(1)

EIGHTH SYMPOSIUM ON

turbulent shear flows

SEPTEMBER 9–11, 1991
TECHNICAL UNIVERSITY OF MUNICH
MUNICH, GERMANY

VOLUME 1

SESSIONS 1–18

EIGHTH SYMPOSIUM ON

turbulent shear flows

Technical University of Munich, September 9-11, 1991

Organizing Committee

F. Durst
Lehrstuhl für Strömungsmechanik
Friedrich-Alexander-Universität
Cauerstraße 4
W-8250 Erlangen, Germany

B. E. Launder
Department of Mechanical Engineering
University of Manchester
Institute of Science and Technology
Manchester M60 1QD - UK

F. W. Schmidt, Secretary
Department of Mechanical Engineering
The Pennsylvania State University
University Park, PA 16802 - USA

J. H. Whitelaw
Department of Mechanical Engineering
Imperial College
London SW7 2BX - UK

Papers Committee

U. Schumann, Chairman
DLR, Institut für Physik der Atmosphäre
W-8031 Oberpfaffenhofen, Germany

R. Friedrich
Lehrstuhl für Strömungsmechanik
Technische Universität München
Arcisstraße 21
W-8000 München 2, Germany

B. E. Launder

J. H. Whitelaw

Local Arrangements Committee

R. Friedrich (Chairman), M. Arnal, A. Dörnbrack, T. Gerz, J. Graf, E. Güntsch, F. Haidinger, R. Hannappel, T. Hauser, U. Schumann, F. Unger, H. Wengle.

PREFACE

This volume and its companion contain the papers presented at the Eighth Symposium on Turbulent Shear Flows held at the Technical University of Munich, September 9-11, 1991. The first of these biennial international symposia took place at the Pennsylvania State University, USA, in 1977; subsequent symposia were held at Imperial College, London, England; the University of California, Davis, USA, the University of Karlsruhe, Germany; Cornell University, Ithaca, USA; the Paul Sabatier University, Toulouse, France; and Stanford University, California, USA. The purpose of this series of symposia is to provide a forum for presentation and discussion of new developments in the field of turbulence, especially as related to shear flows of importance in engineering and geophysics

Nearly 330 extended abstracts proposing papers for this eighth symposium were submitted to the Papers Committee comprising U. Schumann (chairman), R. Friedrich, B E. Launder, and J. H. Whitelaw. Each was evaluated by two members of the Advisory Committee, and by at least one member of the Papers Committee. From the consensus of these evaluations, papers were selected for oral presentation at the Symposium and for inclusion as a full paper of maximum six pages in the proceedings. Because of the large number of excellent contributions, we looked for possibilities to increase the number of papers to be presented. However, because of time and space limitations, not all papers could be orally presented. Therefore, further contributions were invited for presentation as posters during the Symposium. For these contributions, short communications of two pages were included in the proceedings Because of the large number of papers, it was necessary to bind them in two volumes The papers of the poster sessions are included at the end of the second volume. No selection process can ever be perfect, and we very much appreciate the understanding of colleagues whose papers could not be included this time

This Symposium was organized in cooperation with American Meteorological Society, American Society of Mechanical Engineering, and Deutsche Meteorologische Gesellschaft. The Organizing Committee is grateful for this support

In particular, the Organizing Committee wishes to acknowledge the generous financial support of. BMW AG, Deutsche Aerospace AG, Deutsche Lufthansa AG, Deutsche Forschungsanstalt für Luft- und Raumfahrt, Deutsche Meteorologische Gesellschaft European Office of Aerospace Research and Development of the U S Air Force, European Research Office of the U. S. Army, Linde AG, Mercedes Benz AG, and Vieweg-Verlag.

Finally, the Organizing Committee very much appreciates the efforts of the Local Arrangements Committee, which did much to ensure the success of the Symposium

F. Durst, B. E Launder, F. W. Schmidt, J. H. Whitelaw
Organizing Committee

R. Friedrich, U. Schumann
Conference Chairmen

EIGHTH SYMPOSIUM ON TURBULENT SHEAR FLOWS

Technical University of Munich, September 9 - 11, 1991

CONTENTS OF VOLUME 1

SESSIONS 1 - 18

EIGHTH SYMPOSIUM ON TURBULENT SHEAR FLOWS

Technical University of Munich, September 9 - 11, 1991

CONTENTS OF VOLUME 2

SESSIONS 19 - 31 and POSTER SESSIONS

SESSION 25 - COMPLEX FREE FLOWS

SESSION 26 - CLOSURES-I

SESSION 27 - BUOYANT FLOWS AND HEAT TRANSFER - II

SESSION 31 - COMBUSTION - II

POSTER SESSIONS

POSTER SESSION I

* **Note:** *This paper was unavailable at press time. Unbound copies of the full paper may be obtained from the author(s) during the symposium.*

LIST OF AUTHORS

EIGHTH SYMPOSIUM ON
TURBULENT SHEAR FLOWS
Technical University of Munich
September 9-11, 1991

COMPRESSIBILITY EFFECTS ON THE GROWTH AND STRUCTURE OF HOMOGENEOUS TURBULENT SHEAR FLOW

G A Blaisdell[1], W C Reynolds[2,3], N N Mansour[3]

[1] School of Aeronautics and Astronautics, Purdue University
West Lafayette, IN 47907, USA

[2] Department of Mechanical Engineering, Stanford University
Stanford, CA 94305, USA

[3] NASA Ames Research Center
Moffett Field, CA 94035, USA

ABSTRACT

Direct numerical simulations of compressible homogeneous turbulent shear flow are used to provide insight into compressibility effects on turbulence. The simulations show a reduction in the growth rate of the turbulence compared to the incompressible case. Examination of the turbulent kinetic energy budget shows that the reduced growth rate is due to an increase in the dissipation rate due to the divergence of the velocity and to the pressure-dilatation correlation which acts to transfer energy between internal energy and kinetic energy. The structure of the turbulence is also examined. Visualizations of the flow fields reveal the presence of eddy shocklets. These shock structures are important contributors to the increased dissipation of compressible turbulence. A mechanism for the generation of the shocks is suggested.

INTRODUCTION

The renewed interest in hypersonic flight has fostered a need to increase our understanding of turbulence in high Mach number flows. The objective of this work is to aid the development of turbulence models for compressible flows by using direct numerical simulations (DNS) of compressible homogeneous turbulence. The present study focuses on homogeneous shear flow. The growth rate of the turbulence is examined by analyzing the budget for the turbulent kinetic energy (TKE). In addition, physical insight into compressible turbulence is gained by examining flow visualizations. The probability density function (PDF) of the divergence of velocity is considered in order to better understand compressibility effects on the dissipation rate of turbulent kinetic energy.

Our understanding of compressible turbulence is very limited in comparison to what is known of incompressible turbulence. Experiments involving compressible turbulence suffer from a lack of adequate facilities and instrumentation; theoretical studies are made more difficult because the velocity field is no longer divergence free, and because more flow variables are involved, and, finally, numerical simulations have only recently been used to investigate compressible turbulence. Overall, the physics of turbulence in compressible flows is more complicated than that in incompressible flows.

The first published results of numerical simulations of compressible turbulence were those of Feiereisen *et al* (1981ab). They studied homogeneous shear flow at *rms* Mach numbers up to 0.32 using direct numerical simulations with 64^3 grid points. Their simulations did not extend far enough in time to examine effects of compressibility on the growth of the turbulence, however, they were able to see some effects of compressibility on the structure of the Reynolds stresses and the pressure strain terms in the Reynolds stress budgets. Homogeneous shear flow was also considered by Delorme (1985) using large eddy simulation (LES). Erlebacher *et al* (1987) studied decaying isotropic turbulence and investigated sub-grid scale models for LES, but they did not see significant compressibility effects.

Major progress in the simulation of compressible turbulence was achieved by Passot & Pouquet (1987). They performed 2-d DNS of decaying isotropic turbulence for *rms* Mach numbers up to 1.65 using a 256^2 grid and were able to show strong compressibility effects, including the formation of eddy shocklets. Following this work there have been numerous investigations of compressible isotropic turbulence using DNS (Passot *et al* 1988, Sarkar *et al* 1989, Erlebacher *et al* 1990, Erlebacher 1990, Staroselsky *et al* 1990, Dahlburg *et al* 1990, Lee *et al* 1991). These simulations have been used to show the effect of initial conditions, investigate the effect of compressibility on the velocity spectrum, and study the formation of eddy shocklets.

The above simulations are of isotropic turbulence. Homogeneous shear flow has been reconsidered only recently (Blaisdell *et al* 1991 and Sarkar *et al* 1991). There are several reasons for studying homogeneous shear flow. Compressibility effects turn out to be less dependent on initial conditions than for isotropic turbulence. The *rms* Mach number in homogeneous shear flow increases in time, so compressibility effects become stronger as the flow develops, whereas in decaying isotropic turbulence the *rms* Mach number decreases. Also, homogeneous shear flow is a natural extension in complexity over isotropic turbulence.

The simulations described below are from Blaisdell *et al* (1991) and were selected to show specifically the effect of compressibility on the growth rate of the turbulent kinetic energy and to examine the flow structure.

DESCRIPTION OF THE SIMULATIONS

In the current work, the time dependent compressible Navier-Stokes equations are solved using a pseudo-spectral Fourier method with a third order Runge-Kutta time advancement scheme. A mean uniform shear is imposed in the x_2 direction, and a coordinate transformation developed by Rogallo (1981) allows the use of periodic boundary conditions. Details of the numerical method are given in Blaisdell *et al* (1991).

Results from two compressible simulations are presented. The first, designated sha192, uses 192^3 grid points and extends to a nondimensional time $St = 24$, where $S = \partial\tilde{u}_1/\partial x_2$ is the shear rate, u_i is the velocity in the x_i direction and tilde denotes a Favre average. This simulation is used to compare the growth rate of the turbulence to that from the incompressible simulation results of Rogers *et al* (1986). The second compressible simulation is called scb192. This simulation is a refinement of a 96^3 simulation (scb96). It has a smaller computational domain relative to the integral length scale of the turbulence than sha192 and, therefore has finer resolution. The principal use of this simulation is for examining the physical structure of compressible turbulence.

The initial fields are isotropic and generated from random Fourier coefficients with a specified power spectrum. The length scale used to nondimensionalize the problem is chosen such that the nondimensional physical domain for both simulations is of size $4\pi \times 2\pi \times 2\pi$. The simulations use an initial box-like spectrum with fluctuations lying in a given wavenumber band. For sha192 the wavenumber band is $16 \leq k \leq 32$, while for scb96 it is $8 \leq k \leq 16$. Initially the density and temperature fields are uniform. For compressible flow, the velocity can be split into a solenoidal part, which is divergence free, and a dilatational part, which has zero curl. The initial fields of both simulations have no dilatational velocity. However, the simulations quickly develop fluctuations in the density, temperature and dilatational velocity. The initial *rms* Mach number for sha192 is 0.4 and that for scb96 is 0.3.

Homogeneous shear flow also depends on the initial shear rate and Reynolds number. A physically meaningful shear rate is given by $S^* = \bar{\rho} S q^2/\varepsilon$, which has an initial value of 5.0. A Reynolds number relevant to the turbulence is given as $Re_T = \bar{\rho}^2 q^4/\varepsilon\tilde{\mu}$, which has an initial value of 200. q is the turbulent velocity scale, where $q^2 = \overline{\rho u_i'' u_i''}/\bar{\rho}$, and ε is the dissipation rate of turbulent kinetic energy per unit volume. An overbar is used to denote a volume average. Simulation scb192 begins with a refinement of the field from scb96 at $St = 10$ and extends to $St = 12$. Its intended use was to test the accuracy of statistics calculated from the simulations, however, it also provides the best resolved fields of any of the simulations reported in Blaisdell *et al.* (1991) and provides the best flow visualizations.

GROWTH RATES IN COMPRESSIBLE HOMOGENEOUS SHEAR FLOW

Experiments and simulations of incompressible homogeneous shear flow show that the turbulent kinetic energy, $k = \overline{\rho u_i'' u_i''}/2$, grows exponentially in time. Fig. 1 compares the growth of the turbulent kinetic energy from simulation sha192 to that from the incompressible simulations C128V and C128W performed by Rogers *et al.* (1986). While the growth rate of the two incompressible simulations are comparable, the growth rate of the compressible simulation is clearly reduced compared to the incompressible simulations. The development of the turbulent Reynolds number and the nondimensional shear rate for the three simulations is shown in Fig. 2. The values of Re_T and S^* of the compressible simulation are comparable to those of the two incompressible simulations. Therefore, the reduction in the growth rate of the turbulent kinetic energy shown in Fig. 1 is due to the compressibility of the flow rather than other effects.

The turbulent kinetic energy equation is examined in order to determine which terms are responsible for the reduced growth rate. When the turbulent kinetic energy equation is scaled by the shear rate and k, the resulting equation is

$$\frac{1}{\overline{\rho u_j'' u_j''}} \frac{d}{d(St)} \overline{\rho u_i'' u_i''} =$$

$$\frac{2}{\overline{\rho u_j'' u_j''} S} \left\{ \underbrace{-\overline{\rho u_1'' u_2''} S}_{\text{Production}} \underbrace{- \frac{\tilde{\mu}}{Re} \overline{\left[\frac{\partial u_i''}{\partial x_k} \left(\frac{\partial u_i''}{\partial x_k} - \frac{\partial u_k''}{\partial x_i} \right) \right]}}_{\varepsilon_s} \right.$$

$$\underbrace{- \frac{4}{3} \frac{\tilde{\mu}}{Re} \overline{\left(\frac{\partial u_k''}{\partial x_k} \frac{\partial u_i''}{\partial x_i} \right)}}_{\varepsilon_d} \underbrace{+ \overline{p \frac{\partial u_i''}{\partial x_i}}}_{\text{p-dilatation}}$$

$$\underbrace{- \frac{1}{Re} \overline{\mu'' \left(\frac{\partial u_i''}{\partial x_k} \left(\frac{\partial u_i''}{\partial x_k} + \frac{\partial u_k''}{\partial x_i} \right) - \frac{2}{3} \frac{\partial u_k''}{\partial x_k} \frac{\partial u_i''}{\partial x_i} \right)}}_{\text{negligible}}$$

$$\left. \underbrace{- \frac{S}{Re} \overline{\left(\frac{\partial u_1''}{\partial x_2} + \frac{\partial u_2''}{\partial x_1} \right) \mu''}}_{\text{negligible}} \right\} \qquad (1)$$

The reason for using this scaling is that a constant right hand side (RHS) in Eq. (1) indicates exponential growth. The first

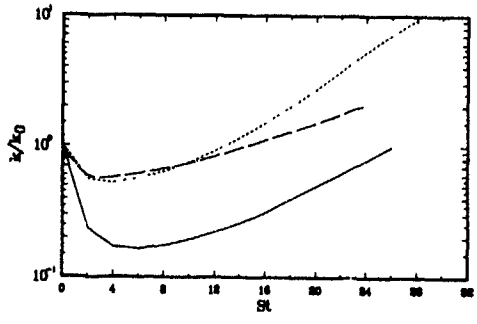

Fig. 1 Evolution of the turbulent kinetic energy in the compressible simulation sha192, — — , and the two incompressible simulations C128V, ——— , and C128W, ----

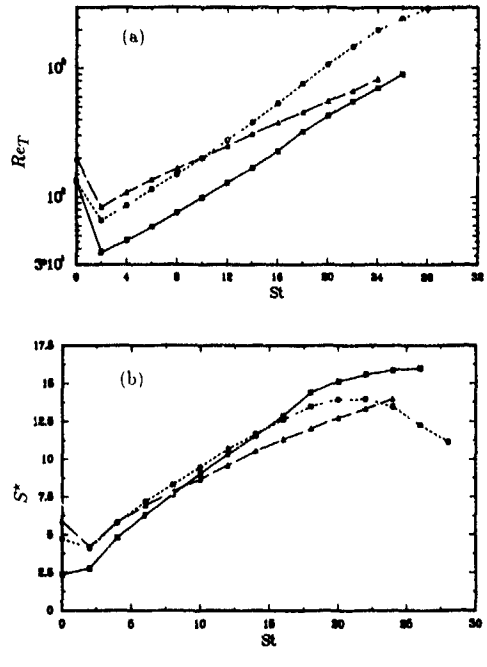

Fig. 2. Comparison of (a) the turbulent Reynolds number and (b) the nondimensional shear rate for sha192 and the incompressible simulations of Rogers *et al.* (1986). C128V, □ , C128W, ○ , sha192, △

term on the RHS is the production term. The second is the solenoidal dissipation rate, ε_s, which is the same as the dissipation rate in incompressible turbulence. For homogeneous turbulence, the solenoidal dissipation rate is proportional to the enstrophy and can be written as $\varepsilon_s = (\bar{\mu}/Re)\overline{\omega_i'\omega_i'}$, where ω_i is the vorticity. The third term, ε_d, is the dilatational dissipation rate. It is proportional to the mean squared fluctuating dilatation (divergence of velocity) and only occurs in compressible flows. The fourth term is the pressure-dilatation correlation and is also only present for compressible turbulence. This term is responsible for the exchange of kinetic and internal energy through the reversible work mode. The last two terms on the RHS are correlations involving fluctuations of viscosity (which is temperature dependent). The simulations show that these two terms are negligible. For incompressible flow, only the first two terms on the RHS are present.

The scaled TKE equation for sha192 is compared to that for the incompressible simulations in Fig. 3. The RHS of the scaled TKE equation for each of the three simulations does reach an approximately constant value, implying exponential growth. The growth rate for C128V is less than that for C128W mainly because of a smaller production term. The RHS for the compressible simulation is reduced compared to both of the incompressible simulations. We are now in a position to determine which of the terms in the scaled TKE equation are responsible for the reduced growth rate of the compressible simulation.

The production term for sha192 is close to that for C128V, which is less than that for C128W. The reason for the difference in the results for the two incompressible simulations is the low Reynolds number of simulation C128V. Because of the difference in the incompressible simulation results, one cannot deduce if the production term for sha192 is reduced because of compressibility effects or because of low Reynolds number effects. In order to make any statements about compressibility effects on the production term, compressible simulations at higher Reynolds numbers are needed.

The solenoidal dissipation term has similar values to the dissipation term from the incompressible simulations. This result confirms the modeling assumptions of Sarkar *et al* (1989) and Zeman (1990a) that the solenoidal dissipation rate could be modeled in the same way as the dissipation rate in incompressible flows. The main reason the RHS is reduced for the compressible simulation is the presence of the additional terms in the TKE equation. The dilatational dissipation rate is about 10% of the solenoidal dissipation rate and is an even more significant fraction of the RHS. The second compressible term in the TKE balance is the pressure-dilatation term. It oscillates considerably but is roughly of the same magnitude as the dilatation dissipation rate and also acts to reduce the RHS. The two terms involving correlations of fluctuating viscosity are essentially zero and can be neglected. Thus, we see that it is both the solenoidal dissipation rate and the pressure dilatation correlation which act to reduce the growth rate of the turbulence in compressible homogeneous shear flow.

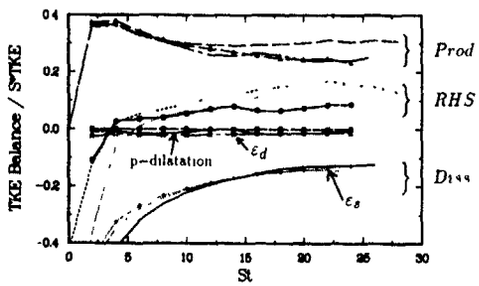

Fig. 3. Comparison of the scaled turbulent kinetic energy budget for sha192 and the incompressible simulations C128V and C128W. Simulation sha192 (symbols) extends to St = 24, C128V to St = 26, and C128W to St = 28. *Prod*, production term, *RHS*, right hand side, *Diss*, dissipation term.

Models for the dilatation dissipation rate have been proposed by Sarkar *et al* (1989) and Zeman (1990ab). The simulations of Blaisdell *et al* (1991) and Sarkar *et al* (1991) show that the model of Sarkar performs very well at low to moderate *rms* Mach numbers, while the model of Zeman does not scale correctly with *rms* Mach number. A model for the pressure-dilatation correlation has been suggested by Zeman (1990b). The simulations of Blaisdell *et al* show that the basic assumptions and scaling of this model are correct at low to moderate *rms* Mach numbers. At higher *rms* Mach numbers, however, the simulation results show some departure from all of these models.

It is clear from the above results that the dilatation dissipation rate is important to the development of compressible turbulence. Insight into the reason for the increased dissipation rate in compressible turbulence is found by examining the structure of the turbulence.

STRUCTURE OF COMPRESSIBLE TURBULENT SHEAR FLOW

Flow visualization of the turbulence structure is a very useful tool for increasing our physical understanding of turbulence. To reveal compressible structures, we examine the divergence of the velocity and the pressure. The flow fields shown are from simulations scb192 at St = 12 and sha192 at St = 24.

Fig. 4 shows contours of pressure in an x_1-x_2 plane from scb192. x_1 is the streamwise direction and x_2 is the direc-

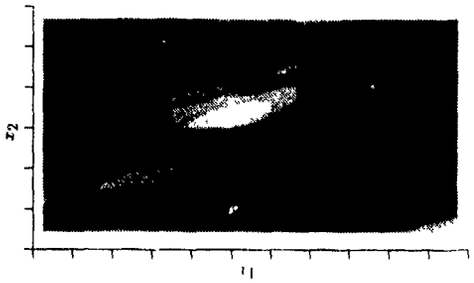

Fig. 4. x_1-x_2 plane of pressure contours in scb192 at St = 12. Dark shading is high pressure and light shading is low pressure.

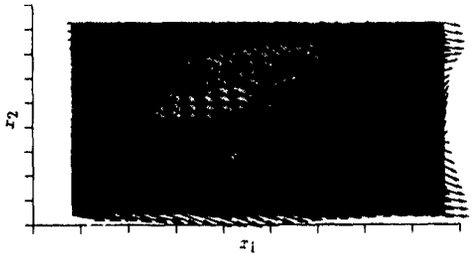

Fig. 5. Close up view of center portion of Fig. 4 showing perturbation velocity vectors.

tion of the mean shear. Only a portion of the plane is shown, and the coordinates on the figure are chosen such that the point with the minimum value of the dilatation in the entire flow field lies in the middle of the figure. This point occurs in a region with a steep pressure gradient. A close-up view of this region showing perturbation velocity vectors is presented in Fig. 5. There is a downward streaming motion through a low pressure region which suddenly changes direction at the location of the steep pressure gradient. The resulting structure appears to be an oblique shock embedded in the turbulence. Eddy shocklets are important for compressible flow because they have a large dilatation dissipation, which is partially responsible for the reduced growth rate of compressible turbulence. The contribution of strong compressions to the dilatation dissipation is considered in more detail in the next section.

Fig. 6 shows the spanwise x_2-x_3 plane that passes through the point of minimum dilatation. The region of high pressure with the steep pressure gradient reveals the location of the shock. From Figs. 4 and 5 we see that the shock is elongated in the streamwise direction, while Fig. 6 shows that it is rather narrow in the spanwise direction. Thus, the shock is shaped more like a ribbon than the broad sheet that might be expected.

In order to determine how the shocklets arise we consider their relationship to the vortical part of the flow field. The pressure contours presented in Fig. 4 show that the shock is inclined at an angle of about 20 degrees to the direction of the mean velocity. The observed behavior is suggestive of typical streamwise vortical structures in shear flows. However, it should be pointed out that the vortical structures in the current simulations resemble the corrugated vortex

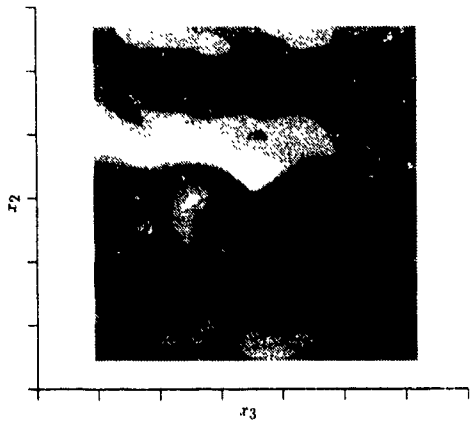

Fig. 6 x_2-x_3 plane of pressure contours in scb192 at $St = 12$. Dark shading is high pressure and light shading is low pressure.

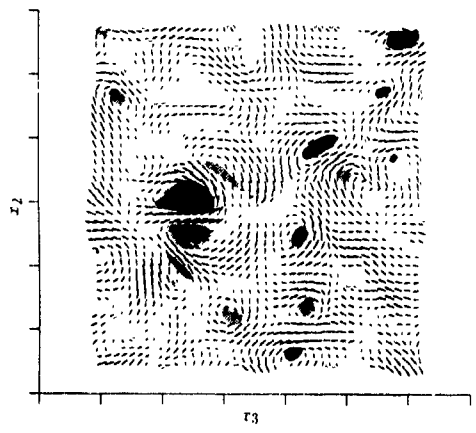

Fig. 7 x_2-x_3 plane of streamwise vorticity with velocity vectors overlaid in scb192 at $St = 12$. Light shading is positive ω_1 and darker shading is negative ω_1. (Velocity vectors are shown at every other grid point.)

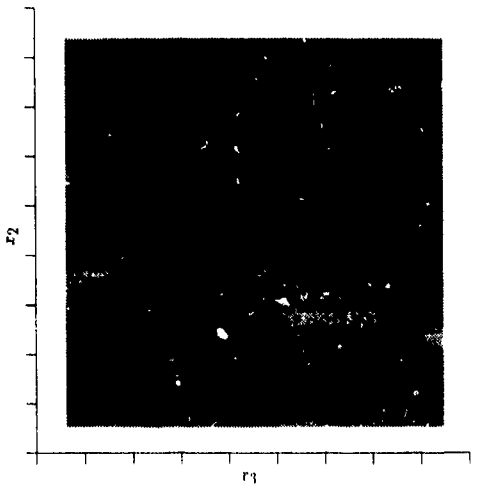

Fig. 8 x_2-x_3 plane of pressure in sha192 at $St = 24$. Dark shading is high pressure and light shading is low pressure.

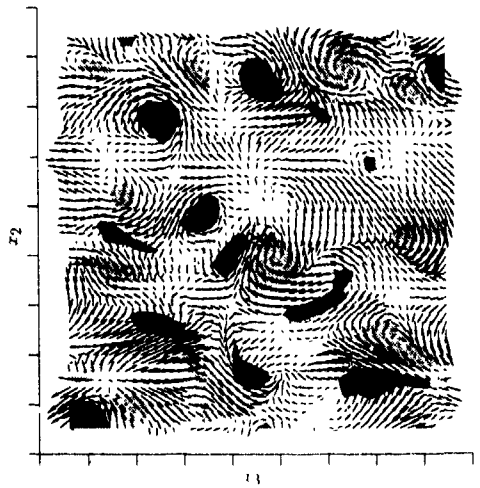

Fig. 9 x_2-x_3 plane of streamwise vorticity with velocity vectors overlaid in sha192 at $St = 24$. Light shading is positive ω_1 and darker shading is negative ω_1.

sheets seen in rapidly sheared turbulence rather than the hairpin vortices typical of higher Reynolds number shear flows

Fig 7 shows contours of the streamwise vorticity in the spanwise plane, with velocity vectors overlaid. There is a contour of negative streamwise vorticity and a contour of positive streamwise vorticity which lie on opposite sides of the shock location and which are associated with a downwash just above the shock The downwash is in the direction of the shear

From this view, a mechanism for the generation of the shocks seems clear The vorticity creates a motion in the direction of the shear, either a downwash or an upwash, which causes high-speed and low-speed fluid to come into contact This causes a compression which results in a shock

Evidence for this mechanism is more clearly seen in Figs 8 and 9 which show contours of pressure and ω_1, respectively, in a spanwise plane from simulation sha192 at $St = 24$ Here an upwash occurs between a pair of contours of streamwise vorticity The shock lies just above this upwash, where the velocity vectors suddenly change magnitude and direction

The spatial resolution of simulation sha192 is not as good as that of scb192. The shock shown in Figs 8 and 9 is the strongest in the entire flow field and represents the greatest resolution problem In spite of the lack of resolution, it is believed that the insights gained from this simulation are still useful

The mechanism discussed above is not the only plausible way shocklets may be generated In order to be certain of the mechanism, the temporal evolution of the eddy shocklet would have to be examined This would be somewhat difficult since the grid moves in time, but such an investigation should provide valuable information

PROBABILITY DENSITY FUNCTIONS

We have seen that eddy shocklets form in compressible homogeneous shear flow These structures are regions of large negative dilatation and, therefore, have large values of the local dilatation dissipation rate However, as pointed out by Sarkar *et al* (1991), these structures are also highly intermittent, and the question therefore arises as to whether eddy shocklets contribute significantly to the dilatation dissipation rate. An indication of how much of the flow field contains strong compression regions is given by examining the probability density function (PDF) of the dilatation and the probability distribution function, or integrated PDF. These are shown in Fig 10 for simulation sha192 at $St = 10$ From the integrated PDF, one can find out how much of the flow has a dilatation more negative than a certain number (negative dilatation indicating compression) However, picking a specific value of the dilatation which represents a "strong compression" is at best arbitrary

A better question to address is this what fraction of the dilatation dissipation rate is due to the most negative dilatations making up a given fraction of the flow field? Since the dilatation dissipation rate is proportional to the mean squared fluctuating dilatation, the answer to this question can be found by examining the weighted PDF

$$\mathcal{P}^{w}_{d''}(d'') = \frac{d''^2 \mathcal{P}(d'')}{\int_{-\infty}^{\infty} d''^2 \mathcal{P}(d'')\, dd''} \tag{2}$$

and probability distribution function

$$f^{w}_{d''}(d'') = \frac{\int_{-\infty}^{d''} d''^2 \mathcal{P}(d'')\, dd''}{\int_{-\infty}^{\infty} d''^2 \mathcal{P}(d'')\, dd''} \tag{3}$$

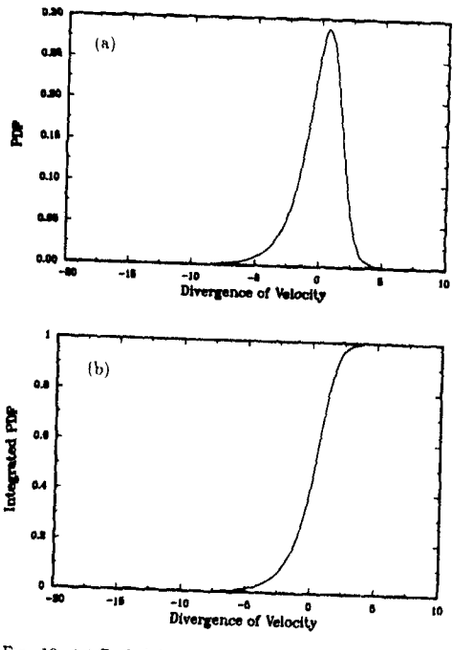

Fig 10 (a) Probability density function of the dilatation, (b) probability distribution function of the dilatation, for sha192 at $St = 10$

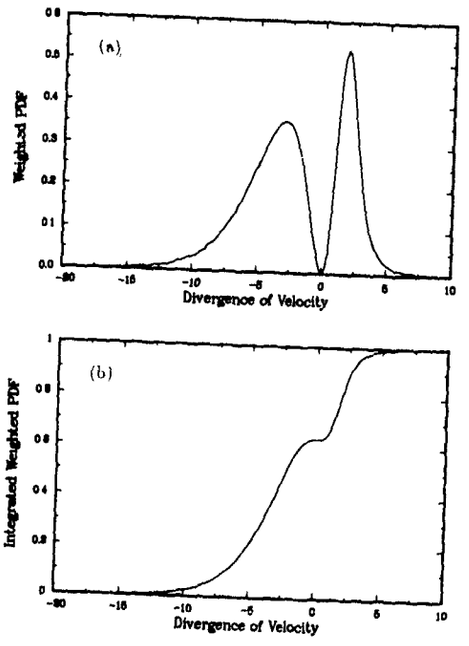

Fig 11 (a) Weighted probability density function of the dilatation, (b) weighted probability distribution function of the dilatation, for sha192 at $St = 10$

The dilatation is denoted by d'' These functions are plotted in Fig 11 for simulation sha192 at $St = 10$ Examining the weighted PDF, $\mathcal{P}^w_{d''}$, we see that most of the dilatation dissipation is due to negative dilatations, or compressions, but that a significant amount of the dissipation also comes from low level positive dilatation This is also seen for the high resolution simulation scb192 and, therefore, is not caused by poor resolution. The most extreme values of the dilatation occur infrequently and, therefore, have a negligible contribution to the dilatation dissipation, while the moderate values of dilatation contribute significantly

We can now answer the question of how much of the dilatation dissipation rate is due to the most negative dilatations making up a given fraction of the flow field From the integrated PDF of the dilatation for sha192 at $St = 10$, we find that 1% of the flow has a dilatation more negative than $-5\,5$ and that 10% of the flow has a dilatation less than $-2\,0$ The probability distribution function, $f^w_{d''}$, shows that

17% of the dilatation dissipation rate is due to the most compressive dilatations making up 1% of the flow field and that 58% of the dilatation dissipation rate is due to the most compressive dilatations making up 10% of the flow The corresponding percentages of the dilatation dissipation rate are 23% and 58% for sha192 at $St = 24$ Therefore, we see that moderately strong negative dilatations, which occupy only a small portion of the flow field, contribute significantly to the dilatation dissipation rate, although they are not entirely responsible for the dilatation dissipation

CONCLUSIONS

We have used direct numerical simulation to study compressible homogeneous turbulent shear flow. We find that the growth rate of the turbulent kinetic energy is reduced compared to the incompressible case. Examination of the turbulent kinetic energy budget reveals that the reduced growth rate is due to the dilatational dissipation rate and the pressure-dilatation correlation Visualizations of the flow fields show the existence of eddy shocklets These structures are important because of their contribution to the increased dissipation rate of compressible turbulence A mechanism for the generation of eddy shocklets in shear flow has been suggested in which vortical motions transport fluid in the direction of the shear The resulting collision of high-speed and low-speed fluid causes a compression and the formation of a shock wave

ACKNOWLEDGEMENTS

We gratefully acknowledge the support for this work by the Air Force Office of Scientific Research under contract F49620-86-K-0022 Computational facilities were made available by the NASA Ames Research Center We also wish to thank Dr. Michael Rogers for providing data from his simulations

REFERENCES

BLAISDELL, G A , N N MANSOUR, & W. C REYNOLDS 1991 Numerical Simulation of Compressible Homogeneous Turbulence. *Report No TF-50.* Department of Mechanical Engineering, Stanford University, Stanford, California.

DAHLBURG, J P R B. DAHLBURG, J H GARDNER, & J M PICONE 1990 Inverse cascade in two-dimensional compressible turbulence I. Incompressible forcing at low Mach number. Phys Fluids A, **2**, 1481-1486

DELORME, P 1985 Simulation numerique de turbulence homogène compressible avec ou sans cisaillement imposé Ph D Thesis, University of Poitiers Available in english as: Numerical Simulation of Compressible Homogeneous Turbulence, *European Space Agency Technical Translation ESA-TT-1030*, 1988, and *NASA Report N89 15965*

ERLEBACHER, G., M Y. HUSSAINI, C G SPEZIALE, & T A. ZANG 1987 Toward the Large-eddy Simulations of Compressible Turbulent Flows. *ICASE Report* No 87-20

ERLEBACHER G. 1990 Direct Simulation of Compressible Turbulence *IMACS First International Conference on Computational Physics*, University of Colorado, Boulder, Colorado, June 11-15, 1990

ERLEBACHER, G , M Y HUSSAINI, H O. KREISS, & S SARKAR 1990 The Analysis and Simulation of Compressible Turbulence. *ICASE Report* No 90-15.

FEIEREISEN, W. J., W. C REYNOLDS, & J H. FERZIGER 1981a Numerical Simulation of a Compressible, Homogeneous, Turbulent Shear Flow *Report No TF-13* Department of Mechanical Engineering, Stanford University, Stanford, California

FEIEREISEN, W J , E SHIRANI, J H FERZIGER, & W C REYNOLDS 1981b Direct Simulations of Homogeneous Turbulent Shear Flows on the Illiac IV Computer: Applications to Compressible and Incompressible Modelling *Turbulent Shear Flows 3*, Springer-Verlag, pp 309-319

LEE, S , S K. LELE, & P MOIN 1991 Eddy-shocklets in decaying compressible turbulence, *Phys Fluids A*, **3**, 657-664

PASSOT, T & A POUQUET 1987 Numerical simulation of compressible homogeneous flows in the turbulent regime *J Fluid Mech* **181**, 441-466

PASSOT, T , A POUQUET, & P WOODWARD 1988 The plausibility of Kolmogorov-type spectra in molecular clouds *Astron Astrophys* **197**, 228-234.

ROGALLO, R S 1981 Numerical Experiments in Homogeneous Turbulence *NASA Technical Memorandum* 81315

ROGERS, M M , P MOIN, & W C REYNOLDS 1986 The Structure and Modeling of the Hydrodynamic and Passive Scalar Fields in Homogeneous Turbulent Shear Flow. *Report No TF-25.* Department of Mechanical Engineering, Stanford University, Stanford, California.

SARKAR, S , G ERLEBACHER, M Y HUSSAINI, & H O KREISS 1989 The Analysis and Modeling of Dilatational Terms in Compressible Turbulence *ICASE Report* No. 89-79

SARKAR, S., G ERLEBACHER, & M Y HUSSAINI 1991 Direct Simulation of Compressible Turbulence in a Shear Flow. *ICASE Report* No 91-29

STAROSELSKY, I., V. YAKHOT, S KIDA, & S A ORSZAG 1990 Long-Time, Large-Scale Properties of a Randomly Stirred Compressible Fluid, *Phys Rev Let* , **65**, 171-174

ZEMAN, O 1990a Dilatation dissipation The concept and application in modeling compressible mixing layers *Phys Fluids A* **2**, 178-188.

ZEMAN, O. 1990b On the decay of compressible isotropic turbulence. *CTR Manuscript* No 115, Center for Turbulence Research, Stanford/NASA Ames

EIGHTH SYMPOSIUM ON
TURBULENT SHEAR FLOWS
Technical University of Munich
September 9-11, 1991

EXPERIMENTS ON FREE TURBULENCE/SHOCK WAVE INTERACTION

by

Jacquin L., Blin E. & Geffroy P.

Office National d'Etudes et de Recherches Aérospatiales
Châtillon-sous-Bagneux FRANCE

Abstract

LDV measurements in two different turbulent free flows impacted by a normal shock wave are presented. The first case is a quasi-homogeneous grid generated flow and the second, a coaxial jet. These two different experiments put into light various aspects of the physics involved in the turbulence/shock interaction.

1. Introduction

Supersonic turbulent flows accelerated by expansion waves or decelerated by compression or shock waves involve different types of compressible effects. The first effect is related to a rapid adaptation of turbulence to the variation in the mean density of the flow. For instance, in the absence of density fluctuations, an axial compression (or expansion) amplifies (or lowers) turbulence in a similar way as an axisymmetric incompressible dilatation or contraction [1].

The other effects are related to the compressible nature of the fluctuating field itself. Small fluctuations of the thermodynamic variables, whose effect could be neglected in equilibrium flows (e.g. in flat plate supersonic boundary layers at moderate Mach number), may constitute non-negligible sources of turbulence when they are coupled with large mean field gradients. Secondly, considering the case of an interaction with a shock wave, the perturbation of the shock by incoming turbulence results in the generation of additionnal temperature and acoustic fluctuations which can interchange energy with the fluctuating velocity field. The great majority of published experimental results in this field concerns the shock/boundary layer problem which evidently constitutes a crucial configuration in supersonic and transonic aerodynamics (see [2] for a review): performance of airfoils, inlets or blade systems is partly conditionned by such interaction phenomena.

Concerning future supersonic combustion systems, while it is now well admitted that effects induced by compressibility inhibite the turbulent mixing, one could take advantage of the shock capability to enhance turbulent mixing. In particular, the various shocks which characterize the inviscid structure of non-adapted jets contribute for a large part to the mixing properties of these flows. Manipulation of supersonic free flows by impinging shocks constitutes an interesting topic for combustion applications. This subject has motivated one of the experiment described in the present paper. Experiments on free flow/shock interaction are scarce. One can cite those of references [3] and [4] which will be evoked in the core of this paper.

Modelling of the interaction regions escapes the basic low speed turbulent models. The direction to be followed to improve these models has not been clearly identified, mainly because the new physics involved in this process need further clarifications (see e.g. [5]).

The aim of our study is precisely to perform new experiments on the shock/turbulence interaction which could help to scrutinize the physics of this problem. These experiments have been conducted in one of the low supersonic continuous wind tunnel of the Fluid Mechanics Laboratory at ONERA Meudon. The results presented in the paper essentially concern mean and fluctuating velocities obtained with a two components Laser Doppler Anemometric system.

2. Theoretical preliminaries

The generation of thermal and acoustic fluctuations and the amplification of the vorticity fluctuations resulting from the interaction of a turbulent field with a shock wave have been first studied by Ribner [6]. This author has considered the linear response of the flow behind a shock which is perturbed by an impinging single shear wave. Several authors have then reformulated and completed this linear approach (see e.g. [7] for a review).

A second candidate, restricted to mean compression (or expansion) effects, is the linear analysis of an homogeneous compressed (or expanded) solenoidal turbulence, the so-called Rapid Distorsion Theory (RDT) ([1], [8]).

These two theories are of very different nature and the similitudes between them are not straightforward. The first is obviously closer to the physics of the problem than RDT.

In a recent paper, Lee et al. [9], have presented results obtained by using Direct Numerical Simulation (DNS), RDT and the "Linear Interaction Analysis" (LIA) of Ribner. They have applied them to the case of an incompressible turbulence passing through a straight shock. As for the linear theories, they conclude that RDT and LIA lead to the same amplification and anisotropy for moderate shock intensities (upstream Mach number $M_0<2$). The differences observed for larger shock

intensities were attributed to unsteadiness and curvature effects of the shock which are not taken into account by RDT. These conclusions may be misleading as they mask the very different nature of the two theories.

As for the similarities between the two approaches, in both cases the amplification factors are fixed by the ratio of the mean densities behind and in front of the shock (subscript 0):

$$C=\rho/\rho_0 \qquad (1)$$

Another point is that both theories lead to the same transmission laws between the incident and the refracted vorticity wave vectors. The relation reads precisely:

$$k_1=CK_1,\ k_2=K_2,\ k_3=K_3, \qquad (2)$$

K and k denote the wave numbers ahead and behind the shock, and subscript 1 refers to the direction normal to the shock. Thus the spectral distorsion of the vorticity field is equivalent in the two theories. In particular, the compression associated with a shock (C>1) induces a shift of energy towards large wave numbers.

In RDT, $C=\exp(-Dt)$, (3)

where D denotes the mean axial velocity gradient normal to the shock, $D=dU/dx_1$. D must be spatially invariant for the flow to be considered homogeneous. Thus, in RDT, the shock effect is represented by a compression (D<0) acting on a solenoidal homogeneous turbulence during a time scale given by (3). Using for example the general methodology given in [8], the RDT solution can be managed analytically. If considering for example the velocity component u normal to the shock, one obtains

$$\overline{u^2}= C^2 \iiint U_{11}(\underline{K})[1+P(\mu)]^2 d\underline{K} \qquad (4)$$

$$\overline{u_0^2} = \iiint U_{11}(\underline{K})\, d\underline{K}$$

with $\mu=K_1/K$, and where $U_{11}(\underline{K})$ is the first diagonal component of the second order spectral tensor. The form given above introduces a directional factor $P(\mu)$ which reads:

$$P(\mu) = \frac{(1-C^2)\mu^2}{1-(1-C^2)\mu^2} \qquad (5)$$

$P(\mu)$ accounts for the pressure effect which constrains $U_{ij}(\underline{K})$ to remain in a plane normal to $\underline{K}$. The above relations show that the result of the distorsion strongly depends on the initial angular distribution of the energy. The maximum amplification concerns the wave vectors parallel to the shock ($K_1=0$). If one supposes that the initial field is isotropic, (4) can be easily integrated. An amplification factor equal to C^2 is obtained if one neglects pressure effects or if the energy is concentrated in wave vectors parallel to the shock ($\mu=0$).

When a shear wave impacts the shock, it is transmitted and amplified, but entropy and acoustic modes are also generated. RDT does not account for these compressible phenomena, whereas the latter are essential in LIA. In particular, the amplification of the impinging shear wave is partly controlled by the perturbation of the shock surface, which is itself sensitive to the generated acoustic field: as shown by Ribner [6], for particular orientations of the upstream mean flow and of the impinging shear wave, the shock oscillations may be strongly amplified by downstream acoustic perturbations. In LIA, this critical regime contributes for a large part to the shear wave amplification [6]. Such a phenomenum has no equivalent in RDT even if, as we said, RDT solutions are also very sensitive to the angular spectral distribution of the incident turbulent field.

On the whole, the anisotropic aspects of the problem seem to play a fundamental role in the two theories, but for very different physical reasons. The integration of the individual wave contributions coupled with the usual isotropic assumption for the incident field (see e.g. [7], [9]), which greatly simplifies the analysis, may mask the differences between various theoretical approaches.

In the most practical applications (e.g. boundary layers), the incident field is anisotropic and the above mentionned directional aspects may be of fundamental importance for the interpretation.

3. First experiment: grid turbulence interaction

The first experiment aimed at producing a very basic test case: an interaction between a nearly homogeneous turbulence with a single normal shock.

Figure 1 shows a schlieren picture of the flow. The turbulence comes from a grid placed in the entrance section of a 100×120×450 mm straight duct. The grid, whose mesh size is m=7mm, serves as a sonic throat and as a turbulence generator, at the same time. It generates a Mach 1.7 flow with low but measurable turbulence fluctuations.

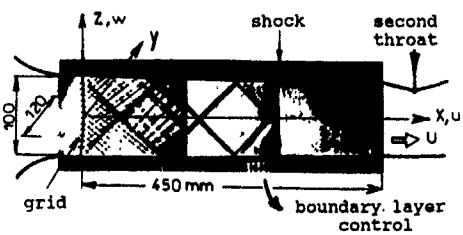

Fig. 1 Schlieren picture of the grid flow

A straight shock wave was controlled by means of a second adjustable throat located downstream. In the absence of nozzle profile, the stabilisation of the shock has been difficult to realize. After having tried different systems, we have been able to ensure a satisfactory control of the shock by means of an aspiration of the bottom wall boundary layer and a slight convergence of the channel.

Figure 1 shows that the flow is perturbed by compression waves issued from the grid. These waves are damped downstream except the intense waves issued from the grid sides. The convergence of the upper wall together with the compression wave effects make the Mach number decreasing from about M=1.7 at the grid level down to M=1.4 just upstream of the shock.

The axial and vertical components of the mean and fluctuating velocities have

been measured by LDV on a fine vertical mesh in the center of the duct (y=0). The probing mesh size is (Δx,Δz)= (10mm,5mm) upstream and downstream of the shock, and (Δx,Δz)=(2mm,5mm) at the level of the shock. Incense smoke particles were used to seed the flow. Each velocity value corresponds to a sample of 2000 instantaneous values. Some corrections have been tested in order to minimize the various usual bias errors. They have been found to be negligible. Another source of errors is related to the response of the particles to the shock induced deceleration (e.g. [10]). But the main weakness of this experiment lies in the low LDV signal-to-noise ratio obtained in such a weakly turbulent flow.

Figure 2(a) shows a map of the mean axial velocity U. The figure at the bottom shows the corresponding velocity contours. The mean velocity is highly perturbed by the compression waves issued from the grid (see Fig. 1). The mark of the diamond-shaped compression waves can be identified. Just behind the shock, an abrupt thickening of the wall boundary layers leads to a slight local re-acceleration of the flow. The velocity then becomes nearly uniform.

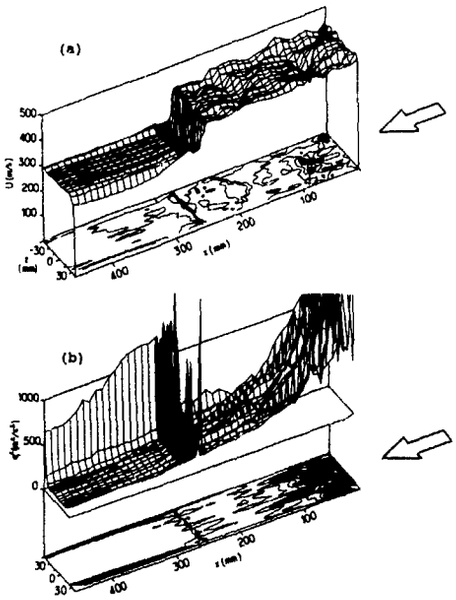

Fig. 2 View maps of mean velocity and of q^2 in the grid flow.

Figure 2(b) shows the corresponding evolution of (twice) the turbulent kinetic energy defined as $q^2=u^2+2w^2$. The energy amplitude is visualized for $-45 \leq z \leq 25$mm so that only the bottom boundary layer is depicted. The oscillations of the shock lead to spurious increases of the fluctuation energy (mainly due to the axial component u^2). The spatial intermittency of the peakiness in the energy at the shock level strongly depends on the location of the mean shock with respect to the probing points. Interactions between the shock and the incoming compression waves should also contribute to this non-uniformities.

We do not observe a substantial increase of q^2, as could be anticipated from the linear theories mentioned above.

Figure 3 shows the evolution of U, $\overline{u^2}$, $\overline{w^2}$ and q^2 and $\overline{u^2}/\overline{w^2}$ calculated by averaging the results in the z direction (the integration is limited to values of z comprised between -30 and +20mm, in order to avoid the influence of the side wall boundary layers). Only the region around the shock is represented here.

The presence of the peaks, preclude a precise evaluation of the levels behind the shock. However we can conclude that there is no significative amplification q^2.

In Fig. 3(c), the anisotropy ratio $\overline{u^2}/\overline{w^2}$, which is equal to about 1.1 before the shock increases up to about 1.25 just behind the shock, then it relaxes to its initial value.

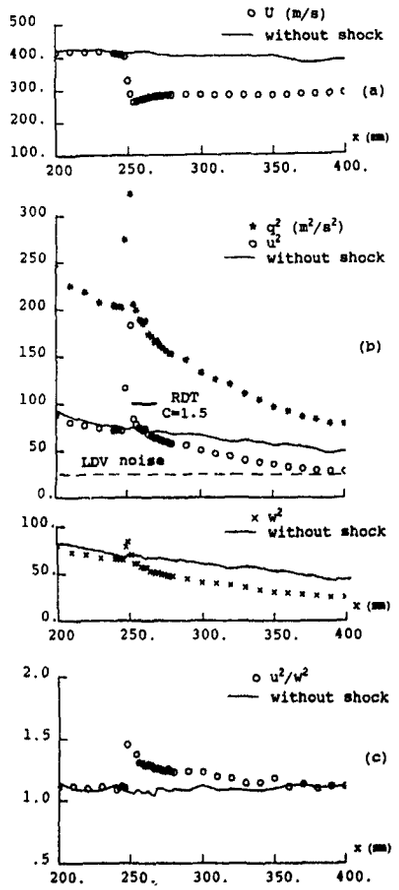

Fig. 3 Z-averaged mean and turbulent quantities

The log-log plot of q^2 versus x/m depicted in Fig. 4(a), shows a significative increase of the decay behind the shock. The exponent o the decay

changes from about -1.2, before the shock (a value similar to that measured to the one in incompressible grid generated turbulences), to about -2.1 behind the shock. The noise of the measuring system contributes to an increase of energy in the last measurement stations.

In a uniform flow, this change of slope could be directly related to a strong increase in the dissipation rate. However, before concluding, one must take into account the changes in mean velocity which make for example the residence time of the turbulence downstream of the shock longer than upstream. This effect is taken into account in Fig. 4(b) where log (q^2) has been plotted versus log(t=$\int$Udx). As expected, the decay is reduced with respect to that in Fig. 4(a), but a change of slope is still apparent. One may conclude to an increase of the kinetic energy decay behind the shock.

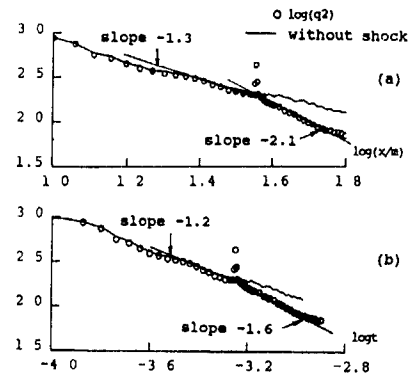

Fig. 4 Turbulent energy decay versus x/m (a) and t (b)

4. Second experiment: jet flow interaction

The second experiment concerns an interaction between a jet and a normal shock. The apparatus and the flow structure are described on the high speed schlieren picture (20 ns exposure) of Fig. 5. A Mach 2 jet is placed coaxially in a supersonic Mach 1.3 half nozzle. The jet exit section, whose diameter is D=17mm, is located in the sonic section of the nozzle in order to avoid the generation of external compression waves. A nearly normal shock is again controlled by the second throat, but the presence of the diverging nozzle is now sufficient to stabilize the shock.

The schlieren picture shows the structure of the over-expanded part of the jet as well as the turbulent structure of the flow. When penetrating into the mixing layer, the shock bends because of the variations in the Mach number. The static pressure in front of the shock is almost uniform (the jet is nearly adapted). The value of the ratio of this pressure and that in the external flow behind the shock precludes a regular reflection of the oblique shock on the axis of the jet. A Mach reflection occurs and a small normal shock takes place in the central part of the jet. Then, successive compressions and expansions develops periodically by

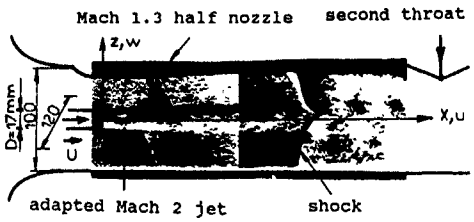

Fig. 5 High speed schlieren picture of the jet flow

multiple reflections on the jet boundaries.

This interaction is obviously far much complex than that of the first experiment. As quoted in the introduction, the structure of such an interaction is of particular interest with regards to supersonic mixing problems. But aside from this interest for engineering applications, our initial motivation in conducting the two different experiments was also to scrutinize various physical aspects of the interaction, particularly the influence of the initial intensity and anisotropic structure of turbulence as well as the response of the fluctuating field to rapid (but not discontinuous) compression or expansion. However, we must admit that this second test case has turned out to be more complex than expected. This configuration needs further investigation before extracting more fundamental information than what we offer here.

Problems inherent to LDV measurements are also present in this flow. The signal-to-noise ratio is large but the main difficulty is now related to the control of the particle population on each side of the jet mixing layer. A discussion of this problem would take much more place than allowed. The results presented below have been obtained by a recombination of the results of separated seeding of the jet and of the external flow. For this combination, an hypothesis is made on the rate of jet fluid concentration across the mixing layer. The arbitrariness of the latter introduces uncertainties in the statistics particularly in the intermittent boundaries of the mixing layer. This problem is still a matter of investigation and definitive results are not yet available. Details are given in [11]. However, our main interest presently concerns the changes in turbulent properties during the interaction. For instance, the relative increase or decrease of turbulent energy in the interaction has turned out to be almost insensitive to the way the data were combined. The results presented below have been obtained using silicium particles (Aérosil R972) whose theoretical size is 0.3 μm.

Figure 6 shows the same quantities as those plotted in Fig. 2. Only half the jet has been probed. One notes that the global expansion rate of the jet mixing layer is small. The potential core is still present at the shock location, that is at x/D=12 . This is primarily a consequence of the acceleration associated with the divergent part of the nozzle. (see Fig. 5). The convective Mach number, which is initially equal to 0.26, is not large enough for compressibility induced effect to be significant.

In Fig. 6, spectacular changes are observed behind the shock. Considering the mean velocity values (Fig. 6(a)), one finds that the jet becomes subsonic behind the shock and then expands on a supersonic regime followed by successive compressions and expansions.

Contrary to the grid flow, the turbulent kinetic energy (Fig. 6(b)) is strongly enhanced by the shock. Then, it decays in the expansion zones and increases again inside the compression zones. The spurious amplification by shock intermittency increases from outside towards the axis of the jet, as the shock strength increases (see [3]).

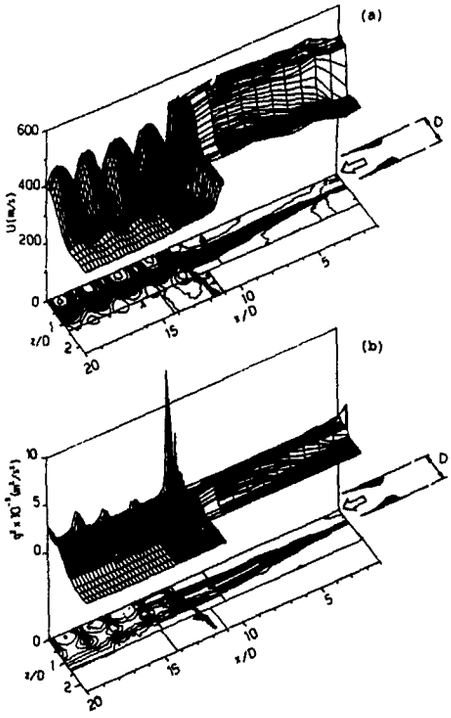

Fig. 6 View maps of mean velocity and of q^2 in the jet flow.

Figure 7, shows the evolution of q^2, $\overline{u^2}$ and $\overline{w^2}$ calculated along the middle mean streamline of the mixing layer (issued from the lip of the ejector and where turbulence is maximum). Note that the shock is oblique at this level: it makes an angle of about 50° with respect to the vertical axis (see Fig. 5). Again, u^2 is much more affected than w^2. One also notes that inside the first cell, just after the peak induced by the shock intermittency, another compression induced amplification occurs.

The results obtained without the shock have been also reported. It is found that turbulence returns periodically to its initial level, without net amplification.

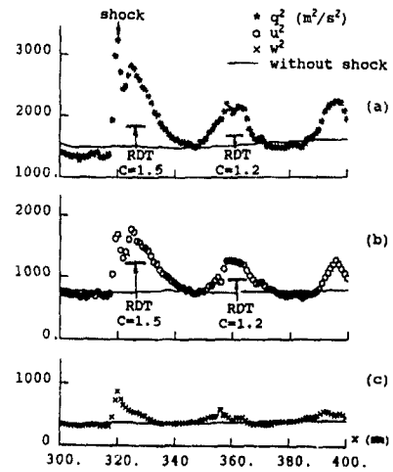

Fig. 7 Normal Reynolds stress components and q^2 in the center mixing layer mean streamline.

5. Discussion

Various aspects of the above results are strinking and will be briefly discussed, particularly into the framework of the linear theories evoked in section 2.

In the grid flow/normal shock interaction, the mean density ratio is equal to the inverse axial mean velocity ratio. One has C=1.5. Even if the Reynolds stress tensor is not sufficient to check the (spectral) anisotropy, we may suppose that the latter, ahead of the shock, is moderate (see Fig. 3(c)). Into the framework of isotropy assumption, relation (4) leads to u^2/u_0^2=1.6 (the total kinetic energy amplification is q^2/q_0^2=1.4, the transverse components being less amplified than u^2). Similar values are obtained from LIA [9]. Such amplifications are not observed in our results. The low signal-to-noise ratio could partly explain this discrepancy. The noise intensity of the LDV system is estimated on Fig. 3(b). Its contribution to q^2 is not amplified by the shock and this leads to a lessening of the overall measured amplification. After substracting the noise contribution, the RDT values indicated in Fig. 3(b) are still too large. It should be noted that the local re-acceleration just behind the shock may also contribute to slightly reduct the energy level (however, from RDT this reduction is not significant).

One must note that, in view of the highly perturbed aspect of the incoming flow, a part of the fluctuations measured upstream the shock may originate from acoustics. RDT does not apply for these acoustic components but LIA does and shows that they are amplified.

As for the downstream behavior, because of the shift of energy towards large k (see(2)), an increase in the dissipation rate ϵ is expected. The solenoidal part of ϵ is given by $\epsilon=\nu\overline{\omega^2}$ where ω denotes the fluctuating vorticity and $\overline{\omega^2}=\overline{\omega_i\omega_i}$, the enstrophy. In RDT, a simple Cauchy solution holds for ω (see

e.g. [1]). For isotropic initial turbulence, one obtains $\overline{w^2}/\overline{w_0^2}=[1+2C^2]/3 \approx 1.8$ (for C=1.5). The turnover time of turbulence, $\tau=q^2/2\epsilon$ is thus divided by 2. This is compatible with the observed increase of the kinetic energy decay in Fig. 4(b). Strong increase in $\overline{w^2}$ has been also reported in the DNS of ref. [9].

The interaction with the jet is much more spectacular and reveals much larger amplifications. Crude theoretical estimations of the magnitude for the amplification can be inferred from an RDT solution of an axial compression or expansion, using the values of C deduced from experiment. Typical results for $\overline{u^2}$ are indicated in Fig. 7(b) for the compression induced by the shock and for the compression which follows the first expansion (for the latter case, one takes for $\overline{u_0^2}$ the lowest value of $\overline{u^2}$ measured at the end of the previous expansion). The values obtained are far below those given by the measurements. The latter are almost analogous to those reported in boundary layer experiments (see [2]). It is strinking to note that a simplification of relations (4) by dropping the pressure effect $(P(\mu)=0)_{\perp}$ which leads to an amplification of $\overline{u^2}$ by a factor C^2, would give results much closer to the experimental data. An equivalent result can be inferred from the theoretical developments proposed in [12] (see also [8]). However, one must note that, in accordance with the developments given in section 2, the strong anisotropy of the mixing layer can largely contribute to the enhancement of the amplification rates. In particular, a concentration of energy in directions normal to the jet axis (in accordance with $\overline{u^2}>\overline{w^2}$) may be expected. This could contribute to an apparent lessening of the damping effect of pressure (RDT) or to an amplification of the contribution of the critical regime described in [6].

A last remark will be done concerning the periodical distorsions developing inside the jet cells. As quoted in the introduction, a complex coupling between the mean field gradient and compressible fluctuations must play an important role in the turbulent kinetic budget. Under its usual form, the latter reads:

$$\bar{\rho} Dk = \Pi_k + D_k - \epsilon + P_k \qquad (6)$$

where Dk denotes the convective derivative of k and where the right hand side is decomposed in production (Π_k), diffusion (D_k), dissipation (ϵ) terms and a compressibility induced pressure term which develops as $P_k=-\bar{u}_k\bar{P}_{,k} + \overline{p'u_{i,i}}$, with $\bar{P}$ and p', the mean and fluctuating pressures.

By linearizing the continuity and the Gibbs equations, one obtains the following leading terms for P_k:

$$P_k = \underbrace{-\tfrac{1}{2}\bar{\rho} Dk_p}_{(1)} + [\underbrace{\tfrac{1}{2}\bar{\rho} k_p \tilde{u}_k}_{(2)} + \underbrace{\overline{u_k p'}}_{(3)}][\frac{\tilde{S}_{,k}}{c_p} + \frac{\gamma-1}{\gamma}\frac{\bar{P}_{,k}}{\bar{P}}] + \underbrace{\frac{-\overline{u_k T'}}{\tilde{T}}\bar{P}_{,k}}_{(4)} \qquad (7)$$

where $k_p=\overline{(p'/\bar{\rho}a)^2}$ is the potential energy, $\tilde{T}$ and T', the mean and fluctuating static temperatures and $\tilde{S}$, the mean entropy. Mass weighted averages are used here. Non-negligible pressure and temperature fluctuations may arise from the shock interaction or in the expansion or compression fans. Considering that mean flow inside the cells is almost isentropic, terms (2) and (4), which are positive terms, may constitute important local sources (or sinks) of kinetic energy in the compressions (or expansions). Concerning term (1), the DNS presented in [13] has shown that large potential energy k_p was rapidly converted into kinetic energy k on the acoustic time scale. Thus term (1) would be positive. So, except perhaps for term (3), the mean gradient induced terms are in phase with the production (Π_k) and may thus contribute to the large variations in the turbulence, as those observed in the experiment.

On the whole, the amplification process seems widely different in the two experiments. The initial anisotropy as well as the extra production terms induced by compressibility could perhaps explain the large increase in turbulence in the jet flow. These mechanisms may be supposed negligible in the grid flow where much less efficient amplification followed by changes in the decay regime have been observed.

References

1. Lee M. J.: Distorsion of homogeneous turbulence by axisymmetric strain and dilatation, Phys. Fluids A, 1, pp 1541-1557, 1989.

2 A survey of measurements and measuring techniques in rapidly distorded compressible turbulent boundary layers. AGARDograph N0 315, 1989.

3 Debiève J.F. & Lacharme J.P.: A shock wave/free turbulence interaction. IUTAM Symposium on Turbulent shear layer/shock wave interactions, Editor J. Delery, Springer Verlag, 1985.

4 Keller J. & Merzkirch W.: Interaction of a normal shock wave with a compressible turbulent flow. Experiment in Fluids, 8, pp. 241-248, 1990.

5 Bushnell D.M.: Turbulence modeling in aerodynamic shear flows-Status and problems. AIAA 91-0214.

6 Ribner H.S.: Convection of a pattern of vorticity through a shock wave. Lewis Flight Propulsion Laboratory. RP 1164,1953.

7 Zang T.A., Hussaini M.Y. & Bushnell D.M.: Numerical Computation of turbulence amplification in shock-wave interactions. AIAA Journal, 23, No1, 1984.

8 Cambon C.: Linear spectral approach to turbulence subjected to mean velocity gradients or body forces. PEPIT Summer Workshop, Lyon, France july 1989.

9 Lee S., Lele S.K. & Moin P.: Direct numerical simulation and analysis of shock turbulence interaction. AIAA paper 91-0523.

10 Boutier A., Lefevre J., Labbe J., Elena M., Lacharme J.P. ONERA RT 27/1883 PN,1985.

11 Geffroy P., Blin E., Jacquin L., D'Humieres, Micheli F. & Papirnick O.: On LDV measurements in a supersonic mixing layer. ONERA report to appear.

12 Debieve J.F.: Etude d'une interaction turbulence onde de choc. Thèse de Doctorat d'Etat. Univ. Aix-Marseille II, 1983.

13 Zeman O.: On the decay of compressible isotropic turbulence, CTR report 115, 1990.

EIGHTH SYMPOSIUM ON
TURBULENT SHEAR FLOWS
Technical University of Munich
September 9-11, 1991

1-3

RAMAN/LIF MEASUREMENTS IN A LIFTED HYDROCARBON JET FLAME

S H Stårner*), R W Bilger*) and R S Barlow**)

*)Department of Mechanical Engineering
The University of Sydney, NSW 2006, Australia

**)Combustion Research Facility
Sandia National Laboratories, Livermore, CA 94550

ABSTRACT

The base of a lifted jet flame of methane has been probed with point Raman/Rayleigh/LIF diagnostics, yielding time– and space–resolved, simultaneous mass fractions of N_2, CH_4, O_2, H_2O, H_2, CO, CO_2 and the OH radical. The results show that the flame is stabilized somewhat outside the mean stoichiometric envelope and outside the turbulent fuel jet. Whilst there are indications of some premixed flame structure at the base, this is not sufficient to support a simple turbulent premixed flame concept of stabilization: the flow is intermittent, and there are composition fluctuations outside the flammability limits at all measured points around the flame base. There is some entrainment of hot fluid into the core of the jet, where it is possible that quenching occurs, but the results do not strengthen the arguments of models proposed for flame stabilization along these lines.

INTRODUCTION

There is considerable diversity of opinion on the processes governing the stabilization of jet flames. Among the models for predicting lift–off height and blowout conditions, perhaps the best known (Vanquickenborne and Van Tiggelen, 1966) rests on the idea that the fuel is premixed at the base of the flame which is stabilized where the mean axial velocity equals the turbulent flame speed. This view is challenged in more recent work by Pitts (1989) showing that at the flame base the flow is highly intermittent. Peters and co–workers (1983), in proposing a stabilization mechanism based on laminar diffusion flame quenching due to high flame stretch, also argue that there is insufficient residence time below the flame base for premixing at the molecular level, so that the premixed flame concept is not justified. However, the experiments by Eickhoff et al. (1985) reveal 40–50 percent burnout just downstream of the stabilization zone, indicating substantial premixedness at the base. They also show that the reaction zone is largely in the quiescent region outside the shear layer. The great sensitivity of lifted flames to co–flow velocity, established by Dahm and Dibble (1989), also indicates that the flame base lies outside the jet boundary. The model by Byggstøyl and Magnussen (1983), like that by Peters and Williams (1983), is based on extinction, but this is argued to occur at the smallest scales, which presumes that the flow is essentially premixed at the flame base. Broadwell et al. (1985) propose a description based on large structure entrainment and extinction, a view contradicted by the results by Savas and Gollahalli (1986) showing that, at least at low lift–off height, flames with a high stoichiometric air/fuel ratio, such as propane, are stabilized outside the turbulent jet boundary, and that combustion does not occur in the cores of the rolled–up vortices. In a recent review of these ideas, Pitts (1989) concludes that present understanding of flame stabilization is poor. Although there exist procedures which predict lift–off height and blowout quite well, models show substantial contradictions and appear to be at variance with observed physical processes associated with stabilization. flamelet quenching ideas do not seem appropriate when stabilization takes place in the tranquil outer zone, and the concept of a premixed flame propagating against the approaching gas flow seems incompatible with the observed intermittency in that region.

The basic problem is that models are ahead of experimentation, not enough is known about the instantaneous mixing – chemistry interactions in the stabilization zone to resolve these model contradictions. Only recently have some such results emerged, such as the 2D images of CH_4, CH and OH by Schefer et al. (1990), the point Raman/LIF data for a lifted H_2 flame in a strong co–flow by Barlow et al. (1989a) and the OH images in H_2–air flames by Seitsman et al. (1990). In the present work we have obtained Raman/OH LIF data for a lifted natural gas jet into still air. This classical geometry, coupled with the simplest hydrocarbon fuel, is thought to be the most suitable for revealing the features at issue, such as the degree of premixing, the departure from equilibrium, and any extinction effects. Results have also been obtained, in the same set of experiments, for fully seated diffusion flames as well as free premixed flames, to allow close comparison with the extremes between which the lifted flame is believed to exist.

This work is undertaken also with a view to clarify how locally extinguished fluid in piloted jet flames with high mixing rates is re–ignited downstream (Masri et al. 1988, Stårner et al. 1990). This is likely to involve some degree of premixing and only limited information is available. However, we do know that when the seated flame is highly intermittent in the upstream region, the re–ignition is noisy, and typically, the fuel is fully burnt in the downstream flame brush.

EXPERIMENTAL

In the present experiments, a natural gas jet (~91% CH_4) issues from a vertical burner tube (of D=7.2 mm diameter and 600 mm length, standing 30 mm proud of a horizontal table), at Reynolds number 28,600, into still air. At this Reynolds number, the flame is stabilized at around 20 nozzle diameters ($x/D \approx 20$, x being the streamwise coordinate). This is the axial location at which a piloted jet flame of the same Reynolds number is mostly extinguished due to high mixing rates (Stårner et al. 1990). A radial traverse is obtained from $r/R = 0$ to 8.3 ($R \equiv D/2$), as well as a set of axial measurements at $r/R = 8.3$, from $x/D = 20$ to 32.

The single–point optical system shown in Fig. 1 is that described in Barlow et al. (1989b). The Raman signals are obtained from 3 μs, 2 J pulses delivered by a flash–lamp pumped dye laser at 532 nm. The LIF OH system operates at 303 nm, driven by a Nd–YAG laser. The coincident probe volumes are 0.5 mm long and 0.7 mm diameter.

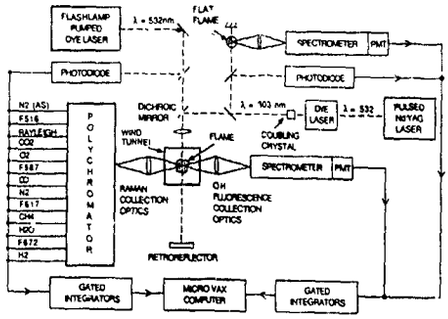

Fig 1 Apparatus for simultaneous point measurements of temperature, major species, and hydroxyl concentration

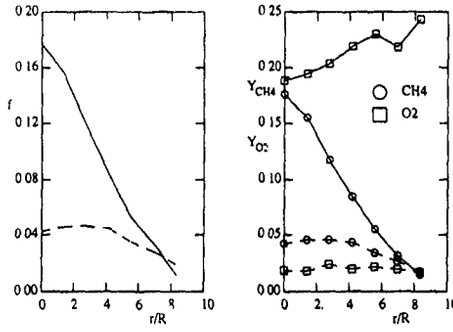

Fig. 2 Radial profiles of mixture fraction and reactants, conditional on T < 450 K at x/D = 20.
—— means; - - - rms.

RESULTS AND DISCUSSION

The appearance of the flame, which is not very far from blowoff, is blue throughout the stabilization region. This high velocity flame is chosen in part to avoid soot interference with the Raman and Rayleigh measurements. There are sometimes fluctuations around the mean axial position of stabilisation at x/D = 20 of up to 10D, rather more than seen in the literature. This is probably due to occasional room draught.

Radial profiles of conventional means and rms of temperature, species mass fractions and the mixture fraction are plotted in Figs. 2–4. Figure 2 shows cold zone data (i.e., samples conditional on the temperature being below the arbitrary threshold 450K), Fig. 3 shows reacting zone averages and Fig. 4 the overall averages. The mixture fraction f, is defined by

$$f \equiv \frac{2Z_C/W_C + Z_H/(2W_H) + (Z_{O,2} - Z_O)/W_O}{2Z_{C,1}/W_C + Z_{H,1}/(2W_H) + (Z_{O,2} - Z_{O,1})/W_O}, \quad (1)$$

where Z_i is the mass fraction of elemental species, i, W_i the atomic mass of species i, and subscripts 1 and 2 denote fuel and oxidant streams, respectively. This formulation preserves the stoichiometric mixture at its mixing value.

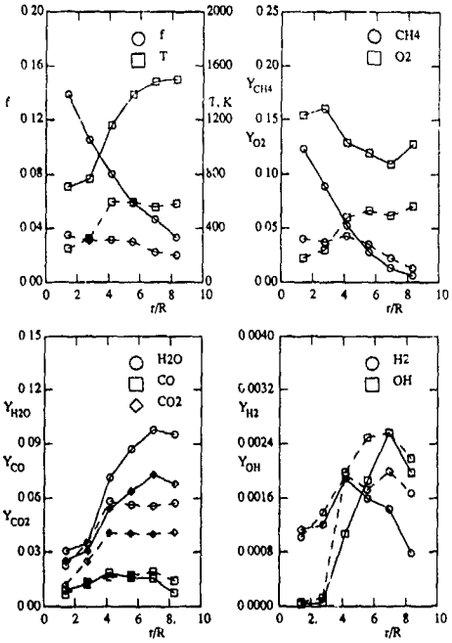

Fig 3 Radial profiles of mixture fraction, temperature and species, conditional on T ≥ 450 K at x/D = 20.
—— means, - - - - rms.

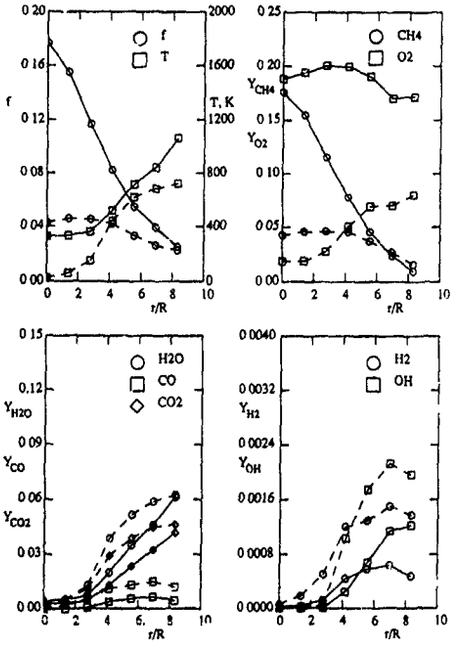

Fig. 4 Radial profiles of mixture fraction, temperature and species, without conditioning, at x/D = 20.
—— means; - - - - rms

The radius R_s at which $\bar{f}$, the mean of f, takes the stoichiometric value, f_s, varies very little with the form of averaging in Figs. 2–4. $R_s/R = 5.5 \pm 0.1$. It is seen in Fig. 3 that the peaks in temperature, products (CO_2 and H_2O) and the radical OH all occur at a larger radius, around 7R. For the overall averages in Fig. 4 these peaks are even further out. It is part of the argument for the propagating premixed flame theory by Vanquickenborne and van Tiggelen (1966) that the radius where the flame is stabilized, R_b, coincides with R_s. Their experiments show, however, that R_b tends to become larger than R_s at high velocity, which is qualitatively consistent with the present high-speed flame. Pitts (1989) has reported intermittency at R_s, and this is also the case here, as seen in Table 1, which lists $\bar{f}$ and the intermittency factor I (as well as unburnt fractions), for x/D = 20 and some further downstream locations. It is hard to reconcile this with the stabilization mechanism of Vanquickenborne and van Tiggelen. Also, at all points near the flame base, the instantaneous mixture fraction deviates outside the flammability limits, 0.03 and 0.08: the fraction of the fluid within the flammmability limits, a_{fl}, in Table 1 is nowhere above 0.6. This is also illustrated in the probability density functions (pdf's) of f, T and the major species, shown in Fig. 5, at five radial locations around the base: the distribution of f is much wider than the flammability limits at all radii. This contrasts with the results by Barlow et al. (1989a) for a lifted H_2 flame, where the wide flammability limits result in almost all of the mixture at the flame base being able to support premixed combustion.

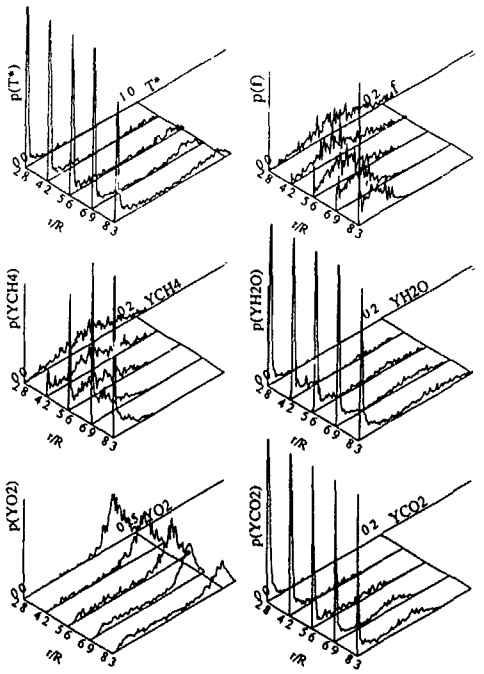

Fig. 5 Probability density functions of mixture fraction, p(f); normalised temperature, p(T^*), $T^* = (T - T_{amb})/(T_{ad} - T_{amb})$, and species, p($Y_i$), at x/D = 20 and various radii, r/R.

Table 1 Mean and rms mixture fraction, $\bar{f}$ and f', cold fraction, a_c ($T<450K$), fraction within flammability limits, a_{fl} ($0.03<f<0.08$), cold fraction within flammability limits, a_{cfl}, and intermittency factor I ($I \equiv 0$ for $f < 0.005$)

x/D	r/R	$\bar{f}$	f'	a_c	a_{fl}	a_{cfl}	I
20	0	0.177	0.043	1.00	0.03	1.00	1.00
20	1.4	0.155	0.046	0.98	0.06	0.97	1.00
20	2.8	0.117	0.045	0.92	0.19	0.91	1.00
20	4.2	0.082	0.042	0.78	0.43	0.72	0.98
20	5.6	0.055	0.033	0.64	0.56	0.56	0.95
20	6.9	0.039	0.026	0.56	0.53	0.42	0.91
20	8.3	0.025	0.022	0.38	0.39	0.15	0.76
22	8.3	0.021	0.023	0.50	0.32	0.22	0.68
24	8.3	0.032	0.028	0.39	0.48	0.19	0.77
26	8.3	0.040	0.029	0.20	0.56	0.08	0.86
28	8.3	0.045	0.030	0.18	0.57	0.09	0.89
32	8.3	0.063	0.032	0.04	0.59	0.02	0.96

It is seen in Fig. 5 that for radii larger than 4R, intermittency spikes appear in the pdf's of f. (These spikes are truncated for clarity in the pdf's of Y_i and T.) At r/R = 2.8 the pdf's of CH_4 and f are almost the same, indicating very little reaction. This is consistent with the low reactedness of H_2O and CO_2 at this radius.

At r/R = 6.9 ($\approx R_b$), all quantities show some bimodality, partly due to intermittency, partly due to the flame base being sometimes above, sometimes below the probe location. There is, however, a significant fraction in the intermediate range between fully reacted and unreacted fluid.

Figure 6 shows scatter plots of temperature and species mass fractions, versus f at x/D = 20. Around stoichiometric ($f_s = .055$) the distribution of all quantities except H_2 and CO is strongly bimodal, as seen in the scarcity of samples half-way between the unreacted and reacted states. For $f > 0.07$, the distribution in Fig. 6 differs markedly from that in undiluted, seated diffusion flames (Stårner et al. 1990): there are no samples near the 'fully burnt' lines (obtained by predictions for a laminar counterflow diffusion flame). This is because cold premixing of fuel and air occurs down to $f \leq 0.17$ in every sample, before any diffusion of heat and products from the reaction zone takes place. Such is also the case much further downstream, at x/D = 32 (Fig. 7), where one expects essentially a diffusion flame structure. However, here a significant fraction of the data is unburnt at stoichiometric showing that some cold mixing is still taking place. There is no clear evidence here of extinguishing fluid of the kind seen in air diluted, piloted flames (Stårner et al. 1990; 3:1 air/CH_4 by volume, corresponding to premixing to $f = 0.16$), the scatter plots of which have the same outlines as those of the lifted flame, except that the intermediate region (half-burnt, or quenched) is densely populated. In fact, the almost complete absence of temperature samples in Fig. 7 at $\approx f_s$ and $900 < T < 1600K$ shows that probe averaging is not a significant occurrence here. Further, the clustering of the burnt samples between the laminar flame lines for $f \leq f_s$ shows that the flame is fairly close to equilibrium, as one expects in a region of low mixing rates. These two observations enable us to infer that the wide distribution of T for $f > f_s$ is not due to nonequilibrium or probe effects. There is clearly some cold premixing to within the rich flammability limit, and subsequent combustion of such samples must, by definition, be premixed. Samples to the rich side of $f = 0.08$ that have already been heated have

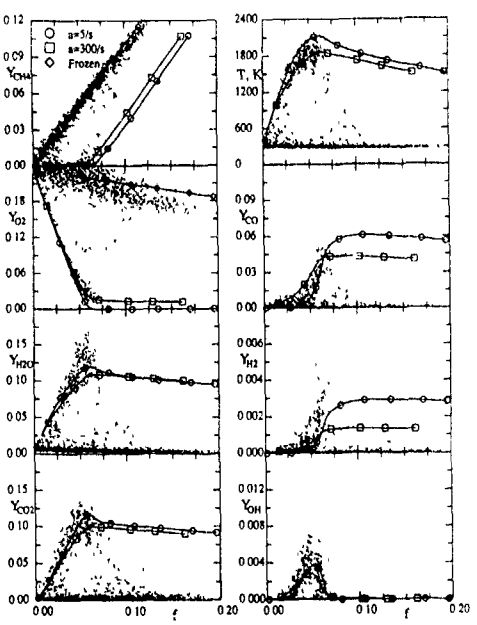

Fig. 6 Scatter plots of temperature and species mass fractions, plotted against mixture fraction, at x/D = 20. Data from r/R = 2.8 to 8.3 are combined, in equal proportions. Lines denote laminar flame calculations at strain rates 5 and 300 s^{-1}, and, for the reactants, frozen flow. (The strain rate $a = 2\,V/R_c$, V being the freestream velocity and R_c the cylinder radius).

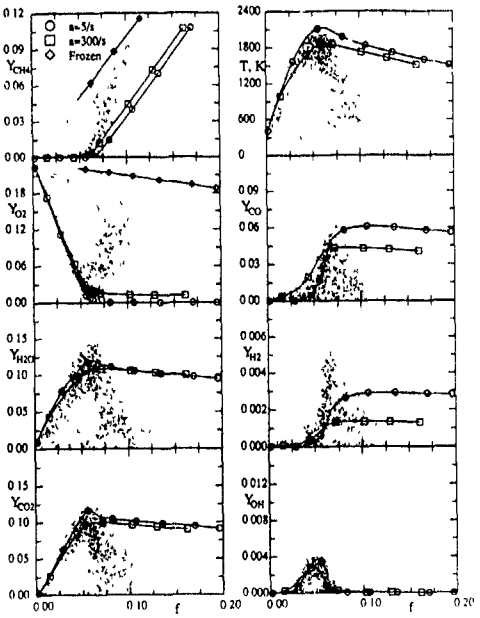

Fig. 7 Scatter plots as in Fig. 5, but at x/D = 32, r/R = 8.3.

obviously been involved in diffusion of heat and products from a nearby reaction zone, and could perhaps be classed as diffusion flame events.

Figure 8 shows scatter plots of data at the flame base, re-plotted versus temperature, and conditional on approximately stoichiometric mixture, $0.9 < f/f_s < 1.1$. In a premixed flame, data above ambient temperature but below 1800K would represent the preheat and main reaction zones, whereas in a steadily burning diffusion flame, there would be no data below the quenching limit (around 1750K for undiluted CH_4) save that at ambient temperature, representing the cold approach flow. There are, however, three possible sources of such data in diffusion flames: probe averaging, signal noise due to dust or soot (resulting in lower measured T through raised Rayleigh scattering), and local quenching. It seems that none of these sources is active here. unpublished 2D Rayleigh images (Stärner and Bilger, 1990) show that the measurements in Fig. 8 are collected in the low turbulence zone at, and outside, the jet boundary, where quenching effects are not expected; probe averaging, as argued above, does not appear to be a problem in a diffusion flame structure where gradients are lower than in a premixed flame, and finally, any soot interference on T would also result in some H_2O samples in Fig. 8 being displaced far to the left of the main cluster; this is clearly not the case here. Therefore, the samples above ambient temperature but below, say, 1750K, seem to indicate a premixed structure. Results of 2D imaging of OH, CH and CH_4 by Schefer et al. (1990) point to a diffusion flame structure downstream of the flame base, but there are instances at the upstream end of the reaction zone of a 'heel' where CH seems to exist on the lower (cold) side and OH on the upper (burnt) side of the flame image, as one expects in a premixed flame. However, this is not consistently the case, and the results are not easily interpreted.

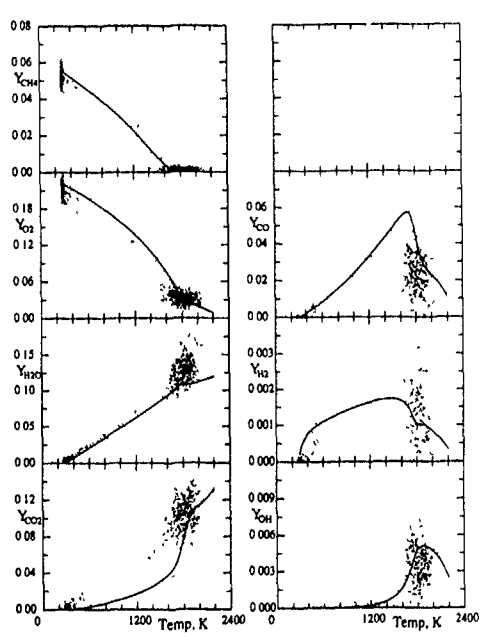

Fig. 8 Scatter plots of species mass fractions against temperature, conditional on $0.9 < f/f_s < 1.1$; x/D = 20, r/R = 6.9 and 8.3 combined. ——: calculations for an unstrained, premixed flame of stoichiometric composition.

The particular species that is thought to be most useful for discriminating between premixed and diffusion flame structure is CO_2: the calculations for a laminar, unstrained, stoichiometric premixed flame in Fig 8 show low CO_2 levels below 1600K and a steep rise in the burnout zone, whereas CO_2 in quenched fluid in a diffusion flame would not have this nonlinear temperature dependence, but would be linear with T to a first approximation, as seen in the results by Stårner et al (1990). In Fig. 9, the CO_2 plot of Fig. 8 is expanded and compared with results for an undiluted seated flame close to extinction (obtained on the same occasion, to minimise systematic bias) where local quenching occurs due to high mixing rates. Typically, CO_2 levels for the seated flame are twice those of the lifted, at the same temperature. It is also seen that the lifted flame data lie somewhat above the laminar flame predictions. If we assume that the lifted flame data indeed represent a premixed flame zone, this must be due in part to probe averaging: the temperature range 600–1800K corresponds to a reaction zone width of ~0.5 mm, approximately equalling the probe size (not accounting for beam thickening by density gradients). The non-linear CO_2–T relationship would result in raised CO_2 levels, particularly around 1400K. In a diffusion flame, the lower gradients and linear CO_2–T correlation would not cause such bias

CONCLUDING REMARKS

The results show that the lifted flame is stabilized somewhat outside the mean stoichiometric contour, where the flow is intermittent and the turbulence level is low. The 2D Rayleigh images by Stårner and Bilger (1990) confirm this and also show that highly distorted hot fluid parcels become entrained into the jet core, and that a smooth-edged outer flame envelope exists, with much larger structures than in the shear layer The hot entrained fluid is consistent with the notion of flamelet entrainment by large structures advanced by Broadwell et al. (1985) but contrasts with the findings of Savas and Gollahalli (1986)

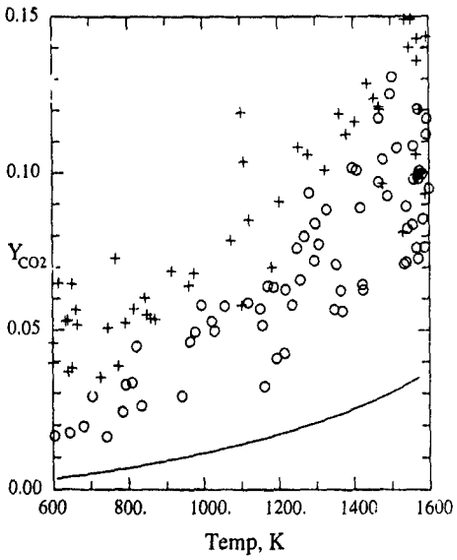

Fig. 9 Data for Y_{CO_2} (o), as in Fig 8, expanded in the intermediate temperature range, and compared with a seated flame (+) of undiluted CH_4 at x/D = 20, r/R = 3.8, at jet velocity 45 m/s.

for a propane flame that the flame base does not propagate into the jet core but jumps from the outer edge of one eddy to the next. However, their fuel jet is slow and the flame is stabilised near the nozzle where regular vortices develop, whereas in the present high-speed flame the turbulence is well developed and three-dimensional. Our 2D Rayleigh images have shown that the higher stoichiometric air/fuel ratio of propane does not suffice to alter the basic structure reported here for the methane flame

There are some indications of premixed burning at the flame base, but the clear evidence of intermittency and the wide variation in mixture fraction outside the flammability limits do not favour the idea of a turbulent premixed flame front propagating steadily into the approach flow However, there may be flow conditions, perhaps such as that of Savas and Gollahalli, where it has more relevance.

Although we have noted the occurrence of fluid entrained into the jet core, which may undergo quenching, this does not happen at the flame base· such parcels are quickly convected downstream and seem unlikely to directly affect the base. Thus, the diffusion flamelet quenching concept of Peters and Williams (1983) in support of their theory of stabilization could not be argued on the basis of these observations The estimate by Peters and Williams that there is insufficient time, Δt, between nozzle and flame base to effect the molecular mixing needed for premixed combustion is not borne out for this flame In calculating Δt, they appear not to account for the flame base being so far out into the low-speed surroundings; here it seems that Δt is almost a magnitude larger However, with a fuel of lower stoichiometric air/fuel ratio, such as a H_2/N_2 mix, the stoichiometric envelope may lie inside the jet shear layer, giving the issue of flamelet quenching more prominence

We have studied a flame of a single fuel, with one nozzle size and at one Reynolds number. Comparisons with work by others indicate that there may be more than one mechanism at work, depending on geometry, turbulence structure and fuel type. It may well be that no single description can satisfy the whole range of conditions for lifted flames. Given the complexity of the problem, it is indeed remarkable that major advances have been made in the development of robust empirical models for liftoff and blowoff phenomena.

ACKNOWLEDGEMENTS

This work is supported by the Australian Research Council and by the US Department of Energy, Office of Basic Sciences

REFERENCES

BARLOW, R.S., DIBBLE, R.W. & FOURGUETTE, D C. 1989a Departure from chemical equilibrium in a lifted hydrogen flame Paper presented at AIAA/ASME/SAE/ASEE 25th Joint Propulsion Conference, Monterey CA, July 10–12

BARLOW, R.S., DIBBLE, R.W. & LUCHT, R.P. 1989b Simultaneous measurement of Raman scattering and laser-induced OH fluorescence in turbulent nonpremixed jet flames, Optics Letters 14 263–265.

BROADWELL, J E., DAHM, W J.A. & MUNGAL, G 1985 Blowout of turbulent diffusion flames, *20th Symposium (International) on Combustion*, The Combustion Institute, 303–310.

BYGGSTØYL, S. & MAGNUSSEN, B.F 1983 A model for flame extinction in turbulent flow. *Proc. of Turbulent Shear Flows 4*, Karlsruhe, West Germany.

DAHM, W.J.A. & DIBBLE, R.W. 1989 Coflowing turbulent jet diffusion flame blowout *22nd Symposium (International) on Combustion*, The Combustion Institute, 801–808

EICKHOFF, H., LENZE, B & LEUCKEL, W 1985 Experimental investigation on the stabilization mechanism of jet diffusion flames. *20th Symposium (International) on Combustion*, The Combustion Institute, 311–318.

JANICKA, J. & PETERS N. 1983 Prediction of turbulent jet diffusion flame lift–off using a pdf transport equation. *19th Symposium (International) on Combustion*, The Combustion Institute, 367–374.

MASRI, A.R., BILGER, R.W. & DIBBLE, R.W. 1988 Turbulent nonpremixed flames of methane near extinction: mean structure from Raman measurements. *Combust. Flame* 71, 245–266

NAMAZIAN, M., KELLY, J. & SCHEFER, R.W. 1989 Near field instantaneous flame and fuel concentration structures. *22nd Symposium (International) on Combustion*, The Combustion Institute, 627–634.

PETERS, N. and WILLIAMS, F.A. 1983 Liftoff characteristics of turbulent jet diffusion flames. *AIAA J.* 21, 423.

PITTS, W.M. 1989 Assessment of theories for the behaviour and blowout of lifted turbulent jet diffusion flames. *22nd Symposium (International) on Combustion*, The Combustion Institute, 809–816.

SAVAS, Ö & GOLLAHALLI, S.R. 1986 Flow structure in near–nozzle region of gas jet flames. *AIAA J.*, 24, 1137–1140.

SCHEFER, R.W., NAMAZIAN, M & KELLY, J 1990 CH, OH and CH_4 concentration measurements in a lifted turbulent–jet flame. Report SAN89–8806, Sandia National Laboratories, Livermore, CA.

SEITZMAN, J., PAUL, P & HANSON, R. 1990 PLIF imaging analysis of OH structures in a turbulent nonpremixed H_2–air flame. Paper 90–0160 presented at the AIAA 28th Aerospace Sciences Meeting, Jan 8–11, Reno, Nevada.

STÅRNER, S.H & BILGER, R.W. 1990 In preparation.

STÅRNER, S.H., BILGER, R.W. & BARLOW, R.S 1990 Piloted diffusion flames of diluted methane near extinction. detailed structure from laser measurements. *Combust. Sci. Technol.* 72, 255–269.

VANQUICKENBORNE, L. & VAN TIGGELEN, A. 1966 The stabilization mechanism of lifted diffusion flames *Combust. Flame* 10, 59–69.

EIGHTH SYMPOSIUM ON
TURBULENT SHEAR FLOWS
Technical University of Munich
September 9-11, 1991

Large-eddy simulation of the convective boundary layer. A comparison of four computer codes.

F T.M. Nieuwstadt [1]), P J. Mason [2]), C.H Moeng [3]), and U Schumann [4]).

[1]) Laboratory of Aero and Hydrodynamics,
Delft University of Technology, Delft, the Netherlands
[2]) Meteorological Office, Bracknell, England
[3]) National Center for Atmospheric Research, Boulder, CO 80307, U S A
[4]) DLR, Institute of Atmospheric Physics,
W-8031 Oberpfaffenhofen, Germany.

Abstract

To test the consistency of large-eddy simulation we have run four existing large-eddy codes for the same case of the convective atmospheric boundary layer The four models differ in various details, such as the subgrid model, numerics and boundary conditions

The agreement between the four models is excellent. In general model results lie within the scatter of available observations Most of the disagreement between the model results can be attributed to the parameter C_s of the subgrid model. The effect of other differences between the four models, such e g due to numerics, is found to be small

Introduction

In large-eddy simulation we seek to compute the large scales of turbulence. This is accomplished by performing on the Navier-Stokes equations a filter operation, designed to remove the small scales from these equations The resulting set of equations is then solved numerically. Large-eddy simulation is considered to be a tool to study the details of turbulence and it is enjoying an increasing popularity.

The most successful application of large-eddy modelling has been to the atmospheric boundary layer and in particular to the convective boundary layer. The reason is of course that the convective boundary layer is dominated by large structures. These are known as thermals and they are responsible for most of the vertical transport processes. They make the convective boundary layer an ideal subject for large-eddy simulation.

The study of the convective boundary layer with large-eddy models has started with the pioneering work of Deardorff in the seventies (e g. Deardorff, 1974). Since then extensive and detailed simulations have been reported by Moeng (1984), Mason (1989) and Schmidt and Schumann (1989). A more general review of large-eddy simulation of convection is presented by Nieuwstadt (1990).

Here, we will not add another simulation to this list. Instead this study has a different objective

The philosophy of large-eddy modelling is to isolate the dynamics of the large scales The small scales are treated by a more or less simple parameterization: the so-called subgrid model. This approach hinges on the hypothesis that the actual details of the subgrid model have only minor effects on the large scales. As this may be considered the fundamental premise of large-eddy modelling there are also other uncertainties. Any large-eddy model requires a large number of assumptions about details of the model, ranging from the choice of a numerical scheme to the selection of boundary conditions It would be very undesirable if a large-eddy simulation turns out to be sensitive to these modelling details.

In this paper we aim to address these questions and investigate whether present large-eddy models are in line with the philosophy mentioned above. Do they lead to consistent simulations for the case of the convective atmospheric boundary layer? Such consistency would present a further argument that large-eddy simulations can be trusted to give a realistic representation of atmospheric turbulence.

To this end four research groups represented by the authors of this paper have decided to test their large-eddy models for a simulation of the convective boundary layer. Besides using different subgrid models, these codes also differ in many other details We run the models starting from the same initial conditions and using the same forcing. By comparing the results we expect to learn the sensitivity of these models to the various parameters

First we shall discuss in some detail the differences between the models Next we shall specify the initial conditions and the calculation procedure Then we turn to a discussion of the results

Description of large-eddy codes

As already mentioned above we shall use in this study existing large-eddy codes which have already been described elsewhere (Mason, 1989; Moeng, 1984 and Schmidt and Schumann, 1989) Therefore, we shall restrict ourselves in this section to highlighting the various differences between the four models

Subgrid model

The main purpose of a subgrid model is to "dissipate" the energy which is passed down the cascade from the large eddies Views at present differ on the complexity needed to model the subgrid terms

The most simple parameterization is the well-known Smagorinsky model, which relates the subgrid stresses to the deformation of the resolved velocity field by means of an eddy viscosity, K_M This eddy viscosity is expressed as

$$K_M = \ell^2 S \tag{1}$$

where S is the absolute value of the strain rate and ℓ is the so-called mixing length. This mixing length is proportional to the filter length.

The Smagorinsky model is used by Mason and for a more detailed discussion we refer to Mason (1989), where an extension of (1) to convective turbulence is introduced. Here, it suffices to mention that in the context of the Smagorinsky model a fundamental role is played by the coefficient C_s It is defined as the ratio between the mixing length and a characteristic grid size Δ

$$C_s = \ell/\Delta. \tag{2}$$

Mason (1989) has considered the effect of several values for C_s and recommends $C_s = 0.32$.

Alongside the Smagorinsky model for subgrid stresses an analogous model is used to parameterize subgrid heat fluxes It relates the temperature flux to the resolved temperature gradient by means of an eddy diffusivity K_H. The K_H is connected to the K_M by means of a Prandtl number

$$Pr = \frac{K_M}{K_H} \tag{3}$$

	Mason	Moeng	Nieuwstadt	Schumann
C_s	0 32	0 18	0 18	0.165
Pr	0.46	0 33	0 33	0 42

Table 1 *Representative values of the coefficient C_s and the Prandtl number Pr for the subgrid model of the four large-eddy codes.*

A slightly more complicated subgrid closure model is used by Moeng and Nieuwstadt It is also based on a relation between the subgrid stress and the resolved deformation rate but in this case the eddy viscosity is defined as

$$K_M = 0\ 12\Delta e^{1/2} \tag{4}$$

where e is the subgrid energy A separate equation for the subgrid energy is formulated, which is then solved along with the other equations of the large-eddy model (Moeng, 1984) If we simplify the subgrid energy equation to a balance between shear production and dissipation we may derive a representative value for C_s. In case of the subgrid model of both Moeng and Nieuwstadt, we find $C_s = 0.18$.

Schumann adopts the most complicated subgrid model It is a second order closure model, in which the following simplifications are made. Only for the subgrid energy a full equation, including time derivatives and transport terms, is solved In the other equations of the subgrid model these terms are neglected Moreover, the production terms in these equations are limited to the isotropic part. As a result the subgrid model can be expressed as a decoupled algebraic system of equations, which can be explicitly solved For further details we refer to Schmidt and Schumann (1989), where it is also derived that their representative value for C_s is: $C_s = 0\ 165$.

Another detail of the subgrid models which varies between the four codes is the formulation of the mixing length. In the interior of the boundary layer all four authors take the mixing length ℓ proportional to a characteristic grid size Δ Moeng and Nieuwstadt use the geometric mean $\Delta = (\Delta x\,\Delta y\,\Delta z)^{1/3}$, whereas Schumann takes the arithmetic average: $\Delta = (\Delta x + \Delta y + \Delta z)/3$ Mason uses a non-uniform grid and he provides no explicit expression of Δ in terms of the grid spacing.

Furthermore, Mason and Schumann allow ℓ to become proportional to height when the surface is approached. Nieuwstadt takes this effect into account through a different parameterization of the dissipation term in the equation for e near the surface

Finally, Mason, Moeng and Nieuwstadt limit the mixing length to a smaller value in stable conditions. This plays for instance a role in the stable layer above the boundary layer.

Nevertheless, we shall see that the most important parameter influencing the effect of the subgrid model is C_s and perhaps to a lesser extent the Prandtl number Pr For convenience we have collected these parameters in table 1

Numerics

The models of Mason, Nieuwstadt and Schumann use a full staggered grid. This means that the velocity components are defined on the sides of the rectangular grid volume with the pressure in the centre. Moeng uses staggering only in the vertical direction, so that in her model all variables are defined on the same x, y-position

The subgrid energy e, used in the subgrid models of Moeng, Nieuwstadt and Schumann, is also defined in the centre of the grid volume This means that in these models the exchange coefficients are located on the same position. Mason adopts a different view and collocates the exchange coefficients with the w-point to avoid vertical averaging of z-derivatives

The resolved temperature is governed by an advection-diffusion equation Therefore, the most obvious location for the temperature is the centre of the grid volume. This view is taken by all participants except Nieuwstadt, who stores the temperature at the w-point. His argument is to avoid vertical averaging of temperature in the w-equation, where buoyancy is the dominant forcing term.

Next we consider the numerical schemes. With respect to time advancement Moeng and Schumann use the Adams-Bashford scheme, whereas Mason and Nieuwstadt employ the leap-frog method The leap-frog scheme is unstable for the diffusion terms Therefore, the latter authors resort for these terms to the simple forward Euler scheme

Mason and Nieuwstadt treat the advection terms by the Piacsek and Williams scheme This is a second-order method designed to conserve variances. Schumann uses standard second-order differencing All three authors take second-order, central differencing to solve the diffusion terms Moeng adopts a somewhat different approach. She uses a pseudo-spectral method to calculate all horizontal derivatives and a finite difference technique to calculate the vertical derivative To avoid aliasing errors in the pseudo-spectral technique all Fourier expansions are truncated beyond the wave number $2/3\,k_{max}$

All four authors use a mixed fast-Fourier and finite difference technique to solve the Poisson equation for the pressure.

Boundary conditions

In all four models horizontal boundary conditions satisfy periodicity. However, differences are found in the specification of the vertical boundary conditions

At the lower boundary the vertical velocity w is set equal to zero. For the horizontal velocities one resorts to Monin-Obuhkov similarity This means that a relation is specified between the surface stress and the horizontal velocity in the first grid cell. Furthermore, it is assumed that the velocity and stress are parallel.

The models of Mason, Moeng and Schumann specify the temperature flux at the surface Surface similarity is then used to obtain the surface temperature T_s from the temperature calculated in the centre of the first grid volume. Nieuwstadt has to adopt a different procedure, because he defines the temperature at the location of the w-variable. He then uses surface-layer similarity to specify a relationship between the surface-temperature flux and the temperature difference across the first grid cell. Note that in convective conditions the temperature profile near the surface is strongly curved. This curvature cannot be resolved within the first grid cell As a result the subgrid exchange coefficients in Nieuwstadt's model are revised in relation to the standard surface-layer expressions.

With respect to the upper boundary conditions all four models agree on stress free conditions: i.e. $\partial u/\partial z = \partial v/\partial z = 0$ Furthermore the temperature gradient at the top of the calculation domain is set equal to the gradient Γ, which is prescribed in the initial conditions as the temperature gradient above the boundary layer

There are however, some important differences in the treatment of the vertical velocity at the upper boundary The goal is to avoid reflecting gravity waves from the top of the model. Moeng and Schumann prescribe a radiation boundary condition which allows gravity waves to propagate out of the calculation domain Mason uses an expanding grid near the top of the calculation domain in conjunction with a damping layer Nieuwstadt also uses a damping layer (but no expanding grid). The role of the damping layer is to dissipate gravity waves before they can reflect back into the boundary layer. This is accomplished by adding to the equations of motion in the upper part of the calculation domain a relaxation term. This relaxation term then damps fluctuations at time scales larger than a prescribed relaxation time scale Nieuwstadt takes the relaxation time scale equal to $50\,s$ at the highest calculation level The relaxation time scale in his model is then increased by a factor of 5 at each computation level for the next 9 levels down.

Calculation

The calculations are performed in a rectangular domain. Its horizontal dimensions are $6400 \times 6400\,m^2$. The vertical domain size is $2400\,m$ for the computations of Moeng, Nieuwstadt and Schu-

	Mason	Moeng	Nieuwstadt	Schumann
N_x, N_y	40	40	40	40
N_z	68	48	40	40
L_x, L_y (m)	6400	6400	6400	6400
L_z (m)	8000	2400	2400	2400
Δt (s)	0 65	3	4 48	10 96
T_{CPU} (s)	23 55	1 15	0 86	1.33
Storage	0.64	0 53	1 75	2.3
Computer	IBM 3084	Cray-YMP	Cray-XMP	Cray-YMP
N_T	20000	4000	2750	1100
N_t	40	10	4	10

Table 2: *Several statistics of the computations; N_x, N_y, N_z number of grid points in the two horizontal and the vertical directions, L_x, L_y, L_z : horizontal and vertical size of the computation domain; Δt: timestep; T_{CPU}. CPU time per time step; Storage. core storage in M words, N_T : total number of time steps to calculate the time period $0 < t/t_* < 11$; N_t number of timesteps used in the calculation of averages*

mann and $8000\,m$ for the computation of Mason (remember that the latter author uses a non-uniform, expanding grid in the upper part of the calculation domain).

To limit the computational effort for this comparison study we took only a modest number of grid points. All authors use 40 grid points for both horizontal directions. This implies a horizontal grid spacing of $\Delta x = \Delta y = 160\,m$ In the vertical direction Nieuwstadt and Schumann use also 40 grid points so in their case $\Delta z = 60\,m$ Moeng takes 48 grid points which implies $\Delta z = 50\,m$. As mentioned before Mason specifies a non-uniform grid with 68 grid points. Near the surface his grid spacing is $\Delta z = 20\,m$ and within the boundary layer a typical grid spacing amounts to $\Delta z = 80\,m$. Near the top of the boundary layer the grid spacing is again reduced to about $\Delta z = 30\,m$ The grid then expands to $\Delta z = 250\,m$ towards the top of the calculation domain.

Convection is driven by a constant temperature flux at the surface of $Q_s =< w'T' >_0 = 0.06\,K m s^{-1}$ This flux is directly prescribed at the surface in the models of Mason, Moeng and Schumann The model of Nieuwstadt requires a different procedure because the heat flux is not defined at the surface due to the w-location of the temperature variable. In his case a constant temperature increase was prescribed at the surface with a magnitude of $(dT/dt)_0 = 0.16K\,hour^{-1}$ With this value of $(dT/dt)_0$ the temperature flux varied slightly during the calculation, say between $0.061\,K m s^{-1}$ and $0.058\,K m s^{-1}$. However, averaged over the whole calculation period the temperature flux was found to be equal to $0.06\,K m s^{-1}$.

The calculations were set up in such a way that boundary-layer height would reach a value in the neighbourhood of $1600\,m$ Therefore, we introduce as a scaling height $z_{i0} \equiv 1600\,m$. We can now define a convective velocity scale w_{*0} as: $w_{*0} = (g/T_0 Q_s z_{i0})^{1/3}$. The gravitational acceleration g is taken here to be $g = 9.81 m s^{-2}$ and the reference temperature $T_0 = 300\,K$ A temperature scale can now be defined as $T_{*0} = Q_s/w_{*0}$ and a time scale as $t_* = z_{i0}/w_{*0}$ With the values of z_{i0} and Q_s mentioned above, w_{*0} becomes equal to $1\,46 m s^{-1}$, T_{*0} equal to $0\,041\,K$ and $t_* = 1096\,s$

Note that in most presentations, to be discussed in the following section, we shall use instead w_* to scale the results This variable is called the convective velocity scale defined by

$$w_* = (g/T_0 Q_s z_i)^{1/3}, \qquad (5)$$

where z_i is a local boundary-layer height That means a boundary-layer height representative for the time period for which the results are evaluated This local boundary layer height has in principle a different value for each calculation.

Other parameters of interest are the constant temperature gradient Γ above the boundary layer. This was specified to be $\Gamma = 0.003\,K m^{-1}$ Furthermore, the roughness length, which enters the surface similarity relationships, is taken to be $z_0 = 0.16\,m$ The density ρ has been normalized to $1\,kg\,m^{-3}$

As initial conditions, we prescribe the following profiles for the temperature T and the three velocity components u, v, w. For $z < z_{i1} = 0.844 z_{i0}$

$$\begin{aligned} T &= T_0 + 0\,1r(1 - \frac{z}{z_{i1}})T_{*0} \\ w &= 0\,1r(1 - \frac{z}{z_{i1}})w_{*0} \\ u &= v = 0 \end{aligned}$$

and for $z > z_{i1}$

$$\begin{aligned} T &= T_0 + (z - z_{i1})\Gamma \\ u &= v = w = 0 \end{aligned}$$

In these equations r stands for a random number uniformly distributed between -0.5 and $0\,5$

In individual calculations these initial profiles are sometimes slightly modified. For instance, Nieuwstadt prescribes for the horizontal velocity components, u and v, at the lowest grid cell the value $0.01 r w_{*0}$ to avoid problems with the surface-layer similarity relationships. Furthermore, he increases the temperature at the surface by $2\,K$ with respect to the value specified by the profile above Finally the subgrid energy is in his model initialized with the profile proposed by Schmidt and Schumann (1989)

Starting from these initial profiles we ran our models with a constant forcing Q_s for a period of $10 t_*$. It was expected that after this period turbulence would reach a quasi-stationary state Next, calculations were continued for $10 < t/t_* < 11$. Within this time interval various quantities were calculated as averages over N_t timesteps. These are the quantities which we shall discuss in the following section It also means that our results have been averaged over only one time-scale. As we shall see, this is too short to obtain stable statistics especially for the higher order moments.

For further information we have summarized in table 2 various statistics of the four computations.

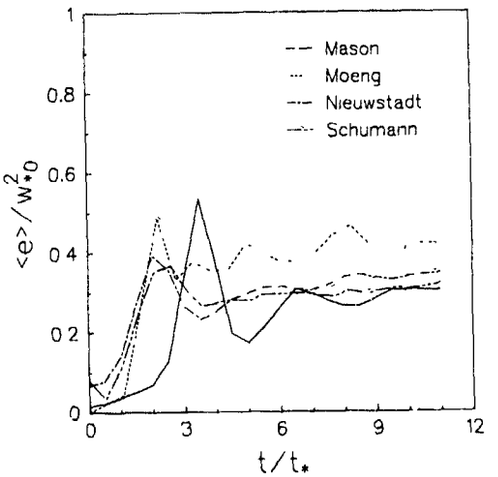

Figure 1. *The total kinetic energy vertically averaged across the boundary-layer height as a function of dimensionless time*

Results

First, we consider whether our simulations have indeed reached a state of quasi-stationary turbulence. To that end we have plotted in figure 1 the kinetic energy averaged across the boundary layer as a function of the dimensionless time t/t_*. Note that we have plotted the total energy, i.e the resolved plus subgrid contribution The energy quickly grows in the initial phase of the computation After an overshoot it settles towards a constant value, which can be interpreted as reaching a state of quasi-stationary turbulence. In the case of Mason's computation the overshoot occurs at a

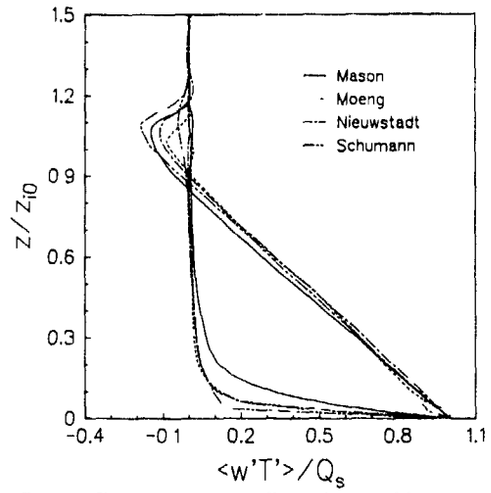

Figure 2: *The temperature flux profile as a function of dimensionless height z/z_{i0}*

later time and it is also larger than for the other models. We believe this to be due to the larger value of C_s in Mason's subgrid model, which leads to a rapid initial loss of energy from the random perturbations. The fact that Moeng's results are somewhat larger than the other calculations seems to agree with her data for the variances to be presented later

Another proof of quasi-stationarity is given in figure 2, where we show the profile of the temperature flux averaged over the time period $10 < t/t_* < 11$ as a function of dimensionless height. Quasi-stationarity should lead to a linear temperature flux profile in the boundary layer This is very well satisfied by all models.

Another well-known property of the convective boundary layer is that the mean temperature is approximately constant over most of the boundary layer. This is corroborated by the calculated temperature profiles (not shown). As additional information on the temperature profile we give in table 3 the value of the surface temperature T_s calculated at $t/t_* = 11$.

The contribution by the subgrid heat flux is small except near the surface, where subgrid effects should dominate by definition. The anomalous value of the temperature flux near the surface in Schumann's model should be disregarded because it is the result of using interpolations for statistics but upwind fluxes in the simulations.

Near the top of the turbulent boundary layer we observe a negative temperature flux. It results from the fact that the boundary layer grows into the stable layer above. This process is called entrainment. The minimum value of the temperature flux is defined as the entrainment flux, $- < w'\theta' >_i$ Its value for the four models is given in table 3. Note that the magnitude of this entrainment flux varies considerably between the four computations As the entrainment flux is largely resolved, this must be a property of the individual models However, we cannot offer at this stage an explanation of this behaviour in terms of the model parameters.

	Mason	Moeng	Nieuwstadt	Schumann
z_i/z_{i0}	1 0563	1 0312	1 0688	1 0900
w_*/w_{*0}	1 018	1 010	1.022	1 029
$- < w'\theta' >_i /Q_s$	0.147	0.106	0.118	0.188
T_s (K)	302 908	301 527	302.542	302.5

Table 3 The actual boundary-layer height z_i, the convective velocity scale w_* and the entrainment temperature flux $- < w'\theta' >_i$ representative for the time period $10 < t/t_* < 11$, the surface temperature T_s calculated at $t/t_* = 11$.

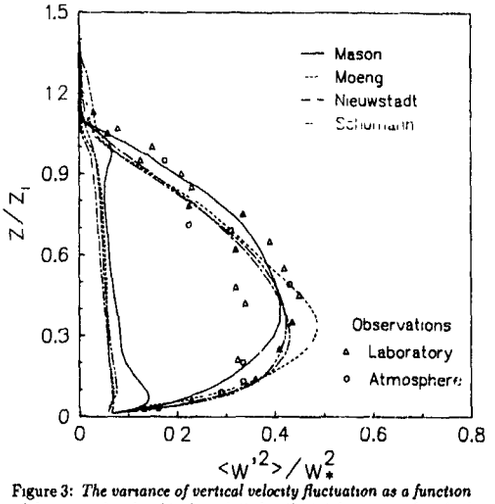

Figure 3: *The variance of vertical velocity fluctuation as a function of dimensionless height z/z_i; plotted is the total variance (resolved plus subgrid) and the subgrid contribution*

Furthermore we note that Schumann's model predicts the largest entrainment heat flux This is partly due to the fact that his model calculates a considerable subgrid contribution to the entrainment flux. The explanation for this result lies in his formulation of the subgrid mixing length ℓ. Remember that Schumann's subgrid model uses a mixing length which is not limited by stability Therefore it will lead to larger subgrid fluxes near the top of the boundary layer

The boundary-layer height z_i is defined as the height where the entrainment temperature flux occurs Its value for the four models is entered in table 3 The height of the boundary-layer seems to correlate positively with the value of the entrainment flux. As already mentioned in the previous section we shall use this actual boundary-layer height to scale the calculation results of each model. In connection we will also use w_*, defined by (5) Its value is also entered in table 3.

Variances

In figure 3 we present the variance of the vertical velocity fluctuations as a function of z/z_i. We have plotted in this figure both the total variance, i e. resolved plus subgrid, and the subgrid contribution.

The subgrid model of Schumann allows a direct estimate of the subgrid contribution to $< w'^2 >$ Moeng and Nieuwstadt calculate the subgrid energy e. They then assume isotropy so that for the subgrid contribution to $< w'^2 >$ results $2/3e$. Mason estimates the subgrid energy from the following diagnostic relationship

$$e = a^{-2}\ell^2 S^2(1 - Ri_f)$$

where $Ri_f = g/(T_0 Pr)\partial T/\partial z/S^2$ is the flux Richardson number The constant a is taken as 0.3 The contribution to $< w'^2 >$ is then calculated by the same method as used by Moeng and Nieuwstadt.

The agreement between the four models is clearly excellent Only Mason's model exhibits a slightly different profile. The other models only differ in their prediction of the maximum value of $< w'^2 >$

We have plotted in figure 3 also some observations obtained from laboratory experiments (Willis and Deardorff, 1974 and Deardorff and Willis, 1985) and from atmospheric field tests (Lenschow et al., 1980) It seems that the differences between the four models are smaller than the scatter in the experimental data. It is therefore not possible to conclude from this figure which model gives the best simulation. We will see that the same statement applies to other comparisons with observational data.

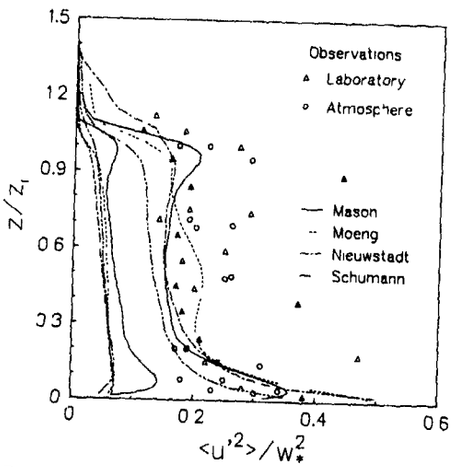

Figure 4. *The variance of horizontal velocity fluctuation as a function of dimensionless height z/z_i, plotted is the total variance (resolved plus subgrid) and the subgrid contribution.*

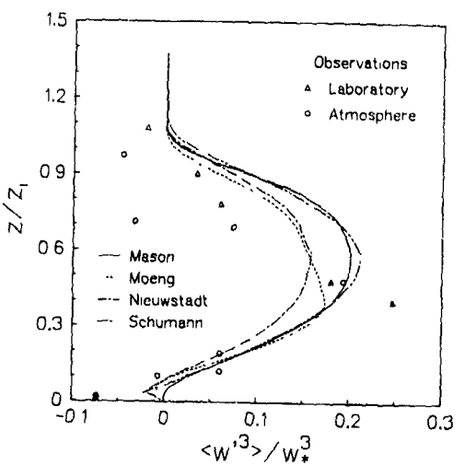

Figure 5 The third moment of the vertical velocity fluctuations as a function of dimensionless height z/z_i

In figure 4 we show a dimensionless plot of the total horizontal velocity variance and its subgrid contribution. The subgrid contributions are calculated by the same method as discussed above for figure 3

In this case differences between the four models are somewhat larger but they lie still within the scatter of the observations, also shown in this figure.

Points to be noted are. Mason's model shows a strong increase towards the top of the boundary layer Moeng's profile exhibits a mid-layer maximum, which we believe to be unrealistic. It explains her somewhat larger values of the boundary-layer averaged energy found in figure 1. Finally, the results of Nieuwstadt show a large value of the variance near and even above the boundary-layer top. This is caused by his upper boundary condition, which uses a damping layer It seems that the damping layer fails to remove fluctuations sufficiently.

Higher order moments

In figure 5 we show the dimensionless profile of the third moment of the vertical velocity fluctuations This variable is strongly influenced by the thermals in the convective boundary layer A boundary layer consisting of isolated thermals with inside these a strong vertical upward motion, necessarily leads to a positive third moment as found in figure 5.

The agreement between the four models is quite acceptable in view of the observations which are also shown in the same figure.

The models of Moeng, Nieuwstadt and Schumann lead to a negative value of $< w^3 >$ near the surface. This is considered unrealistic because it would imply that downdrafts become stronger when they approach the surface. Mason (1989) and Schmidt and Schumann (1989) have investigated the background of negative values of $< w^3 >$ in more detail They conclude that it is a consequence of the subgrid model

Energy budget

The kinetic energy budget of turbulence in a quasi-stationary convective boundary layer reads

$$0 = \frac{g}{T_0} < w'\theta' > - \frac{\partial}{\partial z}(< w'e' > + \frac{1}{\rho} < v'w' >) - \epsilon \qquad (6)$$

where we have omitted shear production term, which is zero in this case because $< u >= 0$

The first term in (6) denotes the production of kinetic energy by buoyancy forces. This production is balanced by the viscous dissipation ϵ. Its vertical profile is given in figure 6. The agreement between the four models is excellent Mason's calculation shows again a maximum near the top of the boundary layer. Moreover, we see that near the surface the ϵ calculated by the models of Moeng, Nieuwstadt and Schumann increase very rapidly. The model of Mason exhibits a more gradual profile Schmidt and Schumann (1989) have pointed out that such rapid increase of ϵ usually goes together with a negative third moment near the surface (see e.g. figure 5). We have also evaluated the transport terms from the four simulations. They show only minor differences.

Spectra

In figure 7 we show the spectra of the resolved vertical velocity fluctuations at three levels in the boundary layer. Remember that Moeng uses a spectral cut-off to avoid aliasing in her pseudo-spectral method. Therefore, her spectra stop beyond wave number

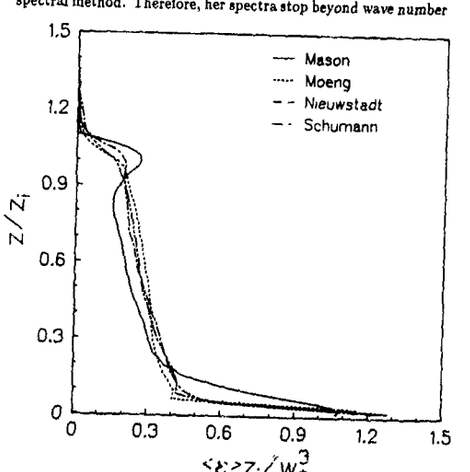

Figure 6: *The dissipation of turbulent kinetic energy as a function of dimensionless height z/z_i*

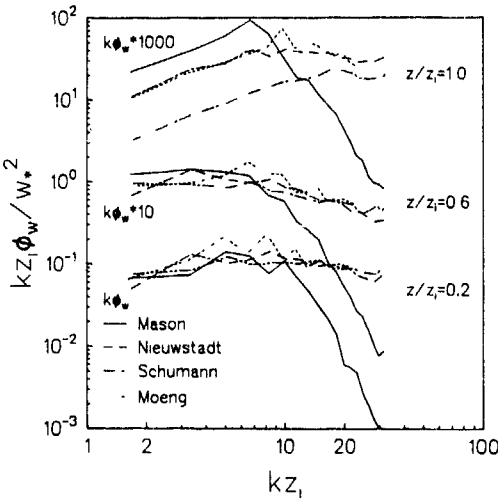

Figure 7. *The spectra of the resolved vertical velocity fluctuations at three levels in the boundary layer*

$kz_{10} = 22$ whereas the other spectra continue until $kz_{10} = 29.84$ (in the figures the spectral values at the last wave number $kz_{10} = 31.41$ have been omitted).

The spectra of Mason have clearly a much steeper slope at high wave numbers than the spectra calculated by the other models. This must be no doubt an effect of the subgrid model.

However, we point to the fact that in figure 7 the spectra of all models are again very close at low wave numbers, i.e. $kz_i \leq 10$. This should not come as a total surprise because it consistent with the good agreement for the variances between all four models. Nevertheless, it supports the fundamental premise of large-eddy modelling, which we have stressed in our introduction: the large eddies do not depend strongly on the details of the subgrid model.

Finally, we should note that none of the spectra seems to follow the well-known $-2/3$ slope of the inertial range. However, there is some evidence (see e.g. Schmidt and Schumann, 1989) that at higher horizontal resolution than 40^2 the spectra become more realistic.

Discussion and conclusion

Our comparison of four large-eddy codes has shown clearly that large-eddy simulation leads to a generally consistent picture of convective turbulence despite differences in many details of the models. This fact should strengthen our confidence in the realism of the simulated turbulence.

However, at this stage such statement can only be made for large-eddy simulation of convective turbulence. In other words, convective turbulence seems to be a rather easy case for large-eddy simulations. A relatively coarse resolution as used in this calculation is able to represent much of the salient characteristics of convective turbulence. Shear turbulence seems to be more challenging test case for large-eddy modelling. Therefore, we are contemplating to perform a similar comparison study for the neutral boundary layer.

As far as differences between the models are concerned, the four models seem to fall into two categories with Mason in the one and Moeng, Nieuwstadt and Schumann in the other. (However, in the latter group the models of Nieuwstadt and Schumann seem to agree slightly better). The most obvious support for this distinction into two groups is given by the results for the w-spectra shown in figure 7. In addition, Mason's model leads also frequently to a different shape of the vertical profile in comparison with results of the other models. Examples are figures 3, 4 and 6.

To explain these differences we consider first the influence of the subgrid model. The main difference of Mason's subgrid model with respect to the others lays in the value of the constant C_s (see table 1). To test the effect of C_s Mason has rerun his model with a value of $C_s = 0.23$. At the same time he changed to an equidistant grid within the boundary layer with a representative vertical grid spacing of $\sim 45\,m$. However, it is expected that the effect of the equidistant versus non-uniform grid will be minimal. Therefore, the new results will primarily reflect the influence of C_s in Mason's model.

We found that for this new calculation Mason's results are much closer to the other models. The spectra for all four models agree now very well at the higher wave numbers while, as expected, agreement at the low wave numbers is hardly affected. This latter fact supports the fundamental hypothesis of large-eddy modelling the large eddies are insensitive to the details of the subgrid model. Furthermore, it seems that the smaller value of C_s also leads to somewhat weaker thermals in comparison with the calculations at $C_s = 0.32$. As a result the vertical profiles, which for the case of $C_s = 0.32$ frequently exhibit a maximum near the top of the boundary layer, are now much closer to the results of the other models. Therefore, we may conclude that most of the differences between the two categories of models, as introduced above, can be explained by C_s.

Another result, which follow from our study, is that the upper boundary condition should be formulated in such a way that gravity waves are not reflected from the top of the boundary layer. Otherwise we should expect to see increased values of the variance above the boundary layer. However, increased variances above the boundary layer do not seem to influence the simulation results inside the boundary layer. Nevertheless, we recommend the use of a radiation condition as upper boundary condition, which lets gravity waves propagate out of the domain. It seems to work very well and it is less expensive than an increase of the vertical computation domain together with an expanding grid.

Other differences between our four models which seem to have had hardly any effect on the calculation results, are: the numerical methods, the details of the staggered grid and the details of the lower boundary condition. For instance, there seems to be no advantage in applying a pseudo-spectral method. Also the use of a non-uniform versus an equidistant grid seems to have negligible influence.

Acknowledgement

U. Schumann is grateful do Dr. Jutta Graf, who cooperated with him in this project. F.T.M. Nieuwstadt acknowledges discussions with J. Eggels and H. Cuypers.

References

Deardorff, J.W. 1974: Three dimensional numerical study of turbulence in an entraining mixed layer. *Boundary-Layer Met.* **7**, 199-226.

Deardorff, J.W. & Willis, G.E. 1985: Further results from a laboratory model of the convective planetary boundary layer. *Boundary-Layer Met.* **32**, 205-236.

Lenschow, D.H., Wyngaard, J.C. & Pennel, W.T. 1980: Mean-field and second-moment budgets in a baroclinic, convective boundary layer. *J. Atmos. Sci.* **37**, 1313-1326.

Mason, P.J. 1989: Large-eddy simulation of the convective atmospheric boundary layer. *J. Atmos. Sci.* **46**,

Moeng, C.-H. 1984: A large-eddy simulation for the study of planetary boundary layer turbulence. *J. Atmos. Sci.* **41**, 2052-2062.

Nieuwstadt, F.T.M. 1990: Direct and large-eddy simulation of free convection. *Proc. 9th Interna. Heat Transfer Conference*, Jerusalem 19-24 August 1990, Amer. Soc. Mech. Engrg., Vol. I, 37-47.

Schmidt, H. & Schumann, U. 1989: Coherent structures of the convective boundary layer derived from large-eddy simulations. *J. Fluid Mech.* **200**, 511-562.

Willis, G.E. & Deardorff, J.W. 1974: A laboratory model of the unstable planetary boundary layer. *J. Atmos. Sci.* **31**, 1297-1307.

EIGHTH SYMPOSIUM ON
TURBULENT SHEAR FLOWS
Technical University of Munich
September 9-11, 1991

BURSTS AND SOURCES OF PRESSURE FLUCTUATION IN TURBULENT BOUNDARY LAYERS

J.F. Morrison* and P. Bradshaw°

* GEC ALSTHOM Turbine Generators Ltd., Aerodynamics Group, Barton Dock Road, Manchester M31 2LD U.K

° Thermosciences Divn., M.E. Dept., Stanford University C.A. 94305-3030 U.S.A.

ABSTRACT

A four-wire array in a flat-plate, zero-pressure-gradient turbulent boundary layer is used to make low-wave-number measurements of the spanwise components of the quantities which appear as source terms in Poisson's equation for the pressure fluctuation. These source terms, referred to as "splat" and "spin", are analysed by use of the VITA+LEVEL conditional sampling scheme and the results are correlated with the local wall pressure.

The results show that the period between successive ejections and sweeps, and the period between successive splats and/or spins both scale with viscous variables (not with wall variables), suggesting that high-wave-number pressure fluctuations trigger the bursting sequence.

NOMENCLATURE

e_{ij}	stress tensor
k_i	streamwise wave number
L	event length = $L(t/\delta t)U_e\delta t$
L_p	event period (length between successive events) - equation (4)
N	number of samples
p	fluctuating pressure
Re_θ	Reynolds number based on momentum thickness
t	time
T	total record time
u_τ	wall friction velocity
U_e	free-stream velocity
U,u,V,v,W,w_i	mean, fluctuating velocity components in x (streamwise) y and z directions respectively
γ	fraction of time for which sampling criteria are satisfied (identity ratio)
δ,δ_{99}	boundary layer thickness
δt	time sampling interval
ϵ	turbulent energy dissipation rate
η	Kolmogorov length scale
κ	von Karman constant
ν	kinematic viscosity
ρ	density
v_ϵ	Kolmogorov velocity scale
ω_i	vorticity vector

Superscripts

′	root mean square
*	non-dimensionalized by wall variables

1. INTRODUCTION

Poisson's equation for the pressure fluctuation in turbulent flow shows that the pressure fluctuation at a point is obtained by integration over the entire velocity field (Townsend 1976 p.43). A Green's function solution for the pressure at a point in the flow, or for the wall pressure in a wall-bounded flow indicates which areas of the velocity field contribute most to the pressure. Using data from a direct numerical simulation of turbulent-channel flow, Kim (1989) shows that although large contributions to the instantaneous pressure at one wall can come from sources near the far wall, contributions to the mean-square wall-pressure fluctuation drop off rapidly with their distance from the wall (see also Kraichnan 1956). An alternative approach for detecting pressure sources used in the past has been to measure a narrow-band-frequency convection velocity of the wall pressure and assume that the associated pressure source in the boundary layer is convected at the local mean velocity (see Bull 1967, Bradshaw 1967, Wills 1970).

The right-hand side of Poisson's equation can be split into rotational and irrotational components.

$$-\frac{\nabla^2 p}{\rho} = e_{ij}\cdot e_{ji} - \tfrac{1}{2}\omega_i^2 \qquad (1)$$

(see Aris 1962 p.97, Bradshaw and Koh 1981), which although not unique (Adrian 1982), is physically meaningful with (in part) measurable terms. Equation (1) describes the generation of pressure fluctuations in terms of two distinct agencies the first term on the right-hand side (referred to as "splat") represents eddy 'collisions' existing near saddle points in the instantaneous stream-function pattern leading to a positive pressure, while the second term (referred to as "spin") represents large local vorticity implying a rapidly rotating eddy with a negative pressure near the axis of rotation. The present work uses this decomposition together with the VITA+LEVEL conditional sampling scheme (Morrison et al. 1989) to detect peaks in the splat and spin signatures immediately above a wall-pressure transducer in a flat-plate, zero-pressure-gradient boundary layer. Correlation of these sources with the wall pressure isolates their contribution to it.

Kim and Lee (1989) have shown that the instantaneous pressure fluctuation from splat and spin contributions are very nearly equal and of opposite sign because $e_{ij}\cdot e_{ji}$ is very nearly equal to $\tfrac{1}{2}\omega_i^2$. However, the present work shows that there are important differences between instantaneous splat and spin contributions (at least in their spanwise components as measured here), most notably near where an "ejection" ($u<0$, $v>0$) or "sweep" ($u>0$, $v<0$) occurs. The detection of ejections and sweeps by use of the VITA+LEVEL conditional sampling scheme operating on the instantaneous uv signature has previously been reported by Morrison and Bradshaw (1989) and Morrison et al. (1991a). Morrison et al. showed that, although ejections are viscous structures, they are part of a larger inertial structure which is the true universal constituent of near-wall

motion. They called these inertial structures "bursts", a more precise extension to the definition originally proposed by Kim et al. (1971), and showed them to be, in fact, Townsend's (1976) "attached" eddies. They further showed that sweeps, which together with ejections effect most of the universal part of spectral energy transfer in the logarithmic region, are also viscous structures, but that in this case, the associated inertial structures are large 'detached' eddies which make the major contribution to inactive motion (Townsend 1961, Bradshaw 1967) in the inner layer. These large eddies were also called splats because that part of the inactive motion caused by pressure fluctuations is generated by the "splatting" mechanism (Moin and Kim 1982): thus the definition of a splat used here is a generalization of that used by Moin and Kim in which a large eddy collides with its instantaneous mirror image at the wall.

2. EXPERIMENTAL ARRANGEMENT

The measurements were made on the floor of a 914 mm x 914 mm closed-circuit wind tunnel, specifically chosen because of its quietness and low vibration. At the traverse position, 3.8 m from the boundary layer trip, the integral parameters are. Re_θ = 14,500, δ^* = 68.2 mm, U_e = 32.8 ms^{-1} and u_τ = 1.09 ms^{-1}. The hot-wire probes, anemometers and data recording equipment were all standard instrumentation, as outlined in Morrison et al. (1989). The signals were recorded on analogue tape and then digitised for subsequent processing in this case, six channels of data were used for which the effective real-time sampling rate was 68,986 sample/s per channel.

Wall-pressure fluctuations were measured using ENDEVCO 8507-2M1 flush-mounted transducers (0 - 2 p.s.i.) for which the associated analogue equipment had a gain-bandwidth product of 6 x 10^6. The effective transducer diameter is approximately d^* = 90. The wall-pressure signal was 'backed-off' by one from a transducer rigidly mounted in the free stream to monitor acoustic resonances, diffuser-induced disturbances and vibration. For further details see Morrison et al. (1991b).

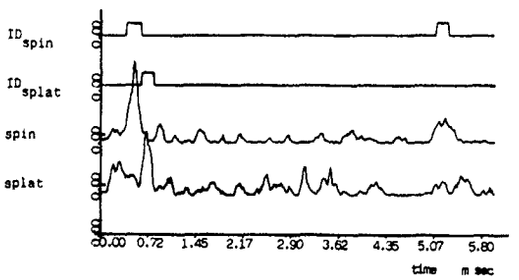

Figure 1. splat and spin signatures with identity traces.

The present work reports wave-number-limited measurements of the spanwise components of strain rate and vorticity made with a four-wire array similar to that used by Foss (1979). Two single hot wires measure $\partial u/\partial y$ directly, while a cross wire between them measures $\partial u/\partial t$ and $\partial v/\partial t$ using Taylor's hypothesis to obtain $\partial u/\partial x$ and $\partial v/\partial x$. The resolution in the two directions is set to be the same, $\delta x = \delta y = 0.0656_{+++}.306\ \nu/u_\tau$. The u-component spectra of Morrison et al. (1991a), taken in the same zero-pressure-gradient boundary layer, indicate that the centroid of the energy-containing range of wave numbers lies at about $k_1 y = 0.18$. Taking the low-wave-number limit of the locally-isotropic range to be say, 20 times this, a worst-case (smallest y) estimate of the largest locally-isotropic wavelength is equal to about half the wire separation, 4.4 mm. This result is important in the interpretation of the results presented in the next section. Subramanian et al., (1985) discuss the resolution of the velocity derivatives in more detail. the restriction of the present data to the low-wave-number end of locally-isotropic turbulence does not preclude a qualitative analysis of the results.

3. RESULTS

In the (x,y)-plane,

$$\text{Splat.}\quad e^2_{xy} = \left(\frac{\partial u}{\partial x}\right)^2 + \tfrac{1}{2}\left(\frac{\partial u}{\partial y} + \frac{\partial v}{\partial x}\right)^2 + \left(\frac{\partial v}{\partial y}\right)^2 , \qquad (2)$$

where the last term was omitted because it is unmeasurable with the present wire array, and.

$$\text{Spin.}\quad \tfrac{1}{2}\omega_z^2 = \tfrac{1}{2}\left(\frac{\partial u}{\partial y} + \frac{\partial v}{\partial x}\right)^2 - 2\,\frac{\partial u}{\partial y}\,\frac{\partial v}{\partial x} . \qquad (3)$$

Peaks in these signatures are identified by the VITA+LEVEL algorithm, see Figure 1. Detection occurs when the short-time variance and amplitude of these signals exceed their thresholds which are multiples of the conventional mean-square and root mean-square (r.m.s.) signal respectively. The thresholds were set by visual examination of the instantaneous splat and spin signatures with the corresponding identity traces. Note that, referred to principal axes, splat becomes $(\partial u/\partial x)^2 + (\partial v/\partial y)^2$ and spin becomes $2(\partial u/\partial y)^2 = 2(\partial v/\partial x)^2$: thus approximately, splats represent large velocity changes along the separation vector while spins represent large velocity changes normal to it.

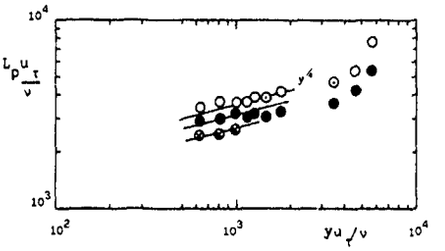

Figure 2. splat, spin periods. ●, splat, ⊙, spin; TH = 0.65. ⊗, splat; TH = 0.4.

Figure 2 shows splat and spin event periods calculated as:

$$L_p = U\left\{\frac{(1-\gamma)}{N}\,T_o + L\,(t/\delta t).\delta t\right\} . \qquad (4)$$

Both splat and spin periods show regions in which they vary as y^4, like the variation of the Kolmogorov length scale deduced by assuming local equilibrium, while the corresponding event lengths (not shown) are approximately constant with y and about one tenth of the corresponding event period. Figure 2 also shows that the y^4 variation persists when splat periods are obtained using a value of threshold reduced by about 40%.

Batchelor and Townsend (1956 p.382) have shown that, at Reynolds numbers high enough for local isotropy, the mean-square pressure gradient and mean-square viscous force, which depend primarily on the small-scale motion, are related by an expression similar to that in isotropic

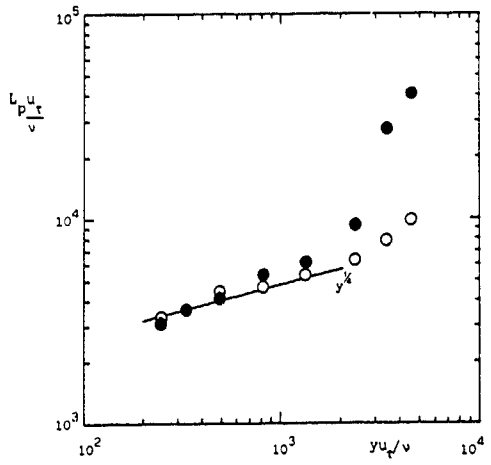

Figure 3. sweep, ejection periods. ●, sweeps; ⊙, ejections.

turbulence, viz.

$$\frac{1}{\rho^2}\overline{\left(\frac{\partial p}{\partial x_i}\right)^2} = 20\,\nu^2\,\overline{\left(\frac{\partial^2 u_i}{\partial x_j^2}\right)^2} \quad . \qquad (5)$$

This shows that the main contribution to the mean-square pressure gradient comes from the smallest eddies, as the viscous force certainly does and that it is independent of Reynolds number. The result implies that even the small scale motion, presumably decaying under the direct influence of viscosity, is driven by peaks in the pressure field from other eddies, and not by viscous forces.

Figure 3 shows event periods generated by application of the VITA+LEVEL algorithm to the uv signature using a threshold that is a universal multiple of the local value of $-\overline{uv}$. Both event lengths and periods show a range in the local-equilibrium region in which they also vary as y^4 (the event lengths are discussed in detail by Morrison et al. 1991a). These results suggest that large excursions in the pressure field, generated by the smallest eddies, trigger the

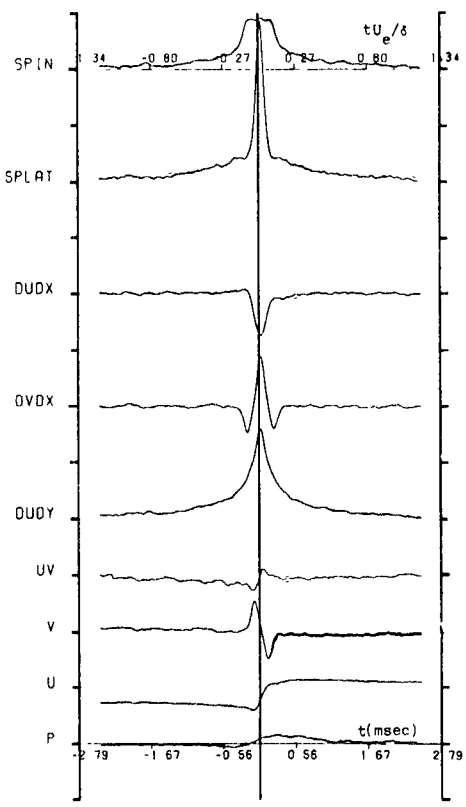

Figure 4. splat-conditioned ensemble-averaged time-histories. 1 vert. division ≡ 0.75 r.m.s. $y/\delta = 0.132$.

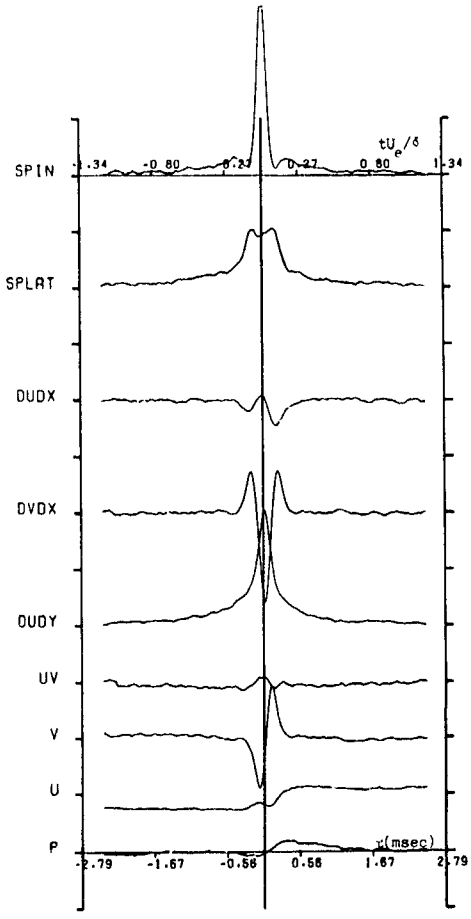

Figure 5: spin-conditioned ensemble-averaged time-histories. 1 vert. division ≡ 0.75 r.m.s. $y/\delta = 0.132$.

bursting sequence and therefore determine its average frequency, as initially suggested by Offen and Kline (1975) and Willmarth (1975), but more recently by the calculations of Aubry et al. (1988).

Moreover, the largest pressure gradients are most likely to occur in regions in which a splat (high pressure) follows a spin (low pressure) or vice versa, and these viscous periods are likely to coincide with either ejections or sweeps or even a combination of both types of event. These results therefore clearly suggest a burst-sweep regenerative cycle which is similar to the Offen and Kline model. In the local-equilibrium region simple scaling laws apply: the expression in equation (5) is proportional to $\varepsilon^{3/2}\nu^{-2}$, so that, where pressure changes occur over distances that are proportional to η, $\delta p'/\rho \propto v_\eta^2$, and, taking $\varepsilon = u_\tau^3/y$,

$$\frac{y}{u_\tau^2}\frac{\partial p'}{\partial x_1} \propto (y^+)^{1/4} \quad . \qquad (6)$$

Thus both the r.m.s. pressure gradient due to splats and spins and the periods between ejections and sweeps, when scaled with wall variables, are proportional to $(u_\tau\delta/\nu)^{1/4}$ for a fixed value of y/δ. See also Morrison et al. (1991b).

Figures 4 and 5 show ensemble-averaged time-histories for splat and spin events respectively, where the vertical centre line corresponds to the centre of events and about which the ensembles are generated. They are non-dimensionalized by the conventional r.m.s. quantities. The principal difference between splat and spin events is the sign of the large peak in $\partial v/\partial x$, as the usual form of the linear (or rapid) source term in Poisson's equation would imply. Quadrant-two motion occurs downstream of the splat-event centre while, in the case of spin events, quadrant-two motion occurs upstream of the event centre. Quadrant-four motion does not appear to be evident. The measured conventional r.m.s. quantities show that $\partial u'/\partial y$ is about 1½ - 2 times $\partial v'/\partial x$. Thus vorticity is large and negative in a spin and strain rate is large and positive in a splat. The wall-pressure ensembles are similar in both cases although it is positive at the centre of a splat but negligibly small at the centre of a spin. None of the ensembles change significantly in character for sampling at larger y/δ.

Figures 6 and 7 show sweep and ejection ensembles respectively: in the case of ejections, the negative vorticity just before detection produces low wall pressure and the positive strain rate just after detection increases the wall pressure. Thus $\partial p/\partial x$ is negative during an ejection while $\partial u/\partial x$ is negligible. The wall pressure during a sweep is dominated by the effects of the associated large-scale splat, particularly at the downstream end of the sweep (see Morrison et al. 1991b) where the wall pressure is large and positive. Although $\partial p/\partial x$ and $\partial u/\partial x$ are of opposite sign immediately downstream of an ejection, $u<0$ also so that Bernoulli's equation is not an accurate approximation for these times. However, immediately downstream of a sweep, $u>0$ and $\partial p/\partial x$ and $\partial u/\partial x$ are again of opposite sign suggesting that here the motion is primarily inertial. Note also that, immediately downstream of ejections and sweeps, $\partial v/\partial x$ is large and of the right sign to suggest that $\frac{\partial U}{\partial y}\frac{\partial v}{\partial x}$, the linear term in Poisson's equation, dominates at these times. These conclusions are corroborated by the splat and spin ensembles.

Figures 8 and 9 show conventional and conditional correlations of velocity derivatives with the wall pressure non-dimensionalized by conventional r.m.s. quantities negative time

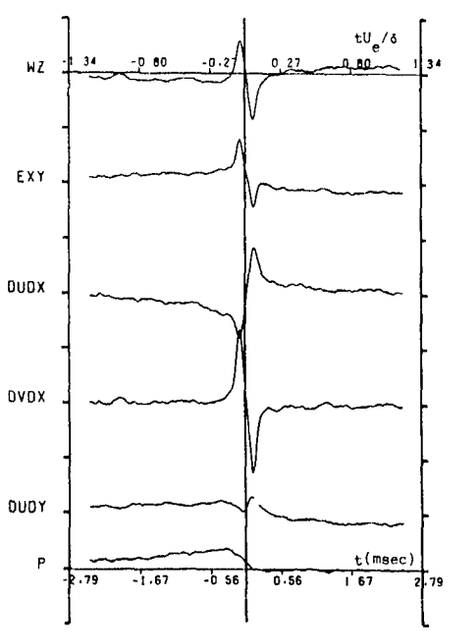

Figure 6 sweep-conditioned ensemble-averaged time-histories. 1 vert. division ≡ 0.75 r.m.s. y/δ = 0.132.

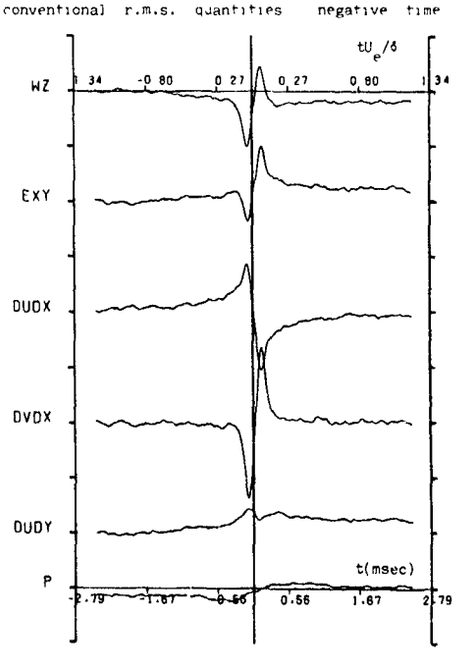

Figure 7. ejection-conditioned ensemble-averaged time-histories. 1 vert. division ≡ 0.75 r.m.s. y/δ = 0.132.

delay corresponds to a positive, downstream displacement of the wire array with respect to the wall sensor. The conditional correlations during splat (Figure 8) and spin (Figure 9) events are expressed as a contribution to the total correlation. Splat and spin correlations are both dominated by large $\partial u/\partial y$, which behaves similarly during splat and spin events (Figures 4 and 5). However, the major difference between the two sets of conditional correlations lies in the nature of the $\overline{p\partial v/\partial x}$ correlation. Its positive value during a splat together with the large positive peak in the $\partial v/\partial x$ ensemble confirms that the rapid term in the usual form of Poisson's equation dominates at these times. But in the spin correlation, $\overline{p\partial v/\partial x}$ changes sign with a negative peak at detection even though the corresponding $\partial v/\partial x$ ensemble also shows a negative peak, implying that the wall pressure would be positive even though the ensemble shows it to be negative. Therefore it is unlikely that the rapid term dominates during a spin and the pressure-generation mechanisms probably involve non-linear terms in this case.

These results suggest the presence of a cyclic process at the wall: a large splat initiates an ejection which has large negative vorticity (spin) at its downstream end. The ejection is toppled by mean vorticity (Morrison et al. 1991a) to produce a sweep further downstream. During this process, the 'detached' burst develops into the associated splat, which subsequently initiates an ejection further downstream. This process is very similar to that described by Offen and Kline, except that the wall-pressure gradient, $\partial p/\partial x$, is favourable beneath an ejection (Figure 7), as Thomas and Bull (1983) also found. See Morrison et al. (1991b) for a fuller discussion.

4. DISCUSSION AND CONCLUSIONS

The VITA+LEVEL algorithm has been used successfully to detect peaks in the instantaneous

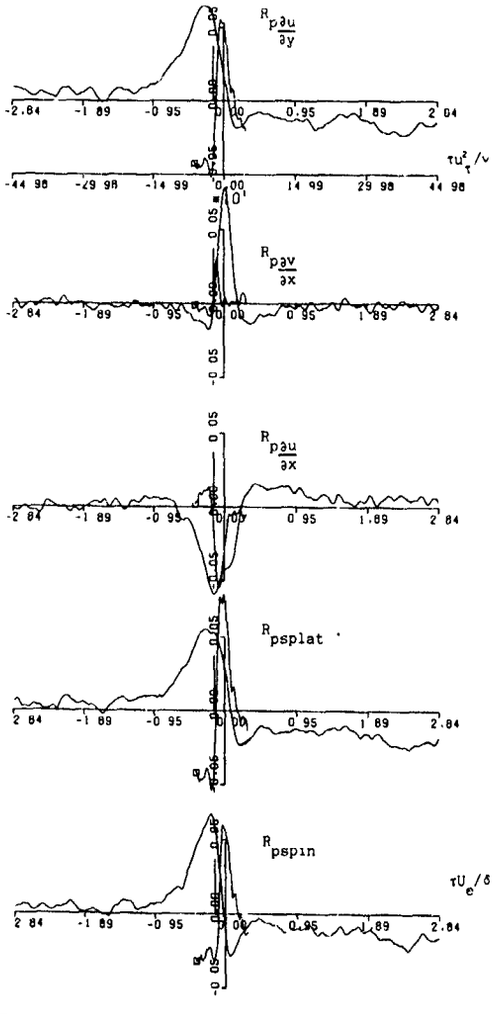

Figure 8. conventional and splat-conditioned (—⊡—) space time correlations with wall pressure. $y/\delta = 0.132$.

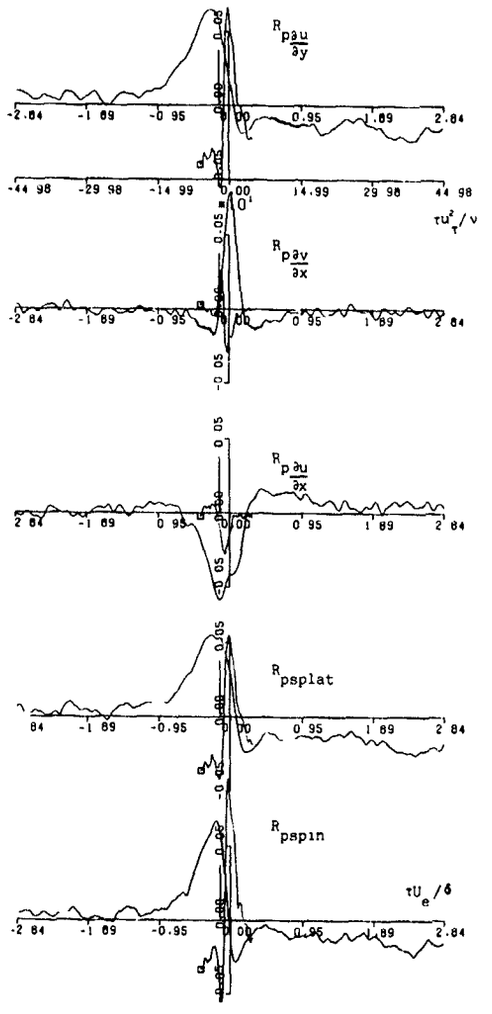

Figure 9 conventional and spin-conditioned (—⊡—) space-time correlations with wall pressure. $y/\delta = 0.132$.

splat and spin signatures. The results show that the spanwise components of $e_{ij}.e_{ji}$ do not always equal those of $\frac{1}{2}\omega_i$ and that the times at which the differences are most apparent play an important part in the bursting process. The period between an ejection and a succeeding sweep (or vice versa) contains numerically large $\partial v/\partial x$, which has the effect of producing large spin, small splat or large splat, small spin depending on its sign. Splat and spin durations occupy (exclusively) about 10% of the time each. Thus these results are not inconsistent with those of Kim and Lee (1989), who showed that the left-hand side of equation (1) is the small difference between two large quantities. The explanation is that shear-layer turbulence consists predominantly of vortex sheets or internal 'shear layers' which have nearly opposite e_{ij} and ω_i and, being approximately plane with nearly-straight streamlines, do not contribute significantly to the pressure.

The exceptions to this general description appear to play an important role in generating pressure fluctuations which drive the bursting sequence. These important pressure gradients are proportional to v_ϵ^2/η in the local equilibrium region. Moreover, the frequency of ejections and sweeps in the local equilibrium region is proportional to $(u_\tau\delta/\nu)^{-\frac{1}{4}}$ when scaled with wall variables. This calls into question the accuracy of wall-variable scaling for the shear-stress-producing eddies, which is usually accepted as a consequence of wall-variable scaling for the mean motion. These results also highlight the importance of the higher wave numbers of the uv cross spectrum (or the momentum field in general) that overlap with the pressure gradient spectra which reach a maximum in the locally-isotropic range of wave numbers. Furthermore, it should be noted that the present measurements are at high enough Reynolds number for the energy-containing and dissipating ranges of wave number to be well separated, whereas in Kim and Lee's low-Reynolds-number simulation, these ranges are less distinct and therefore may affect each other's eddy structure.

ACKNOWLEDGEMENTS

The work was carried out in the Department of Aeronautics, Imperial College; Dr. C.S. Subramanian's help with the four-wire array is gratefully acknowledged. We are indebted to the United States Army for financial support.

REFERENCES

ADRIAN, R.J. 1982. Comment on "A note on Poisson's equation for pressure in a turbulent flow". Phys. Fluids 25, 577.

ARIS, R. 1962. Vectors, Tensors and Equations of Fluid Mechanics. Prentice Hall, Englewood Cliffs, N.J.

AUBRY, N., HOLMES, P., LUMLEY, J.L. and STONE, E. 1988. The dynamics of coherent structures in the wall region of a turbulent boundary layer. J. Fluid Mech. 192, 115.

BATCHELOR, G.K. and TOWNSEND, A.A. 1956. Turbulent diffusion. In: Surveys in Mechanics. (Eds. G.K. Batchelor and R.M. Davies) C.U.P.

BRADSHAW, P. 1967. "Inactive" motion and pressure fluctuations in turbulent boundary layers. J. Fluid Mech. 30, 241.

BRADSHAW, P. and KOH, Y.M. 1981. A note on Poisson's equation for pressure in a turbulent flow. Phys. Fluids 24, 777.

BULL, M.K. 1967 Wall-pressure fluctuations associated with subsonic turbulent boundary layer flow. J. Fluid Mech. 28, 719.

FOSS, J.F. 1979. Transverse vorticity measurements. Dynamic Flow Conference, Skovlunde, Denmark. DISA A/S.

KIM, H.T., KLINE, S.J. and REYNOLDS, W.C. 1971. The production of turbulence near a smooth wall in a turbulent boundary layer. J. Fluid Mech. 50, 133.

KIM, J. 1989. On the structure of pressure fluctuations in simulated turbulent channel flow. J. Fluid Mech. 205, 421.

KIM, J. and LEE, M.J. 1989. The structure of pressure fluctuations in turbulent shear flows. Seventh Symposium on Turbulent Shear Flows. Stanford Univ. U.S.A. Pap. No. 1-1.

KRAICHNAN, R.H. 1956. Pressure fluctuations in turbulent flow over a flate plate. J. Acoust. Soc. Am. 28, 378.

MOIN, P and KIM, J. 1982. Numerical investigations of turbulent channel flow. J. Fluid Mech. 118, 341.

MORRISON, J.F., TSAI, P M. and BRADSHAW, P. 1989. Conditional sampling schemes for turbulent flow based on the variable-interval time-averaging (VITA) algorithm. Expts. Fluids. 7, 173.

MORRISON, J.F. and BRADSHAW, P. 1989. Bursts and wall shear stress fluctuations in turbulent boundary layers. Seventh Symposium on Turbulent Shear Flows. Stanford Univ. U.S.A. Pap. No. 2-2.

MORRISON, J.F., SUBRAMANIAN, C.S. and BRADSHAW, P. 1991a. Bursts and the law of the wall in turbulent boundary layers. Submitted to J. Fluid Mech.

MORRISON, J.F., SUBRAMANIAN, C.S. and BRADSHAW, P. 1991b. Bursts and pressure fluctuations in turbulent boundary layers. Submitted to J. Fluid Mech.

OFFEN, G.R. and KLINE, S.J. 1975. A proposed model of the bursting process in turbulent boundary layers. J. Fluid Mech. 70, 209.

SUBRAMANIAN, C.S. KANDOLA, B.S. and BRADSHAW, P. 1985. Measurements of the low-wave-number structure of a turbulent boundary layer. Imperial College Aero. Rep. No. 85-01.

THOMAS, A.S.W. and BULL, M.K. 1983. On the role of wall-pressure fluctuations in deterministic motions in the turbulent boundary layer. J. Fluid Mech. 128, 283.

TOWNSEND, A.A. 1961. Equilibrium layers and wall turbulence. J. Fluid Mech. 11, 97.

TOWNSEND, A.A. 1976. The Structure of Turbulent Shear Flow. 2nd ed. C.U.P.

WILLMARTH, W.W. 1975. Structure of turbulence in boundary layers. Adv. Appl. Mech. 15, 159.

WILLS, J.A.B. 1970. Measurements of the wave-number/phase-velocity spectrum of wall pressure beneath a turbulent boundary layer. J. Fluid Mech. 45, 65.

EIGHTH SYMPOSIUM ON
TURBULENT SHEAR FLOWS
Technical University of Munich
September 9-11, 1991

THREE-DIMENSIONAL VORTICAL STRUCTURE OF A LARGE SCALE COHERENT VORTEX IN A TURBULENT BOUNDARY LAYER

H. Makita and K. Sassa

Dept. of Energy Engineering, Toyohashi University of Technology
1-1 Tenpaku-cho, Toyohashi 441, Japan

ABSTRACT

The streamwise evolution of three dimensional structure of an artificially induced vortex was pursued by measuring velocity and vorticity fields through a simplified conditional sampling. The artificial vortex developed downstream through the growth, the self preserving and the decay stages. In the growth stage, the vortex grew up to have a horseshoe sculpture and the vorticity confined in it was increased downstream. The grown-up large-scale horseshoe vortex reached about 1.2δ in height, 1.0δ in width and 5.0δ in streamwise length. The vortex became more inclined forward and lost the ability of maintaining its self-similar construction in the decay stage. The convection velocity of the vortex's head was $0.56U_\infty$ in the foregoing two stages and was raised to $0.85U_\infty$ in the decay stage.

NOMENCLATURE

L_x, L_y, L_z	streamwise, normal, and spanwise scales of a large-scale coherent vortex, respectively
Re_θ	Reynolds number based on the momentum thickness
u, v, w	streamwise, normal, and spanwise components of fluctuating velocity, respectively
t	time
U	local mean velocity
U_c	convection velocity of a large-scale vortex
U_∞	free-stream velocity
X, Y, Z	streamwise, normal, and spanwise coordinates, respectively
Ω_z	integrated value of spanwise vorticity
δ	boundary layer thickness
$\|\omega\|^2$	enstrophy
ω_x, ω_y, ω_z	streamwise, normal, and spanwise vorticity, respectively

SUPERSCRIPTS

$(\ )'$	rms value
$\langle\ \rangle$	ensemble-averaged value

INTRODUCTION

Large-scale coherent structures are thought to play important roles in momentum and energy transfer across a turbulent boundary layer. As Kline & Robinson (1989) summarized, the large-scale u-discontinuity spontaneously observed in the turbulent boundary layer reported by Brown & Thomas (1977), Eckelmann et al. (1977), and Platuri & Brodkey (1978) and the turbulent bulge measured by Kovasznay et al. (1970) can be related to the large-scale coherent structures. These observations, however, have caught a large-scale coherent structure only by some characteristic features and also suggest the existence of a large-scale vortical motion in the boundary layer. Actually, many vortical structures, such as an arch, a horseshoe, or a hairpin, have been proposed based on the results of flow visualizations and hot-wire measurements, as reviewed by Robinson (1989).

The coherent vortex has a complex three-dimensional configuration and appears randomly in time and space in a turbulent boundary layer. Moreover, its vortical structure is ambiguous buried in the background turbulence. It is difficult for the hot-wire measurement to catch an arbitrary portion of the vortical structure reaching some stage of the vortex's streamwise growth during its lifetime. As for the authors' knowledge, several researchers, such as Fukunishi & Sato (1987) and Antonia & Bisset (1991), have tried to clarify the three-dimensional structure of the coherent vortex. They gave the coherent vortex similar configurations like a horseshoe, of which the detailed features were, however, still dependent upon the sampling conditions employed in each measurement.

The hot-wire measurements have given only obscure images for the large-scale coherent vortex in a turbulent boundary layer. It is easy to get a two-dimensional image of the coherent vortex by flow visualization. Usually, photographs on visualized planes can not give so much quantitative information, which sometimes causes the lack in objectivity in the interpretation of the observed results. With such experimental difficulties, it seems hopeless to pursue the horseshoe vortex changing its three-dimensional configuration from its birth to death. Antonia & Bisset (1991) suggested that there was no way except for numerical simulations to solve these difficulties. Kim (1987) and Robinson et al. (1989) showed the vortical structure by using LES and DNS numerical methods. Their results, however, seem to have a few doubts because of the assumptions in their calculations, such as the periodic boundary condition.

The present experiment aims to describe the aspect of streamwise evolution of the large scale coherent vortex by determining its three-dimensional vortical structure. In order to make the detection by the hot-wire easy, we tried to induce an artificial coherent vortex having the structure same as a natural one in a fully developed turbulent boundary layer, as shown by Makita et al. (1988, 1989). The other types of the artificial generation of coherent structures were examined by Viets et al. (1981) and Gad-el-Hak et al. (1986, 1987). But for Gad-el-Hak & Hussain (1986), these works seem more interested in the problem of boundary layer control than the detection of the characteristic quantities of the coherent structures. In the present experiment, a seed of the coherent vortex was formed in the lower part of a fully developed turbulent boundary layer. Concentrated spanwise vorticity, ω_z, was induced there through the injection of a pair of fine swirling jets from the flat plate beneath. The existence of the spanwise vorticity in a natural large-scale coherent motion was reported by Platuri & Brodkey (1978). Fukunishi et al. (1987) showed the possibility that a small perturbation of the spanwise vorticity placed in a shear layer grew up to be a large-scale horseshoe vortex, using the vortex filament method. In the present experiment, the vorticity seed was observed to grow up to be a large-scale horseshoe vortex as it drifted downstream. The velocity vectors and the

vorticity components were measured about the artificially induced vortex to pursue the streamwise development of its three dimensional configuration.

EXPERIMENTAL PROCEDURE

As shown in Fig. 1 a turbulent boundary layer without a pressure gradient was developed on a smooth flat plate made of glass settled in a wind tunnel test section of 0.42 × 0.42 × 5.7 m³. No. 40 sand roughness was pasted near the leading edge for 100 mm in streamwise length. The free-stream velocity U_∞ was 5 m/sec and the turbulence level of the free stream, u'/U_∞, was less than 0.1 %. The Reynolds number based on the momentum thickness, Re_θ, was about 1820 at 2 m downstream from the leading edge where a pair of injection slots was placed on the flat plate. The slots were 2 mm in diameter and placed 20 mm apart from each other. They were inwardly facing at the injection angle of ± 45 deg. Swirlers were inserted in the conduits to the slots. As a loud speaker pump was driven, small puffs of swirling jets were ejected from the injection slots. The puffs were connected at about $Y = 0.26\delta$ ($\delta \approx 40$ mm) above the center of the slots and immediately formed a seed of a coherent vortex, having a top spin rotation. The spanwise vorticity, ω_z, had the same sign as that of the mean velocity gradient there. The volume of puffs per each injection was about 0.16 cc, and confirmed not to affect the macroscopic structure of the boundary layer if the jets were not swirled. The coordinates system was set as shown in Fig. 1 and its origin was at the center of the slots.

Measurements were made by using an X-wire or a triple (X) wire probe and constant temperature hot-wire anemometers. The probes were made of tungsten wire of 2.5 μm in diameter and their measuring volumes were 0.7 × 0.7 × 0.2 mm³ (X-wire) and 0.7 × 0.7 × 0.3 mm³ (triple wire). The triple wire was used to eliminate the effect of shear normal to the X-Z plane in the simultaneous measurement of u- and w-components. The anemometers had a good S/N ratio of more than 72 dB and a frequency response flat from DC to about 20 kHz. The data sampling was conditioned by the raising of electric pulses to drive a speaker pump and proper delay time was taken to compensate the travel time of the coherent vortex from the origin to the measuring point. By the present experimental scheme, any arbitrary portion of the coherent vortex can be detected when it reaches the previously imagined stage of its streamwise growth only by traversing the hot-wire probe. The sampled data were ensemble averaged for 1024 times by a 12-bit digital signal analyzer. The temporal resolution of the analyzer was 0.4 msec. The ensemble-averaged velocity fluctuations, $\langle u \rangle$, $\langle v \rangle$ and $\langle w \rangle$, were obtained at several streamwise positions between $X/\delta = 0.13$-45.0. At each streamwise position, the measurements were made at 14 × 13 points locating in every 0.1δ steps in both normal and spanwise directions. In this way, the timewise charts of the ensemble averaged velocity fields were obtained for the coherent structure, see Makita et al. (1989). The ensemble averaged values of the vorticity components, $\langle \omega_x \rangle$, $\langle \omega_y \rangle$ and $\langle \omega_z \rangle$, were numerically calculated from these averaged velocities and their distributions were mapped. The streamwise derivative, $\partial / \partial X$, was obtained from the time derivative, $\partial / \partial t$, assuming Taylor's frozen pattern hypothesis. The error by applying the Taylor's hypothesis on the shear layer was almost negligible in the present case, because the contribution of the term, $\partial / \partial t$, was at most 10 % of each coherent vorticity component, $\langle \omega_y \rangle$ or $\langle \omega_z \rangle$.

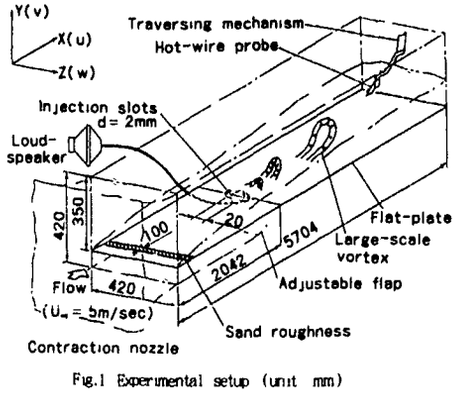

Fig.1 Experimental setup (unit mm)

SYMMETRY OF THE VORTICAL STRUCTURE

Blackwelder (1988) pointed out that coherent structures obtained from conventional ensemble averaged data were apt to become symmetrical even if the individual realizations of the coherent structure were asymmetrical. Actually, some of the recent numerical (Robinson et al. 1989) and experimental (Antonia & Bisset 1991) studies showed that most of individual vortices had asymmetric structure and the symmetric one was rare. In the present study, the magnitude of the initially given artificial disturbance was in the same order as the background turbulence level. Therefore, the individual artificial vortex was also asymmetrical strongly deformed by the background turbulence.

Adding further sampling conditions so as to detect the asymmetry would spoil the expediency of the present method and we can show only averaged symmetric images of the coherent structure. We prefer the averaged symmetric structure as an idealized macroscopic model of the large-scale coherent vortex to the individual asymmetric one. Different from the case of small-scale coherent vortices in the inner layer, the large-scale vortices involve smaller turbulent eddies or random velocity fluctuations in itself. We assume that the asymmetric configuration of the individual vortex results from the superposition of the smaller turbulent eddies on the large-scale symmetric coherent structure. We consider it more useful to grasp the averaged structure in order to clarify the dynamics of the large-scale vortex than to determine the minute structure of the individual vortices deformed by such fine-scale structures.

RESULTS AND DISCUSSION

1. STREAMWISE EVOLUTION OF THE LARGE-SCALE VORTEX

Figs. 2a-e show the distributions of velocity vectors at several streamwise locations to explain the aspect of the streamwise evolution of the artificial vortex. Velocity field around the artificial vortex on the Y-Z plane at $Z/\delta = 0$ is shown in each figure. The abscissa of the figures represents the time, t, passing from right to left. The right-hand side also corresponds to the downstream side of X-direction in each figure. Each arrow in the figures denotes the relative velocity induced by the large-scale artificial vortex from which the local mean velocity of the background turbulent boundary layer is subtracted, $(\langle u \rangle, \langle v \rangle)$. Kovasznay et al. (1970) and Brown & Thomas (1977) showed the velocity vectors as ensemble-averaged velocities subtracted the convection velocity of the coherent structure, $(\langle U + u \rangle - U_c, \langle v \rangle)$. Their representation may show the vortical motion more properly, if the convection velocity of the large-scale vortex is uniform across the turbulent boundary layer. As described later, the convection velocity varies with the portion of the large-scale vortex. The present method of representation gives at least the fluid motion induced by the coherent vortex correctly, though it can not give the completely accurate image of the vortical motion about the coherent structure.

As shown in Fig. 2a, a flow field overlapped by upward

and circulating fluid motions is observed at $X/\delta = 0.5$ just downstream of the injection slots. Such fluid motions, directly induced by the injection of the swirling jets, have not still formed a typical pattern of the induced flow field around the coherent vortex. In the further downstream region of $X/\delta = 2.5$-5, the strong low-speed outflows are observed for $Y/\delta \lesssim 0.8$. Fukunishi & Sato (1987) got a similar flow pattern for a natural large-scale coherent vortex. The outflow resembles to the ejection for the natural small-scale coherent motion in the inner layer (e.g. Willmarth & Lu 1972). The weak clockwise circulating motion existing for $Y/\delta > 0.8$ shows the head of the artificial vortex. The head reached the outer edge of the superlayer at about $X/\delta \approx 12$ downstream of the slots and it became a turbulent bulge (Makita et al. 1988). The momentum in the free-stream is entrained by such fluid motion. The outward motion of the upstream border (back) shows so-called the 'large-scale (δ-scale) u-discontinuity' as observed by Brown & Thomas (1977). In Figs. 2b-e, the magnitude and upward angles of the arrows showing low-speed outflows decrease downstream for about $X/\delta > 2.5$. It shows that the induced velocity decays downstream, and the $\langle v \rangle$-component decays more rapidly. In more downstream region of $X/\delta > 12$, the artificial vortex becomes gradually fragile and more inclined forward as also reported by Antonia & Bisset (1991), keeping its size almost unaltered, see Figs. 2d-e. The convection velocity is known to vary with the portion of the vortex. Judging from the velocity fields, the artificial vortex kept its coherency until about $X/\delta = 45$.

Figures 3a-e present the contour maps of the spanwise vorticity component, $\langle \omega_z \rangle$, on the symmetry plane of the artificial vortex ($Z/\delta = 0$). If the artificial vortex has a horseshoe configuration, it is shown by the distribution of clockwise (negative) vorticity on its symmetry plane. At $X/\delta = 0.5$, the vorticity distributes in a quite complicated manner maintaining the effect of the injection of the swirling jet. Roughly speaking, $-\langle \omega_z \rangle$ distributes upper side of the structure of about $Y/\delta > 0.4$ and $+\langle \omega_z \rangle$ is observed for about $Y/\delta < 0.4$. Such features of the distributions tell us that the induced vorticity has not yet attained the self-similar configuration of the horseshoe vortex there. The upper area of $-\langle \omega_z \rangle$ grows to be the head of a horseshoe vortex as it flows downstream. The lower side $+\langle \omega_z \rangle$ may be a secondary vortex induced between the head of the vortex and the flat plate as suggested by Jiménez et al. (1988). The peak point of $\langle \omega_z \rangle$ shifts upstream in the artificial vortex with the outward growth of the vortex downstream, see Figs. 3a-d. This fact says that the vorticity peak in the large-scale coherent vortex shifts downstream at the velocity smaller than the drift velocity of the coherent vortex. This deceleration of the peak is caused by the influence of the self-induced low-speed outflow shown in Figs. 2b-d. The profile of the artificial vortex stands upright on the flat plate for $X/\delta \lesssim 2.5$. As shown in Fig. 3d, the artificial vortex becomes slightly inclined downstream with its head reaching $Y/\delta \approx 1.2$ at about $X/\delta = 14$. Fig. 3e shows the contour map of $X/\delta = 35$, far downstream region from the slots. Here, the large-scale coherent vortex is split into small blocks before it is smeared out by the background turbulence in the final stage of its streamwise decay.

The positive and negative spanwise vorticities on the symmetry plane ($Z/\delta = 0$) were independently integrated as

$$|\pm\Omega_z| = \iint \frac{|\pm\langle \omega_z(X, Y)\rangle|\delta}{U_\infty} dXdY, \qquad (1)$$

where Ω_z denotes circulation on the symmetry plane. The streamwise integration was converted from the timewise one. The streamwise change in $|\pm\Omega_z|$ is plotted in Fig. 4. It must be noticed that $|-\Omega_z|$ increases in almost proportion to X/δ in the initial growth stage of about $X/\delta \lesssim 2.5$. The seed of artificial vortex seems to be fostered to be a

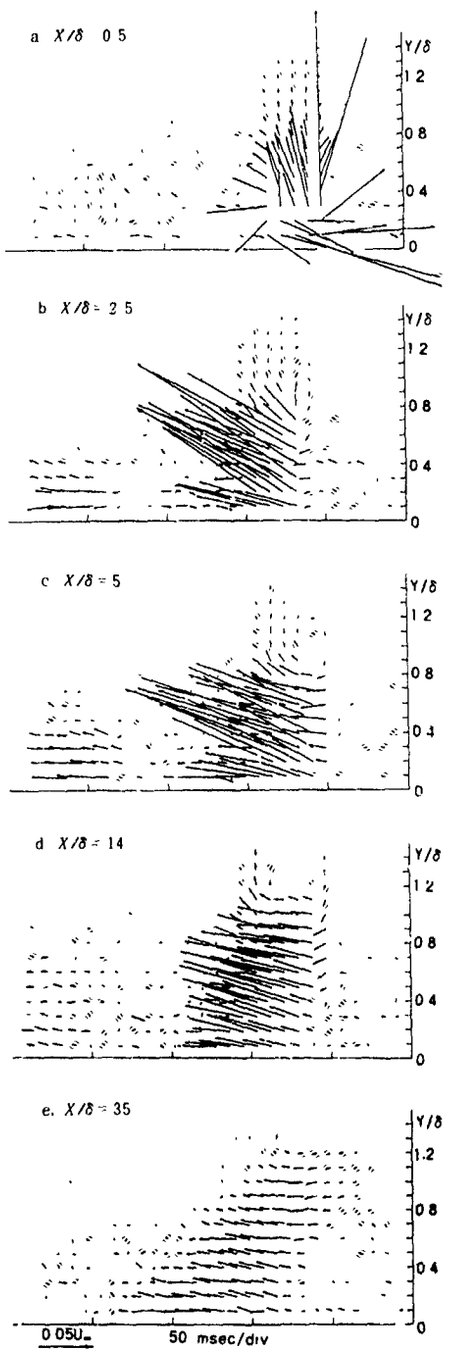

Fig. 2 Induced velocity vectors around the artifical vortex on symetrical T-Y plane ($Z/\delta = 0$) at several streamwise locations. The magnitude of arrow shown bottom of the figures denotes $0.05U_\infty$.

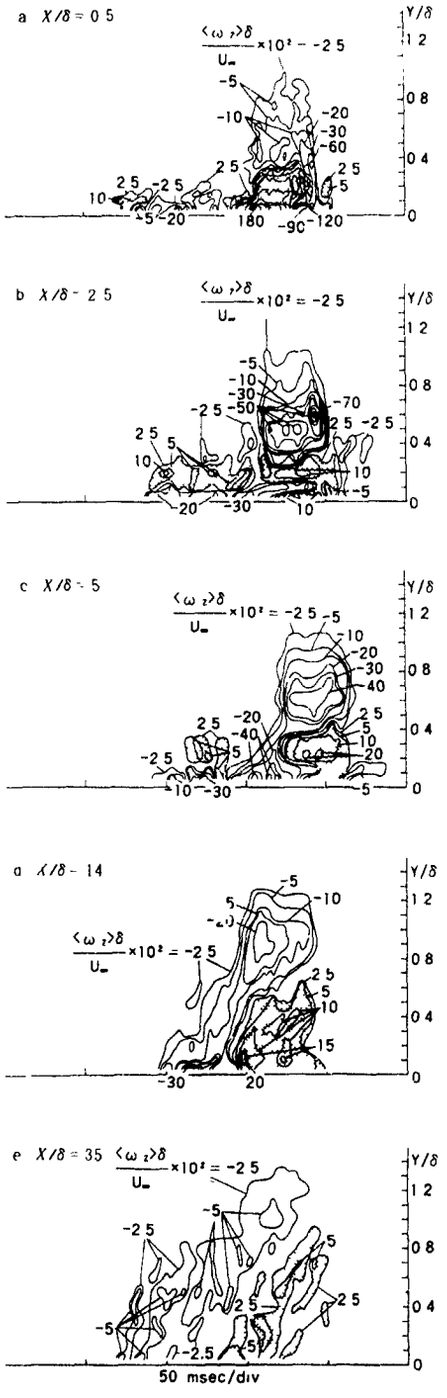

Fig 3 Contour maps of spanwise vorticity, ω_z, on symmetrical I-Y plane ($Z/\delta = 0$) at several streamwise locations. Hatched area denotes $+\omega_z$ distribution

grown-up coherent vortex having naturally receptible structure in the turbulent boundary layer by the velocity gradient, as it travels downstream in the region It is inferred that the artificial vortex becomes able to act as a natural large scale vortex before X/δ 2 5. In the self-preserving stage of about X/δ 2 5 7 5 the height of the coherent vortex gradually increases downstream but $|-\Omega_z|$ is kept almost unaltered In the final decay stage for $X/\delta \geq 7\ 5$, $|-\Omega_z|$ decays monotonously downstream at the slope of about -1.

The convection velocity, U_c, of the large-scale vortex was estimated from the streamwise shift of the vorticity peak in the head It was about $0\ 56U_\infty$ in the growth and the self-preserving stages In the decay stage, U_c was raised to $0\ 85U_\infty$ which was almost equal to the local mean velocity, U, at the peak position.

Good coherency in vortical structure of the large-scale vortex is maintained at most until the beginning of the decay stage. There, the large-scale vortex is known to play some active roles in the momentum and energy transport across the turbulent boundary layer In the decaying stage, the large-scale vortex seems to become merely conveyed downstream on the local mean velocity as a weak structure having only passive functions for the transport process The decay stage is the longest in the total lifetime of the artificial vortex. Not the smaller part of the natural turbulent bulges ever observed in boundary layers is, we guess, such passive structure. The large-scale coherent structure is weakly organic, except for younger one, and does not play important rolls in dynamics of the transport mechanism in a turbulent boundary layer.

At the beginning of the initial growth stage, $|+\Omega_z|$ apparently exceeds $|-\Omega_z|$ This may be because some excessive positive circulation is induced by some extra initial disturbances, such as the mass effect of the injected puffs and the backward motion of the speaker pump in addition to the direct secondary induction by the vortex. $|+\Omega_z|$ decreases monotonously downstream to be smaller than the negative value for $X/\delta \geq 1.25$ The fact implies that it is difficult for the excessive positive vorticity given to the counter clockwise vortex to persist so long in the turbulent boundary layer.

2. THREE-DIMENSIONAL STRUCTURE OF THE LARGE-SCALE VORTEX

As mentioned before, the artificial vortex has only passive structure in the decay stage. Most of the natural large-scale vortices ever observed are, however, those in the decay stage To show the three-dimensional structure

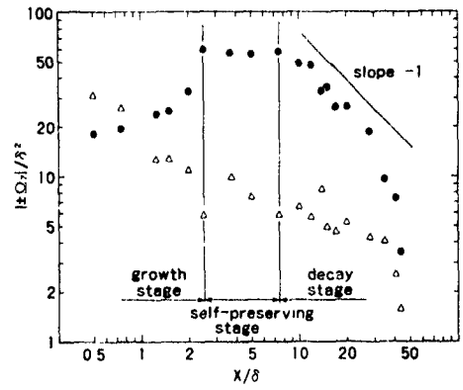

Fig 4 Streamwise evolution of circulation, $|\pm\Omega_z|$, on the symmetrical plane. ● integrated for negative vorticity, △ integrated for positive vorticity

of the artificial vortex, the distributions of vorticity components at $X/\delta = 14$ are illustrated with respect to $\langle \omega_z \rangle$, $\langle \omega_x \rangle$ on the T-Y planes in Figs. 5, 6 and to $\langle \omega_y \rangle$ on the T-Z planes in Fig. 7. Though it is already at the beginning of the decay stage, the coherent vortex still holds the typical self-consistent structure of a horseshoe vortex so well. The distribution of $-\langle \omega_z \rangle$ in Fig. 5 shows the head of horseshoe on the symmetry plane. Outside of the artificial vortex at $Z/\delta = 0.6$, the island of $+\langle \omega_z \rangle$ seems to be a dominant structure, which shows a neighbouring secondary vortex induced by the original artificial one.

Different from the case of $\langle \omega_z \rangle$, the distributions of $+\langle \omega_x \rangle$ and $+\langle \omega_y \rangle$ locate apart from the symmetry plane as shown in Figs. 6 and 7, respectively. These distributions show the existence of a pair of the vortex tube inclined downstream, constituting the legs of the horseshoe vortex. The rate of contribution of three vorticity components to the total vorticity contained in the coherent vortex is nearly the same among them. Antonia & Bisset (1991) obtained the arrangement of the head and the legs similar to that presented here for the natural large-scale vortex.

Three-dimensional distributions of vorticity vectors and ensemble-averaged enstrophy, $|\omega|^2 = \langle \omega_x \rangle^2 + \langle \omega_y \rangle^2 + \langle \omega_z \rangle^2$, obtained from three vorticity components are shown in Fig. 8 and 9, respectively. The vorticity vectors show a half view of the horseshoe configuration of the large scale vortex cut by the symmetry plane. Kim (1987) obtained a similar configuration for a large-scale vortex in a parallel pipe flow by the numerical simulation. The axes of the vortex tubes are located at $Z/\delta \approx \pm 0.2$ and inclined forward at the angle of about 50 deg to the flat plate. The inclination angle is close to the value given by Head and Bandyopadhyay (1981). But, the coherent vortex becomes more inclined in more downstream region, as described before. The distribution of $+\omega_x$ shows that the strength of the vortical motion is highest at the leg. The large scale coherent structure was apt to be grasped as a spanwise vortex, as observed by Platuri & Brodkey (1978). The present result shows that the dominant part of the vortical motion exists not at the head shown by spanwise vortex but at the legs of the horseshoe sculpture.

3. RELATION BETWEEN THE VORTEX AND THE OTHER COHERENT STRUCTURES

We propose a model of the large-scale coherent vortex as illustrated in Fig. 10. It has a horseshoe sculpture. The scales of the horseshoe vortex determined from the vorticity maps were about 5δ in streamwise scale, 1.2δ in height, and δ in horizontal span. The magnitude of the scales agrees well with that experimentally given for the natural large-scale coherent vortex as reviewed by Cantwell (1981). The longitudinal scale is, however, a little larger for the present case. The head forms the turbulent bulge in the superlayer and the fluid motion on the upstream side (the back) causes the u-discontinuity, as described in Section 1. The large-scale vortex is known to induce the coherent motions, such as the outflow around the symmetry plane as shown in Fig. 2d and the 'inrush' in the outside part of

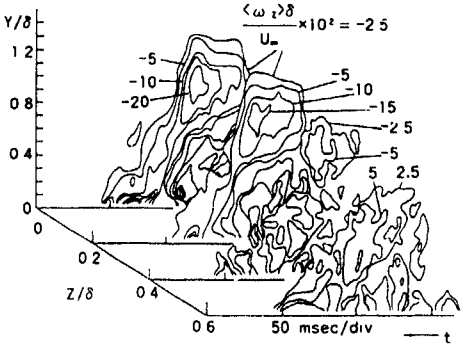

Fig.5 Three-dimensional distribution of spanwise vorticity, ω_z, at $X/\delta = 14$. Hatched area denotes $+\omega_z$ distribution.

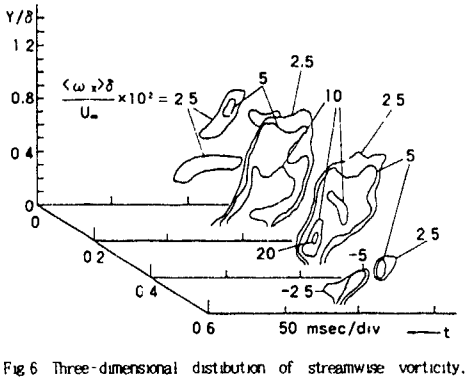

Fig.6 Three-dimensional distibution of streamwise vorticity, ω_x at $X/\delta \simeq 14$. Hatched area denotes ω_x distribution.

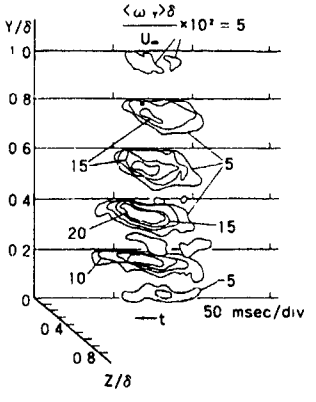

Fig.7 Three dimensional distibution of normal vorticity ω_y, at $X/\delta = 14$. Hatched area denotes ω_y distribution.

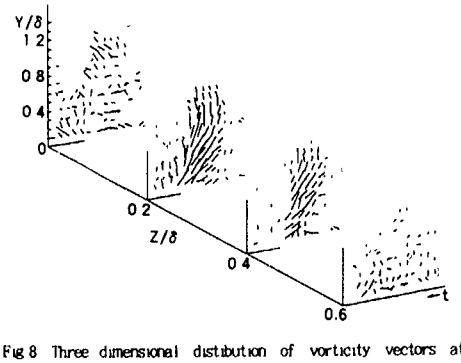

Fig.8 Three dimensional distibution of vorticity vectors at $X/\delta = 14$.

the legs for $Z/\delta > 0.4$ as shown in the velocity fields at $Z/\delta = 0.6$ in Fig. 11. The inrush representing the inward motion of high-speed fluid occurs in the layer lower than the outflow. The Reynolds stress is produced around the outflow and the inrush (Makita et al. 1989).

Moin (1989) demonstrated that the horseshoe vortex was the universal configuration of the coherent structure in the turbulent shear flow. In the same way, the large-scale vortex in the outer layer and the small-scale one in the inner layer must also have similar vortical structure with each other. Under the assumption, the knowledge of the large-scale vortex may be helpful for understanding the small-scale vortex because the large-scale vortex can be measured more minutely by a hot-wire probe with finite spatial resolution than the small-scale one. From the present experimental results, the ejection and the sweep around the small-scale coherent vortex is analogous to

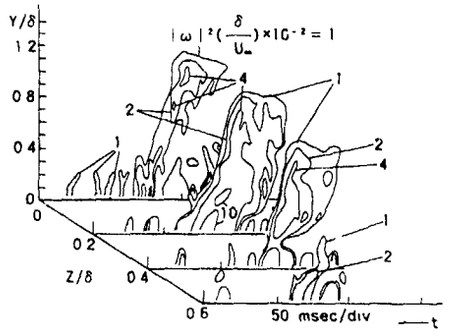

Fig. 9 Three-dimensional distribution of enstrophy, $|\omega|^2$, at $X/\delta = 14$. Hatched area denotes secondary induced vorticity.

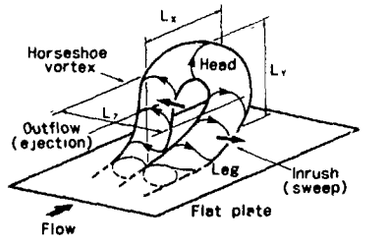

Fig. 10 Idealized model of the large-scale vortex.

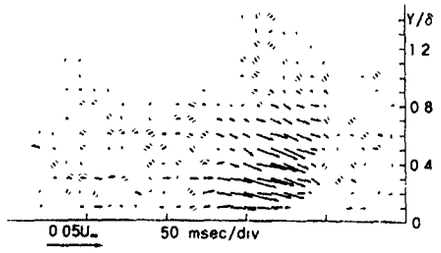

Fig. 11 Induced velocity vectors around the artificial vortex on the T-Y plane at $Z/\delta = 0.6$ at $X/\delta = 14$. The magnitude of arrows are same as those of Figs. 2.

the low-speed outflow and the high-speed inrush of the large-scale horseshoe vortex as follows. The ejection occurs around symmetry plane between the two legs, and the sweep does on the outside of the legs. Such arrangement of the ejection and the sweep around the coherent vortex were also obtained numerically by Robinson et al. (1989). The facts give good similarity between the coherent motions in the outer and the inner layers.

CONCLUSION

The three-dimensional vortical structure of the large-scale coherent vortex in a fully developed turbulent boundary layer was determined. The coherent vortex had a horseshoe-like sculpture. The turbulent bulge in the superlayer corresponds to its head and the large-scale u discontinuity shows the fluid motion on its back.

Though the generation mechanism of the large-scale vortex could not be made clear, the aspects of the streamwise development of the vortical structure were understood throughout its growth, self-preserving, and decay stages in detail. The large-scale horseshoe vortex kept its coherency until the end of the self-preserving stage drifting at the convection velocity of $0.56U_\infty$, but it came to flow downstream on the local mean velocity of $0.85U_\infty$ and then dispersed into small blocks in the decay stage.

REFERENCE

ANTONIA,R.A & BISSET,D.K. 1991 Turbulence and Coherent structures. 141. Kluwer Academic.

BLACKWELDER,R.F. 1988 Transport Phenomena in Turbulent Flows. 89. Hemisphere Pub.

BROWN,G.L. & THOMAS,A.S.W. 1977 Phys. Fluids 20. s243.

CANTWELL,B.J. 1981 Ann. Rev. Fluid Mech. 13. 457.

ECKELMANN,H., NYCHAS,S.G., BRODKEY,R.S., & WALLACE,J.M. 1977 Phys. Fluids 20(10-2). 5225.

FUKUNISHI,Y. & SATO,H. 1987 Fluid Dyn. Res. 2(2). 113.

FUKUNISHI,Y., SATO,H., & INOUE,O. 1987 AIAA Pap. 87-1253.

GAD-EL-HAK,M. & HUSSAIN,A.K.M.F. 1986 Phys. Fluids 29. 2124.

GAD-EL-HAK,M. & BLACKWELDER,R.F. 1987 AIAA J. 25. 1207.

HEAD,M.R & BANDYOPADHYAY,P. 1981 J. Fluid Mech. 107. 297.

JIMÉNEZ,J., MOIN,P., MOSER,R., & KEEFE,L. 1988 Phys. Fluids 31. 1311.

KIM,J. 1987 Turbulent Shear Flow 5. 221. Springer-Verlag.

KLINE,S.J & ROBINSON,S.K. 1989 Near-Wall Turbulence. 200. Hemisphere Pub.

KOVASZNAY,L.S.G., KIBENS,V & BLACKWELDER,R.F. 1970 J. Fluids Mech. 41. 283.

MAKITA,H., SASSA,K. & ABE,M. 1988 Frontiers of Fluid Mechanics. 104. Pergamon Press.

MAKITA,H., SASSA,K., ABE,M. & ITABASHI,A. 1989 AIAA J. 27(2).155.

MOIN,P. 1989 Near-Wall Turbulence. 2. Hemisphere Pub.

PRATURI,A.K & BRODKEY,R.S. 1978 J. Fluid Mech. 89. 251.

ROBINSON,S.K. 1990 Structure of Turbulence and Drag Reduction. 23. Springer-Verlag.

ROBINSON,S.K., KLINE,S.J., & SPALART,P.R. 1989 Near-Wall Turbulence. 218. Hemisphere Pub.

VIETS,S., PIATT,M., & BALL,M. 1981 AIAA Pap. 81-0256.

WILLMARTH,W.W & LU,S.S. 1972 J. Fluid Mech. 55(1). 65.

EIGHTH SYMPOSIUM ON
TURBULENT SHEAR FLOWS
Technical University of Munich
September 9 11, 1991

EFFECTS OF ADVERSE PRESSURE GRADIENTS ON MEAN FLOWS AND TURBULENCE STATISTICS IN A BOUNDARY LAYER

Y Nagano, M Tagawa and T Tsuji

Department of Mechanical Engineering,
Nagoya Institute of Technology
Gokiso-cho, Showa-ku, Nagoya 466, Japan

ABSTRACT

Measurements in boundary layers with 'moderate' to 'strong' adverse pressure gradients are presented and discussed With increasing adverse pressure gradients, the velocity profile in $\overline{U}^+ \sim y^+$ coordinates lies below the standard log law, thus indicating a reduction in the thickness of the sublayer Correspondingly, the turbulence energy components as well as the Reynolds shear stress peak in the outer region of the boundary layer Higher-order moments of velocity fluctuations are also seriously affected by the adverse pressure gradient In strong adverse-pressure-gradient flows, the triple products of velocity have completely opposite signs to those in zero-pressure-gradient flows over most of the boundary layer

NOMENCLATURE

C_p = wall static pressure coefficient $= (\overline{P} - \overline{P}_{ref})/(\rho \overline{U}^2_{ref}/2)$
H = shape factor, $= \delta^*/\theta$
$\overline{P}$ = mean pressure
P^+ = dimensionless pressure gradient parameter $= \nu(d\overline{P}/dx)/\rho u_\tau^3$
R_θ = Reynolds number based on momentum thickness $= \overline{U}_e\theta/\nu$
$S(\chi)$ = skewness factor of χ, $= \overline{\chi^3}/(\overline{\chi^2})^{3/2}$
$\overline{U}$ = mean velocity in x direction
$\overline{U}_e$ = free stream velocity
u_τ = friction velocity, $= \sqrt{\tau_w/\rho}$
u, v, w= fluctuating velocity components in x, y and z directions
x = distance from tripping plate
y^+ = dimensionless distance from wall, $= u_\tau y/\nu$
β = Clauser pressure gradient parameter $= (\delta^*/\tau_w)d\overline{P}/dx$
δ_{99} = boundary layer thickness
δ^*, θ = displacement and momentum thicknesses
ν = kinematic viscosity
ρ = density
τ_w = wall shear stress

INTRODUCTION

Since adverse-pressure-gradient flows often occur in various kinds of fluid machines, it is of both fundamental and practical importance to investigate the effects of adverse pressure gradients on the characteristics of turbulent boundary layers

In this paper, we present the first report of our study planed to quantitatively investigate the effects of an adverse pressure gradient (APG) on the statistics and structures of turbulent boundary layers and to obtain the fundamental data which provides a guide for the development and improvement of turbulence theory and modeling

The main objectives of the present investigation are to answer the following unresolved questions (1) Does the standard log-law in zero-pressure gradient (ZPG) flows

$$\overline{U}^+ = 2.44 \ln y^+ + 5.0 \qquad (1)$$

still hold in APG flows?; (2) How do the near-wall turbulence statistics behave in APG flows?, and (3) How do the higher-order statistics respond to the APG?

There have been several papers investigating the basic characteristics of APG flows For example, Samuel & Joubert (1974) and Cutler & Johnston (1989) investigated the mean flow and fluctuating quantities On the other hand, Kline et al (1967) and Lian (1990) studied turbulence structures by using flow visualization techniques However, the above mentioned problems are still unsettled. In particular, the effects of the APG on near-wall behavior of turbulence are totally unclear, which is mainly due to the difficulties in measurement Furthermore, although we need detailed knowledge of the relationship between turbulence structures and turbulence statistics to develop appropriate turbulence models (Robinson, Kline & Spalart 1990, Nagano & Tagawa 1988, 1990a, 1991), there have been few studies on the APG flows which dealt with this subject

EXPERIMENTAL APPARATUS

The test section is shown in Fig. 1 Working fluid (air) flows successively through the settling chamber, two-dimensional contraction, test section, plenum chamber and blower At the entrance to the settling chamber, a superhigh-performance air filter is equipped to avoid a temporal change in hot-wire responses caused by adhesion of dust. To reduce free-stream turbulence and to establish a desirable two-dimensional flow

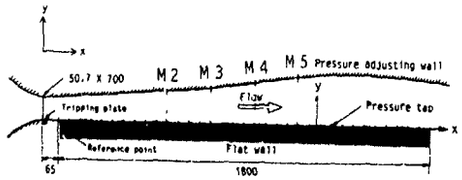

Fig. 1 Test section (flow is from left to right)

field, special care is taken in arranging honeycomb and screens in the light of previous works (e g , for honeycomb, Lumley 1964, and Loehrke & Nagib 1976, for screen, Schubauer et al 1950, and Bradshaw 1965). Thus, in the settling chamber, we installed one honeycomb (cell size. 4 7 mm, length 50 mm) and five screens (mesh 32, s w g #38, open area ratio 65 4 %). The shape of wind-tunnel contraction is designed to conform to the requirements cataloged by Uberoi (1956) and Morel (1977) The contraction ratio is 9 1 and the cross-sectional area of its exit is 50 7 mm × 700 mm Then, the aspect ratio at the inlet to the test section is 13 8 : 1 As a result, nearly ideal, two-dimensional uniform inflow is obtained, whose free-stream turbulence level is below 0 1 % and velocity non-uniformities in the y- (normal to the wall) and z- (lateral) directions are within 0 17 % (2.2 mm $\leq y \leq$ 48 5 mm) and 0.5 % (-200 mm $\leq z \leq$ 200 mm), respectively, under the present measurement conditions. To generate a stable and fully-developed turbulent boundary layer, a row of equilateral triangle plates (length of one side 10 mm, thickness 1 mm) is located at the inlet to the test section The test section is composed of a flat-plate on which a turbulent boundary layer develops and of a roof-plate to adjust pressure gradients The material of both plates is acrylic acid resin and its thickness is 10 mm

Wall static pressures were measured with a Gottingen-type manometer equipped with a microscope (measurement accuracy: $\pm$0.01 mm) The pressure taps with 0 5 mm diameter are located at 20 mm apart form the centerline of the flat-plate and at 50 mm intervals from the inlet

Velocity measurement was done with hot-wire probes, i e , a handmade subminiature (Ligram & Bradshaw 1987) normal hot-wire (dia. 3 1 μm; length 0.6 mm), and two types of specially devised X-probes (dia. 3 1 μm, length. ℓ = 0 6 mm $\simeq 6\nu/u_\tau$; wire spacing Δz = 0 23 mm $\simeq 2\,3\nu/u_\tau$) All these hot-wires were operated using constant-temperature mode hot-wire anemometers (Hayakawa Model HC-30W). As a traversing mechanism, we used a finely adjustable positioning device equipped with a micrometer, the positioning accuracy being $\pm$ 0 005 mm. The absolute distance from the wall is determined by measuring, with a telescope, the distance between the real wire and its reflected image on the flat-plate.

All data were recorded in analog form with an FM data recorder (TEAC SR-31) and then reproduced for conversion to digital form The data digitized with 16 bit analog-to-digital converter (Canopus ADF-16) were stored in a 40 Mbyte hard-disk unit (Logitec LHD-34V) The real-time sampling frequency was 34 08 kHz, and the number of data points per measurement was 262,144 The statistical analysis of the data was performed on an NEC PC-9801 personal computer.

RESULTS AND DISCUSSION

Since the object of the present measurement is concerned with a boundary layer itself which develops on a flat-plate, this boundary layer should be unaffected by the presence of an opposite pressure-adjusting roof-plate Thus, we first investigated a boundary layer formed on the roof-plate under a zero-pressure gradient condition. The result at a measurement location farthest downstream is shown in Fig. 2. As clearly seen from this figure, a highly uniform free stream is formed over a wide portion of the channel. Furthermore, it is confirmed that the velocity profile in the boundary layer on the roof-plate agrees quite well with the Blasius' laminar-flow solution Thus, this boundary layer (boundary-layer thickness δ_{99} = 5 3 mm) is completely laminar even at the end of the test section and separated by the uniform free stream, so that we have concluded that there exists no influence of the pressure-adjusting plate on the objective turbulent boundary layer Also, as seen in Fig 3, ideal zero-pressure-gradient (ZPG) flows are formed in the test section

It is well known that the standard log-law velocity profile given by Eq (1) holds in ZPG turbulent boundary layers Before starting the discussion on APG flows, we re-examine this fact experimentally We estimate the friction velocity, u_τ, using the method similar to McEligot (1984). Thus, with the Van Driest damping function for the mixing length, we may write the velocity profile in the wall region as

$$\overline{U}^+ = 2\int_0^{y^+} \frac{dy^+}{1+(1+4\ell^{+2})^{1/2}} \tag{2}$$

where

$$\ell^+ = \kappa y^+[1-\exp(-y^+/A^+)] \tag{3}$$

In Eqs (2) and (3), $\overline{U}^+ = \overline{U}/u_\tau$ and $y^+ = u_\tau y/\nu$ are the dimensionless velocity and distance, where u_τ is unknown and to be determined On the other hand, in the log-law region, we have

$$y(d\overline{U}/dy) = u_\tau/\kappa = \gamma \tag{4}$$

Here γ can be determined from measurement From Eqs (2)–(4), together with the measurements of mean velocity, we can estimate values of κ, A^+ and u_τ so that Eq (2) gives a best fit to measurements. The optimum values are $\kappa \simeq$ 0 41 and $A^+ \simeq$ 26.5. The universal velocity profiles normalized with

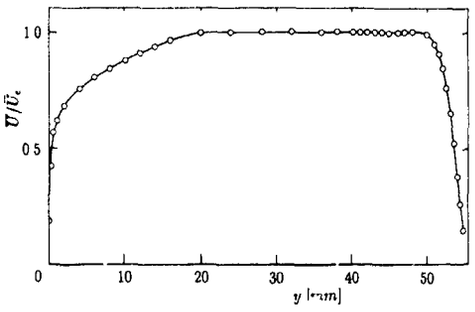

Fig 2 Velocity profile at the end of test section

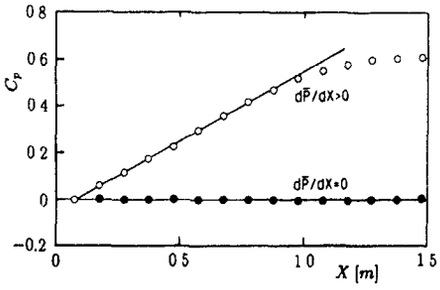

Fig 3 Development of the pressure coefficient

the friction velocity u_τ thus obtained are shown in Fig 4 Obviously, Eq (1) is valid in the log-law region Therefore, it is adequate to estimate the friction velocity by using the established Clauser's method (Clauser 1954), i e , the law-of-the-wall fit, in the cases of ZPG flows. We applied this method to nine ZPG flows different in free stream velocities, and then obtained nine friction velocities, u_τ Figure 5 shows the near-wall distributions of the apparent velocities $\overline{U}_m^+$ ($= \overline{U}_m/u_\tau$) versus y^+ normalized by the friction velocities obtained with the law-of-the-wall fit As clearly seen in Fig. 5, in the vicinity of the wall ($y^+ < 3.6$), $\overline{U}_m^+$ deviates systematically from the 'law of the wall,' $\overline{U}^+ = y^+$, in the viscous sublayer as the wall is approached In general, this can be ascribed to the wall proximity effect of hot-wire outputs Previous extensive studies investigating this wall proximity effect (for example, Oka & Kostic 1972, Hebbar & Melnik 1978, Bhatia, Durst & Jovanovic 1982, Janke 1987) have reported that. once material of a wall, and geometrical factors of a hot-wire and a probe are given, the amount of this deviation can be determined universally, independent of values of wall shear stresses, so that $\overline{U}_m^+ = f(y^+)$. As seen in Fig 5, the apparent velocities $\overline{U}_m^+$ in the present experiments collapse very well onto a unique curve $f(y^+)$, being consistent with the previous findings Therefore, in the following, we use this curve $f(y^+)$ regardless of pressure gradients or wall shear stresses, and determine u_τ by using the least-squares-fitting method to the data in the range $1.1 \leq y^+ \leq 5$ Consequently, the following

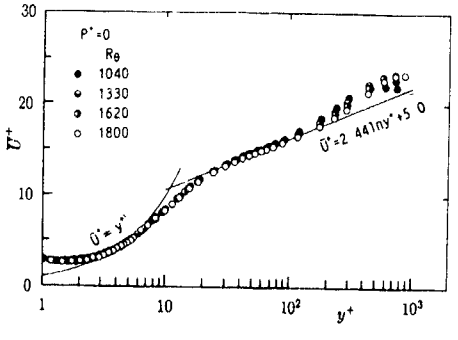

Fig 4 Mean velocity profiles in zero-pressure-gradient flows

Table 1 Mean flow parameters

X mm	$\overline{U}_e$ m/s	δ_{99} mm	u_τ m/s	R_θ	H	P^+	β
523	9.08	16.2	0.390	1290	1.52	8.98×10^{-3}	0.76
723	8.18	24.6	0.307	1880	1.61	1.81×10^{-2}	2.05
925	7.54	34.2	0.251	2660	1.74	2.30×10^{-2}	3.54
1121	6.68	46.1	0.197	3350	1.88	2.51×10^{-2}	4.66

($\overline{U}_{ref} = 10.8$ m/s)

measurements were done with the same probe as that used in this calibration.

The profiles of r m s values of streamwise, wall-normal and spanwise velocity fluctuations ($\sqrt{\overline{u^2}}/u_\tau$, $\sqrt{\overline{v^2}}/u_\tau$ and $\sqrt{\overline{w^2}}/u_\tau$) are shown in Fig 6 It can be seen that all of the present results in the ZPG boundary layer are in good agreement with the existing experiments (Verriopoulos 1983, Barlow & Johnston 1988) and the DNS results (Spalart 1988), thus indicating that the present turbulent boundary layers are canonical

Next, we shall present the results of experiments on adverse pressure gradient (APG) turbulent boundary layers. The distributions of C_p and dC_p/dx are shown in Fig. 3, and the mean flow parameters are summarized in Table 1 In the present APG flow, the pressure gradient dC_p/dx keeps a nearly constant value of 0.6 over 65 mm $\leq x \leq$ 700 mm and then decreases slowly On the other hand, the pressure gradient parameter normalized by inner variables (Huffman & Bradshaw 1972), P^+ ($= \nu(d\overline{P}/dx)/\rho u_\tau^3$), and the Clauser pressure gradient parameter, β ($= (\delta^*/\tau_w)d\overline{P}/dx$), increase monotonously, thus giving 'moderate' to 'strong' adverse pressure gradients.

Figure 7 shows the mean velocity distributions $\overline{U}^+$ in the APG boundary layers These quantities are normalized by the friction velocities obtained by using the above-mentioned method of least-squares curve fitting, in which corrections (Bhatia, Durst & Jovanovic 1982) were done for the mean velocity $\overline{U}^+$ near the wall ($y^+ < 3.6$) by subtracting the quantity $\Delta\overline{U}_m^+ = f(y^+) - \overline{U}^+$ shown in Fig. 5 from the apparent measurement $\overline{U}_m^+$ in APG flows This figure presents the important findings that (i) in the viscous sublayer, the typical linear relationship $\overline{U}^+ = y^+$ holds; but (ii) in the fully turbulent wall region, the velocity profiles $\overline{U}^+$ deviate downwards from the standard log-law profile given by Eq (1) The

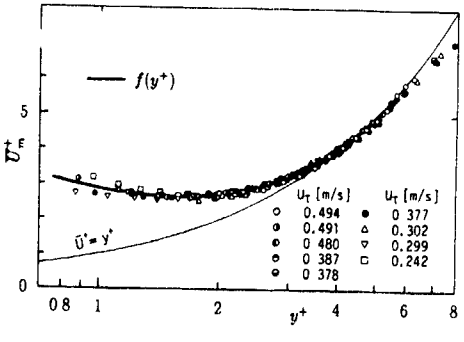

Fig 5 Near-wall distributions of apparent velocities $\overline{U}_m^+$ in various zero-pressure-gradient flows

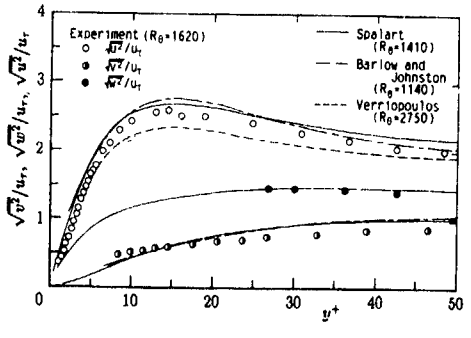

Fig 6 R.m s velocity fluctuations in zero-pressure-gradient flow

amount of deviation increases with an increase of P^+ Using Eqs (2)-(4), the procedure described previously was applied so as to crosscheck the present mean velocity profiles As shown in Fig. 8, it was found that the Von Kármán constant was unchanged ($\kappa \simeq 0.4$) but the Van Driest damping constant A^+ decreased with increasing P^+, which agreed well with a semi-empirical formula obtained by Kays (1971) as.

$$A^+ = 26/(1 + 30.18\,P^+) \qquad (5)$$

The velocity profiles in $\overline{U}^+$ v s y^+ coordinates were almost identical to those presented in Fig 7

These results in the APG flows ($P^+ > 0$) exhibit a striking contrast to those in favorable pressure gradient flows ($P^+ < 0$) in which the velocity profile deviates upwards from Eq (1) (Blackwelder & Kovasznay 1972, Spalart 1986) Kline et al (1967), on the other hand, reported that the $\overline{U}^+$ distributions lay above and below the standard log-law according as $P^+ > 0$ and $P^+ < 0$ The marked difference between their results and the present ones can be attributed mainly to their omission of wall proximity corrections to hot-film outputs and to their over-fitting of measurements to the linear relation $\overline{U}^+ = y^+$ up to $y^+ \simeq 10$ Such an over-fitting may cause the estimation of smaller friction velocity and result in the upward deviation of $\overline{U}^+$ from the standard log-law, Eq (1), even in ZPG turbulent boundary layers (Blackwelder & Haritonidis 1983).

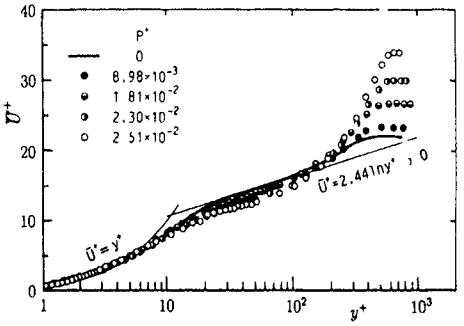

Fig 7 Mean velocity profiles in wall coordinates in adverse-pressure gradient flows

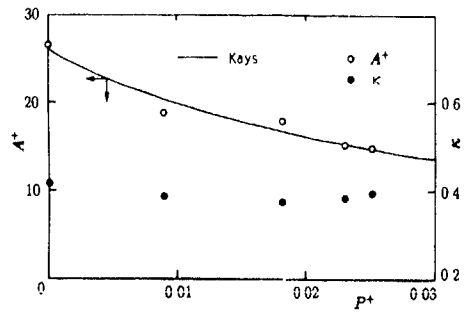

Fig. 8 Von Kármán and Van Driest constants in adverse-pressure-gradient flows

Considering these respects, we have concluded that the standard log-law, Eq (1), does not hold in APG turbulent boundary layers This accords exactly with the conjecture made by Launder (1986) Consequently, this result also serves a warning on the use of the wall functions on which many turbulence models rely (for detailed discussion, see for example Nagano & Tagawa 1990b).

As seen in Fig 9(a-c), the adverse pressure gradient has also a great influence on the distributions of turbulence quantities. As P^+ increases, all of the velocity fluctuation components ($\sqrt{u^2}/u_\tau$, $\sqrt{v^2}/u_\tau$ and $\sqrt{w^2}/u_\tau$) become remarkably large in the outer region of a boundary layer. The increase in $\sqrt{u^2}/u_\tau$ penetrates in the inner region systematically with increasing P^+, and the universal profile of $\sqrt{u^2}/u_\tau$ observed

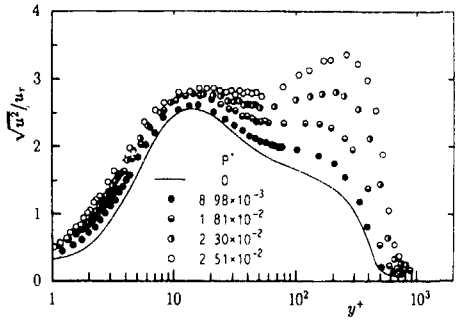

(a) Velocity fluctuations in the streamwise direction

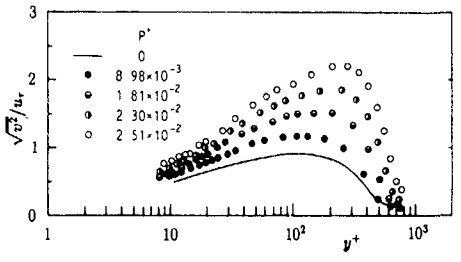

(b) Velocity fluctuations in the wall-normal direction

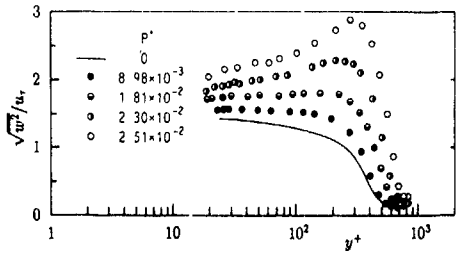

(c) Velocity fluctuations in the spanwise direction

Fig 9 Turbulence intensities in adverse-pressure-gradient flows

in the ZPG flows disappears in the cases of APG flows. As the wall is approached, the distributions of $\sqrt{u^2}/u_\tau$ approach each straight line which coincides with the origin (Fig 10) This is proper because the wall-limiting behavior of u is $u \propto y$ for $y \to 0$. However, the gradients of the linear lines become steeper as P^+ increases Since the wall law, $\overline{U}^+ = y^+$, holds even in the APG flows very near the wall, this leads to a larger wall-limiting value of the relative turbulence intensity $\sqrt{u^2}/\overline{U}$ with increasing P^+, thus indicating that an increase in the dimensionless pressure-gradient parameter P^+ makes the viscous region more turbulent and energetic

The profiles of Reynolds shear stress, $-\overline{uv}/u_\tau^2$, are also seriously affected by the adverse pressure gradient. With increasing P^+, $-\overline{uv}/u_\tau^2$ increases in the outer region as shown in Fig 11 Thus, it should be noted that the constant-stress-layer relationship $-\overline{uv}/u_\tau^2 \simeq 1$ observed in ZPG flows is no longer valid and the turbulent shear stress $-\rho\overline{uv}$ becomes considerably larger than the wall shear stress τ_w, i e , $-\overline{uv} > u_\tau^2$, as P^+ increases This too may account for the nonexistence of the universal law of the wall in APG boundary layers

There is little knowledge of what effects the adverse pressure gradient produces on the higher-order turbulence statistics Figures 12(a) and 12(b) show the turbulent transport, i.e., third-order moments, of turbulence energy component u^2 and Reynolds shear stress uv, respectively The marked effects of the APG are seen on both third-order moments From Fig 12(a), the positive region of $\overline{vu^2}$ observed in the ZPG flows for $y^+ > 15$ disappears partly as P^+ increases. Since third-order moments (i e , triple products) are very sensitive to the change of coherent turbulence structures such as ejections and sweeps (Nagano & Tagawa 1988, 1990a), this result suggests that internal structural changes occur in the APG boundary layers Also, positive values of $\overline{vu^2}$ in the near-wall to outer regions indicate the existence of turbulence energy transport toward the wall from the regions away from the wall This is consistent with the results of Bradshaw (1967) and Cutler & Johnston (1989) From Fig 12(b), it is found that a similar inward transfer takes place in the turbulent diffusion of the Reynolds shear stress In particular, as P^+ increases, turbulent diffusion in the APG boundary layer occurs in the completely opposite direction to that in the ZPG case

The structural change in the higher-order turbulence statistics in the APG flows may be predicted by a 'structural' turbulence model of Nagano & Tagawa (1990a, 1991).

$$\overline{\hat{v}\hat{u}^2} = C\left[\sigma_{\overline{uv}}\frac{1}{2}\pi S(u) + S(v)\right] \tag{6}$$

$$\overline{\hat{v}\hat{u}\hat{v}} = C\left[S(u) + \sigma_{\overline{uv}}\frac{1}{2}\pi S(v)\right] \tag{7}$$

with

$$C = 1/\{3[(\pi/2)^2 - 1]\} \tag{8}$$

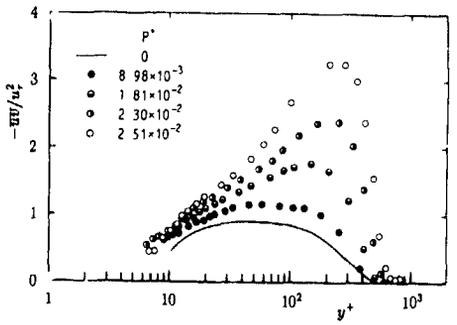

Fig. 11 Reynolds shear stress profiles in adverse-pressure-gradient flows

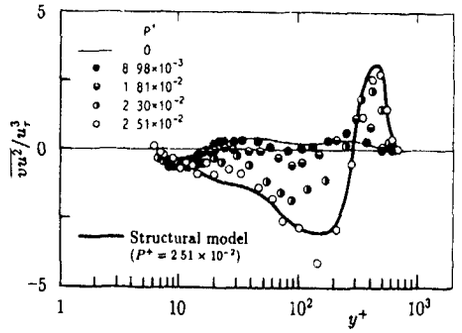

(a) $\overline{vu^2}$

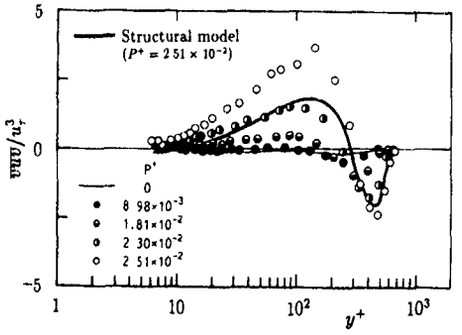

(b) $\overline{vuv}$

Fig 12 Distributions of turbulent transport (third-order-moments) in adverse-pressure-gradient flows

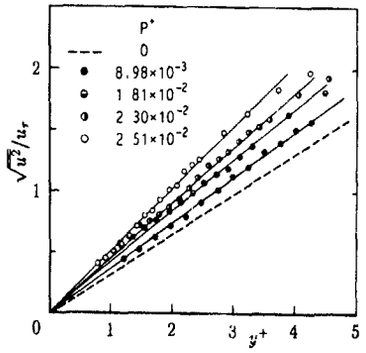

Fig 10 Wall-limiting behavior of $\sqrt{u^2}/u_\tau$ in adverse-pressure-gradient flows

where a circumflex denotes the normalization by the respective r m s value, $S(\chi)$ is the skewness factor of a stochastic variable χ, and $\sigma_{\overline{uv}}$ represents a sign function, i e , $\sigma_{\overline{uv}} = 1$ for $\overline{uv} \geq 0$ and $\sigma_{\overline{uv}} = -1$ for $\overline{uv} < 0$. As can be seen from Figs 12(a) and (b), Eqs (6) and (7) well represent the structural change in the APG boundary layer

CONCLUSIONS

The present experiment reveals that the mean flow and turbulence statistics are seriously affected by increasing adverse pressure gradients The well-known 'law-of-the-wall' established for flows with a zero pressure gradient does not hold in the adverse-pressure-gradient flows. This finding is very important since most of the existing turbulence models in applications are constructed on the basis of the law of the wall Much more drastic change in the structure of turbulence is found in the statistics of higher-order moments of velocity

REFERENCES

BARLOW, R. S & JOHNSTON, J P 1988 Structure of a turbulent boundary layer on a concave surface *J Fluid Mech* **191**, 137-176

BHATIA, J C , DURST, F & JOVANOVIC, J. 1982 Corrections of hot-wire anemometer measurements near walls *J Fluid Mech* **122**, 411-431.

BLACKWELDER, R. F. & KOVASZNAY, L. S G 1972 Large-scale motion of a turbulent boundary layer during relaminarization *J. Fluid Mech* **53**, 61-83

BLACKWELDER, R F & HARITONIDIS, J H 1983 Scaling of the bursting frequency in turbulent boundary layers *J Fluid Mech* **132**, 87-103

BRADSHAW, P 1965 The effect of wind-tunnel screens on nominally two-dimensional boundary layers *J Fluid Mech* **22**, 679-687

BRADSHAW, P 1967 The turbulence structure of equilibrium boundary layers *J Fluid Mech* **29**, 625-645

CLAUSER, F H 1954 Turbulent boundary layers in adverse pressure gradients *J Aeronautical Sciences* **21**, 91-108

CUTLER, A D & JOHNSTON, J P 1989 The relaxation of a turbulent boundary layer in an adverse pressure gradient *J Fluid Mech* **200**, 367-387

HEBBAR, K S & MELNIK, W L 1978 Wall region of a relaxing three-dimensional incompressible turbulent boundary layer *J. Fluid Mech* **85**, 33-56.

HUFFMAN, G. D. & BRADSHAW, P. 1972 A note on von Kármán's constant in low Reynolds number turbulent flows. *J. Fluid Mech* **53**, 45-60.

JANKE, G 1987 Hot wire in wall proximity In *Advances in Turbulence* (ed G Comte-Bellot & J. Mathieu), pp 488-498 Springer

KAYS, W. M. 1971 Heat transfer to the transpired boundary layer. *ASME Paper No. 71-HT-44.*

KLINE, S J , REYNOLDS, W. C., SCHRAUB, F. A & RUNSTADLER, P W 1967 The structure of turbulent boundary layers *J Fluid Mech.* **30**, 741-773.

LAUNDER, B E 1986 Low-Reynolds-number turbulence near walls *UMIST Dept of Mech Eng , TFD/86/4*

LIAN, Q X 199) A visual study of the coherent structure of the turbulent boundary layer in flow with adverse pressure gradient *J Fluid Mech* **215**, 101-124

LIGRANI, P M. & BRADSHAW, P. 1987 Subminiature hot-wire sensors development and use *J Physics E - Scientific Instruments* **20**, 323-332

LOEHRKE, R I. & NAGIB, H M 1976 Control of free-stream turbulence by means of honeycombs a balance between suppression and generation. *Trans. ASME: J. Fluids Engng* **98**, 342-353.

LUMLEY, J. L. 1964 Passage of a turbulent stream through honeycomb of large length-to-diameter ratio. *Trans ASME J Basic Engng* **86**, 218-220

MCELIGOT, D M 1984 Measurement of wall shear stress in accelerating turbulent flows *Max-Planck- Institut für Strömungsforschung (Göttingen) Bericht* 109

MOREL, T 1977 Design of two-dimensional wind tunnel contractions *Trans ASME J Fluids Engng* **99**, 371-378

NAGANO, Y & TAGAWA, M. 1988 Statistical characteristics of wall turbulence with a passive scalar *J Fluid Mech* **196**, 157-185

NAGANO, Y & TAGAWA, M 1990a A structural turbulence model for triple products of velocity and scalar *J Fluid Mech* **215**, 639-657

NAGANO, Y & TAGAWA, M 1990b An improved $k - \epsilon$ model for boundary layer flows. *Trans ASME J Fluids Engng* **112**, 33-39.

NAGANO, Y & TAGAWA, M 1991 Turbulence model for triple velocity and scalar correlations In *Turbulent Shear Flows 7* (ed F Durst *et al*), pp 47-62. Springer.

OKA, S. & KOSTIC, Z. 1972 Influence of wall proximity on hot-wire velocity measurements *DISA Information*, No. 13, pp 29-33.

ROBINSON, S K., KLINE, S J & SPALART, P R 1990 Quasi-coherent structures in the turbulent boundary layer part II verification and new information from a numerically simulated flat-plate layer In *Near-Wall Turbulence* (ed S J Kline & N H Afgan), pp 218-247 Hemisphere

SAMUEL, A E & JOUBERT, P N 1974 A boundary layer developing in an increasingly adverse pressure gradient *J. Fluid Mech* **66**, 481-505.

SCHUBAUER, G B , SPANGENBERG, W G. & KLEBANOFF, P. S. 1950 Aerodynamic characteristics of damping screens *NACA Technical Note* 2001

SPALART, P S 1986 Numerical study of sink-flow boundary layers *J Fluid Mech.* **172**, 307-328

SPALART, P S 1988 Direct simulation of a turbulent boundary layer up to $R_\theta = 1410$. *J. Fluid Mech* **187**, pp 61-98

UBEROI, M S 1956 Effect of wind-tunnel contraction on free-stream turbulence *J. Aeronautical Sciences* **23**, 754-764.

VERRIOPOULOS, C A 1983 Effects of convex surface curvature on heat transfer in turbulent flow. *Ph D Thesis*, Imperial College

EIGHTH SYMPOSIUM ON
TURBULENT SHEAR FLOWS
Technical University of Munich
September 9-11, 1991

The Velocity and Transverse Vorticity Field in a Single Stream Shear Layer

J M Bruns*, R C. Haw**, J F Foss
Department of Mechanical Engineering
Michigan State University
East Lansing, MI 48824

* Exchange student, Rheinisch - Westfalische Technische Hochschule Aachen, Federal Republic Germany, presently at the H F I , T U Berlin Berlin Germany

** Presently, CERL, Urbana-Champagne, Illinois, USA

Abstract

Hot-wire measurements in a large Reynolds number single stream shear layer are reported The stochastic properties of this turbulence field are found to be self-preserving beyond x/θ (0) ~ 200 Stochastic properties of the transverse vorticity field clearly show that the population of vorticity values at a given location are quite widely distributed $\tilde{\omega}_z/\bar{\omega}_z]_{max}$ = 28 at $x/\theta(0)$ = 347 The Kurtosis value is 17 at the same location These measured ratios, albeit large with respect to velocity field statistics, are known to be too small as a result of the spatial smoothing of the 1 mm x 1 mm sample domain

1. Introduction

Documentary measurements have been made in a single stream shear layer for a relatively large $R_{\theta(o)}$ value of the turbulent boundary layer at the separation lip, specifically, $R_{\theta(o)}$ = 7,200 These measurements include the mean and rms velocity profiles at the separation lip and for the upstream region: $-20 \le x/\theta(o) \le 0$ Detailed results are also available for the developing region of the shear layer $0 \le x/\theta(o) \le 200$ and for several streamwise locations in the self-preserving region: $200 \le x/\theta(o) \le 350$.

The intrinsic importance of the single stream shear layer, as one of the basic turbulent shear flows, is considered to be apparent The large $R_{\theta(o)}$ value of the MSU facility makes these data unique. Other studies with a turbulent boundary layer at separation, e g , Hussain and Zaman [1985] and Wygnanski and Fiedler [1970] have involved small $R_{\theta(o)}$ values The present results permit (among other matters) an opportunity to clarify the earlier suggestion (Bradshaw [1966]) that a distance of 1,000 $\theta(o)$ would be required to obtain a self-preserving state. Specifically, the present results indicate that this state is achieved in a distance of 200 $\theta(o)$ from the separation lip, this value is somewhat smaller than the 400 $\theta(0)$ value obtained by Hussain and Zaman (1985) It is instructive that this earlier study was executed with a much smaller initial Reynolds number, viz., $R_{\theta(0)}$ = 480

Section 2 presents the experimental equipment and procedures, the experimental results are presented and discussed in Section 3

2. Experimental Equipment and Procedure

The flow system's test section see Ali, et al. [1985], and Haw and Foss [1989]), is shown schematically in Figure 1. This subatmospheric test section was evacuated by a large centrifugal fan which delivered the combined entrainment and primary flow streams to atmospheric pressure. The subatmospheric test section, which is unusual for such a facility, permits the use of turbulence manipulators in both of these streams with a concomitant low disturbance level in each. The entrainment throttles (not shown) were set such that $dU_o/dx \approx 0$ in the primary stream.

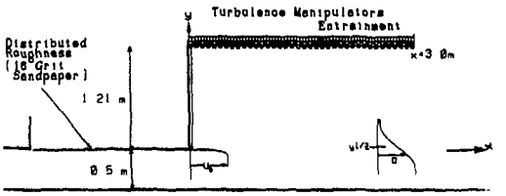

Figure 1 Test Section

Figure 1 also shows the boundary layer and a representative shear layer velocity profile to proper scale in the flow field. An x-y-θ traverse system was used to calibrate the hot-wire probes as a function of the pitch angle and to position the probes in the boundary and shear layers

Hot-wire data were obtained with single wires and with a compact array of 4 wires that provided (u,v) statistics when it was used at a low (200 hz) data rate and (u,v,ω_z) time series when it was sampled at a high (20,000 hz) data rate A thorough description of the probe and the processing algorithms is presented in Foss and Haw (1990) The probe is shown schematically in Figure 2 The data processing algorithms for this probe provide u, v and ω_z values which are spatially averaged over the 1 mm x 1 mm sample domain For reference, the $\theta(x)$ value at the principal location of the measurements is 89 mm and and the shear layer itself is nominally 6θ (or 534 mm) wide

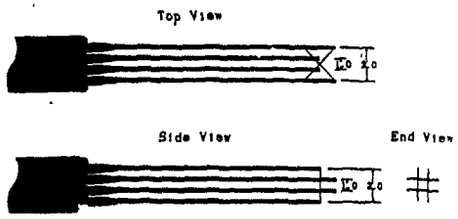

Figure 2 Transverse Vorticity Probe

3. Results and Discussion

3.1 Boundary Layer

An equation presented by Spalding (1961) can be used as a reference condition. Namely,

$$y^+ = u^+ + e^{-kB}\left\{e^{ku^+} - 1 - ku^+ - \frac{(ku^+)^2}{2} - \frac{(ku^+)^3}{3}\right\} \quad (1)$$

This inner region profile can be joined to the Coles [1956] wake expression. The resulting curves are shown in Figure 3.

It can be inferred that the near wall differences between the Spalding and the present profiles are a legacy of the tripping method The

original data of Klebanoff and Diehl [1951] exhibited similar behavior The tripping method of Fig 1 (i e , 60 cm of coarse sandpaper) mimicked the method used in that study

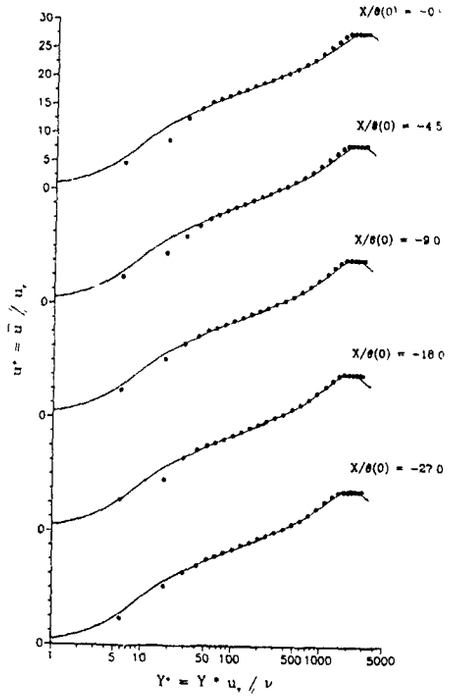

Figure 3 Boundary Layer Mean Velocity Profiles

3.2 Shear Layer

3.2.1 Single wire results

The mean velocity profiles at a number of downstream stations are presented in Figures 4 and 5 These data suggest that a self-preserving condition of the mean velocity distributions is attained for nominally x/θ(o) = 200. An error function polynomial form:

$$\frac{\bar{u}}{U_o} = b_1 + b_2 \operatorname{erf}\left(b_3 + b_4 y + b_5 y^2 + b_6 y^3\right) \qquad (2)$$

can be used to accurately fit these data, see Bruns [1990] for the b_i values Given this expression, the momentum thickness, θ(x), can be evaluated using

$$\theta(x) = \int_{y\,min}^{y\,max} \frac{\bar{u}(x,y)}{U} \left[1 - \frac{\bar{u}(x,y)}{U_o}\right] dy \qquad (3)$$

where y_{max} is a location not yet affected by the outer wall boundary layer and y_{min} is nominally at the velocity ratio $\bar{u}/U_o$ = 0 06 Note that the same form, as used in (2), also describes the velocity profile when the non- dimensional coordinate $\eta = (y - y_{0.5})/\theta(x)$, is used.

The θ(x) values are presented in Figure 6, these also support the inference that a self-preservation condition is obtained for x/θ(o) ≥ 200.

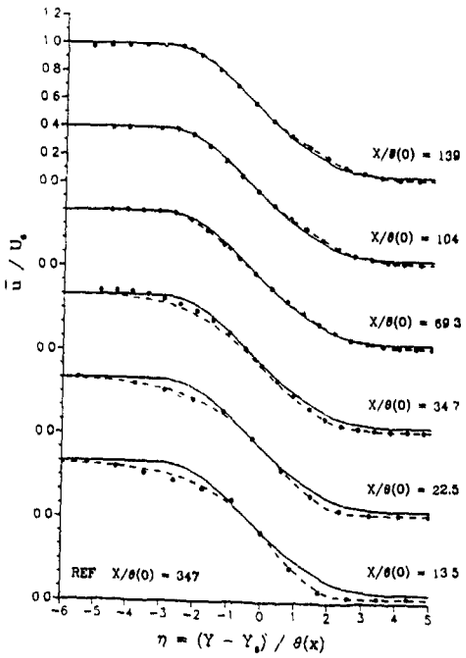

Figure 4 Mean Velocity Profiles - Upstream Region

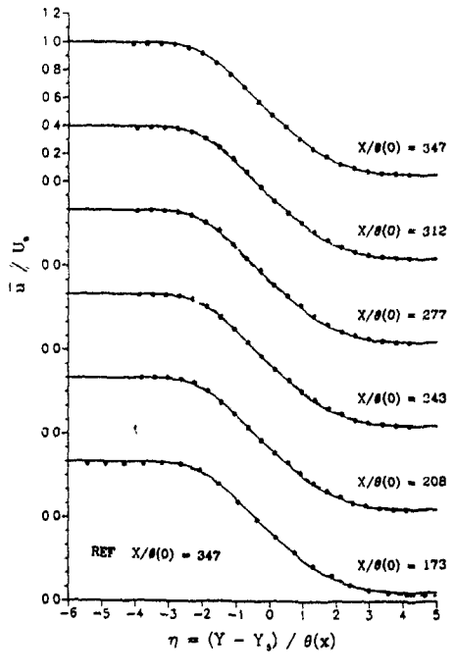

Figure 5 Mean Velocity Profiles - Downstream Region

The $\theta(x)$ values permit an evaluation of the constant $d\theta/dx$ value in the self-preserving region This value is 0.0352 A control volume analysis can be used to derive the result (Bruns [1990]):

$$\frac{V_e}{U_o} = \frac{d\theta}{dx} \qquad (4)$$

in the self preserving region of a single-stream shear layer Independent measurements of V_e/U_o in the same flow field by Ali, et al [1983], showed that

$$0.034 \le \frac{V_e}{U_o} \le 0.035 \qquad (5)$$

The correspondence between V_e/U_o and $d\theta/dx$ is considered to support both the inference of a self preserving state for $x/\theta(o) \ge 200$ and the overall integrity of the measurements

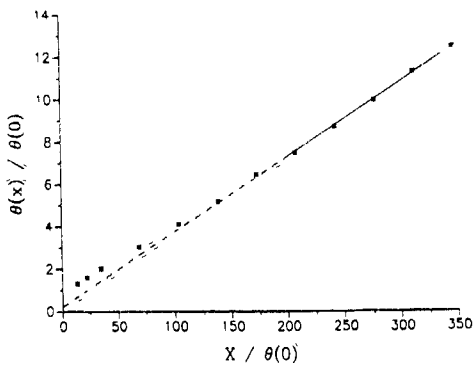

Figure 6 Streamwise Variation of the Momentum Thickness

The corresponding standard deviation profiles are presented in Figures 7 and 8 and the maximum values $\tilde{u}(x,y_{max})/\bar{U}_o$, are shown in Figure 9. The value of 0.165 is typical of other shear layer results and the attainment of this value at nominally $x/\theta(0) = 200$ supports the inference that this location serves as the nominal beginning of the self preserving region.

3.2.2 C.V. Probe Results

The compact vorticity probe was also used to evaluate $\bar{u}$ and $\tilde{u}$ in the shear layer. In general, the results are in good agreement with those of the single wire; see Bruns [1990]

Figure 10 presents the corresponding $\tilde{v}(x,y)$ results and Figure 11 shows the measured and computed Reynolds shear stress magnitudes.

The computed values are derived from the self-preserving form of the momentum and conservation of mass equations. (Note, the latter provides the $u(\eta)$ distribution) The measured values exhibit scatter about the inferred $\overline{uv}(\eta)$ distribution

A detailed analysis of the data record length supports the inference that the differences between the measured and the computed Reynolds stress values can be ascribed to the limited number of independent samples in the data record

4.0 Transverse Vorticity Measurements

4.1 Time Series Data

A short, representative record of $\omega_z(x^*=347, \eta=0.011, t)$ is shown in Fig. 12. The quiescent period in the neighborhood of 0.6 sec is inferred to be a period where irrotational fluid occupied the probe's location. That is, the intermittency

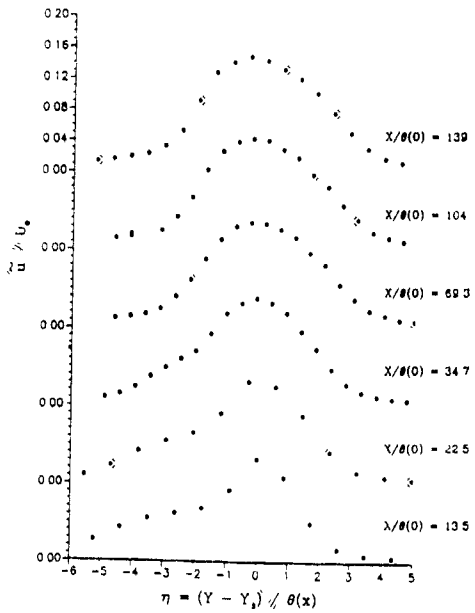

Figure 7 Standard Deviation Profiles - Upstream Region

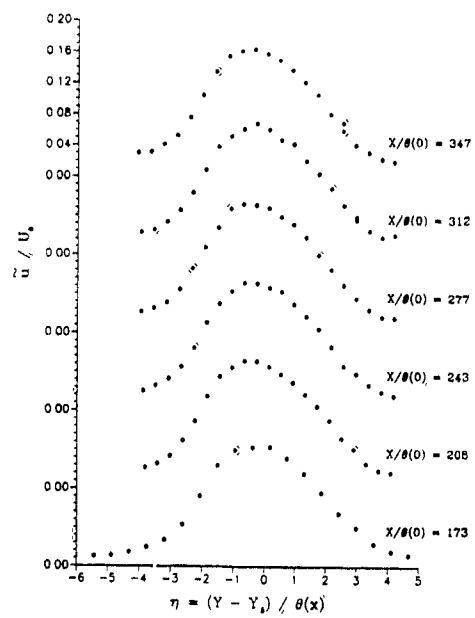

Figure 8 Standard Deviation Profiles - Downstream Region

was zero at that time. Haw, Foss and Foss (1989) provide detailed analyses of the intermittency considerations for this flow field.

Haw, et.al [1989] considered the factors which contribute to the uncertainty of the $\omega_z(t)$ measurements. It was concluded therein that the anemometer noise level (ca 1 mv), the precision of

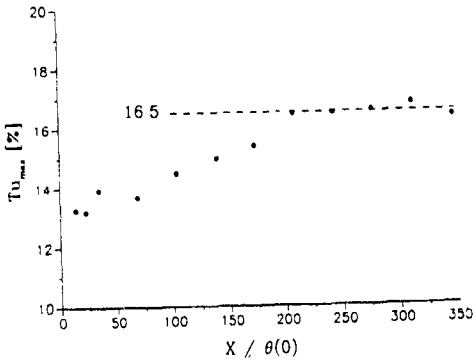

Figure 9 Peak Values of the $\tilde{\omega}_z$ Profiles

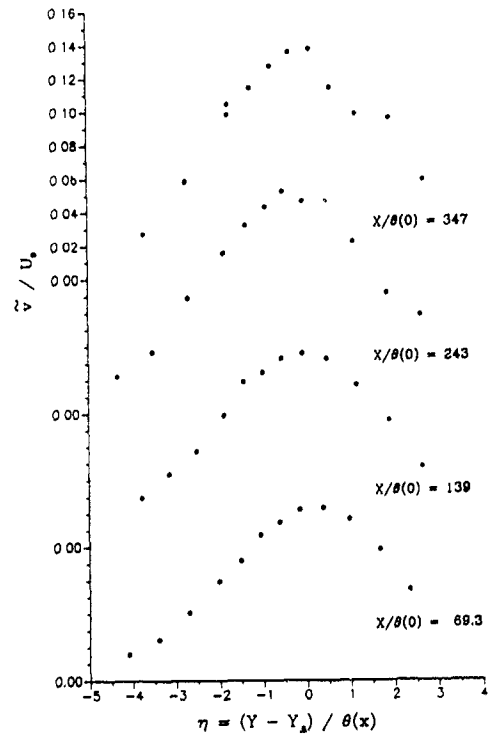

Figure 10 Standard Deviation Profiles of the Lateral Velocity

the A/D converter (1.25 mv), and the standard deviation of the calibration data of the modified Collis and Williams [1959] form

$$E_i^2 = A_i + B_i V^{n_i} \qquad (6)$$

for wires i = 1...4, combined to give an inherent uncertainty of ± 30/sec in the $\omega_z(t)$ signal.

This magnitude is clearly quite small with respect to the typical values exhibited on the figure but it is relatively large with respect to the mean value of 70/sec for the location of Fig 12

Both the uncertainty and the mean value are, however, quite small with respect to the standard deviation of the $\omega_z(t)$ distribution, namely, 1048/sec.

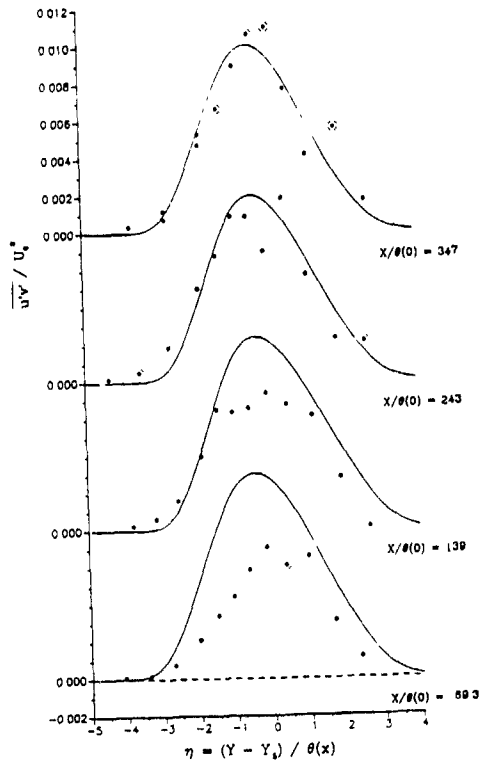

Figure 11 Kinematic Reynolds Shear Stress Profiles

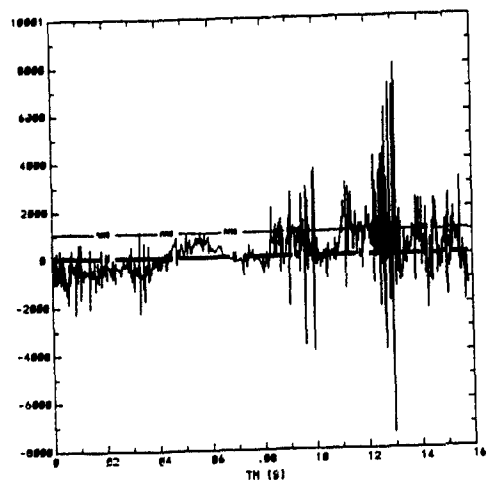

Figure 12 Representative Time Series of $\omega_z(t)$. (Note, x=347 θ(0), η= -0.11)

It is of interest to note that during some periods - e.g., t = 12 5 sec, the $\omega_z(t)$ values can be as large as 100 times the mean value and 7 times the rms. This region, as well as other regions, also exhibits rapid changes in the sign of ω_z. This noteworthy attribute is considered in the following.

4 2 Inferences Regarding the Vorticity Field

The vorticity vector, $\vec{\omega}$, at the center of the probe location can, of course, be represented by three scalar components The present measurement, if successful, resolves the z component of this vector In addition, it provides a low pass spatial filter given its nominally lmmxlmm spatial average of the vorticity filaments which pass through the sample domain. This observation suggests that the observed ω_z magnitudes are smaller than the true values that would be observed if a "point" measurement were better approximated It is appropriate to use the Kolmogoroff scale as nominally representing a "point".

Foss [1991] reports a Kolmogoroff value of ≈ 0 08 mm for the mid portion of the present shear layer at $x/\theta(0) = 347$. With this value, it is noted that nominally 170 "filaments" contribute to the observed ω_z value at a given measurement time. Each filament, however, must satisfy the solenoidal condition

$$\nabla \cdot \omega = 0, \qquad (7)$$

that - in general - implies that a given vorticity filament forms a closed loop in space.

The rapid and strong fluctuations of the sign of ω_z can be understood in this context Namely, that the plane of the probe alternately intercepts the positive and negative z components of the loops that are convected past the probe. It is not suggested that the alternating signs reveal a given loop It is suggested that the vorticity field is represented by a quite compact set of loops whose large ω_z amplitudes suggest the results of "vorticity amplification by stretching".

Specifically, in the transport equation for the vorticity vector

$$\underbrace{\frac{D\vec{\omega}}{Dt}}_{I} = \underbrace{\vec{\omega} \cdot \vec{\nabla}\vec{V}}_{II} + \underbrace{\nu\nabla^2\vec{\omega}}_{III}, \qquad (8)$$

it is noted that term II can increase the magnitude of $\vec{\omega}$ for a given fluid element (of diameter equal to the Kolmogoroff scale) by subjecting the fluid element to a positive longitudinal strain.

The quantitative values of ω_z give insight into these effects with, of course, the understanding that the observed values have been spatially averaged! It is of interest to contrast this perceived understanding of the single stream shear layer - as obtained from Fig. 12 - with that provided by visualizations of "large scale vortex motions".

4.3 Stochastic Representations of ω_z

4.3.1 Histograms

The time series data at $x/\theta = 347$ have been normalized as $\omega_z\theta(x)/U_o$ and represented in histogram form, see Fig. 13. These histograms provide an instructive representation of: i) the width of the distributions compared with the mean value and ii) that a larger sample size would be required to permit the histograms to faithfully approximate the true probability density functions. It would be expected that the p.d f.'s would exhibit smoothly varying shapes as the source location is moved across the shear layer; this is nominally but not precisely obtained.

In this regard, it is instructive to consider the relative record lengths in terms of "convected lengths" represented by the sample. The shear layer width is nominally 6θ and a "convection speed" of $(U_o/2)$ can be used for the present calculation Given the total sample time of T = 3.5 sec, it is noted that

$$\Delta x = T\left[\frac{U_o}{7}\right] = 22\ 75\ m \approx 43 \text{ shear layer widths} \qquad (9)$$

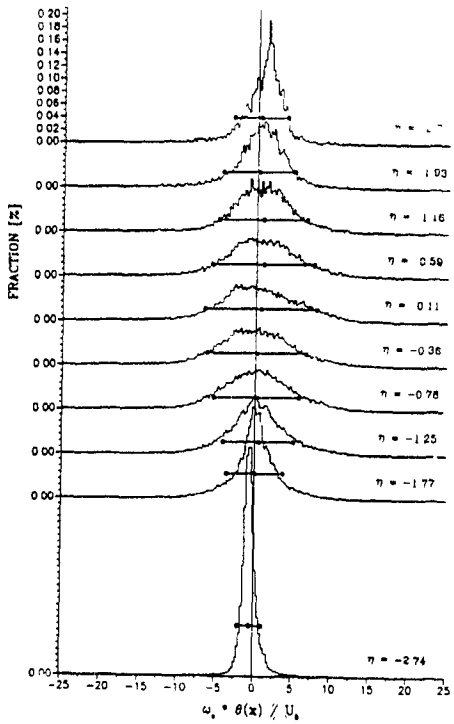

Figure 13 Histogram of ω_z (x,y,t)

4.3.2 Mean Values ($\bar{\omega}_z$)

Bruns [1990] has quantitatively established the expected result that . that $\partial\bar{v}/\partial x \ll \partial\bar{u}/\partial y$ Hence, for $\bar{u}/U_o = f(\eta)$, $\bar{\omega}_z$ can be computed given an expression for $f(\eta)$ Bruns [1990] evaluated the $\bar{\omega}_z$ values using a modified error function for $f(\eta)$; see that reference for these values. Again, detailed differences, which can be ascribed to the limited sample sizes, are evident.

4.3.3 Standard Deviation Values($\tilde{\omega}_z$)

Figures 14 and 15 present the normalized $\tilde{\omega}_z$ distributions and the streamwise evolution of the maximum values respectively The former shows that the shear layer thickness defined using the vorticity is clearly larger than that inferred from the mean velocity field and the latter reveals that the maximum $\tilde{\omega}_z$ value (at a given x location) does not scale on local variables It is suggested that the maximum values decay weakly with downstream distance.

If the probe were able to resolve ω_z over a domain of the order of the Kolmogoroff scale, the measured standard deviation would be expected to approach the "true" value At present, the quantitative relationship between the observed and the true values is unknown; qualitatively, it is recognized that the true values of $\tilde{\omega}_z$ are larger than those of Figures 14 and 15

The Kurtosis (flatness) of the measured distributions are nominally constant across the active portion of the shear layer. $-3 \leq \eta \leq 3$ (See Bruns [1990] for the detailed distribution)

These values, ≈ 17, show that the measured populations are very widely distributed For reference, recall that a Gaussian distribution has a Kurtosis value of 3.0

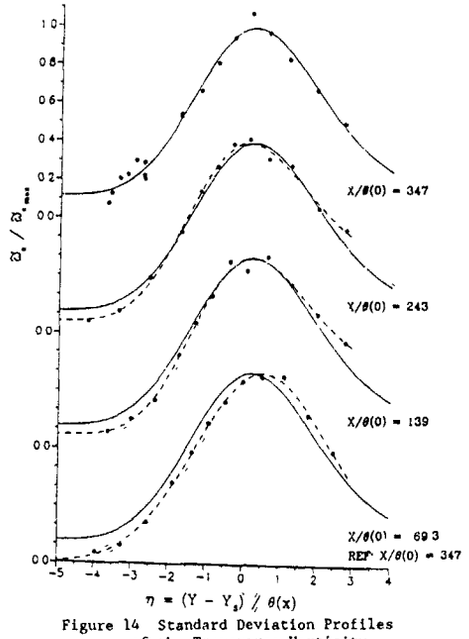

Figure 14 Standard Deviation Profiles of the Transverse Vorticity

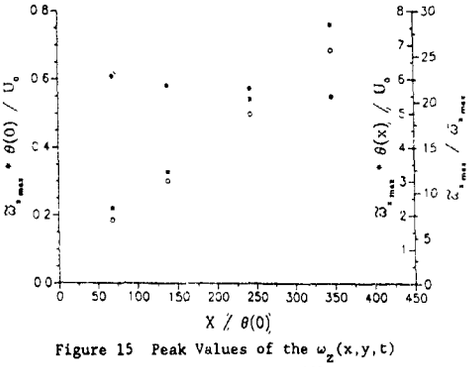

Figure 15 Peak Values of the $\omega_z(x,y,t)$ Standard Deviation Profiles

• $\tilde{\omega}_{max}*\theta(0)/U_o$ ▪ $\tilde{\omega}_{max}/\bar{\omega}_{max}$ ○ $\tilde{\omega}_{max}*\theta(x)/U_o$

5.0 Summary and Conclusions

Mean velocity and standard turbulence quantities for a high Reynolds number single stream shear layer are presented herein These results show that a self-preserving state is achieved in a downstream distance of nominally $x/\theta(0) = 200$ for the high Reynolds number boundary layer at x=0, namely $U_o\theta(0)/\nu = 7,200$.

Transverse vorticity measurements, $\omega_z(t)$, are presented and interpreted The $\omega_z(t)$ populations are characterized by a large ratio between the mean value and the peak standard deviation. $\tilde{\omega}_z/\bar{\omega}_z \approx 28$ at $x/\theta(0) = 347$, and momentary excursions which are quite large. The later is quantified by the Kurtosis values of nominally 17

The "true" standard deviation and Kurtosis values, i e , those which would be provided by a measurement domain nominally equal to the Kolmogoroff scale, are unknown albeit they are certainly larger than the values reported herein

6.0 References

1) Ali, S.K , Klewicki, C L , Disimile, P J., Lawson, I and Foss, J.F , 1985, "Entrainment Region Phenomena for a Large Plane Shear Layer", Fifth Symposium on Turbulent Shear Flows

2) Bradshaw, P , 1966, "The Effect of Initial Conditions on the Development of a Free Shear Layer", *Journal of Fluid Mechanics*, Vol Part 2 pp 225-236

3) Bruns, J. M., 1990, "Evaluation of Hot-wire Velocity and Vorticity Measurements in a Single-stream Shear Layer and Its Parent Boundary Layer", Dioplomarbeit, Michigan State University and Rheinisch-Westfallische Technische Hochschule (Aachen, F R.G)

4) Coles, D , 1956, "The Law of the Wake in the Turbulent Boundary Layer" *Journal of Fluid Mechanics*, Vol. 1, 1954

5) Collis, D C and Williams, M J , 1959, "Two-Dimensional Convection from Heated Wires at Low Reynolds Numbers", Jour Fluid Mech., Vol 6, pp. 357-384.

6) Foss, J.F , June 1991, "Vorticity Considerations and Planar Shear Layers" Proceedings Second World Conference On Experimental Heat Transfer, Fluid Mechanics and Thermodynamics, Dubrovnik, Yugoslavia

7) Foss, J F and Haw, R C , June 1990, "Transverse Vorticity Measurements Using a Compact Array of Four Sensers", Symposium on Thermal Anemometry, Ed D E. Stock, ASME

8) Haw, R C , Foss, J.K and Foss, J.F , 1989, "Vorticity Based Intermittency Measurements in a Single Stream Shear Layer", Proc Second European Turb Conf Advances in Turbulence 2, Ed H H Fernholz and H.E Fiedler Springer Verlag, Berlin.

9) Haw, R C. and Foss, J F , August 1989, "The Effects of Forcing on a Single Stream Shear Layer and Its Parent Boundary Layer", proc Seventh Symp. on Thrb. Shear Flows, Stanford University, Stanford, CA.

10) Hussain, F. and Zaman, K., 1985, "An Experimental Study of Organized Motions in the Turbulent Mixing Layer", *Journal of Fluid Mechanics*, Vol 159

11) Klebanof, P.S and Diehl, J W , "Some Features of Artifically Thickened Fully Developed Turbulent Boundary Layers with Zero Pressure Gradient", NACA Technical Note 2475

12) Spalding, D B , 1961, "A Single Formula for the Law of The Wall" *Journal of Applied Mechanics*, Vol 28, pp 455-457.

13) Wygnanski, I and Fiedler, H E , April 1970, "The Two-Dimensional Mixing Region", *Journal of Fluid Mechanics*, Vol 41, Part 2, pp 327-361

EIGHTH SYMPOSIUM ON
TURBULENT SHEAR FLOWS
Technical University of Munich
September 9-11, 1991

EVOLUTION OF THREE-DIMENSIONALITY IN STABLE AND UNSTABLE CURVED MIXING LAYERS

Michael W. Plesniak*, Rabindra D. Mehta† and James P. Johnston*

*Department of Mechanical Engineering
Thermosciences Division, Stanford University

†Department of Aeronautics and Astronautics
JIAA, Stanford University, Stanford,
California 94305, U.S.A

ABSTRACT

An experiment was conducted on the effects of mild streamwise curvature ($\delta/R < 5\%$) on the three-dimensional structure of a two-stream mixing layer at high Reynolds number ($Re_\delta \sim 2.7 \times 10^4$). Mixing layers with velocity ratios of 0.6 and laminar initial boundary layers were subjected to stabilizing and destabilizing longitudinal curvature by interchanging the high- and low-speed sides. Measurements of the mean and fluctuating velocities were obtained on fine cross-plane grids at eleven streamwise locations using a rotatable cross-wire probe. Well-organized streamwise vorticity was generated in both cases through the braid instability. Although the vortex structures decayed with streamwise distance in both cases, the rate of decay for the unstable case was slower. As a consequence of that the unstable layer exhibited noticeable spanwise variations in the mean velocity and Reynolds stresses. Both cases achieved linear growth, but the rate of growth for the unstable case was higher. The far-field spanwise-averaged peak Reynolds stresses were significantly higher for the destabilized case compared to the stabilized case, which exhibited levels comparable to those of a straight case.

NOMENCLATURE

H	Initial boundary layer shape factor
r	$(RU)_2/(RU)_1$, Velocity ratio
R	Local radius
$\bar{R}$	Mean radius of curvature at mid-profile
Re_l	Reynolds number based on length scale L
U, V, W	Mean velocity in the X (streamwise), Y (normal), Z (spanwise) directions, respectively
U_e	Free-stream velocity in the test section
U_0	$[(RU)_1 - (RU)_2]/\bar{R}$, Velocity difference across mixing layer
u', v', w'	Fluctuating velocity components in the X, Y, Z directions, respectively
δ	Mixing layer thickness (error function fit)
δ_{99}	Initial boundary layer thickness
θ	Initial boundary layer momentum thickness
ω_z	Streamwise component of mean vorticity
$()_{max}$	Maximum value at given X-station (averaged over 30-70 spanwise profiles)
$()_1$	Value for high-speed side
$()_2$	Value for low-speed side

INTRODUCTION

The plane turbulent mixing layer is a desirable free-shear flow for fundamental studies because of its relatively simple mathematical description and common occurance in practice. Although a great deal of effort has been directed toward understanding the structure and development of mixing layers, these phenomena are not yet fully understood because of their sensitivity to initial and boundary conditions (Ho & Huerre 1984). In particular, a mixing layer originating from laminar boundary layers on the splitter plate develops a complex three-dimensional structure in the form of streamwise vorticity.

The presence and role of these streamwise structures in a mixing layer at high Reynolds number ($Re_\delta \sim 2.5 \times 10^4$) were recently investigated by Bell & Mehta (1989). A plane, two-stream mixing layer was generated, with a velocity ratio of 0.6 and laminar initial boundary layers which were nominally two-dimensional. Measurements of the mean streamwise vorticity indicated that small spanwise disturbances in the flow were initially amplified just downstream of the first spanwise roll-up (in the braid region), leading to the formation of streamwise vortices. The vortices first appeared in clusters containing vorticity of both signs, but further downstream, they re-organized to form counter-rotating pairs. The vortex structure was then found to grow in size, scaling approximately with the mixing layer vorticity thickness, and to weaken, the maximum mean vorticity diffusing as approximately $1/X^{1.5}$. The mixing layer appeared to be nominally two-dimensional in the far-field, "self-similar" region. Changing the initial conditions slightly (by interchanging the high- and low-speed sides) has also been investigated recently (Plesniak *et al* 1991) and shown to have negligible effect on the turbulence structure in the far-field.

It is well known that an inviscid instability occurs in any curved flow where the angular momentum decreases away from the center of curvature (Bradshaw 1973). A popular and widely studied example of this is the concave boundary layer flow where the instability results from the no-slip condition at the wall. The instability leads to a substantial increase in the Reynolds stress levels within the boundary layer and, apparently, to the formation of Taylor-Gortler roll cells which appear in counter-rotating streamwise pairs with an approximate spanwise wavelength equivalent to twice the boundary layer thickness (Barlow & Johnston 1988). On the other hand, the boundary layer flow over a convex wall experiences a stabilizing effect such that three-dimensional effects and Reynolds stress levels are suppressed (Muck *et al* 1985). *A mixing layer with curvature in the streamwise direction is expected to experience similar effects, the layer is subject to a destabilizing effect if the low-speed stream is on the outside of the curve and a stabilizing effect if it is on the inside of the curve.*

The subject of streamwise curvature effects on mixing layer structure has received limited attention. Margolis & Lumley (1965), Wyngaard *et al* (1968), Castro & Bradshaw (1976) and Gibson & Younis (1983) investigated curved single-stream layers and showed that curvature affects Reynolds stress production and turbulence transport. Wang (1984) presented flow visualization and mean velocity data for a curved two-stream mixing layer and showed that stabilizing curvature reduced the rate of spanwise vortex pairing whereas destabilizing curvature promoted three-dimensionality. Plesniak & Johnston (1989) investigated the role of stabilizing and destabilizing curvature in suppressing or enhancing the secondary instability responsible for the formation of the streamwise roll cells in a two-stream turbulent mixing layer. These results suggested that the Taylor-Gortler instability mechanism, present in the unstable case, acts to strengthen the streamwise roll cells. Dramatic increases in the primary Reynolds shear stress and enhanced transport of turbulence were documented in the unstable case. Thus, the streamwise structures are believed to play an integral role in the generation and evolution of turbulence in two-stream mixing layers.

The main objectives of the present study were to estab-

lish the effects of stabilizing and destabilizing curvature on the three-dimensional structure of two-stream mixing layers through measurements of the mean and turbulence properties on large cross-plane grids In addition, in the unstable case, the role of the Taylor-Gortler effect, if present, on the streamwise vorticity generated through the braid instability was to be investigated

EXPERIMENTAL PROCEDURE

The experiments were conducted in a *Mixing Layer Wind Tunnel* (Bell & Mehta 1989) consisting of two separate legs which are independently driven The two streams merge at the sharp trailing edge of a slowly tapering splitter plate with an included angle of about 1° The curved test section (Fig 1) has a fixed radius of 305 cm, giving δ/R of less than 5%, and measures 36 cm in the cross-stream (Y) direction, 91 cm in the spanwise (Z) direction and 366 cm in length (X, measured along the centerline arc) One sidewall is adjustable and this was set to give a nominally zero streamwise pressure gradient

The two sides of the wind tunnel were run at free-stream velocities of 9 and 15 m/s, thus giving a mixing layer with velocity ratio, $U_2/U_1 = 0.6$ The high-and low-speed sides were interchanged to produce the stabilizing and destabilizing cases In the free-stream, the measured streamwise turbulence level (u'/U_e) was approximately 0.15%. The boundary layers on the splitter plate were laminar at these running conditions with the integral properties given in Table 1

Measurements were made using a cross-wire probe mounted on a 3-D traverse and linked to a fully automated data acquisition and reduction system controlled by a MicroVax II computer The cross-wire probe (*Dantec* Model 55P51) consisted of 5 μm platinum-plated tungsten sensing elements 1.25 mm long and separated by approximately 1 mm The probe was calibrated statically in the potential core of the flow assuming a 'cosine-law' response to yaw, with the effective angle determined by calibration The analog signals were filtered and amplified before being fed into a fast *Tustin* sample-and-hold A/D converter with 16 bit resolution and a multiplexer for connection to the computer Individual statistics were averaged over 5,000 samples obtained at a rate of 1,500 samples per second.

Data were obtained in cross-sectional (Y-Z) planes with the probe oriented in the uv - and uw-planes Measurements were made at eleven streamwise stations within the test section between X = 11 to 255 cm. Typically, 1200-1500 points were measured on a rectangular, cross-plane grid at a given streamwise station The grid spacing (same in both directions, Y and Z) ranged from 0.1 to 1.0 cm, depending on the streamwise station. The measurements of U, W and $\overline{u'w'}$ were corrected for mean streamwise velocity gradient ($\partial U/\partial Y$) effects, by assuming a linear variation in U between the cross-wire sensors (Bell & Mehta 1989) The streamwise component of mean vorticity (ω_x) was computed using a central difference numerical differentiation of the mean velocity (V and W) measurements

RESULTS AND DISCUSSION

Similarities and differences between the unstable and stable cases are illustrated through detailed comparisons using contour plots at three streamwise stations, covering both, the near- and far-field development regions Included in the streamwise development plots are data for the straight case, run at the same velocity ratio in the same facility, but with straight side-walls (Plesniak *et al* 1991)

Figures 2a-c present contours of the mean streamwise velocity (U/U_0) for the unstable and stable cases. At the first location (X = 11 cm), the velocity contours are corrugated in an irregular fashion in both cases This corrugation may be attributed to the presence of streamwise vortices in the mixing layer Somewhat surprisingly, the stable mixing layer appears more distorted at this first measurement station Further downstream, the distortions become stronger, and more regular and correlated, across the entire mixing layer for the unstable case and by X = 76 cm, the quasi-periodic variation exhibits an average wavelength of approximately 5 cm On the other hand, the velocity contours for the stable case are now hardly distorted. By the station at X = 189 cm, the unstable case still shows some distortion, although the amplitude has decreased while the wavelength has increased. However, the contours for the stable case are almost straight and parallel, suggesting that the streamwise vorticity in this case has decayed almost completely These results imply that the streamwise vorticity decays considerably faster in the stable case compared to the unstable case Note also that the mixing layer is noticeably thinner for the stable case.

Contours of the primary Reynolds shear stress, $\overline{u'v'}$, for the two cases are compared in Figs 3a-c At the first measurement station, the spanwise distribution of $\overline{u'v'}$ is significantly different for the two cases Clearly, the contours for the stable case are more like those usually observed in plane mixing layers, although these contours are somewhat distorted and contain local peaks On the other hand, the contours for the unstable case reveal a patchy distribution with strong local peaks spaced at about 2 cm At X = 76 cm, the contours for the unstable case exhibit a quasi-periodic distortion with local peaks, while those for the stable case appear almost straight and parallel Peak $\overline{u'v'}$ varies by about 12% across the span for the unstable case, compared to about 8% for the stable layer The local peak levels for the unstable case are higher by a factor of two at this streamwise location and this trend of higher $\overline{u'v'}$ continues to the X = 189 cm station At this location, the cross-stream extent of significant levels of $\overline{u'v'}$ is also clearly higher for the unstable case, although the distribution of $\overline{u'v'}$ shows a quasi-two-dimensional behavior for both cases. Spanwise variations of 6.6% are measured peak $\overline{u'v'}$ at this station for the unstable case, versus 3.3% for the stable case

Bell & Mehta (1989) showed that the spanwise variations in mean velocity and Reynolds stresses in the developing region of the mixing layer were governed by the position and strength of the secondary streamwise vortices The mean streamwise vorticity contours for the two cases are presented in Figs 4a and b At X = 11 cm, the streamwise vortices are much stronger (by almost a factor of two) in the unstable case compared to the stable case and they appear in clusters, much like those seen in the straight cases (Bell & Mehta 1989, Plesniak *et al* 1991) The weaker vortices in the stable case appear to be distributed in a less organized fashion The levels of maximum vorticity have diminished by the next station at X = 33 cm for both cases, although by a larger amount for the stable case The distribution is still more or less random for the stable case, but that for the unstable case now shows a regular array consisting of counter-rotating pairs of streamwise vortices — this result is again qualitatively similar to that for the straight case For the stable case, the organization and vorticity levels decrease with streamwise distance such that by X = 76 cm, the measured levels are embedded within the "noise" associated with the entire vorticity measurement scheme Although the levels in the unstable case also decay with streamwise distance, an array of counter-rotating pairs of vortices is still evident at X = 76 cm Further downstream, the vortex size continued to grow in proportion to the mixing layer thickness, but their strength decayed In the far-field region, the vorticity levels for the unstable case were higher than those in the straight case whereas those for the stable case were lower

The streamwise vorticity contour results suggest that the effect of the curvature is to manipulate the streamwise vorticity generated by the braid instability, rather than *producing* new vorticity through the Taylor-Gortler instability in the unstable case, for example The straight case results (Bell & Mehta 1989) showed that the streamwise vortices were produced through the braid instability just downstream of the first spanwise roll-up (at $X \sim 7$ cm) By the first measurement station in the present study (X = 11 cm), the peak vorticity levels are considerably higher for the unstable case While it is not clear from the present measurements if the formation of the vorticity is affected by curvature, the decay rate in the near-field is strongly affected by curvature. The effect of the stabilizing curvature is to hasten the decay of the streamwise vorticity, and hence suppress its associated effects, whereas the effect of the destabilizing curvature is to retard the decay of streamwise vorticity, resulting in more pronounced effects At all

streamwise locations, the peak streamwise vorticity levels and their effects on the mean velocity and Reynolds stresses were higher in the unstable case compared to the straight case, whereas those in the stable case were lower

Streamwise evolution of the mixing layer thickness and peak Reynolds stresses are presented below in Figs 5a-e for the unstable, stable and straight cases All the results are based on spanwise averaged quantities, i e the measurements, obtained on a cross-plane grid, were divided into "slices" through the mixing layer The properties computed from each slice were then averaged with those obtained at other spanwise positions In effect, the mixing layer properties were averaged over 30-70 velocity profiles measured at the defined spanwise locations Due to the large spanwise variations experienced in the near-field, averaging is necessary to obtain an accurate representation of the behavior of the mixing layer

Figure 5a presents the streamwise growth of the mixing layer thickness, δ, for the three cases As suggested by the mean velocity contours, at the first station (X = 11 cm), the stable mixing layer is slightly thicker than the unstable and straight cases, but the trend is quickly reversed further downstream Beyond about X = 76 cm, all three cases exhibit linear growth, but the growth rates ($d\delta/dx$) are different Based on a linear least squares fit to the data downstream of X = 76 cm, $d\delta/dx$ = 0 022 for the straight case, 0 025 for the unstable case and 0 020 for the stable case The growth rate for the unstable case is, hence, increased by about 14% over the straight case while that of the stable case is decreased by about 9%

It has been suggested that the growth rate in the linear region is affected by the initial conditions, namely the presence of organized streamwise vorticity (Bell & Mehta 1990) Most of the growth in a mixing layer is achieved through the pairing of adjacent *spanwise* vortices and entrainment of potential fluid by these structures The presence of organized streamwise vorticity, riding over the spanwise vortices, adds to the entrainment process, resulting in a higher net growth rate Bell & Mehta (1990) found that the straight mixing layer originating from turbulent initial boundary layers did not contain organized streamwise vorticity and had a growth rate of 0 019, approximately 20% lower than the case with laminar initial boundary layers Likewise, the difference in growth rates in the present study may also be attributed to the different strengths of the streamwise vorticity in the three cases It is interesting to note that the growth rate for the present stable case is almost exactly the same as that of the straight case with turbulent initial boundary layers

The streamwise evolution of the peak Reynolds normal stress components ($\overline{u'^2}$, $\overline{v'^2}$, and $\overline{w'^2}$) is shown in Figs 5b-d The trends for the three stresses are very different at the first station (X = 11 cm) — $\overline{u'^2}$ is comparable for the stable and unstable cases, $\overline{v'^2}$ is higher for the unstable case, whereas $\overline{w'^2}$ is higher for the stable case However, beyond the second station at X = 33 cm, the peak normal stress levels for the unstable case are consistently higher than those for the stable case Further downstream, the normal stress levels for the stable case (especially $\overline{v'^2}$ and $\overline{w'^2}$) asymptote to approximately the same values as those for the straight case, while those for the unstable case are consistently higher

Figure 5e illustrates the streamwise evolution of the primary Reynolds shear stress maxima in the three cases At the first station, the peak shear stress levels for both curved cases are higher than those for the straight case Furthermore, the peak stress levels in the curved cases decrease monotonically with streamwise distance until an asymptote is reached, whereas the straight case has a distinct maximum at $X \sim 40$ cm — this is associated with transition in the mixing layer. Once again, the asymptotic level for the unstable case is higher than that for the stable case (which is comparable to that for the straight case) The increased stress levels in the unstable case are partly attributable to "extra" production through terms in the Reynolds stress transport equations which are activated by the angular momentum instability. Note that since the radius of curvature is held constant, δ/R increases with streamwise distance as the layer grows, and so the effects due to curvature should become more pronounced However, shear layer growth also leads to a reduction in the primary shear ($\partial U/\partial Y$), so it is hypothesized that the two effects tend to counteract each other to produce constant stress levels in the far-field

The Reynolds stress data indicate that the turbulence structure of the stable case in the far-field is comparable to that of the straight case, although the growth rate is somewhat lower The turbulence structure of the unstable case also seems to have achieved equilibrium, but different than that of the other two cases When comparing the development of the straight case with laminar initial boundary layers with that originating from turbulent boundary layers it was noted that the asymptotic turbulence structure was comparable for the two cases, although the thickness growth rates were different (Bell & Mehta 1990) It is believed that the straight case (with turbulent initial boundary layers) and the stable layer are structurally indistinguishable, and have achieved a self-similar state completely independent of initial conditions We expect the straight case (with laminar initial boundary layers) will eventually achieve the same self-similar growth rate since the streamwise vorticity decays with downstream distance It is unclear, but unlikely, that the unstable layer will also reach this same state, because the angular momentum instability mechanism is present throughout its development

CONCLUSIONS

A study of the effects of stabilizing and destabilizing streamwise curvature on the three-dimensional structure of a two-stream mixing layer has been completed The mean streamwise vorticity results show that the main effect of the destabilizing curvature is to retard the decay of the streamwise vorticity generated by the braid instability This results in stronger streamwise vorticity at a given streamwise location, producing more entrainment, and hence, higher asymptotic growth rate and higher Reynolds stresses compared to the stable and straight cases Only a part of the increase in Reynolds stresses is due to extra production through terms activated by the angular momentum instability The streamwise vorticity produces a measurable spanwise variation in the mean velocity and Reynolds stress distributions The effect of the stabilizing curvature, on the other hand, is to suppress the three-dimensionality by increasing the rate of decay of the streamwise vorticity, thus leading to a lower growth rate The spanwise variations in mean velocity and Reynolds stress distributions are, therefore, much smaller in this case. The asymptotic peak Reynolds stresses for the stable case are consequently lower than those in the unstable case, but comparable to those for the straight case

ACKNOWLEDGMENTS

This research was supported by The National Science Foundation Grant NSF-CTS-88-15670 and NASA Grant NCC-2-55 from the Fluid Dynamics Research Branch, NASA Ames Research Center

REFERENCES

BARLOW, R.S. & JOHNSTON, J.P. 1988 Structure of a Turbulent Boundary Layer on a Concave Surface *J Fluid Mech* **191**, 1988, 137-176

BELL, J H & MEHTA, R.D 1989 Three-Dimensional Structure of Plane Mixing Layers *JIAA TR-90*, Dept of Aeronautics and Astronautics, Stanford University.

BELL, J H & MEHTA, R D 1990 Development of a Two-Stream Mixing Layer From Tripped and Untripped Boundary Layers *AIAA J* **28**, No 12, 2034-2042

BRADSHAW, P 1973 Effects of Streamline Curvature on Turbulent Flow *AGARDograph* No 169.

CASTRO, I P & BRADSHAW, P 1976 The Turbulence Structure of a Highly Curved Mixing Layer *J Fluid Mech* **73**, 265-304.

GIBSON, M.M & YOUNIS, B A 1983 Turbulence Measurements in a Developing Mixing Layer with Mild Destabilizing Curvature *Exp Fluids* 1, 23 30

HO, C -M & HUERRE, P 1984 Perturbed Free Shear Layers. *Ann Rev Fluid Mech* **16**, 365-424

MARGOLIS, D P & LUMLEY, J L 1965 Curved Turbulent Mixing Layer *Phy Fluids* **8**, 1775-1784

MUCK, K C , HOFFMANN, P H & BRADSHAW, P 1985 The Effect of Convex Surface Curvature on Turbulent Boundary Layers *J Fluid Mech* **161**, 347-369

PLESNIAK, M W & JOHNSTON, J P 1989 The Effects of Longitudinal Curvature on Turbulent Two-Stream Mixing Layers *Report MD-54*, Dept of Mechanical Engineering Stanford University.

PLESNIAK, M W , BELL, J H & MEHTA, R D 1991 Effects of Initial Spanwise Perturbations and Three-Dimensionality in a Plane Mixing Layer. *AIAA*-91-0622

WANG, C 1984 The Effects of Curvature on Turbulent Mix ing Layers Ph D Thesis, GALCIT, CALTECH

WYNGAARD, J C , TENNEKES, H , LUMLEY, J L & MARGOLIS, D P 1968 Structure of Turbulence in a Curved Mixing Layer. *Phy Fluids* **11-6**, 1251-1253

Table 1. Initial Boundary Layer Properties

Condition	U_e (m/s)	δ_{99} (cm)	θ (cm)	Re_θ	H
Stable	15 0	0 40	0 050	525	2 52
Stable	9 0	0 44	0 061	362	2 24
Unstable	15 0	0 34	0 043	432	2 24
Unstable	9 0	0 50	0 065	392	2.55

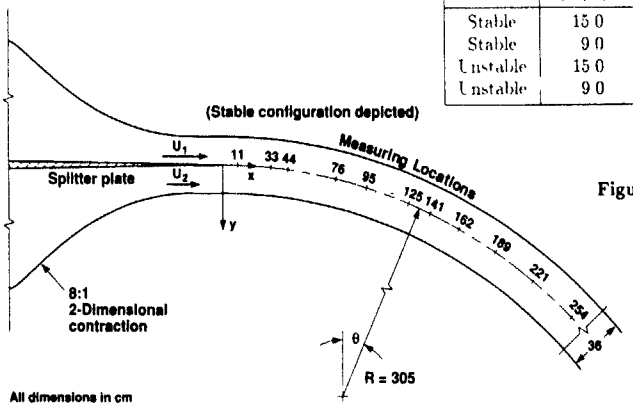

Figure 1. Curved Mixing Layer Test Section Schematic.

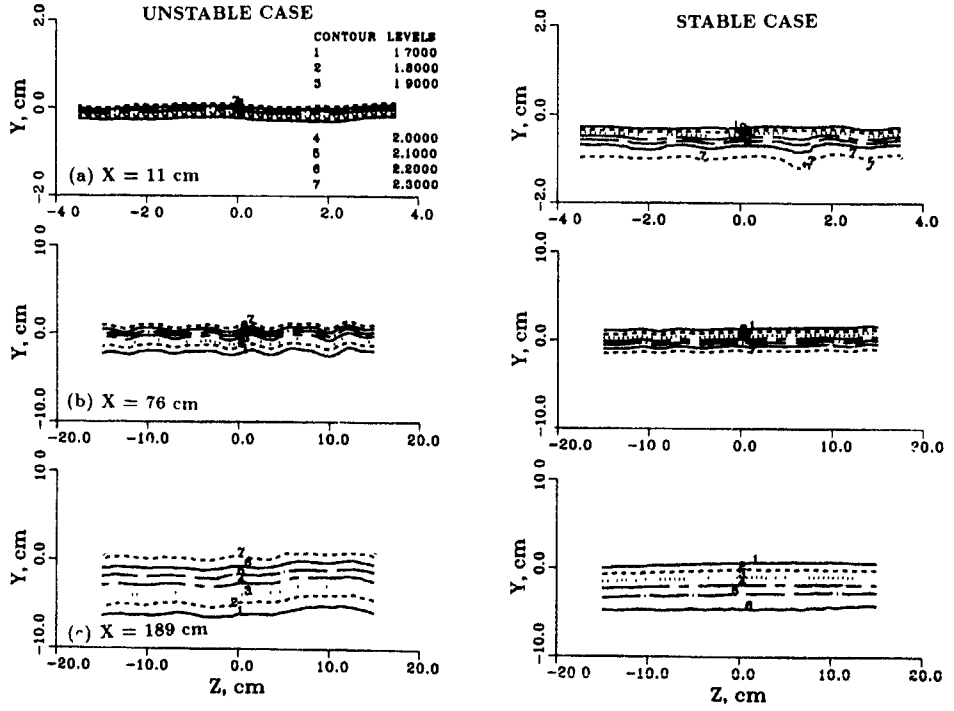

Figure 2. Mean Streamwise Velocity ($U/\overline{R}U_0$) Contours for Unstable and Stable Cases.

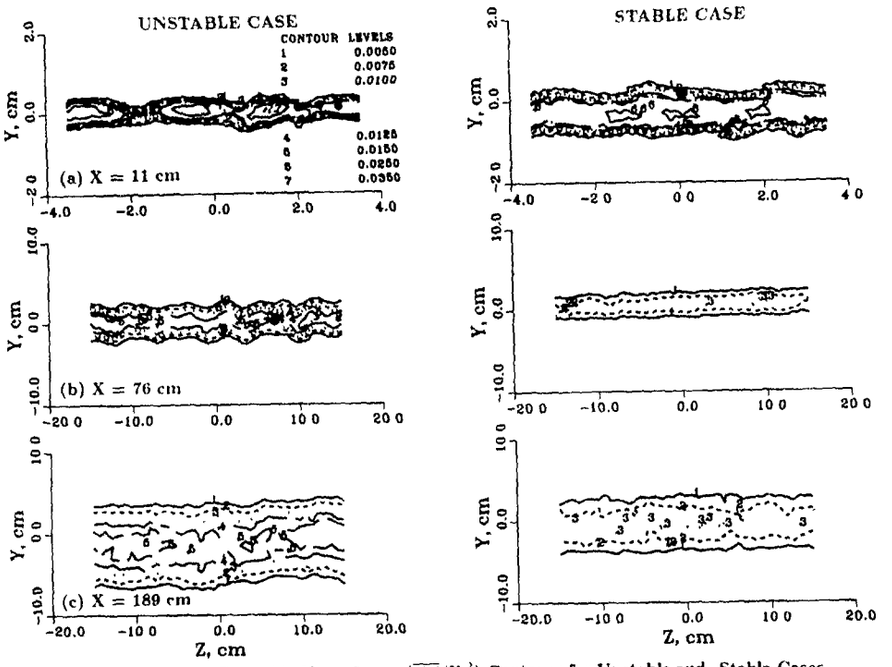

Figure 3. Primary Reynolds Shear Stress ($\overline{u'v'}/U_0^2$) Contours for Unstable and Stable Cases.

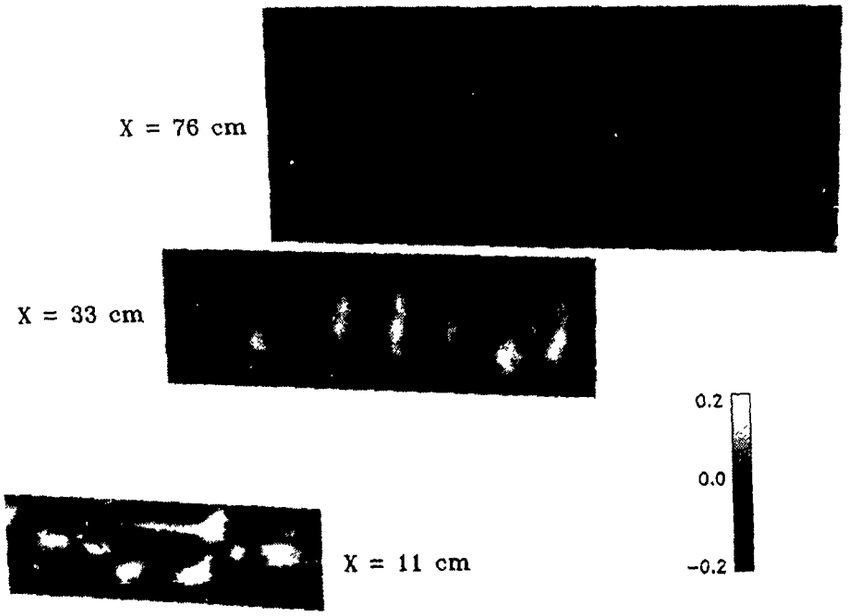

Figure 4a. Mean Streamwise Vorticity ($\omega_x/U_0.cm^{-1}$) Contours for Unstable Case.

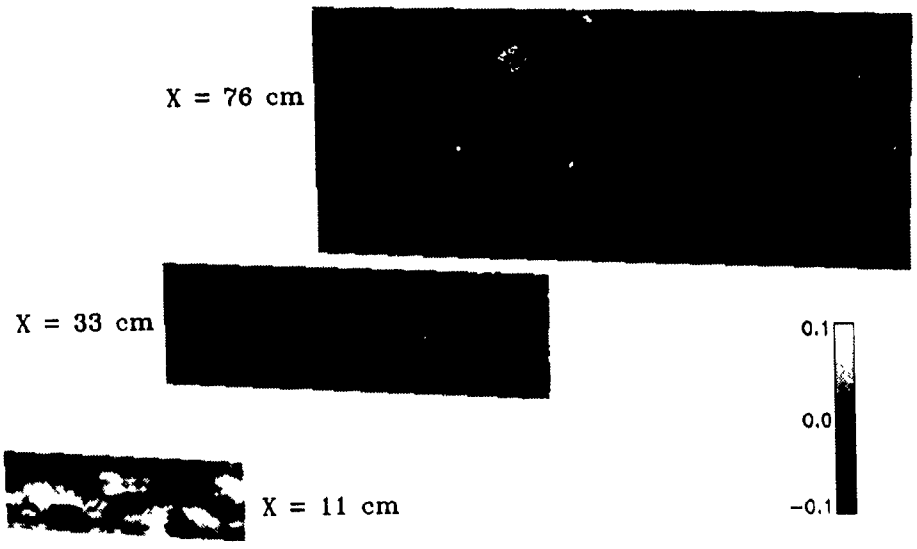

Figure 4b. Mean Streamwise Vorticity ($\omega_x/U_0, cm^{-1}$) Contours for Stable Case.

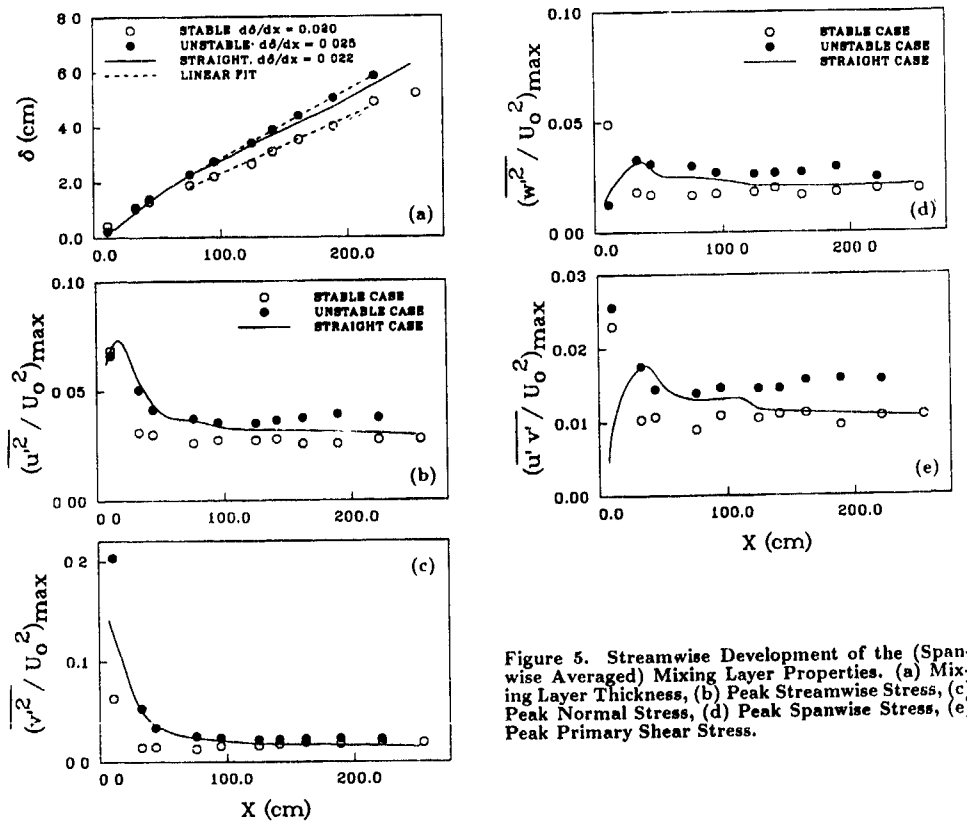

Figure 5. Streamwise Development of the (Spanwise Averaged) Mixing Layer Properties. (a) Mixing Layer Thickness, (b) Peak Streamwise Stress, (c) Peak Normal Stress, (d) Peak Spanwise Stress, (e) Peak Primary Shear Stress.

EIGHTH SYMPOSIUM ON
TURBULENT SHEAR FLOWS
Technical University of Munich
September 9-11, 1991

A Computational Fluid Dynamics Code for the Investigation of Free-Shear-Layer Optics

Y.P. Tsai*) and W.H. Christiansen**)

*) Department of Mechanical Engineering
China College of Engineering
Hsin Chu, Taiwan, 30067 ROC
**) Department of Aeronautics and Astronautics
University of Washington
Seattle, WA 98195 USA

ABSTRACT

The basic vortex dynamics in a plane free shear layer generated by the mixing of two coflowing fluid streams are investigated. Two-dimensional Euler equations are solved directly using the second-order, explicit, MacCormack predictor-corrector and Godunov methods alternately. Detailed description of the numerical algorithm, initial conditions and boundary conditions are given. The density field obtained may be used for optical studies.

I. INTRODUCTION

The extraction of power from high-power gas lasers often involves passing the beam through interface between gases of different indices of refraction. Turbulent shear layers can produce random phase errors in the beam that can substantially reduce the maximum intensity to which the beam can be focused. The main purpose of our reseach is to understand the factors which influence optical degradation and to make useful prediction or correlations with respect to the flow parameters. In order to understand the optical properties of shear layer, first of all, it is improtant to understand the basic fluid mechanics of the shear layer. In the past, the investigations of the shear layer optical properties were based on the assumptions that the natural shear layers were homogeneous and isotropic(Sutton 1969, Legner et al 1978). There has been no study of the optical effects of large-scale structures which are existing during the course of the shear layer development. In this work, the optical effects of coherent structures are identified.

The physical properties of spatially-developing mixing layers between two flows of different velocities and densities are calculated. The 2-D compressible Euler equations are solved directly using the second-order, explicit, MacCormack method and the Godunov method alternately. There is no subgrid scale turbulence in this direct numerical simulation scheme. Two air streams are modelled, each with different enthalpy, so that the density ratio is a parameter other than unity. A hyperbolic-tangent velocity profile is adopted for the initial streamwise velocity distribution at the splitter plate. Large vortical structures and their evolution are investigated for both natural and forced flows. In the forced cases, the forcing frequencies are the fundamental frequency and the first subharmonic. The forcing is applied at the end of the splitter plate. Temporal statistics of fluid dynamical variables of the mixing layer are calculated.

In Sec. II, the numerical method, initial conditions and boundary conditions are discussed in detail. In Sec. III, the results of fluid dynamical statistics computations are given and compared with available experimental or numerical data for validation purposes. The numerical results for both the natural and forced shear layers show that their fluid dynamical properties such as the mean velocity profile, growth rate, turbulence intensity, entrainment ratio and Reynolds stress are all in agreement with the experimental measurements. Finally, the optical effects of the shear layer and the coherent structures within the shear layer are calculated by passing a laser beam through it with circular aperture and uniform phase. The far-field intensity distribution, time averaged Strehl ratio and modulation transfer function are calculated for shear layers with different flow conditions.

II. GOVERNING EQUATIONS and NUMERICAL ALGORITHM

The equations governing Newtonian fluid dynamics have been known for more than a century. However, the closed form analytic solutions can be found only for a few special cases. Now with the development of large, fast scientific computers and in parallel with the improvement in numerical schemes, these equations can be solved directly using the methods of computational fluid dynamics. Since the basic vortex dynamics in a shear layer is essentially inviscid, it is expected that significant simulation can be obtained by solving the Euler equations. Based on the assumptions that there are no external heat addition and body forces, the compressible Euler equations in two-dimensional Cartesian coordinates can be written as

$$\frac{\partial U}{\partial t} + \frac{\partial F}{\partial x} + \frac{\partial G}{\partial y} = 0 \qquad (1)$$

where U, F and G are vectors given by

$$U = \begin{bmatrix} \rho \\ \rho u \\ \rho v \\ e \end{bmatrix}, \quad F = \begin{bmatrix} \rho u \\ \rho u^2 + p \\ \rho u v \\ (e+p)u \end{bmatrix}, \quad G = \begin{bmatrix} \rho v \\ \rho u v \\ \rho v^2 + p \\ (e+p)v \end{bmatrix}$$

and x is the streamwise coordinate, y is the cross-stream coordinate(see Fig 1). The equations written in conservation law form represent conservation of mass, momentum and total energy of invisid fluid motions. The variables ρ, ρu, ρv and e are mass, streamwise momentum, cross-stream momentum and total energy respectively, all per unit volume. p is the pressure. For ideal gas, the pressure is related to equation of state

$$p = (\gamma - 1)\rho\epsilon \qquad (2)$$

where ϵ is the specific internal energy and γ is the ratio of specific heats, i.e., $\gamma = c_p/c_v$. Throughout this paper the value of γ is taken to be 1.40.

The numerical code used in the current work is a direct simulation of the two-dimensional compressible Euler equations with no subgrid scale turbulence model. The code uses the finite volume technique which involves alternating in time the second-order, explicit MacCormack (1969) and Godunov (1959) methods. Since the second-order, explicit MacCormack Scheme has a lagging phase error and the Godunov scheme has a leading phase error (Steger & Warming, 1976), considerable reduction in phase error can be achieved by temporal switching of these two schemes (Fromm, 1971).

MacCormack Scheme

The MacCormack finite difference method is a variation of the two-step Lax-Wendroff scheme. This explicit scheme is second-order accurate both in space and time. The computational domain is shown schematically in Fig 1. A grid of 200 by 50 is adopted. The state variables ρ, u, v, and e are calculated at the center of each computational cell, which is a square mesh, $\Delta x = \Delta y$. A superscript n denotes time $t_n = n\Delta t$. Subscripts j, k denote position (x_j, y_k), where $x_j = j\Delta x$ and $y_k = k\Delta y$. For example, $\rho^n_{j,k}$ represents the volume-averaged density at the point (x_j, y_k) and time t_n. Referring to Fig. 2, the indices of points and lines are shown in the fixed grid system for a general computational volume element. The flow parameters in the center of cell are given the integer index j, k. The cell boundaries surfaces are given a fractional and one integer index; the surfaces are denoted as $S_{j,k-\frac{1}{2}}$, $S_{j,k+\frac{1}{2}}$, $S_{j-\frac{1}{2},k}$, or $S_{j+\frac{1}{2},k}$. Viewing $\bar{U}^n_{j,k}$ as an approximation to the cell average of U rather than as an approximation to the point value $U(x_j, y_k, t_n)$ and using explicit, backward spatial difference method in the predictor step and forward spatial difference method in the corrector step, the solutions at time level n+1 are determined from the data at time level n by creating "interface states" at location such as $(j+\frac{1}{2},k)$, the MacCormack finite volume approximation is

• Predictor Step

$$\Delta \bar{U}^n_{j,k} = -\frac{\Delta t}{V_{j,k}}\left[Q^n_{j,k} \cdot S_{j,k-\frac{1}{2}} + Q^n_{j-1,k} \cdot S_{j-\frac{1}{2},k} + Q^n_{j,k} \cdot S_{j,k+\frac{1}{2}} + Q^n_{j+1,k} \cdot S_{j+\frac{1}{2},k}\right]$$

$$\overline{U}^{n+1}_{j,k} = U^{n}_{j,k} + \Delta U^{n}_{j,k}$$

• Corrector Step

$$\Delta \overline{U}^{n+1}_{j,k} = -\frac{\Delta t}{V_{j,k}}\left[\overline{Q}^{n+1}_{j+\frac{1}{2},k} \cdot S_{j+\frac{1}{2},k} + \overline{Q}^{n+1}_{j,k+\frac{1}{2}} \cdot S_{j,k+\frac{1}{2}} + \overline{Q}^{n+1}_{j-\frac{1}{2},k} \cdot S_{j-\frac{1}{2},k} + \overline{Q}^{n+1}_{j,k-\frac{1}{2}} \cdot S_{j,k-\frac{1}{2}}\right]$$

$$U^{n+1}_{j,k} = \frac{1}{2}\left[U^{n}_{j,k} + \left(\overline{U}^{n+1}_{j,k} + \Delta \overline{U}^{n+1}_{j,k}\right)\right]$$

where $V_{j,k}$ is the cell volume of cell (j,k)

To calculate the flux terms, second–order extrapolations are made of the primitive variables (ρ, u, v, e) from the cell centers to the cell boundaries to give extrapolated values on the two sides of all cell boundaries This procedure is illustrated in Fig 3 On the predictor step, values extrapolated from the left or the bottom side of the cell boundaries are used, on the corrector step, values extrapolated from the right or the top side of the cell boundaries are used. To achieve numerical stability, a simple technique is applied, that is, all extrapolated values of the primitive variables at the cell boundaries must lie between the cell center values at the two adjacent cell centers If any extrapolated value of a primitive variable does not satisfy this condition, it is replaced by the cell center value which is more closer to it (Bogdanoff & Brackett, 1987) For example, as demonstrated in Fig 4, if the extrapolated value $\rho_{j+\frac{1}{2},k}$ lies above the point A, set $\rho_{j+\frac{1}{2},k} = \rho_{j+1,k}$, if it lies below the point B, then let $\rho_{j+\frac{1}{2},k} = \rho_{j,k}$, if $\rho_{j+\frac{1}{2},k}$ lies within point A and B, it is this value to be used for the boundary flux calculations

Godunov Scheme

The basic idea of the Godunov method is emphasized by the use of exact solution of the gasdynamics equations with piecewise constant initial conditions for the construction of the finite difference scheme The use of Riemann problem solution makes Godunov's method a form of the method of characteristics Godunov used the characteristic information within the frame work of conservative method such that Riemann problem was solved forward in time and the solution of the Riemann problem was employed to calculate numerical fluxes at cell edges The physical picture of the wave interactions involved is very clear in this method Detailed derivations of Godunov method are available in many documents (Godunov, 1959, Holt, 1984) The components of $\overline{U}^{n+1}_{j,k}$ are calculated as follows.

$$\rho^{n+1}_{j,k} = \rho^{n}_{j,k} - \frac{\Delta t}{\Delta x}\left[(RU)^{n}_{j+\frac{1}{2},k} - (RU)^{n}_{j-\frac{1}{2},k}\right] - \frac{\Delta t}{\Delta y}\left[(RV)^{n}_{j,k+\frac{1}{2}} - (RV)^{n}_{j,k-\frac{1}{2}}\right],$$

$$(\rho u)^{n+1}_{j,k} = (\rho u)^{n}_{j,k} - \frac{\Delta t}{\Delta x}\left[(P+RU^2)^{n}_{j+\frac{1}{2},k} - (P+RU^2)^{n}_{j-\frac{1}{2},k}\right] - \frac{\Delta t}{\Delta y}\left[(RUV)^{n}_{j,k+\frac{1}{2}} - (RUV)^{n}_{j,k-\frac{1}{2}}\right],$$

$$(\rho v)^{n+1}_{j,k} = (\rho v)^{n}_{j,k} - \frac{\Delta t}{\Delta x}\left[(RUV)^{n}_{j+\frac{1}{2},k} - (RUV)^{n}_{j-\frac{1}{2},k}\right] - \frac{\Delta t}{\Delta y}\left[(P+RV^2)^{n}_{j,k+\frac{1}{2}} - (P+RV^2)^{n}_{j,k-\frac{1}{2}}\right],$$

$$e^{n+1}_{j,k} = e^{n}_{j,k} - \frac{\Delta t}{\Delta x}\left[(EU+PU)^{n}_{j+\frac{1}{2},k} - (EU+PU)^{n}_{j-\frac{1}{2},k}\right] - \frac{\Delta t}{\Delta y}\left[(EV+PV)^{n}_{j,k+\frac{1}{2}} - (EV+PV)^{n}_{j,k-\frac{1}{2}}\right]$$

where R, U and V are the density, x–velocity and y–velocity on the cell boundaries respectively P and E are the pressure and total energy on boundary, where E is related to P by

$$E = \frac{P}{\gamma-1} + 0.5R(U^2 + V^2)$$

Note that prior to the calculation of boundary values for the primitive variables, the initial states to the left and right of the cell boundary are obtained by second–order extrapolation For example, at the boundary $S_{j-\frac{1}{2},k}$ (Fig. 3), we have the two initial states

$$q_l = 1.5q_{j-1,k} - 0.5q_{j-2,k}$$

$$q_r = 1.5q_{j,k} - 0.5q_{j+1,k}$$

The extrapolated primitive variables are subject to the limiting criterion just discussed above, and this set of piecewise constant initial data will give a sequence of Riemann problems

To advance the code in one time step Δt, the numerical stability condition must be applied (MacCormack, 1969, Godunov, 1959) During this time interval, Δt, waves from neighboring Riemann problems will not interact with each other In our calculations, Δx and Δy are of the order of millimeter, Δt is therefore of the order of microsecond to satisfy the stability condition

Boundary Conditions

In numerical simulations, the computational domain must be finite, so appropriate boundary conditions need to be introduced to obtain the correct flow field Based on the hypothesis that the top and bottom boundaries are streamlines, the numerical boundary conditions used at the top and bottom boundaries are

$$v=0$$

and

$$\frac{\partial q}{\partial y} = 0$$

where q is ρ, u, or e For the outflow boundary condition, pressure is assumed to be constant there This is a good approximation provided that the test section is long enough At the exit plane of the computational domain, the "convective condition" of the form

$$\frac{\partial f^*}{\partial t} + U_c \frac{\partial f^*}{\partial x} = 0$$

is used to make this condition absorptive (Lowery & Reynolds, 1986), where U_c is the convective velocity of the large eddies in the mixing layer and f^* is u, v, or ρ The convective velocity is nearly equal to the average of the two free stream velocities U_1 and U_2 At the inlet plane, the inflow boundary conditions are such that both the mass flux and energy flux are kept constant Mathematically, they are

$$\rho u = C_1,$$

$$\frac{\gamma}{\gamma-1}\frac{p}{\rho} + \frac{1}{2}(u^2 + v^2) = C_2$$

where C_1 and C_2 are constants to be determined by the initial conditions Incorporating these two conditions with the linear acoustic wave equation for a wave propagating in the direction upstream from the exit and the equation of state, the primitive variables at the entrance can be determined.

Experimental results show that a natural, spatial, free mixing layer has several characteristic features e g , the growth of its thickness is linear with x, temporal statistics of the mixing layer is self–similar In the plane mixing layer simulation, those facts must be fulfilled. However, it is known that the Euler code can not develop rapidly and achieve the desired roll–up using a steady inflow boundary condition (Chien et al , 1987) In order to simulate a "natural" layer and produce apparent vortex formation, an unsteady boundary condition is also applied at the inlet plane, i e , set

$$v(y,t) = \Delta U\, G(y) \sum_{m=1}^{4} \tilde{A}_m \sin(2\pi f_m t + \phi_m)$$

In the above equation, $\Delta U = U_1 - U_2$ is the difference of the two free stream velocities which measures the strength of shearing, G(y) is a Gaussian distribution function which has a peak value unity at y=0, and half width over six cells, $\tilde{A}_m$ is the forcing amplitude [m=1,2,3,4], f_m [m=1,2,3,4] are the fundamental frequency and its first three subharmonics According to the Rayleigh's inviscid, linear stability theory, the fundamental frequency f_1 satisfies the Strouhal relationship (Ho & Huerre, 1984)

$$\frac{f_1 \theta_0}{\bar{U}} = 0.032 \qquad (3)$$

where $\bar{U} = 0.5(U_1 + U_2)$, which is the average of the two free stream velocities, and θ_0 is the initial momentum thickness The momentum thickness is defined by

$$\theta(x) = \int_{-\infty}^{+\infty} \frac{\bar{u}(x,y) - U_2}{U_1 - U_2}\left[1 - \frac{\bar{u}(x,y) - U_2}{U_1 - U_2}\right] dy$$

Finally, ϕ_m [m=1,2,3,4] are random phases added (Sandham & Reynolds, 1987) The forcing is modified by introducing these random phases to the Rayleigh modes and it is expected that by this modification, the pairing of two vortices will occur randomly in space and in time during the course of simulation and result in linear

growth of the shear layer thickness which is more realistic

Initial Conditions

In this paper, two air streams are modelled, each with different enthalpy, such that the densities and free stream velocities are different The velocity ratio, λ_u, and density ratio, λ_ρ, are defined as

$$\lambda_u \equiv \frac{U_2}{U_1},$$

$$\lambda_\rho \equiv \frac{\rho_2}{\rho_1}$$

Throughout the discussions, the higher speed U_1 will always be in the upper part of the diagram (see Fig 1) So λ_u varies from zero to unity If $\lambda_u = 0$, we have a single stream discharges into a quiescent ambient fluid For $\lambda_u = 1$, this corresponds to a wake flow But the density ratio λ_ρ can be any positive values The free stream velocity U_1 is chosen equal to $7\ 04\times10^3$ cm/sec and U_1 will not be changed throughout the calculation We shall vary the velocity ratio by changing the value of U_2 This velocity $7\ 04\times10^3$ cm/sec, corresponds to a Mach number of 0 2 at temperature 300°K The density of air at temperature 300°K and pressure of 1 atm is $1\ 2019\times10^{-3}$ g/cm^3, which is denoted by ρ_0 The two densities ρ_1 and ρ_2 will be expressed in term of ρ_0 A hyperbolic–tangent velocity profile is adopted for the initial streamwise velocity distribution at the splitter plate, that is

$$u^{init}(y) = \bar{U}\left[1 + \frac{1-\lambda_u}{1+\lambda_u}\tanh\left(\frac{y}{2\theta_0}\right)\right]$$

where θ_0 is the initial momentum thickness The initial density distribution is given by a step function

$$\rho^{init}(y) = \begin{cases} \rho_1 & \text{if } y > 0 \\ \rho_2 & \text{if } y < 0 \end{cases}$$

The initial cross–stream velocity, v, is set equal to zero and the pressure is set equal to 1 atm everywhere

III SHEAR LAYER SIMULATION RESULTS

As mentioned before, the free stream velocity U_1 is set equal to $7\ 04\times10^3$ cm/sec, and density $\rho_0 = 1.2019\times10^{-3}$ g/cm^3 Choosing $U_2=0\ 5U_1$, $\rho_1=\rho_0$ and $\rho_2=1\ 1\rho_0$, so that the velocity ratio is 0 5 and the density ratio is 1 1 The initial momentum thickness, θ_0, is set equal to 0 04 cm and the corresponding fundamental frequency can be determined by Eq (3) Using $A_m = 0\ 05$ [m=1,2,3,4], and incorporating the given initial information, the simulations for natural mixing layers are conducted

Fig 5 provides a sequence of instantaneous flow visualization of the vorticity field for the natural shear layer (the upper one is recorded earlier) The time interval, Δt, between the two consecutive pictures is 0 168 msec where the average time interval for a fluid element to traverse the computation domain is 3 03 msec Several features are found from this figure The sheared fluid makes deeper incursions from the high–speed side into the low–speed side These snapshot pictures clearly show the "pairing phenomenon" between two adjacent vortices Calculations ratify that after the merging interactions among neighboring eddies, the newly formed large vortex convects downstream at nearly constant speed which is approximately the average of the two free stream velocities. This vortex amalgamation process occurs randomly in space and time which is responsible for the linear growth of the mixing layer The spacing between two adjacent vortices and the size of the vortex are increasing with the streamwise coordinate x, which are required by the similarity properties of the mean flow

The nondimensionalized mean streamwise velocity, $\xi_u(x,y)$, is defined by

$$\xi_u(x,y) = \frac{\bar{u}(x,y) - U_2}{U_1 - U_2}$$

where $\bar{u}(x,y)$ is the mean streamwise velocity The dependence of the nondimensionalized mean streamwise velocity on the similarity coordinate, $\eta = y/(x - x_0)$, is shown in Fig 6, where x_0 is the streamwise coordinate of the virtual origin of the flow The lateral distribution of the mean streamwise velocity shown in Fig 6 suggests that the flow is self–similar in the fully–developed region [in this case, x > 8cm] Examining the mean–velocity profile, it is also found that the profile is not symmetric and the shear layer spreads more rapidly into the low–speed region

The growth rate of shear layer depends on both velocity ratio and density ratio The variation of momentum thickness growth rate, $\frac{d\theta}{dx}$, with the velocity ratio parameter, Λ_u, is plotted in Fig 7 together with the experimental data, where $\Lambda_u = \frac{1-\lambda_u}{1+\lambda_u}$ Note that the experimental momentum thickness are obtained for those flows with uniform densities, while as for the numerical calculations, the density ratio is 1 1 The scatter in the experimental data is attributed to the initial conditions of the shear layer and many other reasons yet to be expolred (Oster & Wygnanski, 1982) Other fluid dynamical statistics like the distribution of the u–velocity fluctuations, v–velocity fluctuations, the Reynolds stress and the entrainment ratio all show that these results are consistent with the experimental evidence (Oster & Wygnanski, 1982, Koochesfahani et al , 1983) and other numerical simulations (Riley & Metcalfe, 1980, Grinstein et al , 1986)

The Forced Shear Layer

For the shear layer forced by the fundamental frequency or the first subharmonic, the background noise is kept unchanged Only the amplitude of the component corresponding to the forcing frequency is enhanced (Sandham & Reynolds, 1987) The time averaged isodensity contour plots for the forced cases are illustrated in Fig 8a [fundamental frequency forcing] and 8b [first subharmonic forcing] Three response regions can be classified in the forced mixing layer In region I, growth rate is enhanced, in region II, growth rate is inhibited and in region III, shear layer spreading resumes again (Oster & Wygnanski, 1982) It is seen that in region II, the shear layer thickness stops growing The growth rate of the shear layer is almost zero Vortex pairing is suppressed within this non–growth region and results in a row of well–aligned vortices For the case of fundamental frequency forcing, this behavior occurs earlier in space, while for the subharmonic surging, the mixing layer develops quickly due to merging of two vortices and then growth stops

The effect of fundamental frequency forcing on the streamwise development of the momentum thickness is presented in Fig 9 with λ_u=0 5 and λ_ρ=1 1 This figure shows the general feature of the momentum thickness of the forced shear layer Three regions can be identified as mentioned above In region I, the initial rate of growth of the forced mixing layer exceeds that in the natural case In region II, vortex pairing is prohibited and the growth rate is zero This region is consistent with that shown in Fig 8a Beyond the region II, the mixing layer starts growing again at almost the same rate as that of the natural shear layer Region II starts at x=4 0 cm and ends at x=7 0 cm approximately in this case Fig 10 shows the variation of the momentum thickness of the forced shear layer but the forcing frequency is the first subharmonic Since the computational domain is not long enough for the subharmonic forcing, Region III is not seen in this case Region II starts at x=8 0 cm and ends at x=15 cm Actually, according to Oster & Wygnanski (1982), region II is bounded by

$$\frac{\bar{U}}{\Lambda_u f} < x < \frac{2\bar{U}}{\Lambda_u f}$$

where f is the forcing frequency The numerical results satisfy the above relation quite well In the region of zero growth rate, it is found that the distribution of u' has double peaks which is another charactenstic of region II Also, the lateral distribution of the Reynolds stress is negative all across the layer Due to limited space, however, figures are not shown here These phenomena were observed experimentally by Oster & Wygnanski (1982) and also in the numerical simulation by Riley and Metcalfe (1980) The trends of the computed results to experiments and numerical results of others lend full confidence that the code has been validated satisfactorily

IV SHEAR LAYER OPTICAL RESULTS

The physical properties of the unforced and forced plane mixing layer obtained by solving the two–dimensional Euler equations directly have been examined The calculated results are consistent with the experimental findings Of Brown & Roshko (1974), Oster & Wygnanski (1982), Ho & Huang (1982) and other investigations Since the density fields are correlated with the index of refraction distributions, the optical properties of the shear layer can be calculated using the information of density fields

The electric field amplitude at the far–field point (x_0,z_0) can be written as (Goodman, 1968)

$$\Psi(x_0,z_0) = \frac{1}{i\lambda Y}\exp(ikY)\exp[i\frac{k}{2Y}(x_0^2+z_0^2)] \iint_{-\infty}^{+\infty}\Psi(x,z)\exp[-i\frac{2\pi}{\lambda Y}(x_0x+z_0z)]dxdz,$$

where Y is the distance between the finite aperture plane (x,z) and the far–field observation plane (x_0,z_0), λ is wave length of the incident beam; and the far–field intensity is proportional to the square of the modulus of $\Psi(x_0,z_0)$ Mathematically, the far–field intensity profile is proportional to the square of the Fourier transform of the near–field incident wave distributions. For an uniform monochromatic and coherent circular incident beam, we may set

$\Psi(x,z)=1$ in the above equation and then carry out the integrations to get the far-field intensity distribution where the domain of integration is the circular region defined by the beam This diffraction-limited pattern is plotted in Fig 11 Note that in all figures concerning the far-field intensity distribution hereafter, the far-field coordinates (x_o,z_o) with respect to the center of the incident beam are nondimensionalized by $\frac{\lambda Y}{D}$, where D is the diameter of the beam. The intensity distribution has a central peak value which is normalized to unity The projection shows the far-field intensity contours on the x_o-z_o plane This circular pattern, as a reference, is called the Airy disk

Fig 12 shows the far-field intensity distributions due to the instantaneous natural shear layer at velocity ratio 0 5 and density ratio 1 1 The streamwise location of the center of the beam is x_c=8 cm, and D is equal to 5 12 cm Fig 12 shows the lobes in the far-field intensity distribution pattern, because this beam contains five vortices of the flow field A parameter Strehl ratio, SR, which is defined as the ratio of the maximum light intensity of the diffraction pattern to that of the same optical system without aberrations will be used to evaluate the optical quality quantitatively According o this definition, the Strehl ratio is tilt corrected In Fig 12, the Strehl ratio is 0 585

Strehl ratio provides only the information about peak intensity reduction in the far-field To evaluate the image quality of an optical system in the far-field focal plane, the modulation transfer function (Goodman, 1968) can be used The modulation transfer function is a measure of the reduction in contrast from object to image Even for an ideally perfect optical system, the system is limited by diffraction effects and the image of an object will be somewhat blurred. For a diffraction-limited system, the modulation transfer function as function of spatial frequencies is plotted in Fig 13 Note that here the spatial frequencies f_{xo} and f_{zo} are expressed in term of $\frac{2\Delta x}{\lambda Y}$, and the diameter of the beam used, D, is equal to 5 12 cm The incoherent cutoff frequency refers to the maximum frequency components of the image intensity, which is at $\frac{D}{\lambda Y}$ in this case The cutoff frequency is uniform in all directions in the frequency plane. The MTF shown in Fig 13 may be regarded as a reference modulation transfer function. The MTF for the natural shear layer with λ_u=0 5, λ_ρ=1 1 is shown in Fig 14 The diameter of the beam is 5 12 cm and the beam center passes through the point x_c=8 cm It is seen that aberrations always lower the contrast of each spatial frequency component of image intensity

As discussed in Sec. III, excitation with fundamental or subharmonic frequency produces controlled coherent structures The optical phase variations in the forced shear layer must be different from that of the unforced shear layer In the non-growth region of forced shear layers, the large eddies do not interact with each other The effect of forcing is to rotate and convect those eddies No new irrotational fluids particles are entrained into the mixing zone Also, the thickness and turbulent scale are fixed approximately as a result of excitation Thus the amplitude of phase variation is small there, and thus in turn can improve the optical quality in the far-field

Fig 15 presents this important result In this figure, The instantaneous far-field intensity distribution pattern produced by the shear layer forced by the first subharmonic frequency is plotted, with parameters λ_u=0 5, λ_ρ=1.1, D=5 12 cm, λ=6328 Å and x_c=12 cm In this case, the size of the circular beam is just big enough to cover the whole non-growth region of the shear layer The lobes in the far-field pattern disappear [cf Fig 12] which is due to partial compensation for the phase errors in this region The Strehl ratio is 0 921 The time averaged Strehl ratio is 0 89, which is a significant improvement compared to the value of 0 47 for the natural shear layer under the same conditions The modulation transfer function is depicted in Fig 16 in which the parameters are the same as those just mentioned The MTF is very close to that of an aberration-free system [cf Fig 8] so the image quality is also better

V CONCLUSICNS

A numerical simulation of the spatially-developing, plane, free shear layer and its optical properties have been performed. The numerical scheme involves alternating the second-order, explicit MacCormack method and the Godunov method so that reduction in the numerical phase errors can be achieved The spatial shear layer calculated is asymmetric in the sense that there are more fast fluid particles entrained to the mixing region than that of the slow flow Vortex pairing phenomenon between two neighboring vortices is observed which is responsible for the linearly growth of the natural shear layer Other time averaged calculations for the fluid dynamical variables of the shear layer such as the mean growth rate, rms u-fluctuations, v-fluctuations, Reynolds stress and momentum thickness, all are consistent with the experimental measurements. For the shear layers under periodic forcing, a region with zero growth rate can be identified Numerical calculations show that all the features characteristic of this region are the same as other numerical results and experimental observations These calculations for the two-dimensional free shear layer give very reliable results which can be used for the optical properties investigations

A brief optical calculation shows that, in general, the best image quality, like the best Strehl ratio, is correlated to the shear layer with smaller growth rate provided that all other parameters are kept the same The Strehl ratio in the far-field can be significantly enhanced by retarding the growth rate of the mixing layer via fundamental frequency or first subharmonic forcing And the optical performance of the shear layer is the best when incident beam passes through the non-growth region of the shear layer More optical results are forthcoming

ACKNOWLEDGMENTS

The authors would like to thank J J Riely and S.D Eberhardt and especially D W Bogdanoff for their suggestions in simulating the flowfield Part of the work completed using SDSC CRAY X-MP, which is gratefully acknowledged

REFERENCES

BROWN, G L. & ROSHKO, A 1974 On density effects and large structures in turbulent mixing layers J Fluid Mech. 64, 775-816.

CHIEN, K Y, FERGUSON, R E, COLLINS, J P, GLAZ, H M & KUHL, A L 1987 A study of mixing in forced shear layers with an Euler code AIAA paper 87-1318

FROMM, J E 1971 A numerical study of buoyancy driven flows in room enclosures, in "Lecture Note in Physics", Vol 8, 120-126, Springer-Verlag, Berlin

GODUNOV, S K 1959 A difference method for numerical calculation of discontinuous solutions of the equations of hydrodynamics Matem sb 47, No 3, 271-306

GOODMAN, J W 1968. Introduction to Fourier optics McGraw-Hill, New York

GRINSTEIN, F F, ORAN, E S & BORIS, J P 1986 Numerical simulations of asymmetric mixing layer in planar shear flows J Fluid Mech 165, 201-220

HO, C M & HUANG, L S 1982 Subharmonics and vortex merging in mixing layers J Fluid Mech 119, 443-473

HOLT, M 1984 Numerical methods in fluid dynamics 2nd ed Springer-Verlag, Berlin

KOOCHESFAHANI, M.M, DIMOTAKIX, P E & BROADWELL, J E 1983 Chemically reacting shear layer AIAA paper 83-0475

LEGNER, H H, OTIS, J H THEOPHANIS, G A & FLINBERG, R.M 1978 Laser beam degradation through turbulent interfaces AIAA paper 78-71

LOWERY, P S & REYNOLDS, W C 1986 Numerical simulation of a spatially-developing, forced, plane mixing layer NASA Report No TF-26

MACCORMACK, R W 1969 The effect of viscosity in hypervelocity impact cratering AIAA paper 69-354

OSTER, D & WYGNANSKI, I 1982 The forced mixing layer between parallel streams J Fluid Mech 123, 91-1390

RILEY, J J & METCALFE, R W 1980 AIAA Paper 80-0274

SANDHAM, N.D. & REYNOLDS, W C 1987 Some inlet plane effects on the numerically simulated spatially-developing two dimensional mixing layer Turbulent Shear Flow 22 4.1-22.4.6

STEGER, J L & WARMING, R F 1981. Flux splitting of the inviscid gasodynamic equations with application to finite difference method J of Comput Phys 40, 263-293

SUTTON, G W 1969 Effect of turbulent fluctuations in a optically active medium AIAA Journal 7, 1737-1743

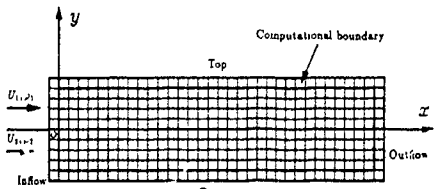

Fig 1 Schematic diagram of the computational domain.

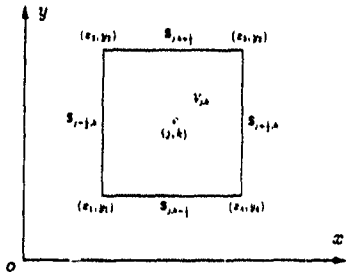

Fig 2 Computational volume element

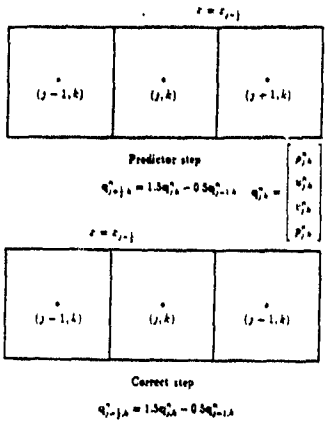

Fig 3 Second-order, linear extrapolation of primitive variables at cell boundary

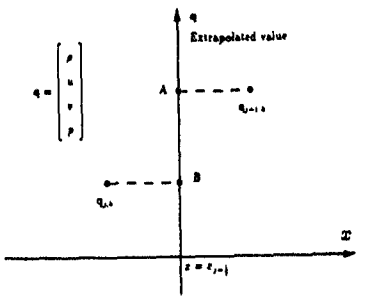

Fig 4 Limiting technique for choice of acceptable cell boundary values.

Fig 5 Instantaneous isovorticity plots for the natural shear layer, λ_u=0 5, λ_ρ=1.1. The pairing processes can be identified clearly in this figure.

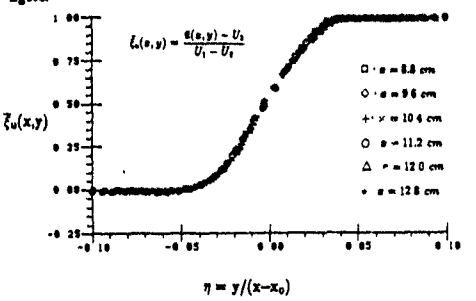

Fig 6 The mean streamwise velocity profile, λ_u=0 5, λ_ρ=1 1

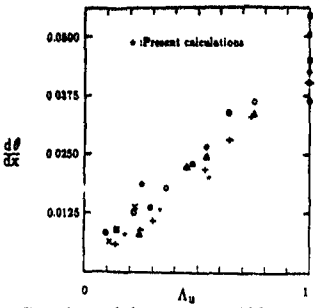

Fig. 7 Dependence of the momentum thickness growth rate on the velocity ratio parameter for the natural shear layer; λ_ρ=1.1 [This figure was taken from Brown & Roshko 1974].

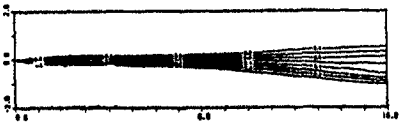

(a) Fundamental frequency forcing

(b) First subharmonic frequency forcing

Fig. 8 Time averaged isodensity plot for the forced shear layer; λ_u=0 5, λ_ρ=1.1.

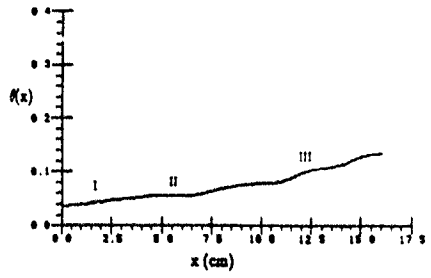

Fig. 9 The variation of momentum thickness for the forced shear layer, the forcing frequency is 4 22 KHz (fundamental) λ_u=0.5, λ_ρ=1 1

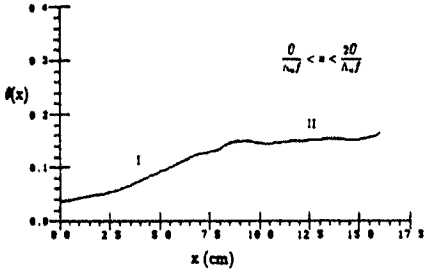

Fig 10 The variation of momentum thickness for the forced shear layer; the forcing frequency is 2 11 KHz (first subharmonic) λ_u=0.5, λ_ρ=1.1.

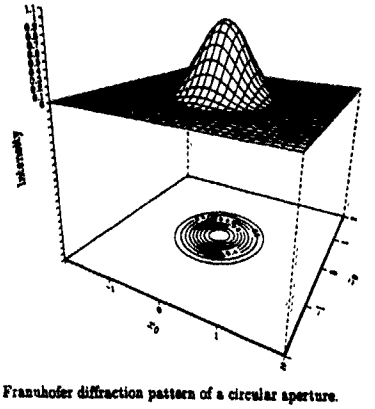

Fig. 11 Fraunhofer diffraction pattern of a circular aperture.

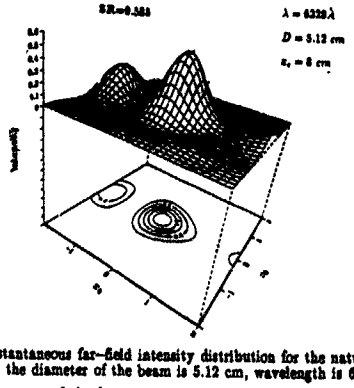

Fig. 12 Instantaneous far-field intensity distribution for the natural shear layer; the diameter of the beam is 5.12 cm, wavelength is 6328 Å, and the center of the beam is at x=8cm. The peak intensity is reduced over 40 per cent compared to its Fraunhofer pattern (see Fig 11).

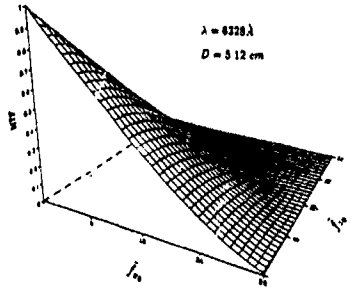

Fig. 13 Modulation transfer function for the diffraction-limited system

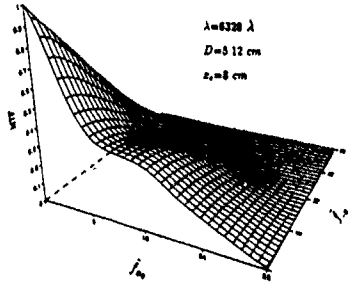

Fig 14 Time averaged modulation transfer function for the natural shear layer; λ_u=0.5, λ_ρ=1.1.

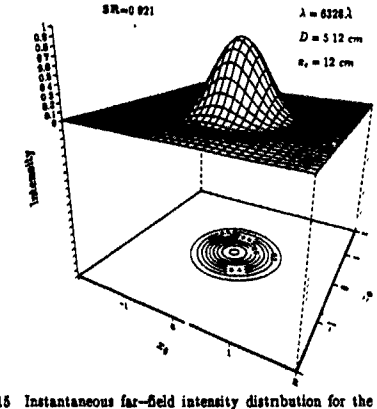

Fig. 15 Instantaneous far-field intensity distribution for the forced shear layer; the forcing frequency is the first subharmonic. The diameter of the beam is 5 12 cm, wavelength is 6328 Å, and the center of the beam is at x=12cm. The peak intensity is recovered significantly when the laser beam passing through this region of "zero" growth rate

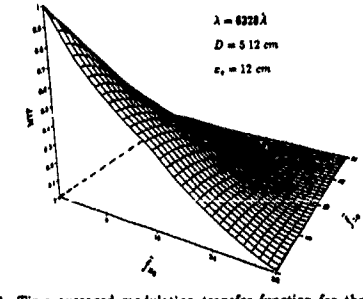

Fig. 16 Time averaged modulation transfer function for the forced shear layer; the forcing frequency is the first subharmonic, λ_u=0 5, λ_ρ=1.1.

EIGHTH SYMPOSIUM ON
TURBULENT SHEAR FLOWS
Technical University of Munich
September 9-11, 1991

EFFECTS OF MULTIPLE-FREQUENCY FORCING ON SPATIALLY-GROWING MIXING LAYERS

Osamu Inoue and **Sakari Onuma**
Institute of Fluid Science, Tohoku University
2-1-1 Katahira, Aoba-ku, Sendai 980, Japan

ABSTRACT

The effect of multiple-frequency forcing on the development of a spatially-growing mixing layer is studied numerically by a two-dimensional vortex method. Forcing is prescribed as a superposition of the predominant frequency of an unforced flow with its sub-harmonic frequencies. Superposition up to three frequencies is considered. The effect of phase shift between forcing frequencies are also examined. Instantaneous plots of discrete vortices and various statistics up to the second order moment are obtained to see the variation of coherent structures. Results show that the number of merging vortices and patterns of vortex merging, and thus the growth of a mixing layer can be effectively controlled by multiple-frequency forcing if forcing frequencies and phase shifts are suitably selected.

INTRODUCTION

Study of the effects of multiple-frequency forcing on the growth of a mixing layer is important, because forcing may have a possibility to drastically change the flow structures and to provide turbulence control (Ho & Huerre 1984; Wygnanski & Petersen 1987). For example, Hussain & Husain (1989) observed in their experimental study of a single-stream mixing layer that, when the mixing layer is forced by two frequencies (the predominant frequency and it first subharmonic), the growth of a velocity fluctuation (r.m.s. u') depends on the phase shift between the two frequencies.

Computational works on multiple-frequency forced mixing layers are not in abundance. In most of simulations except for Mansour, Hussain & Buell (1988) and Inoue (1989, 1991), spatial periodicity was assumed in order to simplify the calculations which consider a temporal evolution of the flow (Jacobs & Pullin 1989; Patnaik, Sherman & Corcos 1976; Riley & Metcalfe 1980). In this work, multiple-frequency forced, spatially-growing mixing layers are studied. Inoue & Leonard (1987) investigated single-frequency forced, spatially-growing mixing layers and reproduced many of the flow features which have been observed experimentally. Statistics up to the second order moment showed excellent agreement with experiments. One of the goals of this study is to increase our understanding of the effects of multiple-frequency forcing on the development and structure of a mixing layer. For this purpose, we use the same flow model and the same flow parameters as those used by Inoue & Leonard.

MATHEMATICAL FORMULATION AND NUMERICAL PROCEDURE

For details of the flow model, readers are referred to Inoue & Leonard (1987). We consider two uniform flows in a wind tunnel which are separated by a splitter plate upstream of the origin (x=0). The two flows meet at the origin and a mixing layer is formed downstream of the origin. To simulate the mixing layer by a vortex method, discrete vortices with the same sign and the same strength are shed one by one at every time-step δt from the origin. The complex velocity potential, f, which governs the flow development for N vortices, is given by

$$f = U_c z + i \sum_{n=1}^{N} \frac{\Gamma}{2\pi} \log(z - z_n) - i \sum_{n=1}^{N} \frac{\Gamma}{4\pi} \log(z - z_{u,n}) - i \sum_{n=1}^{N} \frac{\Gamma}{4\pi} \log(z - z_{\ell,n}) \qquad (1)$$

where $z = x + iy$, and Γ is the circulation of each vortex. The convection velocity Uc is defined as $U_c = (U_1+U_2)/2$, where U_1 and U_2 ($U_1 > U_2$) are the upper- and lower-side velocities of the mixing layer far from the x-axis, respectively. The subscripts u and ℓ denote the upper- and lower-image vortices, respectively. The image vortices are used to approximate the effect of walls in the wind tunnel. The velocity components u in the x-direction and v in the y-direction are given by

$$u - iv = \frac{\partial f}{\partial z} \qquad (2)$$

The time development of an individual vortex is determined from the relation,

$$\frac{dx_n}{dt} = u_n, \quad \frac{dy_n}{dt} = v_n \qquad (3)$$

The simulation parameters were prescribed as follows:

time step: $\delta t = 0.1$,
convection velocity: $U_c = 3.2$ (4)
velocity ratio: $r \ (\equiv U_2/U_1) = 0.6$.

Forcing is applied such that each new discrete vortex that appears at the origin is assigned the velocity

$$u = U_c, \quad v = v_f(t) \qquad (5)$$

in addition to the velocity induced by individual discrete vortices. As our main interest lies in multiple-frequency-forcing up to three frequencies, velocity disturbances are assumed to be of the form,

$$v_f = A_1\sin(2\pi f_1 t) + A_2\sin(2\pi f_2 t + \beta_1) + A_3\sin(2\pi f_3 t + \beta_2) \quad (6)$$

The parameters prescribed for forcing are as follows:

forcing amplitudes: $A_1=A_2=A_3=0.5Uc$ (fixed),

phase angles: $\beta_1,\beta_2=0,\pm\pi/8,\pm\pi/4,\pm\pi/2,\pi$, (7)

forcing frequencies:

f_1 = F (fixed), f_2, f_3 = F/2, F/3, F/4.

In the above expressions, F denotes the predominant frequency of an unforced flow. The mean flow quantities and statistics are obtained by averaging instantaneous values over the period $200 \le t \le 1,400$, which gives 12,000 sampling data for averaging purpose.

RESULTS AND DISCUSSION

In the following figures, for simplicity, the expression $f = f_1 + f_2 + f_3$ denotes the case that $v_f = A_1\sin(2\pi f_1 t) + A_2\sin(2\pi f_2 t+\beta_1) + A_3\sin(2\pi f_3 t+\beta_2)$

Double-frequency forced flows

Distributions of momentum thickness are presented in Fig. 1 where the predominant frequency (F) is combined with its subharmonics F/2, F/3, and F/4, respectively. When the predominant frequency is combined with a subharmonic frequency, the predominant frequency dominates the roll-up process immediately downstream of the origin. The rolled-up vortices then tend to merge regularly and the momentum thickness downstream of the roll-up region increases. The number of merging vortices in this region depends on the subharmonic frequency which is combined with the predominant frequency; that is, every two vortices merge regularly when f=F+F/2, every three vortices when f=F+F/3, and every four vortices when f=F+F/4. New vortices which are produced by multiple-vortex merging lead a saturation region where vortex merging is inhibited. As seen from Fig. 1, the thickness ratio before and after multiple vortex merging is about two for f=F+F/2, three for f=F+F/3 and four for f=F+F/4, respectively. Downstream of the saturation region, the mixing layer recovers its growth. The calculated flow features discussed above are quite similar to those observed experimentally by Ho & Huang (1982).

The range over which the relative phase angle β_1 varies is π when f=F+F/2, $2\pi/3$ when f=F+F/3, and $\pi/2$ when f=F+F/4, respectively. With this phase range in mind, the effect of β_1 on flow features was examined. From Fig. 1(a), we see that when f=F+F/2 two different modes of mixing layer growth exist. That is, when β_1 is close to $\pm\pi/2$, the mixing layer grows immediately downstream of the origin ($40\le x\le 100$). We call this mode as Mode I. On the other hand, when β_1 is close to 0 or π, the growth of the mixing layer is delayed ($100\le x\le 160$). We call this mode as Mode II. In Mode I merging of every two vortices occurs immediately after the roll-up of vortices, leading the rapid growth of the mixing layer in this region. Mode I may correspond to vortex pairing mode (Patnaik, Sherman & Corcos 1976; Riley & Metcalfe 1980). On the other hand, in Mode II vortex merging is delayed, leading the suppression of the mixing layer growth after the roll-up of vortices. It should be mentioned that vortex tearing (or shredding) was observed in Mode II when amplitude ratio, A_2/A_1, was sufficiently large (Inoue 1991).

When f=F+F/3, depending on β_1, three

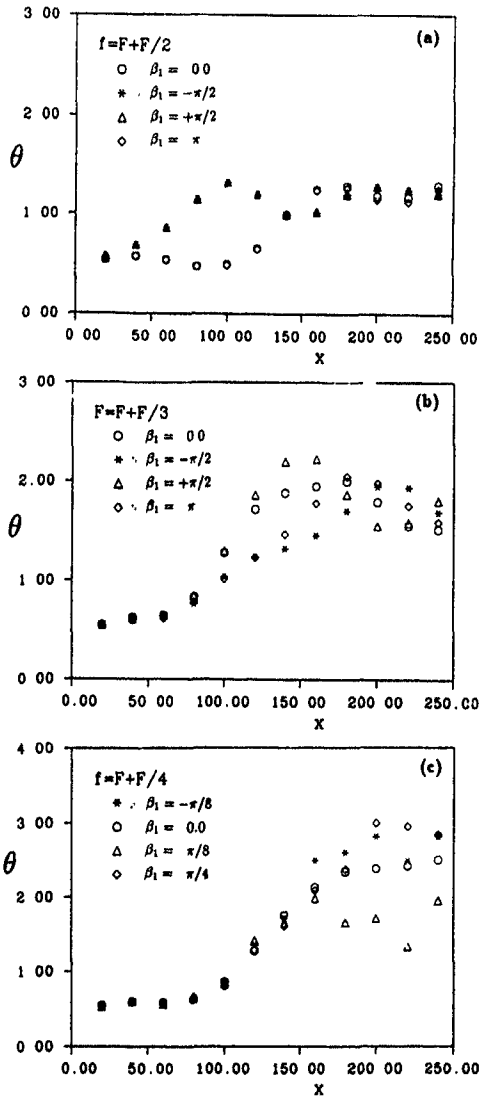

Fig. 1. Effects of double-frequency forcing on momentum thickness distributions. (a) f=F+F/2, (b) f=F+F/3, (c) f=F+F/4.

different patterns of vortex merging are observed, as shown in Fig. 2. When $\beta_1 = -\pi/2$ (or equivalently $\pi/6$ from the view point of the relative phase range mentioned before), downstream two vortices merge first. Then this new vortex merges with a third upstream one. When $\beta_1 = +\pi/2$, three vortices merge simultaneously. When $\beta_1 = \pi$ (or $\pi/3$), upstream two vortices merge first. Then this new vortex merges with a third downstream one. In consistence with the dependency of vortex merging pattern on β_1, Fig. 1(b) shows that the momentum thickness distributions are also dependent on β_1.

When f = F + F/4, depending on β_1, vortex merging patterns change and we observed the following three patterns.

(1) Type A: Among each four vortices, inner two vortices merge into a pair first. Then this pair merges with the third, most downstream vortex. Then, this new vortex merges with the fourth, most upstream vortex.
(2) Type B: As in Type A, inner two vortices merge into a pair first. But, this time the pair merges with the third, most upstream vortex. Then, this new vortex merges with the fourth, most downstream vortex.
(3) Type C: Inner two vortices merge first. Then, this new vortex merges with the other two vortices simultaneously.

Ho & Huang (1982) observed, in their mode IV mixing layer where every four vortices merge, that two vortices usually merge into a pair and two pairs then form a single structure. This pattern of vortex merging was not observed in this case of f=F+F/4. Instead, the pattern of two-stage vortex merging is observed in a triple-frequency forced mixing layer with f=F+F/2+F/4. For more details of the flow features of double-frequency forced mixing layers, readers are referred to Inoue (1989, 1991).

Triple-frequency forced flows

In this paper, effects of triple-frequency forcing were examined for two cases; f=F+F/2+F/3 and f=F+F/2+F/4. In both cases, the results showed different flow behaviors depending on whether β_1 equals 0 or $\pi/2$. It should be remembered that, when f=F+F/2, the double-frequency forced flow with $\beta_1=\pi/2$ is in Mode I where vortex pairing is enhanced while the flow with $\beta_1 = 0$ is in Mode II where vortex pairing is delayed. Keeping this result in mind, the triple-frequency forced flows are analysed.

When $\beta_1=0$, the triple-frequency forced flows show quite similar behavior to the double-frequency forced flows as follows. That is, the flow when f=F+F/2+F/3 with $\beta_1=0$ and $\beta_2=\beta_2$ is similar to the flow when f=F+F/3 with $\beta_1=\beta_2$, and the flow when f=F+F/2+F/4 with $\beta_1=0$ and $\beta_2=\beta_2$ similar to the flow when f=F+F/4 with $\beta_1=\beta_2$. As an example, instantaneous plots of discrete vortices for the case of f=F+F/2+F/3 with $\beta_1=0$ are presented in Fig. 3 for three different values of β_2. By comparing Fig. 3 with Fig. 2, we can readily see that in both double- and triple-frequency forced flows every 3 vortices merge regularly and that the same vortex merging pattern appears for the same relative phase angle to the predominant frequency. The similar results are obtained for the case of f=F+F/2+F/4 Momentum thickness distributions presented in Fig. 4 show that when $\beta_1=0$ each triple-frequency forced flow shows close values to the corresponding double-frequency forced flow. This result indicates that when $\beta_1=0$ the role of the first subharmonic frequency F/2 in the triple-frequency forced flows is small and the flow fields are governed by the predominant frequency and its lower-order subharmonics F/3 or F/4.

When $\beta_1=\pi/2$, on the other hand, the triple-frequency forced flows show different features. Instantaneous plots of discrete vortices and momentum thickness distributions when f= F+F/2+F/3 with $\beta_1=\pi/2$ are presented in Figs. 5 and 6, respectively, for different values of β_2. When $\beta_1=\pi/2$, every two rolled-up vortices tend to merge into a pair regularly immediately downstream of the origin ($40\le x\le 100$), indicating that the flow in this region is governed by Mode I of the double-frequency forced flows, f=F+F/2 with $\beta_1=\pi/2$. Then, an inhibited region of vortex merging is followed ($100\le x\le 160$). Then, downstream of this inhibited region, every three pairs which were produced by the every two-vortices merging tend to merge regularly, as shown in Fig. 5: every six vortices merge eventually. The merging patterns of every three pairs are the same as those of every three vortices in the double-frequency forced flows when f=F+F/3 presented in Fig. 3, except for the case of $\beta_2=\pi/2$. The difference of the merging pattern between the double-frequency forced flow with $\beta_1=\pi/2$ and the triple-frequency forced flow with $\beta_2=\pi/2$ may be due to the unstable nature of the simultaneous merging of every three vortices to irregular disturbances (Inoue 1991). As a result of the successive merging of every two vortices followed by every three pairs, the momentum thickness distributions in Fig. 6 show about 6 times larger values after the vortex mergings than the value immediately downstream of the origin. When f=F+F/2+F/4 with $\beta_1=\pi/2$, every two vortices merge into a pair immediately downstream of the origin, as in the case when f=F+F/2+F/3. In the case when f=F+F/2+F/4, however, every two pairs merged regularly irrespective of β_2 examined in this study. The phase angle β_2 affects on the location where every two pairs start to merge. As an example, instantaneous plots of discrete vortices and momentum thickness distributions are presented in Fig. 7 and 8, respectively. As seen from Fig. 7, immediately after the roll-up process every two vortices merge ($50\le x\le 100$), in accordance with the flow features for the case of f=F+F/2 with $\beta_1=\pi/2$. Then, a inhibited region of vortex merging follows. The distance of the inhibited region of vortex merging depends on the phase shift β_2. Downstream of the inhibited region, the

second region of vortex merging follows where every two pairs produced in the first vortex merging region ($50 \lesssim x \lesssim 100$) merge regularly. In accordance with these vortex merging patterns, the momentum thickness distributions in Fig. 8 show two stage increase in momentum thickness. As mentioned before, Ho & Huang (1982) observed, in their mode IV mixing layer where every four vortices merge, that two vortices usually merge into a pair and two pairs then form a single structure. Our results suggest that three frequencies (F, F/2 and F/4) might have coexisted in the mode IV mixing layer of Ho & Huang (1981).

CONCLUDING REMARKS

The effect of multiple-frequency forcing (up to 3 frequencies) was examined numerically by a vortex method. The results showed that the number of merging vortices and the merging patterns of vortices can be controlled by a combination of the predominant frequency of the unforced mixing layer with its subharmonics. It is also found that the phase shift between forcing frequencies has a profound effect on the process of vortex merging and thus on the growth of a mixing layer.

The computation in this work was done by the use of CRAY Y-MP at the Institute of Fluid Science, Tohoku University.

REFERENCES

Ho. C. M. & Huang, L.S 1982 Subharmonics and vortex merging mixing layers. J. Fluid Mech. 119, -473.

Ho. C. M. & Huerre, P. 1984 Perturbed free shear layers. Ann. Rev. Fluid Mech. 16, 365-424.

Hussain, F. & Husain, H. S. 1989 Subharmonic resonance in a free shear layer. Proc. 4th Asian Cong. Fluid Mech. II, A288-A291.

Inoue, O. & Leonard, A. 1987 Vortex simulation of forced/unforced mixing layers. AIAA Paper 87-0288.

Inoue, O. 1989 Artificial control of turbulent mixing layers. Structures of Turbulence and Drag Reduction, IUTAM Symp., Zurich, Switzerland, ed. A. Gyr, Springer-Verlag, 145-152.

Inoue, O. 1991 Double-frequency forcing on spatially-growing mixing layers. (in preparation)

Jacobs, P. A. & Pullin, D. I. 1989 Multiple-contour-dynamic simulation of eddy scales in the plane shear layer. J. Fluid Mech. 199, 89-124.

Mansour, N. N., Hussain, F. & Buell, J. C. 1988 Subharmonic resonance in a mixing layer. Proc. 1988 Summer Program of NASA/Stanford Center for Turbulence Research (Report CTR-S88), 57-68.

Patnaik, P.C., Sherman, F.S. & Corcos, G.M. 1976 A numerical simulation of Kelvin-Helmholtz waves of finite amplitude. J. Fluid Mech. 73, 215-240.

Riley, J. J. & Metcalfe, R. W. 1980 Direct numerical simulation of a perturbed turbulent mixing layer. AIAA Paper 80-0274.

Wygnanski, I. J. & Petersen, R. A. 1987 Coherent motion in excited free shear flows. AIAA J. 25, 201-213.

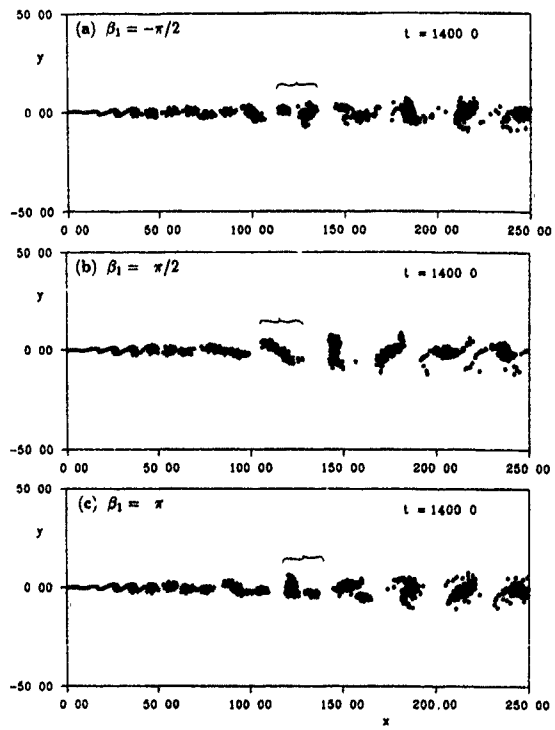

Fig. 2. Effects of double-frequency forcing on vortex merging pattern, f=F+F/3.

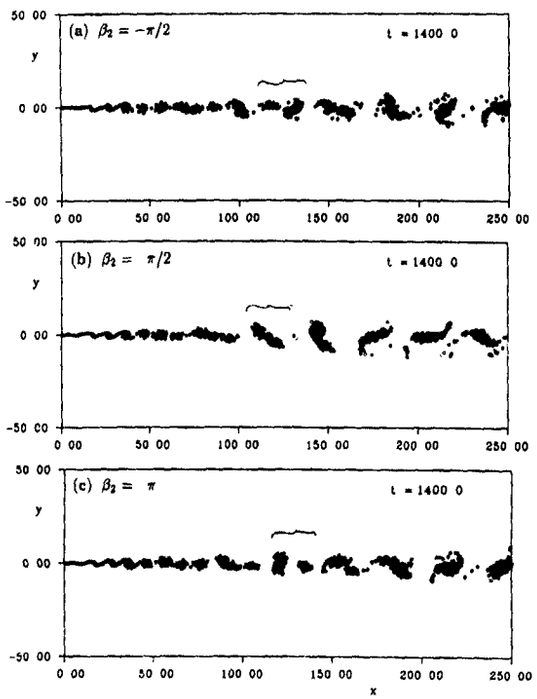

Fig. 3. Effects of triple-frequency forcing on vortex merging (I). f=F+F/2+F/3, β_1=0.0.

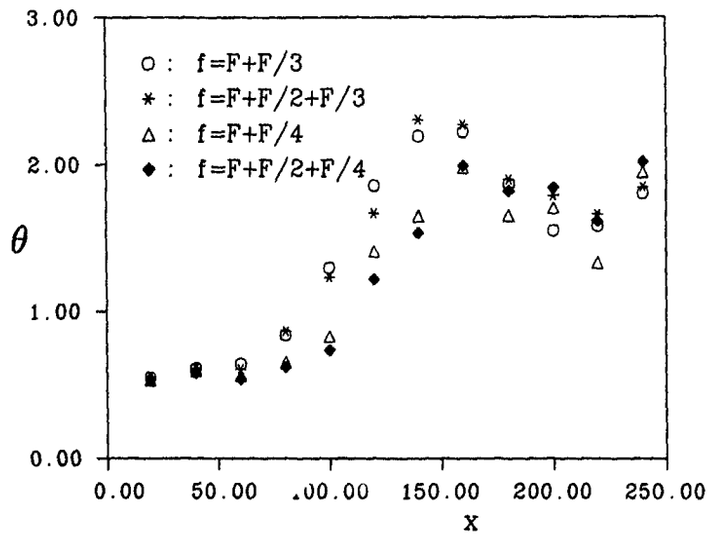

Fig. 4. Comparison of momentum thickness distributions between double- and triple-frequency forced flows.
○ : f=F+F/3, $\beta_1=\pi/2$,
∗ : f=F+F/2+F/3, $\beta_1=0$, $\beta_2=\pi/2$,
△ : f=F+F/4, $\beta_1=\pi/8$,
◆ : f=F+F/2+F/4, $\beta_1=0$, $\beta_2=\pi/8$,

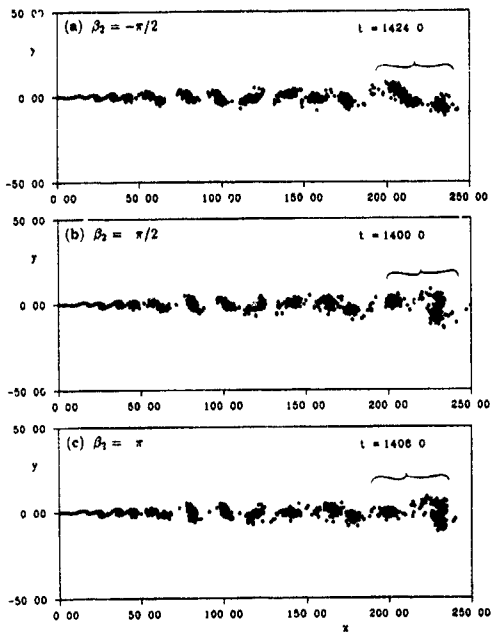

Fig. 5. Effects of triple-frequency forcing on vortex merging (II). f=F+F/2+F/3, $\delta_1=\pi/2$.

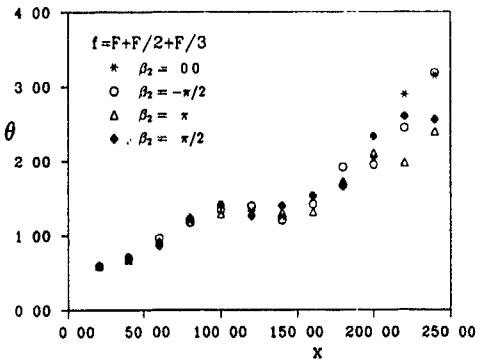

Fig. 6. Effects of triple-frequency forcing on momentum thickness distributions (I). f=F+F/2+F/3, $\delta_1=\pi/2$.

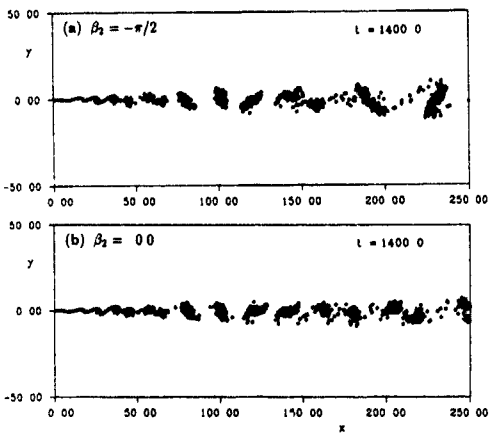

Fig. 7. Effects of triple-frequency forcing on vortex merging (III). f=F+F/2+F/4, $\delta_1=\pi/2$.
(a) $\delta_2=-\pi/2$, (b) $\delta_2=0.0$.

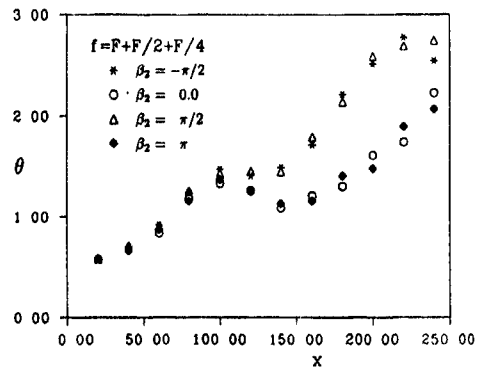

Fig. 8. Effects of triple-frequency forcing on momentum thickness distributions (II). f=F+F/2+F/4, $\delta_1=\pi/2$.

EIGHTH SYMPOSIUM ON
TURBULENT SHEAR FLOWS
Technical University of Munich
September 9-11, 1991

ROLE OF ROLLS AND RIBS IN REACTING MIXING LAYERS

Ralph W. Metcalfe, Fazle Hussain and Kye-Hong Park

Department of Mechanical Engineering
University of Houston
Houston, TX 77204-4792

ABSTRACT

The role of large-scale coherent structures in the enhancement of mixing and chemical reaction in turbulent free shear flows has been investigated. Direct numerical simulations of temporally growing, but spatially periodic mixing layers have been analyzed over a range of Damköhler numbers through rollup and two successive pairings of the spanwise vortices. Mixing layer behavior with controlled forcing at the fundamental, subharmonic, and 3D random frequencies has been studied. The presence of "rolls" and "ribs" and their interactions can significantly modify the species concentration and instantaneous reaction rate fields in a manner that depends critically on the Damköhler numbers. The ribs play a crucial role both in cross-stream transport and in wrinkling the flame sheet, producing enhanced mixing and chemical reaction in both the braid and core regions of the flow. Significant differences are found in the product generation mechanisms in the braid and core regions of the flow. Direct comparison of two simulations with and without 3D modes present shows substantial increase in product generation possible in the presence of 3D modes.

INTRODUCTION

The role of large-scale coherent structures (CS) in the transport processes in reacting and nonreacting turbulent shear flows is now well recognized (Liu 1989; Hussain 1986), but very little is understood about the role as well as the control of CS. We have been investigating some of the mechanisms by which turbulent large-scale coherent structures enhance mixing and promote chemical reaction. In our earlier work on this problem (Lee, Metcalfe & Hussain 1990), we found that the streamwise vortical structures (called "ribs") enhance the reaction rate by convoluting the reaction surface and enhancing the transverse transport mixing of the two species, although the relative significance of this effect is very sensitive to the species diffusivity. For certain Schmidt numbers (Sc), the effects of flame shortening are balanced by flame sheet stretching by the vortex pairing process. Under certain conditions, the ribs remain dynamically active coherent structures over times even longer than the life-times of the rolls (Lasheras, Cho & Maxworthy 1986). The ultimate breakdown of such structures is a very complex process which can significantly affect the interspecies mixing and the reaction rate at higher Sc. The evolution of these structures has also been examined numerically by Buell & Mansour (1990) and Rogers & Moser (1990).

METHODOLOGY

Governing Equations: The simulations described in this paper are of a temporally growing free mixing layer with a binary, single-step, irreversible, isothermal chemical reaction in an incompressible flow. Periodic boundary conditions are applied in the streamwise and spanwise directions, and free-slip conditions in the transverse direction. The basic governing equations are the 3D Navier-Stokes equations with reaction-diffusion equations describing the interaction of the two initially segregated species. The reaction-diffusion equations are

$$\frac{\partial C_1}{\partial t} + u \cdot \nabla C_1 = -\alpha C_1 C_2 + \kappa \nabla^2 C_1 , \quad (1)$$

with two similar equations for C_1, C_2, and C_P, where C_1, C_2, and C_P are the molar concentrations of the two species and the reaction product respectively. The reaction rate coefficient α and the species diffusivity κ are constants. We have also performed simulations of the limiting case of an infinite reaction rate, which can be done using a conserved scalar approach. Details of the numerical methods and problem definition are given elsewhere (Lee, Metcalfe & Hussain 1990; Riley, Metcalfe & Orszag, 1986)

Initial Conditions: The simulations have been initialized using both the most unstable mode (fundamental) derived from linear stability analysis and its subharmonic at various perturbation velocity amplitudes (cf. Table 1) with a hyperbolic tangent mean velocity profile of the form

$$U(z) = \frac{\Delta U}{2} \tanh\left(\frac{z}{\delta_i}\right), \quad (2)$$

Here, ΔU is the velocity difference across the layer and δ_i is the initial mean vorticity thickness. The coordinates (x,y,z) and velocity components (u,v,w) refer to the streamwise, spanwise, and transverse flow directions respectively. The velocity field is nondimensionalized by ΔU and time by $\lambda_f/\Delta U$, where λ_f is the wavelength of the fundamental. The Reynolds number is defined by $Re = \Delta U \delta_i / 2\nu$, the Schmidt number $Sc = \nu/\kappa$, and the first and second Damköhler numbers $D_I = z_o \alpha C_\infty / \Delta U$ and $D_{II} = z_o^2 \alpha C_\infty / \kappa$; the latter two represent the ratio of the convection to the reaction time scales and diffusion to reaction time scales respectively. z_o is the initial thickness of the reaction zone.

In addition to the two-dimensional unstable modes, in most simulations a 3D velocity perturbation field was added in order to simulate the effect of background turbulence and to permit the growth of the most unstable 3D disturbances as well. The energy spectrum of this field had a low wavenumber peak, and then decreased smoothly by about two orders of magnitude to the cutoff wavenumber. The initial peak turbulence intensity varied from about 1% to 8% of ΔU (cf. Table 1). The initial reactant concentrations are defined in terms of error functions to represent initially segregated species (Fig. 1). Details regarding the initialization procedure, equations of motion, and use of pseudo-spectral numerical methods to solve the equations are given elsewhere (Riley, Metcalfe & Orszag 1986, Metcalfe et al 1987).

SIMULATIONS

The simulations analyzed in this work were performed using either 64^3 or 128^3 Fourier modes. The initial Reynolds numbers as defined above ranged from Re ~ 50 - 170, and Schmidt numbers ranged from Sc ~ 0.06 - 2.0. Simulations with Schmidt numbers much larger than 1 become very dif-

ficult due to the discrepancies at high wavenumber scales of velocity and species concentration fields

Both 64^3 and 128^3 calculations were performed with the given initial conditions. The 64^3 simulations involved the rollup of the fundamental mode which saturated at a non-dimensional time of $t \sim 3.2$ for runs 1-8 and $t \sim 2.4$ for runs 11 - 21, while the subharmonic saturation times were $t \sim 7.0$ and 4.8. In the 128^3 simulations, an additional pairing event was simulated. At the time of saturation of the quarter-harmonic f/4 mode, the ribs have become very strong, as can be seen in Fig. 2, which is an isosurface plot of the magnitude of the streamwise vorticity.

Modal Energy Growth: The growth of the streamwise fundamental energy (E_f), first and second subharmonics ($E_{f/2}$ and $E_{f/4}$), and those of non-zero spanwise modes (E_{3D}) are shown in Fig. 3. Here, we have rollup of the fundamental at $t \sim 1.5$, and saturation of the first and second harmonics at $t \sim 4.5$ and 11 respectively. Note the suppression of the growth of the second subharmonic during saturation of the first subharmonic mode, but subsequent growth by extracting energy from $E_{f/2}$, as seen in laboratory experiments (Lasheras, Cho & Maxworthy 1986, Lasheras & Choi 1988). Also, note the strong suppression of the three dimensional modes related to the secondary instabilities during saturation of the subharmonics, suggesting strong nonlinear interaction. Velocity field energy spectra and power spectra of the species concentration fields (Fig. 4) were monitored during the simulations to verify the accuracy of the calculation. The relatively smooth spectral distribution near the cutoff wavenumber is an indication of a well resolved field.

DYNAMICAL EVOLUTION OF SECONDARY INSTABILITIES

Vortex Line Analysis: As discussed above, the secondary instabilities in the flow play a critical role in enhancement of mixing. A useful technique for analyzing the evolution of secondary instabilities in our simulations is vortex line tracing. Although these are viscous calculations, so that there is diffusion of vorticity, it is possible at any instant of time to trace vortex lines which provide an excellent means of characterizing vortical structures and their topology. The vortex line tracing algorithm, developed at the NASA Ames Research Center, is very robust, and was carefully tested during our analysis by comparison with other graphical means for displaying vorticity information and by checking that the determination of a vortex line was independent of the direction of integration along it. The magnitude of the vorticity is shown in the plots by a grey scale code, in which lines of peak vorticity are black or solid, while at lower levels, the lines become grey or dashed.

At early times, the kinked vortex lines in the braids get stretched into horseshoe shaped, counterrotating streamwise vortices which are linked (Fig. 5a). At this point, the ribs have an elliptical cross section prior to their "collapse" into a circular cross section, as in the model of Lin & Corcos (1984). At later times, the stretching continues until well-defined ribs have begun to form (Fig. 5b). By carefully analyzing the mechanisms of their formation, it is clear why the ribs tend to be linked structures, connected to each other, rather than independent forms.

LOCAL EFFECTS OF LARGE SCALE STRUCTURES ON CHEMICAL REACTION

Evolution of Reaction Zone: The importance of these structures to the chemical reaction is characterized in Figs. 6a-c, which are isosurface plots of the instantaneous reaction rate at several times during the rollup and two pairings of the f, f/2, adn f/4 modes in a 128^3 simulation. Early in the simulation, the chemical reaction is largely determined by the dynamics of the 2D spanwise vortex rollup. The three-dimensional secondary instabilities have not yet had time to grow very large. The flame sheet is continuous, with stretching in the vortex cores providing a mechanism to increase product generation. At a slightly later time, $t \sim 3.2$ (Fig. 6a), flame shortening has begun to occur in the rolls, as can be seen in the cross-sectional plane $y = 0$. As f/2 saturates, flame shortening increases, leaving the cores filled with product and hence low levels of reaction there. The ribs are beginning to affect the reaction in the braid region, as can be seen by the uneven thickness of the flame sheet in the cross-sectional plane $x = 0$. At $t \sim 5.3$ (Fig. 6b), the pairing of f/2 entrains non-vortical fluid, and thus unreacted species, into the chemical reaction zone by Biot-Savart induction (Lasheras et al 1986). Thus, the flame sheet again lengthens, and the total rate of product generation increases. The spanwise convolution of the flame sheet due to the ribs also becomes more strongly evident. At the saturation of f/4, i.e. during the second pairing, the new layer of fresh reactants is folded into the core of the rolls, resulting in a multilayered flame sheet (Fig. 6c, $t \sim 8.5$). In the crossectional plane $y = 0$, one can see the remnants of the old flame shortened cores of the fundamental modes with a new layer of reactants separating them. The potential importance of the secondary instabilities and complex vortical motion inside the cores is evident in their effect on the flame sheet wrapped inside the core that is visible in the cross-sectional view in the plane $x = 0$. With the pairing at f/4, the flame sheet stretching/flame shortening cycle is repeated again on a larger scale.

Schmidt number effects: At larger values of $D_{||}$, the flame sheet in the braid region will be thinner, and its distortion by the ribs will tend to become more important, increasing product generation. As $D_{||}$ decreases, however, the thickness of the flame sheet increases, and when the flame sheet thickness becomes significantly larger than the diameter of the ribs, the effect of the ribs becomes less important in product generation. Of course, when both D_f and $D_{||}$ are very large, the presence of the ribs can enhance the reaction rate until flame shortening within the core of the ribs occurs. Similar effects can be seen in the core regions. Figs. 7a and 7b show the flame sheet in the core region at two different Schmidt numbers. At high Sc (Fig. 7a), the concentration gradients are larger and small scale wrinkling or distortion of the flame sheet is more important. Also, flame shortening in the core is delayed due to the lower species diffusivity (see below), and significant product generation continues much longer than at lower Sc. At lower Sc (Fig. 7b), only the larger scale secondary instabilities and vortical modes significantly affect the flame sheet.

At the Re and Sc of the present calculations, it is possible to simulate flows very close to the fast reaction limit. Our simulations show that significant features as well as many smaller details of the product field in the core of the subharmonic at $D_f = 1$ and ∞ are similar. This suggests that $D_f = 1$ is adequate (at these Re and Sc) to capture the asymptotic behavior. The product in the cores is well mixed (small gradients) due in part to the random vortical motion of the trapped ribs. There are steep gradients at the top and bottom where fresh product is carried in from the braid region. The presence of the ribs makes this interface strongly convoluted.

NET EFFECT OF LARGE SCALE STRUCTURES ON CHEMICAL REACTION

Reaction Zone stretching/shortening: The temporal variation of total product generation rate with Damköhler number shows the important effect of the large scale structures. In Fig. 8, the reaction enhancement due to flame sheet stretching up to the saturation of the fundamental is clearly visible from $t \sim 2$ to 4, and by the subharmonic from $t \sim 6$ to 9. It is interesting to note that after fundamental saturation, flame shortening occurs more rapidly at higher values of D_f, so that there is an interval ($5 < t < 6$) during which product generation *decreases* with increasing D_f. This clearly suggests the importance of amplitude and phase in exciting the unstable modes and how critically the effects of the excitation depend on the Damköhler number. The relative importance of the ribs in product generation is also strongly dependant on D_f. At higher reaction rates, when flame shortening occurs sooner in the cores, the *relative* role of product generation in the braid

region, where fresh reactants are continuously brought together, becomes more important (Fig. 9).

Product Generation in Braid and Core Regions: The dramatically different evolution of the flow in the braid and core regions of the mixing layer produces significant differences in product generation and accumulation. Fig. 10 shows the relative accumulation of product in the braid and core at the time of saturation of f/2. The total product at each streamwise location is plotted as a function of the streamwise coordinate x. The streamwise periodicity of the domain in this 64^3 simulation produces the (statistical) symmetry apparent in the figure. At lower Sc, the strong interspecies diffusion in the braids allows more rapid generation of product there, and thus more accumulation than at higher Sc. Note that at higher Sc, there is nearly 10 times as much product in the cores as in the braids. Another important aspect of the differing nature of the instabilities in the braid and core regions is illustrated in Figs. 11a and 11b. Here, the instantaneous product generation at each streamwise plane is plotted in as in Fig. 10 just after saturation of the fundamental (11a) and after saturation of the subharmonic (11b). The product generation, of course, increases with D_I everywhere in the flow, other factors being equal. As the flow evolves, however, the reaction rate remains nearly constant in the braid region, where the ribs have not yet undergone a rescaling to a larger spacing. In the cores, where pairing of vortices has increased reactant concentrations, product generation rises. This suggests that early rescaling of the ribs could be very important in enhancing product generation.

IMPORTANCE OF THREE-DIMENSIONALITY IN PRODUCT GENERATION

We have discussed in some detail in the previous sections the role of secondary instabilities in enhancing the chemical reaction. Thus, it is of some interest to make a direct comparison between the evolution of a reacting flow with and without such modes present. Fig. 12a is a plot of the reaction zone of a simulation in which *only* 2D instabilities were excited. while Fig. 12b is from an identical simulation except that both 2D and 3D instabilities were excited. It is apparent that the presence of the additional modes increases the complexity of the flow, and the possibility for enhanced mixing. As discussed earlier in this paper, the secondary instabilities increase the stretching and convolution of the flame sheet, and appear to enhance product generation. That this is in fact the case is shown in Figs. 13 and 14 in which the volumetrically integrated instantaneous reaction rate is plotted as a function of time for the two simulations. It is clear that the presence of the 3D modes does increase product generation over the entire course of mixing layer with in these simulations. An important issue that is suggested by these comparisons is whether it is possible to determine an optimal strategy for exciting two- and three- dimensional instabilities that will maximize product generation. This will of course depend strongly on the various parameters such as the Reynolds and Damköhler numbers. Nonetheless, we feel it will be instructive to investigate such a possibility for a choice of parameters within the range which can now be approached by direct numerical simulation.

ACKNOWLEDGEMENTS

This work has been supported by the Office of Naval Research under Contract No. N00014-89-J-3231. Computer time has been supplied by NAS of the NASA Ames Research Center.

REFERENCES

Buell, J.C. & Mansour, N.N. 1990 *Turbulent Shear Flows 7* To appear, Springer-Verlag.

Hussain, A.K.M.F. 1986 *J. Fluid Mech* 173, 303-356.

Lasheras, J. C. & H. Choi 1988 *J. Fluid Mech.* 189, 53-86.

Lasheras, J. C., J. S. Cho, & T. Maxworthy 1986 *J. Fluid Mech.* 172, 231-258.

Lee, C., R. Metcalfe, F. & Hussain 1990 *Turbulent Shear Flows 7* To appear, Springer-Verlag.

Lin, S. J. and G. M. Corcos 1984 *J. Fluid Mech.* 141, 130-178.

Liu, J.T.C. 1989 *Ann. Rev. Fluid Mech.* 21: 285-315.

Metcalfe, Ralph W. and Fazle Hussain 1990 in *Topological Fluid Mechanics*, ed. by H. Moffatt & A Tsinober, pp. 659 - 668.

Metcalfe, R. W., F. Hussain, S. Menon, & M. Hayakawa 1987b *Turbulent Shear Flows* 5 110-123

Metcalfe, R. W., S. A. Orszag, M.E. Brachet, S. Menon, & J. J. Riley 1987a *J. Fluid Mech.* 184, 207-143.

Riley, J. J., R. W. Metcalfe & S. A. Orszag 1986 *Physics of Fluids* 29, 406-422.

Rogers, M. M. & Moser, R. D. 1990 *Turbulent Shear Flows 7* To appear, Springer-Verlag.

Table 1. Simulation Parameters

Run #	Re	Sc	D_I	D_{II}	Size	% forcing (2D,3D)*
1	100	0.07	0.1	1.4	64^3	(2, 2)
2	100	0.07	1.0	14.0	64^3	(2, 2)
3	100	0.07	∞	∞	64^3	(2, 2)
4	100	0.7	0 1	14 0	64^3	(2, 2)
5	100	0.7	1.0	140	64^3	(2, 2)
6	100	0.7	∞	∞	64^3	(2, 2)
7	100	0.7	0.1	14.0	64^3	(2. 2)
8	100	0.7	0.1	14 0	64^3	(2, 8)
9	170	0.06	0.125	0.625	128^3	(8, 3)
10	170	0.06	0.125	0 625	64^3	(6, 6)

The notation (a,b) denotes an initial excitation of the 2D and 3D modes having peak rms velocity amplitude of a and b percent with respect to ΔU.

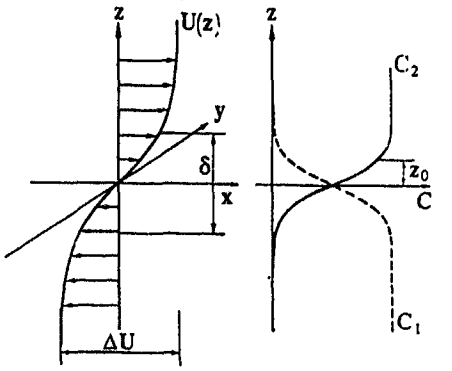

Figure 1 Problem geometry and initial conditions

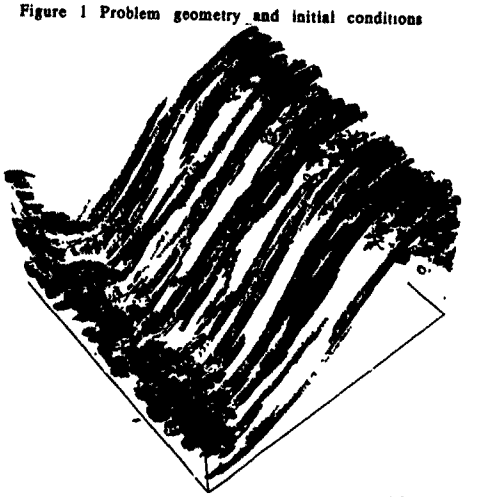

Figure 2 Isosurface plot of $|\omega| = 4\omega_{o,max}$ at T = 4.8

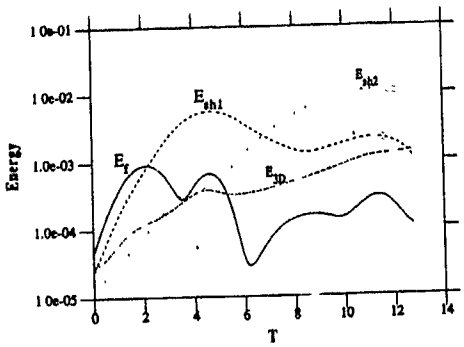

Figure 3 Total energy growth in modes corresponding to the fundamental (E_f), first and second subharmonics (E_{sh1} and E_{sh2}), and those with non-zero spanwise wavenumber (E_{3D}) for a 128^3 simulation

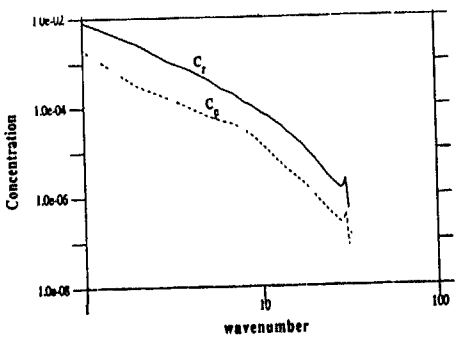

Figure 4 Power spectra of species and product concentration fields at time of first vortex pairing

Figure 5a

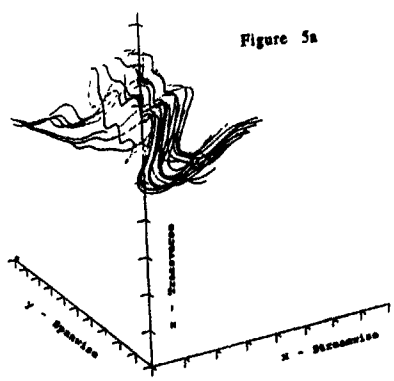

Figure 5b

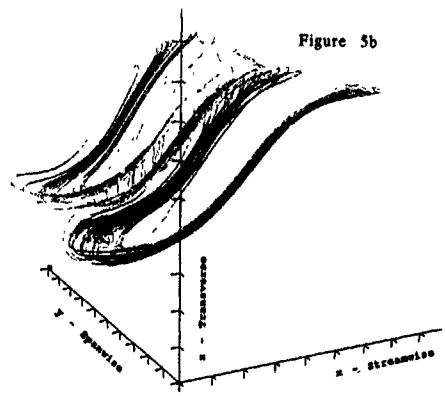

Figures 5a,b Vortex line plots showing rib evolution for 64^3 simulation. 5a: T = 0.8; 5b: T = 2.4

Figure 6a

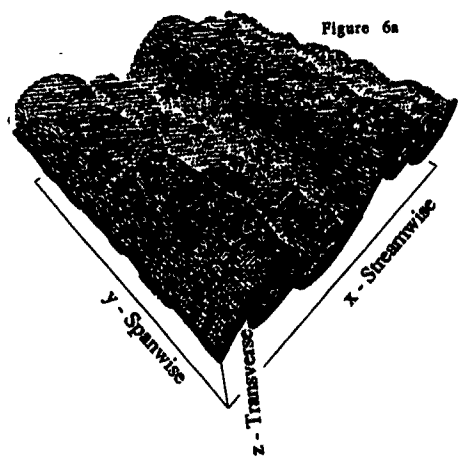

Figure 6b

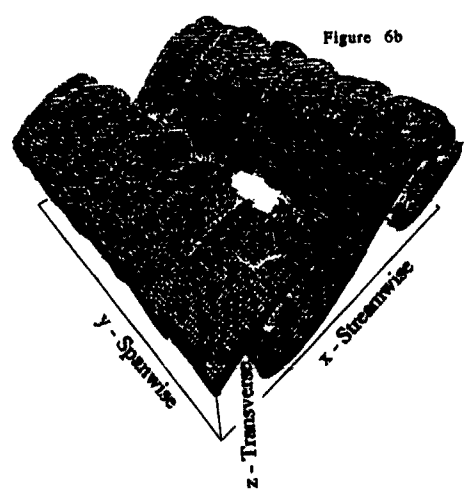

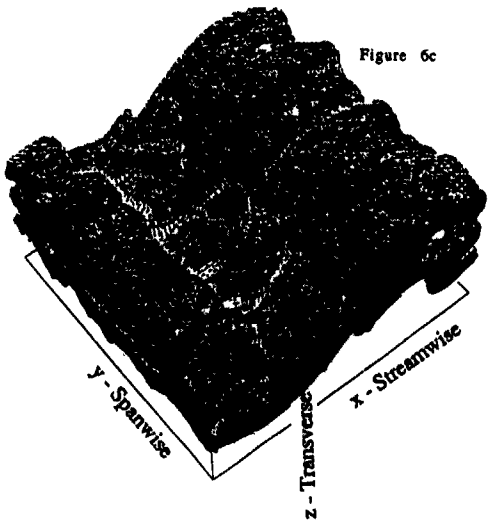

Figures 6a-c Isosurfaces of instantaneous reaction rate $\alpha C_1 C_2$ (reaction zone). 6a: T = 3.2; 6b: T = 5.3, 6c: T = 8.5

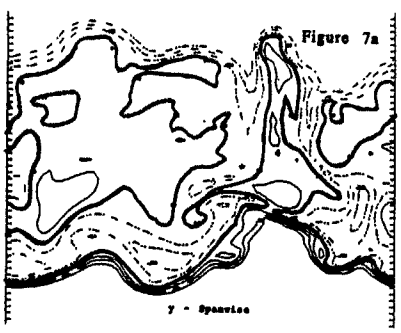

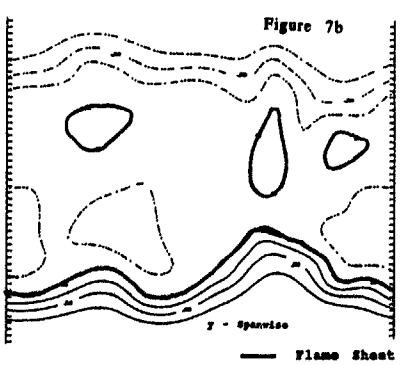

Figure 7a,b Reaction zone contours in the core region at t = 4.8 for $D_I = \infty$. Sc = 0.7 (a), Sc = 0.07 (b)

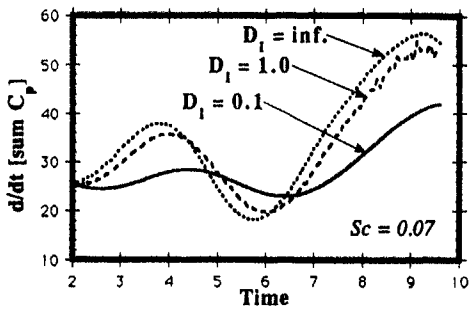

Figure 8 Total rate of product generation

$$P(t) = d/dt \iiint C_p(x,y,z)\,dx\,dy\,dz$$

as a function of Damköhler number

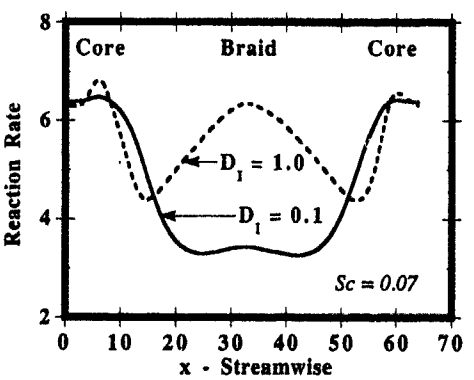

Figure 9 Streamwise variation in instantaneous reaction rate

$$R(x) = \alpha \iint C_1(x,y,z)C_2(x,y,z)\,dy\,dz$$

as a function of Damköhler number

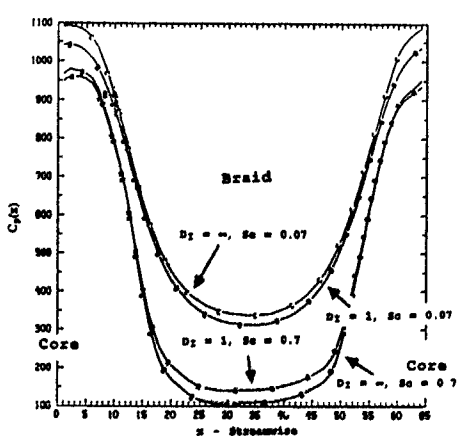

Figure 10 Streamwise variation in total product concentration $C_p(x)$ as a function of Damköhler and Schmidt number

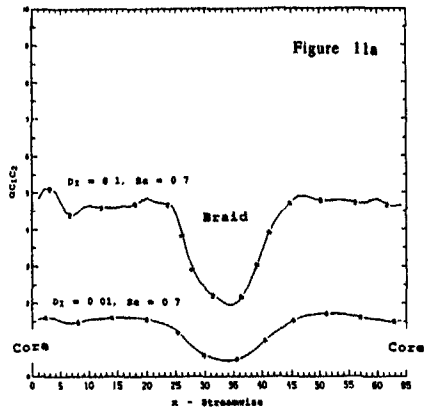

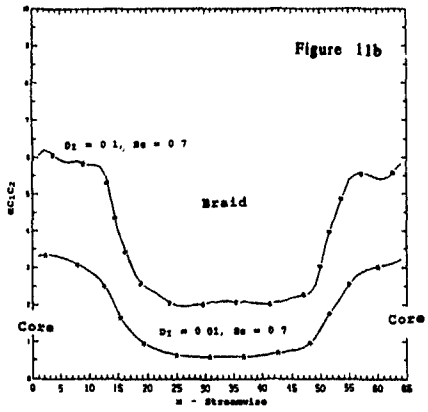

Figure 11a,b Streamwise variation in instantaneous reaction rate R(x) as a function of Damköhler number. 11a: T = 4.8; 11b: T = 7.2

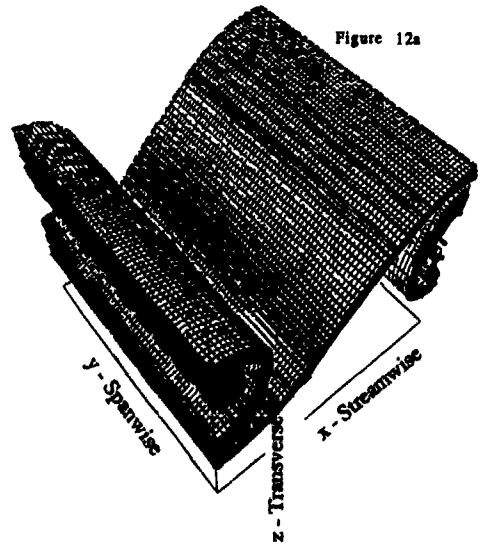

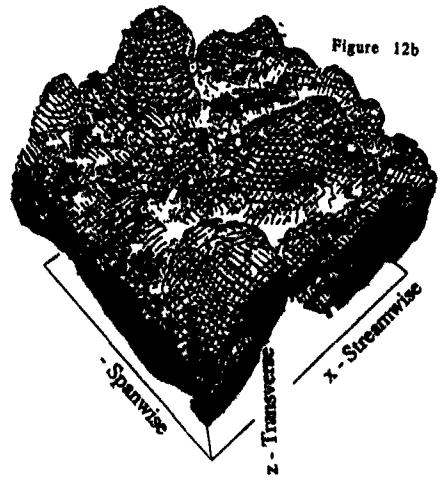

Figure 12a,b Isosurface plots of instantaneous reaction rate $\alpha C_1 C_2$ for 2D excited case with and without 3D excitation

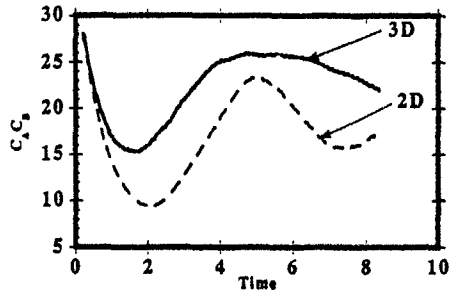

Figure 13 Total rate of product generation P(t). 2D: Only 2D excitations present; 3D: Both 2D & 3D excitations present

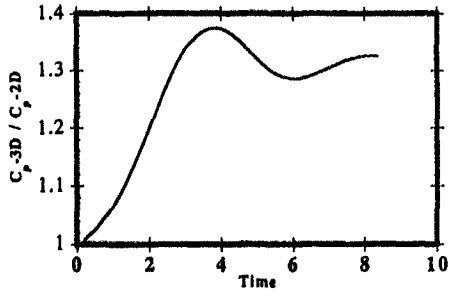

Figure 14 Ratio of 3D to 2D product generation from run with both 2D & 3D excitation to one with only 2D excitation

**EIGHTH SYMPOSIUM ON
TURBULENT SHEAR FLOWS**
Technical University of Munich
September 9-11, 1991

A NEW METHOD FOR VISUALIZATION AND MEASUREMENT OF TURBULENT FLOW PATTERNS

R. H. G. Muller*) and M. Hackeschmidt**)

*) Forschungsinstitut fur Bildverarbeitung,
Umwelttechnik und Stromungsmechanik,
Paul Klee Weg 8, W-4000 Düsseldorf 31, Germany

**) Lehrstuhl für Strömungslehre und Strömungsmaschinen,
Institut für Schienenfahrzeugtechnik der
Hochschule fur Verkehrswesen "Friedrich List"
PSF 82, O-8010 Dresden, Germany

ABSTRACT

A new flow visualization method is presented which can be applied to very complex airflows, including turbulent shear flows and bursted vortices. Based on the idea of J. Steinhoff (Ref. 1), thin and sharp-edged smoke lines are placed within the interesting flow region by projecting small, burning pellets through the flow. The smoke traces behave like time lines and can be photographed using multi-flash photography. By measuring the displacement of the traces between adjacent flashes, the flow velocities can be determined. Flow photographs are presented, showing turbulent shear flows with a spatial resolution of less than one millimeter and flow velocities of up to 20 m/s. Further examples show the development of a tip vortex and the bursting of vortices due to the pressure field of an approaching wing. The flow velocities can be measured relatively accurately using the new method in combination with digital stereometric image processing techniques.

The great advantage of the method is the Lagrangian view of the flow - common for almost all visualization techniques - together with the possibility to produce quantitative results. Interesting flow patterns and their development over space and time can easily be studied.

INTRODUCTION

Flow visualization is an important tool in the study of complex flow patterns. The visualization images allow the qualitative description of the entire flow field and, in some cases, also the quantitative measurement of flow characteristics like the flow velocities. It is very important to obtain these quantitative data for the verification of flow field calculations using Computational Fluid Dynamics codes (CFD).

Currently used methods, like smoke injection, smoke wire, pulsed smoke wire, the helium bubble technique, the spark tracer technique, or the recent phosphorescent tracer techniques all have distinct disadvantages which prevent their application to special flow fields. A more detailed discussion and comparison of these methods is presented in Refs. 2 and 3. Alternatives are the probe-based methods (hot wire) or the Laser Velocimetry (Refs. 4,5). These methods, however, are restricted to the measurement of statistical data of the flow or single point measurements and cannot give the desired Lagrangian view of the flow, which allows the observation and measurement of singular complex flow patterns and their development over space and time. This is very important for the investigation of laminar-turbulent transitions or bursted vortices.

In this paper, a new flow visualization technique and its application to complex fluid flows will be introduced, which has several advantages over the currently used methods. After a short principal description of the method (a more detailed description can be found in Refs. 2 and 3), several flow photographs will be presented and discussed, emphasizing the applicability of the new method to the investigation of turbulent flow fields and the roll-up and bursting of vortices. Finally, the procedure to obtain quantitative results of the entire flow field using digital image processing techniques will be indicated.

THE NEW VISUALIZATION TECHNIQUE

The new method is based on the idea to produce, at one instant, an initially straight line of smoke within the flow at an arbitrary direction or location, normally perpendicular to the main flow. The smoke particles in this smoke trace are very small and follow the airflow very closely. Their motion can be used to determine the flow velocities normal to the smoke trace and, under certain circumstances, also along the trace. The smoke traces have sharp edges, are very thin, can cover distances greater than one meter, and can be placed almost everywhere in the flow field. They are created by heating very small titanium pellets and projecting them through the flow. Due to the heating the pellets are burning and produce a trace of dense, white titanium dioxide smoke which fills the wake of the pellets. As a pellet has a diameter of less than 1/10 of a millimeter, its wake and therefore the smoke trace is not wider than 0.5 millimeter. The disturbance of the flow induced by the pellet and its wake is apparently very small and can be neglected, since when the trace is being observed, the pellet has gone beyond the observation region a distance several orders of magnitude greater than its diameter and all disturbances in the wake have decayed. After being placed within the flow, the smoke trace behaves like a time line. Using a stroboscope or several triggered flashes, the light scattered by the smoke can be photographed. Flow velocities can be determined by measuring the displacement of the smoke traces between subsequent flashes.

The shooting mechanism consists of a thin glass pipette and works according to the principle of an exploding wire (Ref. 6 to 8) (see figure 1). A relatively large (1 millimeter diameter) titanium pellet electrically connects two wires. Power is supplied by large capacitors. Due to the wire explosion the relatively large titanium pellet partially disintegrates into extremely small particles, which start burning (diameter less than 1/10 of a millimeter). The rest of the large pellet, which is of no further interest, and all the burning particles are accelerated by the explosion and leave the glass pipette at a spreading angle of approximately 10 degree and at a speed of 200m/s and more, depending on the energy pro-

vided by the capacitors. At the distance of 0.33m an aluminum screen (figure 2) with a small hole extracts one of these small particles, which then finally continues along its path through the region of interest within the flow. Due to this special screen arrangement, the probability is high that only one particle leaves the apparatus, called "Visualization Gun". Final particle speed is between 50m/s and 150m/s. If necessary for a high speed flow field, it is possible to extend the particle speed with the present apparatus up to about 250m/s. The particle, however, will slow down significantly due to the aerodynamic drag for longer shooting ranges.

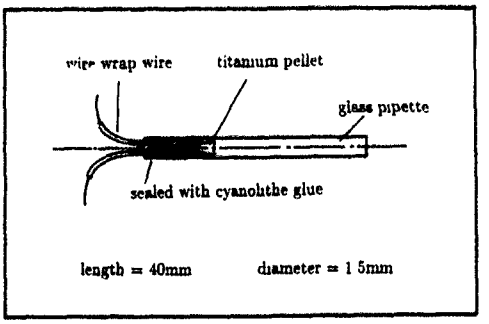

Fig. 1 Glass pipette

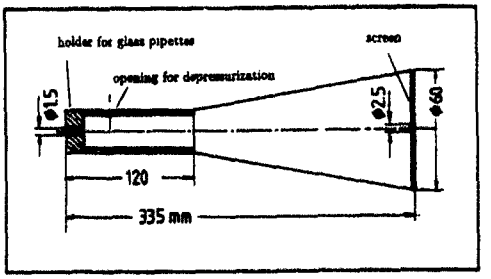

Fig. 2 Visualization Gun

Usable shooting distance with the gun is about 0.5m to 2.0m, depending on the particle speed, size, and temperature. After this distance, the particle becomes thermally unstable and disintegrates or explodes into a firework of even smaller particles.

Since the pellet is incandescent, it leaves a photographic image as it traverses the flow, separate from the illuminated smoke trace. Due to drag forces on the pellet caused by the airflow, its image is not exactly a straight line. This effect can be large and influences the location of the smoke trace. It is therefore not possible to place the line at an exactly predefined position. When the pellet has crossed the whole region of interest, the smoke trace is ready to be photographed. At this time, however, the trace is already influenced by the flow and by flow disturbances. This means that the older parts of the smoke trace have irregularities. This effect, rather than causing a problem, is helpful for determining the flow direction by following distinct recognizable local irregularities over subsequent flashes.

For the illumination of the smoke traces a set of up to four pre-charged flashes is used. Flash rising time is 0.01ms and decay time to half intensity is about 0.5ms. Due to this relatively long decay time, the "leading edge" of the smoke trace image, i.e., the edge in the direction of the flow velocity, is diffuse. The trailing edge (this is the position of the line at the flash rise), however, is very sharp due to the very fast flash rising time. Therefore, just the sharp trailing edge should be used for velocity measurements. Since there is one sharp edge, the relatively large width of the line image has no adverse effect. On the contrary, it can be helpful to determine the flow direction by observation of the fading of the smoke trace image.

Most of the visualization photographs presented in this paper are part of an investigation of the complex flow field of a hovering helicopter rotor. Two cameras were used simultaneously to provide a stereometric view of the smoke traces. One of these (the side view camera) was set to have a radial view towards the tip of the rotor blade, showing the chordwise flow on the blade. The other one (the oncoming view camera) was set to have a tangential view of the rotor, looking at the blade leading edge and showing the radial flow on the blade. The viewing angles of the cameras were rotated slightly from these ideal positions to avoid blade surface light reflections while keeping a good view on the smoke traces. The rotor used has two blades at fixed pitch of 10 degree at the tip with 33° twist and is 1.4m in diameter. The experiments were performed at a rotor speed of 666rpm, giving a tip speed of 48.6m/s. This was actually a constraint of the available test rig. As can be seen in the smoke photographs, however, this should not be a limit for the method.

DISCUSSION OF THE FLOW VISUALIZATION IMAGES

Figure 3 gives a first impression of the capabilities of the method in an initial test. Here, in a simple environment, the wake of an airfoil section in a windtunnel at a very low air speed of 1.3m/s is shown (Ref. 9). The straight line is the image of the incandescent pellet. In a four-flash-sequence the smoke line shows the flow in the wake of the airfoil.

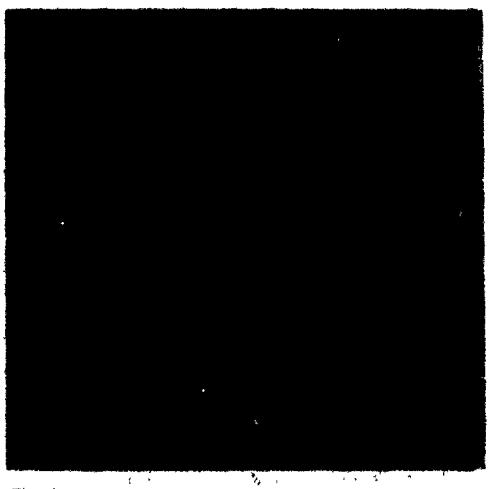

Fig. 3 Wake of an airfoil

As mentioned above, the method has been applied to the flow field of a hovering helicopter rotor to provide a much more complex environment with developing tip vortices, vortex breakdown due to the influence of the fast moving rotor blades, and complex turbulent flow regions.

Figure 4 presents the developing tip vortex with maximum tangential velocities in the vortex of 20m/s. The leading edge of the rotor blade is moving towards the observer. Due to the slight viewing angle of 8 degree relative to the rotor disk which is necessary to avoid light reflections on the twisted blades, the blade seems to move downward in the image. The smoke trace stays at about the same azimuthal rotor position during the four flash sequence, which is in the image plane. The blade (or its quarter chord line), however, moves from a position of shortly behind the image plane at the first flash (uppermost blade image) over the exact image plane position at the second flash to an azimuthal position shortly in front of the image plane at the third flash and finally to the last position, where even the trailing edge has moved in front of the image plane (fourth flash; lowermost blade image).

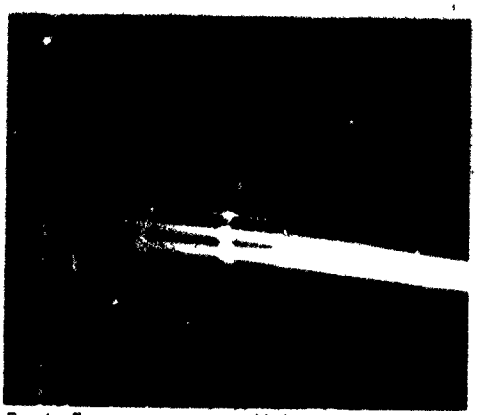

Fig. 4 Tip vortex at a rotor blade

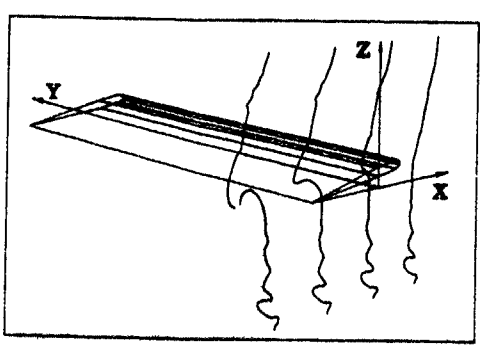

Fig. 5 3-dimensional reconstruction of tip vortex roll-up

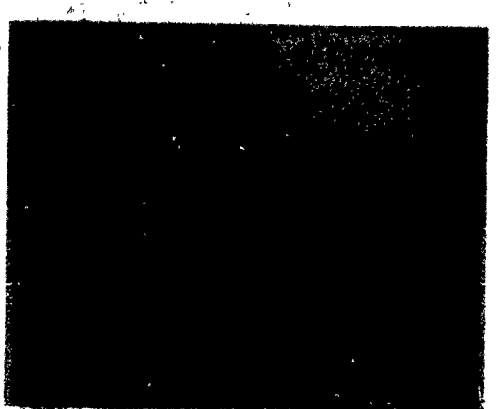

Fig. 6 Contrast-enhanced blow up of the tip vortex

The roll-up of the smoke trace can be observed as the effect of the roll-up of the tip vortex. At the first flash there is almost no influence of the blade on the smoke trace, whereas at the last flash the tip vortex is almost fully developed. The smoke trace could not be placed exactly in the core of the developing vortex. Nevertheless it is possible to observe the radial station of the largest tangential velocity in the vortex. The smooth velocity profile gives evidence to this fact. If the smoke trace had encountered the vortex at a radial station outside of the maximum tangential velocity, a sharp edge of the velocity profile, raising towards the maximum, would then be observed.

Figure 5 shows the development of the tip vortex in a 3-dimensional view, which is reconstructed using a stereometric set of photographs. For this sketch the relations have been changed to a blade-fixed coordinate system and the smoke trace moves past the blade, shaped by the influence of the tip vortex. Figure 6 shows a blow up of the same tip vortex in an inverted (black on white) and contrast-enhanced view. All the following flow field images will be presented in a similar technique, which greatly enhances the visibility of small smoke ructures or faint smoke traces.

The following figures intend to show the capability of the new method to investigate turbulent flow patterns and the bursting of vortices.

For figure 7 two titanium particles have been shot into a flow region in the wake of the helicopter rotor at the same time. Figure 8 shows the reconstructed 3-dimensional view of these smoke traces. The orientation of the coordinate system is not important for the understanding of the figure. The smoke traces have been photographed using a two-flash-sequence. Mean flow velocity can be determined to about 10m/s. It is evident that the two particles have been shot into two regions of completely different flow - one particle into a laminar flow field, the other into a flow field with large local shear flow with shear layers of a thickness of 1 to 5 millimeters and flow disturbances of more than 20% of the mean flow velocity. The existence of these two different flow types within a spatial range of about 20 millimeters could be of great interest and the investigation of the boundary between these two regions could be performed using the new method.

Another interesting flow pattern is shown in figure 9, where little vortices of different orientation start to roll up the smoke line at several locations. Figure 10, again, shows the 3-dimensional reconstruction. Using such photographs, the orientations of the vorticity vectors of a disturbed flow region can be determined.

Depending on the load of the rotor, the wake contraction, and other characteristics, the tip vortex of one rotor blade can come into the vicinity of the following blade and can have a strong influence on this blade. This phenomenon, called "Blade Vortex Interaction" (BVI), causes blade stress, rotor noise, and poor rotor effi-

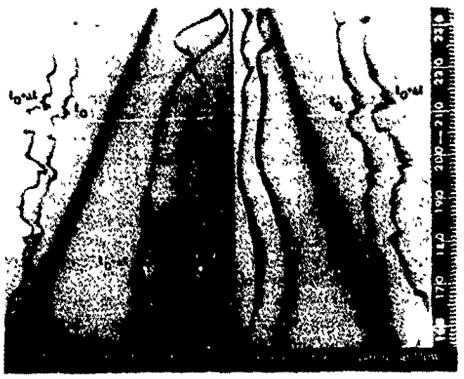

Fig. 7 Laminar and turbulent flow region

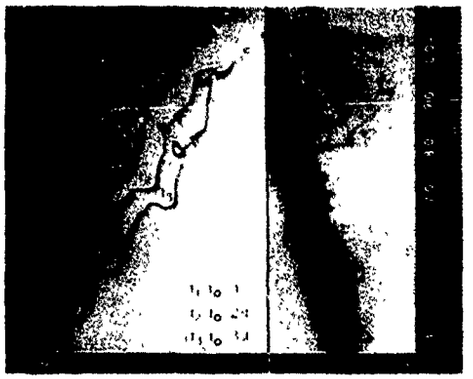

Fig. 9 Flow region disturbed by small vortices

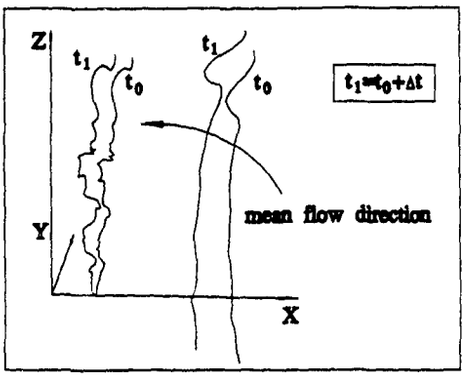

Fig. 8 3-dimensional reconstruct on of the smoke traces

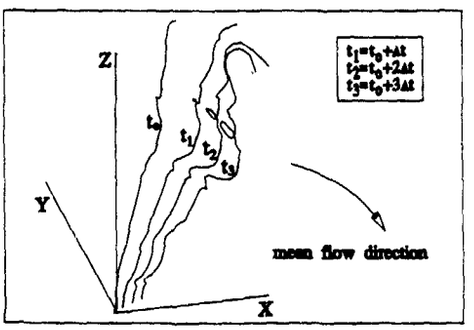

Fig. 10 3-dimensional reconstruction of the smoke trace

Fig. 11
Bursted vortex
by influence
of the approaching
airfoil section

ciency due to the induced velocities of the vortex. The theoretical investigation of this problem is a very difficult task due to the unknown structure of the vortex during BVI. Depending on the distance between blade and vortex at BVI, the pressure field of the approaching blade can cause the bursting of the vortex and therefore produce an even more complex and unknown structure. While the only other possible method for an experimental investigation of this flow type, the laser velocimetry, can only provide statistical data, which normally have to be gathered over many rotor revolutions, the new method can visualize the complete core of the bursted vortex at one instant, showing its dimensions, tangential velocities, and the dimensions of the local turbulent structures. Figure 11 shows such a blade vortex interaction with a bursted vortex in a two-flash-sequence and in an oncoming view like figure 4. The blade is turning towards the observer and moving slightly downward due to the 8 degree shift of the camera relative to the rotor disk. The tip vortex of the preceding blade encounters the blade at about 90% of the rotor radius. The vortex has moved downward only a distance of 25% of the blade chord due to the weak downwash of the rotor.

At the first flash (upper blade image; smoke trace image 'A') the distance between blade leading edge and smoke trace is about 50% of the blade chord and the vortex is already bursted due to the pressure field of the blade. There is a very sharp boundary between the bursted vortex core and the laminar flow outside that core. Figure 12 shows a blow up of the lower part of figure 11, together with the side view of the same flow field. At the second flash, half a chord after the encounter with the smoke trace, the influence of the blade has completely destroyed the smoke trace in its vicinity. Figure 12 and the lower part of figure 11, however, can still be used to determine the mean tangential velocity of the lower part of the bursted vortex during the encounter with the blade. Especially the side view of the vortex (left hand side of figure 12) shows very clearly the turbulent shear flow in axial direction of the bursted vortex (side view: blade moving from left to right).

A similar flow condition is presented in figure 13 Here the boundary between the bursted part of the vortex and the laminar outer flow is less complex. In a final flow photograph figure 14 shows the development of a very complex flow region with many disturbances over a relatively long time interval of 5.4ms. Two smoke traces (A,B) have been set into the flow.

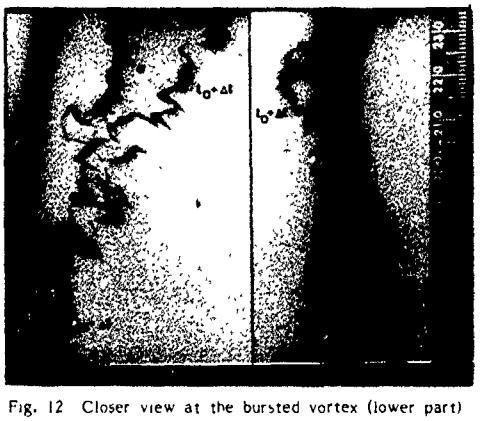

Fig. 12 Closer view at the bursted vortex (lower part)

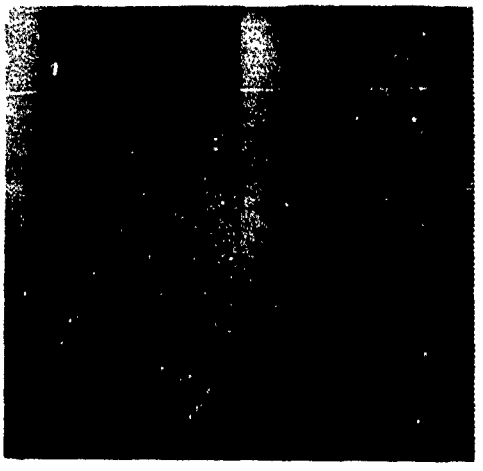

Fig. 13 Bursted vortex

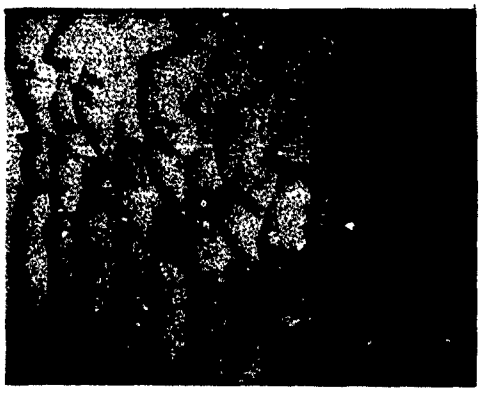

Fig. 14 Distorted flow region

DIGITAL IMAGE PROCESSING

Using digital image processing the computer can help to produce quantitative data of the velocity field. Corresponding points (the earlier mentioned irregularities) on the smoke trace images can be used to calculate the mean local flow velocities between each two subsequent flashes. In the following steps of the procedure, the computer combines two stereometrically taken photographs to produce 3-dimensional images of the smoke traces like the examples of figures 5, 8 and 10 or streamline plots. Even the complete velocity vector plot of a larger flow field can be calculated, using a larger set of stereometric photographs of that flow field and a special 3-dimensional interpolation procedure (figure 15: flow around blade tip including tip vortex of figure 4). More details regarding these topics can be found in Refs. 3 and 10. For a discussion of the possible errors in the velocity determination using time lines see Ref. 11.

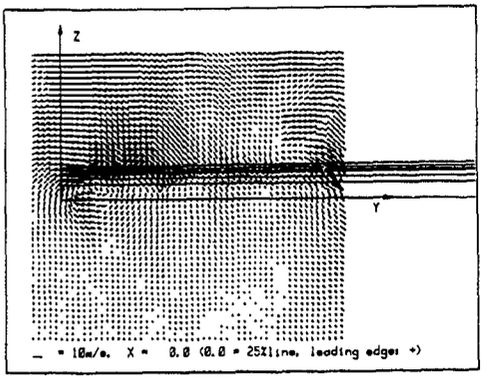

Fig. 15 Interpolated flow velocities at the blade tip

FUTURE WORK

Using the experiences obtained by the helicopter rotor flow study, new experiments will be initiated at the "Hochschule fur Verkehrswesen 'Friedrich List'" in Dresden, concerning the investigation of the development of turbulent spots in a wall boundary layer. These turbulent spots indicate the laminar-turbulent transition by a detachment and bursting of lengthwise vortices which exist in an unstable laminar boundary layer. By shooting the smoke traces directly out of the wall through a very small hole, it will be possible to observe the organization and the characteristics of the flow close to the wall. The new method will be used together with other methods like the "soot-oil-petroleum-layer-"method, which will be helpful to find the most interesting regions within the flow (Refs. 12 and 13). These experiments and several other hybrid applications will be very important steps in the development of the new method, since it is a consequential principle of experimental investigations, to apply at least two different independent methods to get well-defined and interpretable results (Ref. 14). The new method will turn out to be one of very few methods which can be applied to complex small scale flows and can give qualitative as well as quantitative results. Prototypes of the apparatus including the image processing hard- and software are available upon request and can be adapted to different applications.

REFERENCES

1. Steinhoff, J. S., "A Simple Efficient Method for Flow Measurement and Visualization," Flow Visualization III, Hemisphere Publishing Corporation (1985) Springer-Verlag, Edited by W. J. Yang, pp. 19-24.
2. Muller, R.H.G. and Steinhoff, J. S., "Application of a New Visualization Method to Helicopter Rotor Flow," presented at the 8th AIAA Applied Aerodynamics Conference, Portland, Oregon, August 20-22, 1990.
3. Muller, R.H.G., "Eine neuartige Methode zur Visualisierung von Stromungen sowie Auswertung der Stromungsbilder mittels digitaler Bildverarbeitung," Abschlußbericht DFG (Deutsche Forschungsgemeinschaft) Mu802/1-1, 1990.
4. Lorber, P.F., Stauter, R.C., Landgrebe, A.J., "A Comprehensive Hover Test of the Airloads and Airflow of an Extensively Instrumented Model Helicopter Rotor," Proceedings of the 45th AHS Annual Forum, May 1989.
5. Thomson, T.L., Kwon, O.J., Kemnitz, J.L., Komerath, N.M., Gray, R.B., "Tip Vortex Core Measurements on a Hovering Model Rotor," AIAA 25th Aerospace Sciences Meeting, Jan.12-15, 1987, Reno, Nevada.
6. Chace, William G., "Liquid Behavior of Exploding Wires," The Physics of Fluids, Vol. 2, No. 2, March-April 1959, pp. 230-235.
7. Scherrer, Victor E., "An Exploding Wire Hypervelocity Projector," Exploding Wires, Vol. 2, Plenum Press New York, 1962, pp. 235-244.
8. Bohn, J. L., Nadig, F. H., Simmons, W. F., "Acceleration of Small Particles by Means of Exploding Wires," Exploding Wires, Vol. 3, Plenum Press New York, 1964, pp. 330-351.
9. Steinhoff, J. S. and Mersch, T., "A Simple Efficient Method for Flow Field Measurement and Visualization Using Projected Smoke Trails," University of Tennessee Space Institute Report, 1989.
10. Muller, R.H.G., "Visualization and Measurement of Helicopter Rotor Flow Using Projected Smoke Filaments and Digital Image Processing," presented at the 16th European Rotorcraft Forum, Sept. 1990, Glasgow, Scotland.
11. Lusseyran, D. and Rockwell, D.,"Estimation of Velocity Eigenfunction and Vorticity Distributions from the Time Line Visualization Technique," Experiments in Fluids 6, pp 228-236 (1988).
12. Hackeschmidt, M., "Die heutigen Anschauungen zur laminar-turbulenten Übergangsgrenzschicht," Maschinenbautechnik, Berlin 35 (1986) 12, pp 553-559
13. Hackeschmidt, M., "Causes of Vortex Bursting in Transitional Boundary Layers," Laminar-Turbulent Transition IUTAM Symposium, Novosibirsk 1984, Editor: V.V. Kozlow; Springer Verlag, Berlin, Heidelberg 1985
14. Hackeschmidt, M. and Neumann, G., "Two Principles of Application in Analogue Modeling," 11th IMACS World Congress, Aug. 5-9th, 1985, Oslo; Proceedings Vol.5, pp 57-60

EIGHTH SYMPOSIUM ON
TURBULENT SHEAR FLOWS
Technical University of Munich
September 9-11, 1991

TWO-DIMENSIONAL PATTERN RECOGNITION PROCESSING OF NEAR-WALL TURBULENCE

T Ueno*) and T Utami*)

*) Ujigawa Hydraulics Laboratory,
Disaster Prevention Research Institute, Kyoto University
(Yoko-Ohji, Fushimi-Ku, Kyoto 612, Japan)

ABSTRACT

Two-dimensional pattern recognition processing was introduced into two-dimensional vorticity data obtained by flow visualization and picture processing

Several typical patterns of two-dimensional vorticity distribution over a small unit area were correlated with the vorticity distribution to detect the characteristic structure and arrangement of vortex motions Ensemble averaged patterns of each velocity component and vorticity around the detected points were calculated

INTRODUCTION

Conditional sampling techniques (Kovasznay et al 1970, Wallace et al 1972, Willmarth et al 1972, Blackwelder et al 1976 & Wallace et al, 1977) have made remarkable contributions in elucidating the coherent structure of turbulence since they were introduced in the 1970s But, since the techniques had been applied to analyze one-dimensional time-series data, there have been some restrictions in the obtained results First, we can gain information about the structure of turbulence only around the detected point and, secondly, as the detected data sometimes contains phase shift or spanwise shift, their ensemble average may smear out an important phase of a turbulence structure

Recently, Johansson et al (1991) improved the technique by applying it two-dimensionally for processing the database generated from direct numerical simulation of turbulent channel flow, thus removing the second restriction

In this paper, the two-dimensional pattern recognition method was applied to two-dimensional experimental data obtained through flow visualization and picture processing and coherent structures of turbulence in open-channel flow were elucidated

The authors would like to emphasize that, first, the fundamental structure of turbulence is a horseshoe vortex and thus it is important to clarify the structure of horseshoe vortices. Secondly, there are some typical arrangements of horseshoe vortices and, in order to clarify the whole image of coherent structure, every kind of event generated by each arrangement and hierarchical structure of vortices should be examined Thirdly, for these investigations, the two dimensional pattern recognition technique applied for vorticity distribution is particularly effective

EXPERIMENT AND PICTURE PROCESSING

A horizontal cross-section of the 40 cm wide and 3 95 cm deep open-channel water flow was illuminated by a 3 mm thick light sheet and a pair of photographs were taken over the short time span of about 40 ms ($1\ 3\ \nu/u_*$) The friction velocity u_* was 0 57 cm/s The photograph density was digitized into 12 bit data with a spatial resolution of 2 2 viscous scales (0 32mm) using a PDS microdensitometer The digitized data was fed into the computer and the two-dimensional distribution of velocity vectors were calculated using a cross-correlation technique (Utami et al 1991) The map of the x-component of velocity u in the cross-section $y^+ = 21$ is shown in **Fig. 1** In this figure, bands of low-speed and high-speed regions stretching in the flow direction are observed to appear alternately in a spanwise direction

Photographs were taken of the cross-sections of various y^+ locations. In this paper the pattern recognition method was applied to the vorticity distribution calculated from the velocity vector data in the cross-section $y^+ = 21$

TWO-DIMENSIONAL PATTERN RECOGNITION FOR DETECTING A HORSESHOE VORTEX

Fig. 2 shows the map of the y-component of vorticity ω_y in the cross-section $y^+ = 21$ It is commonly concluded that the fundamental structure of near-wall turbulence is a horseshoe vortex The horizontal cross-section of a horseshoe vortex is a vortex pair, which is identified as a pair of high-vorticity regions with opposite signs as in **Fig. 2** Considering that the vorticity distribution of horse-shoe vortices in **Fig 2** has a typical scale and patterns, the map of vorticity (**Fig 3**) over a small area $108\ 6 \times 108.6\ \nu/u_*$ was used to detect horseshoe vortices

The two-dimensional cross-correlation coefficient $C_r(x, z)$ was defined as

$$C_r(x,z) = \frac{\int\int \{\omega_y(x+x_1, z+z_1)\cdot\omega_*(x_1, z_1)\}dx_1dz_1}{\sqrt{\int\int\{\omega_y(x+x_1, z+z_1)\}^2dx_1dz_1\cdot\int\int\{\omega_*(x_1, z_1)\}^2dx_1dz}}$$

where ω_* is the vorticity of the detecting map and ω_y is the y-component of vorticity in **Fig. 2**

The obtained map of C_r is given in **Fig. 4**. In this figure, the detected points which are supposed to be the center of a vortex pair are obtained as a

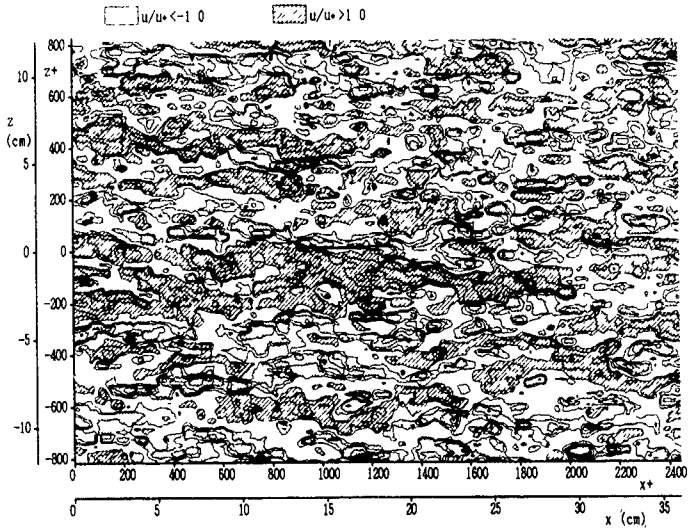

Fig 1 Map of the x-component of velocity u in the horizontal cross-section of the flow ($y^+ = 21$) Contour increment is 1 in viscous unit

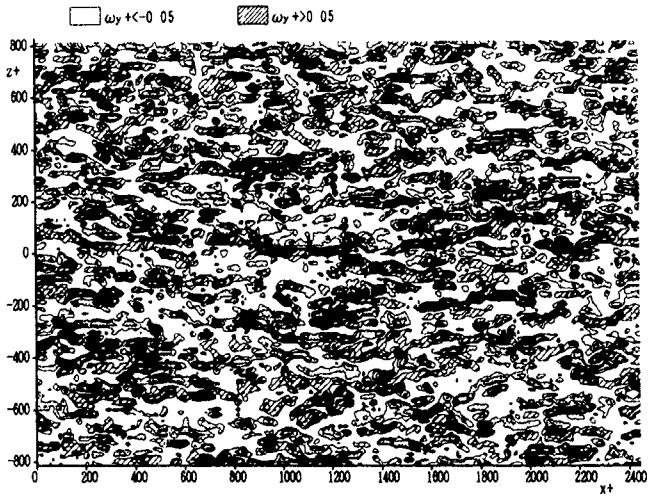

Fig. 2 Map of the y-component of vorticity ω_y in the horizontal cross-section of the flow ($y^+ = 21$) Contour increment is 0 05 in viscous unit

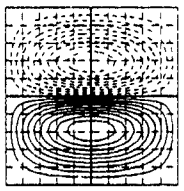

Fig. 3 Map of vorticity for detecting vortex pairs

local peak point of C_r -value greater than the threshold value (in this case, 0 6) and are shown by small dots It is clear, by comparing this figure with Fig 1, that flow velocity is low in a high C_r-value region and vice versa

Fig. 4 shows that some horseshoe vortices are arranged in a line forming longitudinal vortices (Utami and Ueno 1987) The cross-section of a longitudinal vortex has an elliptic shape elongated in the flow direction and its longitudinal axis has an angle $0 - \pm 13^\circ$ in the streamwise direction It is noticeable that longitudinal vortices are generally arranged in a staggered array

The maps of ensemble averaged velocity and vorticity around the detected points are shown in Fig 5, in which the shaded region shows large positive ensemble average values and the dotted region negative values The pattern of a vortex pair is clearly observed in the ensemble average of velocity (Fig. 5(a)) It is emphasized that streamwise and spanwise centering are improved by introducing two-dimensional pattern recognition as compared with the one-dimensional

In the central part of a vortex pair, velocity is low (Fig. 5(b)) As, generally, some horseshoe vortices are arranged in a line in groups, the detected map of vorticity (Fig. 5(d)) is more elongated in the flow direction compared with the detecting map of vorticity

Isolated vortices are also observed in Fig. 2 and

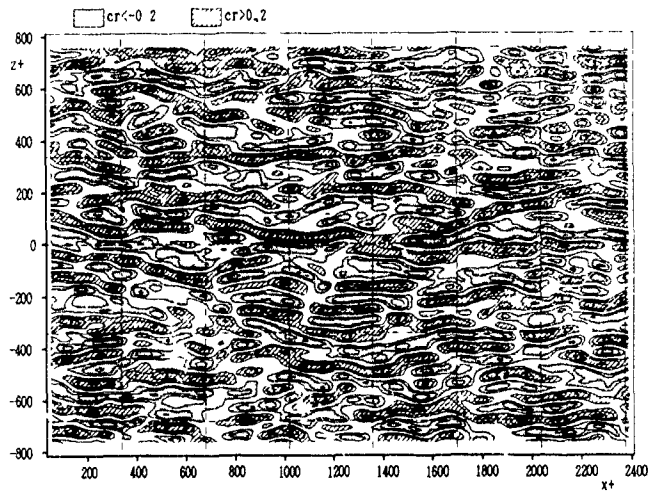

Fig. 4 Map of the cross-correlation coefficient obtained through the detecting pattern of **Fig. 3**. Contour increment is 0.2.

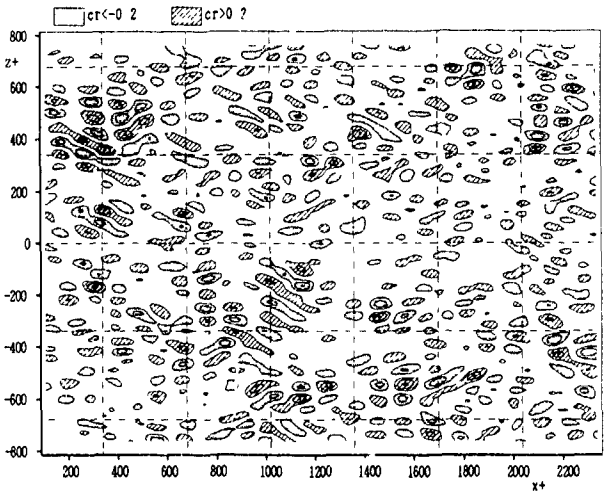

Fig. 7 Map of the cross-correlation coefficient obtained through the detecting pattern of **Fig. 6**. Contour increment is 0.2.

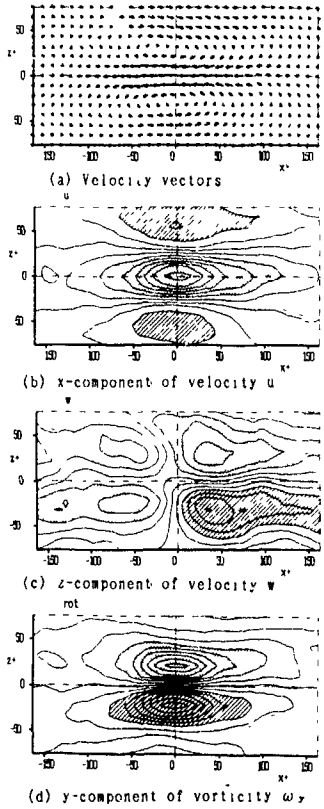

Fig. 5 Two-dimensional ensemble averages of velocity and vorticity obtained through the detecting pattern of **Fig. 3**.

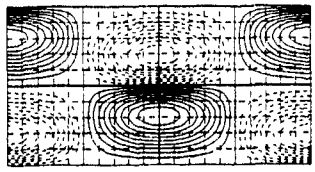

Fig. 6 Detecting pattern for isolated horseshoe vortex.

Fig. 4 In order to detect these vortices, the detecting map of vorticity shown in **Fig. 6** is adopted. The resultant correlation coefficient C_r is shown in **Fig. 7**. The area having a high C_r-value region is significantly smaller than that in **Fig. 4**, which means that few horseshoe vortices are isolated and, generally, 2 - 5 horseshoe vortices are gathered into a group composing a longitudinal vortex (Utami et al. 1987).

The ensemble averages of velocity and vorticity around the detected points are shown in **Fig. 8**. In this case the threshold C_r-value was 0.5. The streamwise scale of detected vorticity is about $100\,\nu/u_\tau$ as shown in **Fig. 8(d)**.

EFFECT OF THE SCALE OF DETECTING PATTERN

In order to examine the effect of the scale of a detecting map, 5 different scales of a detecting map were tried, in which the longitudinal scale L of the central vortex pair of **Fig. 6** was expanded or contracted up to $L^+ = Lu_\tau/\nu$ = 65.1, 108.6, 152.0, 217.1 and 325.7. Some of the results are shown in **Fig. 9**. The ensemble averages of u and ω_y around the detected point for the case L^+ = 217.1 and 325.7 are shown in **Fig. 10** and **Fig. 11**, respectively. It is clear that the larger scale detecting map results in a larger scale detected pattern. But, as a horseshoe vortex having a scale exceeding $200\,\nu/u_\tau$ doesn't exist in **Fig. 2** and **Fig. 4**, the detected patterns

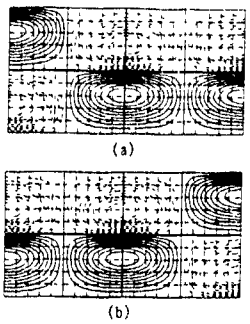

Fig 12 Detecting patterns for (a), the horseshoe vortex at the upstream end and (b), the horseshoe vortex at the downstream end in the longitudinal vortices

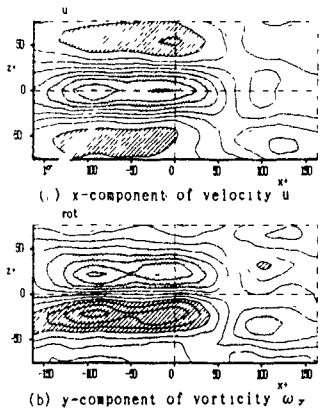

(a) x-component of velocity u

(b) y-component of vorticity ω_y

Fig 14 Two-dimensional ensemble averages of velocity and vorticity obtained through the detecting pattern of Fig. 12 (b)

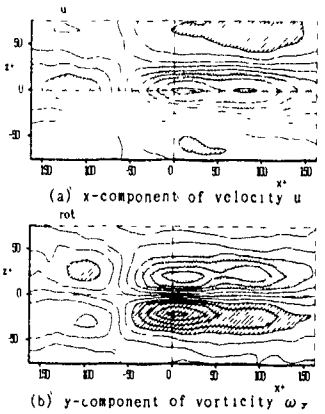

(a) x-component of velocity u

(b) y-component of vorticity ω_y

Fig 13 Two-dimensional ensemble averages of velocity and vorticity obtained through the detecting pattern of Fig 1.(a)

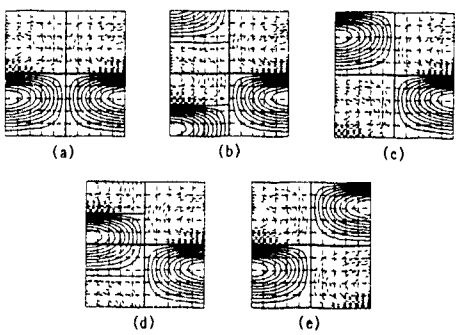

Fig 15 Detecting patterns for typical arrangements of horseshoe vortices

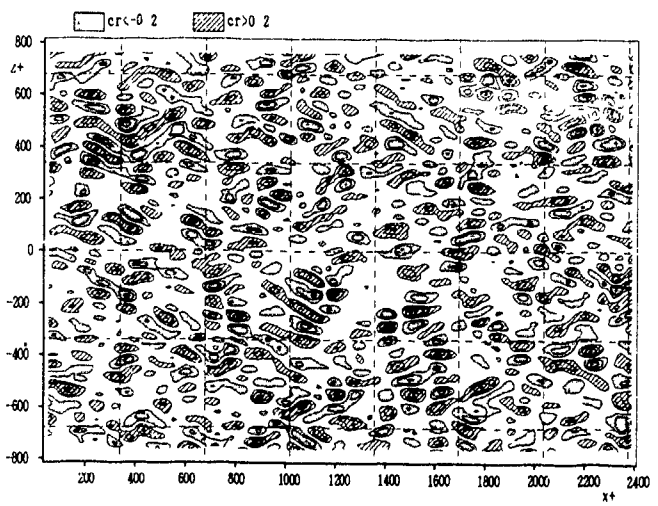

Fig 16 Map of the cross-correlation coefficient obtained through the detecting pattern of Fig. 15(c) Contour increment is 0 2

represents 54 detected points. It is noticed when comparing **Fig 16** with **Fig 4** that most of the detected points are located at the upstream end of longitudinal vortices

The maps of ensemble averaged velocity and vorticity around the detected point are shown in **Fig 17(a)-(d)** The map of u (**Fig 17(b)**) and that of w (**Fig 17(c)**), show quite similar patterns to those obtained by Johansson et al (1991) who used a modified VISA technique It should be noted that the VISA and VITA techniques do not detect events other than the one given in **Fig 17(a)** or **Fig. 17(d)**

CONCLUSIONS

The two-dimensional pattern recognition technique was introduced for processing the turbulence velocity data obtained through flow visualization and picture processing This processing was shown to be more effective in obtaining more exact understanding of the vortex motions in turbulence as compared to one-dimensional pattern recognition processing

It was shown that horseshoe vortices have some typical patterns of arrangement. Some horseshoe vortices are gathered into a group creating a longitudinal vortex and the longitudinal vortices are generally arranged in a staggered array. Some characteristic properties of velocity distribution and vorticity distribution in the longitudinal vortices were shown.

REFERENCES

BLACKWELDER, R F. & KAPLAN, R E. 1976 On the wall structure of the turbulent boundary layer, J Fluid Mech 76, 89-112

BOGARD, D G & TIEDERMAN, W G 1987 Characteristics of ejections in turbulent channel flow. J Fluid Mech 179, 1-19

JOHANSSON, A V, ALFREDSSON, P H & Kim, J 1991 Evolution and dynamics of shear-layer structures in near-wall turbulence J Fluid Mech 224, 579-599

KOVASZNAY, L S G, KIBENS, V & BLACKWELDER, R F 1970 Large-scale motion in the intermittent region of a turbulent boundary layer J Fluid Mech 41, 283-325

UTAMI, T, BLACKWELDER, R F & UENO, T 1991 A cross-correlation technique for velocity field extraction from particulate visualization. Exps Fluids 10, 213-223

Utami, T & UENO, T 1987 Experimental study on the coherent structure of turbulent open-channel flow using visualization and picture processing J Fluid Mech 174, 399-440

WALLACE, J M, BRODKEY, R S & ECKELMANN, H 1977 Pattern-recognized structures in bounded turbulent shear flows J. Fluid Mech 83, 673-693.

WALLACE, J M, ECKELMANN, H & BRODKEY, R S 1972 The wall region in turbulent shear flow J Fluid mech 54 39-48

WILLMARTH W W & LU, S S 1972 Structure of the Reynolds stress near the wall J Fluid Mech 55, 65-92

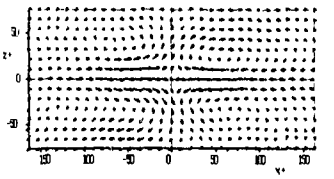

(a) Velocity vectors

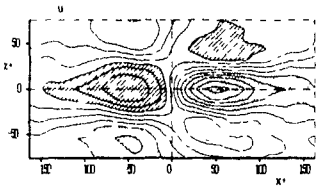

(b) x-component of velocity u

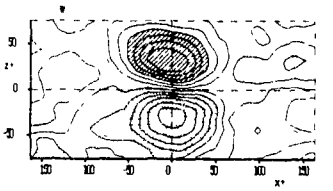

(c) z-component of velocity w

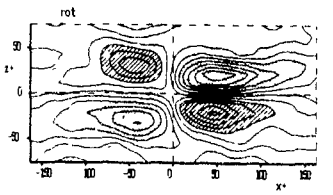

(d) y-component of vorticity ω_y

Fig 17 Two-dimensional ensemble averages of velocity and vorticity obtained through the detecting pattern of **Fig. 15(c)**

EIGHTH SYMPOSIUM ON
TURBULENT SHEAR FLOWS
Technical University of Munich
September 9-11, 1991

4-3

WATER-COMPATIBLE VORTICITY VECTOR OPTICAL PROBE

Michael B. Frish
R. Daniel Ferguson

Physical Sciences Inc
20 New England Business Center
Andover, MA 01810
USA

ABSTRACT

The Vorticity Optical Probe or VOP, a technique for direct non-intrusive measurement of vorticity, is now able to determine all three components of the vorticity vector at well-defined locations in a water flow field with temporal and spatial resolutions better than the Kolmogorov microscales. These developments result from: a) the invention of VOP probe particles that nearly match the refractive index and density of water, and b) data reduction algorithms that fully utilize the information provided by reflections of laser light from the particles. The technique has been tested and demonstrated in laminar and turbulent Couette flows.

INTRODUCTION

A non-invasive instrument capable of measuring and mapping the vorticity vector fields surrounding moving underwater vehicles or along test surfaces in water tunnels has long been sought by researchers performing fundamental fluid dynamics studies or applied studies in underwater technology and aerodynamics. The applications are myriad, ranging from basic understanding of boundary layer turbulence (potentially leading to understanding and control of turbulence production and its concomitant drag), to locating and controlling sources of flow-induced noise, and to studying the effects on maneuverability caused by interactions of large-scale vortices with vehicle control surfaces. In response to this need, the capabilities of an optical technique known as the Vorticity Optical Probe or VOP have been extended so that is now capable of directly measuring all three components of vorticity vectors in water flows.

The Vorticity Optical Probe, invented and developed by these authors, operates by seeding into a liquid flow transparent spherical particles that are tens of microns in diameter with each containing one or more embedded lead carbonate crystals that act as planar reflectors or "mirrors" (Frish and Webb, 1981). Viscous drag on the surfaces of the spheres causes them to rotate with an angular velocity vector equal to half the local vorticity vector (Jeffrey, 1922). The spheres are made invisible by matching their refractive index to that of the flowing medium. A beam of laser light incident upon such a rotating invisible sphere is reflected by the embedded mirror. As described below, the reflected beam is intercepted outside of the flow as it traces a path or "trajectory" along the surface of a detector. That trajectory is uniquely related to the sphere's angular velocity. Methods for measurement and analysis of the trajectory developed initially by Frish (1981) to deduce one vorticity component, and expanded upon by Ferguson and Webb (1983) to deduce two components, have now been refined to enable calculation of the complete vorticity vector.

Other techniques that have been or are being used to determine vorticity actually measure components of velocity vectors at multiple closely-spaced points, and deduce vorticity by calculating the finite-difference curl of the velocity. These techniques, typically employing hot-wire anemometers (Wallace, 1986), laser velocimeters (Lang and Dimotakis, 1982), or particle imaging velocimetry (Adrian, 1991) are cumbersome, difficult to analyze, and generally incapable of small-scale (< 1 to 2 mm) vorticity resolution. This resolution is inadequate for many applications, specifically within liquid boundary layers or in turbomachinery. In contrast, the maximum VOP particle size ($\sim 50\ \mu m$) was selected to be less than the Kolmogorov microscale in a high-speed water tunnels, thereby enabling accurate measurement of the smallest-scale and highest frequency fluctuating vorticity vectors in turbulent boundary layers (Frish, 1981). The particles respond to vorticity fluctuations in the frequency range from zero to 15 kHz.

VOP TECHNIQUE

The VOP deduces the vorticity vector by tracking a small segment of a reflection trajectory as it transits across a two-dimensional surface. It is often asked: "How can one be assured that each trajectory corresponds to a unique vorticity vector?" and "How are all three vector components deduced from a track across a two-dimensional surface?" Answers to those questions are provided here.

Figure 1 illustrates the VOP geometry. A laser beam defines the z-axis of a coordinate system. The beam illuminates a non-translating probe particle spinning with an angular velocity $\bar{\omega}/2$ where $\bar{\omega}$ is the vorticity vector. The laser beam and the unit vector normal to the particle's mirror, called the mirror normal $\hat{n}$, define the $\hat{n}$-$\hat{z}$ plane. The reflection of the laser beam from the mirror, defined as the unit vector $\hat{r}$, lies in the $\hat{n}$-$\hat{z}$ plane, and the angle of laser reflection relative to the mirror normal is equal to the angle of incidence. If $\hat{n}$ is described by the usual spherical coordinates where θ is the elevation relative to the z-axis and ϕ is the azimuth in the x-y plane, then
$\hat{r} \equiv (\theta', \phi') = (2\theta, \phi)$.

As the particle spins, the mirror normal precesses around the vorticity vector according to the equation

$$d\hat{n}/dt = (\bar{\omega} \times \hat{n})/2 \qquad (1)$$

As a result, the trajectory of the mirror normal where it intercepts the surface of a unit sphere drawn around the probe particle describes a circle, illustrated in Fig. 2. The

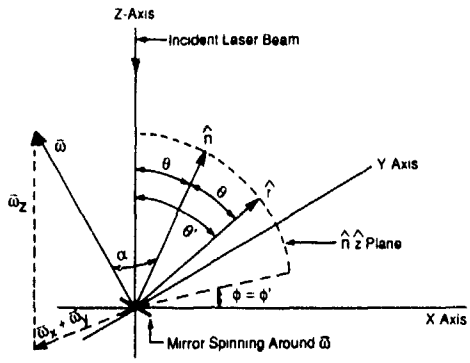

Fig 1 Definition Sketch of VOP Geometry

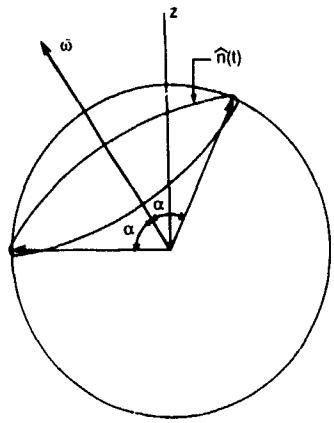

Fig. 2. Trajectory of the Mirror Normal Across the Surface of the Unit Sphere

axis of the circle is colinear with $\bar{\omega}$; its azimuth and elevation specify the direction of the vorticity vector. The vorticity magnitude is simply equal to twice the rate at which the circle is repeated, and can be determined from the time required for the trajectory to sweep an arc of known angular size. The radius of the circle is determined solely by the elevation, α, of the mirror normal relative to the vorticity vector and contains no information about the vorticity. Another probe particle, having the same vorticity but a different mirror orientation, would describe a co-axial circle. Because each vorticity vector direction defines a unique (albeit infinitely large) set of circles, it follows that each circle, and each segment thereof, corresponds to a unique vorticity vector direction.

As discussed above, for each $\hat{n}$ there is a unique $\hat{r}$. Thus, for each circular trajectory described by a mirror normal, there is a corresponding trajectory described by the reflection. Since the mirror normal trajectory is uniquely defined by the $\bar{\omega}$ and α, these two parameters also define a unique reflection trajectory. The converse is also true - each reflection trajectory corresponds to a unique combination of $\bar{\omega}$ and α.

To deduce the vorticity, a segment of a reflection trajectory is tracked as it transits a small (~ 0.5 sr) portion of the unit circle projected onto a flat detector surface. A computer program in essence maps the reflection trajectory segment into a mirror normal trajectory segment on the unit sphere, and calculates both the tilt of the axis around which that segment rotates and the rotation rate, thereby yielding the vorticity. The algorithm requires only knowledge of the orientation of the center of the detector relative to the laser beam, and provides an output in the form of vorticity components relative to a predefined set of axes. The program also provides a calculation of the vorticity uncertainty resulting from imprecise measurement of the reflection trajectory.

VOP PARTICLES AND THEIR MANUFACTURE

As already mentioned, the spherical VOP probe particles, except for the embedded mirrors, must be transparent and made of a material that closely matches the refractive index of the flowing medium. The latter requirement eliminates reflections at the surfaces of the spheres and prevents the spheres from focusing or defocusing the laser beam and reflections of it. In other words, the spheres are made invisible so that, optically, each VOP particle appears as no more than a spinning mirror. Furthermore, for water tunnel studies of boundary layers or turbulence, the particles should be smaller than the boundary layer or Kolmogorov microscales, and they should be nearly neutrally bouyant

Until recently, the VOP particles were made exclusively from polymethylmethacrylate (PMMA, known commercially as Plexiglas). A photograph of a collection of these particles was published by Frish and Webb (1981). The particles are manufactured using a suspension polymerization procedure: An aliquot of the hexagonally-shaped lead carbonate crystals, which are typically 16 μm wide and 0.07 μm thick, is mixed into liquid methylmethacrylate monomer at a concentration suitable to provide, on average, one crystal per 25 μm diameter sphere. The mixture is added to an aqueous suspension fluid in which the monomer is insoluble, and then passed through a high shear created by a food blender. The shear breaks the monomer into droplets having the desired size distribution, and surface tension holds the mirrors within the spheres. Surfactants in the aqueous solution prevent recoalescence of the spheres The entire mixture is heated for several hours, thereby polymerizing the monomer and hardening the particles. Particles made by this procedure have now been in continuous use for over a decade without degrading.

Unfortunately, these original VOP particles can be used only in liquids having a refractive index near 1.49 that do not dissolve the plastic. Only three suitable liquids have been found: the organic materials dibutyl phthalate and p-cymene, and a concentrated (as well as highly-corrosive) solution of zinc iodide in water. Because of the need to use these special liquids, VOP measurements to date have been made only in specially built small-scale flow apparati.

Recently, acquisition of vorticity data in water flows, and thus the application of the VOP to a wide variety of existing flow facilities, has been made possible by to the development of probe particles that nearly match the refractive index of water. These water-compatible particles are made from an acrylamide gel. They are manufactured by a suspension polymerization process that is, in essence, the inverse of the process used to make the PMMA particles. Prior to polymerization, the gel material is a liquid

comprised mostly of water. Lead carbonate mirrors, initially suspended in an alcohol-based slurry, are added to this liquid with the appropriate concentration. A polymerization initiator is added to the mixture, which is then injected into a synthetic oil. The water-based gel mixture is insoluble in the oil and, upon intense stirring, breaks up into the desired droplets that retain the crystalline mirrors. The gel cures without heating in about one hour. The cured gel material is a rubbery solid comprising approximately 95 percent water in a cross-linked polymer network, making the gel's refractive index and density closely matched to those of water. The particles are separated from the oil by washing with tap water and saved for subsequent use. A machine for continuously manufacturing large quantities of these particles is expected to be operational in the near future.

EXAMPLE VOP OPTICAL SYSTEM

There are a multitude of methods that can be conceived for detecting, tracking, and interpreting the reflection trajectories created by reflecting a laser beam from the spinning VOP particles. To date, electro-optical configurations like that illustrated schematically in Fig. 3 have been used to develop and demonstrate the technique. The electro-optical system serves three purposes: It isolates the measurement region or "sampled volume" in a flowfield seeded with probe particles, projects reflection trajectories onto a detector while removing the effects of particle velocity, and converts the trajectories into measurable electrical signals. Each of these functions is described in the following paragraphs.

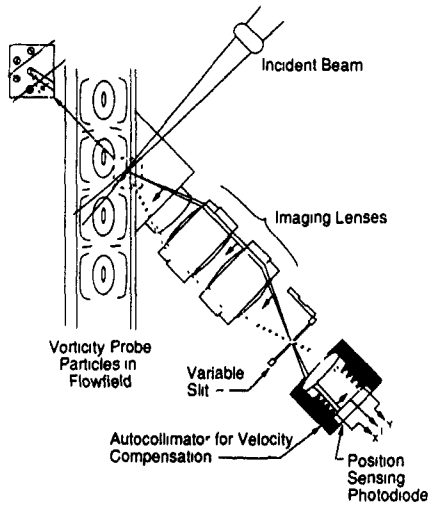

Fig. 3. Example VOP Optical System

a) Sampled Volume Definition

As shown in Fig. 3, the volume of flow sampled by the VOP at any instant of time is isolated by the intersection of a laser beam with the image of a slit projected orthogonally onto the beam. The laser beam is projected through a window into the flow region of interest and illuminates a line of the particle-laden flowfield. Reflections from mirrors embedded within the VOP spheres are transmitted out of the flow through the window (or a different window), and are subtended by a lens or lens system. (Obviously, only those mirrors that are oriented so as to reflect the laser beam into the lens are observed.) The lens images the line illuminated by the laser onto the slit, thereby defining the sampled volume

The image of the sampled volume on the slit serves as a new origin for the reflections, and can be thought of as the center of the unit sphere, discussed previously, on which the reflection trajectories are tracked. The sampled volume can be as small as 100 μm in diameter. Only those reflections that emanate from within this region pass through the slit to impinge upon the detector. The flow is typically seeded with a concentration of about 1000 VOP particles per cm^3, small enough to make it unlikely, but not impossible, for more than one reflection to be observed at any instant of time.

b) Velocity Compensation Lens

Though the sampled volume can be made quite small, there are circumstances in which it is preferable to observe a significant length of the flowfield. Under these conditions, the center of the reflection trajectory moves with the image of the flowing VOP particle. As a result, the projection of the reflection trajectories onto the detector surface can contain contributions from the velocity. To counter this effect, a means of removing the translational contribution to the measured reflection trajectory was incorporated into the VOP optics.

The technique used for this purpose is known as autocollimation. It works on the principle that a ray of light incident upon a lens is refracted to cross the focal plane of the lens at a point that depends only on the angle of incidence at the lens surface and not on the position at which the ray intercepts the lens. In other words, a group of parallel rays incident on the lens are all focused to a single point. The VOP trajectory detector is placed in the focal plane of the autocollimation lens, so that the trajectories sensed represent only the rotation of the VOP particle.

c) Trajectory Detector

The electro-optic detector used in the current VOP apparatus is a two-dimensional position sensing photodiode This device is a 2 x 2 cm photodiode overlaying a planar silicon substrate having uniform electrical resistivity. Photoelectrons are driven through the substrate and discharged through four electrodes, each centered along one of the substrate's four edges. The instantaneous photocurrent is thus divided among the four electrodes according to the position of the centroid of light that illuminates the surface of the photodiode.

The four output currents are subjected to analog processing to yield three time-varying signals. One signal is proportional to the illumination power incident on the surface of the photodiode, and the other two are proportional to the two position coordinates of the centroid of that illumination, all as functions of time. Thus the segment of the reflection trajectory that transits the detector surface is converted to a set of analog current signals. The currents are converted to voltages by transimpedence amplifiers, digitized at a fixed rate by a high speed (1 MHz per channel) a/d converter, and provided to a personal computer. The computer recreates the reflection trajectory and provides it, in the form of a sequence of discrete coordinate pairs, to the data reduction algorithm which calculates the vorticity and

performs statistical analyses. Statistical information about vorticity fluctuations is gathered by analyzing hundreds or thousands of trajectories collected from a fixed sample volume.

DATA REDUCTION ALGORITHM

The primary function of the data reduction program is to numerically perform the mapping that converts a digitized reflection trajectory segment into a segment of mirror normal trajectory across the surface of the unit sphere, and then find the orientation and angular velocity of the circle that best fits the latter trajectory segment. The most efficient algorithm developed to date to perform this function calculates least squares fits to the equations that directly relate the rates of change of the reflection vector coordinates to the vorticity components

$$\begin{aligned} \partial\theta'/\partial t &= a\omega_x + b\omega_y + c\omega_y \\ \partial\theta'/\partial t &= d\omega_x + e\omega_y + f\omega_z \end{aligned} \qquad (2)$$

where the coefficients a-f are geometrically-defined functions of θ' and ϕ'. For each digitized point in the trajectory, there are unique values of θ' and ϕ' and thus of all the a-f coefficients. For each pair of points, values for $\partial\theta'/\partial t$ and $\partial\phi'/\partial t$ are calculated. Thus, for each N points digitized in a trajectory, there are 2N-2 equations that may be solved simultaneously to deduce the three components of vorticity.

In principle, only three equations are needed to find the solution. However, noise in the detector, non-uniformities in the incident laser beam, angular dependencies of the lead carbonate crystal reflection properties, digitizer resolution, and a number of other effects introduce a degree of uncertainty into the measured position of each point along a trajectory. As a result, each set of three equations yields a solution somewhat different from that of any other set The most probable solution is found by a standard linear least squares fit to all available data. This procedure yields the vorticity components, the goodness of fit, and an estimate of the uncertainty in the fit.

This technique also enables rejection of severely compromised measurements Because the mirror normal trajectories must describe circular arcs on the unit sphere surrounding the probe particle (or, equivalently, the reflection trajectories must fit Eq. (2)), measured trajectories which deviate significantly from a circle are assumed to be contaminated by some artifact. These artifacts include multiple reflections striking the detector simultaneously, non-spherical (i.e., broken) probe particles, extraneous scatterers, changes in vorticity occurring faster than the time required to make a measurement, etc. Trajectories that do not fit the equations within limits determined by the signal-to-noise ratio are automatically discarded.

VOP LIMITATIONS

The accuracy of the vorticity measurement is limited by the accuracy with which the measured mirror normal trajectory segment can be fitted to a circle on the unit sphere. If each point on a trajectory was measured with perfect precision, then, as described above, complete determination of the vorticity vector could be made with only three arbitrarily-spaced points per trajectory. Because such precision cannot be achieved, and because accuracy improves with the angular size of the trajectory segment, it is desirable for each trajectory segment to be as long as possible. However, a number of factors limit the length of the detected trajectory, and thus place the ultimate limitations on the accuracy of the measurement. The dominant limiting factors are the size of the optical system and the ratio of the particle's vorticity to its velocity Here, these effects are described qualitatively Ferguson and Frish (1991) provides a complete quantitative discussion

a) Optical Limitations

The size of the optics places an upper limit on the angular size of the reflection trajectory arc that can be intercepted when the reflection sweeps vertically or horizontally across the detector. An F1.4 objective lens is used in the current optical configuration, intercepting slightly more than 30 degrees of arc. This is adequate for determining, with less than 10 percent uncertainty, the x and z components of vorticity which primarily determine the speed and angle at which the trajectory crosses a detector centered on the y-axis. In contrast, small contributions by the y component in the presence of relatively strong x or z components can only be resolved with ± 50 percent uncertainty because they introduce only small and difficult to measure changes in the curvature of the reflection trajectory As the y-component becomes stronger relative to the other two, the accuracy of measuring it improves. Since the data reduction algorithm calculates the measurement uncertainty, it readily identifies poorly measured y-components In these cases, it is usually assumed that the y-component is zero and only the x and z components are calculated

b) Vorticity/Velocity Limitation

Measurement difficulties are encountered when the ratio of vorticity to velocity is small because a probe particle must rotate through a sufficiently large arc while within the sampled volume to provide an accurate fit to the trajectory equations. When the velocity is high and the vorticity small, the particle may be transported through the sampled volume in a time that is less than that needed to collect an acceptable length of trajectory. Thus, only a short trajectory segment may be detected, which, as described above, reduces the accuracy of the measurement

DEMONSTRATION IN COUETTE FLOW

The three-component VOP system was tested and demonstrated in an ideal vorticity measurement laboratory, the Couette flow between a pair of rotating concentric cylinders. This system is ideal because when the relative rotation rates of the cylinders is selected to produce a stable flow between them, the vorticity in the flow is spatially and temporally uniform. It is straightforward to calculate the theoretical value of the vorticity and compare it with measurements.

The Couette flow apparatus shown schematically in Fig. 4 was built for this demonstration It has three concentric cylinders, of which only the center one spins. The flow between the outer cylinder and the spinning central cylinder is stable below a critical Reynolds number (based on cylinder surface velocity and inter-cylinder gap width) of $R_c = 127$. This flow was used to calibrate the three-component VOP, using water as the working fluid. (Note that, above R_c, this flow follows the bifurcation route to turbulence, elucidated by Fenstermacher, Swinney and Gollub [1975]. See Ferguson [1991] or Ferguson and Frish [1991a] for a description of some measurements of vorticity

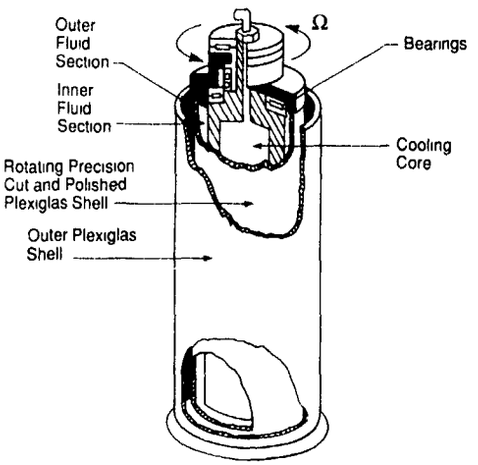

Fig 4 Couette Flow Apparatus Inner fluid bounded by cylinders with radii of 3 944 and 4.477 cm. Outer fluid radii are 5 127 and 5 738 cm

in this regime) The flow between the central and inner cylinders is stable below a Reynolds number of about 100,000 As the Reynolds number is increased, this flow exhibits a catastrophic transition to turbulence that has been used to demonstrate the three-component VOP's capability to track turbulent fluctuations, with p-cymene as the working fluid.

The results of the calibration in the water flow between the central and outer cylinders are plotted in Fig. 5, which shows probability distributions of each of the three vorticity components acquired approximately 500 μm from the wall of the stationary outer cylinder, with the central cylinder spinning at 0.028 Hz The theoretical vorticity values are ω_x = -1 35 s^{-1}, $\omega_y = \omega_z = 0$ where the x-axis is parallel to the axes of the cylinders. The z component of the distribution yields the correct mean value of zero, with a full width at half maximum (FWHM) of 5 percent of the mean vorticity magnitude The x component has a most probable value of 1.25 s^{-1} that corresponds well with the theoretical value, and a FWHM of 0 13 s^{-1}, 10 percent of the mean vorticity magnitude. The x-component exhibits some measurements centered at a value of about half the most probable value. This artifact, which was also seen by Frish (1981), has been attributed by Ferguson and Frish (1991) to pairs of probe particles that stick together in low shear flows. It disappears in high shear and turbulent flows. The y-component, which as described above is difficult to measure using the current optical geometry, has the correct mean value of zero but a standard deviation of approximately 0.7 s^{-1}

The flow between the central and inner cylinders has been used to observe the catastrophic transition to turbulence The working fluid for these experiments was p-cymene, which matches the refractive index of both the cylinders and the PMMA probe particles. Figure 6 shows probability distributions of the x and z vorticity components, scaled in proportion to the cylinder rotation rate, at two Reynolds numbers prior to transition, and one after transition. The increased width of the curves after transition, due to the temporal vorticity fluctuations inherent to the turbulence, is quite clear. Comparisons of the data acquired in these studies with numerical simulations of the flow are

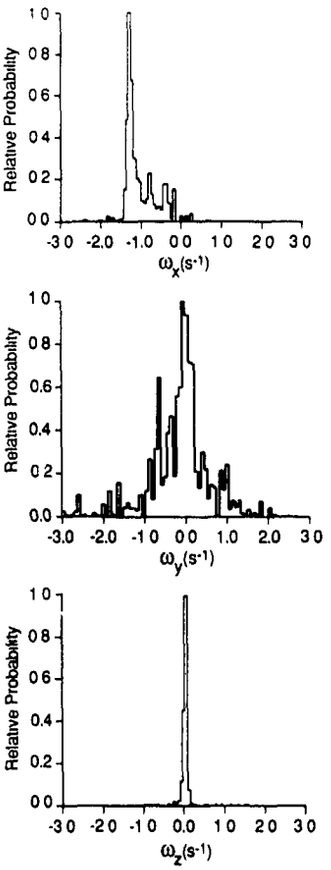

Fig 5. Vorticity Component Probability Distributions Derived from 128 Measurements in Outer Section of Couette Flow. Ω = 0.028 Hz. Fluid is water

made in Ferguson and Frish (1991, 1991a) and Ferguson (1991).

SUMMARY AND FUTURE PLANS

The Vorticity Optical Probe is now able to measure complete vorticity vector statistics at well-defined positions in turbulent water flows. It is an ideal instrument for studying boundary layers where vorticity is high, velocity is low, and access by other instruments is difficult. Preparations for the first such measurements in a high-speed water tunnel are currently underway.

With the development of water compatible probe particles, a difficult obstacle to widespread application of the VOP has been removed. Plans to commercialize the particles and instrumentation are now being formulated. This is expected to facilitate installation of the VOP at university, government, and industrial research sites. In addition, improvements to the instrument are being developed. These include methods for concurrent measurement of a probe particle's vorticity and velocity, for rapidly imaging the vorticity field (the vorticity analog of particle imaging

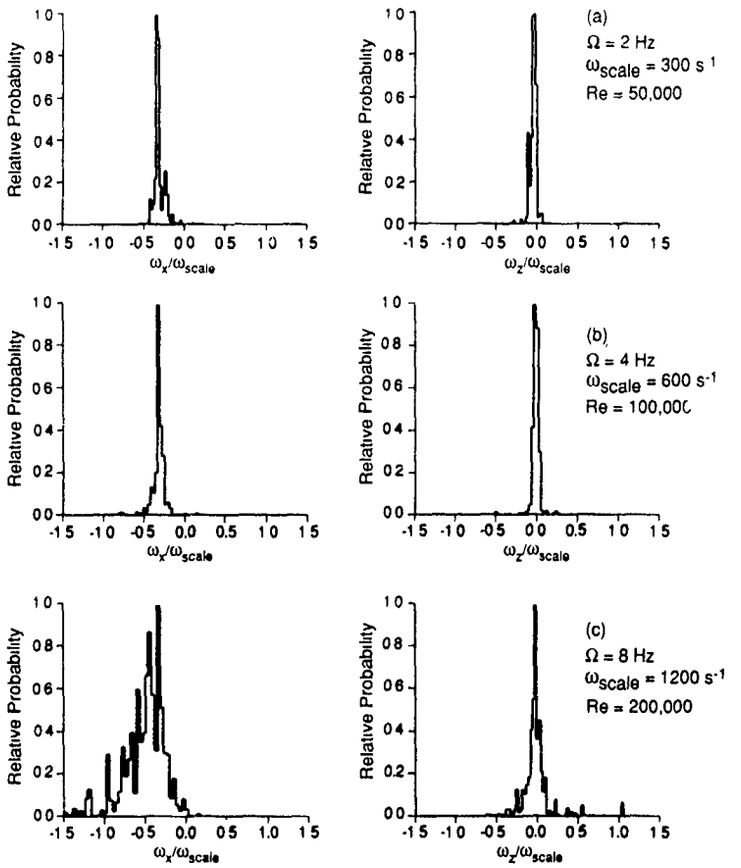

Fig. 6 Measured Vorticity Probability Distributions in Couette Flow Before (a,b) and After (c) Transition to Turbulence

velocimetry), and for manufacturing air-compatible probe particles.

ACKNOWLEDGMENT

This work was sponsored by the Office of Naval Research, via Small Business Innovation Research Contracts N00014-87 C-0865 and N00014-89-C-0004, and by Physical Sciences Inc. The authors are indebted to Mike Reischman, Spiro Lekoudis and John Sullivan for their support.

REFERENCES

Adrian, R.J. (1991), "Particle-Imaging Techniques for Experimental Fluid Mechanics," Ann. Rev. Fluid Mech. 23, 261.

Fenstermacher, P.R., Swinney, H., and Gollub, J.P. (1979), "Dynamical Instabilities and the Transition to Chaotic Taylor Vortex Flow," J. Fluid Mech. 94, 103.

Ferguson, R.D. (1991), "Direct Optical Vorticity Vector Measurement in Turbulent and Transitional Shear Flow", Ph.D. thesis, in preparation for submittal to the Graduate School Faculty of Cornell University.

Ferguson, R.D. and Frish, M.B. (1991), "Measurement of Vorticity Vectors in Couette Flow with the Vorticity Optical Probe", Physical Sciences Inc., Report PSI-1063/TR-1103, Andover, MA.

Ferguson, R.D. and Frish, M.B. (1991a), "Vorticity Vector Fluctuations in Turbulent Couette Flow Measured by the VOP", in preparation for submission to Physics of Fluids.

Ferguson, R.D. and Webb, W.W. (1983), "The Vorticity Optical Probe: A Fast Multicomponent Model," Proc. of the 8th Biennial Symposium on Turbulence, University of Missouri-Rolla.

Frish, M.B. (1981), "Direct Optical Measurements of Vorticity in a Nearly Turbulent Boundary Layer," Ph.D. Thesis, Cornell University.

Frish, M.B. and Webb, W.W. (1981), "Direct Measurement of Vorticity by Optical Probe," J. Fluid Mech., 107, 173.

Jeffrey, J.B., "The motion of ellipsoidal particles immersed in a viscous fluid," Proc. Roy. Soc. A, 102, 161 (1922).

Lang, D.B. and Dimotakis, P.E. (1982), "Measuring Vorticity Using the Laser Doppler Velocimeter," Bull. Am. Phys. Soc. 27, 1166.

Wallace, J.M. (1986), "Methods of Measuring Vorticity in Turbulent Flows," Exper. in Fluids 4, 61.

EIGHTH SYMPOSIUM ON
TURBULENT SHEAR FLOWS
Technical University of Munich
September 9-11, 1991

Development of a Probe for Measuring Pressure Diffusion

M. Nasseri , W. Nitsche

Institut für Luft-und Raumfahrt
Marchstraße 12 D 1000 Berlin 10
Technische Universität Berlin (FRG)

Abstruct

The paper deals with the development and first practical tests of a probe for simultaneous measurements of pressure and velocity fluctuations (X-P-probe) The development of this probe offers for the first time a possibility of considering and evaluating the local pressure fluctuations and their correlations when determining the diffusion term. The behaviour of the probe was closely examined as well as the frequency and yaw characteristics, which were determined by means of operational tests For a first test case (relaxation region behind a 6°-diffuser), the distribution of the pressure diffusion was measured. These results are compared with calculations according to the k-ε-turbulence-model

List of Symbols

A_{cor}	Corrective factor for total pressure
D_p	Pressure Diffusion
f	Frequency
k	Turbulent Kinetic Energy
P,P´	Total Pressure, Total Pressure Fluctuation
P_s	Suction Pressure
p,p´	Static Pressure, Static Pressure Fluctuation
Q_1 , Q_2	Calibrated Signal of the X-Wire
R	Tube Radius
r	Coordinate in Radial Direction
U,V,W	Mean Velocity Components
u´,v´,w´	Velocity Fluctuations
x,y,z	Coordinates
α	Yaw Angle
ε	Dissipation
ρ	Density of Fluid

Indices

c	Centerline

1. Introduction

A comparison of numerical flow calculations with data obtained in experiments shows that differences in turbulent quantities occur even in simple flows. As an example, discrepancies such as these are illustrated in Figure 1, which shows the measured distribution of the turbulent kinetic energy of a 18°- diffuser flow. In this case, the turbulent kinetic energy was determined by means of the LDA-measuring technique in a refractive-index laser test section of the TU Berlin /1/. The numerical data concerning this configuration /2/ are also shown in Figure 1.

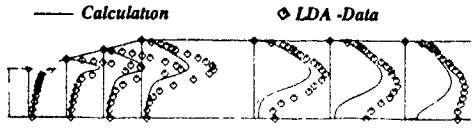

Figure 1 *Distribution of the turbulent kinetic energy. Comparison of LDA-measurement with calculation (k-ε)*

The data are derived from calculations involving the standard k-ε-turbulence-model (Peric´ /3/) A comparison of the curves shows differences regarding the absolute values as well as the distribution of k. These deviations can only be interpreted if further details about the distribution of turbulent quantities of the flow are known. If these terms are to be determined precisely, it will be, amongst other things, necessary to measure the pressure diffusion, whose determination by means of experiment requires a measurement of pressure and velocity fluctuations carried out simultaneously at the same location. The present paper deals with the development of a new

measuring technique aimed at the determination of pressure fluctuations as well as the correlation between pressure and velocity fluctuation. In the paper, the concept, some test measurements and first applications of the new probe for measuring these quantities (X-P probe, Figure 2) are described.

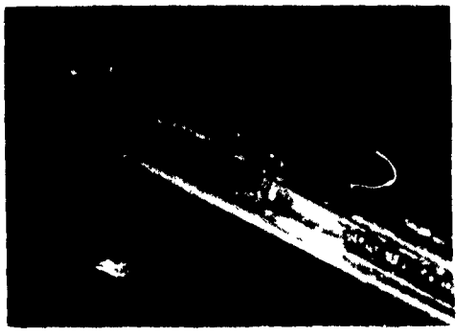

Figure 2 X-P-probe

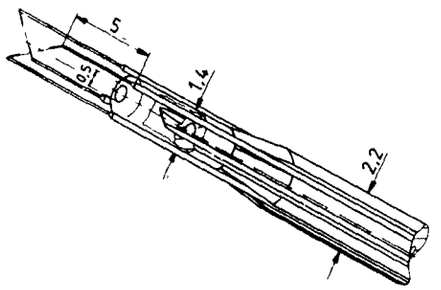

Figure 3 Principle sketch of the X-P-probe

As is plain from its name, the X-P-probe is a combination of two types of probes. Velocity is measured by a conventional hot-wire probe in an X-arrangement, Figure 3

The pressure probe, working according to the principle of an electric variometer, is integrated into the 0 5 mm Pitot probe immediately behind the X-probe, Figures 3 and 4.

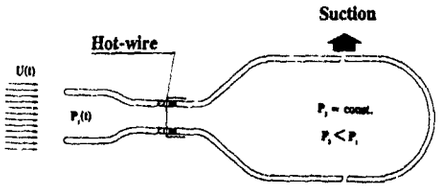

Figure 4 Principle of transducing the total pressure in the electric signal

Aided by this measuring technique, by means of which the time-dependent total pressure on the probe's inlet is transduced into a mass flux and measured by a miniature hot-wire probe (mass -flow meter proportional to pressure), it is possible to produce probes of small dimensions and good frequency response. In view of traditional pressure fluctuation probes (e.g. microphones), suction is another basic part of the X-P-probe concept By lowering the counterpressure in a reservoire, Figure 4, a defined suction rate is generated It reduces the interference influence of the probe and, moreover, steers clear of Helmholtz resonances.

2. Pre-Tests

First, the probe's behaviour was examined under different flow conditions. There are two kinds of these investigations' static and dynamic tests

2.1 Dynamic tests

In order to determine the general frequency behaviour of the P-probe, a calibrated microphone (Brüel & Kjaer) was used as a reference probe In a miniature pressure chamber (Figure 5), the P-probe and the microphone were installed in parallel

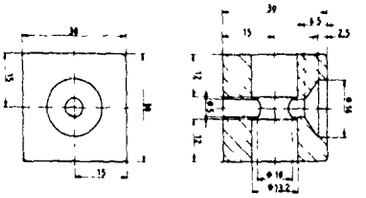

Figure 5 Pressure chamber for dynamic tests

A sine-wave pressure fluctuation was generated in the pressure chamber. The frequency of this pressure fluctuation was incremented from 20 to 10000 Hz, while the amplitude was adapted to the output signal of the microphone The result of these investigations is shown in the form of transfer functions (amplitude ratios as a function of frequency) As follows from Figure 6, curve A (with suction) offers an adequate constancy in the frequency range up to 1.5 kHz. Curve B in Figure 6 describes the much more unsatisfactory frequency behaviour of the pressure probe without suction and thus illustrates the absolute necessity of this measure.

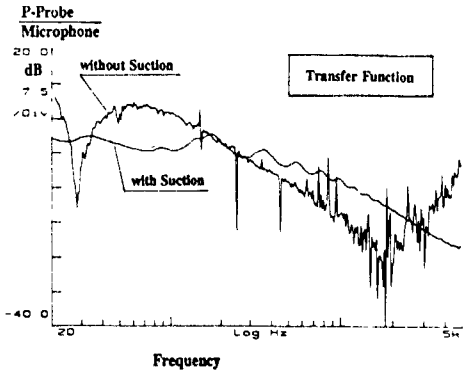

Figure 6 *Transfer function of the P-probe*

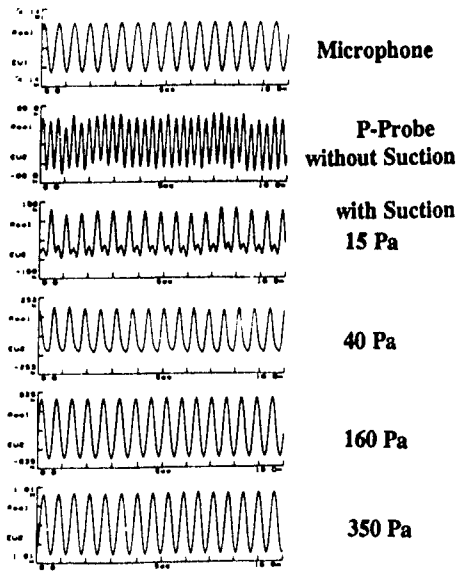

Figure 7 *Comparison of P-probe and microphone at f=1kHz and different suction pressures*

As a further step in this investigation, the pressure signal of the P-probe and the microphone was recorded for an exemplary frequency of 1000 Hz, Figure 7.

In the upper part of Figure 7, the output signal of the measuring microphone is shown. The curves lying below represent the output signal of the P-probe, obtained under suction pressure successively lowered from zero to -350 Pa. This shows that in the case of measurements without suction, the frequency is doubled; a phenomenon, which disappears at an increased suction rate.

2.2 Static Tests

In the static tests, the first step was to calibrate the output signal of the pressure probe versus the total pressure This procedure was repeated within the measurement range for different suction pressures The results are shown in Figure 8.

Further investigations were based on a suction pressure of 65 Pa. It was determined by restrictions such as frequency behaviour (Figure 7), the sensitivity of the probe (Figure 8) and the minimum value of the total pressure in the flow field to be examined

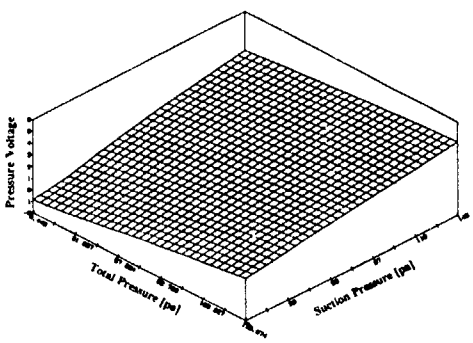

Figure 8 *Calibration of the P-probe at different suction pressures*

3. Yaw Characteristics

Because the probe is usually inclined towards the flow direction, a further pre-test concerning the yaw characteristics of the X-P-probe was carried out. The P-probe's characteristics after first modifications to its head (spherical nose) are shown in Figure 9.

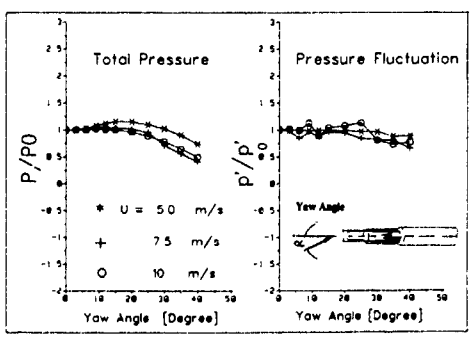

Figure 9 *The probe's yaw characteristics*

It becomes apparent that both the mean total pressure and the pressure fluctuation show harmonic courses up to an angle of ±45°.

3.1 Correction Procedure

In the case a yaw angle occurs, the measured data are subjected to a correction function. Due to the high number of measured data, this function has to be as simple as possible in order to limit the evaluation time. For this reason, the measured data are corrected using "look-up" tables. To draw up these tables, the angle behaviour of the probe was described by means of a Bézier function. Thus, interim points were produced with the aid of an interpolation procedure and set out in a matrix. This matrix, whose elements could be addressed directly by means of the output signal of the X-probe, was stored in a computer and used for correcting the measured data. In Figure 10, a matrix typical for the correction of the total pressure is to be seen. A_{cor} is the correction factor for the measured total presure (P-probe) and Q_1,Q_2 are the calibrated signals of the X-prob, respectively.

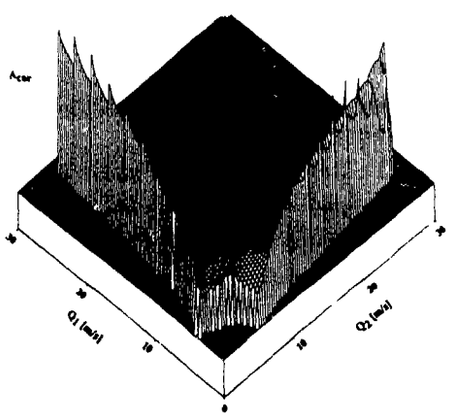

Figure 10 Look-up table for total pressure

4. Practical Tests/ Applications

To begin with, the accuracy of the X-P-probe in total pressure measurements was examined in simple practical tests. For this purpose, the velocity profile of a pipe flow was recorded by means of a X-hot-wire probe, Figure 11.

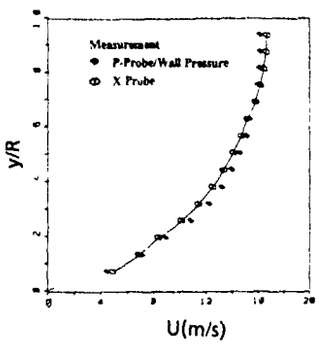

Figure 11 Velocity profile

The same figure shows the velocity values as derived from the total pressure (P-probe) and the static wall pressure. The agreement of the two curves illustrates the ability of the probe to determine total pressures correctly. Moreover, the pressure fluctuations measured as well as their correlations were compared to similar results obtained in a pipe flow by other authors (Komerath/Hedge and Strahle /4/), Figure 12.

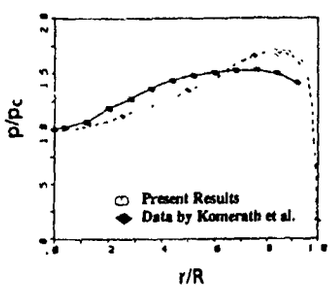

Figure 12a Pressure fluctuation profile in a pipe flow

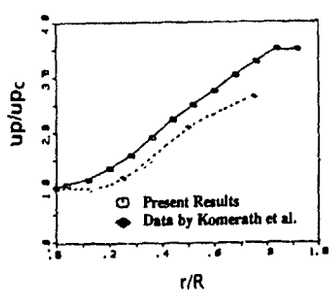

Figure 12b The u´p´ correlation in a pipe flow

These results can be considered as a further confirmation of the measuring technique developed here

For the first practical application of the X-P-probe for measuring the pressure diffusion, the relaxation region behind the 6°-diffuser was chosen This measurement is aimed at detecting the turbulent diffusion in consideration of the static pressure fluctuations. Moreover, the numerical calculations carried out by means of a finite-volume program are to be used as a basis for comparison. As for the calculations shown in Fig 1, this is the k-ε-turbulence model as developed by Launder and Spalding /5/. Figure 13 shows the result of this investigation In order to be able to compare the data in general, the terms determined were standardized with U_c^3 (U_c is the velocity in the centreline of the pipe) The flow field was measured in radial direction by small steps of 1mm. In longitudinal direction, however, a greater distance (30 mm) was chosen because of the smaller gradients of the flow. The measured values themselves were obtained from groups of 36840 measured data which are composed of the three quantities U(t), V(t), p(t) The diffusive transport of k through the velocity and pressure field was determined as follows

$$D_P = -\overline{v'k} - \frac{\overline{v'p'}}{\rho}$$

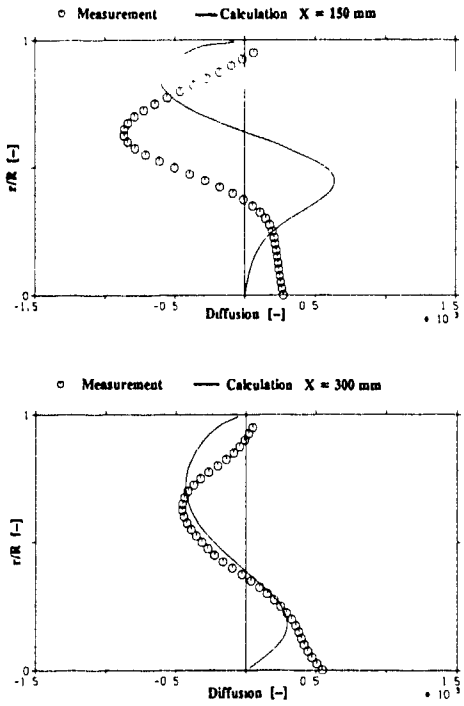

Figure 14 Comparison of the pressure diffusion measured with the k-ε-Turbulence Model

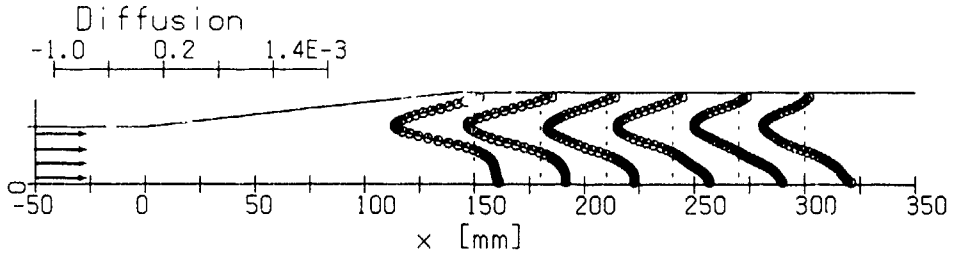

Figure 13 Development of pressure diffusion

In Figure 13, the development of this term in a relaxing flow is depicted. These results show that the diffusion term changes its sign when approaching the wall While the principal course of the diffusion is not influenced by the relaxation process, it is to be noticed that the minimum shifts to smaller values

A comparison with the diffusion term resulting from the k-ε-model (Figure 14) shows that a basic agreement exists between the calculated diffusion and the one determined by way of experiment However, differences in quantity arise, which increase in the near wall region.

5. Concluding Remarks

As is shown in the present paper, the static pressure p(t) and two velocity components U (t) and V(t) can be measured simultaneously by means of the X-P-probe. In axisymmetric flows, the terms in the transport equation for the turbulent kinetic energy can be derived from these measured data, exept for the dissipation wich can be determined indirectly from the equilibrium of these terms However, the determination of the dissipation for complex, three-dimensional flows requires additional information on the third velocity component W(t). Through a modification of the probe (i.e. the integration of an additional hot wire), this aim of development is to be achieved.

References

/1/ Weiser, N ; Bartsch, P. ; Nitsche, W. (1990)
On Turbulent Flow Separation in Axisymmetric Diffusers.
Engineering Turbulence Modelling and Experiments (Eds Rodi / Ganic'), pp Elsevier Science Publ Comp., Inc.

/2/ Bartsch, P. , Weiser, N. , Nitsche, W (1990)
Experimental and Numerical Investigations on Turbulent Separated Diffuser Flows
IUTAM-Symp. "Separated Flows and Jets" (to be published by Springer Verlag)

/3/ Peric', M. (1985)
A Finite-Volume Method for the Prediction of Three-Dimensional Flow in Complex Ducts
Ph D. Thesis, Imperial College University of London

/4/ Komerath, N. ; Hedge, U. ; Strahle, W (1985)
Turbulent static pressure fluctuations away from flow boundaries
AIAA Journal, Vol. 23, pp 1320 - 1326

/5/ Launder, B.E , Spalding, D.B (1974)
The Numerical Computation of Turbulent Flow
Comp. Meth. Appl. Mech and Eng., Vol. 3, pp. 269-289

EIGHTH SYMPOSIUM ON
TURBULENT SHEAR FLOWS
Technical University of Munich
September 9-11, 1991

4-5

WALL SHEAR STRESS DETERMINATION BY MEANS OF OBSTACLE-WIRES

N Weiser, W Nitsche, F Renken

Institut fur Luft- und Raumfahrt
der Technischen Universitat Berlin
Marchstr 14, W-1000 Berlin 10, Germany

ABSTRACT

The paper describes a new technique for detecting local wall shear stresses by means of obstacle-wires From the viewpoint of similarity theorie, this technique is comparable to the sublayer fence measuring technique It is based on the measurement of the pressure difference in front of and behind an obstacle-wire glued on the surface of a test body In a further simplified form of the technique, only the pressure in front of the obstacle wire has to be measured For a wide range of subsonic Mach numbers, the measured calibration curves show a standardizable characteristic, which is independent of the diameter of the obstacle-wire The method is tested for different test cases (airfoil profiles, flat plate flow, relaxing diffuser flow) and compares well with other skin friction measuring techniques

NOMENCLATURE

a	speed of sound
c	chord
$c_f = 2 \cdot \tau_w / \rho \cdot u_0^2$	skin friction coefficient
d	diameter (wire, Preston tube)
D	pipe diameter
h	sublayer-fence height
L	obstacle-wire length
$M = u_0/a$	Mach number
p	static pressure
Δp	pressure difference
$p^+ = \Delta p \cdot d^2/4 \cdot \rho \cdot \nu^2$	dimensionless pressure difference
$Re = u_0 \cdot x/\nu$	Reynolds number
u	velocity in mean flow direction
u_0	free stream velocity
$u^+ = u/u_\tau$	dimensionless velocity
$u_\tau = \sqrt{\tau_w/\rho}$	shear stress velocity
$u_r = \sqrt{2 \cdot \Delta p/\rho}$	reference velocity
x	streamwise coordinate
x_R	reattachment point
y	normal distance from wall
$y^+ = u_\tau \cdot y/\nu$	dimensionless wall distance
α	attack angle
ν	kinematic viscosity
ρ	density
τ_w	wall shear stress
$\tau^+ = \tau_w \cdot d^2/4 \cdot \rho \cdot \nu^2$	dimensionless wall shear stress

INTRODUCTION

The determination of local wall shear stresses as well as the determination of velocity, pressure and temperature belong to the classical problems in experimental fluid mechanics This applies to practice orientated research, i e the optimization of fluid technical systems or the development and examination of new laminar wing concepts and the field of general boundary-layer research, where wall friction is needed as an integral part of boundary layer-similarity laws Additionally, wall shear stress as a boundary condition is a very significant parameter in the experimental verification of modern numerical methods

Up to now, in comparison with other flow quantities, a precise measurement of local wall shear stress requires great experimental demands, e g /1/, /2/ Common skin friction measurement methods are thermo-electric methods (surface hot film) and laser-optic methods (laser interferometer) Apart from these, there are still those methods which are based on pressure measurement such as the sublayer-fence technique and the Preston tube method Both techniques are based on similarity laws of wall boundary layers, i e the law of the viscous sublayer in the case of the sublayer-fence technique and the law of the wall of turbulent boundary layers in the case of the Preston tube technique Unlike the sublayer-fence, which, after having been calibrated individually at the point of later measurements, can also be used in non-classical boundary layers /2/, the standard Preston tube is only valid for simple boundary-layer flows

Here, solid probe geometry (wall-pitot tube with $d_{inside}/d_{outside}$ = 0 6) effects a general calibration curve In the sublayer-fence technique, important restrictions result from the technical effort required (i e fitting a measurement plug into the body wall, individual calibration), whereas the standard classical Preston tube method is restricted to simple flow cases /2/, /3/

This paper presents the obstacle-wire technique as a new wall-shear stress measuring method It combines the advantages of the methods mentioned above, i e the wide application spectrum of a sublayer fence with the standardized calibration and flexible application of a Preston tube In its first step of development, this new method is based on a differential pressure measurement in front of and behind an obstacle-wire of a very small diameter (typical 0 1 - 0 6 mm, L/d 20) Similar to the sublayer-fence technique, the measured pressure difference can be correlated to the local wall shear stress Owing to the form of the device, which can be easily reproduced geometrically , a standard calibration curve can be formulated It is independent of the obstacle-wire diameter and comparable to the standard Preston tube calibration In contrast to the individual sublayer-fence calibration method, this standardizable calibration curve leads to a wide usage spectrum Additionally, the method requires a relatively simple construction technique merely two closely streamwise placed pressure taps are needed Here, the obstacle-wire is glued crosswise in between them on the surface The method needs no plug in probes and is therefore much more flexible and applicable than the sublayer-fence technique

In the following, this paper describes the underlying principle of the obstacle-wire technique Furthermore, it gives a survey of the calibration experiments in the range of 0 01 < Mach number < 0 8 It also describes practical wall shear stress measurements on a turbulent flat plate and in a transitional boundary-layer flow as well as a relaxing diffuser flow Finally, the paper presents a further simplified variation of the obstacle-wire technique Here, only one pressure tap in front of the obstacle-wire is used This configuration allows the application of the technique on almost any wind-tunnel airfoil model with a minimum of construction effort First wall shear stress measurements were carried out on two different airfoil models in sub- and transonic flows They proved the good applicability of this simplyfied technique

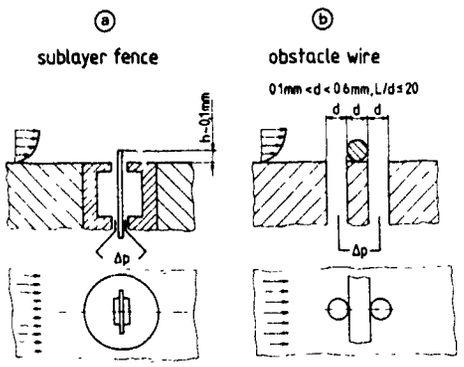

Figure 1: Wall shear stress measurement techniques. a) sublayer fence, b) obstacle-wire

FUNDAMENTALS OF THE OBSTACLE - WIRE TECHNIQUE

The obstacle-wire technique is based on the similarity law of the viscous sublayer and is similar to the sublayer-fence technique, **Figure 1a** The pressure difference measured in front of and behind the thin wire, **Figure 1b**, is correlated to the local wall shear stress via the boundary-layer law through the transformations

$$p^+ = \frac{1}{2} \cdot \left(\frac{u_r}{u_\tau} \cdot \frac{u_\tau \cdot y}{\nu} \right)^2 = \frac{\Delta p \cdot (d/2)^2}{\rho \cdot \nu^2} \qquad (1)$$

$$\tau^+ = \left(\frac{u_\tau \cdot y}{\nu} \right)^2 = \frac{\tau_w \cdot (d/2)^2}{\rho \cdot \nu^2} \quad , \; y = \frac{d}{2} \qquad (2)$$

$$\frac{u}{u_\tau} = u^+ , \quad \frac{u_\tau \cdot y}{\nu} = y^+ , \; u_r = \sqrt{2 \cdot \Delta p / \rho}$$

d = characteristic wall distance, Δp = measured pressure difference, u_r = reference velocity

These transformations, which are both formally similar to the sublayer fence and the Preston tube technique, yield to the required correlation between the dimensionless wall shear stress and the measured pressure difference

$$\tau^+ = A \cdot \left(\frac{\Delta p \cdot (d/2)^2}{\rho \cdot \nu^2} \right)^n \qquad (3)$$

A, n = empirical constants

This correlation is usually determined empirically In **Figure 2a**, two characteristic calibration curves of the sublayer-fence are shown for different heights of the fence

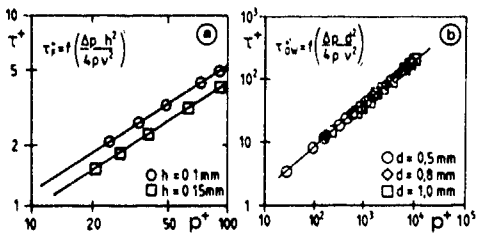

Figure 2: Measured calibration curves
a) sublayer fence, b) obstacle-wire

A standardizable calibration curve can be expected for geometrically more similar configurations like obstacle-wires having the same diameter of pressure taps and wire First calibration experiments employing different sized obstacle-wires confirmed this hypothesis, **Figure 2b** These experiments were carried out in a fully developed pipe flow (D = 50 mm, b l - thickness = 25 mm) The wall shear stresses in these experiments were determined by the pressure drop in flow direction that can be take as a measure for skin friction As shown in Figure 2b, the measuring points for different characteristic diameters of the obstacle-wire make up a standard correlation between nondimensional pressure difference (1) and wall shear stress (2) This forms a contrast to Figure 2a, which shows comparable results for a sublayer fence Here, the influence of the height of the fence is clearly visible and confirms the problem of individual calibration Another result of such calibrating experiments is shown in **Figure 3** In this case, an obstacle-wire (d = 0 15 mm) was calibrated in a turbulent flat plate flow up to Mach numbers of M 0 8 In order to determine the wall shear stress, the standard Preston tube method extended to compressible flows /4/ was used as a referential method The results compare with those shown in Figure 2b and confirm both the applicability of the obstacle-wire technique up to high subsonic Mach numbers as well as the standardizable calibration over a wide velocity range, **Figure 4**

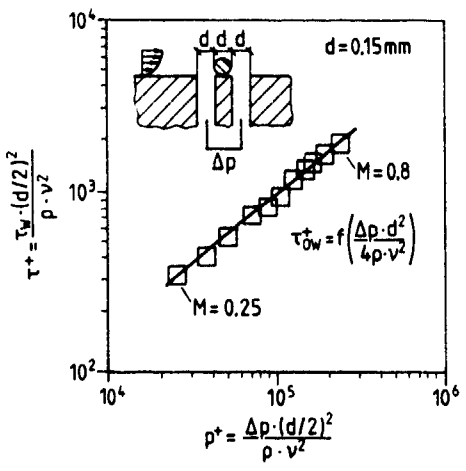

Figure 3: Obstacle-wire calibration curve for high subsonic Mach numbers

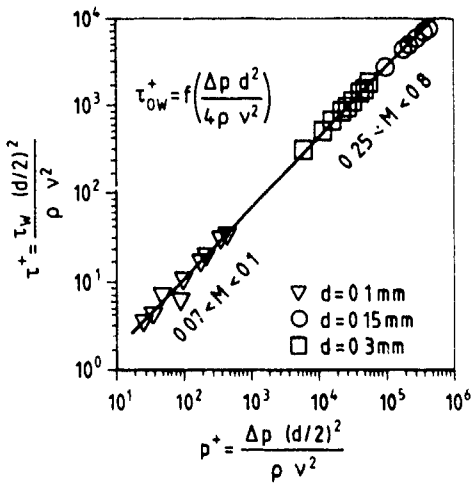

Figure 4. Obstacle-wire calibration for different diameters and Mach numbers

PRACTICAL APPLICATIONS

The first practical application of the method developed took place in a transitional flat plate flow, for both a free laminar - turbulent transition and a fixed transition In these measurements, a calibration curve, as represented in Figure 2b, was used

Figure 5 shows clearly that the obstacle-wire method supplies extremely good reproductions of the theoretical friction laws for laminar and turbulent flows It therefore confirms flexible applicability Similarly convincing results were obtained in the experiments shown in **Figure 6**, which were carried out in a relaxing flow behind an overcritical 10°- diffuser In this case, again the calibration curve which had been assessed in a fully developed pipe flow (Figure 2b), was used for measurements downstream of the reattachment point Comparative results were obtained with a sublayer fence and, thus, also confirmed the method presented here

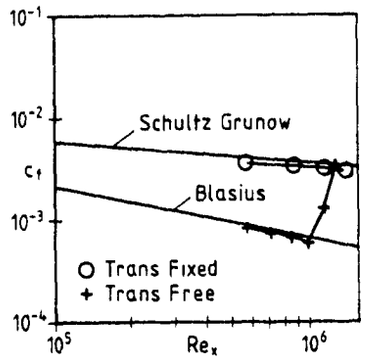

Figure 5 Skin friction measurement with an obstacle-wire (transitional flat plate flow)

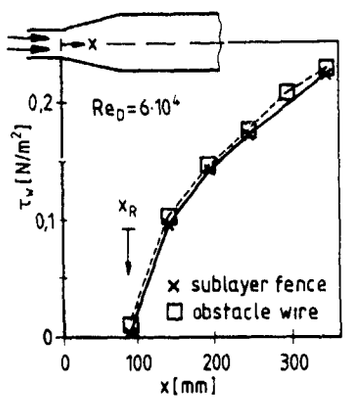

Figure 6. Wall shear stress measurement with the obstacle-wire and sublayer-fence technique (relaxing diffuser flow)

FURTHER DEVELOPMENTS

For further reduction of the technical effort, additional experiments were made, as illustrated in **Figure 7** Here, the pressure difference was no longer used in front of or behind the obstacle-wire As the characteristic pressure difference, the pressure measured in front of the wire (p_3) was used in difference to the calculated value (p_3') obtained by means of interpolation of the pressure tap readings upstream and downstream of the obstacle-wire point Theoretical examinations of this problem are presented in /5/, and show, too, that this pressure difference characterizes the pressure field around wall bounded cylinders The simplified technique

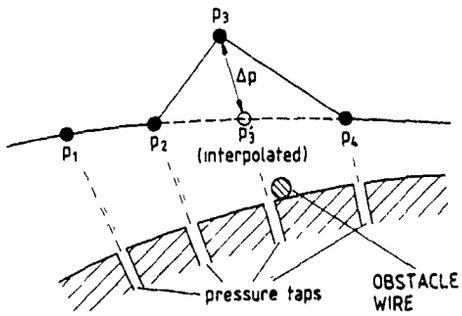

Figure 7: Principle of the modified obstacle-wire technique

presented above was employed on the basis that bodies, which are to be examined in experimental aerodynamics, usually set up with a lot of static pressure taps

The resulting calibration curve of this simplified technique for two different experiments with strongly varied Mach numbers and different wire diameters is shown in **Figure 8** This calibration curve differs slightly from the results shown in Figure 2b, 3 and 4 This is due to the lower pressure difference in case of the simplified technique However, the results in **Figure 8** confirm again that a standardizable calibration exists for geometrically similar configurations of the obstacle-wire **Figure 9** shows both calibration curves of the obstacle-wire technique in comparison with other calibration curves based on pressure measurements as a measure of the wall shear stress

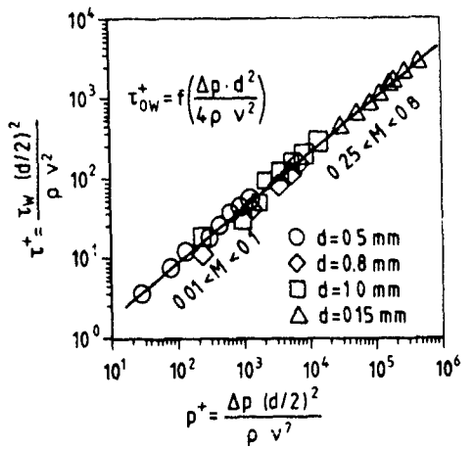

Figure 8. Measured calibration curve for the modified obstacle-wire technique

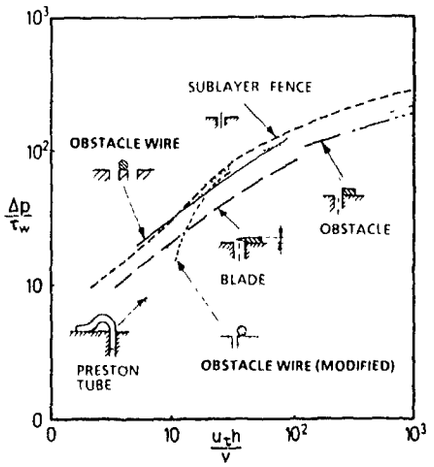

Figure 9 Comparison of the obstacle-wire technique with other wall shear stress measuring devices

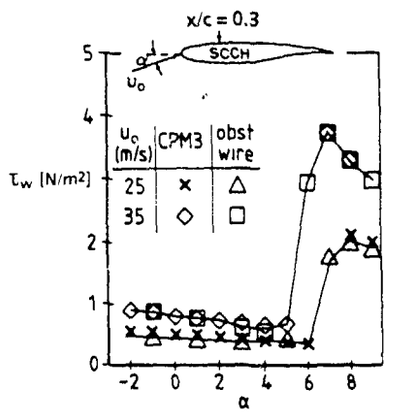

Figure 10. Wall shear stresses on an airfoil (SCCH) measured by means of the modified obstacle-wire and CPM 3-technique

In a first practical application, the extended technique was tested on two airfoil models The Computational Preston-tube Method (CPM 3- triple probe /3/) extended to compressible flows /6/ - served as a referential method **Figure 10** shows a very good correspondence in the wall shear stress measured In this case, only the wall shear stress at x/c = 0 3 is shown, indicating the boundary-layer transition as a function of the attack angle of the profile Another

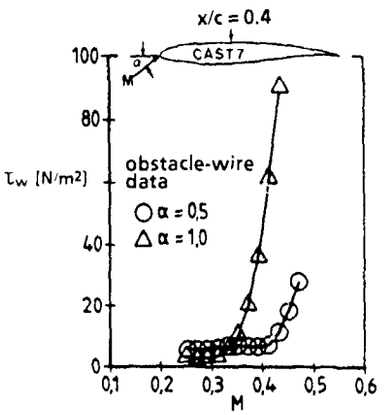

Figure 11: Measured wall shear stresses at x/c = 0 4 as a function of the Mach number for two attack angles of an airfoil (CAST 7)

example is demonstrated in **Figure 11** Here, the transition of the boundary layer - from the low wall shear stress level of the laminar flow to the strongly increasing wall shear stress of the turbulent flow, depending of the Mach number - is clearly visable These first practical tests of the simplified obstacle-wire technique can also be considered as very encouraging with regard to airfoil experiments

SUMMARY

The paper presents a new wall-shear stress measurement method on the basis of obstacle-wires The basic version of the method is founded on the pressure difference measured behind and in front of a thin wire (typical d = 0 1 to 0 6 mm) that is stuck between two pressure taps Although the technique is comparable to the sublayer-fence technique, its flexibility is strongly improved because the device is supported by a standardizable calibration correlation on the condition that the geometrical form (wire diameter / distance between pressure taps / diameter of the pressure taps) remains similar Calibration experiments are shown for different flow cases as well as practical measurements in non-classical boundary-layer flows (transitional air-foil flows, relaxing flow), which illustrate the wide applicability of this technique Finally, an additional simplification of the measuring technique is discussed, employing only one pressure tap in front of the wire The reliability of this technique is confirmed too by calibration experiments and first practical applications on airfoils

REFERENCES

/1/ Winter, K G , An Outline of the Technique Available for the Measurement of Skin Friction in Turbulent Boundary Layers Prog Aerospace Science, Vol 18, pp 1-57, 1977

/2/ Nitsche, W , Thunker, R , Haberland, Ch , Comparative Investigations on Friction Drag Measuring Techniques in Experimental Aerodynamics ICAS 84-2 4 1, Proc Vol 1, 391-403, 1984

/3/ Nitsche, W , Thunker, R , Haberland, Ch , A Computational Preston Tube Method Turbulent Shear Flows 4, Springer Verlag, 261-276, 1985

/4/ Bertelrud, A , Preston-Tube Calibration Accuracy AIAA Journal 14, pp 98-100, 1976

/5/ Solberg, T , Eidsvik, K J , Flow Over a Cylinder at a Plane Boundary - A Model Based Upon (k-ε) Turbulence Journal of Fluids Engineering, Vol 111, pp 414-419 1989

/6/ Weiser, N , Mirow, P , Nitsche, W , Statische und dynamische Meßverfahren zur Transitionsbestimmung an Laminarprofilen DGLR-Jahrbuch 1989 I, pp 427-434, 1989

EIGHTH SYMPOSIUM ON
TURBULENT SHEAR FLOWS
Technical University of Munich
September 9-11, 1991

On the Equations for Higher Order Moments in Wall Bounded Flows

F.Durst* J.Jovanović* T.G.Johansson‡

*Lehrstuhl für Strömungsmechanik Universität Erlangen-Nurnberg
Cauerstrasse 4,D-8520 Erlangen
‡Chalmers University of Technology, Departmant of Appl. Thermodynamics
and Fluid Mechanics, S-41296 Göteborg

Abstract

The present paper considers equations for higher order moments of turbulent velocity fluctuations for wall bounded flows These are derived from the extended Reynolds equations for turbulent property fluctuations. The resultant equations are closed utilizing truncated cumulant expansions as an approximation for the probability density distributions of corresponding turbulence properties.By applying different degrees of truncations of these expansions an alternative set of equations for moments is formulated that contains only velocity correlations From these equations statistical invariants are deduced and are experimentally verified employing data available in literature and also data measured by authors

1 Introduction

It is a general pratice in turbulence modelling to operate with equations for moments of turbulent velocity fluctuations. These involve three different types of unknown correlations:

- higher order velocity correlations
- velocity pressure-gradient correlations
- dissipation correlations

Introducing assumption of local homogenity for the small scale structure of turbulance,Chou [3] developed a sistematic and self consistent procedure to close sets of equations for velocity pressure-gradient and dissipation correlations.In the literature,higher order velocity correlations are usually modeled employing Millionschikov hypothesis [10] or also by gradient transport equations of the corresponding moments of lower order [6].However,the validation of the assumptions introduced in existing closure schemes, i e. presented in ref.[12],revealed significant disagreement between simulated data and data predicted by computer codes involving turbulence models with menthioned closure assumptions Attemts to modify turbulence closure models have not always lead to more improved data predictions of turbulence properties,i.e. see ref.[7].

In a recent publication Durst, Jovanović and Johansson [4] (hereafter referred to as DJJ1) introduced a new statistical approach for treatment of equations for higher order moments of turbulent velocity fluctuations. Starting from the basic conservation laws they derived a set of equations for the central moments of the arbitrary order n:

$$\frac{1}{n+1}\frac{\partial \overline{u_j^{n+1}}}{\partial t}+\frac{U_i}{n+1}\frac{\partial \overline{u_j^{n+1}}}{\partial x_i}+\overline{u_j^n u_i}\frac{\partial U_j}{\partial x_i}+\frac{1}{n+1}\frac{\overline{u_j^{n+1}u_i}}{\partial x_i}-$$

$$\overline{u_j^n}\frac{\partial \overline{u_i u_j}}{\partial x_i}=\overline{u_j^n \Omega_j} \qquad (1)$$

$$\Omega_j=-\frac{1}{\rho}\frac{\partial p}{\partial x_j}+\nu\frac{\partial^2 u_j}{\partial x_i \partial x_i} \qquad (2)$$

For the steady,plane channel flow and approximately also for wall boundary layers, eqn (1) reduces to the following form.

$$\overline{u_j^n u_2}\frac{dU_1}{dx_2}\delta_{1j}+\frac{1}{n+1}\frac{d\overline{u_j^{n+1}u_2}}{dx_2}-\overline{u_j^n}\frac{d\overline{u_j u_2}}{dx_2}=\overline{u_j^n \Omega_j} \qquad (3)$$

Introducing the three-dimensional joint probability density distribution

$$P_j(u_j,u_2,\Omega_j) \qquad j=1,2,3 \qquad (4)$$

and its marginals

$$P^{j,(1)}(u_j,u_2)=\int_{-\infty}^{\infty}P^j(u_j,u_2,\Omega_j)d\Omega_j \qquad (5)$$

$$P^{j,(2)}(u_j,\Omega_j)=\int_{-\infty}^{\infty}P^j(u_j,u_2,\Omega_j)du_2 \qquad (6)$$

DJJ1 formed a basis for statistical consideration to close the hierarcy of equations for higher order moments.

Since the exact analytical forms of the above defined distributions are unknown, DJJ1 proposed to expand them in terms of higher order cumulants.The first terms of these expansions corresponds to Gaussian probability density distributions and the remaining terms express deviations from the normal distribution.By introducing different degrees of truncations of these expansions ,DJJ1, showed that it is possible to formulate an *alternative set of equations for moments that contain only velocity correlations.*

The objective of this work is to analyse,in more detail,the derived system of equations for moments of turbulent velocity fluctuations utilizing double cumulant expansions for the marginal distributions (5) and (6).Equations resulting from fourth,sixth and eighth order truncation approximations of series expansions for the marginal distributions are considered. Since these equations involve only velocity correlations it will be possible to compare them with experimental data measured in a turbulent boundary layer Formulating conditions leading to the asymptotic reduction of the derived system of equations,for moments towards the Gaussian limit,it is possible to deduce the behaviour of higher order correlations across the entire flow field Derived functional relationships for higher order moments are validated against available experimental data obtained in different wall shear flows.

2 Equations for Higher-Order Moments Resulting from Truncated Approximations for the Marginal Probability Density Distributions $P^{j,(1)}$ and $P^{j,(2)}$

To represent marginal distributions (5) and (6) Durst, Jovanovic and Johansson [5] (hereafter refered as DJJ2) utilized a specific type of cumulant expansion which is refered in the literature as Gram-Charlier series expansions They nave extensively investigated the applicability of various relationships for higher order correlations resulting from different degrees of truncations of these expansions Direct testing of the predicted higher order correlations against experimental data gave support for the applicability of the considered type of cumulant expansion over a wide portion of turbulent boundary layer. The analysed data also comfirmed that with increasing order of truncations of the above mentioned series expansions more improved data predictions are obtained Thus the work of DJJ2 has provided an experimental proof that Gram-Charlier series expansions for marginal distributions $P^{j,(1)}$ and $P^{j,(2)}$ provide sufficiently close approximation for the considered types of higher order correlations involved in the basic equations for moments

By expanding the marginal distributions $P^{j,(1)}$ and $P^{j,(2)}$ in the form of Gram-Charlier series expansions and by performing different degrees of truncations of these expansions DJJ1 succeeded in formulating a *nontrivial*[1] set of equations for higher moments.The alternative set of equations for moments is obtained by applying following methodology

> For N^{th} order truncation approximation we consider first $(N+1)$ equations of the system defined by (2). All correlations of order higher than the order of truncation are approximated by relationships valid for truncated Gram-Charlier expansions. Since double expansion is employed for $P^{j,(1)}$ and $P^{j,(2)}$ similar expressions are used for representing $\overline{u_j^n u_2}$ and $\overline{u_j^n \Omega_j}$ correlations for $n > N$. First (N-1) equations for moments are combined with auxiliary relationships derived from truncated Gram-Charlier series expansions to eliminate compound correlations $\overline{u_j^n \Omega_j}$ from the last two equations of the system. From these equations,the final form is obtained by cross elimination of terms that contain spatial derivatives of mixed correlations.

By applying the above procedure the following set of approximate equations is obtained (see also [4])

$$R_j^{3,1}\frac{d\overline{u_j^2}^2}{dx_2} + R_j^{1,1}\frac{d\overline{u_j^4}}{dx_2} - 6R_j^{1,1}\frac{d\overline{u_j^2}^2}{dx_2} - 4R_j^{1,1}\frac{S_j^2}{F_j-3}\frac{d\overline{u_j^2}^2}{dx_2} \simeq 0 \quad (7)$$

$$(R_j^{5,1} - 10R_j^{3,1})\frac{d\overline{u_j^2}^3}{dx_2} + 45R_j^{1,1}\frac{d\overline{u_j^2}^3}{dx_2} - 15R_j^{1,1}\frac{d\overline{u_j^2}\,\overline{u_j^4}}{dx_2} + R_j^{1,1}\frac{\overline{u_j^6}}{dx_2} + 6R_j^{1,1}\frac{(10S_j - SS_j)^2}{15F_j - 30 - SF_j}\frac{d\overline{u_j^2}^3}{dx_2} \simeq 0 \quad (8)$$

$$(R_j^{7,1} - 21R_j^{5,1} + 105R_j^{3,1})\frac{d\overline{u_j^2}^4}{dx_2} + 210R_j^{1,1}\frac{d\overline{u_j^2}^2\overline{u_j^4}}{dx_2} - 28R_j^{1,1}\frac{d\overline{u_j^2}\,\overline{u_j^6}}{dx_2} + R_j^{1,1}\frac{d\overline{u_j^8}}{dx_2} - 420R_j^{1,1}\frac{d\overline{u_j^2}^4}{dx_2} + 8R_j^{1,1}\frac{(21SS_j - 105S_j - HS_j)^2}{315 - HF_j + 28SF_j - 210F_j}\frac{d\overline{u_j^2}^4}{dx_2} \simeq 0 \quad (9)$$

with the following notation:

$$R_j^{m,n} = \frac{\overline{u_j^m u_2^n}}{\sigma_j^m \sigma_2^n}\ ,\ \sigma_j = \sqrt{\overline{u_j^2}}\ ,\ \sigma_2 = \sqrt{\overline{u_2^2}}$$

$$S_j = \frac{\overline{u_j^3}}{\sigma_j^3}\ ,\ F_j = \frac{\overline{u_j^4}}{\sigma_j^4}$$

$$SS_j = \frac{\overline{u_j^5}}{\sigma_j^5}\ ,\ SF_j = \frac{\overline{u_j^6}}{\sigma_j^6}$$

$$HS_j = \frac{\overline{u_j^7}}{\sigma_j^7}\ ,\ HF_j = \frac{\overline{u_j^8}}{\sigma_j^8}$$

The leading equation has been obtained by the application of the fourth order truncation approximation and the remainder equations by the application of sixth and eighth order truncations of the marginal distributions.

The resultant, nontrivial set of equations for higher order moments forms the basis for the advanced statistical treatment of equations that govern the the turbulent wall flows.The system is not closed and contains singular terms at the point where the solution approaches a Gaussian distribution These terms are essential for extracting non-Gaussian behaviour of higher order correlations

3 Derivation of Statistical Invariants from the Equations for Higher Order Moments

The system of equations for moments was derived by expanding marginals (5) and (6) around the normal distribution Therefore it is natural to assume that there exists at least one point in the flow where higher order correlations approachs those corresponding to the Gaussian distribution From derived systm (7)-(9) it is possible to show that the Gaussian solution can be obtained only at the point of maximum intensity

$$\frac{d\overline{u_j^2}}{dx_2} = 0 \quad (10)$$

if higher order central moments are, at the same point, interrelated as follows:

$$\begin{aligned} F_j - 3 &\simeq K_{1,j} S_j^2 \\ 15F_j - 30 - SF_j &\simeq K_{2,j}(10S_j - SS_j)^2 \\ 315 - HF_j + 28SF_j - 210F_j &\simeq K_{3,j}(21SS_j - 105S_j - HS_j)^2 \end{aligned} \quad (11)$$

In the above formulas $K_{1,j}, K_{2,j}$ and K_3, are arbitrary constants. Requesting an unbounded domain of joint variation of higher order moments ($K_{1,j} > 0$), it follows from (11) that the point of maximum intensity zero skewness and minimum flatness coincide in the boundary layer.

Additional constraints for higher order moments can be formulated by considering the possibility to condensate the system of equations (7)-(9) Successive applications of relationships for higher order correlations derived for N^{th} or-

[1] Nontrivial in a sense that the system also posseses non-Gausian solutions

der truncation approximation of series expansion (5) to the equations obtained by applying $(N+2)^{th}$ order truncations of marginal distributions will reduce system (7)-(9) towards the leading equation defined in terms of fourth order correlations. Since the system is not trivial the above described procedure will provide conditions that define a close form solution for the probability density distribution of velocity fluctuations in integral form

Transforming eqns (9) and (8) employing the relationships valid for sixth and fourth order truncation approximations we obtain·

$$5F_j - 15 + 6\lim\frac{(10S_j - SS_j)^2}{15F_j - 30 - SF_j} \simeq 0 \qquad (12)$$

$$SS_j \rightarrow 10S_j$$

$$SF_j \rightarrow 15F_j - 30$$

$$7SF_j - 105F_j + 210+$$

$$8\lim\frac{(21SS_j - 105S_j - HS_j)^2}{315 - HF_j + 28SF_j - 210F_j} \simeq 0 \qquad (13)$$

$$HS_j \rightarrow 21SS_j - 105S_j$$

$$HF_j \rightarrow 28SF_j - 210F_j + 315$$

To enable matching of above deduced algebraic relations for moments to the leading equation of the system, we express eqn (7) as follows

$$2R_j^{3,1}\frac{d\overline{u_j^2}}{dx_2} + R_j^{1,1}\overline{u_j^2}\frac{dF_j}{dx_2} + 2R_j^{1,1}F_j\frac{d\overline{u_j^2}}{dx_2} - 12R_j^{1,1}\frac{d\overline{u_j^2}}{dx_2} -$$

$$8R_j^{1,1}\frac{S_j^2}{F_j - 3}\frac{d\overline{u_j^2}}{dx_2} \simeq 0 \qquad (14)$$

By comparing eqns. (12),(13) and (14) we conclude that they will tend towards a self consistent form only in the following limiting case

$$\overline{u_j^2} \rightarrow 0$$

$$R_j^{3,1} \rightarrow F_j R_j^{1,1} \qquad (15)$$

$$SF_j \rightarrow 15F_j - 30$$

Hence the limiting compressed form of the system reads·

$$2F_j^w - 6 - 4\lim\frac{S_j^2}{F_j - 3} \simeq 0 \qquad (16)$$

$$S_j \rightarrow 0 \quad , \quad F_j \rightarrow 3$$

$$5F_j^w - 15 + 6\lim\frac{(10S_j - SS_j)^2}{15F_j - 30 - SF_j} \simeq 0 \qquad (17)$$

$$SS_j \rightarrow 10S_j \quad , \quad SF_j \rightarrow 15F_j - 30$$

$$\lim\frac{(21SS_j - 105S_j - HS_j)^2}{315 - HF_j + 28SF_j - 210F_j} \simeq 0 \qquad (18)$$

$$HS_j \rightarrow 105S_j \quad , \quad HF_j \rightarrow 210F_j - 525$$

where F_j^w corresponds to the flatness factor evaluated at the wall

The obtained algebraic counterpart of the initial system of equations for moments is valid only at the flow boundaries ($\overline{u_j^2} \rightarrow 0$). Functional forms (16), (17) and (18) are identical to the deduced interrelations between higher order moments (11) found around the point of maximum intensity. Therefore we can write down interpolation formulas for kernels that appear in the equations for moments·

$$ZZ_j^{(1)} = \frac{S_j^2}{F_j - 3} \quad \mapsto const \qquad (19)$$

$$ZZ_j^{(2)} = \frac{(10S_j - SS_j)^2}{15F_j - 30 - SF_j} \quad \mapsto const. \qquad (20)$$

$$ZZ_j^{(3)} = \frac{(21SS_j - 105S_j - HS_j)^2}{315 - HF_j + 28SF_j - 210F_j} \quad \mapsto const. \qquad (21)$$

The above terms are therefore indentified as statistical invariants

4 Experimental Verification

4.1 Verification of Dynamic Equations for Higher Order Moments

The experimental data base of Johansson [8], taken in a fully developed turbulent boundary layer employing three-dimensional LD anemometry, is used to verify the derived set of equations (7)-(9) for higher order moments Individual terms of the above listed equations and final sums were computed from stored LDA data files Verification examples are shown in Figure 1-2.

Experimental data confirm that the derived system of equations holds in the viscous sublayer, logarithmic region and in the outer part of the boundary layer. In the buffer region experimental data systematicly deviate from predictions.This tendency is due to the singularity present in the equation for fourth order truncation approximation and also due to the weak convergence of terms representing velocity-pressure gradient and dissipation correlations [4]. The general conclusion drawn from the analysed data supports the validity of the derived system of equations for moments across 95% of total shear layer thickness.

4.2 Verification of Statistical Invariants

In order to verify the results of the derivations of section 3 a literature survey was performed to collect most of the available data on higher order moments of turbulent velocity fluctuations in wall shear flows. A summary of all collected data is present in Table 1

Verification examples for invariant $ZZ_j^{(1)}$ are shown in Figures 3 and 4 in the form of cross plots of higher order moments Experimental data support the validity of derived invariant for streamwise velocity component across the entire flow domain. For the normal velo·ity component the deduced invariant also holds excluding the buffer region (see also Figure 4-b).Deduced relations between higher order moments are in agreement with conclusions drawn from Figures 1 and 2 regarding the validation of derived system of equations across the boundary layer.

An extension of the analysis presented in this paper permits conclusions to be drawn on the joint variation of higher order moments of all three fluctuating velocity components. This is given in Figure 5 summarizing the existing knowledge on the behaviour of these quantities in wall bounded flows Orderliness, as shown in Figure 5 might help to better understand turbulent momentum transport across wall shear layers

4.3 Limiting Values of Higer Order Moments on the Wall

The condition of asymptotic matching of equations for moments (16) leads to the relation between invariant $ZZ_j^{(1)}$ and

flatness factor F_j^w evaluated at the wall as follows:

$$F_j^w \simeq 3 + 2ZZ_j^{(1)} \tag{22}$$

Comparison of evaluated data presented in Figure 6 shows good agreement with numerical simulations of Kim, Moin and Moser [9] and experiments of Kreplin and Eckelmann [11].

5 Conclusions and Final Remarks

In this paper attempt was made to formulate a statistical closure for equations that define higher order moments Utilizing properties of truncated cumulant expansions, as an approximation for probability density distributions, an alternative set of equations for moments was formulated that contains only velocity correlations. The resultant set of equations provides an interesting insight into the behaviour of successive order moments of turbulent velocity fluctuations across a shear layer. Analysis shows that the point of maximum intensity, zero skewness and minimum flatness coincide in the boundary layer

From statistical considerations of the derived set of equations for moments invariants are deduced that interrelate all even number moments with the first lower odd moment The resultant invariants are in fact conditions for a closed form model for probability density distributions of turbulent velocity fluctuations The reconstruction of the entire density distribution from moments is extremly difficult but the relations (19)-(21), and specially the invariant $ZZ_j^{(1)}$, do resemble properties of inverse Gaussian and hyperbolic probability density distributions These distribution functions play a central role in contemporary statistics of non-Gaussian processes [2].

References

[1] Andreopulos, J. *Comparison test of the response to pitch angles of some digital hot wire techiniques* Report SFB 80/E/182,University of Karlsruhe, 1981.

[2] Barndorff-Nielsen, O. *Models of non-Gaussian variation with application to turbulence.* Proc. Roy. Soc. London, A368, pp. 501-520, 1979.

[3] Chou, P.Y. *On the velocity correlations and solutions of the equations of turbulent fluctuation* Quarterly of Applied Mathematics, Vol.3, pp. 38-54, 1945

[4] Durst, F., Jovanović, J. and Johansson, T.G., *Interrelations of moments of turbulent velocity fluctuations in wall shear flows.* Report 288/ET/90 LSTM, Universität Erlangen-Nürnberg 1990.

[5] Durst, F.,Jovanović, J. and Johansson, T.G., *On the Convergence Properties of Truncated Gram-Charlier Series Expansions in Wall Bounded Flows.* (submitted for publication to Physics of Fluids)

[6] Hanjalić, K and Launder, B.E *A Reynolds stress model of turbulence and its application to thin shear flows.* Journal of Fluid Mechanics, Vol.52, pp 609-638, 1972

[7] Hanjalić, K. *Some results of exploring possible improvements of second order turbulence closure models* Lecture at the LSTM,1991.

[8] Johansson, T G *LDV measurements of higher order mixed moments in a flat plate turbulent boundary layer* Report 880120, Department of Applied Thermodynamics and Fluid Mechanics, Chalmers University of Technology, 1988

[9] Kim, J.,Moin, P. and Moser, R., *Turbulence statistics in fully developed channel flow at low Reynolds number.* Journal of Fluid Mechanics 177, pp. 133-166, 1987.

[10] Kolovandin, B A. and Vatutin, I.A. *Statistical transfer theory in non-homogenious turbulence.* Int J. Heat and Mass Transfer, pp. 2371-2383, 1972.

[11] Kreplin, H.P and Eckelmann, H , *Behaviour of the three fluctuating velocity components in the wall region of a turbulent channel flow* Phys Fluids 22, pp. 1233-1239, 1979.

[12] Mansour, N N.,Kim, J. and Moin, P *Reynolds-stress and dissipation rate budgets in a turbulent channel flow* NASA Technical Memorandum 89451, 1987

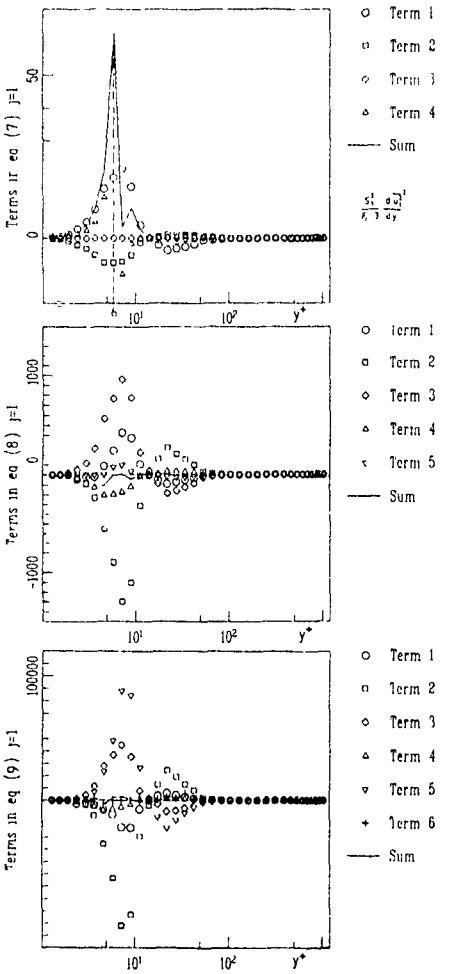

Figure 1: Verification of final equations for moments j=1.

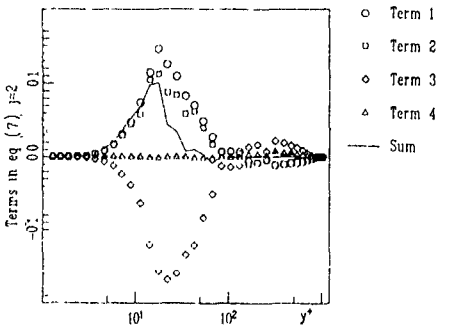

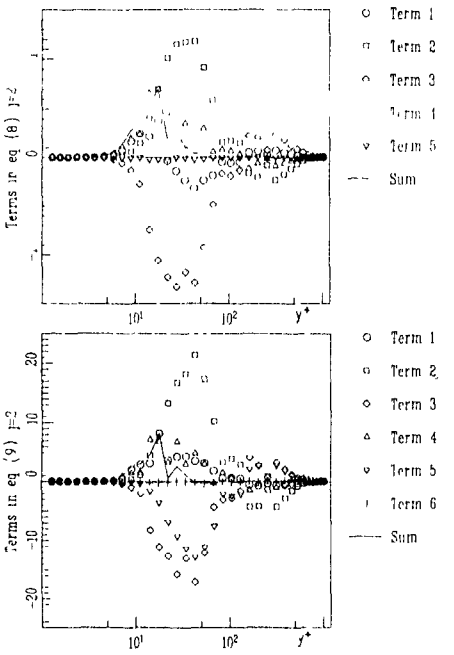

Figure 2: Verification of final equations for moments j=2.

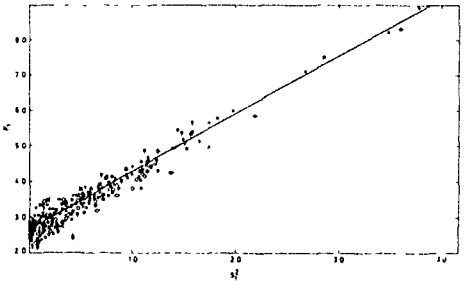

Figure 3: Interrelationship between skewness and flatness factors for streamwise velocity component.

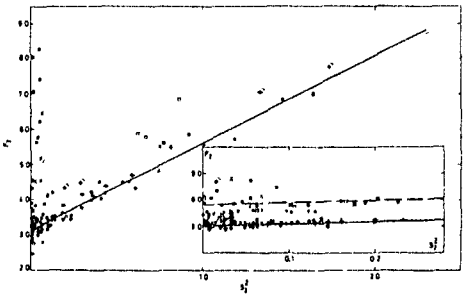

Figure 4-a: Interrelationship between skewness and flatness factors for normal velocity component.

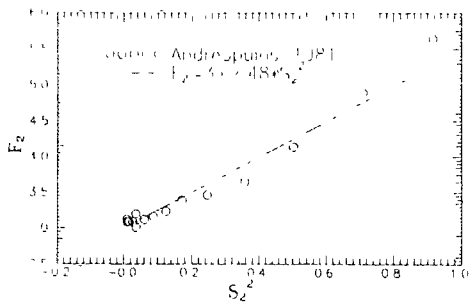

Figure 4-b: Interrelationship between skewness and flatness factors for normal velocity component in the logarithmic region and outer part of boundary layer.

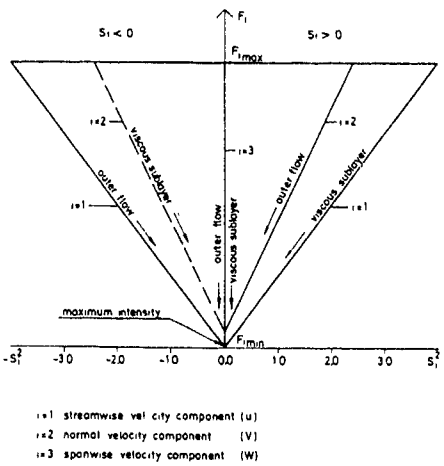

Figure 5: Interpretation of higher order moments in turbulent boundary layers in the form of statistical triangle.

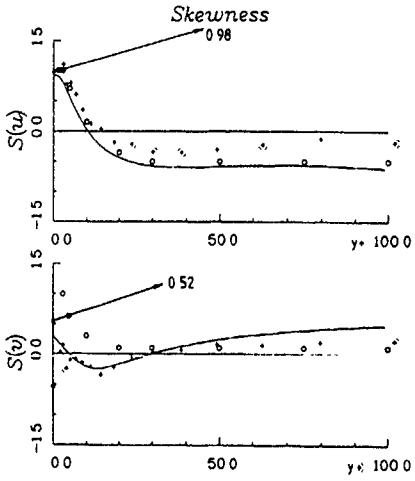

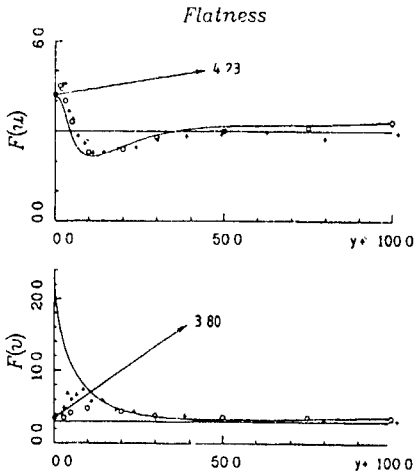

Figure 6: Limiting values of higher order moments on the wall.

Author	Date	Moments						Flow	Technique	Symbol
		S_1	F_1	SS_1	SF_1	S_2	F_2			
Antonia and Luxton	1971	+	+	−	−	+	+	b layer	HWA	●
Comte-Bellot	1965	+	+	−	−	+	+	channel	HWA	◇
Elena	1977	+	+	−	−	−	−	pipe	HWA[a]	⊙
Gupta and Kaplan	1972	+	+	−	−	+	+	b layer	HWA[d]	✱
Kabahpaseva	1976	+	+	−	−	+	+	channel	optical[d]	□
Hedley and Keffer	1974	+	+	−	−	+	+	b layer	HWA[d]	◇
Johansson and Alfredsson	1982	+	+	−	−	−	−	channel	HWA[d]	▲
Johnsan and Eckelmann	1984	+	+	−	−	+	+	channel	HWA[d]	○
Jovanović	1984	+	+	+	+	+	+	b layer	HWA[d]	●
Karlsson and Johansson	1986	+	+	−	−	+	+	b layer	LDA[d]	■
Kastrinakis and Eckelmann	1983	+	+	−	−	+	+	channel	HWA[d]	◆
Keck	1978	+	+	−	−	+	+	pipe	LDA[d]	▼
Kim et al	1986	+	+	−	−	+	+	channel	simulations	×
Kreplin	1973 1976	+	+	−	−	−	−	channel	HWA[d]	◇
Kreplin and Eckelmann	1979	+	+	−	−	+	+	channel	HWA[d]	●
Krishnamoorthy et al	1985	+	+	−	−	−	−	b layer	HWA[d]	▽
Kutateladze et al	1972	+	+	−	−	+	+	channel	optical[d]	◇
Le Stum and Nizou	1971	+	+	−	−	−	−	pipe	HWA[a]	○
Nakagawa and Nezu	1977	+	+	−	−	+	+	channel	HWA[d]	◆
Repik et al	1975	+	+	−	−	−	−	b layer	HWA[a]	▶
Ueda and Hinze	1975	+	+	−	−	−	−	b layer	HWA[d]	✖
Ueda and Mizushina	1977	+	+	+	+	+	+	pipe	HWA[d]	▷
Van Thinh	1982	+	+	−	−	−	−	channel	HWA[d]	✖
Zarić	1974	+	+	+	+	−	−	channel	HWA[d]	+

a - analog data processing
d - digital data processing

Table 1: Summary of collected data on measurements of higher order moments in wall shear flows.

EIGHTH SYMPOSIUM ON
TURBULENT SHEAR FLOWS
Technical University of Munich
September 9-11, 1991

Numerical Study of Axial Turbulent Flow over Long Cylinders

By J. C. Neves *, P. Moin *† AND R. D. Moser †

* Stanford University, Stanford CA 94305

† NASA Ames Research Center, Moffet Field, CA 94035

Abstract

Direct numerical simulations of turbulent axial flow over cylinders have been conducted to study the effects of transverse curvature. Two cases with Reynolds number $Re_\delta = U_\infty \delta/\nu \simeq 3400$ and layer thickness to cylinder radius ratios (δ/a) of 5 and 11 have been simulated. Both cases are in the regime of large δ/a and small $a^+ = a u_\tau/\nu$, the cylinder radius in wall units. All essential turbulence scales were resolved in both calculations. A large number of turbulence statistics were computed. The results are compared with the plane channel results of Kim *et al.* (1987) and with experiments. With transverse curvature the skin friction coefficient increases and the turbulence statistics, when scaled with wall units, are lower than in the plane channel. The momentum equation provides a scaling that collapses the cylinder statistics, and allows the results to be interpreted in light of the plane channel flow. The azimuthal and radial length scales of the structures in the flow are of the order of the cylinder diameter. Boomerang-shaped structures with large spanwise length scales have been observed in the flow.

1. Introduction

The importance of transverse curvature on the development of turbulent boundary layers has been recognized for many years. However, the experimental data available on transversely curved flows is limited, in part because of the difficulties in performing measurements (*e.g.*, Willmarth *et al* [1969, 1976], Luxton *et al.* [1984], Lueptow *et al* [1985, 1987]). Early interest in transversely curved flows arose from the need to predict the skin friction on bodies of revolution. Recently, the need to calculate the drag over cylindrical bodies of very small diameter, as well as the desire to understand the acoustic characteristics of axisymmetric flows that develop over long towed bodies, has renewed interest in these flows. Furthermore, because the area over which turbulence is generated restricts the number of wall structures present, these flows are important for the understanding of the structural mechanisms of wall turbulence.

The presence of a second length scale (the cylinder radius, a) in addition to the boundary layer thickness (δ), results in a two-dimensional space of possible flows that can be parametrized by δ/a and a^+. A comprehensive review of the experimental studies of this flow is provided by Lueptow (1988). For the flow regime studied here (large δ/a and small a^+), experiments are particularly difficult because the long and thin wires used make aeroelastic interactions difficult to isolate.

Close to the wall the total stress must be inversely proportional to the radial coordinate (Glauert *et al.* [1955]), which leads to a viscous sublayer velocity profile that depends on the cylinder radius (Rao *et al.* [1972]). Experiments, however, have shown the viscous sublayer profiles to be independent of transverse curvature. It has also been observed that when both δ/a and a^+ are large the mean velocity profiles exhibit a logarithmic region with a slope that decreases with increasing δ/a (Lueptow *et al* [1985]). But if δ/a is large and a^+ small, there is no longer a logarithmic region (Luxton *et al* [1984]). These studies have also shown that transverse curvature acts to lower the turbulence intensities away from the wall ($y^+ > 20$). However, close to the wall the axial intensity was found to be larger than in the flat plate in some cases (Lueptow *et al* [1985]). Finally, in visual studies of the flow, large structures (larger than the cylinder diameter) have been observed to sweep past the cylinder, which should have a profound effect on the flow.

To study the effects of transverse curvature with large δ/a but small a^+, we simulated a model of the axial flow over a cylinder has been simulated. The model flow is described in section 2. The velocity field statistics and the scaling are discussed in section 3. In section 4 we examine some of the structural characteristics of the flow. Throughout the paper, r, θ, and z denote the radial (normal to the wall), azimuthal, and axial directions, respectively, and the normal coordinate is $y = r - a$. The velocity is denoted by (v_r, v_θ, v_z) and the vorticity is denoted by $(\omega_r, \omega_\theta, \omega_z)$. The friction velocity is $u_\tau = \sqrt{\tau_w/\rho}$, and the Reynolds number $Re_\tau = u_\tau \delta/\nu$.

2. The Model Problem

The boundary layer is modelled by truncating the semi-infinite domain in the radial direction at $r = a + \delta$, thus $r \in [a, a+\delta]$. The flow is driven by a mild pressure gradient

δ/a	L_z^+	$L_{\theta_i}^+$	Δ_z^+	$\Delta_{\theta_i}^+$	$\Delta_{\theta_o}^+$
5	2690	270	14	4	25
11	4524	137	14	1	13

Table 1 Resolution parameters

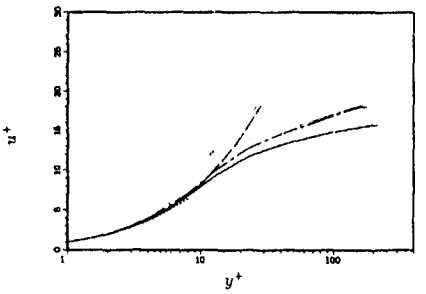

FIGURE 1 Mean-velocity profiles: ——— plane channel, cylinders with —— $\delta/a = 5$ and - - - - $\delta/a = 11$, planar law of the wall ($u^+ = y^+$, $u^+ = 2.5 ln y^+ + 5.5$), cylinder law of the wall ($u^+ = a^+ ln(1 + y^+/a^+)$), — — $a^+ = 21$

and is fully developed On the surface of the cylinder no slip boundary conditions are imposed. At the outer edge of the domain we require $v_r|_{r=a+\delta}$ and the surface shear stress $(\partial(v_\theta/r)/\partial r|_{r=a+\delta}, \partial v_z/\partial r|_{r=a+\delta})$ to be zero The incompressibility constraint at the wall and the pressure field boundary conditions are enforced as in Kleiser *et al.* (1981) Fourier expansions are used in the axial direction, which is homogeneous, and in the azimuthal direction, which is periodic Chebyshev expansions are used in the radial direction Since large velocity gradients are not expected at the outer edge of the domain we use a radial coordinate mapping, which concentrates the grid resolution at the cylinder surface at the expense of the resolution at the outer edge of the domain.

Two cases with $\delta/a = 5$ and $\delta/a = 11$ were computed. The number of modes in (r, θ, z) was $(96, 64, 192)$ for the $\delta/a = 5$ simulation and $(96, 128, 320)$ for the $\delta/a = 11$ simulation Table 1. summarizes the numerical parameters for the two simulations, where $L_z{}^+$ is the length of the computational domain, $L_{\theta_i}^+ = 2\pi a^+$ is the perimeter of the cylinder, Δ_z^+ is the grid resolution in the axial direction, and $\Delta_{\theta_i}^+$ and $\Delta_{\theta_o}^+$ are the the grid resolutions in the azimuthal direction at the wall and at the outer edge of the layer, respectively

3. Turbulence Statistics

The statistics presented in this section were collected after the flow had reached a statistically steady state. They were obtained by averaging over the domain in θ and z and in time from data covering 3 δ/u_τ units.

3.1 Mean Velocity

In transversely curved flow the added length scale provided by the radius of curvature gives rise to three possible flow regimes If δ/a is small, the effects of curvature are insignificant and the flow is like the flat plate flow If δ/a and a^+ are large, the transverse curvature affects only the outer part of the boundary layer. If δ/a is large but a^+ is small, then the inner part of the boundary layer is also be affected by the wall curvature.

δ/a	a^+	C_f	Re_δ	Re_τ	Re_a
0	∞	6.04×10^{-3}	3300	180	∞
5	43	8.07×10^{-3}	3368	214	674
11	21	9.87×10^{-3}	3418	239	311

Table 2 Mean flow parameters

For a boundary layer over a cylinder, dynamical equilibrium near the wall ($ar_w = r\tau$) leads to the near-wall velocity profile $u^+ = a^+ ln(1 + y^+/a^+)$ (Rao *et al* [1972]) This is a good approximation for the simulated velocity profiles for $y^+ < 10$ (Figure 1) Up to second order in y^+, the profile is $u^+ = y^+ - y^{+2}/2a^+$ Thus, the curvature effects can only be significant near the wall if a^+ is sufficiently small In particular, to attain a 10% departure from the planar result at $y^+ = 10$, $a^+ < 50$ is required. In the current simulations $a^+ \leq 43$, which results in the departure from the plane channel shown in Figure 1 In many experiments (*e.g.*, Willmarth *et al* [1969], Rao *et al* [1972], Lueptow *et al* [1987]) there is no perceptible effect of curvature in the velocity profile in the viscous region because a^+ is too large (*e.g.*, $a^+ \approx 140$ and $\delta/a \approx 7$ in Lueptow *et al* [1987]) In some of the experiments by Luxton *et al* (1984), a^+ values close to those of the simulations were used (Table 2) Similar to what is shown in Figure 1, a degeneration of the log-law was observed However, their viscous region velocity profiles follow the planar case profile, $u^+ = y^+$.

Several mean flow parameters are reported in Table 2 for the curved cases as well as the plane channel ($\delta/a = 0$, Kim *et al.* [1987]). Because the Reynolds numbers (Re_τ) of the three simulations are similar, the differences can be attributed to the effects of transverse curvature. In agreement with experimental observations (*e.g.*, Luxton *et al.* [1984]), the skin friction coefficient is larger than in the plane case. However, in our simulations this effect is larger than observed experimentally. The difference may be because in experiments Re_a is much higher (*e.g.*, in Lueptow *et al* [1987], $Re_a \approx 4 \times 10^3$).

3.2 Turbulence Intensities and Reynolds Shear Stress

The turbulence intensities normalized with u_τ are shown in Figure 2 As expected, the streamwise component is the most energetic component and has a peak which moves slightly towards the wall with increasing curvature. The smaller turbulent kinetic energy content of the curved flows is to be expected since there is a smaller surface area over which vorticity fluctuations can be generated. However, the total production and total dissipation of turbulent kinetic energy per unit surface area for the three flows are similar Thus the cylinder surface is not less efficient as a source of turbulent kinetic energy; rather it has to supply a larger volume. The decrease of turbulence intensities with increasing δ/a is in agreement with several experiments (Lueptow *et al.* [1985, 1987] and Luxton *et al.* [1984]). In particular, for comparable a^+ (Luxton *et al.* [1984]), the maximum value of $\sqrt{v_z^2}/U_\infty \approx 0.16$ agrees well with experiments. However, for larger a^+ (Lueptow *et al.* [1987]) the maximum value of $\sqrt{v_z^2}/u_\tau$ is higher than in the flat plate, contrary to the current results.

For the axial flow over a cylinder, the stress equilibrium

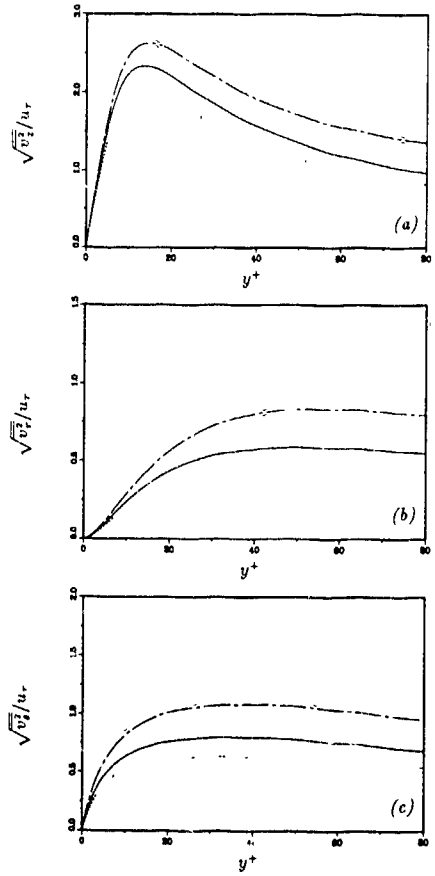

FIGURE 2 Root-mean-square velocity fluctuations normalized by u_τ: (a) Axial intensity, (b) Normal intensity, (c) Azimuthal intensity; —·— plane channel; cylinders with —— $\delta/a = 5$ and ---- $\delta/a = 11$

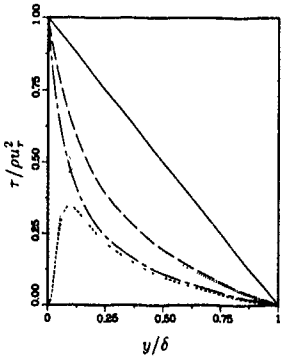

FIGURE 3 Total stress and Reynolds shear stress normalized by u_τ. Total stress. — plane channel, cylinders with — — $\delta/a = 5$ and —·— $\delta/a = 11$ Reynolds shear stress. cylinders with $\delta/a = 5$ and ---- $\delta/a = 11$.

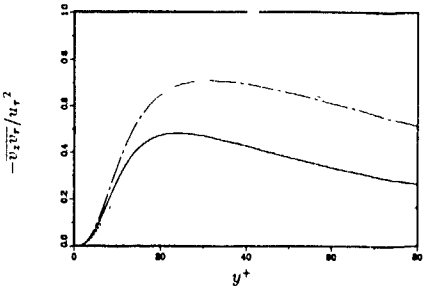

FIGURE 4 Reynolds shear stress normalized by u_τ cylinders with —— $\delta/a = 5$ and ---- $\delta/a = 11$; —·— plane channel

is given by the equation

$$-\overline{v_z^+ v_r^+} + \frac{d\overline{v_z^+}}{dy^+} = \frac{a(\delta - y)}{\delta(a + y)}\left(1 + \frac{y}{2a + \delta}\right), \qquad (1)$$

when scaled in wall variables The total stress and the Reynolds shear stress for the two simulations, as well as the equilibrium stress for a plane channel, are shown in Figure 3 Transverse curvature effects on the equilibrium stress are clearly evident.

As Figure 4 shows, the Reynolds shear stress is strongly reduced by curvature The location of the maximum of the Reynolds shear stress profile is a function of δ/a and moves towards the wall with increasing δ/a This trend, however, does not affect the position of the maximum of the production $(-\overline{v_z v_r} d\overline{v_z}/dy)$ of turbulent kinetic energy located at $y^+ \simeq 12$

3 3 *The Scaling*

The momentum balance in the axial direction expressed in equation (1) shows that, with transverse curvature, the total stress (τ) depends on the curvature parameter (δ/a).

Comparing this expression with the corresponding one for the plane channel, $\tau^+ = 1 - y/\delta$, suggests a new velocity scale $\overline{u} = u_\tau/\sqrt{F(y/\delta, \delta/a)}$, where

$$F(y/\delta, \delta/a) = \frac{a/\delta + y/\delta}{a/\delta}\left(1 + \frac{y/\delta}{1 + 2a/\delta}\right)^{-1} \qquad (2)$$

Note that F is a function of the parameter a/δ as well as the distance from the wall Also, in the flat plate limit, $\delta/a \to 0 \Rightarrow F(y/\delta, \delta/a) \to 1$, the planar result $(\overline{u} = u_\tau)$ is recovered

The axial turbulent intensity and Reynolds shear stress scaled by $\overline{u}$ are shown in Figure 5 The turbulent intensities and Reynolds shear stress collapse very well with this scaling However, the maximum of the production of turbulent kinetic energy (Figure 6*a*) is not well scaled Also, close to the wall $(y^+ < 20)$, the scaled dissipation of turbulent kinetic energy (Figure 6*b*) decreases with increasing curvature.

4. Flow Structures

The streamwise $(\sqrt{\overline{\omega_z^2}})$ and radial $(\sqrt{\overline{\omega_r^2}})$ vorticity intensities are shown in Figure 7. The minimum in $\sqrt{\overline{\omega_z^2}}$ occurs at the same location as in the plane channel and the local maximum becomes progressively weaker with increasing curvature. According to the interpretation of Kim *et al.* (1987), the attenuation of the local maximum of $\sqrt{\overline{\omega_z^2}}$ suggests that the curvature weakens the strength of the near

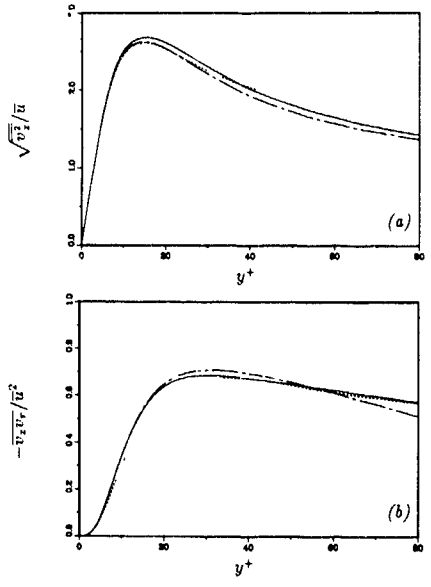

FIGURE 5 Axial turbulence intensity (a) and Reynolds shear stress (b) normalized by $\overline{u}$ cylinders with —— $\delta/a = 5$ and ---- $\delta/a = 11$, —·— plane channel

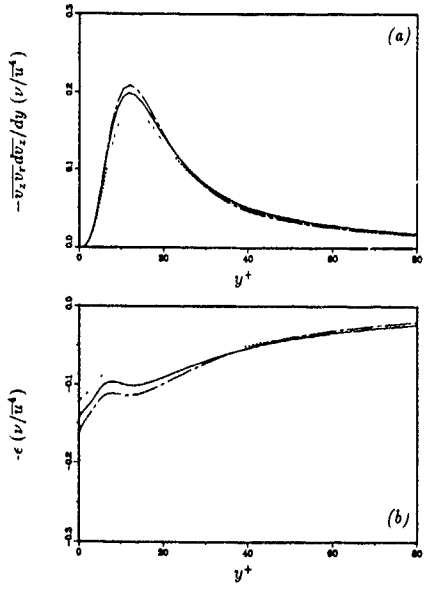

FIGURE 6. Production (a) and dissipation (b) of turbulent kinetic energy normalized by ν and $\overline{u}$: cylinders with —— $\delta/a = 5$ and ---- $\delta/a = 11$; —·— plane channel

wall streamwise vortices. In agreement with this $\sqrt{\overline{\omega_r^2}}$ has a maximum of decreasing magnitude slightly closer to the wall than in the plane channel.

The cylindrical geometry imposes a surface area limitation on the existence of the streamwise streaks, which are

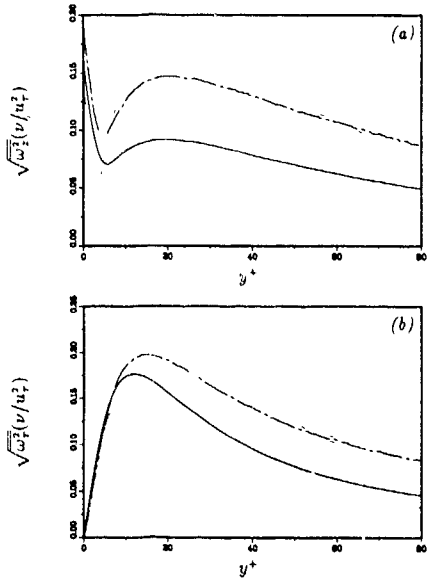

FIGURE 7 Axial (a) and normal (b) vorticity intensities normalized by u_τ and ν —·— plane channel; cylinders with —— $\delta/a = 5$ and ---- $\delta/a = 11$

FIGURE 8. Contours of azimuthal vorticity fluctuations (ω_θ'), normalized by u_τ and ν, on a cylindrical surface at $y^+ \approx 5$ (a) $\delta/a = 5$ (half of the computational domain); (b) $\delta/a = 11$ (third of the computational domain) The contour increment is 0.09 u_τ^2/ν and the positive contours, which correspond to the low speed streaks, are dotted The cylindrical surface is unwrapped.

observed to have a constant mean spacing (about 90-100 wall units) in the three simulations In the $\delta/a = 11$ case, less than two mean streak periods fit around the cylinder perimeter (137 wall units) This restriction is evident in the contours of ω_θ' at $y^+ \approx 5$, shown in Figure 8 At this location $\omega_\theta' \simeq -\partial v_z'/\partial r$, so the regions of positive ω_θ' correspond to the low speed streaks

Contours of ω_θ' on a surface parallel to the cylinder at $y^+ \simeq 10$ are shown in Figure 9. The boomerang-shaped structures evident in the figure are the outer part of shear layers that lift off from the cylinder They occur only when $y/\delta < 0.2$ and have large spanwise length scales (Figure 10), embracing as much as 180° around the cylinder The enhanced coherence of the flow relative to the plane channel flow is also evident from azimuthal views of ω_z' (Figure 11), which also show fewer large scale structures as the transverse curvature increases.

5. Conclusions

Two direct numerical simulations of turbulent flow over a

FIGURE 9 Contours of azimuthal vorticity fluctuations (ω_θ'), normalized by u_τ and ν, on a cylindrical surface at $y^+ \approx 10$: (a) $\delta/a = 5$ (half of the computational domain), (b) $\delta/a = 11$ (third of the computational domain) The contour increment is 0 08 u_τ^2/ν and the positive contours are dotted The cylindrical surface is unwrapped.

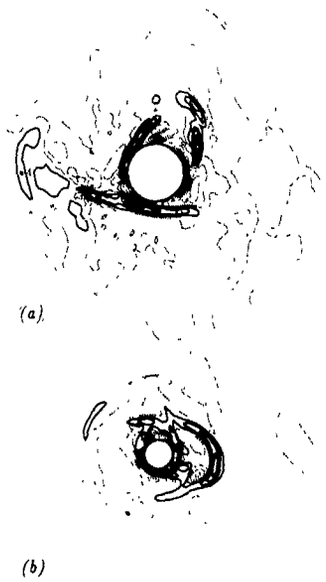

FIGURE 10 Contours of azimuthal vorticity fluctuations (ω_θ'), normalized by u_τ and ν, on an axial plane· (a) $\delta/a = 5$, (b) $\delta/a = 11$ The contour increment is 0 08 u_τ^2/ν and the positive contours are dotted

wire were conducted to investigate the effects of transverse curvature on turbulent boundary layers. The curvature parameters were $\delta/a = 5$ ($a^+ = 43$) and $\delta/a = 11$ ($a^+ = 21$)

Curvature affects the mean velocity profile in the viscous region as predicted from the near wall dynamical equilibrium, $a\tau_\omega = r\tau$ A deteriorated logarithmic-like layer with mild negative curvature was observed in experiments as well as in the simulations.

In agreement with experimental observations, the general effect of curvature is to decrease the levels of turbulence intensities. Close to the wall, turbulence statistics behave qualitatively like those of the plane channel This similarity suggests that the mechanisms of turbulence generation in the cylinder are the same as in the plane channel

A velocity scale, which reflects the effects of transverse curvature in the flow, was derived from the streamwise momentum equation. With this scaling the Turbulence intensities and the Reynolds shear stress collapse throughout the

FIGURE 11 Contours of axial vorticity fluctuations (ω_z'), normalized by u_τ and ν, on an axial plane (a) $\delta/a = 5$, (b) $\delta/a = 11$ The contour increment is 0.03 u_τ^2/ν and the positive contours are dotted.

layer Away from the wall ($y^+ > 20$), the production of turbulent kinetic energy collapses very well, however, its maximum close to the wall ($y^+ \simeq 12$) does not collapse The dissipation of turbulent kinetic energy does not collapse close to the wall ($y^+ < 20$), the range over which the viscous diffusion is also important. Thus, close to the wall the effects of curvature are not accounted for by the scaling alone

The streaks have a spanwise spacing similar to that of the plane boundary layers As the curvature increases, the near-wall streamwise vortices are weakened and the number of large scale structures is reduced Large, boomerang-shaped islands of ω_θ' with large spanwise length scale were observed around the cylinder surface These are several indications that the transversely curved flow is more organized than its planar counterpart

Acknowledgments

This work was sponsored by the Office of Naval Research under contract N00014-88-k-0145, and in cooperation with the Naval Underwater Systems Center, New London, Connecticut

REFERENCES

GLAUERT, M. B. & LIGHTHILL, M. J. 1955 The axisymmetric boundary layer on a long thin cylinder, *Proc Roy. Soc. A*, **230**, 188–195.

KIM, J , MOIN, P. & MOSER, R. 1987 Turbulence statistics in fully developed channel flow at low Reynolds number, *J Fluid Mech* , **177**, 133–166.

KLEISER, L , & SCHUMANN, U. 1981 Treatment of incompressibility and boundary conditions in 3-D numerical

spectral simulations of plane channel flows, *Proc. 3rd GAMM Conf. Numerical Methods in Fluid Mechanics, ed. by E.H. Hirschel (Viewveg, Braunschweig)*, 165-173

LUEPTOW, R. M., LEEHEY, P., & STELLINGER, T. 1985 The thick turbulent boundary layer on a cylinder: Mean and fluctuating velocities, *Phys. Fluids*, **28**, 3495-3505

LUEPTOW, R. M. & HARITONIDIS, J. H. 1987 The structure of the turbulent boundary layer on a cylinder in axial flow, *Phys. Fluids*, **30**, 2993-3005

LUEPTOW, R. M. 1988 Turbulent boundary layer on a cylinder in axial flow, *NUSC T.R. 8389*

LUXTON, R. E., BULL, M. K., & RAJAGOPALAN, S. 1984 The thick turbulent boundary layer on a long fine cylinder in axial flow, *Aero. J.*, **88**, 186-199

RAO, G. N. V. & KESHAVAN, N. R. 1972 Axisymmetric turbulent boundary layer in zero pressure gradient flows, *J. Appl. Mech. Trans. A.S.M.E.*, **94**, 25-32.

WILLMARTH, W. W. & YANG, C. S. 1969 Wall pressure fluctuations beneath turbulent boundary layer on a flat plate and a cylinder, *J. Fluid Mech.*, **41**, 47-80

WILLMARTH, W. W., WINKEL, R. E., SHARMA, L. K. & BOGAR, T. J. 1976 Axially symmetric turbulent boundary layers on cylinders: Mean velocity profiles and wall pressure fluctuations, *J. Fluid Mech.*, **76**, 35-64

EIGHTH SYMPOSIUM ON
TURBULENT SHEAR FLOWS
Technical University of Munich
September 9-11, 1991

THE STRUCTURE OF TURBULENCE IN A SIMULATED PLANE COUETTE FLOW

MOON JOO LEE†‡ AND JOHN KIM†

† *Center for Turbulence Research, Stanford University, Stanford, CA 94305, U.S.A. and MS 202A-1, NASA-Ames Research Center, Moffett Field, CA 94035, U.S.A.*
‡ Present Address *Department of Mechanical Engineering and Advanced Fluids Engineering Research Center, Pohang Institute of Science and Technology, Pohang 790-600, Korea*

Abstract

Turbulent plane Couette flow was numerically simulated at a Reynolds number ($U_w h/\nu$) of 6000, where U_w is the relative wall speed and h is half the channel-height. Unlike in Poiseuille flow, where the mean shear rate changes its sign at the centerline, the sign of mean shear rate in plane Couette flow remains the same across the whole channel. This difference is expected to yield several differences between the two flows, especially in the core region. The most significant and dramatic difference observed in the present work was the existence of large-scale structures in the core region of the plane Couette flow. The large eddies are extremely long in the flow direction and fill the entire channel (i.e. their vertical extent is $2h$). The large-scale structures have the largest contribution from the wavenumber $(k_x h, k_z h) = (0, \pm 1.5)$, corresponding to a wavelength $\Lambda_z/h \simeq 4$. The secondary motion associated with the $k_x h = 0$ mode consists of the large-scale vortices. The large eddies contribute about 30% of turbulent kinetic energy.

1. Introduction

Plane Couette flow is a paradigm of shear flows because of its simple flow geometry and fundamental fluid-mechanical characteristics. A fully-developed plane Couette flow has a constant shear stress, $\tau = \mu\, dU/dy - \rho\overline{uv}$ (equal to its value at the walls, $\tau_w = \mu\, dU/dy|_w$), across the entire channel, $-1 \le y/h \le 1$, be it laminar or turbulent. This prominent property results directly from the zero mean pressure gradient in the flow as it is driven by shear generated at two plane, solid boundaries that are in rectilinear, parallel movement (at speed U_w) relative to each other (see Figure 1).

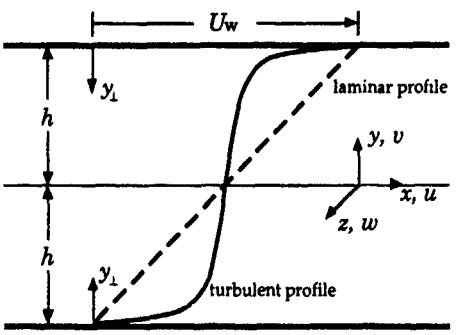

FIGURE 1 Schematic of the flow geometry of plane Couette flow. ——, mean velocity profile in a turbulent flow; ----, linear velocity profile in a laminar flow.

Another interesting characteristic of the flow is that both the mean vorticity (or mean shear rate, $S = dU/dy$) and turbulent shear stress ($-\rho\overline{uv}$) are symmetric about the center plane ($y/h = 0$), yielding a finite production rate ($-\rho S\overline{uv}$) of turbulent kinetic energy even in the core region (say, $0.2\text{-}0.5 \le y_\perp/h < 1$, where $y_\perp$ is the distance normal to a nearest boundary). As a consequence, the profiles of turbulence intensities ($\overline{u^2}$, $\overline{v^2}$, $\overline{w^2}$) differ significantly among the three components (see El Telbany & Reynolds 1982), indicative of a high degree of anisotropy in the flow. We hypothesize here that the structures of turbulence (both statistical and instantaneous) in the core region of plane Couette flow would be quite different from those of Poiseuille flow, which is driven by the pressure gradient. This issue has not been addressed before. In the vicinity of the walls, say $y_\perp/h \le 0.1\text{-}0.2$, however, structures of turbulence in the two flows are expected to be similar, since the near-wall dynamics of a turbulent shear flow is primarily controlled by a mechanism universally represented by the 'law of the wall.' Identification and characterization of the possible new structures in turbulent plane Couette flow is one of the central questions addressed in this study. It is our goal to understand the mechanism by which the shear arising from the boundary movement produces turbulence structures different from those generated in a pressure-driven flow.

Despite its apparent importance as a paradigm of shear flows, turbulent plane Couette flow has been very difficult to realize in a laboratory, and therefore it has not been studied extensively. In previous experiments (Reichardt 1956, 1959, Robertson 1959; Robertson & Johnson 1970, Leutheusser & Chu 1971, El Telbany & Reynolds 1980, 1981), the length of the shearing boundary realized by employing either a (flexible) moving belt or a fluid interface had to be made short ($L_B/h = 10\text{-}80$) since in most cases it is prone to deform at high speeds (or at high Reynolds numbers). Because of the difficulties arising from the moving boundaries, only the profiles of mean velocity, turbulent intensities and turbulent shear stress were obtained in most experiments, and measurements of higher-order turbulence statistics, if any, were limited to the streamwise direction or to the time domain (Robertson & Johnson 1970; Aydin & Leutheusser 1979, 1989). Direct numerical simulation approach taken in this work is ideally suited to study structures of turbulence in plane Couette flow without having such problems.

In this paper, we report the existence of the large-scale eddies in a numerically-simulated turbulent plane Couette flow. Some details of the kinematical characteristics of the kinematical characteristics of the large-scale structures are presented. Both the instantaneous and statistical structures of turbulence in the flow are compared with those in plane Poiseuille flow.

2. Numerical methods

A brief description of the numerical methods employed in the present work is presented here. The three-dimensional, unsteady Navier–Stokes equations were solved numerically for plane Couette flow at a Reynolds number ($\mathrm{Re} = U_w h/\nu$) of 6000; the Reynolds number $\mathrm{Re}_\tau = U_\tau h/\nu$ based on the wall-shear velocity $U_\tau = (\nu\, dU/dy|_w)^{1/2}$ is about 170. The particular choice of Re_τ was made so as to compare with the computation of plane Poiseuille flow by Kim, Moin & Moser (1987) conducted at a comparable Reynolds number $\mathrm{Re}_\tau = 180$. Note that the chosen value of the flow Reynolds number, Re, is higher than the reported critical Reynolds number, 1000.

The simulation reported in the present paper was carried out by using a pseudo-spectral method with Fourier and Chebyshev polynomial expansions in the horizontal (x, z) and vertical (y) directions, respectively. The spectral expansion of the main computation reported here had $128 \times 129 \times 192$ ($3\,170\,304$) modes in (x, y, z). In order to eliminate alias errors, the $\frac{3}{2}$-rule was employed in the horizontal directions, the $\frac{3}{2}$-rule was not employed in the vertical direction because of the incompatibility with the no-slip boundary codition at the wall. The resulting number of the collocation points was $192 \times 129 \times 288$ ($7\,133\,184$) in (x, y, z). No-slip condition was used at the walls, and periodic boundary conditions were used in the horizontal directions. The domain of the main computation has the streamwise and spanwise dimensions of $(B_x, B_z)/h = (4\pi, \frac{8}{3}\pi)$. Many other computations with different sizes of the computational domain were also carried out to ensure that the present choice of the domain size was the optimum choice (for details of this aspect, see §3).

The time advancement was made through a low-storage, third-order Runge Kutta method for the nonlinear terms and the second-order Crank–Nicolson scheme for the viscous terms. The initial field consisted of finite-amplitude random disturbances (about 10% of U_w) in all components of velocity with the linear mean profile, $U/U_w = \frac{1}{2}(y/h+1)$. Subsequent development of the basic statistics such as the mean velocity profile, turbulent kinetic energy and turbulent shear stress was monitored in order to determine whether the flow reached a statistical-steady state. The initial computation was started with a coarse resolution ($32 \times 65 \times 48$ modes), and when the flow reached a statistical-steady state the number of modes was successively increased. The final statistics were compiled after the flow reached the statistical-steady state with the final resolution, $128 \times 129 \times 192$ modes.

3. The large-scale structures

In this section, the existence of large-scale eddies in the core region of plane Couette flow is reported. Figure 2 shows contours of the instantaneous streamwise velocity (u) at the center plane ($y/h = 0$). There are two pairs of high- and low-speed regions (denoted by solid and dashed lines in the figure) that are highly elongated in the flow direction and alternating in the spanwise direction. Note that the eddies are almost uniform in the flow direction (i.e. the eddies do not meander sideways much). The spanwise size of each region as determined from inspection of the contours is about the channel-height ($2h$). In plane Poiseuille flow where the mean shear rate changes sign at the center plane, there are no such organized structures of turbulence in the core region. The spanwise (one-dimensional) energy spectrum, $\Theta_{uu}(k_z h)$, of the streamwise velocity (not shown here) has a distinctive peak at $k_z h = 1.5$, which corresponds to a wavelength $\Lambda_z/h \simeq 4$, consistent with the instantaneous contours shown in Figure 2.

The topological configuration of these structures may appear to be similar to that of the near-wall 'streaks'. However, the lengthscales, Λ_x and Λ_z, of these structures in the core region are much larger than those, λ_x and λ_z, of the streaks in the sublayer: $\Lambda_x^+ \simeq 5000$–7000, $\Lambda_z^+ \simeq 900$, $\lambda_x^+ \simeq 1000$ and $\lambda_z^+ \simeq 100$, where the superscript $+$ denotes a lengthscale made dimensionless by the viscous scale $\ell_v = \nu/U_\tau$ and the subscripts x and z denote the streamwise and spanwise directions, respectively. The wide difference in lengthscales suggests that the generating mechanism of these large-scale structures is different from that repsonsible for generating the wall-layer streaks.

A direct numerical simulation of a turbulent flow is meaningful only when the essential scales (both large and small) in the flow under consideration are properly represented by the computation. We have carried out many other computations with different sizes of the computational domain to make sure that the existence of the large-scale eddies such as those in Figure 2 is not an artifact of the limited streamwise extent, B_x, of the computational domain. It was a pleasant surprise to find that the large-scale structures still persist and are elongated in the flow direction to fill the computational domain with the alternating variation in the spanwise direction even when the streamwise dimension was extended up to $B_x/h = 1024\pi$! (Of course, in this case the 'small' scales were not properly resolved.) It was concluded that the presence of the *very-large-scale* eddies is a true characteristic peculiar to plane Couette flow. Therefore, it is obvious that a computation with a manageable number of modes (typically of the order of 100 in each direction) cannot represent both the

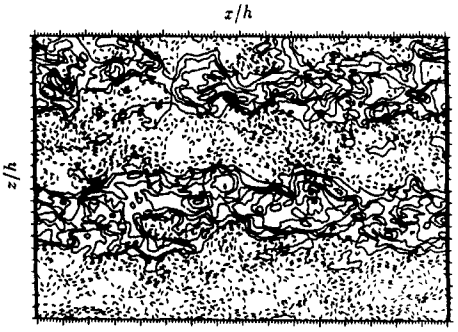

FIGURE 2. Contours of the instantaneous streamwise velocity (u) at the center plane ($y/h = 0$) of plane Couette flow: ——, $u \geq 0$; ----, $u < 0$. Each tick mark denotes the location of a grid point on the computational domain $(B_x, B_z)/h = (4\pi, \frac{8}{3}\pi)$.

largest eddies (of the order certainly greater than $1000h$) and the smallest dissipating eddies (of the order of h/Re_τ, which is about $0.005h$ in our case) simultaneously; the ratio of the two scales is as high as 200 000. We do not really have to include the largest scales in the computation, however, as long as the large-scale eddies contained in the computation are properly treated and the omitted larger scales do not affect the flow dynamics significantly. On the other hand, we must represent the finite, large scales in the wall layer (the sublayer streaks) whose lengthscale is $\lambda_x^+ \simeq 1000$, and they play the dominant

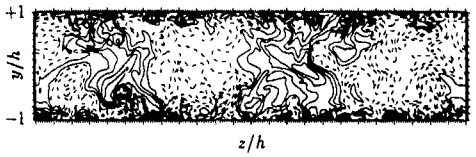

FIGURE 3 Contours of the instantaneous streamwise velocity (u) on a yz-plane (an end view) of plane Couette flow ——, $u \geq 0$, ----, $u < 0$ Each tick mark denotes the location of a grid point on the computational domain $(B_y, B_z)/h = (2, \frac{8}{3}\pi)$.

role in the dynamics of the flow Hence the present choice of $B_z/h = 4\pi$ is appropriate The spanwise extent $B_z/h = \frac{8}{3}\pi$ of the present computation was determined so as to contain two pairs of the large-scale eddies Note that the size of the eddies is not known *a priori* and the present choice of B_z/h was made by examining flow fields computed with much larger domain in the spanwise direction

To examine t' e vertical extent of the eddy structures, contours of instantaneous u are drawn on a yz-plane (an end view) in Figure 3 The figure shows that the eddies are as tall as the whole channel height, $2h$, and hence the aspect ratio of the large eddies is close to unity In the wall region, however, the presence of eddies of much smaller lengthscales is evident. These small wall-region eddies are identical to those found in the wall region of a plane Poiseuille flow (cf. Kim *et al.* 1987)

The two-dimensional energy spectrum, $\Phi(k_x h, k_z h) = \overline{|\hat{u}|^2}$, at $y/h = 0$ (Figure 4) shows that the energy density has two distinctive peaks at $(k_x, k_z)h = (0, \pm 1.5)$; their magnitude is

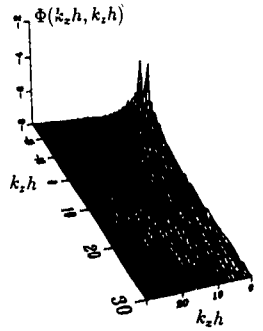

FIGURE 4. Distribution of the two-dimensional energy spectrum $\Phi(k_x h, k_z h) = \overline{|\hat{u}|^2}$ at the center plane ($y/h = 0$) of plane Couette flow, showing that the energy density has two distinctive peaks at $(k_x, k_z)h = (0, \pm 1.5)$. Note that the magnitude of the peaks is about seven times larger than the next largest contribution.

about seven times the next largest contribution. This dominant contribution of the $(k_x, k_z)h = (0, \pm 1\ 5)$ mode persists even close to the walls (the ratio is about three at $y_\perp/h = 0\ 001$), indicating that the large eddies have a significant effect across the whole channel.

To further investigate the characteristics associated with the large eddies, we decompose the flow field as $\mathbf{v} = \mathbf{U} + \tilde{\mathbf{v}} + \mathbf{v}'$, where the field $\tilde{\mathbf{v}} = (\tilde{u}, \tilde{v}, \tilde{w})$ is obtained by averaging over t and x and subtracting the mean value, $\mathbf{U}$, averaged over t, x and z, and $\mathbf{v}'$ denotes the residual field The $\tilde{\mathbf{v}}$ field represents the eddy motion independent of time and the streamwise direction (i e., time-averaged $k_x = 0$ mode), and hence it may be called the large-eddy motion.

Contours of $\tilde{u}$ in the yz-plane (perpendicular to the mean flow) are shown in Figure 5(a) The lengthscales associated with these large eddies are now more apparent; statistical correlations associated with these eddies will be discussed in the next section. Note that the small-scale eddies that are quite strong in the instantaneous field (see Figure 3) are not present in the time-averaged $k_x = 0$ mode any more.

In Figure 5(b), the velocity vectors, $(\tilde{v}, \tilde{w})$, projected on the yz-plane (an end view) show that there exists a secondary motion in the core part of the channel and that the secondary flow consists of large-scale vortices that fill the entire channel (For visual clarity, every fourth data points in the both directions were selected for the vector plot) Because of the large lengthscale of the secondary motion, the magnitude of its streamwise vorticity in the core region is only a few percent of the shear rate at the wall.

In order to compare the magnitude between the velocity components, the profiles of velocities are shown in Figure 6 as a function of the spanwise distance at various selected vertical locations Figure 6(a) shows how smooth the variation of the streamwise component is with the spanwise distance The wavy profile dominates the whole channel except near the walls, and the amplitude of the predominant wave is as large as about 10% of the relative wall speed, U_w The waviness of the vertical component in Figure 6(b), however, is confined in the core region only, and there is a rapid attenuation when the walls are approached. The maximum amplitude of the vertical component is about 1 5% of U_w The high correlation (180° out of phase) between the streamwise and vertical components

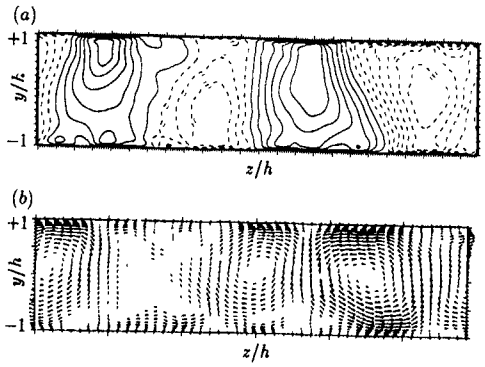

FIGURE 5 Velocity field of the time-averaged $k_x = 0$ mode (or the large-eddy field) in plane Couette flow· (a) contours of $\tilde{u}$ in the yz-plane (perpendicular to the mean flow), where ——, $\tilde{u} \geq 0$, ----, $\tilde{u} < 0$, (b) velocity vectors, $(\tilde{v}, \tilde{w})$, projected on the yz-plane.

in the core region gives rise to a substantial contribution to the Reynolds stress, $-\rho\,\overline{\tilde{u}\tilde{v}}$, from the large-eddy motion (see §4) The profiles of the spanwise velocity in Figure 6(c) shows that the spanwise component is almost antisymmetric about the center plane, $y/h = 0$ (cf Figure 5b), and that the variation is quite strong even near the walls The maximum amplitude of the spanwise component is about 2% of U_w. Comparison with the profiles of the other components reveals that the spanwise component is 90° out of phase with the others, leading to the

secondary flow of roll-cell type shown in Figure 5(*b*)

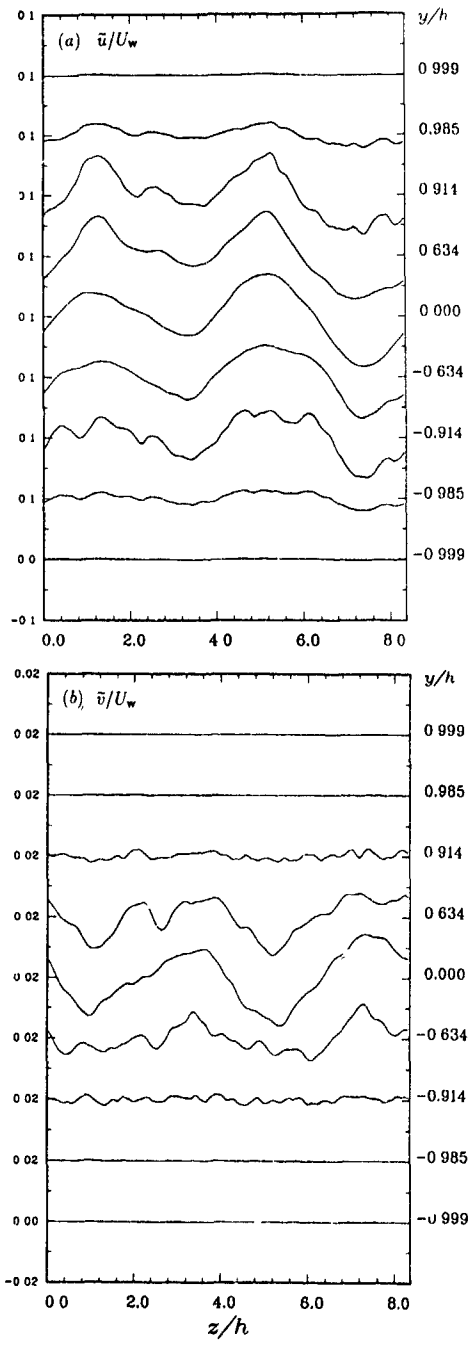

FIGURE 6 Profiles of the velocity components of the time-average $k_z = 0$ mode as a function of the spanwise distance at various vertical locations (*a*) $\tilde{u}(z/h, y/h)$; (*b*) $\tilde{v}(z/h, y/h)$; (*c*) $\tilde{w}(z/h, y/h)$.

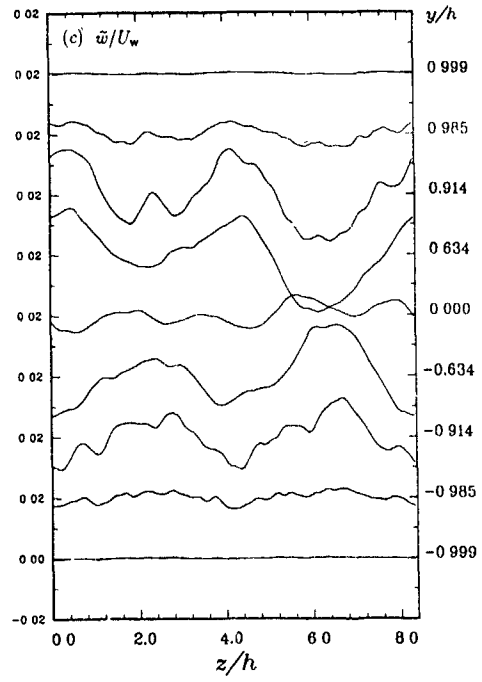

4. Statistics

In Figure 7(*a*), comparison of the mean velocity profile, U, is made between the computation and experiments conducted at different Reynolds numbers (Re = 2900, Reichardt 1959, Re $\simeq 2\times10^4$-4×10^4, El Telbany & Reynolds 1980) Note that the velocity profile at high Reynolds numbers changes rapidly within the narrow region close to the walls (say, $y_\perp/h \leq 0\,1$), and that it has a seemingly constant slope in the core region ($|y/h| \leq 0.5$). The mean velocity gradient at the walls, $S_w = dU/dy|_w$, grows substantially with Reynolds number, whereas at the center plane the slope, $S_c = dU/dy|_{y/h=0}$, decreases with increasing Reynolds numbers The value of S_c is about 5% of the wall value (the total stress) and it is about 30% of the value in an equivalent laminar flow with a linear velocity profile Thus, the total shear stress in the turbulent case is about ten times higher compared with the laminar value

The near-wall profile, U^+ (made dimensionless by the wall-shear velocity, U_τ), *vs* y^+ (the distance normal to the nearest wall scaled by the viscous length, $\ell_\nu = \nu/U_\tau$) is shown in Figure 7(*b*) The dashed and dotted lines denote the law of the wall: $U^+ = y^+$ and $U^+ = (1/\kappa)\ln y^+ + B$ (where $\kappa = 0\,4$ and $B = 5.5$), respectively, which fits the experimental data at a higher Reynolds number (El Telbany & Reynolds 1980)

Figure 8 shows the profiles of turbulent and total shear stresses across the channel. The shear stresses are symmetric about $y/h = 0$, and the uniformity of the total shear stress ($\tau/\tau_w = 1$) is apparent, indicating that the flow has indeed reached a statistical-steady state. Near the walls, the turbulent stress ($-\rho\overline{uv}/\tau_w$) increases rapidly with the distance from the wall. (Hence, the mean shear rate, $dU/dy = (\tau + \rho\overline{uv})/\mu$, decreases rapidly in the same vicinity of the walls) In the core

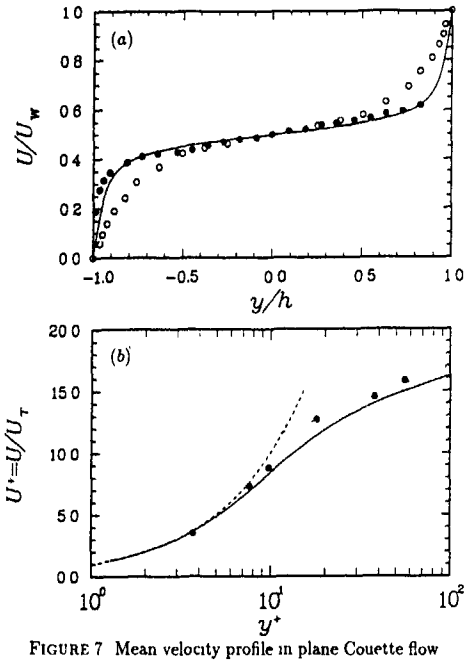

FIGURE 7 Mean velocity profile in plane Couette flow (*a*) global profile, U/U_w *vs.* y/h; (*b*) near-wall profile, U^+ *vs* y^+ ——, present simulation, ○, Reichardt (1959), ●, El Telbany & Reynolds (1980), ----, $U^+ = y^+$; ····, $U^+ = (1/\kappa)\ln y^+ + B$ ($\kappa = 0.4$ and $B = 5.5$)

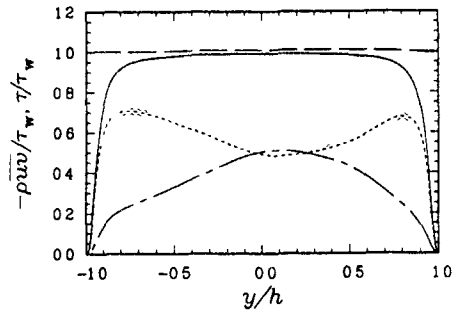

FIGURE 8 Profiles of shear stresses in plane Couette flow —·—, total shear stress (τ/τ_w); ——, Reynolds stress ($-\rho\overline{uv}$) of the full field; — — —, Reynolds stress of the $k_x = 0$ mode, ----, Reynolds stress of the residual field.

region, the total shear stress is completely dominated by the turbulent stress and the viscous stress is only a few percent

It is of interest to examine how much the large-scale eddies contribute to energetics In Figure 8, the contributions to the Reynolds stress from the large-scale eddies and residual field are drawn. The contribution from the large eddies increases with the distance from the wall and at the center line it is about the same as that from the residual field Therefore, the production rate, $-(dU/dy)\overline{uv}$, in the core region has a substantial contribution from the large-scale eddies.

Figure 9 compares the contributions to turbulent kinetic energy from the full, large-eddy and residual fields. Except

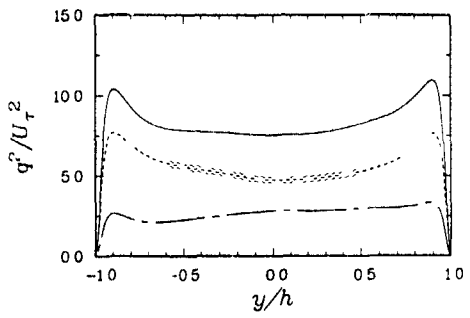

FIGURE 9 Profile of turbulent kinetic energy in plane Couette flow ——, q^2 of the full field, — — —, q^2 of the $k_x = 0$ mode, ----, q^2 of the residual field

in the vicinity of the wall (say $y_\perp/h \leq 0.1$), the contribution from the large eddies is about 30% over the whole channel, indicative of the importance of the large-scale eddies in energetics.

The profiles of turbulence intensities (u'^+, v'^+, w'^+) in Figure 10(*a*) show good agreement with the measurements (El Telbany & Reynolds 1981) at a higher Reynolds number The profiles are almost constant in the core region, suggesting the existence of homogeneous, stationary turbulence states

Comparison with those in a plane Poiseuille flow (Figure 10*b*) at a comparable Reynolds number ($Re_\tau = 180$, Kim *et al.* 1987) shows that the intensities in Couette flow are significantly higher at most locations in the channel, except in the vicinity of the wall ($y^+ \leq 30$) where the Couette values are

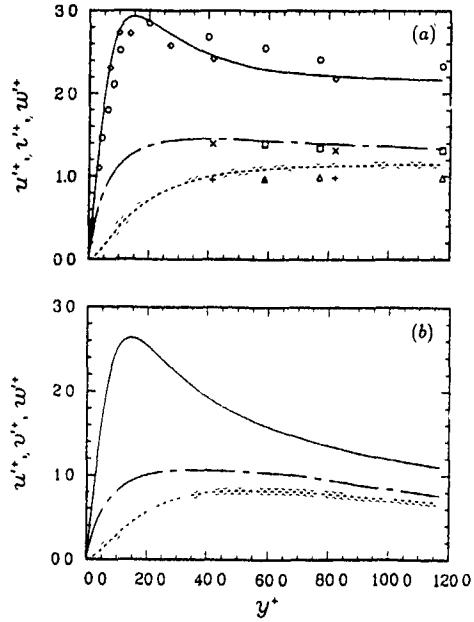

FIGURE 10 Near-wall profiles of turbulence intensities, (u'^+, v'^+, w'^+) *vs* y^+. (*a*) plane Couette flow (present computation), (*b*) plane Poiseuille flow (from Kim *et al.* 1987). ——, u'^+; ----, v'^+; — — —, w'^+ Symbols are the measured data from El Telbany & Reynolds (1981)

only slightly higher The marked difference in the core region is a direct consequence of the finite rate of production of turbulent kinetic energy in plane Couette flow The figure also shows that in the core region the distribution of turbulent kinetic energy among the three components is more anisotropic in Couette flow ($\overline{u^2}$ $\overline{v^2}$ $\overline{w^2}$ $\simeq$ 0 61 . 0 17 · 0 22) than in Poiseuille flow

5. Summary and concluding remarks

Direct numerical simulation of turbulent plane Couette flow at Reynolds number of 6000 was carried out. Examination of the instantaneous and statistical structures revealed the existence of large-scale eddies in the flow The large-scale structures have a extremely long lengthscale in the flow direction and they fill the entire channel They appear as pairs of high- and low-speed regions alternating in the spanwise direction with an average lengthscale of $2h$ so that their aspect ratio is about unity The (x, t)-averaged field shows the existence of secondary vortical motion that fills the entire channel

It has been known that existing turbulence models based on two-dimensional flows have a difficulty in predicting structures of 'three-dimensional' flows such as curved channel flow and rotating channel flow. Despite the flow geometry of these flows is two-dimensional, large secondary flows develop and play a dominant role because of instabilities associated with centrifugal (curved channel) or Coriolis (rotating channel) force. Plane Couette flow does *not* have such instability, but similar large roll-cell-like structures exist in the core region as evidenced in the present work. Therefore, it would be of great interest to see how well the current turbulence models predict the behavior of turbulence in plane Couette flow.

Because turbulent plane Couette flow has uniform shear stress across the channel, there has been an intrinsic interest in the flow from the modeling point of view (Von Kármán, 1937, Henry & Reynolds, 1984, Schneider, 1989. Kim & Gibson, 1989). Kim & Gibson (1989), based on an algebraic-stress model analysis using data of El Telbany & Reynolds (1982), hypothesized that there exists counter-gradient diffusion of turbulence energy from the center of the flow towards the walls. This interesting idea has not been resolved for the lack of measurements of the triple-velocity correlations. In the present work we have computed such data, and we shall address this important issue in a subsequent paper

We have also compiled a variety of turbulence statistics such as all the terms in the transport equations of the Reynolds stresses and the probability density functions (and skewness and flatness) of velocity and vorticity components, etc These and comparison with those in plane Poiseuille flow will be discussed in full later

This work was performed while the first author (MJL) was at the Center for Turbulence Research, Stanford University and NASA-Ames Research Center during 1989-1990 We thank Parviz Moin and Javier Jimenez for the fruitful discussions. This work was supported in part by the National Science Foundation and the computer time was generously provided by the NASA-Ames Research Center, for which MJL is grateful The writing of this paper was supported in part by the Department of Mechanical Engineering and Advanced Fluids Engineering Research Center (AFERC), Pohang Institute of Science and Technology (Postech)

REFERENCES

AYDIN, M & LEUTHEUSSER, H J 1979 Novel experimental facility for the study of plane Couette flow *Rev Sci Instr* **50**, 1362-1366

AYDIN, E M & LEUTHEUSSER, H. J 1987 Experimental investigation of turbulent plane-Couette flow *Forum on Turbulent Flows-1987*, FED vol 51, 1987 ASME Applied Mech , Bioeng & Fluids Eng Conf , Cincinnati, Ohio, June 14-17, 1987 (ed W. W Bower), pp. 51-54 Amer Soc Mech Eng.. New York, New York

AYDIN, E M & LEUTHEUSSER, H J 1989 Plane-Couette flow between smooth and rough walls *J Fluid Mech* (*sub judice*)

EL TELBANY, M M M & REYNOLDS, A J 1980 Velocity distributions in plane turbulent channel flows *J Fluid Mech* **100**, 1-29

EL TELBANY, M. M. M & REYNOLDS, A J 1981 Turbulence in plane channel flows *J Fluid Mech* **111**, 283-318

EL TELBANY, M M M. & REYNOLDS, A J 1982 The structure of turbulent plane Couette flow *Trans ASME, J Fluids Eng.* **104**, 367-372.

HENRY, F. S. & REYNOLDS, A. J. 1984 Analytical solution of two gradient-diffusion models applied to turbulent Couette flow *Trans ASME, J Fluids Eng* **106**, 211-216

KIM, J , MOIN, P & MOSER, R D 1987 Turbulence statistics in fully developed channel flow at low Reynolds number *J Fluid Mech* **177**, 133-166

KIM, K Y & GIBSON, M M 1989 On modelling turbulent Couette flow. *Seventh Symp. on Turbulent Shear Flows· Open Forum Abstracts*, Stanford University, Stanford, California, Aug 21-23, 1989 (ed. F. Durst *et al.*), pp. T8 1.1-T8.1 2.

LEE, M J 1990 The large-scale structures in turbulent plane Couette flow *Center for Turbulence Research Annual Research Briefs-1989*, pp 231-245 Center for Turbulence Research, Stanford University and NASA-Ames Research Center Stanford, Calif

LEE, M J. 1991 Direct numerical simulation of turbulent plane Couette flow *Center for Turbulence Research Annual Research Briefs-1990*, pp 133-143 Center for Turbulence Research, Stanford University and NASA-Ames Research Center Stanford, Calif.

LEE, M J.,· KIM, J. & MOIN, P. 1990 Structure of turbulence at high shear rate *J. Fluid Mech* **216**, 561-583.

LEUTHEUSSER, H J & CHU,· V H 1971 Experiments on plane Couette flow *Proc ASCE, J Hydr Div* **97** (HY9), 1269-1284.

REICHARDT, H. 1956 Über die Geschwindigkeitsverteilung in einer geradlinigen turbulenten Couetteströmung *Zeit angew. Math Mech* **36**, Sonderheft 26-29

REICHARDT, H 1959 Gesetzmäßigkeiten der geradlinigen turbulenten Couetteströmung *Mitteil.* Nr 22 Max-Planck-Inst Strömungsforschung und Aerodynamischen Versuchsanstalt: Göttingen, Germany.

ROBERTSON, J. M. 1959 On turbulent plane-Couette flow *Proc. Sixth Midwestern Conf. Fluid Mech.*, Univ. of Texas, Austin, Texas, Sept 9-11, 1959, pp. 169-182

ROBERTSON, J M & JOHNSON, H. F. 1970 Turbulence structure in plane Couette flow *Proc. ASCE, J. Eng. Mech. Div* **96** (EM6), 1171-1182

SCHNEIDER, W 1989 On Reynolds stress transport in turbulent Couette flow *Z Flugwiss. Weltraumforsch* **13**, 315-319.

VON KÁRMÁN, TH 1937 The fundamentals of the statistical theory of turbulence *J. Aeronaut Sci* **4**, 131-138.

EIGHTH SYMPOSIUM ON
TURBULENT SHEAR FLOWS
Technical University of Munich
September 9-11, 1991

5-4

On the Mechanics of 3-D Turbulent Boundary Layers

By Olav Sendstad and Parviz Moin

Department of Mechanical Engineering, Stanford University, Stanford, CA 94305

ABSTRACT

The effect of an impulsively started transverse pressure gradient on turbulence structures in a planar channel flow was studied using direct numerical simulation. In agreement with experiments, the simulation shows a reduction in the Reynolds shear stress. It also shows a drop in the turbulent kinetic energy. These effects were found to be related to the break-up of the near-wall velocity streaks. The streamwise vortices are convected in the spanwise direction, breaking the original streak structures as they cross over them. It was also found that the vortices with the same sign as the developing mean streamwise vorticity were weakened.

INTRODUCTION

Several experiments have shown a reduction of the Reynolds shear stress when two-dimensional (2-D) turbulent boundary layers are turned by a transverse pressure gradient [1,2,3]. This result is somewhat surprising, since it can be argued that the cross flow would add energy to the flow. Turbulence models most commonly used in 2-D flows do not predict these reductions. This effect cannot be accounted for by coordinate rotation, since many experiments have shown a drop in the invariant structure parameter, $a_1 = \frac{\sqrt{\overline{u'v'}^2 + \overline{v'w'}^2}}{2q}$, where u', v', w' are the velocity fluctuations in the x, y, z directions respectively, and q is the turbulent kinetic energy. The reductions must therefore be caused by changes in the structure of the turbulence. Turbulence in boundary layers contain eddies with long lifetimes which have been found important in the generation of Reynolds shear stress and turbulent kinetic energy [4]. Direct numerical simulation makes it possible to study the dynamics of these eddies in detail. This paper describes how, when subjected to a spanwise pressure gradient, the eddies are changed so as to reduce the turbulent kinetic energy, the Reynolds shear stress and other statistical quantities.

NUMERICAL SIMULATION

The numerical method and the 2-D initial data for this study are the same as those described in Kim, Moin and Moser [5]. This computer program simulates a fully developed turbulent flow between two parallel plates (see Figure 1). The flow is homogeneous in the horizontal (x, z)-planes where a Fourier expansion is used to represent the flow variables. A Chebychev expansion is used in the direction normal to the walls. The Reynolds number based on the channel half-width δ and the 2-D centerline velocity is 3200, and the number of dealiased modes is (128x129x128).

At time zero, a spanwise pressure gradient is imposed on a flow field from a statistically 2-D channel flow. The flow passes through a transient before its mean flow eventually relaxes back to 2-D in a new direction. It is the transient period we are interested in. The spanwise pressure gradient

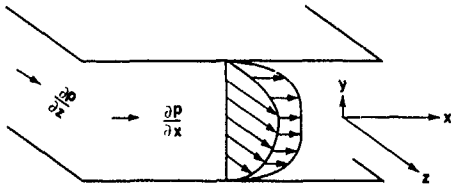

FIGURE 1 Schematic of three-dimensional channel flow

is $10\frac{\tau_w}{\delta}$ where τ_w is the wall shear stress for the 2-D channel flow. The spanwise pressure gradient and the mass flow in the x-direction are kept constant. Additional computations were performed in the minimal channel of Jimenez and Moin [6]. The minimal channel is a channel flow for which the computational box is the smallest possible that can maintain turbulence. It contains only one or two dominating structures and therefore provides a much simpler setting to analyse the flow dynamics.

EVOLUTION OF STATISTICAL QUANTITIES

A detailed description of the evolution of turbulence statistics for the 3-D channel flow is given in Moin et al. [7]. The changes in first- and second-order statistics are outlined below.

All statistics were obtained using averages in x and z directions and ensemble averages of 9 realizations. All velocities are normalized by u_τ, the shear velocity of the 2-D channel flow, and length scales are non-dimensionalized by the channel half width δ.

The mean velocity in the spanwise direction, W will grow linearly in time outside a Stokes layer near the wall; the wall is the source of *mean* streamwise-vorticity, $\overline{\omega_x}$. At early times, the spanwise boundary layer grows like the corresponding laminar boundary layer. The stronger $\frac{\partial p}{\partial z}$, the longer it takes before W deviates considerably from the laminar profile.

In spite of a constant mass flow in the x-direction, the streamwise component of the mean wall stress, $\overline{\tau_x}$, is reduced by about 8 percent. The mean streamwise velocity ,U, is reduced throughout the viscous sublayer. Farther out, U is slightly larger in the 3-D case maintaining the constant mass flux.

The drop in turbulent kinetic energy is mostly caused by a reduction of the root-mean-square (rms) of u' (see Figure 2). The rms of v' is slightly reduced as well, while the rms of w' rises as W builds up. Except in the viscous sublayer, the vorticity component most affected is the vertical component ω_y (see Figure 3). It's rms is reduced across the boundary layer, with maximum reduction around $y^+ = 15$ where it

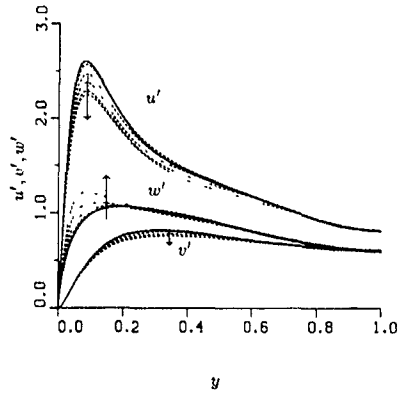

FIGURE 2 Root-mean-square of the 3 fluctuating velocity components. ——— : 2-D flow, 3-D flow $\Delta t = 0.15\delta/u_\tau$ between each curve

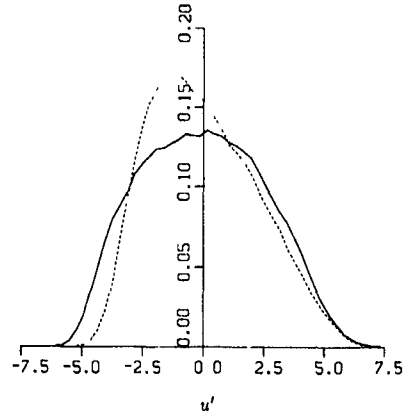

FIGURE 4 Probability density function for u' at $y^+ \simeq 10$. ——— : 2-D flow; : 3-D flow $t = 0.6u_\tau/\delta$ after $\frac{\partial p}{\partial z}$ is imposed.

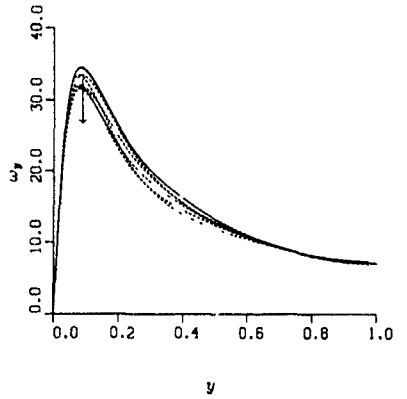

FIGURE 3. Root-mean-square of the vorticity component normal to the walls. ——— 2-D flow, 3-D flow $\Delta t = 0.15\delta/u_\tau$ between each curve.

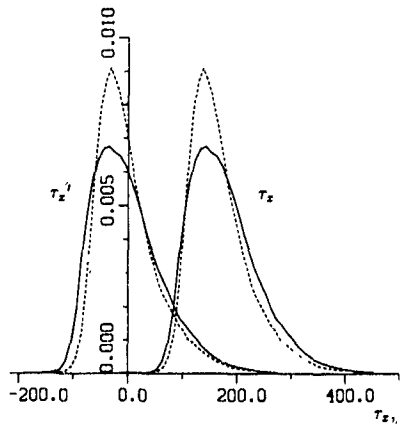

FIGURE 5. Probability density function for τ_z and fluctuating τ_z ——— : 2-D flow, 3-D flow $t = 0.6u_\tau/\delta$ after $\frac{\partial p}{\partial z}$ is imposed.

has its maximum Note that ω_y is invariant to a coordinate rotation parallel to the walls. In the viscous sublayer, the rms of ω_x' grows with growing τ_z (spanwise wall stress) and the rms of ω_z' is reduced.

The reduced statistical quantities will reach a minimum before they recover toward a new steady state. The time at which the minimum is reached, vary for different statistical quantities between t= 0 6 δ/u_τ and 1.1 δ/u_τ

PROBABILITY DENSITY FUNCTIONS

Probability density functions (PDFs) are useful in relating changes in statistical quantities with changes in turbulence structures. By comparing the PDFs for the 2-D and 3-D flows, we can determine the range of values in a flow variable that have been most affected It is then possible to search the instantaneous flow fields for these values and examine the events that create them in the 2-D and the 3-D cases.

The changes in the turbulent kinetic energy were found to be mainly caused by changes in the rms of u'. The PDFs of u' (see Figure 4) show that its rms is reduced because the most intensely negative u' events have become less intense, whereas for positive u' there are smaller reductions, but over a wider range. This is true at all locations across the boundary layer. Rms of $omega_x'$ is reduced in the same manner since in the viscous sublayer, $\omega_x' \simeq -u'y$.

The reduction of high u-events is more pronounced than is indicated by the PDFs of u'. This is especially true in the viscous sublayer, where the change in U is considerable The change in the total streamwise velocity is given by the PDF of u. To get the PDF of u', the PDF of u is shifted U units to the left Since near the wall U is smaller in the 3D case, the 3D PDF is not shifted as far as the 2D PDF. This accounts for the significant weakening of high-speed events which is not pronounced in the PDF of u' changes for low-speed events appear more pronounced This is clearly

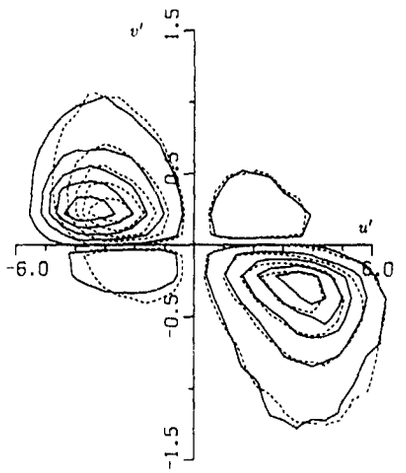

FIGURE 6 Weighted joint probability density function for u' and v' at $y^+ = 10$ —— 2-D flow; 3-D flow t= 0 $6u_\tau/\delta$ after $\frac{\partial p}{\partial z}$ is imposed.

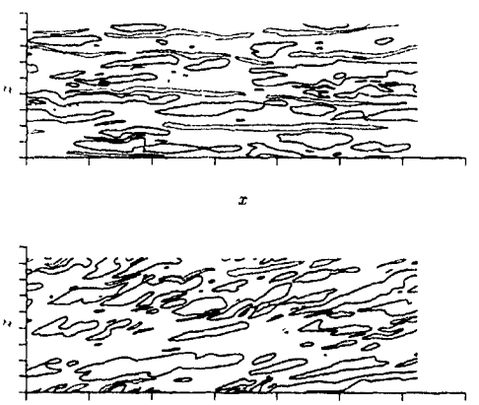

FIGURE 7 Contours of u'-values at $y^+ = 10$ (a) 2-D flow, and (b) 3-D flow t = 0 $6u_\tau/\delta$ after $\frac{\partial p}{\partial z}$ is imposed. u' = -3.5 ( ) and 2 0 (——)

seen in figure 5, which shows the PDFs of τ_x and τ_x' The reduction of the streamwise component of the mean wall stress, $\overline{\tau_x}$, is due to a reduction in the high velocity events

The PDF of ω_y also displays a reduction of the most intense values This alteration is consistent with changes in the structure of the streaks, since the affected values of ω_y are found along the borders between high-speed and low-speed streaks where high values of $\frac{\partial u}{\partial z}$ are found

The weighted joint PDF for u' and v' shows (see Figure 6) that the reduction in the Reynolds shear stress is mostly caused by a weakening of ejections (second quadrant) The changes are consistent with the PDF of u' : the ejections are weakened because the most intensely negative u' have disappeared while the sweeps (fourth quadrant) are weakened in the middle of the range of positive u'

Figure 7 shows the contours of the affected values of u'

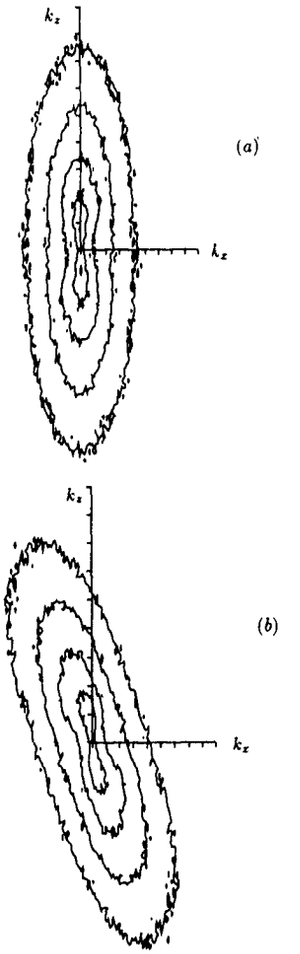

FIGURE 8 Energy spectrum E_{11} at $y^+ = 10\,5$ for (a) 2-D flow, (b) 3-D flow t = $0.6\delta/u_\tau$ after $\frac{\partial p}{\partial z}$ is imposed Contour levels $10^{-1}, 10^{-2}, 10^{-3}, 10^{-4}$.

(obtained from the PDFs of u' in Figure 4) in a 2-D and a 3-D flow field The contours are quite elongated, which indicates that the changes have occured within the wall layer streaks. The low-speed streaks are longer and narrower than the high-speed streaks This is fairly independent of the contour levels chosen to highlight the streaks In the 3-D channel flow, both the low- and the high-speed streaks become shorter

CHANGES IN THE STRUCTURES

The energy spectrum of u,

$$E_{11} = < \hat{u}(k_x, k_z, y)\hat{u}^*(k_x, k_z, y) >$$

where $\hat{u}$ is the Fourier transform of u, $\hat{u}^*$ is the complex conjugate of $\hat{u}$ and k_x and k_z are the wave numbers in the streamwise and the spanwise direction respectively, shows the turning of the structures with the flow (see Figure 8)

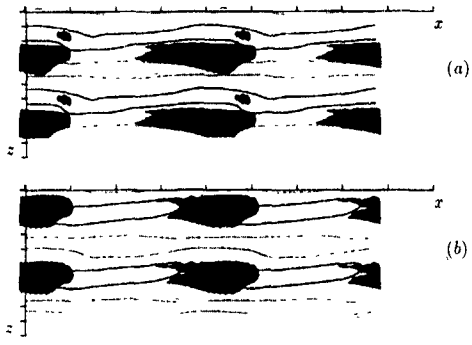

FIGURE 9 Top view of streamwise vortices above the wall stress. ——: high τ_x, . low τ_x. (a) 2-D flow; (b) 3-D flow with spanwise flow in the positive z-direction Both flow fields were initialized from a 2-D minimal channel at t= $0.125\delta/u_\tau$ earlier

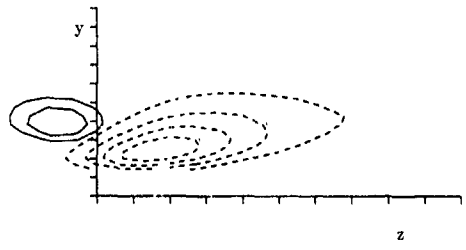

FIGURE 10 Conditionally averaged ω_x conditioned on high wall stress at the origin t = 0.6 u_τ/δ after $\frac{\partial p}{\partial z}$ is imposed.

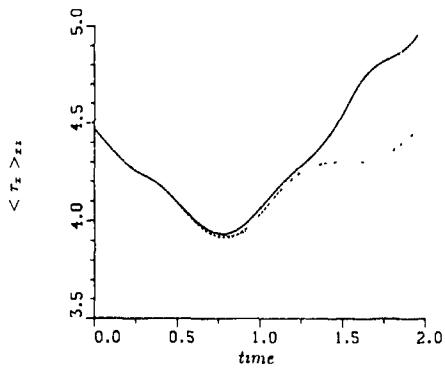

FIGURE 11 Wall stress evolution in the minimal channel —— 2-D flow, ---- 3-D flow with negative $\frac{\partial p}{\partial z}$, 3-D flow with positive $\frac{\partial p}{\partial z}$;

It can also be seen that the largest structures (inner contours) have turned less than the smaller ones The largest structures are affected by the outer part of the flow, which has turned less. Moreover, the smaller structures may have been created after the imposition of the pressure gradient

The rms of ω_x fluctuations have a local maximum around y^+=20. It has been found that contours of ω_x fluctuations of magnitude twice the value of this local maximum are fairly reliable detectors of streamwise vortices Examination of the instantanous flow fields clearly shows that the streamwise vortices turn when the spanwise boundary layer grows to their height above the wall.

Before the vortices start turning, they are convected sideways in the spanwise direction In the 2-D minimal channel streamwise vortices can be found between low-speed and high-speed streaks This is seen in Figure 9a, where the dominant vortex is shown with contours of the wall stress below it. The weaker vortex of oppposite sign is not included for clarity Note that the flow field has been extended four fold using the periodic boundary conditions in x and z directions The sense of rotation of the streamwise vortex shown is such that it pumps high-speed fluid down into the high-speed streak and lifts low-speed fluid up from the low-speed streak When the spanwise mean flow is developed, the vortices are shifted in the spanwise direction relative to the near-wall streaks They then pump high-speed fluid down into the low-speed streak and up from the high-speed streak Both streaks are thus weakened. This is seen in Figure 9b, which is the flow corresponding to 9a, but with a spanwise flow in positive z-direction imposed t=0.125 δ/u_τ earlier.

In the "natural" channel (as opposed to the minimal channel), the distribution of vortices is more chaotic, but their average location is the same as in the minimal channel. The conditionally averaged field of ω_x' conditioned around high wall stress events in the natural channel flow is shown in Figure 10. It is clear that a spanwise shift has occured The corresponding plot conditioned on low wall stress shows a similar shift.

Figure 10 also shows that there are differences in the evolution of vortices with positive and negative signs. The vortices with the same sign as the generated $\overline{\omega_x}$ are weakened This effect also appears in the minimal channel. Figure 11 shows the time evolution of the wall stress for the 2-D flow and two cases of 3-D flow . flow turning in the positive- and negative z-directions. Only a small portion of the intermittant evolution of $< \tau_x >_{xz}$ is shown (see Figure 6 of Jimenez and Moin). The spanwise pressure gradient is imposed at the starting point of the curves. In the case which sets up a streamwise mean vorticity with the same sign as the dominant vortex present at that time, the vortex disintegrates faster causing a lower wall stress Both 3-D cases have a weaker wall stress than the 2-D case, because both experience the shift effect.

Later the vortices start turning Computer animation shows that the streaks are broken as the vortices cross over them. Streaks begin to be formed in a new direction and the turbulent kinetic energy and the Reynolds shear stress begin to recover

CONCLUSION

The reduction of the Reynolds shear stress, turbulent kinetic energy, streamwise mean wall stress and the rms of ω_y have been related to the break-up of the near-wall streaks. The weakening of the streaks occur because the streamwise vortices just above them are shifted relative to the streaks and cut across them. We have also observed reduction of the intensity of the streamwise vortices with the same sign as the mean streamwise vorticity.

AKNOWLEDGMENTS

The authors are grateful to Professor Javier Jimenez for very useful discussions This work is supported by the U S Air Force Office of Scientific Research

REFERENCES

1 Bradshaw, P and Pontikos, N 1985 "Measurements in the Turbulent Boundary Layer on an "Infinite" Swept-Wing," *J Fluid Mech* **159**, pp 105-130

2 Driver, D M and Hebbar, S.K. 1987 "Experimental Study of a Three- Dimensional, Shear-Driven, Turbulent Boundary Layer," AIAA Journal, **25**, 1, pp 35-42.

3 Elsenaar, A , and Boelsma, S., 1974 "Measurements of the Reynolds Stress Tensor in a Three-Dimensional Turbulent Boundary Layer under Infinite Swept-Wing Conditions," National Aerospace Laboratory, The Netherlands, NRL TR 74095 U

4 Moin, P , and Spalart P. R. 1989 "Contributions of Numerical Simulation data bases to the Physics, Modeling, and Measurement of Turbulence," *Advances in Turbulence*, W K George and R Arndt, eds , Hemisphere Publishing Corp., Washington, DC, pp 11-38

5. Kim, J , Moin, P and Moser, R , 1987 "Turbulence Statistics in Fully Developed Channel Flow at Low Reynolds Number," *J Fluid Mech*, **177**, pp 133-166.

6 Moin, P , Shih, T -H , Driver, D and Mansour, N N 1990, "Direct numerical simulation of a Three-Dimensional Turbulent Boundary Layer," *Phys. Fluids*, **2**, 10, pp 1846-1853

7 Jimenez, J., and Moin, P. 1991 " The Minimal flow unit in near-wall turbulence", *J. Fluid Mech* **225**, pp 213-240

EIGHTH SYMPOSIUM ON
TURBULENT SHEAR FLOWS
Technical University of Munich
September 9-11, 1991

On the Origin of Streaks in Turbulent Shear Flows

By Fabian Waleffe & John Kim
Center for Turbulence Research
NASA Ames Research Center, Moffett Field, CA 94035

Abstract

It is shown that the ideas of *selective amplification* and *direct resonance*, based on linear theory, do not provide a selection mechanism for the well-defined streak spacing of about 100 wall units (referred to as 100^+ hereafter) observed in wall-bounded turbulent shear flows. For the direct resonance theory (Benney & Gustavsson, 1981, Jang et al., 1986), it is shown that the streaks are created by the nonlinear self-interaction of the vertical velocity rather than of the *directly forced* vertical vorticity. It is then proposed that the selection mechanism must be inherently nonlinear and correspond to a *self-sustaining* process. The streak formation is only one stage of the complete mechanism and can not be isolated from the rest of the process. The 100^+ value should be considered as a critical Reynolds number for that self-sustaining mechanism. For the case of plane Poiseuille flow the 100^+ criterion corresponds to a critical Reynolds number of 1250, based on the centerline velocity and the channel half-width, which is close to the usually quoted value of about 1000. In plane Couette flow, it corresponds to a critical Reynolds number of 625, based on the half velocity difference and the half-width.

1. Introduction

An intriguing feature of wall-bounded turbulent flows is the existence of bands of low- and high-speed fluid, elongated in the streamwise direction, and with a very consistent spanwise spacing of about one hundred wall units, i.e. $100\nu/u_*$, where $u_* = (\nu dU/dy|_w)^{1/2}$ is the friction velocity. The streaks are known to initiate a localized instability that leads to a "bursting process," during which most of the turbulence production takes place (Kline *et al.*, 1967, Kim *et al.*, 1971). Large momentum is exchanged between the wall and the outer fluid during the bursting process, thus sustaining the turbulent flow.

It is now fairly well accepted that the mechanism for streak generation is a rapid one, meaning that the linear distortion of fluctuations by the mean shear strongly dominates the nonlinear effects (Lee *et al.*, 1990). The physical process is a redistribution of downstream momentum by cross-stream motions (downstream rolls) which are decoupled from the mean flow. The important question remaining is to determine what imposes the characteristic streak spacing. A natural suggestion is that the linear mechanism itself leads to a favored scale (selective amplification). The inner-layer of a typical turbulent boundary layer being about 50 wall units thick, the scale of the largest downstream roll would be also around 50^+ and these would induce streaks with a spanwise wavelength around 100^+. The flaw in that reasoning is that it rests on an intuitive, yet false, assumptions that rolls are necessarily circular while in fact they can be elliptical. Our analysis indicates that while the linear mechanism provides a scale selection, it is much too weak to be significant and does not correspond to the value of 100^+. The weak scale selection shows up in the vertical vorticity spectra but not in the downstream velocity spectra. In a turbulent boundary layer a peak appears in both spectra.

In the direct resonance theory (Gustavsson 1981; Benney and Gustavsson 1981), oblique vertical vorticity modes are forced by the vertical velocity. The physical process is entirely similar to that for the streak generation mentioned above and consists of a redistribution of momentum in oblique planes by oblique rolls. Because of the obliqueness, the two types of fluctuations (oblique rolls and oblique streaks, or in mathematical terms vertical velocity and vorticity) are in general influenced by the mean flow in two different ways. The small vertical velocity fluctuations are governed by the Orr-Sommerfeld equation, while the vertical vorticity fluctuations obey an advection-diffusion equation. The argument is that the forcing of the vertical vorticity by the velocity should be most effective when the eigenvalue of the velocity mode is identical to an eigenvalue of the homogeneous vorticity equation (a so-called direct resonance). The resonance condition is only satisfied for well-defined streamwise (x) and spanwise (z) scales, thus providing a scale selection. If the "resonance" condition is met, the vorticity is expected to reach "large" values. The nonlinear self-interaction of the "large" vertical vorticity then gives rise to downstream rolls (downstream vertical velocity) as shown by Jang, Benney and Gran (1986), and these rolls lead to streaks as explained in the previous paragraph. Unfortunately, our analysis does not support this approach either. The direct resonance criterion does not necessarily select the most amplified vorticity fluctuations. This is because the "resonance" always occurs for damped modes. So the maximum vorticity amplitude that can be obtained is a function of the damping rate, and there are non-resonant modes with a lower damping rate which can reach larger amplitudes. In fact, the largest vorticity amplitudes are obtained for downstream modes, as reported recently by other authors also (Gustavsson 1991; Henningsson 1990), but, as discussed in the previous paragraph, the downstream fluctuations do not yield a significant scale selection. So this approach can not explain the streak spacing either. In any case, our analysis also indicates that the generation of downstream rolls is a result of the nonlinear interaction of the oblique vertical velocities and not of the vorticities, thus bypassing completely the "resonant" amplification of the oblique streaks.

The final part of this paper presents an introduction to on-going research aimed at providing an understanding of the scale selection and the mechanisms taking place in the near-wall region of turbulent boundary layers. We propose that the streak spacing should be considered as a critical Reynolds number for a self-sustaining nonlinear process, of which streak formation is one of the elements. The nonlinear process would not *persists* for scales lower than about 100^+. This is the case, of course, if the largest scale allowed in the domain is smaller than 100^+. Therefore a link is established between the 100^+ characteristic streak spacing and the critical Reynolds numbers, above which turbulence can be maintained. The 100^+ criterion has the potential to be a more universal value for shear flows than other measures of the critical Reynolds number. It translates into a

value of 1250 based on the channel half-width and the centerline velocity in plane Poiseuille flow, and 625 based on the half width and half velocity difference in plane Couette flow. The self-sustaining nonlinear process in question would consists of the following elements First, streaks are created by downstream rolls, the streaks then break down due to an instability of inflexional type i. iated by the spanwise inflexions, the vertical shear might significantly influence the nature of that instability. The streak instability leads to the formation of vortices which reinforce the original downstream rolls, and the process repeats itself provided the scale is larger than 100^+; otherwise it loses intensity and eventually decays The complete process is expected to be itself unstable, or at least "broadband", so that the flow appears disordered if the largest admissible scale is sufficiently bigger than 100^+. In order to capture the process in its simplest form it is necessary to experiment in a domain whose largest scale is close from 100^+.

Insection 2, the idea of selective amplication by the linear nechanism is examined. In section 3, we reexamine the direct resonance theory of Jang et al. (1986). The self-sustaining mechanism for marginal turbulent flows is presented in section 4, followed by a short summary in section 5.

In this paper, x, y, and z denote streamwise, normal (to the wall), and spanwise directions, respectively, while u, v, and w denote corresponding velocities, respectively.

2. Linear Analysis and Selective Amplification

A number of papers (e.g. Lee *et al*, 1990) show that the mechanism for streak generation is linear. The argument is that in the near wall-region the time scale for the mean $(dU/dy)^{-1}$ is much shorter than the time scale for the nonlinear effects, measured by q^2/ϵ, where q is a turbulent velocity scale and ϵ is the dissipation rate. The evolution is then dictated by linear equations and streaks are created from the redistribution of the downstream momentum by vertical and spanwise motions. The mechanism is a simple advection and is most efficient when the fluctuating fields are elongated downstream. The question here is to examine whether the linear mechanism favors spanwise scales of about 100^+. The mathematical description of the mechanism is briefly stated in the next few paragraphs.

The governing equations for the fluctuating field, obtained by eliminating pressure and the continuity constraint, are:

$$(\frac{\partial}{\partial t} + U\frac{\partial}{\partial x} - \frac{1}{R}\nabla^2)\nabla^2 v - \frac{d^2U}{dy^2}\frac{\partial}{\partial x}v = NL_v \qquad (1)$$

$$(\frac{\partial}{\partial t} + U\frac{\partial}{\partial x} - \frac{1}{R}\nabla^2)\eta + \frac{dU}{dy}\frac{\partial}{\partial z}v = NL_\eta \qquad (2)$$

where v and η denote respectively the y-component of velocity and vorticity, and U is the mean velocity. The right-hand sides, NL_v, NL_η, represent nonlinear terms Flows in a channel will be considered in this paper (plane Poiseuille or plane Couette flow) with the boundary conditions $v = \partial v/\partial y = \eta = 0$ at the walls, located at $y = \pm 1$.

In the linear case (NL_v=0), the equation for v is homogeneous and admits eigensolutions of the form:

$$v = \hat{v}(y)e^{i(\alpha x + \beta z - \omega t)} \qquad (3)$$

where $\hat{v}(y)$ satisfies the *Orr-Sommerfeld* equation. In general, for a turbulent mean profile, all of these eigensolutions are decaying. The η-equation on the other hand, is nonhomogeneous for v fluctuations with a spanwise variation. When forced by an eigenmode of the v equation, the linear response of the vertical vorticity has the form:

$$\eta = \hat{\eta}(y,t)e^{i(\alpha x + \beta z)} \qquad (4)$$

with $\hat{\eta}(y,t)$ given by:

$$\hat{\eta}(y,t) = \beta \sum_n \lambda_n \frac{e^{-i\omega t} - e^{-i\mu_n t}}{\omega - \mu_n}\eta_n(y) \qquad (5)$$

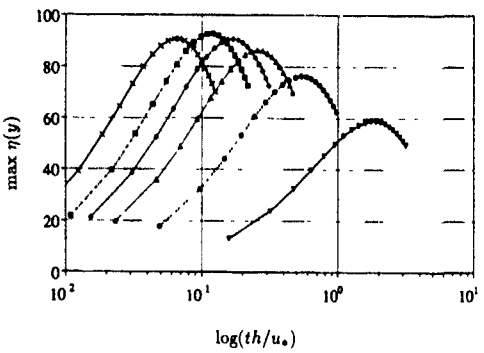

FIGURE 1. Maximum pointwise vertical vorticity response to a single downstream even OS mode ▽ , $\lambda_z^+ = 188$, • , $\lambda_z^+ = 94$; △ , $\lambda_z^+ = 63$, ◇ , $\lambda_z^+ = 47$, □ , $\lambda_z^+ = 38$; × , $\lambda_z^+ = 27$

Where

$$\lambda_n = \frac{\int U'\hat{v}\,\eta_n\,dy}{\int \eta_n\eta_n dy} \qquad (6)$$

and $\eta_n(y)$, μ_n represent the eigenmodes and eigenvalues of the homogeneous η-equation. Note that the vertical vorticity response corresponds to streaks, as opposed to vortices.

When the OS eigenvalue ω is close to the Squire eigenvalue μ_n, the n-th coefficient will behave as $t\exp(-i\mu_n t)$. This corresponds to an algebraic growth followed by exponential decay, as μ_n corresponds to a viscously decaying mode. For a significant algebraic growth to occur the real parts of ω and μ must be sufficiently close. Otherwise the modes will decorrelate. Furthermore, the viscous damping must be small. Thus one expects and verifies numerically that the largest responses occur for downstream modes ($\alpha = 0$) for which the real parts of the eigenvalues vanish (downstream modes are not advected) and the decay rate is inversely proportional to the Reynolds number.

The possibility of a scale selection by the linear mechanism was investigated numerically, by introducing a downstream OS mode, normalized such that the maximum vertical velocity was unity, onto a turbulent mean profile with $R = 180$, based on the friction velocity and the channel half-width. The mean velocity profile was chosen as a Reynolds-Tiederman profile, defined by

$$\frac{dU}{dy} = -\frac{Ry}{(1+\nu_t)}$$

$$\nu_t = \frac{1}{2}\{1 + [\frac{1}{3}KR(1-y^2)(1+2y^2)$$
$$(1 - \exp((1+y)R/A))]^2\}^{1/2} - \frac{1}{2}$$

where K and A were chosen respectively as 0.525 and 37

The forced responses of the vertical vorticity are shown in figure 1. It can be seen that there is a peak around $\lambda_z^+ = 35$, but it is too weak to represent a significant selection. The streamwise fluctuating velocity responses would be obtained by multiplying the vorticity by the wavelength and the largest response would correspond to the largest wavelength. This does not match the experimental observations, which show a scale selection both in the velocity and vorticity spectra. In any case, the "peak" does not correspond to the typical value for the streak spacing, which is between 80^+ and 100^+. We must conclude that the linear mechanism does not provide a scale selection.

3. Direct Resonance Theory

In the direct resonance scenario, streaks originate from a three-step process (Benney and Gustavsson, 1981; Jang *et al*, 1986) The first step is linear and consists of the resonant forcing of the vertical vorticity by the velocity, exactly as in the previous section, but focuses on oblique disturbances, for which the nonlinear effects can be less trivial. The second step is the nonlinear interaction of the vorticity with its mirror image across a vertical downstream plane. This would create downstream vortices which, finally, give rise to the streaks. That sequence of interaction is illustrated by the following diagram.

$$\epsilon v(\alpha, \pm\beta) \longrightarrow \epsilon t \eta(\alpha, \pm\beta)$$
$$\eta\eta^* \longrightarrow v(0, 2\beta)$$
$$v(0, 2\beta) \longrightarrow \eta(0, 2\beta)$$

A nonlinear theory was developed in Benney and Gustavsson (1981) and applied to turbulent boundary layers in Jang *et al* (1986) Using a turbulent boundary layer profile, Jang *et al.* found that an OS eigenvalue coincided with a "Squire" eigenvalue (a *direct resonance*) for the horizontal wavenumbers, $\alpha^+ = 0.0093$ and $\beta^+ = 0.035$. The common eigenvalue was equal to $\omega^+ = 0.090 - \imath\, 0.037$. They showed that the interaction of that mode with its spanwise reflexion induced streamwise vortices with a spanwise wavelength around $\lambda^+ = 2\pi/\beta^+ \simeq 90^+$.

One problem with the direct resonance concept is that it must assume not only that the eigenvalues of the two linear homogeneous operators are close, but also that the damping rates are small. Otherwise, as discussed above, the algebraic growth will be quickly shut off by the exponential viscous decay Another problem comes from multiple resonances or near-resonances There is no a priori criterion for which one should prevail.

The possibility of the direct resonance route to streaks has been explored in the turbulent channel flow (Kim *et al*, 1987). The Reynolds number is about 180, based on the channel half-width and the friction velocity. A direct resonance is found for

$$\alpha^+ \simeq 0.005 \quad \beta^+ \simeq 0\,039$$

with the corresponding eigenvalues

$$\omega_{14}^+ = 0.07871485 - \imath\, 0.02168581$$
$$\mu_{15}^+ = 0\,07871461 - \imath\, 0.02168558$$

These values are different but close to the values reported above for the turbulent boundary layer. The nonlinear interaction of the pair of modes $(\alpha, \pm\beta)$ leads to streaks with a spanwise spacing of about 80^+. The vertical vorticity responses are displayed in figure 2 The initial conditions were such that the maximum v amplitude was 0.1 with no vertical vorticity. As indicated by the subscripts, this direct resonance occurs at the 14th OS mode and the 15th Squire mode, where the modes are ordered according to their decay rate. Although this result looks encouraging, the picture is not as clear when one analyzes other modes.

For instance the linear response obtained from the 13th OS mode for slightly different wavenumbers is very similar to the direct resonance mode, but the nonlinear response is even larger (figure 2). The response to the 19th OS mode for $(\alpha, \beta) = (1\,6, 12)$ revealed rather confusing results (figure 3). The linear response is almost four times larger than the direct resonance one, but the nonlinear response is much smaller. One would expect that if the linear response was four times larger than for the direct resonance modes, the nonlinear response should be sixteen times larger than in the direct resonance case.

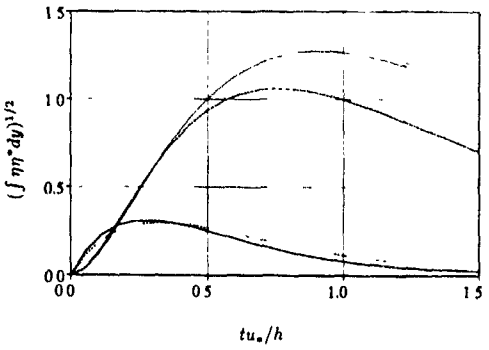

FIGURE 2 Linear (lower curves) and non-linear (upper curves) vertical vorticity response for direct resonance ——— , $(\alpha, \beta) = (0\,9, 7\,07)$ (forced by 14th OS mode), — — , $(0, 14\,14)$; ---- , $(0.8, 6)$ (forced by 13th OS mode), , $(0, 12)$.

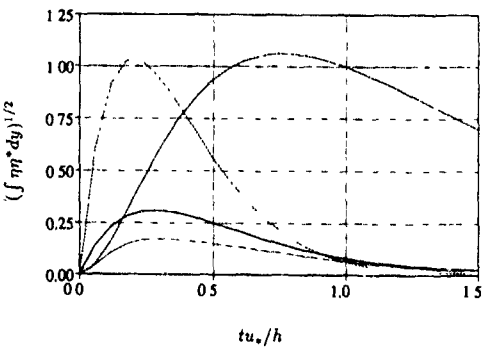

FIGURE 3 Linear and nonlinear vertical vorticity response for direct resonance: ——— , $(\alpha, \beta) = (0.9, 7.07)$ (forced by 14th OS mode), — — , $(0, 14.14)$, ---- , $(1\,6, 12)$ (forced by 19th OS mode); · , $(0, 24)$.

To understand what goes on it is necessary to analyze the nonlinear interactions. The computations and the theory are started with a pair of oblique rolls such as:

$$v = \cos\beta z\,(v_1(y,t)e^{\imath\alpha x} + v_1^*(y,t)e^{-\imath\alpha x})$$

The linear processes then introduce a pair of oblique streaks

$$\eta = \sin\beta z\,(\eta_1(y,t)e^{\imath\alpha x} + \eta_1^*(y,t)e^{-\imath\alpha x})$$

The nonlinear effect of the primary interest is the generation of streamwise vortices $V(y,t)\cos 2\beta z$. The complete equation for $V(y,t)$ is obtained from (1) with the nonlinear forcing provided by the pair of oblique rolls After some manipulations (see e.g. Benney, 1961, Lin and Benney, 1962), one finds:

$$[\frac{\partial}{\partial t} - \frac{1}{R}(\frac{\partial^2}{\partial y^2} - 4\beta^2)](\frac{\partial^2}{\partial y^2} - 4\beta^2)V =$$

$$\beta(\frac{\partial^2}{\partial y^2} + 4\beta^2)(v_1 w_1^* + v_1^* w_1) + 4\beta^2 \frac{\partial}{\partial y}(v_1 v_1^* + w_1 w_1^*)$$

where w_1 is given in terms of v_1 and η_1 by

$$w_1 = k^{-2}(-\beta\frac{\partial v_1}{\partial y} + \imath\alpha\eta_1)$$

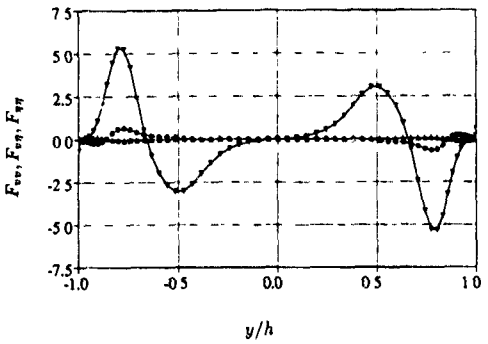

FIGURE 4. Forcing terms for the direct resonance mode at time when η is maximum: ∇ , F_{vv}; $\bullet$, $F_{v\eta}$; and Δ , $F_{\eta\eta}$

with $k^2 = \alpha^2 + \beta^2$. The right hand side can be rewritten as the sum of three forcing terms $F_{vv} + F_{v\eta} + F_{\eta\eta}$, where

$$F_{vv} = 4\frac{\alpha^2\beta^2}{k^2}\frac{\partial}{\partial y}(v_1 v_1^*) + 4\frac{\beta^4}{k^4}\frac{\partial}{\partial y}(\frac{\partial v_1}{\partial y}\frac{\partial v_1^*}{\partial y}) - \frac{\beta^2}{k^2}\frac{\partial^3}{\partial y^3}(v_1 v_1^*)$$

$$F_{v\eta} = \frac{i\alpha\beta}{k^2}[(\frac{\partial^2}{\partial y^2} + 4\beta^2)(\eta_1 v_1^* - \eta_1^* v_1) + \frac{4\beta^2}{k^2}\frac{\partial}{\partial y}(\eta_1^*\frac{\partial}{\partial y}v_1 - \eta_1\frac{\partial}{\partial y}v_1^*)]$$

$$F_{\eta\eta} = \frac{4\alpha^2\beta^2}{k^4}\frac{\partial}{\partial y}(\eta_1\eta_1^*)$$

In the direct resonance theory, the oblique streaks (η_1) are supposed to be much larger than the rolls so that only their nonlinear interaction, i.e the term $F_{\eta\eta}$, is considered The three forcing terms for the direct resonance case at the time when $\eta(\alpha, \pm\beta)$ reaches its maximum amplitude (cf figure 2) are shown in figure 4. Figure 4 shows that the dominant forcing term is the nonlinear interaction of the oblique rolls (v_1) and not of the "directly forced" oblique streaks (η_1) Thus the formation of the streamwise vorticity is owing to the nonlinear interaction of the vertical *velocity* of the oblique rolls, not the vertical *vorticity* as proposed in the direct resonance theory. We must conclude that the formation of streamwise vortices, and the streaks they induce, are not directly associated with "direct resonances."

4. Marginal Flow

In view of the failure of the linear mechanism to provide a scale selection, we hypothesize that the selection must come from the original disturbance. In a turbulent flow the disturbance seems to arise from the breakdown of the streaks themselves (the bursting process). Thus the 100^+ selection must come from the complete *self-sustaining* mechanism Our conjecture is that disturbances with a spacing smaller than about 100^+ can not be maintained. The 100^+ should then be considered as a *critical Reynolds number*. This conjecture is consistent with the observation made by Jimenez and Moin (1991) They show that for a channel flow at three different Reynolds numbers, $U_c h/\nu = 5000$, 3000 and 2000, (U_c is the centerline velocity, h is the half-height), the flow returns to a laminar state when the spanwise width of the periodic box is reduced below about 100^+.

We observe that for channel width of about 100^+ the channel is very narrow. The characteristic length for the scaling of the disturbance should then be taken as the half width as opposed to the half height. In more general terms, the characteristic length should be taken as the smallest of half the channel height and width. Doing so it turns out that turbulence can not be maintained if $u_*\lambda_z/\nu < 100$, which corresponds to $U_c\lambda_z/(2\nu) < 1250$ ($\lambda_z/2$ is the half-width), irrespectively of the value of $U_c h/\nu$ But 1250 is close to the usually quoted value for the critical Reynolds number in channel flow. If one had reduced the height h as opposed to the width λ_z, "turbulence" would have also disappeared when $U_c h/\nu < 1250$ or $u_* h/\nu < 100$.

In order to capture the self-sustaining process in its simplest form, the next step is to reduce both dimensions ($2h$ and λ_z) to their minimum value, so as to eliminate all unnecessary scales. One should be reminded at this point that the streaks are expected to be an essential element of the whole mechanism. The streaks are created from the redistribution of downstream momentum. From the distribution of the mean shear in a channel flow, the simplest self-sustaining non-laminar flow should then consists of a pair of opposite streaks in the spanwise direction and in the direction perpendicular to the walls as well, i.e one pair of streaks in either half of the channel. In Couette flow, where the mean shear has only one sign, the simplest solution should correspond to only one pair of streaks in the middle of the channel Thus, the simplest marginal channel flow should have dimensions $u_*\lambda_z/\nu \simeq 100$ and $u_* 2h/\nu \simeq 100$ (corresponding to Re=1250, based on the centerline velocity), while the simplest marginal Couette flow should have $u_*\lambda_z/\nu \simeq 100$ and $u_* 2h/\nu \simeq 50$ (corresponding to Re=625, based on the half velocity difference). Note that the laminar mean velocity profiles (parabola for plane Poiseuille flow and linear for plane Couette flow) are used to estimate the wall-shear velocity, and the actual critical Reynolds numbers are expected to be somewhat lower than 1250 and 625, accounting for higher wall-shear velocities associated with turbulent mean profiles.

A number of simulations of both flows were performed, and the result support the above reasoning. Turbulent Couette flow, for instance, could not be maintained at Reynolds numbers of 330 and below (based on the half height and half velocity difference) but was maintained for over 2000 convective time units ($2h/2U_w$) at a Reynolds number $U_w h/\nu = 400$. Thus the non-laminar flow was maintained for over 5 viscous units (h^2/ν), a time scale over which the slowest decaying scales would decay by a factor $\exp(-2.5\pi^2)$ if they were not sustained. The computed flow fields in the near-wall region indicated strong similarity to those obtained at a higher Reynolds number (Lee & Kim 1991). The main mechanism appears to be the breakdown of the streaks owing to a spanwise inflectional instability (figure 5) The complete process is still somewhat too disordered to firmly establish the mechanisms at play Energy transfer between the streaks and downstream rolls are being investigated to clarify the nature of the self-sustaining mechanism. It is also planned to investigate these flows with certain symmetries imposed upon in the hope of further constraining and clarifying the nature of the fundamental self-sustaining flow.

5. Summary

The streaks, well-defined bands of low- and high-speed fluid present in the near-wall region of turbulent shear flows, are an integral part of the bursting process, by which momentum is exchanged between the wall and the outer fluid. The formation of the streaks is well described by linear theory and corresponds to the rotation of the vertical mean shear by downstream rolls to create a spanwise shear. The linear theory, however, does not provide an explanation for the well-defined scale selection (100^+). The amplitudes of the streaks obtained from the linear equations for a range of scales around the observed 100^+ did not show any significant peak. The direct resonance theory (Jang et al., 1986) is based on the same linear mechanism but for oblique disturbances, whereby oblique rolls create large oblique streaks. A

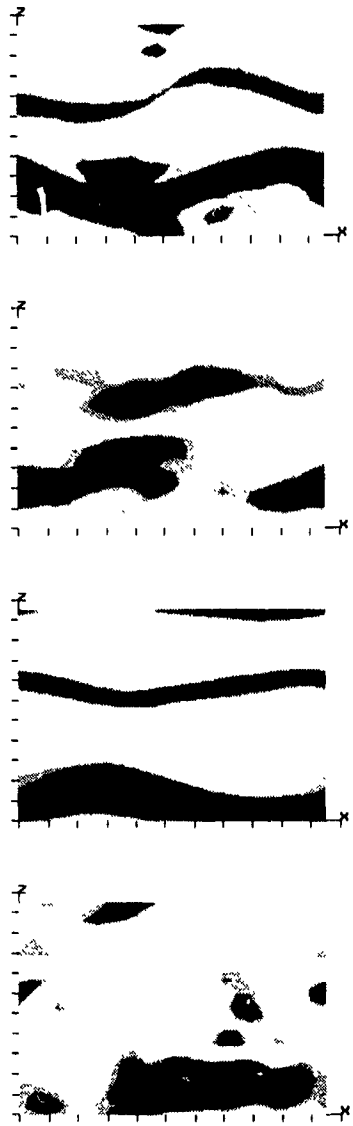

FIGURE 5. Contours of streamwise velocity fluctuations at four different time (time increases from top to bottom) are shown here to illustrate the formation and breakdown of streaks in a marginal plane Couette flow Contours shown here are drawn in the (x, z)-plane in the middle of the channel, and darker contours represent regions of high or low (relative to the local mean) streamwise velocity. The streamwise extent of the figure corresponds to about 6 2 channel half width.

pair of these large oblique streaks then interact nonlinearly to yield downstream rolls, which themselves create downstream streaks In the direct resonance theory, the scale selection comes from the fact that the creation of oblique streaks by oblique rolls would be more efficient for some particular scales. Unfortunately, this was not found to be the case. In fact the largest responses occur for downstream modes which do not show any significant scale selection as stated above Furthermore the analysis of the numerical experiments indicates that the downstream rolls are created owing to the self-interaction of the oblique rolls rather than that of the oblique streaks

Our conclusion is that the scale selection comes from the complete self-sustaining nonlinear mechanism which consists of the creation, destruction and regeneration of the streaks The observed characteristic scale of about 100 wall units corresponds to a critical Reynolds number for that process, below which it would not be self-sustaining This establishes a link between the 100^+ streak spacing and critical Reynolds numbers below which turbulent flows can not be maintained Numerical investigations support this view and a more complete account of that work will be presented in a forthcoming publication

REFERENCES

BENNEY, D J 1961 A non-linear theory for oscillations in a parallel flow *J Fluid Mech* **10**, 209-236

BENNEY, D J & GUSTAVSSON, L.H 1981 A New Mechanism for Linear and Nonlinear Hydrodynamic Stability *Studies in Appl Math* **64**, 185-209

GUSTAVSSON, L H 1981 Resonant growth of three dimensional disturbances in plane Poiseuille flow *J Fluid Mech* **112**, 253-264

GUSTAVSSON, L H 1991 Energy growth of three dimensional disturbances in plane Poiseuille flow . *J Fluid Mech* **224**, 241-260

HENNINGSSON, D. S. 1990 An eigenfunction expansion of localized disturbances *Poster presented at 3rd European Conference, Stockholm*

JANG, P S , BENNEY, D.J. & GRANT, R L 1986 On the origin of streamwise vortices in a turbulent boundary layer *J Fluid Mech.* **169**, 109-123

JIMENEZ, J. & MOIN, P 1991 The minimum flow unit in near-wall turbulence *J Fluid Mech.* **225**, 213-240

KIM, J., MOIN, P & MOSER, R D 1987 Turbulence statistics in fully developed channel flow at l w Reynolds number. *J Fluid Mech* **162**, 339-363.

KIM H T., KLINE, S J. & REYNOLDS, W C 1971 The production of turbulence near a smooth wall in a turbulent boundary layer *J Fluid Mech* **50**, 133-160.

KLINE, S J., REYNOLDS, W.C , SCHRAUB, F.A. & RUNSTADLER, P 1967 The structure of turbulent boundary layers. *J Fluid Mech* **30**, 741-773

LEE, M J , KIM, J & MOIN, P 1990 Structure of turbulence at high shear rate. *J Fluid Mech* **216**, 561-583

LEE, M J. & KIM, J 1991 The structure of turbulence in a simulated plane Couette flow *Proceedings of Eighth Symposium on Turbulent Shear Flows*

LIN, C.C. & BENNEY, D J 1962 On the instability of shear flows *Am Math Soc , Proc Symp.Appl.Math* . **13**, 1

WALEFFE, F. 1989 Organized motions underlying turbulent shear flows. *CTR Annual Research Briefs* **89**, 107-115.

EIGHTH SYMPOSIUM ON
TURBULENT SHEAR FLOWS
Technical University of Munich
September 9-11, 1991

THE TEMPORAL EVOLUTION OF LARGE-SCALE STRUCTURES IN THE TURBULENT JET

M Yoda*), L Hesselink *)†, and M G Mungal‡)

*) Dept. of Aeronautics and Astronautics (and Dept of Electrical Engineering)†,
Durand Building, Stanford University, Stanford, CA 94305-4035, USA

‡) Dept. of Mechanical Engineering, Building 520,
Stanford University, Stanford, CA 94305-3032, USA

ABSTRACT

We investigate the far-field evolution of large-scale structures in both a natural and circularly forced round turbulent (Re = 4000) water jet Sequential axial PLIF cross sections are acquired of the flow, resulting in a 2D time-dependent ($x - y - t$) dataset. After appropriate digital image processing, the marching cubes algorithm is used to extract a 3D isovalue surface from the volume This surface compactly shows the *global* far-field ($x/d \geq 30$) evolution of the flow In both flows the 3D surfaces clearly show the far-field existence and evolution of large-scale organized structures. As expected, the helical instability mode is dominant in the far-field of the natural jet. Circular forcing amplifies this helical mode, and increases its spreading rate.

INTRODUCTION

Although the existence and nature of large-scale or coherent structures has been exhaustively investigated in the fully developed or far-field region of mixing layers (Brown & Roshko [1974]), there has been surprisingly little work on large-scale structures in the far-field region of turbulent round or axisymmetric jets. In the near field of the jet, the early work of Crow & Champagne (1971) showed the existence of "a large-scale orderly pattern." However, the inherent three-dimensionality of these structures in the far-field made them difficult to detect until newer diagnostic and image processing techniques allowed interior details of the flow to be visualized (Hesselink 1988). Dimotakis *et al.* (1983) were among the first to present evidence of far-field organized motion using $x-t$ diagrams from a movie sequence of planar laser induced fluorescence, or PLIF, axial cross sections of a jet Given large-scale structures in the far-field of three-dimensional free shear flows, we are interested in answering two major questions in this work: 1) how do these structures evolve over time?; and 2) what is the effect of circular (instead of axial) forcing on the supposedly dominant helical instability mode?

Our approach involves acquiring a sequence of PLIF axial cross sections of both a natural and circularly forced turbulent round jet under identical conditions (Re = 4000) We analyze the experimental results (consisting of millions of measurements of the jet fluid concentration) by stacking the set of images (frames) sequentially to form a $x - y - t$ volume and extracting an isoconcentration (isovalue) surface from the data. With proper image processing this surface shows the evolution of large-scale structures in the flow both inside and at the surface of the jet.

This three-dimensional visualization technique is useful for revealing aspects of the instantaneous flow physics, but the method is computationally intensive, which makes acquiring flow statistics difficult For example, the relatively brief 20 s sequences used here each consist of 100 449 × 351 images, resulting in about 15MB of raw data. Since we would need a record many times longer to perform any statistical analysis, the memory required merely to store the data and the additional resources required to compute their statistics are impractical. With data compression and faster computers these difficulties may be overcome, but at present we consider that our approach complements the work of researchers such as Tso & Hussain (1989), who used conditional sampling of *point* measurements of the velocity field to detect organized structures and calculate the probability of their occurence.

Related volumetric visualization techniques have also been used on other flows Jiménez *et al.* (1985) first used volume rendering in the mixing layer, while Agüí & Hesselink (1988) visualized in three dimensions the near field of a pulsed coflowing jet. In both of these cases, Taylor's hypothesis was used to relate time to space, and therefore the reconstructed object resembles the flow seen in the experiment More recently, Mungal *et al* (1991) have used volume rendering to investigate the dynamics of high Re (2×10^8) jets Their $x-y-t$ volumes, which bear little resemblance to the actual flow, are the three-dimensional analogs of the $x - t$ diagram, and show evolution and pairing of large-scale organized structures.

Our technique of isovalue reconstruction differs from volume rendering in that it extracts and reconstructs a single surface from a volumetric dataset, while volume rendering uses transparency to render the entire dataset as a single object. Since volume rendering reveals all structures simultaneously, its results are often difficult to interpret because of the lack of high-contrast and easily recognizable internal structures in turbulent flows. In fact, Mungal *et al.* have eliminated the transparency from their volume renderings,

creating an opaque outer isovalue surface, to avoid confusion Our technique (Ning & Hesselink [1991]) provides a more accessible interpretation of the flow, and has the additional advantage of being considerably less computationally intensive

EXPERIMENT

The flow visualized here is a round turbulent jet with a Reynolds number based on the nozzle diameter (d_o = 0 48 cm) of 4000 Pressurized air drives water containing 4 × 10^{-5} M disodium fluorescein from a reservoir tank out the nozzle at a steady exit velocity into a hexagonal tank of still, clear water about 1 m deep The dyed fluid is pushed through a honeycomb section in the reservoir tank before exiting the nozzle to eliminate swirl The jet nozzle can be forced either circularly or axially with a variable speed motor. Both the hexagonal and reservoir tanks are filled and allowed to sit for at least three hours before each run to eliminate stray currents and temperature differences Since the mean turbulent "flame length" becomes independent of Re above 3000 (Broadwell & Mungal 1991), our flow should be fully turbulent

We illuminate the flow along the jet axis from the side with a light sheet 1 mm thick from a 20 W copper vapor laser (MetaLaser Model 251) pulsed at 6 kHz. Each 40 ns laser pulse is brief enough to effectively freeze the flow within a slice The sheet illuminates the region $30d_o$ to $83d_o$ downstream of the nozzle; this corresponds to 1.5–4 local jet diameters ($d = 0.44x$, where x is the downstream location) in the far-field of the jet. The optics for forming the light sheet are designed so that the relatively thick light sheet has a Rayleigh range slightly greater than the region of interest The images are acquired at normal incidence by a VHS videocamera (JVC Model GF-700) with a 0 1 ms shutter at the rate of 30 Hz. Each videotape frame therefore images a single pulse of the laser, and the laser pulses are synchronized with the videocamera framing rate

Individual frames of the videotape are digitized at a rate of 5 Hz; the interframe spacing is then 0.2 s *vs.* local characteristic times t_c of 0.4–2.8 s ($t_c = d/u_c$, where u_c, the centerline velocity, is related to the initial nozzle velocity u_o: $u_c/u_o = 6\,2/(x/d_o)$). Frames are acquired from 6 4 to 26.4 s after the start of the jet, resulting in 100 images per dataset This time range gives us data on fully developed flow with no wall (or floor) effects

These 8-bit images are downloaded to a Silicon Graphics Iris workstation (Model 4D/220GTX), and expanded with linear interpolation in the horizontal (y) coordinate by 1.684 to square the rectangular video pixels We then ensemble average the 100 images, extract the concentration $c_o(x)$ along the vertical centerline (*i.e.* the jet axis) of the average and rescale the average as well as the entire dataset row by row by the vector $r_o(x) = 255/c_o(x)$ The centerline concentration of each image is therefore self-similarly rescaled to be constant and maximum along the centerline, instead of decaying as $1/x$ This rescaling is crucial if we wish to follow the structures as they spread and diffuse downstream. The 100 gray scale images are stacked sequentially to form a $x - y - t$ volume (Fig 1), and median and uniformly lowpass filtered over a 3×3×3 set of sample points to remove artifacts and reduce noise. Finally, since we are interested only in the large-scale structures of the flow, the images are smoothed twice with a uniform lowpass filter over a 5×5 window to suppress the smaller spatial scale details

Isoconcentration surfaces at a specified threshold (in both cases 170 out of 255 gray scales) are reconstructed from the filtered images using the marching cubes algorithm (Lorensen and Cline [1987]) This algorithm thresholds the volume at the specified value and uses linear interpolation between the images to reconstruct a surface consisting of triangles. The number of triangles in the surface is a rough measure of the convolution of the surface. These surfaces can then be viewed with an interactive display program which rotates or translates the isovalue surface in real time. The capabilities of our in-house software are illustrated and described in more detail in Yoda & Hesselink (1990). Less than half an hour of CPU time is required on the Iris workstation to reconstruct these surfaces, which occupy about 50MB of memory each

RESULTS

From various analyses of the stability of the axisymmetric jet in the far-field, it is known that for normal mode disturbances the two most common instability modes present in this flow are the n=0 or axisymmetric mode, which produces a vortex ring-like structure, and the n=1 or helical mode, which produces a single helix. Batchelor & Gill (1962) concluded from their analysis that the helical mode is the only mode which would produce amplified disturbances in an inviscid jet. Fig. 2 shows a sketch of the proposed far-field instantaneous scalar or concentration field of the jet for the axisymmetric (from Dahm [1985]) as well as the helical (from Mungal & O'Neil

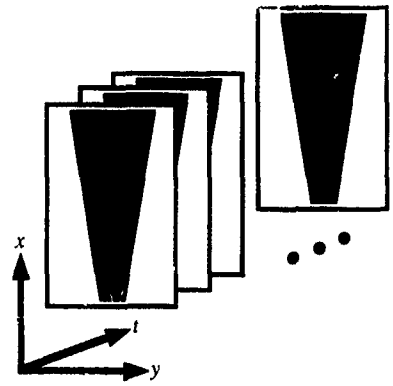

Figure 1. Schematic of image stacking for isovalue surface extraction

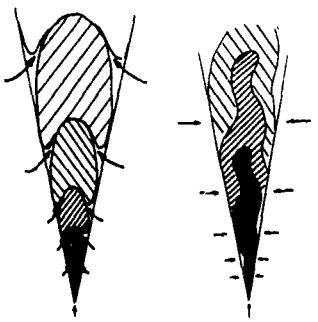

Figure 2. The proposed far-field instantaneous concentration fields of a round turbulent jet in the axisymmetric (left) and helical (right) modes. Arrows indicate entrainment of external fluid. The darkest shading corresponds to the highest concentration fluid

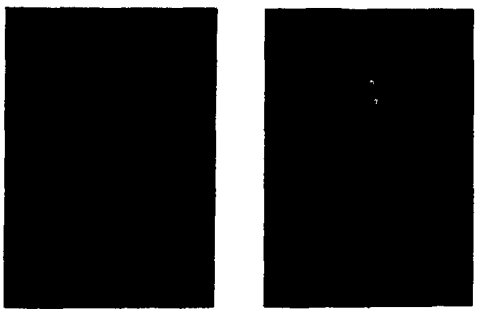

Figure 3. First (left) and last (rigl.t) images of the natural jet dataset (6.4 and 26 4 s, respectively, after the start of the jet). Flow in the 449 row by 351 column pictures goes from bottom to top. We have deliberately limited the number of distinct gray scales to 5 instead of the usual 255 to better enhance the contrast between different gray scale levels (black=0, white=255).

Figure 4. Natural jet isovalue surface at threshold 170 out of 255.

[1989]) mode. These sketches implicitly assume the Lagrangian mixing picture of Broadwell and Breidenthal (1982) where external fluid is entrained by the large-scale structures and is molecularly mixed at the smaller spatial scales Now if the entire shaded area corresponds to an interior axial view of the jet, only the left and right edges of this area would be visible in our surfaces. The bumps on these edges should then become "bands" on the side surfaces (the $x-t$ plane) of the $x-y-t$ volume. And by comparing the left and right side of the isovalue surface and seeing if they are in or out of phase, we will be able to determine whether the natural jet is in the axisymmetric or helical mode, respectively.

Two types of jet flow are presented here, both at $Re = 4000$: a natural jet and a circularly excited jet (Strouhal number $St = 0.3$) with a forcing amplitude of 1 5 mm ($\approx 0.3 d_o$) The fundamental associated with forcing at this critical St is "the most dispersive wave on a jet column" (Crow & Champagne) Both datasets are obtained, processed and reconstructed under identical conditions.

The natural jet

Fig. 3 shows the first and last images from our dataset, while Fig. 4 shows the corresponding three-dimensional isovalue surface In this view the downstream coordinate x increases from bottom to top, and time progresses from left to right A point light source is placed infinitely far away in the upper left-hand corner to highlight the parallel bands in the Gouraud shaded surface which are the large-scale structures traveling downstream (up) as time progresses (to the right). We see from their spacing that these coherent structures increase in size as the local jet diameter increases. The number of bands or structures evident at the top ($x = 83 d_o$) is le·· than that at the bottom ($x = 30 d_o$). Since the structures are of the dimension of the local jet diameter d, which scales with x, the structures must grow either by entraining external fluid or by pairing to produce a yet larger structure (Dahm).

The speed of the coherent structures (*i e* the slope of the bands) seems to decrease with downstream distance. We do not, however, see a continuous $1/x$ decay in the slope, which would be expected on the average from the scaling of the local average centerline velocity. This result agrees with the one-dimensional findings of Dimotakis *et al.*, who observed that the speeds in their jets decreased abruptly with each pairing event, and that the average velocity seemed to decrease "smoothly and monotonically only in an ensemble average sense."

A more interesting result is the frequency with which the coherent structures occur—they appear to be present at all times in the flow—and the large downstream distance (in some cases the full downstream view of $53 d_o$) over which these structures maintain themselves. Tso & Hussain conservatively estimated from the results of their conditional sampling scheme that large-scale structures (whether ax-

isymmetric or helical) existed in the jet about 15% of the time, but our results show that these structures are always present. The robustness of the coherent structures agrees with the results of Tso *et al.* (1981), who concluded from hot-wire measurements that structures on the order of the local jet diameter d persist for up to $3d$ downstream. As a further note, we observe that these surfaces at $Re = 4000$ are very similar to those seen by Mungal *et al* for the natural jet at $Re = 2 \times 10^8$.

Lastly, what is the instability mode of these structures? Since we are interested in analyzing the entire volume, rather than examining the individual images, we decided to try to examine the axi- or antisymmetry of the three-dimensional isovalue surface about its $x - t$ central plane. This approach allows us to qualitatively analyze the surface, instead of using more difficult quantitative correlation techniques (which we are presently pursuing). Each image is flipped around its vertical centerline (whose location is actually determined from the ensemble average), and is averaged with its original version to produce an image that is vertically symmetric (Fig. 5). Now if there exists sufficient overlap between the image and its flip and the gray scales in the images vary smoothly along the horizontal coordinate, the symmetric surface reconstructed from these images at the same threshold (170 out of 255) should be qualitatively smoother than the isovalue surface shown in Fig. 4. We should therefore see little difference between the symmetrized and original surface where the jet is in the (axi)symmetric mode, and a significant difference where the jet is in the helical or antisymmetric mode.

Fig. 6 shows the symmetrized version of the surface in Fig. 4. It is obviously much smoother, even to the extent of almost completely eliminating the bands at the lower downstream locations. The surface in Fig. 6 is about 700,000 triangles, while the surface in Fig. 4 is about 900,000, indicating more surface convolution. Two regions seem to be consistent between the symmetrized and original surfaces—the upper left hand corner, and the rightmost band of the dataset, indicating that the jet is axisymmetric there. The sharp contrast between the two surfaces implies that the jet probably switches between these two modes at different instances of time, instead of following a mixture of both modes at all times. Hence our results suggest that the helical mode is the more dominant one in the far-field of the round turbulent jet, as predicted by Batchelor & Gill and also shown by Tso & Hussain. It is important to remember that swirl has been eliminated in the jet, so there are no helical components in the initial conditions of our flow.

The circularly forced jet

Fig. 7 shows the first and last images from our circularly forced ($St = 0.3$) dataset. Note the strong antisymmetry of the axial cross section and how much the outer boundary deviates from the centerline as compared with Fig. 3. Fig. 8 shows the corresponding isovalue surface. The orientation of the surface is the same as for Figs. 4 and 6. The same "bands" are evident, and they appear to be deeper because of the forcing than those for the natural jet (this surface is about 1.1 million triangles, *vs* 900,000 for Fig. 4).

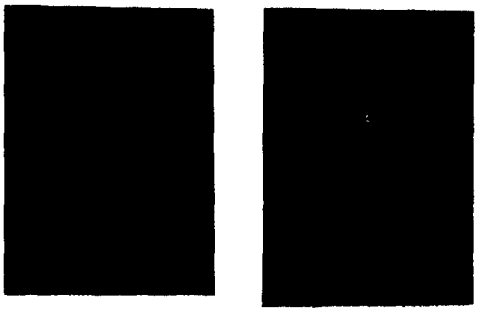

Figure 5. Flipped version (left) of the first image of the natural jet (Fig. 3 left) and its average image with the original (right). Note how much smoother the outlines of the averaged image are compared with the original and its flipped version.

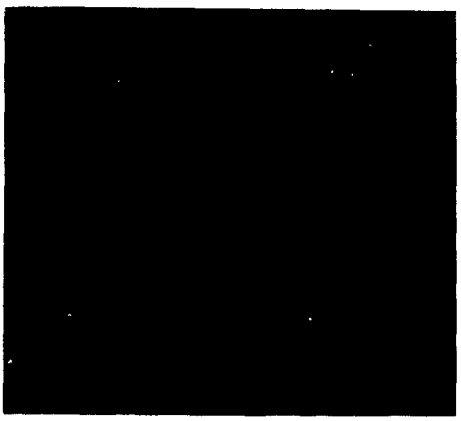

Figure 6. Symmetrized surface for natural jet at threshold 170 out of 255. This isovalue surface is from the averaged images (example shown in Fig. 5 right).

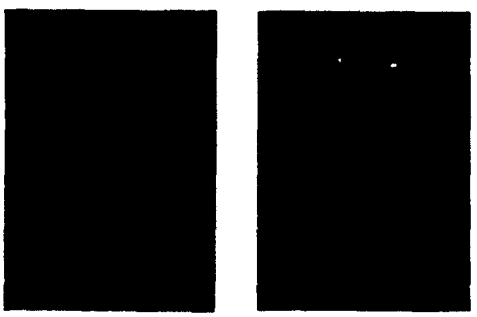

Figure 7. Similar to Fig. 3, but for the circularly forced jet dataset.

The structures again increase in extent and decrease in velocity as the jet progresses downstream We notice here, too, that the coherent structures are present at all times in the flow, and that they maintain themselves over most of the downstream range shown.

The most interesting result from this dataset arises from our two-dimensional ensemble average. If one looks at the rescaled ensemble average from the forced jet and compares it to that for the natural jet (Fig 9), the increase in the spreading rate of the jet is clearly evident Using the first visible edge (around a gray scale level of 50 out of 255, or 20% of the centerline concentration), the natural jet has a spreading angle of about 19°, while the forced jet has a spreading angle of about 22°. Our results in the far-field are not as striking as those of Lee (1985), who reported a near-field spreading angle of 50° at the same St with circular forcing of amplitude 8% of d_o This increase in the angle may be no surprise, considering the amount of radial momentum that is initially imparted to the flow by the nozzle forcing.

We also symmetrized this dataset, but because of the greater deviations from the centerline, the overlap between the image and its flipped version was much smaller and therefore the difference between the original isovalue surface and its symmetrized version is not as significant. Fig. 10 shows the symmetrized surface for the circularly forced jet; it is not nearly as smooth as the surface in Fig. 6 It is nevertheless noticeably smoother than the original surface in Fig. 8—note for example in Fig 10 the much shallower corrugations at the top of the surface as compared with those in Fig 8 This symmetrized surface is about 800,000 triangles, *vs* 1 1 million triangles for the original version.

DISCUSSION AND CONCLUSIONS

We have applied a new technique for analyzing and interpreting large scalar datasets by extracting an isovalue surface from a sequence of axial cross sections of a round turbulent jet This technique has enabled us to easily observe the evolution of the turbulent round jet and the effects of circular nozzle forcing on the far-field instability modes in this flow We wish to emphasize that our technique gives results that could not have been readily obtained using more traditional approaches Although one may have some impression of large-scale structures ,, the overall zigzag shape of the jet while watching the videotape of the flow, their frequency, robustness, velocity and mode are all much more readily evident in the $x - y - t$ isosurface representation Furthermore, *all* of our two-dimensional data (*vs.* point measurements) are represented in our results, and the data are not preconditioned We therefore believe that the results here more fully capture the physics of this flow.

We see that large-scale structures exist at every instant of time in the far-field of both the natural and circularly forced turbulent round jet at $Re = 4000$. The coherent structures increase in extent as the local jet diameter d increases, and their convection speed decreases as the local jet centerline velocity $u_c(x)$ decreases They are surprisingly robust in many cases maintaining themselves over the entire downstream distance observed (about three to four local jet diameters). The helical instability mode is the more

Figure 8. Similar to Fig 4, but for the circularly forced jet dataset

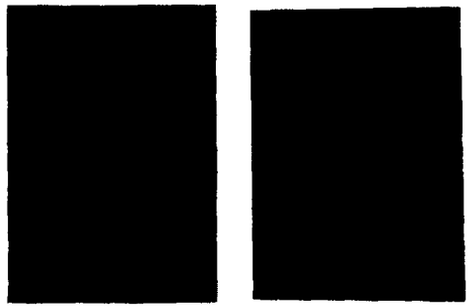

Figure 9. Ensemble averages over 100 jet cross sections for both the natural (left) and circularly forced (right) datasets.

Figure 10. Symmetrized surface for the circularly forced jet.

dominant mode in the far-field of the natural jet as predicted by Batchelor and Gill.

Circular forcing of the nozzle has a pronounced effect on the far-field structure, amplifying the helical mode of the jet. The spreading angle of the forced jet increases by about 15% from the natural jet because of the additional radial momentum imparted by the nozzle forcing. To our knowledge, these are the first far-field measurements on the circularly forced turbulent round jet. The omnipresence of these coherent structures in both types of jets suggests that they play a significant role in the physics of three-dimensional free turbulent shear flows (perhaps in mixing as suggested by Broadwell & Breidenthal).

Until now, this new volumetric visualization technique has have been used to extract mainly qualitative features of the flow. However, this technique can and should be extended to obtaining quantitative results. We therefore plan to next obtain the instantaneous three-dimensional quantitative concentration field of these flows at various *Re* (by sweeping the laser light sheet), and to further develop quantitative data analysis techniques.

ACKNOWLEDGEMENTS

We wish to thank Paul Ning, who wrote the marching cubes software; Prof. R.J. Moffat, for the use of his video digitizing system, and Prof. W.C. Reynolds, for the use of his jet nozzle apparatus. The help of Dr. Abraham Aharoni in optical system design and of Jim Helman in computer related matters is also greatly appreciated. This work was funded by National Science Foundation grant number ECS-8815815. We are grateful for their support.

REFERENCES

Agüí, J.C. & Hesselink, L. 1988. Flow visualization and numerical analysis of a coflowing jet: a three-dimensional approach. J. Fluid Mech. 191, 19–45.

Batchelor, G.K. & Gill, A.E. 1962. Analysis of the stability of axisymmetric jets. J. Fluid Mech. 14, 529–551.

Broadwell, J.E. & Breidenthal, R.E. 1982. A simple model of mixing and chemical reaction in a turbulent shear layer. J. Fluid Mech. 125, 397–410.

Broadwell, J.E. & Mungal, M.G. 1991. Large-scale structures and molecular mixing. Phys. Fluids A 3, 1193–1206.

Brown, G.L. & Roshko, A. 1974. On density effects and large structure in turbulent mixing layers. J. Fluid Mech. 64, 775–816.

Crow, S.C. & Champagne, F.H. 1971. Orderly structure in jet turbulence. J. Fluid Mech. 48, 547–591.

Dahm, W.J.A. 1985. Experiments on entrainment, mixing and chemical reactions in turbulent jets at large Schmidt number. Ph.D. thesis, California Institute of Technology.

Dimotakis, P.E., Miake-Lye, R. & Papantoniou, D.A. 1983. Structure and dynamics of round turbulent jets. Phys. Fluids A 26, 3185–3192.

Hesselink, L. 1988. Digital image processing in flow visualization. Ann. Rev. Fluid Mech. 20, 421–485.

Jiménez, J., Cogollos, M. & Bernal, L.P. 1985. A perspective view of the plane mixing layer. J. Fluid Mech. 152, 125–143.

Lee, M. 1985. Bifurcating and blooming jets. Ph.D. thesis, Stanford University.

Lorensen, W.E. & Cline, H.E. 1987. Marching cubes: a high resolution three-dimensional surface construction algorithm. Computer Graphics 21, 163–169.

Mungal, M.G., Lozano, A. & van Cruyningen, I. 1991. Large-scale dynamics in high Reynolds number jets and jet flames. Expts. in Fluids (to appear).

Mungal, M.G. & O'Neil. 1989. Visual observations of a turbulent diffusion flame. Comb. and Flame 78, 377–389.

Ning, P.C. & Hesselink, L. 1991. Adaptive isosurface generation in a distortion-rate framework. Proceedings of the SPIE 1459 (to appear).

Tso, J. & Hussain, F. 1989. Organized motions in a fully developed turbulent axisymmetric jet. J. Fluid Mech. 203, 425–448.

Tso, J., Kovasznay, L.S.G. & Hussain, A.K.M.F. 1981. Search for large-scale coherent structures in the nearly self-preserving region of a turbulent axisymmetric jet. Trans. ASME I. J. Fluids Engng. 103, 503–508.

Yoda, M. & Hesselink, L. 1990. A three-dimensional visualization technique applied to flow around a delta wing. Expts. in Fluids 10, 102–108.

EIGHTH SYMPOSIUM ON
TURBULENT SHEAR FLOWS
Technical University of Munich
September 9-11, 1991

CONTROL OF AN AXISYMMETRIC TURBULENT JET BY MULTI-MODAL EXCITATION

Ganesh Raman*, Edward J Rice** and Eli Reshotko†

* Sverdrup Technology, Inc , NASA Lewis Research Center Group
Brook Park, Ohio 44142, U S A

** NASA Lewis Research Center
Cleveland, Ohio 44135, U S A

† Case Western Reserve University
Cleveland, Ohio 44106, U S A

ABSTRACT

Experimental measurements of naturally occurring instability modes in the axisymmetric shear layer of a high Reynolds number turbulent jet are presented The region up to the end of the potential core was dominated by the axisymmetric mode. The azimuthal modes dominated only downstream of the potential core region The energy content of the higher order modes ($m > 1$) was significantly lower than that of the axisymmetric and $m = \pm 1$ modes Under optimum conditions, two frequency excitation (both at $m = 0$) was more effective than single frequency excitation (at $m = 0$) for jet spreading enhancement. An extended region of the jet was controlled by forcing combinations of both axisymmetric ($m = 0$) and helical modes ($m = \pm 1$) Higher spreading rates were obtained when multi-modal forcing was applied

INTRODUCTION

The study of the fundamental aspects of natural jets as well as their excitability and control is of great practical importance and shows promise for enhancing mixing, controlling separation and reducing jet noise

Although a vast body of data exists, most of the observations have been made in idealized "clean" jet flows There is a need for studying these phenomena in jets that are more representative of industrial applications, i e , high Reynolds number, fully turbulent initial condition, and high core turbulence In addition, the focus needs to be at and beyond the potential core Such an understanding is essential if any further progress is to be made in the application of these techniques to technologically relevant situations.

In a jet excited by naturally occurring disturbances, the large scale coherent structures occur over a band of frequencies and over various azimuthal mode numbers. The nature of these structures has frequently been characterized using correlation functions (Drubka, 1981, Sreenivasan, 1984, Chan, 1977, Gutmark et al , 1988) Correlations of streamwise velocity with circumferential separation can indicate the relative dominance of the axisymmetric or the azimuthal waves For example, the correlations are independent of circumferential separation if the flow consists of circular vortex rings If the correlations show a circumferential dependence, they may be due to azimuthal waves developing on the circular vortex rings, or by a transverse flapping of the jet. The modal spectrum representation provides the capability of resolving the naturally occurring axisymmetric and azimuthal modes over a range of frequencies

Sample mode spectra have been reported previously (Petersen et al., 1987) but have not been used to characterize the evolution of the various instability modes triggered by natural disturbances. Drubka (1981) examined the evolution of modes in an unexcited jet for both laminar and turbulent exit conditions at various levels of core turbulence However, most of the measurements reported were for $x/D < 1$ at a Reynolds number of 42,000 From the standpoint of practical applications there is a need to study the evolution of modes over an extended region of the jet and at more representative Reynolds numbers

There have been several other investigations of instability modes in jets (Kusek et al , 1989; Corke et al , 1991) In these studies, a very low level of excitation was used to organize shear layer instabilities and to raise the large scale coherent structures over the background levels, in addition to providing a phase reference for the measurements. Even though the levels of excitation were of the same order as the naturally occurring fluctuations, the jet displayed different characteristics For example, in the work of Corke et al., 1991, low amplitude acoustic excitation of the jet at the natural fundamental frequency of the axisymmetric mode suppressed the occurrence of the helical modes observed by Drubka, 1981, in the same jet facility For this reason, it is necessary to document the evolution of natural instability modes without any acoustic excitation

Cohen and Wygnanski (1987-a) calculated the natural evolution of disturbances in the axisymmetric mixing layer. Linear stability analysis was applied to a family of mean velocity profiles for the first seven azimuthal modes after assuming that the flow is inviscid and quasi-parallel These calculations showed that at $x/D = 0.125$ the amplification rates of the first four azimuthal modes are almost indistinguishable from one another As the mixing layer widens the relative importance of the azimuthal modes diminishes and at the end of the potential core, only the $m = 1$ and the $m = 0$ modes remain amplified Their calculations reveal that at the end of the potential core, mode 1 emerged as the dominant instability This was also predicted by Michalke and Hermann (1982) and Batchelor and Gill (1962), and reported by Mattingly and Chang (1974) and Zaman and Hussain (1984) It is suggested, therefore, that the $m = 1$ azimuthal mode is prevalent at the end of the potential core, and one expects this mode to control the evolution of the fully developed jet. However, the experimental evidence for the existence of spinning modes in high Reynolds number jets has been rather sketchy. Direct proof, through detailed measurements, has yet to substantiate these findings

The degree of jet spreading offered by single frequency plane wave excitation may not seem attractive enough to pursue for practical applications However, when the "preferred mode" frequency becomes neutrally stable, its subharmonic, which is then amplifying near its maximum rate, can be used to cause further mixing enhancement The development of a subharmonic in a free shear layer has been observed by several researchers An analysis was presented by Kelly (1967) which showed that there exists a mechanism for the generation of a subharmonic wave in the case of a flow with a hyperbolic tangent velocity profile It was

shown later by Ho and Huang (1982) that the spreading rate of a mixing layer can be manipulated significantly by forcing near the subharmonic of the preferred frequency

Furthermore, when the shear layer is excited simultaneously by the fundamental and subharmonic, an interaction could occur leading to a large augmentation of the subharmonic amplitude Some aspects of this problem have been addressed by Ho and Huang (1982), Mankbadi (1985), Monkewitz (1988), Cohen and Wygnanski (1987-b), and Ng and Bradley (1988).

There have been no experiments reporting two-frequency interactions and their effect on the spreading rate of high Reynolds number ($\sim 10^6$) jets with a turbulent initial condition, possibly because the levels of excitation required to bring about the two-frequency interaction in these jets are too high to be provided by conventional acoustic drivers In addition the two frequency experiment is complicated by a multitude of parameters which need accurate documentation For example, the work of Ng and Bradley (1988) at a Re(D) of about 16,000, documents the phase difference between the two waves and their amplitudes in the input signal, which would be completely different from that present in the flow at the jet exit There is therefore a need for a controlled parametric study of the effects of two-frequency excitation on a high Reynolds number jet with a turbulent nozzle exit boundary layer

However, two-frequency plane wave excitation also has its limitations since the axisymmetric mode only dominates up to the end of the potential core (Batchelor and Gill (1962)) Control in the region downstream can be gained only by forcing modes that are amplified in that region Documented attempts to control the spreading rate of a high Reynolds number turbulent initial condition jet by multi-modal forcing have been quite limited The available data deals mainly with the initial region of low Reynolds number jets with laminar nozzle exit conditions (Strange and Crighton (1983), Cohen and Wygnanski (1987-b), Corke and Kusek (1991))

In summary, the objective of the present work is to study natural as well as excited jets under conditions of technological relevance, i e , high Reynolds number, fully turbulent initial condition and with a focus on the region at and beyond the potential core

EXPERIMENTAL APPARATUS

The axisymmetric jet facility (Figure 1) consists of a 30 inch diameter plenum chamber which is supplied by 40 psi air through an 8 inch line Flow control is made possible through a main butterfly valve and a bypass plug valve The plenum tank includes acoustic treatment as well as flow straightening and turbulence reduction hardware The front end of the plenum tank consists of a contraction which ends in a 3 5 inch diameter nozzle with a 10 inch straight section at the end A trip ring was used on the flange, which attached the nozzle to the plenum tank The trip ring ensured that the nozzle exit boundary layer was fully turbulent Details of the trip ring and the nozzle exit boundary layer are documented in Raman et al (1989)

The high amplitudes required for the multi-frequency interactions were provided by Ling electro-pneumatic drivers (Model EPT 9B) These drivers operate at an air supply pressure of 40 lb/sq inch each, and are capable of producing low frequency ($f < 1000$ Hz) complex waveforms with an acoustic power up to 4000 watts The 40 psi air supplied to the Ling drivers is exhausted into the plenum tank by elbows which turn the flow upstream into the tank Downstream of the elbows, a screen and honeycomb section conditions the flow The exhausted air passed through this flow conditioning and provided the air flow through the nozzle Measurements made at the nozzle exit showed that the mean axial velocity profiles were uniformly "top-hat" and unaffected by this unusual air supply scheme The turbulence intensity measured at the jet exit was 1 5% as compared to 0 1% for the normal air supply scheme (see Raman et al (1988), Raman and Rice (1989))

An azimuthal array of acoustic drivers is used to input various modes into the jet The driver array consists of 8 acoustic drivers mounted on a support ring with an equal circumferential spacing The desired forcing conditions at the nozzle exit were produced as follows An 8 channel signal generator was used to produce variable amplitude and variable phase signals at a prescribed frequency. These signals were then amplified and input to the acoustic drivers The unsteady velocity perturbation caused by the acoustic excitation was measured at the jet exit (at $x/D \approx 0$, $U/U_{CL} = 0.8$) using 8 hot-wire probes and the modal content was determined The iterative fine tuning of the inputs and measurement of the modal content at the jet exit was continued until satisfactory forcing conditions were obtained. This was necessary because the trans-

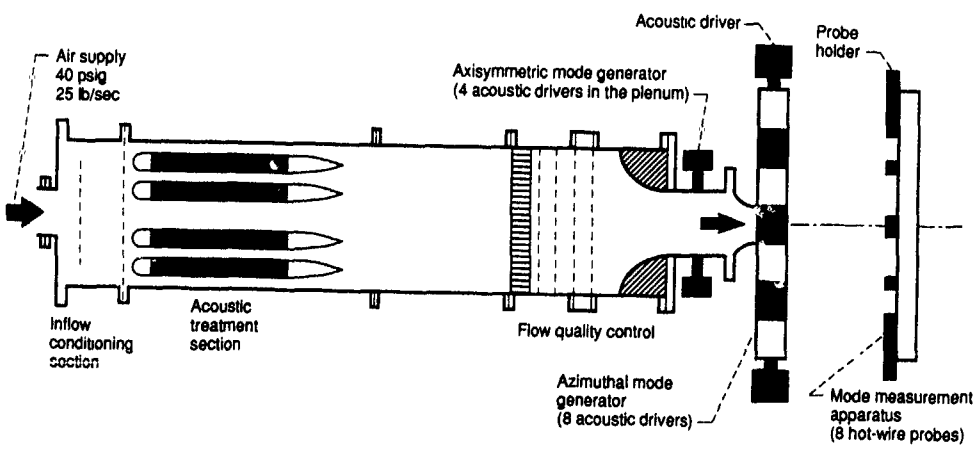

Figure 1.—Schematic of jet excitation facility

fer function associated with the system (amplifiers, cables, acoustic drivers, and tubes) caused the input phases and amplitudes to be different from those measured at the jet exit The radial traversing ring is used to traverse 8 single or x-wires simultaneously in the radial direction.

DISCUSSION OF RESULTS

Naturally Occurring Modes in a Jet

The modal decomposition representation at a discrete frequency of the spectrum can be used to characterize the flow as consisting of various modes of motion of the vortical structures at that frequency The modal spectrum was determined by measuring the unsteady streamwise velocity using 8 hot-wires positioned at intervals of 45° about the circumference of the jet cross-section. Linearized signals from the hot-wires were input to a spectrum analyzer to obtain cross-spectra The cross-spectra are randomly triggered ensemble averages over a long time interval. Using the signal from hot-wire number 1 as reference, 7 cross-spectrum magnitudes and phases were evaluated at each frequency with the 7 cross-spectra (magnitudes and phases) as input the magnitude and phase of the first 3 modes in the clockwise direction and the first 3 modes in the counter-clockwise direction were determined, by solving the 7 simultaneous complex equations To generate the modal spectrum, the decomposition is performed at every frequency in the chosen range The modal spectrum then consists of the amplitude of the mode plotted as a function of the frequency The modal decomposition was performed at every 5 Hz up to 2000 Hz using 8 circumferential measurements providing the magnitude of modes $m = 0, \pm1, \pm2, \pm3$ as a function of frequency

Results will be shown for one case at $M = 0.2$ ($Re(D) = 400{,}000$), with a core turbulence intensity of 0 1% and a turbulent nozzle exit boundary layer The data in Figure 2(a-d) show that the energy content of the higher order modes ($m > 1$) was significantly lower than the $m = 0$ and $m = \pm1$ modes The initial region of the jet is dominated by the axisymmetric mode, whereas the region downstream of the potential core is dominated by helical modes Drubka (1981) found that when the disturbance level in his laminar exit boundary layer was of the order of 5% the probability of finding either mode (0 or 1) was 0 5, near the nozzle exit ($x/D < 1$) The present work (Figure 2) shows that the axisymmetric mode is dominant in the initial region But beyond the end of the potential core ($x/D \sim 6$) the helical modes dominate The damping of the axisymmetric mode beyond the potential core is in agreement with the predictions of Batchelor and Gill (1962) and Morris (1976)

The stability analysis of Strange and Crighton (1983) predicted that helical waves would be more amplified than axisymmetric waves at the preferred frequency Even though the helical modes have a higher growth rate (Raman (1991)), the initial region of the jet is dominated by the axisymmetric mode. This result is attributed to the type of natural disturbances occurring at the jet lip For the 8 89 cm nozzle used, the cutoff frequency for all nonaxisymmetric modes was 2270 Hz (Skudrzyk (1971), page 431) Therefore, acoustic disturbances in the frequency range of 0 - 1000 Hz arriving at the jet lip through the nozzle are axisymmetric Some of these disturbances are of a relatively high amplitude (due to plenum resonances) and they couple

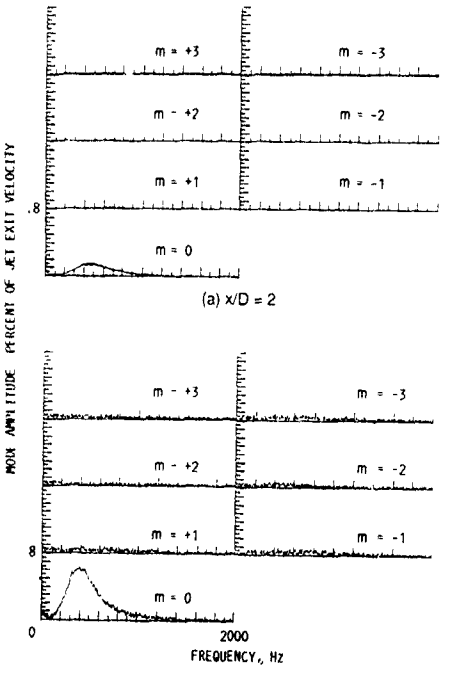

Figure 2.—Axial evolution of the natural modes in a circular jet, turbulent initial boundary layer, velocity measurement at $U/U_{CL} = 0.8$, M = 0.2, Re(D) = 400 000

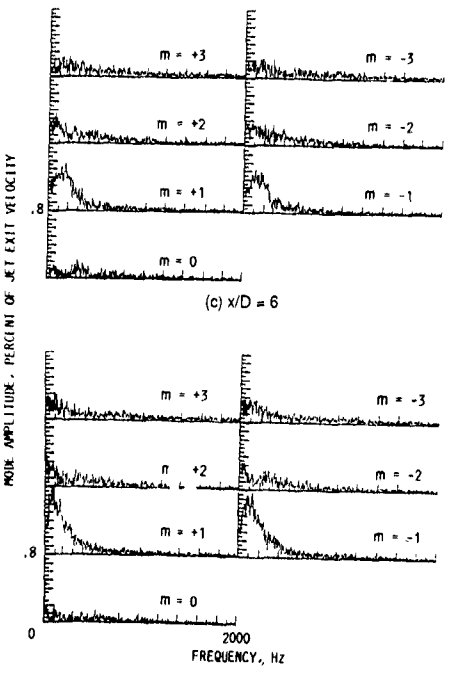

Figure 2 —Concluded.

with naturally occurring disturbances in the initial region of the shear layer Therefore, the axisymmetric "natural excitation" is much higher than the azimuthal "natural excitation" and this in turn causes the initial region of the jet to be dominated by the axisymmetric mode.

Multiple Frequency Axisymmetric Mode ($m = 0$) Forcing

Figure 3 shows the development of the phase-averaged velocities of the fundamental and subharmonic for the Strouhal number pair 0.3, 0.6. The initial forcing level of the fundamental is kept constant, whereas the forcing level of the subharmonic is varied from 0 1 to 3 percent, In Figures 3(a) to (c), both the subharmonic peak and the axial location of the peak depend on the initial phase difference Figure 3(d) shows that the peak attained by the subharmonic is not highly dependent on the initial phase difference when the initial subharmonic forcing level is high. The finding that at high forcing amplitudes of the fundamental and subharmonic, the subharmonic is always augmented irrespective of the initial phase difference is not only useful but it will have a favorable impact on the design of practical excitation devices

The top row in Figure 4 shows the development of the phase-averaged velocities along the jet centerline for axial distances up to 9 diameters (potential core length $\sim$ 6 diameters) The four cases represented are· the fundamental alone, the subharmonic alone, both f and $f/2$ at phase = 180°, and finally both f and $f/2$ at phase = 0° Though the waves do not grow to very large amplitudes individually, the two-frequency interaction causes the subharmonic to be augmented to very high levels (or suppressed), depending on the initial phase difference between the two waves The second row shows the jet center-line velocity along with the unexcited case for comparison The last row shows the momentum thickness development with axial distance Very clearly under optimum conditions, two-frequency excitation is more effective than single frequency excitation for jet spreading enhancement The data presented in Figure (3) and (4) is at $M = 0\,2$ ($Re(D) = 400{,}000$), with a core turbulence intensity of 1 5% and a turbulent nozzle exit boundary layer Measurements at $Re(D)$ up to 870,000 are reported in the paper by Raman and Rice (1989)

The jet centerline velocity and momentum thickness variations are both used as indicators of jet spreading enhancement A drop in the centerline velocity indicates a higher jet spread for most cases. There is, however, a reversal in the jet centerline velocity trend between $x/D = 1$ and 3 This is not to be interpreted as a "reversal of spreading" Due to the shortcomings of the jet centerline velocity as a "spreading" indicator, the momentum thickness is considered to be a better indicator of jet spreading enhancement The jet centerline velocity is, however, retained as it shows a direct relationship between subharmonic augmentation and the "eating up" of the potential core of the jet The high growth rate of the subharmonic wave causes it to extract energy from the mean flow, which causes the destruction of the potential core Based on the theoretical work of Mankbadi and Liu (1981), the results of Figure 4 can be interpreted as follows: the local regions of mean flow "acceleration" might be attributed to modes evolving into their "damped" region where energy is pumped back into the mean flow from the oscillations, with accompanying decrease in the momentum thickness growth rate

The difference between single and two-frequency optimum excitation results is most pronounced on the jet centerline velocity The two-frequency case with phase difference equal to zero produces the same spreading as the single frequency excitation at the fundamental frequency As seen

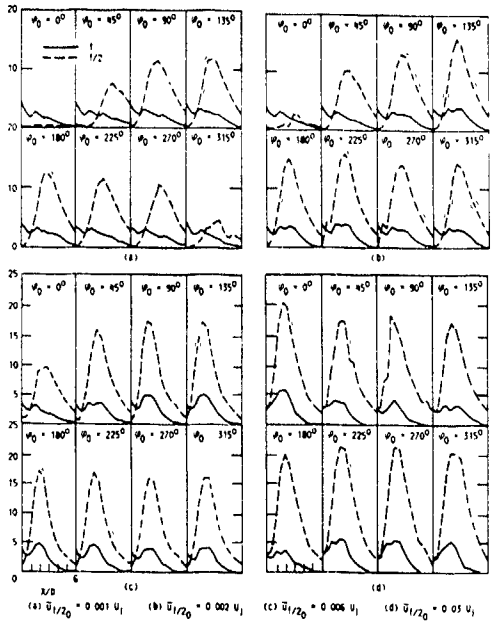

Figure 3.—Axial evolution of phase-averaged unsteady velocity components on the jet centerline for various initial phase differences and subharmonic forcing levels. (St = 0 3, 0 6, $\tilde{u}_{f0} = 0.3U_j$, M = 0 2).

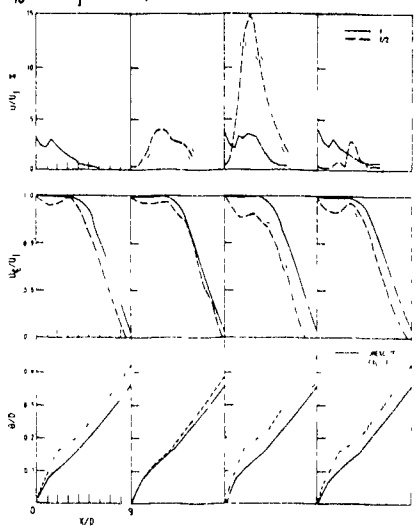

Single Frequency Forcing

(a) $St = 0.6$, $\tilde{u}_{f_0} = 0.03\,U_j$

(b) $St = 0.3$, $\tilde{u}_{f/2_0} = 0.002\,U_j$

Two-Frequency Forcing

(c) $St = 0.3, 0.6$, $\varphi_0 = 180°$, $\tilde{u}_{f_0} = 0.03\,U_j$, $\tilde{u}_{f/2_0} = 0.002\,U_j$

(d) $St = 0.3, 0.6$, $\varphi_0 = 0°$, $\tilde{u}_{f_0} = 0.03\,U_j$, $\tilde{u}_{f/2_0} = 0.002\,U_j$

Figure 4 —Two-frequency excitation effects on jet centerline phase averaged and mean velocities and jet momentum thickness

in Figure 4 (top right), this two-frequency excitation suppresses the coherent subharmonic growth, and additional spreading from forced pairing does not result. Some random pairing may still occur, as might be expected in the single frequency excitation case

Multi-Modal Forcing

Based on the results presented thus far, plane wave ($m = 0$) excitation would be expected to be effective mainly in the region up to the end of the potential core, since beyond this point, the axisymmetric mode is damped. Control of the region beyond the potential core could be accomplished via the forcing of the helical modes. Hence, a combination of both plane wave and helical mode forcing would be expected to be even more effective for controlling the jet than either excitation applied alone. Results will be shown for one case at a Reynolds number of 400,000, with a core turbulence intensity of 0.1% and having a turbulent nozzle exit boundary layer.

Figure 5 shows the evolution of modes for a forcing case. $m = \pm 1$ at $St(D) = 0.15$, and $m = 0$ at $St(D) = 0.6$. The forcing here is in the range of the naturally preferred frequencies determined from the modal spectrum for the unforced jet. The forcing levels measured at $U/U_C = 0.8$, $x/D = 0$ were $(\tilde{u}_0/U)_{St(D)=0.6,m=0} = 0.06$ and $(\tilde{u}_0/U)_{St(D)=0.15,m=\pm1} = 0.02$. The modal decomposition technique used for generating these results is the same as that for the unexcited case. However, only the coherent part of the signal at the excitation frequency was used.

In the initial region, the axisymmetric mode ($m = 0$) grows to about 9 percent of the jet exit velocity. Note that the modes in Figure 5(a) are evolving in the presence of each other. Figure 5(a) shows that the $m = 0$ mode is amplified and saturates in the initial region of the jet. As the $m = 0$ mode becomes damped, the $m = \pm 1$ (combined and denoted by a single curve) grow and peak around $x/D = 6$, beyond which they are damped. Figure 5(b) shows the momentum thickness plotted versus axial distance.

Curves are shown for the following cases: unexcited, plane wave ($m = 0$ at $St(D) = 0.6$), helical modes ($m = \pm 1$, at $St(D) = 0.15$), and the multi-modal case ($m = 0$ at $St(D) = 0.6$ and $m = \pm 1$ at $St(D) = 0.15$). The last two cases are represented by bands bounded by θ_{max} and θ_{min} since θ varies azimuthally. Comparing Figures 5(a) and (b) one observes that the local regions of higher spreading rate (steeper curves in Figure 5(b) for x/D between 0 and 2, 4 and 6) correspond to regions of wave amplification in Figure 5(a), and local regions of lower spreading rate (flattening of curves in Figure 5(b), for x/D between 2 and 4, greater than 6) correspond to regions where the waves are damped. The jet's spreading rate is enhanced in a 2-step process. In step 1, due to $m = 0$ (x/D between 0 and 2), and in step 2, due to $m = \pm 1$ (x/D between 4 and 6). The above interpretation is also supported by the theory of Mankbadi and Liu (1981).

The low frequency helical modes along with the axisymmetric mode of the multi-modal case (Figure 5) are more effective in producing higher spreading rates in the downstream region ($5 < x/D < 10$). Therefore, the choice of the forcing frequencies would vary depending on the region over which maximum control is desired. From Figure 5 it is clear that the combination of a plane wave and two opposing helical modes provides a higher degree of control over the spreading rate of the jet than either excitation applied alone. The plane wave enhances spreading up to the end of the potential core, and helical modes ($m = \pm 1$) cause the jet to flap beyond the potential core.

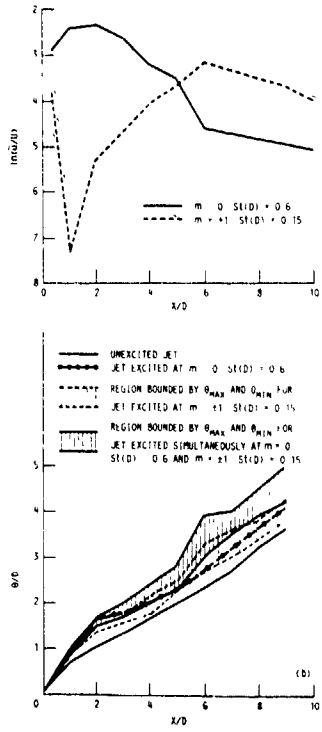

Figure 5 —Multi-modal excitation results (forcing levels, $\tilde{u}_0/U = 0.06$, $(St(D) = 0.6, m = 0)$ $(\tilde{u}_0/U = 0.02$, $(St(D) = 0.15, m = \pm 1))$

SUMMARY AND CONCLUSIONS

The overall objective was to study natural as well as excited jets under conditions more representative of practical applications, i.e. high Reynolds number and fully turbulent initial condition, with a focus at and beyond the potential core. The conclusions are as follows:

(1) The evolution of instabilities resulting from naturally occurring disturbances at the jet lip was studied using the modal frequency spectrum. The region up to the end of the potential core was dominated by the axisymmetric mode. The azimuthal modes grew rapidly but dominated only after the potential core region. For the jet excited by natural disturbances the energy content of the higher order modes ($m > 1$) was significantly lower than the axisymmetric and $m = \pm 1$ modes.

(2) Based on the results from the naturally occurring jet instability mode experiments, target modes for efficient excitation of the jet were determined. The effect of exciting a high Reynolds number, initially turbulent jet simultaneously at fundamental and subharmonic frequencies was studied. The initial phase difference between the two waves was varied in steps of 45°. The effect of varying the initial forcing levels was also studied. It was found that at high amplitudes of fundamental and subharmonic forcing levels, the subharmonic augmentation and the axial location of the peak are independent of the initial phase difference. This finding will have a very favorable impact on the design of practical excitation devices. Two-frequency excitation is indeed more effective than single frequency excitation in jet spreading enhancement. The spreading is quantified by:

(a) Jet centerline velocity, which shows the "eating up" of the potential core

(b) The momentum thickness, which shows the jet spreading rate, and

(3) Forcing combinations of multiple frequencies and multiple modes provides even a higher degree of control over the spreading rate of the jet. When the combination is applied, the plane wave enhances mixing in the region up to the end of the potential core, and the helical modes ($m = \pm 1$) cause the jet to flap beyond the potential core In this way, the region of control is extended

ACKNOWLEDGEMENTS

Funding for this work was provided under NASA contract NAS3-25266 Thanks are extended to Mrs Tammy Langhals of Sverdrup Technology, Inc for the production of this manuscript

REFERENCES

Batchelor, G K and Gill, A , (1962), "Analysis of the Stability of Axisymmetric Jets", J Fluid Mech , 14,529

Chan, Y Y , (1977), "Wavelike Eddies in a Turbulent Jet", AIAA J ,15, 992-1001

Cohen, J and Wygnanski, I , (1987-a), "The Evolution of Instabilities in the Axisymmetric Jet Part 1 Tl Linear Growth of Disturbances Near the Nozzle", J Fluid Mech , 176, 191

Cohen, J and Wygnanski, I , (1987-b), "The Evolution of Instabilities in the Axisymmetric Jet. Part 2. The Flow Resulting from the Interaction Between Two Waves", J Fluid Mech , 176, 221

Corke, T C , Shakib, F , and Nagib, H M , (1991), "Mode Selection and Resonant Phase Locking in Unstable Axisymmetric Jets", J Fluid Mech , 223, pp 253-311

Corke, T C , and Kusek, S M , (1991), "Resonance in Axisymmetric Jets with Controlled Helical Mode Input", AIAA paper 91-0319

Crow, S.C and Champagne, F H , (1971), "Orderly Structure in Jet Turbulence", J Fluid Mech , 48, 547

Drubka, R E (1981), "Instabilities in Near Field of Turbulent Jets and their Dependence on Initial Conditions and Reynolds Number", Ph.D. thesis, Department of Mechanical and Aerospace Engineering, Illinois Institute of Technology, Chicago

Gutmark, E , Schadow, K.C , and Bicker, C J , (1988), "Mode Switching in Supersonic Circular Jets", 1st National Fluid dynamics Congress, Part 2, AIAA, New York, pp. 974-981

Ho, C M and Huang, L S , (1982), "Subharmonics and Vortex Merging in Mixing Layers", J Fluid Mech., 119, pp 443-473

Kelly, R E , (1967), "On the Stability of an Inviscid Shear Layer which is Periodic in Space and Time", J Fluid Mech., 27, 657

Kusek, S M , Corke, T.C , and Reisenthel, (1989), "Control of Two and Three Dimensional Modes in the Initial Region of an Axisymmetric Jet" (AIAA-89-0966)

Mankbadi, R and Liu, J T.C., (1981), "A Study of the Interactions Between Large-Scale Coherent Structures and Fine Grained Turbulence in a Round Jet", Philosophical Transactions of the Royal Society of London, Series A, Vol 298, No 1443, pp. 541-602

Mankbadi, R R , (1985), "On the Interaction Between Fundamental and Subharmonic Instability Waves in a Turbulent Round Jet," J Fluid Mech., Vol 160, pp 385-419

Mattingly, G E. and Chang, C C , (1974), "Unstable Waves on an Axisymmetric Jet Column", J. Fluid Mech , 65, 541

Michalke A , and Hermann, G , (1982), "On the Inviscid Instability of a Circular Jet with External Flow" J Fluid Mech , Vol 114, 343

Monkewitz, P A , (1988), "Subharmonic Resonance, Pairing and Shredding in the Mixing Layer", J Fluid Mech , Vol 188, pp 223-252.

Morris, P.J., (1976), "The Spatial Viscous Instability of Axisymmetric Jets", J Fluid Mech , 77, 511-529

Ng, T T , and Bradley, T A , (1988), "Effect of Multi-Frequency Forcing on the Near Field Development of a Jet"

Petersen, R A , Samet, M M, and Long, T A., (1987), "Excitation of Azimuthal Modes in an Axisymmetric Jet", IUTAM Symposium Bangalore India

Raman, G., Rice, E J , and Mankbadi, R R , (1988) "Saturation and the Limit of Jet Mixing Enhancement by Single Frequency Plane Wave Excitation: Experiment and Theory", 1st National Fluid Dynamics Congress, Part 2, AIAA, New York, pp. 1000-1007 (also NASA TM-100882)

Raman, G , and Rice, E.J , (1989), "Subharmonic and Fundamental High Amplitude Excitation of an Axisymmetric Jet", AIAA paper 89-0993, (also NASA TM-101946). (to appear in the AIAA J , AUG 1991)

Raman, G , Zaman, K B M Q , and Rice, E J , (1989) "Initial Turbulence Effect on Jet Evolution With and Without Tonal Excitation", Physics of Fluids A Vol 1, No. 7, pp 1240-1248

Raman, G., (1991) "An Experimental Study of Natural and Forced Modes in an Axisymmetric Jet", Ph D thesis, Department of Mechanical and Aerospace Engineering, Case Western Reserve University, Cleveland, Ohio (Also NASA TM).

Skudrzyk, E , (1971), "The Foundations of Acoustics", Springer Verlag Wien, New York

Sreenivasan, K R., (1984), "The Azimuthal Correlations of Velocity and Temperature Fluctuations in an Axisymmetric Jet", Physics of Fluids, Vol 27, No 4, pp. 867-875.

Strange, P J R and Crighton, D G , (1983), "Spinning Modes on Axisymmetric Jets", part 1 , J Fluid Mech , 134, 231-245.

Zaman, K B M Q , and Hussain A K M F , (1984), "Natural Large-Scale Structures in the Axisymmetric Mixing Layer," J Fluid Mech , Vol 138, pp 325-351

EIGHTH SYMPOSIUM ON
TURBULENT SHEAR FLOWS
Technical University of Munich
September 9-11, 1991

THE THREE-DIMENSIONAL EVOLUTION OF AXISYMMETRIC JETS PERTURBED BY HELICAL WAVES

James E Martin*) and Eckart Meiburg**)

*)Center for Fluid Mechanics, Division of Applied Mathematics
Brown University, Providence, RI 02912, USA

**)Department of Aerospace Engineering,
University of Southern California, Los Angeles, CA 90089, USA

ABSTRACT

We study the three-dimensional evolution of a helically perturbed nominally axisymmetric jet by means of inviscid vortex filament calculations. For the case of a helical perturbation only, the streamwise vorticity forming in the braids is of the same sign everywhere If the helical symmetry is broken by introducing an additional azimuthal perturbation, we observe the emergence of concentrated streamwise braid vortices all of the same sign, in contrast to the counterrotating braid vortices of ring-dominated jets A Kelvin-Helmholtz-like instability of the braid vorticity layer plays a significant role in their generation While for a jet with $R/\theta = 22.6$, rotation of the vortex helix prevents it from going unstable, we observe in a jet with $R/\theta = 11.3$ the reduction of this rotation and the near exponential growth of the vortex helix's radial corrugation

INTRODUCTION

The present investigation represents an extension of our earlier study focussing on the three-dimensional evolution of nominally axisymmetric jets (Martin and Meiburg 1991) Whereas we previously considered the evolution of jets dominated by axisymmetric coherent structures, we now analyze the effect of non-axisymmetric modes. The motivation for doing so comes from theoretical as well as experimental studies that have demonstrated the importance of non-axisymmetric or helical modes in axisymmetric jet flow. In particular, the stability analysis by Batchelor and Gill (1962) illustrates the importance of both axisymmetric and non-axisymmetric modes While axisymmetric disturbances lead to instability of velocity profiles with relatively thin jet shear layers, non-axisymmetric disturbances satisfy the conditions for instability regardless of the profile chosen. For a bell-shaped profile which models the downstream developed region of a jet, only non-axisymmetric disturbances of azimuthal wavenumber 1 are amplified. From their study, we can conclude that further downstream, as the profile of a jet becomes more smooth, helical perturbations can be more amplified than axisymmetric ones By writing the linearized disturbance equation in terms of the ratio of jet radius to momentum thickness, Cohen and Wygnanski (1987) furthermore demonstrate the dependence of the jet's stability on the streamwise position For large values of this ratio, maximum amplification growth rates are identical for helical and axisymmetric disturbances Smaller values of this ratio, corresponding to downstream development of a jet, show the non-axisymmetric disturbance growth rate overtaking that of the axisymmetric disturbance for all frequencies

In experimental studies, both ring-like and helical organized motions are observed to occur over approximately equal times in the jet's evolution (eg Mattingly and Chang 1974, Browand and Laufer 1975) In helix-dominated flows, the individuality of ring-like vortices is replaced by either a single helical vortex which coils around the jet column, or by double helical formations (Tso and Hussain 1989). Processes similar to pairing which occur amongst vortex rings in ring-dominated jets, also occur in the single helical vortex of helix-dominated jets (Browand and Laufer 1975) Even at extremely high Reynolds numbers, coherent structures in the form of helices are observed by Mungal and Hollingsworth (1989) as well as by Dimotakis, Miake-Lye and Papantoniou (1983). Their studies both suggest that the mechanisms behind the large scale structures' generation and sustenance is largely Reynolds number independent Since these large scale structures dominate the jet's evolution, it appears worthwhile to model the transitional 3-D evolution of a jet dominated by helical vortices with inviscid simulations

Past studies have shown the vortex filament technique (Leonard 1985) to be an efficient tool for simulating the vorticity dynamics of jets dominated by ring-like vortices (Martin, Meiburg and Lasheras 1990, Meiburg, Lasheras and Martin 1991, Martin and Meiburg 1991) and for comparison with experimental results Accounting only for the rotational elements of the flow field, one is able to efficiently gain considerable insight into the full three-dimensionality of jets dominated by rings We will again employ this technique for jets dominated by helical-type vortices

In our analysis of ring-dominated jets we observed three-dimensional features involving a counterrotating streamwise structure in the braid region and a growing three-dimensionality of the rings Furthermore, the rings of a jet were shown to be capable of undergoing instabilities similar to the one discussed by Widnall et al (1974) for isolated vortex rings, with their waviness increasing exponentially (Martin and Meiburg 1991) While flow visualization experiments and simulations have predominantly concentrated on the secondary streamwise structure in ring-dominated jets, the nature of a secondary streamwise structure in helix-dominated jets has largely remained unexplored We will study the form of this secondary structure and its interaction with the primary helical vortex. Furthermore, the observed instability of the jet's vortex rings to additional azimuthal perturbation raises the question of similar instability mechanisms in helix-dominated jets as well (Widnall 1972)

NUMERICAL TECHNIQUE

We employ a vortex filament technique similar to the one used in earlier studies of plane shear layers (Ashurst and Meiburg 1988), wakes (Meiburg and Lasheras 1988), and jets (Martin and Meiburg 1991) Vortex filaments are used for the representation of the vorticity field In the jet, the filaments initially have the form of vortex rings Each filament is represented by a number of nodes, through which a cubic spline is fitted to give it a smooth shape The non-divergent nature of the velocity field in incompressible flows, along with the definition of vorticity, then allows us to obtain the velocity field via the Biot-Savart law (Batchelor 1967) By applying the laws of Kelvin and Helmholtz for an inviscid fluid, the velocity for each node can be obtained and its position advanced according to

$$\frac{D\vec{x}}{Dt} = \vec{u}(\vec{x},t)$$

The Biot-Savart law for the velocity field is evaluated assuming an invariant vorticity distribution of algebraic shape about the filament centerline (e g , Meiburg, Lasheras and Martin 1991), following the concepts outlined by Leonard (1985) The incorporation of this vorticity distribution into the Biot-Savart law reduces the evaluation of the velocity field down to a line integral over all the filaments in the flow field

We limit ourselves to the temporally growing problem Periodicity is assumed in the streamwise direction Since the Biot-Savart law involves integration over the entire vorticity field, a number of periodic images of the filaments must be included in our integration Earlier studies demonstrated that by taking into account three images each in the upstream and the downstream direction, the velocity profile obtained is sufficiently close to the fully converged value Consequently, we carry along three images in our calculations

We take the velocity difference between the centerline and infinity as our characteristic velocity The thickness of the axisymmetric shear layer serves as the characteristic length scale In these units the radius of the jets considered here is 5 The Biot-Savart integration for the velocity is carried out with second order accuracy by employing the trapezoidal rule, while the time-stepping is performed with a predictor-corrector scheme also of second order accuracy We typically discretize the axisymmetric shear layer into 59 filaments per streamwise wavelength of initially 120 nodes each. As the flow develops a three-dimensional structure, the vortex filaments undergo considerable stretching. The spline representation of the filament centerlines then allows us to introduce new nodes to maintain an adequate resolution Furthermore, the time step is repeatedly reduced as local acceleration effects increase The filament core radius decreases as its arclength increases to conserve its total volume

EVOLUTION OF A HELICAL WAVE ALONE

We will first focus on the evolution of a nominally axisymmetric jet perturbed by a single helical wave of azimuthal wavenumber 1 A jet with a ratio of radius R to momentum thickness θ of 22 6 will form the basis of this discussion. Based on this value, we can determine a maximally amplified wavelength for a helical disturbance from the calculations of Michalke and Hermann (1982) These authors give spatial growth rates versus the non-dimensional frequency as a function of the ratio R/θ in spatially evolving, inviscid jets under helical disturbance

By applying Gaster's (1962) transformation we then obtain the wavenumber β for our temporally growing case with R/θ =22 6 as approximately 1

The helical perturbation we impose takes the form

$$x' = \varepsilon R \cos(\beta x + m\phi)$$

where m is the azimuthal wavenumber The perturbation initially displaces the centerline of a vortex filament a distance x' into the streamwise direction The amplitude ε of the perturbation is taken to be five per cent of the jet radius The overall form of the displacement is then the same for all vortex filaments However, there is an azimuthal phase shift in successive filaments which results in the helical nature of the overall perturbation Fig 1 demonstrates the roll-up that results from this

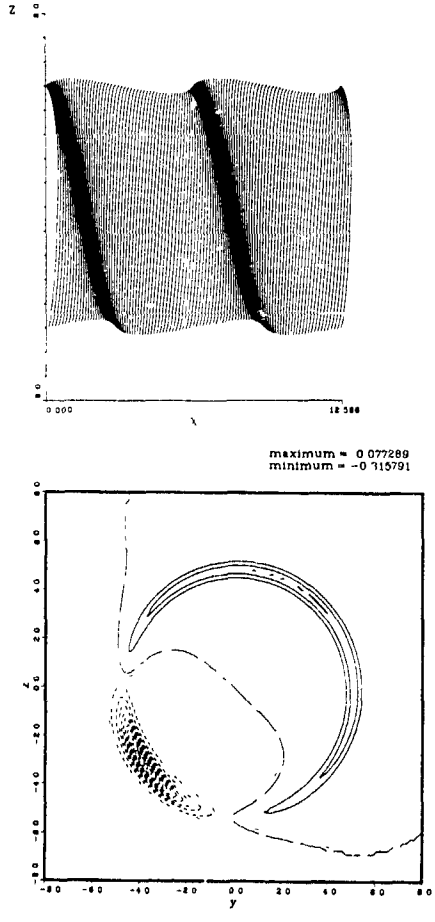

Figure 1 The helically perturbed jet with R/θ=22 6 at time 2 81 a) Side view of the vortex filaments, b) streamwise vorticity contours at x=4 Observe the growth of a vortex helix, corresponding in this case to the region of negative streamwise vorticity The strain field set up by the helix leads to a reorientation of the braid vorticity, which becomes aligned with the direction of extensional strain, thereby resulting in the formation of positive streamwise vorticity

helically symmetric perturbation We show a side view of the filament centerlines along with contours of the streamwise vorticity at a representative streamwise location For clarity, we plot in the side view only those portions of the filament centerlines whose y-location is greater than zero. Instability of the axisymmetric shear layer leads to the formation of a helical vortex As in the case of a ring-dominated jet, a strain field with a stagnation point forms in the braid region between successive segments of the helix However, the stagnation line itself is now a helix The axis of extensional strain in the braid region correspondingly orients itself normal to the emerging helical vortex While the streamwise vorticity contours contain a more concentrated region due to the helix, there is a growing opposite-signed region due to the braid vorticity As the braid vorticity reorients itself in the strain field of the growing helix, streamwise braid vorticity becomes increasingly generated

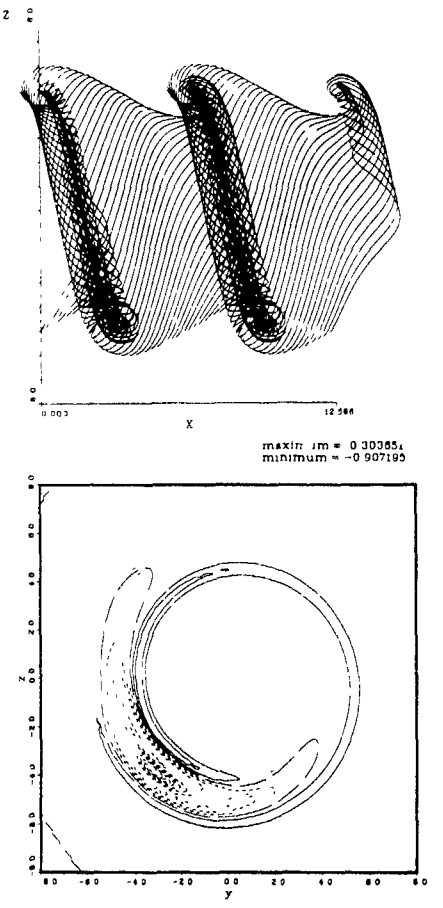

Figure 2 The helically perturbed jet at time 8 75 a) Side view of the vortex filaments, b) streamwise vorticity contours at x=4 The streamwise braid vorticity has the nature of a thin layer of infinite aspect ratio Due to the helical symmetry, concentrated braid structures do not form in this calculation

Figure 2 shows the resulting evolution of the flow later in time While the vortex helix continues to strengthen, the streamwise vorticity contours illustrate the nature of the braid vorticity, which is a flattened sheet of helical shape, occupying the space between the vortex helix The braid vorticity appears to spiral around the concentrated opposite-signed region of streamwise vorticity due to the vortex helix, as it begins to wrap around the vortex The helical symmetry of the present problem prevents any concentrated streamwise structures from forming in the braid region Some insight into how a secondary streamwise structure might evolve in a fully three-dimensional evolution of the helix-dominated jet, can be gained by considering the recent work done by Lin and Corcos (1984) on plane mixing layers The braid vorticity of the mixing layer is modeled as a two-dimensional sheet of streamwise vorticity undergoing a constant plane strain The resulting evolution of the braid vorticity layer is found by Lin and Corcos to be strongly dependent upon its aspect ratio In the helix-dominated jet, the aspect ratio of the braid vorticity tends to infinite value, while in ring-dominated jets the aspect ratio is of finite order This suggests to us that the instability within the braid region of a helix-dominated jet can evolve quite differently from that which occurs in ring-dominated jets In the following section, we will analyze the fully three-dimensional evolution by breaking the helical symmetry of our flow

EFFECT OF NOZZLE CORRUGATION

Figs 3 and 4 show the results of a calculation in which we introduce an additional perturbation in the circumferential direction as well This disturbance periodically displaces the filament centerline in the radial direction in addition to the axial displacement of the helical wave In this way, we duplicate the effect of nozzle corrugation The calculation shown in Figures 3 and 4 contain 5 waves around the azimuthal direction and correspond to times 7 89 and 15 70 respectively Again we consider a jet with a ratio of $R/\theta=22\,6$ The streamwise view of the filament centerlines indicates the form of the additional corrugation, while the side view of the filaments again shows the emergence of a strong helical vortex However, the helical vortex now displays a wavy modulation along its length As in the case of a ring-dominated jet emerging from a corrugated nozzle, the radial displacement brings the local and global induction effects into play, cf Meiburg, Lasheras and Martin (1991) The increased self-induced velocity of the outer sections of the vortex helix with greatest radius of curvature, tends to accelerate those sections into the streamwise direction, more so than the sections of the vortex helix located closer to the jet axis

The streamwise vorticity contours show concentrated structures, all of a single sign, forming within the braid region. This is in marked contrast to the counterrotating streamwise vortices which emerge in ring-dominated jets The sheet-like nature of the braid vorticity layer suggests that a Kelvin-Helmholtz instability is responsible for the braid structure With time, these axial vortices intensify under the extensional strain field of the vortex helix Fig. 4 shows their collapse to very concentrated tubes We expect this collapse to be strongly dependent upon the strain produced by the vortex helix The concentration of the vortices is therefore dependent upon their proximity to the helix

The side view of the filaments in Fig 4 indicates the growth of the streamwise amplitude of the vortex helix waviness, while the streamwise view indicates the near elimination of the radial amplitude of this corrugation In

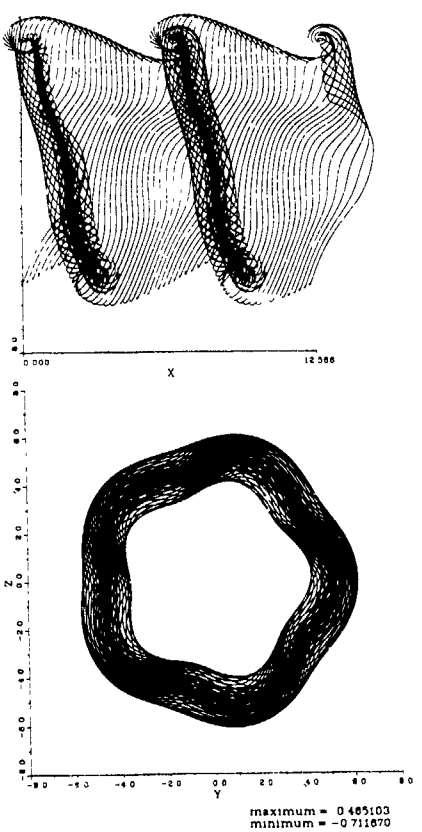

Figure 3. The helically perturbed jet with R/θ=22.6 under the effect of an additional azimuthal perturbation at time 7.89. a) Side view of the vortex filaments, b) streamwise view of the vortex filaments, c) streamwise vorticity contours at x=2 As a result of the additional azimuthal wave, the sheet-like braid vorticity undergoes a Kelvin-Helmholtz instability, so that concentrated streamwise braid vortices form In contrast to the counterrotating streamwise vortices observed in ring-dominated jets, the streamwise braid vortices are all of the same sign in the present case.

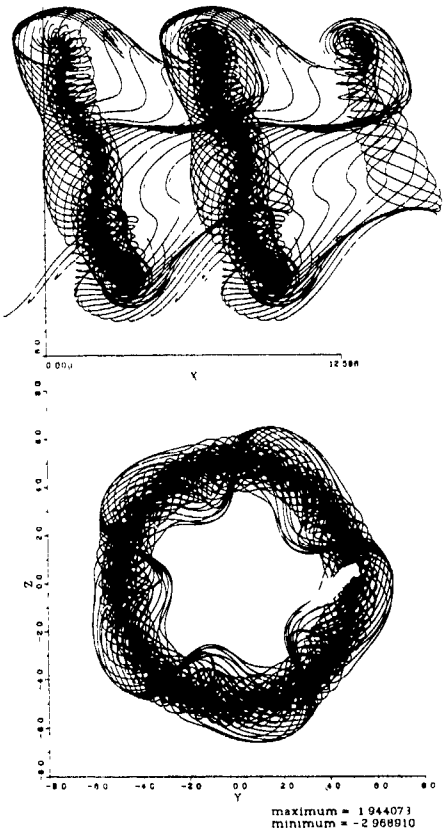

Figure 4 The same jet as in Fig 3 at time 15 70 a) Side view of the vortex filaments, b) streamwise view of the vortex filaments, c) streamwise vorticity contours at x=2 Observe the collapse of the streamwise braid vorticity into concentrated structures, in a way similar to the model case analyzed by Lin and Corcos (1984). Notice the waviness of the vortex helix visible in the side view, while the streamwise view does not display such a waviness

Fig 5, we plot the evolution of the streamwise and radial amplitudes of the vortex helix waviness along with the angle γ, where tan γ is given by the ratio of streamwise to radial amplitudes Variation in γ will then indicate a rotation of the helix It is interesting to note that while the counterrotating braid vortices of a ring-dominated jet act to increase corrugation, no such increase in radial amplitude occurs in the helix-dominated jet The radial amplitude a_r slowly decreases, while the streamwise amplitude a_s initially increases due to the self-induced velocity of the helix, and later levels off As with vortex rings, it is expected that a reduction in the rotation of the helix is necessary for it to undergo instability (Widnall 1972) However, γ increases continually for the present jet parameters as the helix continues to rotate, thus not allowing for an exponentially growing instability

While there is no evidence for a vortex helix instability for the above jet parameters, we expect that by increasing the momentum thickness of the jet, the core radius of the helix will increase as well, thereby reducing the helix's self-induced velocity and its rotation rate Consequently, we perform a similar calculation for a jet with R/θ=11 3. From the calculations of Michalke and Hermann, the decrease in R/θ results in a streamwise wavelength of 3π for maximum amplification. Again, an equal amplitude helical wave is introduced along with a corrugation Side view and streamwise view of this calculation are shown in Fig 6 The side view of the filaments shows a fairly small streamwise amplitude of the vortex helix waviness at this time, while the radial amplitude grows in a nearly exponential fashion (Fig. 7) This is consistent with the graph of γ for this calculation, which demonstrates an almost vanishing rotation rate of the helix, in contrast to the previously considered jet with a ratio of R/θ=22 6 The near exponential growth of the radial amplitude a_r thus suggests that a vortex helix instability is occurring

CONCLUSIONS

Our aim has been to shed light on some of the inviscid mechanisms that govern the three-dimensional evolution of nominally axisymmetric jets. By means of vortex filament simulations, we were able to gain considerable insight into the vorticity dynamics and flow characteristics of such jets perturbed by helical waves

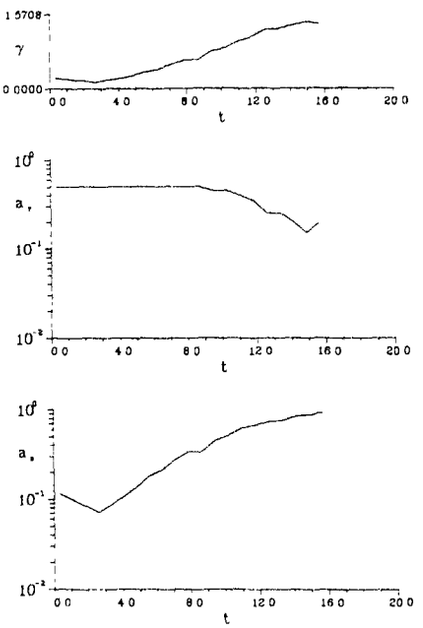

Fig 5 The temporal evolution of the radial (a_r) and streamwise (a_s) amplitudes of the vortex helix waviness for the case R/θ=22 6 These amplitudes are obtained by comparing the curve connecting the computed vorticity maxima in all planes x=const with a helical curve of equal streamwise wavelength. Also plotted is the angle γ, where tan(γ)=a_s/a_r The decrease in a_r and the leveling off of a_s indicate that the continuing rotation of the vortex helix (as reflected by the growth in γ) around its unperturbed centerline prevents the development of an exponentially growing instability

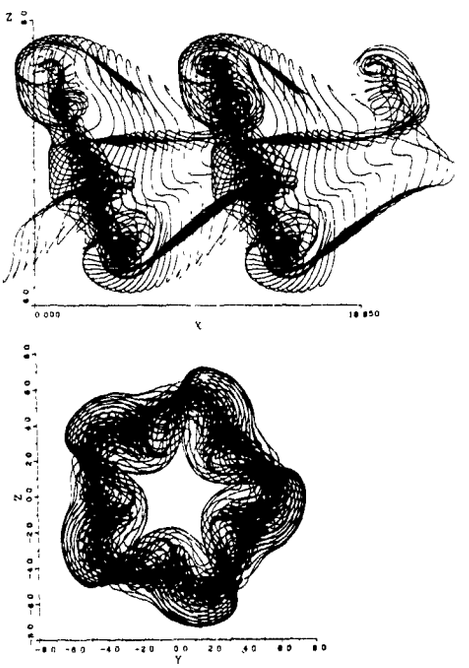

Fig 6 The helically perturbed jet with R/θ=11 3 at time 19 84 a) Side view and b) streamwise view of the vortex filaments For this reduced value of R/θ, the vortex helix develops a stronger waviness (visible especially in the streamwise view), thereby indicating the possibility of a vortex helix instability

The helically symmetric calculation formed the basis for our subsequent discussion of helix-dominated jets If the only perturbation is a single helical mode of azimuthal wavenumber 1, a single helical vortex forms, connected by a braid region of opposite vorticity and infinite aspect ratio If we superimpose an additional azimuthal perturbation, thereby simulating the effect of a corrugated nozzle, the braid vorticity layer develops a Kelvin-Helmholtz-type instability, which leads to the formation of concentrated braid structures These braid vortices are subject to a collpase mechanism similar to the one described by Lin and Corcos (1984) for the plane mixing layer, due to the combined effects of extensional strain provided by the helix and self-induced velocity of the evolving braid structures Furthermore, we observed a principally different evolution of the jet for different values of the ratio of the jet radius R to the jet shear layer thickness θ For $R/\theta=22.6$, the vortex helix had a self-induced rotation rate, which prevented it from developing an instability For $R/\theta=11.3$, on the other hand, this rotation rate almost vanished, so that the waviness of the helix, in its own strain field, kept growing in a nearly exponential fashion The above results suggest ways to actively control the three-dimensional evolution of nominally axisymmetric jets

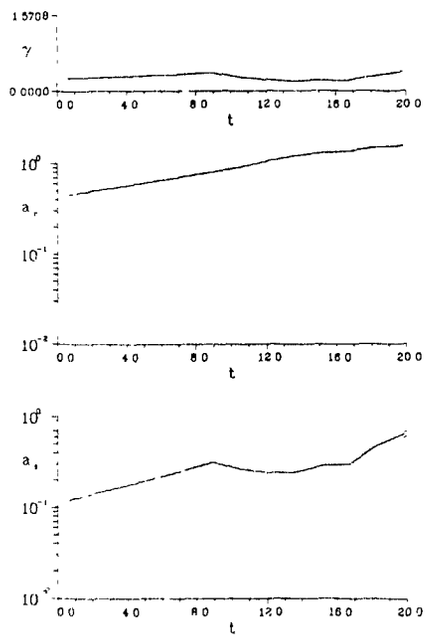

Fig. 7· The temporal evolution of the radial (a_r) and streamwise (a_s) amplitudes of the vortex helix waviness for the case $R/\theta=11.3$ While the graph of the angle γ indicates an almost vanishing rotation rate of the vortex helix, a_r increases continuously in a nearly exponential fashion, thereby lending support to the notion of a vortex helix instability

ACKNOWLEDGEMENTS

This work is supported by the National Science Foundation under grant #CTS-9058065 (to EM), and by DARPA under URI contract #N00014-86-K0754 to Brown University The San Diego Supercomputer Center is providing time on its CRAY-Y/MP

REFERENCES

ASHURST, W T and MEIBURG, E 1988 Three-dimensional shear layers via vortex dynamics J Fluid Mech **189**, p. 87

BATCHELOR, G K 1967 An Introduction to Fluid Mechanics Cambridge University Press.

BATCHELOR, G K and Gill, A E 1962 Analysis of the stability of axisymmetric jets J Fluid Mech **14**, p 529

BROWAND, F.K and LAUFER, J 1975 The role of large scale structures in the initial development of circular jets Proc 4th Biennial Symp Turbulence in Liquids, Univ Missouri-Rolla, pp 333-344 Princeton, New Jersey Science Press

COHEN, J and WYGNANSKI, I 1987 The evolution of instabilities in the axisymmetric jet. Part 1 The linear growth of disturbances near the nozzle J Fluid Mech **176**, p. 191

DIMOTAKIS, P E , MIAKE-LYE, R C , and PAPANTONIOU, D A 1983 Structure and dynamics of round turbulent jets Phys Fluids **26**, p 3185

GASTER, M 1962 A note on the relation between temporally-increasing and spatially-increasing disturbances in hydrodynamic stability J Fluid Mech **14**, p 222

LEONARD, A 1985 Computing three-dimensional incompressible flows with vortex elements Ann Rev Fluid Mech **17**, p 523

LIN, S J and CORCOS, G M 1984 The mixing layer deterministic models of a turbulent flow Part 3 The effect of plane strain on the dynamics of streamwise vortices J Fluid Mech **141**, p 139

MARTIN, J E and MEIBURG, E 1991 Numerical investigation of three-dimensionally evolving jets subject to axisymmetric and azimuthal perturbation To appear in J Fluid Mech

MARTIN, J E , MEIBURG, E , and LASHERAS, J C 1990 Three-Dimensional Evolution of Axisymmetric Jets A Comparison between Computations and Experiments To appear in the Proceedings of the IUTAM Symposium on Separated Flows and Jets, held in Novosibirsk, July 9-13, 1990

MATTINGLY, G E and CHANG, C C 1974 Unstable waves on an axisymmetric jet column J Fluid Mech **65**, p 541

MEIBURG, E and LASHERAS, J C 1988 Experimental and numerical investigation of the three-dimensional transition in plane wakes. J. Fluid Mech **190**, p 1

MEIBURG, E , LASHERAS, J C , and MARTIN, J E 1991 Experimental and numerical analysis of the three-dimensional evolution of an axisymmetric jet Turbulent Shear Flows VII, Springer

MICHALKE , A and HERMANN, G 1982 On the inviscid instability of a circular jet with external flow J Fluid Mech **114**, p 343

MUNGAL, M G and HOLLINGSWORTH, D K. 1989 Organized motion in a very high Reynolds number jet Phys. Fluids A **1**, p 1615

TSO, J and HUSSAIN, F 1989 Organized motions in a fully developed turbulent axisymmetric jet. J. Fluid Mech **203**, p. 425

WIDNALL, S E 1972 The stability of a helical vortex filament J Fluid Mech **54**, p 35

WIDNALL, S E , BLISS, D.B., and TSAI, C-Y 1974 The instability of short waves on a vortex ring J Fluid Mech. **60**, p. 35

EIGHTH SYMPOSIUM ON
TURBULENT SHEAR FLOWS
Technical University of Munich
September 9-11, 1991

VARIABLE DENSITY EFFECTS ON THE MIXING OF TURBULENT RECTANGULAR JETS

B Sarh and I Gökalp

Centre National de la Recherche Scientifique
Laboratoire de Combustion et Systèmes Réactifs
45071 Orleans Cedex 2, France

ABSTRACT

Variable density turbulent rectangular jets are investigated theoretically and experimentally. The theoretical description capitalizes on Rodi (1978), but introduces a new definition for the effective channel width The experimental results are obtained by LDA and fine-wires in strongly heated air jets issuing vertically from a long rectangular channel into still air Both approaches indicate the that axial decay rates of the mean velocity and temperature increase when the density ratio between the ambient medium and the jet is increased The use of the effective channel width defined here allows the global density effect to be taken into account The effect of keeping constant jet exit parameters when the density ratio is varied is also discussed

INTRODUCTION

Variable density effects on turbulent mixing are of importance in several applied situations Mixing of turbulent jets with a medium having a different density is a common engineering feature (Gauldin et al, 1986, Fulachier et al, 1989) The mixing of jet engines exhaust gases, or of industrial gaseous effluents with the surrounding atmosphere are relevant examples In turbulent reacting flows, turbulent jet diffusion flames are often modeled as non-reacting strongly variable density flows, in order to investigate the modification of the flow field by heat release In two phase high pressure systems, such as rocket combustion chambers using liquid propellants or diesel engines, the turbulent mixing of the spray with the surrounding gaseous atmosphere can be analyzed as the mixing between two different density gaseous flows when the chamber pressure is higher than the critical thermodynamical pressure of the liquid, as is often the case

The present paper focuses on the influence of the density ratio between the surrounding atmosphere and the jet, ρ_a/ρ_j, on the mixing and development of turbulent rectangular jets These open jet flows are investigated at LCSR, Orléans in connection with studies of the structure of turbulent diffusion flames stabilized on rectangular burners (Sarh, 1990) The air jet issues vertically into still air from a rectangular channel which has an aspect ratio A of 10 (50 5) and a length of 500 mm. A fully developed turbulent velocity field is thus obtained at the exit The influence of the exit Reynolds number (ranging between 1000 and 10000) and of the aspect ratio (A = 10 and 25) on the mixing characteristics of isothermal turbulent rectangular jets has been previously determined (Sarh, 1990, Sarh & Gökalp, 1991)

The density variation is obtained by preheating the air flow before its entry into the rectangular channel which is thermally insulated The ρ_a/ρ_j ratio is varied between 1 and 2 In the experimental part of the study, the mean and fluctuating longitudinal and one transverse (along the small dimension of the exit section) velocities are determined by laser Doppler anemometry The mean and fluctuating temperature fields are determined by cold-wire anemometry Experimental details are given in Sarh (1990) In the present paper, the main emphasis is put on the structure of the turbulent velocity field. A theoretical description of the density effects on the centerline decay rates of the longitudinal mean velocity and the mean temperature is also developed by following the method first introduced by Rodi (1978) A new definition of the effective channel width to take into account the global density effects is proposed The predictions of the theoretical model are compared with the present experimental results

THEORETICAL DESCRIPTION

In turbulent rectangular jets issuing into a quiescent medium, it can be shown that the mass flow rate Q is related to the momentum flux M_q by the following relationship (Rajaratnam, 1976)

$$\frac{Q}{(x\ M_q\ \rho)^{0.5}} = C_1 \qquad (1)$$

where ρ is the density, x the downstream distance and C_1 a constant At constant static pressure, M_q is independent of downstream distance and, for uniform exit conditions, equal to $M_{qj} = \rho_j U_j^2 H$ where H is the channel width Eq (1) reduces then to

$$\frac{Q}{(x\ M_{qj}\ \rho)^{0.5}} = C_1 \qquad (2)$$

For a small density difference between the jet and the surrounding, the density in Eq (2) can be put equal to ρ_a For a strong density difference, a bulk density ρ_b can be introduced so that

$$\bar{\rho}_b = \frac{\int \bar{\rho}\ \bar{U}^2\, dy}{\int \bar{U}^2\, dy}$$

where y is the transverse coordinate In the present work, in order to simplify the analytical treatment, we propose to use the centerline density ρ_c instead of ρ_b in Eq. (2) The difference between ρ_c and ρ_b in our experiments is less than 4% (Sarh, 1990) By introducing ρ_c and $Q_j = \rho_j U_j H$, Eq (2) becomes

$$\frac{Q}{Q_j} = C_1 \left(\frac{x}{H}\right)^{0.5} \left(\frac{\rho_c}{\rho_j}\right)^{0.5} = C_1 \left(\frac{x}{H_e}\right)^{0.5} \quad (3)$$

where H_e is the effective channel width and is equal to

$$H_e = H \frac{\rho_j}{\rho_c} \quad (4)$$

This definition is different from the one generally used in the literature (Thring & Newby, 1953, Ricou & Spalding, 1960, Pitts, 1991) where the equivalent channel width (or diameter) is expressed as

$$H_\epsilon = H \frac{\rho_j}{\rho_a} \quad (4bis)$$

Rodi (1978) and Chen and Rodi (1980) solved the conservation equations for variable density turbulent non-buoyant free jets by applying the classical boundary layer hypotheses Integration of these equations over the jet cross section, and the use of the perfect gas law to relate the gas density to the temperature yields the following equations .

$$2\int_0^{y_e} \bar{\rho}\, \tilde{U}^2\, dy = M_{qo} \quad (5)$$

$$2\int_0^{y_e} \bar{\rho}\, Cp\, \tilde{U}\, \Delta\tilde{T}\, dy = N_o \quad (6)$$

$$2\int_0^{y_e} \bar{\rho}\, \tilde{U}\, dy = C_1 \sqrt{x} \sqrt{M_{qo}} \sqrt{\bar{\rho}} \quad (7)$$

where y_e is the total jet width, M_{qo} the initial momentum flux and N_o the initial enthalpy flux defined as

$$N_o = \bar{\rho}_j\, Cp\, \tilde{U}\, \Delta T\, H$$

The main assumption of this model is to suppose that in the far field, where density differences are smeared out because of the mixing, the tranverse profiles of the mean longitudinal velocity and of the mean temperature are geometrically similar and conform to the following equations

$$\frac{\tilde{U}}{\tilde{U}_c} = F(\eta) = \exp(-A\,\eta^2) \quad (8)$$

$$\frac{\Delta\tilde{T}}{\Delta\tilde{T}_c} = G(\eta) = \exp\left(\frac{-A}{R^2}\,\eta^2\right) \quad (9)$$

where R is the ratio L_t/L_u between the temperature and velocity jet half-widths and $\eta = y/Lu$ is the reduced transverse coordinate A, R and C_1 are determined from the experiments By combining Eqs (5 -7) and Eqs (8, 9) the following set of equations is obtained

$$2\left(\frac{\tilde{U}_c}{\tilde{U}_{co}}\right)^2 \frac{Lu}{H} \frac{\rho_a}{\bar{\rho}_j} \int_0^{\eta_e} \frac{F(\eta)^2\, d\eta}{1 + \frac{\Delta\tilde{T}_c}{\Delta\tilde{T}_{co}}\left(\frac{\rho_a}{\bar{\rho}_j} - 1\right) G(\eta)} = 1 \quad (10)$$

$$2\frac{\tilde{U}_c}{\tilde{U}_{co}} \frac{Lu}{H} \frac{\rho_a}{\bar{\rho}_j} \frac{\Delta\tilde{T}_c}{\Delta\tilde{T}_{co}} \int_0^{\eta_e} \frac{F(\eta)\, G(\eta)\, d\eta}{1 + \frac{\Delta\tilde{T}_c}{\Delta\tilde{T}_{co}}\left(\frac{\rho_a}{\bar{\rho}_j} - 1\right) G(\eta)} = 1 \quad (11)$$

$$2\frac{\tilde{U}_c}{\tilde{U}_{co}} \frac{Lu}{H} \frac{\rho_a}{\bar{\rho}_j} \int_0^{\eta_e} \frac{F(\eta)\, d\eta}{1 + \frac{\Delta\tilde{T}_c}{\Delta\tilde{T}_{co}}\left(\frac{\rho_a}{\bar{\rho}_j} - 1\right) G(\eta)} = 1 \quad (12)$$

Finally, by combining the Eqs (10-12), the following set of equations is obtained

$$\frac{\Delta\tilde{T}_c}{\Delta\tilde{T}_{co}} = \frac{1}{C_1 \sqrt{\frac{x}{H}} \sqrt{\frac{\bar{\rho}_c}{\bar{\rho}_j}}} \frac{I_3}{I_2} \quad (13)$$

$$\frac{\tilde{U}_c}{\tilde{U}_{co}} = \frac{1}{C_1 \sqrt{\frac{x}{H}} \sqrt{\frac{\bar{\rho}_c}{\bar{\rho}_j}}} \frac{I_3}{I_1} \quad (14)$$

$$\frac{Lu}{H} = C_1^2 \frac{x}{H} \frac{\bar{\rho}_c}{\bar{\rho}_j} \frac{1}{2\frac{\rho_a}{\bar{\rho}_j}} \frac{I_1}{I_3^2} \quad (15)$$

where I_1, I_2 and I_3 refer to the integrals in Eqs (10), (11) and (12) respectively These equations are similar to those established by Rodi (1978), except that the density ratio ρ_c/ρ_j, in addition to ρ_a/ρ_j, appears in these equations The equations are solved numerically by an iterative procedure using the ρ_a/ρ_j ratio as a parameter In solving these equations, we used the following values for the constants A = 0 68, R = 1 4 and C_1 = 0 6, obtained from our measurements for the weakly heated jet (Sarh, 1990, Sarh & Gökalp, 1991)

RESULTS

Theoretical predictions

The predicted variation of the centerline decay rate constants for the axial mean velocity Uc and the mean temperature increase ΔTc are plotted on Fig 1 against the density ratio They correspond to the following linear relations .

$$\left(\frac{U_{co}}{U_c}\right)^2 = K_U\left(\frac{x}{H} - C_U\right) \quad (16)$$

$$\left(\frac{\Delta T_{co}}{\Delta T_c}\right)^2 = K_T\left(\frac{x}{H} - C_T\right) \quad (17)$$

where the subscript o refers to the exit section The higher decay rate of the temperature is confirmed for all density ratios This implies a more efficient mixing of heat as compared to momentum Fig 1 shows that the velocity half-width is only very weakly influenced by the variation

of the density ratio This result seems to contradict the increase in the decay rates with the ρ_a/ρ_j ratio, but could be explained by the strong influence of the density variation on the virtual origins of the jet When plotted in logarithmic coordinates, the data of Fig 1 show a power law relation with the same exponent (which is expected from Eq (9)) equal to 0 81 for the decay rate constants of the velocity, K_U and the temperature, K_T

Theoretical predictions of the effect of the density ratio ρ_a/ρ_j on the centerline variations of the longitudinal mean velocity and the mean temperature and on the downstream variation of the velocity half-width Lu (from which the data of Fig 1 are extracted) are presented on Figs 2, for different values of the density ratio ranging between 0 2 (dense jet) and 5 (light jet) The predictions for the isothermal (or the weakly variable density case) are also presented It is observed that the centerline decay rates of the mean velocity and temperature, increase for increasing density ratio, indicating an increase in mixing efficiency It is also observed that, as expected, the linearity of these evolutions with downstream distance is perturbed when the density ratio ρ_a/ρ_j departs from unity This shows that the introduction of the ratio ρ_c/ρ_j in the previous equations improves the representation of the global density effect on the development of turbulent free jet flows It is clearly shown that the downstream variation of Lu is much less affected by the density ratio

The predictions also show that the virtual origins C_U and C_T vary with the density ratio a value very close to 0 for the isothermal or the weakly variable density cases, positive values for lighter jets and negative values for denser jets This result is also predicted by Thring & Newby (1953) for heated axisymmetric jets, and more recently by Pitts (1991) for isothermal and variable density axisymmetric jets

The capacity of the effective channel width He, introduced here, (Eq 4) to accomodate for the global density effects on the centerline variations of mean flow quantitites is confirmed on Fig. 3, where the curves of Figs 2 are replotted against the normalized downstream distance $(X - X_o)/H_e$, where X_o (= C_U or C_T) is the respective virtual origins for each density ratio

Comparison with experimental results

The experimental results obtained in this study on the axial variation of the mean velocity and temperature are compared in this section with the previous predictions The experimental conditions corresponding to isothermal, weakly heated and strongly heated cases are summarized on Table 1.

nature of the jet	isothermal	weakly heated	strongly heated
ΔT of ejection (K)	0	25	300
ρ_a/ρ_j	1	1 1	2
Exit velocity (m/s)	15 5	18	51
Re	5000	5000	5000
Fr		254	216
Ma	0 045	0 050	0 106

Table 1 Experimental conditions

Figs 4 compare the experimental and predicted variations of the mean centerline quantities and of L_U As shown on Table 1, the experimental results correspond to air jets issuing from the rectangular channel with a constant Reynolds number equal to 5000 for each density ratio The agreement between the experiments and the theoretical predictions are quite satisfactory (see also Fig 1). Figs 5 present the application of the effective channel width to the normalization of the experimental results The density effect is again taken into account by the normalized downstream distance $(X - X_o)/H_e$ This normalization procedure gives also excellent results when applied to the experimental results of Pitts (1986, 1991), as shown in Sarh (1990)

When the density ratio increases from 1 to 2, the mean velocity decay rate K_U increases from 0 19 to 0 35, and the virtual origin C_U from 2 35 to 6 5. The corresponding variations for the mean temperature are respectively (for the density ratios equal respectively to 1 1 and 2) 0 23 to 0 35 and 0 56 to 5 As predicted above, the axial decay rates and the virtual origins of the mean velocity and the mean temperature increase for lighter jets The same data indicate however a decrease in the variation rates of the velocity and temperature half widths, K_{LU} and K_{LT} Indeed, between the weakly and strongly heated cases, the values of these two parameters change from 0 127 to 0 089 and from 0 19 to 0 144 respectively It is noteworthy that this result confirms the above predictions of the variation of L_U with the density ratio (cf Fig 1) For both density ratios, the temperature half-width is higher than the velocity half-width

The downstream variation of the normalized mass flux obtained by integration of the transverse mean velocity profiles is shown on Figs 6, for the isothermal and heated jets having the same exit Reynolds number of 5000 It is observed, first, that the entrainment capacity of the light jet is higher and, second, that the introduction of the effective channel width H_e accounts well for this global density effect The first point above is in agreement with the results reported by Ricou & Spalding (1961)

For isothermal turbulent plane jets, the constant C_1 in Eq (3) was found to be equal to 0 63 by Rajaratnam (1976) and to 0 57 by Schlichting (1968) Our results for the turbulent rectangular jets give C_1 = 0 60 for the isothermal case and C_1 = 0 88 for ρ_a/ρ_j = 2 The entrainment rate E (not shown here), defined as

$$E = \frac{d(\frac{Q}{Q_j})}{d(\frac{X}{H})}$$

shows a maximum value located at X/H = 9 5 for both isothermal and strongly heated jets (Sarh, 1990) The maximum values of E are respectively 0 111 and 0 138 Hussain & Clark (1977) have shown that the location of the maximum entrainment rate is strongly configuration dependent, and is smaller than X/H < 1 for a turbulent plane jet, but varies between X/H = 8 and 10 for a turbulent rectangular jet The maximum value of E is also Reynolds number dependent and decreases with increasing Re for both jet configurations On the other hand, for the same Reynolds number, the values of E_{max} for a turbulent plane jet are approximately twice those of a turbulent rectangular jet This is generally explained by the different nature of the initial boundary layers and it is believed that a jet with laminar initial boundary layers has a higher entrainment capacity (Hussain & Clark, 1977) This should

then explain the lower values of the entrainment rate for a turbulent rectangular jet which has turbulent initial boundary layers In our experiments, the fact that the exit Reynolds number is kept constant between the isothermal and strongly heated cases implies that the Reynolds number is not the factor which explains the increase of the entrainment rate in the strongly heated case

Another important discussion in the literature on variable density turbulent jets concerns the role of the initial or exit conditions (Fulachier et al, 1989). Indeed, when investigating the effects of density variations on the development of turbulent jets, it is important to decide which initial parameter to keep constant for varying density ratios the jet Reynolds number, the jet exit velocity, the mass flow rate, the initial momentum flux or the initial enthalpy flux For example, Pitts (1991) and Birch et al (1978) kept constant the exit Reynolds number, whereas Sforza & Mons (1978) and Panchapakesan & Lumley (1988) fixed the initial momentum flux This point should be considered when comparing the results on variable density effects found in the literature

A contribution to this discussion may be obtained from our experimental results where, for varying density ratios, we kept constant the exit Reynolds number or the initial mass flux or the initial momentum flux Figs 7 show that, for the three modes of operation, the heated jet axial mean velocity decays faster than that of the isothermal jet Figs 8 show the centerline mass flux normalized by its exit value for the three modes of operation The mass flux on the centerline is systematically higher for the heated jet However, when the initial momentum flux is kept constant, the differences between the isothermal and heated jets are reduced and confined to the far downstream region Finally, Figs. 9 show that the normalized centerline momentum flux is not influenced by the density ratio whatever the mode of operation These results need to be confirmed for stronger density variations

CONCLUSION

This paper has focused on the global density effects on the mixing behaviour of turbulent rectangular jets The theoretical description utilized the classical work of Rodi (1978) It has been shown that the effective channel width, defined by using the ratio between the centerline density and the jet exit density accounts for the density effects on the centerline decay rates of mean quantities These effects indicate that the axial decay rates of mean velocity and temperature increase when the density ratio between the ambient medium and the jet is increased and thus show enhanced mixing efficency for lighter jets A weaker influence on the velocity half-width is also predicted It is shown that the decay rate of the temperature is higher than that of the velocity for the density ratio range explored (0 2 to 5), indicating that heat is mixed more efficiently than momentum

These theoretical predictions have been compared with the experimental results of the mixing behaviour of heated turbulent air jets issuing vertically from a long rectangular channel into still air It is found that for a density ratio varying between 1 and 2 and for a constant exit Reynolds number the previous theoretical predictions have been confirmed. It has also been shown experimentally that the axial velocity decay rate increases with increasing density ratio, whether the exit Reynolds number, the initial mass flux rate or the initial momentum flux rate are kept constant This experimental study is currently being extended by increasing the density ratio to higher values by investigating the mixing of isothermal jets with very different densities

REFERENCES

BIRCH, A D et al (1978) **J Fluid Mech** 88 431

CHEN, C.J & RODI, W (1980) **Vertical Turbulent Buoyant Jets**, Oxford Pergamon Press

FULACHIER, L et al (1989) **J Fluid Mech** 203 577

GOULDIN, F.C et al (1986) **Progress in Energy and Combustion Sciences** 12 257

HUSSAIN, A K M F & CLARK, A R (1977) **The Physics of Fluids** 20 1416

PITTS, W M (1986) **Effects of global density and Reynolds number variations on mixing in turbulent axisymmetric jets**, Rep NBIS 86-3340

PITTS, W M (1991) **Experiments in Fluids** 11 125

RAJARATNAM, M (1976) **Turbulent Jets** Amsterdam Elsevier Science Publishing Co

RICOU, F.P & SPALDING, D B (1961) **J Fluid Mech** 11 21

RODI, W (1978) **Influences of density differences on jet development**, University of Karlsruhe Cited in Chen and Rodi (1980)

SARH, B (1990) **Contribution à l'étude des jets turbulents à masse volumique variable et des flammes turbulentes de diffusion** Thèse de doctorat d'Etat, Université Pierre et Marie Curie, Paris

SARH, B & GOKALP, I (1991) **Influence of the Reynolds number and of the aspect ratio on the development of turbulent rectangular jets** Submitted for publication

SFORZA, P M & MONS, R F (1978) **Int J Heat Mass Transfer** 21 371

THRING, M W & NEWBY, M P (1953) **Fourth Sympolsum (Int) on Combustion**, Williams and Wilkins, pp 789-796

PANCHAPAKESAN, N.R & LUMLEY, J M (1988) **Paper presented at the Euromech 237**, Marseille

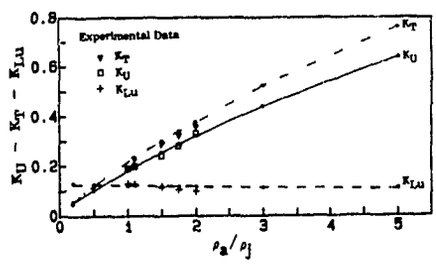

Fig. 1 Predicted variation of the global jet parameters with the density ratio Comparison with experimental data

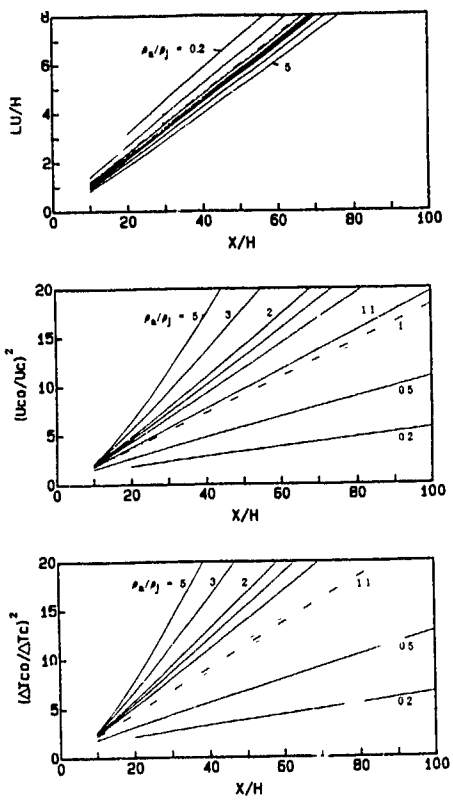

Fig 2 Theoretical prediction of the glob l density effects

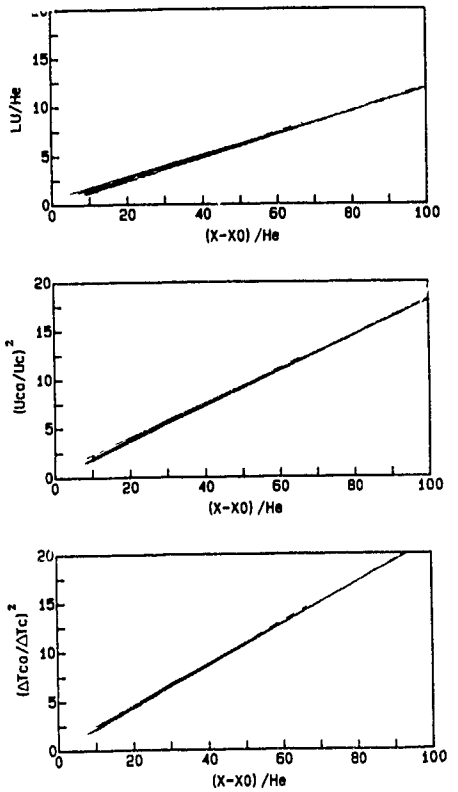

Fig 3 Renormalization of the predictions of Figs 1

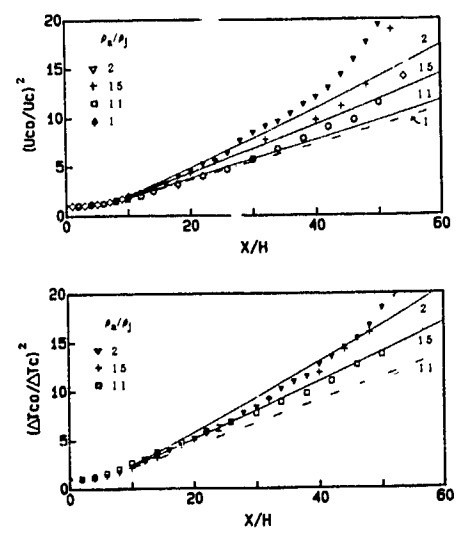

Fig 4 Experimental and predicted variations of the centreline mean quantities

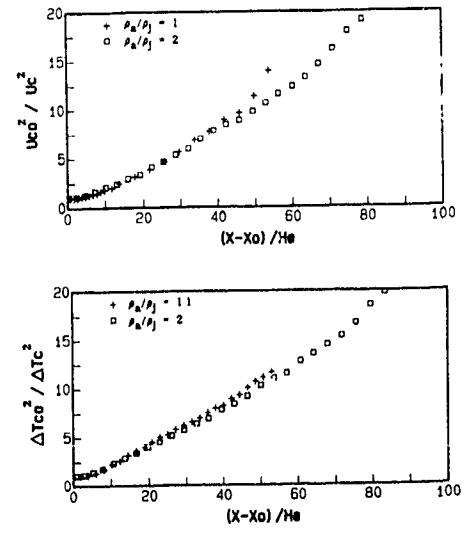

Fig 5 Renormalization of the experimental data of Figs 4

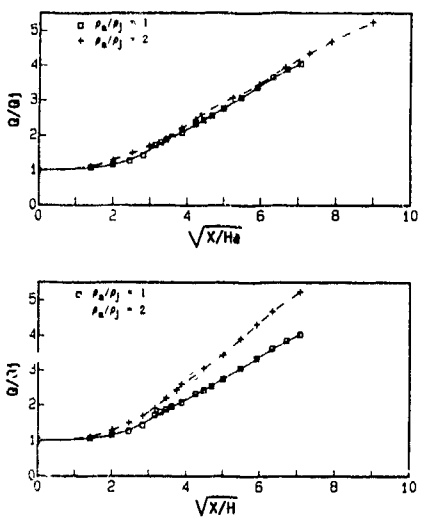

Fig 6 Downstream variation of the normalized mass flux in physical and renormalized coordinates

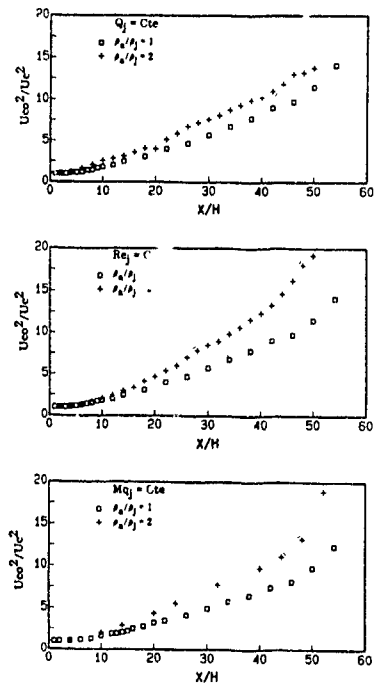

Fig 7 Centerline decay of the axial mean velocity for different constant initial conditions.

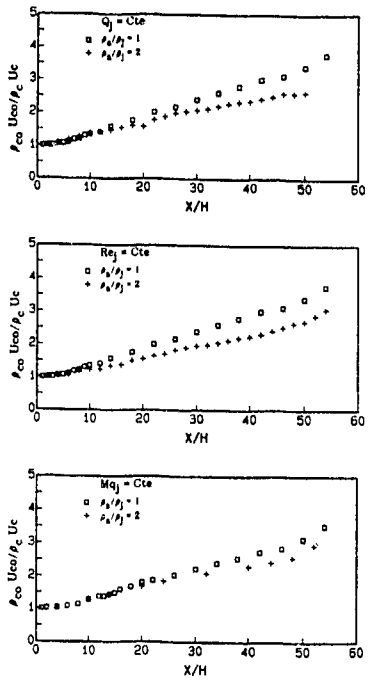

Fig 8 Centerline variation of the mass flux for different constant initial conditions

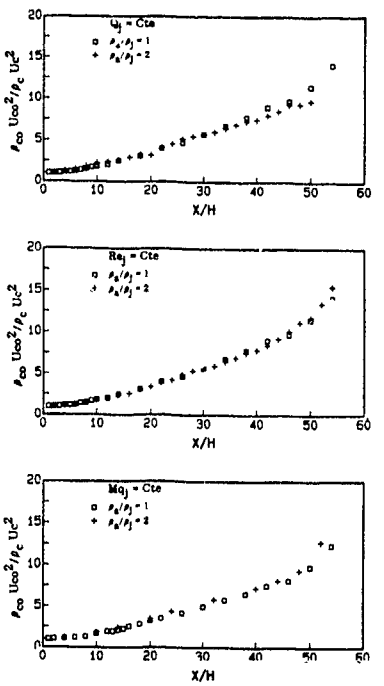

Fig 9 Centerline variation of the momentum flux for different constant initial conditions

EIGHTH SYMPOSIUM ON
TURBULENT SHEAR FLOWS
Technical University of Munich
September 9-11, 1991

LARGE-SCALE STRUCTURES IN WAKES BEHIND AXISYMMETRIC BODIES

S Cannon and F Champagne

Department of Aerospace and Mechanical Engineering
The University of Arizona, Tucson, AZ 85721, USA

ABSTRACT

An experimental study of the evolution of turbulent wakes behind axisymmetric bodies was carried out using arrays of hot-wires and flow visualization The bodies--sphere, disk, and several disk-shaped screens of varying solidity--were tailored to generate the same momentum area The results indicate that the wakes develop in an approximately self-preserving manner, with at least two characteristic velocity scales required Flow visualization studies show that the existence of large-scale coherent structures coincides with the presence of a reverse flow region behind the body Two-dimensional Fourier analysis of data from an axisymmetric rake of hot-wires reveals that these large-scale structures are predominantly helical with both $m = +1$ and -1 azimuthal modes present Special processing of these data allows the amplitudes of the dominant ±1 modes to be determined as a function of time The relative parity between these dominant modes is discussed.

INTRODUCTION

Turbulent wakes behind axisymmetric bodies in the absence of a pressure gradient have been the subject of many experimental investigations (see Torobin and Gauvin, 1959a,b) The results of these studies have generally supported the traditional hypothesis that wake evolution proceeds in a self-preserving manner, based on a length scale l_0 (Fig 1) and a single velocity scale u_0 (Hwang and Baldwin, 1966, Uberoi and Freymuth, 1970, Bevilaqua and Lykoudis, 1978) This support is based on observations that the streamwise variations of l_0 and u_0 were found to be proportional to $x^{1/3}$ and $x^{-2/3}$, respectively, the exponents obtained from the traditional self-preservation analysis Usually, this fit is obtained by introduction of a non-zero virtual origin, x_0 It should be noted that the local Reynolds number ($l_0 u_0/\nu$) decreases with downstream distance for the axisymmetric wake, and this is fundamentally inconsistent with the concept of complete self-preservation Large-scale coherent structures associated with vortex shedding have been observed in the wakes of axisymmetric bluff bodies, they give the wakes a contorted appearance when viewed from the side in flow visualization experiments The azimuthal periodicity imposed by the axisymmetric boundary conditions enables the decomposition of streamwise velocity components into circumferential Fourier modes. Fuchs et al (1979) show that in the near wake behind a disk and cone, the helical mode ($m = 1$) governs the large-scale structures at the vortex-shedding Strouhal number A similar result was obtained by Achenbach (1974) for spheres The manner in which these structures form and evolve has been the subject of continuing controversy (Jeffreys, 1930, Achenbach, 1974, Pao and Kao, 1977, Berger et al., 1990). The focus of the controversy stems from efforts to reconcile interpretation of experimental observations with Thompson's Circulation Theorem The analysis of Pao and Kao for sphere wakes suggests that a double helix with a closed-end start-up loop does not violate Thompson's Theorem and therefore provides a viable explanation for their experimental observations. On the other hand, Berger et al suggest the presence of a single helix that changes its sense of rotation randomly in time, i.e, the alternating presence of $m = \pm 1$ helical modes

The nature and evolution of the large-scale structures were studied using hot-wire anemometry and smoke-wire flow visualization Flow visualization utilizing a 2-D sheet of light gives only a partial picture of the typically 3-D flow fields that develop behind the axisymmetric bodies. Information on the azimuthal organization of large-scale structures in the present study was obtained from 2-D Fourier transformation of the time series of the streamwise velocity component measured simultaneously at eight equally spaced points on a circle of radius r The measurements were obtained with a novel traversing

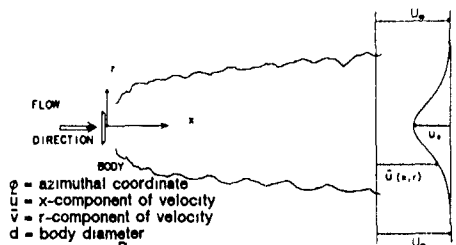

φ = azimuthal coordinate
$\tilde{u}$ = x-component of velocity
$\tilde{v}$ = r-component of velocity
d = body diameter

$$\theta_0^2 = \lim_{R\to\infty} \frac{1}{u_0} \int_0^R (U_\infty - \tilde{u}) r \, dr \Rightarrow \text{similarity length scale}$$

u_0 = similarity velocity scale

Fig 1 Cylindrical coordinate system and nomenclature for wake profiles

mechanism that uses a single stepper motor to move all eight wires simultaneously in the radial direction This arrangement allows for decomposition of the velocity signals into azimuthal modes -3 to +4 (the numbers represent the direction of travel and number of cycles the signal repeats itself in 2π of azimuthal distance). Further, the velocity signals from three of the wires in the array were used to educe time-varying signals indicating the presence of the $m = \pm 1$ helical modes

The wakes behind a solid disk and screens of varying solidity were studied to provide a variety of initial conditions in terms of the strength of vortex shedding from the body The downstream region $35 < x/\theta < 130$ was investigated, it corresponds to $10 < x/d < 35$ for the solid disk The momentum area θ^2 is defined by

$$\theta^2 = \frac{\bar{D}}{2\pi\rho U_\infty^2} = \int_0^R \frac{\tilde{u}(U_\infty - \tilde{u})}{U_\infty^2} r dr = \text{const} \qquad (1)$$

The momentum area was the same for all wake generators A limited hot-wire study of a sphere wake was also carried out to provide information for comparison with the earlier studies mentioned above

EXPERIMENTAL CONSIDERATIONS

All the experiments were carried out in The University of Arizona's low-speed wind tunnel The 19.7-m-long tunnel is a closed-circuit type with a 0.81-m-wide by 0.91-m-tall test section that is made up of a 1.22-m-long removable mounting section followed by a 4.88-m-long measuring section A complete description of this facility is given by Cannon (1991) The test bodies are suspended in the middle of the mounting section with 0.003-in. tungsten support wires The support wires pass through horizontal slots in the two walls and are attached to a set of sliding frames This mounting arrangement provides dampening to effectively eliminate streamwise motions of the mounted body and for fine adjustment of the distance between the aft end of the body and the measuring probes when the axisymmetric rake is used All measurements are referenced to a cylindrical coordinate system whose origin is at the rear end of the wake generator (Fig 1)

The wakes were generated by a disk and three disk-shaped screens of varying solidity σ (ratio of solid to total frontal area) Additionally, a sphere was used to study the momentum balance that exists in the wake and the axial variation in the 1-D spectra These wake generators provide a variety of initial

conditions to the oncoming uniform flow field, but are tailored in size so as to generate the same momentum area, θ^2, and thus the same drag force, D. The average value of θ is approximately 7.5 mm. The solid disk is 28.0 mm in diameter. The diameters of the three screens are 37.5 mm, 30.9 mm, and 30.9 mm, and their solidities are 0.49, 0.62, and 0.84, respectively. The diameter of the sphere is 46.7 mm. The disk and screen wakes were investigated for their sensitivity to body alignment to the flow direction. This was not a critical issue for small misalignment angles up to 3°. The measurements were made at a free-stream velocity of 7 m/s with streamwise fluctuations of 0.0003 U_∞, the corresponding Reynolds number ($Re_\theta = \theta U_\infty/\nu$) is 3,500. To obtain adequate resolution of wake deficits as small as 0.01 U_∞, the free-stream temperature of the wind tunnel was controlled to within a drift range of 0.03°C.

All the velocity measurements were obtained using hot-wire anemometry and digitally recorded with a 12-bit A/D converter onto a Masscomp minicomputer. The mean flow measurements and the momentum balance measurements were obtained with linear rakes of either straight- or x-wire probes. A special axisymmetric rake (provided by Professor Heinz Fiedler) of straight-wire probes was used to explore the modal structure of the $\sigma = 0.49$ screen and disk wakes.

The smoke-wire technique was used to provide flow visualization of the wakes in 2-D slices. Three smoke-wires spaced 5 mm apart were employed to provide a thicker sheet of smoke for better visualization of the highly irregular 3-D wakes. The vertical sheet of smoke particles emanating from the wires is illuminated by a rotating laser beam from a 2-watt argon ion laser. The full width of the wake is scanned within 2.3 msec. The sweep rate of the laser beam sets the exposure time for the photographic records of the smoke-particle streaklines. Trigger delay switches were used to synchronize the camera and the heating of the smoke-wires to the motion of the stepper-controlled laser beam.

FLOW VISUALIZATION

Side-view (x-r plane) photographs of the near and far wakes behind the disk and screen bodies are presented in Fig. 2. The smoke wires are visible under the darkened triangles at the top of each photograph, and the bodies are apparent to the right of the wires in the near-wake photographs. The most distinguishing feature between the bodies for which $\sigma = 1.00$ (disk) and 0.84 and the bodies for which $\sigma = 0.62$ and 0.49 is the shape of the large-scale structures associated with coherent vortex shedding. The wakes of the disk and high-solidity screen are wider, more contorted, and appear to have a characteristic streamwise wavelength associated with large-scale structures of approximately 2.5 θ. The passage frequency of the large coherent structures associated with this wavelength yields $St_d = 0.15$ for the disk ($Re_d = 1.32 \times 10^4$). Spectral measurements for the disk wake display a peak at $St_d = 0.13$. These values compare well with the vortex-shedding frequency $St_d = 0.14$ measured in the near wake of a disk by Hwang and Baldwin (1966) at $Re_d = 1.9 \times 10^4$. In contrast to the wakes of the disk and highest solidity screen, the free-stream boundaries of the wakes of lower solidity screens appear to be less irregular and contorted. Note that this observation applies to both the near and far wakes of the lower solidity bodies, indicating the absence of large-scale coherent structures that scale with the width of the body.

The presence of smoke upstream of the smoke-wire in the near wake of the disk and highest solidity screen (Figs. 2c,d) is evidence of reverse flow, which may indicate that $u_0 > U_\infty$ upstream of the smoke-wire. Sequential photographs of the near-wake region, taken with the spacing between the smoke-wire and the body fixed, alternately show both the absence and presence of smoke upstream of the smoke-wire, an indication that the axial extent of the recirculation bubble oscillates in time. No smoke is present upstream of the smoke-wires for the lower solidity screens (Figs. 2a,b), and none was evident for a variety of spacings between the wire and body up to and including a distance as small of 0.25 of the body diameter, this confirms the absence of reverse flow for the lower solidity screens. While no attempt was made to determine the value $\sigma = \sigma_0$ for which reverse flow exists, Figs. 2b,c suggest $0.60 \le \sigma_0 \le 0.85$. The main difference between the four bodies is the degree of venting in the direction of the flow. It is clear that for a fixed Re_θ, a decrease in solidity corresponds to a decrease in the maximum normalized wake deficit in the near wake, with the eventual disappearance of the region of reverse flow that is attached to the rear of the body. The co-existence of contorted large-scale structures with a recirculation region is consistent with the findings of Monkewitz (1988) regarding the effect of wake deficit on the occurrence of absolute instability of the near wake.

WAKE SIMILARITY

The differences in wake width observed in the photographs were quantified using hot-wire measurements of the u velocity component taken at different x-locations downstream of the bodies. The characteristic scales u_0 and t_0 were determined for each body in order to examine the degree to which the far wakes ($u_0 \le 0.1\ U_\infty$) are self-preserving and to compare their growth rates. Normalized radial profiles of time-averaged velocity,

Fig. 2 Flow visualization comparison for disk-shaped bodies of different solidities: (a) $\sigma = 0.49$ screen, (b) $\sigma = 0.62$ screen, (c) $\sigma = 0.84$ screen, and (d) solid disk ($\sigma = 1$)

$$f(\eta) = \frac{U_\infty - \bar{u}(r, x)}{u_0(x)}, \qquad (2)$$

for each body are presented in Fig 3, η is the normalized radius r/ℓ_0 The normalized profiles for each body collapse fairly well, indicating the mean velocity field develops in an approximately self-preserving manner, though not as self-preserving as the mean velocity field in turbulent wakes behind 2-D planar bodies (Marasli, 1989) All the screen wakes exhibit the same self-preserving form, whereas the disk wake profile is relatively flatter in the center region and has a steeper slope near $\eta = 1$

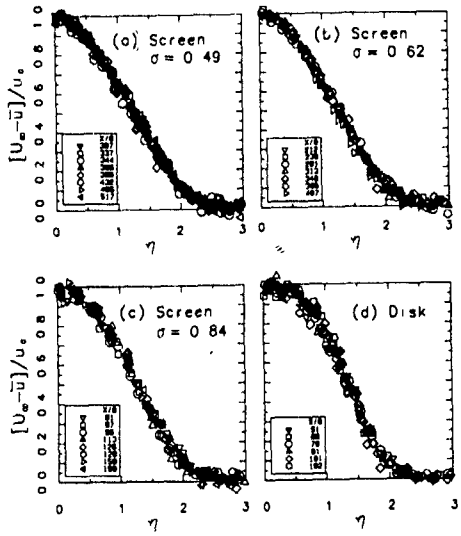

Fig 3 Self-preserving mean velocity profiles.

The variation of $(U_\infty/u_0)^{3/2}$ and $(\ell_0/\theta)^3$ with $(x - x_0)/\theta$ is shown in Figs 4a and 4b, respectively One value of x_0, the virtual origin, was chosen for each wake generator so that the momentum integral constraint, $\ell_0^2 u_0$ = constant, is satisfied and the ℓ_0 data grow in a least squares fashion as $(x - x_0)^{1/3}$ It should be noted that when we plotted U_∞/u_0 and ℓ_0 versus x/θ, the data appeared to fall between the exponents predicted for viscous-dominated growth ($\ell_0 \cong x^{1/2}$ and $u_0 \cong x^{-1}$) and those for turbulence-dominated growth that are given above When x_0 was chosen based on the viscous exponents, a plot similar to Fig 4 was prepared using the viscous exponents The data appear to fit the model as well as those indicated for the turbulence model The concern with the choice of growth exponents was motivated by the fact that the local Reynolds number decreases with x Attempts to fit u_0 and ℓ_0 data to the function $y = a[(x - x_0)/\theta]^b$ using a least squares curve in order to independently determine x_0, a, and b have so far been unsuccessful The data shown in Fig 4a show that the bluff body wakes spread more rapidly because of the vigorous action caused by the large-scale structure associated with vortex shedding The data show some clustering of both length and velocity scales to either side of $\sigma = \sigma_0$, which is consistent with Fig 2

The turbulent velocity field behind 2-D planar bodies is self-preserving based on the velocity and length scales u_0 and ℓ_0 of the mean flow field (Marasli, 1989) Previous experimental investigations (Uberoi and Freymuth, 1970, Bevilaqua and Lykoudis, 1978) have generally supported this same concept for axisymmetric wakes. However, Hinze (1975) and, more recently, George (1987) suggest the possibility that at least two velocity scales, u_0 and $u_{1/2}$ (a scale for the turbulent Reynolds stress), could be required for self-preservation of the streamwise component of the mean momentum equation for wakes behind axisymmetric bodies—a case of incomplete similarity Measured distributions of $\overline{u'^2}$ normalized by $u_0^2(x)$ for the $\sigma = 0.49$ screen are shown in Fig 5a. The direction of the arrow in the figure shows the direction of separation of the profiles with increasing x values, this spread indicates that the normalized distributions do not collapse. It is clear that u_0 decays more rapidly than the rms of the velocity fluctuations Figure 5b shows the same distributions but, here, normalized

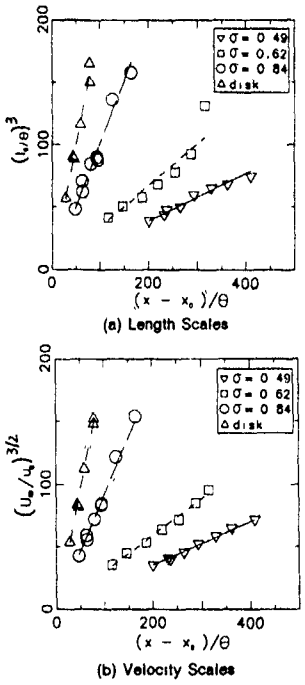

(a) Length Scales

(b) Velocity Scales

Fig 4 Comparison of characteristic scales

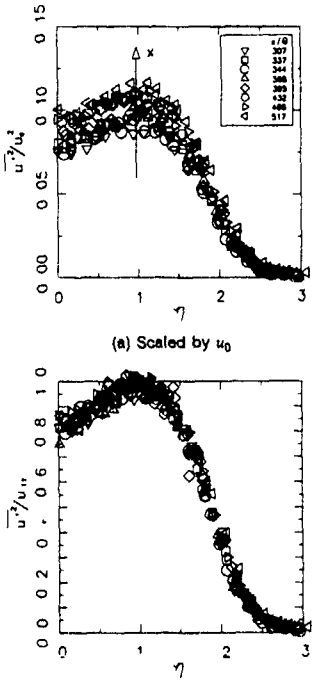

(a) Scaled by u_0

(b) Self-Scaled

Fig 5 Collapse of variance velocity field for $\sigma = 0.49$ screen wake

by the average peak value u_{11} for each distribution The improved collapse of the self-normalized profiles indicates that a new velocity scale is required and that incomplete similarity may exist As the turbulent Reynolds stress $-\rho\overline{u'v'}$ was not measured for the disk and screen wakes, we will use the scale u_{11} to characterize the turbulent velocity field To determine if the two velocity scales are converging with increasing x, their ratio (square root of u_{11} to u_0) is plotted versus downstream distance to log-log scale for the screen and disk wakes in Fig. 6 The two scales appear to maintain separate decay rates to the downstream limit of the present investigation

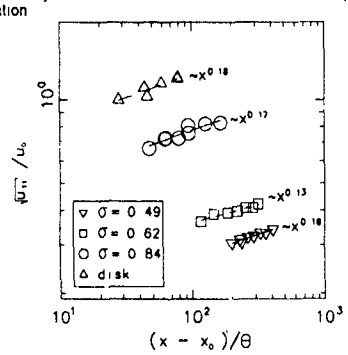

Fig 6 Departure of variance from mean velocity scale

Besides assessing the convergence of the growth rates of velocity scales, Fig. 6 also provides a comparison amongst the different wake generators of the size of the turbulent scale relative to that of the mean scale For example, the ratio of the two scales is approximately one for the disk wake and approximately one-third for the σ = 0 49 screen wake Thus, when comparing the wakes at downstream locations where the defect velocities are the same size, the bluffer bodies have a higher average level of turbulence available for continued mixing and spreading of the wake

Given the ambiguity regarding the growth rates falling between those for viscous- and turbulence-dominated growth and the fact that at least two length scales appear to be necessary for self-preservation, we decided to examine the streamwise momentum balance in these flows A sphere wake was chosen for study, as it has been reported on more frequently in the literature than the disk and screen wakes The size of the sphere was chosen to have the same momentum area as the disk and screens, thereby maintaining Re_θ constant Transverse distributions of mean and turbulent velocity fields were obtained using a linear rake of x-wire probes Measurements were extended to the region where $u_0/U_\infty \cong 0.01$ The results verified that the momentum balance is between the convective acceleration and turbulent Reynolds stress terms and that the momentum integral constraint is satisfied. The measured values of u_0 and l_0 show the same behavior as their counterparts for the disk wake, though the sphere wake is slightly wider As is the case with the other generators, the u_0 and u_{11} velocity scales for the sphere wake are distinct and non-converging to the end of the measuring domain (Fig 7) The downstream variations of $\sqrt{u_{12}/u_{11}}$ and $\sqrt{u_{12}}/u_0$ are also presented in Fig 7. The average peak value

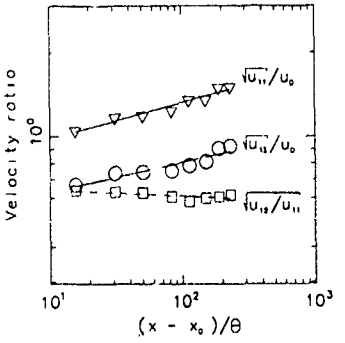

Fig 7 Uniformity of turbulent velocity scales for sphere

from the measured Reynolds stress distributions determines u_{12} The choice of u_{11} to scale the turbulent velocity field is supported by the constant value of the ratio u_{12}/u_{11} The sphere wake results verify that more than one velocity scale is required for self-preservation of the mean and turbulent velocity field, which is contrary to some earlier studies

LARGE-SCALE STRUCTURES

Time series for the streamwise velocity component measured simultaneously at eight equally spaced points on a circle of radius r were obtained for the disk and σ = 0 49 screen wakes using the axisymmetric traversing mechanism These data allow for a 2-D Fourier transformation with respect to time and azimuthal coordinate Normalized power spectra $A(St_\theta, m, \eta)$ of the azimuthal modes m = -3 to +4 were measured at x/θ = 105, η = 1 The spectra are normalized by the sum of the amplitude terms over all frequencies and mode numbers Frequency-weighted modal spectra, $St_\theta A$ are presented in raster format (by mode number) in Figs 8 and 9 for the disk wake and σ = 0 49 screen wake, respectively Also presented are the frequency-weighted 1-D spectra $St_\theta F(St_\theta, \phi, \eta)$ for each of the eight azimuthally spaced locations The disk wake is distinguished by spectral peaks in the m = ±1 mode spectra at St_θ = 0 036 (St_d = 0 13) and peaks in the 1-D spectra at the same St_θ In contrast, the m = ±1 mode spectra for the non-shedding screen exhibit a broad, lower amplitude peak near St_θ = 0.052, while the corresponding 1-D spectra display no evident peaks The relative amplitude of the spectral peaks for m = ±1, along with that of the other modes, is shown in Figs 8c and 9c The amplitudes of the m = ±1 modes dominate the disk wake at the shedding frequency The modal spectra for the disk wake show differences in shape at frequencies below the shedding frequency, with the even-mode spectra being considerably flatter than those for the odd modes The low-frequency structure of all the mode spectra for the screen wake appear to be similar in shape

Contours of constant $St_\theta A$ as a function of normalized radial location η and either frequency (at m = 1) or mode number (at the peak value of St_θ) were examined for the disk and the σ = 0 49 screen wakes For the disk wake, the contours in the St_θ-η plane emphasize the dominance of the +1 (and -1) modes at St_θ = 0 036 in the spectra The peaks in the contours are centered near the radial location η = 1, which is also the location of the highest velocity gradient (and where the peak in the variance profiles occurs) For the screen wake, the contour levels for the +1 (and -1) modes at St_θ = 0 052 are largest near η = 0 and then diminish in prominence with distance from the center of the wake

The sharp peak in the spectra at the *shedding* frequency persists throughout the far wake of axisymmetric bluff-body wakes like that of the sphere and disk Additional spectral measurements of the streamwise velocity component in the sphere wake exhibit a single peak at St_θ = 0 027 (St_d = 0 17) which is invariant with x. This invariance is expected for a globally driven or absolute instability This characteristic Strouhal number St_d = 0 17, obtained at Re_d = 21,800, may be compared with the range of absolutely unstable values of 0 17 ≤ St_{2b} ≤ 0 21 calculated by Monkewitz (1988) His calculations assumed parallel flow and were for a family of wake profiles in which b refers to the radius at which the wake defect velocity is 0 5 U_∞ and the centerline defect is $u_0 = U_\infty$

Unfortunately, x varying mode spectra have not yet been obtained in the wake behind the σ = 0 49 screen Its frequency of peak amplitude would be expected to vary in a manner consistent with a convectively driven instability--to move toward lower frequencies at a rate inversely proportional to the wake spread rate

TEMPORAL VARIATION OF m = ±1 MODES

As mentioned previously, the nature of the large-scale structures associated with vortex shedding in the wakes behind axisymmetric bodies is a controversial issue Information on the azimuthal organization of these large-scale structures was obtained at x/θ = 100 for both the disk and non-shedding screen using the axisymmetric rake

A three-point method of analysis was devised to provide a discriminant for the time-varying features of the m = ±1 structures In the analysis, the measured data are represented by Fourier modes and it is assumed that the spectrum measured by each probe has the same shape Let the de-meaned and variance-normalized velocity measurement by the probe at azimuthal location ϕ be represented by $H_\phi(t, \omega)$ Such a signal that is filtered to pass only angular frequency ω_c and modes m = ±1 could be expressed by

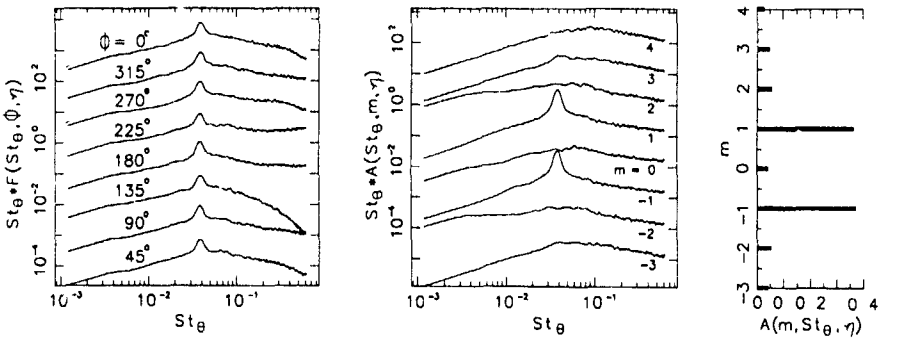

(a) Rasters by Azimuthal Location (b) Rasters by Mode Number (c) Amplitudes at St_θ = 0.036

Notes for Raster Plots (Figs 8, 9, 10a)

Ordinate scale applies to bottom raster
Each raster scaled up by a factor of 10 from the previous raster

Fig 8 One- and two-dimensional Fourier decomposition results for disk wake (x/θ = 105, η = 0.83)

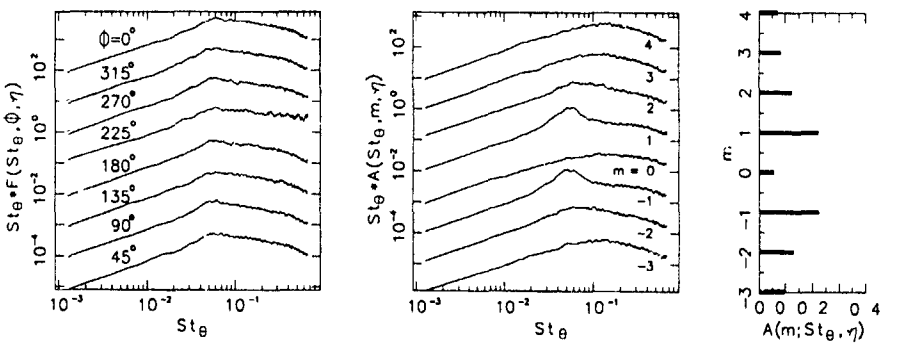

(a) Rasters by Azimuthal Location (b) Rasters by Mode Number (c) Amplitudes at St_θ = 0.052

Fig 9 One- and two-dimensional Fourier decomposition results for σ = 0.49 screen wake (x/θ = 105, η = 0.91) [See notes for raster plots in Fig 8]

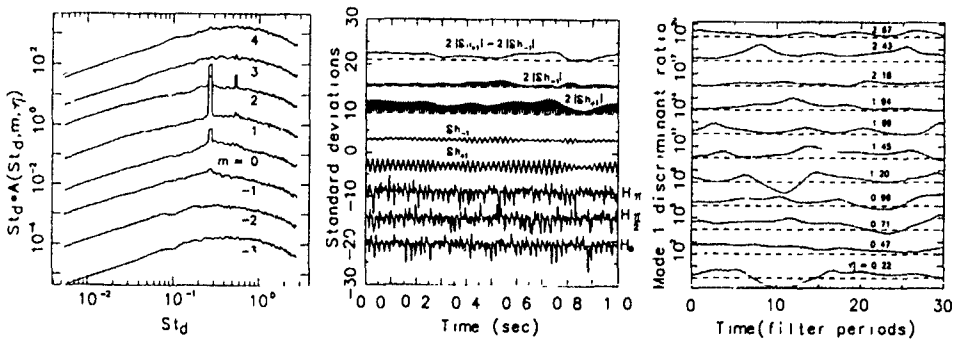

(a) 2-D Spectra ● η = 0.71 (see notes in Fig 8) (b) Construction of Mode Discriminants ● η = 0.47 (c) Radial Variation of Discriminant Ratio

Fig 10 Analysis of ±1 mode parity for a wake forced at m = ±1 and St_d = 0.27

$$h_\phi(t, \omega_c) = H_\phi(t, \omega) - H_\phi(t, \tilde{\omega})$$
$$= b_{+1}\sin\{\phi + \omega_c t + \Phi_{+1}\} - b_{-1}\sin\{\phi - \omega_c t - \Phi_{-1}\}, \quad (3)$$

where $H_\phi(t, \tilde{\omega})$ contains all the terms in $H_\phi(t, \omega)$, except for the two components at m = ±1 for $\omega = \omega_c$. In the above equation, the b's are the amplitude coefficients of the ±1 modes at $\omega = \omega_c$ and the Φ's are phase shifts relative to $t = 0$. Data from probes at $\phi = 0, \pi/2, \pi$ can be combined to yield discriminants for the $m = +1$ and $m = -1$ modes at frequency $\omega = \omega_c$

$$\delta h_{+1}(\tau, \omega_c) = h_0(t, \omega_c) - h_{\pi/2}(t + \frac{\pi}{2\omega_c}, \omega_c)$$
$$= 2b_{+1}\sin\{\omega_c\tau + \Phi_{+1}\} \quad (4a)$$

$$\delta h_{-1}(\tau, \omega_c) = h_{\pi/2}(t + \frac{\pi}{2\omega_c}, \omega_c) - h_\pi(t, \omega_c)$$
$$= 2b_{-1}\sin\{\omega_c\tau + \Phi_{-1}\}, \quad (4b)$$

where τ is the time reference of the combined signals. In practice, the filtering is accomplished in the frequency domain. We utilized a Gaussian shaped filter with an e^{-1} roll-off width of 0.125 ω_c, the outputs so processed will be labeled as δh_{+1} and δh_{-1}.

This method of analysis is first demonstrated for the *forced* wake behind a bullet-shaped body (see Cannon, 1991) because that wake is dominated by the $m = +1$ mode. It will thus provide a figure-of-merit to assess the results for the disk and screen wakes. Fig. 10a is in the same format as Fig. 8b and demonstrates the dominance of the $m = +1$ mode over that of the $m = -1$ mode for the case of forcing at $St_d = 0.27$ and $m = +1$. For this case, the peak amplitude is in the vicinity of $\eta = 0.75$. The different stages in construction of the mode discriminants are shown in Fig. 10b. The bottom three rasters are the de-meaned and variance-normalized velocity signals from three hot-wire probes that are located at azimuthal positions $\phi = 0, \pi/2, \pi$. The scale of the ordinate is in terms of standard deviations of the $H_\phi(t, \omega)$ signals and the dashed lines correspond to the position of the mean values. The velocity signals are filtered and combined, per Eq. (4), to obtain the mode discriminants rastered on lines four ($m = +1$) and five ($m = -1$). The discriminants are then rectified and doubled in amplitude to obtain rasters six ($m = +1$) and seven ($m = -1$) and then smoothed and differenced to obtain the top raster. The dashed line in the top raster represents a zero difference in the amplitude of the two discriminants. For those time periods when the dashed line and the solid raster line are colinear, the two modes contribute equally to the spectral structure (at $St_d = 0.27$). When the raster lies above the dashed line, mode +1 is dominant, below it, mode -1 is dominant. Instead of taking the difference between the rectified signals, their ratio is taken and plotted to logarithmic scale as the second raster from the bottom of Fig. 10c ($\eta = 0.47$). The other rasters in Fig. 10c represent the result of the processing sequence illustrated in Fig. 10b, but for the other radial locations at this axial station. For these rasters, the dashed line represents the point at which the ratio of the two discriminants is 1, and each tic on the ordinate axis represents a factor of ten increase in the magnitude of that ratio. A change in the positive direction from the dashed line corresponds to the $m = +1$ discriminant being larger. Note that the different rasters do not share the same reference time and so time-based comparisons between the rasters are not appropriate. Comparison of Figs. 10a and 10c reveals that, even though the $m = +1$ amplitude (at $St_d = 0.27$) dominates the $m = -1$ amplitude by almost two orders of magnitude in the spectra, that dominance occurs only on average for the mode discriminants. In fact, there are periods when the $m = -1$ discriminant is an order of magnitude larger than the $m = +1$ discriminant. For this particular case, it appears that the cross-over from $m = +1$ dominance to $m = -1$ dominance occurs, on the average, once every 30 filter (and, in this case, forcing) periods for up to 7 periods in duration.

Figure 11 compares the ratio of mode discriminants for the disk and $\sigma = 0.49$ screen wakes. The discriminants are rastered as a function of time (normalized by the center frequency of the band-pass filter) in the same manner as that for the *forced* wake of Fig. 10c. Identifiable features in the plots for the two wakes appear to be the same. For both wakes, the period of time for which the $m = +1$ discriminant is larger than the $m = -1$ discriminant is about the same as for the converse situation, and the maximum excursions from the dashed line (where the discriminants are of equal amplitude) are about the same in both directions and comparable in amplitude to that of the forced wake. Cross-over from $m = +1$ dominance to $m = -1$ dominance occurs approximately twice every 30 filter periods. There are extended time periods for which the ratio of the discriminants is 1 (by comparison with the maximum excursions), but periods of nearly equal length are also evident for the forced wake.

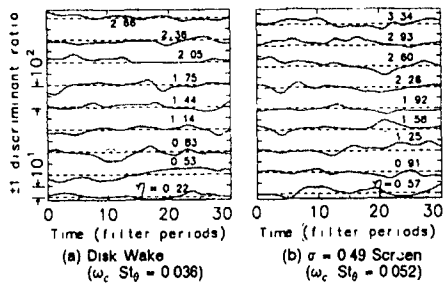

(a) Disk Wake (ω_c St_θ = 0.036)

(b) σ = 0.49 Screen (ω_c St_θ = 0.052)

Fig. 11 Comparison of mode discriminants for disk and $\sigma = 0.49$ screen ($x/\theta = 105$)

The hypothesis that coherent vortex shedding occurs as unwinding double helices (Pao and Kao, 1977) would get some support from a result that the two discriminants remain in a state of parity, but this was not found to be the case for either the *shedding* or *non-shedding* wakes. Even so, the time traces in Fig. 11 suggest that shedding occurs as double helices during some of the time periods. During other periods, one of the modes will clearly dominate the other. Since the principal results of the mode discrimination analysis are the same for the *shedding* and *non-shedding* wakes, there is no evidence to suggest that the strength of the coherent vortex shedding affects the natural interaction that occurs between the two modes. It is interesting to note that even for the case of a wake forced in one azimuthal direction, the other mode will occasionally dominate.

CONCLUSIONS

At least two velocity scales are required to collapse the mean and turbulent velocity fields for the wakes studied, which indicates that incomplete similarity exists. It has been shown that the balance is between the convective acceleration and the Reynolds stress terms in the momentum equation. Flow visualization results indicate that the presence of large-scale structures coincides with the presence of a recirculation bubble in the near wake, both of which are dependent on body bluffness. The axial extent of the recirculation bubble appears to oscillate in time. Two-dimensional Fourier analysis indicates that coherent structures of modes $m = +1$ and $m = -1$ exist in both the *shedding* disk wake and the *non-shedding* screen wake. Analysis of the parity between the +1 and -1 modes suggests that there are periods when one mode will clearly dominate the other, and other periods when the two modes will both be present in equal strength. Temporal variation in the parity between the two modes does not appear to depend on the strength of the coherent structures that are present.

REFERENCES

Achenbach, E. 1974 *J. Fluid Mech.* 62, 209

Berger, E., Scholz, D., Schumm, M. 1990 *J. Fluids and Structures* 4, 231

Bevilaqua, P.M., Lykoudis, P.S. 1978 *J. Fluid Mech.* 89, 589

Cannon, S.C. 1991 Ph.D. thesis, Univ. Arizona

Fuchs, H.V., Merker, E., Michel, U. 1979 *J. Fluid Mech.* 93, 185

George, W.K. 1987 Private communication

Hinze, J. 1975 *Turbulence*, McGraw-Hill

Hwang, N.H.C., Baldwin, L.V. 1966 *J. Basic Engr.* 88D, 261

Jeffreys, H. 1930 *Proc. Roy. Soc. (London) A* 128, 376

Marasli, B. 1989 Ph.D. thesis, Univ. Arizona

Monkewitz, P.A. 1988 *J. Fluid Mech.* 192, 561

Pao, H.-P., Kao, T.W. 1977 *Physics of Fluids* 2, 187

Torobin, L.B., Gauvin, W.H. 1959a *Can. J. Chem. Engr.* 37, 129

Torobin, L.B., Gauvin, W.H. 1959b *Can. J. Chem. Engr.* 37, 167

Uberoi, M., Freymuth, P. 1970 *Physics of Fluids* 13, 2205

EIGHTH SYMPOSIUM ON
TURBULENT SHEAR FLOWS
Technical University of Munich
September 9-11, 1991

USE OF LAGRANGIAN METHODS TO DESCRIBE PARTICLE DISTRIBUTION IN HORIZONTAL TURBULENT FLOWS

JEFFREY L BINDER AND THOMAS J HANRATTY

UNIVERSITY OF ILLINOIS, URBANA, ILLINOIS 61801, U.S.A

ABSTRACT

Lagrangian methods are used to examine the distribution of particles in a two-dimensional turbulent horizontal flow. The concentration field is viewed as resulting from a distribution of line sources of particles. The influence of gravity on the behavior of the particles from one of these sources is assumed, on average, to act independently from the turbulence Two cases are considered gas-liquid annular flow in a two-dimensional channel and sediment transport

INTRODUCTION

A Lagrangian method for analyzing particle distribution in horizontal turbulent flows is explored. The central idea is to describe the concentration field as resulting from a distribution of small sources of particles

This method had been used previously at the University of Illinois to describe the fully developed temperature field that exists when a turbulent fluid is flowing between a hot and a cold plane (Hanratty, 1956; Eckelman & Hanratty, 1972) The flow was assumed to be homogeneous; the hot plane was represented as a series of heat sources, the cold plane was represented as a series of heat sinks. The contributions of these sources and sinks were summed to give the temperature field. In the context of this analysis the spatial variation of the Eulerian turbulent diffusion coefficient is interpreted as resulting from the time-dependency of point source turbulent diffusion (Taylor, 1921) Hot or cold particles close to a wall have, on average, have been in the field for shorter times than hot or cold particles in the center Because of the time-dependency of point source diffusion the effective turbulent diffusivity is smaller close to a wall. Conversely, temperature gradients in the center of the channel are characterized by the long time turbulent diffusivity defined by Taylor

Binder and Hanratty (1991) used these ideas to describe droplet distribution and deposition in a vertical gas liquid annular flow This paper describes recent work by Binder (1991) which considers horizontal turbulent flows where the effects of gravity can cause a stratification of the particles.

POINT SOURCE DIFFUSION

The spread of particles from a point source in a homogeneous field can be represented by the change of the mean-square of the x-component of the displacement, $\overline{X^2}\ (t)$ For molecular diffusion,

$$D = \frac{1}{2}\frac{d\,\overline{X^2}}{dt} \qquad (1)$$

where D is the molecular diffusion coefficient appearing in the mass balance equation,

$$\frac{\partial C}{\partial t} = D\,\nabla^2 C \qquad (2)$$

For point source diffusion of a fluid particle in a homogeneous isotropic turbulence Taylor (1921) showed that

$$\varepsilon = \frac{1}{2}\frac{d\overline{X^2}}{dt} = \overline{v^2}\int_o^t R_L\,(t)\,dt \qquad (3)$$

Here $\overline{v^2}$ is the mean-square of the x-component of the turbulent velocity fluctuations and $R_L(t)$ is the Lagrangian correlation coefficient. A Lagrangian time scale and length scale can be defined as

$$\tau_L = \int_o^\infty R_L\,(t)\,dt \qquad (4)$$

$$\mathcal{L} = \left(\overline{v^2}\right)^{1/2}\tau_L \qquad (5)$$

It is noted from (3) that the turbulent diffusion coefficient is time-dependent At small times it varies linearly with time,

$$\varepsilon = \overline{v^2}\,t \qquad (6)$$

and at large times it is constant,

$$\varepsilon = \overline{v^2}\tau_L \qquad (7)$$

It has been shown that the distribution function describing the spread of fluid particles from a line source is Gaussian The distribution can, therefore, be given as a solution of the following equation

$$\frac{\partial C}{\partial t} = \frac{1}{2}\frac{d\overline{X^2}}{dt}\nabla^2 C + Q\,\delta(y/y')\,\delta(t/t') \qquad (8)$$

for a source located at y', t' The source strength Q has the units of mass per unit area and the delta functions, effectively, have the units of reciprocal length and reciprocal time

This theory can be applied to solid or liquid spheres if the ability of the particle to respond to turbulent velocity fluctuations is taken into account. The reciprocal time constant of the particle is defined for a Stokes drag as

$$\beta = 1/\tau = \frac{18\,\mu}{\rho_p\,d_p^2} \qquad (9)$$

where d_p is the particle diameter.

The dimensionless group $\beta\tau_{LF}$ is the ratio of the Lagrangian time scale of the fluid to the particle time scale For large $\beta\tau_{LF}$ (small particles) the particles follow the fluid motion closely The dimensionless group $\tau^+ = \tau v^{*2}/\upsilon$ is a measure of the ratio of the stopping distance of a particle to the thickness of the viscous wall region For $\tau^+ > 20$ the particles travel by free flight from $y^+ = 30$ to the wall so their deposition is not influenced by non-homogeneities in the turbulent field close to the wall

Measurements by Lee et al (1989) show that

$$\frac{\overline{(v^2)}_{particle}}{\overline{(v^2)}_{fluid}} = \frac{\beta\tau_{LF}}{0.7 + \beta\tau_{LF}} \qquad (10)$$

For small terminal velocities ($V_T / v^* < 1$), a decrease of $\beta\tau_{LF}$ causes a decrease in $\overline{(v^2)}_{particle}$ and an increase in the Lagrangian length scale, $\mathfrak{L}_p$ However, the particle diffusivity, ε_p, remains the same as the fluid diffusivity, ε_F For $V_T / v^* > 1$ the particles fall through the turbulence so rapidly that $\varepsilon_p < \varepsilon_F$

INFLUENCE OF GRAVITY ON THE BEHAVIOR OF WALL SOURCES

Two systems have been considered to show the effect of gravity on turbulent dispersion: gas-liquid annular flow in a two-dimensional channel and sediment transport

In annular flow, liquid moves as a layer along the bottom wall at $y = 0$, and is atomized at a rate per unit area of R_A A differential length of this layer in the flow direction can be considered as a line source of drops These drops diffuse away from the wall and eventually leave the field by depositing on the bottom wall or on the top wall, located at $y = H$ The fraction of these droplets depositing on the top wall is F_{BT} and the fraction depositing on the bottom wall is $F_{BB} = 1 - F_{BT}$. The liquid depositing on the top wall eventually builds up as a layer, which also provides sources of droplets Because of the effects of gravity the droplets tend to stratify so that the concentration is larger at the bottom and $F_{BB} > F_{BT}$. Under fully-developed conditions the rates of atomization from the bottom, R_{AB}, and top, R_{AT}, walls are equal to the rates of deposition, R_{DB} and R_{DT}, and $R_{AT} / R_{AB} = F_{BT} / F_{TB}$, where F_{TB} is the fraction of particles from a source on the top wall that deposits on the bottom wall.

The problem in sediment transport considered in this paper is one in which all of the particles flowing in the liquid originate by entrainment from a layer of sediment on the bottom wall (The analysis is easily extended to take account of particles in the entering liquid by putting line sources in the body of the liquid.) This bottom wall may be considered as a series of line sources of strength $R_A dx$ A fraction of the sediment coming from one of these line sources can redeposit on the bottom wall, F_{BB}, and a fraction F_{BT}, will reach the top of the liquid, which may be a free surface or a channel wall. The solid sediment particles, unlike the drops in annular flow, do not lose their identity on hitting the top boundary We picture them as rolling along the interface and being reentrained (almost immediately) by gravity and turbulence.

In both annular flow and sediment transport τ^+ is usually greater than 20. Therefore, the analysis of a wall source is simplified by assuming plug flow and a homogeneous turbulent field Consequently, the diffusion time can be related to distance in the flow direction by the equation $dt = dx / U$, where U is velocity of the fluid

The equation describing the concentration field resulting from a point source is

$$\frac{\partial C}{\partial t} + V(t - t')\frac{\partial C}{\partial y} = \varepsilon_p(t - t')\frac{\partial^2 C}{\partial y^2} + Q\,\delta(y / y')\,\delta(t / t') \qquad (11)$$

From considerations of conservation of mass and of the free-flight mechanism for impaction on the wall the following equation is derived for the boundary conditions for a single source

$$f(t - t')\sqrt{\frac{2}{\pi}}\left(\overline{v_p^2}\right)^{1/2} C_s = \pm\,\varepsilon_p(t - t')\frac{\partial c}{\partial y}\Big|_s \qquad (12)$$

Term $V(t - t')$ is the average deterministic velocity caused by the gravitational field It is defined by the equation

$$m_p\frac{dV}{dt} = -\frac{1}{2}\rho_L C_D V^2 - g\,m_p\left(1 - \frac{\rho_F}{\rho_L}\right), \qquad (13)$$

where m_p is the particle mass and C_D is the drag coefficient The particles entrained from a liquid film (on the top or bottom wall) or from the sediment bed (on the bottom wall) are pictured to enter the field at a velocity proportional to the turbulence velocity. Because of the limited information about how the particles enter the field the proportionality constant is taken as unity For a particle source on the bottom the boundary condition is that at $t = t'$ velocity $V_o = \left(\overline{v_p^2}\right)^{1/2}$ For a source of drops on the top wall $V_o = -\left(\overline{v_p^2}\right)^{1/2}$ at t Sediment particles that entered the field at $t = t'$ and strike the top boundary at $t = t_s$ are considered to form a source on the top wall for which the boundary condition for (13) is that $V_o = -\left(\overline{v_p^2}\right)^{1/2} + V(t_s - t')$ Equation (13) gives velocities less than the free-fall velocity, V_T Only particles that have been in the field a long time will reach free fall

RESULTS

Calculated results for annular flow and for sediment transport are found to be dependent on two dimensionless groups. Term $\beta\tau_{LF}$ represents the inertia of the particle and

may be thought of as a measure of the particle size The Froude number, v^{*2}/gH, is a measure of gravitational effects The product of these two groups, $Fr\beta\tau_{LF}$, varies inversely as the ratio of the terminal velocity to the friction velocity For example, for Stokesian drag

$$Fr\beta\tau_{LF} = 0.046\ v^*/V_T \qquad (14)$$

For gas-liquid annular flows the Sauter - mean diameter is such that $0.01 < \beta\tau_{LF} < 0.1$ and $V_T / v^* < 1$ Consequently, $\left(\overline{v^2}\right)^{1/2}_{particle} / \left(\overline{v^2}\right)^{1/2}_{fluid} = 0.13 - 0.35$, $\tau_P / \tau_{LF} = 8 - 71$ and $\varepsilon_P \cong \varepsilon_F$ For sediment transport in a liquid, $\beta\tau_{LF}$ is much larger so that $\left(\overline{v_P}\right)^{1/2}$, τ_{LP} and ε_P are approximately the same as the values for the fluid

Figure 1b gives the behavior of a source on the bottom wall for $\beta\tau_{LF} = 1.0$, $Fr = 10$ and $\beta\tau_{LF}Fr = 10$, a case for which turbulent diffusion is dominating over gravitational settling At x/H = 0 and at small x/H the maximum occurs at the wall because $f \cong 0$ At larger x/H deposition occurs at the bottom wall so the maximum moves away from the wall in order to satisfy (12) at the wall Figure 1a gives the behavior of a source on the wall for a case in which both turbulence and gravitational settling are affecting dispersion of the particles $Fr = 10$, $\beta\tau_{LF} = 0.01$ and $\beta\tau_{LF}Fr = 0.1$. It is noted that the particle spread is greatly reduced

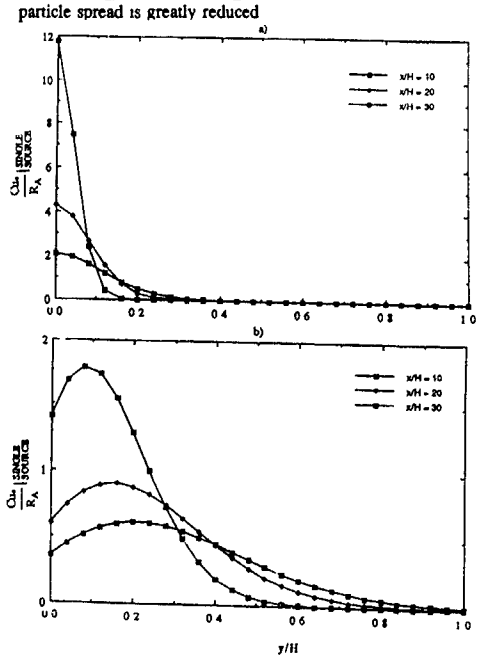

Fig 1 Concentration profile of an instantaneous source on the bottom wall. a) $Fr = 10$, $\beta\tau_{LF} = 0.01$, $Re = 100{,}000$, b) $Fr = 10$, $\beta\tau_{LF} = 1.0$, $Re = 100{,}000$

Figure 2 gives calculated ratios of the fraction of particles that reach the top wall, F_{BT}, to the fraction of particles from a source on the top wall that deposit on the bottom wall. The values of $\beta\tau_{LF}$ correspond to annular flows but the curves do not change much for larger $\beta\tau_{LF}$ The results for $\beta\tau_{LF} = 1$ correspond roughly to sediment transport This plot can be used to define flow regimes For $Fr\ \beta\tau_{LF} < 0.4$ a negligible amount of particles reach the top wall Both gravity and turbulence are affecting the distribution For very much smaller values of $Fr\ \beta\tau_{LF}$ (not studied in this research) turbulence has negligible effect and the concentration distribution is controlled solely by the particle trajectories. This would correspond to the saltation regime in sediment transport For $Fr\ \beta\tau_{LF} > 6$ diffusion is dominating and the particles should be uniformly distributed

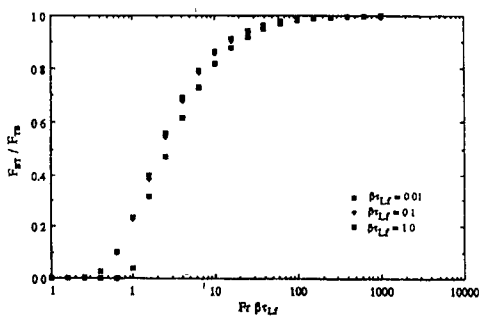

Fig 2 Relative rates of atomization in horizontal annular flow, R_{AT}/R_{AB} versus $Fr\beta\tau_{LF}$.

Concentration fields at different locations in a channel are calculated by adding the contributions from a number of sources Figure 3 gives the fully developed concentration fields for sediment transport of particles of a single size. (This calculation can easily be extended to include a distribution of sizes) The values of $Fr\ \beta\tau_{LF}$ for which these calculations were made are typical of laboratory studies of sediment transport

Calculations have also been made of the dimensionless bulk concentration (or sediment load), given by $C_B v^*/R_A$, as a function of $\beta\tau_{LF}$ and Fr Under fully developed conditions $R_A = R_D$ and the dimensionless bulk concentration equals $(k_D / v^*)^{-1}$, where k_D is a deposition constant defined as $k_D = R_D/C_B$. Such calculations for gas-liquid annular flows reveal that k_D / v^* has a minimum at a certain value of $\beta\tau_{LF}$ (or particle size) For greater $\beta\tau_{LF}$ turbulent diffusion controls deposition, for lesser $\beta\tau_{LF}$ gravitational settling controls. As a consequence, calculations for sources of a range of drop sizes reveal not only a stratification where larger drops are located closer to the bottom but also a ripening for which the distribution of drop sizes in the fluid is different from the distribution at the source

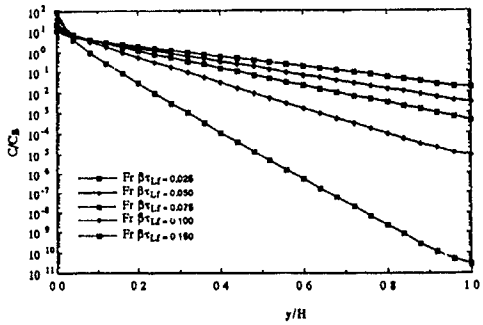

Figure 3 Concentration profiles normalized with the bulk concentration for sediment transport

DISCUSSION

Most of the theoretical work on the stratification of particles in horizontal flows has been related to sediment transport O'Brien (1933) and Rouse (1937) have suggested that the concentration distribution is given by

$$\varepsilon_p\,(y)\,\frac{dC}{dy} + V_T\,C = 0 \qquad (15)$$

where V_T is the terminal velocity The difficulty with this equation is that it predicts an infinite concentration at y = 0 and that a concentration at some location near the bottom boundary needs to be specified empirically.

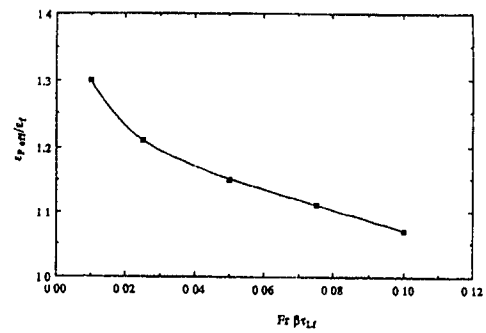

Figure 4 Ratio of effective particle diffusivity to the fluid value.

The application of (15) to the central portion of the concentration profiles shown in Fig. 3 gives the values of ε_p / ε_f in Fig. 4. It is found that ε_p calculated from (15) are 8 - 30 per cent too high. This can be explained in the context of present calculations because the deterministic velocity caused by the gravitational field is not represented very well by V_T

Attempts to generalize (15) so as to consider sediment concentration profiles that are not fully developed have involved the solution of the Eulerian equation

$$U\,\frac{\partial C}{\partial x} + V_T\,\frac{\partial c}{\partial y} = \varepsilon\,(y)\,\frac{\partial^2 C}{\partial y^2} \qquad (16)$$

The condition at the upper boundary is given by (15) and the one at the lower boundary is fixed empirically

The present analysis differs from these approaches in a number of ways: The condition at the lower boundary is defined by specifying the rate of entrainment $R_A(x)$ or the strength of the sources The deterministic velocity is not fixed at the terminal value The time-dependency of turbulent diffusion coefficient is used rather than a spatial variation The condition at the upper boundary is different from (15). The dispersion of particles with a size distribution is taken into account in such a way that the relation of the size distribution in the fluid to the size distribution at the source can be calculated The influence of particle inertia on particle turbulence can be taken into account are in rigorous way.

ACKNOWLEDGEMENTS

This work has been supported by the National Science Foundation under Grant NSF CTS 89-19843 and by the Department of Energy under Grant DOE DEF G02-86 ER 13556

REFERENCES

1 Hanratty, T J 1956 Heat transfer through a homogeneous isotropic turbulent filed AIChE Journal, 2, 42-45

2 Eckelman, L D and T. J. Hanratty 1972 Interpretation of measured variations of the eddy conductivity Int Journal Heat Mass Transfer, 15, 2231-2239.

3 Taylor, G I 1921 Diffusion by continuous movements Proc London Math Soc , 151, 196

4 Binder, J L and T J Hanratty 1991 A diffusion model for droplet deposition in gas/liquid annular flow Int Journal Multiphase Flow, 17, 1-11

5. Binder, J L. 1991 Use of Langrangian Methods to Describe Particle Deposition and Distribution in Dispersed Flows, Ph D thesis, University of Illinois, Urbana

6 Lee, M. M., Hanratty, T J and R J. Adrian 1989 An axial viewing photographic technique to study turbulence characteristics of particles, Int. Journal Multiphase Flow, 15, 787-802

7 O'Brien, M. P 1933 A review of the theory of turbulent flow and its relation to sediment transport, Trans. Amer Geophysical Union, 14, 487.

8. Rouse, H. 1937 Modern conceptions of the mechanics of fluid turbulence, Trans. Am. Soc., Civil Eng., 102, 436

EIGHTH SYMPOSIUM ON
TURBULENT SHEAR FLOWS
Technical University of Munich
September 9-11, 1991

THE DISPERSION AND TRANSPORT BEHAVIOUR OF PARTICLES IN TURBULENT GAS FLOWS

P Neumann and H Umhauer

Institut für Mechanische Verfahrenstechnik und
Mechanik der Universität Karlsruhe (T.H)
Postfach 6980, W-7500 Karlsruhe 1, Germany

ABSTRACT

The paper describes the experimental investigations into the transport- and dispersion behaviour of particles in turbulent gas flows The particles are introduced as strands into a quasi-point-like fashion on the axis of the inlet flow of a vertical test-pipe The decay and fan-out of the particle strands within the turbulent gaseous flow is investigated together with the dispersion of the particles These aspects are to be viewed here as a exemplary situation involved in the investigations concerning the interactions between disperse phase and turbulent fluid phase. Attention is especially focussed on the description of the distribution states of the disperse phase, i.e the spatial distribution of the particles as well as the frequency distributions of their velocity.

INTRODUCTION

The transport and dispersion characteristics of particles of a disperse phase in fluids is of relevance in a variety of technical, natural and ecological sectors This presentation describes this behaviour under defined model conditions in a turbulent pipe flow An important factor is the manner in which the particles are introduced into the pipe flow. *One* possibility is to introduce them in a quasi-point-like region as a compact strand in the axis of the inlet pipe se on This instance is not only suitable for comparison with certain model calculations, but is also of practical interest

It is demonstrated how the highly-concentrated particle strands decay within the turbulent pipe flow and how the particles are distributed across thee downstream pipe regions. One of the main aspects of the investigations is the characterization of the three-dimensional distribution states of the particles of the disperse phase.

The applied measuring techniques mainly involve short-exposure photography and double-pulse holography The latter, being a whole field method, fundamentally differs from temporally-averaging measuring techniques (such as phase-Doppler-technique) in that the instantaneous distribution state of the particle collectives may be exactly determined in addition to their size and velocity

MEASURING TECHNIQUES AND APPARATUS

The presented investigations were based on the following test parameters. The flow channel consists of a vertical pipe of up to 3 m in length, with a diameter of 50 mm The average velocities of the downwards-flowing gas at the pipe axis were 5, 10, and 20 m/s (which correspond to Reynolds numbers of 16 000, 33 000, and 66 000) The disperse phase consisted of three narrow glass sphere fractions with particle sizes of 20-25 µm, 40-50 µm and 90-100 µm To avoid agglomeration, the particles were purified, dried and carefully sieved. The fluid phase was air.

The particles were introduced in a quasi point-like fashion into the inlet section of the flow, 25 mm above the inlet funnel using a dosing apparatus especially developed for the investigations. The heart of this device is a small tube possessing an internal diameter of 1 to 6 mm. A longitudinal ultrasonic oscillation at a frequency of 33.9 kHz serves to avoid both the formation of particle bridges within the inlet, and also guarantees a constant mass flow rate, which can be varied from 0 15 to 10.0 g/s by varying the internal tube diameter.

The spatial distributions and the flow characteristics of the particles as they issue from of the dosing apparatus and through the turbulent pipe stream are registered and recorded with the aid of short-exposure photography, high frequency cinematography, and pulse holography The short-exposure photographs are taken both directly at the particle dosing apparatus outlet and at a transport distance of 103 mm in the pipe through glazed windows. High frequency cinematography is used to investigate the flow of the particles from the dosing apparatus. The pulse holography finally serves the main body of the investigations

The spatial distribution of the particles through the complete pipe cross-section at transport distances of 285 and 3000 mm have been reproduced by means of in-line holography (Schafer et al , 1987). From these holograms, sub-sections were then evaluated, i.e the location, size, and velocity of all particles situated within this sub-section at the instant the hologram was taken were correlatively measured. From this data, the graphs illustrated in Figs 2 up to 6 have been calculated. Being

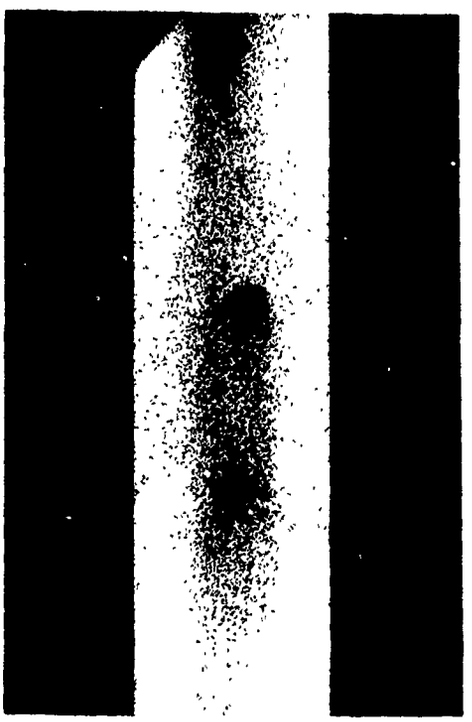

Fig 1 Strands of particles of the fraction 40-50 µm
mass flow. 0.97 g/s; tube diameter (dosing apparatus) 2 mm
velocity of the pipe flow (fluid phase). 10 m/s

a) directly after leaving the dosing unit
b) after a transport distance of 116 mm

a whole field technique, pulse holography particularly yields data from which the instantaneous three-dimensional dispersity state of the collective concerned is revealed, and hence more exactly characterized The characterization does not only employ the concentration profiles but also the frequency distributions of the distances between the particles and the frequency distributions of the local number concentrations This delivers information concerning the homogeneity of the three-dimensional particle distribution state (Neumann & Umhauer, 1989)

RESULTS

Here only the results are presented which concern the particles within the 40-50 µm size range and velocities of 10 and 20 m/s

Fig. 1a illustrates the still coherent particle strand upon leaving the dosing unit through a 2 mm tube. The velocity of the fluid phase was, in this instance, 10 m/s The particle strand is still closely packed, although in the lower regions, necking can already be observed Here, the strand is accelerated and torn apart by the air stream, so that after flowing 116 mm through the pipe, the particles are already carried as disintegrating clusters (Fig. 1b), from which particle trails issue. Fig 1b was taken from a glazed 14 mm wide slot in the pipe.

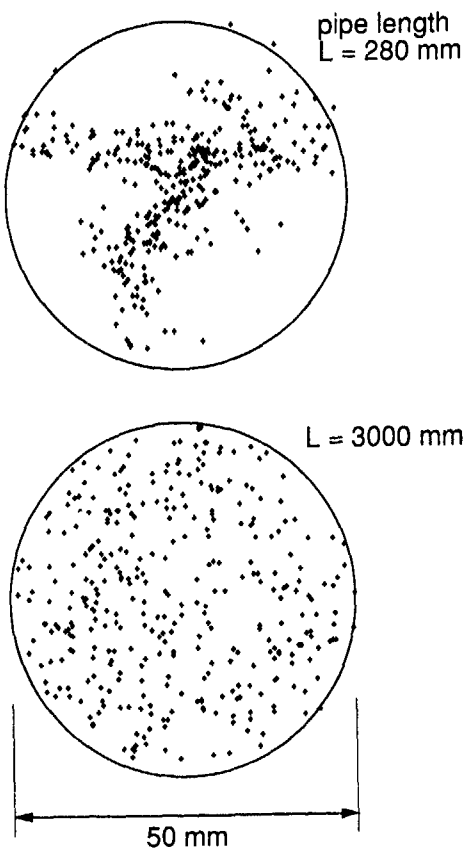

Fig 2: Particle distribution across a pipe section Projection of the particles situated within a thin layer across the flow direction viewed along the flow direction; mean flow velocity. 20 m/s; disperse phase glass spheres 40. 50 µm

In contrast, Fig 2 illustrates situations which originate from the evaluated data of two double-pulse holograms. All particles in a thin layer (0.35 and 0 7 mm thick respectively) across the pipe at transport distances of 280 and 3000 mm have been evaluated. From this data, the spatial particle distributions across the pipe cross-section which existed at the instant of the hologram exposure, are plotted. After the short transport distance of 285 mm, one can still observe a disintegrating cluster From a high central concentration, three particle trails drift outwards in the direction of the pipe wall. After being carried 3000 mm, the particles appear to be more ore less uniformly distributed across the pipe (with local fluctuations which are to be expected for turbulent flows). The results of the evaluation of other holograms shows a similar behaviour

In addition to the representation in Fig. 2, which allows a qualitative assessment, Fig. 3 offers a

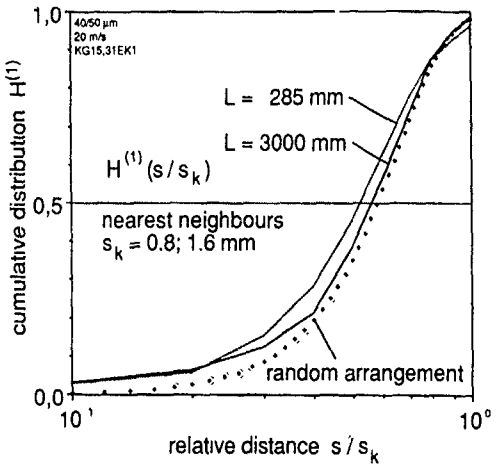

Fig 3: Normalized cumulative frequency distributions of the distances between nearest neighbouring particles (Neumann & Umhauer, 1989, 1991). The curves plotted represent the spatial arrangement of the particles after the two transport distances and the random grouping.

quantitative description of the spatial arrangement of the particles. The graph demonstrates the cumulative distributions of the particle spacing, i e the distance between any single particle of a collective and its nearest neighbour. The abscissa is normalized with respect to a specific average distance, in order to gain a particle concentration independence (Neumann & Umhauer. 1989, 1991) The data refer to a particle collective of the same hologram as in the previous illustration, but here all particles inside a cubical volume have been evaluated. The dotted curve represents the distribution state at the shortest transport distance of 285 mm, and the full line that of 3000 mm. The curve formed by the crosses, is that which would exist for a mathematically randomly distributed, infinitely large particle collective, void of mutual interactions (Raasch & Umhauer,, 1989). This curve can be used as a measure for comparison. Inhomogenities in the particle grouping which are larger than those of the random structure, lead to a shift in the cumulative distribution curve towards smaller particle spacings. This is verified by the median values of the three curves, which are $(s/s_k)_{50}$ = 0 52, 0.56, and 0.58 for the respective shortest, and longest transport distances, and the random distribution

The frequency distribution of the distances between the nearest neighbouring particles is a microscopic measure of the spatial particle grouping The term microscopic is applied because here only the distances between closely neighbouring particles are considered, whilst the global spatial distributions across the whole cross-section remains unregarded Contrary to this the profiles illustrated in Fig. 5 may be regarded as a macroscopic description of the spatial distributions.

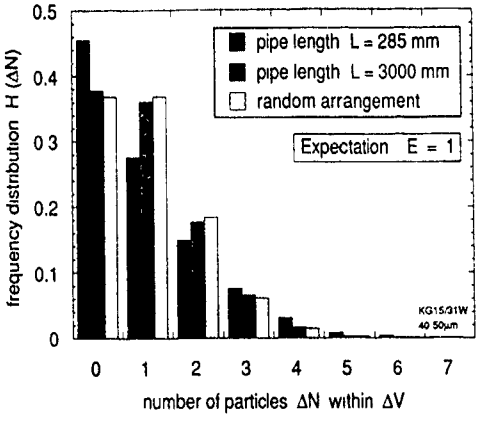

Fig 4 Concentration frequency distribution H (ΔN) of the number of particles within ΔV

A further possibility of quantitatively characterizing the spatial particle distribution is illustrated in Fig. 4 This is the frequency distribution of the local particle number concentrations, which is derived in the following manner. The total evaluated sample volume V, which contains N particles is sub-divided into k sub-volumes of equal size ΔV For the case in question here, i.e. where k = N, each sub-volume ΔV contains, on average, just one single particle (expectation E = 1). Due to the random distribution of the particles caused by the flow turbulence, however, the individual sub-volumes will, in reality, contain no, one, two or more particles. The compilation of the concentration frequency distributions rests on the determination of the frequency of each such case i.e. the number of sub-volumes which contain no, one, two, three etc particles are determined and plotted for each criterion. Such a distribution is discrete. As a variation of this method a number of sub-volumes can be combined, so that an expectation E > 1 emerges The concentration frequency distribution of a collective of statistically random-distributed particles is inevitably a Poisson distribution

Fig 4 illustrates the concentration frequency distribution plotted for a collective of particles distributed at random (Poisson distribution) and for the particle collectives evaluated at transport distances of 285 mm and 3000 mm. The distributions may be observed to differ significantly Whilst the concentration frequency distribution of the particles at the larger transport distance reveals an almost completely random distribution, that of the shorter distance is quite definitely not the case.

Figs 5 and 6 yield information concerning the particle kinetics. These are based on the particle velocity components in the main flow direction v_z.

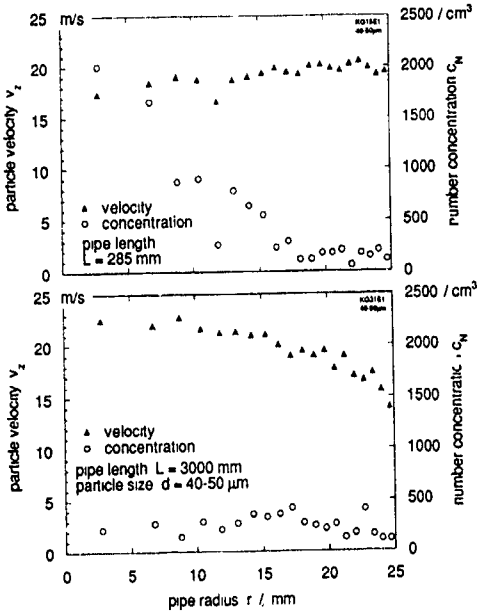

Fig 5 radial profile of the particle velocity v_z in main stream direction and the number concentration c_N after
a) 285 mm and
b) 3000 mm transport length in the pipe

The profiles of the particle velocity v_z and the number concentration c_N have been plotted as function of the pipe radius r in Fig. 5. For this purpose, the thin layer of evaluated particles depicted in Fig 2 have been sub-divided into a number of equi-areal rings. The mean velocity and number concentration of the particles contained within the individual rings were calculated.

At the short transport distance of 285 mm in the pipe, the inlet flow conditions are still predominant The velocity at the pipe axis is still a little lower, than at the wall regions, due to the axially-introduced particle strands, since the high concentration of particles indeed noticeable retards the flow. After a transport distance of 3000 mm the profile of the particle velocities is similar to that of the fluid velocities with the exemption of the wall region.

Fig. 6 finally demonstrates the frequency distributions of the particle velocities at the two investigated transport distances in the form of a standardized number density distribution and a cumulative number distribution. As Fig. 5 already suggests, the distribution at the short transport distance is considerably narrower. Moreover, the mean value for this distance is somewhat lower in comparison to the mean value for the larger distance (see the means and standard deviations specified in the diagrams.

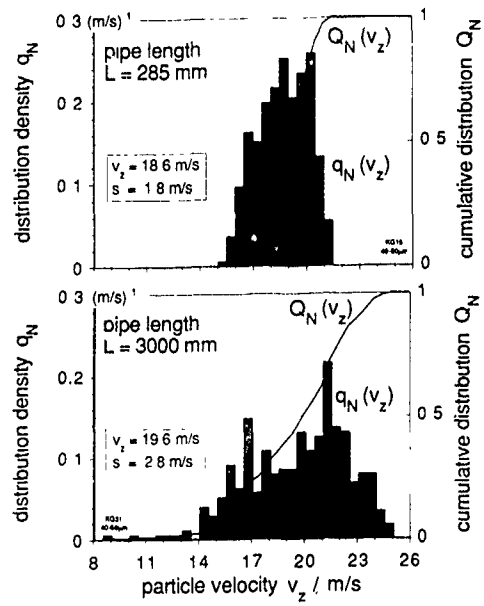

Fig 6 Normalized frequency distributions of the particle velocities in main stream direction plotted as number density distribution (bars) and cumulative number distribution (line)

a) after 285 mm transport length

b) after 3000 mm transport length in the pipe

CONCLUSIONS

This paper concerns the description of the decay and dispersion of a particle strand, transported within a turbulent gaseous pipe flow by means of experimentally obtained data. Special emphasis was laid on the characterization of the spatial grouping of the particles of the disperse phase

The approach of a completely random spatial distribution of the particles in the flow with increasing flow distance has been quantitatively characterized in two different ways by specifying the frequency distributions of the particle spacing, and the specification of the frequency distributions of the local (relative) number concentrations. After 60 pipe diameters of transport distance (at a velocity of 20 m/s and for particles of 40 -50 µm diameter) an almost completely random spatially particle distribution was established After this transport length the frequency distributions of the particle velocities have probably reached their final shape

The further results could not be presented due to the confinements imposed on the length of this contribution.

REFERENCES

Kozikowska, A., Haman, K , Supronowicz, J 1984 Preliminary results of an investigation of the spatial distribution of fog droplets by a holographic method. Quaterly Journal of the Royal Meteorological Society 110· 65-73

Neumann, P , Umhauer, H 1989 Charakterisierung des räumlichen Verteilungszustandes von Partikeln, die in turbulenter Gasströmung transportiert werden 4 Europäisches Symposium Partikelmeßtechnik Nürnberg: 137-151

Neumann, P., Umhauer, H 1991 Characterization of spatial distribution state of particles transported by turbulent gas flow To be published in Experiments in Fluids

Raasch J., Umhauer H. 1989 Computation of the frequency distributions of distances between particles randomly dispersed in a fluid flow. Part Part Syst Charact 6 13-16

Schäfer M., Bottlinger M., Löffler F , Umhauer H 1987 Investigation of the state and transport of particulate phases in a turbulent tube flow Part. Charact. 4: 1-6

Schäfer M., Umhauer H. 1987 Realization of a concept for the complete evaluation of double pulse holograms of particulate phases in flows Part. Charact 4· 166-174

EIGHTH SYMPOSIUM ON
TURBULENT SHEAR FLOWS
Technical University of Munich
September 9-11, 1991

ON THE INTERACTION BETWEEN SOLID PARTICLES AND DECAYING TURBULENCE

S E Elghobashi and G.C. Truesdell

Mechanical and Aerospace Engineering Department,
University of California, Irvine, CA 92717

ABSTRACT

The interaction between small solid particles ($d/\eta < 1$), at a volumetric loading ratio $\Phi = 5 \times 10^{-4}$, and a decaying homogeneous turbulence is studied using direct numerical simulation The results show that the particles increase the fluid turbulence energy at high wave numbers. This increase acts as a barrier to the nonlinear energy transfer from the low wave number range Associated with the energy increase at higher wave numbers, there is a larger increase in the dissipation rate of energy The net result is a reduction in all the turbulence length scales, hence lower turbulent diffusivity of the carrier fluid turbulence Gravity results in a significant turbulence anisotropy and an increase in the diffusivity of the particles and fluid in the gravity direction The correlation $\Psi = \sum_i < \Phi u_i(v_i - u_i)/\tau_p >$ can be *positive or negative* and thus acts as a *source or sink* of fluid turbulence energy

1. INTRODUCTION

It has been known for more than three decades that the addition of a small volumetric concentration ($\leq 10^{-3}$) of particles (solid or liquid) to a turbulent flow modifies the structure of turbulence This modification produces transport rates of momentum and mass (i e turbulent mixing rates) that are different from those in flows without particles Available experimental data show that the addition of particles may *increase or decrease* the turbulence kinetic energy of the carrier fluid However, there is a lack of understanding of the mechanisms responsible for *increasing or decreasing* the turbulence energy Most of the current understanding of turbulence modulation in particle-laden flows is based on the few available experimental observations which are valid only for the conditions of the corresponding experiment and cannot be generalized

When fine droplets or solid particles (diameter $d \leq 250\mu$) are injected into a free turbulent jet the turbulence intensity is reduced, thus lowering the spreading rate of half width of the jet (Hetsroni and Sokolov [8], Popper et al [11], Modarress et al [10] , Fleckhaus et al [3], Tsuji et al [13]). However, there are other experiments (e g Levy and Lockwood [9]) which show that the addition of large particles ($d \geq 500\mu$) increases the turbulence intensity in a free jet whereas smaller particles ($d \leq 250\mu$) suppress turbulence in the jet. Recently, Hardalupas et al [6] measured the velocities of the particles and fluid in turbulent particle-laden jets They showed that the rate of spread of the half width of the jet increased with increasing the loading of 80μ glass beads, whereas it decreased with increasing the loading of 40μ beads Hetsroni [7] suggested that particles with low Reynolds number , R_p , cause turbulence suppression, while particles with higher Reynolds number cause enhancement of turbulence due to wake shedding However, as will be shown later, the present study indicates that particles with low Reynolds number , $R_p < 1$, can also increase the turbulence energy

Gore and Crowe [5] reviewed the available experimental data on turbulence modulation in particle-laden flows and proposed that the critical parameter that predicts whether the turbulence will be augmented or suppressed with the addition of particles is d/ℓ where d is the particle diameter and ℓ is the Eulerian integral length scale of turbulence They concluded that the critical value is $d/\ell \approx 0.1$, above which turbulence intensity is increased and below which it is suppressed Obviously this proposal is too simplistic since the particle material density and fluid viscosity , which affect the particle response time, and particle load ng ratio were different in all these experiments Furthermore, our present results show that turbulence intensity increases for $d/\ell \approx 10^{-3}$, contradicting the proposal of Gore and Crowe

The purpose of this paper is to examine in some detail the interaction between the particles and turbulence in a much simpler flow than the inhomogeneous flows reviewed above In particular, the paper is concerned with the physics of the two-way interaction between a decaying grid-turbulence and a large number of solid spherical particles dispersed within Grid turbulence was selected for the study because of its spatial homogeneity and the independence of its properties on the mean flow velocity We examine the effect of the particles on the time development of turbulence energy and dissipation, their spatial spectra, and the effect of the modified turbulence on the dispersion of particles

The method of direct numerical simulation is used to solve the three-dimensional, time-dependent Navier-Stokes equations which include all the forces exerted by the particles on the fluid The volume fraction of the particles is large enough ($\Phi = 5 \times 10^{-4}$) to modulate the turbulence, but small enough such that there is no collision between the particles.

Only one other direct numerical simulation study (Squires and Eaton [12]) has been reported recently concerning the two-way interaction of particles with homogeneous turbulence However, that study considered only stationary turbulence by forcing the flow at the low wave numbers Stationarity of turbulence was achieved by the addition of energy, at each time step, at a rate equal to that of the energy dissipation. Clearly, the results obtained from a forced simulation are questionable when the goal is to quantify the changes in the fluid turbulence energy spectrum caused by the particles As will be discussed later in section 3, the addition of particles may increase or decrease the turbulence

energy, a result that cannot be obtained from a stationary turbulence simulation Furthermore, the particle motion equation used in that study [12] included only the drag force The present study shows that neglecting the effects of gravity on particle motion results in a significantly different behavior of the turbulence in the carrier fluid

2. MATHEMATICAL DESCRIPTION

The exact time-dependent, three dimensional Navier-Stokes and continuity equations are solved in a cubical domain with periodic boundary conditions The mean flow is vertically upward in the positive x_3 direction The two other coordinates x_1 and x_2 are in the horizontal plane Gravity acts downward in the negative x_3 direction The fluid is incompressible and has a constant kinematic viscosity, ν The dimensionless governing equations are

$$\frac{\partial u_i}{\partial t} + \frac{\partial}{\partial x_j}(u_j u_i) = \frac{1}{Re}\frac{\partial^2 u_i}{\partial x_j^2} - \frac{\partial p}{\partial x_i} - f_i \qquad (1)$$

$$\frac{\partial u_j}{\partial x_j} = 0 \qquad (2)$$

The last term in eq (1) is the force exerted on the fluid by N particles per unit mass of fluid, in the x_i- direction, and calculated from

$$f_i = \sum_{k=1}^{N} f_{k,i} \qquad (3)$$

where $f_{k,i}$ is the instantaneous local sum, in the x_i- direction, of the first four forces on the RHS of eq (4) below acting on one particle k Normalization of f_i is consistent with the other terms in eq. (1) N is the instantaneous number of particles , $[N = N(x_1, x_2, x_3, t)]$, within the control volume at which eq (1) is integrated When we study the dispersion of particles without effects on the fluid (i.e one-way coupling or equivalently particle-free flow) we set f_i equal to zero The direct effect of the particles presence on the continuity equation of the fluid, eq. (2), is assumed negligible since the volume fraction of the particles is less than 10^{-3} The equations are discretized in an Eulerian framework using a second-order finite-difference technique on a staggered grid containing 64^3 points This grid permits an initial microscale Reynolds number $R_{\lambda,o} = 35$. Few additional simulations have been performed with 96^3 grid points and higher $R_{\lambda,o}$ which produced similar results to those in the present paper However, the computation cost (both memory and cpu time) with the 96^3 grid and two-way coupling is quite high at present. A typical simulation requires about 65 cpu hours on the Convex C-240 computer or about 35 cpu hours on the Cray-Y-MP8/864 This is mainly due to the large number of particles to be tracked for the same volumetric loading ratio used here The Adams-Bashforth scheme is used to integrate the equations in time. Pressure is treated implicitly, and is obtained by solving the Poisson equation in finite-difference form using a fast Poisson solver. More details about the numerical method are discussed by Gerz et al [4].

The instantaneous velocity of each particle, v_i, in the x_i direction, is obtained by time integration of the following Lagrangian equation of particle motion

$$\begin{aligned} m_p(dv_i/dt_p) = {} & m_p F(u_i - v_i) \\ & + m_f(Du_i/Dt) \\ & + \tfrac{1}{2} m_f(Du_i/Dt - dv_i/dt_p) \\ & + 6a^2(\pi\rho\mu)^{1/2}\int_{t_{p_o}}^{t_p} \frac{d/d\tau(u_i - v_i)}{(t_p - \tau)^{1/2}}\, d\tau \\ & + (m_p - m_f) g_i \end{aligned} \qquad (4)$$

Equation (4) describes the balance of forces acting on the particle as it moves along its trajectory The term on the left hand side is the inertia force acting on the particle due to its acceleration The terms on the right side are respectively the forces due to viscous and pressure drag, fluid pressure gradient and viscous stresses, inertia of virtual mass, viscous drag due to unsteady relative acceleration (Basset), and buoyancy F is the inverse response time of the particle The response time is the time for momentum transfer due to drag F is calculated from

$$F = 1/\tau_F = \left(\frac{3}{8a}\right) C_D \left(\frac{\rho}{\rho_p}\right) |u_i - v_i| \qquad (5)$$

The quantities a, m_p, ρ_p are respectively the particle radius, mass and material density C_D is the drag coefficient, which is assumed a function of the Reynolds number of the particle, $R_p = 2a\rho|u_i - v_i|/\mu$ The fluid density and viscosity are ρ and μ The derivative d/dt_p is with respect to time following the moving particle, whereas Du_i/Dt is the total acceleration of the fluid as seen by the particle, $\frac{Du_i}{Dt} = [\frac{\partial u_i}{\partial t} + u_j \frac{\partial u_i}{\partial x_j}]$, evaluated at the particle position $\vec{x}_p$ Details of computing particle trajectories and particle dispersion statistics are given by Elghobashi and Truesdell [2]

3. RESULTS

Here we compare the results of four cases (A,B,C and D) to examine the effects of the two-way interaction between the particles and turbulence Only in case A the particles do not affect the flow (one-way coupling) All the other three cases have the same volumetric loading ratio, $\Phi = 5 \times 10^{-4}$ The particle diameter is the same in all cases, $d = 100\mu$, and is smaller than the Kolmogorov length scale throughout the flow development in all the cases ($0.08 \le d/\eta \le 0.15$) Also the particle Reynolds number, R_p, is less than 0.3 throughout

We examine the effect of particle inertia in the absence of gravity, by increasing the initial particle response time, $\tau_{p,o}$, from 0.02 sec in case B to 0.10 sec in case C This is achieved by increasing the material density, ρ_p, from 570 kg/m^3 in B to 2850 kg/m^3 in C The fluid density, ρ_i is constant ($= 1\ kg/m^3$) Thus, the mass loading ratio in C (=1.425) is five times that in B (=0.285). Case D, with the same $\tau_{p,o}$ as in A, examines the effect of gravity on particle dispersion, hence on the turbulence This is accomplished by prescribing the ratio of the initial particle drift velocity $v_{t,o}$ to the initial rms velocity of the fluid u_o Table 1 below summarizes the conditions of the four cases presented here The last two columns contain the ratios τ_p/τ_K and τ_p/τ_f, where the value to the left of $\Rightarrow$ is at the time of particle injection and that to the right is at the end of the simulation The turnover time of the large eddies is $\tau_f = \ell/u_{rms}$, and the Kolmogorov time scale is $\tau_K = (\nu/\varepsilon)^{1/2}$ It is seen that $(\tau_p/\tau_f) < 1$ in all cases, whereas $\tau_p/\tau_K < 1$ for the light particle and > 1 for the heavier particle

Table 1. Conditions of the cases studied

Case	Coupl	$v_{t,o}/u_o$	$\tau_{p,o}$(s)	τ_p/τ_K	τ_p/τ_f
A	1-way	0.0	0.02	$0.7 \Rightarrow 0.2$	$0.09 \Rightarrow 0.02$
B	2-way	0.0	0.02	$0.7 \Rightarrow 0.2$	$0.09 \Rightarrow 0.02$
C	2-way	0.0	0.10	$3.6 \Rightarrow 1.1$	$0.43 \Rightarrow 0.08$
D	2-way	0.4	0.02	$0.7 \Rightarrow 0.5$	$0.09 \Rightarrow 0.04$

3.1 Turbulence modulation

3.1.1 Effects of inertia

Figure 1 shows the time development of the turbulence kinetic energy normalized by its initial value for cases A,B,C and D The particles are injected, at dimensionless time $T = 0.75$, with their velocity equal to that of their surrounding fluid In case A (one-way coupling) the particles do not influence the flow, and thus the dashed curve A follows the standard decay rate of grid turbulence Case B (two-way coupling) is for the light particles in zero gravity, and thus the main force of interaction between the particles and the fluid is the drag The figure shows that up to time $T = 2.0$ the particles in case B cause the turbulence energy to be slightly higher than that in case A After that time, the particles cause a slight reduction in energy relative to A Thus, the effect of the light particles on the turbulence energy is negligible

Now, case C, with larger τ_p and higher mass loading than B, shows a significant deviation from both A and B Because of the large τ_p, the particles in C experience the highest relative velocity fluctuations as seen in Fig 2 which displays the time development of $< v_{rel,1}^2 > = < (v_1 - u_1)^2 >$ for the four cases. Up to $T = 1$ the particles in C provide a source of energy to the decaying turbulence, as will be discussed later with the help of Fig 5-a This transfer of energy from the particles to the turbulence occurs at the small scale level since the particle diameter is less than the Kolmogorov length scale This is seen in Fig 3-a which shows the three dimensional spatial spectrum of fluid energy, $E(k)$, at $T = 2$. Case C has highest energy increase relative to A in the high wave number range This supply of energy to the turbulence at high wave numbers is in sharp contrast to what happens in particle-free turbulence where the energy is extracted from the mean flow at low wave numbers It is important to note the effect on the low wave number part of the spectrum due to the input of energy to the small scale. Fig 3-a shows a reduction of energy in C, relative to A, in the low wave number range This is explained with the help of Fig. 4 which displays the time development of the skewness of the fluid velocity derivative ,

$$S_u = -\frac{1}{3}\sum_{i=1}^{3}\left\langle (\partial u_i/\partial x_i)^3 \right\rangle \Big/ \left[\frac{1}{3}\sum_{i=1}^{3}\left\langle (\partial u_i/\partial x_i)^2 \right\rangle\right]^{3/2} . \quad (6)$$

S_u is a measure of the average rate of production of enstrophy by vortex stretching or the rate of nonlinear energy transfer from smaller to larger wave numbers The turbulence is considered fully developed at about $T = 0.6$ where $-S_u \approx 0.4$ The particles are injected at $T = 0.75$. In case A where the particles have no effect on the flow, the magnitude of S_u gradually increases to about 0.45 indicating no interruption to the energy cascading process. Case B with the lighter particles, the smallest $< v_{rel,1}^2 >$ (Fig. 2), and smallest energy increase at high wave numbers (Fig 3-a), shows the smallest decrease in the magnitude of S_u (Fig 4), but otherwise the development of S_u is similar to that in A.

Case C exhibits the largest rate of reduction in the magnitude of S_u, relative to A, $1 \le T \le 2$, indicating a decrease in the rate of transfer of energy from the large scale to small scale motion. The supply of energy from the particles to the high wave number turbulence acts as a "dam" which results simultaneously in *(i) increasing* the level of the total turbulence energy (Fig. 1), and *(ii)reducing*, the rate of nonlinear energy transfer or equivalently the rate of vortex stretching at the low wave numbers (Fig. 3a), hence the lower magnitude of S_u (Fig 4)

Now $(-S_u)$ is proportional to the production rate of the dissipation rate ϵ Yet the total dissipation rate ε shows a *peak* at $T = 2$ (Fig 6) coinciding with the *minimum* value of $(-S_u)$ This indicates that this increase in ε is a result of *direct particle/fluid interaction* at the small scale level and *not due to a nonlinear transfer of energy* from the low wave number motion This is evident in Fig 7 which displays the spatial spectrum of $\varepsilon(k)$ at $T = 2$ The figure shows that case C has the highest magnitude of ε at high wave numbers, and lowest at low wave numbers relative to all other cases This augmentation of ε due to the direct particle/fluid interaction will be discussed further below

However, for times $T \ge 2$, and due to large τ_p, the energy of turbulence in C experiences the highest rate of decay, relative to A. First, due to the transfer of energy from the particles to the fluid, the relative velocity fluctuation $(v_i - u_i)$ changes sign from positive to negative at $T \approx 1$ as seen in Fig 5a. This figure shows the time development of the correlation $< u_1(v_1 - u_1)/\tau_p >$ which represents the time rate of change of turbulence energy due to the particles. This is seen from the exact dimensionless transport equation of turbulence energy after spatial averaging in the periodic domain for homogenous turbulence,

$$dE/dt = \sum_i < \Phi u_i(v_i - u_i)/\tau_p > - \epsilon \quad (7)$$

$$= \Psi - \epsilon , \quad (8)$$

where

$$\Psi = \sum_i \Psi_i = \sum_i < \Phi u_i(v_i - u_i)/\tau_p > , \quad (9)$$

and ϵ is the rate of energy dissipation Figure 5-a shows that up to $T = 1$, Ψ_1 is positive, hence a reduction in the decay rate of E The magnitude of $E(t)$ itself after particle injection depends on the initial amount of energy transferred from the particles to the turbulence at injection and the subsequent rate of change dE/dt. Figure 5-a indicates that in case C, Ψ_1 becomes negative after $T = 1$, and its maximum magnitude occurs at $T = 2$ This results in the peak value of the *total* dissipation rate, $\varepsilon(t)$, at $T = 2$ as shown in Fig 6, and a subsequent decay of $\varepsilon(t)$, due to the reduction of the magnitude of Ψ_1. When Ψ_1 diminishes to nearly zero for $T \ge 5.5$, (dE/dt) in C approaches its value in B.

It is important here to comment on the significance of the physical meaning of the correlation Ψ Elghobashi and Abou-Arab [1] derived the exact equation of turbulence energy for a fluid laden with particles and classified the correlation Ψ as *" extra dissipation"*. It was believed that this quantity would most probably be always negative because either *(a)* the fluid and particle velocities have, on the average, the same sign, hence their correlation , $< u_i v_i >$, would be positive but its magnitude would be less than the fluid autocorrelation $< u_i u_i >$; or *(b)* the velocities have different signs, then the whole quantity is negative regardless of the relative magnitudes of the correlations. However, the present study indicates that it is possible that u_i and v_i have on the average the same sign and $< u_i v_i >$ is larger than $< u_i u_i >$. Here, the turbulence is decaying and a sufficient concentration of particles, with sufficient inertia is "dragging" the surrounding fluid along, resulting in a positive value of the correlation $< u_i(v_i - u_i) >$, hence a source of energy (see Fig 5-a, all cases for $T \le 1$ and case B for $T > 2.2$). Thus it is recommended here to reclassify the correlation Ψ as an *extra*

source/sink of energy due to particle/fluid interaction This recommendation is strongly supported by the results of the next section

3.1.2 Effects of gravity

Case D is identical to B except that the gravity in D is nonzero We see in Fig 1 that the energy decay rate in D is significantly reduced, relative to the other three cases throughout the computational time This can be explained via Fig 8 which displays the time development of the trace of the anisotropy tensor of the fluid turbulence, B_{ii}, defined as

$$B_{ii} = \frac{< u_i u_i >}{2E} - \frac{1}{3} \qquad (10)$$

The figure shows that the deviation from isotropy is greatest for case D, whereas it is negligible for the other cases In particular, the respective energy contributions of the three components $< u_1^2 >$, $< u_2^2 >$ & $< u_3^2 >$ in D are 26%, 28%&46% at $T = 4$ and 19%, 20%&61% at $T = 8$ In other words, the contribution of $< u_3^2 >$ to E is always larger than the other two components, and it increases monotonically with time Thus, the higher values of $E(t)$ in D relative to the other cases is due only to the increase of $< u_3^2 >$, the component in the gravity direction The effect of gravity on the particles is transmitted to the carrier fluid via Ψ_3 as indicated in Eq (7) and shown in Fig 5. It is seen that for $T \geq 1$, $\Psi_1 (\approx \Psi_2)$ is negative and small whereas Ψ_3 is a large positive Again, the effect of Ψ_i is felt first by the smallest scales as discussed earlier, and then is gradually transmitted to the larger scales as evident in Figs 3-a ($T = 2$) and 3-b ($T = 8$) At $T = 2$, there is an increase in $E(k)$ at high wave numbers, though less than in C. At $T = 8$, that increase propagated to the low wave numbers, i.e the effect of the *energy dam* is now felt by the large scales The reason that the energy dam in D caused, for $T > 4$, an increase in $E(k)$ at low k, whereas it caused a reduction in $E(k)$ in case C is that gravity is a permanent source of energy The effect of the high inertia (τ_p), on the other hand, in C depends on the sign of Ψ_i, a positive sign results in an energy source ($T \leq 1$) and a negative sign results in a sink of energy

It should be emphasized here that the energy increase at the low wave numbers in D is due to the *reverse cascading process* rather than an energy production at the large scales. This is evident in Fig 4 where case D has the smallest magnitude of $(-S_u)$ for $T \geq 4$. Figs. 6 and 7 also show the corresponding behavior of $\varepsilon(t)$ and $\varepsilon(k)$

3.2 Lagrangian statistics of dispersion

Due to space limitations we present only the diffusivities of the fluid points and solid particles in the x_1 and x_3 directions Figure 9 shows the time development of the fluid point diffusivity in the x_1 direction for cases A,B,C and D A fluid point is defined here as a fluid particle that coincided with a solid particle at the injection time of the latter. Note that the time coordinate starts from the injection time, and the reference time is 0 128 *sec* Thus, the simulation ends at 0 93 *sec* corresponding to a dimensionless time $T = 8$.
Curve A (one-way coupling) represents the turbulent diffusivity of a fluid in homogeneous isotropic turbulence, and agrees quite well with Taylor's theory [2]. It is seen that for short time dispersion, the two-way coupling increases the fluid diffusivity slightly above that of the particle-free flow. However, the long time diffusivity in B,C and D is less than that in A. This is expected since the rate of growth of the length scales in B,C and D is less than in A. The dissipation rate $\varepsilon(t)$ in B,C and D (Fig 6) is higher than in A, hence a reduction in the Kolmogorov length scale relative to A Furthermore, the increase of $E(t)$ in C and D relative to A is less than the corresponding increase of $\varepsilon(t)$, hence a reduction of the integral length scale, ℓ
The long time diffusivity of the solid particles in the x_1 direction (Fig 10), is also reduced in B and D relative to A However, in C due to the higher τ_p, the initial inertia of the particles accelerates the surrounding fluid (Fig 5-a), and thus the velocity autocorrelation of the particles is higher than that in a fluid that is not influenced by the particles This higher correlation results in higher displacement and larger diffusivity than in A Of course the velocity autocorrelation diminishes with time, and the particle diffusivity in C approaches that in A

Now, the significant role of gravity in augmenting the turbulent diffusivity the solid particles and simultaneously augmenting the diffusivity of the fluid points is seen in Fig 11 Cases B and C, with zero gravity, show the same asymptotic behavior as in Figs 9 and 10 (note the difference in scales of the ordinate) Case D, on the other hand, shows a monotonic increase of the diffusivity with time, and at the end of the simulation it is about two orders of magnitude higher than that in the lateral directions

4. CONCLUDING REMARKS

The interaction between small solid particles ($d/\eta < 1$), at a volumetric loading ratio $\Phi = 5 \times 10^{-4}$, and a decaying homogeneous turbulence is studied using direct numerical simulation The results show that the particles increase the fluid turbulence energy at high wave numbers. This increase acts as a barrier to the nonlinear energy transfer from the low wave number range Particles with higher τ_p (case C) result in an initial *net increase* of the turbulence energy relative to that of smaller τ_p particles (case B), but a net reduction at longer times Associated with the energy increase at higher wave numbers, there is a larger increase in the dissipation rate of energy The net result is a reduction in all the turbulence length scales, hence lower turbulent diffusivity of the carrier fluid turbulence due to the two-way coupling.
Gravity results in a significant turbulence anisotropy and an increase in the diffusivity of the particles and fluid, in the gravity direction, by two orders of magnitude relative to the zero gravity cases
The correlation $\Psi = \sum_i \Psi_i = \sum_i < \Phi u_i(v_i - u_i)/\tau_p >$ can be *positive or negative* and thus can be considered a *source or sink* of fluid turbulence energy (Eq (7)).

References

[1] S E Elghobashi and T W Abou Arab A two-equation turbulence model for two-phase flows *Phys Fluids*, 26 931, 1983

[2] S.E Elghobashi and G.C. Truesdell. Direct simulation of particle dispersion in decaying isotropic turbulence. *J Fluid Mech* , to appear, 1991

[3] D Fleckhaus, K. Hishida, and M Maeda Effect of laden solid particles on the turbulent flow structure of a round free jet. *Experiments in Fluids*, 5.323-333, 1987.

[4] T. Gerz, U Schumann, and S Elghobashi Direct simulation of stably stratified homogeneous turbulent shear flows *J. Fluid Mech.*, 200·563-594, 1989.

[5] R A Gore and C T Crowe Effect of particle size on modulating turbulent intensity *Int J Multiphase Flow*, 15 279-285, 1989

[6] Y Hardalupas, A M K P Taylor, and J H. Whitelaw Velocity and particle-flux characteristics of turbulent particle-laden jets *Proc R Soc Lond*, A 426 31-78, 1989

[7] G Hetsroni. Particle- turbulence interaction *Int J Multiphase Flow*, 15·735-746, 1989

[8] G. Hetsroni and M Sokolov. Distribution of mass,velocity and intensity of turbulence in a two-phase jet *J Applied Mech*, 38 315-327, 1971

[9] Y Levy and F C Lockwood Velocity measurements in a particle-laden turbulent free jet *Combustion and Flame*, 40 333-339, 1981

[10] D Modarress, H Tan, and S. Elghobashi Two-component lda measurement in a two-phase turbulent jet *AIAA J*, 22 624-630, 1984

[11] J Popper, N Abuaf, and G Hetsroni Velocity measurements in a two-phase turbulent jet *Int J Multiphase Flow*, 1 715-726, 1974.

[12] K D Squires and J K Eaton. Particle response and turbulence modification in isotropic turbulence *Phys Fluids*, A 2:1191-1203, 1990

[13] Y Tsuji, Y Morikawa, T Tanaka, K Karimine, and S Nishida Measurements of an axisymmetric jet laden with coarse particles *Int. J Multiphase Flow*, 14 565-574, 1988

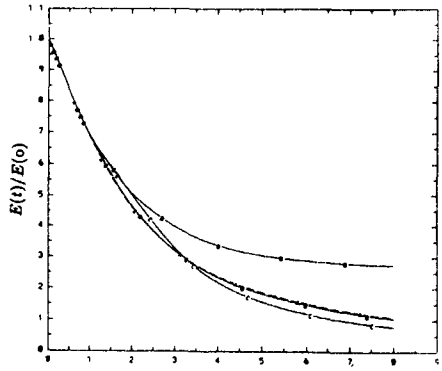

Fig 1 Time development of turbulence energy

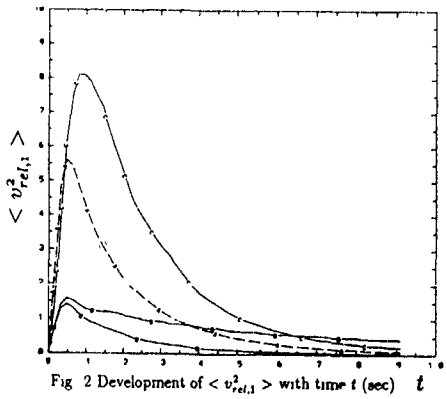

Fig 2 Development of $< v_{rel,1}^2 >$ with time t (sec)

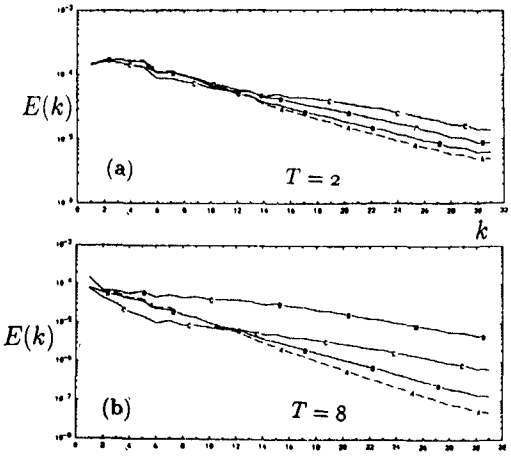

Fig 3 Spatial spectrum of energy

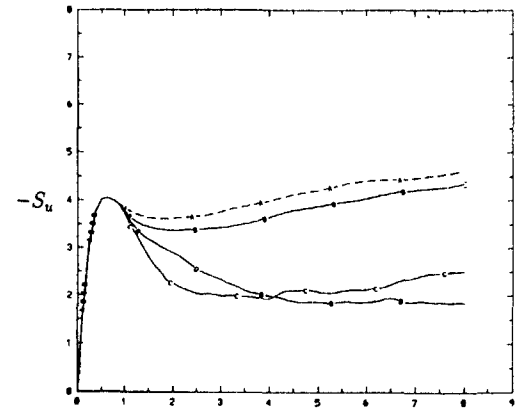

Fig 4 Time development of skewness of velocity derivative

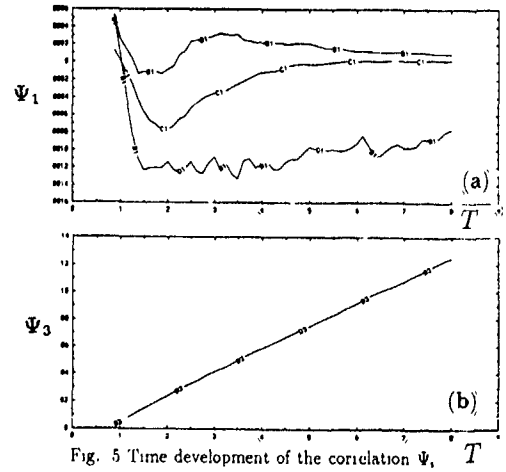

Fig. 5 Time development of the correlation Ψ_i

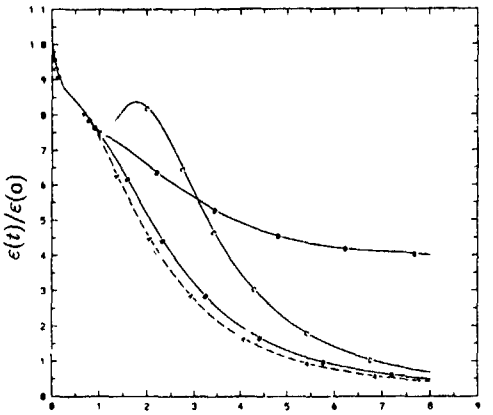

Fig 6 Time development of dissipation rate.

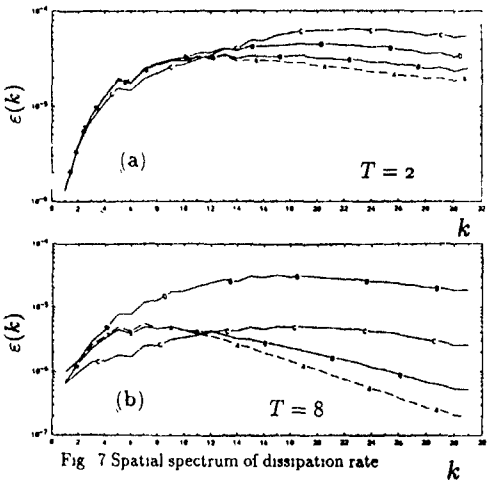

Fig 7 Spatial spectrum of dissipation rate

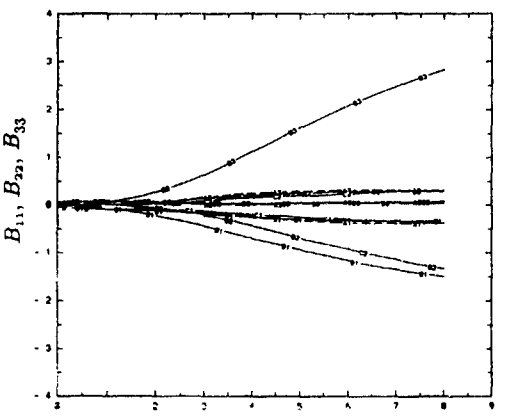

Fig 8 Time development of components of energy anisotropy tensor

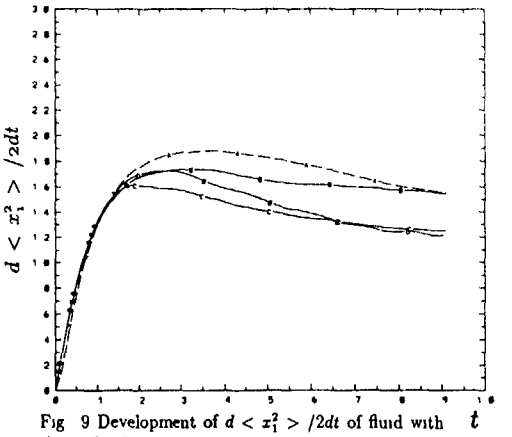

Fig 9 Development of $d < x_1^2 > /2dt$ of fluid with time t (sec)

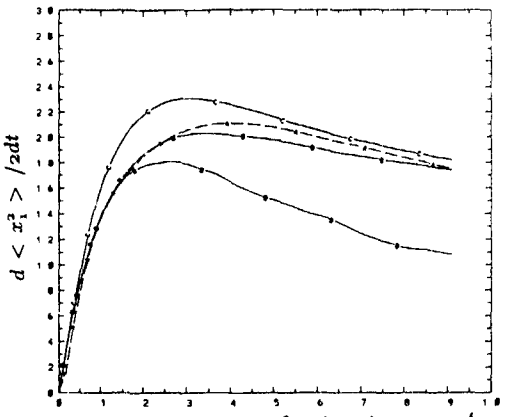

Fig 10 Development of $d < x_1^2 > /2dt$ of particles with time t (sec)

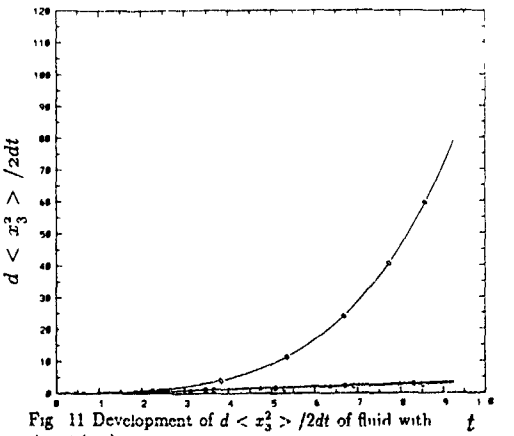

Fig 11 Development of $d < x_3^2 > /2dt$ of fluid with time t (sec)

EIGHTH SYMPOSIUM ON
TURBULENT SHEAR FLOWS
Technical University of Munich
September 9-11, 1991

SECOND-MOMENT PREDICTION OF DISPERSED PHASE TURBULENCE IN PARTICLE-LADEN FLOWS

O Simonin

Laboratoire National d'Hydraulique - EDF
6 Quai Watier, 78400 Chatou, FRANCE

ABSTRACT

A new approach for the modelling of the statistical characteristics of heavy particle clouds in turbulent two-phase flows is proposed, taking into account of the dragging by the fluid turbulence and the interparticle collisions. This model is based on separate transport equations for the dispersed phase Reynolds stress tensor components and the fluid particle velocity correlation The proposed closure assumptions allow to compute dispersed dilute two-phase flows and lead to classical results derived by applying kinetic theory when interparticle collision is the dominating phenomenon

The model is used to predict axisymetric dilute particle-laden jets and a confined swirling gas-particle flow The numerical results compare favourably to available experimental results The model accounts for, among other phenomena, the influence of the radial r m s velocity measured at the nozzle exit on particle dispersion and the high anisotropy of the particle fluctuating motion observed in the main flow

INTRODUCTION

Turbulent dispersed flow is a particular class of two-phase flows, observed in many industrial devices and characterized by the presence of a continuous fluid phase mixed with solid particles, liquid droplets or gas bubbles By assumption, the representative length and time scales of the dispersion (inclusion size, interparticle distance, particle relaxation time) remain small with respect to the ones of the whole flow

The two-fluid Eulerian approach adopted here leads to solve separate mean balance equations for each phase coupled by interfacial transfer terms For dilute particle concentrations, the closure assumptions required for the turbulent correlations and transport coefficients are based on the Lagrangian analysis of the separate particle behaviour (see for example, Elgobashi and Abou-Arab, 1983) Thus, the particle statistical characteristics are assumed to be mainly controlled by the interaction with the fluid turbulence On the other hand, the set of equations obtained from the Eulerian approach may be used for the prediction of gas-solid flows with dense particle concentrations (Lun et al , 1984) But, in this case, the particle random motion is mainly controlled by the interparticle collisions and practical closure assumptions are derived from the kinetic theory.

AVERAGE FIELD EQUATIONS

In the two-fluid model formulation, the field equations for each phase can be derived directly from the local instant conservation equations in single-phase flow by density-weighted averaging with in addition average balances of mass, momentum and energy at the interfaces The average field equations used in this paper are achieved by restricting our attention to isothermal mixtures, where no phase change occurs, and according to the main assumptions that :

- the granular stress due to interparticle collision and the molecular viscous stress in the gaseous phase are negligible compare to the kinetic part of the total stress tensor, the so-called Reynolds stress tensor ;
- the dispersion effect due to the correlation between the gas pressure fluctuations and the instantaneous distribution of particles is negligible compare to the one induced by the fluctuations of the drag force

Mass balance :

$$\frac{\partial}{\partial t}\alpha_k\rho_k + \frac{\partial}{\partial x_i}\alpha_k\rho_k U_{k,i} = 0 \qquad (1)$$

$U_{k,i}$ is the mean velocity i-component for the continuous (k=1) and dispersed phases (k=2) respectively,

α_k is the volumetric fraction and ρ_k the mean density

Momentum balance :

$$\alpha_k\rho_k\frac{\partial}{\partial t}U_{k,i} + \alpha_k\rho_k U_{k,j}\frac{\partial}{\partial x_j}U_{k,i} = -\alpha_k\frac{\partial}{\partial x_i}P_1 + \alpha_k\rho_k g_i - \frac{\partial}{\partial x_j}\alpha_k<\rho u''_i u''_j>_k + I_{k,i} \qquad (2)$$

u''_i is the fluctuation of the local instantaneous velocity and $<\ .\ >_k$ the averaging operator associated to phase k,

$$\alpha_k\rho_k U_{k,i} = \alpha_k<\rho u_i>_k \qquad <\rho u''_i>_k = 0$$

P_1 is the mean pressure of the continuous phase,

$I_{k,i}$ is the part of the interfacial momentum transfer rate between phases which remains after substraction of the mean pressure contributions.

Finally, the closure of the average field equations is achieved using constitutive relations for the interfacial transfer term $I_{k,i}$ and the second-moment correlations of the Reynolds stress tensor $<\rho u''_i u''_j>_k$

THE INTERFACIAL MOMENTUM TRANSFER

In dispersed two-phase flow, the mean spacing between particles is generally assumed to be very small with respect to the variation scale in the mean flow, and the averaging method associated to the dispersed phase can be written at any point as an ensemble average taken over the large number of particles included in a reference time-space domain centred on the point. Thus, if particles are assumed to interact only slightly, the momentum interfacial transfer term $I_{k,i}$ can be obtained, by averaging, from the analysis of the balance of forces acting on an isolated particle in a turbulent flow A special care is required during averaging process in order to take into account the dispersion effect due to the local fluctuations of the momentum transfer term

For heavy particles the momentum interfacial transfert term reduces to the drag force contribution,

$$I_{1,i} = -I_{2,i} = \alpha_2<\rho_1\frac{3}{4}\frac{C_D}{d}|\vec{v}_r|v_{r,i}>_2 \qquad \rho_2 >> \rho_1 \qquad (3)$$

where C_D, the local drag coefficient, may be written :

$$C_D = \frac{24}{Re}\left[1 + 0.15\,Re^{0.687}\right] \qquad Re \le 1000 \qquad Re = \frac{\rho_1|\vec{v}_r|d}{\mu_1}$$

$v_{r,i} = \tilde{u}_{2,i} - \tilde{u}_{1,i}$ is the local instantaneous relative velocity defined on each point included in the particulate phase,

$\tilde{u}_{2,i}$ is the translation velocity of the particle, with diameter d, which contains the point,

$\tilde{u}_{1,i}$ is the characteristic velocity of the surrounding

flow field, defined as the instantaneous fluid flow locally undisturbed by the presence of the particle

The fluid flow field, locally undisturbed by the particles presence, remains turbulent and, assuming that the spatial average of the disturbances (wakes) due to the presence of the particles is negligible, we have

$$\tilde{u}_{1,i} = U_{1,i} + u''_{1,i} \qquad \rho_1 U_{1,i} = <\rho \tilde{u}_{1,i}>_1 \qquad <\rho u''_{1,i}>_1 = 0$$

Neglecting the influence of the drag coefficient fluctuations along the particle trajectory, we finally obtain by averaging

$$I_{1,i} = -I_{2,i} = \alpha_2 \rho_1 F_D V_{r,i} \qquad F_D = \frac{3}{4}\frac{C_D}{d} <|\vec{V}_r|> \qquad (4)$$

$V_{r,i}$, the averaged value of the local relative velocity between each particle and the surrounding fluid, can be expressed in function of the total difference between the mean velocities $\Delta U_i = U_{2,i} - U_{1,i}$ and a drifting velocity $V_{d,i}$ due to the correlation between the instantaneous distribution of particles and the velocity fluctuations of the undisturbed fluid flow

$$V_{r,i} = \left[U_{2,i} - U_{1,i}\right] - V_{d,i} \qquad V_{d,i} = <\tilde{u}_{1,i}>_2 - U_{1,i} = <u''_{1,i}>_2$$

The drifting velocity $V_{d,i}$ takes into account the dispersion effect due to the transport of particles by turbulent fluid motion. According to the limit case of particles with diameter tending towards zero, for which the drifting velocity reduces to the single turbulent correlation between the volumetric fraction of the dispersed phase and the velocity fluctuation of the continuous phase, the velocity $V_{d,i}$ is written as follows

$$V_{d,i} = -D^t_{12,ij}\left[\frac{1}{\alpha_2}\frac{\partial \alpha_2}{\partial x_j} - \frac{1}{\alpha_1}\frac{\partial \alpha_1}{\partial x_j}\right] \qquad (5)$$

Based on theoretical analysis of particle dispersion mechanism in homogeneous turbulence (Deutsch and Simonin, 1991), the binary turbulent diffusion tensor is written in terms of the fluid-particle velocity correlation tensor and an eddy-particle interaction time

$$D^t_{12,ij} = \tau^t_{12} <u''_{1,i}u''_{2,j}>_2 \qquad (6)$$

THE FLUID TURBULENCE

Closure assumptions

Closure assumptions are achieved considering only the turbulent fluid motion at large scales with respect to the mean particle diameter.

$$<\rho u''_i u''_j>_1 \equiv <\rho u''_{1,i}u''_{1,j}>_1$$

Thus, the fluid turbulent predictions are carried out with a standard q^2-ε model supplemented with additional terms taking into account the interfacial turbulent momentum transfer (Simonin and Viollet, 1990a)

The fluid correlations are computed with the help of the eddy viscosity concept

$$<\rho u''_i u''_j>_1 = -\rho_1 \nu^t_1\left[\frac{\partial U_{1,i}}{\partial x_j} + \frac{\partial U_{1,j}}{\partial x_i}\right] + \frac{2}{3}\delta_{ij}\left[\rho_1 q_1^2 + \rho_1 \nu^t_1 \frac{\partial U_{1,m}}{\partial x_m}\right] \qquad (7)$$

$$\nu^t_1 = \frac{2}{3} q_1^2 \tau^t_1 \qquad \rho_1 q_1^2 = \frac{1}{2} <\rho u''_i u''_i>_1 \qquad (8)$$

τ_1^t, the time scale of the energetic turbulent eddies or turbulent dissipation time, is obtained directly from the turbulent kinetic energy q_1^2 and its dissipation rate ε_1

$$\tau^t_1 = \frac{3}{2} C_\mu \frac{q_1^2}{\varepsilon_1} \qquad (9)$$

Particle source terms

The particle fluctuating motion is assumed to influence the fluid turbulence through the following source terms for q_1^2 and ε_1, respectively

$$\Pi_{q_1} = \alpha_2 \rho_1 F_D\left[<u''_{1,i}v''_{r,i}>_2 + V_{d,i}V_{r,i}\right] \qquad (10)$$

$$\Pi_{\varepsilon_1} = C_{\varepsilon 3}\left[\varepsilon_1 / q_1^2\right]\Pi_{q_1} \qquad (11)$$

The first equality (10) can be derived directly from the instantaneous fluid momentum equations. While, the second (11) is modelled according to Elgobashi and Abou-Arab (1983), in terms of the fluid turbulent time scale

If we assume no statistical bias due to the correlation between the particle distribution and the local instantaneous fluid turbulent kinetic energy, we obtain

$$<u''_{1,i}v''_{r,i}>_2 = q_{12} - 2q_1^2 \qquad (12)$$

this late equality (12) clearly implies that the particle presence leads to destruction or production of the fluid turbulence according to the local value of the fluid-particle velocity covariance $q_{12} = <u_{1,i}u''_{2,i}>_2$ with regard to the fluid turbulent kinetic energy

Table 1 Coefficients of the turbulence model

C_μ	$C_{\varepsilon 2}$	$C_{\varepsilon 1}$	σ_q	σ_ε	$C_{\varepsilon 3}$
0.09 (*)	1.92 (*)	1.44	1	1.3	1.2

(*) Turbulence round jet model, see Rodi W. (1972)

THE PARTICULATE FLUCTUATING MOTION

Characteristic times

It is convenient to define several time scales in order to characterize the particulate flow

τ^F_{12}, the characteristic time of particle entrainment by the fluid motion or particle relaxation time, relates to inertial effects acting on the particles

$$\tau^F_{12} = F_D^{-1}\frac{\rho_2}{\rho_1} \qquad (13)$$

τ^t_{12}, the time scale of the fluid turbulent motion viewed by the particles or eddy-particle interaction time, is mainly affected by the mean relative movement of the particles (crossing-trajectories effects) and, following Csanady (1963), can be written

$$\tau^t_{12,\ell} = \tau^t_1\left[1 + C_\beta \xi_r^2\right]^{-\frac{1}{2}} \qquad \xi_r = \left|\vec{V}_r\right| / \sqrt{\frac{2}{3}q_1^2} \qquad (14)$$

in the ℓ direction parallel to the mean relative velocity,

$$\tau^t_{12,j} = \tau^t_1\left[1 + 4C_\beta \xi_r^2\right]^{-\frac{1}{2}} \qquad j \neq \ell \qquad (15)$$

in the orthogonal directions. Comparisons with results of experiments and numerical predictions using Large Eddy Simulation lead to a practical value of $C_\beta = 0.45$

τ^c_2, the inter-particle collision time, can be written in the frame of the kinetic theory as

$$\tau^c_2 = \left[n_2 Q_2 g_2\right]^{-1} \qquad (16)$$

$n_2 = \alpha_2 6/\pi d^3$ is the particle number density,

$Q_2 = \pi d^2$ is the collisional section rate,

$g_2 = \sqrt{\frac{16}{\pi}\frac{2}{3}q_2^2}$ is the particle-particle relative velocity

We must notice that the previous expression given for the particle-particle relative velocity is not fully accurate in turbulent flows due to the spatial extension of the Eulerian velocity correlation function and leads to over-estimate the interparticle collision time but only when the particles are inclined to follow the fluid fluctuating motion ($\tau^F_{12} < \tau^t_{12}$)

Dispersed dilute two-phase flows

The concentration of particles in turbulent two-phase flows is said dilute if the interparticle collision influence is negligible and so the dominant process in the particle random motion is the dragging along by the fluid turbulence (τ^t_{12} and $\tau^F_{12} < \tau^c_2$)

In such flows, the turbulent prediction in the dispersed phase may be achieved by extension of results on dispersion of discrete particles by homogeneous and steady turbulent fluid motions in the framework of Tchen's theory (Deutsch and Simonin, 1991). Transport coefficients and velocity correlations are given in terms of the mean characteristics of the continuous turbulent motion with the help of the particle relaxation time and eddy-particle interaction time ratio.

However, this approach, which assumes local shaking

of particles by the fluid turbulence and neglects the production induces by the mean particle velocity gradient and the memory of injection conditions, leads in particular to underpredict the dispersed phase turbulent kinetic energy and the particle dispersion in particle-laden turbulent jets (Simonin and Viollet, 1990a). Improvements may be achieved using transport equations for the particle statistical characteristics. But a separate treatment of the particle Reynolds tensor components is required, owing the fact that the anisotropy of the dispersed phase turbulence plays a dominant part in the particle dispersion mechanism

Particle collision influence

The extension of gas-particle flow modelling to dense situations prescribes to take into account the particle collision influence. However, as we restrict our attention to particle clouds not too dense ($\alpha_2 < 0.1$), the exchange of momentum due to particle collision is negligible (Lun et al., 1984) and the random motion of particles still provides the principal mechanism for the macroscopic transport of quantities such as momentum and energy

Therefore, contribution to stresses can be derived in the frame of kinetic theory of gases Grad (1949), by assuming a special form for the particle distribution function expanded in Hermite polynomials, has obtained explicit forms of the collision terms appearing in transport equations, up to the triple particle velocity correlation Thus, following Grad's approach, the interparticle collision influence for mono-sized elastic hard spheres reduces to a return-to-isotropy contribution in the particulate stress equations

Finally, the equation set governing particle fluctuating motion includes transport equations for the kinetic stress components of the dispersed phase and for the covariance between the velocity fluctuations of the two phases

Particulate stress equations

$$\alpha_2\rho_2\left[\frac{\partial}{\partial t} + U_{2m}\frac{\partial}{\partial x_m}\right]<u''_{2i}u''_{2j}> = -\frac{\partial}{\partial x_m}\alpha_2\rho_2<u''_{2i}u''_{2j}u''_{2m}> - \alpha_2\rho_2\left[<u''_{2i}u''_{2m}>\frac{\partial U_{2j}}{\partial x_m} + <u''_{2j}u''_{2m}>\frac{\partial U_{2i}}{\partial x_m}\right] - \alpha_2\rho_2\frac{\sigma_c}{\tau_2^t}\left[<u''_{2i}u''_{2j}> - \frac{2}{3}q_2^2\delta_{ij}\right] - \alpha_2\rho_2\frac{2}{\tau_{12}^F}\left[<u''_{2i}u''_{2j}> - R_{12ij}\right]$$

- the first term on the right-hand side of the equation represents the transport of the stress by the velocity fluctuations, and is diffusive in character ;
- the second term represents the production by the mean particle velocity gradient ;
- the third term, which takes account of the interparticle collision ($\sigma_c = 4/5$), leads to destruction of the off-diagonal correlations and redistribution of energy among the various normal stresses ;
- the late term represents the interaction with fluid turbulent motion and leads to creation or destruction of the particle velocity correlations according to the fluid-particle symmetrical correlation tensor R_{12ij} :

$$R_{12ij} = \frac{1}{2}\left[<u''_{1i}u''_{2j}> + <u''_{2i}u''_{1j}>\right]$$

Diffusive transport modelling

The triple velocity correlation contribution is approximated with a gradient diffusion model in terms of a diffusivity tensor obtained from the third-moment equations, by neglecting convective transport and mean gradient effects :

$$K^t_{2mn} = \left[\frac{\tau_{12}^t}{\xi_{12}^t}R_{12mn} + \frac{\tau_{12}^F}{\xi_{12}^F}<u''_{2m}u''_{2n}>\right]\left[1 + \frac{\tau_{12}^F}{\xi_{12}^F}\frac{\xi_2^c}{\tau_2^c}\right]^{-1} \quad (17)$$

Coefficients are given either by the kinetic theory of gases or by standard fluid turbulence second-moment closure (Launder et al., 1975)

$$\xi_{12}^F = \frac{9}{5} \qquad \xi_2^c = \frac{8}{25} \qquad \xi_{12}^t = \frac{3}{2}\frac{C_\mu}{C_s} \qquad C_s = 0.25$$

Fluid-particle covariance equation

The fluid-particle correlation field between fluctuating velocities must be approximated and, unfortunately, there are no direct measurements of the correlations to serve as a guide Nevertheless, closure assumptions must be consistent with the modelling of fluid turbulence when the particle relaxation time is tending towards zero with regards to the eddy-particle interaction time. Thus, in our approach, covariance tensor components are computed with the help of the eddy viscosity concept :

$$<\rho u''_{1i}u''_{2j}>_2 = -\rho_2\nu_{12}^t\left[\frac{\partial U_{1i}}{\partial x_j} + \frac{\partial U_{2j}}{\partial x_i}\right] + \frac{1}{3}\delta_{ij}\left[\rho_2 q_{12} + \rho_2\nu_{12}^t\left[\frac{\partial U_{1m}}{\partial x_m} + \frac{\partial U_{2m}}{\partial x_m}\right]\right] \quad (18)$$

$$\nu_{12}^t = \frac{1}{3}q_{12}\tau_{12}^t \qquad q_{12} = <u''_{1i}u''_{2i}>_2 \quad (19)$$

The fluid-particle covariance equation is written in an approximate form which privileges the particulate transport

$$\alpha_2\rho_2\frac{\partial q_{12}}{\partial t} + \alpha_2\rho_2 U_{2j}\frac{\partial q_{12}}{\partial x_j} = \frac{\partial}{\partial x_j}\alpha_2\rho_2\frac{\nu_{12}^t}{\sigma_q}\frac{\partial q_{12}}{\partial x_j} - \alpha_2\rho_2\varepsilon_{12} + \Pi_{q_{12}} - \alpha_2<\rho u''_{1i}u''_{2j}>_2\frac{\partial U_{2i}}{\partial x_j} - \alpha_2<\rho u''_{2i}u''_{1j}>_2\frac{\partial U_{1i}}{\partial x_j}$$

- the first term on the right-hand side of the equation represents the turbulent transport of the covariance ;
- the second takes into account the destruction rate due to viscous action in fluid and is modelled in terms of the eddy-particle interaction time,

$$\varepsilon_{12} = q_{12}/\tau_{12}^t \quad (20)$$

- the third one represents the interaction between the fluctuating motions,

$$\Pi_{q_{12}} = \alpha_2\rho_1 F_D<u''_{2i}v''_{1i}>_2 - \frac{\alpha_2\rho_2}{\alpha_1\rho_1}\Pi_{q_1} \quad (21)$$

- the last two terms represent the production by the mean velocity gradients

We must notice that the eddy viscosity formalism leads to neglect anisotropy of the fluid-particle correlation field induced by crossing trajectories effects through the eddy-particle interaction time expressions (14) - (15)

Local shaking by fluid turbulence

For the simplest case, that of dilute dispersion of heavy particles suspended in an homogeneous, isotropic and steady turbulent fluid flow, the equation set governing particle and fluid-particle velocity correlations leads to the following expressions :

$$q_2^2 = q_1^2\left[\frac{\eta_r}{1+\eta_r}\right] \qquad \eta_r = \tau_{12}^t/\tau_{12}^F \quad (22)$$

$$q_{12} = 2q_1^2\left[\frac{\eta_r}{1+\eta_r}\right] \quad (23)$$

which are consistent with the analytical expressions obtained in the frame of the Tchen's theory (Deutsch and Simonin, 1991), using exponential form for the fluid turbulence Lagrangian function viewed by the particles

In homogeneous shear flows, the particulate viscosity may be obtained from the second-moment equations, providing that the difference between the fluid and particle mean velocity gradients is negligible

$$\nu_2^t = \nu_{12}^t + \frac{1}{2}\tau_{12}^F\frac{2}{3}q_2^2 \quad (24)$$

we can notice that the particulate Schmidt, $Sc_2 = \nu_2^t / D_2^t$, is about 1/2 for "large" heavy particles ($\eta_r << 1$)

These closure assumptions have been used with some success for the prediction of dilute particle-laden turbulent jets (Simonin and Viollet, 1990a)

RESULTS AND DISCUSSION

Numerical method

A two-dimensional numerical code, named Mélodif, has been developed for several years at the "Laboratoire

National d'Hydraulique" for predicting fluid-inclusions (inclusions standing either for bubbles, drops or particles) turbulent recirculating two-phase flows This numerical code is based on finite discretization and an incremental version of the original fractional step method (Simonin and Viollet, 1990b)

The practical extension to kinetic stress transport modelling was achieved by a standard treatment of additional equations But, in order to enable economical second order discretization and to avoid numerical oscillations, particulate stress components are computed on the pressure half-staggered subgrid

Particle-laden turbulent jets (test cases 1 and 2)

Figures 1 to 8 show comparisons of numerical predictions with velocity measurements in axisymetric particle-laden turbulent round jets (Modarress et al, 1984) The flow set-up consists in a 20mm diameter vertical pipe discharging air and particles in a low velocity coflowing flow particle diameter $d=50\mu m$, density ratio $\rho_2/\rho_1=2550$, mass loading ratio $\phi_0=0.32$ and 0.85 for test cases 1 and 2 respectively Measured flow conditions at the pipe exit were completed by presumed values for the rms velocity in the radial direction given in terms of the axial ones ($v''_2 = 0.7\,u''_2$)

The computations were performed by using the particulate stress transport model, the analytical expressions obtained in the frame of the Tchen's theory (22) to (24), as well as a consistent particle kinetic energy transport model based on the eddy-viscosity assumption There is no adjustment of the parameters used in the equation set, coefficients are given either by the kinetic theory of gases (Grad, 1949) or by standard fluid turbulence moment closure (Launder et al, 1975) Finally, as the interaction with the fluid turbulence has a prominent influence on the radial particle fluctuating motion, the eddy-particle interaction time is computed using the orthogonal expression (15) with respect to the mean relative velocity direction

The numerical predictions with the kinetic stress transport model are in a very good agreement with the experimental data for the gas and particle mean axial velocity distributions (figures 1 and 2) at downstream location x/D1=20 (velocity profiles are normalized by the corresponding single phase centerline value $U_{0,c}$). Fluid turbulent quantities such as kinetic energy (figures 3 and 4) and Reynolds shear stress (figure 7) are correctly reduced from their one-phase jet levels by the presence of the particles (turbulent quantities are normalized by the square of the predicted gas centerline velocity $U_{1,c}$) Concurrently, the kinetic stress transport model accounts for the high anisotropy of the particle fluctuating motion as observed in the available experimental data (figures 5 and 6) As might be expected, the anisotropy stands higher for the particle kinetic stress tensor than for the fluid one, because the redistribution among the various components by interparticle collision is quite ineffective (due to the low particle concentration) in comparison with the one induced by the pressure-strain correlation

The surprising thing is that the closure assumptions assuming a local shaking of particles by the gas turbulence lead to limited discrepencies for the gas and particle mean axial velocity distributions and for the fluid turbulent characteristics, even when the model leads to underpredict the kinetic energy of the particulate fluctuating motion (figures 3 and 4). As a matter of fact, detailed analysis of the numerical results show that the discrepancy is due essentially to the underprediction of the axial velocity fluctuations (figures 5 and 6) mainly controlled by the mean particle velocity gradient production but which are ineffective in these particular flow configuration Whereas, the particle radial velocity fluctuations, which play the dominant part in the particle dispersion mechanism, are controlled by the momentum transfer from the gas phase turbulence and are predicted with a reasonable accuracy in the frame of Tchen's theory.

This result must be related to the predictions of the fluid-particle velocity correlation tensor by using local particle shaking assumption (23), which are almost equal to the predictions using a separate transport equation. So, algebraic stress model, accounting for the anisotropy of the fluid turbulence viewed by the particles (partially due to the crossing-trajectories effects) would be usefully used in place of the eddy-viscosity assumption (18) and the covariance transport equation, which are the more questionable approximations of the model

Figures 1 to 8 show some large discrepencies in the predictions by using the kinetic energy transport model, due to the particle dispersion overvaluation. As a matter of fact, in the two-fluid formalism, the dominant contribution to heavy particle dispersion in turbulent jets is issuing from the kinetic stress contribution in the momentum equation, as proportional to the mean square of the radial velocity fluctuations And, the kinetic energy transport model, which accounts for the production by the particle velocity gradient leaning on the eddy-viscosity assumption, leads to overpredict the radial velocity fluctuations (figures 5 and 6) in spite of a good level for the turbulent kinetic energy (figures 3 and 4). On the other hand, the local shaking assumption which does not account for the initial conditions on the velocity fluctuations leads to underpredict the effective dispersion close to the injection zone This analysis is confirmed by the comparisons between predicted and measured particle mass flux distributions (figures 8). As the initial conditions on the radial velocity fluctuations are probably not the exact experimental ones, further comparisons have to be made with measurements including a more complete description of the injection conditions

Gas-particle swirling flow (test case 3)

In order to test the proposed closure assumptions and the numerical method in a complex flow configuration, computations were performed for a coaxial swirling confined flow with a central nonswirling particle-laden jet The predictions, with the particulate stress transport model, were compared with experimental data obtained by using a phase-Doppler system, which allows the simultaneous measurement of particle size and velocity (Sommerfeld and Qiu, 1991) The test section consist of a 1.5m long tube with an inner diameter of 194mm, and measurements have been performed at several cross sections in the test section, including the inlet, for a swirl number of 0.47, by using glass beads with a mean diameter of 45μm distributed between 20 and 80μm Figures 9 to 14 show some numerical results for three characteristic particle diameters d=30, 45 and 60μm, and the predictions are compared with the corresponding experimental data at location x=155mm downstream the injection, across the central recirculating region

Unfortunately, the fluid flow prediction is not accurate enough to allow quantitative analysis of the particulate results As a matter of fact, the rate with wich the vortex loses its energy is overestimated by using q^2-ε model and the fluid prediction suffered from substancial deficiency in the tangential momentum (figure 13) and the maximum reverse flow velocity (figure 9). We can notice that, due to the low particle concentration level, the particle influence on gas turbulence is quite negligible for this configuration

However, the particle velocity prediction accounts for typical phenomenon according to the experimental observation Thus, the particles have much higher mean axial velocity than the air flow in the core of the test section (figure 9) and so penetrate the central reverse flow region. Due to their higher inertia, the larger particles have the higher velocity and some of the largest are able to cross the recirculating region. The radial and tangential turbulent velocity fluctuations of the particles are lower than the fluid fluctuations, and the smallest particles exhibit the highest fluctuations (figures 12 and 14) On the other hand, the axial velocity fluctuations of the largest particles may become higher than the fluid ones (figure 10) Thus, the measured velocity fluctuations of the particles are not only a result of the inlet conditions and the interaction with the fluid turbulence alone, but also exhibit the mean gradient velocity production

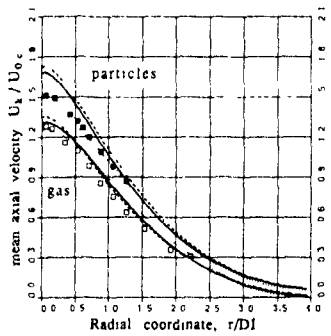

Fig 1 Mean axial velocity profiles (case 1)

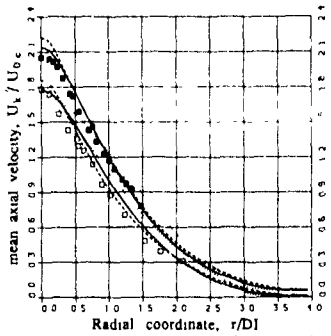

Fig 2 Mean axial velocity profiles (case 2)

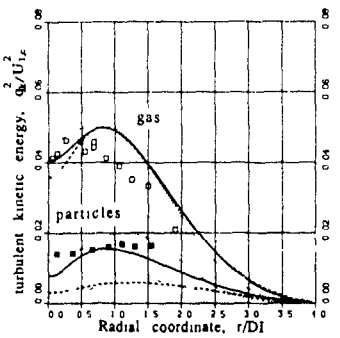

Fig 3 Turbulent kinetic energy profiles (case 1)

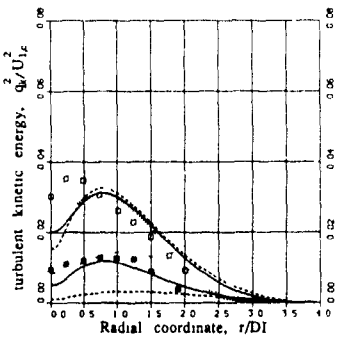

Fig 4 . Turbulent kinetic energy profiles (case 2)

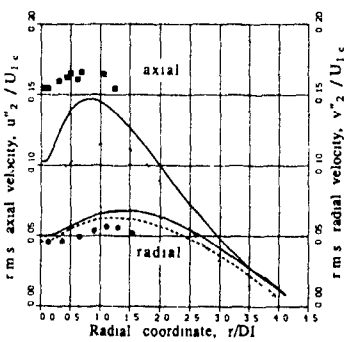

Fig 5 Particle r.m.s velocity profiles (case 1)

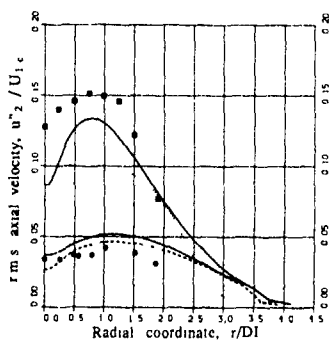

Fig 6 Particle r m s velocity profiles (case 2)

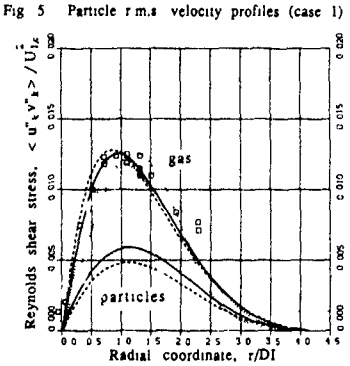

Fig 7 Reynolds shear stress profiles (case 1)

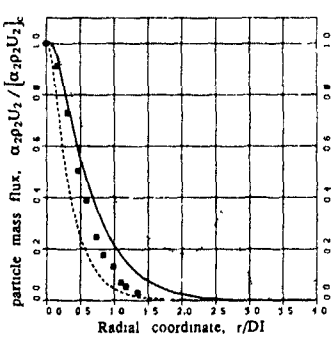

Fig 8 Mean axial particle mass flux (case 2)

Figures 1 – 8 Comparison between numerical predictions and experimental results at x/DI = 20,
—— particulate stress transport model, ---- local particle shaking by fluid turbulence,
particle kinetic energy transport model ; o , • and • experimental results (Modarress et al, 1984)

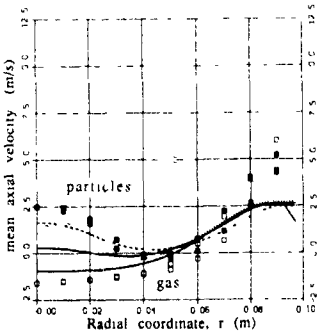

Fig 9 Mean axial velocity profiles (case 3)

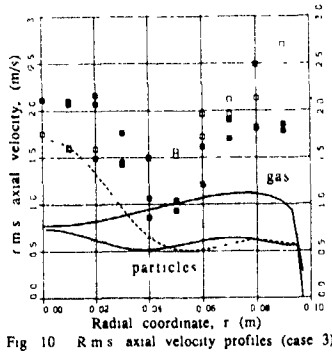

Fig 10 R m s axial velocity profiles (case 3)

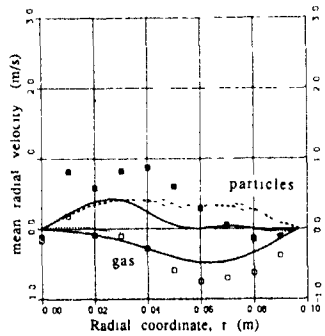

Fig 11 Mean radial velocity profiles (case 3)

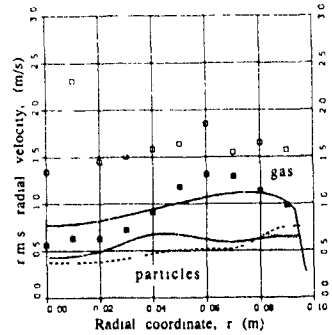

Fig 12 R m.s radial velocity profiles (case 3)

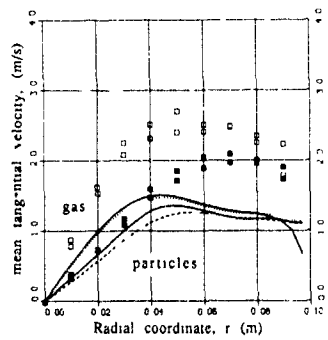

Fig 13 Mean tangential velocity profiles (case 3)

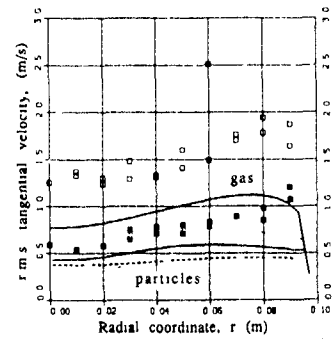

Fig 14 R m s tangential velocity profiles (case 3)

Figures 9 – 14 Comparison between numerical predictions and experimental results in a gas-particle swirling flow at x = 155mm particle diameter d= 30μm , d= 45μm ——, and d= 60μm -·-·- , □ and ■ experimental results for gas and particles respectively (Sommerfeld and Qiu, 1991)

REFERENCES

Csanady, G.T., 1963, "Turbulent Diffusion of Heavy Particles in the Atmosphere", *J Atm Sc*, Vol 20, pp 201-208

Deutsch, E., Simonin, O., 1991, "Large Eddy Simulation Applied to the Modelling of Particulate Transport Coefficients in Turbulent Two-Phase Flows", *Proc 8th Symp on Turbulent Shear Flows*, Munich, FRG

Elgobashi, S E., Abou-Arab, T.W., 1983, 'A Two-Equation Turbulence Model for Two-Phase Flows", *Phys Fluids*, Vol 26, n° 4, pp 931-938.

Grad, H., 1949, "On the Kinetic Theory of Rarefied Gases", *Communications on Pure and Applied Mathematics*, Vol 2, n° 4, pp 331-407

Launder, B.E., Reece, G.J., Rodi, W., 1975, "Progress in the Development of a Reynolds Stress Turbulence Closure", *J Fluid Mech*, Vol 68, pp 537-568

Lun, C.K.K., Savage, S.B , Jeffrey, D.J., Chepurniy, N., 1984, 'Kinetic Theories for Granular Flow Inelastic Particles in Couette Flow and Slightly Inelastic Particles in a General Flowfield", *J Fluid Mech*, Vol 140, n° 4, pp 223-256

Modarress, D., Tan, H., Elgobashi, S., 1984, "Two-Component LDA Measurement in a Two-Phase Turbulent Jet", *AIAA Journal*, Vol 22, n° 5, pp 624-630

Rodi, W., 1972, "The Prediction of Free Turbulent Boundary Layers by Use of a Two-Equation Model of Turbulence", *Ph D Dissertation*, University of London

Simonin, O., Viollet, P.L., 1990a, "Modelling of Turbulent Two-Phase Jets Loaded with Discrete Particles", *Proc Int Conf Phase-Interface Phenomenon in Multiphase Flow*, Dubrovnik, Yugoslavia

Simonin, O., Viollet, P.L., 1990b, "Prediction of an Oxygen Droplet Pulverization in a Compressible Subsonic Coflowing Hydrogen Flow", in *Numerical Methods for Multiphase Flows*, ASME FED, Vol 91, pp 65-82

Sommerfeld, M., Qiu, H.-H., 1991, "Detailed Measurements in a Swirling Particulate Two-Phase Flow by a Phase-Doppler Anemometer", *Int J Heat and Fluid Flow*, Vol 12, pp 20-28

EIGHTH SYMPOSIUM ON
TURBULENT SHEAR FLOWS
Technical University of Munich
September 9-11, 1991

THE NEAR-WALL STRUCTURE OF TURBULENT FLOW ALONG A STREAMWISE CORNER

F B Gessner, H M Eppich, and E G. Lund
University of Washington, Seattle, Washington, USA

ABSTRACT

Experimental results are presented which demonstrate near-wall flow behavior for fully-developed flow in a square duct The results include axial mean velocity, secondary flow velocity, Reynolds stress, and local wall shear stress distributions The data are analyzed in order tc develop wall functions for the turbulence kinetic energy and its dissipation rate which are appropriate for non-circular duct flows Comparisons with experiment show that the proposed model is superior to previously proposed wall function models

INTRODUCTION

Previous experimental work on developing and fully-developed turbulent flow in a square duct with smooth walls has focused primarily on the measurement of flow variables in a quadrant of the flow (Brundrett and Baines, 1964, Ahmed, 1971, Melling and Whitelaw, 1976, Gessner et al., 1979). In more recent work, the nature of fully-developed turbulent flow in a square duct with one or more roughened walls has also been examined (Fujita et al., 1989, Yokosawa et al., 1989) In all of these studies the emphasis has been on global measurements in order to develop a basic understanding of the flow, as influenced by corner generated secondary flows and wall roughness effects By contrast, the present study focuses on mean velocity and Reynolds stress measurements in the near-wall region of a square duct The intent of this paper is not only to present data which can assist in the development of turbulence models applicable to streamwise corner flows, but also to demonstrate that previously applied wall functions must be reformulated if predictive capabilities are to be improved

The discrepancies between predictions and experiment can be illustrated by referring to results based on the k-ε transport equations models proposed by Rodi et al. (1982) and Nakayama et al (1982) Their models underpredict secondary flow along the corner bisector of a square duct, so that U and k contours in the duct cross section do not penetrate as deeply into the corner region as their experimental counterparts During the intervening period between 1982 and the present time, there has been very little improvement in the ability of codes to predict the mean velocity and Reynolds stress fields simultaneously in square duct flows Updated versions of results presented at the 1980-81 Stanford Conference still reflect the shortcomings noted above (Nakayama et al., 1983, Demuren and Rodi, 1984). Results based on recently developed non-linear versions of the k-ε and k-ℓ models (Hur et al., 1990, Bishnoi, 1990) and a non-linear algebraic Reynolds stress model (Barton et al., 1991) also show less-than-complete agreement with experiment, which demonstrates that further work on model development is still needed.

EXPERIMENTAL PROGRAM

The overall flow facility used for the present series of experiments is shown in Fig 1 The results are based on data taken at a location where the flow is nominally fully developed, namely at x/D = 84 where D is the duct width Three operating Reynolds numbers were employed: 250,000, 120,000, and 50,000 ($Re = U_b D/\nu$ where U_b is the axial bulk velocity). In the present paper the emphasis will be on results obtained near the wall y = 0, specifically within the

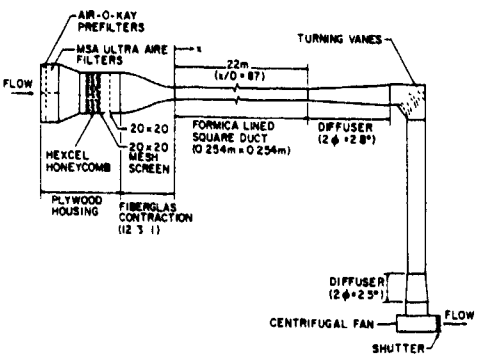

Fig 1 Schematic diagram of overall flow facility

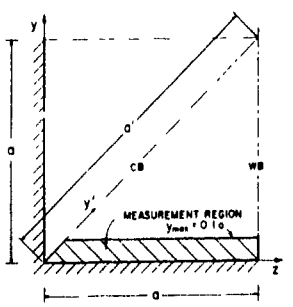

Fig 2 Measurement region relative to a duct quadrant

trapezoidal-shaped measurement region shown in Fig 2 In order to base Reynolds stress results in the corner region on more data, additional data were taken in the triangular-shaped region immediately to the left of the corner bisector (CB). These results were then imaged about the CB in order to calculate representative (average) values for the individual stress components Axial mean velocity distributions were measured by means of a flattened boundary layer probe. Secondary flow profiles were measured by using a rotatable normal-wire probe in conjunction with a Wheatstone bridge and nulling technique Local wall shear stress values were determined by making measurements with three different diameter Preston tubes The six Reynolds stress components were obtained by making measurements with normal and rotatable slant-wire probes connected sequentially to a constant temperature hot-wire anemometer. Details of the probe configurations, calibration techniques, and data reduction procedures are given in two theses which form the basis of the present paper (Lund, 1977, Eppich, 1982)

RESULTS AND DISCUSSION

Axial mean velocity contours measured in the near corner region at Re = 250,000 are shown in Fig 3, contours measured at the other two Reynolds numbers (120,000 and 50,000) are qualitatively similar in appearance The corresponding secondary flow profiles measured in the same region are shown in Fig 4 (W component only) A comparison of the two figures shows that the axial mean velocity contours are relatively unaffected by the presence of the secondary flow, which is in contrast to its known distorting influence in a full quadrant of the flow (cf Fig 7 in Melling and Whitelaw, 1976 or Fig. 3 in Gessner et al., 1979) Although the strength of the secondary flow is maximum near the wall y = 0 (refer to Fig 4), axial mean velocity contours in this region remain essentially parallel to the wall, except in the immediate vicinity of the corner bisector Figure 5 shows that the local wall shear stress τ_w in the interval of interest ($0 \le z/a \le 0.1$) decays monotonically as the corner is approached.

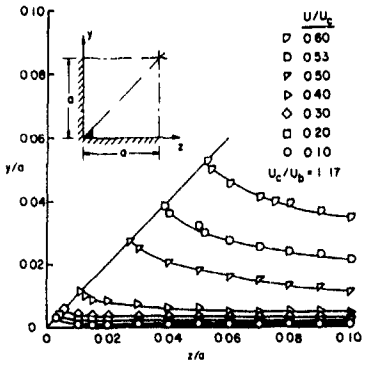

Fig 3 Axial mean velocity contours at Re = 250,000

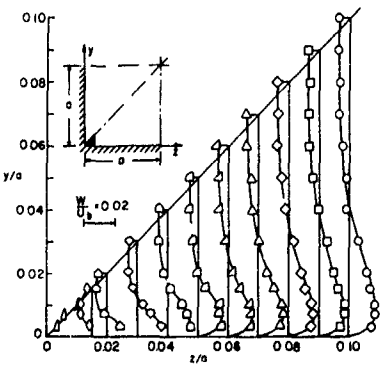

Fig 4 Secondary flow component (W) profiles at Re = 250,000

The nature of the results shown in Figs. 3-5 implies that the two-dimensional form of the law-of-the-wall may apply approximately in the near-wall region. In order to investigate this possibility, law-of-the-wall velocity profiles were plotted at different spanwise locations, as shown in Fig. 6, where $U^+ = U/U_\tau$, $y^+ = yU_\tau/\nu$, κ = von Karman's constant (specified as 0.40 in this study), and U_τ is the local friction velocity calculated from the line distributions shown in Fig 5 ($U_\tau = \sqrt{\tau_w/\rho}$). Profiles within

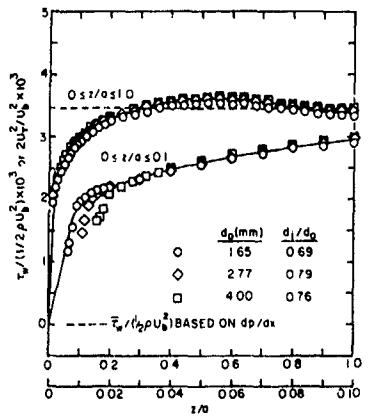

Fig 5 Local wall shear stress distributions at Re = 250,000

the interval $0.01 \le z/a \le 0.1$ are truncated on the CB, and profiles beyond z/a = 0 1 are terminated at $y_{max} = 0.1a$ The results in Fig 6 show that local law-of-the-wall behavior applies in the near-wall region, even in the presence of a secondary flow which is superimposed on the axial mean flow. These results complement those previously obtained by Leutheusser (1963), whose results exhibit more scatter than the profiles shown in Fig 6 and do not extend to the immediate vicinity of the corner In addition to the results shown in Figs 3-6, tabulated data are available in the thesis by Eppich (1982) for the six Reynolds stress components at selected points within the measurement region shown in Fig 2 Corresponding axial mean velocity values are tabulated in the thesis by Lund (1977) for the three operating Reynolds numbers of this study The remainder of this paper will focus on analyzing these results from the point of view of wall function specification for turbulent corner flows

It should first be noted that the near-wall flow appears to be in local equilibrium, inasmuch as the law-of-the-wall applies in this region. If secondary mean strain rate terms are deleted in the Reynolds stress transport equations, then Gessner and Emery (1976) have shown that the following expressions apply for turbulent corner flows in local equilibrium, namely

$$\overline{uv} = -c_\mu \frac{k^2}{\varepsilon}\frac{\partial U}{\partial y} \tag{1}$$

$$\overline{uw} = -c_\mu \frac{k^2}{\varepsilon}\frac{\partial U}{\partial z} \tag{2}$$

$$k = \frac{1}{\sqrt{c_\mu}}\left(\overline{uv}^2 + \overline{uw}^2\right)^{1/2} \tag{3}$$

$$\varepsilon = -\left(\overline{uv}\frac{\partial U}{\partial y} + \overline{uw}\frac{\partial U}{\partial z}\right) \tag{4}$$

$$\ell_p = \frac{c_\mu^{3/4} k^{3/2}}{\varepsilon} \tag{5}$$

where $\overline{uv}$ and $\overline{uw}$ are Reynolds shear stress components, $\partial U/\partial y$ and $\partial U/\partial z$ are primary mean strain rate components, k is the turbulence kinetic energy, ε is the dissipation rate, ℓ_p is Prandtl's mixing length, and c_μ is an empirical constant (specified as 0.09 in this study). Equation (3) can be written in alternate form as

$$\frac{k}{U_\tau^2} = \frac{1}{\sqrt{c_\mu}}\frac{\left(\overline{uv}^2 + \overline{uw}^2\right)^{1/2}}{U_\tau^2} \tag{6}$$

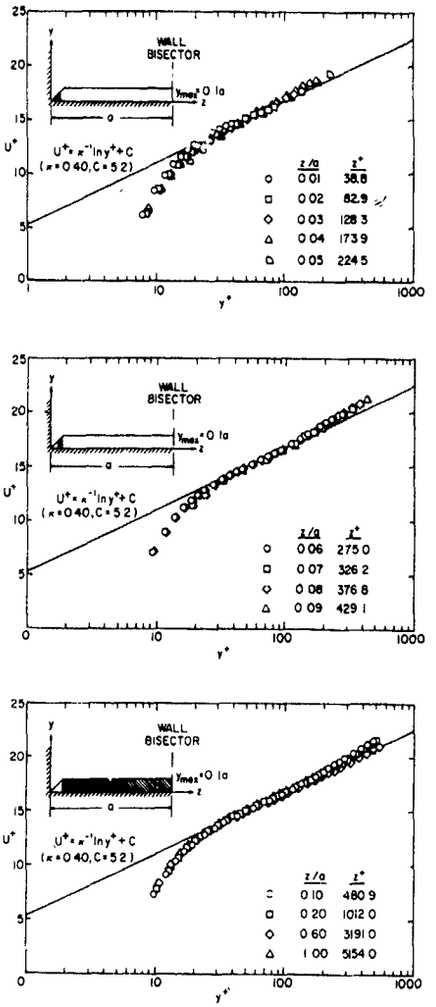

Fig 6 Law-of-the-wall velocity profiles at Re = 250,000

which implies that the reduced form of this expression commonly applied as a wall function in two-dimensional flows, namely $k/U_\tau^2 = 1/\sqrt{c_\mu}$, is applicable to streamwise corner flows only if $(\overline{uv}^2 + \overline{uw}^2)^{1/2}/U_\tau^2 = 1\,0$ throughout the near-wall region Figure 7 shows that this condition is satisfied on the wall bisector where uw is identically zero On the corner bisector, however, where $\overline{uw} = \overline{uv}$ on the basis of symmetry considerations, $(\overline{uv}^2 + \overline{uw}^2)^{1/2}/U_\tau^2 \cong 0\,7$, at least beyond the immediate vicinity of the corner where low turbulence Reynolds number effects influence the results This Reynolds number ($Re_t = k^2/(\varepsilon\nu)$) was evaluated by equating ε to the turbulence kinetic energy production rate, P, corresponding to the right-hand side of Eq (4). From the results shown in Fig. 7 it can be concluded that the two-dimensional form of the wall function for k is inappropriate for turbulent corner flows

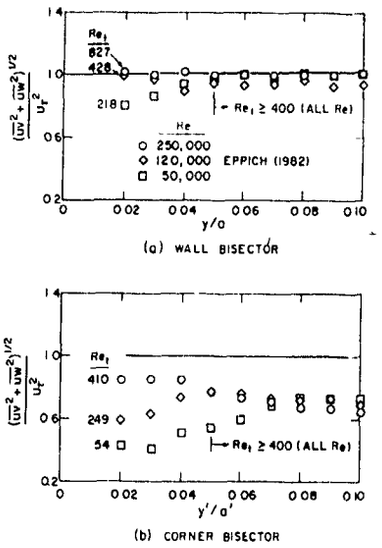

Fig 7 Resultant Reynolds shear stress distributions

As an alternative, Demuren and Rodi (1984) have proposed the following wall functions for corner flows in local equilibrium, namely:

$$\frac{k}{U_\tau^2} = \frac{1}{\sqrt{c_\mu}} F_p^{\frac{1}{2}} \tag{7}$$

and

$$\frac{\varepsilon y}{U_\tau^3} = \frac{1}{\kappa} F_p \tag{8}$$

where, for the measurement region defined in Fig 2,

$$F_p = 1 + \frac{(\partial U/\partial z)^2}{(\partial U/\partial y)^2} \tag{9}$$

Equations (7) and (8) were derived by assuming that $-\overline{uv}/U_\tau^2 = 1\,0$ in the near-wall region and by noting that $\partial U/\partial y = U_\tau/(\kappa y)$ from the law-of-the-wall. In order to investigate the validity of Eqs (7) and (8), k/U_τ^2, $\varepsilon y/U_\tau^3$, and $-\overline{uv}/U_\tau^2$ values were evaluated on grid lines y = constant within the measurement region shown in Fig 2 from data taken by Eppich (1982) The results are shown in Figs 8-10 Superimposed on these figures are the values of these parameters corresponding to the Demuren-Rodi (D-R) wall function model In reference to Fig 8, it can be seen that experimental values of $-\overline{uv}/U_\tau^2$ are near unity on the wall bisector (WB), but then decrease to approximately 0 5 on the corner bisector (CB). A similar trend exists for experimentally measured values of k/U_τ^2, which decrease along each grid line as the corner is approached (refer to Fig 9) This behavior is not simulated by the D-R model, which predicts that k/U_τ^2 should increase by a factor $\sqrt{2}$ between the WB where $F_p = 1$ and the CB where $F_p = 2$ when c_μ is prescribed as a constant (refer to Eq. (7)) The D-R wall function model also overestimates $\varepsilon y/U_\tau^3$ on grid lines y = constant, as is evident from Fig 10, where experimental values cluster about 2.5 ($1/\kappa$ with κ = 0 40), but values referred to the D-R model increase from 2 5 on the WB to 5 0 ($2/\kappa$) on the CB (refer to Eq. 8)

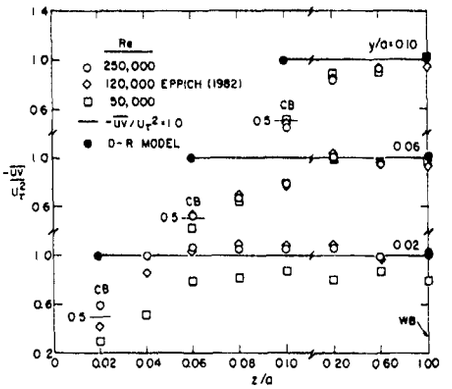

Fig 8 Reynolds shear stress distributions

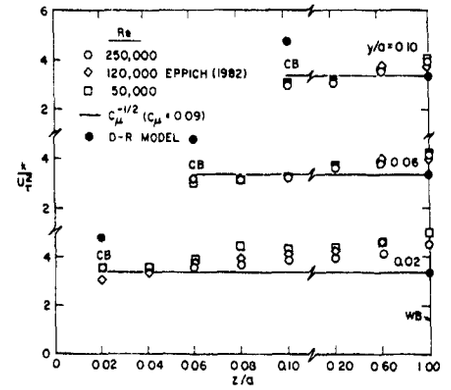

Fig 9 Turbulence kinetic energy distributions

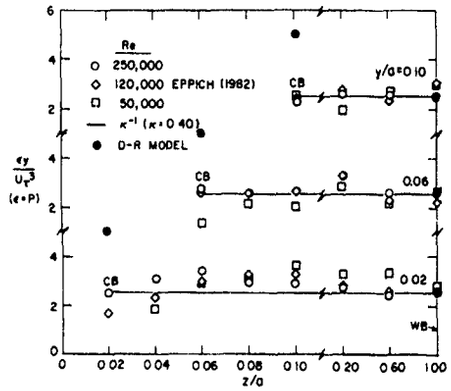

Fig 10 Dissipation rate distributions (ε = P)

Before discussing alternative wall functions, comparisons will be made with the results of other investigators in order to demonstrate that the trends seen in Figs 8 and 9 have been observed by other investigators Figure 11 shows distributions of $-uv/U_\tau^2$ and k/U_τ^2 measured by Po (1975), Lund (1977), and Eppich (1982) in the same flow facility (Fig 1) at x/D = 84 and Re = 250,000 The results of all three investigators are in close agreement and confirm the trends seen in Figs 8 and 9 Figure 12 compares $-uv/U_\tau^2$ and k/U_τ^2 distributions measured by Eppich (1982) with similar distributions based on data obtained by Yokosawa et al (1989) in a square duct at approximately the same streamwise location (x/D = 90) for an intermediate Reynolds number (65,000) Also shown in this figure are distributions based on Ahmed's (1971) square duct flow data at approximately the same Reynolds numbers as those of Eppich's study Ahmed's data were taken at a streamwise location where the flow was not yet fully developed, although the boundary layers on opposite walls of the duct had already merged (x/D = 26.5). In general, the results of all three studies show the same trends, namely $-uv/U_\tau^2$ and k/U_τ^2 values which decrease as the CB is approached The slight differences between Eppich's results and those of Yokosawa et al may be due, in part, to the different flow systems used in these two studies Whereas Eppich's data were taken on the suction side of a centrifugal fan at a streamwise location where the duct was continuous (refer to Fig 1), the data of Yokosawa et al. were obtained near the open end of a square duct which was fed by a blower upstream and discharged into the atmosphere

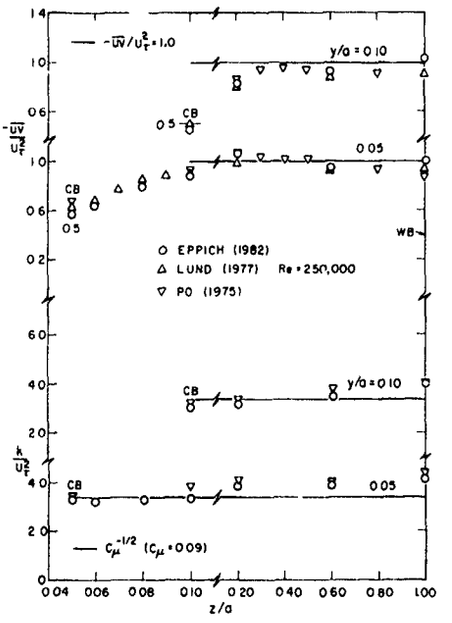

Fig 11 Reynolds shear stress and turbulence kinetic energy distributions (based on data obtained in flow facility shown in Fig 1)

Some insight into the validity of Eq (6) for modeling near-wall behavior can be gleaned by interpreting the results shown in Fig 11 and 12 relative to a reduced form of this equation which applies along the wall bisector of a square duct where $\overline{uw} = 0$, namely

$$\frac{k}{U_\tau^2} = \frac{1}{\sqrt{c_\mu}}\left(\frac{-\overline{uv}}{U_\tau^2}\right) \qquad (10)$$

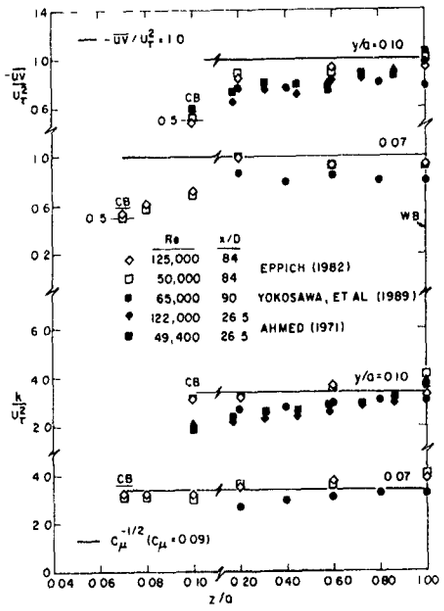

Fig 12 Reynolds shear stress and turbulence kinetic energy distributions (based on data obtained in different flow facilities)

Equation (10) is based on the premise that secondary mean strain rates (e.g., $\partial V/\partial y$ and $\partial W/\partial z$) are negligible in comparison to the primary mean strain rate on the WB ($\partial U/\partial y$). If this is so, then measured values of $-uv/U_\tau^2$ and k/U_τ^2 on the WB should be compatible with Eq (10) to the extent that if $-uv/U_\tau^2 = 1.0$ on the WB, then k/U_τ^2 should equal $1/\sqrt{c_\mu}$ on this traverse. In reference to Fig. 11, k/U_τ^2 values on the WB lie consistently above the line $1/\sqrt{c_\mu}$, even though $-uv/U_\tau^2 \cong 1.0$ on this traverse. Similar behavior can be seen in Fig 12 with respect to Yokosawa et al.'s results. Whereas $k/U_\tau^2 \cong 1/\sqrt{c_\mu}$ on the WB, $-uv/U_\tau^2 \cong 0.8$ on this traverse, which again indicates that Eq (10) is not satisfied identically on the WB. These observations imply that Eq (6) is not adequate for modeling near-wall flow behavior, and that this equation must be modified to account for secondary mean strain rate effects. This would be a formidable task, however, so that in this paper only an approximate analysis based on primary mean strain rates alone will be pursued in order to develop an improved wall function model in comparison to the one proposed by Demuren and Rodi (1984).

The development begins by considering the expressions for $\overline{uv}$ and $\overline{uw}$ derived by Gessner and Emery (1976), which are based on Eqs. (1) – (5) referenced in this paper, namely

$$\overline{uv} = -\ell_p^2 \frac{\partial U}{\partial y}\left[\left(\frac{\partial U}{\partial y}\right)^2 + \left(\frac{\partial U}{\partial z}\right)^2\right]^{1/2} \tag{11}$$

$$\overline{uw} = -\ell_p^2 \frac{\partial U}{\partial z}\left[\left(\frac{\partial U}{\partial y}\right)^2 + \left(\frac{\partial U}{\partial z}\right)^2\right]^{1/2} \tag{12}$$

If the expression for F_p given by Eq. (9) is introduced into Eq (11) and $\partial U/\partial y$ is replaced by $U_\tau/(\kappa y)$ from the law-of-the-wall, then Eq (11) can be written in alternate form as:

$$\frac{\overline{uv}}{U_\tau^2} = -\frac{\ell_p^2}{(\kappa y)^2} F_p^{\frac{1}{2}} \tag{13}$$

A similar approach can be taken to develop a corresponding expression for uw/U_τ^2 from Eq (12). If these two expressions are substituted into Eqs (3) and (4), then the following wall function forms for k and ε apply, namely

$$\frac{k}{U_\tau^2} = \frac{1}{\sqrt{c_\mu}}\frac{\ell_p^2}{(\kappa y)^2} F_p \tag{14}$$

$$\frac{\varepsilon y}{U_\tau^3} = \frac{1}{\kappa}\frac{\ell_p^2}{(\kappa y)^2} F_p^{\frac{3}{2}} \tag{15}$$

A comparison of Eqs. (14) and (15) with Eqs (7) and (8) shows that k/U_τ^2 and $\varepsilon y/U_\tau^3$ now depend on F_p and $F_p^{3/2}$, respectively, rather than F_p and $F_p^{1/2}$, respectively, as in the D-R model. In order to utilize Eqs (13) - (15), it is necessary to specify a functional form for Prandtl's length scale, ℓ_p. For fully-developed flow in a square duct at high Reynolds numbers, this can be done by means of an expression based on Buleev's (1963) length scale, as referenced by Gessner and Emery (1977), namely

$$\ell_p = \frac{2\kappa yz}{yz\left(\frac{1}{y_1^2}+\frac{1}{z_1^2}\right)^{1/2} + y\left(1+\frac{z^2}{y_1^2}\right)^{1/2} + z\left(1+\frac{y^2}{z_1^2}\right)^{1/2} + (y^2+z^2)^{1/2}} \tag{16}$$

where $y_1 = 2a - y$ and $z_1 = 2a - z$, and all four walls influence length scale behavior at a given point in the flow. If the flow develops from an initially uniform axial mean flow at the duct inlet, then length-scale behavior in the near inlet region can be modeled as that for an unbounded corner for which $y_1 \to \infty$ and $z_1 \to \infty$. Under these conditions, only the two walls which bound a corner influence length scale behavior in the corner boundary layer, and Eq (16) reduces to

$$\ell_p = \frac{2\kappa yz}{y + z + (y^2 + z^2)^{1/2}} \tag{17}$$

Equations (16) and (17) were utilized in conjunction with Eqs (13) – (15) to plot the modeled behavior of $-uv/U_\tau^2$, k/U_τ^2, and $\varepsilon y/U_\tau^3$ along the wall and corner bisectors of a square duct for comparison with Eppich's (1982) experimental results. The results are shown in Figs 13 – 15, which also include line distributions based on the D-R wall function model. In general, the wall function expressions given by Eqs (13) – (15), in conjunction with either Eq (16) or Eq. (17), lead to distributions which agree well with experimental values measured on both the wall and corner bisectors of the duct. Distributions referred to the two-wall length scale model are, in fact, in better agreement with experiment than distributions referred to the four-wall length scale model, which indicates that the former model may also be applied when the flow is fully developed. Distributions referred to the D-R wall function model are in good agreement with experiment on the WB, but seriously overestimate local values on the CB. In reference to Fig 14, for example, k/U_τ^2 based on the D-R model is 4.7 on the CB, but experimental values of k/U_τ^2 are much closer to 3.0. Thus, k values on the CB are maintained at artificially high levels when the D-R wall function model is employed. This behavior may account, in part, for the inability of predicted k contours, as calculated by Rodi et al (1982) to penetrate as deeply into the corner region as their experimental counterparts.

CONCLUDING REMARKS

Turbulence and mean flow measurements have been made in the near-wall region of a square duct for fully developed flow conditions. Analysis of the results has led to the development of an improved wall function model. This

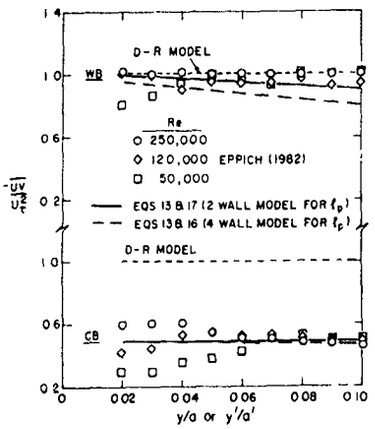

Fig 13 Comparison of wall function distributions with measured Reynolds shear stress distributions

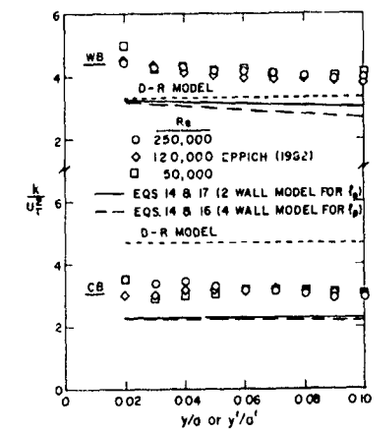

Fig 14 Comparison of wall function distributions with measured turbulence kinetic energy distributions

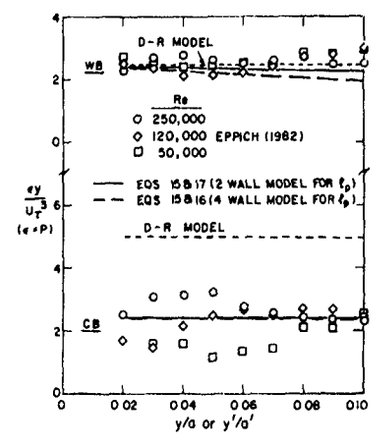

Fig 15 Comparison of wall function distributions with measured dissipation rate distributions (ε = P)

model should be applicable to other non-circular duct configurations, provided that Buleev's length-scale is evaluated from the *linear* formula originally proposed by Buleev. Further work will be required to develop a more representative wall function model which includes secondary mean strain rates in its formulation. This conclusion is based on the observation that $\overline{uv}/U_\tau^2$ and k/U_τ^2 distributions in the near-wall region appear to be influenced by the convecting action of the secondary flow.

REFERENCES

AHMED, S. 1971 Turbulent flow in non-circular ducts. PhD thesis, Dept of Mech Engng, University of Waterloo, Ontario, Canada.

BARTON, J.M., RUBINSTEIN, R. & KIRTLEY, K.R. 1991 Nonlinear Reynolds stress model for turbulent shear flows. AIAA Paper No. 91-0609.

BISHNOI, P.K. 1990 A critical analysis of anisotropic k-ε modeling and its application to turbulence driven secondary flows. PhD thesis, Dept. Mech. Indust. Engng., University of Cincinnati.

BRUNDRETT, E. & BAINES, W.D. 1964 The production and diffusion of vorticity in duct flow. *J. Fluid Mech.*, **19** (3), 375-392.

BULEEV, N.I. 1963 Theoretical model of the mechanism of turbulent exchange in fluid flows. AERE translation 957, Atomic Energy Research Establishment, Harwell, England.

DEMUREN, A.O. & RODI, W. 1984 Calculation of turbulence-driven secondary motion in non-circular ducts. *J. Fluid Mech.*, **140**, 189-222.

EPPICH, H.M. 1982 An experimental investigation of the turbulence structure in the inner region of a three-dimensional streamwise corner flow. MS thesis, Dept. Mech. Engng., University of Washington.

FUJITA, H., YOKOSAWA, H. & HIROTA, M. 1989 Secondary flow of the second kind in rectangular ducts with one rough wall. *Exp. Thermal and Fluid Sci.*, **2**, 72-80.

GESSNER, F.B. & EMERY, A.F. 1976 A Reynolds stress model for turbulent corner flows - Part I: Development of the model. *J. Fluids Engng.*, **98** (2), 261-268.

GESSNER, F.B. & EMERY, A.F. 1977 A length-scale model for developing turbulent flow in a rectangular duct. *J. Fluids Engng.*, **99** (2), 347-356.

GESSNER, F.B., PO, J.K. & EMERY, A.F. 1979 Measurements of developing turbulent flow in a square duct. *Proc. First Symp. Turb. Shear Flows*, Springer-Verlag, New York, 119-136.

HUR, N., THANGAM, S. & SPEZIALE, C.G. 1990 Numerical study of turbulent secondary flows in curved ducts. *J. Fluids Engng.*, **112** (2), 205-211.

LEUTHEUSSER, H.J. 1963 Turbulent flow in rectangular ducts. *J. Hydraulics Div.*, Proc. ASCE, **89** (HY 3), 1-10.

LUND, E.G. 1977 Mean flow and turbulence characteristics in the near corner region of a square duct. MS thesis, Dept. Mech. Engng., University of Washington.

MELLING, A. & WHITELAW, J.H. 1976 Turbulent flow in a rectangular duct. *J. Fluid Mech.* **78** (2), 289-315.

NAKAYAMA, A., CHOW, W.L. & SHARMA, D. 1982 Summary report of computer group no. 23. *Proc. 1980-81 AFOSR-HTTM Stanford Conf. on Complex Turb. Flows*, Vol. III, Stanford University, 1312-1317.

NAKAYAMA, A., CHOW, W.L. & SHARMA, D. 1983 Calculation of fully-developed turbulent flows in ducts of arbitrary cross-section. *J. Fluid Mech.*, **128**, 199-217.

PO, J.K. 1975 Developing turbulent flow in the entrance region of a square duct. MS thesis, Dept. Mech. Engng., University of Washington.

RODI, W., CELIK, I., DEMUREN, A.O., SCHEUERER, G., SHIRANI, E., LESCHZINER, M.A. & RASTOGI, A.K. 1982 Summary report of computer group no. 7. *Proc. of the 1980-81 AFOSR-HTTM Stanford Conf. on Complex Turb. Flows*, Vol. III, Stanford University, 1495-1516.

YOKOSAWA, H., FUJITA, H., HIROTA, M. & IWATA, S. 1989 Measurement of turbulent flow in a square duct with roughened walls on two opposite sides. *Int. J. Heat and Fluid Flow*, **10** (2), 125-130.

EIGHTH SYMPOSIUM ON
TURBULENT SHEAR FLOWS
Technical University of Munich
September 9-11, 1991

PREDICTION OF THREE-DIMENSIONAL TURBULENT BOUNDARY LAYERS USING A SECOND-MOMENT CLOSURE

Nobuyuki Shima

College of Engineering, Shizuoka University
Hamamatsu, 432 JAPAN

ABSTRACT

A second-moment closure, which was previously validated in various two-dimensional boundary layers, is applied to three kinds of three-dimensional boundary layers. The turbulence model faithfully represents a fully-developed pressure-driven flow; a skewed velocity profile itself does not cause difficulties in prediction. For a shear-driven flow and a flow on a swept wing, the predictions show limited success. It is also shown that the decrease in the structure parameter is partially accounted for by the effect of "secondary" velocity gradient terms in the stress transport equations.

NOMENCLATURE

a_1 ratio of shear stress magnitude to twice turbulence energy
C_f skin friction coefficient
d distance from wall
f angular rate of rotation of free-stream velocity vector in Case 1
k turbulence energy
n_i unit vector normal to wall
Q magnitude of velocity vector
Q_e magnitude of velocity vector at boundary layer edge
Re Reynolds number in Case 1 $= Q_e(2/f\nu)^{1/2}$
U_i mean velocity vector
u_i velocity fluctuation vector
U_τ friction velocity
U, V, W mean velocity components in x, y, z directions (or in $\hat{x}, y, \hat{z}$ directions in Case 1)
u, v, w velocity fluctuation components in x, y, z directions (or in $\hat{x}, y, \hat{z}$ directions in Case 1)
u', v', w' turbulence intensities in $\hat{x}, y, \hat{z}$ directions in Case 1
x_i Cartesian coordinates
x' distance from leading edge measured along wind tunnel axis in Case 3
x, z surface coordinates in and normal to external streamline direction (In Case 2, x is measured from the location where the flow encounters wall motion.)
$x, \hat{z}$ surface coordinates in and normal to a direction approximately parallel to [but strictly, separated by an angle of $208/(Re^2 C_f)$ from] direction of wall shear stress in Case 1
y normal coordinate, measured from wall
β angle between direction of velocity vector and that of external streamline
β_g angle between direction of velocity gradient vector and that of external streamline
β_w angle between direction of wall shear stress vector and that of external streamline
β_τ angle between direction of shear stress vector and that of external streamline
Δ reference length in Case 2 $= 0.0254m$
δ boundary layer thickness
ϵ dissipation rate of turbulence energy
ν kinematic viscosity
τ_x, τ_z total shear stress components in $\hat{x}, \hat{z}$ directions in Case 1

The overbar implies averaging, and the superscript $^+$ denotes nondimensionalizing with U_τ, ν, and density.

INTRODUCTION

The prediction of three-dimensional turbulent boundary layers is one of the most challenging problems in turbulence modelling. Although several authors (Rotta 1979; Bradshaw 1987, van den Berg 1982) suggest that the "standard" stress-redistribution model should be revised to reproduce such flows, predictions at the second-moment closure level are rather scarce. Testing of turbulence models at this level in a variety of such flows is clearly needed before a sufficiently general model is established. This paper presents the results of testing of a second-moment closure of Launder & Shima (1989) [with some model functions recasted as in Shima (1989)] in three kinds of three-dimensional boundary layers.

TURBULENCE MODEL

The turbulence model is a full second-moment closure that is applied right up to a wall. It can be summarized as follows.

Stress transport model

$$\frac{D}{Dt}\overline{u_i u_j} = P_{ij} - \frac{2}{3}\delta_{ij}\epsilon + \phi_{(1)ij} + \phi_{(2)ij} + \phi_{(w1)ij} + \phi_{(w2)ij} - \frac{\partial}{\partial x_k}\left(J_{ijk} - \nu\frac{\partial}{\partial x_k}\overline{u_i u_j}\right) \quad (1)$$

$$P_{ij} = -\left(\overline{u_j u_k}\frac{\partial U_i}{\partial x_k} + \overline{u_i u_k}\frac{\partial U_j}{\partial x_k}\right) \quad (2)$$

$$\phi_{(1)ij} = -C_1\frac{\epsilon}{k}\left(\overline{u_i u_j} - \frac{2}{3}\delta_{ij}k\right) \quad (3)$$

$$\phi_{(2)ij} = -C_2\left(P_{ij} - \frac{2}{3}\delta_{ij}P\right) \quad (4)$$

$$\phi_{(w1)ij} = C_{w1}\frac{\epsilon}{k}\left(\overline{u_k u_m}n_k n_m\delta_{ij}\right.$$

$$-\frac{3}{2}\overline{u_k u_i}n_k n_j - \frac{3}{2}\overline{u_k u_j}n_k n_i\Big)\frac{k^{3/2}}{C_t \epsilon d} \quad (5)$$

$$\phi_{(u_i u_j)_2} = C_{w2}\Big(\phi_{(2)km}n_k n_m \delta_{ij}$$

$$-\frac{3}{2}\phi_{(2)ik}n_k n_j - \frac{3}{2}\phi_{(2)jk}n_k n_i\Big)\frac{k^{3/2}}{C_t \epsilon d} \quad (6)$$

$$J_{ijk} = -C_s \frac{k}{\epsilon}\overline{u_k u_l}\frac{\partial \overline{u_i u_j}}{\partial x_l} \quad (7)$$

$$P = -\overline{u_k u_l}\frac{\partial U_k}{\partial x_l} \quad (8)$$

$$C_1 = 1 + 2\,58\,4 A_2^{1/4}\left[1 - \exp\left\{-(0\,0067 R_T)^2\right\}\right] \quad (9)$$

$$C_2 = 0\,75 A^{1/2} \quad (10)$$

$$C_{w1} = -2C_1/3 + 1\,67 \quad (11)$$

$$C_{w2} = \max[2(C_2 - 1)/3 + 0\,5,\ 0]/C_2 \quad (12)$$

$$A = 1 - 9A_2/8 + 9A_3/8 \quad (13)$$

$$A_2 = a_{ij}a_{ji} \quad (14)$$

$$A_3 = a_{ij}a_{jk}a_{ki} \quad (15)$$

$$a_{ij} = \overline{u_i u_j}/k - 2\delta_{ij}/3 \quad (16)$$

$$R_T = k^2/\nu\epsilon \quad (17)$$

$$C_s = 0\,22, \quad C_t = 2\,5 \quad (18)$$

ϵ transport model

$$\frac{D\epsilon}{Dt} = (C_{\epsilon 1} + \psi_1 + \psi_2)\frac{\epsilon}{k}P - C_{\epsilon 2}\frac{\epsilon\tilde{\epsilon}}{k} + \frac{\partial}{\partial x_k}\left(C_\epsilon \frac{k}{\epsilon}\overline{u_k u_l}\frac{\partial \epsilon}{\partial x_l} + \nu\frac{\partial \epsilon}{\partial x_k}\right) \quad (19)$$

$$\tilde{\epsilon} = \epsilon - 2\nu\left(\frac{\partial k^{1/2}}{\partial x_l}\right)^2 \quad (20)$$

$$\psi_1 = 1\,5A(P/\epsilon - 1) \quad (21)$$

$$\psi_2 = 0\,35(1 - 0\,3A_2)\exp[-(0\,002 R_T)^{1/2}] \quad (22)$$

$$C_{\epsilon 1} = 1\,45, \ C_{\epsilon 2} = 1\,9, \ C_\epsilon = 0\,18 \quad (23)$$

The model described above was proposed as an extension of the high-Reynolds-number closure of Gibson & Launder (1978), and was successfully applied to a wide variety of two-dimensional boundary layers (Launder & Shima 1989 , Shima 1989) In three-dimensional boundary layers, however, its success will be limited because, when the transport terms are negligibly small, the model gives the same direction to the shear stress vector and the velocity gradient vector Our aim in the present study is to show the capability and limitation of a second-moment closure of this type

The numerical solutions are obtained with an adapted version of the parabolic solver PASSABLE (Leschziner 1982) For details of the turbulence model and the solution procedure, see Launder & Shima (1989) and Shima (1989)

TEST CASES

The following three-dimensional turbulent boundary layers (3D-TBLs) are considered

Case 1 3D-TBL created by a rotating free-stream velocity vector [direct numerical simulation by Spalart (1989)]

Case 2 3D-TBL formed when an initially two-dimensional boundary layer encounters transverse wall motion [experiment by Lohmann (1976)]

Case 3 3D-TBL on an infinite swept wing [experiments by van den Berg & Elsenaar (1972) and by Elsenaar & Boelsma (1974)]

Cases 1 and 3 are pressure-driven, while Case 2 is shear-driven Case 1 is a fully-developed flow, while Cases 2 and 3 are developing flows These cases are collectively expected to cover essential features of 3D-TBLs Note that Cases 2 and 3 have been employed as test cases by many workers , see e g van den Berg et al (1987)

RESULTS

In Case 1, the velocity profile is skewed by the pressure gradient at right angles to the free-stream velocity vector which rotates at a constant angular rate When the flow is fully developed, averaged quantities in the rotating frame depend only on the distance from the wall Figures 1 - 3 show the mean velocity and stress profiles in a coordinate system with the $\hat{x}$-axis approximately parallel to the direction of the wall shear stress , see Nomenclature for details. The skewed mean velocity profile is faithfully reproduced by the model (Fig 1) The stress profiles are also reproduced well, though some discrepancies are evident in the outer layer (Figs 2 and 3) Midway in the boundary layer w' becomes greater than u' due to the skewing (Fig 3) ; this feature is also captured by the prediction Overall, the agreement between the direct simulation and the prediction is satisfactory As shown in Fig 4, however, in this case the shear stresses are in rather close

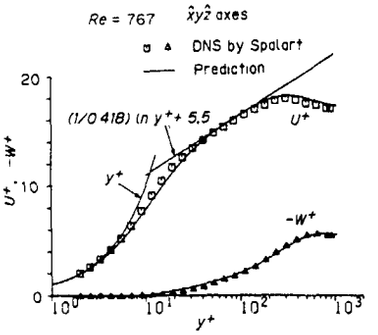

Fig 1 Mean velocity (Case 1)

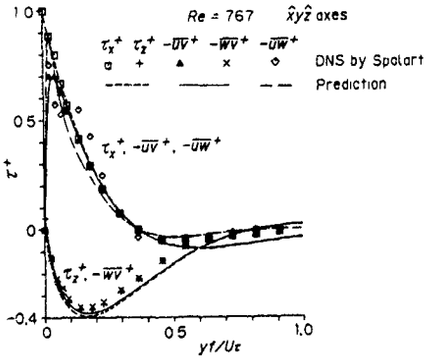

Fig 2 Shear stresses (Case 1)

alignment with the mean shear The result of this case indicates that the present model well reproduces a fully-developed 3D-TBL in which the lag between the shear stress direction and the velocity gradient direction is small

Attention is turned to Case 2 Lohmann (1976) generated the flow field on a cylinder with a stationary front section and a rotating aft section Since the effect of transverse curvature is not entirely negligible, this case has been calculated as an axisymmetric boundary layer using cylindrical coordinates The results are shown in Figs 5 – 9 In the velocity profile, the propagation rate of the influence of the wall motion is somewhat underpredicted (Fig 6) The flow has a nearly constant stress layer in the vicinity of the wall As seen from Fig 7, in the layer, the prediction produces reasonable levels of shear stress components parallel to the wall [the data values being somewhat too low according to Lohmann (1976)] This leads to the good prediction of the magnitude and direction of the wall shear stress (Fig 5) In the outer layer, the experiment shows a rapid growth of the transverse shear stress component (Fig 7) and the resultant lead of the shear stress direction ahead of the velocity gradient direction (Fig 9) This behavior is not captured by the model The redistribution model should be modified to reproduce the large difference between the two directions For other stress components, $\overline{uw}$ (Fig 7) and normal stresses (Fig 8), large discrepancies are evident The developing process of these stresses in the experiment is clearly different from that in the prediction (though the profiles at other stations are not shown for brevity) For instance, the maximum in the measured $\overline{v^2}$ profile is still increasing at

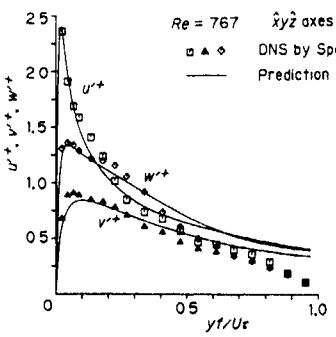

Fig 3 Turbulence intensities (Case 1)

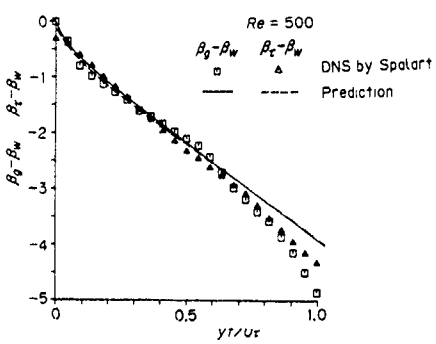

Fig 4 Direction of velocity gradient and shear stress (Case 1)

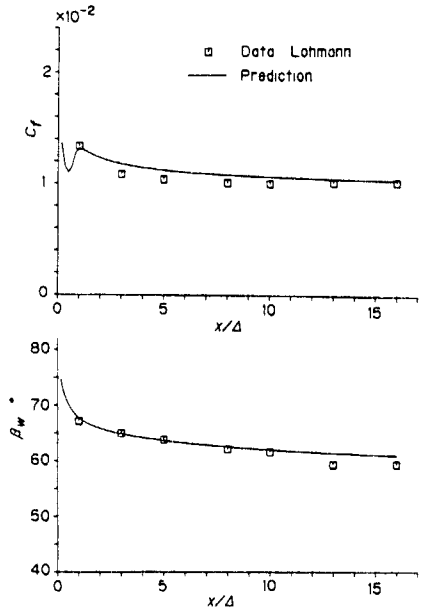

Fig 5 Magnitude and direction of wall shear stress (Case 2)

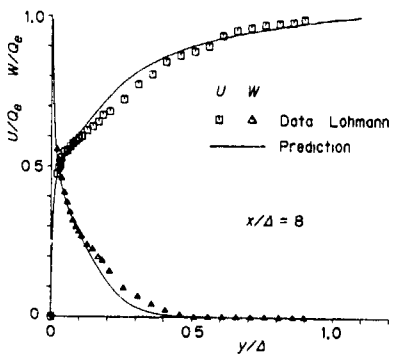

Fig 6 Mean velocity (Case 2)

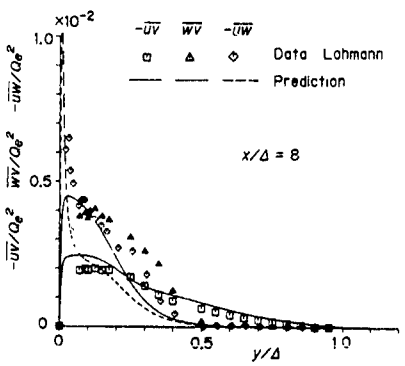

Fig 7 Shear stresses (Case 2)

the station ($x/\Delta = 8$), while the predicted maximum almost attains its asymptotic value

Finally, the 3D-TBL on a swept wing, Case 3, is considered The experiment simulates an infinite 35° swept wing in a wind tunnel The predictions are compared with the experimental data in Figs 10 - 16, where the distance x' is measured along the tunnel axis Two sets of velocity variations at the boundary layer edge (assuming constant pressure across the boundary layer) are tested "External Flow A" uses measured wall pressures, while "External Flow B" employs measured flow angles at the edge In this case, particular attention is given to the effect of approximation of the stress production and rapid redistribution terms "Model Approx 1", as in usual practice, just retains the terms with $\partial U/\partial y, \partial W/\partial y$, while "Model Approx 2" further retains the terms with $\partial U/\partial x, \partial W/\partial x$

Figures 10 and 11 show that the magnitude and direction of the wall friction in downstream regions are too sensitive to the external flow condition to draw a definite conclusion on the model performance , the sensitivity has been pointed out by several authors (e g Cousteix 1982 , van den Berg et al 1987) In Fig 12, the magnitude of mean velocity is faithfully reproduced by the model, but the turn angle of its direction is underpredicted (In Figs 12 - 16, only the results of "External Flow B" are presented for brevity.) Figure 13 shows that even when the wall friction is reproduced fairly well, the maxima in the shear stresses parallel to the wall are too high Perhaps the three-dimensionality is not a main reason for this discrepancy since such a result is also obtained

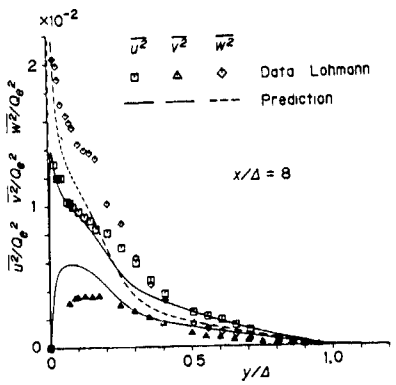

Fig 8 Normal stresses (Case 2)

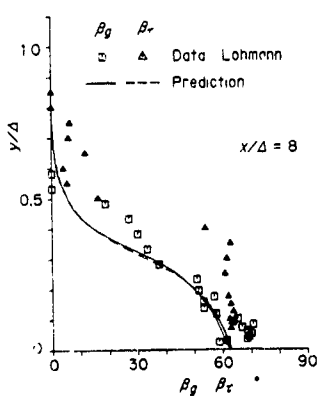

Fig 9 Direction of velocity gradient and shear stress (Case 2)

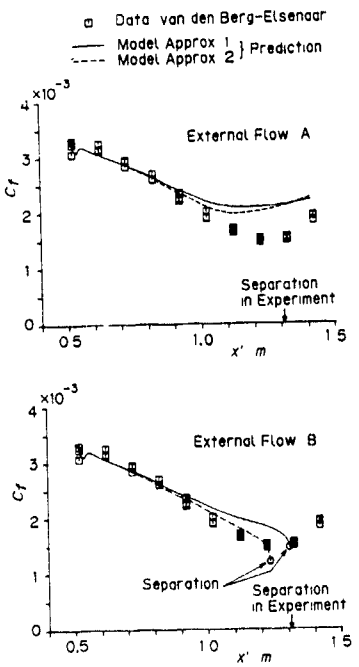

Fig 10 Skin friction coefficient (Case 3)

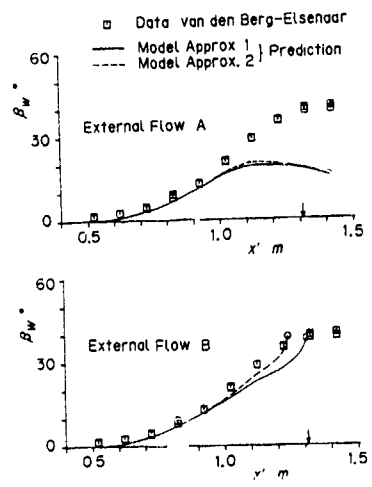

Fig 11 Direction of wall shear stress (Case 3)

in two-dimensional boundary layers in adverse pressure gradients Our main finding in this case is that, as Figs 13 and 14 indicate, the terms with "secondary" velocity gradients considerably augment the stress components acting on the planes normal to the wall $\overline{u^2}$ $\overline{w^2}$ and $\overline{uw}$ This effect can readily be traced to the exact stress production terms The production of those stress components associated with the "secondary" velocity gradients is, in contrast to that of the stresses acting on the plane parallel to the wall, by no means negligible, due to relatively large magnitude of the stresses themselves This effect partially accounts for the decrease in the shear-stress/energy ratio, though quantitative agreement is not satisfactory in Fig 15 due to the overpredicted shear stresses Potentially, the inclusion of the "secondary" terms

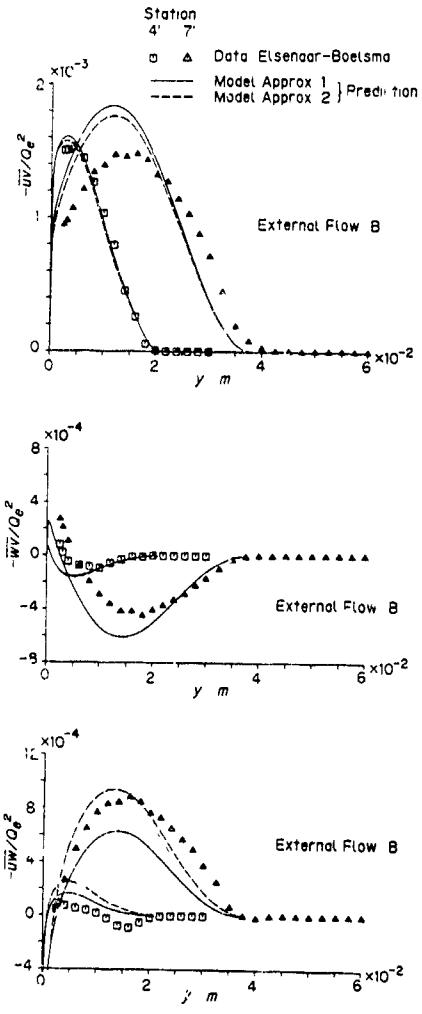

Fig 13 Shear stresses (Case 3 , Station 4' $x' = 0\,795m$, Station 7' $x' = 1\,095m$)

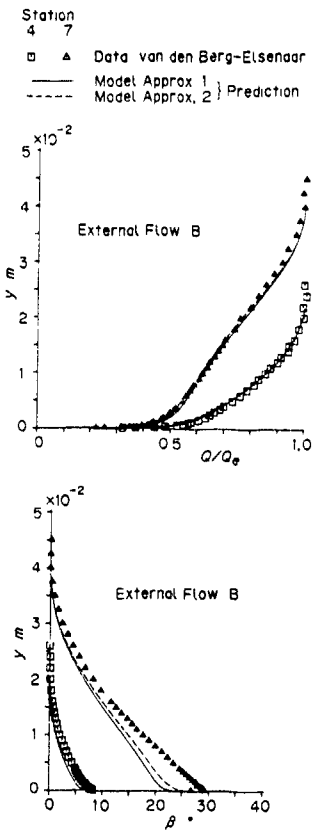

Fig 12 Magnitude and direction of mean velocity (Case 3 , Station 4 $x' = 0\,820m$, Station 7 $x' = 1\,120m$)

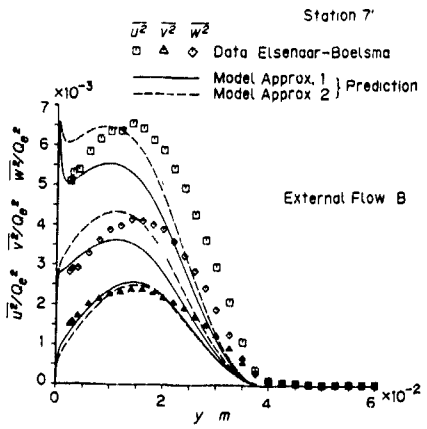

Fig 14 Normal stresses (Case 3)

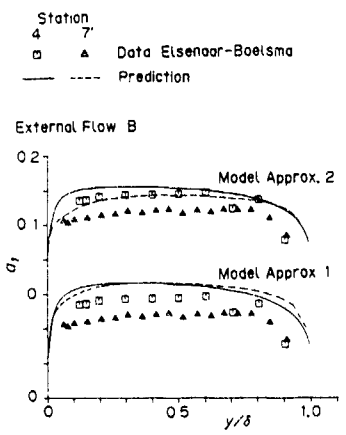

Fig 15 Ratio of shear stress magnitude to twice turbulence energy (Case 3)

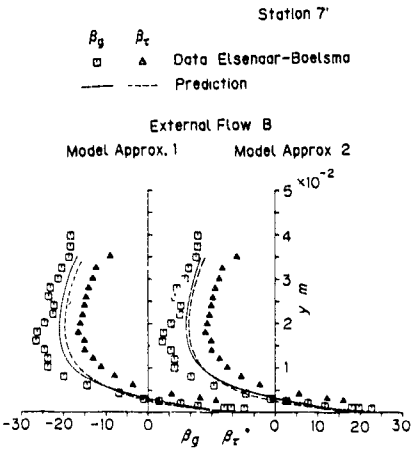

Fig.16 Direction of velocity gradient and shear stress (Case 3)

can also improve the shear stress direction, as suggested by Cousteix (1982) and by Cousteix & Michel (1987) However, Fig 16 shows that the terms make the direction even closer to the velocity gradient direction in the outer layer

CONCLUSIONS

The following conclusions can be drawn from the results

(1) A skewed velocity profile itself does not cause difficulties in prediction , the present model well reproduces a fully-developed flow

(2) Even in developing flows, the model gives a close alignment of the shear stresses with the mean shear, but it does not necessarily lead to unacceptable predictions , the magnitude and direction of wall friction in a shear-driven flow are well reproduced However, the pressure-strain model should be modified to give more accurate prediction of mean velocity profiles and turbulence structures A modification whose effect is limited to developing flows is desirable

(3) The decrease in the ratio of shear stress magnitude to turbulence energy is partially accounted for by the effect of "secondary" velocity gradient terms in the stress transport equations

REFERENCES

BRADSHAW,P 1987 *Ann Rev Fluid Mech* **19**, 53-74

COUSTEIX,J 1982 In *Three-Dimensional Turbulent Boundary Layers* (ed H H Fernholz & E Krause), pp 286-297. Springer-Verlag

COUSTEIX,J & MICHEL,R 1987 In *Perspectives in Turbulence Studies* (ed H U Meier & P Bradshaw), pp 439-472 Springer-Verlag

ELSENAAR,A & BOELSMA,S H 1974 *NLR TR*, 74085 U

GIBSON,M M & LAUNDER,B E 1978 *J Fluid Mech* **86**, 491-511

LAUNDER,B E & SHIMA,N 1989 *AIAA J* **27**, 1319-1325

LESCHZINER,M A 1982 An introduction and guide to PASSABLE Dept Mech Engng , UMIST

LOHMANN,R P 1976 *Trans ASME, J Fluids Engng* **98**, 354-363

ROTTA,J C 1979 In *Turbulent Shear Flows* 1 (ed F Durst et al), pp 267-278. Springer-Verlag

SHIMA,N 1989 In *Proc 7th Symp Turbulent Shear Flows*, pp 5 3 1-5 3.6. Stanford University

SPALART,P R 1989 *J. Fluid Mech* **205**, 319-340

VAN DEN BERG,B 1982 In *Three-Dimensional Turbulent Boundary Layers* (ed H H Fernholz & E Krause), pp 1-18 Springer-Verlag

VAN DEN BERG,B & ELSENAAR,A. 1972 *NLR TR*, 72092 U

VAN DEN BERG,B , HUMPHREYS,D A , KRAUSE,E & LINDHOUT,J P F (eds) 1987 *Three-Dimensional Turbulent Boundary Layers - Calculations and Experiments* Vieweg

EIGHTH SYMPOSIUM ON
TURBULENT SHEAR FLOWS
Technical University of Munich
September 9-11, 1991

TURBULENT ENERGY BUDGETS IN IMPINGING ZONES

by

J M M Barata, D F G Durão and M V Heitor

Instituto Superior Técnico
Technical University of Lisbon
Mechanical Engineering Department
Av Rovisco Pais, 1096 Lisboa Codex
Portugal

ABSTRACT

Budgets of turbulent kinetic energy are presented in the vicinity of the stagnation zone created by the impingement of a turbulent jet on a flat plate through a low-velocity crossflow The analysis is based on laser-Doppler measurements of the time resolved velocity field, which have been carried out for a velocity ratio between the jet and the crossflow of 30, for a Reynolds number based on the jet exit conditions of 60 000 and for an impinging distance of 5 jet-diameters, and provide a basis for better understanding of several related but more complex practical flow fields The results quantify the time-averaged vortex structure developed in this type of flows, as well as the decrease of the Reynolds stresses in the region of strong (stabilizing) curvature, which characterizes the impinging zone, followed by their fast increase before finally decreasing The nature of the turbulent transport of Reynolds stresses is analysed and the related implications for the calculation of complex turbulent flows is discussed

NOMENCLATURE

- D - Diameter of jet nozzle
- H - Height of crossflow channel
- k - Turbulent kinetic energy, $k \equiv 3/4 (\overline{u'^2} + \overline{v'^2})$
- Re - Reynolds number based on jet exit conditions
- U - Horizontal velocity component, $U = \overline{U} + u'$
- V - Vertical velocity component, $V = \overline{V} + v'$
- X - Horizontal coordinate (positive in the direction of the crossflow)
- Y - Vertical coordinate (positive in the direction of the jet flow, i e , downwards)
- Z - Transverse coordinate (zero at central plane, positive in the direction towards the lateral walls
- ν_T - Turbulent viscosity

Subscripts

- j - Jet-exit value
- o - Crossflow value

1. INTRODUCTION

The study of a jet in crossflow which subsequently undergoes impigement on a ground plane provides a basis for understanding the essential dynamics of complex practical flow fields, such as those typical of impingement cooling in engineering applications or those beneath V/STOL aircrafts hovering in a headwind In this application the lift jets interact strongly with the ground plane resulting in lift losses, in enhanced entrainment close to the ground (suckdown), in engine thrust losses following re-ingestion of the exhaust gases and in possible aerodynamic instabilities caused by fountain impingement on the aircraft underside These flows contain in general separated regions bounded by a turbulent stream and include short zones of large ccurvature, which impose mean velocity effects on the turbulent field As a result, and according to the analysis of Castro and Bradshaw (1976), there are zones of the flow which do not satisfy the requirements of the thin-shear-layer approximation (e g Bradshaw, 1973) and may be affected by extra rates of strain Our understanding of these phonomena is particular deficient and this limits the extent of fault diagnosis and the development of calculation methods used to simulate and predict flow situations with practical interest These methods should include a turbulence model, which must reproduce the effect on Reynolds stresses development of the large deformation rates expected to occur in impingement regions To achieve these objectives detailed measurements of all the accessible terms in Reynolds stress transport equations should be obtained and discussed This paper is aimed to help to fulfil these requirements and presents a detailed analysis of an impinging jet through a low-velocity crossflow with a considerably small height

Measurements of the velocity characteristics of normal impinging free jets on a flat surface have been reported for relatively large impingement heights, and normally for H/D>10, using either probe and optical techniques as reviewed for example by Araujo et al (1982) Qualitative information on the effect of the impingement height in a confined flow field has only been given by the visualization studies of Sanpalli (1983) Experiments on the aerodynamics of jets through a confined crossflow are much scarcer, and have been reported not only for large impingement heights, but also for low velocity ratios between the jet and the crossflow, Vj/Uo Sugiyama and Usami (1979), Andreopoulos and Rodi (1984) and Shayesteh et al (1985) report hot-wire measurements for ratios H/D higher than 24 and for values of Vj/Uo respectively up to 1 96, 2 and 16 Kamotani and Greeber (1972) present results for H/D=12 and Stoy and Ben-Hain (1973) give pitot-tube measurements for values of H/D of 3 05 and for jet-to-cross-flow velocity ratios up to 6 8 Only Crabb, Durão and Whitelaw (1981) report LDV measurements, including those of the

shear stress, but for values of H/D=12 and for velocity ratios up to 2 3

This paper is one of a series on turbulent impinging jets (e g Barata et al, 1989, Barata et al, 1991) which have been aimed to document the effect of the complicating influences summarized in the paragraphs above so that some of the calculation methods which have proved satisfactory in simple shear layers can be extended with some confidence to complex impinging flows Laser Doppler measurements are reported for a jet Reynolds number of $Re = 6 \times 10^4$, a velocity ratio between the jet and the crossflow of $V_j/U_0 = 30$ and for the jet exit 5 jet diameters above the ground plate The results include mean and turbulent velocity characteristics along the horizontal and vertical directions, and respective correlations, in a plane containing the jet nozzle axis and aligned with the crossflow The measurements are used tc estimate the convection and production terms in the transport equation of turbulent kinetic energy, which are discussed to improve knowledge of the nature of turbulent transport in impinging zones The analysis quantify the extent up to which the size of the existing terms in the transport equations is changed by extra strain rates associated with the flow distortion in the impingement zone, although they do not contain them explicitly

The remainder of this paper includes three sections, which describe the experimental configuration and procedures, present the results and related discussion and summarizes the more important conclusions

2. EXPERIMENTAL METHOD AND PROCEDURE

This section provides information of the flow investigated and of the instrumentation used to obtain the results The error sources associated with the measurements are briefly considered together with assessments of accuracy The arguments associated with these assessments are based on previous experiments and are provided in condensed form Details can be found in Barata (1989)

The experiments were carried out in a horizontal water channel, 1 50 m long and 0 5 m wide, made of perspex, which was built to allow multi-jet impingement experiments with variable blockage ratio, H/D, but in the present study a single jet of 20 mm exit diameter has been used at a fixed impingement height of 5 jet diameters The crossflow duct extends 20D upstream and 55D downstream of the jet entry which is symmetrically located at 12 5D from each side of the wall The jet unit comprises a nozzle with an area contraction ratio of 16 and a settling chamber 0 56mm long, which begins with a flow distributor (with a aperture of 7 degrees) folowed by flow straighteners The facility has a recirculating system whereby both jet and crossflow water is drawn from a discharge tank and pumped to a constant-head tank or supplied to the jet unit via control valves The uniformity of the crossflow was ensured by straighteners and screens

The origin of the horizontal, X, and vertical, Y, coordinates is taken at the centre of the jet exit in the upper wall of the tunnel X is positive in the crossflow direction and Y is positive vertically downwards

The present results were obtained at the vertical plane of symmetry for jet exit mean velocities of 3 m/s, giving rise to Reynolds numbers based on jet exit conditions of 60000 The nozzle exit velocity characteristics resemble those of a potential jet with a centerline turbulence intensity approximately equal to 2% The crossflow mean velocity was 0 1 m/s, corresponding to velocity ratios between the jet and the crossflow of 30 Measurements obtained in the crossflow without the jet have shown that the local turbulence intensity of the crossflow was 18% and that the wall boundary layer in the jet impingement region had an uniform thickness around 10 mm

The velocity field was measured by a dual beam, forward scatter laser velocimeter, which comprised an argon ion laser operated at a wavelength of 514 5 nm and a nominal power around 1 W, sensitivity to the flow direction provided by frequency shifting from acousto-optic modulation (double Bragg cells), a 310 mm focal length transmission lens and forward-scattered light collected by a 150 mm focal length lens at a magnification of 0 76 The half-angle between the beams was 3 4° (4 64° in air) and the calculated dimensions of the measuring volume at the e^{-2} intensity locations were 2 225 and 0 135 mm The horizontal, U and vertical, V, mean and turbulent velocity components were determined by a purpose built frequency counter interfaced with a microprocessor in the way described by Heitor et al (1984) The fluctuating velocity components were also used, together with those at 45°, to compute the local shear stress distribution, $\overline{u'v'}$, as shown by Melling and Whitelaw (1976) Measurements were obtained up to 2 mm from the ground plate with the transmitting optics inclined half-angle of beam intersection and with the scattered light collected off-axis

Errors incurred in the measurement of velocity by displacement and distortion of the measuring volume due to refraction on the duct walls and the change in refractive index were found to be negligible and within the accuracy of the measuring equipment Non turbulent Doppler broadening (systematic) errors due to gradients of mean velocity across the measuring volume, e g Durst et al (1981), may affect essentially the variance of the velocity fluctuactions, but for the present experimental conditions are sufficiently small for their effect to be neglected the maximum error is of the order of $10^{-4}V_j^2$ and occurs on the edge of the impinging jet Systematic errors incurred in the measurements of Reynolds shear stress can arise from lack of accuracy in the orientation angle of the normal to the anemometer fringe pattern and can be particularly large in the vicinity of the zones characterized by zero shear stress For the present experimental conditions, and based on the results of Melling and Whitelaw (1976), the largest errors are expected to be smallar than -2 5%

The number of the individual velocity values used in the experiments to form the averages was always above 10 000 As a result, the largest statistical (random) errors were 1 5% and 3%, respectively for the mean and variance values for a 95% confidence interval following the analysis of Yanta and Smith (1978)

3 RESULTS AND DISCUSSION

The results presented in the following paragraphs include measurements of mean and turbulent velocities, which are discussed together with estimates of the convection and production terms involved in the budget of turbulent kinetic energy The presentation involves the use of profiles, isometric profiles and contours The choice depends on the intention of the figure and no attempt has been made to provide all data with the same uniformity of precision The contours have been drawn using a bi-cubic interpolation between measurements obtained along 11 (eleven) vertical profiles, and 14 (fourteen) horizontal profiles covering more than 300 measurements stations in the region -10<X/D<7 and 0 75<Y/D<4 9 The estimates of the terms in the transport equation for turbulent kinetic energy are approximate because of the error in evaluating the spatial gradients, but the values are sufficiently accurate for establishing the relative importance of the separated terms in the equation The purpose is to assess the importance of extra source terms derived from the large flow distortion in the impinging zone and to examine the implications for calculation schemes

Prior to the detailed measurements the visualization studies of Barata et al (1991-a) have identified the formation of an impingement region characterized by considerable deflection of the impinging jet The flow becomes almost parallel to the ground plate and originates a recirculating flow region far upstream of the impinging jet due to the interaction of the backward wall jet with the crossflow The result is the formation of a ground vortex wrapped around the impingement jet in the way shown in the sketch of Figure 1, which resembles the "horseshoe" vortex structure known to be generated by the

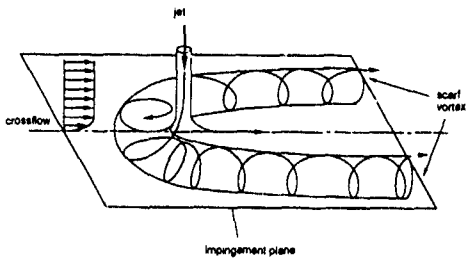

Figure 1 Sketch of flow development for a jet impinging on a flat surface through a low-velocity crossflow

deflection of a boundary layer by a solid obstacle, e g Baker (1981) It should also be noted that the two counter -rotating vortices trailing away from the impingement zone develop in a way indepent of the vortex pair known to exist in a "bent-over" jet in crossflow far from the ground (e g. Crabb et al ,1981, Andreopoulos and Rodi, 1984) The "kidney" shape type of velocity contours found in those situations do not characterize the present impinging jet, which gives rise to a radial wall jet independent of the upstream structure of the impingement zone This flow pattern is created by skewing of pre-existing spanwise vorticity, rather than by the direct action of turbulent stresses, and makes our data particularly interesting to assess the accuracy of calculation methods which should combine the ability to predict the large effects of flow distortion on the turbulence of the impinging zone together with the downstream vortex pair decay

Figure 2 shows the measured mean velocity distribution in the vertical plane of symmetry and identifies respectively i) the impinging jet, which is slightly deflected by the crossflow with the impingement point at X/D = 0 2, ii) the radial wall jets formed after a large distortion of the flow by the impinging plate, and iii) the upstream recirculating flow region noted before due to the interaction of the crossflow with the backward wall jet The flow pattern is peculiar in that it results from the considerably large jet-to-crossflow velocity ratio and small impingement height used throughtout this work As a consequence the influence of the jet exit conditions on the development of the radial wall jet is small and the downstream part of the jet lifts from the ground plane with a maximum inclination of 3 8 ° at X/D = 2 5 The observation is important in that it influences the skin friction and the rate of heat transfer to the ground plate in the practical applications In addition, it can be associated with instantaneous flow separation close to the wall, as dicussed by Walker (1978) for an impinging jet in the absence of crossflow

Figure 3 shows contours of turbulent characteristics and indicates two regions of intense velocity fluctuations, namely the shear layer surrounding the impinging jet and the impingement zone itself Both are located in the zones where the highest mean velocity gradients occur and are associated with near-Gaussian velocity probability distributions suggesting the absence of discrete frequency

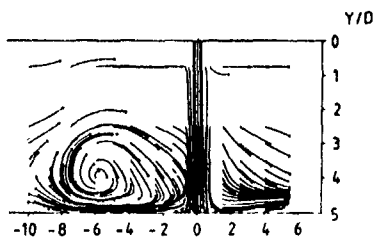

Figure 2. Mean velocity field at the vertical plane of symmetry (i e , Z = 0) for Re = 60 000, V_j/U_0 = 30, H/D = 5 Measured streaklines over 0 2 seconds

oscillations Along the impinging jet, the asymmetry of the distributions of the normal stresses is associated with the comparatively large mean velocity gradient that occurs along the downstream edge of the jet The results show that the turbulent flow is anisotropic in that along the impinging jet, with the exception of the initial potential core, $\overline{v^2}$ is the largest stress with $0.7 \leq \sqrt{\overline{u'^2}}/\sqrt{\overline{v'^2}} \leq 1.0$, while along the wall jets $1.0 < \sqrt{\overline{u'^2}}/\sqrt{\overline{v'^2}} \leq 1.4$

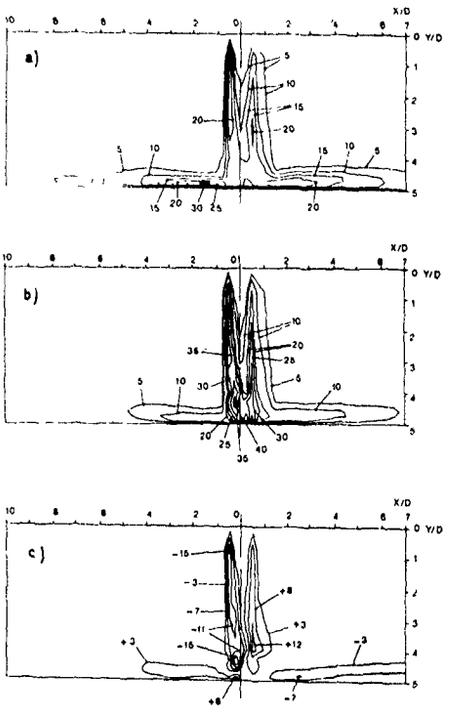

Figure 3 Contours of turbulent velocity characteristics at the vertical plane of symmetry (i e Z = 0) for Re = 60 000, $V_j/U_o = 30$, H/D = 5

a) Variance of horizontal velocity fluctuations, $\overline{u'^2}/V_j^2 \times 10^3$

b) Variance of vertical velocity fluctuations, $\overline{u'^2}/V_j^2 \times 10^3$

c) Reynolds Shear stress $\overline{u'v'}/V_j^2 \times 10^3$

The sign of the shear stress $\overline{u'v'}$ is consistent with the direction of the mean flow, with near zero values at the centre of the impinging jet Away from the impinging zone the sign of the shear stress $\overline{u'v'}$ is related with the sign of the shear strain in accordance with a turbulent viscosity hypothesis, i e $\overline{u'v'} = \nu_T\ (\partial \overline{U}/\partial Y + \partial \overline{V}/\partial X)$, where ν_T is a turbulent viscosity Along the impinging jet the shear strain $\partial \overline{V}/\partial X$ dominates and $\overline{u'v'} = -\nu_T\ \partial \overline{V}/\partial X$, while along the wall jets $\partial \overline{U}/\partial Y > |\partial \overline{V}/\partial X|$ and the shear stress changes its sign and may be represented by $\overline{u'v'} = -\nu_T\ \partial \overline{U}/\partial Y$ Around the impinging point the values of $\partial \overline{U}/\partial Y$ and $\partial \overline{V}/\partial X$ have the same order of magnitude and the "thin shear layer approximation" is (e g Bradshaw, 1973) is no more valid As a consequence, the Reynolds shear stress decrease as expected in the region of high stabilizing curvature, but rise rapidly further downstream with values of $\overline{u'v'}/V_j^2$ higher than those typical of "well-behaved" plane shear layers

We have addressed the question of wether the nature of turbulence has changed owing to the strong stabilizing curvature imposed to the flow by analysing the development of structure parameters, e g Harsha and Lee (1970) Figure 4 a) shows that the correlation coefficient of shear stress falls from values around 0 55 in the shear layer of the impinging jet to values smaller than 0 2 in the impingement zone, but increases again up to 0 5 along the wall jets The distribution of the structure parameter $\overline{u'v'}/k$, figure 4 b), also confirm that the impingement zone is significantly ffected by streamline curvature which increases the shear stress on the upper side and decreases it on the lower side in agreement with the detailed observations of Castro and Brasdshaw (1976) For example, the values of $\overline{u'v'}/k$ plotted along a curved line following the centre of the shear layers bounding the impingement and wall jets fall from around 0 3 to 0 1 in the impinging zone and, then, overshoot again the typical value of 0 3 along the wall jets before decreasing further downstream of the impingement zone All criteria suggest the present impingement zone is characterized by considerable departures from conventional values of dimensionless turbulence parameters, implying unconventional behaviour of the dimensionless "constants" in any turbulence model that is adjusted to fit the data

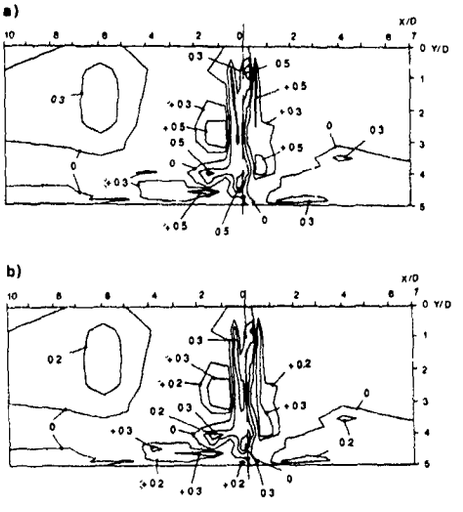

Figure 4. Distribution of turbulence structure parameters at the vertical plane of symmetry (i e , Z = 0) for Re 60 000, $V_j/U_o = 30$, H/D = 5

a) Correlation coefficient for Reynolds Shear stress, Ruv = $\overline{u'v'}/\sqrt{\overline{u'^2}\,\overline{v'^2}}$

b) Ratio between shear stress and turbulent kinetic energy, $\overline{u'v'}/k$

The advection and production terms in the transport equation for turbulent kinetic energy have been calculated from the results obtained in the vertical plane of symmetry and are shown in figures 5

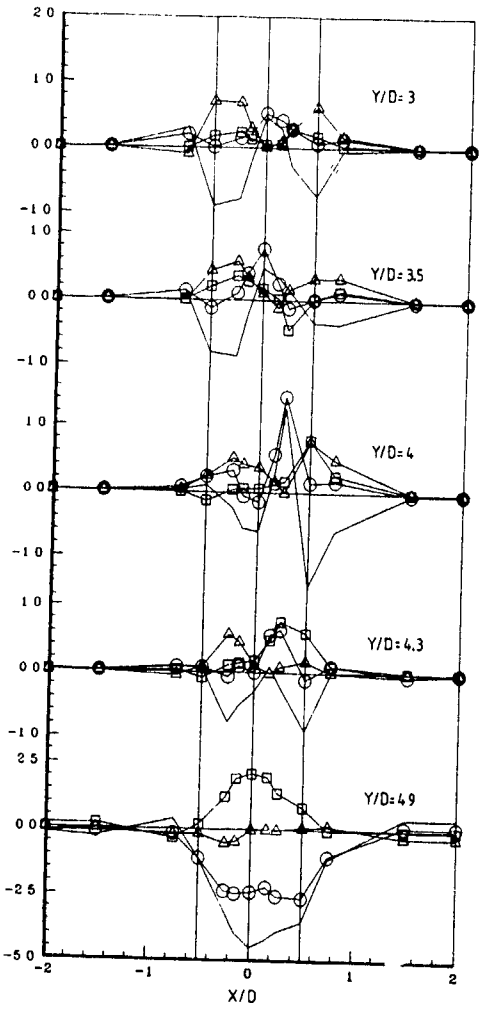

Figure 5. Horizontal profiles of the production and convection terms in the conservation equation for turbulent kinetic energy determined from measurements obtained for Re = 60 000, V_j/U_o = 30, H/D = 5

a) Y/D = 3, b) Y/D = 3.5, c) Y/D = 4.0, d) Y/D = 4.3, e) Y/D = 4.9

KEY: O - Advection $\overline{U}\,\partial K/\partial X + \overline{V}\,\partial K/\partial Y$

□ - Production by normal stresses $\overline{u'^2}\,\partial\overline{U}/\partial X + \overline{v'^2}\,\partial\overline{V}/\partial Y$

▲ - Production by shear stresses $\overline{u'v'}\,(\partial\overline{U}/\partial Y + \partial\overline{V}/\partial X)$

—— Inbalance (diffusion plus dissipation)

and 6, normalized by V_j^3, respectively for five horizontal profiles along the impinging jet and for nine vertical profiles along the upstream and downstream wall jets. The advection term was evaluated assuming that $k = 3/4\,(\overline{u'^2} + \overline{v'^2})$ and is plotted so that a negative value represents a gain of turbulent kinetic energy. The production terms are exact since the transversal derivates vanish at the symmetry plane (i.e., $\partial\overline{V}/\partial Z = 0$) and $\overline{u'w'} = \overline{v'w'} = 0$.

Along the impinging jet, and particularly for Y/D < 3.5, the distributions of figure 5 resemble those for a turbulent free jet (e.g. Tennekes and Lumley, 1972) with production by shear stress has the largest term in the outer edge of the jet and likely to be balance by turbulent dissipation. Along the centre of the jet advection is the largest term, is associated with the spread of the jet and represents a loss of turbulent energy, which is likely to be balanced by turbulent diffusion. With the approach of the impingment zone turbulence production is large and comparatively higher than the largest rate of production by shear stress along the impinging jet, but is through the interaction of normal stresses with normal strain and is comparable with the advection term, which represents a gain of turbulent energy. Turbulent diffusion and dissipation are expected to be large and to balance these terms. This is not surprising given the large distortion of the mean flow in the impingment zone and confirms the likely dominance of extra source terms in the balance of turbulent energy due to streamline curvature. It should be noted that the present analysis has been referred to fixed horizontal and vertical directions similar to those used in any simple calculation scheme aimed to simulate the present flow, and that a more convenient discussion may have to consider a referential following a curved line, as choosen by Castro and Bradshaw (1976). However, for the purpose of this paper the conclusions presented here are valid and can be used to assess the extent up to which current calculation methods for thin shear layers can be extended to simulate complex impinging flows.

The relevance of the present results to the development of engineering calculation methods is that many of the principles used in current schemes for "well-behaved" shear layers and undermined, such as the estimation of a length scale from the shear layer thickness or the gradient-diffusion hypothesis for turbulent transport. Based on the detailed results of Castro and Bradshaw (1976) for a mixing layer bounding a normally impinging plate jet with a irrotational core, one is forced towards the conclusion that a futher level of allowance for history effects on the distortion of the turbulent flow in the impingement zone is necessary, for instance though transport equations for one or more of the empirical constants in engineering models of turbulence. This requires analysis of quantities which are not directly measurable and should involve a more detailed study of length scales in complex flows than we have been able to make in the present case.

The results of figure 6 shows that these features of the flow are limited to the impingement zone and that the budgets of turbulent energy across the radial wall jet resemble those for a conventional wall jet (e.g. Tennekes and Lumley, 1972), with production by shear stress as the largest term and balanced by turbulent diffusion and dissipation (see, for example the profiles X/D = ± 1.5). The decelaration of the radial jet is associated with an increase of the advection term, which represents a gain of turbulent energy and becomes comparable to the rate of production by shear stress at the same vertical station at X/D = ± 4.

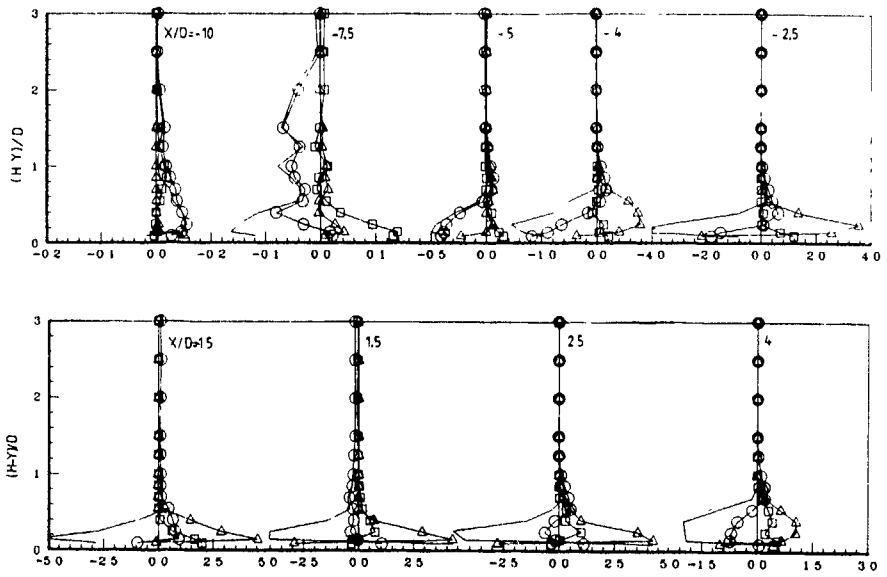

Figure 6 Vertical profiles of the production and convection terms in the conservation equation for turbulent kinetic energy determined from measurements obtained for Re = 60 000, V_j/U_0 = 30, H/D = 5. Symbols as in figure 5

This deceleration process is particularly important upstream of the impinging jet due to the interaction of the backward radial jet with the crossflow, and at X/D = -5 production of turbulent energy across the flow is almost zero and advection is the dominant term, as within other recirculating flows (e.g. Chandrsuda and Braoshaw, 1981). At X/D = -7.5 the approach of the stagnation point associated with the formation of the ground vortex which wrappes around the impinging jet is charactenzed by a fast increase in the production of turbulent energy through the interaction of normal stresses with normal strains. Advection becomes small amd the distribution of figure 6 resembles that for wake flows (e.g. Taylor and Whitelaw, 1984). Again, the observation has important implications for the development of calculation methods because the turbulent structure of the flow in this zone is influenced by the similarity of the normal strains $\partial \overline{V}/\partial X$, and $\partial \overline{U}/\partial Y$, which precludes the use of gradient-diffusion hypothesis for turbulent transport if the length of the ground vortex is to be conveniently predicted.

4. CONCLUSIONS

Laser-Doppler measurements of the flow field created by a single jet impinging on a ground plane through a low-velocity crossflow for Re = 60000, H/D = 5 and V_j/U_0 = 30 have allowed to charactenze the turbulent transport processes typical of impinging flows associated with a large penetration of the impinging jet through the crossflow. The results identify the formation of a fairly thin radial wall jet, which gives rise to a ground vortex wrapped around the impinging jet due to the interaction of the backward radial jet with the crossflow.

The shear layer surrounding the jets is a region of intense velocity fluctuations with maximum values located in the region of highest mean velocity gradients. The sign of the shear stress is consistent with the sign of the shear strain in the sense of gradient diffusion hypothesis, with the exception of the impingement zone and of the stagnation zone associated with the formation of the ground vortex, where it is noted large effects of flow distortion on the tubulence structure parameters that determine the empirical constants in engineering models of turbulence. Inspection of the terms in the conservation equation of turbulent kinetic energy confirms that this behaviour is associated with the interaction between normal sttresses and normal strains. Also, turbulent diffusion and dissipation are likely to be important in the balance of tubulent kinetic energy, particularly in those zones. The evidence suggests that the calculation of complex impinging flows must be found from modelled transport equations rather than from a turbulent-viscosity hypothesis and that allowance for history effects on the distortion of turbulent length scales should be considered.

ACKNOWLEGEMENTS

The expenments were performed at the "Centro de Termodinâmica Aplicada e Mecânica dos Fluídos da Universidade Técnica de Lisboa - CTAMFUTL/INIC". The assistance of Mr. Filipe Carnall in plotting the results is gratefully acknowledge. Thanks are also due to Miss Paula Marques and Miss Marta Neto Pereira for typing the manuscript.

Note: *This paper has been abbreviated by the Editor because it exceeds the given limit of six pages.*

EIGHTH SYMPOSIUM ON
TURBULENT SHEAR FLOWS
Technical University of Munich
September 9-11, 1991

Predictions of a Turbulent Jet Impacting a Flat Surface

M Dianat, M Fairweather and W P Jones*

British Gas plc, Midlands Research Station, Solihull, B91 2JW, England
* Department of Chemical Engineering and Chemical Technology, Imperial College, London SW7 2BY, England

ABSTRACT

A Reynolds stress transport equation model and the k-ε turbulence model have been applied to the calculation of the flow resulting from the orthogonal impact of a circular jet on a solid flat surface. Comparisons of model predictions and measurements made in the radial wall jet region of an impacting air jet demonstrate the superiority of the Reynolds stress transport model In particular, the latter model accurately reproduces mean velocity profiles within the wall jet region, including the magnitude and location of the maximum velocity. As a consequence the spreading rate of the radial wall jet is predicted successfully. None of these flow characteristics is adequately represented by the k-ε model. Predictions of normal and shear stresses also generally confirm the superiority of the higher order turbulence closure.

INTRODUCTION

The impact of a non-reacting, circular jet on a solid flat surface is of interest to many engineering problems. For the case of orthogonal impaction, the flow is axisymmetric and is directed radially outward along the surface giving rise to a radial wall jet. This flow configuration is used in many practical applications to effect cooling, heating and drying, as well as being of importance to the operation of vertical take-off and landing aircraft Of particular interest in the present work, this type of flow is also encountered frequently in assessments of the consequences of gas releases on both onshore and offshore installations involving high pressure pipework and gas handling plant. In addition, such flows are an important test case for the development and validation of mathematical models of turbulent flows since they not only contain both free shear layer and near-wall regions, but also zones of strong, boundary-induced streamline curvature.

Although the case of the turbulent wall jet has received a great deal of attention (Launder and Rodi, 1983), theoretical predictions of the precise flow configuration described above are more rare. However, the main conclusion of the work, in terms of predictions derived using the widely adopted two-equation, k-ε turbulence model (Jones and Launder, 1972), is that the spreading rate in the similarity region of the radial wall jet is generally underpredicted (Malin, 1988) by approximately 25 percent. Sharma and Patankar (1982) did however obtain closer agreement with experimental data by using non-standard values for the k-ε model coefficients. This discrepancy can be attributed to the failure of all turbulence models based on the Boussinesq stress-strain relation to account adequately for the sensitivity of the wall jet to streamline curvature effects induced by the lateral divergence of the flow. The assumption of an effective turbulent viscosity also means that although the position of zero shear stress within the wall jet region is predicted well, the position of the maximum velocity is wrongly predicted since the shear stress does not vanish at the velocity maximum within such flows but at locations closer to the wall Malin (1988) has obtained predictions of the spreading rate of such wall jets by introducing modifications to the k-ε model (Hanjalic and Launder, 1980) to account for the influence of the extra rate of strain, associated with lateral divergence of the flow, on the process of length scale augmentation However, the inclusion of wall-damping effects using the approach of Ljuboja and Rodi (1980) was found to decrease agreement between theory and experiment.

In the present study, predictions of the impacting jet obtained using the standard k-ε turbulence model are compared with those derived through use of a Reynolds stress transport equation model (Jones and Musonge, 1988) in which the influence of streamline curvature arises naturally. Also, because pressure reflections from the wall necessarily impede the transfer of energy from the streamwise direction to that normal to the surface, not just in the immediate vicinity of the surface but also in the outer free shear layer beyond the maximum velocity, the influence of wall-damping terms within the Reynolds stress transport equation model has also been investigated. It is in fact this process which is responsible for both the slower growth rate of the radial wall jet as compared to a free jet, and for the strong sensitivity of the flow to streamline curvature Predictions derived from both turbulence models are compared with experimental data on an impacting air jet obtained by Poreh et al (1967).

MATHEMATICAL MODEL

Governing Equations

Predictions given in this paper were based upon the solution of the ensemble-averaged Navier-Stokes equations using either the k-ε or the Reynolds stress transport equation turbulence model. For solution, the equations were written in a form appropriate to axisymmetric flows but, for reason of brevity, are given below in Cartesian tensor form.

For an incompressible Newtonian fluid, the ensemble-averaged forms of the partial differential equations which describe the conservation of mass and transport of mean momentum may be written as

$$\frac{\partial U_i}{\partial x_i} = 0 \qquad (1)$$

and

$$\frac{dU_i}{dt} = -\frac{1}{\rho}\frac{\partial P}{\partial x_i} + \frac{\partial}{\partial x_j}\left[\nu\left(\frac{\partial U_i}{\partial x_j} + \frac{\partial U_j}{\partial x_i}\right) - \overline{u_i u_j}\right], \qquad (2)$$

with

$$\frac{d}{dt} = \frac{\partial}{\partial t} + U_j\frac{\partial}{\partial x_j} \qquad (3)$$

and where the upper and lower case U's denote the mean and fluctuating components of velocity

respectively, ρ the fluid density, P the mean pressure and ν the kinematic viscosity This set of equations is only closed when the Reynolds stress $\overline{u_i u_j}$ is approximated through the use of a turbulence model.

In the k-ε turbulence model (Jones and Launder, 1972) the Reynolds stress is assumed to be related linearly to the mean rate of strain via a scalar eddy viscosity;

$$\overline{u_i u_j} = \frac{2}{3}\delta_{ij} k - \nu_t \left(\frac{\partial U_i}{\partial x_j} + \frac{\partial U_j}{\partial x_i} \right), \qquad (4)$$

where $k = \overline{u_i u_i}/2$ is the turbulent kinetic energy, $\nu_t = C_\mu (k^2/\varepsilon)$ is the turbulent eddy viscosity and ε is the dissipation rate of turbulence kinetic energy. Values of k and ε are obtained from solution of their modelled transport equations

$$\frac{dk}{dt} = \frac{\partial}{\partial x_j}\left(\frac{\nu_t}{\sigma_k} \frac{\partial k}{\partial x_j} \right) - \overline{u_i u_j} \frac{\partial U_i}{\partial x_j} - \varepsilon \qquad (5)$$

and

$$\frac{d\varepsilon}{dt} = \frac{\partial}{\partial x_j}\left(\frac{\nu_t}{\sigma_\varepsilon} \frac{\partial \varepsilon}{\partial x_j} \right) - C_{\varepsilon 1} \frac{\varepsilon}{k} \overline{u_i u_j} \frac{\partial U_i}{\partial x_j} - C_{\varepsilon 2} \frac{\varepsilon^2}{k}, \qquad (6)$$

where the model constants were taken as $C_\mu = 0.09$, $C_{\varepsilon 1} = 1.44$, $C_{\varepsilon 2} = 1.92$, $\sigma_k = 1.0$ and $\sigma_\varepsilon = 1.3$.

In second moment turbulence closures, the Reynolds stress is obtained directly from solutions of modelled partial differential balance or transport equations. The modelled Reynolds stress transport equation used in the present work may be written as (Jones and Musonge, 1988)

$$\frac{d}{dt}(\overline{u_i u_j}) + \overline{u_i u_l} \frac{\partial U_j}{\partial x_l} + \overline{u_j u_l} \frac{\partial U_i}{\partial x_l}$$

$$= \frac{\partial}{\partial x_l}\left(C_s \frac{k}{\varepsilon} \overline{u_l u_m} \frac{\partial}{\partial x_m}(\overline{u_i u_j}) \right) + A_{ij,1} + A_{ij,2} - \frac{2}{3}\delta_{ij}\varepsilon \qquad (7)$$

where the pressure-strain terms are given by

$$A_{ij,1} = -C_1 \frac{\varepsilon}{k}\left(\overline{u_i u_j} - \frac{2}{3}\delta_{ij} k \right) \qquad (8)$$

and

$$A_{ij,2} = C_2 \delta_{ij} \overline{u_l u_m} \frac{\partial U_l}{\partial x_m} + C_3 \left(\overline{u_i u_j} \frac{\partial U_i}{\partial x_l} + \overline{u_l u_i} \frac{\partial U_j}{\partial x_l} \right)$$

$$+ C_4 k \left(\frac{\partial U_i}{\partial x_j} + \frac{\partial U_j}{\partial x_i} \right)$$

$$- \left(\frac{3}{2} C_2 + C_3 \right) \left(\overline{u_i u_j} \frac{\partial U_l}{\partial x_i} + \overline{u_i u_l} \frac{\partial U_l}{\partial x_j} \right), \qquad (9)$$

and where the model constants were taken as $C_1 = 0.22$, $C_2 = 1.50$, $C_3 = -0.53$, $C_4 = 0.67$ and $C_4' = -0.12$. The turbulence energy dissipation rate is then obtained from solution of the equation

$$\frac{d\varepsilon}{dt} = \frac{\partial}{\partial x_l}\left(C_\varepsilon \frac{k}{\varepsilon} \overline{u_l u_m} \frac{\partial \varepsilon}{\partial x_m} \right) - C_{\varepsilon 1} \frac{\varepsilon}{k} \overline{u_l u_m} \frac{\partial U_l}{\partial x_m} - C_{\varepsilon 2} \frac{\varepsilon^2}{k}, \qquad (10)$$

with $C_\varepsilon = 0.18$, $C_{\varepsilon 1} = 1.40$ and $C_{\varepsilon 2} = 1.90$

Wall reflection effects were incorporated in the second moment closure by including wall corrections in the pressure-strain model according to

$$A'_{ij,1} = C_{w1} \frac{\varepsilon}{k}\left(\overline{u_k u_l} n_k n_l \delta_{ij} - \frac{3}{2} \overline{u_i u_k} n_k n_j - \frac{3}{2} \overline{u_j u_k} n_k n_i \right) f\left(\frac{L}{n_l x_l} \right) \qquad (11)$$

and

$$A'_{ij,2} = C_{w2}\left(A_{kl,2} n_k n_l \delta_{ij} - \frac{3}{2} A_{ik,2} n_k n_j - \frac{3}{2} A_{jk,2} n_k n_i \right) f\left(\frac{L}{n_l x_l} \right), \qquad (12)$$

where n_i is the unit vector normal to the wall and L is a length scale characterising the energy containing motions. The function f reduces the effect of the wall correction with increasing distance from the wall, and was taken as $f = k^{3/2}/(C_w n_i x_i \varepsilon)$ with $C_w = \kappa/C_\mu^{3/4}$ and κ the von Karman constant The constants C_{w1} and C_{w2} were calculated by setting the wall terms (convection and diffusion) terms to zero, i.e local equilibrium, in the equations for thin, two dimensional shear layers and by assuming that only a single component of mean strain is significant These constants were then derived, assuming experimental near-wall values for $\overline{vv}/k = 0.22$ and $\overline{uv}/k = -0.25$, as $C_{w1} = 0.30$ and $C_{w2} = 0.27$

Computational Procedure and Boundary Conditions

The computational results presented below required solution of the full axisymmetric forms of the appropriate transport equations. The equations were solved using a modified, axisymmetric version of a computer program described in detail elsewhere (Fairweather, Jones and Marquis, 1988). The numerical solution method embodied in the program used a cylindrical polar grid and employed a staggered velocity storage arrangement in order to prevent uncoupling between the velocity and pressure fields. A linearised implicit conservative difference scheme was used, with convection terms being approximated by the second order accurate (bounded) TVD scheme originally proposed by Van Leer (1974) and adopted more recently by Zhu (1990). Central differences were

used for all other terms and the resulting quasi-linear algebraic equations were solved using a line Gauss-Seidel method with solution of the velocity and pressure fields being achieved by a pressure correction method (SIMPLE).

The experimental arrangement used by Poreh et al (1967) consisted of a cylindrical chamber from which air was ejected vertically downwards through a circular, sharp-edged orifice, with the jet impacting a horizontal flat surface placed beneath the jet source. This arrangement was approximated for the predictions by the configuration shown in figure 1, where all the experimental results examined below were obtained from a release with a mean exit velocity of 104 ms^{-1}, and with d_j = 51mm and (H-h) = 610mm.

The boundary conditions applied assumed symmetry along the jet centreline and for all surfaces within the computational domain finite-difference solutions were patched onto fully turbulent, local equilibrium wall law profiles. On the impacted surface the matching point was at a fixed distance from the wall for all finite-difference grids and was located at a position corresponding to a value of $y^+ \leq 100$ everywhere. The remaining boundary corresponding to r = constant was treated as an entraining constant pressure surface. In performing the calculations the sensitivity of computed solutions to the positioning of the constant pressure surface and the height h was investigated, and in the results presented below these boundaries were located sufficiently far away from the jet source to have a negligible influence on the flow. Because of uncertainties in the initial conditions, the jet source was assigned mean velocity and turbulence quantities typical of fully developed pipe flow. The validity of this approach was however tested for one particular flow, with U_j = - 113ms^{-1} and d_j = 25mm, for which measurements of mean velocity and turbulence quantities are available in the free jet region mid-way between the jet source and the impacted surface (Tsuei, 1963), with good agreement between theory and experiment being found.

Numerical solutions were obtained using expanding finite-difference meshes of 40 x 26, 75 x 46, 146 x 60 and 146 x 133 in the r and x directions respectively, with the mesh expansion ratio being less than 1.05 in the regions of interest. Results obtained with the four grids suggest that the fine mesh computations were essentially free of numerical error (considered further below).

RESULTS AND DISCUSSION

Calculations performed using both the second moment turbulence closure and the k-ε model indicated that essentially grid independent solutions were obtained using the most refined mesh referred to above. This is illustrated in figure 2 which compares profiles of mean and r.m.s. fluctuating radial velocities through the radial wall jet region, derived using the second moment closure without wall reflection effects, at the position of greatest variation between predictions made using the various grids, i.e. at the largest radial distance from the stagnation point.

Figure 3 compares experimental measurements and predictions of the mean, radial velocity at four radial locations within the turbulent wall jet region. Results obtained using the k-ε turbulence model are seen to overpredict the magnitude of the maximum velocity by as much as 30%, with the position of the peak velocity being unrealistically close to the flat plate. In contrast, the second moment turbulence closure gives good qualitative and quantitative predictions of the velocity profile. In the absence of terms to account for the effects of wall reflection the latter model does tend to slightly overpredict the distance of the peak velocity from the impacted surface; the inclusion of wall reflection terms reduces slightly the deviation between theory and experiment. Both turbulence models also appear to underestimate slightly the mean velocities within the outer regions of the turbulent wall jet.

The k-ε model overpredicts the radial decay of the peak mean velocity and underpredicts the spreading rate of the radial wall jet as shown in figure 4. The rate of decay of peak velocity is, however, in reasonable accord with experimental findings, although the spreading rate of the wall jet appears to be underpredicted by an amount similar to that found by other workers (Malin, 1988). Predictions of the Reynolds stress transport equation model are in much closer agreement with experimental data, particularly when wall reflection effects are included.

Measured and predicted normal and shear stress profiles at the same four radial locations examined above are compared in figures 5 to 8. Overall, there is little to choose between predictions derived using the k-ε turbulence model and the second moment closure without wall reflection effects. The inclusion of wall reflection effects in the latter model does however cause damping of the r.m.s. normal stress perpendicular to the impacted surface resulting in better agreement with experimental data, although as a consequence the remaining two normal stresses are predicted less well. In all cases however, the magnitude of both the normal and shear stresses is overpredicted by the second moment closure, particularly in the outer regions of the wall jet, with similar results being found for k-ε predictions with the exception of the r.m.s. component normal stress. The position of zero shear stress is predicted well by both variants of the second moment closure.

Differences between predictions and experimental data may, however, be to some extent associated with errors in the data. Measurement of local turbulence intensities made within the wall jet were much larger than corresponding intensities found in two-dimensional flow over a plate, pipe flows or circular jets. Values of the local radial turbulence intensity were in fact as high as 0.7 in the outer regions of the wall jet and 0.5 close to the wall (Poreh et al, 1967). The constant temperature, crossed hot-wire anemometer technique used in obtaining mean velocities and both normal and shear stresses within the flow considered is known (Tutu and Chevray, 1975) to be prone to errors when used in such high turbulence intensity flows, resulting, in particular, in Reynolds stresses below actual values. Allowance for such inaccuracies in the measurements considered above would, however, only further confirm the superiority of predictions derived from the transport equation model.

CONCLUSIONS

The k-ε model and a Reynolds stress transport equation turbulence model have been used to predict the flow resulting from the orthogonal impaction of a circular air jet on a solid flat surface. Comparison of predictions with measurements made in the radial wall jet region demonstrate the superiority of the second moment closure, with the transport equation model accurately reproducing mean velocity profiles within this region of the flow and as a consequence the spreading rate of, and the radial decay of maximum velocity in the wall jet. Predictions of normal and shear stresses also generally confirm the superiority of the higher order turbulence closure, particularly when the influence of likely errors in the experimental data used for comparison purposes is taken into account. However, the present comparisons do not provide a rigorous test of the wall reflection model, while it gives reasonable results when the mean flow is parallel to a solid surface it is known to produce undesirable effects in other circumstances. For example, in the vicinity of the stagnation point of the present flow where the mean flow is predominantly towards the solid surface the wall reflection terms quite incorrectly act to augment the fluctuations normal to the wall. To permit a more detailed evaluation of the present and alternative wall reflection approximations further experimental data is needed particularly close to the stagnation point

ACKNOWLEDGEMENT

This paper is published by permission of British Gas plc.

REFERENCES

1. Fairweather, M., Jones, W.P. and Marquis, A J (1988), "Predictions of the Concentration Field of a Turbulent Jet in a Cross-Flow", Combust. Sci. and Tech., 62, 61

2. Hanjalic, K. and Launder, B.E. (1980), "Sensitising the Dissipation Equation to Irrotational Strains", ASME Jl. Fluids Eng., 102, 34.

3. Jones, W.P. and Launder, B.E. (1972), "The Prediction of Laminarization with a Two-Equation Model of Turbulence", Int. J. Heat Mass Transfer, 15, 301.

4. Jones, W.P. and Musonge, P. (1988), "Closure of the Reynolds Stress and Scalar Flux Equations", Phys. Fluids, 31, 3589.

5. Launder, B.E. and Rodi, W. (1983), "The Turbulent Wall Jet - Measurements and Modelling", Ann. Rev. Fluid Mech., 15, 429.

6. Ljuboja, M. and Rodi, W. (1980), "Calculation of Turbulent Wall Jets with an Algebraic Reynolds Stress Model", ASME Jl. Fluids Eng., 102, 350.

7. Malin, M.R. (1988), "Prediction of Radially Spreading Turbulent Jets", AIAA Jl., 26, 750

8. Poreh, M., Tsuei, Y.G. and Cermak, J E. (1367), "Investigation of a Turbulent Radial Wall Jet", ASME Jl. Appl. Mech., 34, 457.

9. Sharma, R.N. and Patankar, S V. (1982), "Numerical Computations of Wall-Jet Flows", Int J. Heat Mass Transfer, 25, 1709.

10. Tsuei, Y G (1963), "Axisymmetric Boundary - Layer of a Jet Impinging on a Smooth Plate", Ph D. Thesis, Colorado State University.

11. Tutu, N.K. and Chevray, R. (1975), "Cross-Wire Anemometry in High Intensity Turbulence", J Fluid Mech., 71, 785.

12. Van Leer, B (1974), "Towards the Ultimate Conservative Difference Scheme. II Monotonicity and Conservation Combined in a Second-Order Scheme", J Comp Phys , 14, 361

13. Zhu, J. (1990), "A Low Diffusive and Oscillation - Free Convection Scheme", Submitted for Publication.

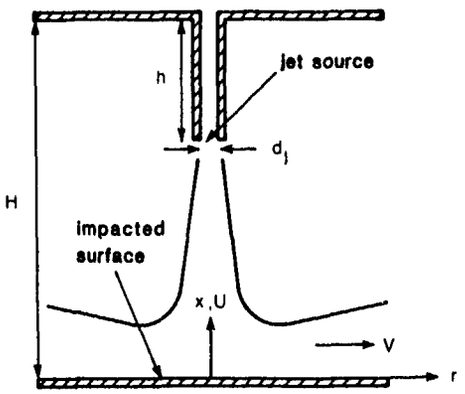

Figure 1. Schematic of a turbulent impacting jet.

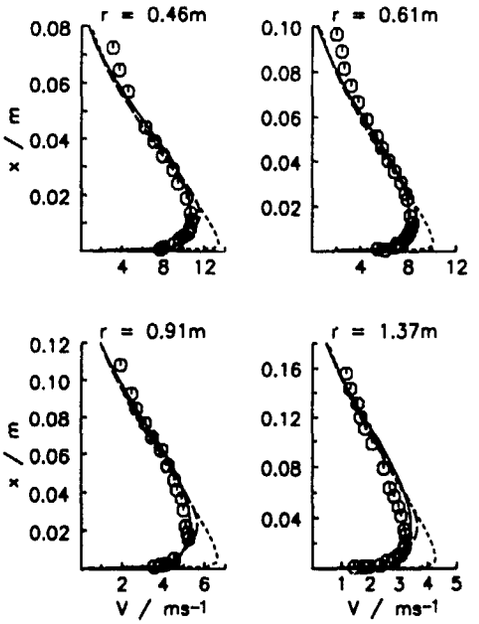

Figure 3. Measured and predicted mean velocity at four radial locations within the wall jet region (o measured, —— predicted second moment closure with wall reflection effects, – – – predicted second moment closure, ----- predicted k-ε).

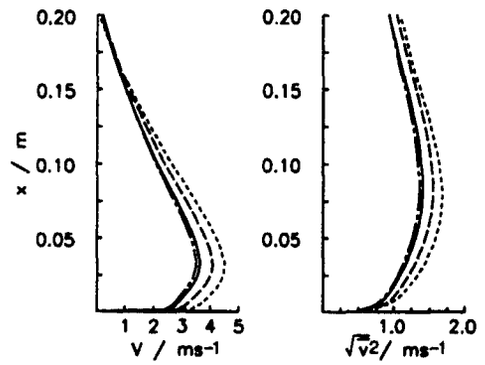

Figure 2. Effect of grid refinement on mean and r.m.s. fluctuating velocities within the wall jet region at r = 1.37m (—— 146 x 133 nodes, —— – —— 146 x 60, – – – 75 x 46, ----- 40 x 26).

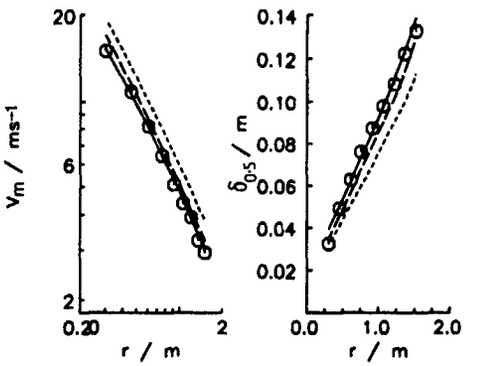

Figure 4. Radial decay of maximum mean velocity and increase in jet mean velocity half-width within the wall jet region (key as figure 3).

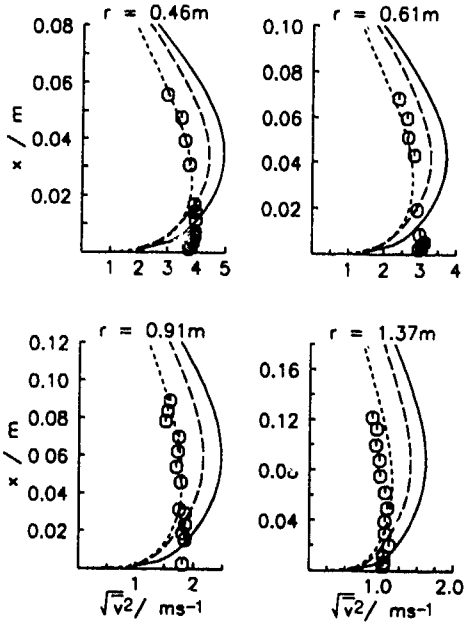

Figure 5. Measured and predicted r.m.s normal stress at four radial locations within the wall jet region
(o measured, —— predicted second moment closure with wall reflection effects, - - - predicted second moment closure, ----- predicted k-ε).

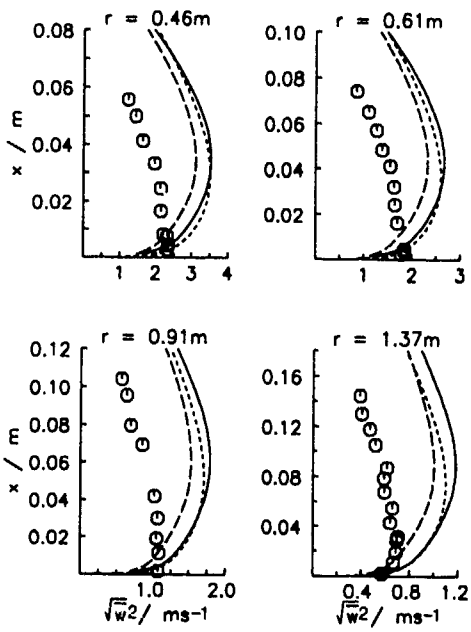

Figure 7 Measured and predicted r m s. normal stress at four radial locations within the wall jet region
(key as figure 5).

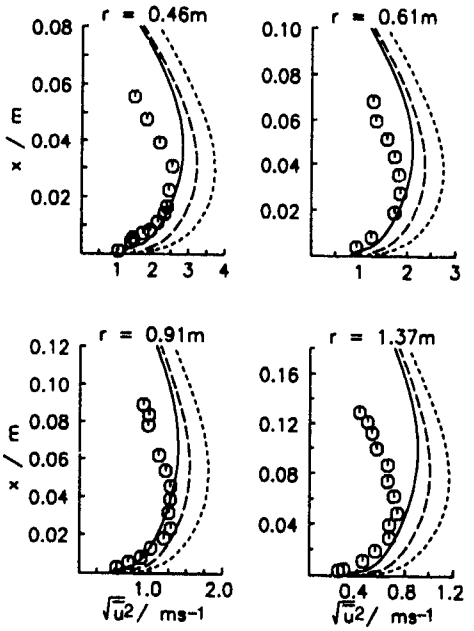

Figure 6. Measured and predicted r.m.s. normal stress at four radial locations within the wall jet region
(key as figure 5).

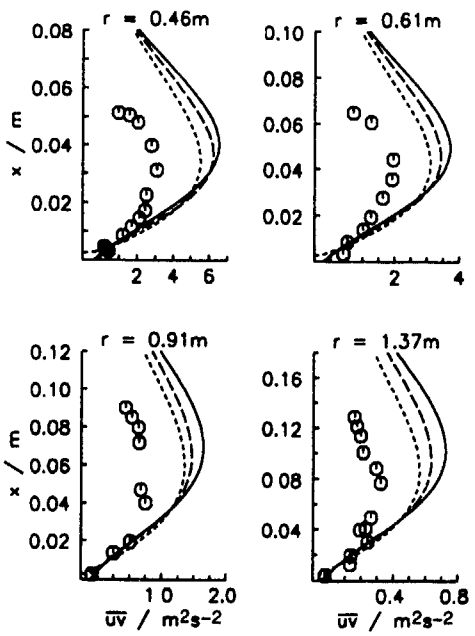

Figure 8 Measured and predicted shear stress at four radial locations within the wall jet region
(key as figure 5).

EIGHTH SYMPOSIUM ON
TURBULENT SHEAR FLOWS
Technical University of Munich
September 9-11, 1991

Computation of Impinging Flows using Second-Moment Closures

T.J. Craft and B.E Launder

Dept. of Mech. Eng., UMIST, P.O. Box 88
Manchester M60 1QD
UK

Abstract

The paper considers the problem of modelling turbulent transport in stagnating jet flows via second-moment closure In the case of colliding jets it is shown that a new model introduced at TSF 7 is more successful than the usually adopted scheme in predicting the high spreading rate of the radial fountain For normal jet impingement against a plane wall it is found that the usually adopted model of pressure-reflection effects gives a correction of the wrong sign in stagnating flows A new version is proposed that gives satisfactory agreement with experiment in impinging strain fields while maintaining the desired form for flow parallel to the surface

1 Introduction

The flow created by the orthogonal impingement of a turbulent jet onto a plane surface is one of considerable interest from both fundamental and practical standpoints It is a configuration that gives rise to very high levels of convective heat transfer coefficients and, thus, is one adopted in numerous industrial heating, cooling and drying processes At a more fundamental level it can be said to be a flow that, while being geometrically simple and easily defined, is emphatically different from a simple shear flow Four major differences from that of a boundary layer flow are worth noting

- a substantial transport of turbulence towards the surface (convective in the outer region, diffusive across the sublayer)
- stress generation near the stagnation point primarily by normal stress/normal strain interactions
- strong streamline curvature
- turbulent velocity fluctuations normal to the wall larger than those parallel to the surface

The first of these is what produces the particularly high levels of Nusselt number, the last, as we shall see later, demands a major rethink of approaches to modelling the role of the wall on the near-surface pressure-strain process.

The impinging axisymmetric jet (together with the related case of a colliding co-axial jet) has thus been selected as a principal flow for guiding the extension of UMIST's second-moment closure for free shear flows (reported at the 7th Symposium on Turbulent Shear Flows [3,4]) so as to be applicable in the vicinity of the wall Parallel research concerning the modelling of channel flow is reported elsewhere in these proceedings [10]

Section 2 details the form of the model for free shear flows and reports the computed behaviour for a pair of colliding axisymmetric jets [11] while the problem of the impinging jet is the focus of Section 3 In both §2 and §3 computational results are also generated with the widely adopted model of Gibson and Launder [6] which we henceforth designate as the "basic" model

Space limitations preclude the possibility of fully reporting numerical aspects of the present research The computations have been made with a version of the TEAM code, an axisymmetric elliptic solver [7] appropriately adapted to incorporate the transport models described in §2 and §3. Grids of up to 100 (axial) × 90 (radial) have been adopted with a concentration of the axial nodes across the viscous sublayer and a concentration of the radial nodes to cover the mixing layer springing from the jet exit Quadratic upstream interpolation has been adopted for mean-flow variables to reduce numerical diffusion It was found that these fine-grid results gave barely perceptible differences from earlier ones obtained with mesh spacings roughly twice as large in regions where property gradients were steepest Results may thus be reasonably regarded as grid independent

2 The Model for Free Shear Flows

The starting point for the present computations is the free flow form of the model whose application to a diversity of homogeneous and inhomogeneous flows was reported at TSF 7 in Stanford [3,4] The transport equation for the Reynolds stress, $\overline{u_i u_j}$, may be written in the symbolic form

$$\frac{D\overline{u_i u_j}}{Dt} = d_{ij} + P_{ij} + \phi_{ij1} + \phi_{ij2} - \varepsilon_{ij} \qquad (1)$$

where the mean strain generation rate, P_{ij}, is handled exactly The dissipation (ε_{ij}) taken as isotropic while diffusive transport (d_{ij}) is modelled by the rudimentary generalized gradient-diffusion hypothesis [5,3] The turbulent (1) and mean strain (2) parts of the non-diffusive pressure interactions in the Reynolds stress ($\overline{u_i u_j}$) budget are represented as

$$\phi_{ij1} = -3\,1(A_2 A)^{1/2}\varepsilon\left(a_{ij} + 1\,2\left(a_{ik}a_{jk} - \tfrac{1}{3}A_2\delta_{ij}\right)\right) - \epsilon a_{ij} \qquad (2)$$

$$\begin{aligned}\phi_{ij2} = {} & -0\,6\left(P_{ij} - \tfrac{1}{3}\delta_{ij}P_{kk}\right) + 0\,3\epsilon a_{ij}\left(P_{kk}/\epsilon\right) \\ & -0\,2\left[\frac{\overline{u_k u_j}\;\overline{u_l u_i}}{k}\left(\frac{\partial U_k}{\partial x_l} + \frac{\partial U_l}{\partial x_k}\right) - \frac{\overline{u_l u_k}}{k}\left(\overline{u_i u_k}\frac{\partial U_j}{\partial x_l} + \overline{u_j u_k}\frac{\partial U_i}{\partial x_l}\right)\right] \\ & -0\,6\left[A_2\left(P_{ij} - D_{ij}\right) + 3a_m\, a_{nj}\left(P_{mn} - D_{mn}\right)\right]\end{aligned} \qquad (3)$$

The numerical coefficients in eq (2) are computer-optimized values while all except the second 0 6 in eq (3) are determined by kinematic constraints [3] Finally ε (the dissipation rate of $k = \frac{1}{2}\overline{u_i^2}$) is obtained from

$$\frac{d\epsilon}{dt} = \frac{\epsilon^2}{k}\left[-\frac{1\,92}{\left(1 + 1\,65A_2^{1/2}A\right)} + 0\,35\left\{\frac{P}{\epsilon} + \frac{\nu_t}{\epsilon}\left(\frac{\partial U_i}{\partial x_j}\right)^2\right\}\right] + d_\epsilon \qquad (4)$$

There are small evolutionary changes in the above model from that reported in [3] that have brought minor improvements to predictions of the test flows considered in that paper

In §3 the question of including 'wall reflection' contributions into the model of the fluctuating-pressure correlations will be examined in order that the impinging jet may be computed However, to provide a test of the model for free flows in an essentially similar strain field to the impinging jet the case of two identical, colliding, axisymmetric jets (shown schematically in Fig 1) is considered. Witze [11] studied such a flow experimentally and found

there were considerable differences between the resultant radial "fountain" and the superficially identical flow produced by a radial nozzle, in particular, the colliding jets lead to a growth of the radial-jet half width of about 0 37, some three times larger than that of the usual radial jet Figure 2 compares the computed and measured growth of the radial jet half width The basic model produces a nearly uniform rate of growth, essentially the same as for the conventional radial jet The present model, however, displays a greatly enhanced rate of growth over the region from 3 to 6 diameters downstream Correspondingly, the development of the centreline mean velocity in Fig 3a is captured with far greater fidelity than with the basic model The origin of the improved behaviour lies in the dissipation rate equation, eq (4) The mean-strain terms herein are only about half as large as in the form of the ε equation adopted in the basic model This, together with the presence of the stress invariants as parameters in eq (4), is why the new form gives values of ε that respond less rapidly to sudden changes in the mean strain field The fluctuating velocity level (Fig 3b) is generally lower with the present model than the basic closure simply because the far too weak spreading rate with the latter produces steeper mean velocity gradients, again experimental data broadly support the new model

Nevertheless, Figure 2 suggests that agreement is not complete At small r/D, in particular, the computed jet width is less than half the measured We suspect the physical reason for this is that high velocity eddy packets approaching the collision plane will centrifuge across to the other side of the flow while low velocity eddies will be rapidly turned, Fig 1 In terms of the stress transport equation, this process gives rise to non-zero values of triple velocity products on the symmetry plane of the radial jet, a feature that is not captured by the very simple model of d_{ij} adopted in the present study The continued high rate of spread beyond 6 diameters downstream that is displayed by the experiment (but not by the computations), may also be a carry-over of the "centrifuging" process occurring in the collision region, that is to say, after crossing the symmetry plane the high-energy packets (Fig 1) will find themselves moving outwards relative to that plane and *will tend to continue in that direction.*

Fortunately, in the case of impingement on to an *impermeable* surface, the physical process discussed in the above paragraph will be absent

3 Model Adaptations for Impinging Near-Wall Flows

3.1 Flow Field Behaviour

This section considers two types of near-wall adaptation: modifications to ϕ_{ij} arising from pressure fluctuations at the wall itself and the handling of viscous influences within the near-wall sublayer Concerning the latter, while strict consistency would require the adoption of second-moment modelling across the viscous sublayer itself, at the time these computations were initiated there was no satisfactory model based on rate equations for $\overline{u_i u_j}$ and ε in this region even for the far simpler case of flow *parallel* to the wall. Accordingly, we have adopted the widely used low-Reynolds-number k ε model of ref [8] to cover the near wall sublayer An amendment to the original form of the ε rate equation is the inclusion of an additional source term S_ε due to Yap [12] (the "Yap correction")

$$S_\varepsilon = 0\,83\frac{\tilde{\varepsilon}^2}{k}\left(\frac{l}{l_e}-1\right)\left(\frac{l}{l_e}\right)^2 \qquad (5)$$

where $\tilde{\varepsilon} = \varepsilon - 2\nu(\partial k^{1/2}/\partial x_j)^2$, a quantity that vanishes at the wall, l is the length scale $k^{3/2}/\varepsilon$ and l_e is the 'equilibrium' near-wall length scale taken as 2 5 times the distance from the wall The effect of the term is to reduce the excessively large length scales that otherwise arise in the viscous sublayer in circumstances where there is a large diffusive transport of k towards the wall. The term has been widely applied in the UMIST group over the past 3 years in separated and three-dimensional wall flows to generally beneficial effect The term is also included in the ε equation employed outside the sublayer (i e in eq (4)) though the effect on the Reynolds stresses there is minor As will be seen later the term exerts a very powerful influence in limiting the level of Nusselt number near the stagnation point

Regarding the handling of wall echo effects in the fully turbulent region, the basic model [6] adopts the following wall reflection terms

$$\phi^w_{ij1} = 0\,5\frac{\varepsilon}{k}\left(\overline{u_k u_m}n_k n_m\delta_{ij} - {}^3/_2\overline{u_k u_i}n_k n_j - {}^3/_2\overline{u_k u_j}n_k n_i\right)\frac{k^{3/2}}{2\,5\varepsilon x} \qquad (6)$$

$$\phi^w_{ij2} = 0\,3\left(\phi_{km2}n_k n_m\delta_{ij} - {}^3/_2\phi_{ik2}n_k n_j - {}^3/_2\phi_{jk2}n_k n_i\right)\frac{k^{3/2}}{2\,5\varepsilon x} \qquad (7)$$

It has been argued [9] that the magnitude of the above terms is unrealistically large because they are partly compensating for weaknesses in the free-shear-flow forms of ϕ_{ij1} and ϕ_{ij2} adopted in the basic model In recent work at UMIST [10,9] only the process ϕ^w_{ij2} has been retained because Brasseur and Lee [2] have shown that the process ϕ_{ij2} is associated with much larger wavelength interactions than ϕ_{ij1} it would thus be the former process that would most "feel" the rigid boundary That is the practice adopted here also

Following [9] we take.

$$\phi^w_{ij} = 0\,3\left(\phi_{km2}n_k n_m\delta_{ij} - {}^3/_2\phi_{ik2}n_k n_j - {}^3/_2\phi_{jk2}n_k n_i\right)\frac{l_n}{0\,8x_n} \qquad (8)$$

where l_n is a length scale normal to the wall $l_n \equiv k\sqrt{\overline{u_p u_q}}n_p n_q/\varepsilon$ and x_n is the distance from the wall $x_k n_k$ (or here simply x)

The impinging-jet test flow selected for consideration is a currently unpublished hot- wire study at UMIST with the jet discharge 2 diameters above the plate, Fig 4 The air delivery pipe is long enough for the flow at discharge to be fully developed, the pipe flow Reynolds number is 23000 Figure 5 compares at $r/D = 1\,0$ (which is typical of the behaviour at other stations) the experimental data with computations for the basic model (including wall corrections eqs (6) and (7)), the present model without wall reflection correction, and the present model with eq (8) as wall correction Without a wall- correction term the present model leads to worse agreement with experiment than the basic model normal velocity fluctuations and turbulent shear stresses too high and consequently a too diffused mean velocity profile results Yet, to our initial astonishment, when the wall correction was added, agreement with experiment became even worse! In fact, the explanation for this behaviour is not difficult to discover Broadly eq (8) impedes the transfer of mean-strain generation into or out of the normal stress perpendicular to the wall In a simple parallel shear flow there is no direct generation in that component and the wall reduces the transfer of energy generation to it that arises from ϕ_{ij2} Hence, as desired, the normal component $\overline{u^2}$ is reduced In an impinging flow, however, the greatest generation rate is in the component normal to the wall and eq (8) hinders the share-out of this generation to fluctuations parallel to the wall It is this that produces the physically spurious behaviour in Fig 4

This anomalous behaviour is intrinsic to eq (8). Evidently a different formulation is needed that will damp the stress component normal to the wall *irrespective* of the strain field From examining all possible combinations of linear products of mean strain, Reynolds stress and unit vectors normal to the wall, the following form was arrived at as one exhibiting broadly the desired behaviour in both a plane channel flow and in the impinging jet

$$\begin{aligned}\phi^w_{ij} = &-0\,044\frac{\partial U_l}{\partial x_m}\overline{u_l u_m}\left(n_q n_q\delta_{ij} - 3n_i n_j\right)f_x\\ &-0\,08k\left(\frac{\partial U_k}{\partial x_m}n_i n_k a_{lm}\delta_{lj} - \frac{3}{2}\frac{\partial U_i}{\partial x_m}n_l n_j a_{lm} - \frac{3}{2}\frac{\partial U_j}{\partial x_m}n_i n_l a_{lm}\right)f_x\\ &+0.6k\frac{\partial U_l}{\partial x_m}n_i n_m\left(n_i n_j - {}^1/_3 n_q n_q\delta_{ij}\right)f_x\\ f_x = &\frac{k^{3/2}}{2\,5\varepsilon x}\end{aligned} \qquad (9)$$

The first line represents a simple redistribution of the turbulence

energy production into components parallel to the wall, whilst the second adds more varied effects The third line is only effective in an impinging flow The results of employing this new wall correction in the impinging jet are shown in Figures 6 8 While the fluctuations normal to the wall, Fig 6, are still rather too large near the stagnation point (r/D = 0 5 and 1 0), there is a very considerable improvement in the overall behaviour As a result of the more accurate shear stress predictions, Fig 7, the mean velocity profile is now also in generally satisfactory accord with the measured data (a feature which serves to confirm the internal consistency of the experimental data)

3.2 Convective Heat Transfer

As remarked in §1, there is considerable practical interest in heat or mass transfer to/from the surface on which the jet impinges Baughn et al [1] have made very careful Nusselt number measurements for dynamic conditions essentially the same as the flow considered in §3 1 The jet temperature is the same as the ambient fluid and a uniform heat flux is applied to the wall Here we compare the measured distribution of Nu with the behaviour predicted by different models

The model for thermal turbulent transport is as follows Across the near-wall viscous layer where the k ε model is applied, we assign a uniform turbulent Prandtl number of 0 9 (the usual value) Over the remainder of the flow transport equations for the turbulent heat fluxes are solved Where the stress field is determined with the basic model, the heat fluxes are obtained from the corresponding model of thermal turbulence [6] With the present dynamic model, we adopt the analogous treatment of the scalar-flux field [3]

$$\frac{D\overline{u_i\theta}}{Dt} = d_{i\theta} + P_{i\theta} + \phi_{i\theta} - \varepsilon_{i\theta} \qquad (10)$$

where the production term $P_{i\theta}$ is handled exactly, $d_{i\theta}$ is represented by the GGDH and the dissipation is assumed isotropic ($\varepsilon_{i\theta}$ = 0) The pressure scalar-gradient correlation is obtained from

$$\begin{aligned}
\phi_{i\theta} = &-1\,7\left[1 + 1\,2(A_2A)^{1/2}\right] R^{1/2}\frac{\varepsilon}{k}\left[\overline{u_i\theta}(1 + 0\,6A_2) - 0\,8a_{ik}\overline{u_k\theta}\right.\\
&\left.+1\,1a_{ik}a_{kj}\overline{u_j\theta}\right] - 0\,2A^{1/2}Rka_{ij}\frac{\partial\Theta}{\partial x_j}\\
&+0\,8\overline{u_k\theta}\frac{\partial U_i}{\partial x_k} - 0\,2\overline{u_k\theta}\frac{\partial U_k}{\partial x_i} + {}^1\!/_3\frac{\varepsilon}{k}\overline{u_i\theta}\frac{P}{\varepsilon}\\
&-0\,4\overline{u_k\theta}a_{il}\left(\frac{\partial U_k}{\partial x_l} + \frac{\partial U_l}{\partial x_k}\right)\\
&+0.1\overline{u_k\theta}a_{ik}a_{ml}\left(\frac{\partial U_m}{\partial x_l} + \frac{\partial U_l}{\partial x_m}\right)\\
&-0\,1\overline{u_k\theta}(a_{im}P_{mk} + 2a_{mk}P_{im})/k\\
&+0.15a_{ml}\left(\frac{\partial U_k}{\partial x_l} + \frac{\partial U_l}{\partial x_k}\right)(a_{mk}\overline{u_i\theta} - a_{mi}\overline{u_k\theta})\\
&-0\,05a_{ml}\left[7a_{mk}\left(\overline{u_i\theta}\frac{\partial U_k}{\partial x_l} + \overline{u_k\theta}\frac{\partial U_i}{\partial x_l}\right)\right.\\
&\left.-\overline{u_k\theta}\left(a_{ml}\frac{\partial U_i}{\partial x_k} + a_{mk}\frac{\partial U_i}{\partial x_l}\right)\right] \qquad (11)
\end{aligned}$$

In eq (11) the time-scale ratio $R \equiv 2\varepsilon_\theta k/(\overline{\theta^2}\varepsilon)$ is obtained by solving rate equations for $\overline{\theta^2}$ and ε_θ, the dissipation rate of ${}^1\!/_2\overline{\theta^2}$ The former may be regarded as exact (save for the GGDH approximation for the diffusion of $\overline{\theta^2}$), while the latter runs:

$$\begin{aligned}
\frac{d\varepsilon_\theta}{dt} &= -\left(2\frac{\varepsilon_\theta^2}{\overline{\theta^2}} + 0\,92\frac{\varepsilon\varepsilon_\theta}{k}\right)\left(\frac{1}{1 + 0\,5A_2^{1/2}A}\right)\\
&\quad + \frac{1\,6}{R}\frac{\varepsilon}{k}P_\theta + \frac{2.6}{R}\nu_t\frac{\varepsilon_\theta}{k}\left(\frac{\partial U_i}{\partial x_j}\right)^2 + d_{\varepsilon_\theta} \qquad (12)
\end{aligned}$$

It is the case that for this flow the level of Nusselt number, particularly near the stagnation point, depends crucially on the distribution of turbulent thermal diffusivity across the sublayer (though this in turn is affected by the Reynolds stress field in the region beyond) The influence of the turbulent heat flux model in the fully turbulent region is by comparison weak For this reason no attempt has been made here to devise a wall correction to $\phi_{i\theta}$ analogous to eq (9)

First it is instructive to note the effect of the Yap correction in the ε equation Fig 9 shows the computed distribution of Nusselt number, employing the present model without wall reflection, with and without the inclusion of the source term, eq (5) Without the term the stagnation point value of Nu is overestimated by a factor of 4 This result is broadly in accord with Yap's [12] experience for heat transfer downstream of an abrupt pipe enlargement The inclusion of the term reduces Nu considerably though the heat transfer coefficient is still too high by 30 60% for values of r/D less than 2 0 Such a departure from the experimental data is to be expected, however, for we have seen in Fig 5 that the level of $(\overline{u^2})^{1/2}$ computed with the basic model is appreciably too high at r/D = 1 whereas at r/D = 2 5 (not shown) it is in reasonable accord with measurements

The computed distribution of the Nusselt number obtained with the present model is shown in Fig 9 Agreement with the measured profile is now considerably closer though for $r/D < 2$ the average value of Nu is still about 15% above the experimental data. This discrepancy can, we suggest, again be attributed to the computed level of $(\overline{u^2})^{1/2}$ being moderately too high in the stagnation region. Indeed, the marked rise in Nu that the experimental data exhibit from r/D = 1 5 to 2.2 is plausibly associated with the measured increase in the level of $(\overline{u^2})^{1/2}$ in this interval. The computations, which fail to predict this rise in Nu, show, consistently, a decrease in the level of $(\overline{u^2})^{1/2}$ over the same interval.

4 Conclusions

The following conclusions may be drawn from this computational study of colliding and impinging jet flows

- The new second-moment closure for free shear flows introduced at TSF 7 performs distinctly better than the widely used basic model [6] in capturing the enhanced spreading rate of the radial fountain arising from the collision of two opposed coaxial jets
- The wall correction to $\phi_{i,2}$ proposed in [6] in fact produces a change in the near-wall Reynolds stress levels *of the wrong sign* in the case of a stagnating flow
- A new version of ϕ_{ij}^w has been developed in the present study (eq (9)) that improves performance in stagnating flows with out detriment to the behaviour in simple shear
- The great importance of the "Yap correction", eq (5), in limiting the near-wall length scale and thereby avoiding excessive levels of Nusselt number in the vicinity of the stagnation point, has been confirmed

Acknowledgements

The research has been supported by AEA Technology (CFD Services) under agreement H2C 4166EMR. Thanks are due to the contract monitor Dr N. Wilkes for his interest and encouragement throughout the project. Our appreciation goes also to Mrs J Buckley for her efforts in preparing the manuscript for publication

Authors are listed alphabetically.

References

1. Baughn, J W , Shimizu, S *ASME J Heat Transfer*, **111**, 1096, 1989.
2. Brasseur, J. and Lee, M , Summer Workshop, Center for Turbulence Research, Stanford 1987

3 Craft, T J and Launder, B E , "A new model for the pressure/scalar gradient correlation and its application to homogeneous and inhomogeneous free shear flows", Paper 17-1, Proc 7th Symp on Turb Shear Flows, Stanford,1989

4 Cresswell, R., Haroutunian, V., Ince, N Z , Launder, B E and Szczepura, R T , 'Measurement and modelling of buoyancy-modified, elliptic turbulent shear flows", Paper 12 4, Proc. 7th Symp on Turb Shear Flows, Stanford, 1989.

5 Daly, B J , Harlow, F H *Phys Fluids*, **13**, 2634, 1970

6 Gibson, M M and Launder, B E , *J Fluid Mechanics*, **86**, Part 3, 491, 1978

7 Huang, P G and Leschziner, M A., "An introduction and guide to the computer code TEAM", UMIST Mech Eng Dept, Rep TFD/83/9(R), 1983

8. Launder, B.E. and Sharma, B I , *Letters in Heat and Mass Transfer*, **1**, 131 138, 1974.

9 Launder, B E and Tselepidakis, D P , AIAA Paper 91-0219, 1991

10 Launder, B.E and Tselepidakis, D P , "Progress and paradoxes in modelling the near-wall sublayer", Paper 29-1, Proc 8th Symp on Turb Shear Flows, Munich, 1991

11 Witze, P O "A study of impinging axisymmetric turbulent flows the wall jet, the radial jet and opposing free jets " Ph D. Dissertation, Mech Eng Dept , Univ of California, Davis 1974

12 Yap, C R , "Turbulent heat and momentum transfer in recirculating and impinging flows", PhD Thesis, Faculty of Science, University of Manchester, 1987

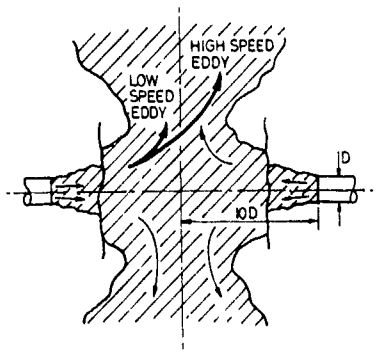

Fig 1 Colliding jet geometry

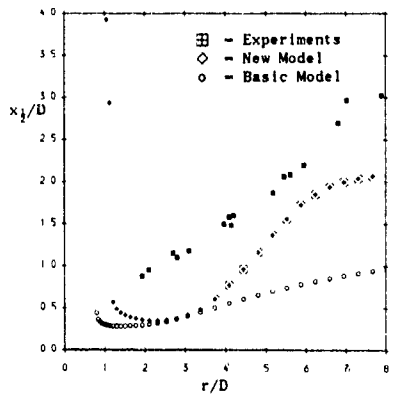

Fig 2· Radial jet half-width

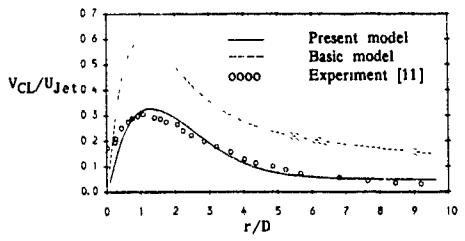

(a)

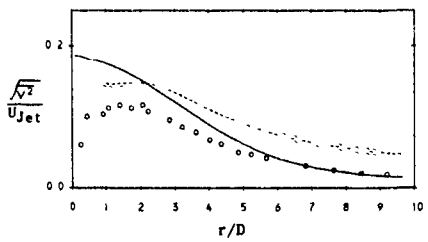

(b)

Fig 3 a) Radial jet centreline velocity
b) Centreline turbulence levels in radial jet

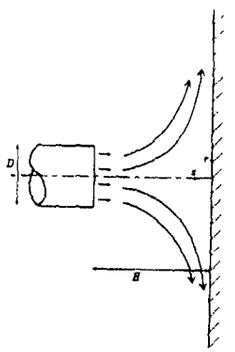

Fig 4 Impinging jet geometry

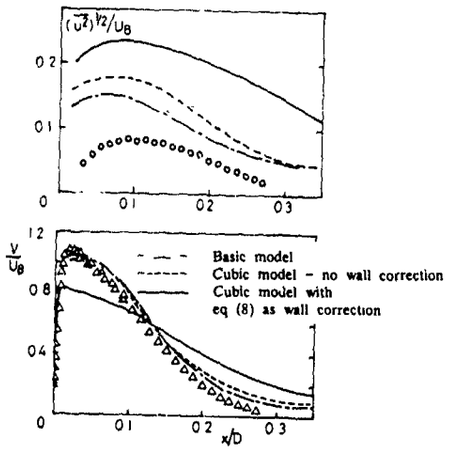

Fig 5 Impinging jet predictions at $r/D = 1$

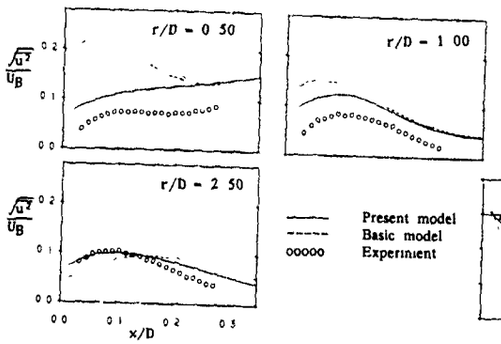

Fig 6 Reynolds stress normal to wall in impinging jet

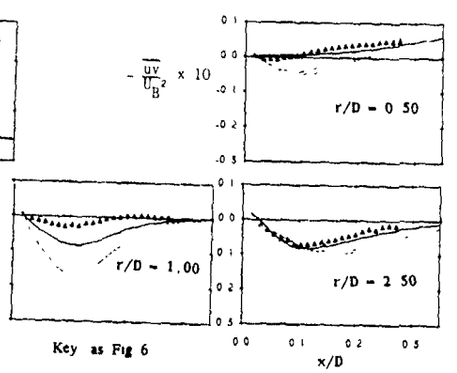

Key as Fig 6

Fig 7 Shear stress in impinging jet

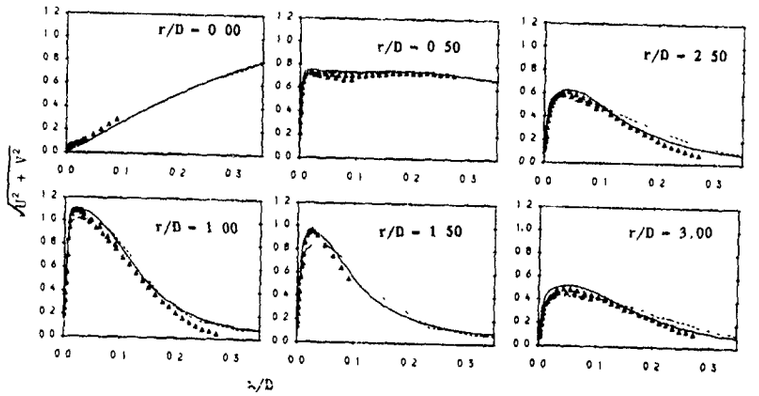

Fig 8 Mean velocity in impinging jet Key as Fig 6

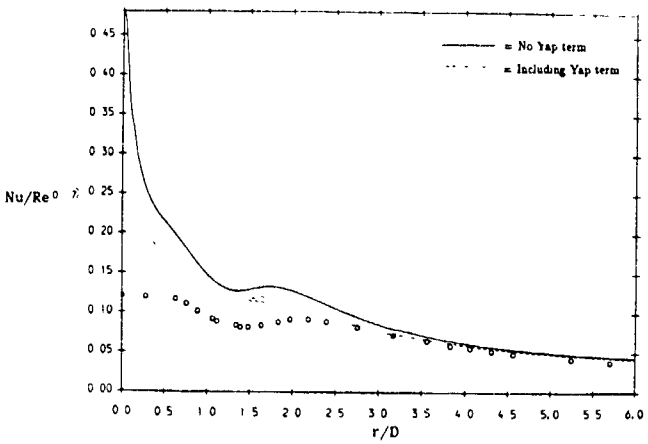

Fig 9 Effect of Yap correction on the Nusselt number

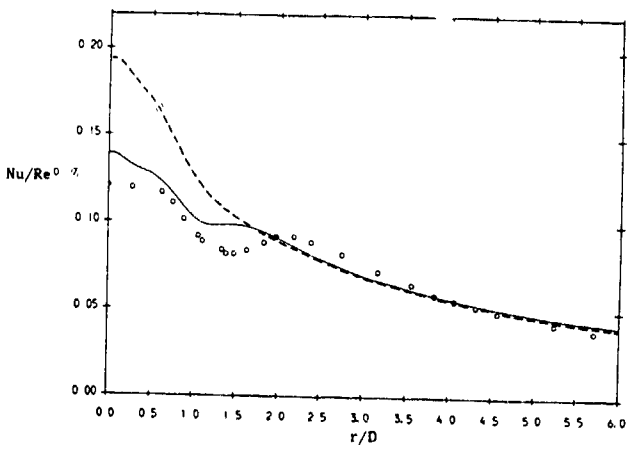

Fig 10 Nusselt number predictions

EIGHTH SYMPOSIUM ON
TURBULENT SHEAR FLOWS
Technical University of Munich
September 9-11, 1991

FAR-FIELD TURBULENCE STRUCTURE OF THE TIP VORTEX SHED BY A SINGLE RECTANGULAR WING

William J Devenport and Gautam Sharma
Department of Aerospace and Ocean Engineering
Virginia Polytechnic Institute and State University
Blacksburg, Virginia 24061, U.S.A.

ABSTRACT

The tip vortex shed by a single rectangular NACA 0012 wing is being studied. Helium bubble flow visualizations and extensive hot-wire velocity measurements have been performed over a wide range of conditions with the intent of revealing the far-field turbulence structure of this flow.

At all conditions the vortex appears insensitive to probe interference and relatively stable. Some very low frequency (fc/U_{ref} = 0.005) lateral motions are present but these have an amplitude of less than ±5% of the wing chord. These motions dominate turbulence measurements made close to the vortex center. Away from the center the effects of the motions are much smaller, however, and the true turbulence structure is visible. This is dominated by the wing wake which forms a spiral around the core.

INTRODUCTION

Surprisingly little is known about the far-field turbulence structure of wing-tip vortices despite the fact that it is important to many applications. This lack of knowledge is a result of the fact that tip vortices generated in wind tunnels tend to be unstable (see Baker et al. (1974), Lee and Schetz (1985) for example) and sensitive to probe interference (see Gasparek(1960)). Useful velocity and turbulence measurements are thus often impossible to make. One solution to this problem has been to make measurements on the wakes of full-scale aircraft (see review by Donaldson and Bilanin (1975)). However, such work is difficult and usually does not yield turbulence measurements. Another solution has been to use a split wing configuration. Here a vortex is generated at the junction between two wings placed tip to tip at equal and opposite angles of attack. Although this type of vortex appears more stable than that produced by a single wing it does not have the same initial turbulence or mean-flow structure, since it is produced by the roll-up of two shear layers rather than one, and is presumably influenced by the wake of the nacelle that is commonly used to join the two wing tips. The turbulence structure of vortices generated in this way have been studied by Phillips and Graham (1984) and Bandyopadhyay et al. (1990).

A possible exception to the problems of stability and sensitivity in wind-tunnel generated vortices lies in the work of Mason and Marchman (1972). They made mean-velocity measurements using a 5-hole yaw probe on a tip vortex generated by a single rectangular NACA 0012-section wing placed in the Stability Wind Tunnel at Virginia Tech. Their results suggest that this particular vortex was comparatively stable and insensitive to probe interference.

The aim of the present investigation is to make detailed measurements of the turbulence structure and spectral properties of Mason and Marchman's vortex over a range of conditions. The investigation has three parts consisting of,

(i) helium bubble visualizations to examine the stability and sensitivity of the vortex,

(ii) single-point measurements of mean-velocities, Reynolds stresses and spectra,

(iii) two-point measurements of correlations and spectra.

This paper describes some of the results of parts (i) and (ii).

Turbulence measurements made in this investigation are to be used to improve methods for the prediction blade-wake interaction noise in helicopter rotors (Glegg (1989)). This is of special interest to NASA Langley who are sponsoring this work under grant NAG-1-1119.

APPARATUS AND INSTRUMENTATION

Only abbreviated descriptions are given here, for full details see Sharma (1991) and Devenport and Sharma (1990).

Wind tunnel

Experiments were performed in the Virginia Tech Stability Wind Tunnel. This closed-circuit facility is powered by a 600 horsepower axial fan. Its test section (figure 1) has a square cross section (1.83m x 1.83m) and a length of 7.33m. Flow in the empty test section is closely uniform and has a very low turbulence intensity (<.05%, see Choi and Simpson (1987)). One wall of the test section has a number of plexiglas and glass windows through which observations may be made.

Wing model

Mason and Marchman's (1972) wing was used. This has a rectangular planform, a NACA 0012 section and a blunt wing tip. The chord and span are .020m and .122m respectively. It is made from solid brass. The wing was mounted vertically at the middle of the test section (figure 1), the root being bolted to a turntable assembly flushed into the upper wall of the wind tunnel. The turntable allowed the wing to be rotated to any angle of attack about its quarter chord location. To eliminate possible unsteadiness and non-uniformity resulting from natural transition, the boundary layer on the wing was tripped. For flow-visualizations 19mm-wide strips of 120-grade sandpaper were glued to both sides of the wing, with their leading edges at the quarter-chord location. For velocity measurements 0.5mm-diameter glass beads were glued to the wing in a random pattern, covering a strip extending from the 20% to 40% chord locations with an average density of 200 beads/cm^2. A few velocity measurements were also performed with no trip.

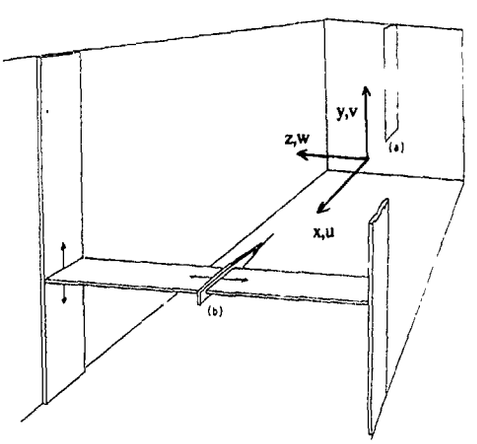

Figure 1. Schematic of the Stability Wind Tunnel test section showing the wing (a), traverse gear (b) and coordinate system.

To eliminate flow-induced vibration the wing was braced at its mid span with two pairs of 2.4mm-diameter steel cables stretched horizontally between the wing and the two side walls of the wind tunnel (figure 1). These cables were covered with a 4.8-mm thick shroud of airfoil cross section to minimize and stabilize their wakes.

The wing was initially placed at zero angle of attack, with an accuracy of about $\pm 0.1^{\circ}$, using a removable wing tip containing 48 static pressure taps. Other angles were then measured relative to this position.

Flow-visualization equipment

Flow visualizations were performed using a Model 3 helium bubble generator manufactured by Sage Action Inc. The generator produces helium-filled bubbles from a probe head supplied with soap solution, air and helium. The flow rates of these are controlled by a series of valves. In the present experiments the valve se. ngs were adjusted so that most of the bubbles were lighter than air and would thus centrifuge into the vortex core. Bubbles were injected into the flow by positioning the probe head 0.54m upstream of the leading edge of the wing tip. To minimize flow interference the probe stem was covered by a 22.5-mm thick shroud of airfoil cross section. At no time did the bubble probe have any visible influence on the flow.

A Varian arc lamp (Model P150S-7) supplied by Sage Action Inc. was used to illuminate the bubbles. For most visualizations the arc lamp was mounted in the diffuser section of the tunnel well downstream of the test section. Photographs of the bubbles were taken using Mamiya and Canon SLR cameras with ASA 3200 and ASA 100 color, and ASA 3200 black and white films. Exposure times ranging from 2 to 60 seconds were used.

Hot-wire anemometry

Single, cross and triple hot-wire probes were used. All sensors were operated using Dantec 56C01 and 56C17 anemometer and bridge units interfaced through an Analogic HSDAS-12 A/D converter to an IBM AT compatible computer. The HSDAS-12 can sample 4 channels simultaneously at rates of up to 100kHz per channel. Raw data was linearized and processed on line using an 18-8 laboratories PL1250 array processor and also stored on optical disc cartridges. All probes were calibrated before and after each traverse. Corrections for temperature drift (typically 1 to 2°C per hour) were applied according to the method of Bearman (1971).

A traversing gear mounted in the wind tunnel test section (figure 1) allowed the horizontal and vertical positions of probes to be controlled from the computer. The probe holder, a 23.6-mm diameter steel tube aligned with the free-stream, positioned the tip of the probe approximately 0.84m upstream of the traverse gear. Two 6.2-mm diameter rods were used to offset the axis of the probes from that of the holder by 114mm (see figure 2(b)). Thus the probe holder did not have to be placed in or near the vortex core for the probes to be positioned there.

The single hot-wire probe (TSI type 1210T1.5) was used to measure profiles of mean velocity and turbulence intensity and spectra in the wing boundary layer as it left the trailing edge. The cross and triple hot-wire probes (Dantec types 55P51 and 55P91) were used to measure radial profiles of all mean velocity, Reynolds stress and triple product components in the vortex at 20, 25 and 30 chordlengths downstream of the wing. Auto and cross spectra of all velocity components were also measured at representative radial positions. To obtain these data with the cross hot-wire probe it was necessary to rotate it about its axis in steps of 45°. These rotations were accomplished using a computer-controlled stepper motor located at the downstream end of the steel tube, connected to the probe stem by a shaft, sprockets and a timing belt.

The axial and pitch sensitivity of all sensors of the cross and triple-wire probes were measured and taken into account during the data reduction, see Sharma (1991). We are working on, but have not yet implemented, a direct angle calibration procedure for the triple-wire and corrections for the finite size of the triple wire measurement volume (2.6mm in width).

For cross and triple-wire statistical measurements, between 30000 and 90000 velocity samples (depending on local turbulence level) were taken at each probe position over a total sampling time of about 50 seconds. For spectral measurements, data were collected in 50, 10240-point records at a 30 kHz sampling rate. At selected locations 10240-point records were also measured at a 1 kHz sampling rate.

α°	Re_c	x/c	Trip	Flow vis.	Hot-wire
0	400000	30	Yes		✓
2.5	400000	30	Yes	✓	✓
5	130000	30	Yes	✓	✓
5	260000	30	Yes	✓	✓
5	400000	30	Yes	✓	✓
5	400000	25	Yes	✓	✓
5	400000	20	Yes	✓	✓
5	530000	30	Yes	✓	✓
5	530000	30	No		✓
7.5	400000	30	Yes	✓	✓

Table 1. Angles of attack (α), Reynolds numbers and streamwise positions (x/c) of hot-wire measurements and helium bubble flow visualizations.

RESULTS AND DISCUSSION

Figure 1 shows the coordinate directions (x,y,z) (u,v,w) to be used in presenting results. The origin of the streamwise coordinate 'x' is the leading edge of the wing tip at zero angle of attack. Coordinates 'y' and 'z' are measured from the nominal vortex center. Distances are normalized on the wing chord 'c' and velocities on the nominal free-stream speed U_{ref} measured using a pitot-static probe located in the forward part of the test section. Angle of attack α is measured rotating from the x to the z axis.

Flow visualizations and velocity measurements were performed at Reynolds numbers ($Re_c = U_{ref}c/\nu$) from 130000 to 530000, angles of attack from 0 to 2.5° and streamwise positions (x/c) from 20 to 30. A full list of conditions is given in table 1. Because of the

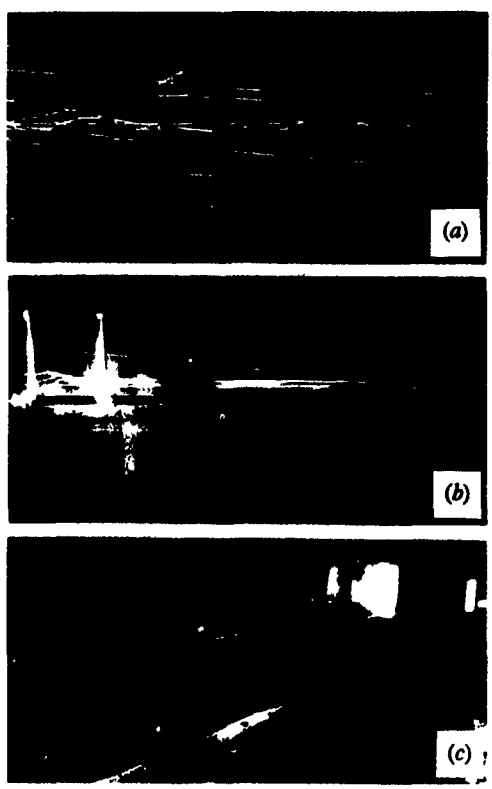

Figure 2. Helium bubble visualizations performed at Re_c = 130000. (a) Side view of the vortex at x/c = 20 with the wing at 5° angle of attack (α). (b) Side view of the vortex at x/c = 30, $\alpha = 5^{\circ}$ in the presence of the dummy probe. (c) View of the vortex from downstream, $\alpha = 7.5^{\circ}$.

volume of results, only a representative sample will be presented and discussed here. Note that some of the velocity measurements listed in table 1 are still in the process of being reduced and analyzed.

Flow visualizations

The purpose of the flow-visualizations was to examine the stability of the vortex and its sensitivity to probe interference. A dummy probe, attached to the traverse gear, was used to simulate the effects of the cross and triple hot-wire probes on the vortex. Photographs were taken with the probe at positions inside and outside the vortex, and traversing through the core at approximately 10mm/s.

Figures 2(a, b and c) are long-time-exposure photographs of the vortex in the presence and absence of the dummy probe at Re_c = 130000. While these photographs have been selected for their clarity, they are representative of the flow patterns seen at all other conditions. In all three pictures the flow is from right to left. Figures 2(a and b) were taken through the transparent side walls of the test section. Figure 2(c) was taken from inside the diffuser looking upstream. Note that these pictures are not instantaneous views of the flow. They are views averaged over the exposure time of 2 or 4 seconds. As a result the paths followed by the bubbles appear as streaks.

The center of the vortex is seen in the photos as a straight line generated by the streaks of the lighter-than-air bubbles passing along it or centrifuging into it. In all the photographs this line appears to have a finite diameter. This is most likely a result of small lateral motions of the vortex core. The extent of these motions may be estimated by comparing the line diameter with the dimensions of the dummy probe. In none of the photographs do the lateral motions appear greater than ±0.047c (± the diameter of the main part of the dummy probe). The frequency of these motions appears to be low since successive bubble streaks along the center of the core are almost parallel (figure 2(a)).

None of the photographs show, and at no time were we able to discern by eye any influence of the dummy probe on the bubble streaks at or close to the probe tip (the measurement point). Figure 2(b) does show some influence of the probe on the bubble streaks, but only well downstream of the tip.

Velocity measurements

Table 2 summarizes measurements made at the wing trailing edge with the single hot-wire probe. Note that, at all but the lowest Reynolds number, the boundary layer leaving both sides of the wing was fully turbulent.

Figures 3 through 6 show mean-velocities, Reynolds stresses and spectra measured with the cross and triple-wire probes during a z-wise traverse through the center of the vortex at x/c = 30, Re_c = 400000, $\alpha = 5^\circ$ with the trip attached. This set of conditions will be referred to as the baseline case. Note that the center of the vortex was located before each traverse by searching for the point of zero mean W and V component velocities. Analysis of the results from the traverses themselves suggests that the vortex center was located with an accuracy of better than ±2mm (±0.01c).

In the vicinity of the vortex center (figure 3(a)) the mean-velocity field much as would be expected given the results of Mason and Marchman (1972). The tangential velocities associated with the vortex are clearly visible in the W component profile. These increase to a peak at the edge of the vortex core, which appears to have a diameter of about .09c. The small core size is circumstantial evidence for the relative stability of the vortex and its insensitivity to probe interference. The U profile shows an axial velocity deficit of about $0.12U_{ref}$ here. The normal and shear stress profiles (figures 3(b and c)) are dominated in this region by a strong central peaks. v^2/U_{ref}^2 and w^2/U_{ref}^2, by far the largest normal stresses, reach peak values of 0.019 (14% turbulence intensity) and 0.012 (11% turbulence intensity). $-\overline{vw}/U_{ref}^2$, by far the largest shear stress, reaches a value of 0.006.

α°	Side	Re_c	δ/c	State
0	S	400000	0.044	Turb.
	P		0.044	Turb.
2.5	S	400000	0.049	Turb.
	P		0.040	Turb.
5.0	S	130000	0.05[illegible]	Trans.
	P		[illegible].034	Trans.
	S	260000	0.052	Turb.
	P		0.038	Low Re Turb.
	S	400000	0.052	Turb.
	P		0.037	Turb.
	S	530000	0.055	Turb.
	P		0.037	Turb.
7.5	S	400000	0.069	Turb.
	P		0.034	Turb

Table 2. Boundary-layer thickness (δ) and state at the wing trailing edge with the trip at various angles of attack (α). (S) - suction side, (P) - pressure side. State inferred from mean-velocity and turbulence intensity profiles.

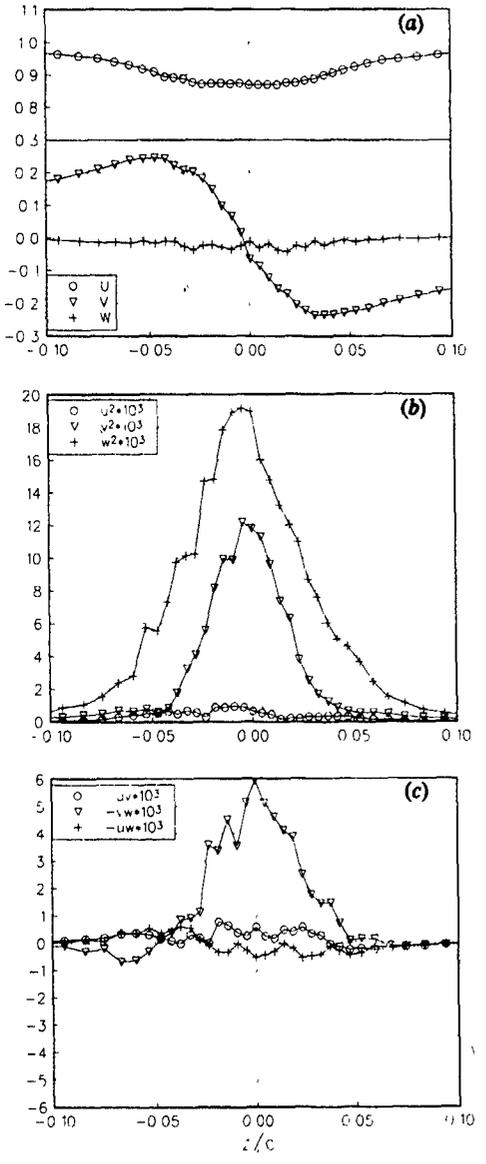

Figure 3. Velocity profiles measured with the cross-wire probe in the vicinity of the vortex core normalized on U_{ref}. Baseline case. (a) Mean velocities. (b) Reynolds normal stresses. (c) Reynolds shear stresses.

These large stresses are quantitatively and qualitatively consistent with the small lateral motions of the vortex observed in the flow visualizations and the steep W gradient in the core. They are clearly not representative of turbulence structure. The fact that v^2 and w^2 are not equal and $-\overline{vw}$ is not zero at the vortex center indicates, surprisingly, that the motions are not isotropic but have a preferred direction.

The effects of the vortex motions can also be clearly seen in velocity power spectra measured at the vortex center (figure 4). These spectra are plotted in terms of non-dimensional frequency fc/U_{ref}, where f is in Hertz. Because of the implied scales it is unlikely that turbulent velocity fluctuations are associated with frequencies much below $fc/U_{ref} = 2$. However, this is where the spectra contain the vast bulk of their energy. The peak frequency of the vortex motions responsible for this energy is remarkably low - about 0.005. This implies a streamwise length scale of about 200 chord lengths (40m). Corresponding cross spectra show a strong coherence between V and W velocity fluctuations between $fc/U_{ref} = 0.001$ and 0.1. This is consistent with the anisotropy of the motions apparent in the Reynolds stresses. While the distinction between the unsteadiness and turbulent parts of the spectra plotted in figure are not that clear, it seems likely that most of the energy above $fc/U_{ref} = 2$ is a result of turbulent fluctuations. Reprocessing the raw data using a filter to extract this energy it may be one way to deduce the Reynolds stresses associated with the true turbulence structure of the core.

Away from the vortex center the effects of the motions are smaller and the true turbulence structure is visible (figure 5). However, this structure is somewhat different from that we had expected. Here the measurements show two, if not three, distinct half turns of the wing wake as it spirals around the vortex. These appear as peaks in the normal- and shear-stress profiles (figures 5(b) and (c)) and inflections and depressions the W and U profiles (figure 5(a)) respectively, centered at z/c = +.75, -.31 and +.19. In contrast to the results and discussions of previous workers studying split-wing vortices (in particular of Phillips and Graham (1984)) there appears to be little or no region surrounding the core where successive turns of the wing wake have merged to form a continuous axisymmetric structure. This may reflect differences in the lift distributions of the wings or, alternatively, may be an important difference between split wing and single wing vortices. Since the former are associated with the roll up of two spiral wakes rather than one we might reasonably expect them to produce a much larger axisymmetric region of merged turbulent flow.

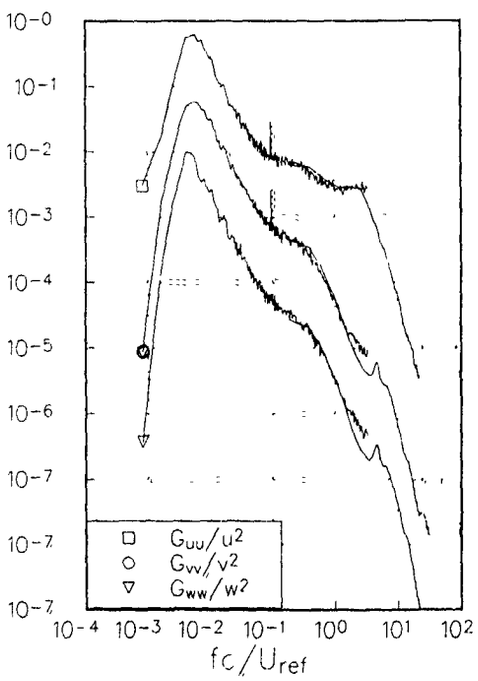

Figure 4. Velocity autospectra measured at the center of the vortex in the baseline case using the triple-wire probe.

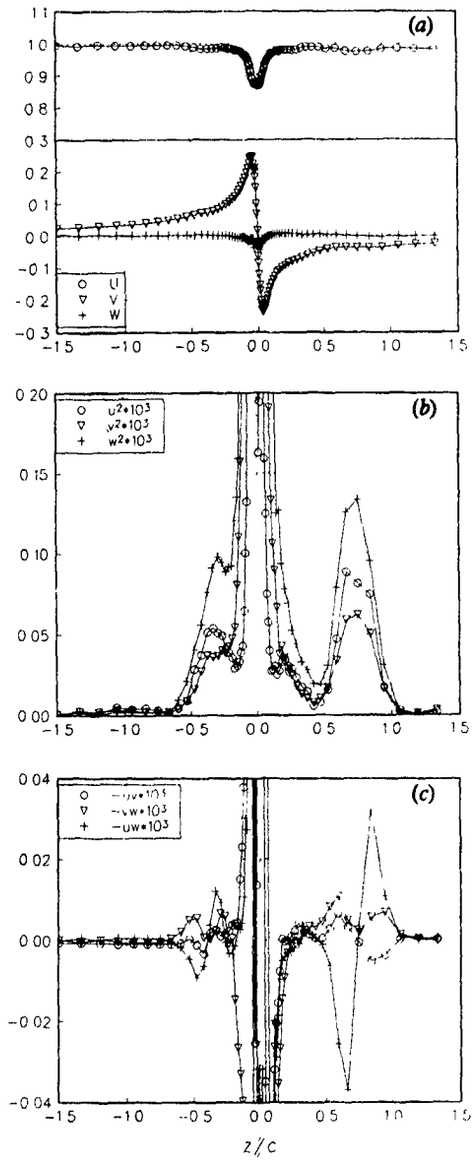

Figure 5. Velocity profiles measured with the cross-wire probe over the entire vortex, normalized on U_{ref}. Baseline case. (a) Mean velocities. (b) Reynolds normal stresses. (c) Reynolds shear stresses.

The behavior of the turbulence stresses in the spiral wake is worth noting. w^2 is easily the largest stress, being typically 1.5 times u^2 and twice v^2. The magnitude of the normal stresses falls by about 40% on each half turn of the spiral. The shear stresses (figure 5(c)), of which $-\overline{uw}$ is the largest, drop even more rapidly. This may indicate that the greater circumferential shear experienced by the wing wake towards the vortex center inhibits the development of, or breaks up, large stress-producing turbulent eddies. This conjecture, however, is not entirely supported by velocity spectra measured in the spiral. Figure 4 shows autospectra of w-component velocity fluctuations measured at x/c=-0.5 and -0.25, to either side of the 2nd half turn of the spiral wake (see figure 5(b)). Note that the discrete peaks in these spectra at non-dimensional frequencies (fc/U_{ref}) above 20 are the result of electrical noise, visible because of the low overall turbulence levels. Despite the substantial difference in turbulence levels at these locations the spectra are almost identical. They both have broad peaks centered at about fc/U_{ref} = 2, corresponding to a streamwise length scale (assuming Taylor's hypothesis) of about c/2, a distance approximately equal to the width of the wing wake at x/c = 30. It is an open question as to whether such large structures truly do exist in this region of high circumferential velocity gradient. Two-point velocity measurements, due to be made in the near future, should be able to answer this question.

Velocity measurements made at other conditions in table 1 reveal a flow structure qualitatively similar to the baseline case. Some quantitative effects are worth noting;

- the core size, as indicated by the mean circumferential velocity measurements, appears almost independent of Reynolds number, angle of attack (i.e. circulation) and wing trip. The increase in core diameter with streamwise position is slow being no more than about 0.006c between x/c=20 and 30.
- the low-frequency unsteadiness of the vortex appears similarly anisotropic at all conditions. It increases in magnitude with distance downstream but appears unaffected by angle of attack. Its variation with Reynolds number is complex, it being greater at Re_c = 130000, and less at Re_c = 130000 and 530000 than at Re_c = 400000.
- the distance between successive half turns of the spiral wake increases with distance downstream and angle of attack, as would be expected. It does not appear influenced by other factors.

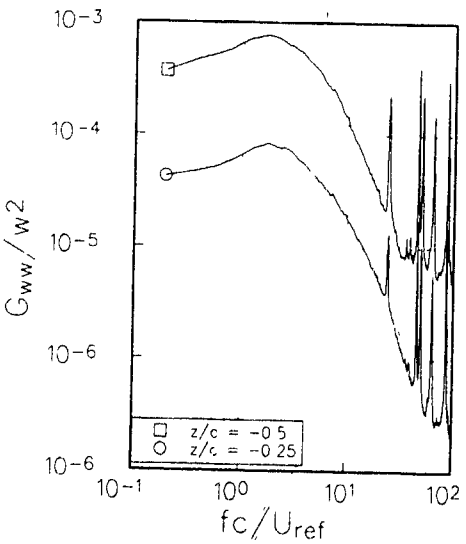

Figure 6. Auto spectra of w component velocity fluctuations measured in the spiral wake with the triple-wire probe. Baseline case. Spectra normalized on w^2.

- turbulence levels in the spiral wake decrease slowly with distance downstream. Otherwise they appear to be strongly dependenc on the properties of the wing boundary layers. Most notably, removing the wing trip at Re_c produced a 60% reduction in turbulence normal stresses in the wake at x/c = 30.

CONCLUSIONS

The tip vortex shed by a single rectangular NACA 0012 wing is being studied. Helium bubble flow visualizations and extensive hot-wire velocity measurements have been performed with the intent of revealing the far-field turbulence structure of this flow. Measurements have been made at Reynolds numbers Re_c from 130000 to 400000, streamwise positions from x/c=20 to 30 and with the wing at angles of attack from 0 to 7.5°.

At all conditions flow visualizations show the vortex to be insensitive to probe interference at the measurement point. It is also relatively stable. Some very low frequency (fc/U_{ref} = 0.005) lateral motions are present but these have an amplitude of less than ±5% of the wing chord. Interestingly, these motions have a preferred direction.

Despite their small magnitude the lateral motions dominate turbulence measurements made close to the vortex center. Mean-velocity profiles, however, clearly show the core which at x/c = 30 has a diameter of about 0.09c. Away from the vortex center the effects of the motions is much smaller and the true turbulence structure is visible. This is dominated by the wing wake which forms a spiral around the core. In contrast to the results of previous workers, there appears to be little or no region surrounding the core where successive turns of the wing wake merge to form a continuous axisymmetric structure. Turbulence shear and normal stresses within the spiral wake fall as the vortex center is approached suggesting that the circumferential shear generated by the vortex inhibits or breaks up the larger stress-producing eddies.

Much of the data taken is still to be reduced and analyzed. Included here are long-time record triple hot-wire measurements at the center and in the outer part of the vortex. These data should reveal the position of the vortex as a function of time, and may ultimately enable us to eliminate the contribution of the vortex motions to the turbulence measurements made in the core.

ACKNOWLEDGEMENTS

The authors would like to thank Allen Roach, Mike Rife, Jeff Zsoldos, Ted Smith and Dr. Stewart Glegg for their help in performing and interpreting these measurements.

REFERENCES

Baker G R, Barker S J, Bofah K K and Saffman P G, 1974, "Laser anemometer measurements of trailing vortices in water", Journal of Fluid Mechanics, vol 65, p 325.

Bandyopadhyay P, Stead D and Ash R, 1990, "The organized nature of a turbulent trailing vortex", AIAA 21st Fluid Dynamics, Plasma Dynamics and Lasers Conference, June 18-20, Seattle, WA. AIAA paper 90-1625.

Bearman P W, 1971, "Corrections for the effect of ambient temperature drift on hot-wire measurements in incompressible flow", DISA Info., vol 11, p 25-30.

Choi K and Simpson R L, 1987, "Some mean-velocity, turbulence, and unsteadiness characteristics of the VPI&SU Stability Wind Tunnel", Report VPI-AOE-161, AOE Dept., VPI&SU.

Devenport W J and Sharma G, 1990, "Flow visualizations of a wing-tip vortex in the presence of a probe", Report VPI-AOE-177, VPI&SU, Blacksburg, VA.

Donaldson C du P and Bilanin A J, 1975, "Vortex wakes of conventional aircraft", AGARD AG 204.

Gasparek E, 1960, "Viscous decay of a vortex", Masters thesis, Syracuse University, NY.

Glegg S A L, 1989, "The prediction of blade-wake interaction noise based on a turbulent vortex model", AIAA 12th Aeroacoustics Conference, San Antonio, TX, April 10-12. AIAA Paper 89-1134.

Lee H and Schetz J A, 1985, "Experimental results for Reynolds number effects on trailing vortices", Journal of Aircraft, vol 22, p 158-160.

Mason W H and Marchman J F, 1972, "Farfield structure of an aircraft trailing vortex, including effects of mass injection", NASA CR 62078.

Phillips W R C and Graham J A H, 1984, "Reynolds stress measurements in a turbulent trailing vortex", Journal of Fluid Mechanics, vol 147, p 353.

Sharma G, MS thesis, VPI&SU, Blacksburg, VA. To be submitted July 1991.

EIGHTH SYMPOSIUM ON
TURBULENT SHEAR FLOWS
Technical University of Munich
September 9-11, 1991

LDV MEASUREMENTS IN THE UNSTEADY TIP-VORTEX BEHIND AN OSCILLATING RECTANGULAR WING

Youxin Zheng and B R Ramaprian

Department of Mechanical and Materials Engineering
Washington State University
Pullman, WA 99164-2920, U.S.A.

ABSTRACT

Data obtained from three-component laser Doppler velocimetry (LDV) in the unsteady tip vortex behind a rectangular NACA0015 wing oscillating sinusoidally in pitch about its quarter-chord axis, are presented. These instantaneous LDV data have been used to obtain information on the distribution of phase locked velocity and vorticity components across the vortex, as well as the phase locked circulation associated with the vortex. Some data on the turbulence intensity in the vortex have also been presented. The data indicate that the oscillating vortex flow is significantly non-quasi-steady. Many of the detailed data obtained in this study are the first of their kind and have been archived for possible future use as a database on unsteady turbulent tip vortex flows.

INTRODUCTION

The study of the structure of the unsteady longitudinal vortex (the so called "wing-tip vortex") in the near wake behind a rectangular wing has important practical applications, notably in helicopter aerodynamics. Flow-visualization studies in steady flow behind a stationary wing have shown that in the near-wake region ($0 < x/c < 1$) of the wing tip, the flow is characterized by the rolling up of the shear layer coming out of the trailing edge, into a spiral. The flow in this region is highly three-dimensional and exhibits strong spatial velocity gradients. A comprehensive project to study the dynamics of this roll-up process in steady and unsteady flows is currently in progress at Washington State University. The results on the steady flow have been reported elsewhere (Zheng and Ramaprian 1991). The present paper reports the results from the unsteady-flow experiments. While there have been several qualitative flow-visualization studies on unsteady wing-tip vortices, such as those of Freymuth (1987) and Freymuth, Finaish and Bank (1985, 1986), and on unsteady three-dimensional flows over wing surfaces such as those of Adler and Luttges (1985), Gad-el-Hak and Ho (1986) and Freymuth (1989), there are no detailed quantitative data on unsteady wing-tip vortices reported in the literature, to the best of our knowledge. Phase-locked measurements of velocity, vorticity and turbulence are reported in this paper. The ultimate objective of the present on-going research project is the understanding of the process of interaction between the longitudinal tip vortex and the spanwise leading-edge vortex under conditions of dynamic stall in three-dimensional unsteady flows. The data can also be used to model the near wake in the wing-tip region more accurately than has been possible in the past.

EXPERIMENTAL DETAILS

The experiments were conducted in a low-speed wind tunnel of test section 1 m × 1 m in cross section. The model tested was a rectangular wing of NACA 0015 profile with a chord (c) of 30 cm and a semispan of 60 cm. The wing was oscillated sinusoidally in pitch about its quarter-chord ($c/4$) axis by a Scotch-Yoke Mechanism driven by a speed-regulated D.C. motor. The mean angle of incidence (α) was 10 degrees. The amplitude ($\Delta\alpha$) and frequency of oscillation (f) were 5 degrees and 1 Hz. respectively. At the test-section velocity (U_∞) of about 8 m/s, this oscillation frequency corresponds to a 'reduced frequency' $k \equiv \pi f c/U_\infty \approx 0.1$, which is relevant to helicopter rotor-blade dynamics. The mean Reynolds number of the flow in the tunnel was about 180,000.

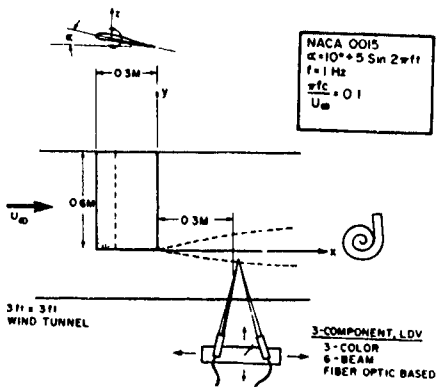

Figure 1 The experimental set up

A three-color, six-beam, fiber-optic based LDV system, mounted on an automated three-dimensional traverse was used to obtain the three components of velocities in the flow field to a resolution of 0.2 mm × 0.1 mm ×0.1 mm. The experimental set-up and coordinate directions are shown in Fig 1.

The seeding for LDV measurements was provided by introducing fine water particles from an ultrasonic humidifier through perforations on the pressure side of the wing surface. Information of the phase angle and instantaneous direction (viz., "up" or "down") of motion of the wing during the oscillating cycle was obtained from an optical encoder (which had a resolution of 4096 parts per revolution) mounted on the pitching axis. This was recorded simultaneously with the velocity signals from the three LDV frequency counters. The instantaneous velocities were subsequently ensemble averaged over a large number of oscillation cycles (ranging from 50 to 500) to obtain phase-locked averages of the flow properties at various phase positions during the cycle. The results presented in this paper were obtained at the downstream location (x) of 30 cm corresponding to $x/c \approx 1$. Measurements were obtained across the vortex (in the $y-z$ plane) at about 500

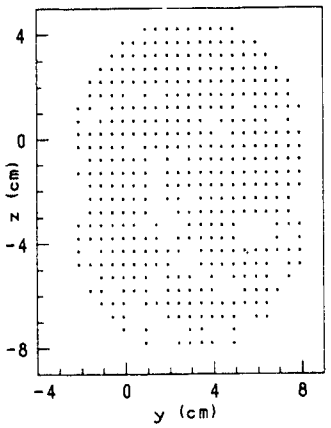

Figure 2 The measurement grid

points which formed a fine grid The grid size and distribution were selected so as to span the region of significant vorticity during the entire oscillation cycle and provide a spatial resolution adequate for the evaluation of the vorticity vector Figure 2 shows the grid used in the present measurements In this paper, the vorticity components ω_y and ω_z have been obtained by assuming $\partial < U > /\partial x$ to be nearly zero This approximation will be dropped as data at several downstream locations become available in the near future

The data from the LDV and the encoder were acquired on an IBM PC based data acquisition system The data were later transmitted over ethernet to a MASSCOMP 5600 computer for processing and display. The data presented in this paper were obtained from a very long experiment, which ran in a fully automated mode for nearly a week

The instantaneous velocity data have been analyzed using the well known principle of double decomposition (see for example, Menendez and Ramaprian 1989) Any instantaneous flow property $\Phi(x, y, z, t)$ is thus represented by

$$\Phi(x, y, z, \alpha, t) = < \Phi > (x, y, z, \alpha) + \phi(x, y, z, \alpha, t) \qquad (1)$$

where $< \Phi >$ is the ensemble averaged or the phase locked component and ϕ the random component of Φ The phase-locked component is obtained by averaging the instantaneous values measured at the same angle of incidence during a number of different oscillation cycles The instantaneous random component ϕ is then obtained from eq (1) The mean square turbulent intensity $\phi'(x, y, z, \alpha)$ is obtained as $[< \phi^2 >]^{\frac{1}{2}}$, where the symbols <> denote ensemble averaging as defined above Note also that by averaging the ensemble-averaged properties over a complete oscillation cycle, one can obtain the time averaged property, $\overline{\Phi}$

RESULTS

The extensive amount of detailed information obtained by processing the LDV data has been stored on tape Only some typical results will be presented and discussed here

Velocity Distribution within the Vortex

Grey level shaded Contours of the phase-locked longitudinal velocity $< U' >$ across the tip-vortex are shown in Figs 3(a) and 3(b) for six typical instantaneous angles of incidence from 5 to 15 degrees. Figure 3(a) corresponds to the "pitch up" situation (increasing α), while Fig 3(b) cor-

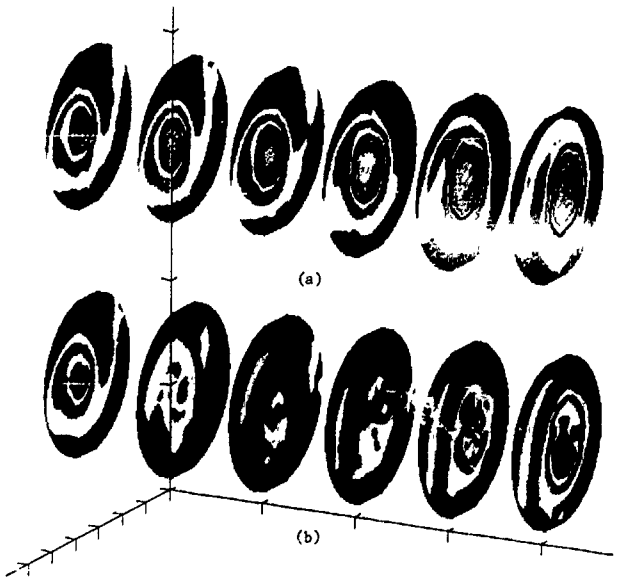

Figure 3 Contours of $< U >$ within the vortex for $\alpha = 5, 7, 9, 11, 13$ and 15 degrees. a)Pitch-up. b)Pitch-down. Minimum contour value is 0.65. Contour interval is .05.

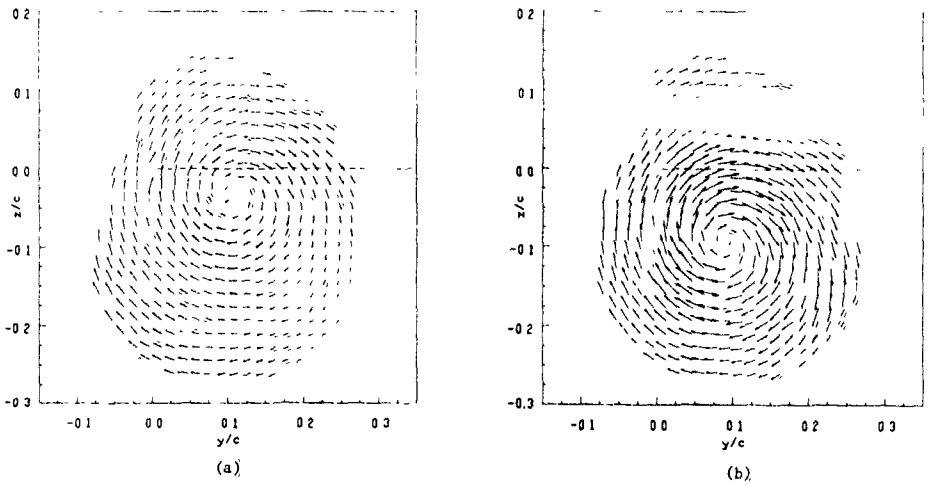

Figure 4 Typical distribution of the cross stream velocity vector ($\vec{j} < V > + \vec{k} < W >$) for $\alpha = 10$ degrees. a)Pitch-up. Maximum magnitude $\approx 0.4 U_\infty$. b)Pitch-down. Maximum magnitude $\approx 0.6 U_\infty$.

responds to the "pitch-down" situation (decreasing α). It is seen that in both cases, the velocity in the interior of the vortex is *generally* lower than in the free stream. However, certain interesting features of the flow are very strongly apparent. For example, it is clearly seen that the decrease of velocity is not monotonic across the vortex from the rim towards the center. Rather, spirals of low velocity can be easily distinguished in the contours, even though in some cases, they are "broken". These spirals correspond to the shear layer from the inboard regions of the flow, which is in a process of rolling up to form the axial tip vortex. One can also notice contours of velocity higher than the local freestream velocity. These are also associated with the flow arriving into the vortex from regions of high velocity in the suction side of the inboard regions of the wing. Another significant feature that can be seen from these figures is the non-quasi-steady nature of the flow, namely, that the flow structure at any given angle of incidence is different for pitch-up and pitch-down situations. In other words, the instantaneous flow "remembers" the wing loading history it passed through. The spiral is far more organized and the flow more nearly axisymmetric during most part of the pitch-up motion than during the pitch-down motion. This difference is due to the fact that during the pitch-up motion the boundary layer over the inboard regions of the wing tends to remain attached to the surface resulting in a wake that is less turbulent and better organized. This shear layer rolls up into the tip vortex. The flow over the wing during the pitch-down motion tends to detach itself from the surface, especially at the larger values of α. This results in a more turbulent and disorganized wake that rolls into the tip vortex. These changes do not, however, manifest neither immediately, nor without distortion at the measuring station. This is due to the lag introduced by the time required for the effects to be convected from the originating regions to the measurement location, as well as due to hysterisis effects. Hence, there is no clear one-to-one correspondence between the results for the pitch-up and pitch-down motions. Also, this non-correspondence cannot be explained as the result of a simple phase shift. This non-quasi-steady behavior of the flow is an important feature that can be observed in all the flow properties studied.

Typical distributions of the phase-locked, cross-stream velocity vectors ($\vec{j} < V > + k < W >$) across the vortex are shown in Figs 4(a) and 4(b). The figures refer to an instantaneous angle of incidence of 10 degrees. Figure 4(a) corresponds to the pitch-up motion of the wing and Fig 4(b) to the pitch-down motion. The magnitude of the cross-stream velocity is shown by the length of the arrow in these figures. The axis of oscillation of the wing is shown by the dashed straight line in each figure. Once again, departure from quasi-steady behavior is clearly seen both with respect to the location of the center of the vortex and the distribution of the velocity vectors across the vortex. The magnitude of the cross-stream velocity vectors was found to be of the order of $0.5 U_\infty$.

From plots like Figs 4(a) and 4(b), one can locate the center of the tip vortex with reasonable accuracy. It was found that the spanwise coordinate of the vortex center essentially remained constant during the entire oscillation cycle at approximately 0.1c in board of the wing tip. The vortex center, however, moved up and down during the cycle. Figure 5 shows the $z-$ coordinate of the vortex center as a function

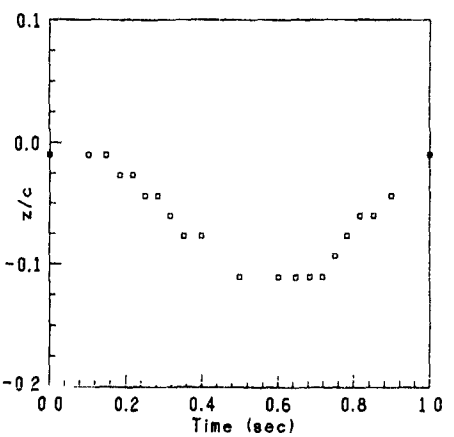

Figure 5 Vertical movement of the vortex center during the oscillation cycle.

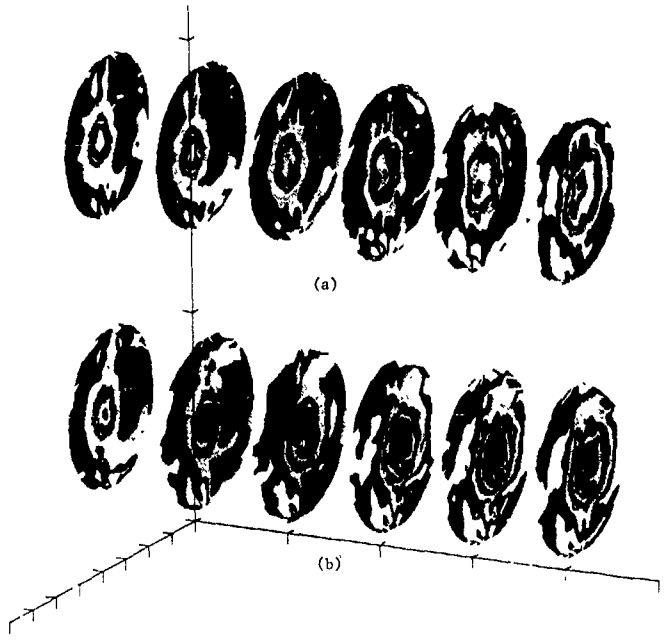

Figure 6 Distribution of $< \omega_x >$ across the vortex for $\alpha = 5, 7, 9, 11,$ 13 and 15 degrees. Minimum contour value is -30 Contour interval is 2.0. a)Pitch-up. b)Pitch-down.

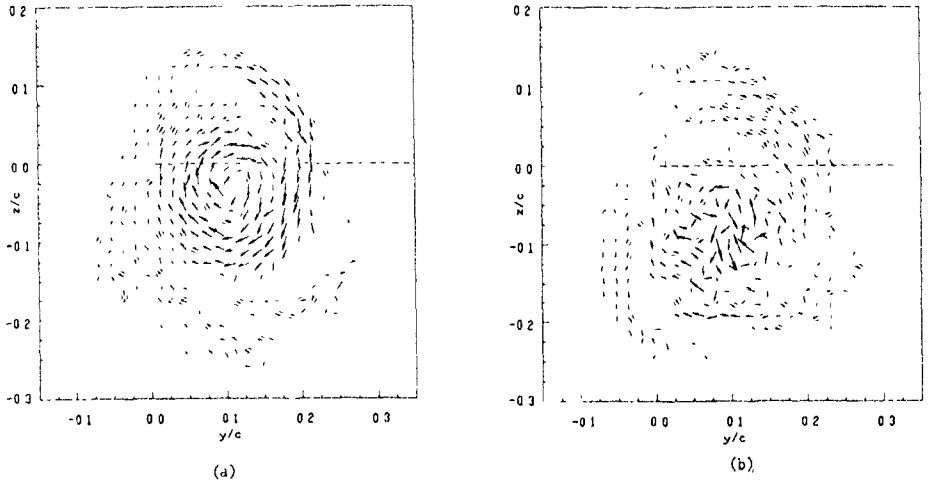

Figure 7 Typical distribution of the cross-stream vorticity vector ($\vec{j} < \omega_y > + \vec{k} < \omega_z >$) across the vortex. $\alpha = 10^0$. a)Pitch-up. b)Pitch-down. Maximum magnitude of vorticity $\approx 0\,2 < \omega_x >_{(max)}$ in both case.

of time during the oscillation cycle While the up and down motion of the vortex center corresponding to a similar motion of the wing tip is expected, it is interesting to note the phase difference between the two motions Also significant is the distortion from the sinusoidal shape in the motion of the vortex center These are further evidences of the non quasi-steady nature of the flow

Vorticity Distributions within the Vortex

The high density of data points obtained in this experiment made it possible to estimate the components of the phase locked vorticity of the flow within the vortex. Some typical results for the evolution of the axial vorticity component ω_x during the pitch-up and pitch-down phases of the oscillating cycle are shown in Figs 6(a) and 6(b) It was observed that nearly 85% of the axial vorticity was concentrated within a radius of the order of 0 1c It is, however, seen that there is a significant distribution of axial vorticity over this radius This distribution is due to viscous and/or turbulent diffusion The maximum (negative) vorticity is observed near the center of the vortex. The magnitude of this vorticity is generally higher, and the vorticity distribution more nonaxisymmetric during the pitch-down motion The non-quasi-steady nature of the flow is thus once again apparent.

As the shear layer from the inboard regions of the wing surface rolls up into the tip vortex, the spanwise vorticity carried by it rotates into the axial direction and augments the axial vorticity of the tip vortex This is clearly seen from Figs 7(a) and 7(b), which show typical plots of the cross-stream vorticity vector $(\vec{j} < \omega_y > + \vec{k} < \omega_z >)$ across the vortex, for $\alpha = 10$ degrees during the pitch-up and pitch down portions of the cycle Once again, the roll-up process resulting in the transfer of the cross-stream vorticity to the longitudinal direction is well organized during the pitch-up process Very little cross stream vorticity is seen in the shear layer during the pitch-down motion which indicates that this layer was detached from the wing surface when it started moving towards the tip

Integration of the axial vorticity over the area of the vortex up to any radius r yields the circulation associated with this vorticity around a circle of that radius Figures 8(a) and 8(b) show typical distributions of the ensemble averaged circulation $< \Gamma >$ as a function of the distance from the vortex center for several angles of incidence during pitch-up and pitch down motions Also shown for comparison in each figure are the distributions of the time average circulation $\bar{\Gamma}$ and the circulation Γ_0 corresponding to the mean angle of incidence of 10 degrees in steady flow There is no spectacular difference between the latter two distributions However, the circulation distribution varies considerably during the oscillation cycle and this variation is significantly non-quasi-steady The circulation during the pitch-down motion is substantially larger than during the pitch-up process. This can be seen by comparing the distributions at a given α, say 10 degrees, during the up and down motions Since the strength of the axial vorte is related to the spanwise distribution of lift over the wing, one can conclude that the latter distribution is quasi-steady during the pitching cycle The circulation has not reached a constant value in som of the distributions at the smaller angles of incidence This is possibly due to the fact that the roll-up of the shear layers at small values of α is slow and hence not complete at this downstream distance The seed particles introduced near the outboard regions of the wing did not spread far enough to allow the measurements to be continued to more inboard locations in the wake (i e , larger values of r)

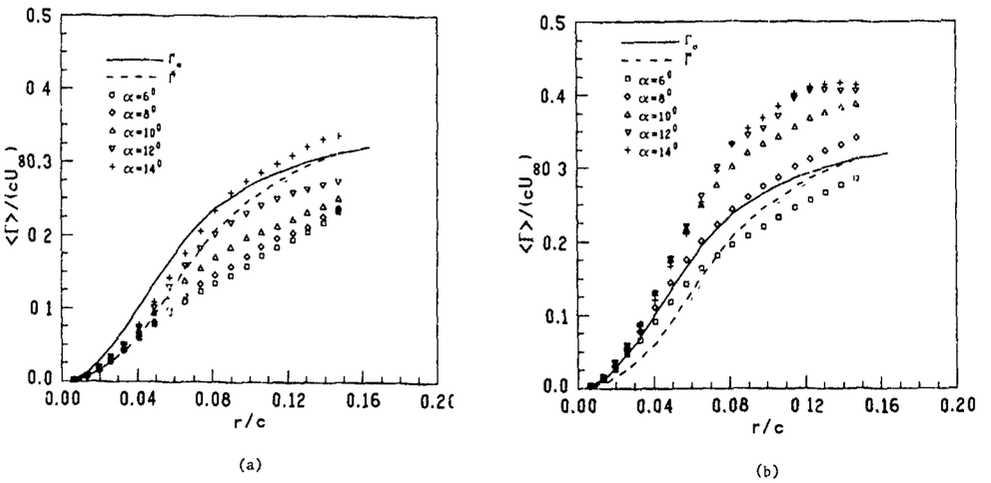

Figure 8 Variation of circulation $< \Gamma >$ with distance r from the vortex center. a)Pitch-up. b)Pitch-down

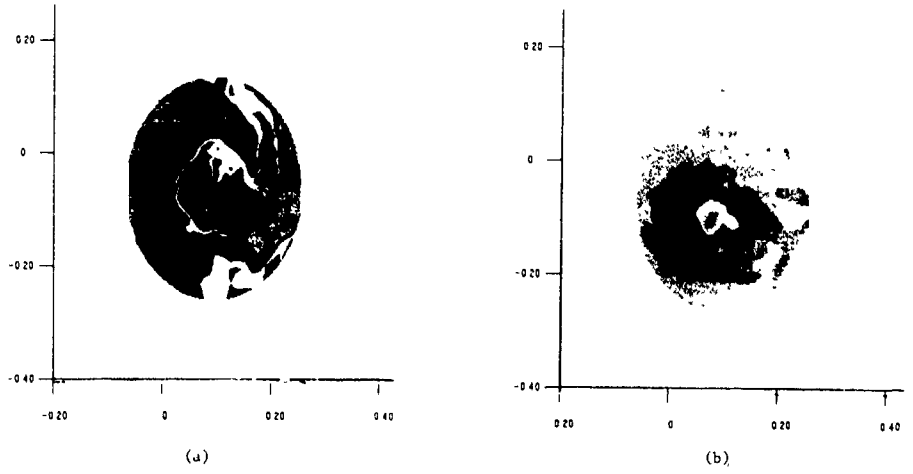

Figure 9 Distribution of turbulent intensity u' across the vortex for $\alpha = 10$ degrees. a)Pitch-up. Maximum contour value is 0 11. Contour interval is 0.01. b)Pitch-down. Maximum contour value is 0.18. Contour interval is 0.02.

Turbulence Intensity in the Vortex

Typical results for the distribution of the rms intensity of turbulence u' across the vortex are shown in the area shaded contours of Figs 9(a) and 9(b) for $\alpha = 10$ degrees The shear layer rolling up into the vortex can be distinguished, in Fig 9(a) corresponding to the pitch-up motion, as a spiral from the relatively higher level of turbulence carried by it The maximum intensity is about 11% and occurs near the center of the vortex The spiral is apparently broken in Fig 9(b) corresponding to the pitch down motion Also, the turbulence level during this part of the cycle is much higher (maximum value of about 18%). These results are consistent with the observations made with regard to the velocity and vorticity data.

CONCLUSIONS

The three-component LDV measurements in the tip vortex of an oscillating wing, obtained at a distance of one chord downstream of the trailing edge have shown that the flow is strongly three-dimensional. While the time-mean flow is not significantly different from steady flow at the mean angle of incidence, the periodic flow is not quasi-steady at the oscillation frequency studied This is due to the non-quasi-steady effects of unsteadiness on the turbulent boundary layer in the inboard planes and the consequent effects on the spanwise lift distribution It will therefore be necessary to use dynamic models to obtain correct predictions of the instantaneous flow The data presented here are probably the first of their kind and will be useful as a database for the development and verification of numerical predictive models

ACKNOWLEDGMENTS

This work was performed under support from the U.S Army Research Office Grants No DAAL03 87-G-0011 and DAAL03-91-G-0026, and U S Air Force Office of Scientific Research Grant No AFOSR-90-0131 The support from these sources is gratefully acknowledged

REFERENCES

Adler, J.N & Luttges, M W 1985 Three-dimensionality in unsteady flow about a wing AIAA Paper No 85-0132.

Freymuth, P 1987 Further visualization of combined wing-tip and starting vortex AIAA Journal, **25**, 1153-1159

Freymuth, P 1989 Visualizing the connectivity of vortex systems for pitching wings J fluids Engrg., **111**, 217-220.

Freymuth, P , Finaish, F & Bank, W 1985 Visualization of wing-tip vortices in accelerating and steady flow J Aircraft, **23**, 9, 730-733

Freymuth, P , Finaish, F & Bank, W. 1986 The wing-tip vortex system in a starting flow ZFW, **10**, 2, 116-118

Gad-el-Hak, M. & Ho, C M 1986 Unsteady vortical flow around three dimensional lifting surfaces AIAA Journal, **24**, 713-721

Menendez, A.N. & Ramaprian, B R 1989 Experimental study of a periodic turbulent boundary layer in zero mean pressure gradient The Aeronautical Journal, **93**, 926, 195-206.

Zheng, Y & Ramaprian, B R 1991 LDV measurements in the roll-up region of the tip vortex from a rectangular wing, AIAA Paper 91-1685

EIGHTH SYMPOSIUM ON
TURBULENT SHEAR FLOWS
Technical University of Munich
September 9-11, 1991

PHASE-AVERAGED TURBULENCE STATISTICS IN A NEAR WAKE WITH AN ASYMMETRIC VORTEX SHEDDING

A Nakayama*) H R Rahai**) and H Unt**)

*) Faculty of Engineering, Kobe University
Rokkodai, Kobe, 657 Japan

**) The Department of Mechanical Engineering
California State University, Long Beach
Long Beach, California, U S A

ABSTRACT

The turbulent near wake of a two-dimensional body influenced by a vortex shedding due to a fixed separation on one side has been measured by a direction-sensitive multi-component split-film probe and the flow characteristics were studied in terms of the phase-averaged statistics of the turbulent velocity components. The contributions to the total apparent shear stress from the periodic motion and the random fluctuation are comparable in one case, but the phase-averaged Reynolds shear stress is fairly well described by a positive eddy viscosity.

INTRODUCTION

It is not yet possible to carry out the direct Navier-Stokes simulation of turbulent flows of at high Reynolds numbers, and, although progress is being made (eg. Le Balleur, 1989), the numerical solutions of the Reynolds equations are still unreliable particularly when there is a separation region of large extent. One of the reasons is that many of these models do not adequately account for the flow unsteadiness when separation is involved The turbulence models must also be examined in these unsteady conditions.

Detailed near wake structures of bluff bodies involving vortex shedding have been investigated by many workers(e.g. Perry & Watmuff(1981), Cantwell & Coles(1983), Kiya & Sasaki(1985), and Perry & Steiner(1987)). These studies are mostly concerned with vortex shedding in otherwise symmetric configurations. However, such flows as the near wake of an airfoil with upper-surface boundary layer separated, imply more one-sided pattern(Nakayama, 1985). Even at high angles of attack, the flow structure is somewhat different from the near wake of symmetric bluff bodies. Perry & Steiner(1987), for example, report that their measurements with inclined flat plate showed the globally-averaged velocity field to be quite different from the theoretically anticipated pattern. Even when the global average shows one-sided separation vortex, the shedding was found alternating. Present experiments were conducted as a step to understand turbulence structures and to provide information for turbulence models under the influence of these asymmetrical vortex shedding-type unsteadiness.

In order to make the flow field easy to model, we chose a configuration that has a fixed separation point. The model is a simple two-dimensional streamline body with a sharp corner on one side that forces a flow separation and flow reversal. This fixed separation made the overall flow condition more stable, but the vortex shedding was less intense than unfixed ones such as that around a cylinder. Our study employs the similar measurement and data reduction techniques used by other investigators of vortex-shedding type wake flows. Since we emphasize the near field where there is instantaneous and mean flow reversals, we have applied the direction sensitive multi-component split-film techniques to measure two simultaneous velocity components. The detailed data were obtained for two cases and were analyzed to reduce the conventional and the phase-averages of fluctuating velocity components.

EXPERIMENTAL METHODS

The geometry of the investigated flow is shown in Fig.1. The model is a 30mm thick 25 cm long wooden board with a variable-length trailing edge piece attached to one side of the aft portion of the body. Fig.1 also shows the arrangement of the field-measurement and vortex-detecting probes.

A special probe shown in Fig.2 that consists of a cylindrical film split into four elements was used to measure the instantaneous velocity components in the center plane of the test flow. Each of the split elements is operated on independent anemometer bridge. If the temperatures of the elements are balanced, two instantaneous components in the plane perpendicular to the sensor axis can be reduced. The magnitude of this velocity component, or the effective cooling velocity is first obtained by inverting the relation between the cooling velocity and the sum of the squares of the outputs of the four elements, which is like the usual King's law of cooling used in the regular hot-film method. Next, the direction of the flow in the plane perpendicular to the sensor axis is determined by finding the direction at which the interpolation of the outputs

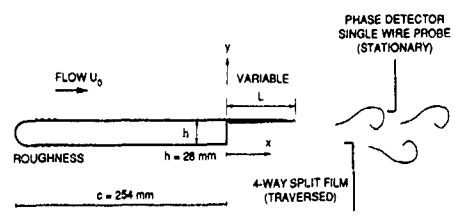

Fig.1. The model and experimental setup

with respect to azimuthal angle between the velocity vector and the reference direction(one of the split planes) direction on the sensor would give the maximum In this interpolation, only the largest three outputs are used to avoid the output of the element that is in the separated zone.

The detailed description and the performance of thethis split-film method is given in Nakayama(1991) The diameter of the sensor cylinder is only 0.15mm and the active length is 2mm. The response characteristics of this probe was compared with that of regular hot-wire probe and a laser doppler anemometer The mean velocity in the region with instantaneous flow reversal was compared with the laser anemometer was found to agree very well, while the frequency response characteristics were compared with a single wire probe in the region where the velocity fluctuation is small and found the response adequate for the present flow.

The phase of the vortex shedding was detected by a separate single-wire probe located just outside the wake about one model thickness downstream of the trailing edge as seen in Fig.1. Examples of this signal for the cases in which the detailed data were obtained are shown in Fig.3. The moment when the output of this phase-detector probe shows a peak is arbitrarily chosen as the phase reference, and the phase angle ϕ is measured from there.

The shedding frequency over a range of Reynolds number Re_h based on the body thickness and geometry parameter L/h, were investigated prior to the detailed measurements, and the results are shown in Fig.4. The results are seen to be very similar to the the case of a rectangular trailing edge with a splitter plate(Nash, Quincey & Callinan(1963) and Bearman(1964)) attached along the centerline, if the present body thickness h is interpreted as one half of the thickness of the rectangular trailing edge and the length L of the overhanging part of the body as the splitter plate length. It can be said that the overhanging part of the trailing edge acted like a splitter plate, and the criteria for the shedding and the frequency are seen to be very similar, too. The maximum Strouhal number is obtained at around L/h=3 and the shedding ceases at about L/h=5 which is related to the reattachment of the separated flow. The present detailed results were obtained at L/h=2.3 and 3.4, which are on opposite sides of the peak frequency. The strength of the vortex shedding was very different for these two cases although L/h is not very different. The Reynolds number Re_h was fixed at 20,000 corresponding to the free-stream velocity of 20 m/s.

The signals from the split-film probe and the phase-detector probe were simultaneously sampled and digitized real time by a MetraByte A/D converter operated on an IBM compatible corputer. The data were also recorded on floppy disks so that they could be re-reduced using different methods

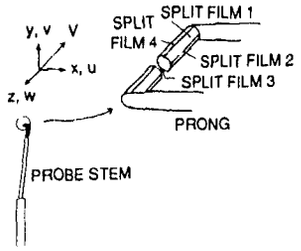

Fig 2 4-way split film probe

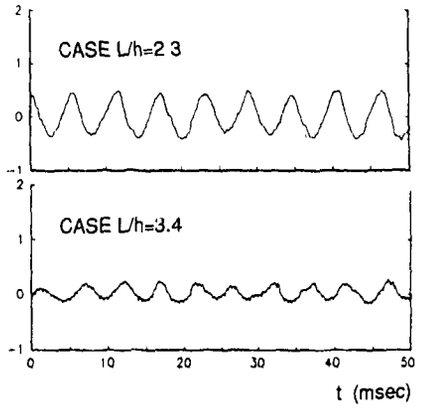

Fig 3. Signals from phase detector wire.

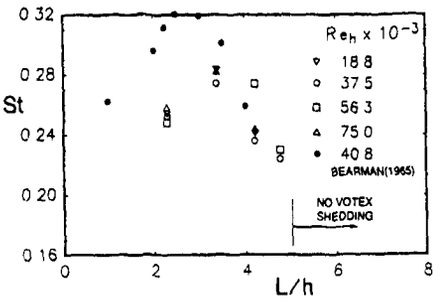

Fig.4. The vortex shedding frequency

DATA REDUCTION

In the present flow with semi-periodic vortex shedding, we use the same notation as used by Cantwell and Coles(1983) and Reynolds & Hussain(1972). The instantaneous velocity component u is written as

$$u = \bar{u} + \hat{u} + u' \qquad (1)$$

where $\bar{u}$ is the global mean, $\hat{u}$ is the periodic mean component, and u' is the randomly fluctuating component. We use < > to indicate the averages at a constant phase, or the phase average. Then the phase average of velocity u is given by

$$\langle u \rangle = \bar{u} + \hat{u} \qquad (2)$$

The phase-averaged Reynolds stress components, that is the Reynolds stresses if the flow is considered periodically unsteady, are $\langle u'u' \rangle$, $\langle v'v' \rangle$, $\langle u'v' \rangle$, etc. While, if the overall flow is interpreted as a stationary flow, the total Reynolds shear stress, for example, is $(u - \bar{u})(v - \bar{v})$ and can be expressed as the sum of two components, $\hat{u}\hat{v}$, and $\overline{u'v'}$. We have

reduced all these Reynolds stresses involving velocity components u and v, but not the spanwise component w It became evident, as the data were analyzed that, the random fluctuation components consisted of cycle-to-cycle fluctuation as well as the purely turbulent fluctuations The problem of the phase jitter was discussed by Perry and Watmuff(1981), but in the present case, the ambiguity due to phase jitter was not as serious The variation in the cycle period is excluded from the random component by subdividing the individual periods between succesive peaks of the phase signal into equal subdivisions. The contribution due to the cycle-to-cycle fluctuation in the strengths is included as a random component.

GLOBAL AVERAGES

The global averages of the velocity components are shown in the vector plots of Fig.5 The sum of the global averages of the periodic and random fluctuations $\overline{(\hat{U}+u)^2}+\overline{(\hat{V}+v)^2}$, which is roughly proportional to the global turbulence energy is plotted in Fig.6 together with the contribution from the periodi motion Similar plots corresponding to the Reynolds shear stress are given in Fig.7. From these plots, it can be said that these flows are like the flow downstream of a backward-facing step, with the length of the wall too short to reattach. In both cases, the separation bubble extends downstream of the trailing edge, but it is more for the case of L/h=2.3. It is this fact that the flow does not reattach the wall induces the vortex shedding In the case of L/h=3.4, the separation bubble closure point is very close to the trailing edge. In both cases, the turbulence intensities and shear stresses are seen to be very large just downstream of the bubble closure point. The relative magnitudes of the global averages and the periodic flow contributions indicate the importance of the periodicity of the vortex shedding It is seen that, in the case of L/h=2.3, the contributions from the periodic motions are very large, while in the case of L/h=3 4, they show up only at downstream locations This point is remarkable sinc he vortex shedding was found to exist up to L/h=5.

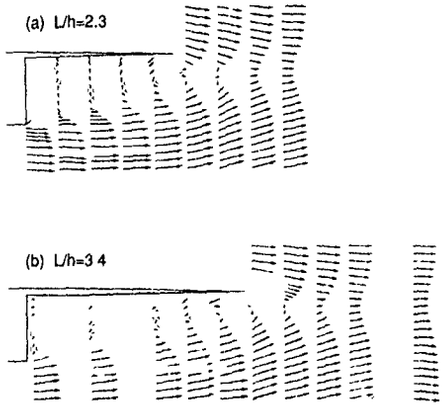

Fig 5 Global average of the velocity vectors

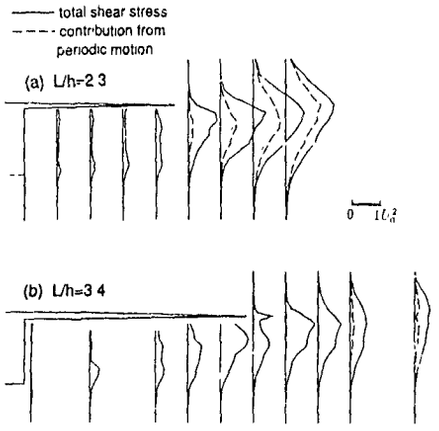

Fig.6 Global averaged turbulence $\overline{(\hat{U}+u)^2}+\overline{(\hat{V}+v)^2}$ and contributions from periodical motion $\hat{U}^2+\hat{V}^2$

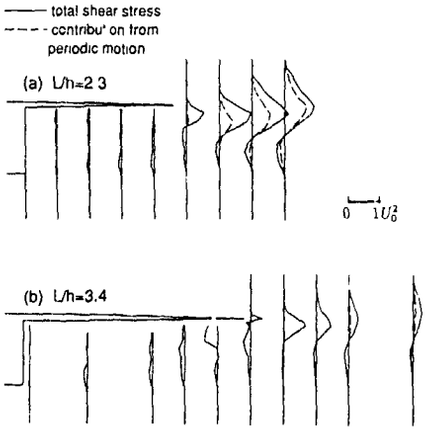

Fig 7. Global averaged shear stresses $-\overline{(\hat{U}+u)(\hat{V}+v)}$ and contributions from periodical motion $-\hat{U}\hat{V}$.

PHASE AVERAGES

The averages of the velocity vectors at constant phase angles are shown in Fig.8 and 9, for the two test cases from ϕ =0 to 300° at 60° interval. The estimated phase-averaged positions of the dividing streamlines are hand drawn in Fig.8. The strength of the vortex shedding is seen to be very weak in the case of L/h=3.4, and the flow pattern for most of the phases are almost the same, except the last few x positions In the case of L/h=2.3, the shedding is seen very strong and one can see how the individual vortices are generated and convected downstream The shedding pattern is seen to be such that the bubble closure point and the dividing streamline move up and down rather than changing the length of the separation bubble. It is seen, however, that even in this case, the motion in the separated shear

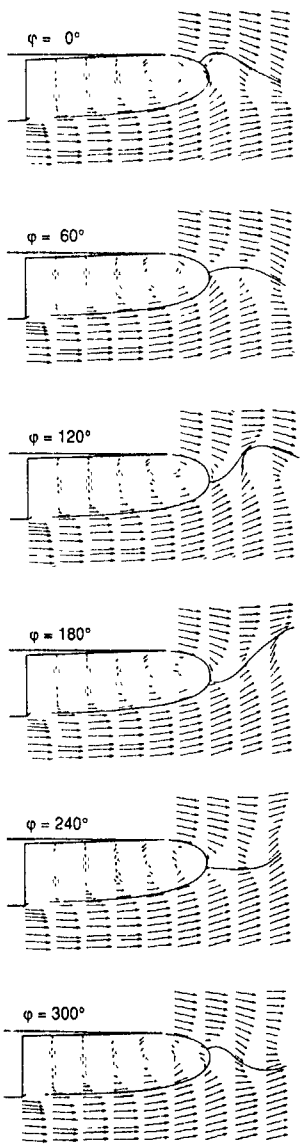

Fig 8 Phase-averaged velocity vectors, L/h = 2 3

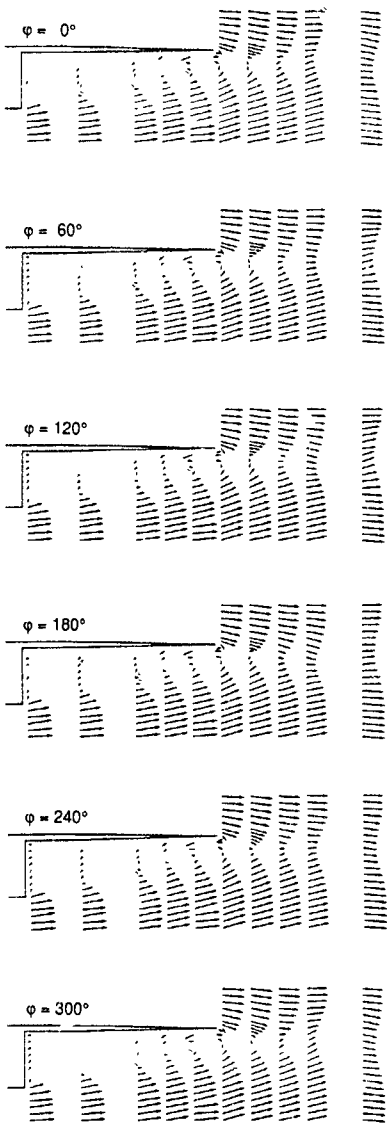

Fig 9 Phase-averaged velocity vectors, L/h = 3 4

layer upstream of the trailing edge is seen to be rather phase-independent suggesting that it is not the large vortex structure in the separated shear layer that is causing the vortex shedding. In fact, additional data taken at locations more downstream than the presently shown region, indicate more periodic motions are detected even for L/h=3 4

The phase averages of the turbulence energy as represented by $\langle u'^2 \rangle + \langle v'^2 \rangle$ are shown in Fig.10 and 11. Since the periodic motion for L/h=3.4 case is very small, the results only at three phase angles are shown. The changes of the distribution of this quantity at different phases is seen to follow the undulating motion of the dividing streamlines.

The distributions of the phase-averaged Reynolds shear stress -u v are shown in Figs. 12-13. It is seen again that the periodic motions are quite strong in the case of L/h=2.3 but it is almost insignificant in most of the regions for the case of L/h=3.4. It was pointed out by Cantwell and Coles(1983) based on

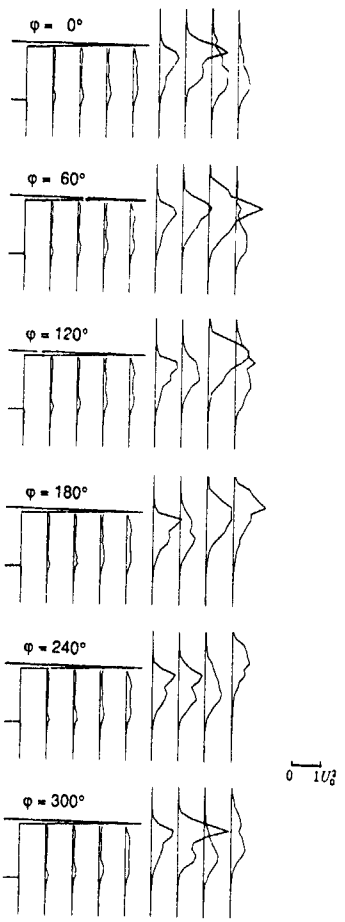

Fig.10. Phase-averaged turbulence $\langle u'^2 \rangle + \langle v'^2 \rangle$, L/h = 2 3

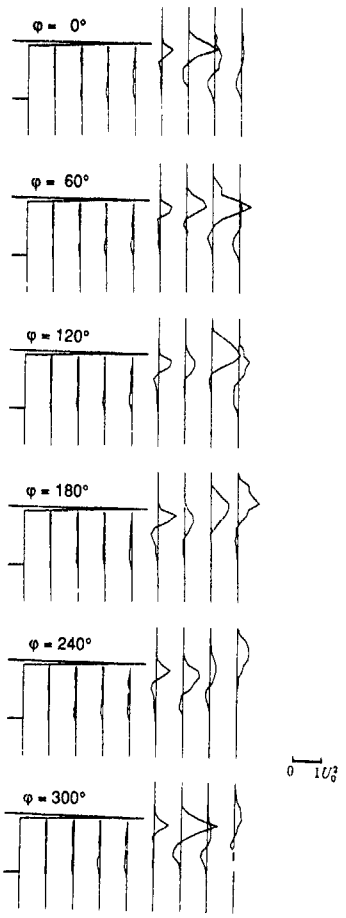

Fig 12. Phase-avereged shear stress $\langle u'v' \rangle$, L/h = 2.3.

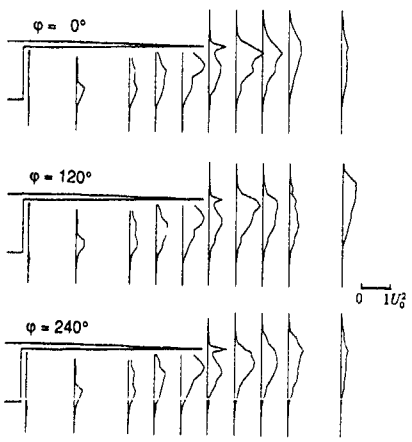

Fig 11. Phase-averaged turbulence $\langle u'^2 \rangle + \langle v'^2 \rangle$, L/h = 3 4.

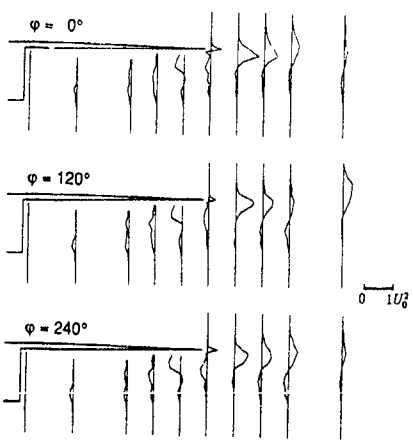

Fig.13. Phase-averaged shear stress $\langle u'v' \rangle$, L/h = 3.4.

their measurements in the wake of a circular cylinder that the turbulence generation is strong at the saddles. By comparing the present turbulence data with the phase-averaged vector fields of Fig. 8 and 9, it can be said that the turbulence intensities are high near the saddle point, which, in the present case, is located at the phase-averaged separation-closure point. Also it seems that the high turbulence intensity and the high shear stress are related to the strong turbulence production indicated by the area of large velocity gradient

In their detailed analysis of Cantwell and Coles data, Franke, Rodi & Schoenung(1989) found that the eddy viscosity coefficient behaved anomalously and found many regions where it was negative. In order to examine the similarity, the eddy viscosity was calculated from the present data, as well Fig 14 shows the eddy viscosity formed by the phase-averaged Reynolds shear stress and the phase-averaged velocity gradient. It can be seen that there is not any significant areas where it behaves anomalous and becomes negative. In fact it seems to behave quite favorably in terms of using it for computational purposes

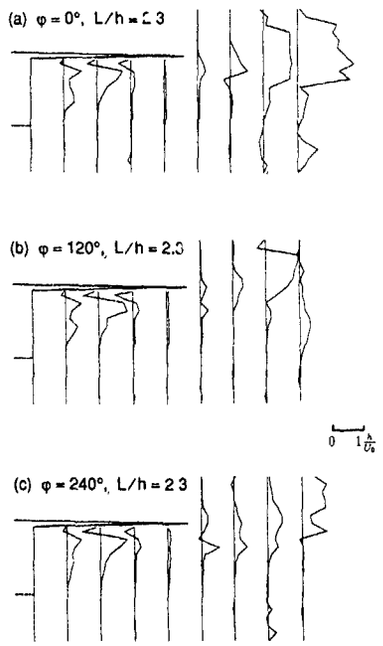

Fig 14 Phase-averaged eddy viscosity – $\langle u'v' \rangle / (\partial \langle u \rangle / \partial y)$

CONCLUSIONS

The vortex-shedding characteristics and the turbulence structure of the turbulent near wake of a two-dimensional streamline body with a sharp cutout for a fixed separation, have been determined in detail using a split-film probe. The contributions to the total apparent stresses from the periodic and random motions depend on the strength of the vortex shedding. When the overhanging length of the trailing edge is shorter than about 3 times the body thickness, the vortex shedding is strong and the periodic-motion contribution becomes significant. In either case, the eddy viscosity defined as constant phase angles appear to stay positive

REFERENCES

BEARMAN, P W 1965 Investigation of the flow behind a two dimensional model with a blunt trailing edge and fitted with splitter plates J Fluid Mech. 21,241-255.

CANTWELL, B. & COLES, D 1983 An Experimental Study of Entrainment and Transport in the Turbulent Near Wake of a Circular Cylinder. J Fluid Mech 136,321-374

FRANKE, R , RODI W. & SCHOENUNG, B. 1989 Analysis of Experimental Vortex-Shedding Data with Respect to Turbulence Modelling. Proc. 7th Symposium on Turbulent Shear Flows, 24.4.1, Stanford University

KIYA, M. & SASAKI, K. 1985 Structure of Large-scale Vortices and Unsteady Reverse Flow in the Reattaching Zone of a Turbulent Separation Bubble J. Fluid Mech. 154,463-491.

Le BALLEUR, J C. 1989 New Possibility of Viscous-Inviscid Numerical Techniques for Solving Viscous Flow Equations with Massive Separation presented at the Fourth Symposium on Numerical and Physical Aspects of Aerodynamic Flows, Long Beach, California, U.S A

NASH, J F , QUINCEY, V G. & CALLINAN J. 1963 Experiments on Two-Dimensional Base Flow at Subsonic and Transonic Flow Speeds. NPL R & M No. 3427.

NAKAYAMA, A 1985 Measurements of Separating Boundary Layer and Wake of an Airfoil Using Laser Doppler Velocimetry. AIAA Paper 85-0181.

NAKAYAMA, A 1991 Multi-Component Split Film Probes Applied in the Measurement of Flows with High Turbulence Intensities. AIAA Paper 91-0164.

PERRY, A.E. & STEINER, T.R. 1987 Large-scale Vortex Structures in the Turbulent Wakes Behind Bluff Bodies. Part 1. vortex formation. J Fluid Mech 174,233-270.

PERRY, A E. & WATMUFF, J.H 1981 The Phase-Averaged Large-Scale Structures in Three-dimensional Turbulent Wakes. J. Fluid Mech.103,33-51.

REYNOLDS, A E. & HUSSAIN, A.K.M.F 1972 The Mechanics of an Organized Wave in Turbulent Shear Flow. Part 3. Theoretical Models and Comparisons with Experiments. J. Fluid Mech.54,263-288.

EIGHTH SYMPOSIUM ON
TURBULENT SHEAR FLOWS
Technical University of Munich
September 9-11, 1991

AN EXPERIMENTAL EVALUATION OF SOME TURBULENCE MODELS FROM A THREE-DIMENSIONAL TURBULENT BOUNDARY LAYER AROUND A WING-BODY JUNCTION

by

Semih M Olçmen and Roger L Simpson
Department of Aerospace and Ocean Engineering
Virginia Polytechnic Institute and State University
Blacksburg, VA, 24061, USA

ABSTRACT

Detailed three-dimensional LDV measurements have been made in a three-dimensional turbulent boundary layer that approaches a wing-body junction. These measurements are used here to evaluate several turbulence models These models require or imply a relationship between the angles of the turbulent shear-stress and mean velocity gradient vectors. In the present flow these angles are not only different but do not follow any simple relationship. The ability of several turbulence models to calculate the magnitude and direction of the shear stress vector is examined Among the best are the Cebeci-Smith and Johnson-King models

NOMENCLATURE

β_{FS} angle between x axes of the tunnel and free-stream coordinates
β_{MS} angle between x axes of the tunnel and mean velocity vector direction at the maximum normal stress location
β_w wall shear stress direction with respect to x axis of the free-stream coordinate
$()_{FS}$ quantity in free-stream coordinates
All other quantities are explained in the text

I. OUTLINE OF THE PRESENT WORK

In the present study, a three-dimensional boundary layer (3D TBL) formed by a cylinder setting on a flat plate was studied. The pressure, skin-friction, mean velocity, fluctuating velocity and Reynolds stresses were measured and used in examining the validity of some turbulence models in the calculation of the turbulence structure of these types of flows

The body used is a 3 2 elliptical nose, NACA 0020 tail symmetric profile which has a chord length of c=30.5 cm (12 inches), maximum thickness of t=7 17 cm (2 824 inches), and height of 22 9 cm (9 016 inches) The measurements were carried out in the Boundary Layer Tunnel at Virginia Tech The nominal reference velocity was U_{ref}=27 m/sec and the Reynolds number based on the momentum thickness at 0 75 chord upstream of the body on the centerline of the tunnel was Re_θ= 5936 (Olçmen, 1990).

The mean velocity and stress data for all components were obtained with hot-wire (HW) and laser-Doppler velocimeter (LDV) techniques. Due to the differences observed near the wall between the HW and LDV data the LDV measurements were taken twice with both sets in close agreement. This permitted the study of the uncertainties of the mean velocities and the stresses. Pressure distributions on the wing and the on the bottom plate were obtained with a Scanivalve and an inclined manometer. Skin friction vectors at several locations on the wall were measured by Ailinger (1990) with an oil-flow laser interferometer technique.

The future development of turbulence models still necessitates reliable, complete data sets of flows which are encountered in engineering practice. This test flow is encountered in many cases of engineering interest, for example in the wing/body junction on aeroplanes and the appendage and hull junction on submarines The boundary conditions and the characteristics of the approaching boundary layer to the wing were carefully documented. Pressure data were taken at closely enough spaced locations to obtain pressure gradients from the data.

Another important aspect of the present study is that it is a unique data set which documents the flow characteristics on a line along the direction of the mean velocity vector component parallel to the floor, at a point in the boundary layer where $\overline{u^2}$ kinematic normal stress is maximum (Figure 1) Since most of the turbulent kinetic energy of the flow is stored in the $\overline{u^2}$ normal stress term, the flow along this path must follow approximately the path of the shear and turbulence producing eddies. The data show that the eddy viscosity of the flow is not isotropic, but that the ratio of eddy viscosities perpendicular and parallel to the direction of the mean velocity vector component parallel to the wall at the point in the layer where $\overline{u^2}$ is maximum is close to unity The shear-stress vector direction in the flow lags behind the flow gradient vector direction (Olçmen, 1990).

$A_1=\frac{\sqrt{-\overline{vw}^2+-\overline{uv}^2}}{2^k}$, is not a constant of 0.15 as expected for 2-D flows, but is much lower near the wall for 3-D flows The skin friction velocity is not the scale of the turbulence in such a flow. Table 1 gives some important characteristics of the profiles measured.

In the next sections, selected Algebraic Turbulence Models will be described and then their performance in simulating the shear-stress magnitudes and the shear-stress vector directions throughout the layers will be discussed comparatively The data used were from stations 0, 2, 4, 6.

II. SELECTED ALGEBRAIC TURBULENCE MODELS

Turbulence models selected were chosen among the models which did not necessitate solving the governing continuity, momentum, and turbulent transport equations. This restricts the discussion to algebraic eddy viscosity models

The comparison of the computed and experimental data was performed using two parameters, a magnitude ratio and direction angle difference which are described below. The shear stress vector in the plane parallel to the floor with components of $-\overline{vw}_{FS}$ and $-\overline{uv}_{FS}$ can be expressed using complex numbers in the form $|\tau|e^{i\alpha}$, where $|\tau|=(-\overline{uv}^2_{FS}+-\overline{vw}^2_{FS})^{1/2}$ and α is the shear stress angle. The ratio of the measured and computed shear stresses presented in the complex form give two parameters:

$$\frac{|\tau_m|}{|\tau_c|} = \textit{Magnitude ratio}$$
$$\alpha_m-\alpha_c = \textit{Direction angle difference}$$

where m denotes the measured quantities and c stands for the computed values. If a model were able to calculate the magnitude and the direction of the measured shear stress vector data perfectly, the ratio of magnitudes would be 1, and the difference between the shear stress directions would be zero.

All computations were carried out using the data in free-stream coordinates, and U and W denote the mean velocity components in the x_{FS} and z_{FS} directions, respectively. (x_{FS} is in the direction of the velocity vector at the boundary layer edge; y_{FS} is in the perpendicular direction to the wall; z_{FS} completes a right-handed coordinate system) The necessary mean flow gradients to calculate computed shear stresses for each flow were found by fitting a parabola to 5 consecutive points and computing the gradients at the third or the middle point. Except at the zeroth

station, the shear stresses at the wall were taken from Ailinger (1990). At station 0, the wall stress was found using the 2-D Law of the Wall Clauser plot. The required mean flow quantities were also taken from the data, as if the solutions of the governing equations were same as the data. The necessary maximum shear stress magnitudes in the layers for the Johnson-King model at each station were taken as the measured maximum shear stress magnitudes which satisfy the realizability conditions (Schumann, 1977).

II.A. CEBECI-SMITH MODEL

The Cebeci-Smith model used in this study is the one described by Cebeci (1984). The model uses two different eddy-viscosity definitions, one described for the inner region and one for the outer region.

In the inner region, the eddy-viscosity is defined as

$$\nu_{ti}=F^2 l^2\left[\left(\frac{\partial U}{\partial y}\right)^2+\left(\frac{\partial W}{\partial y}\right)^2\right]^{1/2}$$

$$l=\kappa y \ , \quad F=1-\exp(-y^+/A^+)$$

$$y^+=\frac{y\,u_\tau}{\nu} \ , \quad u_\tau=\left(\frac{\tau_w}{\rho}\right)^{1/2}$$

$$\tau_w=\nu\left[\left(\frac{\partial U}{\partial y}\right)_w^2+\left(\frac{\partial W}{\partial y}\right)_w^2\right]^{1/2}$$

$$A^+=26 \qquad \kappa=0.4$$

in which l is the mixing length, F is the van Driest damping function, u_τ is the friction velocity, and τ_w is the wall shear stress magnitude.

The outer region eddy-viscosity is given by

$$\nu_{to}=0.0168\,\delta_2^*\gamma_k U_e$$

$$\delta_2^*=\int_0^\infty\left(1-\frac{(U^2+W^2)^{1/2}}{U_e}\right)dy$$

$$\gamma_k=\left[1+5.5\left(\frac{y}{\delta}\right)^6\right]^{-1}$$

where γ_k is Klebanoff's intermittency correction, and δ_2^* is the displacement thickness. The boundary layer thickness δ is defined as the point in the layer where $(U^2+W^2)/U_e^2$ is 0.99. By using a smoothing function, the eddy-viscosity distribution in the layer can be defined as.

$$\nu_t=\nu_{to}[1-\exp(-\nu_{ti}/\nu_{to})]$$

and the shear stresses are found by using.

$$-\overline{uv}_{FS}=\nu_t\frac{\partial U}{\partial y} \ , \quad -\overline{vw}_{FS}=\nu_t\frac{\partial W}{\partial y}$$

II.B. ROTTA'S MODEL

This anisotropic eddy-viscosity model is based on work by Rotta (1979). An analysis of the pressure strain terms in the governing equations for the stresses led Rotta to an anisotropic eddy-viscosity model (Rotta, 1977). The model uses an anisotropy constant T

$$T=\frac{(\nu_T)_{transverse}}{(\nu_T)_{streamwise}}$$

defined as the ratio of the transverse eddy-viscosity to the streamwise eddy-viscosity in local free-stream coordinates.

By assuming T constant in the layer, ν_T in the free-stream coordinates can be computed as

$$\nu_T=F^2 l^2\left[\left(\frac{\partial U}{\partial y}\right)^2+\left(\frac{\partial W}{\partial y}\right)^2+\frac{(T-1)\left(W\frac{\partial U}{\partial y}-U\frac{\partial W}{\partial y}\right)^2}{U^2+W^2}\right]^{1/2}$$

and the stresses are related to the mean flow gradients with

$$\nu_t=\nu_{to}[1-\exp(-\nu_T/\nu_{to})]$$

$$-\overline{uv}_{FS}=\nu_t\left(a_{xx}\frac{\partial U}{\partial y}+a_{xz}\frac{\partial W}{\partial y}\right)$$

$$-\overline{vw}_{FS}=\nu_t\left(a_{xz}\frac{\partial U}{\partial y}+a_{zz}\frac{\partial W}{\partial y}\right)$$

where

$$a_{xx}=\frac{U^2+TW^2}{U^2+W^2} \ , \quad a_{zz}=\frac{W^2+TU^2}{U^2+W^2} \ , \quad a_{xz}=(1-T)\frac{UW}{U^2+W^2} \ , \quad l=\kappa y$$

In this study, ν_T defined by Rotta was used as the inner layer eddy-viscosity and the outer layer eddy-viscosity was kept the same as the Cebeci-Smith model. For the present data, three different anisotropy constants, T=0.3, T=0.5 and T=0.7, were tested.

II.C. PATEL'S MODEL

The third model selected is the one equation (k) model of Wolfshtein (1969), as used by Chen and Patel (1988) in the k-ϵ turbulence model with the fully elliptic Reynolds-averaged Navier-Stokes equations to compute the flow characteristics in the boundary layer or wake of axisymmetric bodies. The eddy-viscosity in this model is defined as:

$$\nu_t=C_\mu\sqrt{k}\,l_\mu$$

$$l_\mu=C_l y[1-\exp(-R_y/A_\mu)] \ , \quad C_l=\kappa C_\mu^{-3/4}$$

$$R_y=\frac{\sqrt{k}\,y}{\nu}=\text{Turbulent Reynolds number}$$

$$A_\mu=70 \ , \quad C_\mu=0.09 \ , \quad \kappa=0.418 \ , \quad k=TKE=\frac{\overline{u^2}+\overline{v^2}+\overline{w^2}}{2}$$

and the stresses in cartesian coordinates could be computed using(Stern, Yoo and Patel, 1988).

$$\overline{u_i u_j}=-2\nu_t S_{ij}+2k\delta_{ij}/3$$

$$S_{ij}=\frac{1}{2}(U_{i,j}+U_{j,i})$$

$$\delta=1 \ \text{ if } \ i=j$$

$$=0 \ \text{ if } \ i\neq j$$

After neglecting the derivatives other than those with respect to y, the stresses in this study are computed using

$$-\overline{uv}_{FS}=\nu_t\frac{\partial U}{\partial y} \ , \quad -\overline{vw}_{FS}=\nu_t\frac{\partial W}{\partial y}$$

The validity of the equations for the turbulence model as given was defined to be restricted to the viscous sublayer, buffer layer, and a part of the fully turbulent layer. Therefore, the comparison with the data is only meaningful below $y^+=150$ (Patel and Chen, 1987).

II.D. JOHNSON-KING MODEL

The eddy viscosity model introduced by Johnson and King (1984) for 2-D flows subject to strong pressure gradients and separation was extended to 3-D flows by Abid (1988). Instead of using the wall skin friction as the Cebeci-Smith model does, the model utilizes the maximum shear stress in the layer to define the eddy viscosities and the Van Driest damping function which is effective near the wall. The inner layer eddy viscosity, which has the same form as the Cebeci-Smith model, differs due to the use of the maximum shear stress in the layer. The model is defined as follows:

$$\nu_{ti}=F^2 l\left(\frac{\tau_M}{\rho}\right)^{1/2}$$

$$F=1-\exp\left(-y\frac{(\tau_M/\rho)^{1/2}}{\nu A^+}\right) \ , \quad l=\kappa y \ , \quad \frac{\tau_M}{\rho}=(\overline{uv}^2+\overline{vw}^2)_{max}^{1/2} \ , \quad A^+=15$$

The outer eddy viscosity was also modified to take into account the effect of the maximum shear stress in the outer layer. The outer layer eddy viscosity is defined as:

$$\nu_{to}=\sigma(0.0168)\gamma_k\int_0^{\bar{\delta}}(V_e-V)\,dy$$

where σ is found when the relation

$$\left(\frac{\tau_M}{\rho}\right)=\nu_t\left[\left(\frac{\partial U}{\partial y}\right)^2+\left(\frac{\partial W}{\partial y}\right)^2\right]_{max}^{1/2}$$

is satisfied at the location in the layer where the shear stress is maximum. Once σ is found the shear stresses are found using

$$-\overline{uv}=\nu_t\frac{\partial U}{\partial y} \ , \quad -\overline{vw}=\nu_t\frac{\partial W}{\partial y}$$

where

$$\nu_t=\nu_{to}(1-\exp(-\nu_{ti}/\nu_{to}))$$

The maximum shear stress magnitude was found by Johnson-King and Abid using an ordinary differential equation derived from the T.K.E. equation, which is

valid along a path where the shear stress is maximum. In this study it was assumed that this equation could exactly compute the maximum shear stress The location of it in the layer, which would be found once the governing equations are solved, was also assumed to be found accurately. Once these assumptions are made, the constant multiplier σ in the v_{t_o} equation was found by Newton iteration and by using the experimental τ_M and mean flow gradients

III. RESULTS AND DISCUSSION

The comparison of the computed and measured stress magnitudes and angles for the present data are presented using log(y/t) as the abscissa of the plots. To distinguish the different regions in the layers, different symbols corresponding to inner, semi-logarithmic and outer regions were used Also the uncertainties in the dependent variables were found using the uncertainties in each experimental shear-stress and assuming that the computed shear-stresses did not induce any uncertainty These uncertainties are plotted as bars at each point. The uncertainty of the magnitude ratio was also used to eliminate the data points which had large uncertainties The data presented are those with uncertainties less than ±1 and which satisfy the realizability conditions (Schumann, 1977), (Figs 2-5).

The Cebeci-Smith model at the zeroth station of the present data set seems to overpredict the magnitude of the computed shear stresses in the inner layer and underpredict in the outer region (Fig 2) Since this flow profile is closely 2-D and since the model was developed using available 2-D data, the ratio of stresses should be 1 The high shear stresses observed are attributed to the uncertainties, and the ratio of magnitudes is 1, within the limits of the uncertainty, in most of the log and outer regions. The direction difference is zero at this station within the uncertainty limits. Station 2 profiles show a higher $|\tau_M|/|\tau_c$ within the inner region and part of the log region Although including the uncertainty bands, the magnitude ratio is still 1.0, the values were seen to be ≈ 1.2 in the part of the log and outer regions.The direction difference at this station was seen to be decreasing down to 0° at the log region starting from a value of ≈ 60° in the near wall region. At station 4 the inner layer and part of the outer layer ratios were seen to be less than 1. However, most of the log region values were 1 within the uncertainty bands. Angle differences at this station reach to 90° near the wall and decrease down to zero in the log region. At station 6 the decrease of magnitude ratio near the wall is most visible. The low, near wall values steadily increase to reach to a maximum at y/t≈0.05 with a value of ≈1.65. The outer region values were seen to be ≈1.0 including the uncertainty bands. The angle difference was seen to form a peak at y/t≈0.015 at a value of ≈50° and a lower peak at y/t≈0.08 at ≈25°. Overall it was observed that the Cebeci-Smith

At station 0, even though the very near wall and most of the outer region magnitude ratios are less than 1.0, the log region values were seen to be≈1.0, and the direction difference at the same station was zero in the most of the layer (Fig 5). Within the uncertainty bands, log region magnitude ratios of station 2 are ≈1.0. Near wall and outer regions show underestimated ratios. The log region and outer region directions of the two stress vectors were the same, which was reached after a gradual decrease starting from a value of ≈ 100° near the wall. For station 4, the values are scattered within 0.7~1.1, closer to 0.9 in the average. The high direction difference on the order of ≈ 100° near the wall decreases to zero in the logarithmic region. At station 6 the near wall values as seen in most of the profiles were lower than 1.0. Starting with y/t≈0.03 the ratios were close to being 1.0 in the uncertainty bands. The difference in the directions of the computed and experimental stress vectors parallel to the wall were seen to be reaching to a peak at y/t≈0.02 at a value of 50°. Further out in the layer, the difference was gradually reduced and was zero within the bands in the log and outer regions.

IV. CONCLUSIONS

Overall, the Cebeci-Smith model and the modification to it by using Rotta's anisotropy constant were seen to overpredict the magnitude ratios in the logarithmic and outer layers and underpredict very near the wall. Even though the Johnson-King model inherently includes the maximum stress to find the stress distribution in the layers, it was observed that it underpredicted the magnitude ratios within the near wall and outer regions. None of the models was able to calculate well the stress direction Except Rotta's model, which overpredicts the direction in most of the stations, they all seemed to work equally well. The range of the computed magnitude ratios and angle differences at y^+=200 for the present flow studied may be found in Table 2

Even though the Cebeci-Smith model overpredicts the magnitude ratio for the almost 2-D flow station, the calculated ratios decrease for the downstream stations. The angle differences in most of the profiles are on the positive side

Rotta's model with anisotropy constant T=0.3 for the present data calculates the angle differences and the magnitude ratios in a wider band compared to the Cebeci-Smith model. The constants T=0 5 and T=0.7 result in magnitude ratios and angle differences between the predicted values of the Cebeci-Smith model and T=0.3.

In the same y^+ range Patel's model was observed to calculate magnitude ratios lower than the Cebeci-Smith model for stations 2 and 4 but the ratios were much closer to 1 in the inner regions For magnitudes, Patel's model is the best of these four in the inner region. The angle differences are the same as the Cebeci-Smith model.

The Johnson-King model in the form used in this study underpredicts the magnitude ratios in the almost 2-D flow station of the present data, especially in the outer region. For the stations where 3-D flow is developed, the scatter of the magnitude ratios are around 1.0 and in a narrower band than the Cebeci-Smith or any other model.

In conclusion, none of the models predict the shear stress data well especially near the wall. A good model near the wall should capture the fact that τ_R is much lower near the wall for a developing 3-D flow than for a 2-D flow with the same mean velocity gradients. If there must be choices made among these model resulted in lower magnitude ratios near the wall and higher magnitude ratios in the outer region. The shear stress direction difference was most noticeable in the near wall and beginning of the log region.

Rotta's model with T=0.3 seems to be effective in raising appreciably the magnitude ratios in the log region, in the range y/t≈0.01~0.1, (Fig 3). This effect at station zero was negligible. At station 2, the log region values were seen to be shifted up as much as 0.1, but the effect was reduced in the outer region. This is due to the use of v_t only in the inner region. Very near wall values were also less affected than the log region values. The increment in the magnitude ratios for station 4 was similar to the station 2 values. The maximum shift in the magnitude ratio at station 4 was ≈0.5. While the magnitude ratio for most of the outer region of station 4 was ≈1.0, and the near wall ratios were less than 1, the logarithmic regions had ratios on the order of ≈0.9-1.6. At station 4, while the very near wall direction difference was ≈ 100°, it was seen to be ≈ 30° in the log and outer regions. In the upper part of the log region and the lower part of outer region, the magnitude ratio increase at the next station was also accompanied with a direction difference increase. The increment at y/t≈0.03 was ≈0.7 for station 6. Station 6 direction angle difference increment was seen to be ≈ 25° for the log and outer regions.

Using different anisotropy constants, T=0.5 and 0.7, to compute v_t, results in the magnitude ratios and direction differences which are between the results found using Cebeci-Smith (T=1) and Rotta's models with T=0.3. For this data set, it was observed that using an anisotropic eddy-viscosity amplified the existing differences of the measured and computed shear stress magnitude and directions as compared with the Cebeci-Smith model.

Discussion of Patel's model is restricted to the inner layer for y^+ values less than 150 Patel's model was seen to calculate the magnitude ratios very near the wall lower than the Cebeci-Smith model (Fig 4).

For the zeroth station, in the log region, the magnitude ratio was ≈1.0, and the stress vector direction difference was seen to be zero within the uncertainty bands. The magnitude ratio for the second station was again seen to be 1.0 within the uncertainty limits, and the direction difference except near the wall below y^+ < 40 about zero. Station 4 magnitude ratios were seen to be ≈1 within the uncerta nty limits especially in the inner layer and at the beginning of the semi-log region. The 100° angle difference in the near wall region reduced to zero in the log region. The gradual increment in the ratio observed in the next profile was accompanied by less difference in the directions. The magnitude ratio starting from the near wall is seen to be increasing up to ≈1.05 at y/t≈0.04. The angle difference at

station 6 peaked at y/t=0.02 at a value of 50° In comparison to Cebeci-Smith or Rotta's models, Patel's model seems to underpredict the magnitude ratios for station 2 and overpredict for station 4 in the inner and semi-log regions but with ratios much closer to 1, and the direction difference was similar to the Cebeci-Smith model calculations.

Since, the maximum shear stress for the Johnson-King model was used to find the σ parameter in the outer eddy-viscosity definition, the shear stress computed is the same as the experimental value, so one point in each of the magnitude ratio profiles is assured to be 1.0. In the application of the Johnson-King model, this maximum value is obtained from a solution of an ordinary differential equation. As mentioned before, in this study it was taken from the data as if the solution of this equation were same as the data.

models, Patel's model is the best in the inner region and, the Johnson-King model is suggested for overall performance, although this recommendation is contingent on good calculations of τ_M by the differential equation

REFERENCES

Abid, R., "Extension of the Johnson-King Turbulence Model to 3-D Flows", AIAA Paper-88-0223, AIAA 26th Aerospace Sciences Meeting, Jan 11-14, 1988, Reno, Nevada.

Ailinger, K., (1990) " Measurements of Surface Shear Stresses under a Three-Dimensional Turbulent Boundary Layer using Oil-Film Laser Interferometry", M.S Thesis, Dept. of Aerospace and Ocean Eng., VPI&SU,

Cebeci, T., (1984) "Problems and Opportunities with Three-Dimensional Boundary Layers", AGARD-Report, 719.

Chen, H.C., and Patel, V.C., (June, 1988) "Near-Wall Turbulence Models for Complex Flows Including Separation", *AIAA Journal*, 26, No 6, pp. 641-648

Johnson, D A., and King, L.S , (Jan 9-12, 1984) "A New Turbulence Closure Model for Boundary Layer Flows with Strong Adverse Pressure Gradients and Separation", AIAA Paper-84-0175, AIAA 22nd Aerospace Sciences Meeting, Reno, Nevada

Olcmen, M.S , (1990) " An Experimental Study of a Three-Dimensional Pressure-Driven Turbulent Boundary Layer", Ph D Thesis, Aerospace and Ocean Eng Dept., Virginia Polytechnic Institute and State University, Blacksburg, VA

Patel, V C., and Chen, H.C.,(Aug. 1987) "Turbulent Wake of a Flat Plate", *AIAA Journal*, Vol 25, No 8, pp. 1078-1085.

Rotta, J.C., (July, 2-4, 1979) "On the Effect of the Pressure Strain Correlations on the Three-Dimensional Turbulent Boundary Layers", Turbulent Shear Flows, Imperial College, London

Rotta, J.C , (April, 18-20, 1977) "A Family of Turbulence Models for Three-Dimensional Thin Shear Layers", Turbulent Shear Flows 1, University Park, Pennsylvania.

Schumann, U., (May 1977) "Realizability of Reynolds-Stress Turbulence Models", *Phys. Fl.*, 20, pp.721-725.

Stern, F., Yoo, S.Y., Patel, V C., (Sept. 1988) "Interactive and Large-Domain Solutions of Higher-Order Viscous-Flow Equations", *AIAA Journal*, 26, No 9, pp 1052- 1060

Wolfshtein, M., (March 1969) "The Velocity and Temperature Distribution in One-Dimensional Flow with Turbulence Augmentation and Pressure Gradient", *Int. J. Heat and Mass Trans*, 12, pp.301-318.

Table 1. LASER-DOPPLER VELOCIMETER LOCATIONS.

station number	file name	x (inches)	z (inches)	U_{ref} m/sec	β_{FS} (degree)	β_{MS} (degree)	β_M (degree)	u_τ m/sec
0	LDV0	-4.487	-1.316	27.57	-1.684	-6.1	-3.816	1.152
1	LDV1	-3.496	-1.449	27.44	-2.288	-8.52	-17.712	0.864
2	LDV2	-2.287	-1.752	27.40	-5.576	-21.5	-21.724	0.865
3	LDV3	-1.328	-2.035	27.60	-8.774	-18	-39.823	0.957
4	LDV4	-0.472	-2.578	27.62	-10.163	-30.22	-26.337	1.105
5	LDV5	0.258	-2.939	27.59	-9.392	-25.326	-9.808	1.154
6	LDV6	1.193	-3.295	27.25	-6.509	-20.82	-4.692	1.162
7	LDV7	2.165	-3.527	27.29	-3.753	-10.92	-1.048	1.203

Table 2 THE RANGE AND ABSOLUTE RANGES OF ANGLE DIFFERENCES ($\alpha_R - \alpha_{\tau_R}$) AND MAGNITUDE RATIOS (τ_R/τ_R-1) CALCULATED WITH SEVERAL TURBULENCE MODELS AT y=200 FROM ALL STATIONS

Cebeci - Smith		Rotta 0.3		Rotta 0.5		Rotta 0.7	
-31.9°+25.5° 57.4°	-0.32+0.4 0.72	-25.5°+35.1° 60.6°	-0.3+0.85 1.15	-28.7°+22.3° 51.1°	-0.34+0.64 0.94	-31.9°+12.8° 44.7°	-0.3+0.34 0.64
Johnson-King				**Patel**			
-35.1°+25.5° 60.6°		-0.28+0.21 0.49		-32.5°+17.5° 50°		-0.4+0.05 0.45	

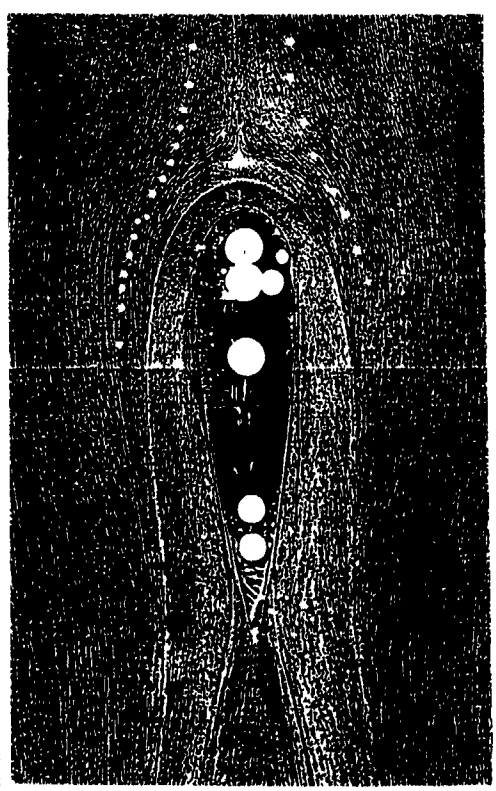

Figure 1: Oil flow visualization picture taken on the test wall surrounding the wing, at 27 m/sec nominal reference velocity. The dots on both sides denote the velocity and stress measurement locations. Hot-wire measurements were obtained on both sides and laser velocimeter measurements were made on the right half.

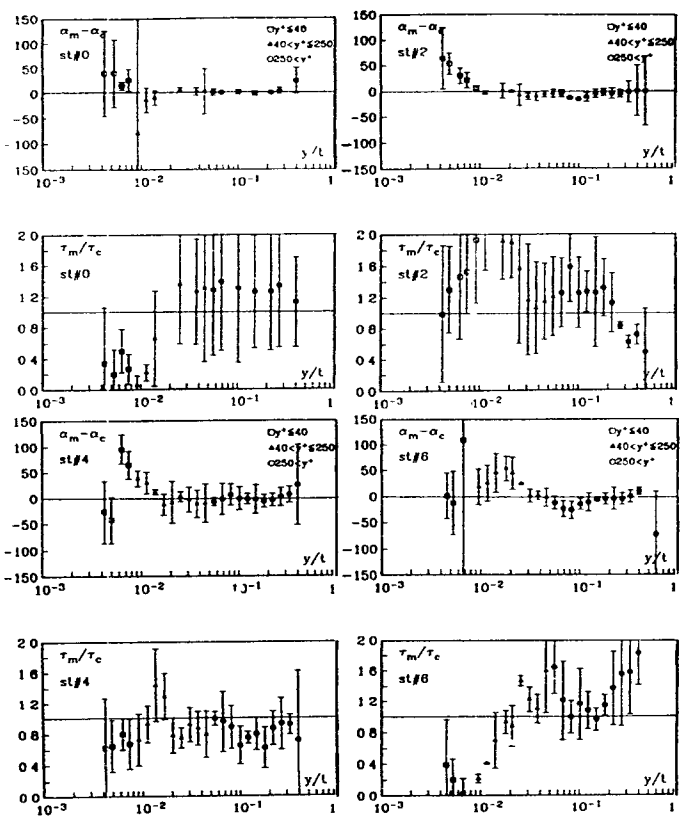

Figure 2: Present data in Cebeci-Smith model.

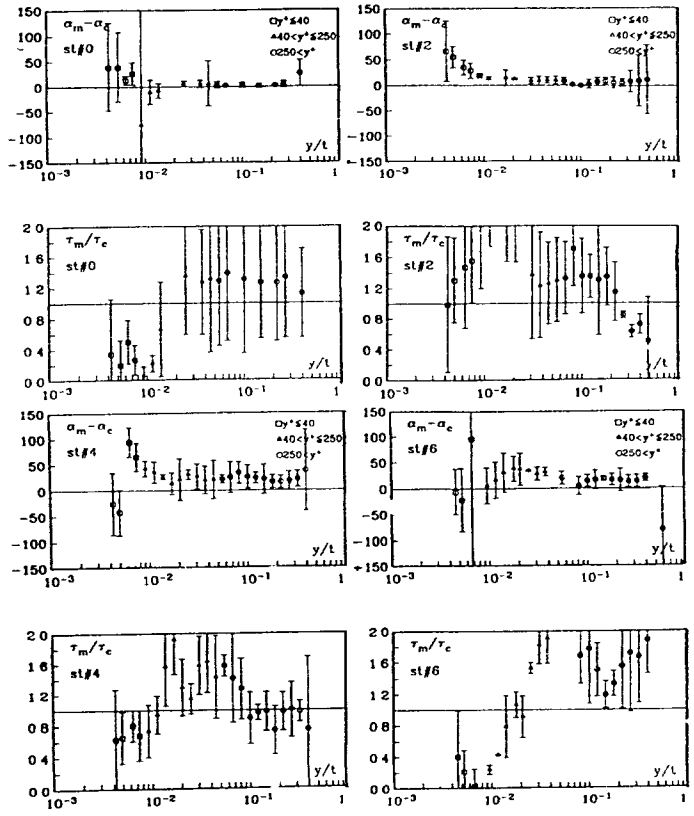

Figure 3: Present data in Rotta's model with T=0.3.

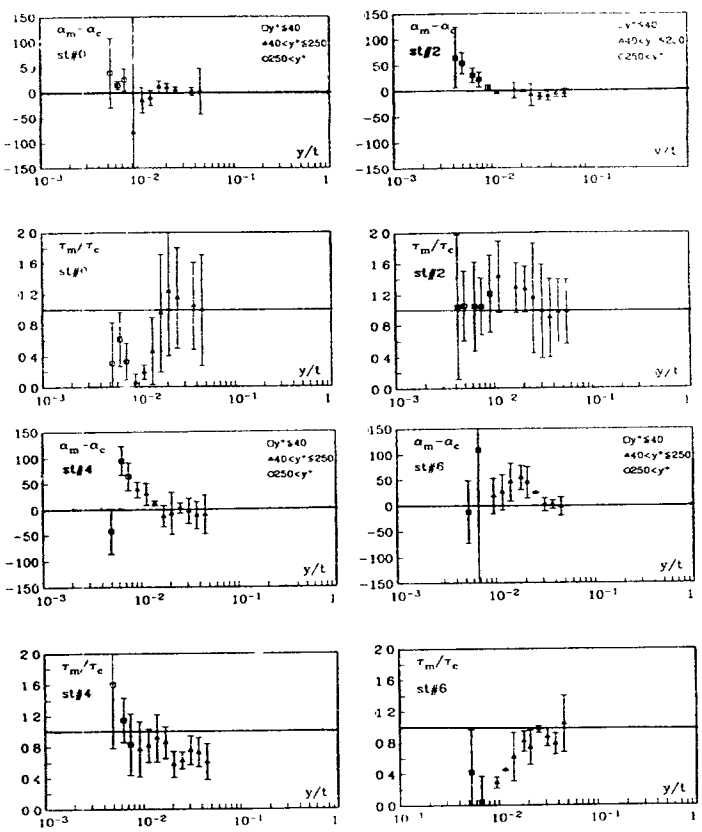

Figure 4 : Present data in Patel's model.

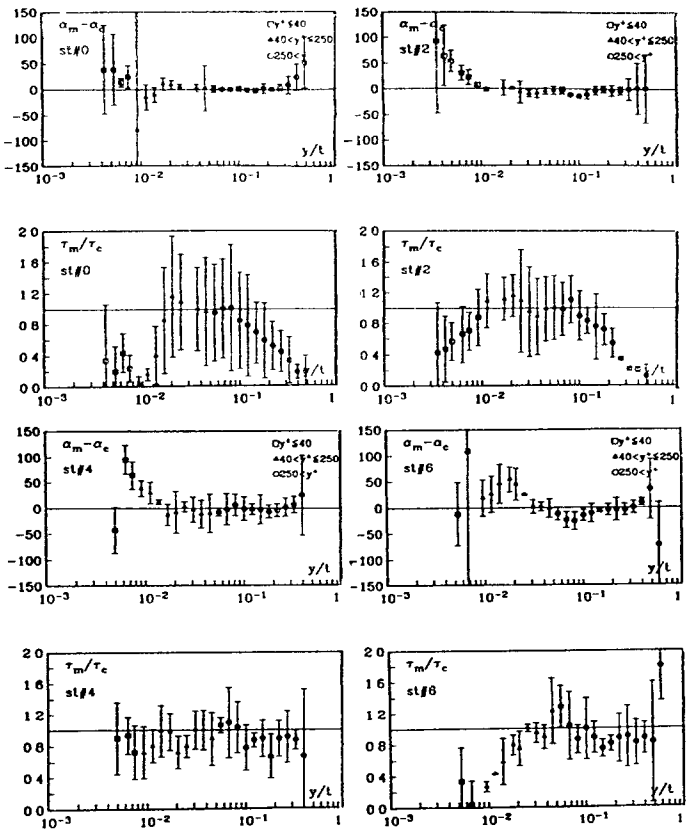

Figure 5: Present data in Johnson-King model

EIGHTH SYMPOSIUM ON
TURBULENT SHEAR FLOWS
Technical University of Munich
September 9-11, 1991

THREE-DIMENSIONAL SEPARATED FLOWS

F.McCluskey, P E Hancock, and I P Castro,

Department of Mechanical Engineering,
University of Surrey, Guildford, GU2 5XH, U K

ABSTRACT

In a preliminary study, three regions of three-dimensional separated turbulent flow have been considered, in the first instance, by means of surface flow patterns The three regions have particular significance in terms of extra rates of strain Some mean velocity and Reynolds stress measurements have been made using pulsed-wire anemometry in one of these - a nominally spanwise-invariant region Even for large aspect ratios (compared with those used for previous detailed studies) the type of flow near the 'upstream side-wall' may affect the flow near reattachment, and the wind-tunnel side walls cause an apparently significant spanwise variation in pressure

NOMENCLATURE

C_p	Surface pressure coefficient
h_f	Fence height above splitter plate
p	Pressure
p_o	Free-stream pressure upstream of fence
U,V,W	Mean velocities in x-, y-, z- directions
U_o	Free-stream velocity upstream of fence
u,v,w	Fluctuating velocities
X_A	Distance to attachment line (normal to fence)
x,y,z	Spatial coordinates - figure 1
W	Width of separation (= 610mm)
W_A	Width of nominally spanwise invariant region
δ	Height of separation bubble

INTRODUCTION

An understanding of separated flow and ability to predict its behaviour is of major practical importance in many fields of engineering and applied sciences Accurate and detailed prediction of the various features of such flows, necessary in many applications, will be a demanding test of turbulence modelling Of course, the mean flow of most separations of practical importance is three-dimensional. Sensibly, at least in a primafacia sense, most detailed investigations of turbulence structure have confined attention to (nominally) two-dimensional separations Such separations may be sub-divided into two groups, namely 'open' and 'closed' separations, the distinction being whether or not the separated flow reattaches on the surface from where it separated, forming a closed separation bubble. Most detailed investigations of closed separations have been made on sharp-edged configurations, the advantage being that the separation point (or line) is fixed.

The present work comprises a first phase of experimental work, currently in progress, extending work already done at the University of Surrey on two-dimensional separated flows A main objective of the current work is to establish a number of three-dimensional separated flows for detailed investigation, followed by more detailed measurements in one or more of these Initial investigations were by means of standard surface flow visualisation techniques Surface streamlines are indicative of the flow near the surface, and to some extent, of the whole flow further away, so standard surface flow visualisation techniques were used as an initial means of assessing the suitability of particular flow geometries Mean flow velocities and some Reynolds stresses have been measured by means of pulsed-wire anemometry

Detailed studies of the turbulence structure within supposedly two-dimensional separations have been made by Ruderich & Fernholz (1986), Castro & Haque (1987) and Jaroch & Fernholz (1989) However, it is suggested here that even the flow of Jaroch & Fernholz, which had the largest aspect ratio in these studies, may have been significantly affected by three-dimensional effects orginating from the wind tunnel side walls Wolf (1987) has made surface measurements and some simple mean-flow measurements in a separated flow generated on a swept thick flat plate Handford (1986) has made detailed measurements in a highly three-dimensional separation downstream of a profiled smooth body with a blunt rear end, mounted on a plane surface.

SOME SEPARATED FLOWS

A useful way to view the outer part of a separation is as a mixing layer subjected to extra rates of mean and fluctuating strain, where the latter strain is imposed by the recirculating flow (and is always three-dimensional, of course). If $\partial U/\partial y$ is the primary mean strain rate, where (for the moment) x is the direction of the mixing layer and y is perpendicular to it, then for a two-dimensional separation the extra strain rates are $\partial V/\partial x$, $\partial U/\partial x$ and $\partial V/\partial y$ (Johnson & Hancock, 1991) All three are associated with curvature of the mean streamlines and the second and third sum to zero by continuity Depending on its sign, curvature has either a substantial suppressing or intensifying effect on the turbulence structure Castro & Haque (1987) found that (suppressing) curvature effects are weak compared with the (intensifying) effect of the strain imposed by the recirculating flow. The recirculating flow is also subjected to straining by curvature of the mean streamlines as well as by mean shear. For a three-dimensional separation further extra rates of strain arise; the terms in these are $\partial W/\partial x$, $\partial W/\partial y$, $\partial U/\partial z$, $\partial V/\partial z$ and $\partial W/\partial z$.

Three regions A major feature of three-dimensional flow is that, unlike the ideal two-dimensional separation, the mean flow is not co-planar. Therefore, an obvious modification of a two-dimensional separation is one in which the flow, while not co-planar, is otherwise invariant in the spanwise direction Such a flow has the advantage that it minimises the additional measurements required, and should be relatively easy to handle computationally However, it is less useful if history effects associated with spanwise convection are not small, and several features typical of three-dimensional separations are precluded

Figure 1 illustrates a portion of a periodic separation

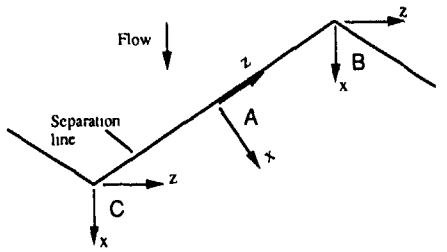

Fig 1 Regions A, B, C, downstream of separation line

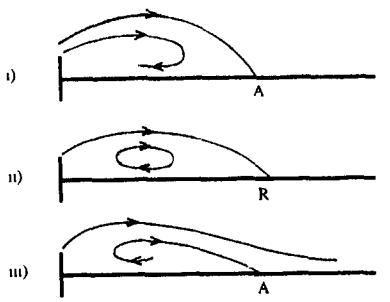

Fig 2 Streamlines on x-y planes, i) Region B ($\partial W/\partial z > 0$), ii) Region A ($\partial W/\partial z = 0$), iii) Region C ($\partial W/\partial z < 0$)

line, where the flow upstream of separation is from top to bottom. Three regions, A, B and C are identified, as are the axes to be used in the discussion of each region. y is perpendicular to x and z. Region A is the spanwise invariant region (if one exists) - that is, where $\partial/\partial z$ is everywhere zero. Assuming that the flow is spanwise-invariant in A and symmetrical in B and C (about the x-y planes) then some strain rate terms are zero, as shown below ($\partial U/\partial y$ is the primary strain if x is taken in the mixing-layer direction, and y perpendicular) The pressure gradient is also included

In region A: $(\partial U/\partial x) \neq 0$, $(\partial U/\partial y) \neq 0$, $(\partial U/\partial z) = 0$,
$(\partial V/\partial x) \neq 0$, $(\partial V/\partial y) \neq 0$, $(\partial V/\partial z) = 0$,
$(\partial W/\partial x) \neq 0$ $(\partial W/\partial y) \neq 0$ $(\partial W/\partial z) = 0$
and $(\partial p/\partial z) = 0$

On planes of symmetry in B and C:

$(\partial U/\partial x) \neq 0$, $(\partial U/\partial y) \neq 0$, $(\partial U/\partial z) = 0$,
$(\partial V/\partial x) \neq 0$, $(\partial V/\partial y) \neq 0$, $(\partial V/\partial z) = 0$,
$(\partial W/\partial x) = 0$, $(\partial W/\partial y) = 0$ $(\partial W/\partial z) \neq 0$
and $(\partial p/\partial z) = 0$

Thus the flows on the symmetry planes of B and C appear to be of particular interest in that, compared with the two-dimensional case, only $\partial W/\partial z$ is non-zero and is expected to be of opposite sign in A and B (see below) However, experimental determination of $\partial W/\partial z$ would need careful measurements either side of the symmetry plane Of course, a symmetrical geometry is only a necessary condition for symmetrical flow not a sufficient one The flows *in* Regions B and C, as distinct from flows on the symmetry planes, are examples of more general three-dimensional flows A further feature of symmetry of flow in Regions B and C is that mass flow is conserved between the symmetry planes through B and C, and this would have computational advantages in a domain between these planes

Kinematic constraints Integrating the continuity equation over the x-y plane (to an arbitrary closed boundary in the plane) gives

$$\iint(\partial U/\partial x)\,dx\,dy + \iint(\partial V/\partial y)\,dx\,dy + \iint(\partial W/\partial z)\,dx\,dy = 0$$

By Green's theorem the first two terms become contour integrals, to give

$$\oint U dy - \oint V dx + \iint(\partial W/\partial z).dx\,dy = 0, \qquad (1)$$

where the contour integrals are taken counter clockwise Now, on a (projected) streamline $dy/dx = V/U$, so

$$\int U\,dy - \int V\,dx = 0 \qquad (2)$$

along a streamline The third term in equation (1) represents the net mass flow into or out of the plane and equations (1) and (2) imply that a separating streamline is not the attaching streamline except in the spanwise-invariant case (where $\partial/\partial z = 0$), as illustrated in figure 2 for a separation on a fence and splitter-plate, where it has been supposed the flow is from B towards C. Figure 3 is an illustration of the flow in the three regions (assuming symmetry in B and C and spanwise invariance in A).

EXPERIMENTAL TECHNIQUES

In all cases reported here the separations have been developed on a fence-plus-splitter-plate arrangement (as in figure 3), with the splitter-plate mounted horizontally in the centre of a wind tunnel working section of 0.61m width x 0.76m height. The plate thickness was 3mm and the fence height, h_f, was 4mm for the surface patterns, and 3.5mm for most of the remainder Surface (limiting) streamlines were determined using conventional surface paint and the ink-dot method of Langston & Boyle (1982) which, unlike surface paint, is able to distinguish the stress vector direction, and was also found to be better in regions of very low shear stress. Mean velocities and Reynolds stresses were measured by means of a 'small' pulsed-wire probe, of 6mm pulsed and sensor wire lengths, supported from the underside of the splitter plate and passing through a small hole in the plate Interference effects associated with the probe support were negligible Surface pressures were obtained by means of pressure tappings. The upstream speed was about 9m/s, limited primarily by the maximum-velocity of the pulsed-wire anemometer

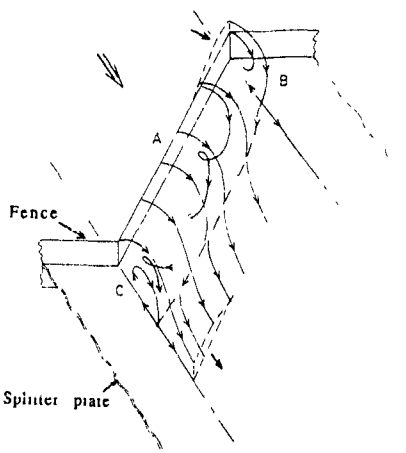

Fig 3. Sketch of separation and attachment streamlines downstream of a fence-plus-splitter plate

RESULTS

Surface streamlines Figures 4 and 5 show the limiting streamlines for a fence and splitter plate spanning the width of the tunnel, for sweep angles of 0°, 4°, 10°, and 25° Saddle and foci singularities of shear stress are indicated by S and F, respectively (No node singularities were observed in these cases) As the sweep angle is increased the singularities move; the numbers attached to each denote corresponding singularities Assistance in interpretation in some parts of the surface flow was gained from surface patterns (not shown) downstream of a larger fence which gave a larger distance to reattachment and greater detail, but at a reduced aspect ratio Reducing the thickness of the boundary layers on the wind tunnel side walls by means of end plates fitted parallel to the side walls resulted in very similar surface patterns though of slightly reduced aspect ratio

The aspect ratio of the present measurements, W/h_f = 155, is more than twice as large as than that used by Jaroch & Fernholz, and considerably larger than that used by Ruderich & Fernholz and Castro & Haque However, the surface lines in the centre of the unswept case (fig 4a) are not highly two-dimensional. Though not observed clearly there was a secondary separation line at roughly X_A/δ (≈$4h_f$) from the fence, possibly with a node of separation in the region of X The motion between the fence and the secondary separation was obviously weak, but it should not be automatically supposed that the flow in this region is therefore unimportant Another possibility for the surface pattern in the region of appears to be a saddle of separation and a pair of foci of opposite sense, as illustrated in figure 4b The latter is considered more plausible in that it is consistent with the patterns observed at non-zero sweep, and with the pattern (at zero sweep) observed by Jaroch & Fernholz at an aspect ratio of W/h_f = 63 That is, there is no 'switch' in the type of surface pattern, though the foci F3 and F4 (figure 4b) would appear to become stronger as the aspect ratio is reduced, and change in strength as the sweep is increased. The pattern of Jaroch & Fernholz appears to imply that S2 and S3 are "pushed" near to the side walls as the aspect ratio is reduced below some threshold; crudely, supposing S2 and S3 do not move with respect to the side walls until they are very close this threshold would appear to be about 50 On this basis, previous detailed measurements would appear to have been significantly affected by three-dimensional effects - ie by significant (negative) $\partial W/\partial z$

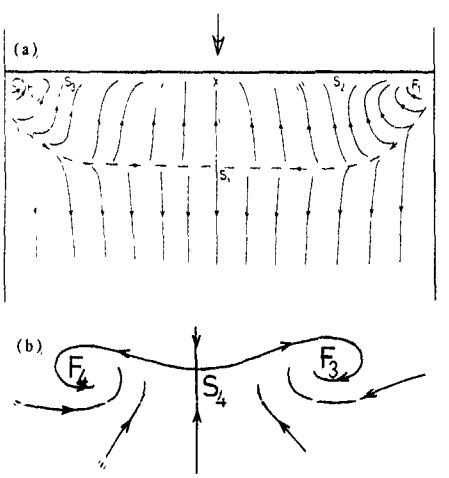

Fig 4 Limiting streamlines for unswept fence a) 0°, b) conjecture near X - not same scale as a).

As the sweep is increased S1 moves rapidly to the "downstream side" - ie to the left in figures 5a, b and c - and the focus, F3, becomes apparent The existance of S5 (in fig 5b) was clearer from surface patterns (not shown

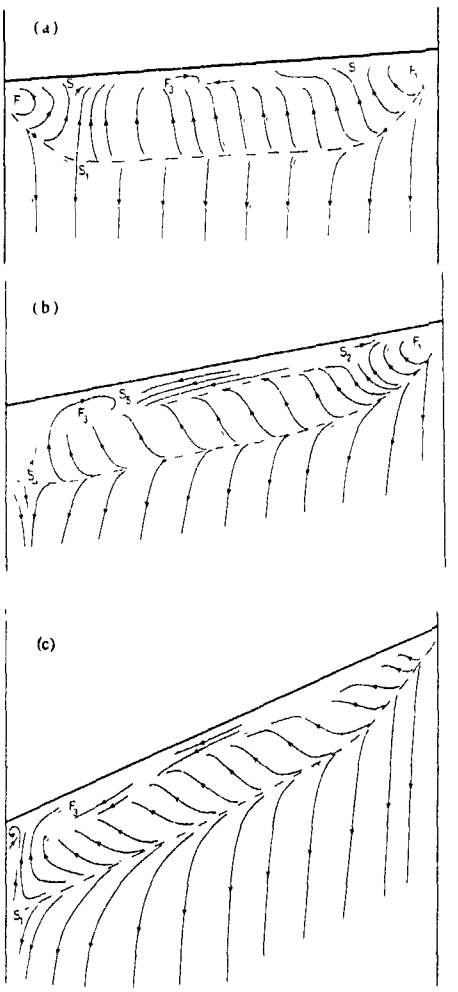

Fig 5 Limiting streamlines for swept fence. a) 4°, b) 10°, c) 25°

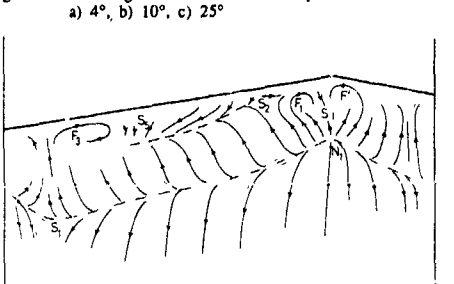

Fig 6 Limiting streamlines for 'cranked' fence - 10° sweep

here) downstream of a larger fence Above about 10° sweep the centre portion of the separation appears to be reasonably spanwise invariant, but for smaller sweep angles the presence of F3 near the centre suggests a still larger aspect ratio is required, assuming the position of F3 is primarily associated with the flow pattern on its downstream side F1 and S2 do not move much for sweep angles less than 10°, but would seem to move rapidly to the "upstream side" (right side in figure 5) for larger sweeps. (Surface patterns were also observed at sweeps of 2°, 6° and 8°, but not at intervals between 10° and 25°.) S3, S4 and F4 are moved to the downstream side as the sweep is increased F4, perhaps, becomes very weak Figures 5b and c suggest that about the central 20-25% of the span - ie, about 1 5 reattachment lengths - is spanwise invariant, and it seems highly likely that a spanwise-invariant region would not exist for $W/h_f <$ ~120 The distance to attachment measured normal to the fence is roughly invariant with sweep, though the distance to the secondary separation increases to roughly $8\,h_f$ for sweep angles greater than about 10° Surprisingly, the limiting streamlines of the secondary separation were repeatedly observed to be closely parallel to the fence, rather than towards the secondary separation line as would be normally the case, though this behaviour may be associated with the motion in the direction normal to the fence remaining relatively weak

In view of the above constraint on aspect ratio we would not expect to see a spanwise-invariant region in figure 6 There is, nevertheless, a clear topological similarity between the central regions in figures 5b and 6. Moreover, in these regions, there is good quantitative agreement in the limiting streamlines between the attachment and secondary separation lines Thus, it does seem reasonable that a region of spanwise invariance in the pattern would have existed for the case of figure 6 had the width, W, been larger, by about 25% Importantly, these results also suggest that if a region of spanwise invariance existed it would be quantitatively independent of whether the flow from the 'upstream side' originated near a wind tunnel side wall or from a Region-B flow The region B flow is somewhat distorted in the flow of figure 6 because of the proximity of the wind tunnel wall)

In a geometry (not shown) symmetrical to the wind tunnel side walls the region B flow was found to be symmetrical However, compared with the foregoing cases the aspect ratio was then effectively halved, and either F3 and F1 had merged or one had become very weak, neither S1 nor S5 were observed In a systematic study of separated flows as outlined earlier it is preferable that a spanwise invariant region should exist adjacent to Region B, requiring a total aspect ratio, W/h_f, approaching 300 The flow in Region C (not shown) was also found to be symmetrical in a symmetrical geometry, with S1 on the symmetry axis, and F3 and its mirror image either side

The variation with sweep of the distance to reattachment, X_A, in the nominally spanwise-invariant region, as measured from the surface patterns was constant at about $29h_f$, and agreed with measurements made by means of a simple two-tube pressure-difference probe This distance is consistent with the blockage dependence given by Smits (1982) Wolf also found the distance X_A independent of sweep angle

Surface pressures Figures 7a and b show C_p as functions of x and z respectively, for the geometry of figure 5c, but with an h_f of 3 5mm From the limiting streamlines (fig 5c) one would anticipate the central, say, 20% or more to be a region of spanwise invariance However, $\partial C_p/\partial z$ is clearly not zero in this region, changing sign about half-way along the bubble The general form of figure 7a is in good agreement with that measured by previous workers (eg Smits, 1982) The spanwise variation in C_p is caused by the presence of the wind tunnel side walls, primarily on the external flow and the linear variations (in figure 7b) are probably fortuitous Surface-pressure measurements downstream of a smaller fence (h_f= 3 m m) exhibited relatively smaller spanwise gradients, as expected Wolf (1987) implies that the spanwise pressure gradient was negligible for an aspect ratio W_A/X_A of about 5, compared with the present W_A/X_A of about 1 5, where W_A is measured parallel to the separation line

Making the simplistic assumption that the pressure does not vary with y, a change in C_p of ΔC_p, implies a fractional change in external velocity of $0\,5\Delta C_p$ So, for ΔC_p = 0 05, say, the velocity near the edge of the separation will change by 2 5% Broadly, this is in agreement with the measured variation with z of the velocity near the edge, though it is also close to the accuracy that can be expected for the velocity measurements However, although in these terms $\partial p/\partial z$ fairly small it is not small compared with the expected magnitude of the stress gradient $\partial \overline{vw}/\partial y$ which also appears in the z-momentum equation. Taking $\overline{vw}$ as comparable to uv in a two-dimensional mixing layer, ie about $0\,01U_0^2$ (Johnson & Hancock), and the length y as comparable with the bubble height, δ, then (in non-dimensional terms) $\partial p/\partial z$ in figure 7b is of the same magnitude as $\partial \overline{vw}/\partial y$ Also, although $\partial p/\partial z$ is an order of magnitude larger than $\partial p/\partial x$ in the downstream half of the separation, it is comparable with $\partial p/\partial x$ in the upstream half Thus, although the limiting streamlines of figure 5c) appear to be closely span-wise invariant it does not follow that $\partial/\partial z$ is negligible In that the width of the apparently spanwise-invariant zone is not much larger than one reattachment length this is not surprising, but neither was it obvious that $\partial p/\partial z$ - and

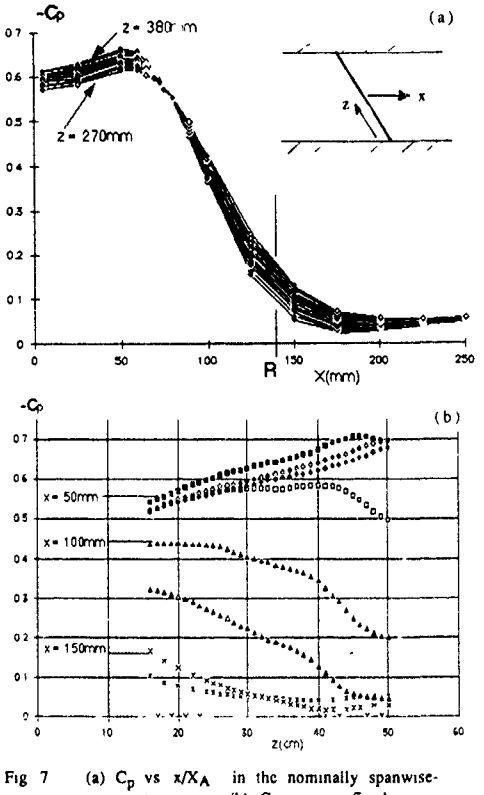

Fig 7 (a) C_p vs x/X_A in the nominally spanwise-invariant region (b) C_p vs z at fixed x, symbols not labelled refer to other x values (25° sweep)

presumably at least some other $\partial/\partial z$ terms - would be significant at the aspect ratio of figure 5c In simplistic terms, if the pressure fields associated with the regions near the wind tunnel side walls were constant, $\partial p/\partial z$ would vary inversely with the width of the nominally spanwise-invariant zone Wolf's geometry had a higher aspect ratio so that $\partial p/\partial z$ was probably smaller than in the present case (but not zero), unless there is some fortuitous difference arising from their use of a bluff thick plate rather than the present fence-plus-splitter plate

A partial explanation of the spanwise invariance of the limiting streamlines follows by supposing the velocity field, but not the pressure field, to be spanwise-invariant A two-dimensional velocity field implies a spanwise-invariant surface stress pattern, while in the equations of motion it permits the pressure to vary linearly in the spanwise sense - ie $p=f(x,y)+kz$, where k is a constant Such a dependence cannot apply above the separation as it implies non-zero vorticity

Mean velocities and Reynolds Stresses Figures 8 and 9 show U and W, and $\overline{u^2}$, $\overline{w^2}$ and $\overline{uw}$ measured in three planes $0.4X_A$ apart, in the nominally spanwise invariant region (As for the pressure distributions, the planes were in fact parallel to the tunnel axis, rather than perpendicular to fence, as probe traversing was easier, but U and W are, respectively, perpendicular and parallel to the fence) Measurements, not included here, were also made at $x/X_A = 0.54$ and 1.09 U and W show very little variation with z One noticeable point is that W is almost constant over most of the separation near reattachment (ie at 0.94 and 1.09) The measurements of stress in the three planes are generally in good agreement, although the scatter in $\overline{w^2}$ is rather large This amount of scatter was the worst observed $\overline{uw}$ is substantial, and comparable with $\overline{uv}$ in a two-dimensional mixing layer

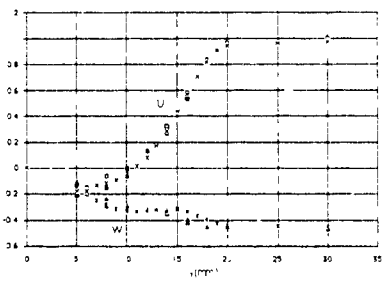

Fig 8a U and W in three spanwise planes $0.4X_A$ apart $x/X_A = 0.27$ (25° sweep) U, □, ·, ■, W, Δ, ×, ▲ (Symbol order is in direction of increasing z)

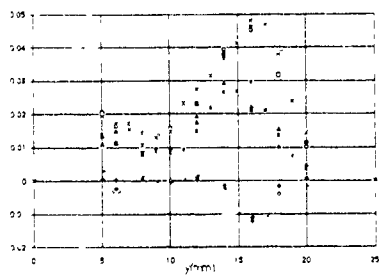

Fig 8b $\overline{u^2}$, $\overline{w^2}$ and $\overline{uw}$ in the three planes of a) $\overline{u^2}$, □, ×, ■, $\overline{w^2}$, Δ, ✱, ▲, $\overline{uw}$, ◊, –, ◆ (Symbol order is in direction of increasing z)

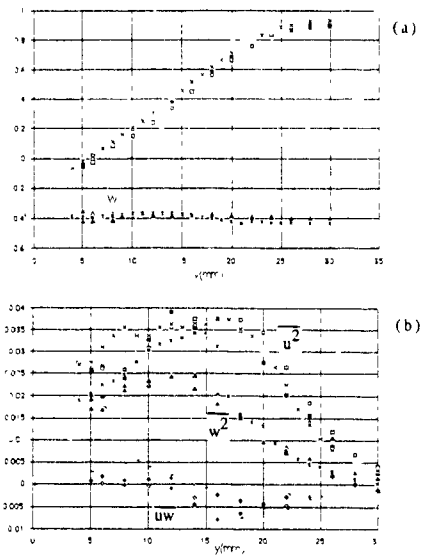

Fig 9 As for fig 8a (a) and 8b (b) but at $x/X_A = 0.94$

Figures 10 and 11 show U and W, and $\overline{u^2}$, $\overline{w^2}$ and $\overline{uw}$ in nominally spanwise invariant zones, where ' one case the cross flow originated near a wind-tunnel side wall, and in the other case from a Region-B flow (as in figure 6 but at 25° sweep) In the latter case the fence height was smaller in order to maintain a comparable aspect ratio for the spanwise invariant region Midway along the two separations there is little difference in the mean velocities or stresses, the slight difference in negative U being attributable to the small difference in x/X_A However, near reattachment, the differences in U near the edge of the separation, and in the stresses, are more marked Thus, though provisional at this stage, it appears that there is some residual side-wall effect even at the present, comparatively large aspect ratio

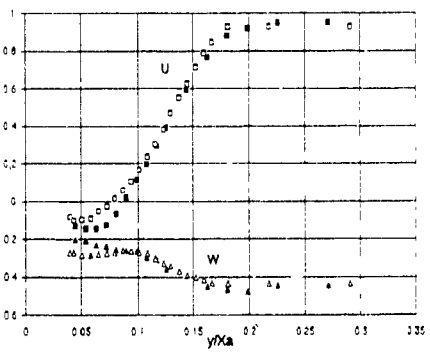

Fig 10a U and W open symbols - geometry as in fig 3c ($x/X_A = 0.54$) Filled symbols - cranked fence as in fig 6, but 25° sweep ($x/X_A = 0.58$)

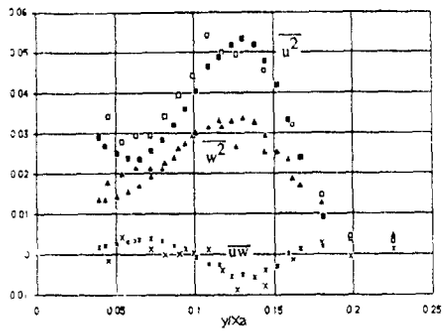

Fig 10b $\overline{u^2}$, $\overline{w^2}$ and $\overline{uw}$ corresponding to fig 10a

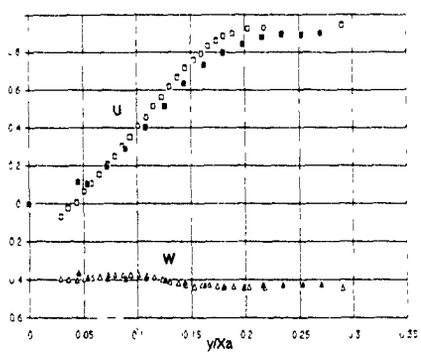

Fig 11a U and W as fig 10a but at $x/X_A = 1.0$ (filled symbols) and $x/X_A = 0.94$ (open symbols)

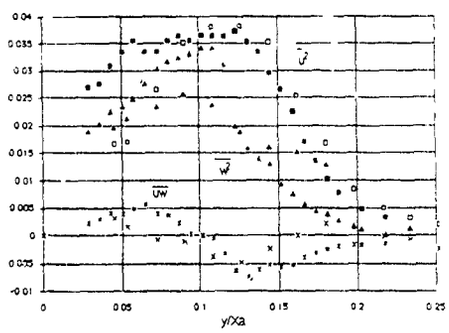

Fig 11b $\overline{u^2}$, $\overline{w^2}$ and $\overline{uw}$ corresponding to fig 11a

CONCLUSIONS

Three types or regions of three-dimensional separated flow have been considered, and are of particular interest in terms of extra strain rates Even for W/h_f =1.55 surface flow patterns showed distinct three-dimensionality in the unswept case The topology of the surface pattern seems to show a continuous change as the strength of the cross-flow increases Some singularities become strong, while others become very weak Spanwise invariance in the surface flow is a necessary though not sufficient condition for genuine spanwise invariance. The wind-tunnel side walls cause significant departure from spanwise invariance even for W/h_f = 1.74, though the effect on the flow structure, except perhaps near the surface, is small. The effect of flow near the 'upstream sidewall' may be significant near reattachment even for large aspect ratios of W/h_f = ~1.70 Flows in regions B and C (figure 2) are symmetrical

ACKNOWLEDGEMENTS

The authors wish to thank the Science and Engineering Research Council for their financial support throughout this work

REFERENCES

Castro, I P & Haque, A (1987) The structure of a turbulent shear layer bounding a separation region *J Fluid Mech* 179, 439

Jaroch, M P & Fernholz H H (1989) The three-dimensional character of a nominally two-dimensional separated turbulent shear flow *J Fluid Mech* 205, 523

Johnson, A F & Hancock, P E (1991) The effect of extra strain rates of curvature and divergence on mixing layers 7th Turbulent Shear Flows Symp Springer-Verlag

Handford, P M (1986) Measurements and calculations in three dimensional separated flow PhD thesis, Imperial College

Langston, L S & Boyle, M T (1982) A new surface streamline flow visualisation technique *J Fluid Mech* 125, 53

Ruderich, R & Fernholz H H (1986) An experimental investigation of a turbulent shear flow with separation, reverse flow, and reattachment *J Fluid Mech* 163, 283

Smits, A J (1982) Scaling parameters for a time-averaged separation bubble *Trans ASME, J Fluids Eng* 104,178

Wolf, F D B (1987) Swept and unswept separation bubbles PhD thesis, University of Cambridge

EIGHTH SYMPOSIUM ON
TURBULENT SHEAR FLOWS
Technical University of Munich
September 9-11, 1991

LARGE EDDY SIMULATION APPLIED TO THE MODELLING OF PARTICULATE TRANSPORT COEFFICIENTS IN TURBULENT TWO-PHASE FLOWS

E Deutsch and O Simonin

Laboratoire National d'Hydraulique - EDF
6 Quai Watier, 78400 Chatou, France

ABSTRACT

Statistical characteristics of particles suspended in an homogeneous and steady fluid turbulence have been studied using Large Eddy Simulation (L E S) Computations have been carried out for three typical particle/fluid density ratio (ρ_2/ρ_1 = 2000, 2 and 0 001) with the particle equation of motion including dragg, fluid pressure and added-mass forces

Numerical predictions are compared with analytical expressions obtained by an extended approach of the Tchen's theory which takes into account crossing-trajectories effects In parallel, the computation of the particulate transport coefficients validates closure assumptions used in the frame of the Eulerian two-fluid modelling with a special care about the separate contribution to dispersion induced by the transport of particles by the turbulent fluid motion

INTRODUCTION

This study takes part in a more general work on the numerical prediction of turbulent dispersed two-phase flows using Eulerian equations for both phases In this approach, the general equations set governing particle motion in homogeneous and steady turbulent two-phase flow leads to identify several terms which contribute simultaneously to the particle dispersion mechanism

Thus, the correlation between the instantaneous distribution of particles and the fluid velocity fluctuations at large scale with respect to the particle diameter, induces a separate contribution which predominates for particle diameter tending towards zero Based on semi-empirical analysis, this contribution may be written in terms of a binary turbulent dispersion coefficient proportional to the mean product between velocity fluctuations of the two phases and an eddy-particle interaction time (Simonin, 1990)

In order to analyse the accuracy of closure assumptions used to compute dispersed phase transport coefficients mean-square of velocity fluctuations and fluid-particle turbulent interaction terms, we have investigated the statistical characteristics of particle clouds suspended in an homogeneous and steady fluid turbulence using Large Eddy Simulation results

BASIC EQUATIONS

Averaged field equations

In the two-fluid model formulation, the field equations for each phase can be derived directly from the local instant conservation equations in single-phase flow by density-weighted averaging with in addition average balances of mass, momentum and energy at the interfaces By assumption, the mean spacing between particles is assumed to be very small with respect to the scale of variations in the mean flow Therefore the method of averaging associated to the dispersed phase can be expressed at any point as an ensemble average taken over the large number of particles included in a reference time-space domain centred on the point.

Restricting our attention to isothermal mixtures, where no phase change occurs, the field equations for the two-fluid model is written assuming that the granular stress due to interparticle collision and the molecular viscous stress in the fluid phase are negligible

Mass balance

$$\frac{\partial}{\partial t}\alpha_k\rho_k + \frac{\partial}{\partial x_j}\alpha_k\rho_k U_{kj} = 0 \qquad (1)$$

U_{ki} is the mean velocity i-component for the continuous (k=1) and dispersed phases (k=2) respectively,

α_k is the volumetric fraction and ρ_k the mean density

Momentum balance

$$\alpha_k\rho_k\frac{\partial}{\partial t}U_{ki} + \alpha_k\rho_k U_{kj}\frac{\partial}{\partial x_j}U_{ki} = -\alpha_k\frac{\partial}{\partial x_i}P_1 + \alpha_k\rho_k g_i - \frac{\partial}{\partial x_j}\alpha_k<\rho u''_i u''_j>_k + I_{ki} \qquad (2)$$

u''_i is the fluctuation of the local instantaneous velocity and $<\ >_k$ the averaging operator associated to phase k,

$$\alpha_k\rho_k U_{ki} = \alpha_k<\rho u_i>_k \qquad <\rho u''_i>_k = 0$$

P_1 is the mean pressure of the continuous phase,

I_{ki} is the part of the interfacial momentum transfer rate between phases which remains after substraction of the mean pressure contributions

Interfacial momentum transfer

If we consider a dilute dispersion of small rigid spheres in translation with relative motions of low Reynolds number, the resulting force induced by the surrounding nonuniform fluid flow on each point included in the dispersed phase can be written

$$f_{2i} = -\rho_1 F_D v_{ri} - \rho_1 C_A\frac{dv_{ri}}{dt} - \rho_1 C_H\int_{t_0}^{t}\frac{dv_{ri}}{d\tau}\frac{d\tau}{\sqrt{t-\tau}} + \left[\rho_1\frac{D\tilde{u}_{1i}}{Dt} - \rho_1 g_i\right] \qquad (3)$$

v_{ri} is the local instantaneous relative velocity defined on each point included in the particulate phase and given by $v_{ri} = \tilde{u}_{2i} - \tilde{u}_{1i}$,

$\tilde{u}_{2i}$ is the translation velocity of the particle which contains the point,

$\tilde{u}_{1i}$ is the characteristic velocity of the surrounding flow field locally undisturbed by the presence of the particle but which remains turbulent

The first three terms on the right-hand side of Eq (3) correspond to the drag, the added mass and the Basset history force respectively The last two terms are due to the stress applied on the particle by the undisturbed surrounding fluid flow The derivative d/dt is used there to denote a time derivative following the moving particle

Since Tchen's proposal, several papers have appeared correcting or modifying terms in the equation of particle motion According to Gatignol (1983), the approximate form used there is valid at low particle Reynolds number, if the representative time of the variation rate of the undisturbed fluid flow is of the same order as the characteristic time of the viscous effects acting on the particle At high particle Reynolds number, we must notice that the fluid velocity

derivatives in the equation (3) should be expressed in terms of the change along the fluid element trajectory This modification could be especially important in predicting the motion of bubbles in a liquid

Finally, constitutive relations for the interfacial transfer terms I_k, in the basic Eulerian equations may derive by averaging from the particulate expression Special care is required to take into account the dispersion effect due to the fluctuations of the momentum transfer terms (Simonin, 1990)

EULERIAN MODELLING OF PARTICLE DISPERSION

Particle dispersion in homogeneous turbulence

In the framework of the diffusion approximation, the flux induced by the random motion of fluid (or discrete) particles is written in terms of the gradient of the volumetric fraction as

$$\alpha_k U_{k,i} = - D^t_{k,ij} \frac{\partial \alpha_k}{\partial x_j} \qquad (4)$$

the effective turbulent diffusion (or dispersion) tensor components are given by

$$D^t_{k,ij} = \frac{1}{2} \frac{d}{dt} < y_{k,i} y_{k,j} >_k \qquad (5)$$

where $< y_{k,i} y_{k,j} >_k$ is the time-dependant displacement tensor of fluid (k=1) and discrete (k=2) particles

For long time dispersion, the dispersion tensor can be related to the velocity correlation field by

$$D^t_{k,ij} = \sqrt{< u^2_{k,i} >_k < u''^2_{k,j} >_k} \int_0^{\infty} R_{k,ij}(\tau)\, d\tau \qquad (6)$$

where the Lagrangian correlation tensors R_1 and R_2 are computed along the fluid and discrete particles trajectories respectively and correspond with the energy spectrums E_1 and E_2 by Fourier transformations

Finally, it is convenient to define a Lagrangian integral time scale

$$\tau^t_{k,ij} = \int_0^{\infty} R_{k,ij}(\tau)\, d\tau \qquad (7)$$

In order to steady turbulent dispersion phenomenon in the two-fluid model formalism, we consider a dilute distribution of particles ($\alpha_2 << 1$) suspended in an homogeneous and steady turbulent fluid flow T' 'n, the particulate flux can be written

$$\alpha_2 U_{2,i} = \alpha_2 \left[V_{r,i} + V_{d,i} \right]$$

$V_{r,i}$, the averaged value of the local relative velocity, can be obtained from the momentum equation (2) as

$$\alpha_2 V_{r,i} = - \left[\tau^F_{12} < u''_{2,i} u'_{2,j} >_2 - b\, \tau^F_{12} < u'_{1,j} u'_{2,i} >_2 \right] \frac{\partial}{\partial x_j} \alpha_2$$

where τ^F_{12} is the characteristic time of particle dragging by the continuous fluid motion or particle relaxation time

$$\tau^F_{12} = F_D^{-1} \left[\frac{\rho_2}{\rho_1} + C_A \right] \qquad b = \left[1 + C_A \right] \left[\frac{\rho_2}{\rho_1} + C_A \right]^{-1} \qquad (8)$$

$V_{d,i}$, the drifting velocity, is equal to the correlation between the instantaneous distribution of particles and the velocity fluctuations of the undisturbed fluid flow

$$V_{d,i} = < \tilde{u}_{1,i} >_2 - U_{1,i} = < u''_{1,i} >_2 \qquad (9)$$

and takes into account the dispersion effect due to particles transport by turbulent fluid motion According to the limit case of particles with diameter tending towards zero, for which the drifting velocity reduces to the single turbulent correlation between the volumetric fraction of the dispersed phase and the velocity of the continuous phase, the velocity $V_{d,i}$ is written as follows :

$$V_{d,i} = - D^t_{12,ij} \left[\frac{1}{\alpha_2} \frac{\partial \alpha_2}{\partial x_j} - \frac{1}{\alpha_1} \frac{\partial \alpha_1}{\partial x_j} \right] \qquad (10)$$

Thus, according to the previous expression of the particulate flux, the effective turbulent dispersion tensor for discrete particles can be directly related to the fluid-particle one

$$D^t_{2,ij} = D^t_{12,ij} + \tau^t_{12} \left[< u_{2,i} u'_{2,j} >_2 - b < u'_{1,i} u_{2,j} >_2 \right] \qquad (11)$$

Finally, the effective dispersion tensor of the particulate phase is obtained as the sum of a binary turbulent dispersion coefficient and a contribution due to the random motion of particles and the fluctuations of the fluid pressure and added mass forces This last contribution is proportional to the particle relaxation time and so becomes negligible when the particle diameter tends towards zero And the other hand, the equation (11) points out the prominent part plays by the mean-square of velocity fluctuations when the particle relaxation time is increasing Thus, accurate predictions of particle-laden turbulent flows in the Eulerian formalism require reliable knowledge of the individual components of the dispersed-phase Reynolds stress tensor (Simonin, 1991)

Particles suspended in turbulent fluid flow

The traditional approach used to compute the statistical characteristics of the particulate fluctuating motion, is based on a direct extension of fundamental results concerning the motion of dicrete particles suspended in an homogeneous and steady turbulent fluid flow In the frame of the Tchen's theory, the dynamic equation for particle motion is Fourier transformed to the frequency domain where it can be solved directly

For this purpose, we now introduce the Lagrangian correlation tensor $\mathcal{R}_1$ associated to the fluctuating motion of the fluid computed along the particles trajectories

$$\mathcal{R}_{1,ij}(\tau) = < u'_{1,i}(t)\, u''_{1,j}(t+\tau) >_2 \Big/ \sqrt{< u^2_{1,i} >_2 < u'^2_{1,j} >_2} \qquad (12)$$

which corresponds with the energy spectrum tensor $\mathcal{E}_1$

Then, from the particle motion equation (3), using Fourier transformations, we may establish a linear relation between energy spectrums with the help of the so-called particle response coefficient Q_{12} (Gouesbet et al., 1984) written analytically in terms of three independant dimensionless parameters

$$\mathcal{E}_{2,ij}(\omega) = Q_{12}(\tau^F_{12}\, \omega, C_H/\sqrt{\omega}, b)\, \mathcal{E}_{1,ij}(\omega) \qquad (13)$$

Thus, the turbulent correlation tensor, the effective dispersion tensor and the mean-square velocity of the dispersed phase (but also the velocity covariance between phases) can be computed by numerical integration using a given form of the fluid Lagrangian correlation tensor $\mathcal{R}_1$, for instance one obtains

$$D^t_{2,ij} = \tau^t_{12,ij} \sqrt{< u'^2_{1,i} >_2 < u''^2_{1,j} >_2} \qquad \tau^t_{12,ij} = \int_0^{\infty} \mathcal{R}_{1,ij}(\tau)\, d\tau \qquad (14)$$

where $\tau^t_{12,ij}$, the fluid-particle Lagrangian integral time scale, or eddy-particle interaction time, characterize the fluid turbulence viewed by the particles

But, we must notice that the fluid correlation tensor $\mathcal{R}_1$, which leads to the previous results, is written in terms of the fluid velocity fluctuations encountered along the discrete particle trajectories In general, this correlation tensor can not be identified directly with the standard one R_1 computed along the fluid element trajectories As a matter of fact, this identification is probably the more questionable approximation of the Tchen's theory and is justified by the assumption that, during its motion, the neighbourhood of each particle will be formed by the same fluid element But, for instance, for a non-zero mean relative velocity between phases, the modifications in the fluid turbulence viewed from a reference frame moving with the particulate phase lead to the so-called crossing-trajectories effects which clearly reduce the dispersion of the particles

Crossing-trajectories effects

Using a slightly different method than the one proposed by Csanady (1963), we can note that, when the instantaneous displacement of the particles is dominated by the mean relative velocity, the Lagrangian correlation $\mathcal{R}_{1,ij}$ stands for an Eulerian space correlation of the fluid velocity fluctuations Thus, restricting our attention to homogeneous and isotropic fluid turbulent

flows, the Lagrangian correlation, parallel to the mean relative velocity direction ℓ, is written

$$\mathcal{R}_{\ell\ell}(\tau) = \exp\left[-\tau / \tau^{t}_{12\ell}\right] \qquad (15)$$

where the eddy-particle interaction time is given by

$$\tau^{t}_{12\ell} = \tau^{t}_{l}\left[1 + \beta^2 \xi_r^2\right]^{-\frac{1}{2}} \qquad \beta = \frac{\tau^{t}_{l}}{L^{t}_{l}}\sqrt{\frac{2}{3}q_l^2} \qquad \xi_r^2 = \frac{3}{2}\frac{V_r^2}{q_l^2} \qquad (16)$$

q_l^2 is the fluid turbulent kinetic energy, L^{t}_{l} is the Eulerian length-scale and τ^{t}_{l} is the fluid Lagrangian time macroscale

Neglecting the Basset force, we can compute analytically from equation (13) the longitudinal velocity variance of the dispersed phase, and the velocity covariance between the two phases, in terms of the fluid turbulent kinetic energy viewed by the particles

$$< u'_{2\ell} u''_{2\ell} >_2 = < u'^{2}_{1\ell} >_2 \left[\frac{b^2 + \eta_{r,\ell}}{1 + \eta_{r,\ell}}\right] \qquad \eta_{r,\ell} = \frac{\tau^{t}_{12\ell}}{\tau^{F}_{12}} \qquad (17)$$

$$< u''_{1\ell} u''_{2\ell} >_2 \sim < u'^{2}_{1\ell} >_2 \left[\frac{b + \eta_{r,\ell}}{1 + \eta_{r,\ell}}\right]$$

we can notice that previous expressions are affected by inertial and crossing-trajectories effects simultaneously, through the characteristic times ratio η_r

If the instantaneous distribution of particles and the fluid turbulent kinetic energy are uncorrelated so that

$$< u''^{2}_{1\ell} >_2 = < u'^{2}_{1\ell} >_1 = 2/3\, q_l^2$$

we obtain from (14) the expression proposed by Csanady for the effective particle dispersion coefficient

$$D^{t}_{2\ell} = D^{t}_{1}\left[1 + \beta^2 \xi_r^2\right]^{-\frac{1}{2}} \qquad (18)$$

Comparison of the previous equation with experimental results (Wells and Stock, 1983) shows a good agreement and leads to the approximate value of $\beta^2 = 0.45$

Following Csanady proposal, we may assume same forms for the lateral turbulent characteristics than for the longitudinal one, but with a different eddy-particle interaction time because of the continuity effect

$$\tau^{t}_{12\,j} = \tau^{t}_{l}\left[1 + 4\beta^2 \xi_r^2\right]^{-\frac{1}{2}} \qquad j \neq \ell \qquad (19)$$

Finally, the fluid-particle dispersion coefficient may be written in terms of the velocity covariance and the eddy-particle interaction time as

$$D^{t}_{12\,ij} = \tau^{t}_{12\,ij} < u''_{1i} u''_{2j} >_2 \qquad (20)$$

Thus, substituting analytical expressions for the kinetic stress tensor components in the definition of the effective particle dispersion tensor from the two-fluid model formalism (11), we obtain the equality (14) due to the direct Fourier resolution of particle motion equation

Particle kinetic stress in simple shear flow

The computation of particle velocity fluctuations depends on the interaction with the fluid turbulent motion, but is also modified by the mean gradient of the particle velocity Restricting our attention to dilute concentrations of heavy particles, we may obtain from the second-moment transport equations (Simonin, 1991), by neglecting convective and diffusive transport, the following equation for the off-diagonal correlations

$$< u''_{2i} u''_{2j} >_2 = R_{12,ij} - \frac{1}{2}\tau^{F}_{12}\left[< u'_{2i} u'_{2m} >_2 \frac{\partial U_{2j}}{\partial x_m} + < u''_{2j} u''_{2m} >_2 \frac{\partial U_{2i}}{\partial x_m}\right] \qquad (21)$$

where the first contribution, which results from the local dragging by the fluid turbulent motion, is equal to the fluid-particle symmetrical correlation tensor $R_{12,ij}$

$$R_{12,ij} = \frac{1}{2}\left[< u''_{1i} u_{2j} >_2 + < u'_{2i} u''_{1j} >_2\right] \qquad (22)$$

The set of equations governing the fluid-particle correlation tensor cannot be derived exactly from the local instantaneous equations Nevertheless, from an approximate form of the fluid velocity fluctuation equation of the Langevin type, we may obtain a practical form of the second-moment equation, which reads, neglecting convective and diffusive transport, as follows

$$< u_{1i} u''_{2j} >_2 = \frac{\eta_r}{1 + \eta_r} < u_{1i} u_{1j} > - \frac{\tau^{t}_{12}}{1 + \eta_r}\left[< u''_{1i} u'_{2m} >_2 \frac{\partial U_{2j}}{\partial x_m} + < u''_{2j} u'_{1m} >_2 \frac{\partial U_{1i}}{\partial x_m}\right] \qquad (23)$$

Thus if the fluid Reynolds shear stress viewed by the particles may be computed with the help of the eddy viscosity concept in terms of the eddy-particle interaction time and the fluid-particle velocity correlation, providing that the mean gradient of the relative velocity may be neglected, we obtain the eddy-viscosity of heavy particle clouds suspended in homogeneous turbulence as

$$\nu^{t}_{2} = \tau^{t}_{12}\frac{1}{3}q_{12} + \frac{1}{2}\tau^{F}_{12}\frac{2}{3}q_2^2 \qquad (24)$$

where $q_{12} = \sum_{i=1}^{3} < u'_{1i} u'_{2i} >_2$ and $q_2^2 = \frac{1}{2}\sum_{i=1}^{3} < u''_{2i} u'_{2i} >_2$

Like the dispersion coefficient, the particulate eddy-viscosity is written as the sum of two separate contributions proportional to the eddy-particle interaction time and the particle relaxation time respectively According to the effective dispersion coefficient expression, the Schmidt leads to 1/2 for "large" heavy particles ($\eta_r << 1$) And the other hand, the previous expression is consistent with the modelling of the fluid turbulence when the particle diameter is tending towards zero ($\eta_r >> 1$)

On the contrary, if the fluid turbulence remains fully isotropic corresponding to a zero fluid velocity gradient, the effective eddy-viscosity of the particle clouds reduces to the following expression

$$\nu^{t}_{2} = \frac{1}{2}\left[\frac{\tau^{t}_{12}}{1 + \eta_r}\right]\frac{1}{3}q_{12} + \frac{1}{2}\tau^{F}_{12}\frac{2}{3}q_2^2 \qquad (25)$$

which is decreasing with the particle relaxation time, but has the same limit than (24) for "large" particles

LARGE EDDY SIMULATION METHOD

Fluid turbulence predictions

The computations of particle trajectories in homogeneous fluid turbulence require the knowledge of the instantaneous three-dimensional velocity field Though the Direct Simulation is the approach the most satisfactory from the theoretical point of vue, it is not practical owing to the limitation to low Reynolds number turbulence But, as the dominant process in particle displacement is the interaction with the large scales of the fluid velocity field, we can used Large Eddy Simulation with a good accuracy The numerical methods used there have been developed for many years at the "Laboratoire National d'Hydraulique" (Khoudli, 1988)

The fluid equations are unchanged by the presence of the particles since the volume fraction of the particles and the interfacial momentum transfer are assumed to be negligible The homogeneous and isotropic turbulence field, obtained from simulation using 64^3 grid points, stands still artificially by adjustement of the spectrum by comparison with the theoretical von Karman-Pao form Fluid turbulent characteristics correspond to the initial measurements of Wells and Stock experiment (1983) in a grid-generated turbulence

Particle tracking algorithm

In order to minimize numerical bias, statistical results for each case were obtained from an ensemble of about 25000 particle trajectories Special attempts were made in the treatment of the particle motion concerning the projection of instantaneous fluid characteristics on the position of the particles and the time integration of the dynamic equation (Deutsch and Simonin, 1991)

The particle momentum equation was time advanced using a second-order Runge-Kutta scheme with the same

time step as for the fluid velocity field calculation The particles were released with an initial velocity equal to the local instantaneous fluid velocity To remove the influence of the release conditions, the particles were allowed to disperse somewhat before the statistics were calculated The Basset force contribution is assumed to be negligible, this assumption may reduce the practical accuracy of the simulations for the lightest particles but does not affect the comparison with the theoretical results obtained in the frame of the Tchen's theory and based on the same assumption

RESULTS AND DISCUSSION

Particles suspended in turbulent fluid flows

In a first step, computations were carried out for zero-mean relative velocity (without gravity) and three typical particle/fluid density ratio (ρ_2/ρ_1 = 2000 , 2 and 0 001) with various particle diameters in order to modify appreciably the particle relaxation time

The results validate the theoretical expressions derived, in the frame of two-fluid model formalism, for the dispersion coefficient (figure 3) and the velocity fluctuations (figures 4 to 9) in terms of the fluid turbulent characteristics viewed by the particles Thus, in order to improve the accuracy of Eulerian predictions, the closure assumptions should take into account the tendency of the fluid-particle Lagrangian integral time scale, or eddy-particle interaction time, to increase for large values of the particle relaxation time (figure 2)

As the particle dispersion coefficient can be written as proportional to the 'eddy-particle interaction time" using Eq (14), it may be pointed out (figure 3) that the particle dispersion coefficient may be greater than that of fluid elements But, for practical purpose, this effect must be compared with the increase of effective dispersion (up to ten times more) observed in particle-laden jets predictions (Simonin, 1990) and due to the memory of injection conditions on the particle velocity correlations distribution

And the other hand, the results of simulation for the lightest particles (ρ_2/ρ_1 = 0 001) exhibit large statistical bias (figure 1) due to the correlation between the distribution of the particles and the local instantaneous fluid turbulent kinetic energy, corresponding to a strong preference to collect in regions of low velocity According to the analysis based on the Fourier transformation of the dynamic equation (Gouesbet et al , 1981), the kinetic energy of the lightest particles is locally larger than the one of the fluid turbulence viewed by the particles (figure 6), but, due to the statistical bias, remains smaller than the average turbulent kinetic energy of the whole fluid flow

In addition, Figures 10 to 12 show the separate contribution of the fluid-particle dispersion coefficient induces by transport of particles by fluid turbulent motion These results are consistent with the idea that the dispersion of the very small discrete particles is mainly controlled by the fluid turbulent mixing However, we can note the surprising results that the fluid-particle dispersion coefficient for the lightest particles may be larger than the effective one owing to the fact that undisturbed fluid pressure and added mass effects induce a negative contribution

Crossing-trajectories effects

The effect of non-zero mean relative velocity of particles crossing a stationary homogeneous turbulent field is studied based on results of the Large Eddy Simulation for different values of the external force applied on the heavy particles (ρ_2/ρ_1 = 2000)

Figures 13 compare the fluid-particle Lagrangian integral time scales, computed from the L E S results, with analytical expressions (16) and (19) with β^2 = 0 45 We can note a fine agreement between the simulation data and equations, specially for increasing values of the mean relative velocity. Consistent with the so-called continuity effects, the fluid-particle Lagrangian time scale in direction perpendicular to the mean relative velocity are becoming half as large as the one along the parallel direction Thus, we obtain that the effect of crossing trajectories reduces the dispersion of the particles, but also the particle and fluid-particle velocity correlations, unequally in directions parallel and normal to the mean relative velocity.

Figures 14 show an extremely good agreement between simulated velocity correlations and analytical expressions (17) obtained in the frame of the Tchen's theory Finally, figure 15 shows an improvement in the accuracy of the closure assumptions used in the Eulerian two-fluid modelling for non-zero mean relative velocity

Particle kinetic shear stress

The influence of the mean velocity gradient on the heavy particle kinetic shear stress is studied based on particle clouds with a x_3 linear variation of the mean velocity component $U_{2\,i}$ imposed by a non-uniform external force field acting on the particles

Firstly, figures 16 and 17 show that the computed particle and fluid-particle velocity correlations stand in good agreement with the analytical expressions (17) And the other hand, the particle dispersion coefficient, which may be computed from the displacement tensor (5) in the x_2 direction, is in very good agreement with the theoretical expressions obtained in the frame of two-fluid modelling and is correctly reduced according to an average crossing trajectories effect (figure 19)

Concerning the L E S predictions of the particle Reynolds shear stress component $< u''_{2\,i}\, u'_{2\,3} >_2$ influenced by the particle mean velocity gradient, figure 20 shows a fine agreement with the one obtained as the sum of the separate predicted contributions from (21) Thus, the separate contribution $R_{12\,i}$ due to the particle dragging by the fluid turbulence is decreasing with the increase of the particle relaxation time

And the other hand, figure 21 show the separate fluid-particle velocity correlations which contribute to the particle shear stress We obtain a fairly good agreement with the semi-empirical equation (23), specially for the component $< u''_{2\,i}\, u''_{i\,3} >_2$ influenced by the particle mean velocity gradient Unfortunately, a part of these correlations is due to the residual anisotropy of the predicted fluid turbulence and thus limit the accuracy of the analysis concerning the particle eddy-viscosity

However, figure 18 shows the comparison of the theoretical expressions (24) and (25) for particle eddy-viscosity with the effective one computed as the particle shear stress predictions and the mean velocity gradient ratio The deviation between predictions and the equation (25) is due to the residual fluid turbulence anisotropy in the L E S predictions Thus, the agreement is increasing with the particle relaxation time, when dispersion effects are mainly controlled by the random motion of particles, and finally, the results validates the limit value 1/2 obtained for the particle Schmidt ($\eta_t < 1$)

REFERENCES

Csanady, G.T., , 963, "Turbulent Diffusion of Heavy Particles in the Atmosphere", *J Atm Sc*, Vol 20, pp 201-208

Deutsch, E , Simonin, O., 1991, Large Eddy Simulation Applied to the Motion of Particles in Stationary Homogeneous Fluid Turbulence", *Proc Workshop Turbulence Modification in Multiphase Flows*, June 23-26, Portland, U S A

Gatignol, R., 1983, "The Faxen Formulae for a Rigid Particle in an Unsteady Non Uniform Stockes Flow", *J de Méc Th et Appl*, Vol 1, n° 2, pp 143-160

Gouesbet, G , Berlemont, A., Picart, A., 1984, "Dispersion of Discrete Particles by Continuous Turbulent Motions", *Phys Fluids*, Vol 27, n° 4, pp 827-837

Khoudly, M., 1988, "Macrosimulation de Turbulence Homogène en Présence de Cisaillement et de Gradients Thermiques Application aux Modèles de Fermeture en un Point", *Thèse Ecole Centrale de Lyon* , Lyon

Simonin, O., 1990, "Eulerian Formulation for Particle Dispersion in Turbulent Two Phase Flows", *Proc 5th Workshop on Two-Phase Flow Predictions*, Mars 19-22, Erlangen, R F A

Simonin, O., 1991, "Prediction of the Dispersed Phase Turbulence in Particle-Laden Jets", *Proc 4th Int Symp on Gas-Solid Flows*, June 23-26, Portland, U S A.

Wells, M R., Stock, D.E., 1983, "The Effects of Crossing Trajectories on the Dispersion of Particles in a Turbulent Flow", *J Fluid Mech*, Vol 136, pp 31-62

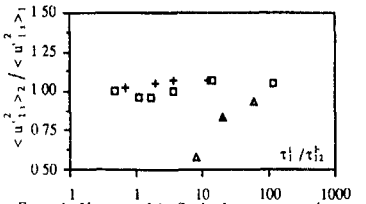

Figure 1 Variance of the fluid velocity computed along particle trajectories □ $\rho_2/\rho_1 = 2000$, + $\rho_2/\rho_1 = 2$, ▲ $\rho_2/\rho_1 = 0.001$

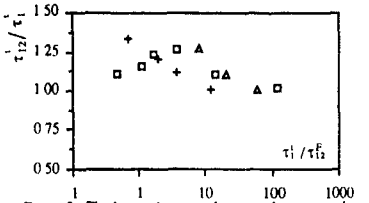

Figure 2 Fluid particle integral time scale computed from L E S results □ $\rho_2/\rho_1 = 2000$, + $\rho_2/\rho_1 = 2$, ▲ $\rho_2/\rho_1 = 0.001$

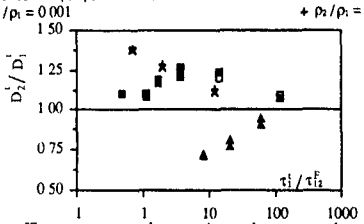

Figure 3 Particle dispersion coefficient, comparison between theorical expression obtained in the framework of diffusion approximation (Eq 5) and Eulerian two-fluid model formalism (Eq 11) respectively
□ and ■ for $\rho_2/\rho_1 = 2000$, + and × for $\rho_2/\rho_1 = 2$, ▲ and ▲ for $\rho_2/\rho_1 = 0.001$

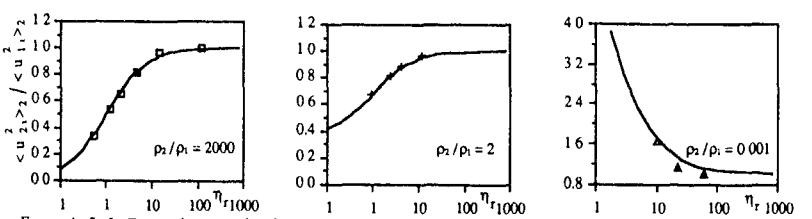

Figures 4, 5, 6 □ , + and Δ, particle velocity variances computed by L.E.S , — Tchen's theory extension (Eq 17)

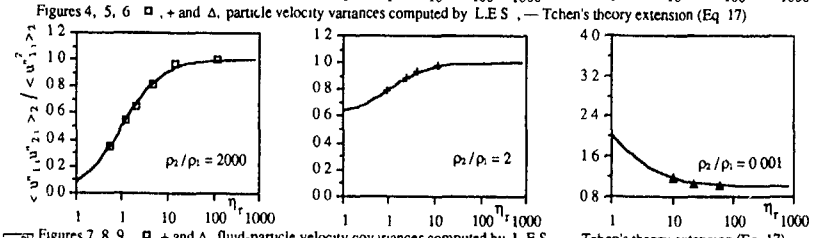

Figures 7, 8, 9 □, + and Δ, fluid-particle velocity covariances computed by L E S , — Tchen's theory extension (Eq 17)

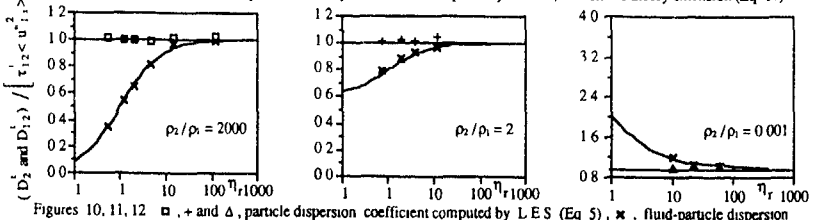

Figures 10, 11, 12 □ , + and Δ , particle dispersion coefficient computed by L E S (Eq 5) , × , fluid-particle dispersion coefficient computed from L E S results (Eq 20) , — dispersion coefficients (Eq 11 and 20) computed from the particle and fluid-particle Reynolds stress expressions of the Tchen's theory extension (Eq 17)

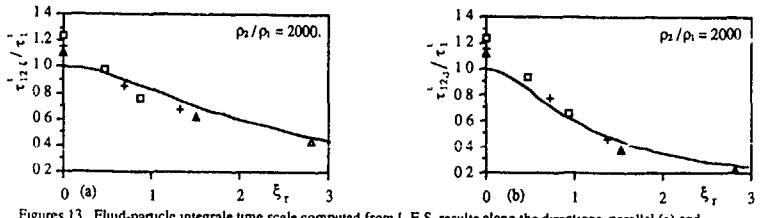

Figures 13 Fluid-particle integrale time scale computed from L E S results along the directions parallel (a) and perpendicular (b) to the mean relative velocity, comparison with Csanady expression (β^2=0.45)
□ , + and Δ L E S (particle diameter d= 45 μm, 57 μm and 90 μm respectively), — Csanady expression

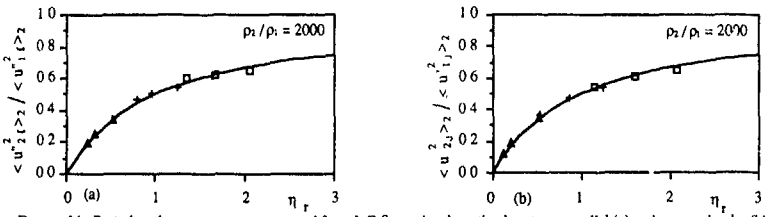

Figures 14 Particle velocity variances computed from L E S results along the directions parallel (a) and perpendicular (b) to the mean relative velocity, comparison with prediction of the Tchen's theory extension
□ , + and Δ L E S (particle diameter d= 45 μm, 57 μm and 90 μm respectively), — Tchen's theory extension

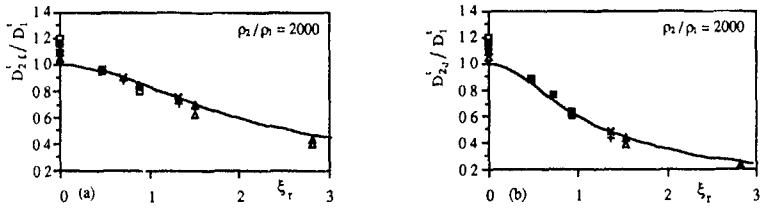

Figures 15 Particle dispersion coefficient computed from L E S results along the directions parallel (a) and perpendicular(b) to the mean relative velocity, comparison between theorical expression obtained in the framework of diffusion approximation (Eq 5) and Eulerian two-fluid model formalism (Eq 11) respectively , □ and ■ for particle diameter d= 45 μm, + and ✖ for particle diameter d=57 μm, Δ and ▲ for particle diameter d=90 μm,
— Csanady expression (Eq 18)

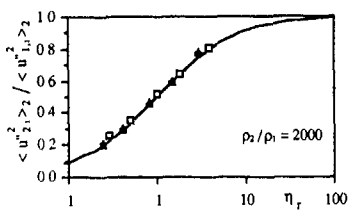

Figure 16 □ , ▲ , + , particule velocity variances computed by L E S , — Tchen s theory extension (Eq 17)

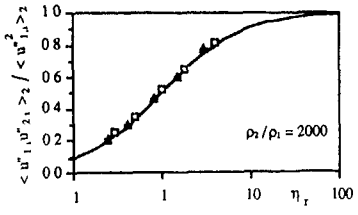

Figure 17 □ , ▲ , + , fluid-particule velocity covariances computed by L E S , — Tchen's theory extension (Eq 17)

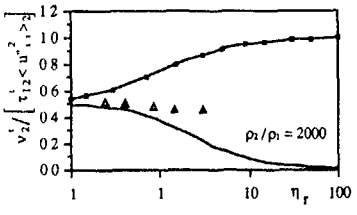

Figure 18 . ▲ , effective particle viscosity computed from L E S results , -●- and — theorical expressions obtained in the framework of Eulerian two fluid modelling (Eq 24 and 25)

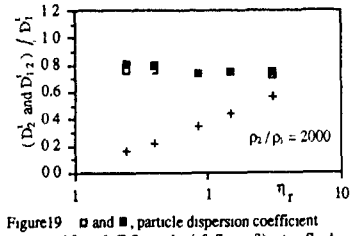

Figure19 □ and ■ , particle dispersion coefficient computed from L E S results (cf figure 3) , + , fluid-particle dispersion coefficient

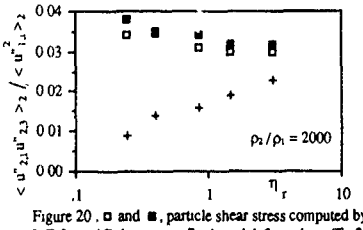

Figure 20 . □ and ■ , particle shear stress computed by L E S and Eulerian two fluid model formalism (Eq 21) , + fluid-particle symmetrical tensor (Eq 22)

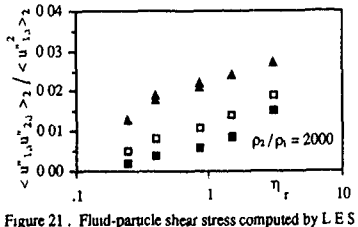

Figure 21 . Fluid-particle shear stress computed by L E S and Eulerian two fluid model formalism (Eq 23) respectively □ and ■ for $<u''_{1,1}u''_{2,3}>_2$, ▲ and ▲ for $<u''_{2,1}u''_{1,3}>_2$

EIGHTH SYMPOSIUM ON
TURBULENT SHEAR FLOWS
Technical University of Munich
September 9-11, 1991

MODELING OF PARTICLE DYNAMICS AND HEAT TRANSFER IN TURBULENT FLOWS USING EQUATIONS FOR FIRST AND SECOND MOMENTS OF VELOCITY AND TEMPERATURE FLUCTUATIONS

L I Zaichik *) and A A Vinberg *)

*) Krzhizhanovsky Power Engineering Institute
Leninsky Prospekt 19 Moscow V-71 USSR

ABSTRACT

The paper is aimed at the derivation of a closed system of equations for dynamics and heat transfer in turbulent flows. The equation for the probability density of particle velocity and temperature in a turbulent flow, a set of equations for velocity and temperature moments, the closure technique for the system of equations for the moments of velocity and temperature fluctuations as well as applications of the derived equations for transfer of momentum and heat transfer in the near-wall region and in a free jet are presented.

INTRODUCTION

Presently for modeling of two-phase (dispersed) turbulent flows use is mostly made of the method based on the combined Eulerian-lagrangian approach: equations of motion and energy for the continuous carrier phase are presented and solved in terms of Eulerian variables, while the equations of motion and energy of the dispersed phase are written and solved using Lagrangian variables, i.e. by integration along the individual particle (droplet) trajectories. Accounting for the stochastic particle motion in this case significantly increases calculations because the statistically valid information requires sufficiently representative number of realizations. With decreasing particle size the number of realizations to obtain statistically valid averaged characteristics must increase due to larger contribution of particle interaction with smaller eddies. Therefore application of the Lagrangian technique for modeling of the dispersed phase dynamics is probably reasonable with regard to the inertial particles only. The Eulerian approach to the description of the disperse phase is based on the continuum presentation of the particle ensemble and, hence, allows the use of numerical algorithms close in their forms both for the disperse and the carrier phases. The approach provides adequate description of particle inertia movement induced effects, it would be a rational alternative to the Lagrangian technique.

NOMENCLATURE

τ	- time
$\vec{R}_p$, $\vec{V}_p$, ϑ_p	- particle coordinate, velocity and temperature
F_i	- external force
Q	- density of internal heat sources in a particle
τ_u, τ_t	- particle dynamic and thermal relaxation times
T_p	- time of particle interaction with gas high energy pulsations
T_L	- Lagrangian time macroscale of turbulence.
$H(x)$	- Havisaid function
y	- distance from wall
δ	- viscous sublayer thickness
ν_t	- turbulent viscosity of gas
Pr_t, Sc_t	- turbulence Prandtle and Schmidt numbers for single phase flow.
C_μ, C_1, C_2, σ_K, σ_ε	- constants in K-E model.
x, r	- longitudinal and radial coordinates.
d_p	- particle diameter.
D	- nozzle diameter
m_0	- particles loading ratio.
U_0	- nozzle gas velocity
U_{0s}	- nozzle gas velocity in single phase flow.
T_0, T_∞	- gas temperature in nozzle and environment

PROBABILITY DENSITY EQUATION

The flow and heat transfer of solids in a turbulent gas flow is considered assuming maximum possible solids volumetric concentration where particle-particle interactions may be neglected. Velocity and temperature fluctuations of particles are caused by their entrainment into the turbulent flow of the carrier phase, i.e. by the interaction with random fields of gas velocity and temperature due to viscous friction and thermal conductivity.

The motion and heat transfer of a single particle are described as follows

$$\frac{dR_{pi}}{d\tau} = V_{pi}, \quad \frac{dV_{pi}}{d\tau} = \frac{U_i(\vec{R}_p,\tau)-V_{pi}}{\tau_u} + F_i(\vec{R}_p,\tau), \qquad (1)$$

$$\frac{d\vartheta_p}{d\tau} = \frac{t(\vec{R}_p,\tau)-\vartheta_p}{\tau_t} + Q(\vec{R}_p,\tau). \qquad (2)$$

Then kinetic equation for the particle ensemble is used instead of Lagrangian equations for a single particle, the probability density distribution of particles with respect to coordinates, velocities and temperature is introduced

$$P(\vec{x},\vec{V},\vartheta,\tau) = \langle \delta(\vec{x}-\vec{R}_p(\tau))\,\delta(\vec{V}-\vec{V}_p(\tau))\,\delta(\vartheta-\vartheta_p(\tau)) \rangle \qquad (3)$$

Averaging in equation (3) is made using realizations of random turbulent fields of velocity $\vec{u}(\vec{x},\tau)$ and temperature $t(\vec{x},\tau)$ of the carrier phase. Differentiating Eq (3) with respect to time and accounting Eqs (1) and (2) and representing the gas velocity and temperature as averaged and pulsating summands $u_i = U_i + u_i'$, $t = T + t'$, we obtain

$$\frac{\partial \rho}{\partial \tau} + V_\kappa \frac{\partial \rho}{\partial x_\kappa} + \frac{\partial}{\partial V_\kappa}\left(\frac{U_\kappa - V_\kappa}{\tau_u} + F_\kappa\right)\rho + \frac{\partial}{\partial \vartheta}\left(\frac{T-\vartheta}{\tau_t} + Q\right)\rho =$$

$$= -\frac{\partial}{\partial V_\kappa}\left(\frac{\langle u_\kappa' \rho\rangle}{\tau_u}\right) - \frac{\partial}{\partial \vartheta}\left(\frac{\langle t'\rho\rangle}{\tau_t}\right). \qquad (4)$$

For the closure of the equation for ρ the required correlations

$$\langle u_\kappa' \rho\rangle = \langle u_\kappa' \delta(\vec{x}-\vec{R}_p)\delta(\vec{V}-\vec{V}_p)\delta(\vartheta-\vartheta_p)\rangle;$$

$$\langle t'\rho\rangle = \langle t'\delta(\vec{x}-\vec{R}_p)\delta(\vec{V}-\vec{V}_p)\delta(\vartheta-\vartheta_p)\rangle$$

are derived using the Furutsu-Novikov formula /1/, assuming random fields u_i', t' to be Gaussian

$$\langle z(\vec{x},\tau)R[z]\rangle = \iint \langle z(\vec{x},\tau)z(\vec{x}_1,\tau_1)\rangle \times$$

$$\times \left\langle \frac{\delta R[z(\vec{x},\tau)]}{\delta z(\vec{x}_1,\tau_1)}\right\rangle d\vec{x}_1 d\tau_1, \qquad (5)$$

where $z(\vec{x},\tau)$ - random process in space $\vec{x}$, $R[z]$ - random process dependent functional $\delta R/\delta z$ - functional derivative. Using Eq (5), accounting Eq (1) and (2) and ignoring the spatial nonuniformity of fields $\vec{U}$, t we arrive at

$$\langle u_i'\rho\rangle = -\tau_u g_u \langle u_i' u_\kappa'\rangle \frac{\partial \rho}{\partial x_\kappa} - f_u \langle u_i' u_\kappa'\rangle \frac{\partial \rho}{\partial V_\kappa} -$$

$$- f_{ut}\langle u_i' t'\rangle \frac{\partial \rho}{\partial \vartheta}, \qquad (6)$$

$$\langle t'\rho\rangle = -\tau_u g_{ut}\langle u_\kappa' t'\rangle \frac{\partial \rho}{\partial x_\kappa} - f_{ut}\langle u_\kappa' t'\rangle \frac{\partial \rho}{\partial V_\kappa} -$$

$$- f_t \langle t'^2\rangle \frac{\partial \rho}{\partial \vartheta},$$

where $\langle u_i' u_\kappa'\rangle$, $\langle u_i' t'\rangle$, $\langle t'^2\rangle$ - single-time moments of gas velocity and temperature pulsations

$$g_u = \int_0^\infty \frac{\langle u_i'(\vec{x},\tau)u_\kappa'(\vec{R}_p(\tau_1),\tau_1)\rangle}{\langle u_i' u_\kappa'\rangle}\left[1 - \exp\left(\frac{\tau-\tau_1}{\tau_u}\right)\right]\frac{d\tau_1}{\tau_u},$$

$$f_u = \int_0^\infty \frac{\langle u_i'(\vec{x},\tau)u_k'(\vec{R}_p(\tau_1),\tau_1)\rangle}{\langle u_i' u_\kappa'\rangle}\exp\left(-\frac{\tau-\tau_1}{\tau_u}\right)\frac{d\tau_1}{\tau_u},$$

$$f_{tu} = \int_0^\infty \frac{\langle u_i'(\vec{x},\tau)t'(\vec{R}_p(\tau_1),\tau_1)\rangle}{\langle u_i' t'\rangle}\exp\left(-\frac{\tau-\tau_1}{\tau_t}\right)\frac{d\tau_1}{\tau_t},$$

$$g_{ut} = \int_0^\infty \frac{\langle u_i(\vec{R}_p(\tau_1),\tau_1)t'(\vec{x},\tau)\rangle}{\langle u_i' t'\rangle}\left[1 - \exp\left(-\frac{\tau-\tau_1}{\tau_u}\right)\right]\frac{d\tau_1}{\tau_u},$$

$$f_{ut} = \int_0^\infty \frac{\langle u_i(\vec{R}_p(\tau_1),\tau_1)t'(\vec{x},\tau)\rangle}{\langle u_i' t'\rangle}\exp\left(-\frac{\tau-\tau_1}{\tau_u}\right)\frac{d\tau_1}{\tau_u},$$

$$f_t = \int_0^\infty \frac{\langle t'(\vec{x},\tau)t'(\vec{R}_p(\tau_1),\tau_1)\rangle}{\langle t'^2\rangle}\exp\left(-\frac{\tau-\tau_1}{\tau_t}\right)\frac{d\tau_1}{\tau_t}.$$

One can see computation of the degree of particles entrainment by turbulent pulsations of the carrier phase, two-time correlation functions of gas velocity and temperature pulsations along the particle path are required. Stepwise approximation of two-time correlation functions /2/

$$F(\tau-\tau_1) = 1 - H(\tau-\tau_1-T_p)$$

gives

$$g_u = g_{ut} = T_p/\tau_u - 1 - \exp(-\tau_u/T_p),$$

$$f_u = f_{ut} = 1 - \exp(-\tau_u/T_p),$$

$$f_{tu} = f_t = 1 - \exp(-\tau_t/T_p).$$

Introducing Eq (6) in Eq (4) we obtain the closed equation for the probability density distribution of particles with respect to coordinates, velocities and temperature in a nonuniform turbulent flow

$$\frac{\partial \rho}{\partial \tau} + V_\kappa \frac{\partial \rho}{\partial x_\kappa} + \frac{\partial}{\partial V_\kappa}\left(\frac{U_\kappa}{\tau_u} + F_\kappa\right)\rho + \frac{\partial}{\partial \vartheta}\left(\frac{T-\vartheta}{\tau_t} + Q\right)\rho =$$

$$= g_u \langle u_i' u_\kappa'\rangle \frac{\partial^2 \rho}{\partial V_i \partial x_\kappa} + \frac{f_u}{\tau_u}\langle u_i' u_\kappa'\rangle \frac{\partial^2 \rho}{\partial V_i \partial V_\kappa} +$$

$$+ \frac{\tau_u}{\tau_t} g_{ut}\langle u_\kappa' t'\rangle \frac{\partial^2 \rho}{\partial \vartheta \partial x_\kappa} + \frac{f_t}{\tau_t}\langle t'^2\rangle \frac{\partial^2 \rho}{\partial \vartheta^2} +$$

$$+ \left(\frac{f_{tu}}{\tau_u} + \frac{f_{ut}}{\tau_t}\right)\langle u_\kappa' t'\rangle \frac{\partial^2 \rho}{\partial V_\kappa \partial \vartheta}. \qquad (7)$$

It is worth noting that in the case of δ-correlated with time random fields $\vec{U}$, t, i e, ignoring the finite time of the turbulent pulsation decay, first two terms in the right-hand part of Eq (7) equals zero, and the equation becomes that of the Fokker-Plank type. For the case of a homogeneous and steady-state turbulence, the normal distribution is the solution of the Eq (7). With larger particle size where particle entrainment decreases, the probability density distribution tends to become a beta - function

$$\lim_{\tau_u, \tau_t/T_p \to \infty} \rho = \Phi\delta(\vec{V}-\vec{V})\delta(\vartheta-\theta)$$

THE EQUATIONS FOR MOMENTS

The probability density equation was used to derive the system of equations for the second order and triple correlations of particle velocity and temperature fluctuations. Average particle concentration, velocity and temperature are defined

$$\Phi=\int\rho_d\vec{V}d\vec{v}^0,\ V_i=\frac{1}{\Phi}\int v_i\rho_d\vec{V}d\vec{v}d\vartheta,\ \theta=\frac{1}{\Phi}\int\vartheta\rho_d\vec{V}d\vec{v}d\vartheta.$$

Integrating Eq (7) on the velocity and temperature we obtain equations for particle concentration, average velocity and temperature, second order correlations of particle velocity and temperature fluctuations

$$\frac{\partial\Phi}{\partial\tau}+\frac{\partial\Phi V_\kappa}{\partial x_\kappa}=0, \tag{8}$$

$$\frac{\partial V_i}{\partial\tau}+V_\kappa\frac{\partial V_i}{\partial x_\kappa}=-\frac{\partial\langle V_i'V_\kappa'\rangle}{\partial x_\kappa}+\frac{U_i-V_i}{\tau_u}+F_i-$$
$$-\left(\langle V_i'V_\kappa'\rangle+g_u\langle u_i'u_\kappa'\rangle\frac{\partial\ell n\Phi}{\partial x_\kappa}\right), \tag{9}$$

$$\frac{\partial\theta}{\partial\tau}+V_\kappa\frac{\partial\theta}{\partial x_\kappa}=-\frac{\partial\langle V_\kappa'\vartheta'\rangle}{\partial x_\kappa}+\frac{T-\theta}{\tau_t}+Q-$$
$$-\left(\langle V_\kappa'\vartheta'\rangle+\frac{\tau_u}{\tau_t}g_{ut}\langle u_\kappa't'\rangle\right)\frac{\partial\ell n\Phi}{\partial x_\kappa}, \tag{10}$$

$$\frac{\partial\langle V_i'V_j'\rangle}{\partial\tau}+V_\kappa\frac{\partial\langle V_i'V_j'\rangle}{\partial x_\kappa}+\left(\langle V_i'V_\kappa'\rangle+g_u\langle u_i'u_\kappa'\rangle\right)\frac{\partial V_j}{\partial x_\kappa}+$$
$$+\left(\langle V_j'V_\kappa'\rangle+g_u\langle u_j'u_\kappa'\rangle\right)\frac{\partial V_i}{\partial x_\kappa}+\frac{1}{\Phi}\frac{\partial}{\partial x_\kappa}=$$
$$=\frac{2}{\tau_u}\left(f_u\langle u_i'u_j'\rangle-\langle V_i'V_j'\rangle\right), \tag{11}$$

$$\frac{\partial\langle V_i'\vartheta'\rangle}{\partial\tau}+V_\kappa\frac{\partial\langle V_i'\vartheta'\rangle}{\partial x_\kappa}+\left(\langle V_i'V_\kappa'\rangle+g_u\langle u_i'u_\kappa'\rangle\right)\frac{\partial\theta}{\partial x_\kappa}+$$
$$+\left(\langle V_\kappa'\vartheta'\rangle+\frac{\tau_u}{\tau_t}g_{ut}\langle u_\kappa't'\rangle\right)\frac{\partial V_i}{\partial x_\kappa}+\frac{1}{\Phi}\frac{\partial}{\partial x_\kappa}\Phi\langle V_i'V_\kappa'\vartheta'\rangle=$$
$$=\left(\frac{f_{uu}}{\tau_u}+\frac{f_{ut}}{\tau_t}\right)\langle u_i't'\rangle-\left(\frac{1}{\tau_u}+\frac{1}{\tau_t}\right)\langle V_i'\vartheta'\rangle, \tag{12}$$

$$\frac{\partial\langle\vartheta'^2\rangle}{\partial\tau}+V_\kappa\frac{\partial\langle\vartheta'^2\rangle}{\partial x_\kappa}+2\left(\langle V_\kappa'\vartheta'\rangle+\frac{\tau_u}{\tau_t}g_{ut}\langle u_\kappa't'\rangle\right)\frac{\partial\theta}{\partial x_\kappa}+$$
$$+\frac{1}{\Phi}\frac{\partial}{\partial x_\kappa}\Phi\langle V_\kappa'\vartheta'^2\rangle=\frac{2}{\tau_t}\left(f_t\langle t'^2\rangle-\langle\vartheta'^2\rangle\right). \tag{13}$$

The equations (9), (10) for the particle average velocity and temperature incorporate terms for turbulent stresses and turbulent particle heat flux resulted from the particle entrainment into the pulsating fluid, transfer of momentum and heat due to turbulent diffusion caused by the nonuniform particle space distribution. The equations (11) - (13) for the second order correlations of velocity and temperature fluctuations include convection diffusion, generation of pulsations because of gradients of the averaged small-size particle velocity and temperature, generation and dissipation due to the interaction between the particles and the fluid flow turbulent pulsations. In the case of a homogeneous steady-state turbulence the algebraic expression for turbulent stresses, turbulent heat fluxes and small-size particle and fluid flow temperature fluctuations was drawn from the equations for second moments

$$\langle V_i'V_j'\rangle=f_u\langle u_i'u_j'\rangle,\ \langle V_i'\vartheta'\rangle=\frac{\tau_u f_{ut}+\tau_t f_{tu}}{\tau_u+\tau_t}\langle V_i't'\rangle,$$
$$\langle\vartheta'^2\rangle=f_t\langle t'^2\rangle.$$

For the inhomogeneous turbulent flow equations for triple correlations are used to determine diffusion terms in the equations for second moments. To describe the momentum and heat transfer in the disperse phase in terms of second moment equation the terms defining time variations, convective transfer and initiation of pulsations due to averaged velocity and temperature gradients are ignored in the third moment equation. Assuming normal distribution of fluctuations which allows presentation of 4th moments as a sum of products of second moments, the relationship for triple correlations for particle velocity and temperature fluctuations were derived

$$\langle V_i'V_j'V_\kappa'\rangle=-\frac{\tau_u}{3}\left[\left(\langle V_i'V_n'\rangle+g_u\langle u_i'u_n'\rangle\right)\frac{\partial\langle V_j'V_\kappa'\rangle}{\partial x_n}+\right.$$
$$\left.+\left(\langle V_j'V_n'\rangle+g_u\langle u_j'u_n'\rangle\right)\frac{\partial\langle V_i'V_\kappa'\rangle}{\partial x_n}+\left(\langle V_\kappa'V_n'\rangle+g_u\langle u_\kappa'u_n'\rangle\right)\frac{\partial\langle V_i'V_j'\rangle}{\partial x_n}\right], \tag{14}$$

$$\langle V_i'V_j'\vartheta'\rangle=-\frac{\tau_u\tau_t}{\tau_u+2\tau_t}\left[\langle V_i'V_\kappa'\rangle+g_u\langle u_i'u_\kappa'\rangle\right)\frac{\partial\langle V_j'\vartheta'\rangle}{\partial x_\kappa}+$$
$$+\left(\langle V_j'V_\kappa'\rangle+g_u\langle u_j'u_\kappa'\rangle\right)\frac{\partial\langle V_i'\vartheta'\rangle}{\partial x_n}+\left(\langle V_\kappa'\vartheta'\rangle+\frac{\tau_u}{\tau_t}g_{ut}\langle u_\kappa't'\rangle\right)\frac{\partial\langle V_i'V_j'\rangle}{\partial x_\kappa}\Big], \tag{15}$$

$$\langle V_i'\vartheta'^2\rangle=-\frac{\tau_u\tau_t}{2\tau_u+\tau_t}\left[\left(\langle V_i'V_\kappa'\rangle+g_u\langle u_i'u_\kappa'\rangle\right)\frac{\partial\langle\vartheta'^2\rangle}{\partial x_\kappa}+\right.$$
$$\left.+2\left(\langle V_\kappa'\vartheta'\rangle+\frac{\tau_u}{\tau_t}g_{ut}\langle u_\kappa't'\rangle\right)\frac{\partial\langle V_i'\vartheta'\rangle}{\partial x_\kappa}\right]. \tag{16}$$

With the particle relaxation time tending to zero the above relationships become as those proposed by Launder B E et al for a single phase fluid /3,4/. Also these relationships are capable of closing the system of equations for transfer of momentum and heat for small-size particles.

NEAR-WALL REGION INCLUDING VISCOUS SUBLAYER

Turbulent transport models based on differential equations for second moments for the dispersed phase velocity fluctuations are capable of accounting for nonlocal effects due to particle inertia

Therefore such models can be to advantage used for particle dynamics calculations in the near-wall region where large gradients of all turbulent characteristics are observed The widely applied algebraic (local equilibrium) models for example /5 - 9/ for prediction of the near-wall region turbulent stresses of the carrier phase may give large errors

Main qualitative effects in approximating the carrier phase pulsations were revealed by using a simple model incorporating a viscous sublayer with no pulsations, and a turbulent region with constant pulsations i e $\langle u_y'^2 \rangle = u_*^2 H(y-\delta)$ The time of particle interaction with gas turbulent pulsations are considered constant $T_p = T_L = \delta/u_*$ The equations for particle concentration and pulsation intensity of particle velocity obtained from equations (8), (9) (11), (14) were analytically solved by joining decompositions for the above regions The boundary conditions for velocity pulsations were as $d\langle V_y'^2 \rangle / dy = 0$ at $y = 0, \infty$. Distributions of velocity pulsation intensity vs the particle inertia parameter $\tau_* = \tau_u u_*/\delta$ are shown in Fig.1

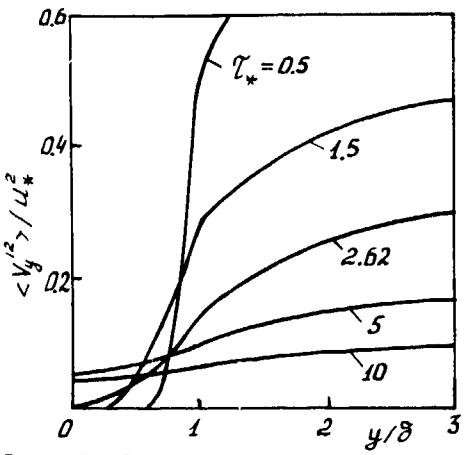

Figure 1 Particle pulsation intensity in the near-wall region

The small-size particle pulsation intensity equals to zero in the viscous sublayer while the intensity of the large-size particles in the viscous sublayer and on the wall is a non-zero value The velocity pulsations of the dense phase can be described by the nonlocal model only and is explained by the diffusion-controlled transfer of pulsations from the turbulent region to the viscous sublayer due to particle inertia

TWO-PHASE JET FLOW AND HEAT TRANSFER

In free jet flows turbulent characteristics are substantially closer to isotropic state than in the near-wall flows Therefore, turbulent stresses in a jet flow dispersed phase can be calculated using the particle turbulent energy equation only To simplify calculations of two-phase jet flows, the set of equations for second moments of particle velocity fluctuations (11) is reduced to a gradient type correlation similar to Boussinesq correlation for single phase turbulent stresses

$$\langle V_i' V_j' \rangle = \frac{2}{3} k_p \delta_{ij} - \nu_p \left(\frac{\partial V_i}{\partial x_j} + \frac{\partial V_j}{\partial x_i} - \frac{2}{3} \frac{\partial V_k}{\partial x_k} \delta_{ij} \right),$$

where turbulent viscosity coefficient for the dispersed phase is governed by both the particle relaxation time and turbulent energy

$$\nu_p = f_u \nu_t + \tau_u k_p / 3 .$$

The particle turbulent energy $k_p = \langle V_i' V_i' \rangle / 2$ was obtained from the differential equation derived from (11) with accounting (14) The carrier phase characteristics are described by the K-E turbulence model modified to account for the particle effect on turbulence The equations for the gas turbulence energy $k = \langle u_i' u_i' \rangle / 2$ and its dissipation ε are

$$U_i \frac{\partial k}{\partial x_i} = \frac{\partial}{\partial x_i} \left(\frac{\nu_t}{\sigma_k} \frac{\partial k}{\partial x_i} \right) + \langle u_i' u_j' \rangle \frac{\partial U_i}{\partial x_j} - \varepsilon -$$

$$\frac{\rho_p}{\rho \tau_u} \left[2\Phi (1 - f_u) k - \tau_u g_u \langle u_i' u_j' \rangle (U_i - V_i) \frac{\partial \Phi}{\partial x_j} \right], \qquad (17)$$

$$U_i \frac{\partial \varepsilon}{\partial x_i} = \frac{\partial}{\partial x_i} \left(\frac{\nu_t}{\sigma_\varepsilon} \frac{\partial \varepsilon}{\partial x_i} \right) - C_1 \frac{\varepsilon}{k} \langle u_i' u_j' \rangle \frac{\partial U_i}{\partial x_j} - C_2 \frac{\varepsilon^2}{k} -$$

$$- \frac{2 \rho_p \varepsilon}{\rho \tau_u} \left[\Phi (1 - f_\varepsilon) - \frac{\tau_u g_\varepsilon}{3} (U_i - V_i) \frac{\partial \Phi}{\partial x_i} \right] \qquad (18)$$

First terms in square brackets of Eqs (17) and (18) are defined by the pulsating interphase slip, while second terms - by the averaged slip and nonuniform particle distribution. The degree of particle entrainment into the micropulsating motion of the carrier phase is defined in Eq (18) as

$$f_\varepsilon = 1 - \exp(-\tau_u / T_\varepsilon), \quad g_u = T_\varepsilon / \tau_u - 1 + \exp(-\tau_u / T_\varepsilon),$$

where turbulence time microscale, with the assumption on isotropic small-scale pulsating motion is described by $T_\varepsilon = (15 \nu / \varepsilon)^{1/2}$ The time of particle interaction with high energy gas pulsations is approximated by

$$T_p = \left[1 + \left(T_L / |\bar{U} - \bar{V}| / L \right) \right]^{-1/2},$$

where $L = (2k/3)^{1/2} T_L$ spatial turbulence macroscale The time macroscale of gas velocity pulsations is determined by $T_L = 3 C_\mu k / 2 C_\varepsilon \varepsilon$.

The proposed set of equations for two-phase flows comprises no extra empirical constants The described system of equations was used for calculating two-phase round jet characteristics for a wide range of particle size and mass concentration Fig. 2-4 show results of these calculations. Predictions and experiments /10 11/ are compared showing good agreement Most important calculation findings are: increased range and decreased thickness of a two-phase jet as compared to a single phase jet; laminarization effect of particles on the

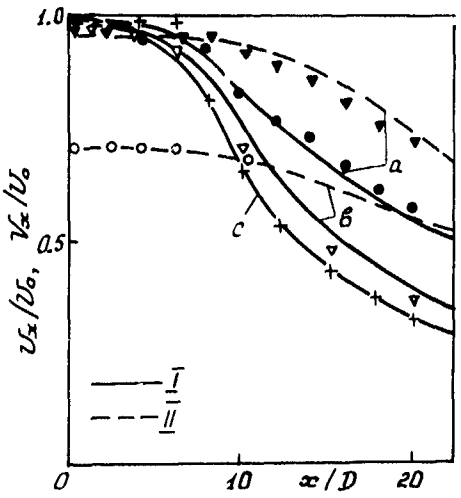

Figure 2 Centre-line longitudinal mean velocity of gas (I) and particles (II) distributions a, d_p=170 μm, b d_p=500 μm c single-phase flow

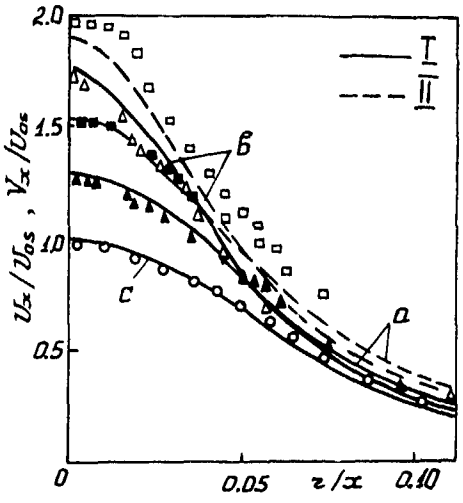

Figure 3 Radial distributions of mean velocity of gas (I) and particles (II) a m_0 =0 32, b m_0 =0 85 c single-phase flow

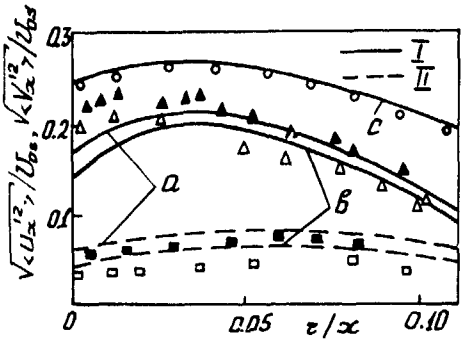

Figure 4 Gas (I) and particles (II) velocity pulsations intensity a m_0 =0 32, b, m_0 =0 85 c, single-phase flow

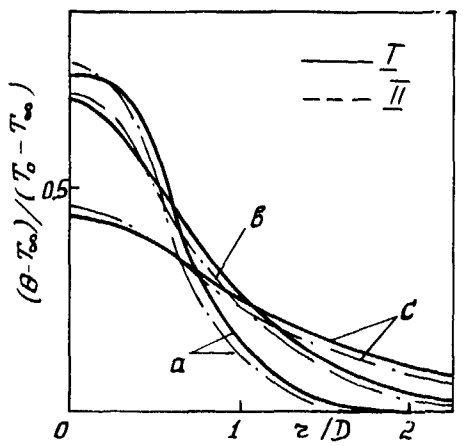

Figure 5 Radial distributions of particles temperature, =50 μm a, x/D =5, b, x/D =10; c x/D =20

fluid flow Good agreement between the predictions and the experiments for the average velocity distributions and the intensity of pulsations for the dense phase proves the validity of the proposed model to describe particle dynamics in turbulent jets

The two-phase round jet heat transfer was calculated using the equation for the turbulent heast flux of the dispersed phase (12) accounting (15) or the formula, resulting from simplifying the equation for the turbulent heat flux

$$\langle v_i' \vartheta' \rangle = -\left[\frac{(\tau_u f_{u\tau} + \tau_t f_{t\omega})\nu_t}{(\tau_u+\tau_t)Pr_t} + \frac{2\tau_u\tau_t}{3(\tau_u+\tau_t)} k_p\right]\frac{\partial\theta}{\partial x_i} = -\frac{\nu_p}{Pr_p}\frac{\partial\theta}{\partial x_i} \quad (19)$$

The turbulent Prandtl number obtained

$$Pr_p = \frac{(\tau_u+\tilde{\tau}_t)(f_u\nu_t + \tau_u k_p/3}{(\tau_u f_{u\tau} + \tilde{\tau}_t f_{t\omega})\nu_t/Pr_t + 2\tau_u\tau_t k_p/3}$$

illustrates the effect of the particle thermal-physical properties (particle dynamic and thermal relaxation times) on transfer of momentum and heat

The results obtained by both techniques are close This conclusion is illustrated in Fig 5 showing radial distributions of the particle temperature in diferent jet sections (I - using equation for $\langle v_i' \vartheta' \rangle$,II -using Eq (19))

Therefore particle turbulent Prandtl number may be recommended for two-phase jet flow heat trasfer calculations

Thus the proposed model can adequately be applied to predict transfer of momentum and heat in the near-wall region and two-phase free jet flows requiring no extra empirical constants

REFERENCES

1 Klyatskin,V I 1980 Stochastic equations and waves in randomly nonuniform media (in Russian) Moscow Nauka

2 Derevich I V & Zaichik,L I 1988 Particle deposition from a turbulent flow (in Russian) Izvestiya Akademii Nauk SSSR Mekhanika Zhidkosti i Gaza 5 96-104

3 Hanjalic,K & Launder,B.E 1972 A Reynolds stress model of turbulence and its application to thin shear flows J Fluid Mech 52, 609-638.

4 Launder,B E , Reece,G.Y & Rody,W. 1975 Progress in the development of a Reynolds-stress turbulence closure. J.Fluid. Mech 68, 537-566

5 Shraiber,A.A , Gavin,L B., Naumov,V A & Yatsenko,V P 1990 Turbulent flows in gas suspensios Hemisphere publishing corporation

6 Pourahmadi,F. & Humpfrey,J.A.C 1983 Modeling solid-fluid turbulent flows with application to predicting erosive wear Phys Chem Hydrodyn 4, 191-219

7.Chen,C P & Wood P E 1986 Turbulence closure modeling of the dilute gas-particle axisymmetric jet AIChE Journ 32, 163-166

8 Mostafa,A A. & Mongia,H C 1987 On the modeling of turbulent evaporating sprays Eulerian and Lagrangian approach Int J Heat and Mass Transfer 30, 2583-2593.

9.Rizk M A & Elghobashi,S.E. 1989 A two-equation turbulence model for dispersed dilute confined two-phase flows Int J. Multiphase Flow 15, 119-133

10 Modarress,D , Tan,H & Elghobashi, S 1984 Two-component LDA measurement in a two-phase turbulent jet AIAA Journ 22, 624-630.

11 Tsuji Y , Morikava,Y , Kerimine,K , Tanaka,T & Nishida,S 1988 Measurement of an axisymmetric jet laden with coarse particles. Int J Multiphase Flow 14, 565-574

EIGHTH SYMPOSIUM ON
TURBULENT SHEAR FLOWS
Technical University of Munich
September 9-11, 1991

A TIME-CORRELATED STOCHASTIC MODEL FOR PARTICLE DISPERSION IN ANISOTROPIC TURBULENCE

Q Zhou and M.A. Leschziner

Mechanical Engineering Department
University of Manchester Institute of Science and Technology,
Manchester, M60 1QD, UK

ABSTRACT

The dispersion of particles, tracked by a LaGrangian method within a continuous carrier modelled by an Eulerian scheme, is effected by imposing on the particle turbulent velocity perturbations of the carrier fluid. Within a Reynolds-averaged framework, these perturbations must be extracted, by some sampling method, from statistical information provided by the turbulence closure. This paper presents a sampling scheme which accounts (i) for the correlation in time between successive perturbations, and (ii) for the directional correlation in space reflected by anisotropy of the normal Reynolds stresses and the finite values of the shear stresses. The scheme is intended to be used in conjunction with Reynolds-stress closure in modelling two- and three-dimensional flows. The properties of the correlated sampling method are first illustrated by tests which aim to reconstitute the joint PDFs pertaining to anisotropic states identified by prescribed sets of Reynolds-stress components. The scheme is then applied to particle dispersion in a free shear layer.

INTRODUCTION

Within a statistically steady Eulerian framework, the motion of the carrier is described in terms of its time-averaged velocity, $\vec{V}_f$. The instantaneous velocity, $\vec{\tilde{V}}_f$, is thus given by

$$\vec{\tilde{V}}_f = \vec{V}_f + \vec{v}_f \qquad (1)$$

If $\vec{v}_f$ were known, modelling particle dispersion would not be an issue, for dispersion would arise naturally as a consequence of the randomly time-dependent nature of $\vec{v}_f$. But the fluctuation is not known or simply determinable. Rather, the correlations $\overline{u_i u_j}$ (the *Reynolds stresses*) are usually given as the outcome of a turbulence model. The central task is thus to construct a model which is able to provide a description for $\vec{v}_f$ which, while obviously not conforming to the real variation, gives the same dispersion effect, viewed in statistical terms.

The traditional approach to modelling dispersion is to extract an isotropic turbulent velocity fluctuation u_f from the predicted carrier turbulence energy and a Gaussian PDF having a standard deviation of $(2/3k)^{0.5}$, without taking temporal correlation or directional anisotropy into account. This approach was first proposed by Yuu et al (1978). Irrespective of the computational time step adopted for advancing the solution, $\vec{v}_f$ is extracted, by random sampling, from the same PDF. The question of the period over which u_f acts on a particle is addressed via two time scales: the *eddy-life time*, t_ℓ, and the *eddy-transit time* t_t. The interaction period is evaluated from

$$t_s = \min\,(t_\ell, t_t) \qquad (2)$$

Several proposals have been made for determining the above time scales. Gosman and Ioannides (1981) evaluate t_ℓ from

$$t_\ell = \ell_e / |\vec{v}_f| \qquad \ell_e = C_\mu\, k^{3/2} / \epsilon \qquad (3)$$

$$t_t = -\tau \ln\,(1 - \ell_e / (\tau |\vec{V}_{f,p} - \vec{V}_f|)) \qquad (4)$$

where τ is the "particle relaxation time"

$$\tau = \frac{4}{3}\frac{D_p}{C_D}\,/\,|\vec{V}_f - \vec{V}_{f,p}| \qquad (5)$$

The above expression for t_t is obtained by solving a simplified and linearised form of the particle-motion equation with V_f held invariant. Sampling for a new fluctuation u_f is performed after the interval t_s. Shuen et al (1983) suggest the modification

$$t_\ell = \ell_e / (2/3k)^{0.5} \qquad (6)$$

while Kallio & Stock (1986) proposed that (6) be multiplied by a flow-dynamics-related constant which experimental studies suggest to lie in the range 0.15 to 2.

All the above methodologies share the same three important weaknesses:

(i) No account is taken of the fact that turbulent fluctuations are correlated in time, i.e. $\overline{u(t)u(t+\delta t)}$ does not vanish unless δt is large.
(ii) There is no clear-cut rationale for prescribing the magnitude of the aforementioned time scales.
(iii) No account is taken of anisotropy and the fact that cross-correlations of velocity fluctuations are non-zero.

The third item above might be acceptable when an eddy-viscosity approach is used for characterising carrier turbulence. However, when a Reynolds-stress model is employed, the traditional approach does not exploit effectively the information arising from the Eulerian framework.

Recognising the above limitations, Berlemont et al (1990) have recently proposed a model which accounts for temporal correlation and anisotropy via a combination of LaGrangian and Eulerian correlation functions. Our work, proceeding independently in parallel to that above, has given rise to a modelling framework which, whilst sharing the same philosophy, adopts a different, arguably simpler route to representing dispersion without dependence on the details of the statistical sampling process and on time-scale assumptions. This paper exposes the modelling framework in detail and verifies its validity.

TEMPORALLY AND DIRECTIONALLY CORRELATED SAMPLING

Preliminary considerations

Attention is focused in Fig. 1 on a single discrete particle at time $t-\delta t$, located at $\vec{r}_{p,t-\delta t}$ relative to an origin 'O'.

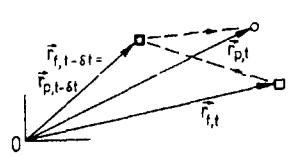

Fig. 1 Motion of particle and carrier-fluid packet in time interval δt

At time t, a fluid (i e carrier) particle originating at $\vec{r}_{f,t-\delta t}=\vec{r}_{p,t-\delta t}$, will have moved to $\vec{r}_{f,t}$ while the discrete particle will, in general, be located at $\vec{r}_{p,t}$. The task is to determine the carrier fluctuation at $\vec{r}_{p,t}$. The velocity fluctuation of the carrier phase at time t at location $\vec{r}_{f,t}$ may be related to the velocity fluctuation at t-δt by

$$\vec{v}(\vec{r}_{f,t}) = \{\beta\}\ \vec{v}(\vec{r}_{f,t-\delta t}) + \vec{d}_t \qquad ..(7)$$

where $\{\beta\}$ accounts for effects arising from previous time levels, while $\vec{d}_t$ represents effects arising from randomness during the time interval δt. Similarly, the carrier velocity fluctuation at location $\vec{r}_{p,t}$ can be related to the fluctuation at location $\vec{r}_{f,t}$ by

$$\vec{v}(\vec{r}_{p,t}) = \{\gamma\}\ \vec{v}(\vec{r}_{f,t}) + \vec{e}_t \qquad (8)$$

Unless the discrete particle is large and dense, and the time step δt is long, it may be assumed that the departure of $\vec{r}_{p,t}$ from $\vec{r}_{f,t}$ is sufficiently modest for the statistical state of the fluid at both positions to be close. In this case, the velocity fluctuation at the particle's position at time level t is simply represented by equation (7). This restriction, whilst not essential, simplifies the modelling considerations to follow and may be readily relaxed at a later stage, if desired, via the use of an Eulerian correlation function in conjunction with relation (8). The task is thus reduced to determining the matrix $\{\beta\}$ and the vector $\vec{d}_t$. An analogous path leads to similar expressions for $\{\gamma\}$ and $\vec{e}_t$. The primary objective pursued below is to 'retrieve' $\vec{v}$, by some sampling process, in such a way that a sufficiently large set of sampling events satisfies the statistical constraints imposed by the available time-averaged correlations of the velocity fluctuations.

Temporal correlation

As a precursor to the full model, it is instructive to restrict attention to isotropic turbulence. The present approach is based on the proposition that temporal correlation between velocity fluctuations at two successive time steps at which sampling is performed be accounted for via the *time-correlation coefficient* R(δt) defined as

$$R(\delta t) = \frac{\overline{u_t\, u_{t-\delta t}}}{\overline{u^2_{t-\delta t}}} \qquad (9)$$

According to Hinze (1975), a reasonable approximation for R(δt) is

$$R(\delta t)=\exp(-\delta t/T) \qquad (10)$$

If k and ε are the only turbulence parameters available from the Eulerian framework, the time scale T may be assumed given by

$$T = f(C_\mu^{0.75} k^{1.5}/\epsilon)/(^2/_3 k)^{0.5} \qquad ..(11)$$

where f may be determined on the basis of analytical and experimental considerations.

Given δt, k, and a sampled fluctuation $u_{t-\delta t}$ (the subscript 'f' is omitted henceforth for brevity), the objective is to construct a PDF whose variance is not simply $(2/3k)^{0.5}$ but which reflects correlation (9). There are two quite different routes to achieving this objective, both lead to identical end points and are detailed in Zhou & Leschziner (1991). Here, the gist of one route is outlined.

For isotropic turbulence, equation (7) for u_t, may be written

$$u_t = \beta u_{t-\delta t} + d_t \qquad (12)$$

where β and d_t are here scalar quantities which are to be determined. From

$$\overline{u_t u_{t-\delta t}} = \beta\ \overline{u_{t-\delta t}\ u_{t-\delta t}} + \overline{e_t\ u_{t-\delta t}} = \beta\ \overline{u^2_{t-\delta t}} \qquad ..(13)$$

β is seen to be simply R(δt). Since

$$\overline{e_t} = \overline{u_t} - \beta\overline{u_{t-\delta t}} = 0 \qquad (14)$$

it follows that

$$\overline{e_t^2} = \overline{(u_t-\beta u_{t-\delta t})^2} = \overline{u_t^2} - R^2(\delta t)\overline{u^2_{t-\delta t}} \qquad (15)$$

If the PDFs describing u_t and $u_{t-\delta t}$ are assumed Gaussian in shape, that governing e_t is also Gaussian, and $P(d_t)$ follows from

$$P(d_t)=\frac{1}{\sqrt{2\pi\ (\overline{u_t^2} - R^2(\delta t)\overline{u^2_{t-\delta t}})}}\exp\left\{\frac{-(u_t - R(\delta t)u^2_{t-\delta t})}{2(\overline{u_t^2} - R(\delta t)\overline{u^2_{t-\delta t}})}\right\} \qquad (16)$$

Hence, with R(δt) and turbulence intensities at t and t-δt given, (12) and (16) allow u_t to be determined for any chosen step δt and a previously sampled value $u_{t-\delta t}$.

Temporal and directional correlation

Attention is now directed towards anisotropic turbulence. Assume that at any time level, t, the velocity fluctuations are to be sampled from a directionally correlated PDF $P(\vec{v}_t|\vec{v}_{t-\delta t})$ which is conditional on the velocity fluctuation $\vec{v}_{t-\delta t}$ sampled at level t-δt. The nature of the PDFs will be considered later. The statistical correlation between $\vec{v}_{t-\delta t}$ and $\vec{v}_t$ is assumed to be described by the (as yet unknown) correlation functions $R_{ij}(\delta t)$

$$R_{xx} = \frac{\overline{u_t\, u_{t-\delta t}}}{\sqrt{\overline{u_t^2}}\sqrt{\overline{u^2_{t-\delta t}}}},\quad R_{xy} = \frac{\overline{u_t\, v_{t-\delta t}}}{\sqrt{\overline{u_t^2}}\sqrt{\overline{v^2_{t-\delta t}}}},\quad R_{xz} = \frac{\overline{u_t\, w_{t-\delta t}}}{\sqrt{\overline{u_t^2}}\sqrt{\overline{w^2_{t-\delta t}}}}$$

$$R_{yx} = \frac{\overline{v_t\, u_{t-\delta t}}}{\sqrt{\overline{v_t^2}}\sqrt{\overline{u^2_{t-\delta t}}}},\quad R_{yy} = \frac{\overline{v_t\, v_{t-\delta t}}}{\sqrt{\overline{v_t^2}}\sqrt{\overline{v^2_{t-\delta t}}}},\quad R_{yz} = \frac{\overline{v_t\, w_{t-\delta t}}}{\sqrt{\overline{v_t^2}}\sqrt{\overline{w^2_{t-\delta t}}}}$$

$$R_{zx} = \frac{\overline{w_t\, u_{t-\delta t}}}{\sqrt{\overline{w_t^2}}\sqrt{\overline{u^2_{t-\delta t}}}},\quad R_{zy} = \frac{\overline{v_t\, v_{t-\delta t}}}{\sqrt{\overline{w_t^2}}\sqrt{\overline{v^2_{t-\delta t}}}},\quad R_{zz} = \frac{\overline{w_t\, w_{t-\delta t}}}{\sqrt{\overline{w_t^2}}\sqrt{\overline{w^2_{t-\delta t}}}} \qquad (17)$$

from which (δt) has been omitted, for brevity, and which may be expressed compactly as

$$\{R\}=\begin{Bmatrix} R_{xx} & R_{xy} & R_{xz} \\ R_{yx} & R_{yy} & R_{yz} \\ R_{zx} & R_{zy} & R_{zz} \end{Bmatrix} \qquad ..(18)$$

With the subscript 't' denoting '$\vec{r}_{f,t}$' henceforth, the turbulent fluctuation $\vec{v}_t=(u_t,v_t,w_t)^T$ can be expressed by

$$u_t = (\beta_{xx}\, u_{t-\delta t} + \beta_{xy}\, v_{t-\delta t} + \beta_{xz}\, w_{t-\delta t}) + d_{tx}$$
$$v_t = (\beta_{yx}\, u_{t-\delta t} + \beta_{yy}\, v_{t-\delta t} + \beta_{yz}\, w_{t-\delta t}) + d_{ty}$$
$$w_t = (\beta_{zx}\, u_{t-\delta t} + \beta_{zy}\, v_{t-\delta t} + \beta_{zz}\, w_{t-\delta t}) + d_{tz}$$

or compactly as

$$\vec{v}_t=\{\beta\}\ \vec{v}_{t-\delta t} + \vec{d}_t \qquad (19)$$

Multiplication of eq (19) by $\vec{v}^T_{t-\delta t}$ followed by time-averaging – denoted by the operator 'E' – gives.

$$E(\vec{v}_t\ \vec{v}^T_{t-\delta t}) = E[(\{\beta\}\vec{v}_{t-\delta t}+\vec{d}_t)\ \vec{v}^T_{t-\delta t}] \qquad (20)$$

where the left-hand side is

$$E(\vec{v}_t\ \vec{v}_{t-\delta t}) = \{C\} = \begin{Bmatrix} \overline{u_t u_{t-\delta t}} & \overline{u_t v_{t-\delta t}} & \overline{u_t w_{t-\delta t}} \\ \overline{v_t u_{t-\delta t}} & \overline{v_t v_{t-\delta t}} & \overline{v_t w_{t-\delta t}} \\ \overline{w_t u_{t-\delta t}} & \overline{w_t v_{t-\delta t}} & \overline{w_t w_{t-\delta t}} \end{Bmatrix}$$

$$= \begin{Bmatrix} R_{xx}\sqrt{\overline{u^2}_t}\sqrt{\overline{u^2}_{t-\delta t}} & R_{xy}\sqrt{\overline{u^2}_t}\sqrt{\overline{v^2}_{t-\delta t}} & R_{xz}\sqrt{\overline{u^2}_t}\sqrt{\overline{w^2}_{t-\delta t}} \\ R_{yx}\sqrt{\overline{v^2}_t}\sqrt{\overline{u^2}_{t-\delta t}} & R_{yy}\sqrt{\overline{v^2}_t}\sqrt{\overline{v^2}_{t-\delta t}} & R_{yz}\sqrt{\overline{v^2}_t}\sqrt{\overline{w^2}_{t-\delta t}} \\ R_{zx}\sqrt{\overline{w^2}_t}\sqrt{\overline{u^2}_{t-\delta t}} & R_{zy}\sqrt{\overline{w^2}_t}\sqrt{\overline{v^2}_{t-\delta t}} & R_{zz}\sqrt{\overline{w^2}_t}\sqrt{\overline{w^2}_{t-\delta t}} \end{Bmatrix} \tag{21}$$

while the right-hand side becomes

$$E[(\{\beta\}\vec{v}_{t-\delta t}+\vec{d}_t)\ \vec{v}^T_{t-\delta t} = \{\beta\}E(\vec{v}_{t-\delta t}\ \vec{v}^T_{t-\delta t}) + E(\vec{d}_t\ \vec{v}^T_{t-\delta t})$$

$$= \{\beta\}\{cov\}_{\vec{v}_{t-\delta t}} + 0 \tag{22}$$

In the above, {cov} is the covariant matrix of $\vec{v}_{t-\delta t}$,

$$\{cov\} = E(\vec{v}\ \vec{v}^T) = E\begin{bmatrix} u^2 & uv & uw \\ vu & v^2 & vw \\ wu & wv & w^2 \end{bmatrix} = \begin{Bmatrix} \overline{u^2} & \overline{uv} & \overline{uw} \\ \overline{vu} & \overline{v^2} & \overline{vw} \\ \overline{wu} & \overline{wv} & \overline{w^2} \end{Bmatrix} \tag{23}$$

which is thus fully determined within a Eulearean solution scheme for the carrier phase employing a Reynolds-stress turbulence model. The r h s zero in equation (22) arises because $\vec{d}_t$ is clearly not correlated to the fluctuations at t-δt. Hence, equation (22) may be written

$$\{C\} = \{\beta\}\ \{cov\}_{\vec{v}_{t-\delta t}}$$

or

$$\{\beta\} = \{C\}\ \{cov\}^{-1}_{\vec{v}_{t-\delta t}} \tag{24}$$

Reference to equation (21) shows {C} to depend on Reynolds stresses and correlation functions only. Hence if the latter are known, all elements of {β} may be determin

Attention is next directed towards $\vec{d}_t$. This is obtained by manipulating equation (19), rearranged to give

$$\vec{d}_t = \vec{v}_t - \{\beta\}\ \vec{v}_{t-\delta t} \tag{25}$$

Multiplication of (25) by its transpose and time-averaging gives

$$E(\vec{d}_t\ \ \vec{d}_t{}^T) = \begin{Bmatrix} \overline{d_{tx}{}^2} & \overline{d_{tx}d_{ty}} & \overline{d_{tx}d_{tz}} \\ \overline{d_{ty}d_{tx}} & \overline{d_{ty}{}^2} & \overline{d_{ty}d_{tz}} \\ \overline{d_{tz}d_{tx}} & \overline{d_{tz}d_{ty}} & \overline{d_{tz}{}^2} \end{Bmatrix} = \{cov\}_{\vec{d}_t}$$

$$= E[(\vec{v}_t - \{\beta\}\ \vec{v}_{t-\delta t})(\vec{v}^T_t - \vec{v}^T_{t-\delta t}\{\beta\}^T)]$$

$$= E[(\vec{v}_t\ \vec{v}^T_t)] - \{\beta\}\ E[(\vec{v}_{t-\delta t}\ \vec{v}^T_t)]$$

$$- E(\vec{v}_t\ \vec{v}^T_{t-\delta t})\{\beta\}^T + \{\beta\}E(\vec{v}_t\ \vec{v}^T_{t-\delta t})\{\beta\}^T \tag{26}$$

Use of the definition for {C} given in equation (21) allows (26) to be written.

$$\{cov\}_{\vec{d}_t} = \{cov\}_{\vec{v}_t} - \{\beta\}\{C\}^T - \{C\}\{\beta\}^T + \{\beta\}\{cov\}_{\vec{v}_{t-\delta t}}\{\beta\}^T \tag{27}$$

From equation (23) it is apparent that the last two terms in eq (26) cancel each other so that:

$$\{cov\}_{\vec{d}_t} = \{cov\}_{\vec{v}_t} - \{\beta\}\{C\}^T \tag{28}$$

The next task is to relate the elements of the vector $\vec{d}_t$ to $\{cov\}_{\vec{d}_t}$. To this end, an assumption is required about the nature of the PDF governing the vectorial fluctuation $\vec{v}$ and hence also $\vec{d}_t$. Here, all components are assumed to be governed by Gaussian distributions. This permits $\vec{v}$ and $\vec{d}_t$ to be described by the *joint normal distributions*:

$$P(\vec{v}) = \frac{1}{(2\pi)^{n/2}|cov|^{\frac{1}{2}}_{\vec{v}}}\exp\left\{-\tfrac{1}{2}(\vec{v})^T\ \{cov\}^{-1}_{\vec{v}}\vec{v}\ \right\} \tag{29}$$

and

$$P(\vec{d}_t) = \frac{1}{(2\pi)^{n/2}|cov|^{\frac{1}{2}}_{\vec{d}_t}}\exp\left\{-\tfrac{1}{2}(\vec{d}_t)^T\ \{cov\}^{-1}_{\vec{d}_t}\ \vec{d}_t\right\} \tag{30}$$

In the above, n identifies the dimensionality of the problem, i e the number of elements correlated via {cov}. The question is now how to effect by computational means a sampling methodology which reflects the correlation implicit in equation (30)

If $\vec{Z}$ is a set of random components with independent standard normal distribution N(0,I), then the *correlated* components of the vector $\vec{d}_t$ may be determined, in principle, from:

$$\vec{d}_t = \{B\}\ \vec{Z} \tag{31}$$

Where $\{B\}=b_{ij}$ is the matrix expressing the degree of correlation between components of $\vec{d}_t$. Post-multiplication of equation (31) by $\vec{d}_t{}^T$ gives

$$E(\vec{d}_t\ \vec{d}_t{}^T) = E[\{B\}\vec{Z}\ (\{B\}\vec{Z})^T] = \{B\}\ E(\vec{Z}\ \vec{Z}^T)\ \{B\}^T = \{B\}\{B\}^T \tag{32}$$

and hence,

$$\{cov\}_{\vec{d}_t} = \{B\}\{B\}^T \tag{33}$$

which obviously contains products of elements b_{ij} only. The variables Z_1, Z_2 and Z_3 may be taken to represent uncorrelated velocity perturbations (of incorrect magnitude, however) in the linearly independent co-ordinate framework (1,2,3). Because of the spherical symmetry of constant P($\vec{Z}$) surfaces, there is a degree of ambiguity in relation to the orientation of $\vec{Z}$ relative to $\vec{d}_t$ (and $\vec{v}$). This ambiguity offers some flexibility in 'aligning' the $\vec{Z}$ and $\vec{d}_t/\vec{v}$ co-ordinate system. Here, we have chosen to align d_{tx} (one of the three components of $\vec{d}_t$) with the Z_1 direction. In this manner, {B} can be made to become lower triangular (ie $b_{12} = b_{13} = b_{23} = 0$). An element-by-element comparison of the left- and right-hand sides of the above equation then leads to:

$$\left.\begin{aligned} b_{11}{}^2 &= \overline{d_{tx}{}^2}, \quad b_{11}b_{21} = \overline{d_{tx}d_{ty}} \\ b_{11}b_{31} &= \overline{d_{tx}d_{tz}}, \quad b_{21}{}^2 + b_{22}{}^2 = \overline{d_{ty}{}^2} \\ b_{21}b_{31} &+ b_{22}b_{32} = \overline{d_{tz}d_{ty}} \\ b_{31}{}^2 &+ b_{32}{}^2 + b_{33}{}^2 = \overline{d_{tz}{}^2} \end{aligned}\right\} \tag{34}$$

From which the coefficients follow as

$$\left.\begin{aligned} b_{11} &= (\overline{d_{tx}{}^2})^{\frac{1}{2}}, \quad b_{12} = 0, \quad b_{13} = 0 \\ b_{21} &= \frac{(\overline{d_{tx}d_{ty}})}{b_{11}}, \quad b_{22} = [\overline{d_{ty}{}^2} - b_{21}{}^2]^{\frac{1}{2}}; \\ b_{23} &= 0, \quad b_{31} = \frac{(\overline{d_{tx}d_{tz}})}{b_{11}} \\ b_{32} &= \frac{(\overline{d_{ty}d_{tz}} - b_{21}b_{31})}{b_{22}} \\ b_{33} &= [d_{tz}{}^2 - b_{31}{}^2 - b_{32}{}^2]^{\frac{1}{2}} \end{aligned}\right\} \tag{35}$$

Hence the elements of $\vec{d}_t$ become

$$\left.\begin{aligned} d_{tx} &= b_{11}\ Z_1 \\ d_{ty} &= b_{21}\ Z_1 + b_{22}\ Z_2 \\ d_{tz} &= b_{31}\ Z_1 + b_{32}\ Z_2 + b_{33}\ Z_3 \end{aligned}\right\} \tag{36}$$

In what follows, tests are presented in two-dimensional space only. In this case the components of {β}, after expanding equation (24), take the following forms

$$\left.\begin{aligned}
\beta_{xx} &= \frac{1}{|\mathrm{cov}|_{\tilde{v}_{t-\delta t}}}\left(R_{xx}\sqrt{\overline{u^2}_t}\sqrt{\overline{u^2}_{t-\delta t}}\;\overline{v^2}_{t-\delta t} - R_{xy}\sqrt{\overline{u^2}_t}\sqrt{\overline{v^2}_{t-\delta t}}\;\overline{u_{t-\delta t}v_{t-\delta t}}\right)\\
\beta_{xy} &= \frac{1}{|\mathrm{cov}|_{\tilde{v}_{t-\delta t}}}\left(R_{xy}\sqrt{\overline{u^2}_t}\sqrt{\overline{v^2}_{t-\delta t}}\;\overline{u^2}_{t-\delta t} - R_{xx}\sqrt{\overline{u^2}_t}\sqrt{\overline{u^2}_{t-\delta t}}\;\overline{u_{t-\delta t}v_{t-\delta t}}\right)\\
\beta_{yx} &= \frac{1}{|\mathrm{cov}|_{\tilde{v}_{t-\delta t}}}\left(R_{yx}\sqrt{\overline{v^2}_t}\sqrt{\overline{u^2}_{t-\delta t}}\;\overline{v^2}_{t-\delta t} - R_{yy}\sqrt{\overline{v^2}_t}\sqrt{\overline{v^2}_{t-\delta t}}\;\overline{u_{t-\delta t}v_{t-\delta t}}\right)\\
\beta_{yy} &= \frac{1}{|\mathrm{cov}|_{\tilde{v}_{t-\delta t}}}\left(R_{yy}\sqrt{\overline{v^2}_t}\sqrt{\overline{v^2}_{t-\delta t}}\;\overline{u^2}_{t-\delta t} - R_{yx}\sqrt{\overline{v^2}_t}\sqrt{\overline{u^2}_{t-\delta t}}\;\overline{u_{t-\delta t}v_{t-\delta t}}\right)
\end{aligned}\right\} \quad (37)$$

Moreover, equation (27) gives

$$\left.\begin{aligned}
\overline{d_{tx}^2} &= \overline{u_t^2} - \left[\left(\beta_{xx}\overline{u^2}_{t-\delta t} + \beta_{xy}\overline{u_{t-\delta t}v_{t-\delta t}}\right)\beta_{xx} + \left(\beta_{xx}\overline{u_{t-\delta t}v_{t-\delta t}} + \beta_{xy}\overline{v^2}_{t-\delta t}\right)\beta_{xy}\right]\\
\overline{d_{tx}d_{ty}} &= \overline{u_tv_t} - \left[\left(\beta_{xx}\overline{u^2}_{t-\delta t} + \beta_{xy}\overline{u_{t-\delta t}v_{t-\delta t}}\right)\beta_{yx} + \left(\beta_{xx}\overline{u_{t-\delta t}v_{t-\delta t}} + \beta_{xy}\overline{v^2}_{t-\delta t}\right)\beta_{yy}\right]\\
\overline{d_{ty}^2} &= \overline{v_t^2} - \left[\left(\beta_{yx}\overline{u^2}_{t-\delta t} + \beta_{yy}\overline{u_{t-\delta t}v_{t-\delta t}}\right)\beta_{yx} + \left(\beta_{yx}\overline{u_{t-\delta t}v_{t-\delta t}} + \beta_{yy}\overline{v^2}_{t-\delta t}\right)\beta_{yy}\right]
\end{aligned}\right\} \quad (38)$$

These expressions are then used in equations (35) and (36)

There remains the important question of how to obtain the correlation functions R_{ij} While some experimental data has been reported for these functions, the data are judged to be insufficiently general and conclusive to be used in the present context We have therefore followed Berlemont et al's suggestion (1990) and adopted the following forms

$$R_{ij} = \frac{\overline{u_iu_j}}{\sqrt{\overline{u_i^2}}\sqrt{\overline{u_j^2}}}\exp\left\{\frac{-\delta t}{T_{ij}}\right\}\cos\left\{\frac{\delta t}{T_{ij}}\right\} \quad (39)$$

(no summation on i or j in denominator) with T_{ij} being equivalent to expression (10).

$$T_{ij} = \zeta(C_\mu^{0.75}k^{1.5}/\epsilon)/\left(\sqrt{\overline{u_i^2}}\sqrt{\overline{u_j^2}}\right)^{0.5} \quad (40)$$

(no summation on i or j) The value of ζ was taken as 0 8 on the basis of an optimisation carried out by the authors for isotropic turbulence [Zhou & Leschziner (1991)]

VALIDATION

Basic characteristics of sampling scheme

The validity of the present sampling methodology may be verified by contrasting the PDF fields obtained from the joint normal distribution (30), in conjunction with relation (19), with the corresponding fields reconstituted by repeated sampling via the route (31) to (36) To this end, a set of Reynolds stresses u_iu_j needs to be chosen together with a dissipation rate ϵ and a time interval δt It should be evident that, in practice, these would be available within an Eulerian Reynolds-averaged treatment of the carrier phase Hence, the correlation functions R_{ij} may be evaluated from (39), and from these follow the elements of $\{\beta\}$ via (37) This then permits the correlations of d_{tx} and d_{ty} to be determined from (38), from which the covariance of d_t follows.

For two-dimensional conditions, the PDF (30) may be expanded to read·

$$P(d_{tx},d_{ty}) = \frac{1}{(2\pi)\left(\overline{d_{tx}^2}\cdot\overline{d_{ty}^2} - \overline{d_{tx}d_{ty}}^2\right)^{\frac{1}{2}}} \times \exp\left\{-\frac{\left(\overline{d_{tx}^2}\,d_{ty}^2 - 2\,\overline{d_{tx}d_{ty}}\,d_{tx}d_{ty} + \overline{d_{tx}^2}d_{ty}^2\right)}{2\left(\overline{d_{tx}^2}\,\overline{d_{ty}^2} - \overline{d_{tx}d_{ty}}^2\right)}\right\} \quad (41)$$

For any pair (d_{tx},d_{ty}), the above thus yields $P(d_{tx},d_{ty})$ Given any particular choice of pairs $\tilde{v}_{t-\delta t}$, relations (19) allows the corresponding pair $\tilde{v}_t$ and the associated value P(u,v) to be determined, since the elements of $\{\beta\}$ are known

To test the conditional sampling process documented in Section 2, a large number of pairs $[Z_1,Z_2]$ (typically, 8000) were independently sampled from standard normal PDFs, from which the correlated fluctuations u and v were obtained, subject to the prescribed triples $(\overline{u^2}, \overline{v^2}, \overline{uv})$ and values for $u_{t-\delta t}$, $v_{t-\delta t}$ and δt used above The number of 'events' in which a pair (u,v) fell within any prescribed range $(\Delta u,\Delta v)$ was determined, and this was held to represent the probability of that event occurring·

It is instructive to consider first the case in which the time step δt is large, in which case temporal correlation is negligibly weak Here, δt was chosen such that the ratio $\delta t/T_{ij}$ varied between 4 and 5. Figs 2-4 shows contours of P(u,v) for three triples $\overline{u^2}$,$\overline{v^2}$, and $\overline{uv}$ In all three, the normal stresses are identical The first case is uncorrelated, reflected by uv=0, while in the second and third cases correlation is imposed via a positive or negative $\overline{uv}$ value Each figure contrasts the 'expected' PDF (obtained via (41)) with that reconstituted from the sampling methodology As is evident, there is close agreement between the pairs Typically, the stress triple computed from the sampled set differs from that originally prescribed by about 1%. The slight tendency for the centres of the sampled PDFs to wander into the third (-u,-v) quadrant is due to a programming detail relating to the allocation of sampling events to squares $(\Delta u,\Delta v)$, coupled with the relative coarseness of the $(\Delta u,\Delta v)$ grid; this is thus a cosmetic flaw which is easily cured

The performance of the scheme in the presence of time and directional correlation is illustrated in Figs 5 and 6 Here, δt is small, typically 1/2 of T_{ij}, and the choice made for $(u_{t-\delta t},v_{t-\delta t})$ is (0 2,0 2) or (-0 2,-0 2). Again, the figures contrast the 'expected' behaviour with that arrived at via the sampling route Two features deserve to be highlighted here. First, although the stress triples are identical to those adopted for Fig 3, the PDF is considerably narrower This is entirely in accord with expectations, for temporal correlation implies that the degree of randomness associated with the link $(u_{t-\delta t},v_{t-\delta t}) \longleftrightarrow (u_t,v_t)$ diminishes with decreasing δt Second, the contours are seen to be biased towards the sampling origin at $t-\delta t$ Here again, this is expected As δt increases, tests show that the centre of the contours shifts towards the origin (0,0) Overall, the agreement between the expected and sampled behaviour may be said to be satisfactory and to confirm the validy of the approach

Particle dispersion

We report initial results obtained from the application of the present model to the dispersion of fine water droplets in a free shear layer, examined experimentally by Lazaro & Lasheras (1989) The two-dimensional experiment involves the mixing of a spray with a stagnant air region At the start of the mixing region, information is available on mean velocity, turbulence intensity, mean-particle concentration and mean droplet dimeter

Modelling of the above flow proceeded in two parts the flow field was first computed with a boundary-layer algorithm incorporating the second-moment closure of Gibson and Launder (1976) and applied over a flow-adaptive 61x400 grid The aerodynamic field was then interpolated to a 31x61 Cartesian grid in which particle tracking was performed. The particle stream at the initial plane was represented by 144 groups, each relating to a different lateral position in the spray stream and each containing particles of a mean diameter (varying between 10 and 30 μm) commensurate with measurements A total of 6000 time steps were performed,

and 144 particle groups were discharged at intervals of 100 time steps Hence the total number of groups discharged was 86400 However, at any one time, the maximum number of groups tracked and processed was 2880 If more than 2880 groups resided in the solution domain, only the latest 2880 groups were tracked The sampling time step δt was taken as $4\,10^{-5}$ seconds This value was chosen such that the fastest particles trave"ed no further than one tenth of the grid size within the time step

At the time of writing, computations are being performed for different sampling intervals, δt, to investigate the extent to which particle dispersion is sensitive to this interval In an earlier investigation [Zhou & Leschziner (1991)], the dispersion in isotropic turbulence was demonstrated to be virtually insensitive to δt. Results are given here for $\delta t=4\,10^{-5}$ only An indication that the aerodynamic state has been captured correctly is provided in Fig 8 which demonstrates that the computed velocity thickness ($y_{0.9}-y_{0.1}$) is in close accord with the measurements Predicted variations of the Reynolds stresses indicate maximum levels of the ratio $\sqrt{\overline{u^2}}/\sqrt{\overline{v^2}}$ to be of the order 1 7 Computed particle-concentration profiles are shown in Fig 7, while Fig 8 compares predicted and experimental spreading rates of concentration, expressed in terms of ($y_{0.9}-y_{0.1}$) As seen, the computed spreading rate is a little too low but quite respectable. Calculations performed with other models not accounting for time-correlation or directional sensitivity show, for the same value of δt, spreading rates of only 20% of the experimental value

CONCLUSIONS

The paper has provided a modelling framework for sampling turbulent velocity fluctuations from statistical correlations of such fluctuations Key features of the method are: (i) its ability to account for correlation in time arising from shortness of sampling interval, and (ii) its ability to account for anisotropy and correlation between velocity fluctuations A series of tests have been presented, constituting a preliminary validation By reconstruction of the PDF fields, via the conditional sampling sequence, it has been demonstrated that the method yields velocity fluctuations which, in a statistical sense, satisfy the constraints imposed upon it by the given set of correlations of the fluctuations The method is being applied to particle dispersion in an anisotropic shear layer Initial results given herein are encouraging and justify the tentative conclusion that the method gives a statistically realistic representation of particle dispersion

REFERENCES

BERLEMONT, A , DESJONQUERES, P and GOUESBET, G , (1990), Int J Multiphase Flow, 16, pp 16-34

GIBSON, M M and LAUNDER, B E , (1987), J Fluid Mechanics, 85, p 491

GOSMAN, A D and IOANNIDES, E , (1981), "Aspects of computer simulation of liquid-fueled combustor", AIAA Paper 81-0323, 19th Aerospace Science Meeting, St. Louis

HINZE, J O , (1975), *Turbulence*, 2nd ed , McGraw-Hill, New York

KALLIO, G A and STOCK, D E , (1986), "Turbulent particle dispersion A comparison between Lagrangian and Eulerian modelling approaches",Proc of Gas-Solid Flow, The AIAA/ASME 4th Fluid Mechanics, Plasma Dynamics, and Lasers Conference, Atlanta, Georgia, 1986, pp 23-34

LAZARO, B J and LASHERAS, J C (1989), "Particle dispersion in turbulent, free shear flow", Proc 7th Symp on Turbulent Shear Flows, Stanford, pp 15 3 1 - 15 3 6

SHUEN, J S , CHEN, L D and FEATH G M., (1983), J AIChE, 29, No 1, pp 167-170

WELLS, M.R. and STOCK, D E , (1983), J Fluid Mechanics, 136, pp 31-62

YUU, S , YASUKOUCHI, N , HIROSAWA, Y and JOTAKI, (1978), J AIChE, 24, pp. 509-519

ZHOU, Q., and LESCHZINER, M A , (1991), "A LaGrangian particle dispersion model based on a time-correlated approach", Proc 1st joint JSME-ASME Fluids Engineering Conf., 4th Symp on Gas-Solid Flow, Portland

Acknowledgement· The authors gratefully acknowledge the financial support provided by SHELL Research, Amsterdam

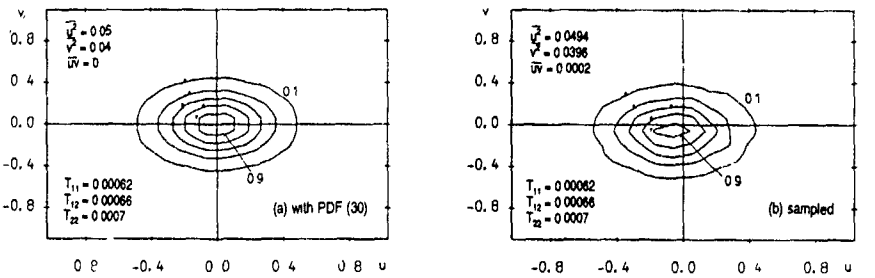

Fig 2 Contours of joint PDF P(u,v), $(\overline{u^2},\overline{v^2},\overline{uv})$ = (0 05,0.04,0), $(u_{t-\delta t},v_{t-\delta t})$ = (0 2,0 2), δt=0 03

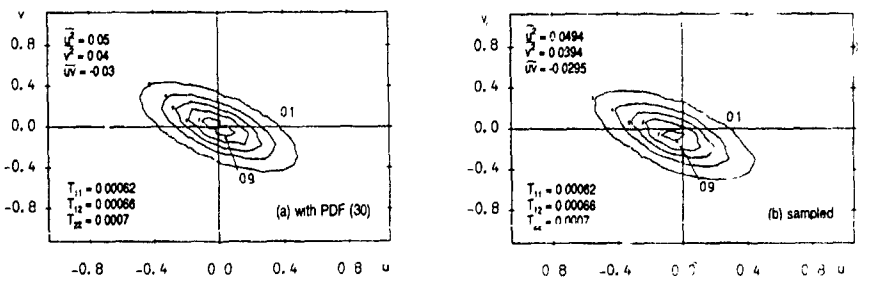

Fig 3 Contours of joint PDF P(u,v), $(\overline{u^2},\overline{v^2},\overline{uv})$ = (0 05,0 04,0 03), $(u_{t-\delta t},v_{t-\delta t})$ = (0 2,0 2), δt=0 03

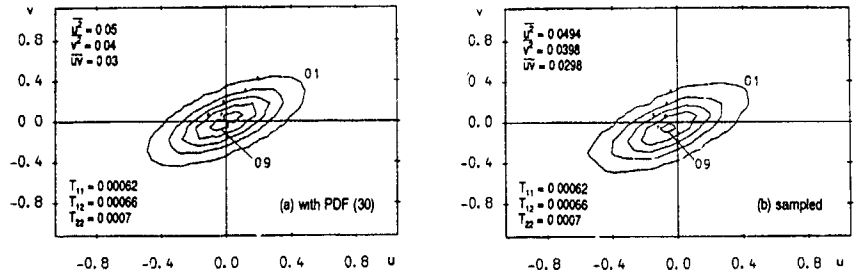

Fig 4· Contours of joint PDF P(u,v), $(\overline{u^2},\overline{v^2},\overline{uv})$ = (0.05,0.04,-0.03), $(u_{t-\delta t},v_{t-\delta t})$ = (0.2,0.2), δt=0.03

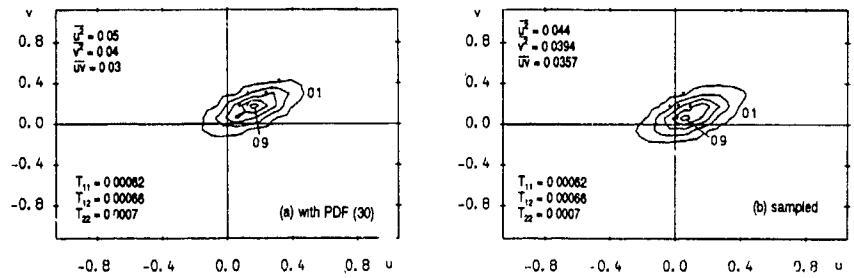

Fig 5 Contours of joint PDF P(u,v), $(\overline{u^2},\overline{v^2},\overline{uv})$ = (0.05,0.04,0.03), $(u_{t-\delta t},v_{t-\delta t})$ = (0.2,0.2); δt=0.0003

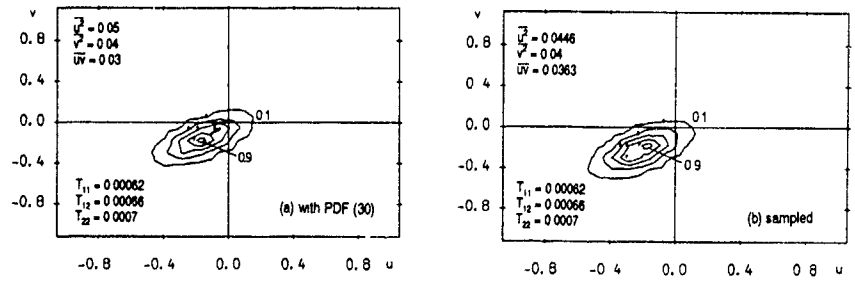

Fig 6. Contours of joint PDF P(u,v), $(\overline{u^2},\overline{v^2},\overline{uv})$ = (0.05,0.04,0.03), $(u_{t-\delta t},v_{t-\delta t})$ = (-0.2,-0.2), δt=0.0003

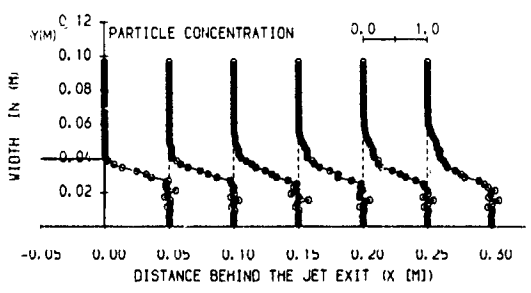

Fig 7: Mixing layer predicted particle-concentration field

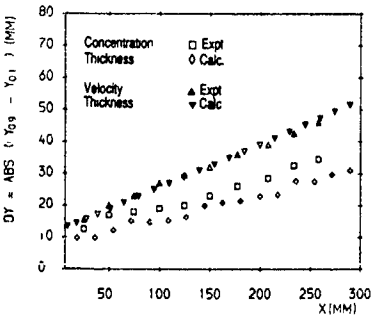

Fig. 8: Mixing layer· aerodynamic and concentration spreading rate

EIGHTH SYMPOSIUM ON
TURBULENT SHEAR FLOWS
Technical University of Munich
September 9-11, 1991

THE STATISTICAL CONCEPT OF COARSE PARTICLE MOTION IN A TURBULENT PIPE FLOW

I V Derevich

Krzizanovsky Power Engineering Institute
Moscow, USSR, Leninsky Prospect 19

ABSTRACT

On the basis of modern theory of stochastic processes the closed equation for probability function (PDF) velocity and coordinates of particles in inhomogeneous turbulent flow has been derived The gaseous phase turbulent pulsations are approximated by the random Markov process with fixed correlation function The system for the averaged velocity and pulsation motion of dispersed phase are presented The boundary conditions for the equation accounting particle-wall interaction are given The equations have been solved and the deposition rate, intensity of normal velocity of particles, particle concentration profiles, averaged velocity of dispersed phase have been obtained Predictions are in a good agreement with measurements

INTRODUCTION

Three general approaches allow to model two-phase turbulent flow gas with particles One is the Lagrangian approach usually known as a 'trajectory model' where the turbulent motion of individual particles which of traced by solving their equation of motion The trajectories of many particles(usually thousands) are realized in order to form the averaged characteristics of dispersed phase The fluid velocity pulsations are modelled as Gaussian noise with given auto correlation function (Kallio& Reeks 1989, Govan, Hewitt & Ngan 1989,Kyle &Eaton 1990, Sclen, Chen & Faeth1983) Lagrangian-type trajectory models give a detailed and realistic behavior of particles in pulsation motion of fluid But stochastic model is computational expensive and difficult to specifying boundary layer turbulence ,especially in the shear flows The second, Eulerian approach, often called a 'two-fluid' model, where the particles are treated as a continuous phase The motion of the particulate phase is mathematically described by equations of mass momentum and energy conservation The difficult task in Eulerian method is descriptions of closed equations for first and second moments of velocity pulsation of particles The relations between intensity of particles motion usually are derived in local-equilibrium approach, when a pulsation characteristics of particulate phase in a given point are connected with characteristics of fluid flow in the same point(Rizk & Elghobashi, 1985, Shraiber, Gavin, Naumov & Yatcenko 1987, Derevich, Yeroshenko & Zaichik, 1989) The local-equilibrium approach is valid only for small particles whose relaxation time is smaller than the life of energy-containing turbulent eddies (turbulent time macro scale) For inertial particles, whose dynamic relaxation time exceeds the time scale of turbulence nonlocal transfer is significant in inhomogeneous turbulent flow The analysis of such flow is only possible on the basis of nonlocal models In channel flows of inertial particles the intensity of particle velocity does not become zero on the walls unlike the pulsations of fluid velocity The intensive turbulent motion of particles normally to the wall determined the particles deposition from turbulent flows,and averaged slip velocity The diffusion and free-flight model are used to estimate of the inertial transfer of pulsation energy of particulate phase toward the walls (Fridlender & Johnstone ,1975, Reeks & Skyrme, 1976) Note, that the slip velocity is of great importance to calculate the diffusion coefficient and turbulent intensity of dispersed phase These effects usually are called as crossing trajectory effects' (Yudine, 1959, Csanady 1963, Nir & Pismen 1979, Reeks, 1980) Correct description of motion of particles near the channel wall is possible only if we have into consideration the interactions between particles and boundary The third approach to model the motion of particles in turbulent shear flows is method of probability density functions of characteristics of dispersed phase In the problem of turbulent fluid flow this method has been discussed (Lundgren, 1969,Pope,1985,Chung 1976)

EQUATION FOR PROBABILITY DENSITY FUNCTION

Equations of motion for single particle are

$$\frac{dR_{pk}}{dt} = V_{pk} \quad , \quad \frac{dV_{pk}}{dt} = \frac{1}{\tau}\left(U_k(R_p(t),t) - V_{pk}\right)$$

V_{pk} -velocity of particle, R_{pk} -coordinates of particle, $U_k(x,t)$- velocity of carrying gas We use description of probability density function of velocity and coordinates of particles (PDF) in the following way

$$\Phi(x,V,t) = \delta(x - R_p(t))\,\delta(V - V_p(t))$$

We averaged over the ensemble of turbulent realisation and obtain the non-closed

equation for PDF

$$\frac{\partial\langle\Phi\rangle}{\partial t} + V_K \frac{\partial\langle\Phi\rangle}{\partial x_K} + \frac{1}{\tau}\frac{\partial}{\partial V_K}\left[(\langle U_K\rangle - V_K)\langle\Phi\rangle\right] = -\frac{1}{\tau}\frac{\partial}{\partial V_K}\langle u_K\Phi\rangle$$

where $U_k(x,t) = \langle U_K(x,t)\rangle + u_K(x,t)$, $\langle U_K(x,t)\rangle$ – averaged velocity, $u_K(x,t)$ pulsation gas velocity

Modelling pulsation gas velocity as Gaussian stochastic process (Klyatskin, ..80) we find the following expression

$$\langle u_K\Phi\rangle = \int dx_1 \int_0^\infty d\xi \langle u_i(x_1,\xi) u_K(x,t)\rangle \left\langle \frac{\delta\Phi(x,V,t)}{\delta u_i(x_1,\xi)}\right\rangle$$

where functional derivation looks as

$$\frac{\delta\Phi(x,V,t)}{\delta u_i(x_1,\xi)} = -\frac{\partial}{\partial x_j}\Phi\frac{\delta R_{pj}(t)}{\delta u_i(x_1,\xi)} - \frac{\partial}{\partial V_j}\Phi\frac{\delta V_{pj}(t)}{\delta u_i(x_1,\xi)}$$

As a result we obtain approximate solution for functional derivations

$$\frac{\delta V_{pi}(t)}{\delta u_j(x_1,\xi)} = \frac{\delta_{ij}}{\tau}\exp\left(-\frac{t-\xi}{\tau}\right)\delta(x_1 - R_p(\xi))$$

$$\frac{\delta R_{pi}(t)}{\delta u_j(x_1,\xi)} = \delta_{ij}\left[1-\exp\left(-\frac{t-\xi}{\tau}\right)\right]\delta(x_1 - R_p(\xi))$$

The expression for correlator $\langle u_K\Phi\rangle$ is

$$\langle u_K\Phi\rangle = -\int_0^t d\xi\left[1-\exp\left(-\frac{t-\xi}{\tau}\right)\right]\langle u_i(R_p(\xi),\xi)u_K(x,t)\rangle\frac{\partial\langle\Phi\rangle}{\partial x_j} - \frac{1}{\tau}\int_0^t d\xi\exp\left(-\frac{t-\xi}{\tau}\right)\times$$

$$\langle u_i(R_p(\xi),\xi)u_K(x,t)\rangle\frac{\partial\langle\Phi\rangle}{\partial V_j}$$

This expression is described in terms of probability of particles transition

$$\langle u_i(R_p(t_1),t_1)u_K(x,t)\rangle = \int dx_1\langle u_i(x_1,t_1)u_K(x,t)G(x,t|x_1,t_1)\rangle$$

$$G(x,t|x_1,t_1) = \delta(x - R_p(t))\delta(x_1 - R_p(t_1))$$

Using the equation of particle motion, we find the following equation (Reeks, 1980)

$$G(x,t|x_1,t_1) = \delta(x - x_1 + \tau(v_p(t) - v_p(t_1)) - (t-t_1)\langle W\rangle - (t-t_1)\langle U\rangle - \int_{t_1}^t ds\, u(R_p(s),s))$$

where $\langle W\rangle = \langle V\rangle - \langle U\rangle$ averaged drift velocity, $v_p(t) = 1/\tau\int_0^t ds\, e^{-\frac{t-s}{\tau}}u(R_p(s),s)$ pulsation velocity of single particle. The function $G(x,t|x_1,t_1)$ gives the density of probability of particle transition from point (x_1,t_1) to point (x,t). The displacement of the solid particle is composed of the inertial movement (second term in the argument of δ -function) the movement under the external mass force and the displacement together with turbulent eddies, the velocity of which is calculated on the trajectory of reference particle (the last two terms). The displacement of fluid eddies with trajectory crossing the single particle path we denote by $R_f^p(t-t_1) = \langle U\rangle(t-t_1) + \int_{t_1}^t ds\, u(R_p(s),s)$ Using the variables $x' = x_1 + R_f^p(t-t_1)$ we obtain

$$\langle u_i(R_p(t_1),t_1)u_K(x,t)\rangle = \int dx'\langle\langle u_i(x',t_1)u_K(x,t)\rangle\rangle\langle G'(x,t|x',t_1)\rangle, \langle\langle u_i(x',t_1)u_K(x,t)\rangle\rangle =$$

$$\langle u_i(x' - R_f^p(t-t_1),t_1)u_K(x,t)\rangle, \langle G'(x,t|x',t_1)\rangle = \langle\delta(x - x' + \tau(v_p(t) - v_p(t_1)) -$$

$$-\langle W\rangle(t-t_1))\rangle$$

In the assumption of Gaussian type pulsation of particle velocity we can write a closed expression for transition probability function

$$\langle G'(x,t|x_1,t_1)\rangle = \prod_{i=1}^3 (2\pi\ell_{pi}^2)^{-1/2}\exp\left[-(x_i - x_i' - \langle W\rangle(t-t_1))^2/(2\ell_{pi}^2)\right],$$

$$\ell_{pi}^2 = \tau^2\left[\langle v_{pi}^2(t_1)\rangle\left(1-\exp\left(-\frac{t-t_1}{\tau}\right)\right)^2 + \langle v_{pi}^2(t-t_1)\rangle\right].$$

Finally we have a closed equation for PDF

$$\frac{D\langle\Phi\rangle}{Dt} - \frac{D\langle V_i\rangle}{Dt}\frac{\partial\langle\Phi\rangle}{\partial v_i} + v_k\frac{\partial\langle\Phi\rangle}{\partial x_k} + \frac{\langle U_i\rangle-\langle V_i\rangle}{\tau}\frac{\partial\langle\Phi\rangle}{\partial v_i} - v_k\frac{\partial\langle V_i\rangle}{\partial x_k}\frac{\partial\langle\Phi\rangle}{\partial v_i} - g\langle u_i u_j\rangle\frac{\partial^2\langle\Phi\rangle}{\partial x_i\partial v_j} -$$

$$(1-\delta_{ij})\frac{\sigma_{ij}}{\tau}\frac{\partial^2\langle\Phi\rangle}{\partial v_i\partial v_j} = \hat{L}\langle\Phi\rangle,\ \frac{D}{Dt} = \frac{\partial}{\partial t} + \langle V_k\rangle\frac{\partial}{\partial x_k},\ \sigma_{ij} = f\langle u_i u_j\rangle - \tau g\langle u_i u_k\rangle\frac{\partial\langle V_j\rangle}{\partial x_k},$$

$$\hat{L} = \frac{1}{\tau}\frac{\partial}{\partial v_i}v_i + \frac{\sigma_{ii}}{\tau}\frac{\partial^2}{\partial v_i\partial v_j},\ f\langle u_i u_j\rangle = \frac{1}{\tau}\int_0^t dt_1 \exp\left(-\frac{t-t_1}{\tau}\right)\int dx'\langle\langle u_i(x,t)u_j(x',t_1)\rangle\rangle\langle G'\rangle.$$

Note that the above equation for PDF is similar to Fokker-Planck (Ahmadi & Hayday, 1988, Chung, 1976)

EQUATIONS FOR FIRST AND SECOND MOMENTS OF PARTICLE VELOCITY FLUCTUATIONS

The equation of particle number concentration $\langle N(x,t)\rangle = \int dV\langle\Phi(x,V,t)\rangle$ is

$$\frac{\partial\langle N\rangle}{\partial t} + \frac{\partial\langle N\rangle\langle V_k\rangle}{\partial x_k} = 0$$

The equation of averaged velocity of dispersed phase $\langle N\rangle\langle V_i\rangle = \int dV V_i\langle\Phi\rangle$ is

$$\frac{\partial\langle V_i\rangle}{\partial t} + \langle V_k\rangle\frac{\partial\langle V_i\rangle}{\partial x_k} + \frac{\partial\langle v_i v_k\rangle}{\partial x_k} = \frac{\langle U_i\rangle-\langle V_i\rangle}{\tau} - \frac{D_{ik}}{\tau}\frac{\partial\ell_n\langle N\rangle}{\partial x_k}$$

where $D_{ik} = \tau(\langle v_i v_k\rangle + g\langle u_i u_k\rangle)$ - coefficient of turbulent diffusion of particles The system of equations for second moments of particles velocity pulsation is

$$\frac{\partial\langle v_i v_j\rangle}{\partial t} + \langle V_k\rangle\frac{\partial\langle v_i v_j\rangle}{\partial x_k} + \frac{1}{\langle N\rangle}\frac{\partial\langle N\rangle\langle v_i v_j v_k\rangle}{\partial x_k} + \langle v_i v_k\rangle\frac{\partial\langle V_j\rangle}{\partial x_k} +$$

$$+\langle v_j v_k\rangle\frac{\partial\langle V_i\rangle}{\partial x_k} = \frac{2}{\tau}(\sigma_{ij} - \langle v_i v_j\rangle)$$

Note that operator $\hat{L}$ in the right side of PDF equation describes 'collisions' of particles with turbulent eddies We suggest the procedure for solution the above PDF equation which is similar to the Chapman-Enskog methods of solving kinetic equations in the theory of gases As a zero approximation we have equilibrium relations for the velocity distribution of particles The full form of PDF in the approximation

$$\langle\Phi(x,V,t)\rangle = \langle N\rangle A\exp\left(-\frac{v_i v_j}{2\sigma_{ii}}\right)\left\{1 + \frac{1}{2}(1-\delta_{ij})\sigma_{ij}\frac{v_i v_j}{\sigma_{ii}\sigma_{jj}} - \frac{\tau}{2\sigma_{ii}}(v_i v_k - \delta_{ik}v_k v_k)\times\right.$$

$$\left.\frac{\partial\langle V_i\rangle}{\partial x_k} - \frac{\tau}{3}\frac{v_i}{\sigma_{kk}}\left[\frac{v_k v_k}{2\sigma_{kk}} - (\delta_{ik}+\frac{1}{2})\right]\left(1 + g\frac{\langle u_i u_j\rangle}{\sigma_{jj}}\right)\frac{\partial\sigma_{kk}}{\partial x_i}\right\},\ A = \prod_{i=1}^{3}(2\pi\sigma_{ii})^{-1/2}$$

The second correlation of velocity pulsations for $i \neq j$ of dispersed phase is

$$\langle v_i v_j\rangle\langle N\rangle = \int dV v_i v_j\langle\Phi\rangle = \langle N\rangle\left[\sigma_{ij} - \frac{\tau}{2}\left(\sigma_{ii}\frac{\partial\langle V_j\rangle}{\partial x_i} + \sigma_{jj}\frac{\partial\langle V_i\rangle}{\partial x_j} - \frac{2}{3}\delta_{ij}\sigma_{kk}\frac{\partial\langle V_k\rangle}{\partial x_k}\right)\right]$$

The triple correlation of the velocity pulsations is determined in terms of eddy diffusion of particles

$$\langle v_i^2 v_k\rangle\langle N\rangle = \int dV v_i^2 v_k\langle\Phi\rangle = -\langle N\rangle\frac{\delta_{ik}+2\delta_{ii}}{3}D_{ik}\frac{\partial\sigma_{ii}}{\partial x_k}$$

Thus we have the system of closed equations for concentration, momentum and pulsation energy of dispersed phase balances

THE BOUNDARY CONDITIONS

The boundary conditions are formulated in the frame of wall-particle interactions We assumed that reflected particles have lower speed than dropped ones $V_i = \varkappa_i V_i'$ The PDF of reflected particles ($\langle\Phi_+\rangle, V_y > 0$) is connected with PDF of particles before collisions ($\langle\Phi_-\rangle, V_y \leq 0$) with the channel wall

$$\langle\Psi_+(x,V,t)\rangle = \int dV'\varphi(V,V')\langle\Phi_-(x,V',t)\rangle,\ V_y' \leq 0;\ \langle\Phi_-(x,V',t)\rangle = \langle\Phi(x,V,t)\rangle,$$

$$\varphi(V,V') = \delta(V_x - \varkappa_1 V_x')\,\delta(V_y + \varkappa_2 V_y')\,\delta(V_z - \varkappa_3 V_z')$$

where function $\varphi(V,V')$ describes the interactions dispersed phase and boundary $\varkappa_i$ - coefficient of restitution of impuls in i -th direction Using the balance

of rate transfer characteristics of deposited and reflected particles, the boundary conditions are formulated for equations of mass, averaged velocity,and the level of turbulent pulsations of particles normal to the wall

$$\left(\frac{2}{\pi}\sigma_{yy}\right)^{1/2}\frac{1-\varkappa_2}{1+\varkappa_2}+\langle V_y\rangle=0\ ,\quad \sigma_{yy}\langle W\rangle=\int dv\, v_y^2\langle\Phi\rangle=\langle N\rangle\langle v_y^2\rangle,$$

$$\left[\left(\frac{2}{\pi}\sigma_{yy}\right)^{1/2}\frac{1-\varkappa_1\varkappa_2}{1+\varkappa_1\varkappa_2}+\langle V_y\rangle\right]\langle V_x\rangle=\frac{\tau\sigma_{yy}}{2}\frac{\partial\langle V_x\rangle}{\partial y},$$

$$\left[\left(\frac{2}{\pi}\sigma_{yy}\right)^{1/2}\frac{1-\varkappa_2^3}{1+\varkappa_2^3}2+\langle V_y\rangle\right]\sigma_{yy}=\mathcal{D}\frac{\partial\sigma_{yy}}{\partial y}\ ,\quad \mathcal{D}=\tau\left(\sigma_{yy}+g\langle u_y^2\rangle\right).$$

Note that boundary conditions for particle consentration in homogeneous flow is similar to reflected boundary conditions for Brownian motion (Mennon & Sahni,1985)

RESULTS AND DISCUSSION

For illustration let us consider a problem in the approximation of homogeneous turbulence Neglecting the effect of particle inertia ($\ell_p=0$, on T_p(macro scales of turbulent pulsations of fluid velocity on the particle path)we defined relation between T_p, L_p and Eulerian (T_E, L_E) and Lagrangian(T_L, L_L) macro scales

$$\beta_p=\frac{T_p}{T_E}=\frac{L_p}{L_E}\ ,\ \beta=\frac{T_L}{T_E}=\frac{L_L}{L_E}\ ,$$

$$\beta_p=\frac{\gamma+\beta}{\gamma+1}\ ,\ \gamma=\langle W\rangle/u\ ,\ u=E^{1/2}.$$

For cons derably drift velocity the scales of the pulsation field of gas along the path of the particle coincide with Eulerian macro scales For low drift velocity the turbulent field around the particle has the Lagrangian characteristics For exponential approximation we have $\varphi(y,t)=\exp(-|y|/L_p-|t|/T_p),\ \Omega=\tau/T_E$,

$$f=\left[1+\Omega/\beta_p(1+\gamma)\right]^{-1},\ g=\beta_p/\Omega(1+\gamma)^{-1}-f$$

It is possible to obtain analytical formula for Lagrangian time scale of particle velocity pulsations

$$\frac{T_{pL}}{T_E}=\beta_p\frac{1+\Omega/\beta_p(1+\gamma)}{1+\gamma}\ .$$

Figure 1,2 show dependence of Lagrangian scales of particle on relative velocity (x/M - position in the wind-tunnel test section β =0 5, Sato & Yamamoto,1987) We see that as the slip velocity of small inertial particles (Ω << 1) becomes significant turbulent Lagrangian time scale of particle pulsation becomes smaller However, for inertial particles Ω >>1 , order in high slip velocity γ >>1, Lagrangian time scale of particles is about particle relaxation time

We calculate the intensity of particle turbulent pulsations in the case of inhomogeneous turbulence in a pipe Figure 3 compares the results of author calculations (β =0 3) of the normal pulsating velocities of particles with the results of stochastic simulations and experimental data We see that as the infertility of particles($\Omega=\tau/T_E$)increases, the dispersed phase penetrate more and more into viscous sub layer, which results in the non zero values of the pulsating velocity on the channel wall As the infertility of particles further increases, the intensity of turbulent fluctuations goes down (Hinze, 1959, Pismen & Nir,1978) This is due to the lower intrainment of heavy particles into the turbulent motion Figure 4 compares author calculation results with the experimental data on the deposition rate of particles from turbulent flow

The calculations show substantial slip velocity of dispersed phase and gas because of the intensive momentum transfer between the turbulent core and near-wall region in the flow of particle gas suspension (Figure 5) In this case, the particle velocity in the core is smaller than carrier phase velocity, but in the near-wall region the particle velocity exceeds of the gas The predictions and experiments are in satisfactory agreement (Figure 6 R+ -tube radius in universal coordinates,Vm/Um - relation of mean velocities of phases)

Fig 1 The effect of slip velocity on Lagrangian autocorrelation time of particle velocity pulsations (points by Wells & Stock,1983,lines-calculations)
1 - x/M=41 2 - 79 3 - 171

Fig 2 Lagrangian autocorrelation time dependence on particle dynamic relaxion time (points by Snyder & Lumley, 1977, lines - calculations)
1 - x/M=30, 2 - 45, 3 - 90

Fig 3 Particle pulsation velocity in the

Fig 4 Particle deposition rate (points by Papavergos & Hedley, 1984,lines - calculations)
1 - R+=5 E3, 2 - 3 E3, 4 - 1 E3, 5 - 6 E2

Fig 5 The averaged velosity of dispersed phase in the pipe (R+=2300)
1 - τ +=1 E5,$\varkappa_2$=0, 2 - τ +=1 E5,$\varkappa_2$ =1,$\varkappa_1$=0 8, 3 - τ +=1 E5,$\varkappa_2$=1,$\varkappa_1$=0 5, 4 - τ+=1 E5,$\varkappa_2$=1, $\varkappa_1$ =0, 5 - τ +=1 E4,$\varkappa_2$ =1,$\varkappa_1$=0 8, 6 - τ+= 1 E6 $\varkappa_2$ =1, $\varkappa_1$ =0 8

Fig 6 The mean velosity of particles in

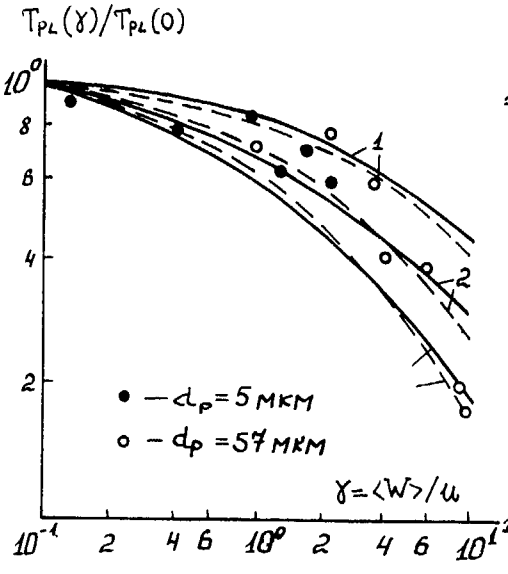

Fig. 1

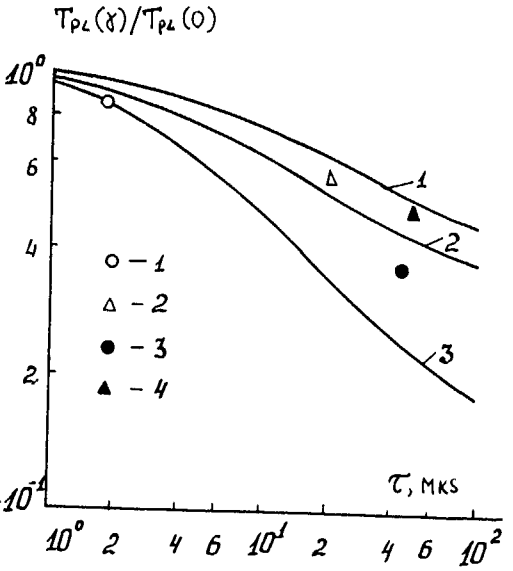

Fig. 2

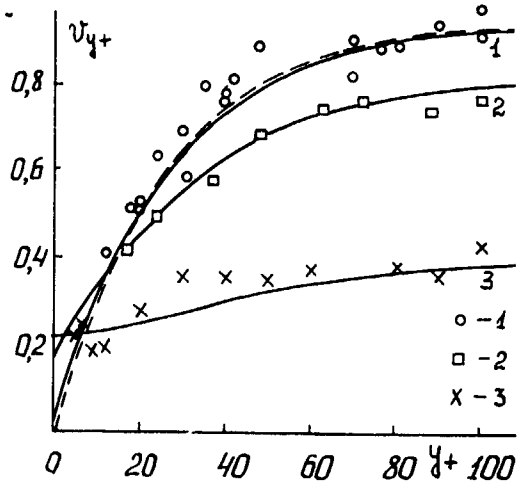

Fig. 3

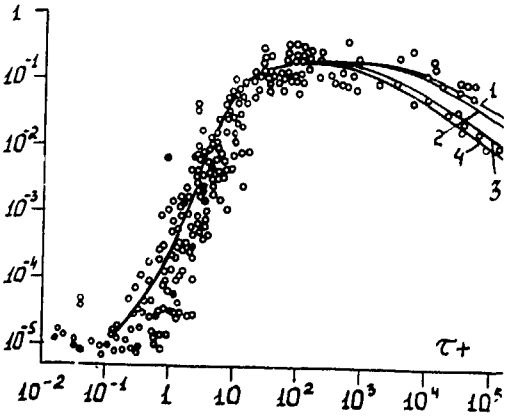

Fig. 4

Fig 3 Particle pulsation velocity in the wall region (points by Kallio & Reeks, 1989, lines - calculations)
1 - τ_+=1, 2 - 15, 3 - 100

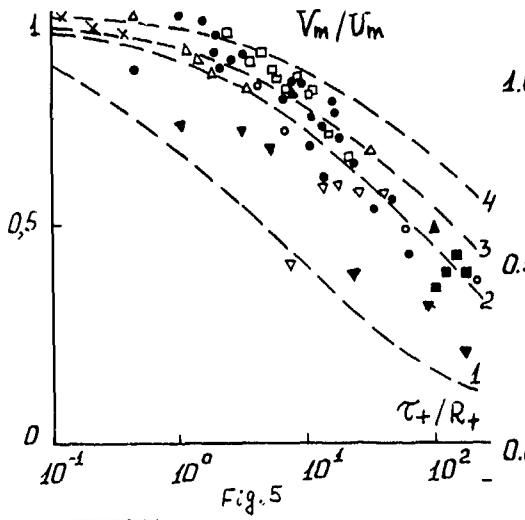

Fig.5

Fig 6 The mean velosity of particles in a pipe (points - experimental data, lines - calculations, $\mathcal{R}_2$ = 1)
1 - $\mathcal{R}_1$ = 0,2 - 0 6, 3 - 0 7,4 - 0 8

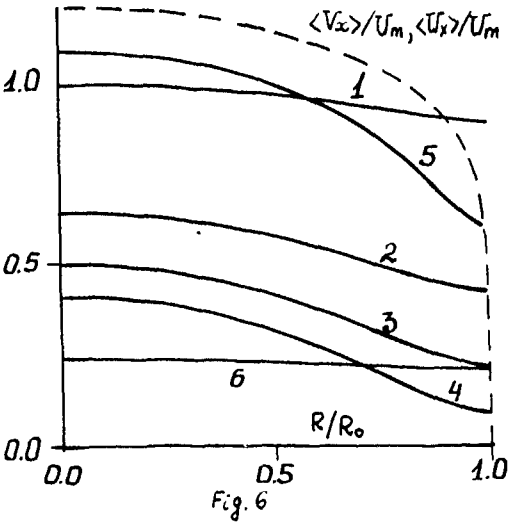

Fig.6

REFERENCES

Ahmadi, G & Haydav A A 1988 A probability density closure model for turbulence Acta Mechanica 72,55-71

Chung,P M 1976 On kinetic-theory approach to turbulent chemically reacting flows Combust Sci Tech 13,1123-147

Csanady,G T 1963 Turbulent diffusion of heavy particles in the athmosphere J Atmospheric Sci 20,201-208

Derevich,I V , Yeroshenko,V M & Zaichik L I 1989 Hydrodynamics and heat transfer of turbulent gas suspension flow in tubes I Hydrodynics, II Heat trasfer Int J Heat & Mass Transfer 32, 2329-2350

Friedlender,S K & Jounstone,H F 1957 Deposition of suspended particles from turbulent gas streams Ind Engn Chem 49,1151-1156

Govan,A H ,Hewitt,G F & Ngan,C F 1989 Particle motion in a turbulent pipe flow Int J Multiphase Flow 15,471-481

Hinze, J A 1959 Turbulence, Ney York,Mc Grow Hill

Kallio,G A &Reeks,M W 1989A numerical simulation of particle deposition in turbulent boundary layers Int J Multiphase Flow 15,433-446

Klyatskin,B I 1980 Stochastic equatins and waves in a random media Nayka, Moscow (USSR,in Russian)

Kyle,D S & Eaton,J K 1990 Particle response and turbulece modification in isotropic turbulence Phys Fluids A 2, 1191-1203

Lee,M M ,Hanratty,T J & Adrian,R J 1898 The interpritation of droplet deposition measuremrnts with a diffusion mo-

Lundgren,T S 1969 Model equacion for nonhomogeneous turbulence Phys fluids 12 485-497

Mennon,S V G & Sahni,D C 1985 Derivation of the diffusion equation boundary condition from the Fokker-Planck equation Phys Fluids 32,3832-3834

Nir,A & Pismen,L M 1979 The effect of steady drift on the dispersion of a particles in turbulent fluid J Fluid Mech 94,369-481

Papavergos,P G & Hedley,A B 1984 Particle deposition behaviour from turbulent flows Chem Eng Res Des 62,275-295

Pismen,L M & Nir,A 1978 On the motion of suspended particles in stationary homogeneous turbulence J Fluid Mech 84,193-206

Reeks,M.W 1980 Eulerian direct interaction applied to the statistical motion of particles in a turbulent fluid J Fluid Mech 97,569-591

Rizk,M A & Elghobashi,S E 1985 The motion of spherical paritcle suspended in a turbulent flow near a plane wall Phys Fluids 28,806-817

Sato,Y & Yamamoto,k 1987 Lagrangian measurement of fluid-particle motion an isotropic turbulent field J Fluid Mech 175,183-199

Shraiber,A A , Gavin,L B ,Naumov,B A & Yatzenko, 1987 Turbulent flow of gas-solid suspension Naukova Dumka,Kiev (USSR,in Russian)

Shyen,J-S ,Chen,L-D & Faeth,G M 1983 Evaluation of a stochastic model of particle dispersion in a turbulent round jet AIChE Jl 29,167-170

Snyder,W H & Lumley,J L 1977 Some measurements of particle velocity autocorrelation functions in a turbulent flow J Fluid Mech 48,41-71

Yudine,M I 1959 Physical consideration on heavy-particle diffusion Advances in Geophysics,6, New York,Academic Press, 185-191

Wells,M R & Stock,D E 1983 The effects of crossing trajectories on the dispe sion of particles in a turbulent flow J Fluid Mech 136,31-62

EIGHTH SYMPOSIUM ON
TURBULENT SHEAR FLOWS
Technical University of Munich
September 9-11, 1991

PARTICLE DISPERSION IN HIGHLY SWIRLING, TURBULENT FLOWS

E.Blumcke, M.Brandt, H.Eickhoff, C.Hassa

DLR - Institut for Propulsion Technology
Linder Hohe, D-5000 Koln 90
Telefon: 02203-601-2478
Germany

Abstract

Transport processes of monosized droplets in a turbulent swirling shear layer were investigated experimentally and theoretically. A model experiment was designed that represents the spray dispersion produced by airblast atomizers.
Based on the experimental results a stochastic dispersion model was developed.
The analysis of the numerical results emphasizes the importance of an accurate description of gas phase turbulence characteristics.
The implementation of a socalled "Multiple-Particle-Option" enables the model to resolve instationary dispersion characteristics.

Introduction

During the last years it became more feasible to design combustion chambers of modern gas turbine engines with the aid of numerical computations, see e.g. Burrus (1989). For that purpose a suitable description for the transport of the liquid phase in the two-phase flow is essential. Therefore, the main scope of the present investigation is the development of a so-called "Spectral Dispersion Model" and its evaluation with detailed experimental results. To furnish the experimental data required for that purpose ,the experiment should exhibit some essential features of the two-phase flows found in combustors with airblast atomizers. In order to ensure well defined boundary and initial conditions for the liquid phase, a model experiment was designed that clearly separates transport phenomena from effects originating from the atomization process.
The present paper describes an approach for the modelling of turbulent particle dispersion and the application of the model to the experiment mentioned above.

Two-Phase Flow Model

The axisymmetric gas flow field was described by the time mean equations for conservation of mass and momentum, supplemented by a standard k-ε-turbulence model. The numerical predictions were based on a finite-volume method using a computational mesh of 79 x 61 nodes.
The liquid phase is considered in a Lagrangian frame. The assumption of a dilute spray is justified by the low mass loading as well as by the large droplet spacings in the experiment considered here.

The major problem in modelling the turbulent particle dispersion in a Lagrangian frame is the determination of the actual gas velocity experienced by the droplet. In the present approach, it is assumed, that for the calculation of stochastic droplet trajectories the gas turbulence can be characterized by a Gaussian probability density distribution (PDF) and a predefined Lagrangian autocorrelation function R of the velocity fluctuations. Thereby, the turbulent kinetic energy of the gas phase is distributed over a range of frequencies (hence the name "Spectral Dispersion Model"). This means, that the model accounts for gas velocity fluctuations being connected with "eddies" of different sizes. Such a procedure was first proposed by Desjonquères (1987). The present approach is described in detail in Blumcke (1991).
At its core is a digital filter, that numerically generates the velocity fluctuations for the Lagrangian trajectories, as demonstrated by Olivari&Benocchi (1987). The transfer function of such a filter has to be identical with the autocorrelation function of the Lagrangian velocity fluctuations and therfore requires as input parameter the Lagrangian integral time T_L or length scales I_L. The transfer function is now z-transformed and the discrete transform is multiplied with a random number sequence having a Gaussian probability density distribution and a "white noise" spectrum, i.e. the convolution theorem in its discrete form is used to generate step by step a number sequence that exhibits a Gaussian PDF as well as the behaviour of a digital filter with a predefined spectral function. The filter output signal is then multiplied by the RMS-velocity to yield the actual velocity fluctuation. Each of the velocity components is assigned to one digital filter. This technique, which can easily be extended to account for anisotropic turbulence, Blumcke et al. (1990), enables the calculation of the trajectory of a fluid particle.
Due to the inertial force, the spectral manipulation technique, working solely in time, is not sufficient for the provision of velocity fluctuations along the path of a droplet, see Fig.1a. Therefore, a fluid particle and a discrete particle are always followed simultaneously in the dispersion model . To that effect the spatial evolution of velocity fluctuations between the location of the fluid particle and that of the discrete particle also have to be resolved by the spectral manipulation technique, which is now applied in the

space domain as long as the droplet stays in a correlation domain. A correlation domain is defined by the volume, in which there is a correlation between the velocity fluctuations at the location of the fluid point and that of the particle. Leaving its correlation domain, the particle experiences a crossing-trajectory-effect.

a: Trajectories of a fluid and a discrete particle, resp.

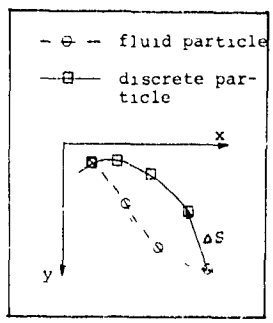

b: Link of the two digital filters
I: Trajectory of a discrete particle in the time-space-domain
II: Correlation domain in time
III: Correlation domain in space

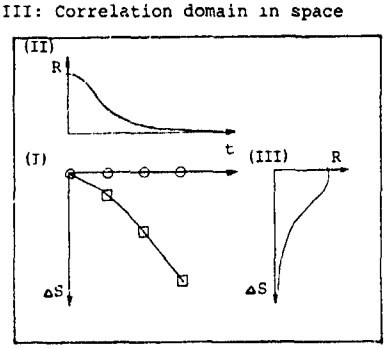

Fig. 1: Spatial evolution of gas velocity fluctuations

The initial position in the new correlation domain, sketched in Fig. 1bI, is then re-established while the digital filters are restarted.
The remaining task of the proper matching of the two digital filters, working in time, Fig. 1bII. and space, Fig. 1bIII, resp., requires that the filter input signals have to be stored. The matching instruction originates from an assumed link of Lagrangian time and length scales.
The anisotropic Lagrangian integral length scales L_i of the coordinate directions i can be calculated following Hinze (1975) as:

$$L_i = C_L * T_L * u_{rms,i} \qquad (1),$$

where C_L is a model constant and $u_{RMS,i}$ is the root mean square of the PDF of velocity component i. With the experiment of Snyder& Lumley (1971), serving as validation test case, the constant C_L was set to 0.4 as a result of computer optimization.
Hence, the Lagrangian integral length scales enter the procedure twice via the filter transfer function and the dimensions of the correlation domains.
The link between length and time scales also requires to assume the same shape of the autocorrelation functions of the digital filters working in time and space.
As has been mentioned, associated with the linkage is the burden of storing the filter input sequence. This problem was overcome by storing only one very long sequence of input signals. On this very large vector each particle is assigned to a separate start index and a separate increment for every velocity component. Thereby, it is guaranteed that each velocity component of every particle experiences an individual filter input sequence.

Diagnostics

For the measurements of gas- and particle velocities a two component Laser-Doppler-Anemometer (LDA) was used. The dispersion and velocity of the monosized drops were measured under 90° scattering angle to limit the nominal measurement volume size. This size was varied from about 50x50x200 µm near the nozzle to 150x150x600 µm further downstream in order to adapt to the different droplet concentrations.
The liquid mass flow was determined by an algorithm proposed by Saffman (1987). A validation test of the algorithm using monosized droplets showed a good agreement between measured and theoretical data.
The errors of this measurement technique were estimated to be less than 20% for the present investigation, Hassa (1991). The same error margin is claimed for the reproducibility of the measured data, mainly caused by minor fluctuations of the operation characteristics of the droplet generator.

Model Experiment

The purpose of the model experiment was the quantitative evaluation of models for the turbulent dispersion of particles in a flow exhibiting the features of gas turbine combustor flows, that are relevant to dispersion: a swirling recirculating shear layer, creating a strong source of turbulent kinetic energy where drops prevail, before they are vaporized in a combusting environment.
Consequently, the gas flow in the model configuration, Fig. 2a, consists of a swirling air jet discharged in a low velocity co-flowing air stream. Great care was taken to ensure the axial symmetry of the flow, see Hassa et al. (1988).
By the use of a monodisperse droplet generator the initial conditions for the liquid phase: location, size, velocity and concentration of the droplets are known. For this investigation, water droplets of 23, 30 and 44 µm were produced with initial velocity fluctuations of about 2%. By positioning the generator off-axis in the annulus between the swirling and the non-swirling airflow - the analogon to the atomizing lip of an atomizer nozzle -, the axial symmetry of the liquid phase flow is lost and it becomes fully threedimensional, reflecting the ability of studying threedimensional effects by a Lagrangian dispersion model even if the underlying gas flow is axially symmetric.

a: Schematic layout of the experiment

1 inner airflow
2 coaxial airflow
3 swirler
4 swirl channel
5 droplet generator
6 annulus
7 flow straightener

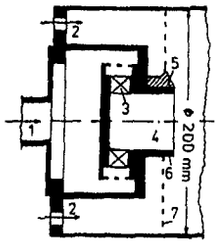

b: Calculated isothermal flow field

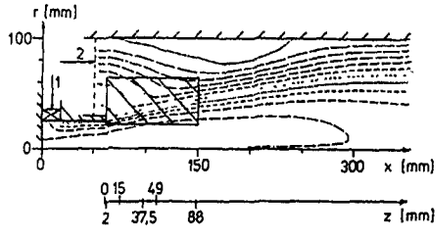

Fig. 2: Model experiment "Turbulent Particle Dispersion"

The ultimate prerequisite for the evaluation of the particle dispersion model is the knowledge of the correct gas flow field including the Reynolds stress tensor and the dissipation. The comparison of calculated and measured data showed a reasonable, but not yet sufficient agreement for the mean gas flow field, Blümcke et al. (1988). Therefore, measured data, like the mean gas velocity and the turbulent kinetic energy, replaced whenever possible the calculated data. The turbulent input parameters of the Lagrangian code are formed by a combination of the values from k and ε. While ε could not be measured, the calculated Lagrangian integral time scales were judged by the evaluation of measured power spectral density distributions of the gas fluctuations, Hassa et al. (1990).

Results

The three dropsizes considered in the experiment are within the range of interest for airblast atomizers. The particle Reynolds numbers were kept similar to the ones in a combustor in order to provide a rough check for the applicability of the chosen particle drag description. Moreover mean and turbulent particle Stokes numbers of the model experiment are within a range guaranteeing that the droplets react on the gas flow in about the same way as in a combustor, Hassa et al. (1990).

Fig. 3 shows a perspective view on a recontructed hologram of the dispersion process of the 44 µm-droplets. There, two different dispersion regimes were identified: the acceleration regime, characterized by drops staying together in chains, and the regime, where the drops reach the mean gas velocity and disperse in clouds, Blümcke et al (1988).
An overall impression of the mean disper-

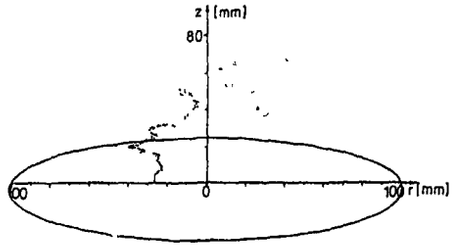

Fig. 3: Snapshot of the drop dispersion after the point source located off-axis: Perspective view of a reconstructed hologram

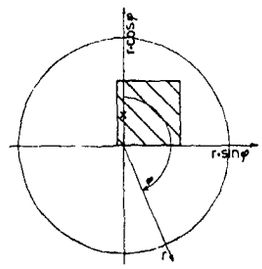

Fig. 4: Position of the cartesian sector where drop quantities are shown
x - Position of the drop ejection

sion process of 44 µm diameter droplets gives Fig. 5, where calculated number flux

[kHz/mm²]

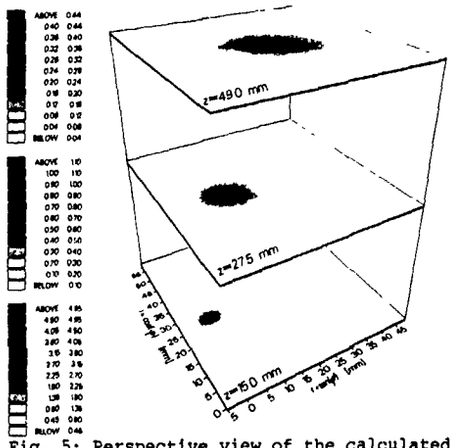

Fig. 5: Perspective view of the calculated flux density distribution of the 44 µm-drops in 3 cross-sections (attention: scale splits !)

density distributions over three successive cross-sections of the experimental facility are shown. In order to resolve graphically the threedimensional dispersion in the radial-tangential plane, only a rectangular sector of the whole plane is sketched, as indicated in Fig. 4.
Under the action of gas turbulence, the

droplets disperse more and more, while they are highly accelerated by the mean gas flow field. As can be seen in more detail in Fig. 6b, there exists a preference for the dispersion in the circumferential direction, which cannot be seen in the measurements, Fig. 6a. These discrepancies lead to the structure of the relative error of the number flux density as is exemplary shown in Fig. 6c. The relative error of the number flux density accumulates to 80% in the measurement plane z = 49.0 mm.

a: Measured flux density distribution

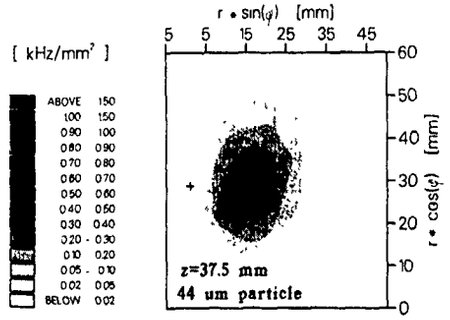

b: Calculated flux density distribution

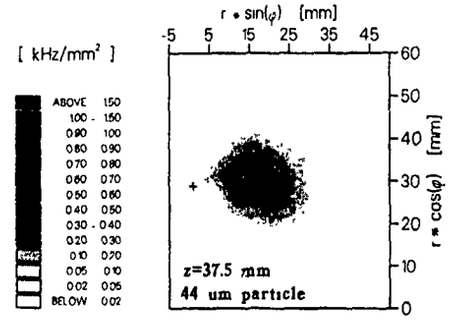

c: Relative error of the calculated flux density

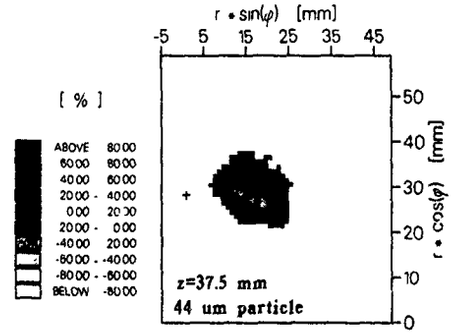

Fig. 6: Comparison between the measured and the calculated flux density of the 44 µm-drops at z = 37.5 mm

The analysis of the comparison between measured and calculated mean particle velocities at a height z = 37,5 mm, Fig. 7 I and Fig. 7 II, resp., reveals the reasons for this behaviour of the numerical simulations. In the measurements there can be seen a quite different gradation of the mean velocity distributions of the three components, resulting mainly from the history of individual droplet trajectories, i.e. from inertia effects. Only in the radial velocity component the gradation qualitatively resembles that of the underlying gas flow, while there is a very smooth distribution of the axial velocity component, contrary to the results of the simulation. This latter fact is primarily due to the differences observed in the radial component: The dispersion model doesn't reproduce the range of the radial velocities of the droplets (from -8 m/s up to 10 m/s) on the base of the measurements of the gas flow - where in the region under consideration only positive radial velocities exist - under the assumption of Gaussian probability density distributions of the velocity components.

Some deviations from the Gaussian shape of the PDF were observed in the experiment in the radial velocity component combined with a high degree of anisotropy of the Reynolds normal stresses, Hassa (1991): The radial normal stress component dominates the two other components in the shear layer.

The measured radial velocity distribution of the droplets causes an extensive exchange in the radial direction. Because of the inertia of the droplets, this increased exchange results in a smooth distribution of the mean axial velocity component as well as in a high turbulence intensity of that component. Additionally the steep gradients of the underlying mean gas flow amplify the differences between measurement and simulation in the tangential velocity distribution. Therefore it can be concluded that the wrong prediction of the radial velocity component of the droplets is the main reason for the discrepancies observed in the calculated drop dispersion.

In order to investigate the influence of the shape of the gas PDF on the dispersion process calculations were performed which were based on extremly bimodal probability density distributions of the radial gas velocity component, also simulating the increased level of the radial normal stress. Thereby, it could be proved that the shape of the PDF can determine the flux distribution via the radial velocity distribution.

These calculations show, that the dispersion model can treat more information than the k-ε -turbulence model of the gas phase delivers. "Large-Eddy-Simulations" yielding information about the shape of the gas PDF's might be a remedy here.

Another difficulty in the calculations arises from the uncertainty concerning the used empirical correlations for the determination of the Lagrangian integral time and length scales. These uncertainties are mainly reflected in the differences between calculated and measured variances of the droplet velocity distributions.

The analysis of the measurements of the smaller droplets delivers no additional information related to the quality of the

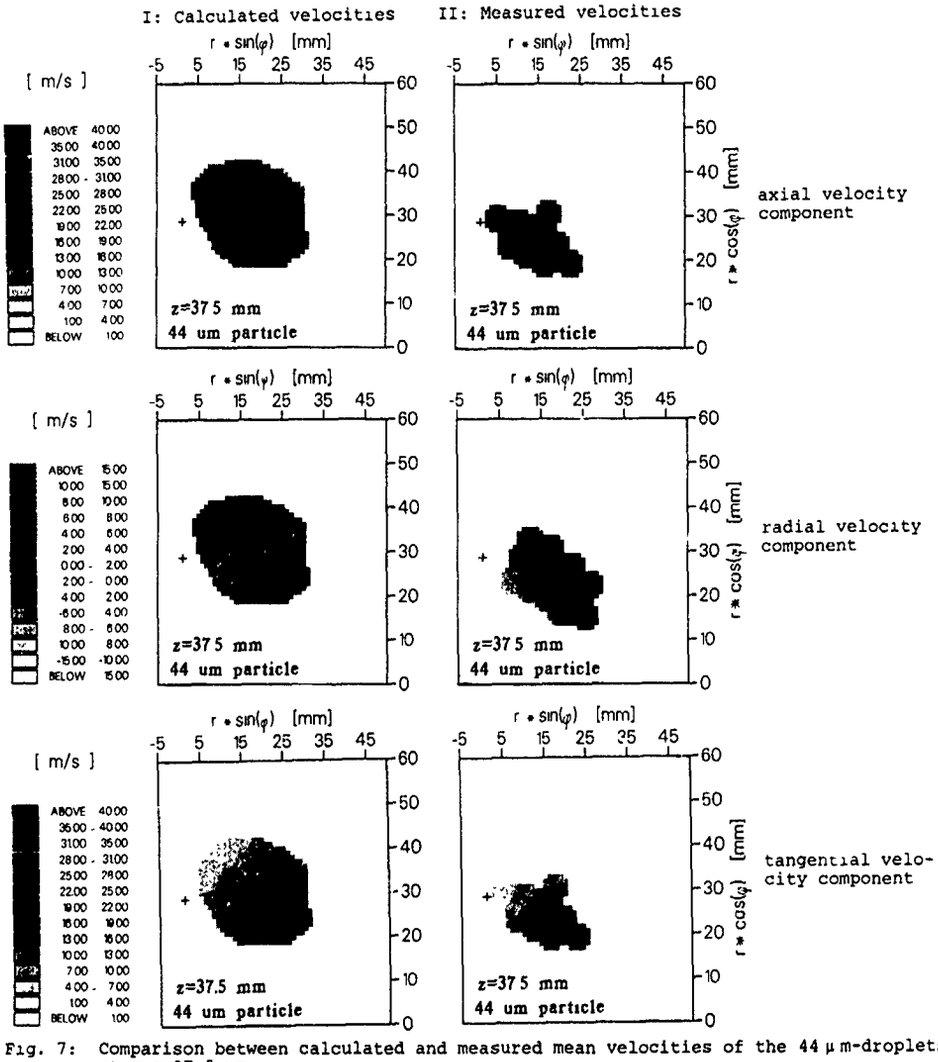

Fig. 7: Comparison between calculated and measured mean velocities of the 44 µm-droplets at z = 37.5 mm

presented dispersion model, emphasizing the fact, that the influence of particle relaxation time is correctly reproduced by the dispersion model. For more information the reader is referred either to Hassa (1991) or Blümcke (1991).

Instationary dispersion characteristics

Another interesting feature of the dispersion process, which is important for mixing processes in two-phase flows, is the existence of droplet clusters, moving through the model combustor. Similar effects were also observed in plain-jet atomizers, Faragó&Chigier (1990).
This transport phenomenon, which is apparent in the snapshot of the dispersion, Fig.3, can be modelled assuming that neighbouring drops experience correlated gas velocity fluctuations, as far as they can be described by the macroscopic properties of stochastic turbulence. The aim of the "Multiple-Particle-Option" (MPO) is realized as follows:

1. All particles are handled simultaneously.
2. Starting form a randomly sampled droplet, called "leading" drop, the MPO recognizes neighbouring droplets found in the correlation domain of the "leading" drop and assignes individual filter output sequences to them. These are correlated because they are based on the same starting index and increment on the vector of filter input signals as the "leading" drop. The only difference is caused by the individual positions of the particles.
Thus, the drops are subdivided in groups, respectively exhibiting a similar dispersion behaviour.

3. The individual droplet remains in that cluster as long as it stays in its own correlation domain. If the droplet has left its correlation domain, the MPO searches another correlation domain of a "leading" drop, to which the droplet can be assigned. If there is no such correlation domain, the droplet itself becomes "leading" drop with its own start index and increment on the vector of filter input signals.

Fig. 8a shows a typical arrival time statistics plot, measured at the position of the maximum number flux density at z = 10.0 mm. The character of the droplet chain observed in the first dispersion regime, is responsible for the high probability of short arrival times as well as for a higher probability of long arrival times, compared to the arrival time statistics of a homogeneous mixture of droplets in a laminar flow (Poisson statistics).

a: Experimental result

b: Simulation without MPO

c: Simulation with MPO

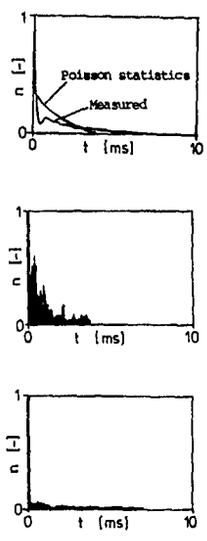

Fig. 8: Arrival time statistics of the 44 µm-droplets at z = 10.0 mm, at a radius of 27.0 mm and an angle of 0^0 relative to the droplet ejection point: Comparison of results of the experiment and of simulations

The result of the presented spectral dispersion model without MPO is illustrated in Fig. 8b: The trend of this arrival time statistics plot resembles qualitatively the Poisson statistics. The situation changes for the calculated arrival time statistics using the "Multiple-Particle-Option", Fig. 8c: As was seen in the measurements, there is a high probability for short arrival times, accounting for the fact, that neighbouring drops stay together.
In the measurements this fact, which might have a strong impact on drop vaporization, was observed over the whole flow field.

Conclusions

It could be shown that the model experiment is suitable for the quantitative evaluation of dispersion models.

A theoretical model for the description of liquid phase transport processes in turbulent swirling flows was developed.

The analysis of the deviations of measured from calculated data for the dispersion process in the model experiment emphasizes the importance of the correct description of gas phase turbulence properties in the vicinity of the nozzle. Instationary dispersion characteristics were numerically simulated proving the fact that the dispersion of droplet clusters is effected by the macroscopic stochastic gas turbulence.

References

Blumcke,E.; Eickhoff,H.; Hassa,C.: "Dispersion of monosized droplets in a turbulent swirling flow", Proc. 4th Int. C. on Liquid Atomization and Spray Systems, 1988

Blümcke,E.; Eickhoff,H.; Hassa,C.: "Evaluation of a spectral dispersion model with exp. results ..", Proc. 5th Int. Workshop on Two-Phase Flow Predictions, 1990

Blümcke,E.: "Turbulente Partikeldispersion in eingeschlossenen Drallströmungen", PhD University of Bochum, Germany, to be published in 1991

Burrus,D.L.: "Appl. of numerical models for predictions of turbine engine combustor performance", ASME 89-GT.251, 1989

Desjonquères,P.J.: "Modélisation Lagrangiense du comportement de particules discrètes en ecoulement turbulent", PhD University of Rouen, France, 1987

Farago,Z.; Chigier,N.: "Parametric experiments on coaxial airblast jet atomization", ASME 90-GT-91, 1990

Hassa,C.; Blümcke,E.; Eickhoff,H.; Racnner,M.: " The influence of a radial swirl generator on the flow field from a fuel nozzle model", Proc. 4th Int. S. on Appl. of Laser Tech. to F. Mech., 1990

Hassa,C.; Blümcke,E.; Eickhoff,H.: "Measurements of Eulerian macro timescales in highly swirling flows and comparison with a computational model", Proc. 5th Int. S. on Appl. of L. Tech. to F. Mech., 1990

Hassa,C.:"Experimentelle Untersuchungen der turbulenten Partikeldispersion in Drallströmungen", PhD University of Bochum, Germany, to be published in 1991

Hinze,J.O.: "Turbulence", McGraw-Hill, 1975

Olivari,D.; Benocchi,C.: "Modelling of scalar transport in turbulent shear flows with a spectral manipulation technique", Proc. 6th S. on Turbulent Shear Flows, 1987

Saffman,M.: "Automatic calibration of LDA measurement volume size", Applied Optics, Vol. 27, No. 13, 1987

Snyder,W.H.; Lumley,J.L.: "Some measurements of particle velocity autocorrelation functions in a turbulent flow", J. Fluid Mech., Vol. 48, No. 1, 1971

EIGHTH SYMPOSIUM ON
TURBULENT SHEAR FLOWS
Technical University of Munich
September 9-11, 1991

MEASUREMENT OF WALL SHEAR RATE IN LARGE AMPLITUDE UNSTEADY REVERSING FLOWS

ZHUOXIONG MAO AND THOMAS J HANRATTY

UNIVERSITY OF ILLINOIS, URBANA, ILLINOIS, 61801, U S.A

ABSTRACT

This paper shows how electrochemical probes can be used to measure the wall shear stress for unsteady flows - even when the oscillations are large enough to cause temporary flow reversal at the wall New experimental results are presented for turbulent flows with and without imposed sinusoidal flow oscillations Of particular interest is the finding that large amplitude flow oscillations can cause a decrease in the time - averaged drag

INTRODUCTION

Small mass transfer probes, mounted flush to a wall over which a fluid is flowing, have been used for many years to measure the wall shear stress in flow systems. A chemical reaction is carried out on the surface of an electrode under conditions for which the reaction rate is fast enough that the concentration of the reacting species is zero at the surface and the electrochemical process is controlled by the rate of mass transfer, N, to the test electrode A solution of the mass balance equation for steady flow conditions shows that the measured electric current is proportional to the one third power of the wall shear rate, S.

The sampling volume is the concentration boundary-layer over the electrode, δ_c. Because of the large Schmidt number characterizing the process and the small size of the probe, δ_c is typically 0 003 - 0 02 mm. As a consequence, the electrochemical probe is capable of measuring flow closer to a boundary than any other known technique. However, its use has been mainly limited to forward moving flows with small amplitude oscillations. This paper describes a new method that has been developed to apply this technique to situations in which large amplitude oscillations exist and in which the flow is changing direction at the wall

The present practice in using wall probes in unsteady flows is to apply a pseudo-state approximation whereby the relation between the mass transfer rate and the velocity gradient developed for steady flow is applied to an unsteady flow. If oscillations of small amplitude are imposed on a mean flow, a linearized form of the mass balance equation can be used to correct for frequency response.

Mao and Hanratty (1991a, b) developed an inverse mass transfer method which recovers shear rate variations from measured mass transfer signals from a single electrode. This can be used in reversing flows if additional information on the flow direction is given They suggested that two rectangular electrodes in a sandwich arrangement, as reported by Son & Hanratty (1969) and by Py (1973), can be used to provide information about flow direction. However, this idea could not be implemented because the frequency response of the sandwich probe was not understood, especially in large amplitude unsteady flows. Consequently, the inverse mass transfer method has been used to determine the response of the sandwich probe to an imposed sinusoidal flow variation with an amplitude that is large enough to create temporary flow reversal In practice, the insulation layer between the two rectangular electrodes cannot be made negligibly thin Therefore, an important aspect of the calculation is the determination of the effect of insulation thickness on the behavior of the sandwich probe.

THEORETICAL ANALYSIS

The behavior of a wall shear stress probe can be calculated from the mass balance equation

$$\frac{\partial C}{\partial t} + Sy \frac{\partial C}{\partial x} = D \frac{\partial^2 C}{\partial y^2} \qquad (1)$$

where S is the velocity gradient at the wall This is solved for the boundary conditions that $C = C_b$ at large y and that $C = 0$ at $y = 0$.

The solution of (1) for a steady flow is given as

$$\frac{KL}{D} = 0.807 \left(\frac{\ddot{S} L^2}{D} \right)^{1/3} \qquad (2)$$

where L is the electrode length and K is the mass transfer coefficient Finite difference methods can be used to calculate from (1) the time - varying mass transfer coefficient, K(t), from the time - varying velocity gradient at the wall, S(t). Of course what needs to be solved is the inverse problem: K(t) is known and S(t) is to be calculated.

Mao & Hanratty (1991a) have recently developed such an inverse analysis Suppose, that at time t, the velocity gradient S(t) and the concentration field are known The velocity gradient at $t+t\Delta t$ is assumed. Equation (1) is used to calculate, by finite - deference methods, the concentration field and the mass transfer coefficient at $t+\Delta t$. If this calculated mass transfer coefficient agrees with the measurement the assumption is correct; if not, a new assumption is explored

This approach has been successfully employed in turbulent flows (Mao & Hanratty, 1991b) without flow reversals. In these studies data are digitized at 25,600 points so considerable computer time is needed to solve equation (1) by trial and error techniques at each of these points. In order to study reversing flows equation (1) is solved for the case of two rectangular electrodes separated by a layer of insulation about one-half the thickness of the electrodes.

EXPERIMENTS

Experiments were carried out in a 5 cm pipe. An aqueous solution, 0.1 M in K1 and 2×10^{-3}M in I_2, was circulated The test section was made of plexiglas In the turbulence studies without imposed oscillations, a platinum

wire, 0 0127 cm in diameter, was inserted into the test section and polished flush with the wall It served as the cathode in an electrolysis cell and a stainless steel pipeline with much larger area served as an anode The test electrode was controlled at a high enough voltage that the reaction was mass transfer controlled The current flowing in the electrolysis circuit is then proportional to the mass transfer coefficient. For the conditions studied the diameter of the electrode made dimensionless with wall parameters was less than 5, so no spatial averaging of the velocity fluctuations occurred

For experiments with large amplitude flow oscillations a sandwich probe was used It was made from two pieces of 0.0102 cm thick platinum sheet. The actual dimensions of each of the electrodes was 0 011 x 0 093 cm The thickness of insulation between them was 0.0024 cm

RESULTS

Figure 1a shows a signal representative of the measured variation the velocity gradient, S(t) in a turbulent flow. Figure 1b shows the dimensionless mass transfer coefficient obtained from the results in figure 1a by a direct finite difference solution of (1) Figure 1c shows values of S(t) calculated from K(t) shown in figure 1b by using inverse mass transfer calculations The ability of these methods to analyze a randomly varying signal is demonstrated by the equivalence of the tracings figures 1a and 1c.

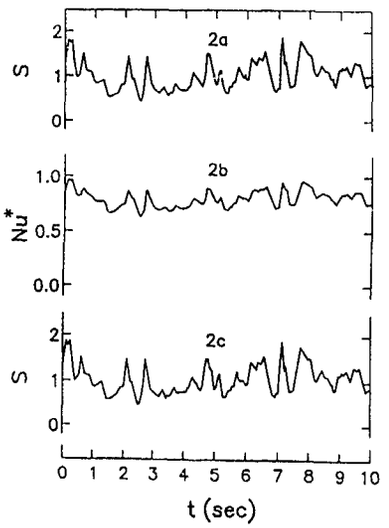

Fig. 1a. Input of velocity gradient variation

Fig 1b Prediction Nu^* using Fig. 2a as in the input of velocity gradient variation

Fig. 1c Estimated S using Fig 2b as input for the inverse mass transfer problem

The analysis of the random signals obtained from laboratory measurements revealed small but significant differences from results obtained by using linear theory to correct for frequency response The root-mean-square (made dimensionless with the time - average velocity gradient), the skewness and the flatness of the fluctuating wall shear stress were found to be 0 39, 0 96 and 4 2 A measured frequency spectrum is shown in figure 2

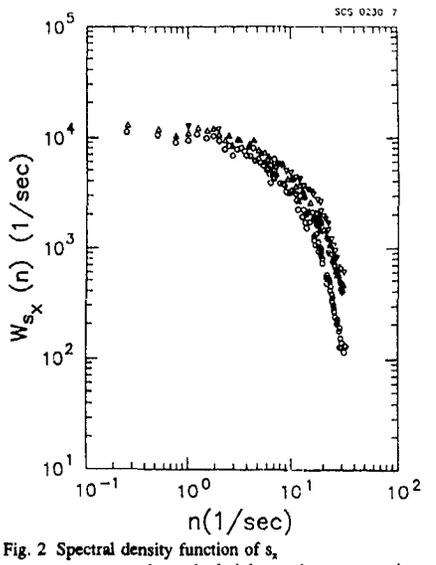

Fig. 2 Spectral density function of s_x
o quasi-steady method, Δ linear theory correction,
∇ inverse method
(Re = 29270, sampling frequency, 64 Hz)

Figure 3a shows the dimensionless time - varying wall velocity gradient for a case in which a large amplitude oscillation was imposed on a flow The Reynolds number was 10,610. The dimensionless circular frequency was ω^+ = 0 0506 It is noted that negative values of the velocity gradient at the wall were measured.

The phase - average of a large number of cycles gave the results shown in figure 3b. The time average of this gives $\overline{S}$ = 0.89. This indicates an 11 per cent drag - reduction since S was made dimensionless with the time - average of the velocity gradient with no oscillations.

Figure 3(c) gives the root-mean-square of the fluctuations of the phase average This indicate peaks near locations where <S> is going through zero These results could be real, but a more likely explanation is errors in the iteration procedure in this region. These errors could be avoided but a larger number of iterations and considerably more computer time would be required.

Because of the importance of the discovery of drag - reduction, numerical experiments were carried out to determine whether this result was associated with errors in the iteration procedure. A turbulent fluctuating signal such as shown in figure 1a was added to a signal given by S = 1 + 2 cos ωt. The combined signal has flow reversals of the type shown in figure 3a and a time - average of 1.0.

This combined signal was used to calculate a time - varying mass transfer rate by a direct numerical solution of (1) The inverse technique was then used to analyze this K(t). The phase average of the results are shown in figure 4. The calculated intensities in 4b show the same type peaks at flow

reversals that were obtained by analyzing the laboratory measurements However the phase average is approximated by $S = 1 + 2 \cos \omega t$ so that $\overline{S} = 1.0$ This suggests that the drag - reduction observed for turbulent flows with imposed large amplitude, sinusoidal variations is real

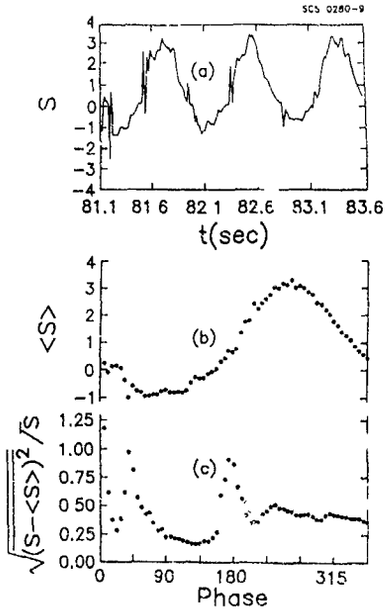

Fig 3 A turbulent flow with large imposed oscillations. Re = 10,600, $\omega^+ = 0.0506$,

$$I_{u_c} / \overline{u}_c = 0.377,\ \overline{S} = 0.89,\ \left(\overline{s^2}\right)^{1/2} / \overline{S} = 0.41$$

Other tests have been performed with large amplitude imposed non-sinusoidal (saw-tooth) oscillations Under certain conditions these show drag - reductions of the order of 5 to 10 per center, even when flow reversals at the wall were not observed. These seem to be associated with sharp drops in the phase - averaged velocity gradient during periods of unfavorable pressure gradient and a slow relaxation during periods of favorable pressure gradient

Acknowledgement :- This work was supported by the National Science Foundation under Grant CBT 88-00980 and by the Office of Naval Research under Grant N00014-82 K0324, and by the National Science Foundation of China

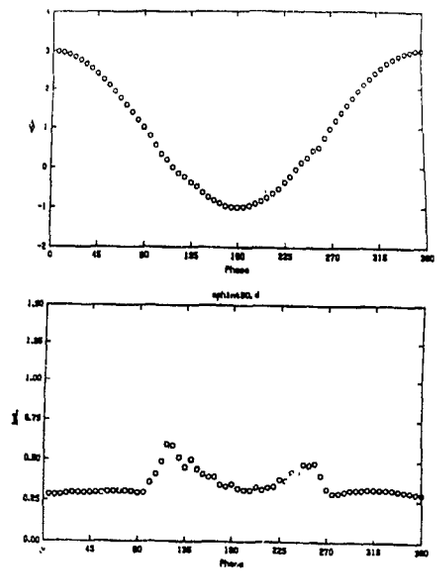

Fig 4 Numerical experiments with a signal given by $S = 1 + 2 \cos \omega t$ + turbulence. Results gives $\overline{S} = 0.997$ and $\left(\overline{s^2}\right)^{1/2} / \overline{S} = 0.363$

REFERENCES

(1) Mao, Z. and T. J. Hanratty 1990a "Analysis of wall shear stress probes in large amplitude unsteady flows", *Int J Heat Mass Transfer*, 34, 281-290.

(2) Mao, Z., and T J Hanratty 1991b "Application of an inverse mass transfer method to the measurement of turbulent fluctuations in the velocity gradient at the wall", To be published in *Experiments in Fluids*

(3) Son, J S., and T. J Hanratty (1969) "Velocity gradients at the wall for flow around a cylinder at Reynolds numbers from 5×10^3 to 10^5", *J Fluid Mech*, 35, 353-368

(4) Py, B. 1973 "Etude tridimensionnelle de la sous couche visqueuse dans une veine rectangulaire par des measures de transfert en paroi", *Int. J Heat Mass Transfer*, 15, 129-144.

EIGHTH SYMPOSIUM ON
TURBULENT SHEAR FLOWS
Technical University of Munich
September 9-11, 1991

WALL SHEAR-STRESS MEASUREMENTS IN UNSTEADY TURBULENT FLOWS IN DIVERGING CHANNELS

R.D. Maestri, S. Tardu, G. Binder

Institut de Mécanique de Grenoble
B.P. 53 X 38041 Grenoble Cédex-FRANCE

ABSTRACT

Wall shear stress (WSS) measurements in pulsating flows in diverging channels are reported. The total divergence angles were 2.4° and 6°. The velocity oscillations at the diffuser entrance had amplitudes of 20 and 40% and frequencies ranging from ω^+=0.0015 to 0.04. It is found that the time-mean WSS value and WSS turbulent intensity are increased by forced oscillations. The oscillations of WSS are smaller and the modulation of the turbulent intensity of the WSS are larger than in constant area unsteady channel flows in similar forcing conditions. These effects increase with the divergence angle of the channel.

NOMENCLATURE

h(x) = half height

τ = wall shear stress u_τ=shear velocity

l_s=viscous Stokes length ; frequency parameter

$l_s^+ = l_s u_\tau/\nu$ $\omega^+ = 2/(l_s^+)^2$

$\tau = \bar{\tau}+\tilde{\tau}+\tau'$: triple decomposition of τ into time mean, periodic and turbulent parts $\langle\tau\rangle = \bar{\tau}+\tilde{\tau}$ phase average of τ

$\langle\tau'\tau'\rangle = \overline{\tau'\tau'}+\widetilde{\tau'\tau'}$ phase average of $\tau'\tau'$

$A_{\tilde{\tau}}$, $A_{\widetilde{\tau'\tau'}}$, $\Phi_{\tilde{\tau}}$, $\Phi_{\widetilde{\tau'\tau'}}$ amplitudes and phases of the fundamental modes of $\tilde{\tau}$ and $\widetilde{\tau'\tau'}$

$a_{\tilde{\tau}} = A_{\tilde{\tau}}/\bar{\tau}$ and $a_{\widetilde{\tau'\tau'}} = A_{\widetilde{\tau'\tau'}}/\overline{\tau'\tau'}$ relatives amplitudes

$\bar{\tau}_{unst}/\bar{\tau}_{st}$ ratio of $\bar{\tau}$ measured in unsteady and steady flow for the same time mean inlet conditions

INTRODUCTION

The aim of this investigation is to determine to which extend time mean adverse pressure gradients affect the features of unsteady turbulent wall flows. In previous adverse pressure gradient experiments (SCHACHENMANN & ROCKELL (1976), COUSTEIX, HOUDEVILLE & JAVELLE (1977), MENENDEZ & RAMAPRIAN (1983), SIMPSON, CHEN & SHIVAPRASAD (1983), BREKENTON, REYNOLDS & JAYARAMAN(1990)) only a few different cases could be explored so that, despite their interest, it is not possible to infer some general trends in unsteady flow features from these data. Such a picture could only emerge from a set of data covering a significant range of the flow parameters.The purpose of the present work is to attempt to obtain such a general --although in no sense complete-- picture of this flow family. A major difficulty for systematic measurements is the complexity of these flows since, besides the Reynolds number, they depend upon four additional parameters, namely the amplitude and the frequency of the imposed oscillations (when the unsteadiness is periodic), the pressure gradient and its streamwise variations. Divergence angles θ =2.4° and 6° were selected in order to have a mild and a steep adverse pressure gradient, not too steep, however, so as to avoid separation in the channel.

APPARATUS

The flow facility is the same as the one described in TARDU (1988) except for the test section which in the present experiments was diverging. After the first 1.6m of the channel the wall can be inclined with respect to the channel axis. The 1m long test section (≈ 20 h_0) can thus be transformed in a diffuser with a total divergence angle that can be set at any value between 0° and 40°.

MEASUREMENT TECHNIQUES

The velocities were measured with LDA or with hot film probes (BINDER et al 1985). The former was used for mean velocity measurements while the latter were used for the determination of the oscillating flow characteristics on the channel axis. The wall shear-stress was measured with flush mounted hot-film gages at four different stations along the test section (see Table 1).

The calibration procedure consists in determining the relationship between the centreline velocity U_c and the wall shear stress τ from the measurement of $\partial u/\partial y$ near the wall with the LDA (Fig 1). With the τ vs. U_c relationship the wall hot film gage (WHFG) calibration curve E vs. τ (Fig 2) has then obtained (or E vs. U_c).

Because of the low velocities near the wall the sensitivity of the WHFG is poor especially in comparison to the offset caused by parasitic non-convective heat losses. The reproducibility of the measurements is about ± 7%. The maximum error on τ is estimated to be at most 15%. Data acquisition and phase averaging were made on an PC computer equipped with an A/D board (12 bit accuracy).

EXPERIMENTAL CONDITIONS

1.The steady flow conditions.

The time-mean entrance conditions for all flows investigated were, $U_{c\,0} \cong 17{,}5$ cm/s and $Re_{h\,0} \cong 8\,750$. The pressure gradient $(PG)_{MB}$ was determined from the momentum balance. The values are given in Table 1 where they are non-dimensionalised by δ^* and $(1/2)\rho U_C^2$ and multiplied by 10^3. The values of $(PG)_{Uc}$ have simply been computed by assuming $dp/dx = - U_c\, d(U_c)/dx$. The real pressure gradient is about three times smaller than the one computed by assuming potential flow with uniform velocity profiles in the diverging channel.

The decrease of the friction coefficient (multiplied by 10^3 in Table 1) and increase of the Clauser parameter $\beta=\delta^*/\tau\,(\partial p/\partial x)$ with downstream distance show that the flow encounters increasing more adverse conditions and approaches separation.

Stat.	h_{mm}	δ^*_{mm}	θ	β	C_f	$(PG)_{Uc}$	$(PG)_{MB}$
S1	59	9.04	6.27	3.4	3.23	5.7	3.5
S2	74	13.1	8.91	4.9	2.80	6.7	4.4
S3	83	19.7	11.3	6.4	2.34	7.4	5.0
S4	99	23.6	15.0	12.7	1.13	8.3	6.0

TABLE 1 Flow parameters θ=6°.

2 - Oscillating flow conditions.

Oscillations with three different amplitudes and six frequencies were imposed on the mean flow. The three nominal amplitudes at the entrance were : 10, 20 and 40%. The six forcing periods were : 2.7; 4; 8; 16; 32; 60s.

The corresponding values of the l_s^+ parameter $l_s^+ = (u_\tau/\nu)\sqrt{2\nu/\omega}$ at the entrance were: $(l_s^+)_0 = 7; 9; 13; 18; 27; 36$.

The mean flow rate and hence the mean entrance conditions to the diffuser were always the same **in steady flow**. The eccentricity of the driving mechanism of the pulsator was adjusted so as to produce either ±10, ±20 or ±40% ($(a_{uc})_0$) velocity variations with respect to the mean in the **quasi-steady regime** ($(a_{uc})_0$ = **nominal amplitudes** at diffuser entrance). The actual amplitudes at the entrance dependent somewhat upon the forcing frequency and on the geometry. For a given nominal amplitude all the geometrical parameters were kept constant and only the frequency of oscillation was changed. This does insure neither an invariable time-mean flow nor an invariable oscillating flow when the frequency is changed. The changes in the mean flow rate were, however, quite small since the headloss through the diffusor is small compared to the total headloss. This way of proceeding is, of course, not ideal, but for this study it seemed more important to cover a wide frequency range than to maintain the amplitude strictly constant.

The amplitude and phase of u_c(as of any other quantity) are obtained from Fourier analysis of the phase averaged velocity $\langle u_C \rangle$ (see TARDU 1988). "Amplitude" and "phase" will hereafter be used to designate the parameters of the fundamental mode. The actual amplitudes are, smaller than the nominal values which are roughly reduced by the value 0.75 .

RESULTS

The results at different stations are plotted versus the local value of l_s^+ (or versus $\omega^+=1/(l_s^+)^2$) since it was shown in TARDU (1988) that this is the correct similarity parameter for the near wall flows in particular for τ in the case of parallel wall channel flow. It is recalled that l_s^+ varies with u_τ which varies with X position.

1 - Time-mean properties

TIME-MEAN WALL SHEAR-STRESS

The ratio of τ in unsteady flow with respect to the steady steady value is plotted on Fig. 3. The most striking feature of these figures is the large increase of the ratio in both geometries in the high amplitude and high frequency forcing regime. In the 6° diffuser the ratio reaches the value two. Worth noting is that the highest ratios are reached at the most downstream station where the pressure gradient is the largest. These results are highlighted by the fact that this ratio remains equal to one in the constant area channel .

There is, of course, some scatter in the data, but even the pessimistic estimate of 15% error quoted earlier can certainly not account for the measured increase in τ in the flows forced at 40% in the diverging channels.

BRERENTON, REYNOLDS & JAYARAMAN (1990) also found an increase in $\overline{\tau}$ in unsteady flow. This increase is about 8% in their case for an amplitude $a_{Uo} \cong 15\%$ in a pressure gradient equivalent to those in the 6° degree diffusor.

TIME-MEAN RMS-VALUE OF THE TURBULENT WALL SHEAR STRESS FLUCTUATIONS

It is first recalled that the ratio $\sqrt{\overline{\tau\tau}}/\bar{\tau}$, from experimental data and direct numerical simulations, in steady turbulent wall flows is about 0.36. It was found by TARDU (1988) that this value is not appreciably modified by forced oscillations in channel flow (i.e. channel with parallel walls; by "channel" we shall hereafter mean channel with parallel walls) even when their amplitude near the wall is so large as to produce periodic flow reversal.

With the reference level 0.36 drawn on the graph of Fig. 4, it is immediately apparent that the turbulence level of τ in the adverse pressure gradient flows is almost systematically larger than this value. Turbulence levels of 0.6 which represent more than a 50% increase with respect to the standard reference value are actually not uncommon in these flows.

These are not only large increases but very high absolute turbulent intensities. A relative RMS-turbulent intensity of 0.60 implies the existence of frequent instantaneous values larger than one, i.e. of instantaneous flow reversal. Since the hot film rectifies the velocity signal, the present measurements are on the conservative side.

2 - The oscillating flow properties.

THE THE WALL SHEAR-STRESS OSCILLATIONS.

It was shown that the amplitude of the viscous Stokes solution $A_{\tilde{\tau}\ Stokes} = \sqrt{2}\ A_{\tilde{u}c}/l_s$ (see BINDER et al 1985), was a useful reference quantity for the amplitude the wall shear stress oscillations in the channel flow since it does involve the centreline amplitude (in all rigour this should be the amplitude at infinity) and a frequency dependence. The same scaling is adopted here. The mean curve from the channel experiments is the solid line drawn on Fig. 5. It is seen that in the 2.4° diffusor (Fig.5 a) the variations of the amplitude ratio with l_s^+ is roughly the same as in the constant area channel : at high frequencies the values are of order one and at lower frequencies the values increase with l_s^+ due to the progressively larger effect of the turbulence on the oscillating wall shear-stress. The amplitude ratio in this geometry is, however, systematically larger than in the channel. There is no explanation for the fairly large scatter of data points at the present time.

The amplitude behaviour in 6° diffusor displayed on Fig.5b contrasts sharply with that of the previous figure. The amplitude ratios are almost systematically smaller than one, values of order 0.8 may be explained by destructive interference of the shear wave with the strongly damped wave reflected by the buffer-layer where the effective viscosity suddenly increases, but for values of order 0.2 , the same reasoning would require that the shear wave suffers nearly no damping which is rather unlikely. Quite a different mechanism should, therefore, be operating.

The increase of the ratio with l_s^+ when $l_s^+ > 15$ does no longer seem to occur. This statement is only conditional because the l_s^+ values in the wide angle diffusor are smaller than in the small angle diffusor owing to the smaller values of u_τ. In any case, it is clear that under the same forcing conditions the wall shear stress oscillations are considerably smaller in strong mean adverse pressure gradients than in a mild or favourable pressure gradient.

The phase shift of τ with respect to the phase of the centerline velocity are shown on Fig. 6. The full line is again a schematic representation of the channel data. It is recalled that in this case the phase shift data is remarkably well correlated by the l_s^+ parameter. As for the amplitude, it is seen that measurements from the 2.4 ° diffusor follow the same trend as those from the channel with notably larger values, however, at high frequencies and larger values at low frequencies when $l_s^+ \geq 20$.

The first impression from the phase-shift results of the 6 ° diffusor (Fig.6b) is the large scatter among the data points. There are large differences from one station to the other and in some instances also from one frequency to the next at the same station. One part of this scatter is certainly due to experimental uncertainties which are compounded by the added effects of two factors: firstly the relatively small value of the maximum phase shift of τ which is only 1/8 or 1/6 of the cycle and, secondly, the small amplitudes of τ in this geometry which slows down the statistical convergence of $\langle\tau\rangle$, the much the more so that the turbulent intensity is high as observed earlier . Despite these irregularities it is possible to guess a general trend when following the points corresponding to the same measuring station : at small l_s^+ values the phase shift is only about 20 to 30 °, it increases with l_s^+, reaches a maximum value between 45 and 60 ° when $l_s^+ =$ 15 to 25 and finally decreases to zero as may be expected. From the amplitude as well as the phase shift data it is also quite clear that a strong adverse pressure gradient has a large effect on the oscillating wall shear stress.

MODULATION OF THE TURBULENT WALL SHEAR STRESS FLUCTUATION INTENSITY

The modulation $\widetilde{\tau'\tau'}$ of the phase averaged wall shear stress intensity is defined by : $\widetilde{\tau'\tau'} = \langle\tau'\tau'\rangle - \overline{\tau'\tau'}$ where $\langle\tau'\tau'\rangle = \langle\tau^2\rangle - (\langle\tau\rangle)^2$. $\widetilde{\tau'\tau'}$ is also the response of the turbulence to the forcing. Since the turbulent intensity is driven by the shear via the production and since the shear scales with wall shear stress, $\tau'\tau'$ may be considered as the result of the τ-oscillation. The ratio of relative amplitudes $a_{\widetilde{\tau'\tau'}}/a_{\widetilde{\tau}}$ may then be interpreted us the response function of the turbulent wall shear stress fluctuations to the periodic forcing. If the system were linear, this ratio would be independent of forcing amplitude. It should be stressed that this ratio involves four independent quantities.

The results are presented versus ω^+ on Fig. 7 ($\omega^+=2/l_s^{+2}$). Again, the full line is a schematic indication of the channel flow results.

Two features are immediately apparent on these figures. Firstly, the turbulence response in the diverging channels follows the same trend as in channel with parallel walls, in particular the amplitude ratio $a_{\widetilde{\tau'\tau'}} / a_{\widetilde{\tau}}$ starts decreasing when $\omega^+ \sim 0.005$ and stays at a roughly constant low level. It is also confirmed in a variety of situations that the turbulence modulation decreases with increasing frequency once $\omega^+ > \sim 0.005$. Secondly, the ratio $a_{\widetilde{\tau'\tau'}} / a_{\widetilde{\tau}}$ is systematically higher in the diverging ducts than in the channel. The increase of the turbulence response is particularly large in the 6 ° diffusor, nearly a factor two with $(a_{\widetilde{uc}})_0 = 10\%$. It is seen recalled that in the quasi-steady linear approximation limit (TARDU 1988): $a_{\widetilde{\tau'\tau'}}/a_{\widetilde{\tau}} = 2$. It is seen that values of this order are reached in the 6 ° diffusor. From the quasi-steady linear approximation limit, saturation effects have to be expected at large forcing amplitudes, so that $a_{\widetilde{\tau'\tau'}} / a_{\widetilde{\tau}}$ cannot remain independent of amplitude under these conditions.

It is not sure that the ratio $a_{\widetilde{\tau'\tau'}} / a_{\widetilde{\tau}}$ is the best way to account for the effect of the channel divergence on the turbulence modulation since its variations incorporate those of $a_{\widetilde{\tau}}$. It has, in particular, been observed in the previous section that the shear stress oscillation is considerably reduced in the strong adverse pressure gradient. The increase in $a_{\widetilde{\tau'\tau'}} / a_{\widetilde{\tau}}$ in the diffusors as compared to the values in the channel are, therefore, at least partly, if not essentially, due to the changes in the shear stress oscillations.

In order to give another view of the modulation of the turbulent shear stress fluctuations, the data has been reploted on Fig. 8 by normalizing $a_{\widetilde{\tau'\tau'}}$ with the local centerline velocity amplitude $a_{\widetilde{uc}}$. In order to have a feeling for the values of the ratio $a_{\widetilde{\tau'\tau'}} / a_{\widetilde{uc}}$, it should be remembered that in the quasi-steady small amplitude limit in channel flow the value should be 7/2. Values around 4 are, therefore, "normal" in the case of small amplitude forcing. The large scatter among the data points of Fig.8b makes it difficult to draw any definite conclusions.

The decrease of $a_{\widetilde{\tau'\tau'}} / a_{\widetilde{uc}}$ with increasing frequency is clear for the 2.4 ° diffusor flows but not for the 6 ° diffusor flows because of the scatter especially at the high forcing frequencies. One does, however, observe many values of this ratio around 4 or above - even as large as 6 - which reveal quite strong modulations of the turbulence. Such large values in the case of 40% amplitude forcing are absurd. Indeed $\langle\tau'\tau'\rangle$ is strictly positive so that $a_{\widetilde{\tau'\tau'}} \leq 1$. How is then $a_{\widetilde{\tau'\tau'}} / a_{\widetilde{uc}} \geq 4$ possible when $(a_{\widetilde{uc}})_0 = 0.4$? The answer lies in the fact that the local a_{uc} can be appreciably smaller than $(a_{\widetilde{uc}})_0$. Some particularly large values of $a_{\widetilde{\tau'\tau'}} / a_{\widetilde{uc}}$ may, of course, be due to underevaluations of the centerline amplitude.

CONCLUSION

From the measurements of the wall shear stress in unsteady turbulent flows in diverging channels, it may be concluded that imposed oscillations :

- modify the mean flow at the wall to considerable extend if their amplitude is large and their frequency is high ;
- increase the time mean turbulent intensity by as much as 50% ;
- produce smaller shear stress oscillations than in channels with parallel walls when the adverse pressure gradient is steep and modify their phase shift ;
- produce larger modulations of the turbulent shear stress fluctuations with respect to the centerline velocity oscillations.

These effects are, in general, more important when the adverse pressure gradient is steeper. Since an increase in the wall shear stress and in the turbulent intensity delay separation, these conclusions are in agreement with the observations of airfoil stall retardation by imposed unsteadiness.

ACKNOWLEDGMENTS.

Financial Support of the European Research Office of the US Army under contract DAJA 45-87-0015 is greatfully ackowledged.

REFERENCES

BINDER, G., TARDU, S., BLAKELDER, R.K. & KUENY, J.L. 1985 Large amplitude periodic oscillations in the wall region of a turbulent channel flow. *Proc. Fifth Symposium on Turbulent Shear Flows*, pp. 16.1-16.7. Cornell University, Ithaca, New York.

BRERENTON, G.J., REYNOLDS, W.C. & JAYARAMAN, R. 1990 Reponse of a turbulent boundary layer to sinusoidal free-stream unsteadiness. *J. Fluid Mech.* **221**, 131-159

COUSTEIX, J., HOUDEVILLE, R., JAVELLE, J., 1977 Structure and development of a turbulent boundary layer - effects of periodic free-stream unsteadiness. *J. Fluid Mech.* **131**, 319-340

MENENDEZ, A.N. & RAMPRIAN, B.R., 1983 Study of unsteady turbulent boundary layers, *Report* IIHR **270**, University of Iowa, Iowa City, Iowa.

SCHACHENMANN, A.A. & ROCKELL, D.O., 1976 Oscillating turbulent flow in a conical diffuser. *Trans. ASME I: J. Fluids Engng* **98**, 695-701

SIMPSON, R.L., CHEW, Y.-T. & SHIVAPRASAD, B.G. 1983 The structure of a separating turbulent boundary layer - Effcts of periodic free-stream understeadiness *J. Fluid Mech.* **131**, 319-340

TARDU, S. 1988 Ecoulement Turbulent Instationnaire près d'une paroi: Réponse des Structures Turbulentes. *Thèse* Universit' Joseph Fourier. Grenoble

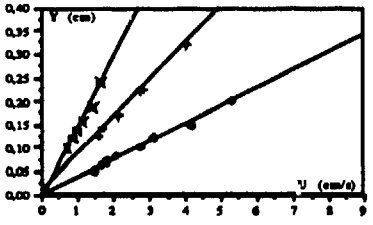

Figure 1: Velocity profiles near the wall in staedy flow (station 4).$(a_{\widetilde{uc}})_0$ = 40% and θ=6°. ⊕ , + and × are maximun, mean and minimum velocity.

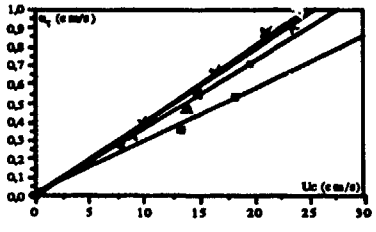

Figure 2:Shear velocity vs centerline velocity θ = 6°. += station 1; × = station 2; Δ= station 3; □ = station 4

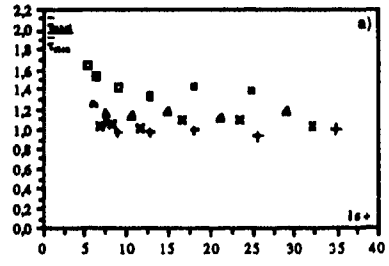

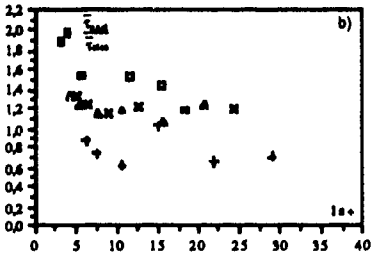

Figure 3: Ratio of unsteady/steady time-mean wall shear stress vs l_s^+, $(a_{\widetilde{uc}})_0$=40%. (a) C=2.4° and (b) θ=6°

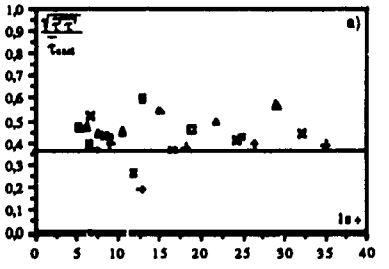

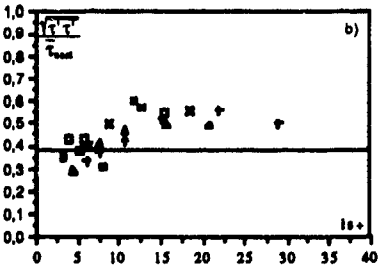

Figure 4: Time mean turbulent intensity of wall shear stress vs l_s^+.
(a) $(a_{\widetilde{uc}})_0$=10% θ=2.4° (b) $(a_{\widetilde{uc}})_0$=40% θ=6°.

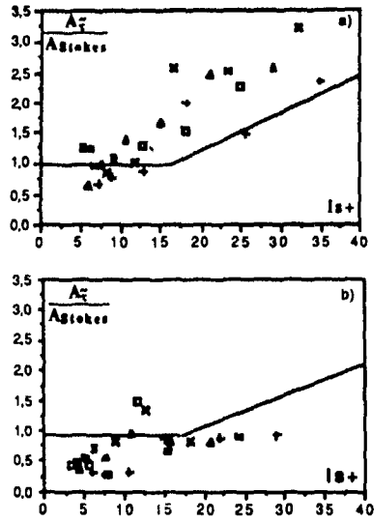

Figure 5: Amplitude of the wall shear-stress with respect to the Stokes value
(a) $(a_{\widetilde{uc}})_0$=10% θ=2.4° (b) $(a_{\widetilde{uc}})_0$=40% θ=6°.

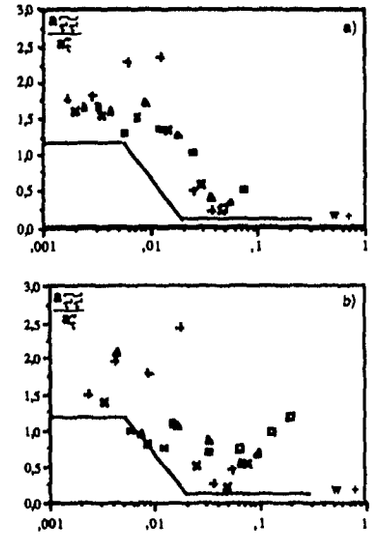

Figure 7 Relative amplitude of the modulation of the turbulent fluctuation intensity referred to the relative amplitude of velocity oscillation in the centerline vs. ω^+.
(a) $a_{\widetilde{uc}}$=10% and θ=2,4° (b) $(a_{\widetilde{uc}})_0$=40% θ=6°

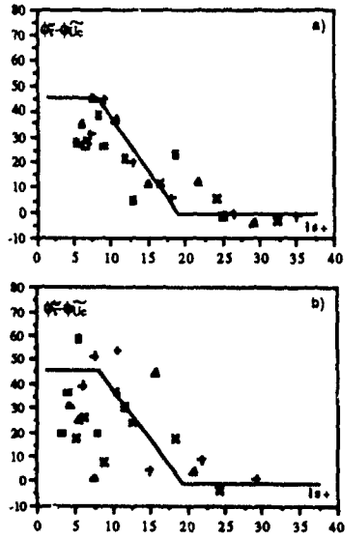

Figure 6:Phase shift of wall shear-stress oscillations with respect to the centerline velocity oscillation
(a)$(a_{\widetilde{uc}})_0$=10% θ=2,4°(b)$(a_{\widetilde{uc}})_0$=40% θ=6°

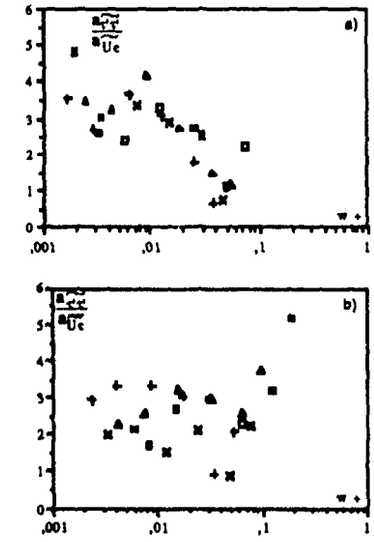

Figure 8: Relative amplitude of turbulent wall shear stress fluctuation modulations refered to relative amplitude of velocity oscillation in the centerline vs ω^+
(a) $a_{\widetilde{uc}}$=10% and θ=2,4° (b) $(a_{\widetilde{uc}})_0$=40% θ=6°

EIGHTH SYMPOSIUM ON
TURBULENT SHEAR FLOWS
Technical University of Munich
September 9-11, 1991

Turbulence in High-Frequency Periodic Fully-Developed Pipe Flow

by

J.-L. Hwang and G. J. Brereton

Dept. of Mechanical Engineering and Applied Mechanics

The University of Michigan

Ann Arbor, Michigan 48109, USA

ABSTRACT

The effects of high frequency organized unsteadiness on wall-bounded turbulence have been studied experimentally at higher frequencies than have been achieved in previous investigations A detailed examination was made of the contention that non-linear resonant interactions might be found if oscillation were induced at a frequency characteristic of turbulence in the parent boundary layer It was found that the response of turbulence to forced unsteadiness around and above the burst frequency constituted a monotonic approach to a "frozen state" No resonant behavior was detected However, when the period of forced oscillation reached a timescale characteristic of the lifetime of a low-speed streak in the sublayer, the streaks underwent spatial organization with a significant reduction in their spanwise meandering motion This effect is a minor one and does not appear to be a precursor to any resonant behavior

INTRODUCTION

While unsteady turbulent flows are of prime importance in large numbers of engineering systems, in which unsteady forcing covers a broad range of frequencies, studies of their response to organized unsteadiness have focused predominantly on low-frequency effects, where information is accessible with relative ease The purpose of this study is to carry out a detailed investigation of the response of wall-bounded turbulence to forced oscillation at high frequencies, superposed upon a mean flow, in order to address the issue of whether forced oscillation around the burst frequency in the parent boundary layer can cause interaction with the turbulence producing motions of the mean flow.

The motivation for this study is that it has long been speculated that non-linear resonant interactions might be found if oscillation were induced at a frequency characteristic of turbulence in the parent boundary layer While a number of investigators have reported measurements in the neighbourhood of the burst frequency in unsteady flow experiments, they have, in almost all cases, been restricted to a single data set at a frequency thought to be comparable to the burst frequency — usually the highest attainable in the particular apparatus A survey of the relevant literature reveals differing opinions on whether such any interaction takes place The pipe-flow experiments of Ramaprian & Tu (1983) revealed an orderly decrease in amplitude of phase-dependent turbulence intensity with increasing frequency, towards a "frozen" state, as did the channel flow experiments of Binder & Kueny (1981) In the adverse pressure gradient boundary-layer experiments of Brereton *et al* (1990, 1991), when the frequency of forced oscillation was of the order of the burst frequency, phase-conditioned turbulent motions tended towards a "frozen" state everywhere except in the region of peak production of the parent boundary layer ($y^+ \simeq 11$, at $Re_\theta = 3200$), where a small first-harmonic oscillation in $\langle u'u' \rangle$ could still be detected (where $\langle\ \rangle$ represents the phase average and u' the turbulent component of streamwise velocity) It was not clear if this peak would disappear at higher frequencies of oscillation. No modification of profiles of mean velocity or of time-averaged components of the Reynolds-stress tensor was observed. The conclusions of this study were that all periodic production of turbulence was primarily a modulation of the robust turbulence producing motions of the parent (mean) boundary layer, and that any resonant interaction might only come about if both spatial and temporal control of the turbulence producing motions could be achieved The conclusion that there is no noticeable interaction over other ranges of frequency has been supported by a number of other studies in other unsteady turbulent boundary-layer, channel, and pipe flows when the frequency of forced oscillation approaches the estimated burst frequency (Shemer *et al* (1985), (Cousteix & Houdeville 1983)) At frequencies of forced unsteadiness very much higher than characteristic turbulence frequencies, the observation of a smooth approach to a "frozen" state has been supported by the experiments of Brown *et al* (1969) — in these experiments phase-conditioned friction factor measurements exhibited a quasi-laminar dependence on frequency, and turbulence was reported as "frozen"

Amongst the numerous observations of comparability between steady and mean unsteady effects, several contradictory findings have been reported at high frequencies of forced unsteadiness Amongst the first to look at the detailed structure of unsteady turbulent pipe flow were Mizushina *et al* (1973, 1975), who inferred that significant changes in turbulence structure occur when the frequency of oscillation reached a critical frequency which scaled with estimates of the burst frequency While the trustworthiness of their data has been the subject of some criticism (Tardu *et al*, 1987), their findings have still to be contradicted by a comparable study Ramaprian & Tu (1983) studied oscillatory fully-developed pipe flow at different frequencies of forced unsteadiness and reported slight difference in profiles of mean quantities for oscillation close to the burst frequency, attributing these effects to non-linear interactions caused by the imposed oscillatory flow More recently, Mao & Hanratty (1986) measured the wall shear in oscillatory pipe flow,

at frequencies which appeared to be as high as the mean-flow burst frequency They noted that the phase-conditioned turbulence intensity in wall shear constituted a distinctly non-linear response to a harmonic phase-conditioned wall shear stress, which they attributed to an unexplained interaction between organized flow oscillation and turbulence close to the wall Abrams & Hanratty (1985) also noted similarities between flows with forced spatial variation and those subjected to forced temporal variation In their studies of flow over a wavy wall, they observed relaxation effects in the phase of the response of turbulence to a wavy surface of short wavelength, consistent with non-linear behavior observed in their high-frequency smooth-wall pipe-flow results (Mao & Hanratty, 1986) In the channel-flow study of Acharya & Reynolds (1975), the response of a fully-developed turbulent channel flow to forced oscillation was compared at a low frequency and at a frequency of the order of the burst frequency Although their correlation technique allowed measurement only of the first-harmonic response, some of the discrepancies between data at the two frequencies were attributed to interaction with the turbulence-producing motions More recently, Tardu & Binder (1987, 1989) have considered aspects of turbulence structure in these flows Using conditional sampling techniques to monitor bursting activity, they observed a strong modulation of bursting frequency during each oscillation and identified differences in educed bursting characteristics when the oscillation frequency approached the burst frequency Their results showed that one effect of imposed oscillation at a frequency of the order of the burst frequency was to decrease the average ejection frequency, while maintaining the same burst frequency. Moreover, bursts which result in multiple ejections, and bursts which produce single ejections appeared to react differently to imposed oscillation, leading to the notion that, in unsteady flow, each might be governed by somewhat different mechanisms.

In summary, there are a number of different experiments, conducted in different flows, from which contradictory conclusions have been drawn concerning the interaction between turbulence and forced oscillatory motion in the neighborhood of the burst frequency of the mean flow. The objective of this study was to conduct a systematic study of effects of forced oscillation on wall-bounded turbulence, over a wide range of frequencies which would exceed by an order of magnitude the mean-flow burst frequency A turbulent pipe flow is a good candidate for a study of this kind because the compact geometry of this flow translates to lower mechanical power requirements for forced oscillation at high frequencies than its channel-flow or boundary-layer counterparts The parameter space of the study (Reynolds number vs. mean flow burst frequency (as estimated by the correlation of Luchik & Tiederman (1987)) is shown in Fig 1, together with the parameter space covered by other pertinent pipe-flow studies

EXPERIMENTAL APPARATUS

The test facility comprised a standard recirculating water loop with a constant-head tank, sump, pump, and a test section of translucent pipe (57mm in diameter, 160 diameters long, assuring fully-developed flow over most of the test section) The final stage of the test section was of bronze, and flow control was achieved by motoring a profiled sleeve around a longitudinal slot milled in the bronze pipe section Rotational position and speed of the profiled sleeve were controlled by a DC motor and amplifier with position feedback, which operated under the control of a laboratory computer The average area presented for outflow from the test section to the sump resulted in a mean flow Reynolds number (referenced to centerline velocity and pipe diameter) of 11,700, corresponding to a burst frequency of about 1 7 Hz (according to the correlation of Luchik & Tiederman (1987), and consistent with hydrogen-bubble visualization and VITA measurements). Forced oscillation at up to 10 Hz could be achieved in this apparatus, with temporal variation of phase-averaged velocity always a good representation of a sine wave The amplitude of flow oscillation decreased with increasing frequency, consistent with the impedance characterization of the pipe by Shemer *et al* (1985). In these experiments the amplitude of oscillation at the pipe centerline varied between 19% of the mean centerline velocity at 0.25 Hz and 12% at 3 0 Hz

Phase-conditioned and time series measurements of streamwise velocity were made using a laser-Doppler anemometer with frequency shifting and a counter, which was interfaced with a laboratory computer to allow phase-resolved measurements of the instantaneous velocity of the flow Since highly repeatable periodic motion could be imposed by the flow-control apparatus, a phase-averaging procedure was adopted for decomposition of flow variables into mean, oscillatory and turbulent components All measurements were averaged over at least 1000 ensembles Statistical convergence in data was assumed to have been reached when the fractional tolerance (a measure of differences in $\langle u'u' \rangle$ over the first and second halves of the data set, normalized by the rms level in $\langle u'u' \rangle$) reached 0 1% For oscillation at 3 0 Hz, the typical number of cycles required to satisfy this tolerance was around 5000.

The relatively low Reynolds number of the flow allowed the use of hydrogen-bubble visualization to study timelines and streaklines of the unsteady flow, in the manner outlined by Schraub *et al* (1965). In order to view timelines initiated a constant distance from the wall, a very thin flat strip was inserted at the surface, at the observation station in the manner described by Achia & Thompson (1977) Visual information was recorded using either phase-conditioned photography or a high speed video camera (Kodak Ektapro Motion Analyzer).

EXPERIMENTAL RESULTS

Measurements of the time-averaged values of mean velocity (U) and mean square of turbulence $\overline{u'u'}$ across a radius of the pipe were in good agreement with reference steady-flow data and showed no variation with frequency, even when oscillation was forced at six times the estimated burst frequency of the mean flow These results are well established and consistent with those of nearly every unsteady flow experiment and so are not shown here. Of more interest were power spectra of u', as deduced from time series measurements from which the phase-averaged velocity had been subtracted These power spectra are shown in Fig 2, for forced oscillation at frequencies as high as 8 Hz, measured at $y^+ \simeq 15$ — close to the position of peak production of turbulence in the parent boundary layer While there is considerable low-frequency noise in these data, caused by the differing lengths of time series processed

and the variance of the FFT as a power-spectral estimator, the general trend is one of qualitative agreement There is no convincing evidence of any re-arrangement of the spectral content of the flow, reinforcing the notion of invariance of all scales of motion of the parent boundary layer to forced sinusoidal oscillation

The high-frequency response of the organized component of streamwise velocity is illustrated in Fig 3, in which the amplitude of $\langle u \rangle$ at its first harmonic is plotted in the near-wall region For frequencies above 1 Hz, these profiles are in good agreement with the asymptotic high-frequency (Stokes) solution to the streamwise momentum equation in the oscillatory field of flow. They also illustrate clearly that, at these frequencies, all oscillatory shear is confined to a very thin region within the viscous sublayer and so is unlikely to provide direct interaction with the turbulence producing motions of the parent boundary layer

The first harmonic response of the streamwise component of turbulence is shown in Fig 4, normalized by u_τ, the friction velocity of the mean flow In this figure, the amplitude of the square root of the oscillatory component of $\langle u'u' \rangle$ is plotted — the square root represents a more robust statistical measure which is less sensitive to false measurements than the phase average of the square of u' (though it is more indirect in relevance to decomposed forms of the Navier-Stokes equations). It is clear from this figure that the trend is a monotonic one towards "frozen" turbulence with increasing frequency, with the peak in the turbulence response coincident with the peak of turbulence production in the parent boundary layer ($y^+ \simeq 11$). It is worth pointing out that the amplitudes of the phase-conditioned turbulence response are extremely small. Therefore they are very sensitive to minor cycle-to-cycle variations in the organized forcing, which are interpreted as turbulence by the phase-average decomposition We were initially misled by such organized variation (in the form of a noisy signal from a position encoder, which produced the effect of an occasional phase shift in $\langle u \rangle$) which manifested itself as a second-harmonic response when it exceeded in amplitude the true turbulence response However, once this problem was resolved, second harmonic motion was always an order of magnitude smaller than that at the fundamental frequency

The phase dependence of the deviation of $\langle u'u' \rangle$ from its mean is shown in Fig 5 for three selected frequencies, measured at $y^+ = 12$ The attenuation of phase-dependent variation in turbulent intensity with increasing frequency may be seen plainly, together with the obvious variance from a sinusoidal response For the phase average of $u'u'$ measured at 2 0 Hz, a Fourier decomposition still reveals a dominant first-harmonic response The similarity between these data and the equivalent measures of turbulence in wall shear stress (Mao & Hanratty (1986)) prompted a more thorough examination of whether the variance of these data from a sinusoidal response was due to an inability to distinguish between harmonic components and background noise, or whether it did indeed represent the growing importance of higher harmonics with increasing frequencies

This issue was examined by estimating the power spectrum of the square of u' (and thus organization in magnitude of u') from a time series of $u(t)$ from which the phase-averaged velocity $\langle u \rangle$ had been subtracted Spectra of the square of u' are shown in Fig 6 for time series measured at $y^+ = 12$, with oscillation at 0 5 Hz and 2 0 Hz From the high-frequency content of the spectra, it appears that there is no obvious broadening due to instrumentation noise for the case of forced oscillation at 2 Hz, even though the signal level (shown in Fig 5 is significantly lower) The spectra reveal enhanced organization in magnitude of u' at the fundamental and second-harmonic and hint at the possibility of weak peaks appearing at higher harmonics The second harmonic arises through the non-linear character of the periodic Reynolds-stress equations in coupling first harmonic shear ($\langle \partial u/\partial y \rangle$) and first harmonic Reynolds stress ($\langle u'v' \rangle$) to yield a second-harmonic production term for $\langle u'u' \rangle$. Through the same coupling, multiple higher harmonics in $\langle u'u' \rangle$ may be generated in this kind of flow However, it appears that the energy in $\langle u'u' \rangle$ is only transferred from the fundamental to higher harmonics when the period of oscillation approaches a characteristic time scale of the parent flow (burst frequency, large-eddy turn-over time, *etc.*).

The indication from these results is that variance about the sinusoidal response shown in Fig. 5 is turbulence at higher harmonics and not noise Thus the proportional role of higher harmonics grows as turbulence approaches a "frozen" state, though it is not clear that higher harmonics supercede the first harmonic response in importance.

The coincident in position between peaks in amplitudes of periodic measures of turbulence and turbulence production in the parent boundary layer reinforces the contention that the former is predominantly a modulation of the latter Thus it is informative to examine statistical features descriptive of turbulence producing motions in this region In Fig 7, conditional averages from time series of the turbulent component of streamwise velocity are presented, as deduced by a positive-slope VITA technique These conditional averages span a range of frequencies of oscillation from steady flow to 2 Hz The general trend in these results appears to be one of qualitative agreement at all frequencies, with no dramatic dependence on frequency There are, however, subtle variations which may be indicative of structural change in the motions which are identified by this particular statistical technique This notion appears to support the more detailed investigations into identification of structural information in unsteady turbulent flow, carried out by Tardu *et al* (1989) which characterized subtle changes in statistical measures of this kind with frequency variation.

Further information on possible modifications of the structure of the near-surface turbulence field was sought using hydrogen bubble visualization A high-speed video camera was focused on the flowfield downstream of a platinum wire positioned at $y^+ \simeq 15$ and the evolution of timelines during unsteady oscillation was recorded Video footage demonstrated clearly that streak initiation (and the peak level in $u'u'$) becomes organized in time by the superposed oscillation, favoring the beginning of the deceleration phase when the flow is most susceptible to the as-yet-unidentified destabilization effect which drives the bursting phenomenon. This result was consistent with measurements of the phase of $\langle u'u' \rangle$ relative to that of the oscillatory forcing, and in agreement with similar measurements made by Tardu *et al.* (1987). As the period of forced

oscillation was decreased, the streak signature (indicative of features of the robust turbulence producing motions of the mean flow) began to survive whole periods of oscillation Moreover, the dying signature of a streak generated during the deceleration phase of the previous unsteady cycle appeared to mark the position upstream of which new streaks were most likely to appear during the next deceleration phase of the unsteady cycle.

Selected frames from these recordings are shown in Figs 8, 9 and 10 for the cases of steady flow, low-frequency unsteady flow (at one seventh of the mean-flow burst frequency) and high frequency unsteady flow (at a frequency approximately equal to three times the mean flow burst frequency) In the steady flow sequence, attention is drawn to the apparently random appearance of a new streak (at the bottom of the frame) below the existing one (near the top of the frame), as it twists and loses its coherence For the sequence at low-frequency unsteadiness, the streak (towards the top of the frame) forms during the deceleration phase and maintains it characteristic "V" signature as it meanders before being swept downstream during the acceleration phase of the unsteady cycle (during which the final frame was taken)

In the high-frequency case, the sequence of images spans a complete period, beginning with a well-established region of low-speed flow in the center of the frame As this region is swept downstream during the acceleration phase, the characteristic "V" signature of a newly initiated streak begins to form in the wake of the previous one The "V" signature continues to develop during the deceleration phase, establishing a new broad region of low-speed fluid The subsequent convection downstream during the acceleration phase then precedes the initiation of a new streak in its wake until, eventually, spanwise meandering breaks this pattern

These visualizations were quite repeatable at frequencies at and above the burst frequency, when viewed as a continuous video sequence. A second observation from these recordings was that spanwise meandering of streak signatures was reduced when organized oscillation was imposed Thus high-frequency forced unsteadiness appears to play the role of stabilizing the location at which the turbulence producing motions (as marked by accompanying streak patterns) are generated close to the wall The comparison with the almost random localization of streaks in steady flow is quite dramatic and might be exploited if spatio-temporal flow-control techniques were to be targeted at stabilizing the turbulence producing motions of the boundary layer. It would seem that plausible explanations for this observation should be linked with the elusive instability which drives bursting motion, or with feedback from the outer flow of the organized oscillatory pressure field, which would overwhelm the turbulent pressure fluctuations which act in steady flow However, exploration of these issues remains a topic of future research

DISCUSSION AND CONCLUSIONS

The effect of high-frequency oscillation on wall-bounded turbulence appears to be predominantly one of reducing the response time afforded to the turbulence-producing motions of the mean flow to adapt to momentary changes in the bulk flow. Phase-conditioned production is thus weaker and loses its coherence after outward diffusion over shorter distances, as frequency of oscillation increases A monotonic approach to "frozen" turbulence follows, characterized by a proportionally greater energy content in higher harmonics. It does not seem to matter whether the characteristic turbulence time scale is gauged as a reciprocal burst frequency, a large-eddy turnover time scale, a streak lifetime, or a turbulent kinetic energy/dissipation rate ratio, as these are all characterizations of the robust turbulence producing motions of the parent boundary layer and are all of the same order in a given low Reynolds number experiment in wall bounded turbulent flow

While it appears that temporal forcing can impose weak organization on some aspects of turbulent motion, there is no evidence of any resonance or strong interaction with the turbulence-producing motions of the parent boundary layer The spatial disorganization of these motions prohibits such simple interference The weak interference which is achieved by temporal forcing arises when the time scale of forced oscillation approaches that of the response of turbulence, and promotes subtle organizational effects in the localization of turbulence-producing motions These effects are essentially cosmetic changes to the signature of an active motion and appear to have no effect on $u'u'$

REFERENCES

Abrams, J & Hanratty, T J Relaxation effects observed for turbulent flow over a wavy surface *J Fluid Mech* **151** (1985), 443-455

Acharya, M & Reynolds, W C Measurements and predictions of a fully developed turbulent channel flow with imposed controlled oscillations *Report TF-8*, Department of Mechanical Engineering, Stanford University, Stanford, California, (1975)

Achia, B U & Thompson, D W Structure of the turbulent boundary layer in drag-reducing pipe flow *J Fluid Mech* **81** (1977), 439-464.

Binder, G & Kueny, J. L. Measurements of the periodic velocity oscillations near the wall in unsteady turbulent channel flow In *Turbulent Shear Flows 3*, Springer-Verlag, New York, 1982

Brereton, G J Reynolds, W C. & Jayaraman, R. Response of a turbulent boundary layer to sinusoidal free-stream unsteadiness *J Fluid Mech* , 221 (1990), 131-159.

Brereton, G. J. & Reynolds, W. C Dynamic response of boundary-layer turbulence to oscillatory shear. *Phys Fluids A* **3** (1) (1991), 178-187

Brown, F T., Margolis, D L & Shah, R. P. Small-amplitude frequency behavior of fluid lines with turbulent flow *Trans ASME D J. Basic Engng* , **91** (1969), 678-693

Cousteix, J & Houdeville, R. Couches limites instationnaires *Rapport Technique 53/2259 AND*, Departement d'Etudes et de Recherches en Aerothermodynamique, Centre d'Etudes et de Recherches de Toulouse, 1983

Luchik, T S & Tiedermann, W G Timescale and structure of ejections and bursts in turbulent channel flows *J. Fluid Mech* **174** (1987), 529-552

Mao, Z -X & Hanratty, T J Studies of the wall shear stress in a turbulent pulsating pipe flow *J Fluid Mech* 170 (1986), 545-564

Mizushina, T , Maruyama, T. & Hirasawa, H Structure of the turbulence in pulsating pipe flows *J Chem Engng Japan* 8 (1975), 210-216

Mizushina, T , Maruyama, T & Shiozaki, Y Pulsating turbulent flow in a tube *J Chem. Engng Japan* 6 (1973), 487-494.

Ramaprian, B. R. & Tu, S W Fully developed periodic turbulent pipe flow Part 2 The detailed structure of the flow *J Fluid Mech* 137 (1983), 59-81

Schraub, F A , Kline, S. J , Henry, J , Runstadler, P. W & Littell, A Use of hydrogen bubbles for quantitative determination of time-dependent velocity fields in low-speed water flows *Trans ASME* D *J. Basic Engng* 87 (1965), 429-444

Shemer, L , Wygnanski, I & Kit, E Pulsating flow in a pipe *J Fluid Mech* 153 (1985), 313-337

Shemer, L , Kit, E & Wygnanski, I On the impedance of the pipe in laminar and turbulent pulsating flows *Expt Fluids* 3 (1985), 185-189 Tardu, S , Binder, G & Blackwelder, R Modulation of bursting by periodic oscillations imposed on channel flow *Sixth Symposium on Turbulent Shear Flows*, Université Paul Sabatier, Toulouse, 1987

Tardu, S & Binder, G Ejections and bursts in pulsatile turbulent wall flow measurements and visualizations *Seventh Symposium on Turbulent Shear Flows*, Stanford University, Stanford, 1989

Tardu, S , Binder, G & Blackwelder, R Response of turbulence to large amplitude oscillations in channel flow In *Advances in Turbulence* (eds. G Compte-Bellot & J Mathieu), Springer-Verlag, New York, 1987

Figures

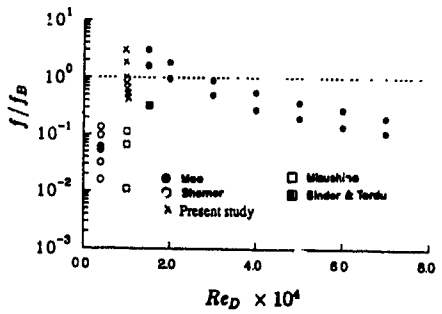

Fig. 1 Oscillation frequency vs. Reynolds number parameter space for unsteady turbulent pipe flow experiments

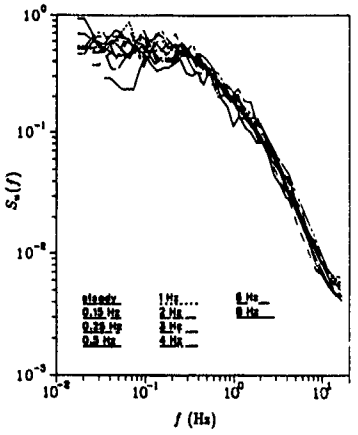

Fig 2 Power spectra of u' at $y^+ = 15$ for steady and decomposed unsteady turbulent flow The burst frequency of the parent boundary layer is about 1 4 Hz

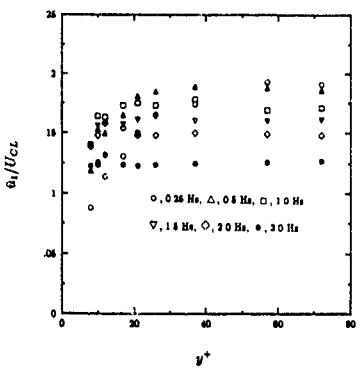

Fig 3 Amplitude of the first harmonic response of $\langle u \rangle$, normalized by the centerline amplitude

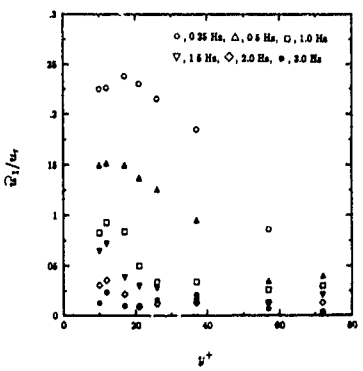

Fig. 4. Amplitude of the first harmonic response of $\langle u' \rangle$, normalized by u_τ

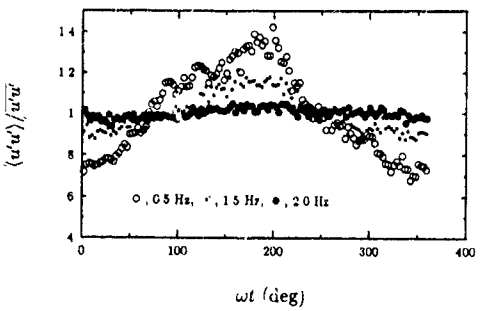

Fig 5 Dependence of $(u'u')$ with phase, at $y^+ = 12$

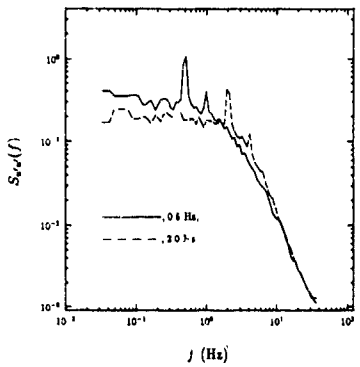

Fig 6 Spectrum of the square of u' at $y^+ = 12$ for oscillation at 0 5 Hz and 2 0 Hz, representing the frequency dependence of organization in magnitude of u'

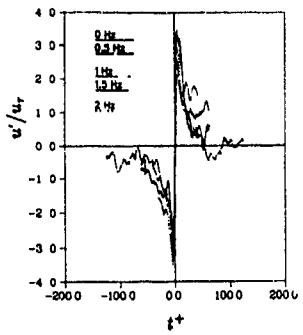

Fig 7 VITA positive-slope conditional averages for forced oscillation over a range of frequencies, at $y^+ \simeq 15$ The abscissa is in viscous time units

Fig 8 The decay of one streak and the disorganized initiation of another, in steady flow. The time sequence is from left to right.

Fig 9 The deceleration-phase growth and acceleration-phase downstream convection of a streak, in low-frequency unsteady flow

Fig 10 The downstream convection of one streak and the subsequent initiation of a new one in its wake, in high-frequency unsteady flow.

EIGHTH SYMPOSIUM ON
TURBULENT SHEAR FLOWS
Technical University of Munich
September 9-11, 1991

Direct Simulation of Turbulent Pulsed Plane Channel Flows.

S. Rida, K. Dang Tran

Office National d'Etudes et de Recherches Aérospatiales

BP 72, 92322 Chatillon, FRANCE

1. Abstract.

The aim of this study is the understanding of the behaviour of turbulent wall shear flows submitted to time dependent external forces. Experimental studies and theoretical considerations [3,4,6,7] have already given some insights on the influence of an imposed unsteadiness on turbulent motions in the case of pulsed plane channel and boundary layer flows: the time averaged turbulent quantities seem to be unaffected by the imposed periodical forces, mostly at high frequencies, and the phase averaged quantities follow merely the evolution of the linear viscous Stokes solution on the major part of the flow domain. However these experimental results may be completed and tuned by means of numerical direct simulation. This numerical work, completed in the case of a pulsed plane channel flow at a mean Reynolds number $\overline{<R_e>} = 2000$ for the steady case, brings out that non linear interactions can be found between the turbulent flow and the imposed unsteadines., in the range of low frequencies where the computations have been carried out.

2. The continuous problem.

We are interested in the case of a plane channel flow driven by a periodically time varying mean adverse pressure gradient. This problem has an exact solution in the linear case, called the Stokes solution U_s. It is obtained by solving the following equation

$$\frac{\partial U_s}{\partial t} - \frac{1}{R_e}\frac{\partial^2 U_s}{\partial x_3^2} = -\frac{\partial P}{\partial x_1}\,(1 + \varepsilon\cos(\omega t)) \tag{1}$$

which solution is the real part of.

$$U_s(x_3,t) = \frac{e^{i\omega t}}{i\omega}\varepsilon\frac{\partial P}{\partial x_1}\left(\frac{e^{kx_3} + e^{-kx_3}}{e^{k} + e^{-k}} - 1\right) - \frac{R_e}{2}\frac{\partial P}{\partial x_1}(1-x_3^2)$$

with $x_3 \in [-1,1]$. k is denoting the wavenumber equal to $\sqrt{i\omega R_e}$, and R_e is the Reynolds number based on the value of the velocity in the middle of the channel and the half height of the channel. In the non linear case, the solution of the Navier-Stokes equations at supercritical Reynolds numbers, with the imposed mean gradient and the continuity equation, provides us with the turbulent value of the velocity and the pressure fields. These equations are:

$$\begin{cases} \dfrac{\partial U_i}{\partial t} + U_j\dfrac{\partial U_i}{\partial x_j} = -\dfrac{\partial P}{\partial x_1}(t)\delta_{1i} - \dfrac{\partial p}{\partial x_j}\delta_{ij} + \dfrac{1}{R_e}\dfrac{\partial^2 U_i}{\partial x_j \partial x_j} \\ \dfrac{\partial U_j}{\partial x_j} = 0 \end{cases}$$

As it is commonly done, we will use the triple decomposition, to bring out the non linear interaction which may arise between the mean turbulent field and the imposed force.

$$U(x_1,x_2,x_3,t) = \overline{<U>}(x_3) + <\tilde{U}>(x_3,t) + u'(x_1,x_2,x_3,t) \tag{2}$$

where $\overline{<U>}$ is the mean steady part, $<\tilde{U}>$ its mean time dependent part, and u' its turbulent fluctuation. Taking the advantage of the direct simulation procedure $<U>$ is defined as the mean value taken by U over planes of homogeneneity x_3=cte and over a large number N of cycles for a given phase angle ϕ

$$<U>(x_3,\phi) = \frac{1}{N}\sum_{n=1}^{N}\frac{1}{L_1}\frac{1}{L_2}\int_0^{L_1}\int_0^{L_2} U(x_1,x_2,x_3,n\,\omega T+\phi)\,dx_1 dx_2 \tag{3}$$

where L_1 and L_2 are the streamwise and spanwise dimensions of the channel

3. The numerical method.

The numerical method has been developed for direct simulations of plane channel flows and is detailed in [1][2]. The Navier-Stokes equations in velocity-pressure formulation, are discretized on a non uniform cartesian grid and are solved by a semi-implicit finite difference scheme which is second order accurate in time and fourth order accurate in space. The pressure defined at the same discretization points as the velocity, is computed iteratively at each time step in order to minimize a norm of the velocity divergence. In the present case streamwise periodic boundary conditions are prescribed in order to simulate a temporally evolving flow. The semi implicit time discretization uses an Adams-Bashforth scheme for the convective term, and an Euler scheme for the diffusion term.

$$L\left\{\frac{U_i^{n+1}-U_i^n}{\Delta t}\right\} = -\varepsilon_{ijk}\omega_j^{*}U_k^{*} - \frac{\partial Q^{n+\frac{1}{2}}}{\partial x_i} - \frac{\partial P}{\partial x_1}(t)\delta_{1i} + \frac{1}{R_e}\frac{\partial^2 U_i^n}{\partial x_k \partial x_k}$$

$$\text{with } Q = \frac{U_i U_i}{2} + p \text{ and } \omega_i^{*} = \varepsilon_{i,k}\left(\frac{3}{2}\frac{\partial U_k^n}{\partial x_j} - \frac{1}{2}\frac{\partial U_k^{n-1}}{\partial x_j}\right)$$

where L is an implicit operator, factorized in the three space directions.

$$L = \left\{1-\eta_1\frac{\partial^2}{\partial x_1^2}\right\}\left\{1-\eta_2\frac{\partial^2}{\partial x_2^2}\right\}\left\{1-\eta_3\frac{\partial^2}{\partial x_3^2}\right\}$$

The pressure field is determined by solving the following equation obtained by taking the discrete divergence of the momentum equation :

$$-\frac{\partial}{\partial x_k}L^{-1}\frac{\partial Q^{n+\frac{1}{2}}}{\partial x_k} = -\frac{1}{\Delta t}\frac{\partial U_k^n}{\partial x_k} + \frac{\partial}{\partial x_i}L^{-1}\varepsilon_{ijk}\omega_j^{*}U_k^{*} + \frac{\partial}{\partial x_i}L^{-1}\left\{\frac{\partial P}{\partial x_1}(t)\delta_{1i} - \frac{1}{R_e}\frac{\partial^2 U_i^n}{\partial x_k \partial x_k}\right\}$$

It is computed iteratively in order to minimize a discrete norm of the velocity divergence. A special treatment of the pressure at the internal points, eliminates spurious pressure modes [5], and enhances the convergence of the iterative computation.

4. Results

4.1 Direct simulation procedures.

The laminar viscous Stokes solution is taken as the initial field whose steady part is the laminar Poiseuille flow. Therefore, destabilization is achieved by adding the suitable 2-D and 3-D Tollmienn Schlichting waves [1,2] of wavelength $\alpha = 1.25$. After a transient state the computed field becomes fully turbulent. The dimensions of the computational box are $2\pi/\alpha$, π, 2, respectively in streamwise, spanwise and normal to the wall directions, discretization is achieved with 18x32x65 points respectively in these directions.

The computations are carried out for two values of the period: T= 2.6 s and T= 60. s, corresponding to high and low values of the frequency ω, and for an amplitude ratio $A = [\tilde{U}_x]/\overline{U_x}$ in the middle of the channel equal to 40%. The characteristics of these two cases transcribed in the Binder-Kueny [3] parameter ls_+ which is defined as the ratio of the Stokes layer $ls = \sqrt{2/R_e\omega}$ to the thickness of the steady turbulent viscous sub-layer $1/R_e\langle u_\tau \rangle$, are equal respectively to 1.81 and 8.74. The Reynolds number of the initial field based on the half height of the channel $\overline{U_x}(h/2)h/2\nu$ is equal to 5000.

Periodically time dependent solutions have been obtained for which amplitudes $[\tilde{U}]$ follow fairly well the Stokes solution on the major part of the channel height, as shown on figures 1 and 2 respectivily for T= 2.6 s and T= 60 s, with better agreement for the high frequency case as expected, except very near the walls.

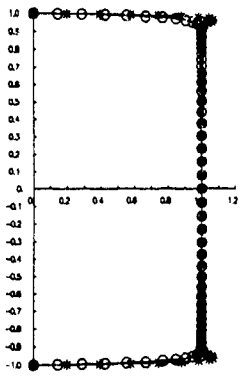

Fig 1 Amplitudes ratios for $A = 0.4$ and $T = 2.6s$
* $[\tilde{U}_x]/A$
o $[\langle U \rangle]/A$

In the high frequency case, the linear solution U_s and the non linear solution $\langle U \rangle$ are in phase in the middle of the channel and out of phase very near the wall as shown by Lissajoux curves of figure 3 denoting linear interactions due to viscosity. The interesting result is found in the low frequency case. The same trends concerning the relative phase of $\langle U \rangle$ and U_s can be observed on figure 4, but in

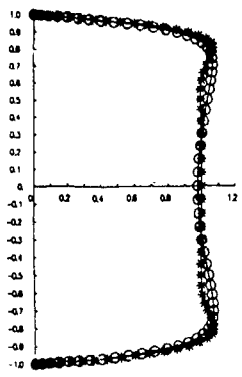

Fig 2 Amplitudes ratios for $A = 0.4$ and $T = 60.s$
* $[\tilde{U}_x]/A$
o $[<\tilde{U}>]/A$

this case, Lissajoux curves are not closed, neither in the middle of the channel nor near the wall, which denotes a non linear interaction between the turbulent flow and the unsteady external forces.

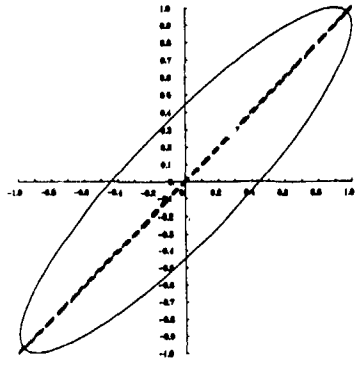

Fig 3 Relative phase of $[\tilde{U}_x]/A$ versus $[<\tilde{U}>]/A$ $T = 2.6s$.
---- in the middle of the channel
— at the point nearest to the wall

4.2 Time averaged quantities.

As observed experimentally [3,4,7], time averaged quantities $\overline{<>}$ seem effectively not much influenced by the forcing frequency and amplitude The frequency invariance may be observed first, on the averaged Reynolds number $\overline{<U>}(h/2)h/2\nu$ and on the time averaged wall velocity In effect, computed values of these quantities in both high and low frequency cases $\overline{<R_e>} = 1787, 1590$ and $\overline{u_\tau} = 2.05510^{-2}, 2.01010^{-2}$ do not differ much from those obtained in the steady case ($\overline{<R_e>} = 1866$ and $\overline{u_\tau} = 2.02710^{-2}$)

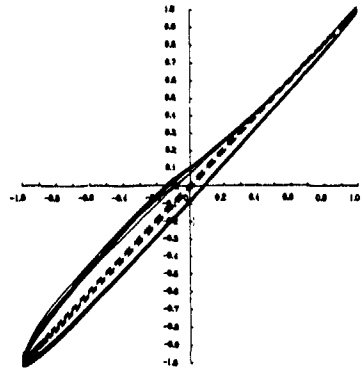

Fig.4 Relative phase of $[\tilde{U}_x]/A$ versus $[<\tilde{U}>]/A$ $T = 60.s$.
---- in the middle of the channel
— at the point nearest to the wall

The same conclusions can be drawn for time averaged velocity $\overline{<U>}/\overline{u_\tau}$, and shear stress $\overline{<u'_1u'_3>}/\overline{u_\tau^2}$ distributions displayed on figures 5 and 6. On the contrary normal stress distributions $\overline{<u'_1u'_1>}/\overline{u_\tau^2}$ (Fig.7), seem to depend on frequency. However, this dependency found in some experiments, and not in others [7] is not yet clearly established. The amplitude invariance of our simulation results has been verified by simulating again the low frequency case with the forcing amplitude of $A = 0.1$. Results obtained for the previous quantities are the same as for $A = 0.4$(Fig 5,6,7). This seems to indicate that non linear interactions between the turbulent flow and the forcing at this low frequency, discussed here after, are not related to relaminarization of the flow which may occur for $A = 0.4$ due to the low mean Reynolds number of the simulation

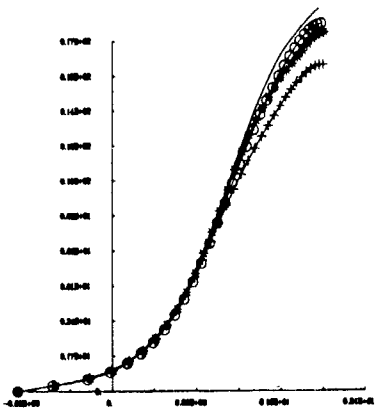

Fig 5 Velocity distribution of $\overline{<U_1>}/\overline{u_\tau}$ versus $Log(x_3^+)$
- $T = \infty$, + $T = 60\,s$, * $T = 2.6s$
o ($A = 0.1$, $T = 60\ s$)

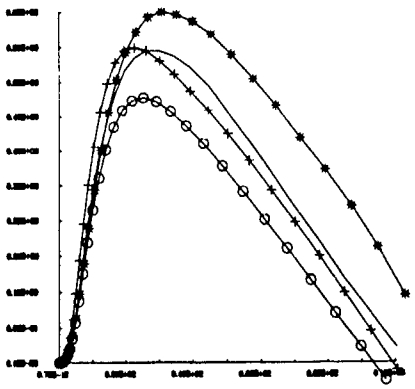

Fig 6 Shear stress distributions $\overline{<u'_1u'_3>}/u_\tau^2$ versus x_3^+
- $T = \infty$, + $T = 60.s$; * $T = 2.6s$
o ($A = 0.1$, $T = 60.\ s.$)

4.3 Phase averaged quantities.

Fig 8.a and Fig 8.b show the time evolutions of $<u'_1\tilde{u}'_3>$ in the high and low frequency cases, respectively recorded over ten and five periods of forcing at $x_3^+ = 5$. Power spectra of these signals are displayed on figures 9.a and 9.b In the high frequency case, the shear stress oscillates almost sinusoidally at the forcing frequency A modulation of the signal at a lower frequency observed on figure 8.a and 9.a may be due to a lack of spatial homogeneity of the computed flow and is eliminated by phase averaging the signal as defined by (3) (Fig 10.a) In the low frequency case, the turbulence response is very different: the signal is periodic but far from sinusoidal (Fig 8.b and 10.b) The power spectrum displays a great number of harmonics enhanced by non linear interactions

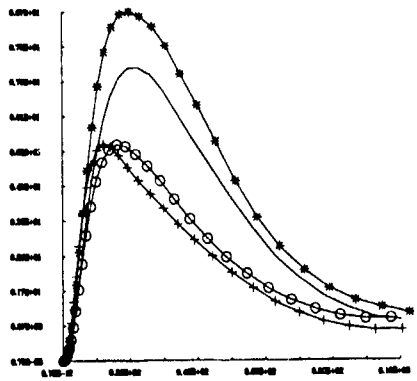

Fig.7 Normal stress distributions $\overline{<u'_1u'_1>}/u_\tau^2$ versus x_3^+
- $T = \infty$, + $T = 60\,s$, * $T = 2.6s$
o ($A = 0.1$, $T = 60\ s$)

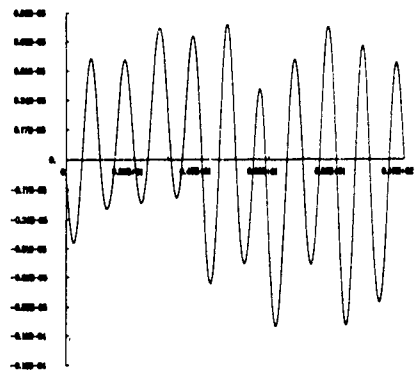

Fig.8.a Time evolution over ten periods of $<u'_1\tilde{u}'_3>$ versus t/T $T = 2.6\ s$ at $x_3^+ = 5$

In the mean, the complex evolution of the time dependent part of the shear stress seems to have no influence upon the time averaged value. Some insights in the complex underlaying energy transfers may be gained by considering in the energy budget of $\overline{<u'_1u'_1>}$ the production term P_{11} which is the largest contributor to the gain of turbulent kinetic energy in the steady case. Time averaging this term and using the decomposition (2) gives

$$P_{11} = -\overline{\langle u'_1 u'_3 \rangle \frac{\partial \langle U_1 \rangle}{\partial x_3}}$$

$$= -\overline{\langle u'_1 u'_3 \rangle} \frac{\partial \overline{U_1}}{\partial x_3} - \langle u'_1 \tilde{u}'_3 \rangle \frac{\partial \tilde{U}_1}{\partial x_3} \qquad (4)$$

Figure (11) displays the spatial distribution of the first steady term of (4) which does not depend on the forcing frequency, so that the distributions found in each case are similar as found also by experiment [6]. The "unsteady" contribution of the second term to the production P_{11} is compared to the "steady" contribution on figure 12 It is negligible in the high frequency case while it is very important in the low frequency one, acting as a supply of energy No simple explanation as the one suggest in [3,7]

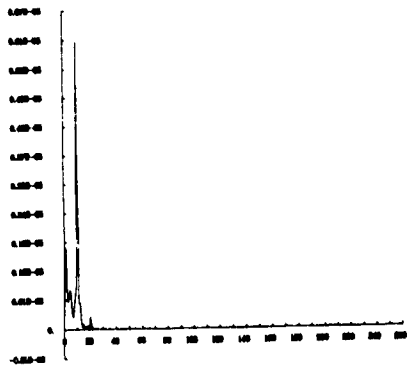

Fig 8 b Power spectrum of $\langle u'_1 \tilde{u}'_3 \rangle$ $T = 2.6$ s

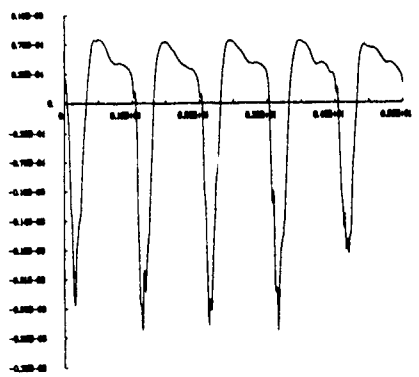

Fig 9 a Time evolution over five periods of $\langle u'_1 \tilde{u}'_3 \rangle$ versus t/T $T = 60.$ s at $x_3^+ \approx 5$.

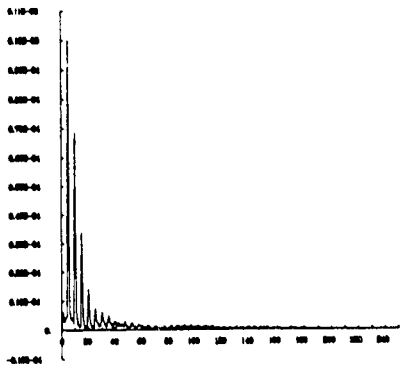

Fig.9.b Power spectrum of $\langle u'_1 \tilde{u}'_3 \rangle$ $T = 60$ s

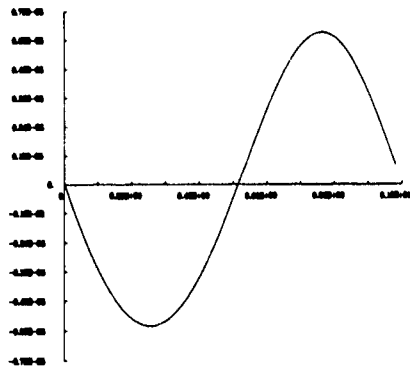

Fig.10.a Phase averaged evolution of $\langle u'_1 \tilde{u}'_3 \rangle$ versus t/T $T = 2.6$ s at $x_3^+ \approx 5$.

seems to exist for the frequency invariance of the time averaged values. Other terms of the energy budgets of the Reynolds stress terms must be computed to complete the analysis.

5. Conclusions

Direct simulations of turbulent plane channel flows submitted to imposed periodic time evolving streamwise mean pressure gradient have been carried out for two frequencies of the external force. At high frequency, the non linear solution is periodic and follows fairly well the linear periodic Stokes solution, but with an increasing phase lag, when approching the wall. At low frequency, the non linear solution is no more periodic due to non linear effects.

These non linear effects have no direct influence on time averaged second order moments of the velocity field, except for $\overline{<u'_1u'_1>}$ The analysis of the production term of the energy budget of $\overline{<u'_1u'_1>}$ shows a complex effect of the forcing frequency, but seems to be not sufficient to explain the results obtained. Consequently, computations of other terms involved in energy budget of the Reynolds stress tensor are required to describe the non linear effects of the low frequency forcing on energy redistribution between velocity components and the role of the pressure

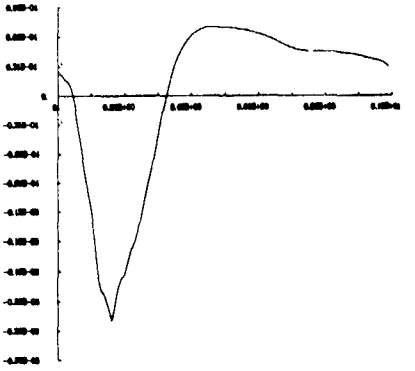

Fig 10.b Phase averaged evolution of $\overline{<u'_1u'_3>}$ versus t/T $T = 60$ s at $x_3^+ \approx 5$

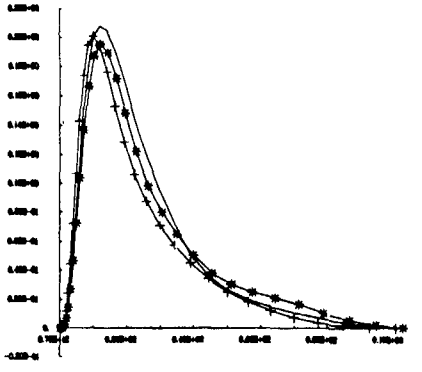

Fig 11 Spatial distribution of $-\overline{<u'_1u'_3>}\dfrac{\partial \overline{U_1}}{\partial x_3}$ versus x_3^+

- $T = \infty$, + $T = 60\,s$, * $T = 2.6s$

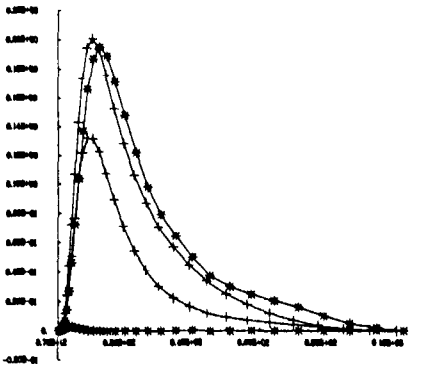

Fig.12 Spatial distribution of $-\overline{<u'_1u'_3>}\dfrac{\partial \overline{U_1}}{\partial x_3}$ and $-\overline{<u'_1u'_3>}\dfrac{\partial \overline{U_1}}{\partial x_3}$ versus x_3^+, + $T = 60.s$, * $T = 2.6s$.

6. References

[1] Dang Tran K., Deschamps V "Simulations numériques d'écoulements turbulents de canal plan", On fluid dynamics of 3-D turbulent shear flows and transition, Cesme (Turquie), 3-6 oct 1988 Agard CP438

[2] Dang Tran K , Morchoisne Y. "Numerical methods for direct simulation of turbulent shear flows", V K I Lecture Series 1989-3 on "Turbulent Shear Flows", Rhode-Saint-Genese (Belgique), February 6-10, 1989

[3] Binder G., Tardu S., Blackwelder R F. "Modulation of bursting by periodic oscillations imposed on channel flows", 5th Symposium on Turbulent Shear Flows -1987

[4] Cousteix J.,Houdeville R., "Effects of unsteadiness on turbulent boundary layers", onera/cert report.

[5] Lê T. H., Morchoisne Y , "Traitement de la pression en incompressible visqueux", C R A.S. Paris 1991 ref II 369.

[6] Brereton G J., Reynolds W. C., "Dynamic response of boundary-layer turbulence to oscillatory shear", Phys Fluids A 3(1), January 1991.

[7] Tardu S., Binder G.,"Turbulent channel flow with large amplitude velocity oscillations", to be submitted to J.F M .

EIGHTH SYMPOSIUM ON
TURBULENT SHEAR FLOWS
Technical University of Munich
September 9-11, 1991

A THEORETICAL AND NUMERICAL INVESTIGATION OF WAVE TURBULENCE INTERACTIONS

J Magnaudet and J Queyron

Institut de Mécanique des Fluides de Toulouse

31400 - Toulouse - France

ABSTRACT

The dynamical interactions occuring between periodic surface waves, turbulence and mean current are analysed by considering the orbital vorticity balance closed using an eddy-viscosity model It is theoretically shown how these interactions induce an energy transfer from the waves to the mean motion and then modify the mean momentum and turbulence energy balances Numerical computations using a simple one point closure with boundary conditions appropriate for interfacial turbulence are presented The results show that the turbulence energy is highly increased by these interactions and reaches the unusual level that has been measured below wind waves

1 INTRODUCTION

The aim of this paper is to try and present a coherent explanation of the dynamical interactions occuring between wind waves and water turbulence in lakes and oceans Evidence of the existence of such interactions has been demonstrated in several sets of experiments

- for instance field measurements have been performed on Lake Ontario (Kitaigorodskii et al 1983) Since in this case the waves were random, the total velocity fluctuations have been separated using a linear filtration method (Benilov et al 1974) into an orbital contribution linearly related to the wave height and a turbulent fluctuation The results showed that in presence of large wind waves, the ratio K/u^{*2} (K denoting the *turbulent* kinetic energy and u^* the interfacial friction velocity) can reach values two orders of magnitude higher than in wall flows,

- laboratory experiments using paddle-generated waves sheared by the wind have been performed in the Stanford Wind Wave Facility (Cheung 1985, Cheung and Street 1988) In this situation, the waves were periodic so that a phase-averaging procedure could be used in order to obtain the turbulent contribution The ratio K/u^{*2} below the free surface was found to range between 9 and 11, nearly three times the near-wall value

In order to explain the first group of results, Kitaigorodskii and Lumley (1983), following previous proposals of Kitaigorodskii and Miropolskii (1968) and Benilov (1973) have proposed an interaction mechanism based on an irrotational behavior of the orbital motion supposed to be governed by a linear Bernoulli equation. Several additional terms appear in the K-balance but it has been shown by an order of magnitude analysis that, within previous hypotheses, the diffusion of wave kinetic energy by the turbulent motion is the only significant source of transfer between orbital and turbulent motions However, subsequent experimental data (Terray and Bliven 1985) have shown that the corresponding term in the K balance is in fact negligible Furthermore, this mechanism can only act with random waves in contradiction with the second group of results which is showing that the interactions are efficient even with periodic waves. Thus it is clear that other mechanisms must exist Among them of course, wave breaking is supposed to play a very important role However in the two sets of experiments previously mentioned, wave breaking was unsignificant Another possibility, based on the creation of an orbital component of the vorticity field has been explored by Magnaudet (1989)

2 THEORETICAL ANALYSIS

In order to summarize this mechanism, let us consider the basic case of a periodic wave with wave-number k propagating at the surface of the water in the direction x The wave is sheared by the wind which also creates a mean current and generates turbulence A frame of reference moving with the velocity c of the wave is used in order to freeze the shape of the free surface This allows us to define a phase average ($\langle\ \rangle$) of each variable which only depends on spatial coordinates Then the triple decomposition (Reynolds and Hussain 1972) is used to write exact balance equations for the mean ($\bar{\ }$), orbital ($\tilde{\ }$) and turbulent ($'$) motions In this approach the orbital velocity $\tilde{\mathbf{v}}$ is defined as the part of the velocity field which is periodic in x with the wavelength $2\pi/k$, no assumption is made concerning the dynamical properties of $\tilde{\mathbf{v}}$ Defining the orbital vorticity $\tilde{\omega} = \nabla \times \tilde{\mathbf{v}}$, the mean momentum balance writes

$$(\bar{\mathbf{V}} - \mathbf{c})\,\nabla \bar{\mathbf{V}} = -\nabla\left(\bar{P}/\rho + \frac{\overline{\tilde{v}^2}}{2}\right) + \nabla\,(\nu \nabla \bar{\mathbf{V}} - \overline{\mathbf{v}'\mathbf{v}'}) - \overline{\tilde{\omega} \times \tilde{\mathbf{v}}} \quad (1)$$

Thus the effect of waves on the mean flow can appear either through a modification of the Reynolds stress tensor $\bar{\mathbf{R}} = \overline{\mathbf{v}'\mathbf{v}'}$ or through the vortex term $\overline{\tilde{\omega} \times \tilde{\mathbf{v}}}$ The $\bar{\mathbf{R}}$ balance may be written

$$\frac{D\bar{R}_{ij}}{Dt} = P_{ij} - \varepsilon_{ij} + \Phi_{ij} + D_{ij} - (\overline{v'_i v'_k \tilde{v}_{j,k}} + \overline{v'_j v'_k \tilde{v}_{i,k}} + (\overline{v'_i v'_j \tilde{v}_k})_{,k}) \quad (2)$$

where P_{ij}, ε_{ij}, Φ_{ij} and D_{ij} represent the usual production, dissipation, pressure-strain and diffusion terms Two kinds of extra terms due to wave-turbulence interactions appear in the $\bar{\mathbf{R}}$ balance they represent the production of turbulence by the gradients of $\tilde{\mathbf{v}}$ and the diffusion of turbulence by $\tilde{\mathbf{v}}$ but it can be shown by an order of magnitude analysis that they are not large enough to modify strongly $\bar{\mathbf{R}}$. So in the following it will be shown that the increase of the turbulence level can be explained by the vortex-term $\overline{\tilde{\omega} \times \tilde{\mathbf{v}}}$

First of all we have to examine the $\tilde{\omega}$ balance

$$(\overline{V} \cdot \nabla)\tilde{\omega} = \nabla\times[\overline{\tilde{\omega}\times\tilde{v}} - \tilde{\omega}\times\tilde{v}] + \tilde{\omega}\cdot\nabla\overline{V} - \nabla\times(\overline{\tilde{\omega}}\times\tilde{v}) - \nabla\times[\nabla\cdot(\tilde{v}'\tilde{v}')] + \nu\nabla^2\tilde{\omega} \quad (3)$$

(1) (2)

(1) and *(2)* are the two source terms which can create an orbital component of the vorticity It is worth noting that, in contrast with the study of coherent structures where equation (2) is untractable analytically, the situation is much more comfortable here because

- at first order (without wind) $\tilde{v}$ is potential and can be found using the Stokes expansion for gravity waves,

- the problem is periodic in the direction of the primary mean flow (x)

In order to solve (1) it is necessary to model $\tilde{R} = \tilde{v}'\tilde{v}'$ which represents the variations of the Reynolds stress along the wave profile This question has been thoroughly studied by several authors either in the context of turbulent flows excited by an oscillatory plate (Hussain and Reynolds 1970, Reynolds and Hussain 1972) or in order to describe the boundary layer *over* gravity waves (Davis 1970 and 1972, Thorsness et al 1978)

Since the $<\tilde{R}>$ balance and consequently the $\tilde{R}$ equation contain a lot of non-linear terms, this equation cannot be used safely in an analytical approach Thus the simplest way of going further is to assume an eddy viscosity relation for the phase-averaged Reynolds stress tensor

$$<R> = 2/3 < K > 1 - 2 < \nu_T > < S > \quad (4)$$

where $<S>$ denotes the phase averaged rate of strain tensor

$$< S >= 1/2\,(\nabla<V> + {}^t\nabla<V>)$$

This closure assumption is of course very restrictive and must be understood like a model from which consequences can be examined and not like an unquestionable physical representation From (4) we derive

$$\tilde{R} = 2/3\,\tilde{K}1 - 2\,\tilde{\nu_T}\,\overline{S} - 2\,\overline{\nu_T}\,\tilde{S} + 2\,(\tilde{\nu_T}\tilde{S} - \overline{\tilde{\nu_T}\tilde{S}}) \quad (5)$$

It can be shown (Magnaudet 1989) that to first order with respect to small parameters (to be defined later) and excepted in a very thin layer below the free surface, (5) implies

$$\tilde{R} = 2/3\,\tilde{K}1 - 2\,\overline{\nu_T}\,\tilde{S} \quad (6)$$

This means that the principal effect of the waves on the spatial structure of the turbulent field is to redistribute the Reynolds stresses This is in agreement with the conclusions of Reynolds and Hussain (1972) and Davis (1972) who obtained satisfactory results using (6) Introducing (6) in the $\tilde{\omega}$ balance leads to

$$-(\nabla\times[\nabla\cdot(\tilde{R})])_i = (\overline{\nu}_T\,\tilde{\omega}_{i,j})_j + \overline{\nu}_{T,j}(\tilde{\omega}_{j,i} - \tilde{\omega}_{i,j}) + 2\varepsilon_{ijk}\,\overline{\nu}_{T,l}\tilde{S}_{kl} \quad (7)$$

The first term on the right hand side represents the classical Taylor model for the diffusion of vorticity whereas the two other terms take into account the stretching mechanisms associated with scales changes in inhomogeneous turbulence (Tennekes and Lumley 1972) Introducing the wave steepness ε and the dimensionless mean shear rate $\delta = (\overline{S}\,\overline{S})^{1/2}/ck$ and assuming these two parameters to be small, it becomes possible to perform an asymptotic expansion of (3) The resulting equation obtained at leading order $\varepsilon\delta$ writes with dimensionless variables

$$\tilde{\omega}^*_{i,x^*} = \varepsilon\delta\,(\overline{\omega}^*_k\,\tilde{v}^*_{i,k^*} - \tilde{v}^*_k\,\overline{\omega}^*_{i,k^*} + 2\varepsilon_{izk}\,\overline{\nu}^*_{i,z^*z^*}\,\tilde{\Omega}^*_{kz}) \quad (8)$$

(8) can then be integrated and the final result is attained (Magnaudet and Masbernat 1990)

$$\tilde{\omega} = \nabla\times(\overline{\omega}\times\int\frac{\tilde{v}}{c}dx) + 2\,\overline{\nu}_{T,zz}\,\frac{\tilde{w}}{c}\,e_y \quad (9)$$

(z denotes the vertical axis directed upwards and y the spanwise axis , e_y is the unit vector in the y direction)

This equation demonstrates that when surface waves are superimposed on a mean turbulent shear flow the periodic motion cannot remain strictly irrotational because of two kinds of interactions

- the first term was found previously by Craik and Leibovich (1976) Craik (1977) showed that, due to a spanwise instability mechanism, this term generates large x-axis mean vortices known as Langmuir circulations the basic one-dimensional mean current is unstable and the steady mean motion is an helical one This is typically a three-dimensional aspect of wave-mean current interactions which will be disregarded here

- the second term arises from wave-turbulence interactions : it shows that when an inhomogeneous turbulence (such as the one present in the surface boundary layer) and a periodic plane strain (due to the wave motion) exist together, they interact and produce a periodic spanwise component of the vorticity at the wavenumber of the strain
This means that the total amount of energy associated with wavenumber k below a train of surface waves is the sum of three components one corresponds of course to the potential motion induced by the waves (this is the common definition of the orbital motion), the second is due to the classical turbulence induced by the wind stress and the third one is the result of a non-zero value of $\tilde{\omega}$ From an experimental point of view this means that any filtration technique where the orbital motion is defined with the aid of a Bernoulli equation will lead to a "turbulent" spectrum with a peak arising from wave-turbulence interactions This is indeed the case as was recently found with a non-linear filtration method by Jiang et al (1990)

Let us now turn to the consequences of (9) on the mean flow Using boundary layer assumptions the mean vortex-term $\overline{\tilde{\omega}\times\tilde{v}}$ reduces to $\overline{\tilde{\omega}\times\tilde{v}} = \overline{\tilde{u}\tilde{w}}_{,z}$ so that (9) can be integrated to obtain with the aid of the Airy solution for water waves :

$$\overline{\tilde{u}\tilde{w}} = -2\,\overline{\nu}_{T,z}\,\frac{\overline{\tilde{w}^2}}{c} = -\varepsilon^2\,\overline{\nu}_{T,z}\,c\,e^{2kz} \quad (10)$$

Since $\tilde{u}\tilde{w}'$ vanishes on the free surface as will be shown later, $\overline{\nu_T}$ must also vanish on the interface Since in the bulk $\overline{\nu_T}$ is mainly positive, there is a region near the interface where $\overline{\nu_T}_{,z} < 0$ so that, following (10), $\overline{\tilde{u}\tilde{w}}$ must be positive This is in complete agreement with the experimental results of Cheung and Street (1988) showing a positive $\overline{\tilde{u}\tilde{w}}$ over a significant depth below the waves It is worth noting that $\overline{\tilde{u}\tilde{w}} > 0$ means that the mean flow extracts energy from the orbital motion as it often occurs when coherent structures exist in a turbulent flow.

Let us now consider the turbulence production. The approximate mean momentum balance (to first order in the wave steepness) writes :

$$-\overline{u'w'} = u^{*2} + \overline{\tilde{u}\tilde{w}} \quad (11)$$

This shows that the turbulent shear stress is enhanced by the interaction Since $-\overline{u'w'}$ governs turbulence production in

shear layers it seems reasonable to expect a higher ratio $\overline{K}/u^{*2}$ in the present situation than in usual flows It must be noted that, due to the fact that the typical wave energy $\varepsilon^2 c^2$ is generally much greater than u^{*2}, weak interactions which do not modify seriously the orbital motion can completely change the turbulent balance The efficiency of this mechanism in terms of turbulence level was first demonstrated with the aid of a very simple one-dimensional numerical model solving (10) - (11) together with a K- ε model (ε meaning here the dissipation rate of K) (Magnaudet et al , 1991) The results obtained using the experimental parameters of Cheung and Street have shown to be promising More precisely a ratio K/u^{*2} ranging between 9 and 12 was obtained near the mean interface in accordance with the experimental levels

3 NUMERICAL APPROACH

In this section are presented the first results of a full numerical approach which was carried on in order to check the previous theory and to explore more carefully various aspects of wave-turbulence interactions without all the limitations inherent to the analytical expansions In this first step the three-dimensional aspect of wave-current interactions is disregarded and we focus as previously on wave-turbulence interactions

For this purpose, the two-dimensional Reynolds phase-averaged equations are solved below a prescribed Stokes wave As we want to describe accurately the interfacial zone, the equations are written in a curvilinear orthogonal system of coordinates moving with the phase velocity c This curvilinear system is identical to the one used by Gent and Taylor (1976) or Al-Zanaidi and Hui (1983) in numerical investigations of wind-waves generation Thus we solve

$$\nabla \langle V \rangle = 0 \tag{12a}$$

$$(\langle V \rangle - c)\, \nabla \langle V \rangle = - \nabla \langle P \rangle / \rho + \nabla\, (\nu \nabla \langle V \rangle - \langle v'v' \rangle) \tag{12b}$$

Denoting by **n** and **t** the normal and tangential unit-vectors respectively, the boundary conditions on the free surface $z = \eta(x)$ write

$$(\langle V \rangle - c)\, \mathbf{n} = 0 \tag{13a}$$

$$\mathbf{t}\ \nu (\nabla \langle V \rangle + {}^t \nabla \langle V \rangle)\, \mathbf{n} = u^{*2} \tag{13b}$$

The bottom of the domain ($z = - H$) is considered as a symmetry plane and periodic conditions are imposed on $\langle P \rangle$ and $\langle V \rangle$ at $x = 0$ and $x = 2\pi/k$ A linear term $\frac{2\pi}{kH} u^{*2}$ has to be added to the pressure in order to represent the hydrostatic effect of the mean slope of the free surface It must be noted that, since the interface has a prescribed form, it is not possible to satisfy a constant pressure condition on $z = \eta(x)$ together with the kinematic condition (13a). However the phase velocity c can be calculated by minimizing the surface integral

$$I(c) = \int_0^{2\pi/k} | \mathbf{t} \cdot \nabla \langle P \rangle |^2 ds$$

The solution of equations (12a)-(12b) is obtained by means of a second-order accurate finite volumes technique using a velocity-pressure formulation on a staggered grid The momentum equations are solved with an explicit predictor-corrector method (the Brailovskaya scheme) whereas the divergence-free condition is satisfied by means of a fully implicit Poisson equation

4 TURBULENCE MODELING

The representation of the phase-averaged Reynolds stress tensor is achieved by means of one-point closures In this preliminary study only very simple models of the K-ε type were used However these models must take into account the specificities of interfacial turbulence contrarily to a solid wall behavior, turbulent fluctuations exist on the interface at least with clean water Let us consider first a shear-free interface The boundary conditions for the turbulent fluctuations write

$$\mathbf{v}' \cdot \mathbf{n} = 0 \tag{14a}$$

$$\mathbf{t}\ \nu (\nabla \mathbf{v}' + {}^t \nabla \mathbf{v}')\, \mathbf{n} = 0 \tag{14b}$$

Then denoting by u', v' and w' the turbulent velocity fluctuations parallel and normal to the free surface respectively and by x, y and z the corresponding coordinates, it becomes possible (with the aid of the continuity equation) to expand the fluctuations with respect to z within the form (Hunt 1984)

$$u'(x,y,z,t) = a_0(x,y,t) + a_2(x,y,t) z^2 +$$

$$v'(x,y,z,t) = b_0(x,y,t) + b_2(x,y,t) z^2 +$$

$$w'(x,y,z,t) = c_1(x,y,t)\, z + c_3(x,y,t) z^3 +$$

Thus the exact $\langle K \rangle$ and $\langle \varepsilon \rangle$ boundary conditions on $z = \eta(x)$ write (Magnaudet 1989)

$$\frac{\partial \langle K \rangle}{\partial n} = 0 \tag{15a}$$

$$\frac{\partial \langle \varepsilon \rangle}{\partial n} = 0 \tag{15b}$$

Of course when a wind is blowing over the free-surface, fluctuations occur in the surface stress so that condition (14b) does not remain exact However the ratio between the viscosities of water and air is high enough to keep (14b) and the subsequent conditions (15) as an accurate approximation Furthermore, combining conditions (15) with the previous asymptotic expansions leads to the remarkable statement that all the flux-terms in the $\langle K \rangle$ and $\langle \varepsilon \rangle$ balances (written under an integral form) are exactly zero on the free surface This is straightforward, due to the boundary condition (13a), for the advective terms $\int \langle K \rangle (\langle V \rangle - c)\, \mathbf{n}\, ds$ and $\int \langle \varepsilon \rangle (\langle V \rangle - c)\, \mathbf{n}\, ds$ and, due to (14a)-(15a), for the diffusive term of the $\langle K \rangle$ balance $\int (- \langle K' \mathbf{v}' \cdot \mathbf{n} \rangle - \langle \frac{p'}{\rho} \mathbf{v}' \cdot \mathbf{n} \rangle + \nu \frac{\partial \langle K \rangle}{\partial n}) ds$

It can be also shown with the aid of the w' momentum balance that $\frac{\partial p'}{\partial n} = 0$ on the free surface due to the fact that $\frac{\partial^2 (\mathbf{v}' \cdot \mathbf{n})}{\partial n^2} = 0$ (because w' does not contain any z^2 term) This leads to the result that the diffusive term of the $\langle \varepsilon \rangle$ equation

$\int (- \langle \varepsilon' \mathbf{v}' \cdot \mathbf{n} \rangle - 2\nu \langle \frac{\nabla p'}{\rho} \nabla (\mathbf{v}' \cdot \mathbf{n}) \rangle + \nu \frac{\partial \langle \varepsilon \rangle}{\partial n}) ds$ also vanishes at the interface

Taking these results into account and setting the modeling constants to their classical values (Rodi 1980), the $\langle K \rangle$-$\langle \varepsilon \rangle$ system is solved with the method previously described for the momentum equations

5 DISCUSSION OF THE RESULTS

The computations allow a detailed investigation of several quantities of interest including the mean current $\overline{U}(z)$ (Fig 1), the orbital velocities $\tilde{u}$, $\tilde{w}$, the turbulent mean shear stress $-\overline{u'w'}$ (Fig 2), the correlation $\tilde{u}\tilde{w}$ (Fig 3), the mean turbulent kinetic energy $\overline{K}$ (Fig 4), ..It must be kept in mind that $\overline{\ }$ denotes here a spatial average following the curvilinear x axis so that the averaging procedure is carried out at a constant distance from the real interface and not at a constant distance from the mean surface level

The value found for the eulerian surface drift $\overline{U}(0)$ is about $13.0\, u^*$ which is in qualitative agreement with experimental results exhibiting for the lagrangian drift $\overline{U_L}(0)$ values of about $15.8\, u^*$, more commonly expressed as $\overline{U_L}(0) = 0.55\, u^*_A$ (Phillips and Banner 1974) (u^*_A denoting the friction velocity in the air). The analysis of the $\overline{U}(z)$ profile shows that a

logarithmic region exists, the Von Karman constant κ being equal to 427 This value does not agree with the results of Cheung (1985) showing $6 \leq \kappa \leq 8$ depending on the waves characteristics This desagreement is probably due to the c_ε constant associated with the diffusion term of the ε equation this constant ($c_\varepsilon = 1\,3$) is determined by the requirement that production balances dissipation in the near wall region and the classical value of κ is explicitely used in this determination

Concerning $\widetilde{u}\widetilde{w}$, the results confirm the existence of an important region of the flow where this correlation is positive in agreement with (10) A thin layer where $\widetilde{u}\widetilde{w} < 0$ is also shown to exist in the immediate vicinity of the interface due to the large variations of the eddy viscosity along the wave profile in this region (the $\widetilde{\nu_T}$ terms of equation (5) which have been neglected in equation (6)) This layer will be studied in a following paper The behavior of $-\overline{u'w'}$ is quite complex because this quantity is influenced by the existence of the correlation $\widetilde{u}\widetilde{w}$ as well as by the centrifugal terms resulting from the curvature of the interface

The most important result concerns of course, the $\overline{K}$ level It can be seen that, for the set of parameters specified in this run (wavelengh $\lambda = 2\pi/k = 1$ m, wave amplitude a = 012 m, phase velocity $c = 1\,25\ ms^{-1}$, $Re = 2ac/\nu = 3\ 10^4$, friction velocity in the water $u^* = 01\ ms^{-1}$) the maximum value of $\overline{K}/u^{*2}$ is about 19 0, nearly 5 times the maximum value near a solid wall It must be noted that the maximum value obtained for $\widetilde{u}\widetilde{w}/u^{*2}$ is about 0 1 and that such a rather weak value is able to modify completely the turbulence level The influence of the free surface boundary conditions derived for $\langle K \rangle$ and $\langle \varepsilon \rangle$ is seen to be rather weak since, right at the interface, $\overline{K}/u^{*2}$ is damped to about 4 0

The values obtained for the $\overline{K}/u^{*2}$ level must be confirmed with the aid of improved turbulence models taking into account the complete real behavior of turbulent fluctuations near a free surface and especially the anisotropy between the normal and the tangential components Nevertheless they agree qualitatively well with the previously cited measurements Furthermore, they demonstrate that the turbulence level is highly influenced by the creation of a positive correlation $\widetilde{u}\widetilde{w}$

So, the theoretical mechanism based on the generation of $\widetilde{\omega}$ by means of wave-turbulence interactions is confirmed to be a good candidate in order to explain the level of turbulence below wind waves

REFERENCES

AL-ZANAIDI M A & HUI W H 1984, Turbulent air flow over water waves A numerical study, *J Fluid Mech* **148**, 225-246

BENILOV, A Y 1973, On the generation of turbulence in the ocean by surface waves, *Izv Acad Sci USSR, Ser Atmos Ocean Phys* **9**, 293-303

BENILOV, A Y , KOUZNETSOV, O A & PANIN, G N 1974, On the analysis of wind wave-induced disturbances in the atmospheric boundary layer, *Boundary Layer Met* **6**, 269-285

CHEUNG, T K. 1985, A study of the turbulent layer in the water at an air-water interface, *Tech Rep 287, Dpt Civ Eng*, Stanford University.

CHEUNG, T.K. & STREET, R L 1988, The turbulent layer in the water at an air-water interface, *J Fluid Mech* **194**, 133-151

CRAIK A D D 1977, The generation of Langmuir circulations by an instability mechanism, *J Fluid Mech* **81**, 209-223

CRAIK, A D D & LEIBOVICH, S 1976, A rational model for Langmuir circulations, *J Fluid Mech* **73**, 401 426

DAVIS R.E 1970, On the turbulent flow over a wavy boundary, *J Fluid Mech* **42**, 721-731.

DAVIS R E 1972, On prediction of a turbulent flow over a wavy boundary, *J Fluid Mech* **52**, 287-306

GENT P R &TAYLOR P A 1976, A numerical model of the air flow above water waves, *J Fluid Mech* 77, 105-128

HUNT J C R 1984, Turbulent structure and turbulent diffusion near gas-liquid interfaces, in *Gas Transfer at Water Surfaces*, Brutsaert & Jirka ed , D Reidel Publishing Company

HUSSAIN, A K M F & REYNOLDS, W C 1970, The mechanics of an organized wave in a turbulent shear flow, *J Fluid Mech* **41**, 241-258

JIANG J Y , STREET R L , KLOTZ S P 1990, A study of wave -turbulence interaction by use of a nonlinear water wave decomposition technique, *J Geo Res* **95**, 16037-16054

KITAIGORODSKII, S A K , DONELAN, M A , LUMLEY J L & TERRAY, E A 1933, Wave-turbulence interactions in the upper ocean Part II Statistical characteristics of wave and turbulent components of the random velocity field in the marine surface layer, *J Phys. Ocean* **13**, 1988-1999

KITAIGORODSKII, S A.K. & LUMLEY, J L 1983, Wave turbulence interactions in the upper ocean Part I The energy balance of the interacting fields of surface wind waves and wind-induced three-dimensional turbulence, *J Phys Ocean* **13**, 1977-1983

KITAIGORODSKII, S A K & MIROPOLSKII Y A 1968, Turbulent energy dissipation in the ocean surface layer *Izv Acad Sci USSR, Ser Atmos. Ocean. Phys* **4**, 647-659

MAGNAUDET, J 1989, Interactions interfaciales en écoulement à phases séparées, *PhD Thesis*, INP Toulouse

MAGNAUDET J , GEORGE J., MASBERNAT L., CAUSSADE B 1991, Turbulence level below wind waves and its relation with absorption, to appear in *J Environ. Eng. (ASCE Trans)*

MAGNAUDET, J & MASBERNAT, L 1990, Interactions des vagues de vent avec le courant moyen et la turbulence, *CRAS Paris série II* **311**, 1461-1466

PHILLIPS O M & BANNER M L 1974, Wave breaking in presence of wind drift and swell, *J Fluid Mech* **66**, 625-640

REYNOLDS, W.C. & HUSSAIN, A K M F 1972, The mechanics of an organized wave in a turbulent shear flow. Part 3 Theoretical models and comparisons with experiments, , *J Fluid Mech.* **54**, 263-288

RODI, W. 1984, Examples of turbulence-models applications, *Turbulence models and their applications*, Eyrolles

TENNEKES, & LUMLEY J L 1972, *A First Course in Turbulence*, MIT Press.

TERRAY, E A. & BLIVEN, L.F. 1985, The vertical structure of turbulence beneath gently breaking waves, *The Ocean Surface*, Toba & Mitsuyasu ed , D Reidel Publishing Company

THORSNESS C.B., MORRISROE P E & HANRATTY T.J 1978, A comparison of linear theory with measurements of the variation of shear stress along a solid wave, *Chemical Eng Sc.* **33**, 579-592.

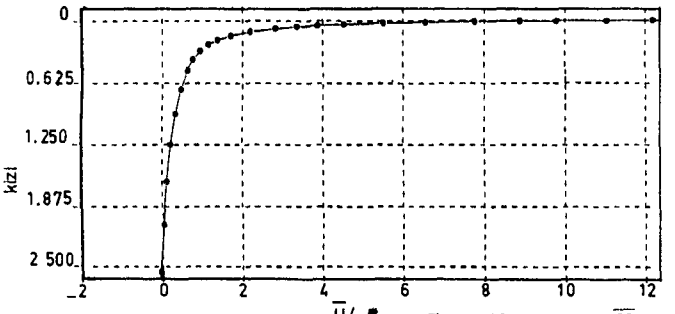

Fig 1. Mean current $\overline{U}$

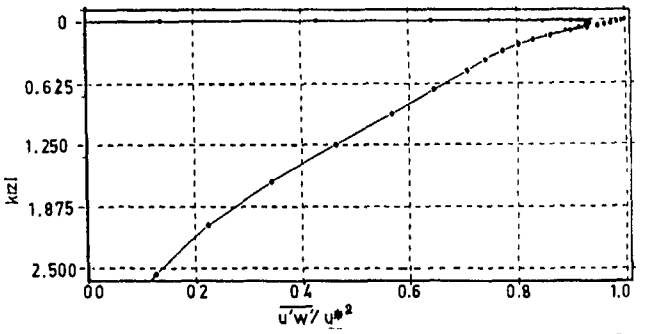

Fig 2. Turbulent shear stress - $\overline{u'w'}$

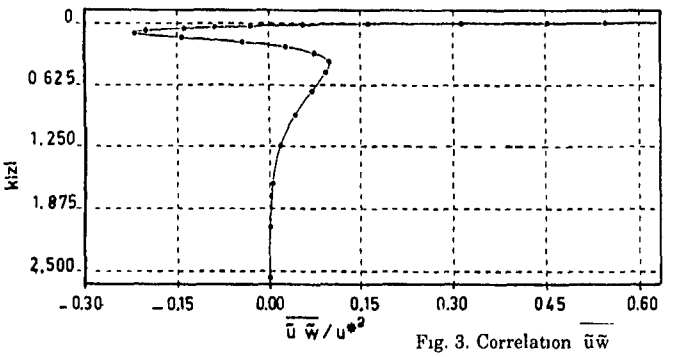

Fig. 3. Correlation $\overline{\tilde{u}\tilde{w}}$

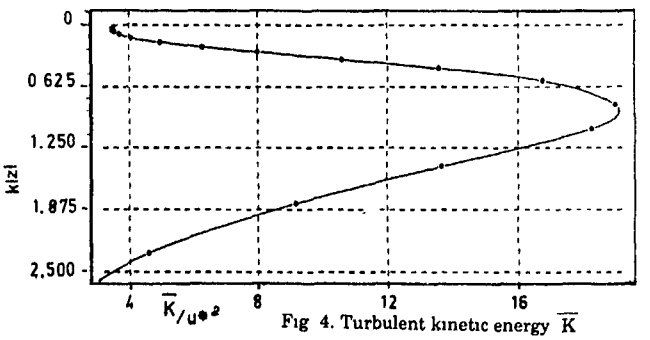

Fig 4. Turbulent kinetic energy $\overline{K}$

EIGHTH SYMPOSIUM ON
TURBULENT SHEAR FLOWS
Technical University of Munich
September 9-11, 1991

ESTIMATION OF EDDY CHARACTERISTICS FROM TIME SERIES USING LOCALIZED TRANSFORMS

L Mahrt and J Howell

Atmospheric Sciences
Oregon State University
Corvallis, Oregon 97331 USA

ABSTRACT

We examine the physical characteristics of local transforms to decompose coherent turbulent structures extracted from time series or numerical data. The windowed Fourier transform, the wavelet transform and decomposition into eigenvectors of the lagged covariance matrix are compared by projecting the latter two decompositions onto Fourier space The results are applied to turbulence time series from the Lammefjord experiment. The eigenvector decomposition is able to separate the variances due to the coherent eddy microfronts from that due to the random fine scale structure. In the Fourier spectrum, both appear together at the higher wavenumbers and their individual contributions cannot be separated. Other advantages and disadvantages of the eigenvector and wavelet decomposition are noted.

1 INTRODUCTION

Because turbulent eddies are local and nonperiodic, the usual Fourier decomposition into trigonometric functions can be physically ambiguous (Tennekes, 1976). The aperiodic local behavior is particularly evident in the spatial variations of the flux which is more intermittent and event-like compared to variances (Haugen et al, 1971; Shaw and Businger, 1985).

The study of turbulent structures or events in time series can be posed in terms of local transforms or decompositions which are local in contrast to conventional global decompositions such as the Fourier transform (Figure 1). Local decompositions include the windowed Fourier transform (Gabor transform), the wavelet transform (Daubechies, 1988; Mallet, 1989; Grossmann, et al, 1989; Meyer, 1989) and decomposition into eigenvectors of the lagged covariance matrix (Busch and Petersen, 1971; Lumley, 1970; Panofsky and Dutton, 1984; Sirovich, 1988, Mahrt and Frank, 1988). Eigenvectors of the lagged covariance matrix are also referred to as empirical orthogonal functions. For historical reasons, the above local decomposition techniques have enjoyed application in specific and separate areas of research. The main goal of this paper is to compare the different techniques by applying them to the same data.

The basis sets for the windowed Fourier transform and wavelet transforms are specified while the basis set for the eigenvector decomposition is determined by the data. In this sense the eigenvector decomposition is more "natural". The cost of this flexibility is the large number of samples required to adequately estimate the lagged covariance matrix. The number of eigenvectors which are statistically significant depends on the sample size. If the events are not phase-locked into the same relative position within each sample, then the eigenvectors approach sines and cosines in the limit of random phase

Therefore the eigenvector approach applied to time series requires a conditional sampling procedure In contrast the wavelet transform can be applied as a simultaneous sampling and decomposition analysis.

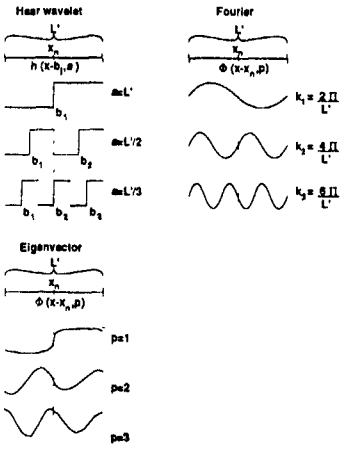

Figure 1. The first three basis functions for the different decomposition methods The eigenvectors are from the data set described in Section 5

The eigenvector decomposition maximizes covariance explained with the fewest number of modes As a result, discarding the less important eigenvectors often serves as an efficient filter which removes noise. Such eigenvector filtering can preserve the sharp edges of the main structures in contrast to windowed Fourier decomposition where the sharp edges of the main structures and the noise both appear at high frequencies. Since the eigenvectors maximize explanation of the lagged covariance, the leading eigenvectors are generally less noisy than a simple composited average of the structures. In some cases the simple composite is an average of the leading types of structures and therefore is not similar to any of the individual structures. The eigenvectors seem to have the ability to sort out different types of structures although such a capability is not mathematically guaranteed. The extension to the multivariate case is straight forward (Petersen, 1976).

A principal advantage of the wavelet transform is localization where the resolution or spacing of the transform decreases with decreasing scale That is, small scale features are decomposed with finer spatial resolution compared to large scale features The wavelet transform contains the additional flexibility of specification of the basis function in terms of the physical goal of the analysis For example, symmetric basis functions might be applied to study large deviations from the local mean while asymmetric basis functions might be specified to study sharp changes or edges in the signal The nonorthogonal wavelet transform with spatial oversampling can be applied to enhance spatial phase resolution or a nonorthogonal wavelet transform can be constructed to provide higher spatial resolution

Advantages of the windowed Fourier transform are inherited from the global Fourier transform Advantages include universitality as a standard of comparison and the fact that derivatives of the basis functions lie in the same basis. The latter is especially useful for studies in connection with dynamical systems based on differential equations

2 LOCAL DECOMPOSITION

We assume that samples of coherent structures of width L' have been selected in terms of some form of conditional sampling or generating process For example, such sampling might seek thermals, vortices or eddy microfronts. We then decompose the samples into different scales in terms of a local transform of the sample $f(x - x_n)$ where x_n designates the position of the center of the n^{th} sample. The samples $f(x - x_n)$ can be multivariate

Mathematically, we can expand the sampled structure centered at $x = x_n$ in terms of a discrete basis set defined over the interval $x = [x_n - L'/2, x_n + L'/2]$. In the case of windowed Fourier bases and eigenvector basis, the decomposition of the n^{th} sample can be written as

$$f(x-x_n) = \sum_p W\{f(x-x_n),p\}\,\phi\,[x-x_n, p] + \text{error} \qquad (1)$$

$$x = [x_n - L'/2, x_n + L'/2].$$

where f is the basis function and the sum in (1) is performed over the P basis functions $W\{f(x), p, b\}$ are the transform coefficients defined as

$$W\{f(x-x_n),p\} = (1/M)\sum_m g(x-x_n)\phi[(x-x_n),p]f(x-x_n) \qquad (2)$$

$$L' = M\,\Delta x$$

where the sum in (2) is defined for a given basis function over the M points in the sample window of width L' and Δx is the interval between data points The value of the transform is proportional to the amplitude of the structure contained in $f(x - x_n)$ and its similarity to the shape of the basis function. The error in (1) is due to possible incompleteness of the transform or intentional discarding of terms to remove noise in which case the first term on the right hand side of (1) acts as a filter on the original signal.

For the windowed Fourier transform, the basis functions $\phi[(x-x_n),p]$ are defined as sines and cosines, where a is the wavelength, and $g(x-x_n)$ is the windowing function (Daubechies, 1988) In Section 3, we consider the discrete Fourier transform where $g(x-x_n)$ is everywhere one When the basis functions are the eigenvectors of the lagged covariance matrix computed from the samples themselves, $g(x-x_n)$ is also everywhere one and $p = 1, 2 \ldots M$ is the eigenvector number The first eigenvector maximizes sample covariance-explained, the second eigenvector maximizes explanation of the remaining covariance of the samples and so forth

With the above class of decompositions, each of the P basis functions $\phi[(x-x_n),p]$ generates only one transform coefficient $W\{p, f(x - x_n)\}$ for each sample In the orthogonal wavelet transform, the basis function of width ("dilation") a generates L'/a coefficients for each sample as the transform incrementally translates through the sample at an increment of a (Figure 1) The center positions of the transforms for dilation scale a are then

$$b_j = (x_n - L'/2) + (j - 1/2)a\,; \quad j = 1 \ldots L'/a \qquad (3)$$

Consequently the transform provides higher spatial resolution at smaller scales (smaller a) at the expense of more coefficients compared to the Fourier and eigenvector expansions

The expansion of the original signal into the wavelet basis set can then be written as

$$f(x - x_n) = G(x_n)\sum_a \sum_j W\{f(x-x_n),a,b_j\}\,h[x-b_j,a] + \text{error} \qquad (4)$$

$$x = [x_n - L'/2, x_n + L'/2].$$

where $h[x-b_j,a]$ is the basis function defined to be nonzero over the interval $[b_j - a/2 \le x \le b_j + a/2]$ and $W\{f(x-x_n),a,b_j\}$ is the wavelet transform defined as

$$W\{f(x-x_n),a,b_j\} = (1/M)^{1/2}\sum_m h[(x-b_j),a]f(x-x_n) \qquad (5)$$

where $G(x_n)$ is a normalization factor required for nonorthogonal wavelet expansions (Daubechies, 1988) here equal to unity and M is now the number of points in the transformation interval of width $a \le L'$. The division of the sum in (2) by $M^{1/2}$ provides the transform with a conservation of energy property.

For comparison with Fourier and eigenvector decompositions, it will be necessary to compute the variance or energy of the wavelet transform at a given scale a by summing over the different positions of the transform

$$\text{Var}\,[f(x-x_n),a] = \sum_j W^2\{f(x-x_n),a,b_j\} \qquad (6)$$

The dependence of $\text{Var}\,[f(x-x_n),a]$ on the dilation scale a provides the distribution of the variance of $f(x-x_n)$ over the different scales and is the quantity most comparable to the coefficients of the Fourier decomposition and coefficients of the eigenvector decomposition

4 EIGENVECTOR DECOMPOSITION IN FOURIER SPACE

We begin with the comparison between the eigenvector and Fourier decomposition of the covariance between two variables $f_1(x-x_n)$ and $f_2(x-x_n)$ for the n^{th} turbulent structure. This covariance can be projected onto the eigenvector basis set

$$[f_1(x-x_b)\, f_2(x-x_b)] = \sum_p \sum_s [a(p,n)\, \phi_1(p,x-x_n)\, a(s,n)\, \phi_2(s,x-x_n)] + \text{error} \quad (7)$$

Here we compute the eigenvectors for the two variables simultaneously by stacking variables into one observational vector (Petersen, 1976) to study the total lagged covariance between the variables. Then $\phi_1(p,x-x_n)$ and $\phi_2(p,x-x_n)$ are the parts of the eigenvector associated with $f_1(x-x_n)$ and $f_2(x-x_n)$, respectively and the expansion coefficient $a(p,n)$ applies to the entire eigenvector.

To compute the total covariance for the population of sampled structures, we average (7) over the N samples and note that the expansion coefficients for the different eigenvectors are uncorrelated. We then obtain

$$(1/N)\sum_n [f_1(x-x_n)\, f_2(x-x_n)] = \sum_p \mathrm{Var}(a_p)[\phi_1(p,x-x_n)\, \phi_2(p,x-x_n)] \quad (8)$$

$$\mathrm{Var}(a_p) = (1/N)\sum_n a^2(p,n) \quad (9)$$

The covariance for a given eigenvector is proportional to the energy attributed to the eigenvector, as represented by the square of the expansion coefficient (9). The covariance is also proportional to the correlation between the two parts of the eigenvector corresponding to the respective variables in the covariance.

For comparison, the eigenvector decomposition can be projected onto a more traditional basis set (Sirovich, 1988) such as sines and cosines. The decomposition of the pth eigenvector for variable $f_1(x-x_n)$ into a Fourier series can be written as

$$\phi_1(p,x') = \sum_r A(r,p,1)\sin(k_r x') + B(r,p,1)\cos(k_r x') \quad (10)$$

$$k_r = 2\pi\, r/L'$$
$$x' = x-x_n$$

where here A(r,p,1) and B(r,p,1) are the coefficients of the Fourier series for the pth eigenvector for variable 1. Substituting (10) and the analogous expression for $f_2(x-x_n)$ into the expression for within-sample covariance (8), we obtain

$$(1/N)\sum_n [f_1(x')\, f_2(x')] = \sum_p \mathrm{Var}(a_p)[(\sum_r A(r,p,1)\sin(k_r x') + B(r,p,1)\cos(r_n x')\{\sum_r A(r,p,2)\sin(k_r x') + B(r,p,2)\cos(k_r x')\}] + \text{error} \quad (11)$$

where the first sum on the right hand side is over the P eigenvectors, the square brackets again designate an average over the sample window and Var (a_p) is defined in (9).

Applying the orthogonality of the sine and cosine modes when averaged over the sampled structure, (11) becomes

$$(1/N)\Sigma_n [f_1(x')\, f_2(x')] = \sum_p \mathrm{Var}(a_p)\sum_r C^2(r,p) \quad (12)$$

where

$$C^2(r,p) = A(r,p,1)\, A(r,p,2)/2 + B(r,p,1)B(r,p,2)/2$$

represents energy of the p^{th} eigenvector described by the r^{th} Fourier mode. In the simpler example of decomposition of the variance where $f_2(x-x_n) = f_1(x-x_n)$, the product A(r,p,1) A(r,p,2) reduces to $A^2(r,p,1)$ and so forth.

A Fourier cospectra can be recovered by noting that Var (a_p) is independent of the Fourier wavenumber and switching the order of summation in (12) in which case we obtain

$$(1/N)\sum_n [f_1(x')\, f_2(x')] = \sum_r C_r^2 \quad (13)$$

where

$$C_r^2 = \sum_p \mathrm{Var}\,(a_p)\, C^2(r,p)$$

This decomposition of variance in the Fourier spectral domain relates the covariance in each Fourier mode to the contributions from the P different eigenmodes. Therefore the projections (12,13) show the relationship between the scale dependence based on the eigenvector decomposition and the scale dependence based on the Fourier modes.

5. JOINT DECOMPOSITION OF THE DATA

We apply the above joint decomposition to a 43 hour record of turbulence collected from the 45 m tower level in the Lammefjord experiment (Kristensen et al, 1989) during a relatively stationary period of strong winds. We select gust events by choosing samples centered about locations of maxima of the Haar transform (Mahrt and Frank, 1988) applied to the longitudinal velocity component. In this way the samples are centered about microfronts or zones of significant horizontal convergence. The transform is computed over the suspected scale of the main eddies, about 500 m. Here psuedo-distance is inferred from Taylor's hypothesis using a mean wind speed of 12 m/s. The 500 m wide samples are not allowed to overlap. This procedure selects 2976 samples which occupy slightly more than 50% of the record.

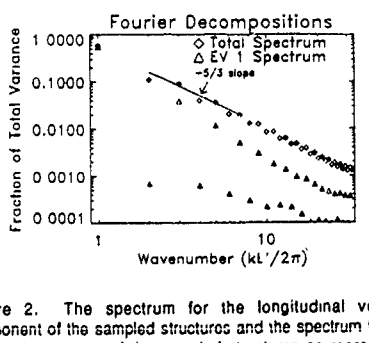

Figure 2. The spectrum for the longitudinal velocity component of the sampled structures and the spectrum for the main coherent part of the sampled structures as represented by the first eigenvector.

In this section, we decompose only the longitudinal velocity component. The first eigenvector explains 60% of the variance within the gust samples and is characterized by a sharp microfront across which the wind increases sharply with time (Figure 1). Such structure is expected from the sampling criteria. Because of the sharpness of the microfront, the energy associated with the first eigenvector spreads to higher wavenumbers in Fourier space (Figure 2). Since the shape of the first eigenvector is similar to the Haar function most of the spectral energy is in the odd wave numbers (The coefficients of the Fourier transform of the Haar function are zero for even wave numbers)

The eigenvector technique is able to separate out the variance due to the narrow microfront edges of the coherent parent eddies (which appears in the first eigenvector) from the more random fine scale structure which appears in the higher numbered eigenvectors. On the other hand in the Fourier transform, the energy due to both random fine scale structure and the eddy microfronts occur at high wavenumbers in a non-separable way. Even though the microfront zones are associated with main eddies, they may contribute directly to the energy dissipation without a sequential energy cascade to smaller scales.

Figure 2 also shows the total spectrum which has been computed for each sample and then averaged. The difference between the total within sample spectrum and the spectrum associated with the first eigenvector is due to the variation of the structure of the gusts between samples and due to the contribution of smaller scale eddies not represented by the first eigenvector The envelope of the spectra associated with the first eigenvector is near a 7/3 slope while the total within sample spectra is closer to a 5/3 slope. The main coherent structures represented by the first eigenvector contribute most of their energy to the low wave numbers but also contribute a systematic amount of energy to the high wave numbers.

The second and third eigenvectors appear more as trigonometric functions with wavelengths less than the window width L'. The expansion coefficients for the eigenvectors (a(p,n) in Eq 7) occur with either sign with equal probability. Since the eigenvectors for hypothetical structures with random phase are Fourier modes (Panofsky and Dutton, 1984), the samples can apparently be roughly approximated as a Haar function plus Fourier components with random phase. Higher order eigenvectors generally mimic smaller scale Fourier modes.

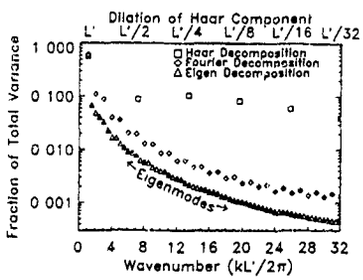

Figure 3. The decomposition of variance with respect to scale for the three decomposition approaches

The partitioning of energy between the different scales is shown in Figure 3 for each decomposition method The left side of the figure corresponds to the largest scale For the Fourier and wavelet transforms, the scale decreases systematically to the right while for the eigenvector decomposition, the scale *generally* decreases to the right. Consequently, the different decompositions are not numerically comparable Since the sample window contains 64 points, 64 eigenvectors are generated although only the first eigenvector contains more than 10% of the energy Each Fourier mode contains one coefficient for the real part and one coefficient for the imaginary part so that the 64 coefficients correspond to 32 different wavenumbers Even allowing for the fact that the Fourier decomposition requires two coefficients at each scale, the eigenvector vector decomposition converges faster with scale when summing the decomposition Disadvantages of the eigenvector decomposition are noted in the Introduction.

The Haar decomposition leads to 63 coefficients distributed over six different dyadic scales The variance at each scale in Figure 3 has been summed over the different subintervals by using (6). The Haar decomposition appears to contain more energy at the smaller scales compared to the other two methods This is due to the fewer number of wavelet dyadic scales which at smaller scales integrate information from a greater number of wavenumbers.

6 MULTIVARIATE STRUCTURE

The actual spatial structure of the first eigenvector in the preceding section is dictated mainly by sampling with the Haar basis function Therefore, we have also computed the eigenvectors of the *multivariate* lagged covariance matrix constructed from the three velocity components using the samples from the previous section. Given the samples centered about the microfronts in the longitudinal velocity component, what is the structure of the other two velocity components? For the first eigenvector (Figure 4), the structure of the vertical velocity component is similar to the shape of the longitudinal velocity component but smaller amplitude and characterized by large negative correlation with the longitudinal velocity component This corresponds to efficient downward transport of longitudinal momentum The first eigenvector explains 9% of the within-sample variance of the vertical velocity, 58% of the longitudinal velocity variance and 60% of the momentum flux. Consequently, the coherent part of the samples explain slightly more of the momentum flux than the longitudinal velocity variance even though the samples are selected in terms of the longitudinal velocity variance! Additional analyses not reported here also indicates that the flux is more intermittent than the variances and more concentrated in the most coherent structures

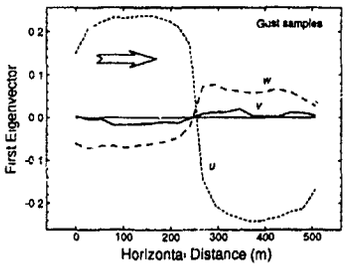

Figure 4 Multivariate eigenvectors for the three velocity components

Using basis functions for the sample selection which are smoother than the Haar function produces similar results except that the first eigenvector is smoother and explains a slightly lower percentage of the flux and variances

Acknowledgments The comments of Nimal Gamage are greatly appreciated This material is based upon work supported by the Physical Meteorology Program of the National Sciences Foundation under grant ATM-8912736 and by USARO under contract DAAL03-89-K-0113.

REFERENCES

Busch, N & Petersen, E L 1971 Analysis of nonstationary ensembles *Statistical Methods and Instrumentation on Geophysics Teknologisk Forlag, Oslo, 71-92.*

Daubechies, Ingrid 1988 Orthonormal bases of compactly supported wavelets *Comm Pure and Appl Math* **61**, 909-996.

Grossmann, A , Kronland-Martinet R & Morlet, J. 1989 Reading and understanding continuous wavelet transforms *Wavelets* Springer Verlag, 315 pp

Haugen, D A., Kaimal J C & Bradley E. F. 1971 An experimental study of Reynolds stress and heat flux in the atmospheric surface layer. *Quart J Roy Meteor. Soc*, **97**, 168-180.

Kristensen, L , Lenschow D H., Kirkegaard P. & Courtney, M. 1989 The spectral velocity tensor for homogeneous boundary-layer turbulence *Boundary-Layer Meteor*, **47**, 149-193

Lumley, J L. 1970 *Stochastic tools in turbulence* Academic Press, New York, 194 pp.

Mahrt, L 1991 Eddy asymmetry in the sheared heated boundary layer *J Atmos Sci* **48**, 472-492

Mahrt, L & Frank, H 1988 Eigen structure of eddy microfronts. *Tellus*, **40A**, 107-119

Mallet, S G. 1989 Multifrequency channel decompositions of images and wavelet models. *Trans. Acoustics, Speech and Signal Proc*, **37**, 2091-2109.

Meyer, Y 1989 Orthonormal wavelets *Wavelets.* Springer Verlag, 315 pp.

Panofsky, Hans A & Dutton, John A. 1984 *Atmospheric Turbulence* John Wiley and Sons, 397 pp

Petersen, E L. 1976 A model for the simulation of atmospheric turbulence. *J. Appl Meteor*, **15**, 571-578.

Shaw, W. J., & Businger, J. A 1985 Intermittency and the organization of turbulence in the near-neutral marine atmospheric boundary layer. *J. Atmos Sci.*, **42**, 2563-2584.

Sirovich, L. 1987 Turbulence and the dynamics of coherent structures Part I: Coherent structures. *Quart of Appl Math* , **45**, 561-571.

Tennekes, H., 1976 Fourier-transform ambiguity in turbulence dynamics. *J Atmos. Sci*, **33**, 1660-1663.

EIGHTH SYMPOSIUM ON
TURBULENT SHEAR FLOWS
Technical University of Munich
September 9-11, 1991

STRUCTURE OF TURBULENT BOUNDARY LAYERS PERTURBED OVER SHORT LENGTH SCALES

S E Belcher†, W S Weng‡ and J C R Hunt†‡

†Department of Applied Mathematics and Theoretical Physics
University of Cambridge, Cambridge CB3 9EW, UK

‡Cambridge Environmental Research Consultants Ltd
3D King's Parade, Cambridge CB2 1SJ, UK

ABSTRACT

Research on the structure of turbulent boundary layers over undulating surfaces and large applied pressure gradients turbulence has given rise to some clarification of concepts (validity of logarithmic wall functions, and when equilibrium or memory effects are more important), new approximate turbulence models, and better understanding of the accuracy of existing turbulence models (mixing-length, $k-\epsilon$, and second-order). The aim of this paper is to describe a few of these developments and highlight recent developments (some of which will be reported at the meeting).

1 LENGTH AND TIME SCALES

We particularly focus on very high Reynolds number flows when the horizontal length scale, L, of the variation of the pressure gradient is small compared with h_*, the natural length scale of adjustment of a turbulent boundary layer, which is given by $h_* = hU(L)/u_*$, where h is the boundary layer depth, $U(L)$ is the approach flow mean velocity at the height L and u_* is the upstream friction velocity, furthermore, since the Reynolds number is high $u_*/U(L)$ is small (typically from 0.03 to 0.05). The significant changes to the flow then occur well within the boundary layer, in a region of depth $\ell \sim Lu_*/U(L)$ (i.e. $\ell \ll h \sim L \ll h_*$). Here we focus on the turbulent processes which occur close to a rigid wall.

In practical problems the varying pressure gradient may arise from a variety of different sources, but the best specific example is the flow of the atmospheric boundary layer over a hill (Fig. 1) perhaps surprisingly to laboratory experimentalists, the fine detail of these flows is at least as well defined as laboratory studies especially in the inner region! The hill has the effect of accelerating the flow on the upwind slope (a favourable pressure gradient) and decelerating the flow on the downwind slope (an adverse pressure gradient).

The pressure gradient changes the structure of the turbulence through two processes. Firstly, the mean flow is altered by the pressure gradient and hence strains the turbulent eddies. The time scale, T_D, of these straining distortions is the time taken for an eddy to be advected by the mean flow over the distance L, i.e.

$$T_D(x_3) = L/U(x_3) = L/[(u_*/\kappa)\ln(x_3/z_0)], \qquad (1a)$$

assuming the approach flow profile is logarithmic. Secondly, the turbulence is changed by the interactions between the eddies, so that the second fundamental time scale is the time, T_L, taken for an eddy to decorrelate or turnover. Assuming that at a height x_3 above the surface, the large energy containing eddies have a vertical size of order x_3 (an idea which is refined in §2), T_L may be estimated as

$$T_L = \kappa x_3/u_*. \qquad (1b)$$

where κ is the von Karman constant whose value is taken as 0.4.

These two time scales are of the same order of magnitude at a height $x_3 = \ell$ defined by equating (1a) and (1b)

$$\ell \ln(\ell/z_0) \sim L \qquad (2)$$

Thence the perturbed flow can be separated into two regions (Fig.1), whose different properties can be defined with aid of the kinetic energy equations. Different turbulent models are appropriate within the inner region and above it.

2 TURBULENCE PROCESSES AND MODELS

The rate of changes of kinetic energy per unit mass k of the turbulent velocity fluctuations in a steady turbulent flow is given by

$$\underbrace{U_j\frac{\partial k}{\partial x_j}}_{A} = \underbrace{-\overline{u_iu_j}\frac{\partial U_i}{\partial x_j}}_{Pr} \underbrace{-\frac{\partial}{\partial x_j}\left[\frac{1}{\rho}\overline{u_jp} + \frac{1}{2}\overline{u_iu_iu_j} - 2\nu\overline{u_is_{ij}}\right]}_{T} \underbrace{-2\nu\overline{s_{ij}s_{ij}}}_{\epsilon}, \qquad (3)$$

where $s_{i,j} = \partial u_i/\partial x_j + \partial u_j/\partial x_i$, and u_i, U_i, P, ρ and ν are the ith components of the fluctuation and mean velocity, the pressure, density and kinematic viscosity. The relative order of magnitude can be estimated by assuming $\overline{u_iu_j} \sim k$, $\epsilon \sim k^{3/2}/\ell_\epsilon$, where ℓ_ϵ is the dissipation length scales (a functional rather than physical length scale, Hunt, Newley and Weng 1990), and by considering the changes, denoted by $\Delta(\ )$, in each term when the boundary layer is perturbed. Upwind $k = k_0$ and $U = U_0(x_3)$, so

$$\underbrace{\frac{U_0\Delta k}{L} \sim \frac{k_0^{1/2}\ln(x_3/z_0)\Delta k}{L}}_{\Delta A}, \quad \underbrace{-\Delta k\frac{\partial U_0}{\partial x_3} \sim \frac{k_0^{1/2}\Delta k}{x_3}}_{\Delta Pr}, \quad \underbrace{-\frac{k_0^{1/2}\Delta k}{(\ell,\ L)}}_{\Delta T}, \quad \underbrace{-\frac{k_0^{1/2}\Delta k}{\ell_\epsilon}}_{\Delta\epsilon}, \quad \underbrace{k_0^{3/2}\Delta\left(\frac{1}{\ell_\epsilon}\right)}_{\Delta\epsilon}, \qquad (4)$$

where the length scale for the different transport term, ΔT, is of order ℓ within the inner region and L in the outer region. If ℓ_ϵ has the same value as in the unperturbed layer, then $\ell_\epsilon \sim x_3$ near the surface. It follows that when $x_3\ln(x_3/z_o) < L$ or $x_3 < \ell$ where $\ell\ln(\ell/z_o) \sim L$, production and dissipation terms balance each other. However, when $x_3 \gg \ell$, the advection and production terms are dominant

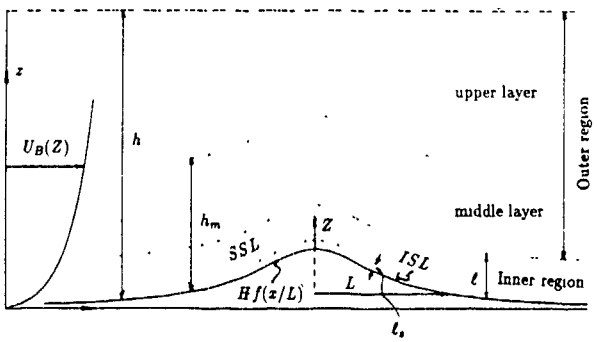

Figure 1 Schematic diagram of flow regions over a hill

and in the intermediate region where $x_3 \sim \ell$, all the terms are of same magnitude This was examined in detail using a second-order closure model by Hunt *et al.* (1990), Newley (1986)

To investigate the form of the solutions in the inner region, two simple models have been used that are consistent with the turbulence being close to local equilibrium The shear stress is modelled by an eddy viscosity formula

$$\Delta\overline{u_1u_3} = -k^{1/2}\ell_\tau\partial\Delta U_1/\partial x_3 \qquad (5a)$$

(i) In the simplest model, the closure is completed with the relations,

$$k^{1/2} \propto u_*, \quad \text{and} \quad \ell_\tau = \ell_\epsilon \propto x_3, \qquad (5b)$$

and ℓ_ϵ is independent of Δu_1 This leads to the mixing-length expression

$$\Delta\overline{u_1u_3} = -2\kappa u_*\partial\Delta U_1/\partial x_3, \qquad (5c)$$

and no subsidiary turbulence equation is required

(ii) The second, more complex, model involves calculating k from a modelled form of the turbulent kinetic energy equation, (4) To account for the changes in mean profile and separation it is necessary to allow for ℓ_τ to vary with $\Delta U(\underline{x})$ This can be done by solving another approximate PDE for ϵ, or, more simply, by noting that in perturbed shear layers the length scales are determined by the *straining* (dU_1/dx_3) and the *blocking* effect of the wall From theoretical analysis, experiments and direct numerical simulation (Hunt *et al.* , 1989) and higher order closure calculation (Hunt *et al.* , 1990), it is found that (outside any viscous wall region or roughness elements)

$$1/\ell_{\epsilon(w)} \approx A_B/x_3 + A_S\,\langle\partial u_1/\partial x_3\rangle/\sqrt{\overline{u_3^2}}, \qquad (6a)$$

where $\langle\partial u_1/\partial x_3\rangle$ is averaged over the eddy scale ℓ_ϵ, and A_B, A_s are coefficients Near the wall this approximates (for neutral stratified boundary layer) to

$$1/\ell_{\epsilon(s)} \simeq A_B/x_3 + A_S\langle\partial u_1/\partial x_3\rangle/k^{1/2}, \qquad (6b)$$

Note that (6a) and (6b) are still consistent with production and dissipation being in balance

Above the inner region where $x_3 > \ell$, as shown by (1) and (2), the turbulence is not in equilibrium with the local *mean* strain rate so that using equations of the form (5a) is wrong in principle and typically gives the wrong *sign* for $\Delta\overline{u_1u_3}$ (e g. over surface undulations). However, either second-order closure models or rapid distortion theory can provide useful estimates in this region

3 SPECIFIC RESULTS USING THE MODEL

(i) *Perturbed boundary layers very close to a rigid surface*

Using the simple mixing-length formula (equation 5c) in the inner region only, analytic solutions for linear perturbations to the boundary layer may be obtained Very close to the surface, when $x_3 \le \ell_s = \sqrt{\ell z_0}$, the perturbed profile then has a logarithmic form

$$u_1 \approx \frac{u_*}{\kappa}\left(1 + \frac{\Delta\tau_{13}}{2u_*^2}\right)\ln\frac{x_3}{z_0} \qquad (7)$$

For a hill that is 1km long and 100m high, with a roughness length of $z_0 = 0.01m$, the inner region depth is $\ell \sim 10m$ and the logarithmic law holds up to a height of order $\ell_s \sim 0\,3m$, see figure 2a. Above this height, in the range $\ell_s \lesssim x_3 \lesssim \ell/3$, the streamwise velocity, in the limit $u_*/U_\infty \ll 1$, is

$$u_1 \approx \frac{u_*}{\kappa}\left(1 + \frac{\Delta\tau_{13}}{2u_*^2}\right)\ln\frac{x_3}{z_0'}, \qquad (8a)$$

see figure 2b, where the *apparent* roughness length is

$$z_0' \approx z_0 e^{-(4\gamma+1)\Delta\tau_{13}/u_*^2}, \qquad (8b)$$

where γ is Euler's constant ($= 0.577\ \cdot$). When $\Delta\tau_{13}/u_*^2 \approx 1$, as in the Askervein field experiments of flow over a hill, the apparent roughness length is about 1/30 of the upstream value This agrees with the field data of Taylor(1990).

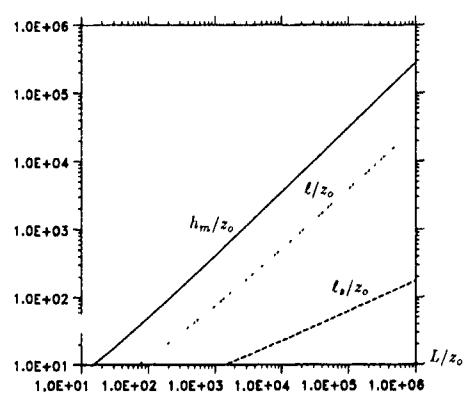

Figure 2a Variation of the heights of the asymptotic layers with L.

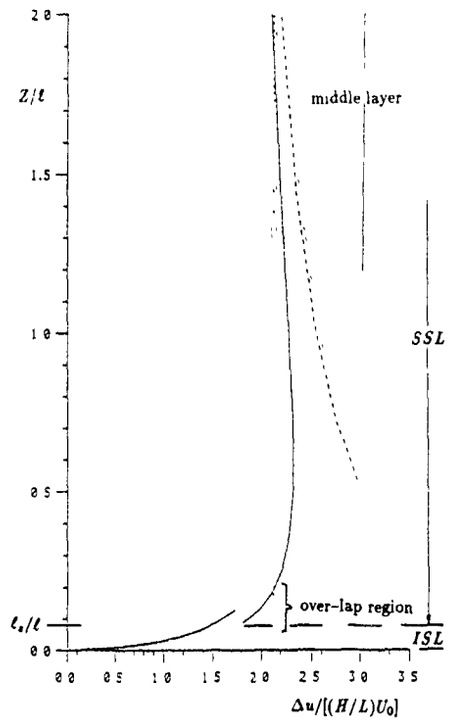

Figure 2b Streamwise velocity perturbation at the crest of sinusoidal topography in the inner region $H/L = 0.04$, $L/z_0 = 2500$ and $\delta \approx 0.2$

: solution to $O(\delta^0)$
—— solution to $O(\delta^1)$
– – middle layer solution

This result suggests the need to replace wall functions by results of local calculations based on simple turbulence models with the correct surface boundary conditions (*c.f.* Rodi, 1989)

(ii) *The relation between perturbation pressure and surface shear stress*

The mixing-length model (5c) can also be used to show how asymptotically when $u_*/U_0 \ll 1$, the surface shear stress $\Delta\tau_{13}$ varies *in phase* with the pressure, Δp (Hunt & Richards, 1984) $\Delta\tau_{13}$ has small phase lead by angle $\Delta\phi$ over an undulating surface, which is of the order of $O(\ln^{-1}(\ell/z_o))$ (say by about $15° - 25°$ in geophysical flows). Data will be shown to demonstrate this point. Consequently over surfaces where $u_*/U_\infty \ll 1$ (or in very high Reynolds number flow) the *location of separation* is approximately determined by the value of the *pressure* (rather than the pressure gradients in laminar flows) which has been verified by experimental and computational studies (eg Tampieri, 1987)

(iii) *Mean velocity distributions near the surface*

The form of the perturbed velocity profile $\Delta U_1(x_3)$ near the surface departs significantly from a logarithmic form, in accelerating or decelerating flows In that case the ordinary mixing-length (OML) formula (5c) is less accurate than using (5a) together with the shear-blocking mixing-length (6a). Asymptotic analysis of the kinetic energy equation shows that the mean shear varies near the wall according to

$$\frac{\partial u_1}{\partial x_3} = \frac{\partial U_1}{\partial x_3} + \frac{\partial \Delta U_1}{\partial x_3} = \frac{u_*}{\kappa x_3}\left\{1 + \frac{\Delta\tau_{13}}{2u_*^2} + \alpha\ell_1 \ln\frac{x_3}{z_o}\frac{\partial\tau_{13}/\partial x_3}{u_*^2}\right\}, \qquad (9)$$

where $\alpha = 17$ using the OML and 71 using the SBML (6a)

The latter value shows how sensitive the turbulence profile is to small changes in the production whether caused by acceleration or body force (eg buoyancy or electromagnetic fields), because any perturbation first changes the shear $\partial u_1/\partial x_3$, but then changes ℓ_ϵ and ϵ, which then requires greater production Typically any increase in production by a factor $\delta(= 1/\ln(\ell/z_o))$ lead to an increase in dissipation by about 4δ (Turner, 1973, Hunt *et al*, 1990)

Equation (7) agrees well with computed profiles of u_1 (using a second-order closure) over a boundary layer with an sinusoidal pressure $p(x_1)$ caused by flow over undulating surface) Note how the agreement is better with the SBML results, see figure 3

(iv) *Turbulent flows close to separation*

The different OML and SBML formulae for ℓ_ϵ and ℓ_τ have been used to compute turbulent flows that are just separating on the downwind slope of a hump (or equivalently in a region of rising pressure) (Weng, Richards and Carruthers, 1989) Figure 4 shows that although ℓ_τ only varies by about 10% between OML and SBML formulae this leads to large changes in $\partial\tau_{13}/x_3$, so that flow is significantly different, in the case not separating and with other separating Further results and comparison with experiment will be shown

(v) *Turbulence above the inner region*

Above the height ℓ, at the value of x_1 where the perturbations are maximum, and

$$\frac{\partial p}{\partial x_1} \approx -\frac{\partial u_1}{\partial x_1} \approx 0, \qquad \frac{\partial \Delta U_1}{\partial x_3} < 0, \qquad (10)$$

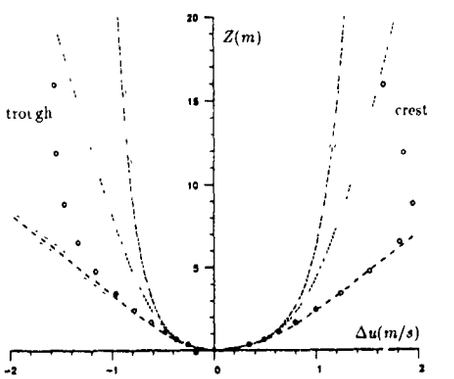

Figure 3. Comparison of the mean streamwise velocity perturbation at the crest and trough of a sinusoidal undulation The value of the surface shear stress is determined from the results of the second-order closure model (1986)

∘ ∘ ∘ second-order closure model (Newley, 1986)
—— log-law
..... mixing-length (log-linear)
- - - - shear-blocking mixing-length (log-linear)

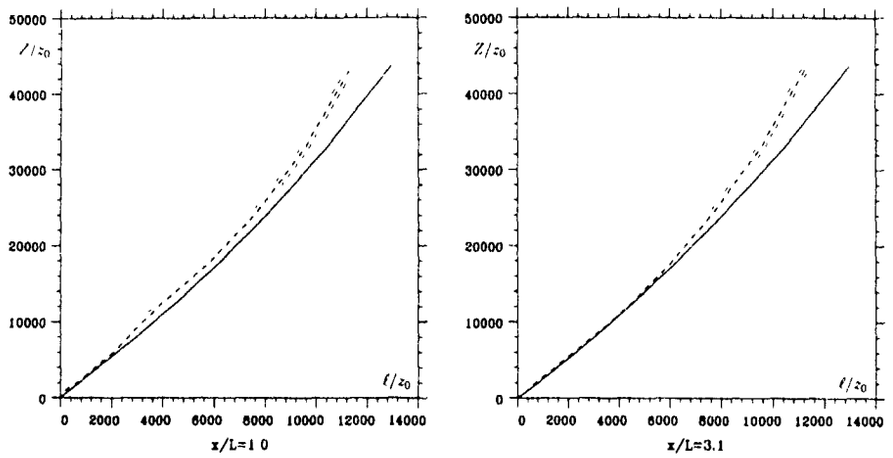

Figure 4 Vertical distribution of the mixing length in the wake region of flow over a Gaussian hill $z(x) = H\, e^{-x^2/L^2}$ with $H = 2000 z_0$ and $L = 5000 z_0$

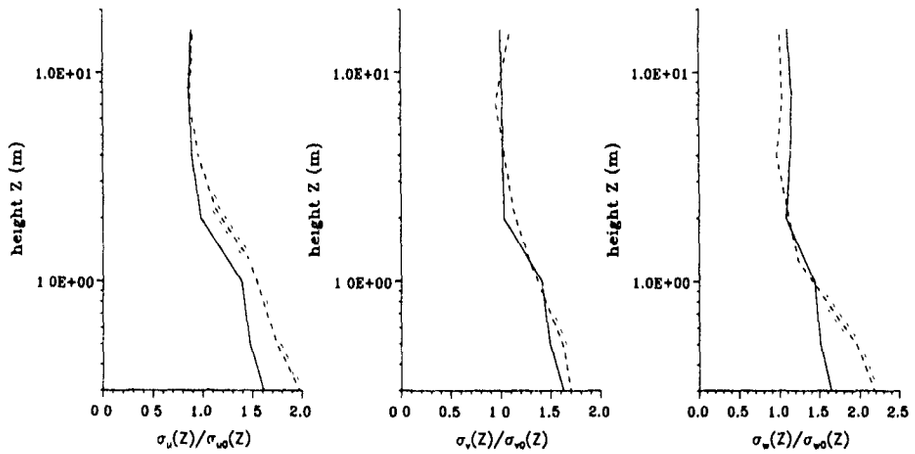

Figure 5 Comparison of normalised variances of turbulent velocities at the summit of Nyland hill

observations (Mason, 1986) —— calculation

it follows from (5a) that the usual eddy viscosity calculation yields $\Delta\tau_{13} < 0$ But in fact, experiments and second-order closure show that the stretching of the eddies leads to $\Delta\tau_{13} > 0$ and of a smaller order of magnitude, $O(u_*^2 \Delta U_1/u_1)$ Similarly the assumption of isotropic eddy viscosity indicates that all the components of kinetic energy decrease, whereas the changes in turbulence are anisotropic $\overline{u_1^2}$ is reduced and $\overline{u_3^2}$ increased, much like the changes in a wind tunnel contraction These changes can be estimated by second-order closure models (eg. Zeman & Jensen, 1987), or outside the wake region, by simple formulae derived from rapid distortion theory

The new concept presented here is that for these kind of perturbed flows there is only a relatively narrow region between the inner local equilibrium region and the outer, rapid distortion region, where all the complex processes of turbulence occur (including curvature effects over curved surfaces) If the details of the turbulence in this region are unimportant, they can be estimated by extrapolation between the outer and inner regions. This is incorporated into a simple computer program for turbulence over undulating terrain, see figure 5

An important consequence of this difference in the turbulence structure between the inner and outer regions is that it effects the *drag* force on undulating terrain surfaces (whether solid or liquid) because the drag is too large if an eddy viscosity model is applied in the outer region. Figure 6 shows that the analytical solution, based on ignoring shear stress in the outer region, agrees with the second-order closure calculation (and force measurements) and is about 50% of the value of F_x derived when eddy viscosity model is applied throughout the flow.

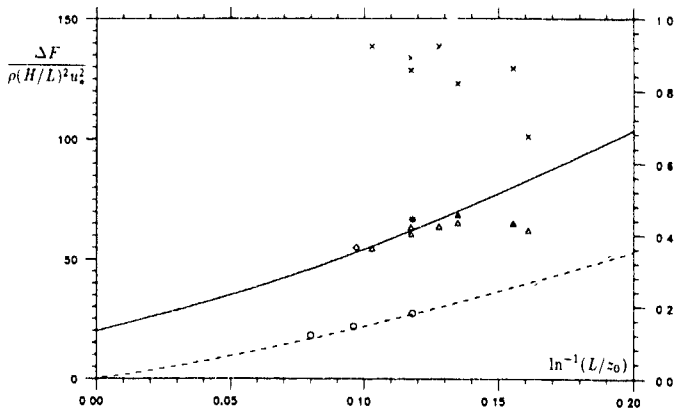

Figure 6 Variation of drag coefficient with relative surface roughness for sinusoidal topography

-- present theory (left scale)
variation of $\delta(=1/\ln(\ell/z_o))$ (right scale)
△ value computed with second-order closure model (Newley, 1986)
× value computed with mixing-length closure model (Newley, 1986)
○ value computed by Townsend (1972)
* value computed by Townsend (1980)
◇ experimenta, result (Zilker & Hanratty, 1979)

REFERENCES

Hunt, J C R , Newley, T M.J & Weng, W.S. **1990** Analysis and computation of turbulent boundary layers with varying pressure gradients Proc. of IMA conf on *Computational Method in Aeronautical Fluid Dynamics* ed. P Stow. Clarendon Press, Oxford

Hunt, J C R & Richards, K J **1984** Stratified airflow over one or two hills *B L Met* **30,** 223—259

Hunt, J C R , Moin, P , Lee, M , Moser, R D , Spalart, P Mansour, N N., Kaimal, J C & Gaynor, E **1989** Cross correlation and length scales in turbulent shear flows near surfaces *Proc Second European Turbulence Conf* (ed H. Fernholtz and H Fiedler), pp 128-134. Springer-Verlag

Mason, P J **1986** Flow over the summit of an isolated hill *B.L Met.* **37,** 385—405

Newley, T M J **1986** Turbulent air flow over hills Ph D thesis, University of Cambridge

Rodi, W. **1991** Current trends in turbulent modelling Prec. of SIAM/IMA conference on *Computational Aeronautical Dynamics* (1989) Clarendon Press, Oxford

Tampieri, F. **1987** Separation features of turbulent boundary -layer flows over valleys *B L Met* **34,** 295--307

Taylor, P A **1990** The Askervein experiment data on the flow over a hill. Presented at ERCOFTAC workshop, 30-31 Aug., 1990, Bologna, Italy

Turner, J.S **1973** Buoyancy Effects in Fluids C U P

Weng, W S , Richards, K J. & Carruthers, D.J. **1989** Some numerical studies of turbulent wake over hills *Proc Second European Turbulence Conf* (ed H Fernholtz and H Fiedler), pp 412-417 Springer-Verlag

Zeman, O & Jensen, N.O. **1987** Modifications to turbulence characteristics in flow over hills. *Quart J R Met Soc* **113,** 55—80

EIGHTH SYMPOSIUM ON
TURBULENT SHEAR FLOWS
Technical University of Munich
September 9-11, 1991

COMPARISON OF DIRECT AND LARGE-EDDY SIMULATION OF TURBULENT SCALAR TRANSPORT IN STABLY STRATIFIED SHEAR FLOWS

Hans-J. Kaltenbach, Thomas Gerz and Ulrich Schumann

DLR, Institut für Physik der Atmosphäre
W-8031 Oberpfaffenhofen, Germany

ABSTRACT

We determined the tensor of turbulent diffusion of passive scalar tracers in homogeneous turbulence under the presence of shear and stable density stratification by means of numerical simulation Results of DNS (Direct Numerical Simulation) and LES (Large-eddy simulation) with Smagorinsky closure with similar (mean) viscosity show little differences in a neutrally stratified flow LES runs deviate from DNS runs under thermally stable stratification mainly because the mean turbulent viscosity adjusts itself to the reduced turbulence activity Only two out of nine tensor components - the vertical and the spanwise diffusion coefficient - are of practical interest for dispersion problems Stable stratification reduces the vertical more than the spanwise diffusivity which leads to an enhanced anisotropy of the diffusivity tensor

METHOD

In continuation of a previous study (Kaltenbach, Gerz & Schumann 1991) we extend the work of Rogers, Mansour & Reynolds (1989), who calculated the dispersion of a passive scalar in homogeneous shear flow, to thermally stably stratified flows By means of highly resolving numerical simulation we computed the development in time of the turbulent diffusivity tensor D_{ij}, which relates a turbulent flux $\overline{u_i c}$ of a scalar fluctuation c to its mean value according to $\overline{u_i c} = -D_{ij}(d\bar{C}/dx_j)$ Horizontal bars denote a spatial mean value which represents an ensemble mean because of homogeneity In order to calculate all tensor components we integrated balances for passive scalar fluctuations c_1, c_2 and c_3 which have uniform (stationary) mean gradients in the directions of the mean flow (x), the spanwise direction (y), and the vertical direction (z), respectively (Fig 1) As Rogers et al. (1989) explained, a height dependent source term has to be assumed in order to maintain a stationary mean gradient $d\bar{C}_1/dx$. Mean velocity and mean temperature have uniform vertical gradients

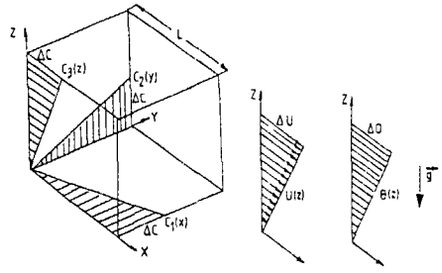

Fig. 1 Sketch of the computational domain with uniform gradients of the mean quantities

Buoyancy influence is approximated using the *Boussinesq*-assumptions. Because of equal molecular diffusivity, temperature fluctuation T and scalar fluctuation c_3 behave identically Our code uses central differences and a pseudo-spectral approximation of the advection by the mean velocity (Gerz, Schumann & Elghobashi, 1989) We use a 96^3 cubic grid, which allows for an initial Reynolds number $Re_{\lambda_{11}} = q \cdot \lambda_{11,1}/\nu$ of 44 We extended our code to a LES-version using the Smagorinsky model for the subgrid scale stresses $\overline{u'_i u'_j}$ and fluxes which are defined by a box filter in the physical space The eddy diffusivity $\nu_t = (c_s\Delta)^2\sqrt{0\,5\,S_{ij}S_{ij}}$ is calculated with the mesh size Δ and the local deformation $S_{ij} = \partial u_i/\partial x_j + \partial u_j/\partial x_i$ We do not include the mean shear dU/dz in the calculation of S_{ij} For SGS scalar diffusivity $\gamma_t = \nu_t/Pr_t$ we use $Pr_t = 1$ We compare turbulence statistics of the *resolved scales* of the LES runs with the corresponding DNS values without any "defiltering". The value of the closure constant $c_s = 0\,17$ was chosen in order to produce a *mean* turbulent viscosity $\bar{\nu}_t$ similar to the constant molecular viscosity of the DNS reference cases. Incidentally it is close to the value 0 165 deduced in Schmidt & Schumann (1989) for isotropic turbulence. LES runs have zero molecular viscosity

RESULTS

According to Table 1 we performed three pairs of simulations at different Richardson numbers $Ri = N^2/S^2$ where N denotes the Brunt-Vaisala frequency and S the mean shear

Table 1. Simulation parameters

Case	type	Ri	c_s	$q\lambda_{11}/\nu$
DNS0	DNS	0.	-	44
LES0	LES	0	0 17	(33 4)
DNS13	DNS	0 13	-	44
LES13	LES	0 13	0 17	(33 4)
DNS25	DNS	0 25	-	44
LES25	LES	0 25	0 17	(33 4)

Comparison of the two unstratified cases DNS0 and LES0 with similar (mean) viscosity (Fig 2h) corroborates the findings of Ferziger & Leslie (1979) and Bardina, Ferziger & Reynolds (1983) that turbulence statistics which are dominated by large scales, e g Reynolds stresses and scalar fluxes, behave nearly identical in both types of simulations The development in time of the turbulent kinetic energy $q^2/2 = 0.5(\overline{u^2} + \overline{v^2} + \overline{w^2})$, the sink term ε (dissipation rate for DNS, $\overline{u_i' u_j'} S_{ij}$ for LES respectively), the energy partition $\overline{u_i u_j}/q^2$, correlation coefficients and the scalar diffusivity ratios D_{ij}/D_{22} show little effect of using a weakly fluctuating ($\nu_t'/\bar{\nu}_t \approx 0.3$) eddy diffusivity instead of a constant molecular viscosity (Fig. 2 a-g) More differences are found on small-scale related statistics like vorticity and velocity-gradient skewness coefficients Both runs behave similar to the spectral simulations of Rogers et al (1989) The initial period ($St < 2$), which is dominated by the dissipation, is followed by an approximately exponential growth of q^2 The mean turbulent viscosity $\bar{\nu}_t$ behaves very similar as ε which grows slowly because stages of quasi-isotropic decay and steady growth due to shear-production overlap (Fig 2b,h) This slow time variation of ε and subsequently $\bar{\nu}_t$ is one cause for the conformity of DNS and LES results under neutral conditions For $St > 6$ the flow looks self-similar with characteristic anisotropy of Reynolds stresses and diffusivity tensor component ratios Self-similarity, however, implies independence on initial conditions which is only partly fulfilled. Strong influence of the initial conditions on the results is often reported (Bardina et al , 1983, Rogers, Moin & Reynolds, 1986) We found that the approximately self-similar stage will only be reached if the initial Reynolds number $Re_{\lambda_{11}} > 40$ Simulations with lower values show stronger anisotropy which decreases after several shear times (Rogers et al , 1986) Strong anisotropy arises if the growth rate of the momentum flux, which is weakly affected by viscosity, is fast in comparison to the growth of the vertical velocity variance, which strongly depends on the initial amount of dissipation This causes $|\overline{uw}/\overline{ww}| > 1$, which is greater than usually measured values The eddy viscosity model removes energy from the small scales more effectively than the DNS which leads to steeper energy spectra (Fig 3a) The spectral slope highly depends on the value of the viscosity or c_s respectively Hence, the agreement of the observed slope close to k^{-2} with the predictions of Hunt & Carruthers (1990) is rather incidentally

Analysis of the spectral energy balance sheds light on the reasons for the little influence of SGS parameterization on the results As shown by Domaradzky, Rogallo & Wray (1990) the right hand side of the spectral energy balance per spherical wave number shell k with thickness $\Delta k = 1$ of the unstratified cases

$$\frac{\partial E(k)}{\partial t} = -S\Phi_{uw}(k) + T_{lin}(k) + T_{nonlin}(k) - \varepsilon$$

includes energy production by shear, linear transfer due to mean shear, nonlinear transfer and energy dissipation The linear transfer term is omitted in the plot (Fig 3c) because it shows fluctuations around zero with large amplitude but without clear sign preference. For wave numbers 1 to 20, most of energy production (92%) occurs whereas only 40% of dissipation take place There reside 82% of the kinetic energy At higher wave numbers, nonlinear energy transfer and dissipation approximately balance each other This detailed analysis shows again no significant difference between LES and DNS. The Smagorinsky closure has no back-scattering characteristics Therefore it only changes the energy sink at small scales whereas the large scales are unaffected On the other hand, greater differences between DNS and LES of isotropic decaying turbulence are found where dissipation provides the largest contribution to the spectral balance Reynolds number independence of a shear flow (Ferziger & Leslie, 1979) therefore means separation of an energy-producing from an energy-dissipating wave number range which is more a question of number of resolved scales than of details of the energy sink. The number of resolved scales is much too small to find an universal equilibrium range with inertial subrange The assumptions for proper use of the Smagorinsky model are therefore not given which is indicated by the low value of the ratio $|S_{ij}|/(dU/dz) < 2.5$, i e mean local deformation and overall shear have the same order of magnitude In contrary to expectation, the anisotropy of small scales is augmented in the LES which seems to be connected to the steeper energy spectrum and therefore *less* dissipation on small scales (Fig 3b) An "anisotropy minimum" occurs at medium wave numbers where dissipation is largest

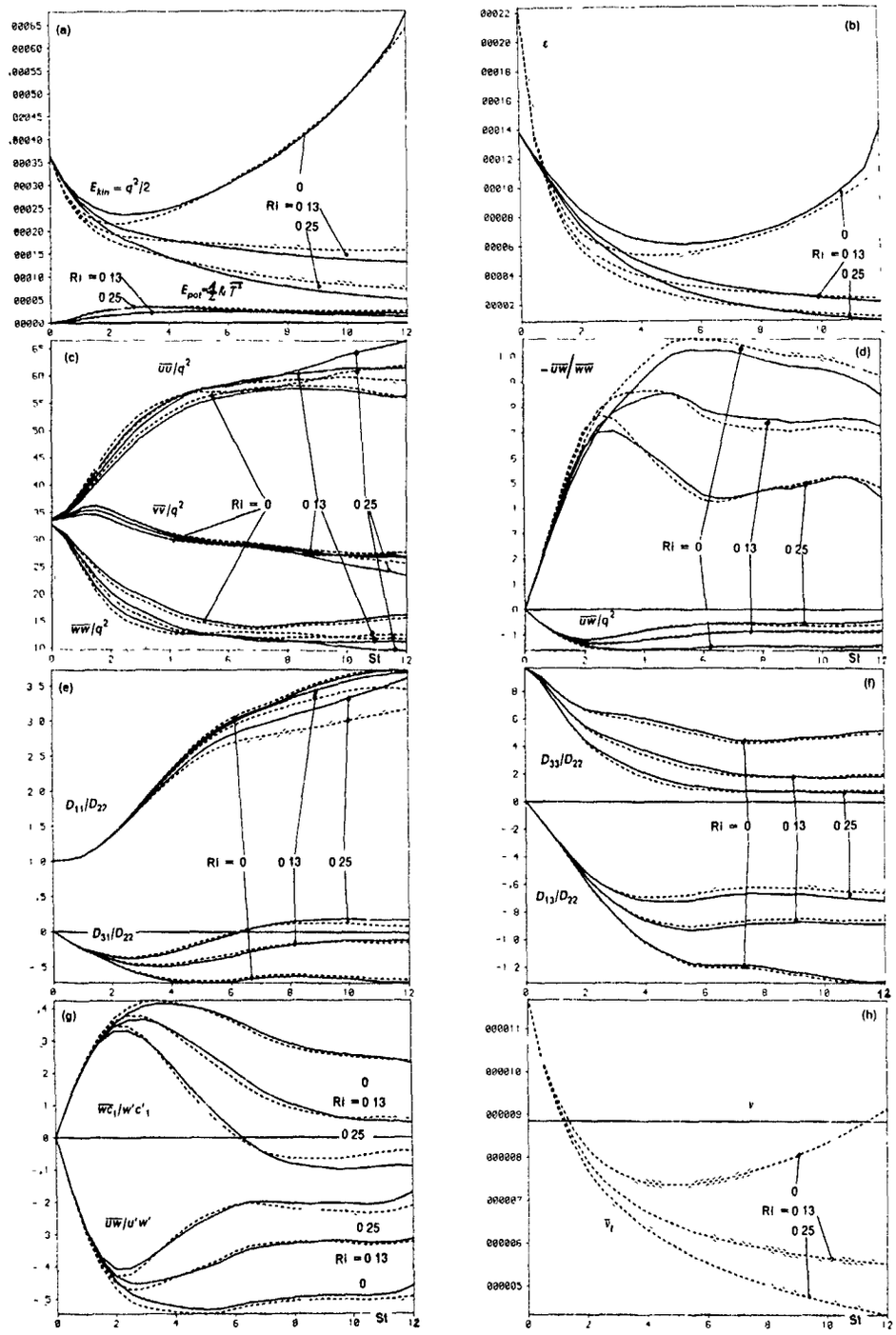

Fig 2 Turbulence statistics versus shear time St a) Kinetic energy $q^2/2$ and potential energy $0\,5\,Ri\,\overline{TT}$ b) Dissipation rate ε c) Energy partition d) Shear stress ratios e) and f) Normalized diffusivity tensor component ratios g) Correlation coefficients h) Mean turbulent viscosity $\overline{\nu}_t$ and constant molecular viscosity ν
—— DNS, - - - - LES

Other small scale effects like counter gradient contributions of momentum or vertical heat flux in a *neutrally* stratified flow (Kaltenbach et al 1991) only occur if the energy spectrum slope is steeper than k^{-2}

SCALAR TRANSPORT

Rogers et al (1986) derived an algebraic flux model similar to the second order closures of Freeman (1977) and Dornbrack (1989) to predict the tensor components D_{ij} from the Reynolds stresses and the mean strain-rate dU/dz The diagonal components $D_{11} > D_{22} > D_{33}$, which describe gradient transport, are more anisotropic than the related Reynolds stresses but show the same relations in magnitude, i e $\overline{u^2} > \overline{v^2} > \overline{w^2}$ D_{ij} has two more components which differ from zero, $|D_{13}| \neq |D_{31}|$ The tensor asymmetry is the essential difference between turbulent and molecular diffusion D_{31} describes a vertical flux which stems from a horizontal gradient, for D_{13} it is vice versa Both fluxes make sense only if a gradient in x-direction exists which is not very realistic. two parcels which are initially vertically neighboured are soon separated over a wide horizontal distance due to the mean advection $U(z) = dU/dz \cdot z$ An initially round spot of concentration in the x-z-plane soon looks like an inclined streak Turbulent diffusion in the x-direction plays a minor role compared to mean advection Therefore, for practical purposes, constant scalar distribution in x-direction may be assumed Then only D_{22} and D_{33} are of interest Generally the diffusion concept becomes questionable, if it is applied to problems with streamwise (x-direction) varying concentration There the characteristic length scale of the resulting *vertical* concentration profile soon gets smaller than the mixing length of the turbulence, which violates the scale-separation assumption

THERMALLY STABLE STRATIFICATION

The work against buoyancy forces is an additional sink term in the kinetic energy balance

$$\frac{\partial q^2/2}{\partial t} = -S\overline{uw} + Ri\overline{wT} - \varepsilon$$

For the present Reynolds number flows Gerz & Schumann (1991) found an almost steady flow state at a critical Richardson number $Ri_{crit} = 0.13$ Simulations with $Ri > Ri_{crit}$ show decaying kinetic energy Our case DNS13 behaves weakly supercritical whereas LES13 approaches almost a stationary value for q^2 (Fig. 2a) More differences in the evolution of q^2 and ε between LES and DNS are found for the two stably stratified simulation pairs than for the neutral case Whereas the mean turbulent viscosity stays similar to the constant molecular viscosity of the reference DNS in the neutral case, the reduced turbulence activity causes an permanent decrease of $\bar{\nu}_t$ in the stratified cases (Fig 2h) At St = 12 ν of case DNS25 is twice larger than $\bar{\nu}_t$ of LES25 Correlation coefficients and normalized values like energy partition and scalar diffusiviy ratios show again little difference between DNS and LES They reach stationary values which implies self-similarity A DNS with smaller molecular viscosity would probably produce similar results as this LES, e g a larger Ri_{crit} This point of view is corroborated by the work of Holt (1990) He found that Ri_{crit} approached the theoretical value 0 25 of the linear inviscid case when the Reynolds number in the DNS was increased Whereas the LES spectra are steeper than the DNS spectra in our neutral cases, LES spectra show flatter slopes than DNS spectra in the stratified cases at both Richardson numbers (Fig 3e,f) One cause is the reduced mean viscosity. Probably more important is the reduction of the nonlinear energy transfer due to the buoyancy influence (Holt, 1990) The small scales are less excited by the large scales in the stratified cases than in the neutral case The constant molecular viscosity then reduces strongly the small scales in the DNS whereas in the LES the reduced ν_t "cares for" a sufficient amount of small scales to develop a constant spectral slope at the high wave number end Whereas nonlinear transfer and dissipation balance each other in the neutral case, dissipation is three times bigger than transfer for Ri = 0 25 (Fig 3c,d) Hence the difference in small scale behaviour of DNS and LES under stable stratification is the same as in simulations of decaying isotropic turbulence. For both Ri numbers the energy spectra of the LES runs have spectral slopes close to $k^{-5/3}$ Reducing the value of ν_t, either with a smaller c_s or through inclusion of buoyancy influence on ν_t, leads to flatter energy spectra. If one accepts this, one has to abandon the idea that the high wave number end extends into an inertial subrange Holt (1990) showed that Ri_{crit} only weakly depends on Re if the Reynolds number is high enough This means, DNS can describe flow stages which are nearly Reynolds number independent and therefore refer to an infinite Reynolds number Our results suggest that the implicit assumption of infinite Reynolds number for LES may not necessarily be true We suppose that, provided the flow is not extremly unsteady as in decaying isotropic turbulence or strongly stably stratified flows, a DNS may predict similar properties as a LES of the same problem

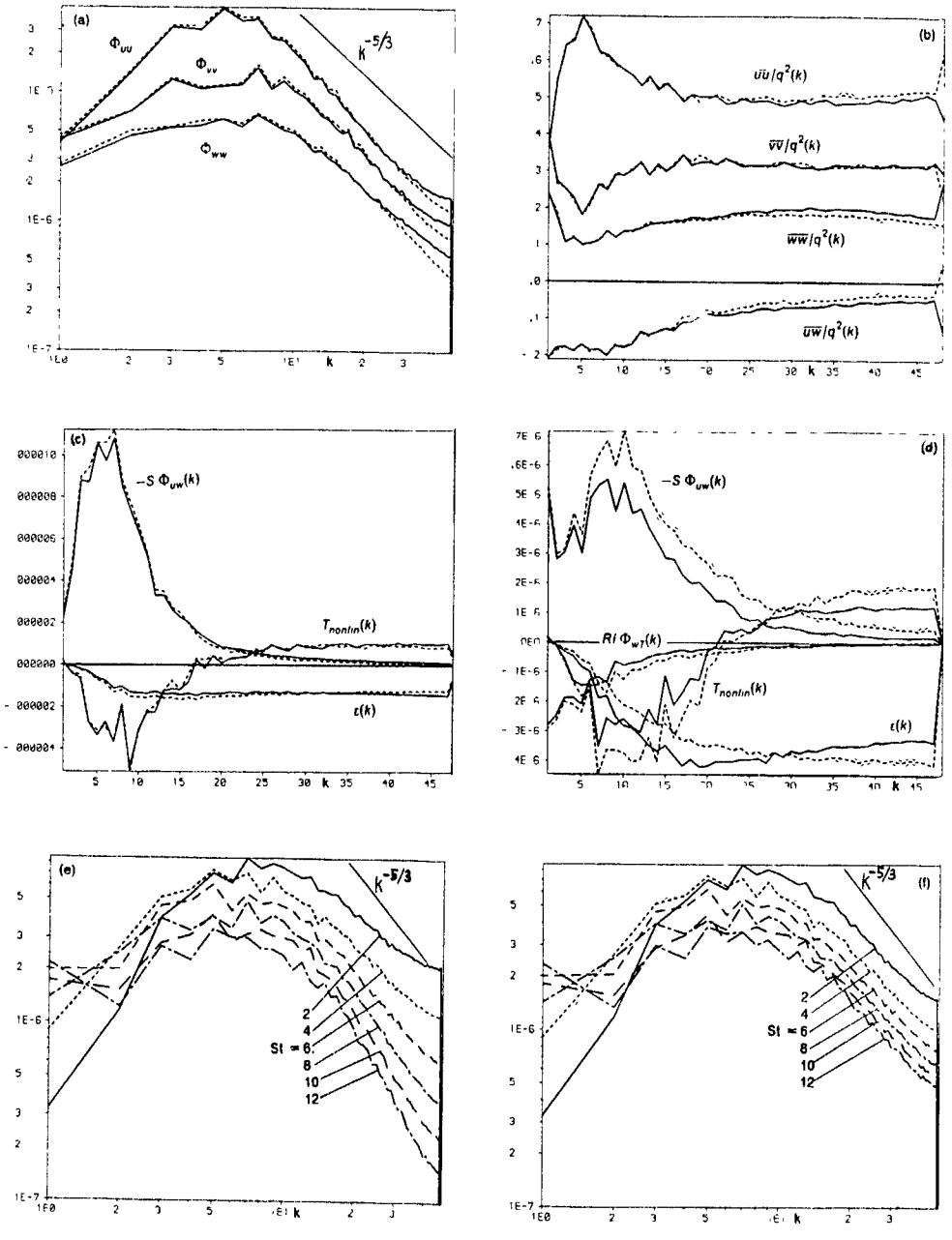

Fig 3 Turbulence statistics versus dimensionless wave number k for cases DNS0 and LES0 (a-c) and DNS25 and LES25 (d-f) The spectra are integrated over spherical wave number shells with radius k a) Power spectra of velocities Φ_{uu}, Φ_{vv} and Φ_{ww} at St = 8 (LES0 dashed) b) Local anisotropy $u_i u_j(k)/q^2(k)$ at St = 8 (LES0 dashed) c) Terms of the spectral energy balance for Ri = 0 at St = 8 (LES0 dashed) d) Terms of the spectral energy balance for Ri = 0 25 at St = 8 (LES25 dashed) e) Kinetic energy spectra of DNS25 f) Kinetic energy spectra of LES25

The momentum flux ratio $\overline{uw}/q^2$ and other statistics which are related to vertical velocity fluctuations show strong buoyancy influence (Fig 2d-g) Derbyshire & Hunt (1991) argued that at high Reynolds numbers the shear stress ratio $-\overline{uw}/\overline{w^2}$ only weakly depends on Ri We find a strong decrease from ~ 1 at $Ri = 0$ to ~ 0.5 at $Ri = 0.25$ Again there is no significant difference between DNS and LES The scalar diffusivity ratio D_{33}/D_{22} changes from 0 5 at $Ri = 0$ to 0 1 at $Ri = 0.25$ The spectral energy balances of the stably stratified cases reveal that buoyancy acts on large scales similar as the momentum flux (Fig 3d) Whereas the absolute values of each contribution deviate considerably in DNS and LES at the same time due to different flow histories, caused by changes in viscosity the relative weights of the balance terms are similar in DNS and LES Holt (1990) defined a transient Richardson number which separates a shear dominated from a buoyancy dominated flow regime For $Ri > Ri_{trans}$ many quantities show oscillating behaviour caused by exchange of kinetic energy and potential energy $0.5\,Ri\,\overline{TT}$ The diffusivity tensor component ratios are no longer stationary values which simply depend on the value of Ri Hunt, Stretch & Britter (1988) revealed the important role of the initial conditions on the time development of the flows which do not reach self-similar stages

CONCLUSIONS

Numerically simulated neutrally and moderately stratified shear flows with $Ri < Ri_{trans}$ reach self-similar stages with constant energy partition on velocity components and diffusivity tensor component ratios These are large-scale related quantities which only weakly differ between high resolution direct numerical simulation or LES A LES of Smagorinsky type has similar properties as a DNS with comparable molecular viscosity as long as the energy containing scales are well resolved

ACKNOWLEDGMENT

The work of H -J Kaltenbach was supported by the Volkswagen-Stiftung with help of the DECHEMA, Frankfurt am Main

REFERENCES

Bardina J , Ferziger J H & Reynolds W C 1983 Improved turbulence models based on large eddy simulation of homogeneous incompressible, turbulent flows, Report TF-19 Dep of Mech Eng , Stanford University

Derbyshire, S H & Hunt, J C R , 1991 Structure of turbulence in stably stratified atmospheric boundary layers, comparison of large eddy simulations and theoretical models Proc 3rd I M A Conf on Stably Stratified Flows Ed S D Mobbs Clarendon Press Oxford, 1991

Dörnbrack, A 1989 Approximative Berechnung turbulenter Flüsse und des Tensors der turbulenten Diffusion auf der Grundlage der Schließung 2 Ordnung, Dissertation Humboldt Univ Berlin

Domaradzki, J A , Rogallo, R S & Wray, A A 1990 Interscale energy transfer in numerically simulated turbulence In Studying turbulence using numerical simulation databases - III, Proc of the 1990 summer program, Center for Turbulence Research Stanford

Ferziger, J H & Leslie D C 1979 Large eddy simulations a predictive approach to turbulent flow computation AIAA paper No 79 1471 (pp 234-246)

Freeman, B E 1977 Tensor diffusivity of a trace constituent in a stratified boundary layer, J Atmos Sci 34 124-136

Gerz, T , Schumann U & Elghobashi S E 1989 Direct numerical simulation of stratified homogeneous turbulent shear flows, J Fluid Mech 200 563-594

Gerz, T & Schumann U 1991 Direct simulation of homogeneous turbulence and gravity waves in sheared an unsheared stratified flows In *Turbulent Shear Flow 7* (F Durst et al , ed) Springer Verlag, in press

Holt, S E 1990 The evolution and structure of homogeneous stably stratified sheared turbulence, Diss at Dep of Civil Eng Stanford University

Hunt J C R , Stretch, D D & Britter, R E 1988 Length scales in stably stratified turbulent flows and their use in turbulence models in Stably Stratified Flows and Dense Gas Dispersion (J S Puttock, ed) Clarendon Press, Oxford, pp 285-321

Hunt, J C R & Carruthers, D J 1990 Rapid distortion theory and the 'problems' of turbulence, J Fluid Mech , 212, 497-532

Kaltenbach, H -J Gerz, T & Schumann, U 1991 Transport of passive scalars in neutrally and stably stratified homogeneous turbulent shear flows, In Advances in Turbulence 3 (Proc of the 3rd Europ Turbulence Conf , A Johansson & H Alfredsson ed), in press

Rogers, M M , Moin, P & Reynolds, W C 1986, The structure and modeling of the hydrodynamic and passive scalar fields in homogeneous turbulent shear flow, Report TF-25 Dep of Mech Eng , Stanford University

Rogers, M M , Mansour, N N & Reynolds, W C 1989, An algebraic model for the turbulent flux of a passive scalar J Fluid Mech 203, 77-101

Schmidt, H & Schumann, U 1989, Coherent structure of the convective boundary layer derived from large-eddy simulations J Fluid Mech , 200 511 562

EIGHTH SYMPOSIUM ON
TURBULENT SHEAR FLOWS
Technical University of Munich
September 9-11, 1991

THE TEMPERATURE STRUCTURE FUNCTION FOR COMPLEX TERRAIN

Anne F. de Baas *) and Marc Sarazin **)

*) Risø National Laboratory, 4000 Roskilde,Denmark

**) European Southern Observatory, K Schwarzschild-str 2,
D8046 Garching bei München, Germany

ABSTRACT

Design studies are being conducted with the aim of constructing a very large telescope (ø 16 m) to observe the night-time sky. A numerical model is developed to calculate the temperature structure function on top of the mountain and the results are compared to measurements The model consists of an equation for the wind-components, where the turbulence model is the well-known $\varepsilon - E$ model, an equation for the temperature variance and its dissipation. From the values for ε and ε_θ we derive the temperature structure function

$$C_t^2 = 1.6\ \varepsilon_\theta\ \varepsilon^{-1/3}, \qquad (1)$$

(Wyngaard et al, 1971). The numerical results were compared to C_t^2 derived from the fine-scale temperature fluctuation measurements The results show the impressive achievement of this model despite its severe approximations

INTRODUCTION

The European Southern Observatory (ESO) wants to construct a new Very Large Telescope (VLT) in Chile They are looking for a mountain with optimal conditions for observation purposes. This means that the wind and turbulence fields have to meet certain criteria For the contract the wind field was modeled over some chosen sites with WASP (Troen et al, 1989) Also some possible alterations in the site were considered like cutting the top of the mountain. The other part of the contract here described comprised modeling the 'seeing', which is a function of the temperature structure function C_T^2 The question concerned the possible effects of different mountains on the seeing.

DESCRIPTION OF THE MODEL

The situation at the telescope site to be considered is nighttime flow over a steep hill, without separation We confine ourselves to situations with higher winds so that the stability is weakly stable In such situations the effect of the orography on the wind is much larger than the stability effects, and the buoyancy terms in the 'flow' equations (U, E, ε) can be neglected This means a decoupling from the 'temperature' equations (T, $\overline{\theta^2}, \varepsilon_\theta$). As stationarity is required we do not solve the temperature equation, which is basically instationary in stable situations, but assume that the temperature profile is lifted over the hill.
In our two equation (E-ε) turbulence model the fluxes are approximated by a gradient approach with en eddy diffusivity $K_m = c_\mu \frac{E^2}{\varepsilon}$.

$$\begin{aligned}
\overline{u_i u_j} &= -K_m \left(\frac{\partial U_i}{\partial x_j} + \frac{\partial U_j}{\partial x_i}\right), \\
-\frac{1}{2}\overline{u_j u_i^2} - \overline{u_i p} &= \frac{1}{2} K_E \frac{\partial \overline{u_i^2}}{\partial x_j} = K_E \frac{\partial E}{\partial x_j} \\
-\overline{u_j \varepsilon'} &= K_\epsilon \frac{\partial \varepsilon}{\partial x_j} \\
\overline{u\theta} &= -K_h \frac{\partial \Theta}{\partial x} \qquad (2) \\
\overline{w\theta} &\equiv u_* \Theta_* = -K_h \frac{\partial \Theta}{\partial z} \\
\overline{u_j \theta^2} &= -2K_h \frac{\partial \overline{\theta^2}}{\partial x_j}
\end{aligned}$$

where $K_E = K_m$, $K_\epsilon = K_m/\sigma_\epsilon$ and $K_h = \alpha K_m$
The constants σ_ϵ and α^{-1} are called Prandtl numbers

Substituting these flux modeling in the 'flow' equations for stationary flow without buoyancy effects we have for

momentum:

$$U_j \frac{\partial U_i}{\partial x_j} = \frac{\partial}{\partial x_j}\left(K_m \frac{\partial U_i}{\partial x_j}\right) - \frac{1}{\rho_0}\frac{\partial P}{\partial x_i} \qquad (3)$$

kinetic energy

$$U_j \frac{\partial E}{\partial x_j} = \frac{\partial}{\partial x_j}\left(K_m \frac{\partial E}{\partial x_j}\right) + K_m \left(\frac{\partial U_i}{\partial x_j}\right)^2 - \varepsilon \qquad (4)$$

temperature variance:

$$U_i \frac{\partial \overline{\theta^2}}{\partial x_i} = \frac{\partial}{\partial x_j}\left(K_h \frac{\partial \overline{\theta^2}}{\partial x_j}\right) + 2K_h \left(\frac{\partial \Theta}{\partial x_i}\right)^2 - 2\varepsilon_\theta \qquad (5)$$

The modeling of the dissipation equation can be found in Hanjalic and Launder, 1972

$$U_j \frac{\partial}{\partial x_j}\varepsilon = \frac{\partial}{\partial x_j}\left(K \frac{\partial \varepsilon}{\partial x_j}\right) + 2c_{\varepsilon 1} K_m \left(\frac{\partial U_i}{\partial x_j}\right)^2 \frac{\varepsilon}{q^2} - 2c_{\varepsilon 2}\frac{\varepsilon^2}{q^2}, \qquad (6)$$

The modeling of the thermal dissipation equation can be found in Newman et al, 1981:

$$\frac{\partial}{\partial x_j}(U_j \varepsilon_\theta) = \frac{\partial}{\partial x_j}\left(\frac{K_h}{\sigma_{\epsilon_\theta}}\frac{\partial \varepsilon_\theta}{\partial x_j}\right) + a_1 K_h \left(\frac{\partial \Theta}{\partial x_i}\right)^2 \frac{\varepsilon_\theta}{\overline{\theta^2}} - a_2 \frac{\varepsilon_\theta^2}{\overline{\theta^2}} - a_3 \frac{\varepsilon \varepsilon_\theta}{q^2}, \qquad (7)$$

CONSTANTS IN THE EQUATIONS

The constants in the 'flow' part of the model for the atmosphere (Duynkerke,1982) can be determined to be $c_\mu = A^{-2} = (5\,48)^{-2} = 0\,033$, $c_{\varepsilon 2} = 1\,83$, $c_{\varepsilon 1} = 1\,46$ and $\sigma_\varepsilon = 2\,38$

The neutral and stable surface layer profiles found on flat terrain (Businger,1971) satisfy the $\overline{\theta^2}$ equation For the ε_θ equation the situation becomes too involved if stability is taken into account and in this model the coefficients are tuned to the neutral situation It follows that

$$\frac{u_*^2\Theta_*^2}{z^2}\left[\frac{1}{\sigma_\theta}+\frac{1}{\kappa^2}\left[a_1\frac{(0\,74)^2}{B}-a_2\frac{(0\,74)^2}{B}-a_3\frac{(0\,74)}{2A}\right]\right]=0 \quad (8)$$

We assumed that $\sigma_\theta = \sigma_\varepsilon = 2\,38$ There are various solutions to this equation We tested $\{a_1,a_2,a_3\}=\{1,1,1\}$, $\{2.36,2\,02,1\,5\}$ and $\{5,3\,38,3\,38\}$ for the atmosphere, where the second combination keeps a_2 as given by Newman and the other two combinations are chosen such that the a_1 are wide apart. We found that the results for the temperature structure function C_T^2, (our ultimate goal) are the same on flat terrain no matter what the constants are

The weakly stable profiles turned out to be close to a solution of the ε_θ equation with these sets of coefficients, in the sense that only slight changes in C_T^2 occurred downstream.

TEMPERATURE STRUCTURE FUNCTION

The temperature structure function is defined as

$$C_T^2 = \frac{\overline{(\Theta(\vec{r}_o)-\Theta(\vec{r}+\vec{r}_o))^2}}{r^{\frac{2}{3}}} \quad (9)$$

and can be related to the 3D temperature spectra S_T normalized as

$$\overline{\theta^2} = \int_0^\infty S_T(k)d(k)$$

Scaling the temperature spectrum with the parameters of the inertial subrange gives (Tennekes and Lumley, 1984 p. 283 with $S_T = 2E_\theta$)

$$S_T(k) = \beta\varepsilon_\theta\varepsilon^{-\frac{1}{3}}k^{-\frac{1}{3}}$$

Here ε_θ is defined (as before) to be the rate of dissipation of half the temperature variance

From the definition of S_T and C_T^2 it follows

$$C_T^2 = \gamma\varepsilon_\theta\varepsilon^{-\frac{1}{3}}, \quad (10)$$

where Tennekes and Lumley's variables (1984) give $\gamma = 2.4$, Dutton and Panofsky (1983, p182) $\gamma = 2\,8$ and Wyngaard et al (1971) $\gamma = 3.2$. All authors agree that the constants are very difficult to measure and a factor 2 in uncertainty is not uncommon

Wyngaard 1973, page 128 finds from measurements for the neutral and stable case

$$C_T^2\frac{(\kappa z)^{\frac{2}{3}}}{\Theta_*^2} = 2\,66(1+2\,1(\frac{z}{L})^{\frac{2}{3}})$$

which for neutral stability with $\kappa = 4$ reads $C_T^2\frac{(\kappa z)^{\frac{2}{3}}}{\Theta_*^2} = 2\,66$ and which has as very stable limit $C_T^2\frac{z^{\frac{2}{3}}}{\Theta_*^2} = 11.76\xi^{\frac{2}{3}}$

Using the surface layer profiles

$$\begin{aligned}\varepsilon &= \frac{u_*^3}{\kappa z}\phi_m(\xi),\\ \varepsilon_\theta &= \frac{u_*\Theta_*^2}{\kappa z}\phi_h(\xi),\end{aligned} \quad (11)$$

where the stability parameter ξ and Monin-Obukhov length L are given by

$$\begin{aligned}\xi &= \frac{z}{L},\\ L &= -\frac{\Theta_0}{\kappa g}\frac{u_*^3}{\overline{w\theta}_0} = \frac{\Theta_0}{\kappa g}\frac{u_*^2}{\Theta_*}\end{aligned} \quad (12)$$

in the scaling equation for C_T^2

$$C_T^2 = \gamma\frac{\varepsilon_\theta}{\varepsilon^{\frac{1}{3}}} = \gamma\frac{\Theta_*^2}{(\kappa z)^{\frac{2}{3}}}\frac{\phi_h}{\phi_m^{\frac{1}{3}}} \quad (13)$$

For stable conditions we have the stability functions are $\phi_m = 1 + 4\,7\xi$ and $\phi_h = .75 + 4.7\xi$. This gives the measured neutral limit mentioned above if $\gamma = 3\,6$ and the very stable limit if $\gamma = 2\,3$

In our model we calculate with neutral ϕ_m and stable ϕ_h, thus

$$\gamma = 2.66\left[1+2.4\xi^{\frac{2}{3}}\right][.75+4.7\xi]^{-1} \quad (14)$$

E.g. for $\xi = 1$ we have $\gamma = 1\,6$. If necessary, a different value of γ can directly be applied to the results by a simple scaling if the C_T^2 axis and all conclusions are still true in a relative sense

INNER LAYER THEORY

The relation between the wind profile at the top and the inlet profile in 2D cases can be described by inner layer theory (Jackson and Hunt, 1975).

For a hill with height h, width L and roughness z_0

$$\frac{\ell}{L}\ln\left(\frac{\ell}{z_o}\right) = 2\kappa^2 \text{ and} \quad (15)$$

$$\Delta S_{max} \sim 2h/L, \quad (16)$$

ℓ is the inner layer height where the speedup S is maximum.

With an inlet U_0 the differential speedup is defined as

$$\Delta S(x,z) \equiv \frac{U(x,z)-U_o(z)}{U_o(z)} = \frac{\Delta u_*}{u_*}. \quad (17)$$

Our model will show that the changes in ε_θ are much smaller than the ones in ε. If ε at the top is taken equal to the inlet (frozen thermal turbulence) and inserting surface layer scaling for ε we get

$$C_T^2 = 1.6\,\varepsilon_\theta\,\varepsilon^{-\frac{1}{3}} = 1.6\,\varepsilon_\theta\,\frac{\kappa z}{u_*} \qquad (18)$$

Applying inner layer theory we get with x_o the x-coordinate of the inlet and x_t the x-coordinate of the top

$$C_T^2(x_t, z=l) = \frac{1}{1+\frac{\Delta u_*}{u_*}}\,C_T^2(x_o, z=l) \qquad (19a)$$

with

$$C_T^2(x_0, z=l) = \frac{\gamma\Theta_*^2}{(l\kappa)^{\frac{2}{3}}}\left(0.75 + \frac{l}{L}4.7\right) \qquad (19b)$$

These results are only valid in case $L_y = \infty$. The influence of finite L_y is not taken into account. For finite L_y the flow can go around the hill and the turbulence increases less than in the 2D case. This means that the temperature fluctuations do not get mixed so efficiently and it is expected that the seeing is higher than pedicted by 2D inner-layer theory.

THE PU MODEL

The pressure that drives the flow over a hill of small slope can be approximated by the potential pressure (Prandtl's boundary layer). The correct way of proceeding would be to write the flow equations in a boundary following coordinate system. The assumption that the pressure is potential is only valid for small slopes and we will make a next assumption, also based on this fact. We stretch the surface of the hill into a straight line and assume that we can keep the Cartesian flow equations in this coordinate system while keeping the pressure as described by the potential pressure. We therefore assume that no transformation of the flow equations is necessary or in other words that the extra terms due to the curvature of the coordinate system are small.

From the equation of motion for potential flow we can easily derive an expression for the horizontal Fourier transform of the pressure $\hat{P}(\vec{k}, z)$

$$\hat{P}(\vec{k}, z) = -\frac{(\vec{u}_0\cdot\vec{k})^2}{|\vec{k}|}\hat{h}\exp(-|\vec{k}|z) \quad . \qquad (20)$$

The procedure is as follows. We specify the height of the terrain $h(x,y)$ and Fourier transform this into $\hat{h}(\vec{k})$. Substitution and a back Fourier transformation give $P(x,y,z)$. The value of the background wind $u_0(z)$ will be taken at a height $z = c\,|\vec{k}|^{-1}$, as used in Troen and de Baas (1987). The constant c gives a tuning freedom. With this the pressure is determined and kept fixed in the further proceedings.

RESULTS

THE PU-MODEL APPLIED TO 2D FLOW OVER HILLS

First the constant in the potential pressure formulation was tuned against the Askervein measurements. The vertical wind profile at the hill top and the wind at 10 m height across the hill were checked against the measurements. A good accordance was found for $c = 1$.

Then the model could be tested against the 2D inner layer theory. These equations were confirmed and it was indeed found that the inner layer height ℓ is independent of the height of the hill and the maximum speedup is independent of the roughness.

The PU-model was checked against the second-order model of Zeman and Jensen (1987) which also accounts for curvature effects. Both models use a potential pressure. The results for a low slope Lorenzian hill

$$\eta = \frac{h}{1+(x/L)^2}, \qquad (21)$$

were compared with $h = 50$ m, $L = 250$ m and $z_o = 0.03$ m. Speedup, kinetic energy and dissipation profiles before, at and after the hill top were compared (Fig. 1). We can see that the second order model gives more difference in the speedup as function of downwind distance. The profiles, also the ones for kinetic energy and dissipation, differ most behind the hill. However, considering the much larger sophistication of the Zeman and Jensen model the overall agreement is much better than expected.

We conclude that the E-ε turbulence model is very useful and that the violation of the flow equations without making the correct boundary following coordinate transformation is of minor importance.

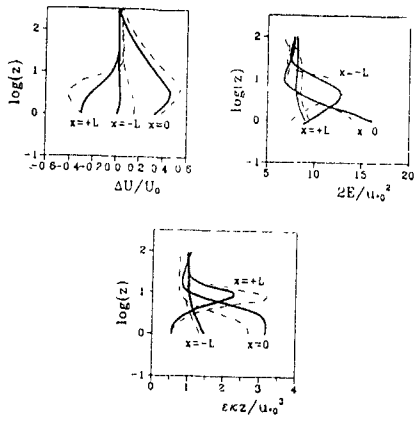

Fig. 1 Comparison of the E-ε model (solid lines) and the second order model by Zeman and Jensen (dashed lines) for a Lorenzian hill with h=50 m, L = 250 m, and z_0 = 0.03 m. a) speedup, b) kinetic energy, c) dissipation

THE 'FLOW' AND 'TEMPERATURE' EQUATIONS APPLIED TO FLOW OVER HILLS

Characteristic for a nonneutral boundary layer is that the heat flux at the ground is non-zero, while zero at the top. In a homogeneous terrain this means that the diffusive term in the temperature equation is non-zero and the solution is necessarily nonstationary However, to reduce the output of our model we restrict ourselves to stationary situations and are thus forced to consider only constant flux regions (surface layers). These regions extend to heights that are luckily sufficient for our purpose of predicting the seeing in the first 100m

With the analytical inlet profiles of $\overline{\theta^2}$, ε_θ, the U, E, ε fields calculated with the PU model and the analytical T field throughout the domain, we solve the equations for $\overline{\theta^2}$ and ε_θ and derive C_T^2. The equation for ε_θ contains three constants with a wide variety possible This gave us the opportunity to tune the constants to the measurements made at La Silla (VLT report no 55, p88) In our model La Silla is described by a Lorenzian hill with h=300 m, L_x=1 km, L_y=100 km, z_0= 01 m, and the measurement conditions by u_*= 6 m/s and θ = 0 09K.

The different set of constants tried are :

set 1 : $\{a_1, a_2, a_3\}$ ={1,1,1},
set 2 : $\{a_1, a_2, a_3\}$ ={2 36, 2.02, 1 5} and
set 3 : $\{a_1, a_2, a_3\}$ ={5, 3 38, 3.38}

The different C_T^2 profiles at the top of the hill for set 1, 2 and 3 are shown in Fig. 2.
Only set 1 gives the undisturbed flow at higher heights in this case of stable flow over a hill (not shown here) The set $\{a_1, a_2, a_3\}$ ={1,1,1} represents the data best if the constant γ in the C_T^2 relation to ε and ε_θ (Eq(8)) is set equal to γ=1.6. Set 2 would require a larger γ causing unrealistic values for C_t^2 at higher heights. The reverse is true for set 3 Here smaller values are required whereas the theory discussed before indicates that γ should rather be larger

We settle for the combination of set 1 and γ=1.6

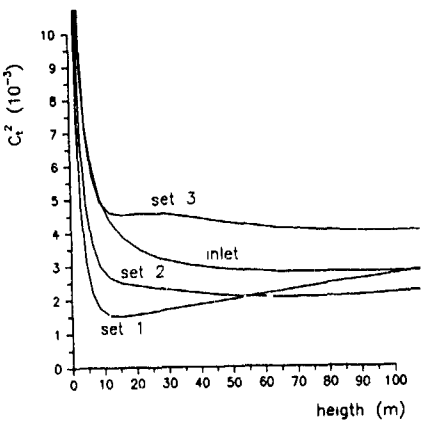

Fig 2. Measurements (•) and calculated profile of the temperature structure function $C_t^2(z)$ (in $10^{-3} K^2 m^{-2/3}$) on top of La Silla modelled by a Lorenzian hill with h=300 m, ω_x=1000 m, L_y=100000 m, z_0= 01 m, u_*= 58 m/s for different constant sets $\{a_1, a_2, a_3\}$ in the ε_θ equation
set 1 $\{a_1, a_2, a_3\}$ ={1,1,1},
set 2 $\{a_1, a_2, a_3\}$ ={2 36, 2 02, 1 5} and
set 3 : $\{a_1, a_2, a_3\}$ ={5, 3 38, 3 38}.
◇ inner layer results.

MODELLING OF LA SILLA, PARANAL, MONTURA AND ARMAZONI

Different mountains in Chile were considered as potential sites for the VLT and measuring campaigns were set up. A first preliminary modeling of the mountains Paranal, Armazoni and Montura is made with Lorenzian shapes The combinations of variables determining the hill shape are chosen so that La Silla, Paranal, Montura and Armazoni were approximated as best we could

mountain	h	L_x	L_y	z_o	ℓ	ΔC_T^2	$C_T^2(\ell)$
La Silla	300 m	1 km	100 km	01 m	6 m	62	3 84
Paranal	600 m	1 km	1 km	1 m	14 m	45	1 59
Montura	300 m	1 km	5 km	05 m	11 m	62	2 59
Armazoni	300 m	1 km	1 km	01 m	6 m	62	3 84

Measurements are found in VLT report No 55 and VLT report No 62, p 106, Fig 4 72 The model results fit the data very well (Fig. 3)

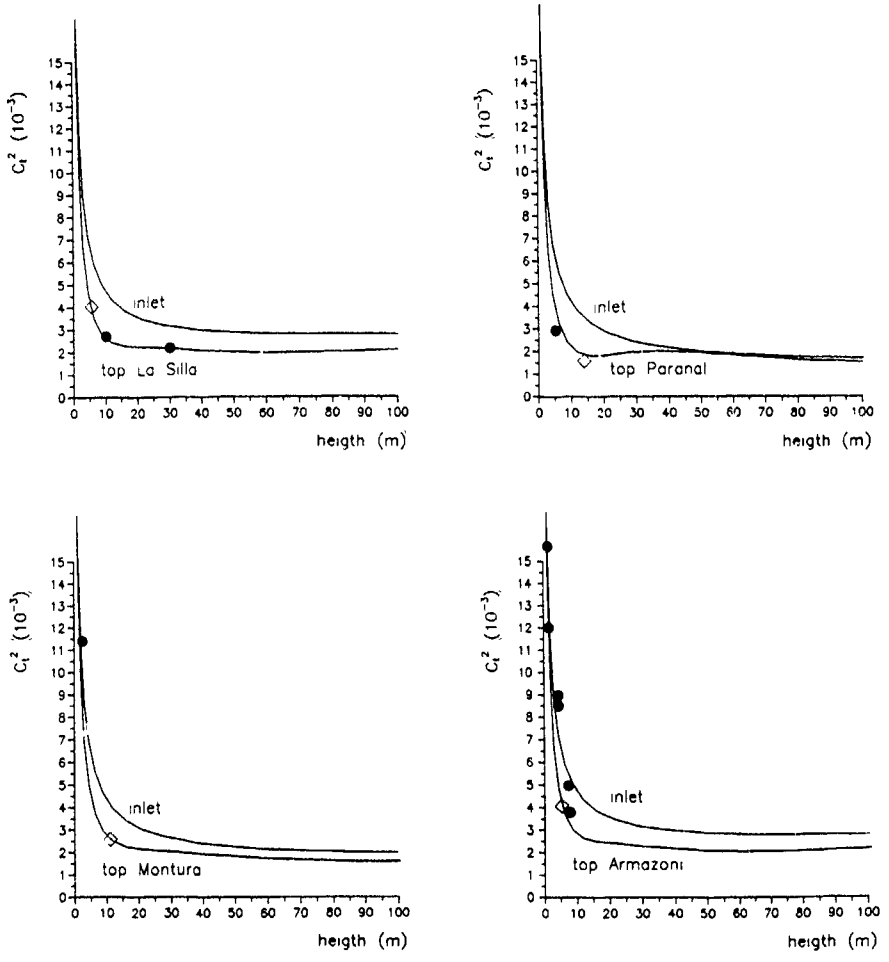

Fig. 3. Measurements (•) and calculated profile of the temperature structure function $C_T^2(z)$ (in $10^{-3}\,K^2\,m^{-2/3}$)
a) on top of La Silla modelled by a Lorenzian hill with h, L_x, L_y, z_0 = 300, 1000, 100000, .01 m and u_* = 58 m/s
b) on top of Paranal modelled by a Lorenzian hill with h, L_x, L_y, z_0 = 600, 1000, 1000, .1 m and u_* =.87 m/s
c) on top of Montura modelled by a Lorenzian hill with h, L_x, L_y, z_0 = 300, 1000, 500, 05 m and u_* =.75 m/s
d) on top of Armazoni modelled by a Lorenzian hill with h, L_x, L_y, z_0 = 300, 1000, 1000, .01 m and u_* =.58 m/s
◇ inner layer results

DISCUSSION

We feel that our model has the following shortcomings.

- The assumption in the PU model that the pressure is potential and that the extra terms are small in the equation of motion due to the curvature of the coordinate system is only valid for flow over small slopes This means that we have to restrict ourselves to lower hills.
- The vertical velocity plays a very important role in the temperature equation A velocity of 3 cm/s already has an effect of a°C. In our stretched coordinate model we were forced to exclude the temperature from calculation. For the cases considered in this report that was not of great importance as the thermographic investigations of the undeveloped sites showed that the hills were thermally homogeneous (VLT report No 62, page 142). However in order to catch influences of heat flux differences occuring due to roads and buildings we would need to calculate the temperature distribution in the flow.

To be able to improve on all these shortcomings a new model is being developed at Risø National Laboratory. The flow equations are written in a boundary following coordinate system, enabling us to calculate separation in front and behind obstructions as well as the temperature distribution in the air

REFERENCES

BUSINGER, J.A 1984 Equations and concepts, in Atmospheric Turbulence and Air Pollution Modelling, Ed Nieuwstadt and v Dop, Reidel Publ Co , Holland

DUYNKERKE, P G. 1988 Application of the $E-\varepsilon$ turbulence closure model to the neutral and stable atmospheric boundary layer *J A S* , **45-5**, 865-880

DUTTON J & H PANOFSKY 1984 Atmospheric turbulence models and methods for engineering applications. J Wiley and Sons.

HANJALIC, K. & B.E LAUNDER 1972 A Reynolds stress model of turbulence and its application to thin shear flows *J Fluid Mech* , **52**, 609-638.

JACKSON, P.S & J.C.R. HUNT 1975 Turbulent wind flow over a low hill. *Quart J Roy Meteor. Soc.*, **101**, 929-955

NEWMAN G.R., B.E. LAUNDER & J.L. LUMLEY 1981 Modelling the behaviour of homogeneous scalar turbulence. *J. Fluid Mech*, **111**, 217-232

SARAZIN M , 1987. Site testing for the VLT, LASSCA, La Silla seeing campaign Ffeb 1986, Data analysis part 1: seeing, VLT reports No. 55 ESO Garching bei Munchen, Germany.

SARAZIN M 1990 VLT site selection working group final reports, VLT reports No 62 ESO Garching bei Munchen, Germany

TENNEKES, H. & J.L. LUMLEY 1972 A first course in turbulence, MIT press.

TROEN I. & A.F de BAAS 1986 A spectral diagnostic model for wind flow simulations in complex terrain Proceedings of the EWEC'86 European Wind Energy Association, Conference and Exhivition, Rome 7-9 October Eds W. Palz and E Sesto Published by A. Raguzzi, Rome, Vol. I, 243-250

TROEN I. & N.G. Mortensen 1989 WAsP- Wind atlas analysis and application programme. An Introduction Third edition. Risø National Laboratory, 12pp.

ZEMAN, O. & N.O. JENSEN 1987 Modification of turbulence characteristics in flow over hills *Quart J. Roy. Meteor. Soc* , **113**, 55-80.

EIGHTH SYMPOSIUM ON
TURBULENT SHEAR FLOWS
Technical University of Munich
September 9-11, 1991

SECOND MOMENT CLOSURE PREDICTIONS OF JET-ON-JET IMPINGEMENT FLOWS

S J Baker* and J.J McGuirk**

* Dept of Mechanical Engineering, Imperial College, London, SW7 2BX, U K.

** Dept. of Transport Technology, Loughborough University, Leicestershire, LE11 3TU, U.K

ABSTRACT

Calculations are presented which contrast the performance of eddy viscosity and second moment closure turbulence models for confined flows dominated by jet-on-jet impingement. Flow configurations relevant to gas-turbine and ramjet side-dump combustors are chosen, with emphasis laid on two-dimensional systems, one plane and one axi-symmetric, to allow sufficiently fine meshes to avoid numerical errors. The particular second moment closure adopted is the Gibson-Launder Reynold stress transport model, using two alternative sets of constants in the pressure-strain model For the axi-symmetric case, the second moment closure performs significantly better than the eddy viscosity model, improved predictions are obtained for both the strength of recirculation upstream of impingement and the rate of recovery of the downstream velocity profiles. This is attributed to the much improved resolution of the highly anisotropic turbulence field created at impingement. Much smaller differences between the two models are seen in the plane flow case. This is shown to be partly caused by the flow being more pressure dominated in the plane geometry. Evidence also exists however to indicate the presence of large-scale periodic oscillations which are not well modelled by any long-time-averaged closure.

INTRODUCTION

Many fluid flow systems which require rapid mixing involve the impingement of two or more fluid streams. In ramjet side-dump combustors and in all gas-turbine combustors, multiple air jets distributed around the periphery of a flame tube are radially injected to impinge on each other, creating both a mean flow pattern conducive to flame stability (recirculating primary zone vortex) and a high turbulence field to encourage rapid fuel/air mixing. The ability to predict the turbulence levels in the primary zone impingement area is an essential pre-requisite for any useful mathematical model of such systems, since this is the 'environment' into which the fuel is injected. As a first step, we may examine the turbulence environment created by the impingement process under isothermal conditions and without fuel injection, to avoid complications arising from variable density, combustion and fuel spray modelling. Koutmos and McGuirk (1989) have performed an LDA study of this region in a model gas-turbine combustor and noted the highly anisotropic nature of the turbulence at impingement; radial and azimuthal normal stresses were typically twice as large as the axial component. Attempts to predict this flow with a two-equation eddy viscosity model (k-ε) (Koutmos and McGuirk (1991)) failed to reproduce this feature, leading to a large underprediction (≈ 100%) of the level of turbulence activity in the jet-on-jet impingement zone. It must be stated however that the 3D nature of the flow and the correspondingly rather coarse meshes which were used did leave some doubt that all numerical errors had been completely eliminated from these results. A second moment closure route is likely to be in a much stronger position to reproduce the large turbulence anisotropy in such flows, but since obtaining a numerically accurate solution of the Reynolds stress equations in a 3D recirculating flow is currently a daunting task, it is felt that recourse should first be made to an attempt to address this problem in a 2D flow.

Fortunately, the main features of jet-on-jet impingement can be reproduced in two dimensions Measurements are available in both an axi-symmetric (Green and Whitelaw (1980)) and a plane flow (Miau et al (1989), Liou and Wu (1990)). The former was intended to be an idealised 2D version of an annulus-fed can-type gas-turbine combustor, whilst the latter flow resembles more that found in ramjet combustors. Similarly anisotropic turbulence fields at impingement have been measured as in the fully 3D flow of Koutmos and McGuirk (1989). One further feature which has also been noted in the plane 2D flow impingement is the presence of bi-modal pdf's of the velocity components. Jet flapping or periodic instability of the impingement process itself have been suggested as the origin of these. It is not known to what extent the 3D impingement process is also subject to such phenomena, although the 2D system may be more prone to strong flapping modes. Such phenomena, if present to any significant level in energy terms, will contribute to the level of 'turbulence' measured and hence the anisotropic structure, whilst being impossible to predict with long-time-averaged closure models of any level.

The turbulence structure of jet-on-jet impingement flows is therefore seen to contain questions of importance to both practical combustor designers and turbulence model developers and users. The purpose of the present paper is to use the two 2D impingement flows mentioned above as a testing ground for addressing the question: to what extent can a second moment closure model improve on the ability to predict the impingement zone turbulence levels (and the mean velocity field which these influence) compared with an eddy viscosity level of closure?

MATHEMATICAL MODEL AND COMPUTATIONAL DETAILS

The flows considered are all high Reynolds number, constant property, incompressible flows, governed by the mean flow equations:

$$\frac{\partial(U_i)}{\partial x_i} = 0$$

$$\frac{\partial}{\partial x_j}(U_j U_i) = -\frac{1}{\rho}\frac{\partial P}{\partial x_i} - \frac{\partial}{\partial x_j}(\overline{u_i u_j})$$

The unknown Reynolds stresses in these equations are obtained either using the standard high Reynolds number k-ε model (Launder and Spalding (1974)) with the standard set of constants, or the Gibson-Launder (1978) second moment closure:

$$\frac{\partial}{\partial x_k}(U_k \overline{u_i u_j}) = \frac{\partial}{\partial x_k}(C_s \frac{k}{\varepsilon}\overline{u_k u_l} \frac{\partial}{\partial x_l}\overline{u_i u_j})$$

$$+ P_{ij} + \varphi_{ij} - \frac{2}{3}\delta_{ij}\varepsilon$$

$$\frac{\partial}{\partial x_k}(U_k \varepsilon) = \frac{\partial}{\partial x_k}\left(C_\varepsilon \frac{k}{\varepsilon} \overline{u_k u_l} \frac{\partial \varepsilon}{\partial x_l}\right)$$

$$- C_{\varepsilon 1} \frac{\varepsilon}{k} \overline{u_i u_j} \frac{\partial U_i}{\partial x_j} - C_{\varepsilon 2} \frac{\varepsilon^2}{k}$$

$$P_{ij} = -\left(\overline{u_i u_k} \frac{\partial U_j}{\partial x_k} + \overline{u_j u_k} \frac{\partial U_i}{\partial x_k}\right)$$

$$\varphi_{ij} = -C_1 \frac{\varepsilon}{k}\left(\overline{u_i u_j} - \frac{2}{3}\delta_{ij} k\right) - C_2\left(P_{ij} - \frac{1}{3}\delta_{ij} P_{mm}\right)$$

The constants involved in the second moment closure model were initially adopted unchanged from the work of Gibson and Launder (1978). Some calculations were however carried out using the alternative set of constants suggested by Gibson and Younis (1986) for the pressure-strain component (i.e. C_1=3.0, C_2=0.3 as opposed to C_1=1.8, C_2=0.6) and some comments are included below on this. In the results presented, no terms for wall-reflection have so far been included into the pressure-strain model

The equations were solved using an iterative finite-volume, pressure-correction method which adopted grid-staggering for both the velocity components and the Reynolds shear stresses for numerical stability reasons. The convection terms in all equations were discretised using the second-order accurate QUICK method. For the present 2D flows, sufficiently fine meshes could be used such that the cell Peclet numbers were small enough that the QUICK method caused no spatial oscillation or boundedness problems. On the fine mesh, maximum cell Peclet numbers were of order 100 in the k-ε calculations and 5000 in the Reynolds stress predictions. The only convective stabilising measure adopted therefore was to remove all negative coefficient contributions into the source terms in the algebraic equations to retain the diagonal dominance of the matrix. As an example of the grid-dependancy tests carried out Fig 1 shows results for the axi-symmetric problem discussed below.

Coarse, medium and fine meshes were used, the results are sensibly grid-independent on the fine mesh (122x83), with the turbulence quantities most sensitive; maximum changes were less than 10% on the fine mesh which was therefore used in all further predictions. The current 2D calculations do not therefore suffer from any doubts concerning numerical error as the 3D calculations of Koutmos and McGuirk (1989), and true turbulence model comparisons are possible. It should be noted that high Reynolds number log-law based wall functions were used for the near-wall cells, and care was taken to retain the near-wall mesh line at the same position during the mesh refinement process

RESULTS AND DISCUSSION

Initial calculations were made for the 2D axi-symmetric geometry of Green and Whitelaw (1980) shown in Fig. 2. The flow configuration comprised a slot entry into a cylindrical tube, with an upstream cavity representing the 'head' of the combustor. Measurements were available at the annulus entrance which avoided the need to calculate the flow over the domed head, but allowed the flow from the small height annulus through the slot to be part of the predictions. Fig. 3 displays the predicted streakline flow patterns using the k-ε model and the second moment closure. Noticeable differences appear in all three recirculation zones present: in the upstream head cavity, in the downstream annulus and in the separation zone near the tube wall in the wake of the bent-over jet. The second moment closure predicts tighter, stronger and smaller recirculation patterns for the first two zones, but an elongated jet wake separation zone In the head cavity particularly, large differences are observed; the eddy viscosity model shows a recirculation which fills the available space and indicates a solid body recirculation pattern The Reynolds stress model on the other hand shows the upstream edge of the inflowing jet to produce an eddy which penetrates less than a quarter upstream, with almost stagnant fluid filling the remainder of the cavity. Clearly the amount of jet fluid which contributes to the upstream eddy is an important parameter in the context of combustor modelling, with the Reynolds stress model indicating a weaker backflow than the k-ε model. Which is the more correct is assessed below by comparison with measurements of the axial velocity profiles taken at the dashed lines indicated on Fig. 3. Both models predict the effect of the annulus velocities on the inflowing jet trajectory to allow fluid to flow into the upstream 25% of the slot width, again the Reynolds stress model indicates this effect to be somewhat weaker.

Fig. 4 allows a quantitative assessment of the accuracy of the two models by comparing predictions with measured mean axial velocity profiles at several stations both up- and downstream of the slot (the origin of the x-co-ordinate is at the slot centre; quantities are non-dimensionalised by the downstream bulk velocity and the tube diameter) The Reynolds stress predictions are seen to be in closer agreement with the data at all stations (extra profiles have been taken from Green (1981). In particular the weaker upstream recirculated flow predicted by the second moment closure is vindicated by the measurements The rate of mixing-out of the profile as it proceeds towards a developed pipeflow shape is also better in the Reynolds-stress predictions Examination of the $\overline{uv}$ shear stresses predicted by the two models showed that the k-ε model produced positive values in the region of the tube wall and a negative zone in the vicinity of the axis for the entire downstream region (consistent with the velocity gradients). The Reynolds stress model on the other hand shows the positive values spreading rapidly towards the axis and positive shear stresses over the whole radius from about one slot width downstream of impingement. This change in the sign of the dominant shear stress has brought about the improved profile shapes.

The too-slow rate of mixing in the k-ε prediction may also be a result of the underprediction of the turbulence levels generated by the impingement process. Only measurements of the axial normal stress are available, and these are compared with predictions in Fig. 5 on the basis of normalised turbulence intensity. Although the Reynolds stress model does reduce the underprediction implied by the eddy viscosity calculations, (increasing levels typically by a factor of 2), the results still fall far short of the measurements, particularly in the impingement zone. The possibility that large-scale unsteadiness is contributing to this deficiency cannot be excluded, particularly given the close agreement in the mean velocity profiles in this region shown in Fig. 4. Further downstream the Reynolds stress predictions are considerably better, showing close agreement with measured stress levels at the two furthest downstream stations, with the eddy viscosity predictions being a factor of two in error It may also be noted here that the use of the Gibson and Younis pressure-strain constants improved the stress level predictions slightly, by about 10%, but did not alter the impingement zone behaviour. One final feature of impingement is the anisotropy of the turbulence structure Fig. 6 indicates that the Reynolds stress model reproduces the anisotropy well, with the two transverse normal stresses 2.5 times the axial level The k-ε model produces only a factor of 1.5, with all three levels lower.

Turning to the 2D plane flow geometry of Liou and Wu (1990), a sketch of the flow configuration and predicted particle path trajectories with the two models are given in Fig. 7 This flow differs from the first in possessing parallel side inlet ducts and a smaller upstream cavity. Inlet condition information was available one duct height upstream of the jet exits, so that flow in the inlet ducts itself was part of the calculation, allowing an upstream effect on the exit velocity profiles. Once again the stress model seems to predict a different nature to the upstream eddy, although the short duct length for the combustor head no longer allows the size to differ. The velocity profile shape through the eddy is significantly different however; k-ε predicts a clear solid body rotation throughout the eddy whereas Reynolds stress displays this only at the very eye of the vortex, with uniform velocity in the outer regions.

Velocity profile information is available at the four downstream stations marked in Fig. 7. In contrast to the previous case, very little difference is now observed (see Fig. 8) between the two turbulence models for either axial or

transverse velocities The Reynolds stress model predicts a steeper velocity gradient in the shear layer on the edge of the downstream recirculation, and this is closer to measured data, but the larger separation zone in the second moment closure prediction is not borne out by the measurements Similarly close predictions between the two models are obtained for the normal stress levels which are therefore not shown here The transverse normal stress is substantially underpredicted on the symmetry plane (a factor of 2). Together with the occurrence of non-zero transverse mean velocity on the central plane in the measurements (see Fig 8), this encourages the belief that large-scale jet flapping across this plane is occuring and some of this unsteadiness is appearing as v^2 turbulence level This is further supported by the evidence from additional measurements in the geometry reported by Liou et al (1990) of bi-modal pdf's of the transverse velocity in the same region Clearly the use of a true symmetry plane in the calculations and long-time averages over all scales of motion, will cause problems when trying to predict flows with such strong oscillations. Finally, the axial momentum equation budgets along the centre-planes of the two flows shown in Fig 9 indicate that although the impingement region is highly pressure-dominated in both flows, this also applies in the rest of the downstream region in the plane flow, whereas the Reynolds-stress gradient provides a non-negligible contribution in the axi-symmetric case. The plane flow does not therefore allow the benefits of the second moment closure to be displayed for both the above reasons, whereas it seems the cylindrical flow suffers less from such problems

SUMMARY

(i) Grid independent predictions have been obtained using the QUICK convection scheme for k-ε and Reynolds stress models applied to two confined flows containing jet-on-jet impingement zones

(ii) Little difference was observed between the two alternative sets of pressure-strain constants recommended for the Gibson and Launder second moment closure.

(iii) For the axi-symmetric case studied, although the impingement region was pressure-dominated, the presence of an annulus-fed system and a large upstream cavity allowed the superior prediction of the turbulence field provided by the Reynolds stress model also to improve predictions of the mean velocity field The higher levels of anisotropy and turbulence energy and the de-coupling of the shear stress from the velocity gradient produced a better prediction of the recovery region downstream of impingement.

(iv) For the plane flow case, pressure domination extended over almost the entire impingement and recovery zones In this flow however there were several indications of the presence of large-scale flow oscillations which were not possible to predict with the calculation methods adopted

(v) Jet-on-jet impingement zones in 3D may not suffer from such strong oscillations, and will therefore benefit from the improved predictive accuracy of second moment closures. This will be true in the scalar fields into which the turbulence feeds even if pressure effects provide some insensitivity in the velocity field. If oscillations are still important then the second moment calculations will at least need to abandon use of symmetry conditions and adopt solution of the transient form of the equations to capture these effects

ACKNOWLEDGEMENTS

This work has been carried out with the support of Procurement Executive, Ministry of Defence The authors would also like to acknowledge useful discussions with colleagues at Imperial College (Mech.Eng. and Chem Eng. Depts.), at Rolls-Royce and at RAE (Pyestock).

REFERENCES

KOUTMOS, P and McGUIRK, J J 1989 Isothermal flow in a gas turbine combustor a benchmark experimental study, Expts. in Fluids, 7, pp. 344-354.

KOUTMOS, P. and McGUIRK, J.J 1991 Isothermal modelling of gas turbine combustors a computational study To appear in AIAA Jnl. of Propulsion and Power

GREEN, A and WHITELAW, J H. 1980 Measurements and calculations of the isothermal flow in axi-symmetric models of combustor geometries. Proc I Mech E , Jnl. of Mechanical Engineering Science, 22, pp. 119-124.

MIAU, J J , SUN, D.J , YAO, L S 1989 Streamwise vortices generated by impinging flows in a confined duct Expts. in Fluids, 7, pp 497-500

LIOU, T M , WU, S.M 1990 LDV measurements of triple velocity correlations in confined opposing jets Proc of 5th Int Symp on Applications of Laser Techniques in Fluid Mechanics, Lisbon

LAUNDER, B.E. and SPALDING, D.B 1974 The numerical computation of turbulent flows. Comp Methods in Applied Mech. and Eng , 3, pp 269-289

GIBSON, M.M and LAUNDER, B E 1978 Ground effects on pressure fluctuations in the atmospheric boundary layer. Jnl Fluid Mech , 86, pp 491-511

GIBSON, M M. and YOUNIS, B.A. 1986 Calculation of swirling jets with a Reynolds stress closure Physics of Fluids, 29, pp 38-48

GREEN, A S 1981. Isothermal models of combustion chamber flows Ph D. Thesis, University of London

LIOU, T.M , WU, S.M and HWANG, Y.H. 1990 Experimental and theoretical investigations of turbulent flow in a side inlet rectangular combustor AIAA Jnl. of Propulsion and Power, 6, pp 131-138.

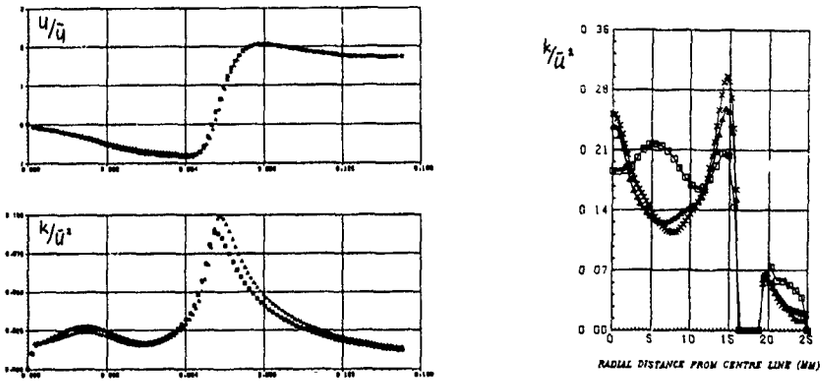

Figure 1 Grid dependency tests - axi-symmetric problem
(a) centre-line mean axial velocity and turbulence energy (⊡- medium mesh, ▲- fine mesh)
(b) radial profile of turbulence energy near impingement (□- coarse mesh, ▲- medium mesh, X - fine mesh)
(coarse - 62x33, medium - 96x58, fine - 122x83)

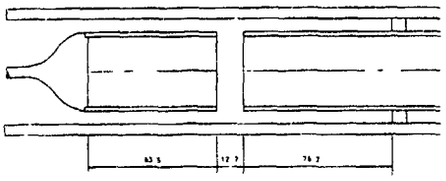

Figure 2 Flow configuration - axi-symmetric problem

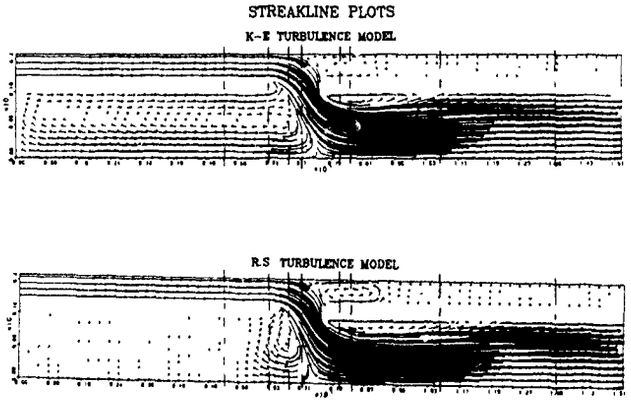

Figure 3 Predicted streakline patterns k-ε model (top) and second moment closure model (bottom)

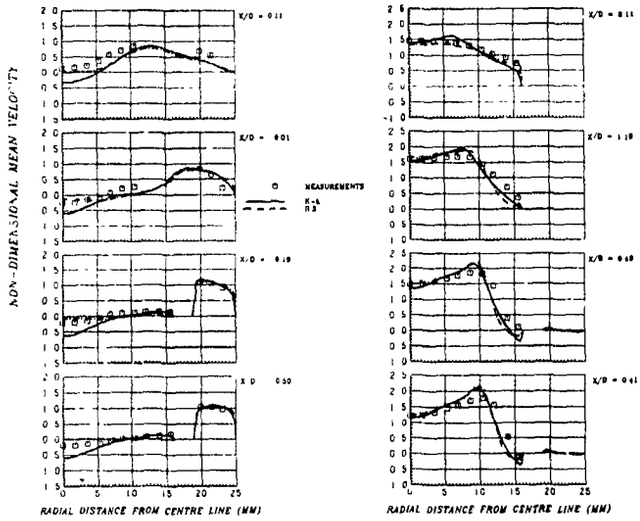

Figure 4 Comparison between measurements and model predictions for axial velocity profiles

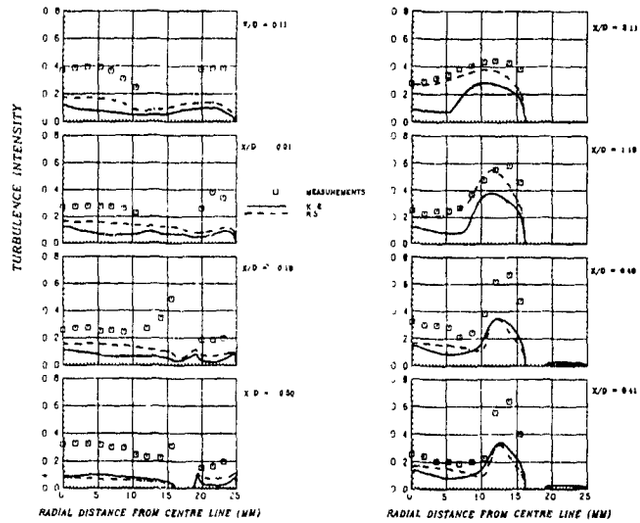

Figure 5 Comparison between measurements and model predictions for axial normal stress intensity

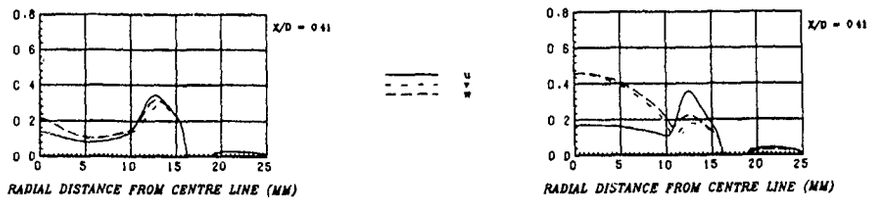

Figure 6 Individual normal stress predictions near impingement k-ε model (left) and second moment model (right)

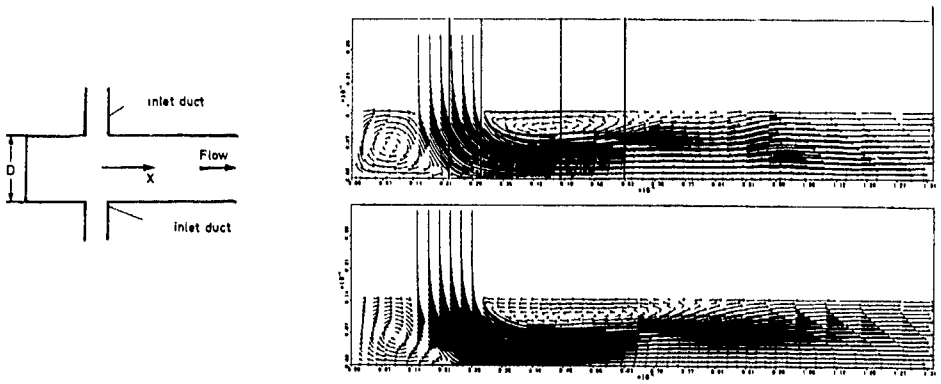

Figure 7 Flow configuration and predicted streakline patterns, plane problem, kε (top), second moment model (bottom)

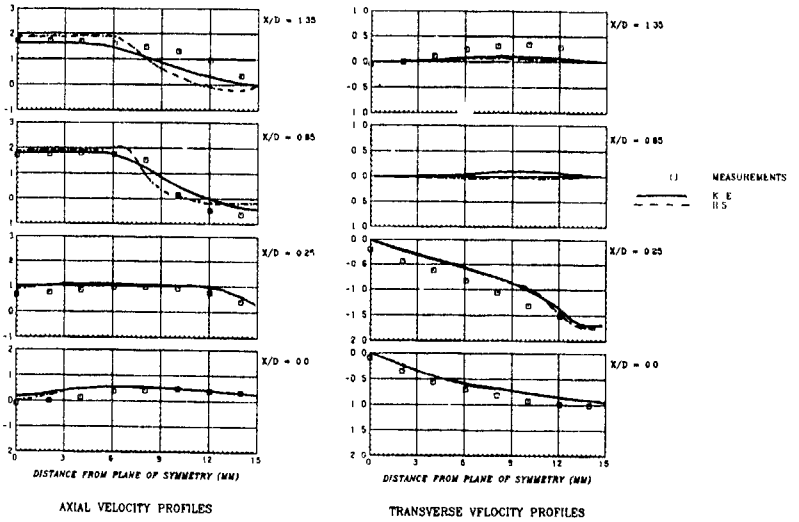

AXIAL VELOCITY PROFILES TRANSVERSE VELOCITY PROFILES

Figure 8 Comparison between measurements and model predictions for axial and transverse velocity profiles

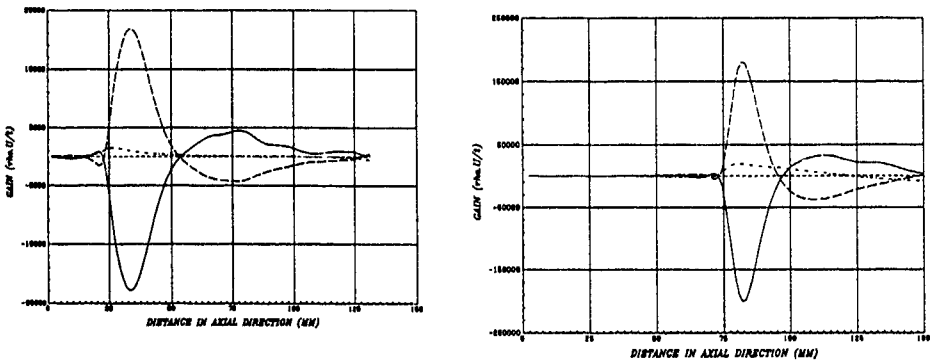

Figure 9 Budgets of axial momentum equation along centre-line, plane flow (left), axi-symmetric flow (right)

EIGHTH SYMPOSIUM ON
TURBULENT SHEAR FLOWS
Technical University of Munich
September 9-11, 1991

MEASUREMENTS AND SIMULATION OF THE FLOW AROUND A POPPET VALVE

Ž. Lilek**, S Nadarajah*, M Perić**, M.J Tindal* and M. Yianneskis*

*Centre for Heat Transfer and Fluid Flow Measurement
School of Physical Sciences and Engineering
King's College London, Strand, London WC2R 2LS, U.K

**Lehrstuhl für Strömungsmechanik
Friedrich-Alexander-Universität Erlangen-Nürnberg
Cauerstraße 4, D-8520 Erlangen

ABSTRACT

The flow through an axisymmetric inlet port was investigated experimentally and numerically. Laser-Doppler anemometry was used to measure the three ensemble-averaged mean and r m s velocity components for two valve lifts, 6 and 10 mm. Numerical calculations of the flows were carried out using a finite volume multigrid method and a standard k-ε turbulence model Comparison of the predictions with the experimental results shows good agreement for the mean velocities for the 10 mm lift case. However, for the 6 mm lift case the predicted flow differs substantially from the experimental results This indicates the extreme sensitivity of the flow to the valve lift and the need for more sophisticated turbulence modelling when predicting such flows.

INTRODUCTION

In the design of medium and high speed diesel engine inlet ports, the two major considerations are the volumetric efficiency of the engine and the mixing of fuel and air The requirement to improve fuel economy often conflicts with the need to reduce harmful exhaust emissions; both are affected by the mixing of air and fuel and the breathing capacity of the engine, which in turn depends on the design of the inlet port. The study of the air motion through ports is thus essential if port design is to be optimised.

Most studies of air motion in internal combustion engines have been restricted to the flow inside the engine cylinder, partly due to experimental and computational difficulties in dealing with the flows inside inlet ports. From such studies, it has been found that flow unsteadiness and valve operation have a negligible effect on the flow through the port and around the valve, but the valve lift was identified as having a significant effect on the flow (Bicen et al, 1985). The present work makes use of the demonstrated validity of the quasi-steady flow assumption so that measurements and predictions can be made with significantly reduced esxperimental and numerical complexities.

In the present study, which is part of a long term investigation, the flow through an idealised port design is considered in order to study the effects of essential features of port design under relatively simple conditions. In this way the influence of geometrical parameters such as seat width, valve lift etc. can be effectively quantified.

The work constitutes an extension of that previously reported by Demirdžić et al (1987). In the present geometry the valve seat width is larger and the recirculation regions along both the seat and crown are also larger and have a more significant effect on the flow. While in the earlier study the experimental results at both inlet and outlet cross-section were used as boundary conditions for calculations and only one valve lift was considered, here a full prediction without reference to experimental data was attempted.

APPARATUS AND EXPERIMENTAL TECHNIQUE

The test section geometry is shown in Figure 1. In order to enable optical access to all parts of the flowfield without beam refraction, a mixture of liquids was used as the working fluid Oil of turpentine and tetraline were mixed in a volume ratio of *31.3* to *68.7*. The resulting density and kinematic viscosity of the fluid were *899 kg/m^3* and *1.67x10^{-6} m^2/s* respectively. The temperature of the liquid was controlled to *+/-0.02 °C* throughout the experiments. The refractive index of the mixture at *23 °C* was *1.4892*, which matched the refractive index of the acrylic material of the test section In this way, the beams could enter the port and cylinder without suffering deflection at the walls It has been previously established (Cheung et al, 1990) that the flow of the mixture through the port is dynamically similar to that of air, subject to an upper limit where compressibility effects will become significant. The main features of the steady flow rig and of the experimental procedures have been described by Tindal et al (1988).

The test section was placed downstream of a constant head tank. In the absence of any swirl generation, the magnitude of the tangential component was near zero (to within the precision of the measurements). The liquid flowed through the port and valve discharging into the cylinder The flow rate was *1.742x10^{-3} m^3/s*. The flow Reynolds number, based on the hydraulic diameter of the annular passage around the valve guide, *26 5 mm*, was *24600*.

The laser-Doppler anemometer is shown schematically in Figure 2. It comprised a *10 mW* Helium-Neon laser, a rotating diffraction grating and a frequency counter (TSI model 1990B) for processing the Doppler signals. The ensemble-averaged data were processed by a microcomputer interfaced to the digital output of the counter, and the mean and r.m s velocities were calculated for a preset number of samples The errors in the mean and r.m.s. velocity measurements are

estimated at *5%* and *10%* respectively. The principal characteristics of the anemometer are listed in Table 1

Table 1: Principal characteristics of the laser-Doppler anemometer

Half-angle of beam intersection in air	*3.9°*
Frequency-to-velocity conversion constant, m/s/MHz	*4.65*
Intersection volume diameter at 1/e2 intensity (mm)	*0.060*
Intersection volume length at 1/e2 intensity (mm)	*1.320*
Number of fringes in intersection volume without frequency shift	*13*

NUMERICAL SOLUTION METHOD

Calculations were performed using a finite volume method (Demirdžić and Perić, 1990) with a full multigrid algorithm for convergence speedup (Perić et al, 1989). Three grid levels were used with *54 × 16, 108 × 32* and *216 × 64* control volumes, respectively. Figure 3 shows the coarsest grid (a) and an enlarged section of the finest grid (b). A standard k-ε turbulence method was employed (Launder and Spalding, 1974). The convection and diffusion fluxes were discretized with second order central-differences, except for the k and ε equations where upwind scheme was used for the discretization of convection fluxes. The ILU-decomposition method of Stone (1968) was used as a solver.

The standard wall functions were employed to specify the boundary conditions at walls (Launder and Spalding, 1974). Due to the relatively low Reynolds number of the flow, further systematic grid refinement could not be done without violating the wall function boundary condition. Outlet boundary was placed far enough downstream for zero gradient extrapolation to be justifiable. At the inlet cross-section - which was also placed sufficiently far upstream of the valve passage - only the flow rate and variable values typical for plug flow were specified. The sensitivity of the results to the inlet boundary conditions was checked by imposing also the fully developed annulus flow conditions, which were obtained in a separate calculation: the solution was not significantly affected in the region of interest The numerical results represent thus a pure prediction of the flow: comparisons with experiments were not used to tune the calculation results

RESULTS AND DISCUSSION

Measurements of the three ensemble-averaged mean and r.m.s. velocity components and turbulent shear stress were performed for a dense matrix of measurement points covering the whole cylinder cross-section from z = *- 5 mm* to z = *25 mm* The valve lifts of *6 mm* and *10 mm* were chosen to represent two of the four main flow regimes occuring in the valve passage (cf Tindal et al, 1988): one with a separation from the valve head (*6 mm*) and one with a separation from the valve seat (*10 mm*) At an intermediate valve lift the flow separates from both valve head and seat, and at low lifts there is no separation in the valve passage.

The velocity vectors obtained from the axial and radial component mean velocity measurements with valve lifts of *6* and *10 mm* are shown in Figures 4 and *5*, respectively. In both cases the flow emerges through the velve as an annular jet. It strikes the cylinder wall around *20 mm* downstream of the cylinder head with the *6 mm* lift, while with the 10 mm lift the impingement point moves about *10 mm* further downstream. Two large recirculation regions are formed, one on either side of the incoming annular jet. The recirculation below the cylinder head shows higher velocities than that below the valve. Differences between the flows obtained with the different valve lifts are found primarily in the vicinity of the valve passage. These differences stem from the aforementioned variation of the flow pattern with valve lift (Kastner et al, 1963; Tindal et al, 1988).

Predicted streamlines and isobars for the *10 mm* valve lift are shown in Figure 6 (a) and (b), respectively. Comparisons with earlier experimental results of Tindal et al (1988) indicate that the flow in the region upstream of the valve passage is well predicted, including small features such as the recirculation region at the end of the valve guide, cf Fig. 6 (a). The flow measured in one cross-section in this region (z = *- 20 mm*) is also in good agreement with predictions. Tindal et al (1988) also showed that the flow in the port is not significantly affected by the valve lift which was also found in the present measurements and predictions

The axial and radial mean velocity profiles measured with a valve lift of *10 mm* are presented and compared with the corresponding predicted profiles in Figures 7 (a,b) and (c,d), respectively. The predicted axial component profiles are in a good agreement with experimental data at all cross-sections; the radial component shows somewhat larger discrepancy in the jet impingement region. The agreement is especially good inside the two main recirculation regions. The secondary eddy in the corner of the cylinder head and wall shown in Fig 6 (a) is also indicated by the measured velocity profiles in this region, cf. Fig 7 (a).

Contours of the measured kinetic energy of turbulence, k, are shown in Fig. 8 for the *10 mm* valve lift flow The values of k vary from *0.04* m^2/s^2 away from the jet region to *0.4* m^2/s^2 near the centre of the jet The values are low near the exit of the port and they increase as the flow passes through the valve passage. The values of k continue to increase in the jet region as it spreads. The levels in the vortices are consistently lower than in the jet region; in the recirculation region along the cylinder head the levels increase progressively from the valve seat to the wall. The predicted and measured profiles of k are compared in Fig. 9 for three typical cross-sections. While the qualitative agreement is noticable everywhere, the data and predictions agree quantitatively only in the recirculation region beneath the valve The turbulence levels near the wall are siginificantly underpredicted for both valve lifts. One of the reasons for this is

thought to be the instabilities present in the flow, which are known to exist for both steady and unsteady flow regimes, cf Yianneskis et al. 1989. These amount to what is often termed "flapping" of the jet and will result in broadening of the velocity distributions and thus in an increase of the turbulence levels indicated by ensemble-averaged measurements. The measurements of the normal stresses indicated that the flow inside the cylinder is strongly anisotropic, especially for a distance of *30 mm* from the cylinder head Further downstream and in the port the turbulence is approximately isotropic, which was also found by Tindal et al, 1988.

Figure 10 shows predicted streamlines for the *6 mm* valve lift flow. The separation at the valve head observed in the experiment is not predicted and hence a lower jet angle and longer reattachment length then in the experiment resulted, cf. Fig 4 This is also evident from the comparison of predicted and measured axial and radial velocity component profiles shown in Fig 11. Due to the missing valve head separation, all downstream profiles differ substantially from the measured ones

Since for both valve lifts the same solution method, the same equations and the same grids were employed, it is obvious that the above disagreement is due to the incapability of the standard k-ε turbulence model to mimic the change in the flow regime when the valve lift is reduced. The reasons for this might lie in the stronger acceleration, streamline curvature and pressure gradients at lower lifts Future studies will involve variation of turbulence modelling (low-*Re* k-ε and Reynolds stress models) in order to clarify the above uncertainty

CONCLUSIONS

Steady turbulent flows through an axisymmetric port and poppet valve assembly were investigated. The mean velocity and turbulent kinetic energy were measured by laser-Doppler anemometry and then compared with corresponding predictions obtained with a multigrid finite volume numerical method.

The results obtained with valve lifts of *6* and *10 mm* show that the mean flow and turbulence structure are similar in both cases: the flow is essentially that of an annular jet surrounded by two axisymmetric ring vortices. There are differences in the flow in the valve passage due to the separation from the valve head at lower lift; this separation affects significantly the annular jet leaving the gap, especially its direction and hence the size of main recirculation regions.

The predictions show good quantitative agreement with the mean flow data for the *10 mm* valve lift case, but differ significantly for the *6 mm* lift case This discrepancy appears to stem from the incapability of the employed standard k-ε turbulence model to predict the small separation at the valve head. The distribution of the turbulent kinetic energy is qualitatively well predicted, but the levels are substantially underpredicted near the cylinder wall. It is anticipated that this is caused partly by the instabilities present in the flow leaving the valve which are not accounted for in the modelling.

ACKNOWLEDGEMENTS

The authors are grateful to the Deutsche Forschungsgemeinschaft which supported the numerical work through the grant *Pe 350-2/2*

REFERENCES

BICEN, A.F., VAFIDIS, C. & WHITELAW, J.H., (1985), Steady and unsteady airflow through the intake valve of a reciprocating engine. *J.Fluids Engng.*, **107**, 413-420.

CHEUNG, R.S W , NADARAJAH, S , TINDAL, M.J. & YIANNESKIS, M , (1990), An experimental study of velocity and Reynolds stress distributions in a production engine inlet port under steady flow conditions. *SAE Paper 900058.*

DEMIRDŽIĆ, I., PERIĆ, M & YIANNESKIS, M , (1988), Numerical Predictions of the Mean Flow and Turbulence in an Axisymmetric Port and Their Assessment Against Experimental Data, in D.B Spalding and N. Afgan (Eds), Heat and Mass Transfer in Gasoline and Diesel Engines, Hemisphere Publishing Corp., New York.

DEMIRDŽIĆ, I & PERIĆ, M., (1990), Finite Volume Method for Prediction of Fluid Flow in Arbitrary Shaped Domains with Moving Boundaries, *Int. J. Num Methods in Fluids,* **10**, 771-790.

KASTNER, L.J., WILLIAMS, T.J. & WHITE J.B., (1963), Poppet inlet valve characteristics and their influence on the induction process, P oc. *I Mech. Eng,* **178**, 955-975.

LAUNDER, B.E. & SPALDING, D.B., (1974), The numerical computation of turbulent flows, *Comp. Meth. Appl. Mach. Eng.*, **3**, 269-289.

PERIĆ, M., RUGER, M. & SCHEUERER G., 1989, A Finite Volume Multigrid Method for Calculating Turbulent Flows, Proc. *7th Symposium on Turbulent Shear Flows,* **1**, 7 3.1-7.3.6, Stanford University, August 1989.

STONE, H.L , (1968), Iterative solution of implicit approximations of multi-dimensional partial differential equations, *SIAM J Numer Anal.*, **5**, 389-403

TINDAL, M.J., CHEUNG, R S.W & YIANNESKIS, M., (1988), Velocity characteristics of steady flows through engine inlet ports and cylinders. *SAE Paper 880383.*

YIANNESKIS, M., TINDAL, M.J. & SUEN K.O., (1989), A comparison of cycle-resolved and ensemble-averaged velocity variations in a diesel engine, *SAE Paper No. 890617.*

FIGURES

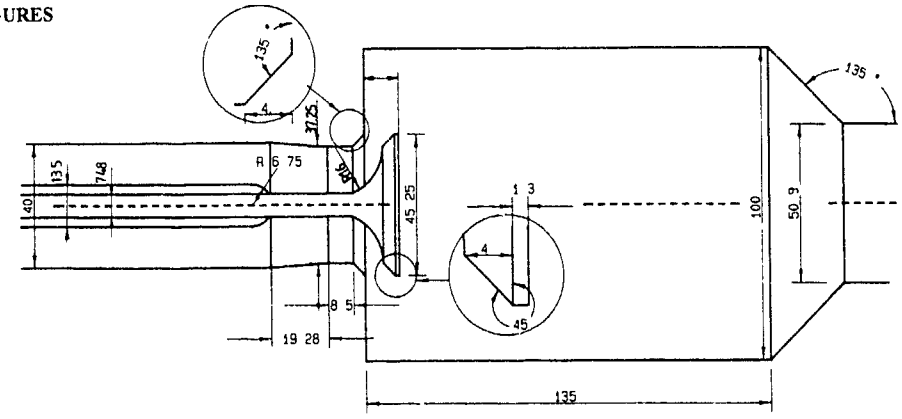

Fig 1: Cross-section of axisymmetric port test section

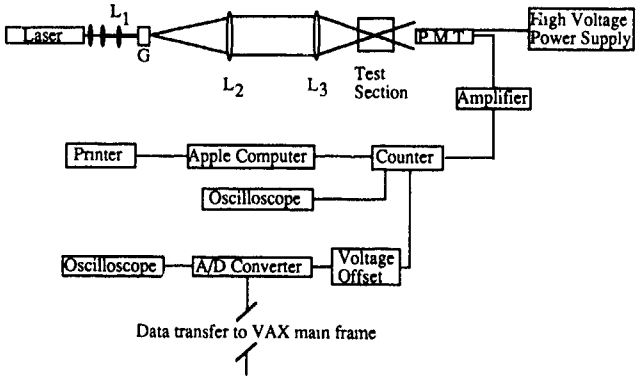

Fig. 2: Schematic diagram of the laser-Doppler anemometer optical and signal processing system. G. grating; P.M T : photo-multiplier tube; L1: beam expanding and focussing compound lens, 100 mm focal length, L2,L3: 200 mm plano-convex lenses

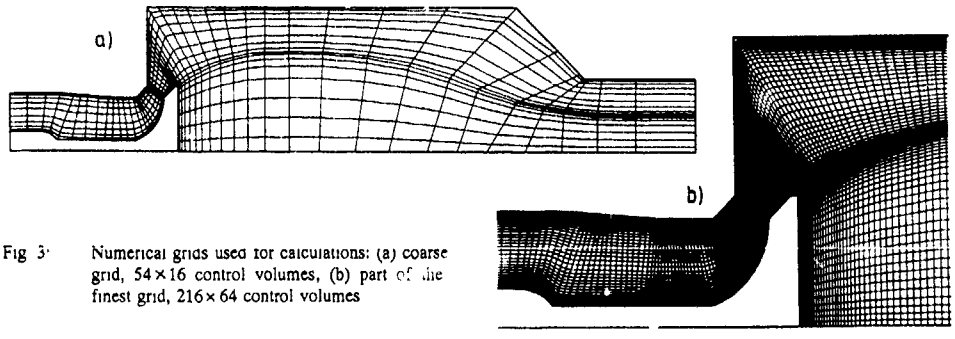

Fig 3: Numerical grids used for calculations: (a) coarse grid, 54×16 control volumes, (b) part of the finest grid, 216×64 control volumes

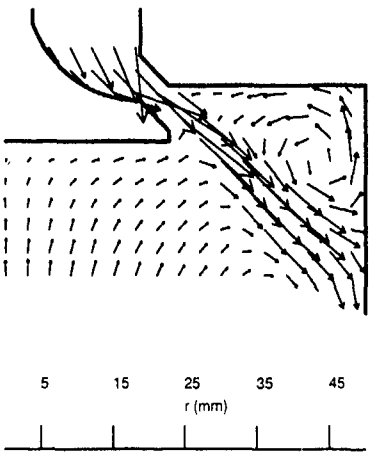

Fig 4. Measured mean velocity vectors, 6 mm valve lift

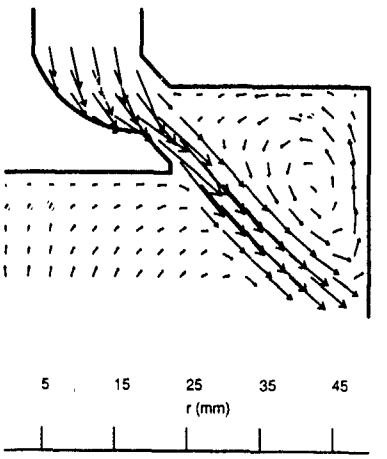

Fig. 5. Measured mean velocity vectors, 10 mm valve lift

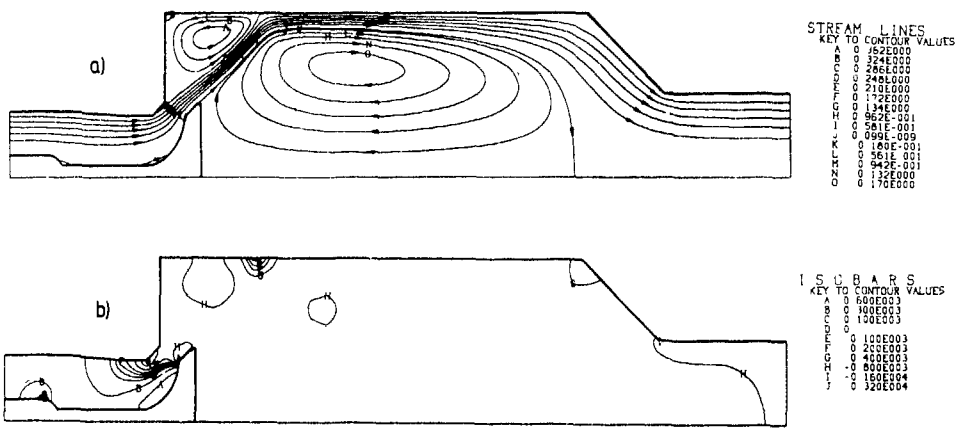

Fig. 6. Predicted streamlines (a) and isobars (b), 10 mm valve lift

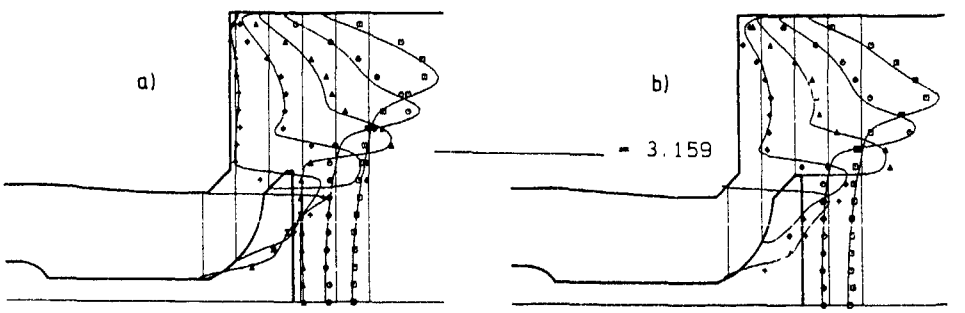

Fig. 7: continued

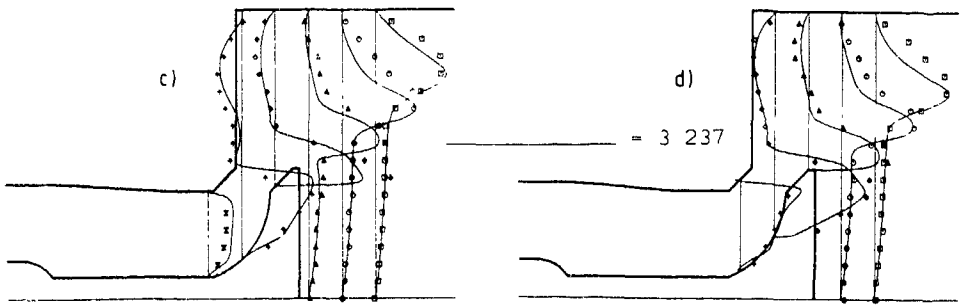

Fig 7 Comparison of measured and predicted axial (a,b) and radial (c,d) velocity components, 10 mm valve lift

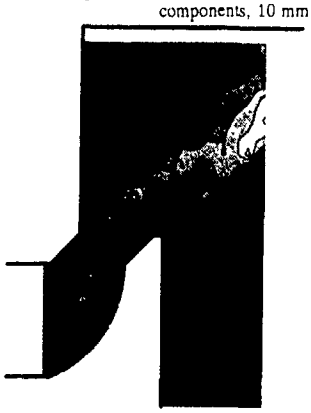

Fig 8: Contours of the measured kinetic energy of turbulence, 10 mm valve lift

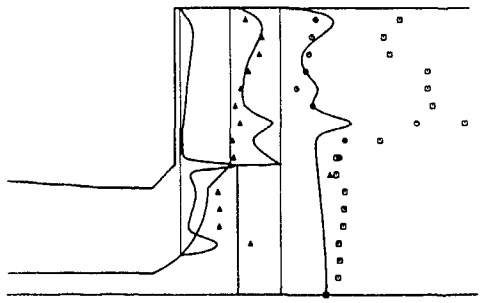

Fig. 9· Comparison of predicted and measured profiles of turbulent kinetic energy, 10 mm valve lift

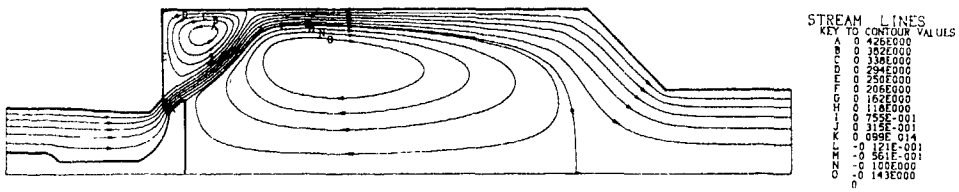

Fig 10: Predicted streamlines, 6 mm valve lift

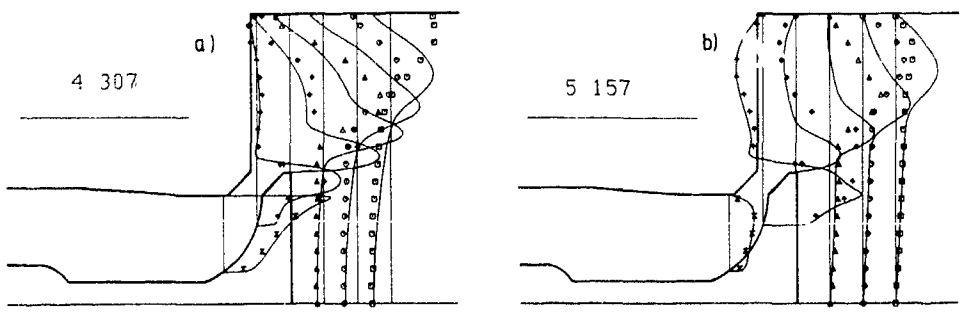

Fig. 11 Comparison of predicted axial (a) and radial (b) velocity components, 6 mm valve lift

EIGHTH SYMPOSIUM ON
TURBULENT SHEAR FLOWS
Technical University of Munich
September 9-11, 1991

13-3

EXPERIMENTAL AND NUMERICAL ANALYSIS FOR FLOWS IN NEGATIVE CORONA PRECIPITATOR

J N Sørensen*), P S Larsen*) and J Zamany**)

*) Dept of Fluid Mech., Techn Univ of Denmark
Building 404, DK–2800 Lyngby, Denmark

**) FLS–Miljø, DK–2500, Valby, Denmark

ABSTRACT

In a negative corona, barbed–wire, smooth–plate electrostatic precipitator the nonuniform electrostatic field represents a three–dimensional vorticity source distribution acting on the charged gas flow

At large values of the electrical Froude number Fe, the ratio of fluid inertia to electrical force, LDA–experiments show that the fields drive regular secondary flows of low turbulence intensity, in the form of rolls of axial vorticity superposed the axial bulk flow As Fe decreases rms–values, normalized by bulk velocity, increase dramatically, suggesting the presence of large scale vortical structures and turbulence At small values of Fe, the amplitude of rms–velocity appears to be limited by viscous effect

The model problem of a three–dimensional harmonic vorticity source distribution acting on a unit cell with through flow has been studied numerically by solving the Navier–Stokes equations in the velocity–vorticity formulation Results reveal a complex steady vortical structure at zero flow,the unsteady vortical structure at low values of Fe, and the steady regular roll pattern at high values of Fe.

1 INTRODUCTION

In the common wire–plate electrostatic precipitator, a particulate–laden gas flows horizontally past a row of vertical wire electrodes placed along the center plane between grounded plates The axial bulk velocity is typically 0 5 – 3 m/s and plate spacing 0 2 – 0 4 m. For power plant applications the electrodes are usually energized to negative polarity DC–voltage in the range 30–60 kV, and corona points of discharge are often fixed at pins along electrodes

In the laboratory precipitator we employ fine pins, equally spaced along wires that are thin to minimize wake effects (figure 1) The current density is then localized to these pins, and the body force density $\mathbf{f_e}$ (being proportional to the local current density **J**) becomes steady and three–dimensional and may drive secondary flows Specifically, since an irrotational body force field merely contributes by a pressure gradient, it is the vorticity source $\boldsymbol{\Omega} = \nabla \times \mathbf{f_e}$ of the electrical force density that may drive such flows

For the precipitator geometry of figure 1, at high values of the bulk flow, it may be shown (Larsen 1986) that weak sources of y– and z–vorticity, seen by the moving fluid to alternate in sign, have a vanishing effect on the mean flow However, weak sources of x–vorticity, being of one sign although of varying strength along a given cell, persistently drive secondary flows in the form of rolls of axial vorticity

This pattern of secondary flows, shown schematically in figure 1, has been found earlier by laser sheet visualization and by LDA–experiments (Thomsen et al 1982, Larsen & Christensen 1988) Figure 2 shows a typical vertical traverse of the y–component of velocity v(z) at two axial locations in the duct The flow is directed towards the wall at level of pins and away from the wall at level between pins The aforementioned earlier results have also shown that the strength of the rolls, as well as the associated rms–velocity fluctuations, increase with increasing electrical field for fixed bulk velocity For a given field, rms–velocities also increase with decreasing bulk velocity, a fact also noted by Leonard, Mitchner & Self (1983) It is anticipated that the observed rise in rms–velocity, observed at one point of the flow, starts as an inviscid flow phenomenon, but being limited in amplitude by viscous effect

From the equations of motion, the inviscid instability of the gas flow should be characterized by the electrical Froude number, the ratio of fluid inertia to electrical force, which may be expressed in two forms (Larsen & Christensen 1988)

$$Fe = \rho U_0^2/(L_y J_m/b) \quad \text{or} \quad Fe = \rho U_0^2/(L_y^2 \Omega_m) , \qquad (1)$$

where U_0 is the axial bulk velocity, ρ the fluid density, L_y the electrode–to–wall distance, J_m is a representative mean current density, say, that at the plate electrode, and it is related to the electrical force by $J = b \cdot f_e$, where b ($\simeq 2\ 1 \times 10^{-4}$ m^2/Vs for air) denotes the ion mobility; Ω_m is an appropriate norm of $\boldsymbol{\Omega} = \nabla \times \mathbf{f_e}$ Here, J_m can be readily measured while values of Ω_m rely on numerical solutions of the field equations In addition, inertia relative to viscous effects are governed by a Reynolds number, $Re = \rho U_0 L_y/\mu$, where μ denotes the dynamic viscosity Unsteady phenomena associated with bulk convection past electrodes spaced L_x apart, may be scaled by time L_x/U_0 Finally, geometry effects, not studied here, involve also the pin spacing $2 \cdot L_z$ (figure 1)

It is the purpose of present study to elucidate the nature of the shear flows of an electrostatic precipitator for a range of electrical Froude numbers, partly by LDA–experiments and partly by a numerical study of a related model problem

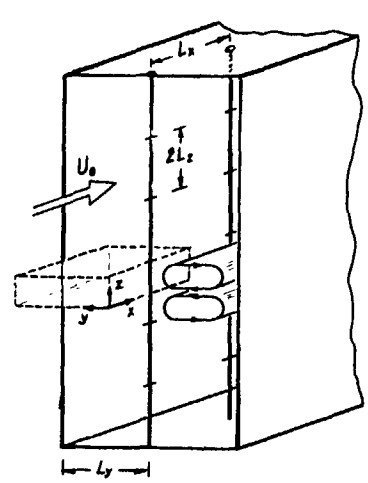

Figure 1 Precipitator geometry, 0.3 m wide by 0 6 m high test section with barbed wire electrodes, observed rolls of secondary flow, and computational box, (L_x, L_y, L_z) = (0 1 m, 0 15 m, 0.05 m).

2 EXPERIMENTS

The laboratory precipitator facility is a standard windtunnel with a screened 8:1-contraction, giving a uniform velocity field with 2-4% turbulence intensity at at he inlet to the test section The test section is a 5 0 m long, 0 3 m wide by 0 6 m high duct with smooth, electrically grounded walls and nonconducting, transparent top and bottom giving access to visualization and LDA-measurements

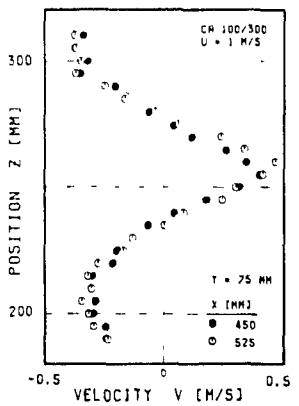

Figure 2 Vertical traverse of transversal velocity v(z) midway between electrode and wall, at two axial positions

Negative DC-voltage was applied to five vertical, 3 mm diameter wire electrodes, equipped with 1 mm diameter by 12 mm long pins, spaced $2 \cdot L_z = 0.10$ m apart Electrodes were positioned along the center plane of the duct at a spacing of $L_x = 0\ 10$ m, starting 0 25 m downstream of the inlet. All LDA-data were recorded at one fixed point, halfway between electrode no 3 and 4, 0 75 m from the sidewall, and at the level of pins, midway between top and bottom of the duct A two-component, back-scatter LDA-system (DANTEC 55x) with counter processors was used to record velocity data LDA-sample sizes were 300 for mean and rms-velocity, and 24000 for autocorrelation Residence-time weighting was used in all cases

Because particles become charged they precipitate out on plates, making it difficult to attain data-rates above about 50 Hz Also, recorded particle velocities differ from the gas velocity due to their electrical drift which furthermore depends on their size For the glycerine droplets used and at the location of measurements, the resulting bias to mean and rms-velocities have been estimated to be 0 1 and 0 03 m/s, respectively No attempts have been made to correct the data for these bias effects

First, velocities were recorded for the accessible range of bulk velocities ($U_0 = 0\ 1 - 1\ 8$ m/s) at four values of the electrical field, 0, 26, 36, 45 kV, corresponding to mean current densities $J_m = 0, 0\ 526, 2\ 261$, and $4\ 161$ mA/m^2 As seen in figure 3, which shows U-rms/U_0 versus bulk velocity U_0, increasing fields and decreasing bulk velocity give a marked rise in U-rms/U_0 relative to its background value, the turbulence intensity, recorded at zero field

Figure 4 shows the same data, now versus reciprocal electrical Froude number, calculated from the first expression of eq (1) Despite the scatter of data, which is partly due to the natural rise in turbulence intensity with decreasing bulk velocity, figure 4 suggests the onset of instabilities to occur about $Fe \simeq 20 - 50$ For large values of 1/Fe, the slope of 0 5 implies that U-rms levels off at values proportional to the current density to the one-half power The viscous effects set these limits

Next, time-series of U-velocity (see figure 5 for samples, each representing one batch of 150 data) were recorded at three values of bulk velocity at each of two values of electrical field, 26 and 36 kV Subsequent numerical analysis, employing the scheme described by Buchhave et al (1979), gave autocorrelations shown in figure 6 and one-dimensional spectra, such as figure 7 The poor resolution of time series and spectra, are due to low data-rates of the random sampling governed by the arrival of seeding particles The random sampling in the burst mode LDA gives alias-free spectra but the spectral variance become significant at frequencies near the mean sampling rate

To interprete figures 5-7 we note that any periodic information should be characterized by the period of structures of length scale L_x moving with bulk velocity U_0 For the three velocities $U_0 = 0\ 2$, 0 5, and 1 5 m/s this gives the periods $L_x/U_0 = 0\ 5$, 0 2, and 0 07 s At the lowest velocity, the period 0 5 s in figure 6 and frequency 2 Hz in figure 7 can be discerned At higher velocities, structures become too irregular to appear as distinct periods in signals.

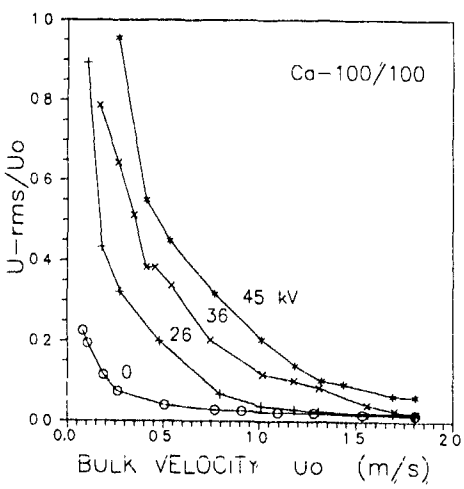

Figure 3. Axial component of rms-velocity, normalized by bulk velocity, versus bulk velocity All data from same point in the flow, at four values of electrical field, 0, 26, 36, 45 kV

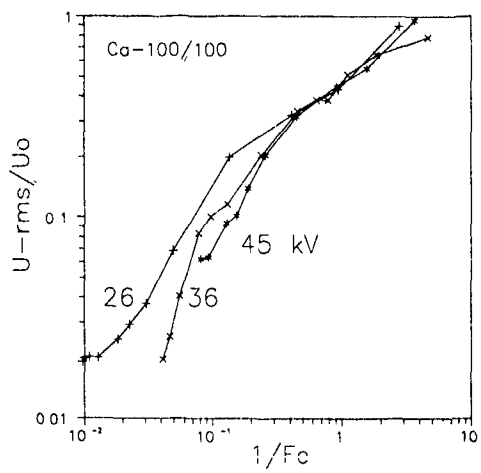

Figure 4 Data from figure 3 (for nonzero field) plotted versus reciprocal electrical Froude number

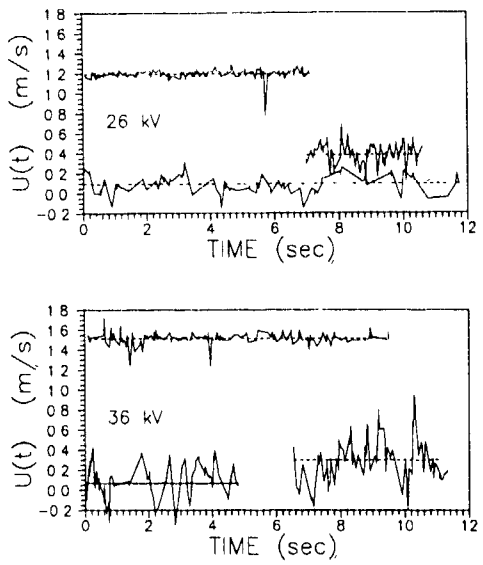

Figure 5 Samples of time series at 26 and 36 kV for three values of bulk flow

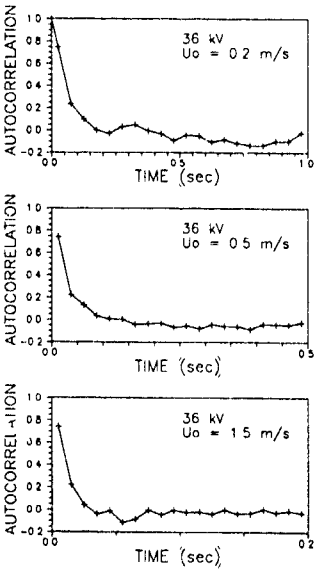

Figure 6 Time–autocorrelation of u(t) at 36 kV for U_o = 0 2, 0 5, and 1 5 m/s

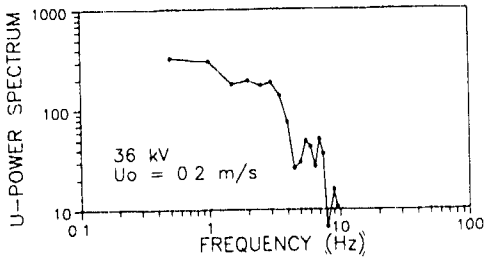

Figure 7 One–dimensional power spectrum (arbitrary units) at 36 kV for U_o = 0 2 m/s

3 THE NUMERICAL MODEL PROBLEM

The motion of the incompressible, constant–property gas phase is governed by the conservation of mass and momentum balance,

$$\nabla \cdot \mathbf{V} = 0 , \qquad (2)$$

$$\frac{\partial \mathbf{V}}{\partial t} + (\mathbf{V}\cdot\nabla)\mathbf{V} = -\nabla(p/\rho) + \nu\nabla^2\mathbf{V} + \mathbf{f_e}/\rho , \qquad (3)$$

where the velocity vector $\mathbf{V} = (u,v,w)$ is given in Cartesian co–ordinates (x,y,z), p is the static pressure and ν the kinematic viscosity. The electrical body force per unit volume, $\mathbf{f_e} = \rho_1\mathbf{E}$, is determined by the charge density of ions ρ_1 and the electrical field strength E, which are both solutions to the Maxwell equations. When the convective current of charge is negligible the electrodynamic problem is decoupled from that of the fluid motion.

In the present study, considering vorticity–driven secondary flows, we replace the momentum equation (3) by its curl. This results in the vorticity transport equation

$$\frac{\partial \omega}{\partial t} + (\mathbf{V}\cdot\nabla)\omega = (\omega\cdot\nabla)\mathbf{V} + \nu\nabla^2\omega + \nabla\times(\mathbf{f_e}/\rho) , \qquad (4)$$

where the vorticity is $\omega = \nabla\times\mathbf{V}$ (5)

Taking the curl of eq (5) and employing the continuity, the velocities are given by the Poisson equations

$$\nabla^2\mathbf{V} = -\nabla\times\omega \qquad (6)$$

As model problem we consider a harmonic distribution of volume forces $\mathbf{f_e} = (f_x,f_y,f_z)$, where

$$f_x = A_x\cdot\mathrm{sign}(x-L_x/2)\cdot|f|,\ f_y = -A_y\cdot|f|,\ f_z = -A_z\cdot|f|, \qquad (7)$$

$$|f| = 1/4(1-\cos(2\pi x/L_x))\cos(\tfrac{1}{2}\pi y/L_y)(1-\cos(\pi z/L_z)) \qquad (8)$$

Preliminary calculations of the electrical field have shown that these expressions both qualitatively and quantitatively give a fairly good representation of the actual distribution of volume forces obtained by solving the field equations. These solutions show the non–uniformity of the components of volume force, expressed as rms–values, to be of the same order as the mean values. At 36 kV, for example, the mean value of f_y is about 1 1 N/m^3 while that of f_x and f_z are considerably smaller. This case is thus considered to be well represented by setting the amplitudes A_x, A_y, and A_z equal to unity.

The closure of the system of equations is achieved by prescribing slip conditions at the collector wall, and symmetry on the centerplane and the lower and upper planes of the computational domain (see figure 1). In the axial direction we assume periodicity, corresponding to fully developed flow.

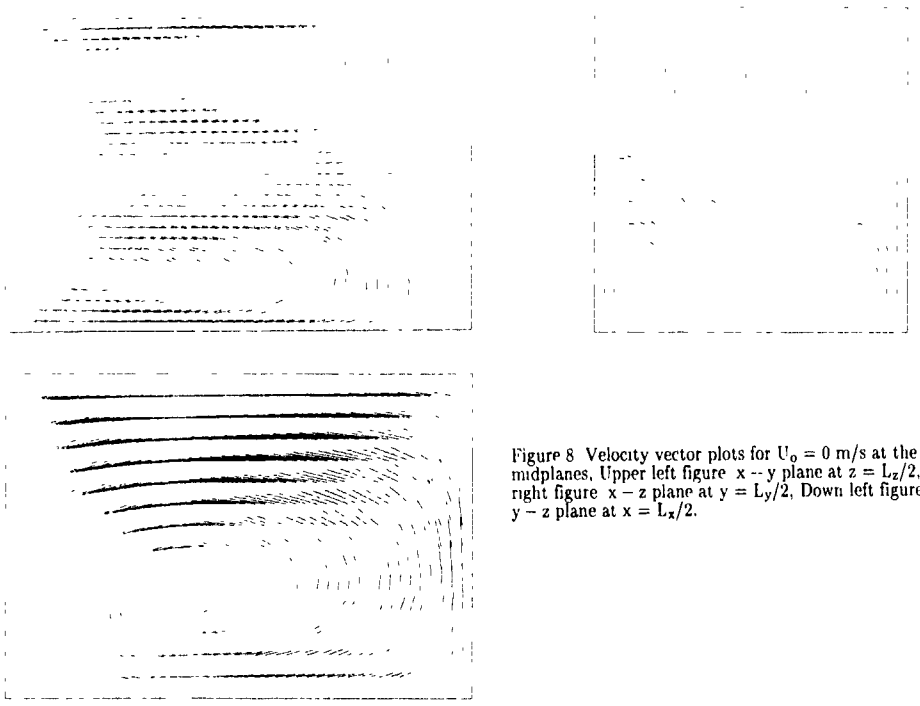

Figure 8 Velocity vector plots for U_o = 0 m/s at the three midplanes, Upper left figure x -- y plane at $z = L_z/2$, Upper right figure x – z plane at $y = L_y/2$, Down left figure y – z plane at $x = L_x/2$.

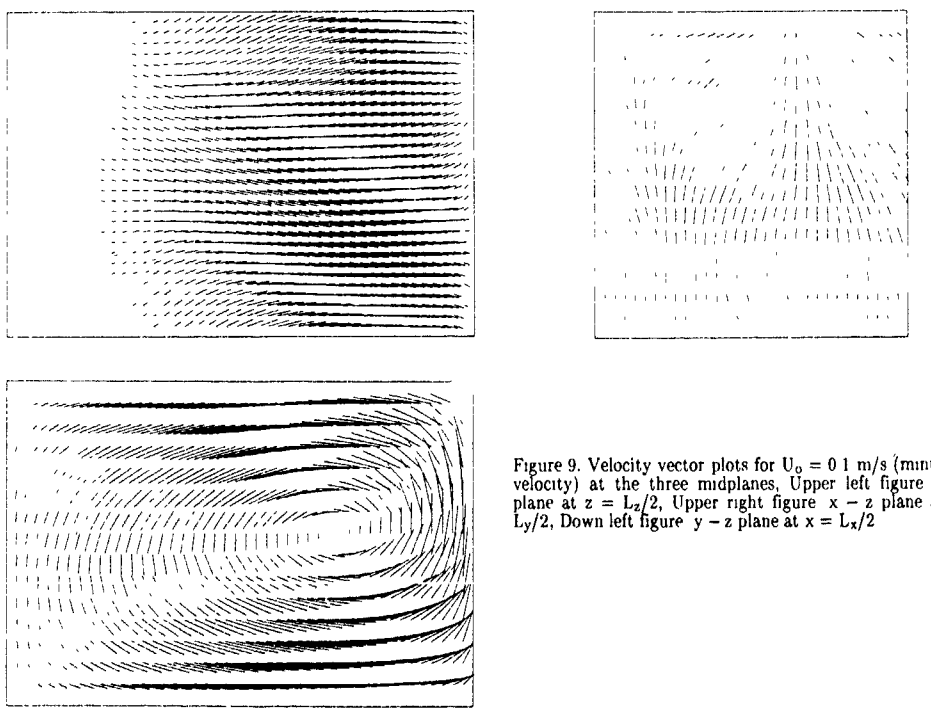

Figure 9. Velocity vector plots for U_o = 0 1 m/s (minus bulk velocity) at the three midplanes, Upper left figure x – y plane at $z = L_z/2$, Upper right figure x – z plane at $y = L_y/2$, Down left figure y – z plane at $x = L_x/2$

The solution of eqs (4) and (6) is accomplished by employing second order accurate differences solved by the ADI technique in space in a time–marching, second–order scheme (see Toumi & Ta Phuoc 1987) In all calculations an equal grid spacing of $\Delta x = \Delta y = \Delta z = L_x/40$ is employed resulting in a discretization of 31x16x16 nodepoints To ensure the time–true nature of the computations the time–step obeys the CFL condition, i e $\Delta t \leq 0.5\Delta x/V_{max}$

4 NUMERICAL RESULTS

To supplement the experimental results and to obtain information on the structure of the flow field at small bulk velocities calculations were carried out for $U_0 = 0$ m/s, 0 1 m/s, and 0 2 m/s In figure 8 is shown the calculated velocity field, projected as velocity vectors on the midplanes $x = L_x/2$, $y = L_y/2$, and $z = L_z/2$, respectively, for the case of zero bulk flow, $U_0 = 0$ m/s The flow is here completely induced by the electrical volume forces and the figure shows that the electrical field induces a complex but highly organized structure of three–dimensional rolls At the x–y midplane we see the flow being forced against the collector wall along the centerline Due to symmetry two concentrated rolls of z–vorticity are formed with center points located symmetrically about $x = L_x/2$ near the electrode plane Projected on the x–z plane the flow exhibits a rather curious topology We here identify four points with concentrated y–vorticity also located symmetrically about the $x = L_x/2$ line Two of these vortex centers are located near the down corners of the midplane, whereas the two other ones are found near the centerline at about $z = 3/4L_z$ On the last midplane, the x–z plane, only one concentrated x–vorticity center is seen to be projected These projections suggest a rather complicated topology of a deformed vortex ring which as yet has not been analyzed in details However, symmetry considerations suggest the structure sketched in figure 10

In order to avoid numerical stability problems the calculations were performed with a kinematic viscosity $\nu = 10^{-4}$ m²/s, corresponding to about 6 times the value of air Although this damps out small scale motions and gives a different balance between the electrical force field and the diffusion, it is believed that the gross behaviour of the flow is reflected in our calculations The calculation with zero bulk velocity was carried out in what in physical time corresponds to 4 seconds We here employed a time–step of $\Delta t = 2 \cdot \Delta x = 1/150$ s , corresponding to 600 time–steps A steady solution was not obtained, but oscillations did not appear and by comparing velocity vector plots at different times, it was found that after being established the vortical structures did not change appreciably Thus, it is assumed that the final steady solution corresponds closely to the one shown in figure 8 Maximum velocities were found to be in the order of 0 2 m/s

Increasing the bulk velocity to $U_0 = 0$ 1 m/s, keeping the electrical field at the same level, results in the flow field shown in figure 9 Note that the bulk velocity has been subtracted from the velocity vectors, which then represent the topology of perturbed vortex structures We here see that the vortex center passing through the y–z plane now is located somewhat nearer the electrode Furthermore no vortex lines are now passing through the the x–z midplane Although the flow still is undulated in this plane, vortex stretching along the axial direction now has diminished the x– and z–vorticity, leaving the flow dominated by axial vorticity.

Increasing the bulk velocity further to $U_0 = 0$ 2 m/s, this tendency of axial stretching becomes even more pronounced Here the perturbation velocity in the x–z plane is almost parallel to the z–direction indicating that y–vorticity has almost vanished. In the x–y plane variations of perturbed in–plane velocities still exist, but are small in magnitude, leaving most part of the vorticity to be directed in the axial direction

In figure 8–10 only spatial structures are shown Following time–histories for velocities at arbitrary located points, both for $U_0 = 0$ 1 m/s and for $U_0 = 0$ 2 m/s, the flow field was found to be dominated by periodic motions For $U_0 = 0$ 1 m/s the flow oscillated with 1 Hz and for $U_0 = 0$ 2 m/s a characteristic frequency of 2 Hz dominated By simple dimension analysis of the time scale connected to bulk velocity past electrodes, it may be seen that these frequencies are identical to U_0/L_x Indeed, the present model problem could be replaced by a problem in which the bulk velocity is put equal to zero and the parameter x/L_x in the expression for the volume forces is replaced by the unsteady parameter $(x/L_x - U_0/L_x t)$

5 DISCUSSION AND CONCLUSIONS

The present experimental and numerical study of the electrostatic precipitator flow provides some preliminary understanding of the development and nature of a three–dimensional turbulent shear flow This flow arises from spatially periodic volumetric vorticity sources acting on an incompressible duct flow which is uniform upstream of the first electrode Wall boundary layers are thin and may be neglected in the present context

The flow of practical interest (finite non–zero Fe) falls in between two extreme cases, Fe = 0 and Fe >> 1, that is, that of zero bulk velocity and that of large inertia These limiting cases lend themselves to ready interpretation

At Fe = 0, so far not studied experimentally, our numerical solutions show a stable three–dimensional vortical flow structure that appears to be a stable laminar mode for the field strength studied This flow is considerably more complex but generically the same as that of a single point of corona discharge facing an infinite plate

At Fe >> 1, experiments and numerical simulations show a regular pattern of secondary flow in the form of axial rolls The flow appears to be stable and for all practical purposes laminar, as experimental rms–levels coincide with those of the case of no electrical field and same bulk velocity (figure 3) This case can also be anticipated, as mentioned in the introduction. At large x–inertia, vorticity sources in y– and z–directions impart vanishing perturbations to the flow The vorticity source in x–direction, being of one sign although of varying magnitude, drive the rolls We stress that the development of axial rolls depends itself on fluid inertia, extending over increasing axial distances as the bulk velocity increases However, this effect should not affect the present study

The case of practical interest, that of finite, non–zero values of Fe, can be approached from either of the foregoing limits Reducing inertia, for example, causes perturbations from y– and z–direction vorticity sources to increase in amplitude Experiments have shown rms–values that increase pronounced with decreasing Fe (figure 4) Preliminary numerical results show a periodic motion with complex vortical structures, where the period can be traced to the time scale of electrode spacing and bulk velocity It is anticipated that long time simulations, at a sufficiently small scale and with a realistic low viscosity, would show the evolution of instabilities leading to turbulence It is suggested that a stability limit may exist at Fe ≃ 20–50

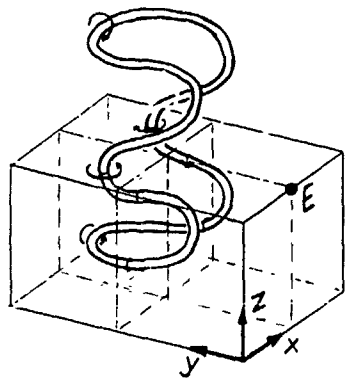

Figure 10 Inferred topology of vortex structure at $U_0 = 0$ m/s Electrode at E

REFERENCES

BUCHHAVE, P , GEORGE JR ,W K & LUMLEY, J L 1979 The measurement of turbulence with the laser–doppler anemometer Ann Rev Fluid Mech 11, 443–503

LARSEN, P S 1986 Secondary flow in negative corona precipitator DCAMM Report no 337, Techn Univ of Denmark

LARSEN, P S & CHRISTENSEN E M 1988 Secondary flow and turbulence in electrostatic precipitator Laser Anemometry in Fluid Mechanics, Ladoan, Lisbon, 361–371

LEONARD, G L , MITCHNER, M & SELF, S A 1983 An experimental study of the electrohydrodynamic flow in electrostatic precipitators J Fluid Mech 127 123–140

THOMSEN H P LARSEN, P S CHRISTENSEN E M & CHRISTIANSEN, J V 1982 Velocity and turbulence fields in negative corona wire–plate precipitator Techn Univ of Denmark, Report AFM 82–08

TOUMI, A & TA PHUOC LOC 1987 Numerical study of three–dimensional viscous incompressible flow by vorticity and velocity formulation 5th Int Conf on Num Meth in Laminar and Turbulent Flow, Pineridge Press 595–606

EIGHTH SYMPOSIUM ON
TURBULENT SHEAR FLOWS
Technical University of Munich
September 9-11, 1991

VORTICAL FLOW SIMULATION BY THE SOLUTION OF THE NAVIER-STOKES EQUATIONS

Longo J M A and Radespiel R
Institute for Design Aerodynamics
DLR, Am Flughafen, D-3300 Braunschweig (FRG)

Abstract

The validation of a finite-volume scheme for the solution of the 3-D Navier-Stokes equations for the prediction of vortical flow fields around delta and strake-delta wings is presented. The current technique is based on central difference approximations (cell-vertex formulation) with a Runge Kutta integration in time. Using local time stepping, implicit residual smoothing, a multigrid method and carefully controlled artificial dissipative terms, the convergence rates are dramatically improved for the complex flow problems tested. The reliability of the present scheme for engineering applications is established by comparing the numerical results with wind tunnel measurements at subsonic and transonic speeds.

1. Introduction

Vortex flow associated with flow separation from leading-edge plays an important role in the high-angle-of-attack aerodynamics. While the application of Navier-Stokes solvers to delta wings with vortical flows have been already discussed in the literature [1] to [3], the use of this technique was restricted mainly due to their high requirements in computer time and storage.

Recently subtantial improvements have been reported in the numerical solution of the Navier-Stokes equations [4], making this technique attractive for engineering applications. Using explicit Runge-Kutta schemes as the basic time integration algorithm the problem of slow convergence rates for highly clustered meshes near solid walls was overcome by application of local time stepping, implicit residual averaging and multigrid. Converged solutions of sub- and transonic flows around airfoils and wings with significant shock-boundary layer interaction were obtained within less than 100 multigrid cycles [4]. Subsequently, the code was extended to allow multi-block decomposition of the computational domain [5] which is important not only to treat complex aircraft geometries but also to allow three-dimensional calculations on computers with limited amount of core memory. It has been demonstrated that the multi-grid-multiblock code converges rapidly for some generic inviscid and viscous test cases [5] [6].

The purpose of the present paper is to validate the code for the prediction of vortical flows around delta wings. The accuracy of the code is established by comparing solutions with different grid densities and with experimental data. Also, convergence rates of the present scheme to the steady state with and without multigrid technique are shown to demonstrate the usefulness of the code within an aerodynamic design process.

2. Governing Equations and Numerical Method

The integral form of the mass-averaged Navier-Stokes equations using nondimensional variables can be written as

$$\frac{\partial}{\partial t}\iiint_V \vec{W}\,dV + \iint_{\partial V} \bar{\bar{F}}\cdot\vec{n}\,dS = 0 \qquad (1)$$

where

$$\vec{W} = (\rho, \rho u, \rho v, \rho w, \rho E)^T$$

is the vector of conserved quantities with ρ, u, v, w, and E denoting the density, the cartesian velocity components, and the specific total internal energy. The quantity V denotes an arbitrary control volume with boundary ∂V and outer normal $\vec{n}$. The definition of the flux density tensor $\bar{\bar{F}}$ is given in [4]. The equation of state for an ideal gas is used to calculate the pressure and the temperature. The viscosity is assumed to follow an empirical power law and the heat conductivity is obtained by using a constant Prandlt number.

2.1 Turbulence Model

For turbulent flows the laminar viscosity μ, is replaced by $\mu + \mu_t$ and μ/P_r is replaced by $\mu/P_r + \mu_t/P_{rt}$, where the eddy viscosity μ_t and the turbulent Prandlt number P_{rt}, are provided by a turbulence model. In the present work the algebraic turbulence model of Baldwin and Lomax [7] with the modifications proposed by Degani and Schiff [8] to treat cross flow separations is used.

2.2 Spatial Discretization

The discretization of Eq (1) in space and time is done separately. The discrete values of the flow quantities are located at the vertices of the mesh cells and the integral equation is approximated by

$$\frac{d}{dt} W_{i,j,k} = \frac{-1}{V_{i,j,k}} (\vec{Qc}_{i,j,k} + \vec{Qv}_{i,j,k} + \vec{D}_{i,j,k}) \qquad (2)$$

where $\vec{Qc}_{i,j,k}$, $\vec{Qv}_{i,j,k}$ and $\vec{D}_{i,j,k}$ are the convective, the viscous and the artificial dissipative terms, respectively The discretization of the convective part follows [9] The eight cells surrounding a vertex form a super cell as is shown in Figure 1-a The surface integral of Eq (1) of the convective part of the flux density tensor is evaluated for each cell face using an arithmetic average of the flux quantities at the vertices The convective flow is first-order accurate if the normal vector of each surface segment is smooth and the shape of the segment approaches a parallelogram with grid refinement On smooth meshes the scheme is second-order accurate [10]

The viscous fluxes are approximated using the auxiliary cell with the dashed boundary shown in Figure 1-b The first derivatives of the flow variables which are needed to compute the viscous fluxes are obtained by central differences using a local transformation from Cartesian coordinates to curvilinear coordinates [4] The thin layer approximation is employed in the present coding A one-dimensional error analysis of the discrete approximation of the viscous terms has shown first-order accuracy on general strech ' meshes and second-order accuracy on smoothly varying meshes [11]

The convergence of this scheme to the steady state is strongly influenced by the choice of the artificial dissipative terms $\vec{D}_{i,j,k}$ The present artificial dissipation model uses a blend of fourth and second differences to provide third-order background dissipation in smooth regions of the flow and first-order dissipation at shock-waves The scaling factor of the dissipative fluxes is a nonlinear function of the spectral radii of the Jacobian matrices associated with the three computational coordinate directions, λ_ξ, λ_η and λ_ζ which accounts for varying cell aspect ratios λ_ξ/λ_η, $\lambda_\xi/\lambda_\zeta$ and $\lambda_\eta/\lambda_\zeta$ [4]

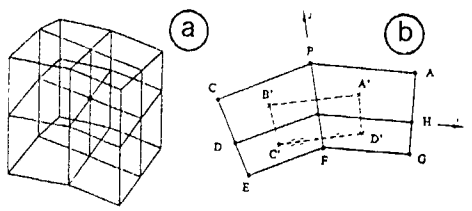

Figure 1. Control volume (a) around point (i,j,k), (b) in a plane grid

2.3 Boundary Conditions

At subsonic inflow-outflow boundaries locally one-dimensional flow normal to the boundary is assumed and the concept of characteristic variables is used Characteristic variables corresponding to outgoing waves are extrapolated from the interior while those corresponding to incoming waves are determined from the free stream At solid walls, the no-slip condition is enforced The continuity and energy equations are solved at the grid points on the surface assuming an adiabatic wall [4]

2 4 Time Stepping Scheme

The system of ordinary differential equations (2) is advanced in time with a five-stage Runge-Kutta scheme [12] The steady-state solution is independent of the time step, and hence several numerical techniques are applied to accelerate convergence Using local time stepping, the solution at each mesh point is advanced at the maximum Δt allowed by stability With implicit smoothing of residuals the stability range of the explicit time stepping scheme is extended to large Courant numbers For three-dimensional flows, a factored form is used The ability of the scheme to damp out high frequency oscillations in the solution depends strongly on the choice of the smoothing coefficients Consider cells with the edge lengths in the ξ and ζ directions much larger than in the η direction The explicit time step is limited by the characteristic wave speed along the short cell edge For extension of the time step beyond the explicit stability limit, implicit residual smoothing is required in the η direction On the other hand, one expects that no smoothing is required in coordinate directions where the characteristic wave speeds are much smaller than the stability limit Simple formulas for the smoothing coefficients as functions of the spectral radii of the Jacobian matrices associated with the ξ, η and ζ directions have been devised in [4]

Finally, a multigrid algorithm according to [9] is implemented Coarser meshes are defined by eliminating every other mesh line in each coordinate direction The solution is transferred to the coarse meshes by injection Transfer of the residuals from fine to coarse meshes is done by a weighted average of the fine-mesh grid points surrounding the point on the coarse mesh A forcing function is constructed so that the solution on a coarse mesh is driven by the residuals collected on the next finer mesh Corrections obtained on the coarse meshes are transferred to the fine mesh by trilinear interpolation A postsmoothing step is applied to the total corrections before the solution is updated The postsmoothing reduces high-frequency oscillations introduced by the linear interpolation of the coarse-mesh corrections, and hence improves robustness of the overall scheme.

2.5 Multiblock Code

The present multiblock version of the code is described in detail in [5] The main problem in the design of a multiblock code is to define the arrangement of the block loops, that is, how often should data be transferred between blocks The simplest option is clearly to execute a complete multigrid cycle in a given block before moving to the next Indeed it was found in [5] that convergence properties of the present time-asymptotic flow solver does depend on an appropiate sequencing of the boundary conditions and hence on the definition of the block loops For exam-

ple, lag or lead of ghost points which are used to update internal cut boundaries must be carefully controlled because it may produce unphysical spatial derivatives near the boundary This problem is particularly evident with a multigrid code designed for rapid convergence On the other hand, if the multiblock code is used on computers with limited amount of core memory the complete elimination of lag and lead effects by extensive sweeps through the blocks introduces penalties for I/O operations even on machines with solid-state device (SSD) In the present scheme lag and lead effects are eliminated by updating boundary conditions in two passes, before and after each Runge-Kutta stage

3. Configuration and Grids

Figure 2 shows the configurations investigated in the present study These are a cropped delta wing with a 65° sweep sharp leading edge, and two flat plate strake-wings with round leading edges with sweep angles for the strake and the wing of 80°/60° and 80°/50° respectively For all three configurations extensive wind tunnel results have been reported in [13] [14] [15] [16] For the numerical simulation the physical domain is discretized using O-O topologies of different sizes In all cases the distance to the first grid point away from the wall is $\leq 10^{-5}$ times the root chord (only the 24x48x24 mesh does not satisfy this criteria), which results in an average value of $y^+ \leq 1\,3$ for for the turbulent computation

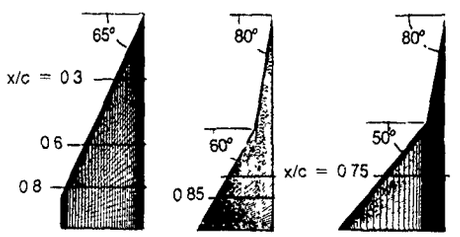

Figure 2. Configurations.

4. Numerical Results

As mentioned in the introduction the purpose of the present paper is to show that the current approach is able to (i) accurately predict vortical flow fields, (ii) in moderate computer times, (iii) even for configurations using more than one block Figure 3 shows the convergence rates of the present scheme without multigrid (a) and with a 4 level multigrid (b) for the 65° cropped delta wing at a Mach number $M_\infty = 0\,4$ and an incidence $\alpha = 10°$ The results have been obtained using a single block mesh of 150000 cells with 48X48 cells in stream- and spanwise directions and 64 cells normal to the wall Also the corresponding multigrid convergence rate for a two block mesh using the same total number of points is shown in Figure 3(c)

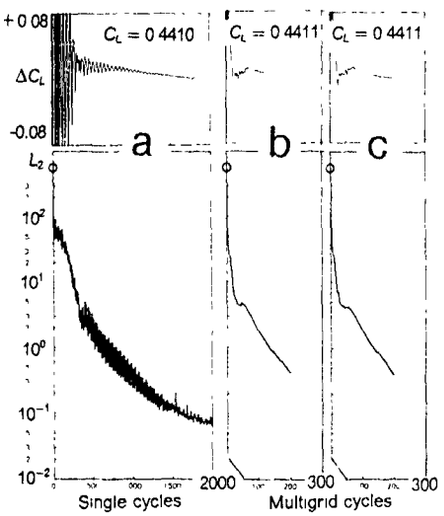

Figure 3. Convergence rates: Cropped delta wing $M_\infty = 0\,4, \alpha = 10°$ (a)single grid (b)multigrid (c)multigrid-multiblock

While the flow solution is the same for the three cases there is a factor 6 8 in computer time reduction by using the multigrid option That means that converged results within 0 015% of the global force coefficients needs only 40 min computer time on a Cray-YMP using the multigrid technique for meshes consisting on 150000 cells Whereas 4 5 hs are needed for computation without multigrid When using a two block configuration, the penalties introduced for I/O operations are below 10 % of the computer time of a single block mesh

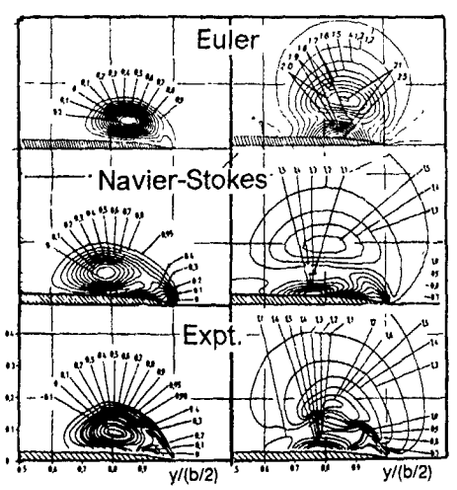

Figure 4. Cross flow fields: Cropped delta wing $M_\infty = 0.1, \alpha = 10°$ (a)Total pressure, (b)Dynamic pressure

The significance of the viscous terms on the prediction of vortical flow fields around delta wings is assessed in Figures 4 and 5 Results for the 65° cropped delta wing using an Euler code have been already published in [17] and [18] The numerical simulation based on the Euler equation is done for a single block mesh consisting of 48x48x48 cells To perform the Navier-Stokes calculations in the same mesh a subgrid consisting of 16 cells between the solid wall and the first mesh line away from the wall is injected Figure 4 shows the viscous effects at the vortex core Computed flow fields values are performed for the experimental flow conditions defined in [13], i e $\alpha = 10°$, $R_e = 1.4 \times 10^6$ $M_\infty = 0.1$

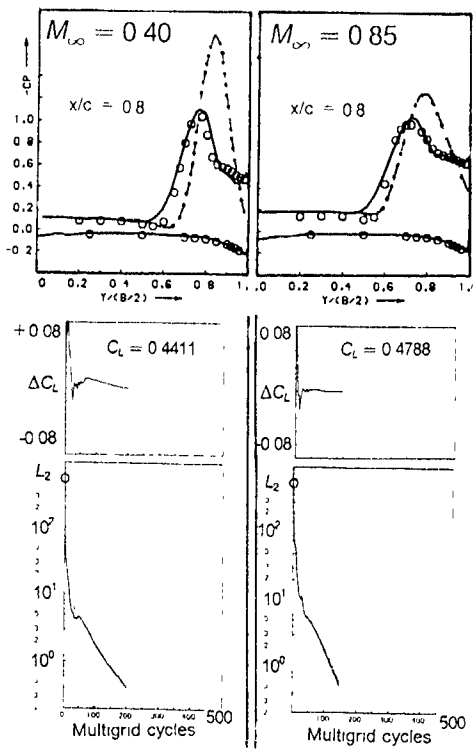

Figure 5. Cp distributions ; Cropped delta wing $\alpha = 10°$, x/c = 0.8 —Navier Stokes, ←·←·← Euler, o Expt

The effects of the viscosity on the surface pressure distribution are shown in Figure 5 for two different Mach numbers Computed values are compared with measurements [14] and [15] at $R_e = 9 \times 10^6$, $\alpha = 10°$, $M_\infty = 0.4$ and $M_\infty = 0.85$ Also, the rates of convergence of the Navier Stokes code for the two Mach numbers are included in the Figure

The influence of the discretization error on the surface pressure distribution is assessed by increasing and decreasing the size of the 48x64x48 mesh, by a factor of 2 in each coordinate direction Figure 6-a shows the pressure distributions obtained on the three meshes compared with the experimental data at $M_\infty = 0.4$, $\alpha = 10°$, $R_e = 9 \times 10^6$ Figure 6-b shows the convergence rate of the code for the finest mesh tested To perform the results on the one million point, eight block mesh , a full multigrid strategy was used wich was started from the second level mesh

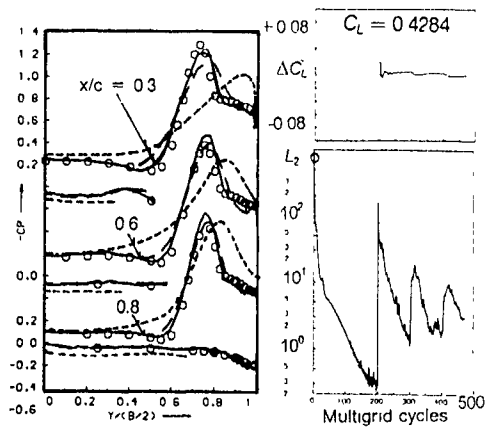

Figure 6 Mesh refinement ; Cropped delta wing $M_\infty = 0.4$, $\alpha = 10°$ —— 96x128x96, — — — 48x64x48, --- 24x32x24, o Expt

Figure 7 shows that the wind tunnel model support has an strong influence on the prediction of the surface pressure distribution The computations were carried on the 48x64x48 mesh at $M_\infty = 0.4$, $\alpha = 10°$, $R_e = 9 \times 10^6$

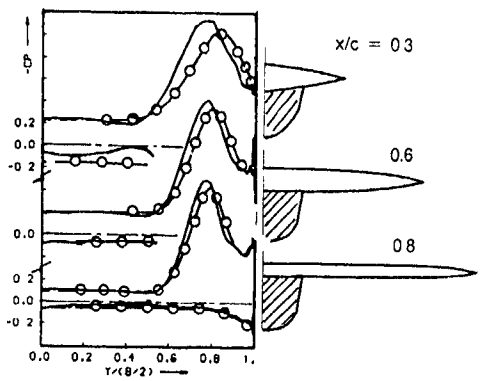

Figure 7. Cp distributions : Cropped delta wing $M_\infty = 0.4$, $\alpha = 10°$ -o-without body, —— with body

Figure 8 shows a comparison between a surface oil-flow picture (left) and the numeric stream lines near to the wing surface (right) at $M_\infty = 0.85$, $\alpha = 20°$ All ingredients of surface flow topology like primary attachment, secondary separation and secondary attachment (although vague in the experimental data) can be observed

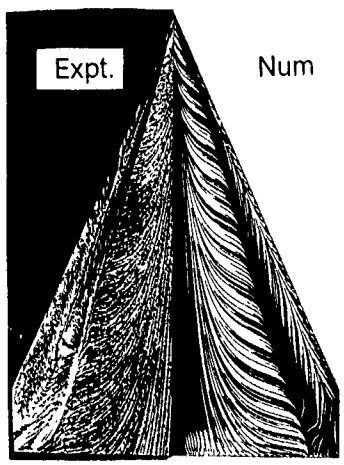

Figure 8. Cropped delta wing $M_\infty = 0.85, \alpha = 20°$

Solutions for the strake-delta wings have been obtained using a 3 level multigrid two block mesh consisting of 96x48 cells in stream- and spanwise directions and 48 cells normal to the surface Results are compared with measurements [16] at $R_e = 1.3 \times 10^6$ and $M_\infty = 0.1$ At lower angles of attack the two system of vortices originating from the wing apex and the leading-edge kink remain distinguishable over the entire wing (Fig 9-a)

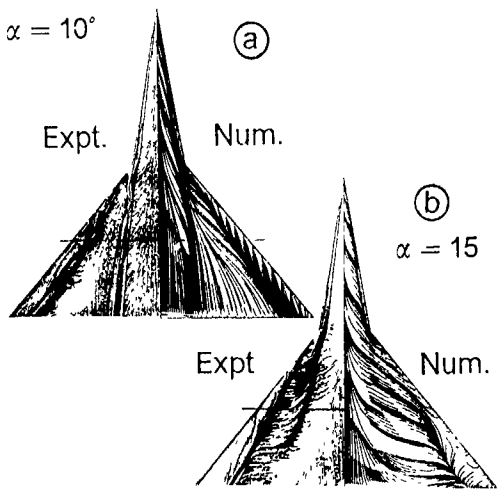

Figure 9. Strake-wing (outer sweep angle 50°)
$M_\infty = 0.1, R_e = 1.3 \times 10^6, (a)\alpha = 10°, (b)\alpha = 15°$

At medium angles of attack both vortex systems interact about each other and merge into one stable vortex over the rear part of the wing The mergin process is quantitatively and qualitatively well reproduced for the two wings with different outer sweep angle (Figs 9-b and 10)

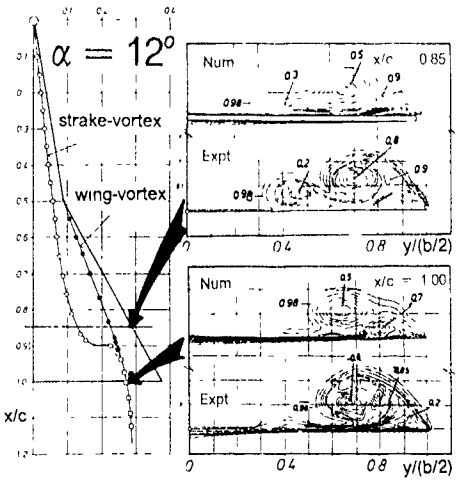

Figure 10. Strake-wing (outer sweep angle 60°)
$M_\infty = 0.1, \alpha = 12°, R_e = 1.3 \times 10^6$

As the angle of attack is increased the mergin point moves upstream Further increase of the incidence leads inevitable to vortex breakdown The whole process is summarized in Figure 11, for a single cross section plane

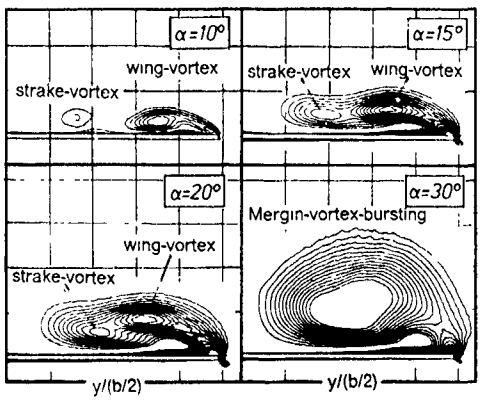

Figure 11. Strake-wing (outer sweep angle 50°)
$M_\infty = 0.1, R_e = 1.3 \times 10^6, x/c = 0.75$

Finally, Figure 12 shows that the integral values for lift, drag and pitching moment are in good agreement with the experimental data

5. Conclusions

The validation of a finite-volume scheme for the solution of the 3-D Navier-Stokes equations for the prediction of vortical flow fields around delta and strake-delta wings is presented The efficiency of the current multigrid-multiblock strategy is demonstrated for a variety flow cases which are strongly determined by

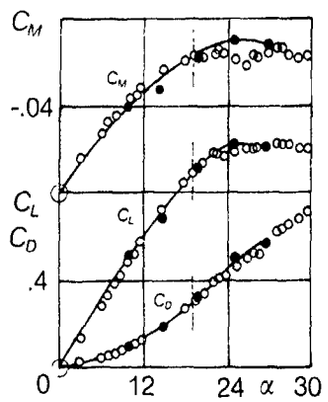

Figure 12 Strake-wing (outer sweep angle 50°)
$M_\infty = 0.1, R_e = 1.3 \times 10^6$

viscous effects Basic flow features due to changes of incidence, Mach number and geometry as well as flow phenomena due to vortex vortex and shock-vortex interactions are well simulated Converged solutions with sufficient accuracy are obtained in less than 40 minutes on a Cray-YMP computer The investigation clearly demonstrates the usefulness of the present code as a suitable tool within an aerodynamic design cycle

6. Acknowledgement

This investigation was carried out as a joint-program of the DLR Braunschweig and DASA-MBB Munchen

Bibliography

[1] Fujii K and Schiff L B *Numerical Simulation of Vortical Flows over a Strake-Delta Wing* AIAA 87-1229 (1987)

[2] Hartwich P M, Hsu C H, Luckring J M and Liu C H *Aerodynamic Application of an Efficient Incompresible Navier-Stokes Solver* ICAS Proc (1988), pp 1417-1427

[3] Rizzi A, Drougge G and Muller B *Navier-Stokes and Euler Solutions for Vortex Flow over a Delta-Wing* Symposium Transonicum III (1988), pp 305-316

[4] Radespiel R, Rossow C and Swanson R C *Efficient Cell-Vertex Multigrid Scheme for the Three-Dimensional Navier-Stokes Equations* AIAA Journal (1990), Vol 28, No 8, pp 1464-1472

[5] Atkins H *A Multiple-Block Multigrid Method for the Solution of the Three-Dimensional Euler and Navier-Stokes Equations* DLR-FB 90-45 (1990)

[6] Longo J M A and Das A *Numerical Computation of Vortical Flows Around Double-Delta Wings Using Navier-Stokes Equations* 7th DGLR-Fachsymposium "Strömungen mit Ablösung", Aachen (1990)

[7] Baldwin B S and Lomax H *Thin Layer Approximation and Algebraic Model for Separated Turbulent Flows* AIAA 78-257 (1978)

[8] Degani D and Schiff L B *Computation of Turbulent Supersonic Flows around Pointed Bodies Having Cross-flow Separation* Journal of Computational Physics (1986), No 66, pp 173-196

[9] Jameson A *A Vertex Based Multigrid Algorithm for Three-Dimensional Compressible Flow Calculations* Numerical Methods for Compressible Flows Finite Difference, Elements and Volume Techniques (1986) Ed by T E Tezduar and T J R Hughes, Applied Mechanics Revision 78, ASME, pp 45-73

[10] Rossow C Ch *Berechnung von Strömungsfeldern durch Lösung der Euler Gleichungen mit einer erweiterten Finite-Volumen Diskretisierungsmethode* DLR-FB 89-38 (1989).

[11] Radespiel R and Swanson R C *An Investigation of Cell Centered and Cell Vertex Multigrid Schemes for the Navier-Stokes Equations* AIAA 89-0548 (1989)

[12] Martinelli L and Jameson A *Validation of a Multigrid Method for the Reynolds-Averaged Equations* AIAA 88-0414 (1988)

[13] Oelker H-Chr *Aerodynamische Untersuchungen an kurzgekoppelten Entenkonfigurationen bei symmetrischer Anströmung* TU Braunschweig ZLR-Forschungsbericht 90-01 (1990)

[14] Hirdes R H C M *US/European Vortex Flow Experiment Test Report of Wind-Tunnel Measurements on the 65 degree wing in the NLR High Speed Wind Tunnel HST* NLR TR 85046 U (1985)

[15] Elsenaar A and Hoeijmakers H W M *An Experimental Study of The Flow over a Sharp-edged Delta Wing at Subsonic and Transonic Speeds* AGARD FDP Symposium on "Vortex Flow Aerodynamics", Scheveningen, The Netherlands (1990)

[16] Brennenstuhl U *Experimentelle und Theoretische Untersuchungen über die Wirbelbildung an Doppeldeltaflügel* Dissertation der TU Braunschweig (1985)

[17] Longo J M A. *The Role of the Numerical Dissipation on the Computational Euler Equations Solutions for Vortical Flows*, AIAA 89-2232 (1989)

[18] Longo J M.A and Das A *Numerical Simulation of Vortical Flows over Close-Coupled Canard Wing Configuration* AIAA 90-3003 (1990)

EIGHTH SYMPOSIUM ON
TURBULENT SHEAR FLOWS
Technical University of Munich
September 9-11, 1991

A STUDY OF THREE DIMENSIONAL TURBULENT BOUNDARY LAYER SEPARATION AND VORTEX FLOW CONTROL USING THE REDUCED NAVIER STOKES EQUATIONS

by

Bernhard H. Anderson
NASA Lewis Research Center
Cleveland, OH 44135

and

Saeed Farokhi
University of Kansas
Lawrence, KS 66045

ABSTRACT

A Reduced Navier Stokes (RNS) initial value space marching solution technique has been applied to a class of vortex generator and separated flow problems and has demonstrated good predictions of the engine face flow field This RNS solution technique using PLARL approximations can adequately describe the topological and topographical structure flow separation associated with vortex liftoff, and this conclusion led to the concept of a subclass of separations which can be called 'vorticity separations', i e separations dominated by the transport of vorticity Adequate near wall resolution of vorticity separations appears necessary for good predictions of these flows

INTRODUCTION

This paper represents one in a series of studies on the design issues associated with inlet-engine compatibility problems, and in particular, engine face distortion and its control These studies center on the development of CFD tools and techniques which look promising within an analysis-design environment, and the application of these new analysis approaches to understand and control inlet-engine distortion The first paper in this series by Anderson (1991), deals with the aerodynamic characteristics of vortex interaction within the P A-18 inlet duct, where the vortex interaction arises as a result of a vortex ingestion Later studies will involve the effect of vortex ingestion on the engine face flow field itself In the second paper in this series, by Anderson and Levy (1991), it was demonstrated that an installation of co-rotating vortex generators could be constructed to tailor the development of secondary flow to minimize engine face distortion Of special interest is the conclusion that there exists an optimum axial location for this installation of co-rotating vortex generators, and within this configuration, there exists a maximum spacing between generators above which the engine face distortion increases rapidly This study also showed that the vortex strength, generator scale, and secondary flow field structure have a complicated and interrelated influence on the engine face distortion, over and above the influence of the initial arrangement of generators

Thus the overall goal of this paper is to advance the understanding and control of engine face distortion, and in particular, to effectively analyze the basic interactions that influence this important design problem Specifically, the present paper achieves two goals (1) it extends and validates a 3D RNS solution technique for class of vortex generator and separated flow problems which will be shown to be dominated by the transport of vorticity, and (2) it examines the role of near wall resolution for the class of vorticity dominated separated flow problems

THEORETICAL BACKGROUND

The reduced Navier-Stokes (RNS) equations originally termed parabolized Navier-Stokes (PNS) equations and more recently semi-elliptic, or partially parabolic, are used here as an initial-value space marching method for the evaluation of subsonic compressible flow with strong interactions and/or separation arising from internal vortex flows Techniques that use space marching with an approximate form of the RNS equations, namely initial-value methods and those that require three-dimensional global iterations, have been used for a number of years to predict flows in curved ducts and turbomachinery blade cascades Unfortunately, this terminology does not identify the relevant mathematical approximations nor does it distinguish these approximations from the properties of the solution algorithm and the differential or difference equations In other words, different methods within the same category will in some instances give significantly different results

Three dimensional viscous subsonic flows in complex inlet duct geometries are investigated by a numerical procedure which allows solution by spatial forward marching integration, utilizing flow approximations from the velocity-decomposition approach of Briley and McDonald (1979 and 1984) The goal of this approach is to achieve a level of approximation that will yield accurate flow predictions, while reducing the labor below that needed to solve the full Navier Stokes equations The governing equations for this approach have been given previously for orthogonal coordinates, and the approach has been applied successfully to problems whose geometries can be fitted conveniently with orthogonal coordinate systems However, geometries encountered in typical subsonic inlet ducts cannot be treated easily using orthogonal coordinates, and this led to an extension of this approach by Levy, Briley, and McDonald (1983), to treat ducted geometries with nonorthogonal coordinates The nonorthogonal capability has been validated over a wide range of inlet flow conditions

Although the analysis itself was general, the class of ducted geometries that could be analyzed was represented by superelliptic cross-sections normal to a reference line space curve having continuous second derivatives The description of the superelliptic cross-sections was specified by polynomials defined in terms of a marching parameter, τ In generalizing the geometry formulation, Anderson (1991) extended the analysis to cover ducted geometries defined by an externally generated gridfile This version of the 3D RNS computer code is called RNS3D The geometry description within the gridfile is a 'ducted' geometry which has a variable cross-sectional area and shape and a centerline which is curved and possibly twisted In addition, the duct described by the gridfile is considered to have a defined centerline with continuous second derivatives The surface geometry is described in terms of cross-sectional planes which lie perpendicular to the duct centerline, and thus represent the flow area at each streamwise station Since the inlet duct geometry definition has been reduced to a cross section specification which is placed perpendicular to a centerline space curve, a number of grid and geometry pre-processing functions may be performed using RNS3D. These pre-processing functions include (1) reclustering the existing gridfile mesh points for more accurate solutions in regions of high shear, (2) redefining the centerline space curve to satisfy design constraints, and (3) altering the cross-sectional shape of the inlet duct to reflect specified design iterations. The approach taken by Anderson (1991), is to develop a geometry pre-processor to augment the existing geometry and grid generation programs for internal inlet duct configurations, i e. to partition the "work" of mesh generation between the grid generator and the flow solver

RESULTS AND DISCUSSIONS

Comparison and Validation with Experimental Data

To demonstrate the accuracy of the numerical results obtained with RNS3D for internal duct flows typical of high angle-of-attack conditions, a series of numerical simulations were carried out using the University of Tennessee diffusing S-duct. In this experimental investigation sponsored by NASA Lewis Research Center Vakili, Wu, Liver, and Bhat (1986) obtained a series of measurements in a 30-30 degree diffusing S-duct of area ratio 1.5 with and without vortex generators (Fig. 1). The 30-30 degree circular cross-section S-duct, shown in Fig. 1, was made from two symmetric sections. The inlet duct diameter D_i was 16.51 cm and the mean radius of curvature R was 82.55 cm. A straight pipe section of length $4.75D_i$ was installed upstream of the curved section to allow for the development of the turbulent boundary layer to the desired thickness. Another pipe of length $9.0D_e$ was installed downstream of the S duct.

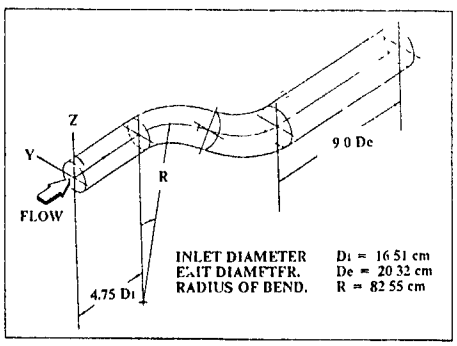

Fig. (1) Geometry definition of the Univ. Tennessee diffusing S-duct configuration.

All measurements were made at a nominal inlet Mach number of 0.60 at the reference measurement station in the straight section at $X/D_i = -1.54$. The flow parameters at this station were used as reference conditions for non-dimensionizing the experimental data. The experimental survey stations correspond to $X/D_i = 0.0$, 1.29, 2.49, and 5.2. At each survey station, a five-port cone probe was traversed radially at ten azimuthal angles, approximately 20 degrees apart, on both sides of the symmetry plane. At least seventy points were measured at each traverse.

A polar grid topology (Fig. 2), was chosen for the University of Tennessee diffusing S-duct, consisting of 49 radial, 49 circumferential, and 101 streamwise nodal points in the half-plane. The internal grid was constructed such that the transverse computational plane was perpendicular to the duct centerline. Grid clustering was used both in the radial and circumferential directions to redistribute the nodal points along these coordinate lines to resolve the high shear region near the wall and the separation region in the second bend. The flow in the inlet duct was turbulent, with an entrance Mach number of 0.6, Reynolds number based on an inlet diameter of 1.76×10^6, and the inflow corresponds to a shear layer $\delta/D_i = 0.05$. These initial conditions were applied at an axial station 1.54 inlet diameters (D_i) upstream of the duct entrance.

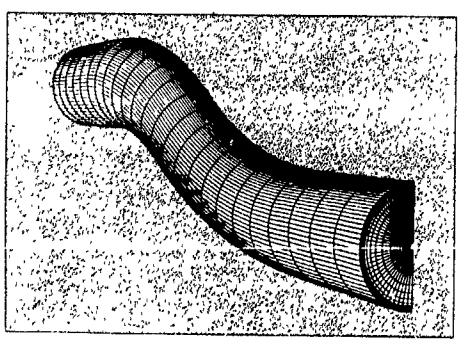

Fig. (2) Computation grid for the Univ. Tennessee diffusing S-duct configuration.

Fig. 3 shows a comparison between the experimental and computed total pressure coefficient contours at $X/D_i = 5.2$. In both the experiment and analysis, the flow in the S-duct separated and reattached in the second bend upstream of $X/D_i = 5.2$. This flow separation was caused by both adverse pressure gradients and the effect of pressure-driven secondary flow resulting from duct curvature. Experimental measurements and computational results from the 3D RNS code show excellent agreement for a simple mixing length turbulence model.

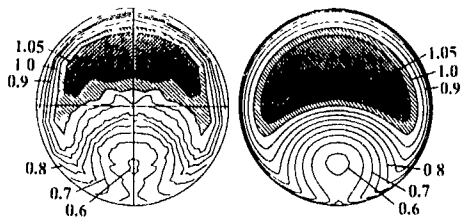

EXPERIMENTAL DATA ANALYSIS, $y+ = 0.5$

Fig. (3) Total pressure coefficient contours without vortex generators, $X/D_i = 5.2$.

As separation was encountered in the second bend of the S-duct, three pairs of vortex generator devices were installed in the duct at $X/D_i = 0.09$, and at azimuthal angles of -38.0, 0.0, and 38.0 degrees with respect to the streamwise direction. The vortex generator pairs had geometric incidence angles of +16.0 and -16.0 degrees relative to the duct centerline. Fig. 4 shows the comparison between the experimental and computed total pressure coefficient contours at $X/D_i = 5.2$. Comparison of contour levels between the separated case (Fig. 3), and the vortex generator case (Fig. 4), shows that the vortex generators successfully mixed the high energy core flow with the low energy flow in the wall region to suppress separation. In general, the computed interaction between the induced vortex generator flow and the pressure driven secondary flow was physically realistic and the agreement between experiment and analysis is considered very good, although more improvements on the generator model must be made.

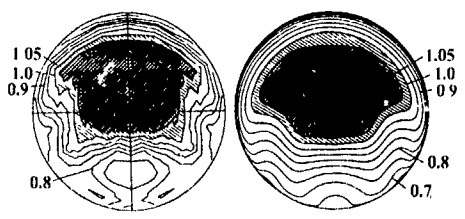

EXPERIMENTAL DATA ANALYSIS, $y+ = 0.5$

Fig. (4) Total pressure coefficient contours with vortex generators, $X/D_i = 5.2$.

Figs. 5 and 6 show additional flow characteristics obtained with the 3D RNS analysis with the vortex generator modeling. The secondary flow structure from the vortex generator model just downstream of the generator region, i.e. at $X/D_i = 0.18$, is shown in Fig. 5, and clearly reveals the three pairs of vortices that arise from the three pairs of counter-rotating generators. The limiting streamline signature shown

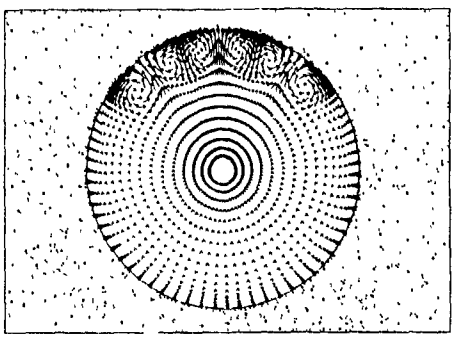

Fig. (5) Reduced Navier Stokes (RNS) solution showing secondary flow structure from vortex generator model, $X/D_i = 0.18$

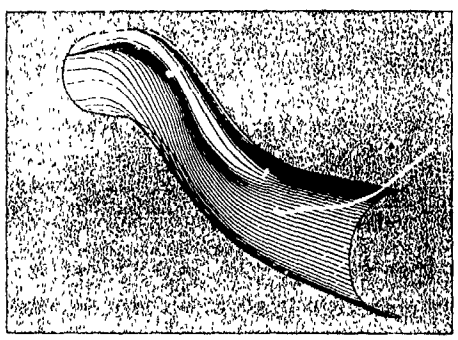

Fig. (6) Reduced Navier Stokes (RNS) solution showing limiting streamline signature of vortex generator region.

in Fig 6 indicates that the generator configuration tested eliminated the flow separation encountered in the second bend, and reveals the familiar topographical pattern through the generator region itself.

Flow Separation and Vortex Liftoff

The three dimensional separation encountered in the University of Tennesse diffusing S-duct was very large in area and thin in extent (Figs 7 and 8), and this separation did not alter the pressure distribution in a substantial manner Secondary flow resulting from duct curvature caused an accumulation of boundary layer near the innerwall of the first 30 degree bend The thick boundary layer thus established was

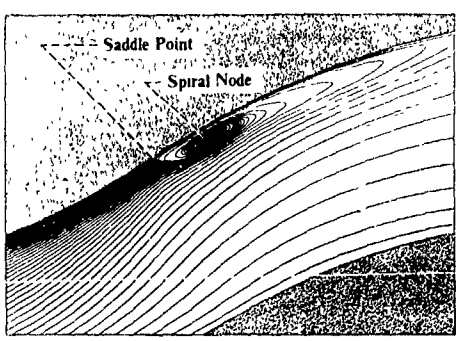

Fig. (7) Reduced Navier Stokes (RNS) solution showing limiting streamline signature of separation region within Univ. Tennessee diffusing S-duct.

Fig. (8) Surface oil flow patterns showing separation region within Univ. Tennessee diffusing S-duct.

especially susceptible to flow separation because of the adverse pressure gradients induced by the reverse curvature section of the second 30 degree bend A comparison between the computed oil flow patterns (represented by the limiting streamline topology in Fig 7) and the experimental oil flow patterns presented in Fig 8 shows excellent correspondence Of exceptional importance is the fact that the space marching RNS analysis method using FLARE approximations captures the reverse flow region of this separation

To meet the required confidence level of code validation, it is also essential that the 3D RNS marching analysis be able to capture the known topographical structure of the limiting streamlines in the vicinity of 3D separation A very striking and significant feature captured by the analysis (Fig 7), and seen in the oil flow pattern (Fig 8), is the convergence of the limiting streamlines as an indication of three dimensional separation taking place in this duct Another important and striking feature is the symmetric pair of spiral nodes and pair of saddle points that were clearly captured by the 3D RNS analysis The topological patterns, as shown in the analysis Fig 7, and the photograph of surface oil flow pattern Fig 8, also reveal the remarkable characteristic that the limiting streamlines forming the spiral node enter only from downstream of the nodal point The very familiar topological pattern shown in Figs 7 and 8 is known to describe the important stage in the development of the pair of counter rotating vortices that form in the first 30 degrees of turning resulting in vortex liftoff in the second bend

Table I presents a summary of the computed and experimental results for the separation characteristics in the University of Tennessee diffusing S-duct for RNS3D and two FNS (Full Navier Stokes) codes currently in use, PARC3D and CFL3D In general, all three computer codes show remarkable consistancy with regard to the location of separation,

Source	Separation Point (X_s/D_i)	Reattachment Length ($\Delta X_s/D_i$)	Computational Grid ($N_x \times N_\theta \times N_r$)	CPU Time (Min.)
RNS (RNS3D)	2.5	2.6	49x49x95	6.5
FNS (PARC3D)	2.4	1.7	26x49x65	600.0+
FNS (CFL3D)	2.4	2.6	26x49x65	600.0+
Experiment	1.8	1.2	———	———

Table I Summary of computed and experimental separation characteristics for the Univ. Tennessee diffusing S-duct.

while two codes, RNS3D and CFL3D, show very good agreement with regard to the reattachment length. However, none of the computer codes showed very good agreement with regards to this particular set of experimental data. In general, RNS3D was able to capture the essential features of separation location and reattachment length as well as the two INS solutions, certainly with far more computational efficiency.

The topography of this very important flow interaction is shown schematically in Fig. 9, while Figs. 10 and 11 show the computed particle traces associated with vortex liftoff for particles orignating at $y/\delta = 0.03$ (Fig. 10), $y/\delta_i = 0.30$ (Fig. 11).

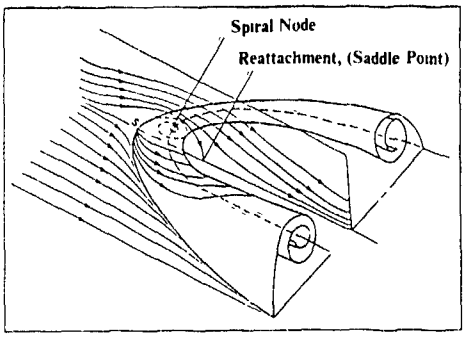

Fig. (9) Topography of the streamlines associated with vortex liftoff.

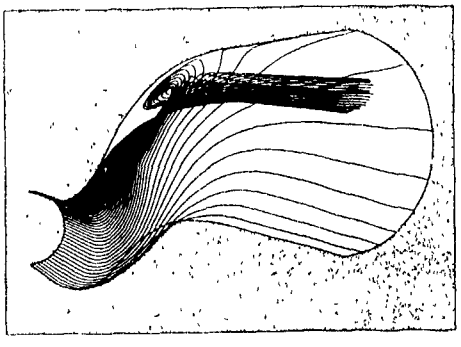

Fig. (10) Reduced Navier Stokes (RNS) solution showing particle traces associated with vortex liftoff, $y^+ = 0.5$, $y/\delta_i = 0.03$.

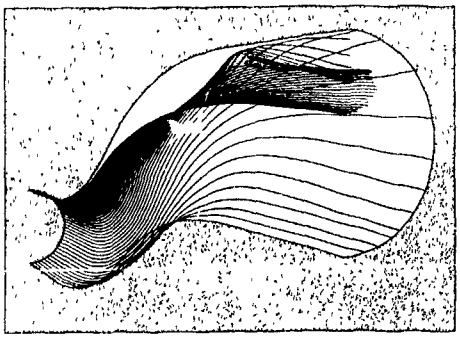

Fig. (11) Reduced Navier Stokes (RNS) solution showing particle traces associated with vortex liftoff, $y^+ = 0.5$, $y/\delta_i = 0.30$.

It is quite apparent that fluid particles that originate well inside the entrance boundary layer can influence the core region of the engine face station.

In general, the flow separation studied here was dominated by pressure forces rather than shear forces, as would be the case with massive separation in the inlet duct, such that the influence of the stress-driven flows was small and the effective viscosity approach surprisingly successful. In order to explain the success of space marching 3D RNS methods in describing the detailed topographical structure of vortex liftoff, it must be concluded that there exists a class of separated flows that are dominated by the transport of vorticity. This class of separation interactions can be called 'vorticity separations', since they differ fundamentally from shear-driven separations.

Vorticity Dominated Internal Flow Fields

Several numerical factors can affect the accuracy of predictions of high Reynolds number vorticity-dominated internal flows. These include (1) the nature of numerical smoothing (in the case of Full Navier Stokes analyses), (2) the kind of turbulence model used to describe the turbulent transport properties, and (3) the form of the grid distribution to resolve the details of the viscous boundary layer in the near wall region where the vorticity is the largest. For the computations of the flow within the University of Tennessee diffusing S-duct, two calculations were made to study the effects of near wall grid resolution. In the first case, the radial grid spacing was chosen to give a nominal y^+ of 8.5 at first grid point above the duct wall, and in the second case, a nominal y^+ value of 0.5 was chosen, both determined at the duct enterence plane $X/D_i = 0.0$. Figs. 12 and 13 show the effects of this near wall grid lattice resolution on the total pressure coefficient contours (Fig. 12), and the secondary flow structure (Fig. 13), both at the engine face station, $X/D_i = 5.2$. It was the case of $y^+ = 0.5$ which gave the best agreement with the experimentally measured engine face flow field (see Fig. 3). The very strong effect of near wall grid resolution on structure and strength of the engine face flow results from the very nature of vorticity dominated internal flows. Since the largest value of vorticity occurs in the near wall region, and secondary flow is generated by turning of transverse shear, a very strong effect of near wall grid resolution was realized as stronger secondary flow (Fig. 13), which had consequently an appreciable influence on the primary flow (Fig. 12). This interaction is really an inviscid

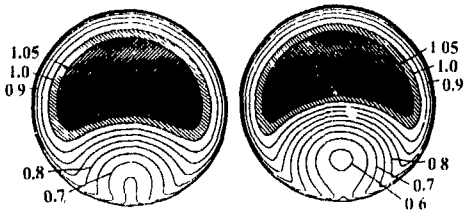

ANALYSIS, y+ = 8.5 ANALYSIS, y+ = 0.5

Fig. (12) Effect of near wall grid lattice resolution on total pressure coefficient contours, $X/D_i = 5.2$.

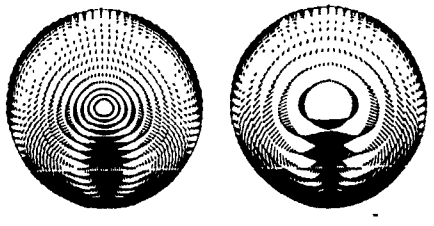

ANALYSIS, y+ = 8.5 ANALYSIS, y+ = 0.5

Fig. (13) Effect of near wall grid lattice resolution on secondary flow structure, $X/D_i = 5.2$.

rotational phenomenon rather than a viscous phenomenon, and indicates that secondary flow has its ultimate origin very near the wall The turbulence model will thus also strongly influence the strength of secondary flow, but only as an inviscid rotational phenomena through the near wall vorticity distribution and not necessarily as part of the turbulent properties of the flow

Figs 14 and 15 show the limiting streamline signatures obtained with the Reduced Navier Stokes code for $y^+ = 8.5$ (Fig 14) and for $y^+ = 0.5$ (Fig 15) Both figures clearly reveal the size of the flow separation region encountered in the University of Tennessee diffusing S-duct, as well as the characteristic topology associated with vortex liftoff However, there is a marked difference in the calculated extent of the separated region between the two cases, i e lack of near wall resolution diminishes the size of the separated region It is quite evident that near wall resolution plays a very important role in determining the structure of the separation associated with vortex liftoff

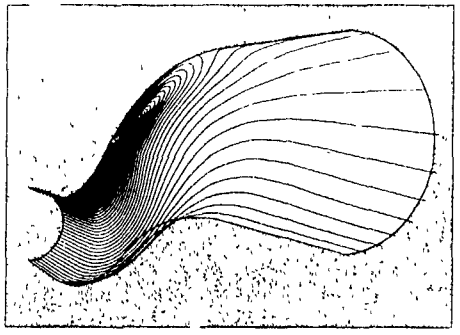

Fig (14) Reduced Navier Stokes (RNS) solution showing limiting streamline signature of separation region, $y^+ = 8.5$.

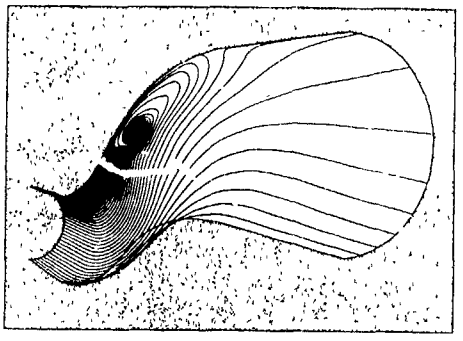

Fig. (15) Reduced Navier Stokes (RNS) solution showing limiting streamline signature of separation region, $y^+ = 0.5$.

The significance of near wall resolution with regards to engine face distortion is presented in Figs 16 and 17, where the distortion parameters used for comparision are the more advanced ring distortion descriptors, introduced in the late 1960 s and 1970 s These parameters, which are defined by Anderson (1991), take into account the distortion of each ring of total pressure measurements, or in this case, at each ring of the radial computational mesh In comparing the two calculations in Figs 16 and 17, it can be seen that a maximum difference of 0 02 can be incurred in the radial pressure ring distortion, while a maximum uncertainty of 0 01 can be realized in the calculation of the 60°-sector circumferential ring

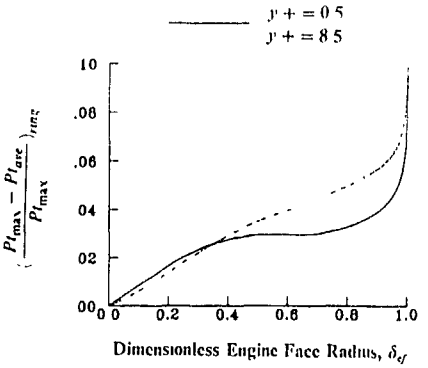

Fig. (16) Effect of near wall resolution (y^+) on engine face radial pressure ring distortion.

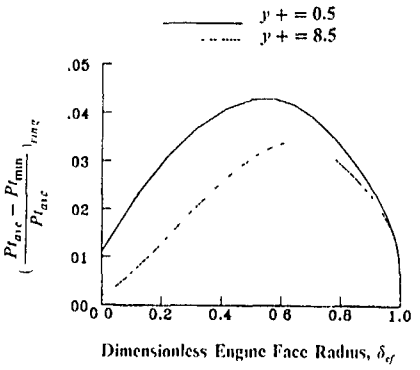

Fig. (17) Effect of near wall resolution (y^+) on engine face 60°-sector circumferential pressure ring distortion.

distortion descriptor The uncertainty of 0 01 represents a 33% error in the maximum 60°-sector circumferential ring distortion indicator

CONCLUSIONS

The present results provide a validation of the initial value space-marching 3D RNS procedure and demonstrates accurate predictions of the compressor face flow field, with a separation present in the inlet duct as well as when vortex generators are installed to suppress separation The computing time, CPU = 6 5 min on the CRAY XMP for 2 28 x 10^5 grid points, for both the baseline case and the case with three pairs of counter-rotating vortex generators, is sufficiently rapid for routine use in an analysis-design engineering environment

Initial value space marching 3D RNS procedures using FLARE approximations can adequately describe the topological and topographical features of 3D flow separations associated with vortex liftoff within inlet ducts The success of this RNS analysis in describing this phenomenon is due to the existence of a class of separated flows, which can be called "vorticity separations", which are dominated by the transport of vorticity rather than turbulent shear effects

Adequate near wall resolution of "vorticity separated turbulent flows are necessary to obtain accurate calculations of the strength of secondary flows that develop in typical inlet ducts, and in particular, the size and shape of the separated region and the engine face total pressure recovery map and distortion level

REFERENCES

ANDERSON, BERNHARD H. 1991. The Aerodynamic Characteristics of Vortex Ingestion for the F-18 Inlet Duct. AIAA Paper No. 91-0130.

ANDERSON, BERNHARD H. & LEVY, RALPH. 1991. A Design Strategy for the Use of Vortex Generators to Manage Inlet Engine Distortion Using Computational Fluid Dynamics. AIAA Paper No. 91-2474.

BRILEY, W. R., & MC DONALD, H. 1979. Analysis and Computation of Viscous Subsonic Primary and Secondary Flow. AIAA Paper No. 79-1453.

BRILEY, W. R., & MC DONALD, H. 1984. Three-Dimensional Viscous Flows with Large Secondary Velocities. Journal of Fluid Mechanics, 144, 47-77.

LEVY, R., BRILEY, W. R., & MC DONALD, H. 1983. Viscous Primary Secondary Flow Analysis for Use with Nonorthogonal Coordinate Systems. AIAA Paper No. 83-0556.

VAKILI, A. D., WU, J. M., LIVER, P. A., & BHAT, M. K. 1986. Experimental Investigation of Secondary Flows in a Diffusing S-Duct with Vortex Generators. NASA NAG-233.

EIGHTH SYMPOSIUM ON
TURBULENT SHEAR FLOWS
Technical University of Munich
September 9-11, 1991

AN EXPERIMENTAL AND NUMER CAL STUDY OF CONFINED AXISYMMETRIC JET WITH A BLUFF BODY

M. Senda, S. Okamoto and S. Kikkawa

Department of Mechanical Engineering, Doshisha University, Kyoto 602, Japan

ABSTRACT

Experimental and numerical studies have been made on a confined axisymmetric jet with two types of bluff bodies one is a cylindrical ring and the other a disk both having a same blockage ratio The velocity characteristics in the near wake have been measured with a laser Doppler velocimeter, the results of which have been compared with the numerical calculations using the k-ε model of turbulence

The size of the recirculating region behind the ring was not affected by the velocity ratio U_j/U_s of the jet and the circumferencial flows, whereas both the axial and radial extent of the recirculating region behind the disk became larger with increasing U_j/U_s In the near-wake region, the positions where the values of the mean axial velocity gradient and the Reynolds shear stress were respectively at zero did not necessarily coincide, and the present flow indicates the existence of the region of the negative production. The numerical calculation using the k-ε model predicted fairly well the mean velocity field in the near wake of the ring, but the prediction of the near wake of the disk was not satisfactory in respect of both the axial and radial extent of the recirculating region.

1 INTRODUCTION

Turbulent recirculating flows occur in a variety of engineering situations. flows over steps (Etim, Kline & Johnston, 1980, Kondo & Nagano, 1991) or ribs (Durst & Rastogi, 1980, Benodekar et al., 1985), and around bluff bodies (Fujii, Gomi & Eguchi, 1978; Taylor & Whitelaw, 1984) are typical ones Because of the large heat and mass transfer rates associated with the high turbulent intensities, flame stabilization of many practical combustion chambers is often achieved in the recirculating region We are concerned with the locally recirculating flows which are established behind bluff bodies. Since the intense turbulent mixing in the near wake is the decisive factor to understand the mechanism of the flame stabilization, the aerodynamics of the near wake have been studied in the isothermal flows (Fujii, Gomi & Eguchi, 1978, Taylor & Whitelaw, 1984)

In the present paper, an axisymmetric confined jet is studied both experimentally and numerically, in which two kinds of bluff bodies (one is a cylindrical ring and the other a disk both having a same blockage ratio) are installed coaxially at a downstream position of the jet nozzle. The axial and radial velocity components have been measured with a laser Doppler velocimeter and the detailed characteristics of the flow field in the wake region are presented A further purpose in making these measurements is to compare the experimental results with the numerical calculation using a turbulence model Applicability of the k-ε model of turbulence to the present flow is discussed based on the comparison of the measured results with those of prediction.

2 EXPERIMENTAL AND NUMERICAL PROCEDURES

Experiments were carried out in a circular tube in which the nozzle and the bluff body were installed coaxially The working fluid was water The main constructional details and dimensions of the test section is shown schematically in Fig 1 The inner diameter D of the tube was 60mm, and the blockage ratio of both the bluff bodies was same and equal to 0 15 Measurements were made at the cross sections of x/D=0 4, 0 6, 1 0 and 2.0 for three different velocity ratios of the jet and the circumferencial flows (U_j/U_s=1 0, 1 5 and 2 5) The mean velocity of the circumferencial flow Us at the inlet of the test section was kept constant at 1 10m/s.

A two-color four-beam laser Doppler velocimeter has been used in the present experiment, and the axial and the radial velocity components have been measured simultaneously In order to detect a negative velocity in the recirculating region behind the bluff body, an optical frequency shift of the laser beam has been accomplished with the Bragg cell The light scattered by small particles suspended in the fluid was collected by a lens on the same side of the transmission optics (backward scattering optical arrangement) and focused at a pin hole in front of a photomultiplier The output of the photomultiplier was processed by a frequency counter which provided an output voltage proportional to the frequency of the input signal. The output signal from the counter was transferred to a digital computer and processed to give the mean velocities, the rms values of their fluctuations and the Reynolds shear stress Since the refractive indexes of air, the material of the circular tube (Pyrex glass) and the working fluid (water) are different from each other, the four beams do not intersect at a single point after passing through the tube wall with a curvature. In the present experiments, the circular tube was enclosed in a rectangular duct and a water solution of NaI having the same refractive index as that of the Pyrex glass was filled in the space between the duct and the circular tube In addition, two of the beams (blue) were geometrically shifted by passing them through the optical glass plates outside the duct in order to bring four beams to intersect at a single point

Although the results presented in the next section are shown for the half cross section, symmetricity of the flow was confirmed at every cross section by measuring the mean axial velocity profile both vertically and horizontally in a plane containing the tube's axis.

The governing partial differential equations for a two-dimensional axisymmetric flow (Pope & Whitelaw, 1976) are as follows:

$$\frac{\partial}{\partial x}(\rho U) + \frac{1}{r}\frac{\partial}{\partial r}(r\rho V) = 0 \qquad (1)$$

$$\frac{\partial}{\partial x}(\rho U^2) + \frac{1}{r}\frac{\partial}{\partial r}(r\rho UV) = -\frac{\partial}{\partial x}(\rho\overline{u^2}) - \frac{1}{r}\frac{\partial}{\partial r}(r\rho\overline{uv}) - \frac{\partial p}{\partial x} \quad (2)$$

$$\frac{\partial}{\partial x}(\rho UV) + \frac{1}{r}\frac{\partial}{\partial r}(r\rho V^2) = -\frac{\partial}{\partial x}(\rho\overline{uv}) - \frac{1}{r}\frac{\partial}{\partial r}(r\rho\overline{v^2}) - \frac{\partial p}{\partial r} + \rho\frac{\overline{w^2}}{r} \quad (3)$$

where U and V are the mean axial and radial velocity components, ρ the density of the fluid, and p the mean pressure, respectively x and r stand for the axial and radial coordinates Each component of the Reynolds stresses appeared in the momentum equations has been described using the eddy viscosity μ_t, and the k-ε two equation model of turbulence has been applied The transport equations of the turbulent kinetic energy k and its dissipation rate ε are

$$\frac{\partial}{\partial x}(\rho Uk) + \frac{1}{r}\frac{\partial}{\partial r}(r\rho Vk) = \frac{\partial}{\partial x}\left(\frac{\mu_t}{\sigma_k}\frac{\partial k}{\partial x}\right) + \frac{1}{r}\frac{\partial}{\partial r}\left(r\frac{\mu_t}{\sigma_k}\frac{\partial k}{\partial r}\right) + P - \rho\varepsilon \quad (4)$$

$$\frac{\partial}{\partial x}(\rho U\varepsilon) + \frac{1}{r}\frac{\partial}{\partial r}(r\rho V\varepsilon) = \frac{\partial}{\partial x}\left(\frac{\mu_t}{\sigma_\varepsilon}\frac{\partial \varepsilon}{\partial x}\right) + \frac{1}{r}\frac{\partial}{\partial r}\left(r\frac{\mu_t}{\sigma_\varepsilon}\frac{\partial \varepsilon}{\partial r}\right) + \frac{\varepsilon}{k}(C_{\varepsilon 1}P - C_{\varepsilon 2}\rho\varepsilon) \quad (5)$$

where $\mu_t = \rho C_\mu k^2/\varepsilon$ and

$$P = -\rho\left\{\overline{uv}\left(\frac{\partial U}{\partial r} + \frac{\partial V}{\partial x}\right) + \overline{u^2}\frac{\partial U}{\partial x} + \overline{v^2}\frac{\partial V}{\partial r} + \overline{w^2}\frac{V}{r}\right\}$$

The Reynolds stresses can, then be expressed as follows

$$\rho\overline{uv} = -\mu_t\left(\frac{\partial U}{\partial r} + \frac{\partial V}{\partial x}\right), \qquad \rho\overline{u^2} = \frac{2}{3}\rho k - 2\mu_t\frac{\partial U}{\partial x} \quad (6)$$

$$\rho\overline{v^2} = \frac{2}{3}\rho k - 2\mu_t\frac{\partial V}{\partial r}, \qquad \rho\overline{w^2} = \frac{2}{3}\rho k - 2\mu_t\frac{V}{r}$$

The values of the empirical constants appearing in Eqs (4) and (5) are the standard values recommended in Launder and Spalding (1974)

The finite-difference equations have been obtained by integrating the basic equations over the control volume with a hybrid central/upwind differencing scheme being used for the convection terms A staggered nonuniform grid arrangement (40 × 27 grid points) was employed for the velocities, while all other equations were solved at the pressure nodes In obtaining the coefficients of the difference equations at the grid points adjacent to the corners of the bluff body the convection and the diffusion contributions were such that it accounts for the fact that half of the control volume face is the wall and the other half exposed to the flow (Durst & Rastogi, 1980) The solution algorithm employed here was the SIMPLER (Patanker, 1980) in which the axial and radial velocity components are solved iteratively together with the pressure correction, and the solution procedure was a line by line method in conjunction with a tridiagonal matrix solver

Since the turbulence model used in the present calculations is applicable to the high Reynolds number flows, the wall functions (Rodi, 1980) were used for the boundary condition of all the walls The dependent variables at the inlet of the computational domain (at the exit of the nozzle) were given based on the measurements, and at the exit of the computational domain, the fully developed flow was assumed

3 RESULTS AND DISCUSSION

3 1 Mean Velocity

The mean axial velocity profiles are shown in Figs. 2 and 3, where Um is the mean velocity of the cross section, x the axial distance from the exit of the nozzle, r the radial distance from the axis of symmetry and R(=D/2) the radius of the circular tube. At the position of x/D=0 4, there existed a region where the mean axial velocities were negative. The size of the recirculating region behind the ring are seemed not to be affected by the velocity ratio U_j/U_s of the jet and the circumferencial flows in both the axial and radial directions The recirculating region extended downstream, at most, up to x/D=0 6 in all cases of U_j/U_s, as the velocity profiles at the position of x/D=1 0 indicated that the flow disturbed by the ring began to redevelop to a fully developed one On the other hand, the recirculating region behind the disk was larger than that of the ring and its size changed with the velocity ratio The axial and radial extent of the recirculating region became larger with increasing U_j/U_s, since the jet flow impinged on the frontal plane of the disk was bended towards the tube wall more strongly with increasing jet velocity. The streamline angle near the training edge of the disk increased, which can be confirmed from Fig. 4 of the velocity vector in the near wake

In Figs 2 and 3, the numerical calculations using the k-ε model of turbulence are compared with the experiments The

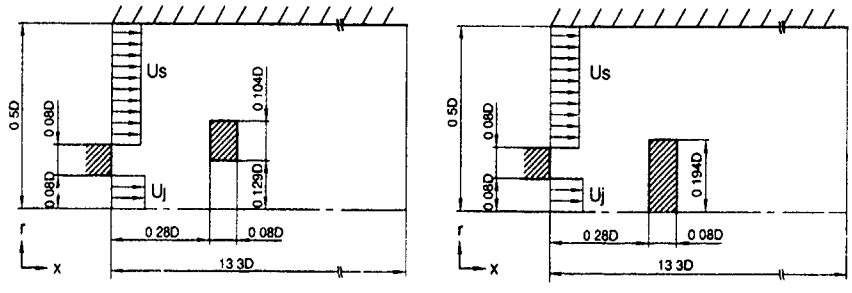

Fig. 1 Schematic diagram of the test section.

agreement between them is fairly good in the case of the ring, although the experimental data at the position of x/D=1 0 indicated somewhat lower values near the axis of symmetry This difference between the numerical and the experimental results has been slightly improved, when the algebraic stress model was used in the calculation (Senda et al , 1991) In the case of the disk, the numerical calculation predicted well the effect of U_j/U_s on the mean velocity profiles in the recirculating region, but the agreement with the experiments is not so good quantitatively As will be seen in Fig 6, the high turbulent intensities were observed in the recirculating region of the disk For those flows in which there is large production of the turbulent kinetic energy through the normal stresses, calculations using a scalar eddy viscosity like the standard k-ε model would be inaccurate Leschziner and Rodi (1981) proposed a variant of the k-ε model which accounts for the effects of the streamline curvature on turbulence In their paper, it was also pointed out that the hybrid central/upwind differencing scheme is a deficient tool for simulating a recirculating flow, unless exc dingly fine grids are used The k-ε model modification together with the hybrid differencing scheme was not effective in improving the present results Therefore, a higher-order differencing scheme in respect of the numerical diffusion should be employed for the calculation

3 2 Turbulent Intensities

The turbulent intensities, u' and v', of the axial and radial velocity components are shown in Figs 5 and 6 In the case of the ring, the u' profiles at x/D=0 4 had three peaks, the radial positions of which corresponded to the steep mean velocity gradients· two of which are due to the separating shear layers from the inner and outer edges of the ring and the third one, which became conspicuous with increasing U_j/U_s, is due t· ·e free shear layer of the jet The large values of v' resulted from the separating shear layers are also seen in the figure. In the case of the disk, the u' and v' values of the separating shear layer increased and their peak positions moved towards the tube wall with increasing velocity ratio, which also indicated the larger extent of the recirculating region in the radial direction On the other hand, both u' and v' were large in the recirculating region behind the bluff bodies, but their values were almost constant and equal independent of the velocity ratio The intense turbulent mixing in this region can be inferred from these figures

3 3 Reynolds Shear Stress

In Fig. 7 are shown the distributions of the Reynolds shear stress $\overline{uv}$ for the case of the ring Corresponding to the sign of the mean axial velocity gradient, the Reynolds shear stress profile at x/D=0 4 had a local maximum (a large positive value) or a local minimum (a large negative value). It is also seen that the local maximum due to the free shear layer of the jet increased with the velocity ratio At the downstream positions of x/D=1.0 and 2 0, the experimental data shows that the positive values of $\overline{uv}$ did not exist near the axis of symmetry in the cases where the excess jet velocity over the circumferencial flow disappeared

In the same figure, the numerical calculations using the k-ε model of turbulence are compared with the experimental results The calculations did not agree well with the experiments at the positions of x/D=1 0 and 2 0, especially in the region from the axis of symmetry to r/R=0 4 This caused from the fact that a little higher values of the mean velocity than the experimental data were predicted near the axis of symmetry In the case of U_j/U_s=1 0, for example, the mean velocity gradient of the calculation at these positions was negative in sign near the axis of symmetry, while the local maximum of the velocity profile on the

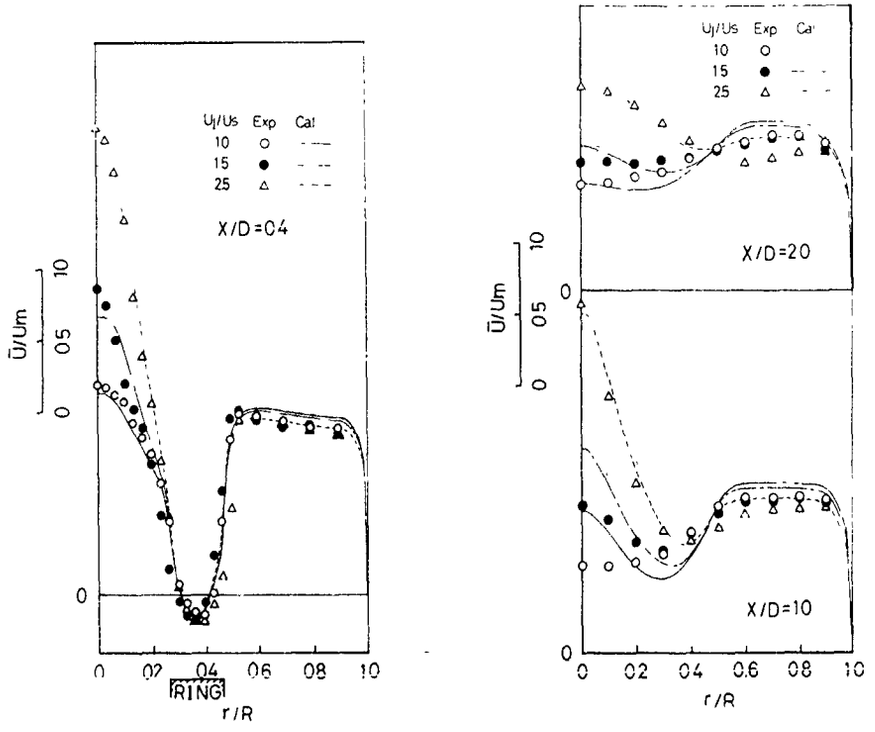

Fig. 2 Mean axial velocity (Ring)

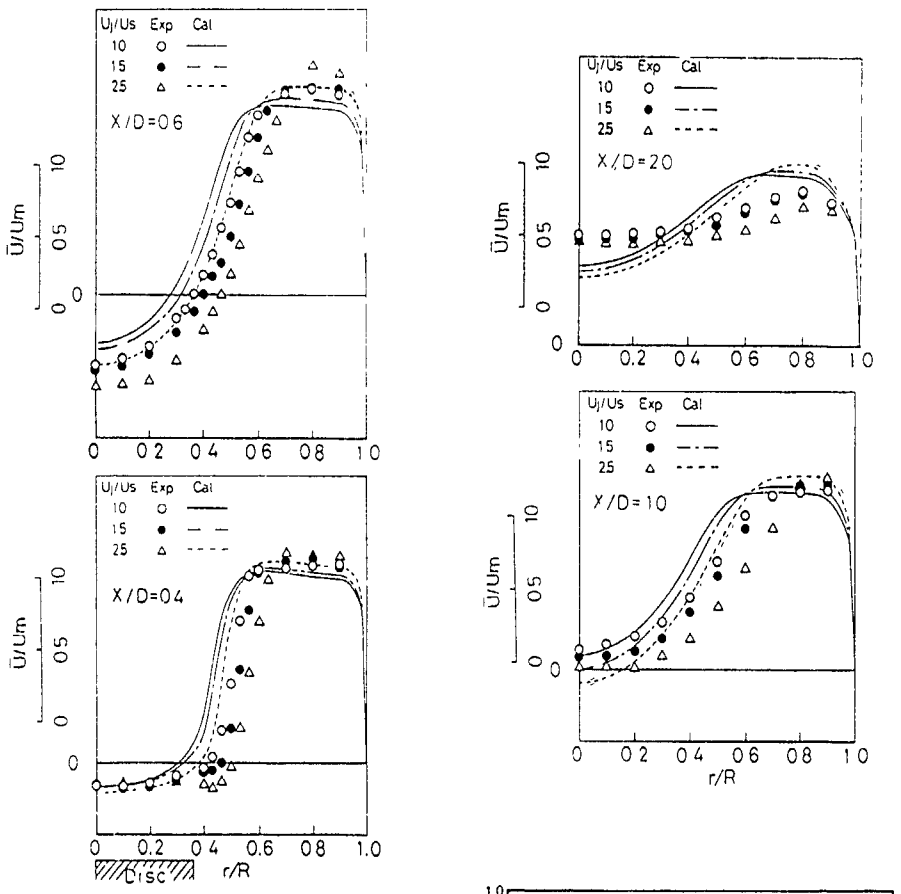

Fig 3 Mean axial velocity (Disk).

axis disappeared in the results of the experiments Therefore, the positive values of the Reynolds shear stress near the axis of symmetry were predicted numerically in contrast to the negative values of the experiments Figure 8 shows the comparison between the numerical and the experimental results of the Reynolds shear stress for the case of the disk As seen from the Fig 3, the prediction of the mean velocity profile was not satisfactory in respect of both the narrow width and the short length of the recirculating region This reflected on the results of the Reynolds shear stress, leading to a large difference between them in the region from r/R=0 4 to 0 8.

An important fact which is of interest experimentally is that the radial positions, where the values of the mean axial velocity gradient and the Reynolds shear stress were respectively at zero, did not necessarily coincide It was then confirmed that there is a region of the turbulent energy reversal (that is, the negative production), which is indicated in the figures as the shaded portion The region of the turbulent energy reversal is seen to exist in the recirculating region, and the same phenomenon has been reported for a flow behind a two-dimensional nozzle and bluff body combination (Fujii, Gomi & Eguchi, 1978) Further examination which is in progress is required on the turbulence structure in this region

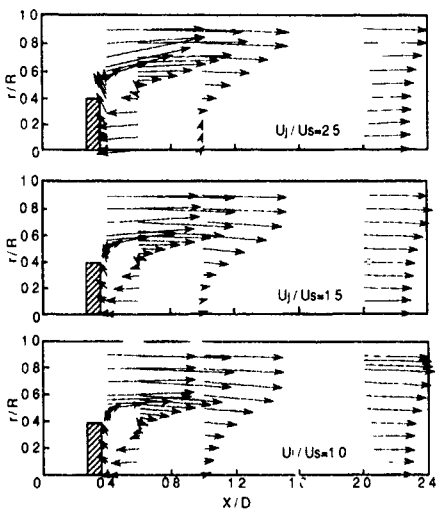

Fig 4 Velocity vector in the near wake of the disk.

4. CONCLUDING REMARKS

Experimental and numerical studies have been made on a confined axisymmetric jet with a bluff body The velocity characteristics in the near wake have been measured with a laser Doppler velocimeter, the results of which have been compared with the numerical calculation using the k-ε model of turbulence The main results obtained are summarized as follows:

(1) In the case of the ring, the size of the recirculating region was not affected by the velocity ratio U_j/U_s of the jet and the circumferencial flows On the other hand, both the axial and radial extent of the recirculating region behind the disk became larger with increasing U_j/U_s, since the jet flow impinged on the frontal plane of the disk was bended more strongly towards the tube wall

(2) The turbulent intensities profiles in the near wake indicated the local maxima, which are due to the separating shear layer from the edge of the bluff body, and due to the free shear layer of the jet in the case of the ring

(3) In the recirculating region, the positions where the values of the mean axial velocity gradient and the Reynolds shear stress were respectively at zero did not necessarily coincide, and the present flow is further experimental evidence of the phenomenon of the negative production

(4) The numerical calculations using k-ε model of turbulence predicted fairly well the mean velocity field in the near wake of the ring, whereas the prediction of the mean velocity field of the disk was not satisfactory in respect of both the axial and radial extent of the recirculating region

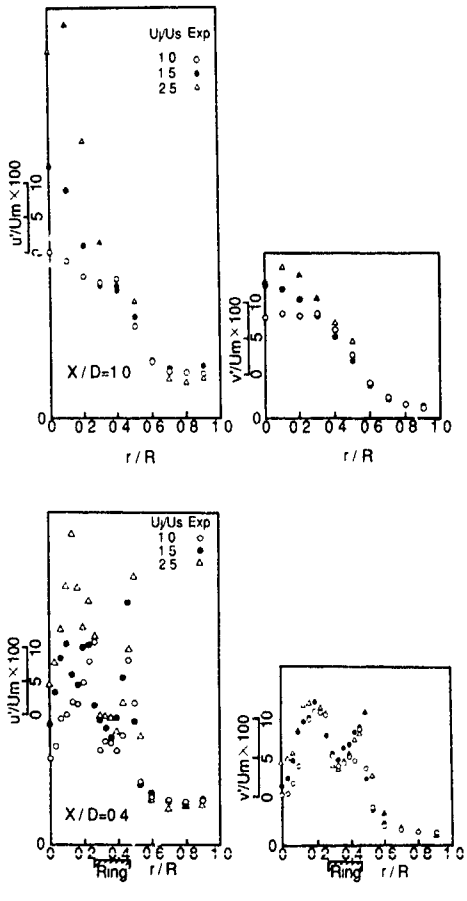

Fig. 5 Turbulent intensities (Ring)

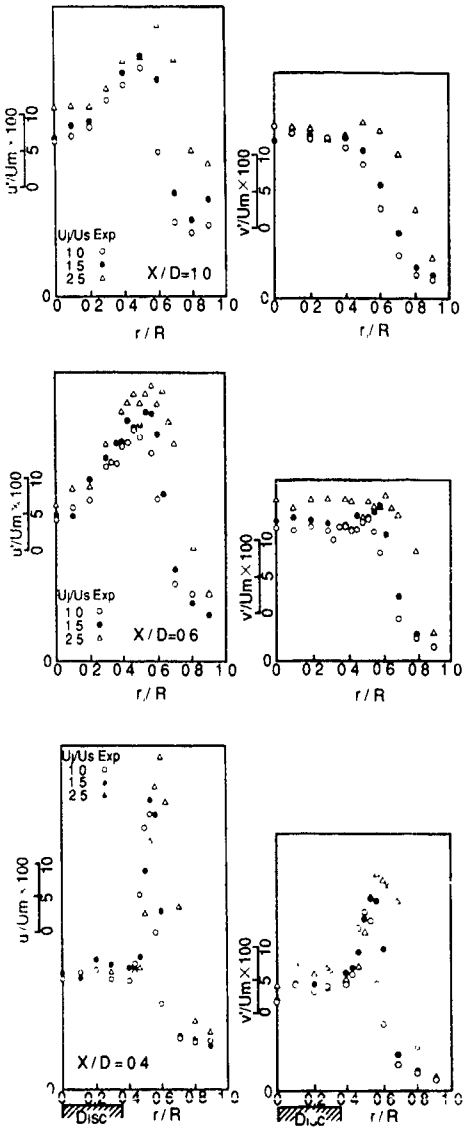

Fig 6 Turbulent intensities (Disk)

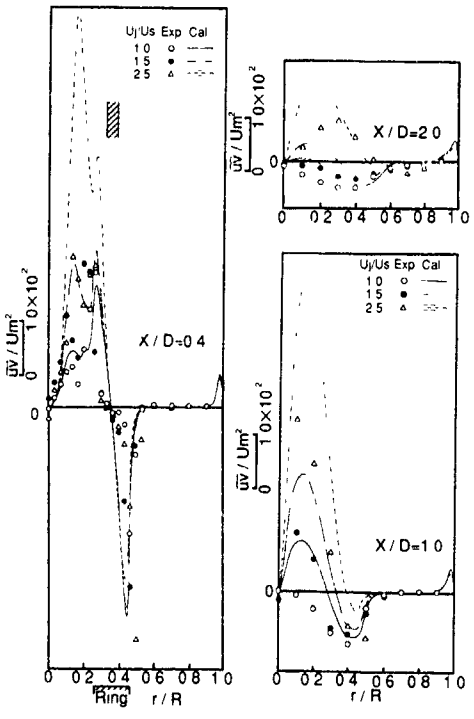

Fig 7 Reynolds shear stress (Ring).

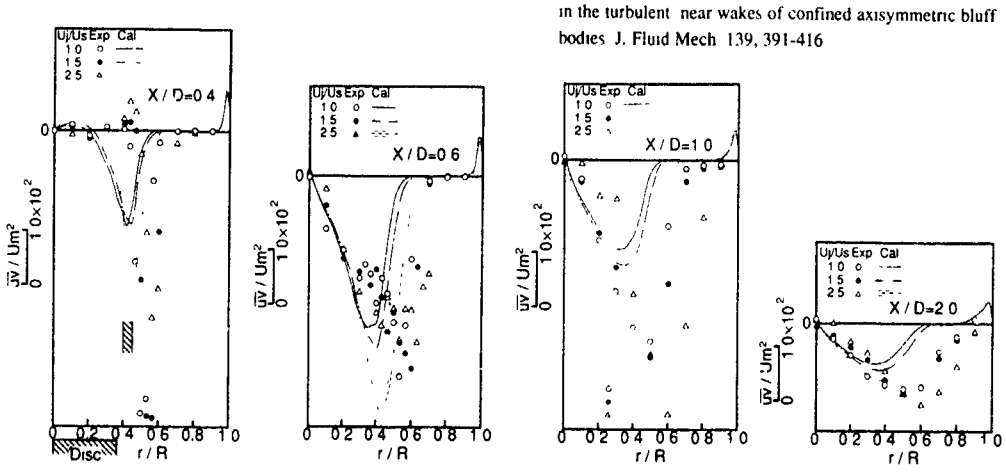

Fig 8 Reynolds shear stress (Disk)

REFERENCES

Benodekar,R W Goddard,A J H , Gosman,A D,& Issa,R I 1985 Numerical prediction of turbulent flow over surface-mounted ribs AIAA J 23, 359-366

Durst,F & Rastogi,A K 1980 Theoretical and experimental investigations of turbulent flows with separation Turbulent Shear Flows 2 (ed F Durst et al) Springer, 208-219

Fujii,S , Gomi,M.& Eguchi,K 1978 Cold flow tests of a bluff-body flame stabilizer Trans ASME, J. Fluids Eng 100, 323-333

Kim,J , Kline,S J & Johnston,J P. 1980 Investigation of a reattaching turbulent shear layer Flow over a backward-facing step Trans ASME, J Fluids Eng 102, 302-308

Kondo,T & Nagano,Y 1989 Computational study of separating and reattaching flows behind a backward-facing step (Simulation of a large-scale flow structure)Trans. JSME(B), 55, 1016-1021.

Launder,B E & Spalding,D B 1974 The numerical computation of turbulent flow Comput Mech Appl Mech Eng 3, 269-

Leschziner,M A & Rodi,W 1981 Calculation of annular and twin parallel jets using various discretization schemes and turbulence-model variations. Trans ASME, J Fluids Eng 103, 352-360

Patankar,S V 1980 Numerical Heat Transfer and Fluid Flow McGraw-Hill

Pope,S B & Whitelaw,J H 1976 The calculation of near-wake flows J Fluid Mech 73, 9-32

Rodi,W 1980 Turbulence Models and Their Applications in Hydraulics IAHR

Senda,M , Nishimura,M, Hayama,K & Taira,T 1991 Numerical analysis of an axisymmetrical confined jet with a bluff body Trans JSME(B), 57, 360-365.

Taylor,A M K P & Whitelaw,J.H. 1984 Velocity characteristics in the turbulent near wakes of confined axisymmetric bluff bodies J. Fluid Mech 139, 391-416

EIGHTH SYMPOSIUM ON
TURBULENT SHEAR FLOWS
Technical University of Munich
September 9-11, 1991

Flow Structure and Mixing in Obstructed and Confined Jets

S.G Bryce and R E J. Fryer-Taylor

Shell Research Ltd, Thornton Research Centre
P.O. Box 1, Chester CH1 3SH, U K

ABSTRACT

A comprehensive series of smoke flow visualisation and laser induced fluorescence experiments was perfoimed in a study of the dispersion processes of obstructed and confined incompressible gas jets It was found that large-scale vortical structures dominated the entrainment of ambient air into a free jet The presence of obstacles within the flowfield generated additional vorticity which locally enhanced the concentration decay within the release However, the creation of recirculatory regions in the wake of certain obstacles reduced entrainment into these areas For hazardous releases, this could give rise to a steady flammable or toxic mixture within the wake

NOMENCLATURE

d	cylinder diameter or flat plate width
I(x)	laser sheet intensity distribution
l	distance from source to obstacle
N_{jet}	number density of jet
N^{seed}	number density of seeding material
Re^{seed}	Reynolds number
S_f	fluorescent intensity
x	downstream coordinate

INTRODUCTION

The possible ignition of an accidental release of pressurised flammable gas poses a major hazard to the production, processing and transport operations of the natural gas industry In the majority of cases, the release would initially take the form of an underexpanded jet (Ewan and Moodie, 1986) Downstream of this highly compressible region the flow would decelerate but would remain momentum-dominated Buoyancy effects would become important at a further distance downstream This paper examines the behaviour of experimental releases within the momentum dominated region

Given the highly congested nature of the gas production environment, it was necessary to determine the effects on flow behavio of an obstruction within this momentum-domina ed region In particular, it was necessary to characterise the resulting variation in dispersion characteristics, as preliminary flow visualisation experiments had indicated that such obstruction might have a major impact on the inital dispersion of a low Reynolds number release

This paper considers three types of release for $Re < 1 \times 10^4$ no obstruction, obstruction by a circular cylinder, and obstruction by a flat plate Details of the flow structure were obtained by smoke flow visualisation The concentration measurements were determined through image analysis of the results of laser induced fluorescence of iodine seeded flows

EXPERIMENTAL METHOD

A vertical flow wind tunnel was designed which is suitable for use in both smoke flow visualisation and laser induced fluorescence (LIF) experiments The tunnel is shown schematically in Fig 1 The illumination for the experiments was provided through window 1 by a laser light sheet formed from the 514 5 nm line of an Argon-ion laser (5W all lines). Each experiment was video recorded through window 2 via a CCD camera (plus image intensifier for LIF tests) for later analysis on an Imaging Technology Series 151 image processing system.

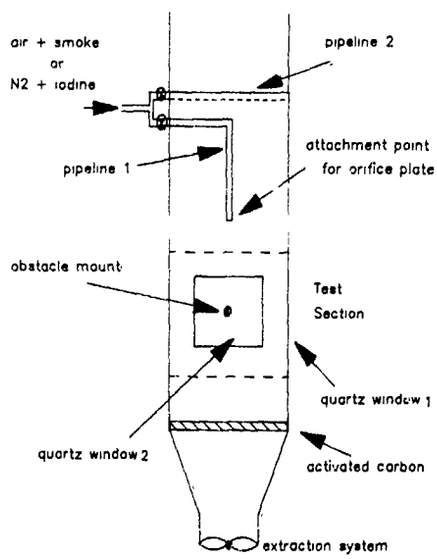

Fig 1 Experimental apparatus

Two types of smoke flow visualisation were possible In both cases pressurised air from a cylinder supply was fed to a Dreschel chamber where a cigarette was burning Vortical flow within the chamber ensured that the incoming air was thoroughly mixed with the smoke before passing out of the chamber Thereafter the seeded air flow followed one of two routes It could simply pass through pipeline 1 before being discharged through an orifice plate into the tunnel test section as a jet flow This permitted direct visualisation of the jet and its subsequent dispersion

Alternatively, the smoke seeded flow could be directed across the tunnel through pipeline 2 in which a series of holes were drilled The resulting smoke lines were drawn through the tunnel by a fan located at its base If an air alone jet was simultaneously released into the test section along pipeline 1, it was possible to study the entrainment behaviour of the initial region of the jet as it mixed with the ambient smoke seeded airstream

For LIF tests, it was necessary to seed the flowfield with a suitable fluorescing medium For an incompressible release, it may be found at any point in a jet flowfield illuminated by a laser sheet of intensity variation I(x) that

$$S_f = \text{constant} \times I(x) \times N_{seed} \qquad (1)$$

where S_f is the resulting fluorescent intensity and N_{seed} is the number density of the seeding material at that point It is further possible to directly relate N_{seed} to N_{jet}, where N_{jet} is the number density of the injected gas (Hartfield et al, 1989) Therefore, when I(x) is known, it is possible to obtain relative concentration values at each point in the flow by relating the local fluorescent intensity to its value at the exit from the orifice plate, where the fluorescence is assumed to correspond to a 100% concentration of the injected gas Relative concentration maps were routinely obtained via the image processing system

Gaseous iodine will fluoresce strongly when excited by light at 514 5 nm and was therefore selected as the seeding material for these experiments It was generated by sublimation through the application of heat to a pressure bomb containing iodine crystals Nitrogen was used as the carrier gas to prevent the formation of iodic acid through the reaction of iodine with the water content of air It was also necessary to fit trays of activated carbon in the bottom part of the tunnel in order to prevent the release of iodine to the outside environment

LIMITATIONS

An initial application of the LIF technique to an unobstructed release at Re = 800 revealed two particular shortcomings Firstly, the low signal-to-noise ratio (SNR) associated with use of the image intensifier at low fluorescent light levels precluded any analysis based on a single video frame Some time-averaging was required, i e the averaging of n successive video frames Consequently, it was not possible to resolve short period concentration fluctuations within the shear layers (Mungal and Hollingsworth, 1989) However, it was possible to obtain the mean concentration field for these regions Flow visualisation data provided additional information on unsteady phenomena, e g vortex development

The second shortcoming was the occurrence of optical thickness for an initially laminar flow A region of a seeded flow is deemed to be optically thick if the seeding absorbs sufficient laser energy to significantly reduce the laser illumination of other regions of the flow which lie behind it Although the iodine seeding level produced no problems for fully turbulent releases, the limited expansion of the laminar region and the associated low levels of entrainment did not provide sufficient dilution of the iodine seeding to allow quantitative analysis in this region (Qualitative information was available) It was considered that the very limited extent of laminar flows in this study does not make this a major shortcoming

THE UNOBSTRUCTED RELEASE

Flow visualisations and concentration measurements were obtained for releases from a 2mm diameter circular nozzle Exit velocities ranged between 3 m/s and 60 m/s The corresponding Reynolds number range lies from 400 to 8000 based on the characteristic dimension of the initial jet diameter

Fig 2 shows that an initially laminar release at Re = 800 underwent a transition to turbulent flow at some distance downstream The instability of the turbulent shear layer lead to the formation of large scale vortices which rapidly accelerated the entrainment of ambient air into the jet (Tso and Hussain, 1989) As Re was increased, it was found that a critical value existed beyond which the flow was fully turbulent from the exit Increases in Re beyond this value caused an increased diffuseness of the vortical structures

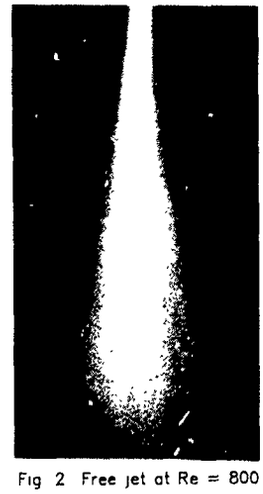

Fig 2 Free jet at Re = 800

The unsteady nature of the jet vorticity is shown in Fig. 3, an average over 32 video frames (1 28 seconds) of the Re = 800 release It can be seen that, as discussed in the introduction, such an averaging process removes the short period time-dependent detail of the shear layer

structure The L I F experiments provided only mean flow information

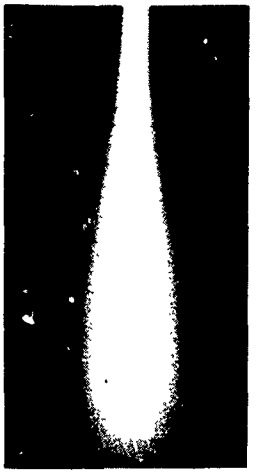

Fig 3 Time-averaged image at Re = 800

It was found that L I F results could be fully quantified for Re > 1700, i e there was no optical thickness problem above this value The centreline concentration profile for a release at Re = 2700 is shown in Fig 4, where it can be seen that the initial decay was near-linear, with a gradual decrease in decay rate with increasing distance downstream

Fig 4 Centreline concentration for free jet, Re = 2700

With increases in Re above 2700 it was found that there was only a very limited effect on the centreline concentration distribution Fig 5 shows the cross-jet concentration profiles for Re = 2700 and 8000 at 25 exit diameters downstream of the exit The profiles both have a Gaussian form with a slightly reduced peak concentration value at the higher Reynolds number There was no noticeable change in the lateral extent of the Gaussian with increasing Reynolds number These results indicate that the increasing diffuseness of the vortical structures, noted in the smoke experiments, did not significantly alter the entrainment of air into the centre of the jet

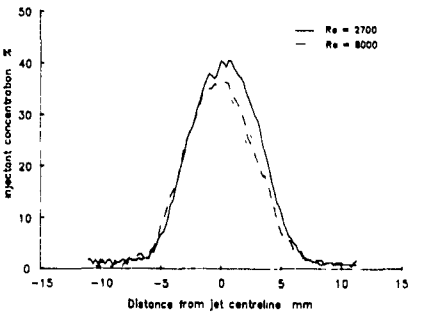

Fig 5 Cross-jet concentration distribution at 25d downstream

OBSTRUCTION OF A JET BY A CIRCULAR CYLINDER

The impingement of a jet on a structure of circular cross-section is highly likely if a release occurs within the congested environment of, for example, a production platform or refinery This investigation studied the effects of impingement on a cylinder of high aspect ratio, i e length-to-diameter ratio The high aspect ratio was chosen in order to minimise any three dimensional effects A range of cylinder diameters (d) and jet-to-cylinder distances (l) were considered The flow was studied in the plane of the jet centreline, perpendicular to the cylinder axis As for the unobstructed case, the flow was studied for releases from a 2mm nozzle over a Re range of 400 to 8000

As for the unobstructed jet, smoke flow visualisation revealed that a jet obstructed by a circular cylinder underwent a transition from laminar to turbulent behaviour at some value of Re. It was noted that where transition occurred downstream of the obstacle the post-impingement flow took the form of two laminar jets, where the rapid widening of these jets marked the transition to turbulence The transition point moved upstream with increasing Re Once the transition point had moved upstream of the obstacle, a slight increase in Re caused the jet to become fully turbulent from the exit This could have been a consequence of accelerated instability of the jet shear layers through the upstream reflection of downstream propagating disturbances by the cylinder surface

Analysis of the series of visualisation experiments suggests that for l/d = 5 and Re > 2700 there was a Coanda effect around the cylinder, i e the jet core split at the point of impingement, followed the curvature of the cylinder and then recombined to the rear of the cylinder As shown in Fig 6, the jet shear layers also followed this curvature to a limited exetent and, as a consequence, there was an apparent "waist" in the immediate wake of the cylinder Downstream of this "waist" large-scale vortical structures could be seen in the flow

For those configurations where the Coanda effect occurred, it was further found that there existed a range of Re within which there was a pronounced lateral oscillation of the wake It was also noted that for an asymmetric geometry, i e one where the jet was not properly aligned with the centre of the cylinder, the Coanda effect produced a marked deviation of the wake to either the left or the right depending on the initial asymmetry This indicates that the wake oscillation described above for a symmetric

geometry was a consequence of disturbances in the shear layer upstream of the cylinder creating an effectively asymmetric jet at the point of impingement As a result there was a very strong Coanda effect on one side of the cylinder such that the flow remained attached until close to the rearmost point This caused a pronounced movement of the wake to the other side of the cylinder Further disturbances moved the upstream asymmetry to this side, which resulted in the above cycle repeating in the opposite direction

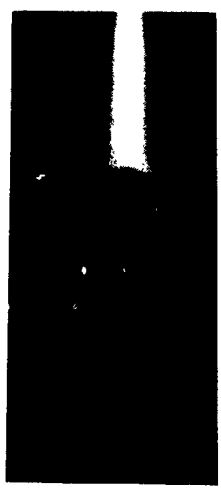

Fig 6 Re = 2700, l = 25mm, d = 5mm

The Coanda effect was not found for l/d > 5 For these higher values of l/d, it can be seen from Fig 7 that there was little apparent effect of the cylinder on the visible flow structure for fully turbulent releases However, there remained considerable vortical activity within the flow

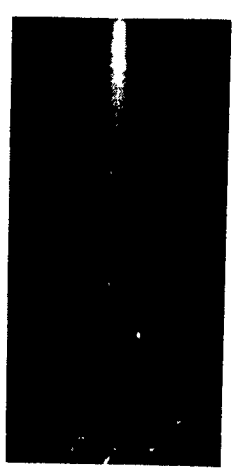

Fig 7 Re = 2700, l = 50mm, d = 5mm

It was found that L I F results could be quantified for Re > 1700 Fig 8 shows the centreline concentration decay for l = 25mm and d = 5mm at Re = 2700 It can be seen that the concentration immediately downstream of the cylinder cannot be obtained by linear extrapolation of the immediately upstream value, although Fig 9 shows that cross-jet concentration profiles both upstream and downstream of the cylinder have an approximately Gaussian form Comparison with the free jet distribution at the same Re revealed that entrainment into the jet was reduced upstream of the cylinder. This was a consequence of the blockage of the upstream effect of any downstream vortices. However, the concentration decay downstream was far greater than that of the free jet This was a consequence of the enhanced turbulent mixing promoted by the Coanda effect Increasing Re was found to further increase this mixing

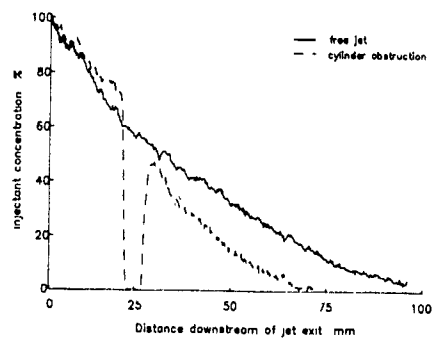

Fig 8 Effect of cylinder on centreline concentration
Re = 2700, l = 25mm, d = 5mm

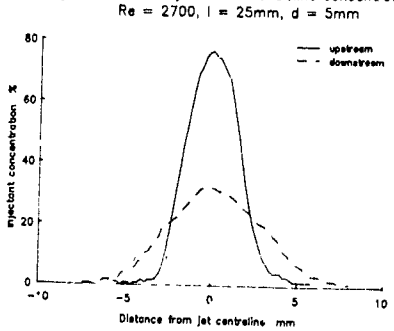

Fig 9 Effect of cylinder on cross-jet concentration distribution
Re = 2700, l = 25 mm, d = 5mm

An increase in l to 50mm for the same cylinder had a marked effect on the flow development For fully turbulent releases there was no Coanda effect It would appear that if the width of the jet at the point of impingement exceeded the width of the cylinder by greater than a critical margin, then the radial pressure gradient normal to the cylinder could not balance the centrifugal force exerted by the flow. Consequently, the jet expanded linearly past the cylinder. Upstream of the cylinder, the dilution of the jet was slightly increased above free jet levels as a result of increased vortical behaviour There was little notable difference between the decay curves downstream of the cylinder, and increasing Re had little effect on this behaviour.

The results suggest that, for those configurations where the Coanda effect did not occur, it might be possible to represent the concentration distribution arising from the impingement on a circular cylinder of a fully turbulent, incompressible jet by some simple modifications to a free jet model

These experiments also provided some evidence of the respective sizes of the boundary layer and jet shear layer over the cylinder Fig. 10 shows the concentration distribution along a radial line from the 5mm cylinder for l = 25mm and Re = 8000 It can be seen that the initial rise in concentration occured very rapidly within the boundary layer, whereas the subsequent gradual decrease to zero indicates the presence of a considerably wider jet shear layer

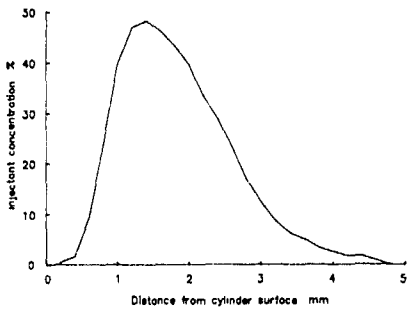

Fig. 10 Radial concentration distribution for cylinder Re = 8000, l = 25mm, d= 5mm

OBSTRUCTION OF A JET BY A FLAT PLATE

As for the preceding case, there is a very high probability of jet impingement on a flat plate if a release should occur within a congested environment The plates studied were of high aspect ratio, and the releases were again from a 2mm diameter nozzle over the Re range of 400 to 8000

Smoke flow visualisations showed that at Re = 800, the laminar upstream jet struck the surface of the plate and spread laterally At both edges of the plate the flow again took the form of a laminar jet, which then underwent transition at some distance downstream of the plate A recirculation region was obvious in the wake of the plate between the two jets The transition points moved upstream with increasing Re, until at Re = 1700 the jets were fully turbulent from the plate edges It should be noted that his was a highly unstable flow state and any slight variation in flow conditions caused a sudden upstream or downstream movement of the transition location For higher values of Re, the flow was wholly turbulent from the jet exit

Fig 11 shows a smoke visualisation of a release at Re = 3500, where the flow can be seen to have a bell-shaped outline, i e there was a pronounced lateral expansion of the flow as it passes the plate It was found that the magnitude of this expansion was reduced with increasing l, as a consequence of the associated increase in jet width at the point of impingement At a critical value of l there was no marked expansion and the linear growth of jet width upstream of the plate continued downstream This occured where the width of the jet exceeded the width of the plate at the point of impingement, and indicates that the downstream transfer of momentum far exceeded the lateral transfer induced by the impingement of the inner part of the jet However, there was evidence of the persistence of a wake region immediately behind the plate

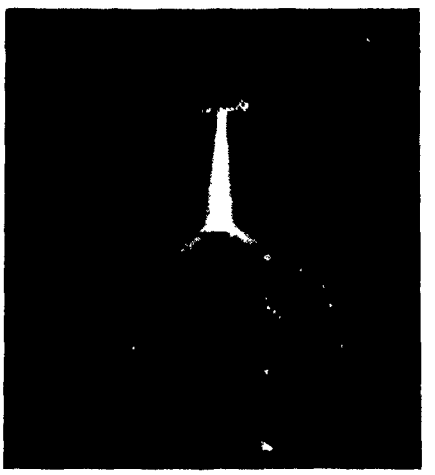

Fig 11 Re = 3500, l = 25mm, d = 5mm

It was found that full quantification of the flat plate flowfield was possible with L I F for Re > 1700 Fig 12 shows the centreline concentration distribution for Re = 2700, l = 25mm and d = 5mm It can be seen that upstream of the plate the concentration decayed more slowly than for a free jet As for the case of the cylinder, this was a consequence of a reduction in the upstream effect of downstream vortices as a result of blockage by the obstacle On passing through the plate there was an instantaneous large decrease in concentration, which reduced the concentration to far below free jet levels This was a consequence of both the sudden expansion of the jet as it passed the plate (which lead to a major increase in air entrainment), and the ecirculatory flow pattern resulting from separation of the jet at the edges of the plate Thereafter the concentration decayed only very gradually in the downstream region

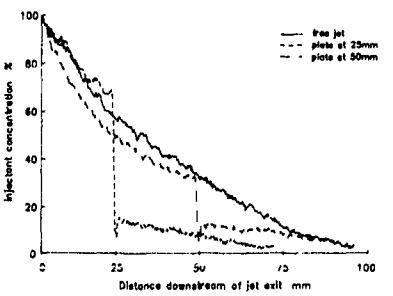

Fig 12 Effect of plate on centreline concentration Re = 2700, d = 5mm

Fig 13 shows four crossjet concentration profiles taken at different downstream locations for the Re = 2700 release Profile 1 was taken upstream of the plate and has a Gaussian form Profile 2 was taken across the right-hand edge jet just downstream of the plate and has a near-Gaussian profile The higher baseline on the left-hand-side of the curve was a result of the higher gas concentrations in the wake of the plate Profile 3 was taken downstream of, but parallel to, the plate At this point the concentration profile had a twin peak distribution corresponding to the two edge jets The area between the peaks shows that turbulent mixing provided a near-uniform distribution in the wake. Profile 4 was taken in the same direction as 3, but further downstream. It can be seen that the concentration profile there exhibited a near-uniform distribution, indicating that mixing had taken place between the two edge jets.

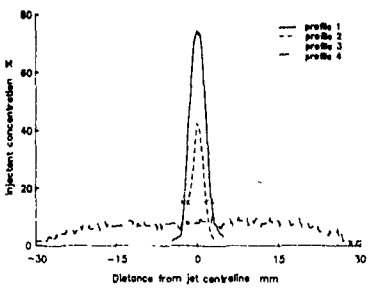

Fig 13 Cross-jet concentration distributions for plate obstacle Re = 2700, l = 25mm, d = 5mm

It was found that increasing Re to 8000 had little effect or the flow development detailed above

From Fig 12 it can be seen that an increase in l to 50mm for d = 5mm and Re = 2700 resulted in a more marked decay of the initial region of the jet Again, as for the cylinder case, this was a consequence of increased vortical behaviour. For this configuration, the drop in centreline concentration on passing through the plate was less marked than for l = 25mm In this instance the flow expansion past the plate had a near-linear form, and the reduction in concentration within the wake was simply a result of the recirculating flow It was interesting to note, however, that this drop in concentration reduced its value to approximately that found in the l = 25mm case Once again, there was only a very limited reduction in concentration downstream of the plate The effect of an increase in Re was minimal

Analysis of a series of results suggested that there was no simple way of representing the concentration distribution arising from the impingement of a fully turbulent, incompressible jet on a flat plate. It appeared that there was only very limited entrainment into the central region of the wake behind the plate In certain circumstances this could lead to the formation of a steady flammable or toxic mixture in this region

DISCUSSION

Smoke flow visualisation and laser induced fluorescence experiments were performed in a study of the dispersion processes of incompressible gas jets It was confirmed that the formation of coherent vortical structures within the jet flow lead to the dilution of the released gas by the entrainment of ambient air An examination was made of the interaction of such a flow with cylindrical and flat plate obstacles It was found that, where such an obstacle lies close to the source of the jet, the dilution of the jet was reduced upstream of the obstacle For obstacles of circular cross-section, a Coanda effect around the surface of obstacles of circular cross-section enhanced turbulent mixing within the wake and increased the dilution of the release However, its occurrence also promoted lateral oscillations of the wake region Where the obstacle was a flat plate the jet expanded rapidly as it passed the plate, and its separation from the plate edges created a recirculatory region in the immediate wake There was limited entrainment into this region of the flow

Where the obstacle was further removed from the source of the release, there was a slight increase in the dilution of the inital region of the jet as a consequence of increased vortical effects There was a near-linear expansion of the flow past cylindrical and flat plate obstacles, although a recirculating flow persisted behind the flat plate

For fully turbulent, incompressible releases it appears that, outwith the Coanda regime, the concentration distribution arising from the impingement of a jet on a circular cylinder may be represented by some simple modification to a free jet model However, this is not possible for a flat plate obstacle, where the recirculatory flow could lead to the creation of a steady flammable or toxic mixture for a hazardous release The modelling of such a flowfield requires further investigation

REFERENCES

HARTFIELD,R J , ABBITT,J D & MCDANIEL,J C 1989 Injectant mole-fraction imaging in compressible mixing flows using planar laser-induced iodine fluorescence Optics Letters, 16, 850 - 852

MOODIE,K & EWAN,B C R 1986 Structure and velocity measurements in underexpanded jets Combustion Science and Technology, 45, 275 - 288

MUNGAL,M G & HOLLINGSWORTH,D K 1989 Organized motion in a very high Reynolds number jet Pysics of Fluids A 1(10), 1615 - 1623.

TSO,J & HUSSAIN,F 1989 Organized motions in a fully developed turbulent axisymmetric jet Journal of Fluid Mechanics, 203, 425 - 448

EIGHTH SYMPOSIUM ON
TURBULENT SHEAR FLOWS
Technical University of Munich
September 9-11, 1991

TURBULENT SHEAR FLOW OVER ROWS OF TWO-DIMENSIONAL SQUARE RIBS ON GROUND PLANE

SHIKI OKAMOTO and KOUICHIROU NAKASO

Department of Mechanical Engineering ,
Shibaura Institute of Technology ,
Tokyo , Japan

ABSTRACT

This paper describes the detailed study of the flow structure over the rows of two-dimensional square ribs on the ground plane for various values of S/D and the optimum value of S/D to augment the turbulence of the free stream The pitch between the centers of two adjoining square ribs was varied at $S/D = 2, 3, 4, 5, 7, 9, 13$ and 17 The time-mean velocity and the velocity vectors were measured by the Pitot- and static pressure tubes, and the cylindrical yawmeter of 6 mm diameter having three pressure holes The turbulence intensities, auto-correlation and power spectrum were obtained using the data processing system and the F.F.T. analyzer connected to the hot wire anemometer As a result it is concluded that the pitch ratio $S/D = 9$ is optimum to augment the turbulence intensity

NOMENCLATURE

D	side length of square section of two-dimensional ribs
Eu	power spectrum of u'
L_X	integral scale in X-direction
Ru	auto-correlation of u'
Re	Reynolds number $= U_\infty D/\nu$
S	pitch between the centers of two adjoining square ribs
U	time-mean velocity
U_1	velocity at outer edge of shear layer
U_∞	velocity in free stream
u', v', w'	X, Y and Z components of fluctuation velocity
X, Y, Z	co-ordinates with origin above 10 mm at the center of the leading edge of the ground plane (see Fig.1) X is chosen along the ground plane, Y and Z for the vertical and horizontal directions respectively
$\overline{X}$	distance in X-direction from the center of the rib
$\overline{Y}$	distance in Y-direction from the base in the groove
$\overline{X}_1$	distance from the center of square rib to the reattachment point
δ	thickness of turbulent shear layer
τ	time delay

1. INTRODUCTION

The flow over the rough wall has been hitherto investigated in relation to determination of the drag of rough wall and early establishment of the turbulent boundary layer and augmentation of the heat transfer Nikuradse[1] studied first the turbulent flow in the pipe roughened by sands, and after then Schlichting[2] investigated the resistance of the wall with the rows of various roughness elements Perry et al[3] studied the turbulent boundary layer developed over the rough wall and proposed to devide it into two types - the one is "d-type" independent on the size of roughness element for $S/D \lesssim 4$, where S is the pitch between adjoining roughness elements and D is the height of roughness element, and the other is "k-type" dependent of the roughness size for $S/D > 4$ Antonia and Luxton[4] studied the "k-type" and Osaka et al[5] investigated the "d-type" boundary layer

In connection with the problem of augmenting the heat transfer, Nunner[6] measured the heat transfer and the pressure loss in the pipe whose inner wall was set with wires of various sizes Webb et al[7] studied the relation between the heat transfer and the resistance of tubes roughened with the rows of ribs for the cases of $10 < S/D < 40$, and Berger and Hau[8] measured the mass- and heat transfer in the pipe roughened with the rows of square ribs for cases of $3 < S/D < 10$.

It seems that these above-mentioned studies did not almost investigate the detailed flow structure over the wall roughened with the rows of ribs. Recently Hijikata et al[9] and Mori et al[10] studied the flow between adjoining ribs among the repeated two-dimensional ribs on the ground plane for case of $S/D = 15$ Moreover, Ichimiya et al[11] measured the flow over the rows of ribs on the lower insulated wall of duct whose upper wall was heated for case of $S/D = 5$, 7 and 15 However, these studies were performed for the limited case of S/D and did not describe the variation of flow properties with the pitch ratio S/D

The present paper describes the detailed study of the flow structure over the rows of two-dimensional square ribs on the ground plane for various values of S/D and the optimum value of S/D to augment turbulence of the free stream

2. EXPERIMENTAL APPARATUS AND MEASUREMENT PROCEDURES

The experiment was carried out in an N.P.L type wind tunnel having a 500mm × 500mm working section of 2000mm length The ground plate, an aluminium plate of 4mm thick-

ness, was set with a spacing of 25mm from the lower wall of tunnel exit in order to avoid the boundary layer developed on the tunnel wall, as shown in Fig 1 The half-ogival forebody of 150mm length was placed on the leading-edge portion of the ground plate The two-dimensional square ribs of 10 mm side length were aligned with equal pitch on the lower wall of the test section of tunnel The pitch between the centers of two adjoining square ribs was varied at S/D = 2, 3, 4, 5, 7, 9, 13 and 17 The time-mean velocity and the velocity vectors were measured by the Pitot- and static pressure tubes, and the cylindrical yawmeter of 6mm diameter having three pressure holes. The turbulence intensities, auto correlation and power spectrum were obtained using the data processing system and the F F T analyzer connected to the hot wire anemometer. Measurements were made at the 14 locations of the centers of the square ribs and the grooves between the square ribs under the wind velocity of U_∞ = 16 0 m/s corresponding to $Re = U_\infty D/\nu = 1.0 \times 10^4$.

3. EXPERIMENTAL RESULTS AND DISCUSSIONS

3.1. Velocity Profiles in Shear Layer over the Rows of Square Ribs

Figure 2 shows the distribution of the velocity in the section at the center of grooves between two adjoining squares ribs It can be seen from this figure that the turbulent shear layer is developed in the downstream distance and the velocity profiles tend to be similar with an increase in the downstream distance The thickness of the turbulent shear layer is defined by the value of Y where U is equal to $0.99U_1$ Figure 3 shows the variation of the thickness of the turbulent shear layer with the pitch ratio S/D The thickness increases with an increase in the downstream distance in like manner as a naturally developed turbulent boundary layer on the ground plate, and it increases in the range of $2 \leqq S/D \leqq 9$, but is almost unchanged in the range of $S/D \geqq 9$ as the value of S/D increases

3.2. Turbulence Intensities in Shear Layer over the Rows of Ribs

Figure 4 shows the downstream change of X - component of turbulence intensity in the shear layer at the centers of groove between square ribs for the case of S/D = 5 The turbulent shear layer is developed over the square ribs along the downstream distances. It can be supposed that the mixing phenomenon in the shear layer becomes strong due to the existence of square ribs Figures 5 and 6 show the X-component of turbulence intensity in the shear layer at the rib- and groove centers for the cases of S/D = 5 and 9 The profiles of turbulent intensity become self- preserving at the rib- and groove centers for the case of S/D = 5 shown in Fig.5 The difference between the turbulence intensity at both positions is less in like manner as the velocity profile The profiles of turbulence intensity in the shear layer at the rib center become self-preserving in the downstream distance except at X/D = 23 5 for the case of S/D = 9 as shown in Fig.6(a) But Figure 6(b) shows that the turbulence intensity in the shear layer at the groove is seen to be decaying with an increase in the downstream distance, and especially does not yet accomplish the self-preserving profile in contrast to the velocity profiles at the same position In order to examine the variation in turbulence intensity with the pitch ratio S/D, the profiles of the turbulence intensity were measurec at the typical three posi-

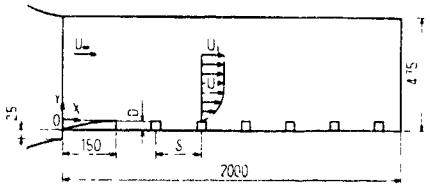

Fig 1 Apparatus and nomenclature

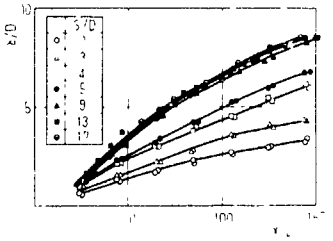

Fig 3 Thickness of shear layer

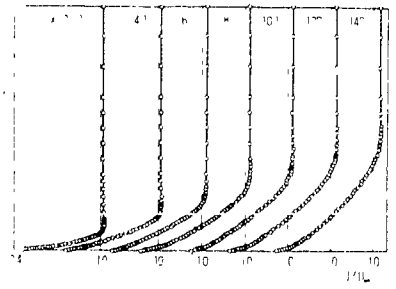

Fig 2 Velocity profile of shear flow over the rows of square ribs above the centers of grooves for S/D = 5

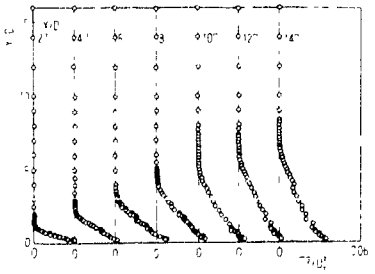

Fig 4 X-component of turbulence intensity above grooves for S/D = 5

tions near X/D = 67, 103, 142 for the rib centers and X/D = 69, 108, 147 for the groove centers. Figures 7 and 8 show the variation of turbulence intensity in the shear layer at three positions with the pitch ratio S/D. It is obviously found from these figures that the turbulence intensity increases for $S/D \leq 9$ and decreases for $S/D > 9$ as the value of S/D increases. Figure 9 shows the variation of turbulence intensity at the positions of Y/δ = 0.1 to 0.5 in the groove with the pitch ratio S/D, in order to find the optimum pitch ratio to augment the turbulence intensity as a turbulence promoter. It can be seen from this figure that the turbulence intensity attains maximum at S/D = 9. Hence when the two-dimensional square ribs are aligned on the wall as a turbulence promoter, the pitch ratio S/D = 9 is optimum to augment the turbulence intensity.

Furthermore, the Y- and Z-components of turbulence intensities and Reynolds stresses were measured for various values of S/D. Figure 10 shows the Y-component, Z-component of turbulence intensities and Reynolds stresses in the shear layer above the groove near X/D = 147. It can be seen from these figures that they attain maximum value at S/D = 9 in like manner of X-component of turbulence intensity.

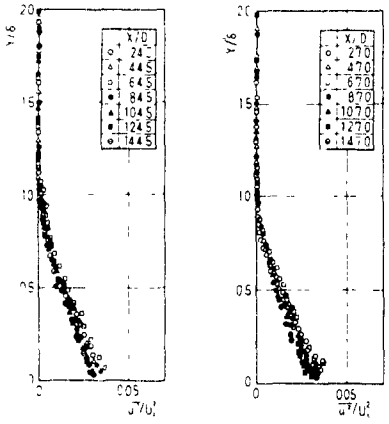

(a) Rib (b) Groove

Fig 5 X-component of turbulence intensity for S/D = 5

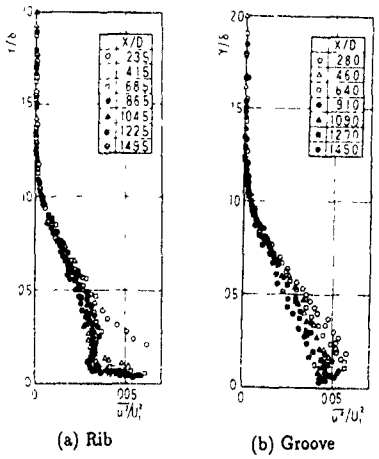

(a) Rib (b) Groove

Fig.6 X-component of turbulence intensity for S/D = 9

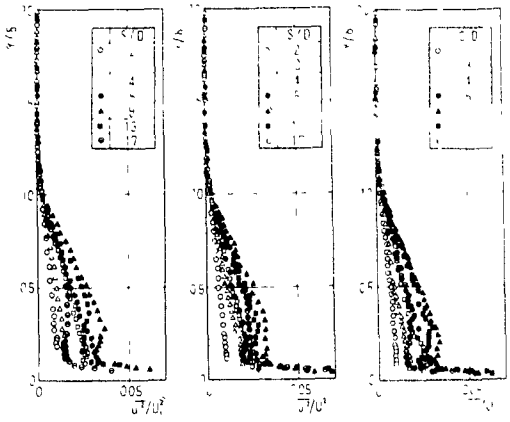

(a) X/D = 67 (b) X/D = 103 (c) X/D = 142

Fig 7 X-component of turbulence intensity for rib

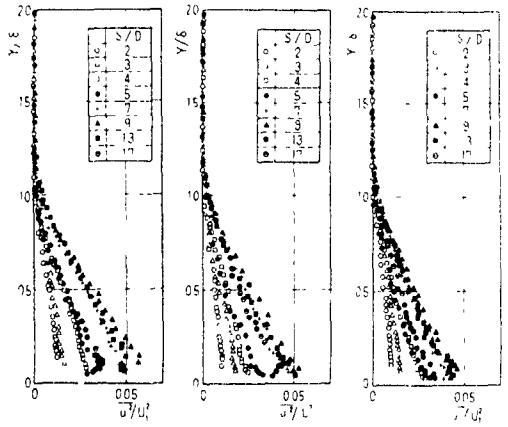

(a) X/D = 69 (b) X/D = 108 (c) X/D = 147

Fig.8 X-component of turbulence intensity for groove

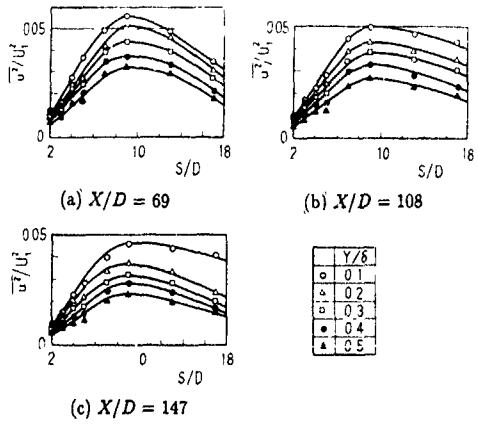

(a) X/D = 69 (b) X/D = 108

(c) X/D = 147

Fig.9 Variation of X component of turbulence intensity above groove with S/D

3.3. Flow Pattern and Turbulent Eddies in the Groove

As described in the article 3 2 , when the two dimensional square ribs are aligned on the wall as a turbulence promoter, the turbulence intensity attains maximum at $S/D = 9$, which means that the mixing phenomenon is more active for the pitch ratio $S/D = 9$ than that for other values of S/D. Figure 11 shows the velocity vectors in the flow in the groove for the case of $S/D = 9$ in order to investigate the feature of the flow in the groove between two square ribs It is found from this figure that there is back-flow in the region of $\overline{X}/D \leq 4$ behind the upstream square ribs and favourable flow in the region of $4 \leq \overline{X}/D \leq 7.5$. Hence the free streamline left from the edge of the upstream square rib encloses the recirculation region and reattaches to the ground plate at $\overline{X}/D \approx 4$ as shown in Fig 11 The length of recirculation region, namely the distance from the rib center to the reattachment point for the pitch ratio S/D is shown in Fig 12 The abscissa D/S is selected to show the result for the case of the single rib simultaneously. The existing experimental results are denoted in this figure for the sake of comparison. Mantle[12] reported that the free streamline left from the edge of the upstream square ribs does not reattach in the groove for the case of $S/D < 6\,6$, but reattaches at $\overline{X}r/D = 4$ for the case of $6\,6 \leq S/D \leq 12$ and at $\overline{X}r/D = 8.5$ for the case of infinite pitch ratio, namely, the case of single rib. Mori et al[10] showed $\overline{X}r/D = 4\,5$ for the case of $S/D = 15$. Their results and the present result are put in the single curve as shown in Fig 12 Therefore the present result ($\overline{X}/D = 4$) is consistent with the results by Mantle[12] and Mori et al[10] The author reported[13] the shear flow behind a flat plate normal to a plane boundary and pointed out that the turbulence intensity is largest immediately behind the reattachment point and decreases gradually in the downstream flow.

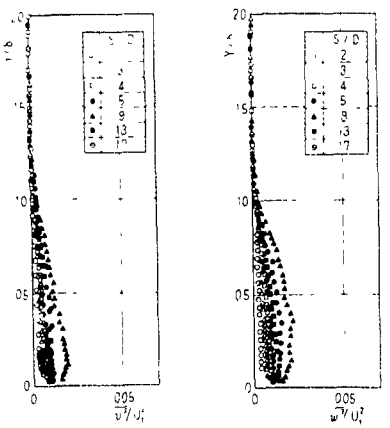

(a) Y-component of (b) Z-component of turbulence intensity

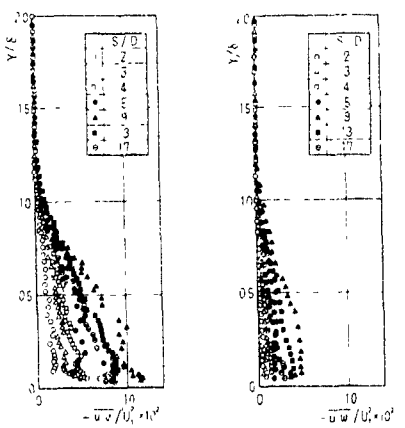

(c) Reynolds stresses

Fig.10 Y- and Z-components of turbulence intensity and Reynolds stresses for groove

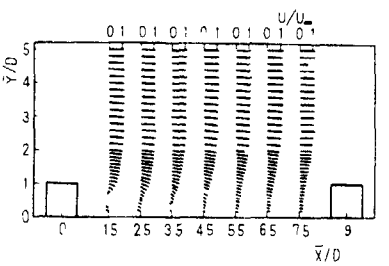

Fig 11 Velocity vectors in flow above the groove for $S/D = 9$

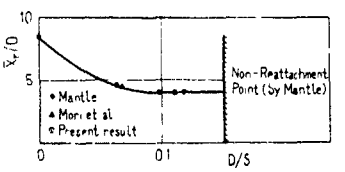

Fig 12 Reattachment point

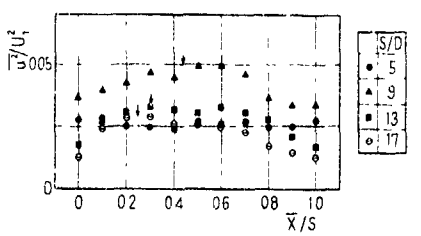

Fig 13 X-component of turbulence intensity at $Y/\delta = 0.1$ above groove

As mentioned in the article 3.2, the turbulence intensity at the groove decays gradually with an increase in the downstream distance for the case of $S/D = 9$. Figure 13 shows the variation of turbulence intensity at $Y/\delta = 0.1$ in the groove of the range, $X/D = 116.5 \sim 133.5$ with the pitch ratio S/D. The mark "↓" in this figure denotes the position of the reattachment point for the cases of S/D= 17, 13 and 9 from left to right respectively. The turbulence intensity has almost the same and low value in the groove for the case of S/D= 5. However for the cases of $S/D = 9$, 13 and 17 the turbulence intensity attains maximum near the reattachment point. For the case of $S/D = 5$, the square ribs are closely placed and the stable vortices are set up in the grooves and, so the recirculation region occupies the whole groove between the square ribs without reattachment, because the length of recirculation region is nearly $4D$ (see Fig.14(b)). Hence the turbulence intensity becomes low as compared with those of $S/D = 9$, 13 and 17. On the other hand, for the case of $S/D > 5$, there is the recirculation region behind the upstream square ribs and the reattached flow goes downstream from the reattachment point (see Fig.14(c)). This was confirmed by the flow visualization experiment($Re \approx 1000$) by using the water channel. Figure 14 shows the photographs of vortices generated behind the upstream square rib for the cases of $S/D = 2$, 5 and 9. The small stable vortices exist in the grooves between the two adjoining square ribs for the case of $S/D = 2$. Furthermore a large stable vortex occupies the whole groove without reattachment for $S/D = 5$. For the case of $S/D = 9$, the recirculation region exists behind the upstream ribs and the length of recirculation region is approximately $4D$ as previous-mentioned, and the reattached flow goes downstream. The reattachment point which corresponds to the position of the maximum turbulent intensity near the ground plane is near the midpoint in the groove for the case of $S/D = 9$. Furthermore, for the cases of $S/D = 13$ and 17, the turbulence intensities decrease as compared with that for $S/D = 9$. The distance from the reattachment point to the next downstream square rib is longer for the cases of S/D= 13 and 17 than for $S/D = 9$. Hence the turbulence intensity decays with an increase in the downstream distance behind the recirculation region so that it becomes largest for S/D = 9, and larger for $S/D = 13$ than for $S/D = 17$.

This phenomenon can be explained from the feature of the turbulent eddies in the flow above the groove between two ribs. The power spectrum was measured to confirm the vortices shed periodically from the square ribs. Figure 15 shows the power spectrum in the shear layer at $Y/D = 0.5$ above the midpoint, $X/D = 124.5 \sim 127.0$, in the groove between the square ribs. The highest value of $Eu(n)$ always occurs at the low frequency. The energy of turbulence is transferred from the large scale eddy to the small scale eddy in the inertial subrange. The energy of the micro eddy decreases under the action of kinematic viscosity at the high frequency. The power spectrum has the steep peak at the frequency which corresponds to that of the vortices shedding. It can be seen from Fig.15 that a steep peak does not appear in the spec-

(a) $S/D = 2$ (b) $S/D = 5$ (c) $S/D = 9$

Fig.14 Photographs of vortices

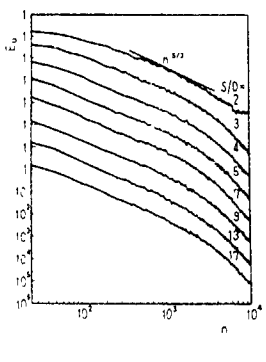

Fig.15 Power spectrum at $Y/D = 0.5$ above midpoint of groove

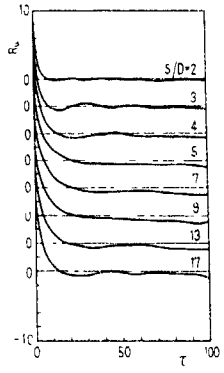

Fig.16 Auto-correlation at $Y/D = 0.5$ above midpoint of groove

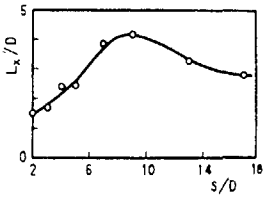

Fig.17 Integral scale at $Y/D = 0.5$ above midpoint of groove

trum curves independently of the value of S/D, and so the existence of periodical vortices shedding was not confirmed at this position

The auto-correlation of X-component of fluctuation velocity was measured in order to investigate the structure of large scale turbulence. Figure 16 shows the auto-correlation coefficient of u' at the same position as in Fig 15 There is no large negative correlation in the correlation curves due to the existence of the periodical vortices shedding The time-delay of first zero correlation increases in the range of $S/D \lesssim 9$ and decreases in the range of $S/D > 9$ as the value of S/D increases The time-delay of first zero correlation attains maximum at $S/D = 9$. The time-delay which becomes firstly zero correlation lengthens with an increase in the value of S/D for $S/D \lesssim 9$, which shows that the correlation vanishes slowly and the decay of a large eddy is slow The average scale of the large turbulent eddy is predicted to be largest for $S/D = 9$

The integral scale, which identifies the average scale of the large eddy, is obtained by integrating the auto-correlation function

$$L_X = U \int_0^\infty R_u(\tau) d\tau$$

where the convection velocity is estimated by the local time-mean velocity according to Taylor's hypothesis. Figure 17 shows the integral scale in the shear layer at $Y/D = 0.5$ above the midpoint in the groove. The integral scale becomes largest at $S/D = 9$, which means that the average scale of the large eddy is maximum The integral scale becomes small for the case of $S/D < 5$ as predicted by Perry et al[3] who pointed out that the eddies shed from the roughness element into the flow will be neglgible for "d-type" rough wall.

4. CONCLUSION

The results of the present study are summarized as follows :

(1) The thickness of the turbulent shear layer increases with an increase in the downstream distance. It increases in the range of $2 \lesssim S/D \lesssim 9$, but is almost unchanged in the range of $S/D \gtrsim 9$ as the value of S/D increases.

(2) The profiles of turbulent intensity in the shear layer become self-preserving at the ribs and grooves for the case of $S/D \lesssim 5$. But for the case of $S/D = 9$, the turbulence intensity is seen to be decaying in the shear layer at the grooves with an increase in the downstream distance and does not yet accomplish the self-preserving profile, while it becomes self-preserving in the shear layer above the ribs.

(3) The pitch ratio $S/D = 9$ is optimum to augment the turbulence intensity. The rows of two-dimensional square ribs for $S/D = 9$ may be used as a turbulence promoter.

(4) The free streamline left from the edge of the upstream square rib reattaches to the ground plate at $X/D \approx 4$ The turbulence intensity is highest immediately behind the reattachment point and decreases gradually in the downstream flow. Hence for the case of $S/D \lesssim 5$, the turbulence intensity becomes relatively low due to non-reattachment Since the position of the maximum turbulent intensity is the midpoint in the groove for the case of $S/D = 9$, the turbulence intensity becomes highest at $S/D = 9$ Moreover, the distance from the reattachment point to the next square rib is longer for $S/D = 13$ and 17 than for $S/D = 9$ so that the turbulence intensity decays in the downstream flow behind the recirculation region

(5) The time-delay of first zero correlation increases in the range of $S/D \lesssim 9$ and decreases in the range of $S/D > 9$ as the value of S/D increases. The time-delay of first zero correlation attains longest at $S/D = 9$ and hence the average scale of the large eddy is maximum at $S/D = 9$

REFERENCES

(1) Nikuradse,J.. Strömungsgesetze in rauhen Rohren, VDI-Forschungsheft 361 (1933)

(2) Schlichting, H. : Experimentelle Untersuchung zum Rauhigkeitsproblem, Ing -Arch. 7 (1936) pp 1 - 34

(3) Perry,A.E. , Schofield,W.H., and Joubert, P.N.: Rough wall turbulent boundary layers, J Fluid Mech 37-2 (1969) pp.383 - 413

(4) Antonia,R A and Luxton,R.E.: The response of a turbulent boundary layer to an upstanding step change in surface roughness, Trans.ASME Ser.D 93-1 (1971) pp.22 - 34

(5) Osaka,H.,Nakamura,I.and Kageyama,Y.: Time averaged quantities of a turbulent boundary layer over a d-type rough surface, Trans.JSME 50-458B(1984) pp.2299 - 2306

(6) Nunner,W. : Warmeubergang und Druckabfall in rauhen Rohren, VDI-Forschungsheft 455 (1956)pp.1 - 38

(7) Webb,R.L.,Eckert,E R G.and Goldstein,R.J.: Heat transfer and friction in tubes with repeated-rib roughness, Int.J.Heat Mass Transfer,14 (1971) pp 601 - 617

(8) Berger,F P.and Hau,K.-F.,F.-L.. Local mass / heat transfer distribution on surfaces roughened with small square ribs, Int.J.Heat Mass Transfer, 22 (1979) pp. 1645 - 1656

(9) Hijikata,K.,Mori,Y and Ishiguro,H.: Turbulence structure and heat transfer of pipe flow with cascade smooth turbulence surface promoters, Trans JSME 50-458B (1984) pp 2555 - 2562

(10) Mori,Y ,Hijikata,K and Ishiguro,H : Fundamental study of heat transfer augmentation by smooth turbulence surface promoters, Trans JSME 51-461B (1985) pp.160 - 168

(11) Ichimiya,K.,Yokoyama,M.and Shimomura,R Effects of several roughness elements for the heat transfer from a smooth heated wall, Proc ASME / JSME Thermal Eng Joint Conf ,1 (1983) pp.359 - 364

(12) Mantle,P.L.: A new type of roughened heat transfer surface selected by flow visualization techniques, Proc.3rd Int.Heat Transfer Conf ,1 (1966) pp.45 - 55

(13) Okamoto,S : Shear layer behind two- dimensional flat plate normal to plane boundary, Theoretical and Applied Mechanics,27 (1979) pp 563 - 570

EIGHTH SYMPOSIUM ON
TURBULENT SHEAR FLOWS
Technical University of Munich
September 9-11, 1991

FLOW AROUND SURFACE-MOUNTED, THREE-DIMENSIONAL OBSTACLES

by

A Larousse, R. Martinuzzi and C Tropea
Lehrstuhl für Strömungsmechanik
Universität Erlangen - Nürnberg
Cauerstr 4, D-8520 Erlangen

Abstract

The flow around surface-mounted obstacles placed in a turbulent channel flow (Re= 10^5) has been experimentally studied with the aim of determining separation and reattachment patterns and to investigate the major flow differences between two- and three-dimensional geometries. Obstacles of square cross-section and half channel height were studied while varying the cross-channel width between that of a cube and a two-dimensional rib. Surface flow patterns were obtained to study the flow topology. A two-component laser Doppler anemometer (LDA) was used to gain detailed information about the time-averaged and time-resolved turbulence parameters.

The results of this study lead to a picture of the flow pattern over a surface-mounted cube with quantitative data describing the mean and fluctuating velocity field. Major differences between the two- and three-dimensional flow patterns are identified, both upstream and downstream of the obstacle. Analysis of the time-dependent behaviour reveals a distinct unsteadiness of the upstream flow field for three-dimensional obstacles, which also leads to large contributions to the Reynolds shear stress.

Introduction:

The study of the flow around sharp-edged obstacles placed in a channel contributes directly to the understanding of the flow mechanisms for complex two- and three-dimensional geometries Past studies have often concentrated on two-dimensional geometries, for instance ribs or fences, because, as a diagnostic flow, the two-dimensional geometry is easier to handle experimentally and numerically. Hence, there exists a considerable amount of published data on two-dimensional, surface-mounted obstacles. However, little data exist on the flow development upstream of the obstacle The present work indicates the importance of this flow region for understanding the rest of the flow field.

There has been very little work published on the flow around three-dimensional obstacles and no data has been found for such flows in a channel. Typically, the three-dimensional obstacle is studied as a perturbation to a boundary layer, for instance for purposes of artificial thickening or increasing overall drag (Castro (1979), Castro and Robins (1977)). Correspondingly, only few studies concentrated on describing the detailed flow patterns around the obstacle. Of the existing work, the theoretical analyses of Hunt *et al* (1978), Perry and Horning (1984) and Fairlie (1980) address directly the expected separation and reattachment patterns around the obstacle. There exists, however, a severe lack of experimental data in this regard, a fact also recognized in a recent review of the flow over surface-mounted obstacles presented by Schofield and Logan (1990) The present work provides such data.

The transition between a two-dimensional obstacle flow and a three-dimensional one is not well defined. Work by de Brederode and Bradshaw (1972), in which the base pressure of a backstep flow was measured for various channel widths, is often cited as prescribing a 10.1 width-to-height ratio to ensure two-dimensionality in the recirculation region behind the step. In light of the complex nature of the obstacle flow as compared with a backstep flow, this ratio is not expected to be directly applicable in the present case The nature of the two-dimensional to three-dimensional transition in flow pattern remains obscure. Therefore, a second focus of the present work was to investigate the effect of varying the obstacle cross-channel width on the resulting surface flow patterns. Detailed velocity data for two-dimensional geometries already exist (Dimaczek *et al.* (1989)) and can be used for comparison with the present measurements for three-dimensional obstacles.

Experimental Apparatus and Methods

The flow geometry to be studied and the nomenclature used are shown in Fig. 1. Some preliminary work, especially concerning the flow pattern on the front face of the obstacle, was performed in a water channel (550 mm (W) x 50 mm (h)). Most of the experiments were performed in a 600 mm (W) x 50 mm (h), blower-type air channel at a Reynolds number of 10^5 ($Re = U_B h/\nu$). Trip wires were placed at the inlet

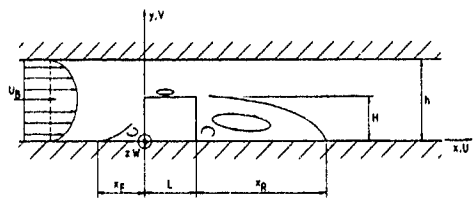

Figure 1: Sketch of the obstacle geometry in a channel flow

of the air channel flow. The obstacles were placed on the centre line at a downstream distance of 52 channel heights The channel could be mounted either horizontally or vertically, as sketched in Fig 2, to allow either the U-V (forward scatter) or the U-W (backscatter) velocity components to be acquired with a three-beam, two-component LDA (TSI 9100), also shown in Fig. 2 Beam expansion was used in the LDA system to achieve a measuring volume of 84 μm diameter and 610 μm length Two counter processors (TSI 1980B) with a 5 μs coincidence acquisition window were connected to a PC for data reduction. Data rates of 500 Hz to 4000 Hz were typical A di-ethylglycol/water mixture atomized by a medical nebulizer was used as seeding material The particles were introduced upstream of the channel inlet in the settling chamber of the blower

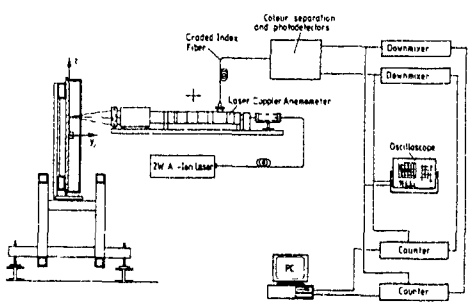

Figure 2 Schematic representation of the test-rig

Surface flow pattern visualization was performed in the air channel using a mixture of kerosene, light transmission oil and carbon dust (toner) Visualization results were then photographed for analysis and documentation purposes In the water channel, the crystal violet visualization technique (Dimaczek *et al.* (1988)) was used

Experimental Results and Discussion

The obstacles used in this study were 25 mm in height (H) and length (L) and varied between 25 mm and 600 mm in width (W) Before mounting the obstacle, the channel flow was verified to be fully turbulent and uniform in mean velocity to within 2% over 85% of the channel width. With the cube obstacle mounted, the mean velocity about the z-axis was verified to be symmetric within 2%. Also, the measured quantities $\overline{W}$ and $\overline{uw}$ were acceptably close to zero on the z-plane of symmetry.

Flow Around the Cube

To begin with, the flow in front of the cube will be examined in more detail Fig. 3 shows the mean streamlines corresponding to the measured flow patterns, surface oil patterns on the channel floor upstream of the obstacle and results of the mean velocity measurements in the z-plane upstream of the cube. The mean streamline pattern in this work correlates well with that of Hunt *et al* (1978) except for the region upstream of the horseshoe vortex No evidence could be found supporting the existence of two secondary vortices

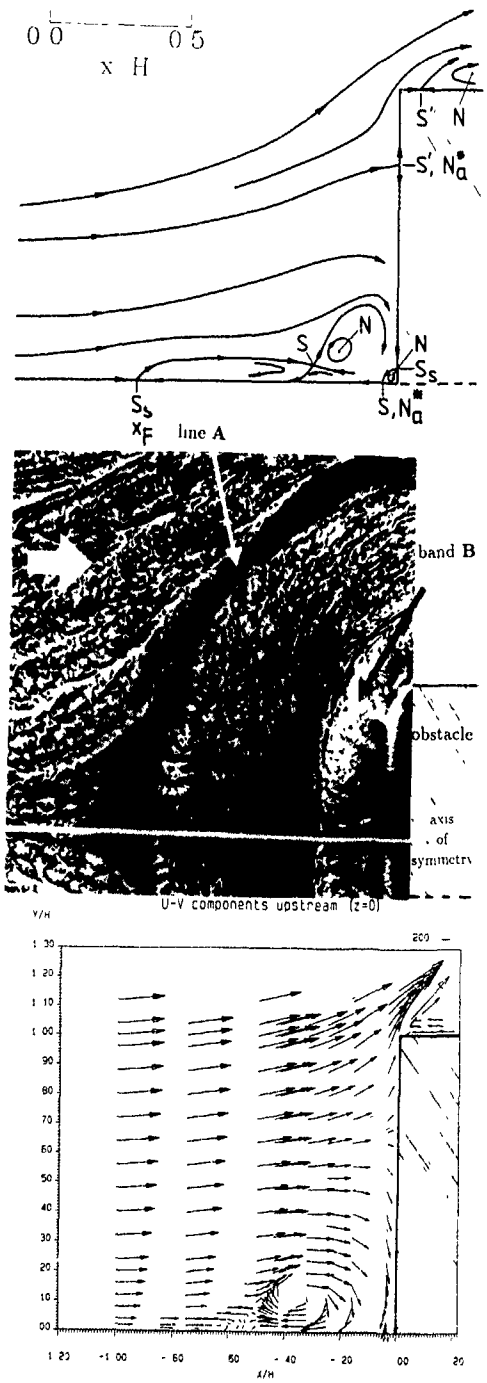

Figure 3: Flow upstream of the cube Legend. S= saddle, N= node, '= half saddle or node,*= when point viewed perpendicularly to the wall; subscripts· s-separation and a-attachment

in this region.

Dark regions in Fig 3b correspond to an accumulation of visualization pigment Line **A** in Fig 3b, for instance, a half saddle point in the X-Y plane which is considered to correspond to the primary separation of the flow, marked x_F in Fig. 1, and is located at a distance of $x_F = -1.04H$ upstream of the cube This separation is caused by the strong adverse pressure gradient imposed by the obstacle in this region

The horseshoe vortex is easily recognized in the velocity vectors of Fig 3c. It extends from the obstacle upstream to a point approximately over the centre of a second large dark area in the visualization photograph ($x \approx -0.5H$) This location corresponds roughly to the streamwise position of a free-stream saddle above the channel floor The white visualization band labelled **B** in Fig 3b is caused by the strong backflow and the correspondingly high wall shear stress The border between this white band and the dark zone directly upstream coincides with the centre of the horseshoe vortex

A secondary corner vortex was observed in the velocity vectors of Fig. 3c, which yields another light and dark visualization band immediately in front of the obstacle. Also a half saddle is observed at a height of approximately 0.7 on the obstacle front face This is the stagnation point of the on-coming flow

The region between the primary separation and the horseshoe vortex exhibits a very thin layer, at times no longer measurable, of reverse flow In this region, the velocity distributions show a distinct bimodal form, as illustrated in Fig. 4 The bimodal form of the distribution could also be measured out of the plane of symmetry, always corresponding to a region between line **A** and band **B** in Fig 3b. This form of distribution indicates that the velocity takes one of two preferred states, a behaviour studied recently by Devenport and Simpson (1990) for the flow upstream of a wing-body junction In this region, there is a thin layer of reverse flow extending back to the separation line, as can be seen in Fig. 3a.

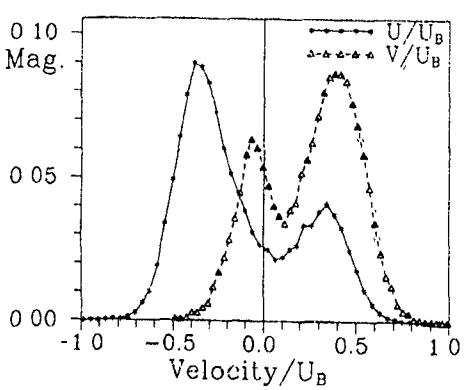

Figure 4 Velocity PDF at x= -0.44H, y= 0.10H and z= 0

Devenport and Simpson (1990) conditionally analysed the velocity field according to which one of the two preferred modes the flow was in and concluded that this area is a region of intense turbulence production, arising from a large-scale unsteadiness between the two flow modes A similar analysis of the present data, shown in Fig 5, shows strong similarities with the behaviour observed by Devenport and Simpson (1990).

Fig. 5a shows the time-averaged velocity field in the X–Y plane with the regions of bimodal velocity distributions measured in the U and V components superimposed. Separating the bimodal distributions into two independent distributions, in a manner similar to that of Devenport and Simpson (1990), the mean flow pattern in mode 1 or mode 2 can be constructed as shown in Fig 5b and c However, these representations have been constructed without considering any phase shift of mode transition between neighbouring measuring positions This information would only be available if spatial correlations were performed.

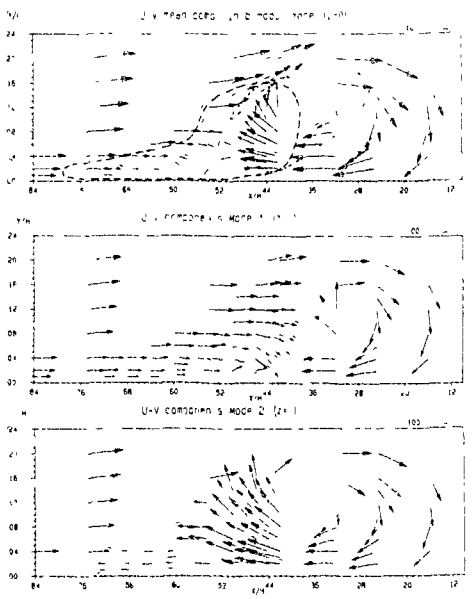

Figure 5 Vector fields for the different flow modes
— — — — — Bimodal in U - - - - Bimodal in V

Further analysis of this data reveals extremely high values of the Reynolds shear stress in the region of measured bimodal velocity distributions suggesting that this production is associated with large-scale unsteadiness Future analysis will investigate the cross spectral density of the U and V velocity fluctuations to determine the time scales of the $\overline{uv}$ contributions and their relative magnitude.

The cause of this unsteadiness, and consequently the cause of a very thin reverse flow layer, is postulated to be related to the origin of the recirculating fluid (Devenport and Simpson (1990)) Low momentum rotational fluid from the boundary layer is easily integrated into the junction vortex while high momentum irrotational fluid coming from the outer flow transforms into a jet of near-wall backflow seen clearly in mode 2 in Fig 5c. The present study indicates that this flow behaviour is not only present for the wing-body junction as given by Devenport and Simpson (1990) but also for the obstacle placed in a channel flow The ma-

jor difference between these two geometries is that the flow can go over the top of the obstacle but can only go around a wing-body junction

A further region studied in more detail is the flow separation at the upper leading edge of the obstacle, shown in Fig 6 There exists a mean recirculation region over the top surface which also exhibits very strong velocity fluctuations and bimodal PDF's Measurements of the U and V velocity components, taken just inside of the separating streamline

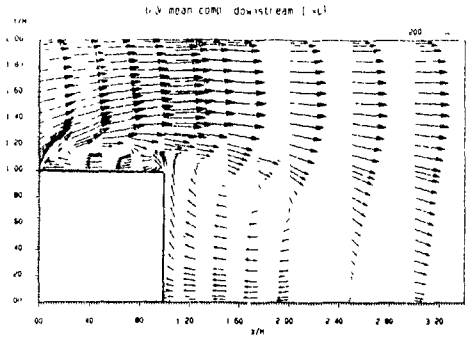

Figure 6 Flow over and behind the cube

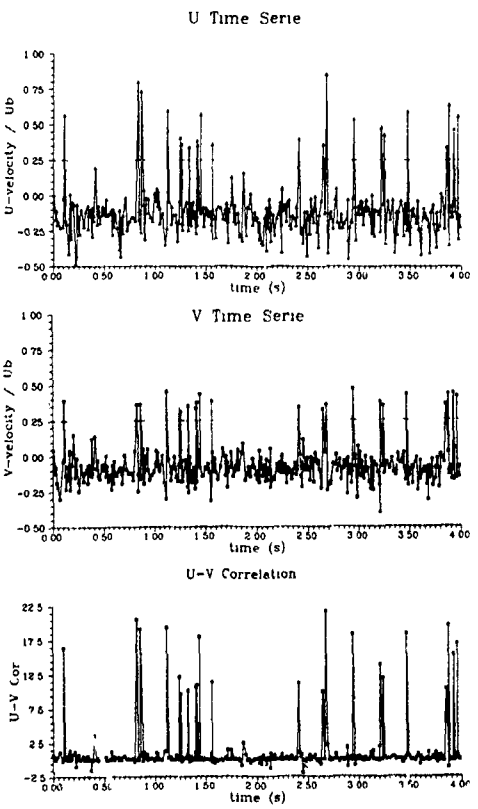

Figure 7 Velocity time series at x= 0 04H, y= 1 024H, z= -0.24H

above the obstacle, are shown in Fig. 7 as time traces. For the most part, the fluctuations are random in nature and contribute weakly to the Reynolds stress. At some instances, however, a very organized motion occurs in which the U and V velocity fluctuations become highly correlated This would correspond to intense turbulence production and can be interpreted as a large-scale unsteadiness in the recirculation region similar to the behaviour seen in front of the obstacle

The recirculation region behind the cube, also shown in Fig. 6, exhibits a structure similar to that described by Hunt *et al.* (1978) The two corner vortices visible on the floor behind the cube (as seen in the top view given in Fig. 10a) extend upwards to join in the plane of symmetry forming an arch along which strong velocity fluctuations and bimodal velocity distributions have been measured As was the case for the regions of bimodal measurements previously described, this region also corresponds to one where the kinetic turbulent energy is very large A map of the turbulent kinetic energy, $k = \frac{1}{2}(\overline{u^2} + \overline{v^2} + \overline{w^2})$, measured in the Y-Z plane immediately behind the obstacle, shows that large values of k clearly trace out the postulated arch vortex behind the cube (see Fig. 8).

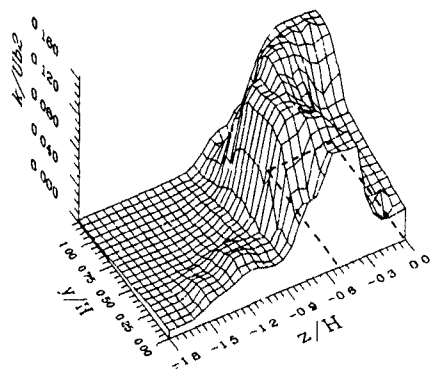

Figure 8: Map of the turbulent kinetic energy at the plane x=1.25H (- - - - - back face of the cube).

Velocity measurements performed behind the obstacle show that the two arms of the horseshoe vortex downstream of the reattachment point remain adjacent to one another, with no further streamwise vortices occuring in between. This is in contradiction to recent flow patterns proposed by Shofield and Logan (1990). These results also show that the location of the horseshow vortex centres change from $z \approx \pm 1.24H$ at $x = 1\ 75H$ to $z \approx \pm 0\ 95$ at $x = 5\ 3H$ This

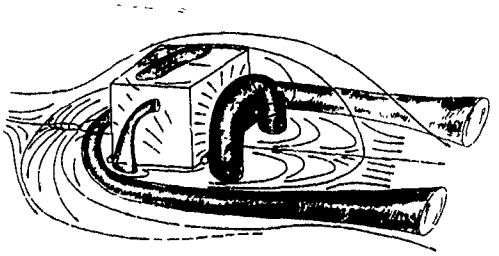

Figure 9 Sketch of the flow around a cube.

narrowing is due to the influence of the recirculation region vortex which entrains inner portions of the horseshoe vortex and draws the arms towards the axis of symmetry

Further analysis of the wall visualization results with support from LDA velocity measurements, leads to a picture of the overall mean flow field as sketched in Fig. 9

Flow around Obstacles of various Aspect Ratios

The aspect ratio of the obstacle, defined as the width to height ratio (W/H), was varied between 1 (cube) and 24 (rib). The results of the visualization experiments are shown in Fig. 10 for five of the tested obstacles

Observing first the dark line of primary separation in front of the obstacle, it is clear that at large obstacle aspect ratios ($W/H > 10$), it looses its curvature and becomes a separation line The separation distance, x_F, shown in Fig 11, increases with the aspect ratio to values of W/H $\approx$ 5 and then becomes independent of the obstacle width. This result is in contradiction to the visualization measurements of König (1990), who indicates a decrease of x_F for large obstacle widths up to 20H. This latter value coincides with the aspect ratio for which the separation line has negligible curvature.

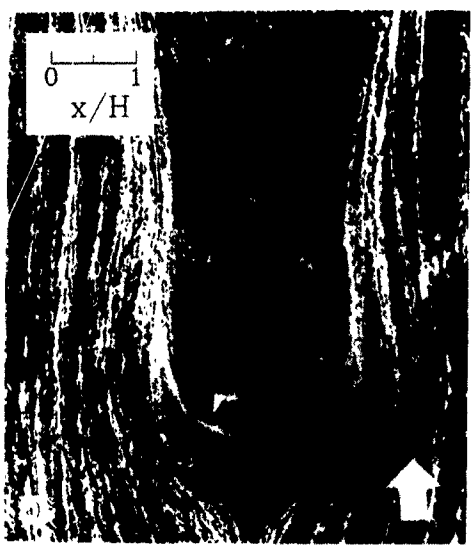

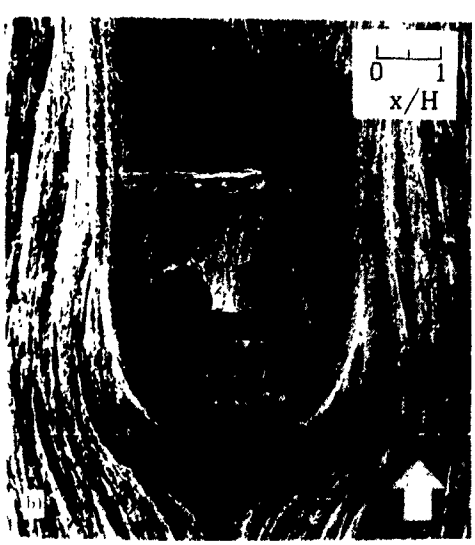

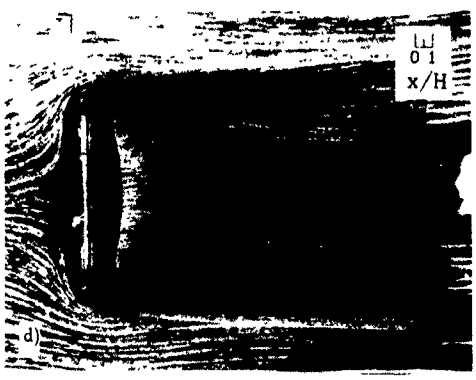

Figure 10: Flow visualization results for obstacles of different aspect ratio: a) W/H=1, b) W/H=2, c) W/H=4 and d) W/H=10

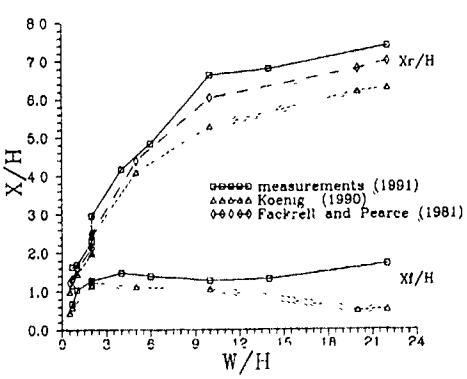

Figure 11: Separation $\frac{X_F}{H}$ and reattachment lengths $\frac{x_F}{H}$ versus $\frac{H}{W}$

Preliminary work in a water channel (König (1990) and Theisinger (1990)) showed that for obstacle aspect ratios greater than 10, an alternating series of node and saddle points could be observed on the obstacle front face as shown by the crystal violet visualization in Fig. 12. Whereas the on-coming flow can easily be diverted around short obstacles, it must go over wider obstacles and the structure of the forward recirculation region apparently changes. In addition,

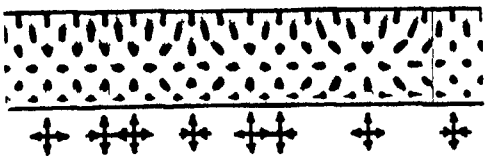

Figure 12: Crystal violet results for a rib showing saddle and nodal points on part of the front face.

no bimodal velocity distributions could be measured for the wider obstacles. Thus, the large-scale unsteadiness, which appears to be typical of three-dimensional obstacles, must be closely linked to the evacuation of recirculating fluid to the sides and around the obstacle, probably in the form of a horseshoe vortex.

Inspection of the series of photographs in Fig. 10 also reveals major differences downstream of the obstacles for different aspect ratios. For the cube obstacle, the horseshoe vortex narrows at a downstream distance near the rear reattachment point. This behaviour has been briefly described in the previous section. For wide obstacles ($W/H > 6$), the two arms of the horseshoe vortex appear to continually grow further apart, presumably with little interaction between them. In the region between the two arms, the W velocity component appears to be zero which is characteristic of a two-dimensional flow.

The reattachment length, x_R, normalized with the obstacle height is also plotted as a function of the aspect ratio in Fig. 11. It can be seen that there is little variation in this parameter for aspect ratios greater than 10. Reasonable agreement is found between the present results, previous results from König (1990) and a correlation relation proposed by Fackrell and Pearce (1981) for obstacles placed in boundary layers.

The trailing edge vortices on either side of the obstacle also change character with aspect ratio. These are indicated in Fig. 10 by the strong accumulation of pigment on each side and immediately behind the obstacles Whereas these elliptically shaped patterns strongly point outwards for the cube obstacle, they point strongly inwards for obstacles with W/H greater than 6. Separate measurements of the wall pressure show that the base pressure is much lower for the two-dimensional obstacle flow than for the cube obstacle flow, which accounts therefore for the stronger in-flow in the immediate obstacle wake

Conclusions

This experimental study has provided further details of the mean flow patterns around three-dimensional obstacles and a comparison of these patterns to those for two-dimensional obstacles Major differences in the mean and fluctuating velocity field upstream of the obstacle between two- and three-dimensional obstacles was identified In particular, a large scale unsteadiness was found in the case of the three-dimensional obstacle. This unsteadiness leads to very high values of the Reynolds shear stress For wider obstacles, a flow of 'two-dimensional' character about the centre plane is only achieved for width-to-height ratios above 10 Even above these values, however, the flow upstream and downstream of the obstacle does exhibit spanwise variations, in particular an alternating saddle/node structure on the obstacle front face.

References:

CASTRO, I.P. (1979) Relaxing Wakes Behind Surface-Mounted Obstacles in Rough Wall Boundary Layers, J. Fluid Mech. **93** 631-659.

CASTRO, I.P., ROBINS, A.G. (1977) The Flow Around a Surface-Mounted Cube in Uniform and Turbulent Streams, Ann. Rev. Fluid Mech. **11** 443-503

de BREDERODE, V., BRADSHAW, P. (1972) Three-Dimensional Flow in Nominally Two-Dimensional Separation Bubbles I: Flow Behind a Rearward-Facing Step, IC Aero Report 72-19, Imperial College, London

DEVENPORT, W.J. and SIMPSON, R.L. (1990) Time-Dependent and Time-Averaged Turbulence Structure Near the Nose of a Wing-Body Junction. J. Fluid Mech. **210** 23-55

DIMACZEK, G., KESSLER, R., MARTINUZZI, R. and TROPEA, C. (1989) The Flow Over Two-Dimensional, Surface-Mounted Obstacles at High Reynolds Numbers, 7th Symp. on Turb. Shear Flows, Stanford CA

DIMACZEK, G., EH, C., TROPEA, C. (1988) Sichtbarmachung von Wasserströmungen mit Hilfe des Kristalviolettverfahrens, DLGR Workshop 2D-Meßtechnik, Marktdorf, DLGR-Bericht 88-04

FACKRELL, J.E., PEARCE, J.E. (1981) Parameters Affecting Dispersion in the Near Wake of Buildings, CEGB Report No. RD/M/1179/N81

FAIRLIE, B D. (1980) Floe Separation on Bodies of Revolution at Incidence, Proc. 7th Australian Conf. on Hydr. and Fluid Mech., Brisbane.

HUNT, J.C.R., ABELL, C.J., PETERKA, J.A., WOO, H. (1978) Kinematical Studies of the Flows Around Free or Surface-Mounted Obstacles; Applying Topology to Flow Visualization, J. Fluid Mech. **86** 179-200

KÖNIG, J (1990) Anwendung des Kristallviolettverfahrens zur Untersuchung der dreidimensionalen Hindernisströmung, Studienarbeit at the Lehrstuhl für Strömungsmechanik, University Erlangen-Nürnberg.

PERRY A.E, HORNING, H. (1984) Some aspects of Three Dimensional Separation, Z Flugwiss. Weltraumforschung **8** Heft 3, 155-160

SHOFIELD, W.H. and LOGAN, E. (1990) Turbulent Shear Flow Over Surface Mounted Obstacles, J. of Fluid Engineering, Trans. of the ASME **112** 376-385.

THEISINGER,J (1990) Untersuchung der Dreidimensionalität einer Rippenströmung im Flachkanal mittels LDA. Diplomarbeit at the Lehrstuhl für Strömungsmechanik, University Erlangen-Nürnberg.

EIGHTH SYMPOSIUM ON
TURBULENT SHEAR FLOWS
Technical University of Munich
September 9-11, 1991

INSTABILITY OF FLOW PAST AN ISOLATED ROUGHNESS ELEMENT IN THE BOUNDARY LAYER

K. Ono*) , T. Tamura**) , K. Kuwahara***) and T. Motohashi****)
*)College of Science & Technology, Nihon University, Chiyoda,Tokyo,101,Japan.
**) Ohsaki Research Institute, Shimizu Corporation, Chiyoda,Tokyo,101,Japan.
***) Institute of Space & Astronautical Sciences, Sagamihara,Kanagawa,229,Japan.
****)College of Science & Technology,Nihon University, Funabashi,Chiba,274,Japan.

ABSTRACT

Flowfield around an isolated roughness element (a circular cylinder) is investigated by experimental and computational approaches. The roughness element is totally submerged in the laminar boundary layer of the flat plate. Our final goal is to make clear the transition process of the wake to the turbulence. At the present paper the structure and the instability of the wake near the cylinder is mainly focused. Newly developed return-type wind tunnel is used to measure the velocity field, using a hot-wire anemometer. The three-dimensional Navier-Stokes equations with a body-fitted coordinate system are also solved by the finite difference method. The computational results show the formation and development of the horse-shoe vortex and the arch vortex. In addition to the arch vortex, longitudinal twin vortices are found to be formed just downstream of the circular cylinder. These vortices explain the characteristics of the experimental results.

NOMENCLATURE

Dc	Diameter of a cylinder.
f	Frequency of the velocity fluctuation.
H	Height of a cylinder.
h	Spacing of the grid.
Re	Reynolds number based on Uo & H.
Rer	Roughness Reynolds number based on Ur & H.
p	Pressure.
Uo	Inflow velocity.
Ur	Flow velocity at the height of a cylinder in the boundary layer.
u,v,w	Flow velocity components.
x,y,z	Coordinate system. x is the inflow direction. y is perpendicular to the flat plate. The origin is located at the center of the cylinder on the plate.

INTRODUCTION

The objective of this research is to investigate basic mechanism that elucidates an abrupt change of flow around a small roughness element in a boundary layer of a flat plate. The small roughness element in the laminar boundary layer is believed to produce at least two vortex systems(Gregory & Walker(1951)) ; (i) a horse-shoe vortex in the upper stream part of the roughness and (ii) an arch or a trailing vortex in the wake. A breakdown of the flow is induced. The transition to the turbulent flow, followed by the interaction of these vortices, forms the turbulent wedge. The mechanism of the interaction among these vortex systems and the velocity shear layer at the element height has not yet been understood. So two methods of approaches are undertaken ; experiment and numerical computation.

This problem has been not only one of classical themes for the boundary layer theory(Tani(1969)), but also a crucial problem for the aircraft designers. They have eagerly desired to evaluate the permissible height of the roughness to keep the boundary layer laminar.(Klebanoff, et al(1987)) The laminar boundary layer generates smaller skin friction than the tubulent one. Judging from Gregory & Walker(1951), the flowfield is categorized into three patterns, depending on the roughness Reynolds number Rer , based on Ur and H.

(1) At smaller Rer (Rer < 200) a pair of streaks appear immediately behind the roughness element and disappear at the downstream
(2) At intermediate Rer (200 < Rer <500) the abrupt breakdown of a pair of streaklines happens and the turbulent wedge is formed.
(3) At larger Rer (Rer > 500) the turbulent wedge seems to start at the roughness element.

Our attention is mainly focused on the second case. The role of the horse-shoe vortex and the arch or the trailing vortex for the transition process to the turbulent wedge must be made clear. Also the possibility of the formation of other vortices should be investigated.

EXPERIMENTAL SETUP

The experiment is carried out using a newly constructed small wind tunnel. (Fig.1) This wind tunnel is return-type. Its test section is 30 cm x 30 cm x 2 m. The wind speed is controlled by the AC-fan motor from 0.8 to 14 m/s. The contraction ratio is 13.4. Residual turbulence is about 0.12% of the free stream at Uo=5m/s. A laminar boundary layer is generated on a flat plate installed in the test section. The flat plate is 20 cm x 90 cm x 0.3 cm and its leading edge has half wedge shape with an apex angle of 15 degrees. A cylindrical roughness with 2 mm height and 2 mm diameter is located 10 cm downstream of the leading edge. The longitudinal velocity component was measured with the constant temperature type hot wire anemometry. The hot-wire sensor is 2.5 m diameter and 0.5 mm span. The coordinate system adopted in the present paper is shown in Fig.2. The frequency of fluctuation was analyzed with FFT analyzer(CF-360,ONO-SOKKI).

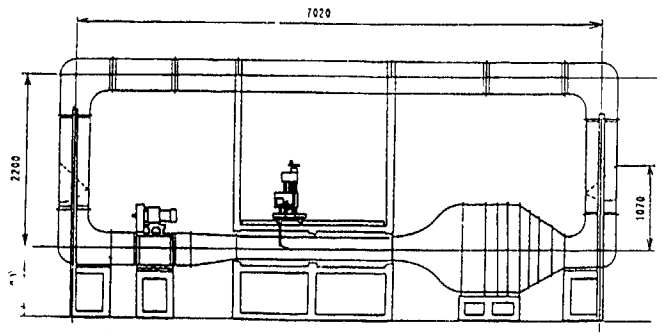

Fig. 1 Low speed wind tunnel

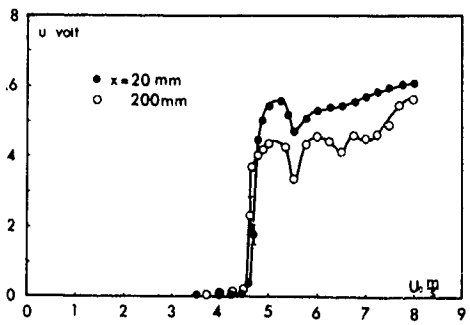

Fig. 3 Critical velocity. (y = 2 mm, z = 0 mm)

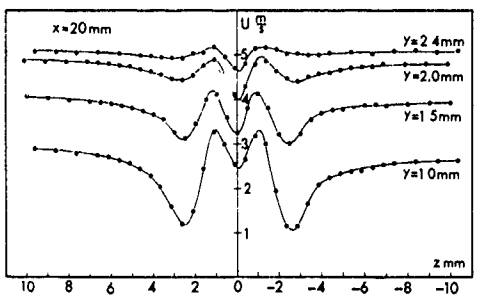

Fig. 4 Spanwise distributions of mean velocity. (x = 20 mm)

NUMERICAL COMPUTATION

Flowfield around a circular cylinder placed in the boundary layer of a flat plate is solved by applying the finite difference method to the three dimensional incompressible Navier-Stokes equations.(Tamura, et al.(1989)) Computational conditions are determined in accordance with the experimetal ones as much as possible. All spacial derivatives execpt those of convective terms are approximated by the central difference. The third order upwind scheme is applied to the convection terms.(Kawamura & Kuwahara(1984)) The semi-implicit scheme, which is eqivalent to the Euler implicit scheme , is used for the time marching except the convection terms, which are linearized in time. The

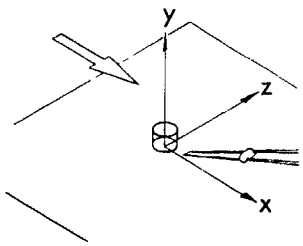

Fig. 2 Coordinate system.

poisson equation for pressure is solved by SOR method. The divergence free term is added according to MAC method.(Harlow & Welch(1965)) The generalized curvilinear body-fitted grid system is used to treat the boundary conditions easily. For the pressure boundary conditions the Neumann condition is applied and the normal derivative of the pressure is set to zero. For the velocity conditions, the uniform flow is assumed at the inflow area and the Neuman condition is applied for other outer boundaries. On the surface of the cylinder and on the ground non-slip conditions are used.

EXPERIMENTAL RESULTS

CRITICAL VELOCITY

The flow around a three-dimensional roughness is characterized by an abrupt flow change. The change occurs when the speed of fluid exceeds a threshould value. This value is called "Critical Velocity". As a first step of the experiment the critical velocity has to be checked. Fig. 3 shows the rms value of fluctuation at x=20 mm and x=200 mm(y=2 mm, z=0 mm). The abscissa is the uniform velocity. At x=200 mm turbulent signals break out at Uo=4.5 m/s. The hot-wire signals at the velocity are intermittent. Real turbulent waves are observed at Uo=4.65 m/s. Intermittent character of the velocity fluctuation is remarkable. In the vicinity of the roughness element (x=20 mm), sinusoidal fluctuations were found at Uo=4.5m/s. The amplitude of the periodic fluctuation increases as the uniform velocity up to 5.15m/s It increases again at Uo=5.5 m/s.

Based on these data,the experiment conditions are determined as follows:

*Uniform velocity	:	Uo=5.11 m/s
*Thickness of the boundary layer at the roughness location	:	2.64 mm
*Displacement thickness	:	0.88 mm
*Reynolds number	:	Re =677
*Roughness Reynolds number	:	Rer=650

MEAN VELOCITY FIELDS

Detailed measurement of mean velocity profile was made at x=20 mm. Mean velocity distributions in the spanwise direction are shown in Fig.4. At y=1.0 mm, there are two pairs of the peak and the valley on both sides of the center-line. The horse-shoe vortex and the acceleration effect of the side-walls of the cylinder bring about such wavy

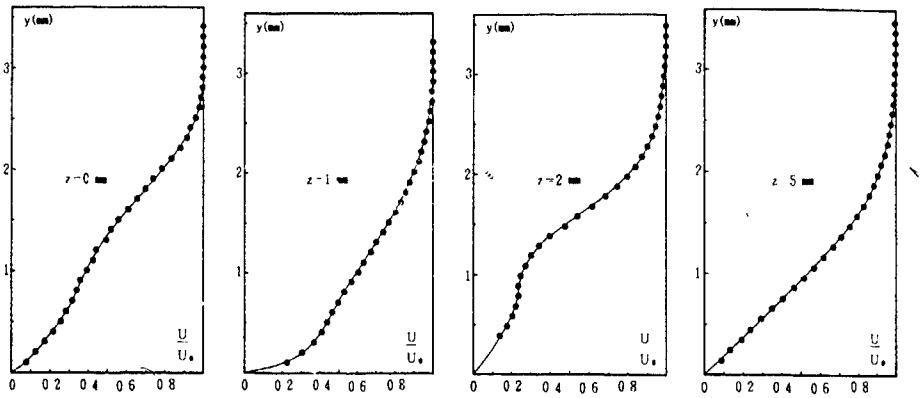

Fig. 5 Spanwise variation of velocity profiles.
(x = 20 mm)

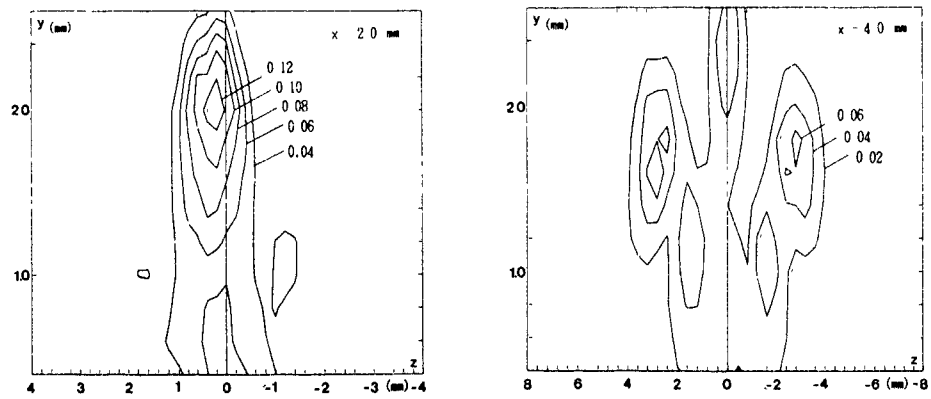

Fig. 6 Iso-intensity contours
of velocity fluctuation.

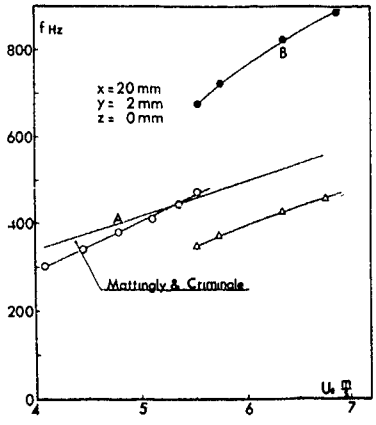

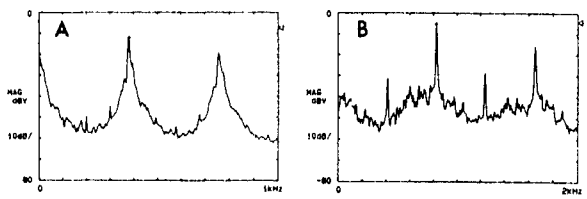

Fig. 7 Frequency of the velocity fluctuation
vs. uniform velocity.

structure. The velocity difference between the peak and the valley decreases as the probe moves away from the plate. The location of the peaks, however, is almost fixed at the side edge of the roughness element. Fig.5 shows the vertical distribution of the mean velocity at various spanwise positions. On the center-line the velocity defect due to the roughness is observed throughout the boundary layer, but at z=5 mm its influence is hardly detected in the vicinity of the wall and in the outer edge of the boundary layer. The effect of the roughness reveals itself as making the velocity profile inflectional. At z=2 mm the inflectional point is situated about y=1.7 mm. If the infletional instability is responsible for the instability at the downstream stage as mentioned by Klebanoff , et al.(1987), fluctuations develop near this position. The velocity profile at z=5 mm shows some velocity defect, suggesting that a rather long relaxation distance is needed in the lateral direction. We notice that small deviation from Blasius profile exists from y=1 to 2 mm.

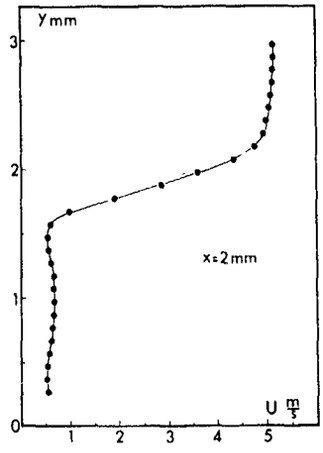

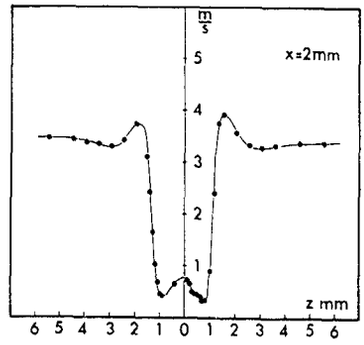

Fig. 8 Mean velocity distributions at high shear layers. (x = 2 mm)

FLUCTUATIONS

The velocity fluctuation at x=20 mm begins to appear at Uo=4.5 m/s as mensioned before. The amplitude of the fluctuation shows a rapid increase in the flow direction. Maximum amplitude of fluctuation occurs on the center-line. Magnitude of the maximum fluctuation reaches over 12 % of the uniform velocity. According to the visualization, a pair of counter-roatating vortex filaments exist in the vicinity of the center-line and they would realize two peaks in the amplitude distribution. But the spacial resolution of the hot-wire is not sufficient to discriminate two vortex cores Figs.6 show iso-intensity contours of the velocity fluctuation with regards to the uniform velocity. A splitted structure of the peaks of the amplitude distribution occurs at X=40 mm. A distortion of the trailing vortices is believed to be largely associated with this change. The frequency of the fluctuation is measured with the spectrum analyzer(Fig.7). The hot-wire probe was set at the roughness top and on the center-line, The dominant frequency of fluctuation is proportional to the uniform velocity and its shape becomes gradually dull.At about Uo=5.5 m/s a pair of new components appears suddenly . A fundamental component of 670 is Hz and its subharmonics is 345Hz. The new components are so-called "line-spectra". The previously dominant component diminishes with the increase of the uniform velocity. The solid line is calculated from the stability prediction of two-dimensional wake by Mattingly and Criminale(1972). The present results agree well with their prediction in the case of lower uniform velocity.

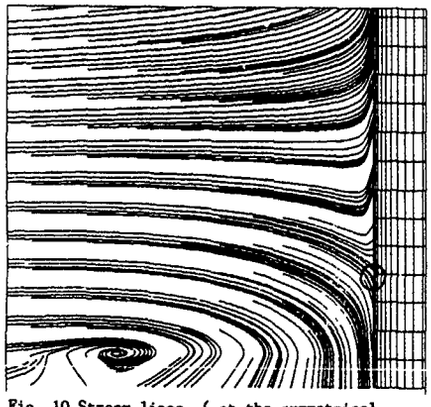

Fig. 10 Stream lines. (at the symmetrical cross section)

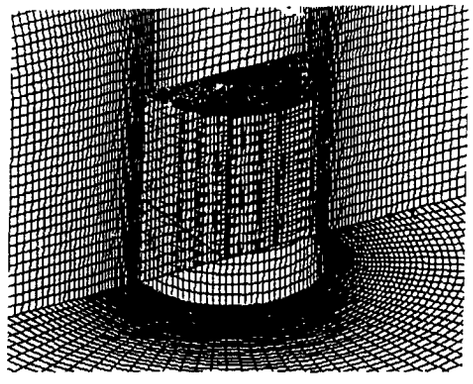

Fig. 9 Grid system. (102 x 100 x 100)

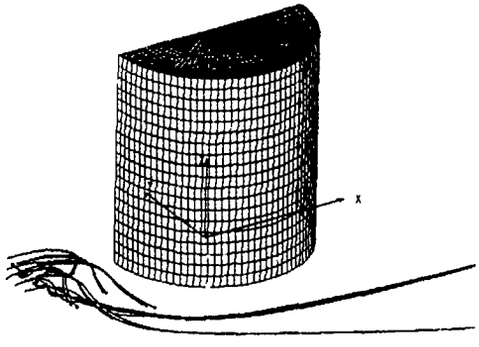

Fig. 11 Stream lines. (front view)

INSTABILITY

In the near field of the roughness element, the complex high shear layer is established; the separated flow at the top of the roughness generates vertical high shear layer and sheds unsteady vortices. A high shear layer also is made in the spanwise direction. These locations corespond just to those of side walls of the cylinder. Detailed measurements of the flow immediately behind the roughness at $x = 2$ mm show such features in the profiles (Fig.8). The vertical velocity gradient of the back ground flow , normalized with the uniform velocity and the roughness height , is 0.078. Maximum velocity gradient in the vertical direction is 3.3. The spanwise one is also 3.3. The strength of these shear lavers is the same order.

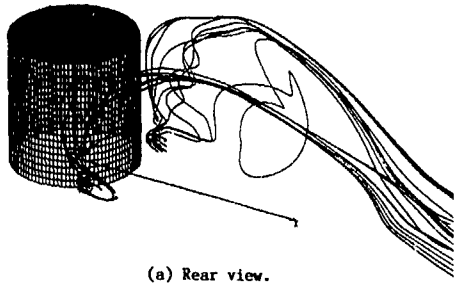

(a) Rear view.

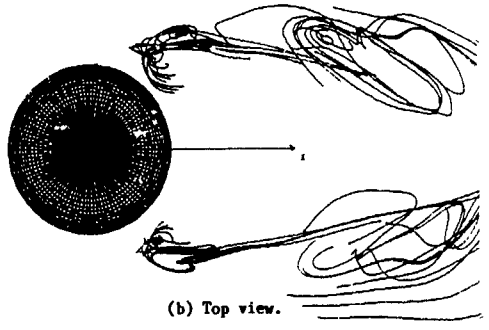

(b) Top view.

Fig. 12 Stream lines in the wake.

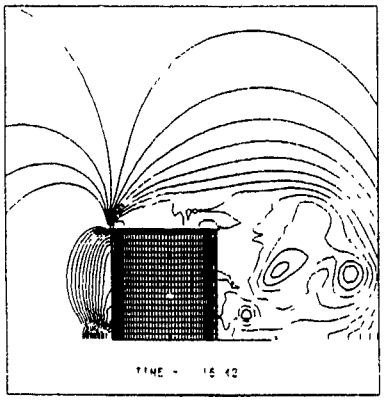

Fig. 14 Pressure contours. (at the symmetrical cross section)

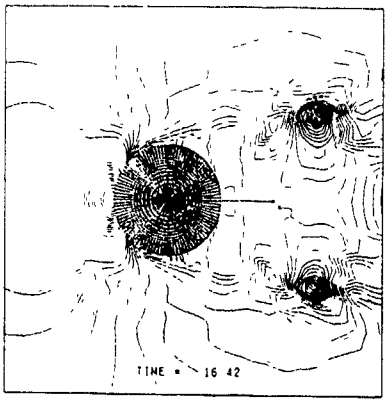

(a) on the flate plate.

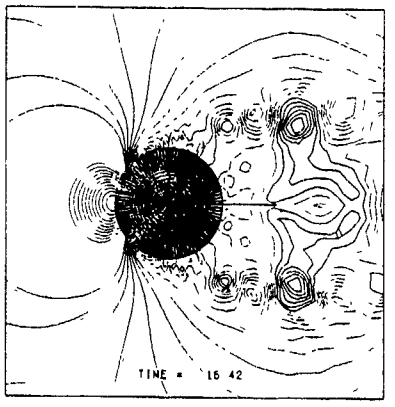

(b) at the half height of the cylinder.

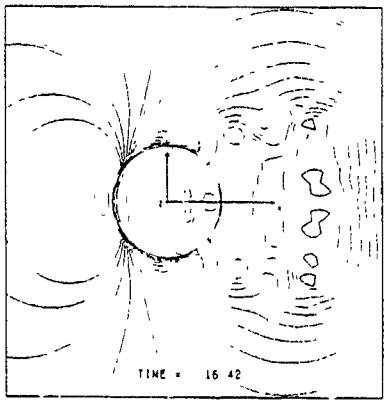

(c) at the top height of the cylinder.

Fig. 13 Pressure contours.

COMPUTATIONAL RESULTS

The computation was carried out, simulating the experimental conditions as much as possible. Reynolds number Re was set to 600. The grid system used in this computation is shown in Fig 9. The mesh size is 102 for the radial direction, 100 for the circumfencial one and 100 for the height. The 'O-type' grid is adopted at any section of constant height near the cirlular cylinder. And the whole grid system is made up by putting the 'O-type' grid on another. Such grid system is believed to be suitable because the abrupt variation of Jacobian can be avoided in the computational domain.

In Fig. 10 the stream lines on the upperstream part of the roughness is shown. This figure is the view at the longitudinally symmetrical cross section. The non-dimensionalized ellaped time (time x the inflow velocity / the cylinder diameter) from the start of the computation is 16.42, as well as that of the following figures. The formation of the horse-shoe vortex is clearly detected Also the stagnation point is found on the surface of the circular cylinder. (Marked with a circle in the figure.) It is difficult to determine the location of the stagnation point precisely, because the spacial resolution is insufficient. But the curved stream lines around the stagnation point can be recognized.

The development of the stream lines around the horse-shoe vortex is shown in Fig. 11. These stream lines flow away without interacting with the wake. It means that there in no interference between the horse-shoe vortex and the wake in this computation.

In Figs. 12 (a) and (b) the selected stream lines in the wake are presented. From the top view (Fig. 12 (b)) the periodic shedding of pair vortices in the wake is clearly found. Supposing one stream line just behind the circular cylinder in Fig. 12 (a) is focused, it is shown that this stream line goes up first, change its direction about the cylinder height and flow straight to downstream.

Figs. 13 (a),(b)and (c) are the pressure contours at the various cross sections respectively. The higher pressure region is formed just upperstream of the cylinder. This is corresponding to the stagnation point. It is easily found that pair of vortices are sheded simultaneously and periodically. They spread a little transversially in the wake. These vortices almost diappeared at the height of the cylinder.

The pressure contours at the symmetrical cross section (Fig. 14) shows the transverse vortex in the wake.

Judging from these vortex structure , it is concluded that the arch type vortices are shedded periodically and flow downstream. They stretch at most to the level of the cylinder height and spread transversially a little. It can be mentioned that the arch vortex is formed by the shear between the acceleration of the side-walls and the deacceleration of the wake, and that the higher velocity region in the velocity distribution(Fig. 4) is explained by the formation of the arch vortices.

From Fig. 14 the flow is known to be separated on the top of the cylinder. The lower flow speed region at the centerline (Fig. 4) and the turbulence intensity structure (Fig. 6) correspond to this separation.

Fig. 15 is the stream lines at the section just downstream of the cylinder. The viewing direction is marked in the figure. A pair of vortices are recognized. The center of these vortices are located below the top of the cylinder and inside the side walls.

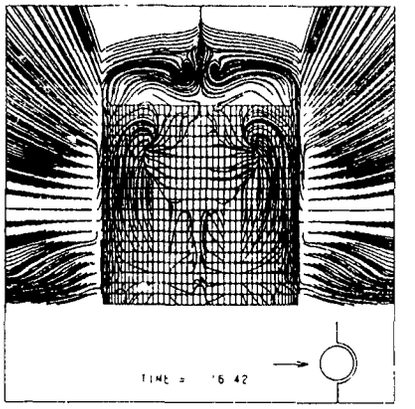

Fig. 15 Stream lines (just downstream of the circular cylinder)

CONCLUSION

Experiment and numerical computation are being conducted to make clear the structure and the instability of the flow past a circular cylinder placed on a flat plate in the laminar boundary layer. Accordig to Gregory and Walker's experiment, an intermediate roughness Reynolds number case was examined. It is confirmed that in this case the horse-shoe vortex is formed but does not interact with the wake. The flow separation on the top of the cylinder determines the deaccleration and the high turbulence intensity at the centerline of the wake. The arch vortices are formed in the wake. These vortices determine the acceleration region at the side walls. Another pair of longitudinal vortices are forme just behind the circular cylinder. Such computational results explain well the charactersitics of the experimental results.

REFERENCES

GREGORY,N. & WALKER,W.S. 1951 The Effect on Transition of Isolated Surface Excrescences in the Boundary Layer. Aero. Res., Council Reports & Memoranda No.2779.

TANI,I. 1969 Boundary-Layer Transition. Ann. Rev Fluids Mech. vol 1.

KLEBANOFF,P.S, CLEVELAND,Jr,W.G. & TIDSTROM,K.D. 1987 Interaction of a Three-Dimensional Roughness Element with a Laminar Boundary Layer AEDC-TR-87-7 US AIR Force.

TAMURA,T.,KUWAHARA,K. & SUZUKI,M. 1989 Numerical Study of Wind Pressure on a Domed Roof and Near Wake Flows. Proc. 6th U.S.National Conf. Wind Eng..

KAWAMURA,T. & KUWAHARA,K. 1984 Computation of High Reynolds Number Flow around a Circular Cylinder with a Surface Roughness. AIAA Paper 84-340.

HARLOW,F.H. & WELCH,J.E. 1965 Numerical Calculation of Time-Dependent Viscous Incompressible Flow of Fluid with Free Surface. Phys. Fluids vol 8 .

MATTINGLY,G.E. & CRIMINALE,W.O 1972 The Instability of an incompressible two-Dimensional Wake. J.Fluid Mech. vol.51 233-292.

EIGHTH SYMPOSIUM ON
TURBULENT SHEAR FLOWS
Technical University of Munich
September 9-11, 1991

Paper presented at the *8th Symposium on Turbulent Shear Flows*
Technische Universitat, Munich, September 9-11, 1991

THE NATURAL AND FORCED FORMATION OF SPOT-LIKE Λ-STRUCTURES CAUSED BY VORTEX DISLOCATIONS IN A WAKE

C.H.K.Williamson

Mechanical and Aerospace Engineering
Upson Hall, Cornell University,
Ithaca, NY 14853

ABSTRACT

In the present paper, the three-dimensional transition of the flow behind a bluff body, at low Reynolds numbers, is studied. It has previously been found that there are two fundamental modes of three-dimensional vortex shedding in the wake of a circular cylinder (dependant on the range of Reynolds number), with a spanwise length scale of the same order as the primary streamwise wavelength. However, it is shown in the present study that the wake transition also involves the appearance of low-frequency intermittent wake oscillations, which are the result of the generation of large-scale "spot-like" structures that grow downstream to a size of the order of 10-20 primary wavelengths. These massive structures, which are caused by "vortex dislocations", have some similarities with turbulent spots found in bounded shear flows, as well as with some flow structures found in free shear flows. It will also be shown that such spot-like structures can be passively forced to occur in the wake using a small localised disturbance near the body. The disturbance causes the periodic generation of "vortex dislocations" that grow into the large-scale "spots". By forcing such phenomena, we are better able to study their structure and characteristics, in much the same way as investigators have studied turbulent spots that have been artificially forced in boundary layers.

1. INTRODUCTION

A number of investigations have recently been concerned with the general problem of the development of three-dimensional structure in turbulent shear flows, and with the corresponding implications for mixing in such flows. The form and development of such structures can often be studied to advantage in the transition region, where smaller scales have not yet developed.

In the transition regime, it has been found that there are differences in the development of streamwise vorticity in the wake of bluff bodies as compared with the "unseparated" wake from a splitter plate. (Such developments are discussed in detail in Williamson, 1988b, 1991a-d). These differences arise from the presence of the bluff body in the former case, which causes the main part of the streamwise vorticity to originate primarily from a spanwise instability of the primary vortices (the 2-D rollers). Over a range of Reynolds numbers, two modes of three-dimensionality are found, and the appearance of each mode, as we increase Reynolds number, corresponds with a discontinuity in the Strouhal-Reynolds number relationship as can be seen in Figure 1. Above Re=180, there is a discontinuous change in the wake formation, as the primary wake vortices become unstable and generate large-scale vortex loops. This "mode A" three-dimensional shedding correponds with Strouhal curve A in Figure 1. Between Re=230-260 there is a transition to a mode B three-dimensional shedding involving the inception of finer-scale streamwise vortex structure, with a shedding frequency corresponding to curve B in Figure 1. At this discontinuity there is no hysteresis (as occurs at the first discontinuity), and it is found that two modes of vortex shedding (modes A and B) alternate in time. There are thus two stages in the transition to three-dimensionality in the wake of a bluff body, each of which is associated with a different scale of streamwise vortex structure, and with a different vortex shedding frequency.

However, it is found that the transition to three-dimensionality involves a further phenomenon, and one that is largely responsible for the low-frequency fluctuations and break-up to turbulence in the wake, namely the presence of "vortex dislocations" in the near wake. Vortex dislocations are generated between spanwise cells of different frequency, when the primary "Karman" vortices in each cell move out of phase with each other. Across the cell boundaries, a rather contorted web of vortex linking occurs, in what is termed here a dislocation, in analogy with dislocations that appear in solid mechanics. These dislocations grow downstream into large-scale spot-like structures (in a manner not unlike the "transverse contamination" of boundary layer spots, as described for example by Schubauer & Klebanoff, 1956, and Gad-El-Hak et al., 1981).

In the transition regime, cells of different frequency appear (along with vortex dislocations), due in part to the alternating of different-frequency modes of 3-D shedding along the span, as discussed above. In the laminar regime also (Re<180), it is found that cells occur, but in a more ordered fashion than for the transition regime, and these cells are associated with certain oblique vortex shedding modes (Williamson,1988a, 1989a; Eisenlohr & Eckelmann, 1989; Konig, Eisenlohr & Eckelmann 1990). These laminar oblique-shedding modes, involving cells and dislocations, are influenced by the end boundary conditions.

Browand and Troutt (1985) had earlier found vortical structures to be generated naturally in the shear layer between spanwise cells of different frequency, or between cells of similar frequency but which are out of phase with each other. These vortical structures were inferred from velocity measurements using a rake of hot wires along the span. Browand and Ho (1987) suggested that these "defects" or dislocations could be due to slight non-uniformities in the flow, causing differences in frequency along the span. Although the "defects" in the free shear layer observed by Browand et al. are found to be produced randomly in space and time, it has proved possible to organise them by acoustic forcing (Browand and Ho, Browand and Prost-Domasky, 1988,1989) and so to study their evolution more clearly. A process similar to the vortex splitting (mentioned above) could be inferred from their velocity measurements. The defects cause an increase in the low-frequency velocity fluctuations as the shear layer travels downstream, and it has been found that they are dynamically important in promoting vortex pairing interactions locally in the shear layer. They seem to be of fundamental importance in the development of such shear layers. Efforts are underway to describe such topological effects from theoretical considerations (Yang, Huerre & Couliet 1989).

Nygaard & Glezer (1990) have constructed a highly-sophisticated heater-strip forcing technique for use in water, with the intention of forcing many different spanwise patterns of vortex formation in a free shear layer. By imposing a spanwise phase modulation on the evolving primary vortices, they have induced the primary vortices to split or dislocate at certain spanwise positions in a remarkably neat manner, and thereby to produce strong streamwise vorticity in the flow. The study has some similarities and is complementary to the flows being studied, using a different technique, by Browand et al.

Experiments by Gharib and by Williams (at the University of California) have extended the work of Van Atta, Gharib and Hammache (1988), where a vibrating wire created spanwise structures due to interactions of the wire frequency with the natural shedding frequency. They considered the case of a shear layer forced to have different frequencies over each half span, similar to

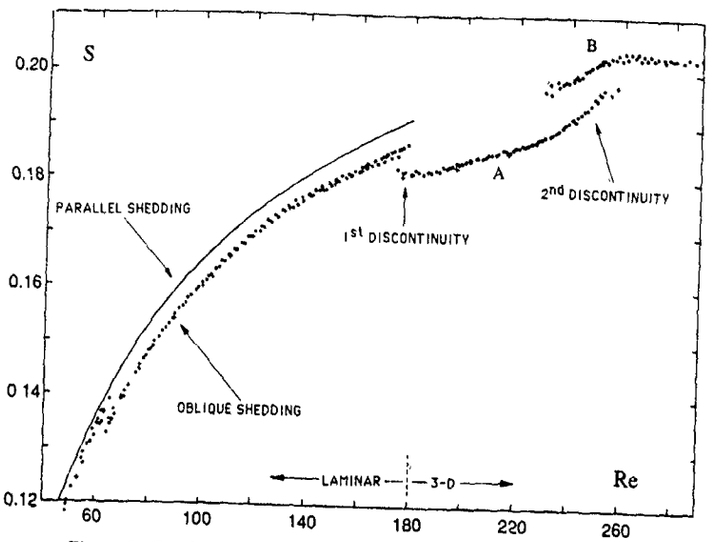

Figure 1. *Strouhal number versus Reynolds number over the laminar and transition regimes.*
The two discontinuities are associated with the inception of different modes of three-dimensional shedding (modes A and B). D = 0.104 cm. (L/D = 140)
D = 0.061 cm. (L/D = 200) D = 0.051 cm. (L/D = 240)

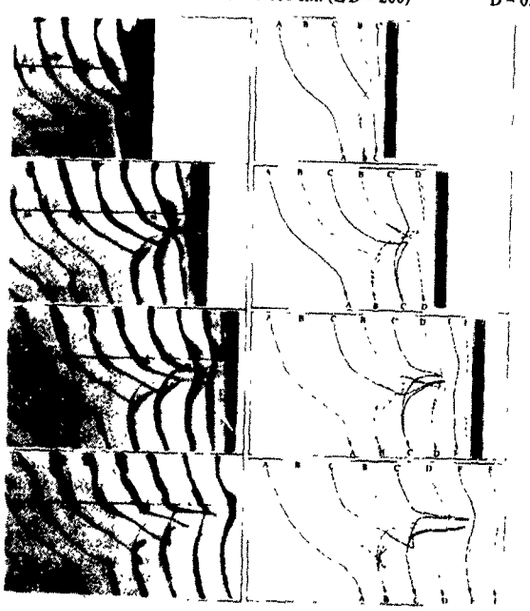

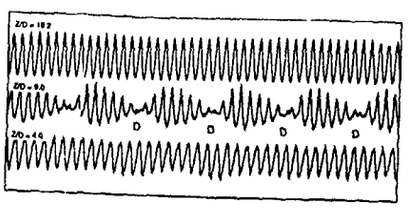

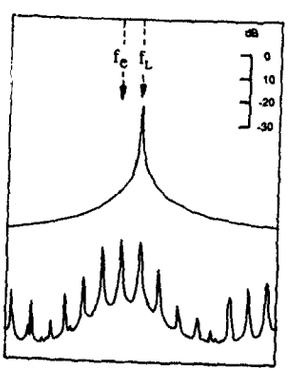

(c)

Figure 2. *Development of a "vortex dislocation" in the laminar shedding regime.*

(a) This visualisation sequence shows a vertical cylinder moving to the right, leaving behind a higher shedding frequency in the top half of each photograph relative to the bottom half, and demonstrates the vortex linking process when vortices in each frequency-cell move out of phase with each other.

(b) Time traces of velocity fluctuation taken with a hot wire probe at different spanwise positions, across a dislocation. The central trace corresponds with a position between the cells, whereas the upper and lower traces are for positions well within the two different frequency-cells.

(c) Spectra of velocity fluctuations well within a frequency-cell (upper spectrum), and between two cells (lower spectrum), the latter showing the characteristic quasi-periodic form.

the experiments of Browand et al., but in this case further utilising the control of heater strips. They made the suggestion that vortical structures between cells of different frequency could be part of the fundamental process by which streamwise vorticity is generated in shear flows.

It can be seen from the above that dislocations can be generated in free shear flows, as well as in other flows, of which one type is perhaps to be expected; namely the non-uniform flow past a body. Gaster (1969,1971) and recently Papangelou & Gaster (1991), and also Piciriello & Van Atta (1991) have investigated the flows past cones, and it has been found in these studies that cells of different frequency appear, along with the expected dislocation structures between the cells. The agreement between typical experimental results for flow past cylinders and cones with computations made on a Connection Machine by Jesperson and Levit (1991) is remarkably good for such complex flows, and much may be learnt from such computations. Further work by Lewis & Gharib (1991) has also found interacting cells of different frequency in the wake of a stepped-cylinder, which have similarities to the interaction of cells in the wakes of cones. Finally, different-frequency cells may be found in the wake of a cylinder placed in a shear flow, and this was shown by Maull & Young (1973) and is discussed in a review by Griffin (1988). In fact, ongoing work by Rockwell (1991) and by Bearman & Szewczyk (1991) seem also to exhibit interacting cells of different frequency in the wakes of bluff bodies with spanwise geometric variations. It seems from the above that there are several investigations being conducted on the *non-uniform flows* past bodies, and primarily in the laminar shedding regime.

The present work has stemmed from studies concerning the three-dimensional aspects of cylinder wakes in *uniform flow conditions*. It has been shown before that cells of different frequency appear in the wake of a cylinder in a uniform flow, in the laminar-shedding regime (Gerich & Eckelmann, 1982). In the laminar regime these cells are influenced by the end boundary conditions and have recently been found to be the origin of a number of phenomena in the cylinder wake, including that of oblique vortex shedding, and also the possible discontinuous changes of shedding mode with variation of Reynolds number (Williamson, 1988a, 1989a; Eisenlohr & Eckelmann, 1989; Konig, Eisenlohr & Eckelmann 1990). Of particular importance in the present study is the fact that vortex dislocations are found to be a fundamental feature of the natural 3-D transition in the cylinder wake, and it is found that very slight phase variations due to the 3-D modes of shedding can naturally produce dislocations in the wakes of long cylinders. One of the prime characteristics of dislocations is their reasonably fast growth in the spanwise direction, and they seem to trigger a rapid breakdown to turbulence with a broad spectrum within several primary (Karman) vortex wavelengths downstream of the body. The natural occurrence of dislocations as part of the transition process is discussed below in Section 2.

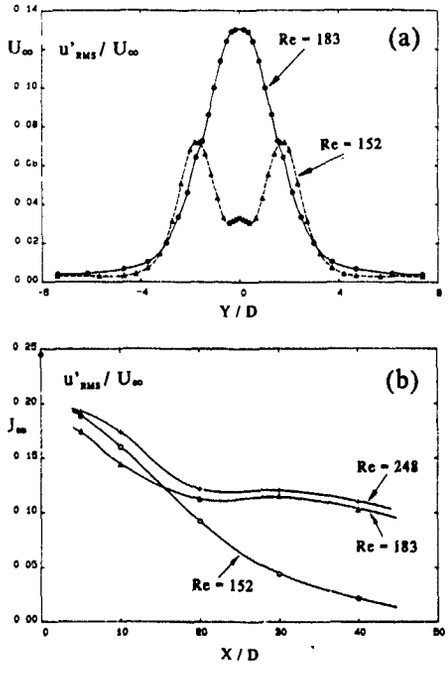

Figure 3. *Velocity fluctuations for the laminar wake versus the natural 3-D turbulent wake.*
(a) Transverse profiles of (u'_{rms} / U_∞) velocity fluctuations, showing the marked contrast between the laminar wake (Re=152) and 3-D transition wake (Re=183). (Y/D = distance perpendicular to wake centreplane / diameter.)
(b) Downstream decay of (u'_{rms} / U_∞), showing the much slower decay for the 3-D turbulent wake (Re=183 and 248), as compared with the laminar wake (Re=152). (X/D = distance downstream from cylinder axis / diameter.)

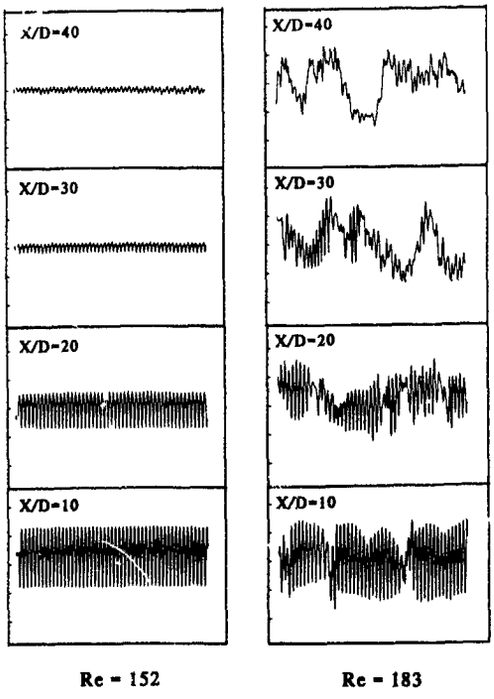

Figure 4. *Downstream decay of u' fluctuations for the laminar and 3-D turbulent wakes.*
The time traces of velocity fluctuations on the left are for the laminar wake (Re=152), and these show a rapid decay of energy. This is in marked contrast with the 3-D turbulent wake on the right (Re=183), for which the energy at the shedding frequency rapidly gives way to large low-frequency oscillations. The origin of these large oscillations downstream (x/d=40) comes from the "glitches" in the time traces found upstream (x/d=10), and are due to the formation of vortex dislocations. (Time traces are scaled correctly relative to each other, although the scale is arbitrary.)

In Section 3, it will be shown that "vortex dislocations" can be simply triggered artificially, with the intent that the periodic evolution of these structures can more easily be studied as they progress downstream. The dislocations are generated by a small disturbance in the form of a small ring of slightly larger diameter than the cylinder, which is placed at a certain spanwise position on the cylinder. This ring generates a slightly lower frequency of shedding (f_R) than is found over the rest of the cylinder (f), which then results in vortex dislocations appearing at the low beating frequency ($f_D = f - f_R$) The observation that such a ring would generate dislocations originated from a study of possible end conditions for a cylinder (in early 1988), where a large range of endplate diameters was investigated. It was found that even for very small endplates, which were both thin (in the spanwise direction), and had a diameter only slightly larger than the cylinder, that the vortices of the main cylinder span did not end smoothly at the endplate, but rather were interacting with the wake of the endplate itself to generate large spot-like structures. Interestingly, as the endplate became smaller, so the dislocations became larger, because they scale on the inverse of the dislocation frequency f_D ! It was decided at that time to study these large-scale vortex dislocations for their own sake,with the feeling that whether or not it had any significant connection with natural transition, it was a phenomenon of intrinsic interest. Fortunately, this study has proved most fruitful, as it provides much-needed insight to the naturally occurring dislocations that are part of transition Examples (shown in colour) of forced dislocations have been shown in Williamson (1989b), in the Gallery of Fluid Motion.

2. NATURAL FORMATION OF "VORTEX DISLOCATIONS" AS PART OF THE TRANSITION PROCESS

Some features of vortex dislocations can be shown clearly from investigations in the laminar regime, as shown in Figure 2. The photographs in (a) show the formation of a vortex dislocation for a vertical cylinder which is moving to the right, and which has a higher shedding frequency in the top part of each photograph relative to the bottom half. (The cylinder is towed in a water tank, and the visualisation shows dye washed off the body) The dislocation involves vortex division, whereby vortices of one sign in one cell are divided up and are linked to vortices of the same sign in the other cell. These dislocations occur at the beat frequency ($f_1 - f_2$) between the frequencies of each of the neighbouring cells (f_1 and f_2), and cause modulations in the time traces of velocity fluctuation when a probe is placed between the cells, as shown in the central trace of (b) (The velocities are measured using a hot wire placed in the wake of a cylinder in a wind tunnel.) The top and bottom periodic velocity fluctuation traces correspond to the different frequencies that are found within the different cells (found by placing the hot wire at different spanwise positions). As one could expect, the corresponding spectra are shown to be periodic well within a frequency cell, but are quasi-periodic close to the cell boundaries, as seen in (c). In the case of the natural three-dimensional transition at higher Reynolds numbers, the appearance of vortex dislocations is not, in general, periodic as in the above example, but seems to be random in time and space.

Figure 5. *Natural formation of a symmetric "vortex dislocation" as a fundamental part of the transition process, Re=210*

These "vortex dislocations" appear when there is a local phase variation of the shedding, and these are found when locally a part of a vortex moves out of phase with the vortex formation to each side. The photograph shows a symmetric "vortex dislocation" recently formed in the near wake of the cylinder, and travelling downstream. Flow is upwards, and the horizontal cylinder is shown as the thick white line at the bottom

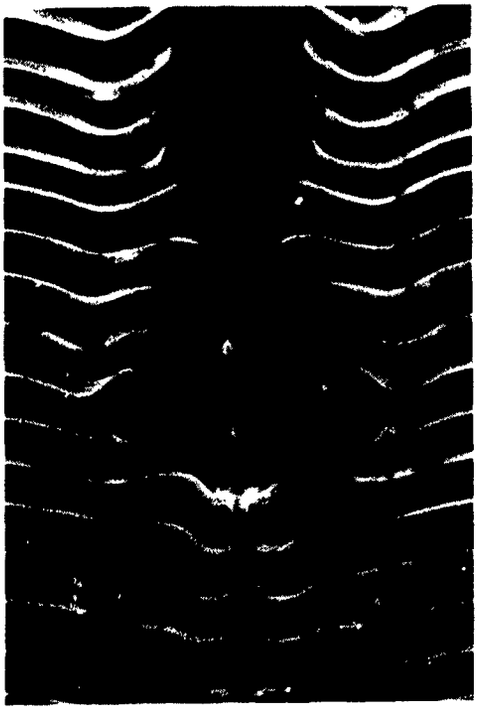

Figure 6. *Forced formation of symmetric "vortex dislocations" (large-scale A structures).*

The colour visualisation shows the formation of a vortex dislocation at a low frequency. The large-scale A structure is forced to occur in the wake of a cylinder, due to the presence of a small ring disturbance on the cylinder surface. This generates a slightly lower frequency at a local spanwise position (marked by the yellow dye), which causes the vortices behind the disturbance to dislocate from those vortices to either side (seen as the almost-horizontal green lines to each side). Flow is upwards, and the vertical extent of the photographs is around 60 diameters. (Re=120).

Striking differences in the character of the wake between the laminar and the transition regimes can be seen in Figure 3 and 4. The transverse profile of u' fluctuations for x/d=30 in Figure 3(a) when there is laminar shedding (Re=152) shows two peaks corresponding to the two organised rows of laminar vortices travelling downstream, whereas the turbulent case of Re=183 shows much larger overall fluctuation energy with a maximum in the wake centre. Clearly, the character of the turbulent fluctuation profile is very different from the laminar profile. Figure 3(b) shows that the energy (which is related to u'_{rms}) decays downstream much slower in the three-dimensional (turbulent) shedding case than for the laminar case (which decays exponentially beyond about x/d=10). These differences correspond in Figure 4 with the much larger velocity fluctuations downstream for the transition Reynolds number (Re=183) than for the laminar case

One can see that the large fluctuations are of much lower frequency than the upstream vortex shedding frequency, and are related to the occurence of the low frequency intermittent "glitches" appearing in the time traces further upstream at x/d=10. These intermittent glitches are themselves associated with the formation of vortex dislocations (these features are discussed at length in Williamson, 1991d). In summary, it is the growth of these dislocations into massive structures downstream that causes the large velocity fluctuations at low frequency, and the relatively slow decay of fluctuation kinetic energy as compared with the laminar wake.

Visualisation of vortex dislocations occuring in the natural wake transition are shown in Figure 5 (from laser-induced fluorescence of a cylinder wake in a computer-controlled XY Towing Tank). Dislocations can occur due to the interaction of cells of different frequency along the span causing an asymmetric type of dislocation, but a different type of dislocation can be caused when the shedding frequency along a section of the span changes relative to the frequencies on either side (i.e. if there is a local phase variation). In this case two dislocations occur side-by-side along the span to cause a large-scale symmetric structure. The dislocations spread out into the spanwise regions to either side as they travel downstream, and this spanwise "contamination" is partly associated with axial flow in the vortices when they are divided across the dislocations. The angles of spreading of such large-scale Λ-structures is typically around 10-12° (half angle).

3. PASSIVELY-FORCED FORMATION OF "VORTEX DISLOCATIONS"

Often it is found that vortical structures which occur in shear flows can conveniently be investigated by forcing them to appear in a controlled manner. An example of this is the generation of turbulent spots in a boundary layer either singly or periodically using roughness elements on the boundary surface, or by initiating an electric spark on the surface, and also by fluid injection (amongst many studies involving forcing of spots are: Schubauer and Klebanoff, 1956; Gad-el-Hak, Blackwelder & Riley, 1981; Wygnanski et al. 1976; Itsweire & Van Atta, 1984). In the present case, vortex dislocations are produced in an otherwise laminar wake (Re=120) by using a small disturbance at a local spanwise position, in the form of a ring of slightly larger diameter than the cylinder diameter. This causes locally a vortex frequency of slightly lower frequency than over the rest of the span, and induces

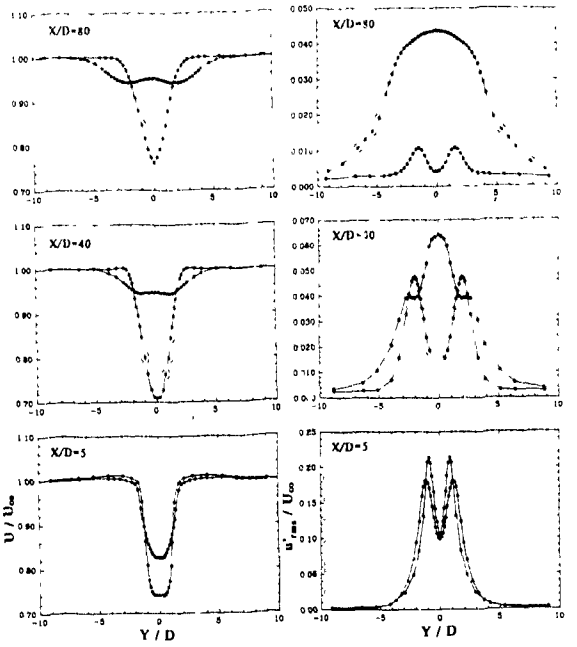

Figure 7. *Comparison of mean and fluctuating velocity profiles at different downstream distances for the normal wake and for the wake with forced vortex dislocations.*

On the left are shown mean velocity (U / U_∞)profiles in the laminar wake (solid symbols), and in the path of the vortex dislocations (open symols). There is a marked reduction in momentum defect in the case of the wake with dislocations. On the right are shown corresponding fluctuating velocity (u'_{rms} / U_∞) profiles. The growth of the large peak in the centre of the wake is associated with the growth of the large-scale Λ-structures or vortex dislocations, as we travel downstream. The profiles in the central figure are markedly similar to those found when the wake undergoes natural 3-D transition from the laminar state (see Figure 3(a))

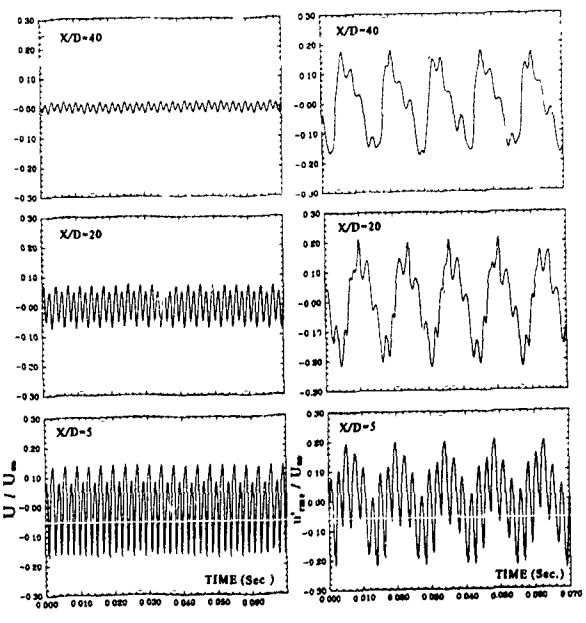

Figure 8. *Comparison of velocity fluctuations at different downstream distances for the normal wake and for the wake with forced vortex dislocations.*

On the left are shown velocity fluctuations that rapidly decay downstream for the normal wake, whereas for the wake with dislocations (on the right) there is a large growth of oscillation energy at the low dislocation frequency at the expense of the higher vortex shedding frequency. These differences in wake fluctuations are similarly observed when the wake undergoes natural 3-D transition from the laminar state (see Figure 4).

frequency than over the rest of the span, and induces "symmetric" vortex dislocations to be produced periodically at a low beat frequency. A typical large-scale structure formed from a dislocation can be seen in Figure 6, travelling downstream and spreading out spanwise. Each of the white almost-horizontal lines (to each side of the large dislocation) marks a primary vortex shed by the cylinder. It can be seen that this large structure has good similarity with the natural dislocation in Figure 5.

A comparison is shown in Figure 7 of mean and fluctuating velocity profiles between a position in the wake of the disturbance (i.e. within the path of large-scale dislocations) and a position outside the dislocation region (i.e. within a laminar vortex wake at this Reynolds number). The mean velocity profile in the wake affected by the dislocation has a much lower momentum defect, as compared with the normal wake. A particularly interesting comparison can be made for the fluctuation profiles. Upstream, the profiles both within and outside of the dislocation region are similar (although the energies are associated with slightly different frequencies). However, downstream at x/d=40, the fluctuation profile within the dislocation shows a much higher overall energy compared with the normal wake profile, and shows a large maximum at the wake centre, rather than the two peaks (associated with the two rows of vortices) at the sides of the normal laminar wake. At this point, we can see that the character of the change from the laminar wake to that wake involving the dislocations is very similar to the change from the laminar wake to the natural 3-D transition wake found earlier in Figure 3(a). Further downstream at x/d=80, Figure 7 shows that the fluctuations in the path of the large-scale dislocation structures becomes almost an order of magnitude larger than those in the normal laminar wake !

A further comparison of wake velocity fluctuations in Figure 8 shows that the large fluctuation energy found for the wake profiles in the previous Figure 7 is directly associated with the growth of low frequency oscillations. These oscillations are at a beat frequency and correspond with the periodic passage downstream of the large-scale vortex dislocations. It can be seen again that there is a similarity (Figs 4 and 8) between the effects of these forced structures and the effects of natural transition where, in both cases, the large oscillations are due to low-frequency vortex dislocations.

Other comprehensive details and measurements concerning the influence of vortex dislocations, primarily for the forced case, have been included in Williamson (1991c), and where in particular they have an effect on the natural 3-D transition process, such dislocations are discussed in detail in Williamson (1991d).

4. CONCLUSIONS

The present work shows that the natural three-dimensional transition in the wake of a bluff body involves not only the two different modes of shedding whereby small-scale streamwise vortex structures are formed, but also involves the formation of vortex dislocations, which can grow downstream into much larger-scale "spot-like" structures. These dislocations are responsible for the large low-frequency oscillations in the time traces of velocity fluctuations, and for the much slower decay of turbulent energy as the wake travels downstream, as compared with a laminar wake.

The character of the 3-D transitional wake involving *natural dislocations* is found to be distinctly similar to that of a wake involving *passively-forced dislocations* induced by a small disturbance. These similarities are evident both from flow visualisation and from measurements of wake velocity.

It appears that there are similarities in the occurence of vortex dislocations in the natural transition of the wake with those stuctures which are to be found in the free shear layer, and it seems that such structures play a not insignificant part in the process of 3-D turbulent transition in shear flows in general.

Acknowledgements: The author would like to thank Kristen Gledhill at Cornell for her most efficient help in organising some of the plots of data. This work was supported by an O.N.R. Contract No. N00014-90-J-1686, as part of the "Bluff Body Wake Vortex Dynamics" Accelerated Research Initiative.

REFERENCES

BEARMAN, P W & SZEWCZYK, A 1991 Effects of 3-D imposed disturbances on bluff body near wake flows Presentation at O N R Workshop on Bluff Body Wake Dynamics, Arizona Sate University, Tempe, Arizona

BROWAND, F.K. & HO, C.-M 1987 Forced unbounded shear flows *Nuclear Physics B (Proc Suppl.)*, 2, 139

BROWAND, F K & PROST-DOMASKY, S.A 1988 Technique for acoustic excitation of separated shear flows: preliminary results A S.M E Winter meeting, Chicago, Illinois

BROWAND, F.K. & PROST-DOMASKY, S A 1989 Experiment on pattern evolution in the 2-D mixing layer To appear in *New trends in nonlinear dynamics and pattern forming phenomena* (ed P Coullet & P Huerre), NATO ASI Series 8, Plenum, New York

BROWAND, F.K. & TROUTT, T.R 1985 The turbulent mixing layer geometry of large vortices *J Fluid Mech* 158, 489

EISENLOHR, H 1986 Investigations of the wake of a plate parallel to the flow with a blunt trailing edge (In German) Diplom Thesis, Bericht 3/1986, Max-Planck-Inst fur Stromungsforschung, Gottingen

EISENLOHR, H & ECKELMANN, H 1989 Vortex splitting and its consequences in the vortex street wake of cylinders at low Reynolds number *Phys. Fluids*, A1, 189.

GAD-EL-HAK, M., BLACKWELDER, R.F & RILEY, J.J 1981 On the growth of turbulent regions in laminar boundary layers. *J Fluid Mech.* 110, 73

GASTER, M. 1969 Vortex shedding from slender cones at low Reynolds numbers *J Fluid Mech* 38, 565

GASTER, M. 1971 Vortex shedding from circular cylinders at low Reynolds numbers *J Fluid Mech.* 46, 749

GERICH, D & ECKELMANN, H. 1982 Influence of end plates and free ends on the shedding frequency of circular cylinders *J Fluid Mech.* 122, 109

GRIFFIN, O.M. 1988 The effects of current shear on vortex shedding Marine Technology Division Report, Naval Research Laboratory

ITSWEIRE, E.C. & VAN ATTA, C.W. An experimental investigation of coherent substructures associated with turbulent spots in a laminar boundary layer. *J Fluid Mech.* 148, 319

JESPERSON, D C. & LEVIT, C 1991 Numerical simulation of flow past a tapered cylinder AIAA Paper 91-0751 29th Aerospace Sciences Meeting, Reno, Nevada.

KOENIG, M., EISENLOHR, H., ECKELMANN, H. 1990 The fine structure in the S-Re relationship of the laminar wake of a circular cylinder *Phys Fluids* A 2, 1607.

LEWIS, C & GHARIB, M. 1991 An experimental exploration of three-dimensionality in the laminar wake of a stepped cylinder Submitted for publication

MAULL, D. J. & YOUNG, R. A. 1973 Vortex shedding from bluff bodies in a shear flow. *J. Fluid Mech.* 60, 401

NYGAARD,K.J. & GLEZER,A. 1990 Core instability of the spanwise vortices in a plane mixing layer. *Phys Fluids* A 2, 461

PAPANGELOU, A., & GASTER,M 1991 Private Communications, Cambridge University

PICIRILLO, P.S., & VAN ATTA, C W. 1991 An experimental study of vortex shedding behind a linearly tapered cylinder at low Reynolds number Submitted for publication

ROSHKO, A 1954 On the development of turbulent wakes from vortex streets *NACA Report* 1191.

SCHUBAUER, G.B. & KLEBANOFF, P.S. 1956 Contributions on the mechanics of boundary layer transition *NACA Report* 1289.

VAN ATTA, C., GHARIB, M. & HAMMACHE, M. 1988 Three-dimensional structure of ordered and chaotic vortex streets behind circular cylinders at low Reynolds Numbers. *Fluid Dynamics Research*, 3, 127

WILLIAMSON, C.H.K. 1988a Defining a universal and continuous Strouhal-Reynolds number relationship for the laminar vortex shedding of a circular cylinder *Phys. Fluids*, 31, 2742.

WILLIAMSON, C.H.K. 1988b The existence of two stages in the transition to three-dimensionality of a cylinder wake *Phys Fluids*, 31, 3165

WILLIAMSON, C.H.K. 1989a Oblique and parallel modes of vortex shedding in the wake of a circular cylinder at low Reynolds numbers *J Fluid Mech* 206, 579.

WILLIAMSON, C.H.K. 1989b Generation of periodic vortex dislocations due to a point disturbance in a planar wake", In the Gallery of Fluid Motion, *Physics of Fluids A*, 1, 1444

WILLIAMSON, C.H.K. 1991a 2-D and 3-D aspects of the wake of a cylinder, and their relation to wake computations, Proc of Conf on Vortex Dynamics and Vortex Methods ,AMS-SIAM *Lectures in Applied Mathematics*, in press

WILLIAMSON, C.H.K. 1991b Three-dimensional aspects and transition in the wake of a cylinder, *7th Symposium on Turbulent Shear Flows*, ed.F Durst & J. Launder, Springer-Verlag, Berlin. in press

WILLIAMSON, C.H.K. 1991c The formation of spot-like A-structures caused by vortex dislocations in a wake. Submitted to *J. Fluid Mech*

WILLIAMSON, C.H.K. 1991d The onset of three-dimensionality in the wake of cylinders, in preparation for submission to *J. Fluid Mech*

YANG, HUERRE,P., COULLET, P. 1989 A 2-D model of pattern evolution in mixing layers, *New Trends in Nonlinear Dynamics and Pattern Phenomena*, ed P.Coullet & P.Huerre, NATO ASI Series 8, Plenum, New York.

EIGHTH SYMPOSIUM ON
TURBULENT SHEAR FLOWS
Technical University of Munich
September 9-11, 1991

The route to turbulence in nominally two-dimensional free shear flows

George S. Triantafyllou

The Benjamin Levich Institute for Physico-Chemical Hydrodynamics
Mechanical Engineering, The City College of New York
New York, New York 10031, USA

George Em. Karniadakis

Department of Mechanical and Aerospace Engineering
Princeton University, Princeton, N J 08544, USA

Abstract

The transition to turbulence in the wake of a nominally two-dimensional circular cylinder is studied numerically, through direct simulation of the three-dimensional Navier Stokes equations using a spectral element method The computations are conducted for three representative Reynolds numbers Re=300, 333 500 It is found that the transition process consists of a succession of period doublings At Reynolds number 300 the first period-doubling bifurcation has occured At Re=333, a second period doubling bifurcation has occured, whereas at Reynolds number 500 the wake has become chaotic The occurence of the period-doubling bifurcations is only possible in a flow with three-dimensional structure, because of the coexistence of different accessible flow states with symmetric spanwise structures It is proposed that period-doubling is a natural route to chaos for nominally two-dimensional flows with an absolute instability mechanism

1 Introduction

Sheared flows away from no-slip boundaries, such as wakes, jets and free shear layers, are often referred to as "free" shear flows Because of the inflectional form of their basic velocity profile, such flows are strongly unstable and undergo transition into turbulence at relatively low Reynod numbers (considerably lower than say, channel flows) The wakes of bluff objects in particular are known to undergo a transition into turbulence in the Reynolds number range 200-400 (Bloor, 1964) It is at the lower part of this range (Reynolds number around 200) that three-dimensionality also appears, so experiments suggest there is clear relation between the two Additional indirect support for this relation has been provided by two dimensional numerical simulations which show in the same Reynolds number range periodic vortex shedding It appears therefore that three-dimensionality somehow triggers the transition into turbulence, and the two key questions are (a) how the three-dimensionality is initiated and (b) how the three-dimensionality triggers the transition process

In recent years it has been demonstrated that a better conceptual description of vortex wakes than the classical arrary of point vortices is that of a wave of vorticity, sustained from a hydrodynamic instability of the flow (Koch, 1985, Triantafyllou et al , 1986, Monkewitz and Nguyen, 1987, Hannemann and Oertel, 1989, Karniadakis and Triantafyllou, 1989) By considering an instability around the mean, rather than an initial state, this concept can be used even for turbulent wakes (Triantafyllou et al 1986) As the instability of a two-dimensional mean flow invariably creates two-dimensional flow states (Triantafyllou, 1990), it is reasonable to seek the source of three-dimensionality in a secondary instability of the saturated two-dimensional vortex street More specifically, the saturated two-dimensional vortex street is stable to two-dimensional perturbations in the Reynolds number range 200-500, as it can be inferred from the nearly perfect periodic behaviour predicted by two-dimensional simulations It becomes however unstable to three-dimensional perturbations, once a certain critical value of the Reynolds number is exceeded This has been demonstrated numerically by Karniadakis and Triantafyllou 1990, through direct numerical simulation of the three-dimensional Navier-Stokes equations The Reynolds number value for the onset of the secondary instability was found to be around 200, in agreement with experimental observations about the appearnce of three-dimensionality (Williamson, 1989) The secondary instability of the wake is therefore similar to the ones observed in other flows (see for example, Pierrehumbert and Widnall, 1981, Orszag and Patera, 1983), but with the important difference that the final three-dimensional asymptotic state created by the secondary instability is periodic in time (which is not always the case with the other cited studies) We may conclude therefore that after the appearance of three-dimensionality additional bifurcations are required to render the wake turbulent

The purpose of the present study is to report on a numerical study of the transition process in a two-dimensional wake, which can be considered as a case-study, with potential extensions to other free shear flows The main issues which are discussed here are (i) the route to turbulence, i e whether it follows any of the so-called "universal routes" to chaos, and (ii) why the occurence of these bifurcations is tied to the three-dimensional structure of the flow

2 Numerical Method and Results

We consider an incompressible flow of speed U_∞ past a cylinder of diameter D the kinematic viscosity of the fluid is ν The system of coordinates has its x axis parallel to the stream its z axis parallel to the span, and its y axis perpendicular to the other two The governing equations are the three-dimensional Navier Stokes and continuity equations, written in the following non-dimensional form

$$\frac{\partial \mathbf{v}}{\partial t} + \mathbf{N}(\mathbf{v}) = -\nabla p + R^{-1}\nabla^2 \mathbf{v} \tag{1}$$

$$\nabla \mathbf{v} = 0 \tag{2}$$

where $R = U_\infty D/\nu$ is the Reynolds number, $\mathbf{v}$ is the velocity vector (non-dimensionalized with respect to U_∞, p the non-dimensional pressure and the operator N is defined as

$$N(\mathbf{v}) = \frac{1}{2}\left(\mathbf{v}\nabla\mathbf{v} + \nabla(\mathbf{v}\mathbf{v})\right) \tag{3}$$

The Navier-Stokes equations have been written in the above form for better aliasing control (Honuti 1987)

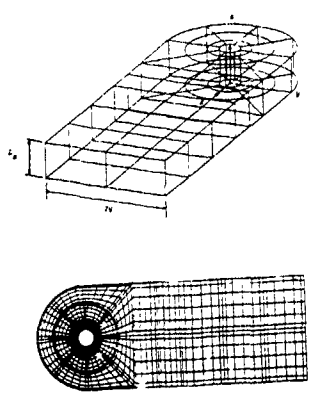

Figure 1: Top Perspective view of the computational domain Bottom Spectral element mesh used for the Fourier modes

The computational domain is shown in figure 1 The upstream boundary lies at a distance of six radii from the center of the cylinder; the downstream boundary at twentyfive radii The side boundaries are twelve radii apart, and the spanwise dimension was taken to be equal to pi (=3 14) radii At the upstream boundary

uniform flow conditions are applied whereas at the downstream boundary mixed Neumann/viscous sponge" (Tomboulides et al 1991) boundary conditions are implemented to eliminate spurious numerical instabilities At the other two boundaries periodicity conditions are assumed

In the spanwise direction because of the homogeneity of the geometry we expand the velocity and pressure field into a Fourier series Each coefficient of the series is a function of x and y, is solved for using a spectral-element methodology (For a discussion of spectral elements see Patera 1984 Korczak and Patera, 1986 and Karniadakis, 1989) Sixteen Fourier modes were used in the spanwise direction, and thirty four spectral elements with sixth and eight order interpolants With this choice of parameters the required CPU time on a single processor CRAY Y/MP was typically two seconds for each time step Since each period of vortex shedding consisted of about 795 time steps, reaching the asyptotic state of the flow required several hours of CPU time

In order to study the transition process, the flow was computed at three representative Reynolds numbers 300, 333, and 500 The first two Reynolds numbers lie in the range that experiments have characterized as "transitional", whereas the third Reynolds number lies in the range that experiments characterize as "turbulent" Thus the idea is to confirm that even in a perfectly two-dimensional geometry (like the one of figure 1) the wake will be turbulent at Reynolds number around 500, and to observe some characteristic intermediate stages of the transition to turbulence process Although computation of the flow at many more Reynolds numbers would ideally be desirable, the enormous amount of required computation and practical limitations of computer resources led to the above choice

At each Reynolds number the two-dimensional vortex street was computed first and three-dimensional noise was subsequently introduced to trigger the secondary instability of the vortex street (which is present after Reynolds number 200) Then the computation was carried out over several periods of vortex shedding and power spectral densities of the velocity fluctuations were used to characterize the temporal behaviour of the flow Streamline-plots were used to study the spatial structure of the flow As mentioned in the introduction, for Reynolds numbers close to 200 the flow asymptotically settles into a three-dimensional oscillation, which is periodic in time (Karniadakis and Triantafyllou, 1990) For the sequence of Reynolds numbers considered here however the final asymptotic state in the wake exhibited an increasingly complex behaviour, which became chaotic at Reynolds number 500

More specifically at Reynolds number 300 a period-doubling bifurcation occured more visible in the spanwise velocity component This can be seen in the spectra of the velocity fluctuations in the near wake (figure 2) Then at Reynolds number 333 a second period doubling followed (figure 3) Finally when the Reynolds number was further increased to 500, broad-band spectra were obtained indicative of a chaotic behaviour (figure 4) At this Reynolds number time-traces of the velocity become ariodic, with intermittent periods of organized motion (figure 5) Figures 2 3, and 4 show the specta of the velocity fluctuations of the same point in the near wake for the three values of the Reyolds number (Similar behaviour is observed in any other location in the computational domain) Figures 2, 3, and 4 suggest therefore that the flow in a two-dimensional wake follows the period doubling route to chaos How closely does the sequence of period-doublings follows the universal route as described by Feigenbaum, 1978, i e whether a complete cascade of period doublings occurs, and whether Feigenbaums (1978, 1979) scaling laws are satisfied, is a question that can not be answered based on the numerical results presented here In fact the required amount of computation for a systematic investigation is so large, that it seems unlikely that it will be performed in the immediate future It is however a very interesting fundamental question and a real challenge for further research

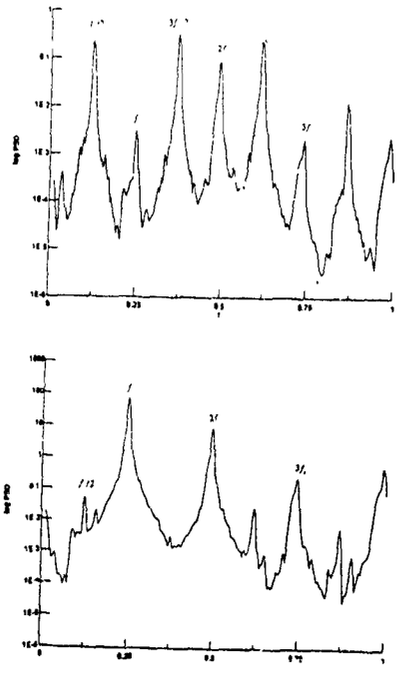

Figure 2: Power spectral density of the spanwise velocity component (top), and the streamwise velocity component (bottom) in the near wake at Re=300 The presence of the subharmonic is visible in both

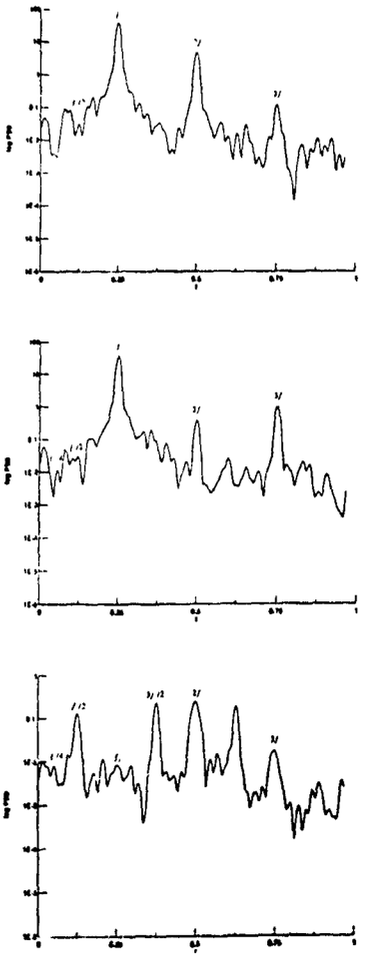

Figure 3: Power spectral density of the three velocity components at Re=333 From top to bottom the three components u,v,w A second subharmonic is present (corresponding to four times the Strouhal period)

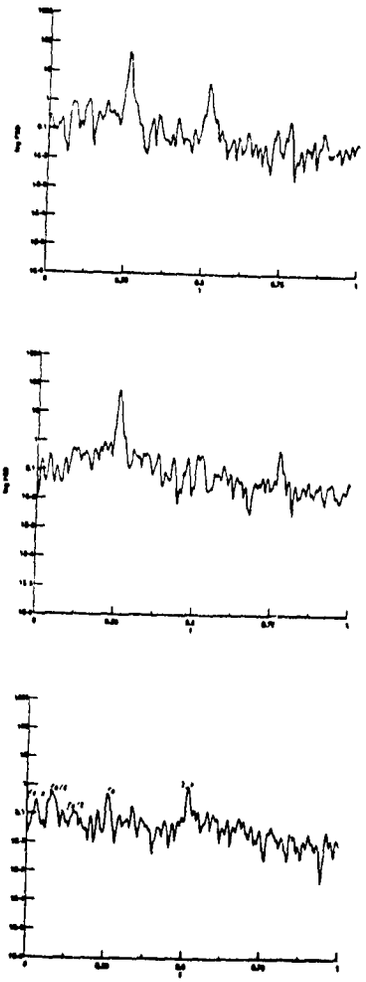

Figure 4: Power spectral density of the three velocity components at Re=500, indicative of a chaotic behaviour

The period doubling bifurcations are possible only in a three-dimensional flow, since two-dimensional simulations show at the range of Reynolds numbers a periodic behaviour The reason for this seems to be that for a given Reynolds number in the transitional regime several three-dimensional states are possible with different spanwise structure, and the flow can alternate between them multiplying (doubling, quadrupling, etc) its period The process of physically identifying the flow states that allow the succession of period doublings is not an easy task In the next section we discuss the physics of the first period doubling bifurcation, which can be considered to be the most significant, since it initiates transition

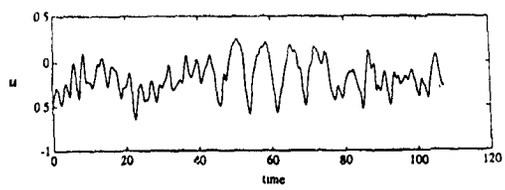

Figure 5: Typical time-trace of the streamwise velocity component at Re=500 exhibiting intermittent organized behaviour interchanged with intervals of "random" behaviour

3 Discussion

Our interpretion the period doubling bifurcation relies on the consideration of the oscillatory part of the flow as the instability mode of the time averaged part of the flow Once the secondary instability has been triggered and the wake settles into its three-dimensional mode of self-oscillation, the time-average flow acquires modulations along the spanwise direction We can then think of the fluctuating part of the flow as the absolute instability mode of this modulated time-average flow For a slowly varying modulation of the time-average flow, a quantitative way to represent its spanwise modulation is by plotting at each location the growth-rate of the local two-dimensional perturbation, say $\omega_i(z)$ This will have a variation with z like the curve (0) in figure 6 Then it can be shown (Triantafyllou, 1990) that the spanwise structure of the instability mode is related to that of the time-average flow in the manner sketched in figure 6 The instability mode (curve (a) in figure 6) has twice the wavelength of curve (0) and the maximum spanwise inclination in absolute value occurs where $\omega_i(z)$ has a maximum, likewise, zero spanwise inclination occurs where $\omega_i(z)$ has a minimum The justification is based on Squire's transformation

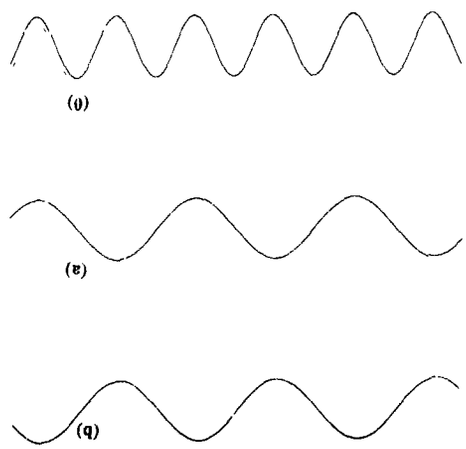

Figure 6: Sketch of the spanwise structure of a three-dimensional wake Curve (0) variation of the local growth rate of two-dimensional perturbations with z Curves (a), (b) Spanwise structure of the two possible instability modes corresponding to the time-average flow with curve (0)

We note that the variation of $\omega_z(z)$ is followed very closely by the variation of the u component along the centerline $y=0$, thus a numerical confirmation of the analytical argument (data from Karniadakis and Triantafyllou 1990 for Reynolds number 225) can be seen in figure 7 where the spanwise variation of the time average and the fluctuating parts of u are plotted The fact that the fluctuating part of u has twice the spanwise wavelength of the time-averaged part is clearly seen Moreover the maximum spanwise inclination of the fluctuating flow occurs indeed where the average flow is most negative and $\omega_z(z)$ has therefore a maximum likewise the slope of the fluctuating part of u is zero where the average u is least negative, and $\omega_z(z)$ has therefore a minimum The argument of the previous paragraph describes correctly the relation between the spanwise structure of the time-average and the fluctuating part of the three-dimensional flow in the wake It turns out that this relation is crucial for the occurence of period-doubling bifurcations, as discussed below

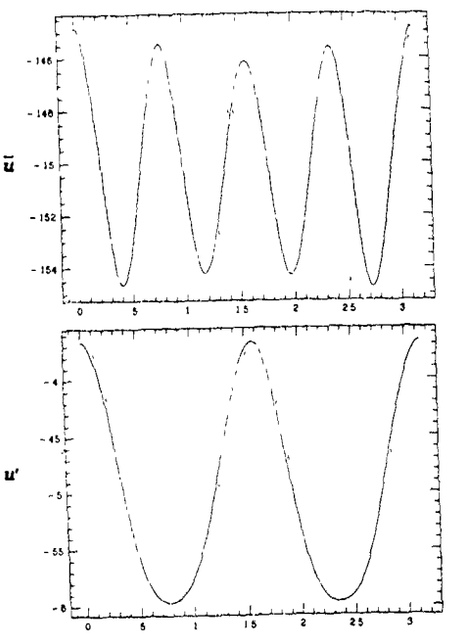

Figure 7: Top Spanwise variation of the time average streamwise velocity component at Re=225 (this closely approximates curve (0) in figure 1) Bottom Spanwise variation of the fluctuating streamwise velocity component at Re=225, confirming the theoretical result of figure 6

Because of the symmetry of the flow to rotations in the x-y plane, a second instability mode sketched as curve (b) in figure 6), is possible for the same time-average flow (0) Mode (b) is identical with mode (a), except that at each point they have spanwise inclinations of opposite signs The fact that there are two possible instability modes of the time-average flow suggests that there are also two possible asymptotic states for the flow We assume that the two asymptotic states will have a similar spanwise structure as the curves (a) and (b) sketched in figure 6, although not necessarily as perfectly sinusoidal as these two curves Since there are two attainable flow states, the flow in the wake can alternate between the two doubling its period In physical space, the flow will produce a vortex filament of type (a), then one Strouhal period later will produce a filament of type (b) then another Strouhal period later a filament (a) will appear again and so on The time that elapsed between two (a) filaments is therefore twice the Strouhal period We note that for a two-dimensional time-average flow, the only possible filaments are straight lines, so period-doubling can not occur according to this scenario This is consistent with the fact that two-dimensional simulations predict a periodic vortex street for this Reynolds numbers range Moreover, the two states in figure 6 differ only in the sign of the spanwise velocity component w When state (a) has positive w, state (b) has negative w and vice-versa Consequently, in a "phase-space", where the two states (a) and (b) are represented each by one closed trajectory, the two trajectories are symmetric around the $w=0$ plane

Numerical confirmation of the presence of the two states at Reynolds number 300 can best be made by plotting the trajectory in the "phase-space" This is done in figure 8, where the two connected trajectories can clearly be seen, consistently with the argument given above We note that at Reynolds number 225, where the period doubling has not occured, the phase-space plots contains only one of the two curves (see Karniadakis and Triantafyllou, 1990) The reason is that although both states are possible, only one of the two can be realized The two trajectories intersect at a finite angle, so the system would require infinite acceleration in order to switch from one to the other We can infer therefore that the first period doubling occurs when the two trajectories "merge" at the points where they both intersect the $w=0$ plane forming a single trajectory with twice the period The "merging" here means that they both become tangent to the $w=0$ plane, allowing the system to switch from one trajectory to the other

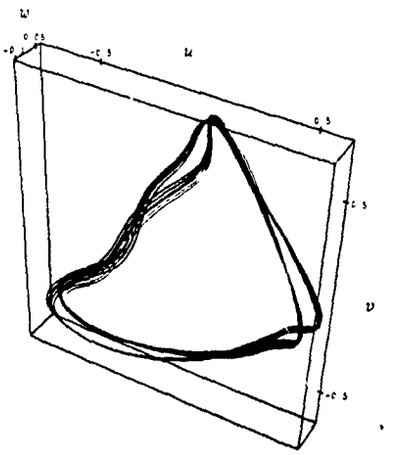

Figure 8. "Phase-space" plot of (u-v-w) at Re=300, showing the presence of two states in the flow (the two connected trajectories)

The explanation for the rest of the period doublings is not known currently One could speculate of course that "similar" symmetries exist which allow the coexistence of several states with different spanwise structures, but further investigation is required to identify those states (Interestingly, in a recent study Nuzzi et al., 1991, have experimentally observed a cascade of period doublings in the wake behind a vibrating nonuniform cylinder, their flow visualization technique shows indeed the switching between several different flow states, which seems to support the intuitive argument given here) The unambiguous conclusion that can be drawn however is that in a nominally two-dimensional wake three-dimensionality triggers transition by opening the route to period-doubling It seems therefore reasonable to anticipate that period doubling is the natural route to chaos for other two-dimensional flows with an absolute instability mechanism

Acknowledgements

The financial support of the Office of Naval Research, Contracts N00014-87-K-0356, N00014-90-J-1215, and N00014-91-J-1373 is greatly appreciated

References

Bloor, S 1964 J Fluid Mech 19, p 290

Feigenbaum, M J , 1978, J Stat Phys , 19 p 25

Feigenbaum, M J , 1979, Phys Lett , 74A(6), p 375

Hanneman K and Oertel, H , 1989, J Fluid Mech 199, p 55

Honuti, K , 1987, J Comput Phys , 71 p 343

Karniadakis, G E 1989, Appl Num Meth , 6, p 85

Karniadakis, G E and Triantafyllou G S , 1989, J Fluid Mech 199, p 441

Karniadakis G E and Triantafyllou G S , 1990, AIAA paper 90-0113

Koch, W , 1985, J Sound Vibr 99, p 53

Korczak, K Z , and Patera, A T , 1986, J Comput Phys 62 p 361

Monkewitz, P A and Nguyen, L , 1987, J Fluids Struct , 1, p 165

Nuzzi, F , Magness, C and Rockwell, D , 1991, submitted for publication

Orszag, S A and Patera, A T , 1983, J Fluid Mech , 128, p 347

Patera, A T , 1984, J Comput Phys , 54, p 468

Pierrehumbert and Widnall, 1981, J Fluid Mech , 114, p 59

Tomboulides, A G Israeli, M , and Karniadakis G E , 1990, J Sci Computing, 4, p 291

Triantafyllou, G S , 1990, in Proceedings, Symposium on NonSteady Fluid Mechanics, ASME, FED, vol 92, Toronto, Canada, p 395

Triantafyllou, G S , Triantafyllou M S , and Chryssostomidis, C , 1986 J Fluid Mech , 170, p 461

Williamson C H K , 1989, J Fluid Mech 206, p 579

EIGHTH SYMPOSIUM ON
TURBULENT SHEAR FLOWS
Technical University of Munich
September 9-11, 1991

ABSOLUTE INSTABILITY IN VARIABLE DENSITY PLANE JETS

J-L. HARION, R. RIVA, G. BINDER, M. FAVRE-MARINET

Institut de Mécanique de Grenoble
BP53X 38041 Grenoble Cedex-FRANCE

ABSTRACT

The stability of two-dimensional helium-air jets has been investigated experimentally. Velocity fluctuation spectra and Schlieren images show that the jet is absolutely unstable in definite ranges of velocity and ratio of jet to ambient fluid density S. A fixed frequency is associated to the lower range of velocity and no scaling with the jet parameters could be found for this case. In the higher range, the frequency of the fluctuations scales with the jet velocity. The absolute instability disappears when S>0.2, a limit which is far from the predictions of stability theory. Visualizations confirm the development of strong side jets when the flow becomes absolutely unstable.

AIM OF RESEARCH

If the concept of absolute or convective instability is not new, the search for conditions under which shear flows such as jets may actually become absolutely unstable has only been undertaken in the past few years. The ideas are, for instance, described in the book on Hydrodynamic Stability by P.G. DRAZIN & W.H. REID (1) first published in 1981 but no concrete examples of absolutely unstable flows are given.

The first suggestion that jets less dense than the ambient fluids are absolutely unstable was made in 1985 by HUERRE and MONKEWITZ (2). Since then inviscid parallel flow computations for variable density jets by MONKEWITZ and coworkers (3,4) have demonstrated that round as well as plane jets can be absolutely unstable when the density ratio $S=\rho_j / \rho_\infty$ is less than the critical values respectively equal to 0.7 and 0.95. The other control parameter in their computations is the thickness of the shear layer δ_ω.

Experimental evidence of absolute instability in axisymmetric jets was provided nearly at the same time as the theory by SREENIVASAN & al (5) or shortly after by MONKEWITZ & al (6) and by RIVA & al (7,8). The three experiments demonstrate that in certain ranges of S and δ_ω the power spectra are line dominated as is expected when the flow is absolutely unstable since it should then behave as an oscillator. They also reveal that as a consequence of absolute instability, strong intermittent side jets may be generated. There are, however, differences between the experimental observations mainly about the critical Reynolds number above which absolute instability may occur and about the critical value of the density ratio S. Furthermore in reference 8 it was found that for a given S there are several absolute-convective transitions when the velocity is increased, suggesting the existence of several distinct regions of absolute instability in the S,Re (or δ_ω)-plane, a feature which theory has not shown so far.

The absence of any published experimental results on plane jets with variable density has motivated the present investigation, but it should be added that such an experiment is also announced in reference 4. The aim is to demonstrate the existence of absolute instability in this flow, to determine the ranges of the control parameters where it occurs and to find out whether side jets do also exist in this geometry.

It should be mentioned that variable density jets occur in flows of practical importance as in engine exhaust or in combustion where the density difference may first be due to the different nature of gases (H_2 and O_2 as in some rocket engines) and later on to the temperature difference.

APPARATUS AND FLOW CONDITIONS

- Jet : slot width d variable from 1 to 11 mm.
  - Exit velocity : U_j
  - Reynolds number based on the initial jet viscosity : $Re = U_j d / \upsilon_{\infty}$

Most measurements were obtained in the following conditions :

- Slot d = 3.7 mm
- aspect ratio : 13.5
- End plates
- $7.5 < U_j < 20$ m/s
- Nozzle contraction : 28
- Vorticity thickness : $\delta_{\omega} \approx 8.8\ Re^{-1/2}$ nondimensionalized by d/2
- Turbulence level at exit ≈ 0.16%
- No forcing is applied

- 2D checks showed mean velocity variations in mid-plane of less than 0.4%

- Density variations are produced by concentration changes of air-helium mixtures (the ambient fluid is air). The mixtures are produced via a set of calibrated sonic throats.

- Measurements : microphone (dia ≈ 10 mm at x=0 and y=120 mm) and hot wire anemometers; 15 bit A/D conversion; spectra computed with 1024 points, averaged over 8 realisations. For all results presented in this paper the probe was located in the mid-plane of the nozzle exit (x=0, y=0), therefore it is sensitive to the velocity fluctuations only.

- Vizualisations : Schlieren method.

RESULTS

Probe interference effects

Microphone measurements with a probe and without probe in the same flow show that interference effects are small (Fig. 2) : the frequency of the main spectral peaks is unaffected. In some instances there may be a small influence on the signal level of the perturbations. Figure 7 shows spectra from a hot wire and from the microphone measured in same conditions. It is seen that the spectra from the two signals resemble each other very closely; in particular the same peaks are found on both and occur at the same frequencies. In order to reduce the noise level the microphone signal was filtered between 100 and 900 Hz.

Absolute/convective instability in helium/ air jets

Figure 1 shows hot wire spectra in the pure helium jet (S=0.14) and in the air jet at same Reynolds numbers. The strong contrast between the spectra is evident : there are sharp peaks of high level in the helium jet, characteristic of absolute instability and low level broad peaks in the air jet. Note that the peaks are at least two orders of magnitude (even four orders for Re=245) above the neighbouring level. The sound emitted by the absolutely unstable jet is easily perceived directly by ear and a fortiori from the amplified microphone signal played back through a loudspeaker. Video recordings were performed by illuminating the flow with a flash driven by the microphone signal. On the movies, symmetric structures which develop near the nozzle are observed. Since these initial structures are perfectly synchronized with the microphone signal, it may be deduced that they are responsible for the high sound level.

It was checked that the absolutely unstable mode is of the varicose type as predicted by the theory (4). This was done by comparing the signal from two hot wires placed symmetrically with respect to the mid-plane (the two signals are in phase). This is also clearly shown by the vizualisations (fig.6-7).

Side jets

Vizualisations of Fig. 6 and 7 show that side jets also occur in the plane jet but these are less spectacular than in the round jet. Video recordings with sound from the microphone show that when the velocity is increased and the jet becomes absolutely unstable, the development of side jets coincides with the increase in sound level. Hence, side jets are concomitant with absolute instability. It may be remarked that the development of the side jets coincides with the loss of coherence of the initial structures.

Evolution of instability with velocity, S=0.14

On Fig 3 which displays spectra for increasing velocity the following observations are made :

- There is a sharp transition to absolute instability between 7.5 and 7.6 m/s.
- The frequency of the first peak at about 250 Hz is nearly independent of U_j. It nearly disappears at 11 and 13 m/s and emerges again at 15 m/s with a level three orders magnitude above the plateau.
- A second frequency which is not an harmonic of the previous one appears at 11 m/s. This frequency is nearly proportional to U_j. This peak reaches also a high level at U_j=15 m/s. Fig. 4 shows the evolution of the Strouhal numbers of the dominant peaks ($S_\delta = f\ \delta_{\omega} / U_j$). The curve has two branches. The lower one corresponds to the fixed frequency f_1 observed at the first transition of the jet. The second one shows that the higher frequency f_2 of instability scales very well

with vorticity thickness $\delta\omega$. On Fig. 5, the Strouhal number has been computed with the slot width d scale for comparison with the computations of YU & MONKEWITZ (4) ($\omega_{or} = (2\pi\ f\ d/2)\ /\ U_j/2$). These authors have computed the stability characteristics in terms of the density ratio S and a parameter N related to the shape of the velocity profile. N^{-1} is proportional to the shear layer thickness $\delta\omega$. In the present facility $N = 0.18Re^{1/2}$. The observed tendency for f_2 is the same as in the reference (4), but since the results given in (4) are limited to $S > 0.7$, direct comparison with our results could not be made. The opposite trend is observed for f_1; when U_j is increased, $\delta\omega$ and consequently N^{-1} decrease, whereas ω_{or} is inversely proportional to U_j. The observation of a fixed frequency when the velocity increases has not been explained at the present time.

Evolution of the instability with density ratio S

Spectra for increasing S at constant velocity U_j≈8 m/s and U_j≈15 m/s are shown on figures 6 and 7. For U_j=8 m/s, the peak in the spectrum becomes broader and its value drops sharply when S increase from 0.2 to 0.22. The same thing occurs to the main peak at U_j=15 m/s but at a lower value of S, at about S=0.16. In this case a new peak emerges at a higher frequency. The frequency of this peak shifts to higher values as S is increased. Since the viscosity changes with S ($\upsilon_{He} \approx 8\upsilon_{air}$) the shear layer thickness at the exit is also affected by the changes in S. This higher frequency mode scales roughly with δ_ω

The transition at $S \approx 0.2$ is also very clearly seen on the relative RMS levels (Fig 8) of the two signals : the level drops by a factor 5 or more through the transition. Since the flow is more unstable when it is absolutely unstable, one is tempted to conclude that the transition to convective instability occurs around $S \approx 0.2$ at these velocities. This does not agree at all with the theory (4) which predicts the transition for $S \approx 0.85$ for the values of δ_ω corresponding to the present experiments.

CONCLUDING REMARKS

There clearly are several points of disagreement between the present experimental observations and the results of the stability computations of YU & MONKEWITZ (4). The real flow is, of course, neither inviscid, nor parallel, nor without buoyancy forces contrary to the theory. Even if jet instability is essentially inviscid, one may wonder about the influence of the large difference in viscosity between the jet and the ambient fluid on the stability characteristics. It may further be noted that while the theory assumes the profiles of U_j and ρ to be the same with a finite shear layer thickness, in the experiments with different gases the ρ-profile at the exit has a true discontinuity but not the U_j-profile. Effects of mass diffusivity are, therefore, large in the initial region. These differences may, however, not be sufficient to account for the discrepancies between the theory and the present experiment. For the latter, this raises question of the influence of the features of the facility on the observed results. Some experiments have already been performed in order to find out to which extent the present observations depend upon the particular features of the facility and more are being carried out. Changes in the supply line (longer tubing, insertion of damping chamber), experiments performed by discharging a reservoir (without use of the sonic throats), changes in the inlet to settling chamber (feed through a porous plug), runs in quieter surroundings at night have produced no marked changes with the results reported here. The acoustic characteristics of the settling chamber will be investigated next. One may, however, note already that the frequency f_1 is more than an order of magnitude smaller than the organ-pipe resonant frequency.

ACKNOWLEDGMENTS

This work was supported by the HERMES R&D Program through the *Centre National d'Etudes Spatiales* and *Dassault Aviation*.

REFERENCES

(1) DRAZIN P.G. and REID W.H. 1981, "Hydrodynamic Stability", Cambridge Univ. Press.

(2) HUERRE P. and MONKEWITZ P.A. 1985, *J.Fluid Mech.* **159**, 151.

(3) MONKEWITZ P.A. and SOHN K.D 1988, *A.I.A.A. J.* **26**, 911.

(4) YU M.-H., MONKEWITZ P.A. 1990, *Phys. Fluids* **A2**,7,1175.

(5) SREENIVASAN K.R., RAGHU S. and KYLE D. 1989, *Experiments in Fluids* **7**, 309.

(6) MONKEWITZ P.A., BECHERT D.W., BARSIKOW B. and LEHMANN B. 1990, *J.Fluid Mech.* **213**,611.

(7) RIVA R., BINDER G., TARDU S., FAVRE-MARINET M. 1990, "Turbulence and Coherent Structures", Métais O. & Lesieur M., eds Kluwer Academic Publishers,113.

(8) RIVA R., BINDER G., FAVRE-MARINET M., *3rd European Turbulence Conference*, Stockholm 3-6 july 1990 Advances in Turbulence III, Springer-Verlag 1991

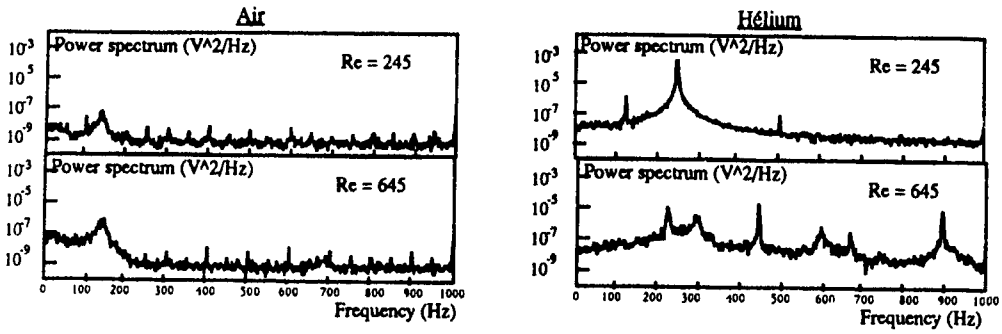

Figure 1 : Spectra in Air and He at same Reynolds numbers
Hot wire, d = 3.7 mm

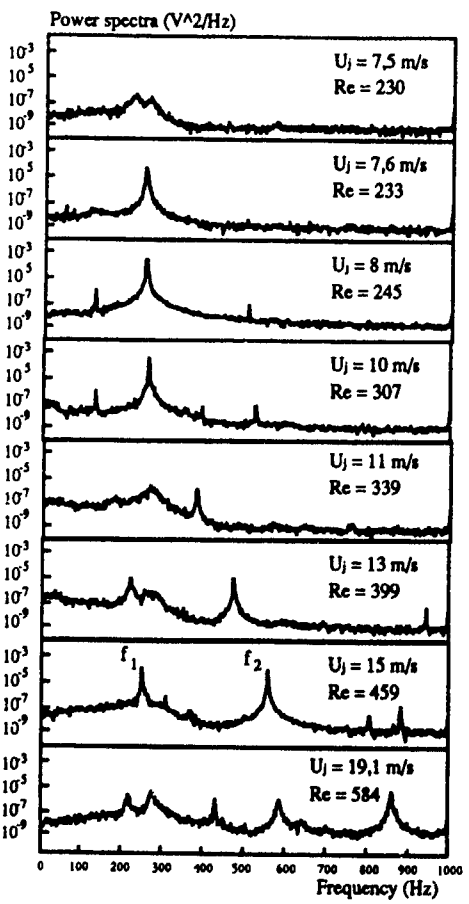

Figure 3 : Spectra in pure Helium with increasing velocity
Hot wire, d = 3.7 mm

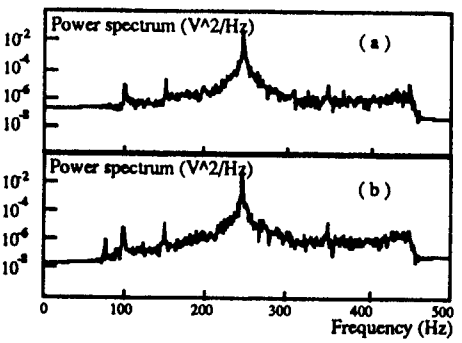

Figure 2 : Microphone signal power spectra
(a) with a probe at x=0
(b) without probe

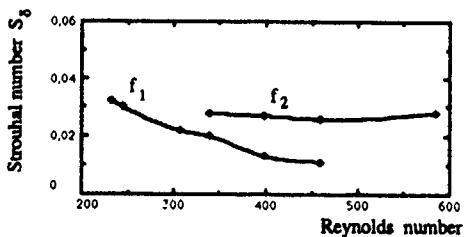

Figure 4 : Strouhal number S_δ of dominant frequencies versus Reynolds number.
Pure Helium (S = 0.14)

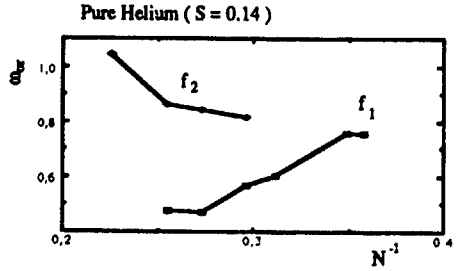

Figure 5 : $\omega_{ad} = (2\pi f d/2) / U_j /2$ of dominant frequencies versus shape parameter N^{-1}
Pure Helium (S = 0.14)

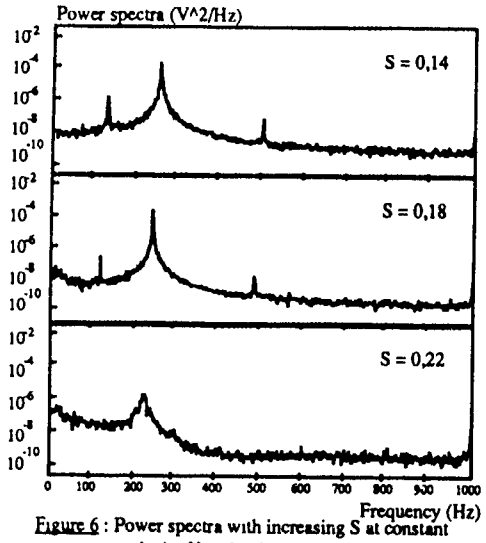

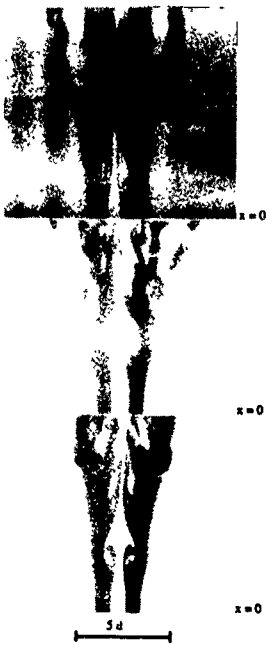

Figure 6 : Power spectra with increasing S at constant velocity U_j = 8 m/s
Hot wire, d = 3.7 mm
Schlieren visualizations
Horizontal knife edge for S =0.14
Vertical knife edge for S =0.18 and 0.22

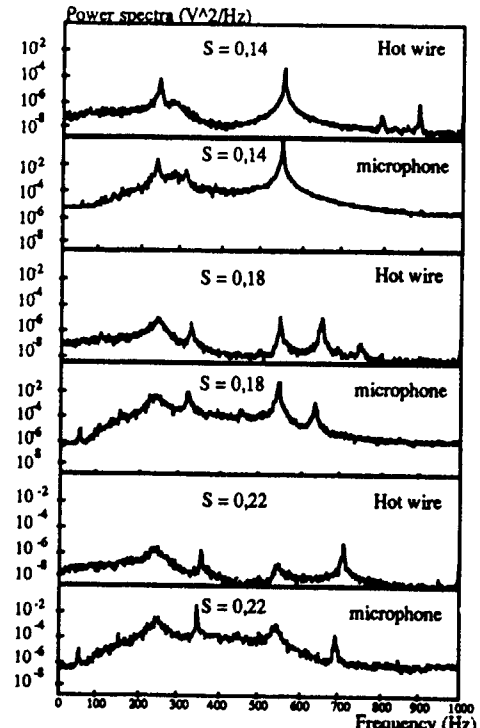

Figure 7 : Power spectra with increasing S at constant velocity U_j = 15 m/s
Hot wire and microphone, d = 3.7 mm
Schlieren visualizations
Horizontal knife edge for S =0.14
Vertical knife edge for S =0.18 and 0.22

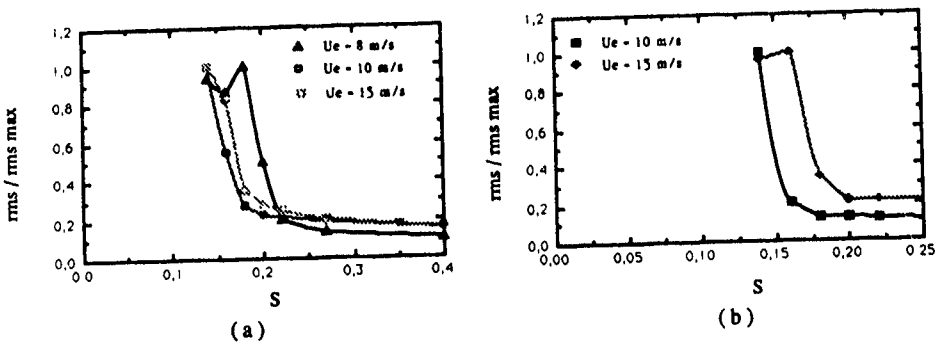

Figure 8 : Relative RMS levels of the signals versus S
(a) Hot wire
(b) Microphone

EIGHTH SYMPOSIUM ON
TURBULENT SHEAR FLOWS
Technical University of Munich
September 9-11, 1991

Direct and large-eddy simulations of transition in the compressible boundary layer over an insulated flat plate

P. COMTE, X. NORMAND and M. LESIEUR
Institut de Mécanique de Grenoble*
BP 53 X - 38041 Grenoble-Cedex, France.

Abstract.

Transition to turbulence in a three-dimensional compressible boundary layer over a semi-infinite insulated flat plate in studied by means of direct and large-eddy simulations Results are presented in quasi-incompressible (Mach number equal to 0.5) and high supersonic (Mach number equal to 5) cases, both in temporal and spatial configurations At low Mach number, a direct-numerical simulation shows that the fundamental mode is selected, leading to the *peak-valley* structure found by Klebanoff *et al.* (J Fluid Mech., **12**, pp 1-34, 1962). In the high Mach number case, no direct-numerical simulation is possible, and we use a subgrid-scale model, the structure-function model, in order to perform a large-eddy simulation of the transition. In this case, the subharmonic mode appears, giving rise to a staggered pattern of Λ vortices

Introduction

The study of supersonic transitioning and turbulent flows is more than ever a current issue, both from a fundamental point of view and for technological applications such as, e.g., the development of the European shuttle *Hermès* or the US National Aerospace Plane. Compressible boundary layers have been studied extensively from the point of view of linear (Mack, 1969) and weakly non-linear stability theory (see e.g. Nayfeh and Harper, 1989; Masad and Nayfeh, 1990) The first stages of a *fully-controlled* transition have also been simulated numerically [Erlebacher and Hussaini (1987, 1990), Maestrello *et al.* ,(1989) and Thumm *et al* (1989)], by forcing the instability in a deterministic way

We present here deterministic simulations of transition to turbulence in the boundary layer above a flat plate, both in weakly-compressible (Mach 0.5) and fast (Mach 5) cases Here, we study *controlled* transition, where the instability is excited by the superposition of a deterministic and a random perturbations The random perturbation is three-dimensional, and of amplitude small with respect to the two-dimensional forcing. This is a more correct way of simulating forced flows in the laboratory, where a residual turbulence is always present. We solve numerically the Navier-Stokes equations in a boundary-layer above a flat plate, with the aid of a direct-numerical simulation using finite-differences methods. At high Mach numbers, the simulation requires a subgrid-scale model

2. Numerical method

The compressible Navier-Stokes and energy equations for a perfect gas are, written in conservation form:

$$\frac{\partial U}{\partial t} = \frac{\partial F}{\partial x} + \frac{\partial G}{\partial y} + \frac{\partial H}{\partial z} \quad . \tag{1}$$

with

$$U = \begin{pmatrix} \rho \\ \rho u \\ \rho v \\ \rho w \\ e \end{pmatrix} \quad , \tag{2}$$

the fluxes F, G and H being computable out of U. Equation (1) is written in dimensionless form Lengths are non dimensionalized by the initial (in the temporal case) or inflow (in the spatial case) displacement thickness δ^*. Reference values for velocity, density, pressure, temperature, and viscosity are their free-stream values (indicated by a subscript ∞). Specific energy e is normalized with respect to the pressure p_∞ The Prandtl number Pr is assumed equal to 1, and Sutherland's law is prescribed for the viscosity μ M is the free stream Mach number and the Reynolds number Re is based on δ^*.

The numerical scheme is due to Gottlieb and Turkel(1976), and has been previously used in the spatial instability study of the compressible boundary layer over a flat plate by Bayliss *et al.* (1985) and Maestrello *et al.* (1989). For the one-dimensional equation $\frac{\partial V}{\partial t} = \frac{\partial F}{\partial x}$ where $F = F(V)$, we have

$$\tilde{V}_i = V_i^n + \frac{\Delta t}{6\Delta x}\left(7(F_{i+1}^n - F_i^n) - (F_{i+2}^n - F_{i+1}^n)\right)$$

$$V_i^{n+1} = \frac{1}{2}\left[V_i^n + \bar{V}_i + \frac{\Delta t}{6\Delta x}\Big(7\,(\bar{F}_i^n - \bar{F}_{i-1}^n) - (\bar{F}_{i-1}^n - \bar{F}_{i-2}^n)\Big)\right] \tag{3}$$

denoting by V_i^n the value of V at point $i\Delta x$ and time $n\Delta t$, and with $\bar{F} = F(\bar{V})$. The scheme (3) is second-order accurate in time and fourth-order accurate in space, provided F does not feature derivatives. In the presence of viscous terms, first-order derivatives arise in F. They are calculated with the aid of a second-order centered scheme and the global scheme is then only second-order accurate in space.

For the temporal calculations, source terms must be added to the second and fifth components of the transverse flux G, so that the laminar state becomes stationary. Otherwise, the mean flow would degenerate into an error-function profile. This would have no physical meaning and the stability of the flow would be deeply modified (see e.g. Spalart and Yang (1987)).

For the three-dimensional equation (1), the scheme (3) is used together with operator splitting, with the same global accuracy. Thus, if $\mathcal{L}_x$ is the one-dimensional operator defined by (3) ($\mathcal{L}_y$ and $\mathcal{L}_z$ corresponding respectively to the equations $\frac{\partial V}{\partial t} = \frac{\partial G}{\partial y}$ and $\frac{\partial V}{\partial t} = \frac{\partial H}{\partial z}$), we have

$$U^{n+2} = \mathcal{L}_x\,\mathcal{L}_y\,\mathcal{L}_z\,\mathcal{L}_z\,\mathcal{L}_y\,\mathcal{L}_x\;U^n \tag{4}$$

Stretching is applied in the y direction, normal to the plate, in order to improve the resolution near the wall and keep the upper boundary of the calculation domain at a sufficient distance from the plate. At the wall, no slip and no heat transfer conditions are imposed, i.e.,

$$u = v = w = 0\,, \qquad \frac{\partial T}{\partial y} = 0\,. \tag{5}$$

The condition for the pressure is derived from the second component of the momentum equation at the wall, which gives

$$0 = -\frac{1}{\gamma M^2}\frac{\partial p}{\partial y} + \frac{1}{Re}\left(\frac{4}{3}\frac{\partial^2 v}{\partial y^2} + \frac{1}{3}\frac{\partial^2 u}{\partial x \partial y} + \frac{1}{3}\frac{\partial^2 w}{\partial y \partial z}\right) \tag{6}$$

An inflow/outflow boundary condition, using one-dimensional normal characteristics, is used at the upper boundary. Linearization of the inviscid equations gives the five characteristic variables C_1 to C_5 and their corresponding velocities λ_1 to λ_5. Outgoing characteristics ($\lambda_i > 0$) are extrapolated from the interior of the calculation domain, whereas incoming characteristics ($\lambda_i < 0$) are kept constant at the boundary. In the temporal calculations, periodicity is assumed in the streamwise direction x, whereas the inflow/outflow boundary condition described above is used at $x = 0$ and $x = L_x$ in spatial simulations. In both cases we have periodicity in the spanwise direction z.

The initial condition consists of the superposition of the laminar solution and a perturbation. The laminar flow is obtained by solving the similarity equation. In the temporal case, the flow is made parallel by taking $\bar{v} = 0$ and $u = \bar{u}(y)$. The perturbation is the superposition of the eigenfunction corresponding to the most amplified mode (which is two-dimensional in the two cases considered hereafter), at an amplitude ε_{2D} and some three-dimensional random noise at an amplitude ε_{3D}. In practice, the two-dimensional eigenfunction is provided by a randomly-forced two-dimensional simulation performed with the same numerical code. In the temporal calculation, the perturbation is only applied at the initial time, t=0. In the spatial case, it is also used at the upstream boundary, the random noise being refreshed every timestep.

As already stressed, high Mach numbers require high Reynolds numbers for transition to develop. These can be reached, with the limited resolution offered by the computer, only by means of large-eddy simulations, where the effect of the small unresolved scales upon the explicitely-simulated large scales has to be modelled. A very efficient subgrid-scale parameterization, based on a spectral eddy-viscosity (Kraichnan, 1976), was developped by Metais and Lesieur (1990). Turbulence is supposed to be locally, at a position $\vec{x}$, isotropic at scales smaller than the grid mesh Δx. A local kinetic energy spectrum $E_{\vec{x}}(k_c)$ (with $k_c = \pi/\Delta x$) is then calculated in terms of the local 2nd order velocity structure function

$$\overline{F_2} = \left\langle \|\vec{u}(\vec{x},t) - \vec{u}(\vec{x}+\vec{r},t)\|^2 \right\rangle_{\|\vec{r}\|=\Delta x} \tag{7}$$

of the large scale velocity field (where $\langle\,\rangle$ is a proper spatial average upon points $\vec{x}+\vec{r}$, a distance Δx apart of $\vec{x}$). Then the isotropic EDQNM expression for the eddy-viscosity is used:

$$\nu_t(\vec{x},t) = 0.4\,\sqrt{\frac{E_{\vec{x},t}(k_c)}{k_c}}\,, \tag{8}$$

which varies with the instantaneous and local turbulent activity. It is found

$$\nu_t(\underline{x},t) = 0.06\,\Delta x\,\sqrt{\overline{F_2}(\underline{x},\Delta x,t)}\,. \tag{9}$$

An analogous eddy-conductivity is built taking a turbulent Prandtl number equal to 0.6, as given by the isotropic incompressible studies[2]. Afterwards, these eddy-coefficients are substituted with the viscous coefficients into the full compressible Navier-Stokes equations. Notice that our model gives a better agreement with laboratory experiments than the Smagorinsky model, at least for two incompressible flows: behind a backward-facing step (Silveira *et al.*, 1990), and the channel flow (Comte *et al.*, 1990). In the last paper was given evidence of acceptable behaviour of the structure-function model, even near the walls, where the assumption of

homogeneity and isotropy is certainly not fulfilled The use of the incompressible eddy-viscosity (9) and its associated eddy-conductivity for compressible calculations may be only justified by assuming that the subgrid-scales are negligibly affected by compressibility.

3 Low Mach number boundary-layer simulations

In this section, we present temporal direct numerical simulations at $M = 0.5$ (which is low enough to permit comparison with incompressible experiments and computations) and at an initial Reynolds number of 1000.

For a simulation at a resolution of $60 \times 20 \times 45$ involving two TS wavelengths, Figure 1 shows, from (a) to (g), the successive evolution of a set of vortex lines in the same run for times ranging from 470 to 500 δ^*/U_∞. We observe the formation of Λ vortices in an *aligned pattern*, and thus we can conclude that they correspond to the fundamental mode of the secondary instability This fundamental mode may be physically explained as an in-phase spanwise oscillation of the vortex filaments, which is amplified by the straining due to the basic shear. The wavelength in the spanwise direction λ_z is half the calculation domain and is of the same order as λ_{TS}, the longitudinal wavelength of the Tollmien-Schlichting waves It is obviously not possible to conclude that the observed spanwise mode is the most amplified one, since spanwise periodicity leads to the selection of particular modes.

The selection of the secondary instability fundamental mode in a case in which TS waves are forced with a relatively high amplitude is consistent both with experiments, theoretical calculations (Herbert, 1988) and computations (Spalart and Yang, 1987; Zang and Hussaini, 1987; Kleiser and Zang, 1991).

At $t = 490\ \delta^*/U_\infty$, the flow clearly displays a *peak-valley* structure, as in the laboratory experiments of Klebanoff *et al.* (1962). The peak planes corresponds to the tip of the Λ structures and the valley planes to their bases. In the peak planes (parallel to x, y), the vertical velocity v is positive and the streamwise velocity u is lower than the mean value. Indeed, slow fluid close to the wall is lifted between the legs of the Λ The opposite behaviour characterizes the valley planes.

The present simulation stopped before a developed turbulent regime was reached. It has thus been resumed for a longer time (up to 2300 δ^*/U_∞), but at a lower resolution ($30 \times 25 \times 20$) in a domain of length equal to one TS period instead of two. Despite this low resolution, a good qualitative agreement with experimental measurements made in incompressible boundary layers at a comparable Reynolds number was obtained: our shape factor, for instance, goes from 2.6 to 1.4, as in the experimental incompressible data Our friction coefficient peaks after the transition at $5.1\ 10^{-3}$. Our computed r.m.s. of the three velocity components peak respectively at 0.13, 0.04 and 0.06 (see Normand, 1990 , Normand and Lesieur, 1991).

4. Mach 5 simulations

At a Mach number of 5, a high Reynolds number of the order of 10 000 is needed in order to reach the turbulent regime Such a Reynolds number is to high to allow for a direct-numerical simulation of the whole transition process, and we have chosen to perform a large-eddy simulation using the above-discussed *structure-function model*. Another choice was done by Erlebacher and Hussaini (1990), who use (at a Mach number of 4.5) no subgrid model, and are able to observe the development of a secondary instability This requires very low time steps, and lengthy calculations Ours (which blow up if the eddy-viscosity is suppressed) allow longer time evolutions

The question of the validity of the subgrid-scale parameterization for the simulation of the transitional stages is crucial, and an important criterion is that the eddy-viscosity should be negligible during the linear stage of the evolution. This will be well verified. We will now present results obtained in the temporal case and in the spatially-growing case

4.1 *Temporal boundary layer at Mach 5*

We present here a simulation at $M = 5$ and $Re = 10\,000$. The resolution is of $50 \times 20 \times 40$ for a domain of length equal to twice the most-amplified wavelength at this Mach number (the second mode) and the initial perturbations are of the same order as in the previous case.

Figure 2 shows the streamwise velocity field u in the plane $y = 0.5\ \delta^*$ at $t = 300\ \delta^*/U_\infty$. We observe very clearly a staggered pattern. This marks a radical change compared with the low Mach number case, since the subharmonic mode of the secondary instability seems now to be selected. This subharmonic mode corresponds to an out of phase spanwise oscillation of the vortex filaments, which is intensified by the straining due to the mean shear Unfortunately, we did not find any experimental or theoretical work with which this results could be compared However, the above-mentioned calculations of Erlebacher and Hussaini (1990), which are forced initially with a secondary fundamental perturbation, might go in favour of our findings: instead of seing the development of the spanwise in-phase oscillation of the vortex filaments, they observe that the peak and valley planes *lose their most distinctive characteristics.*

4.1 *Spatial simulation at Mach 5*

The higher growth rate of the instability makes a spatial simulation at Mach 5 possible, whereas it was not the case at low Mach number. The resolution is of $300 \times 40 \times 20$. The domain's size is of $600 \times 30 \times 20$ the displacement thickness

upstream, where the flow is forced using the same eigenfunctions as in the temporal case The upstream Reynolds number, based upon this thickness, is of 10 000

Figure 3 shows an isosurface of ω_z viewed from the top (*Fig 3-a*), with enlarged top and side views in the downstream region (*Fig 3-b* and *3-c* respectively), visualized with the aid of the FLOSIAN software (developped at I.M G by Y Foullet, E. David, M.A. Gonze and P Comte) The flow is going from left to right. We first observe the two-dimensional waves resulting from the forcing Then a subharmonic secondary mode emerges, as in the temporal case, giving rise to Λ-shaped structures staggered in the spanwise direction These Λ waves break up and pair as they travel downstream. They also seem to be more stretched in the streamwise direction than the analogous staggered vortices observed experimentally in an incompressible case of natural transition.

5. Conclusion and discussion

Transition to turbulence of a compressible boundary layer over a semi-infinite insulated flat plate was studied numerically by solving the complete unsteady Navier-Stokes equations. Direct numerical simulations were performed at low Mach number ($M = 0.5$, $Re_{\delta^*} = 1000$), whereas the use of a subgrid-scale parameterization was necessary for the high Mach number ($M = 5$) case, since we had to increase the Reynolds number ($Re_{\delta^*} = 10\,000$). A new subgrid-scale model, based on the second-order velocity structure function was used here for the first time in a compressible shear flow.

At low Mach number, the fundamental mode of the secondary instability (in-phase spanwise oscillation of the T.S filaments) was found to be predominant, as predicted by the incompressible theory when the TS wave amplitude is high The complete transition process was observed and explained on the basis of vortex filament dynamics. Finally, the transition to small-scale turbulence was proved to be well simulated in a calculation at low resolution, at least with regard to the main average quantities of the flow (mean velocity, shape factor and friction coefficient, r.m s. velocity fluctuations).

In the high Mach number case, the predominant unstable mode (second mode) is two-dimensional and results from the generalized inflection-point instability criterion A controlled-transition numerical experiment, with a 3D white-noise perturbation superimposed on the second mode, shows a drastic change of behaviour compared with the incompressible case: now the subharmonic mode of the secondary instability (out-of-phase spanwise oscillation of the vortex filaments) seems to be selected. This was confirmed by a spatial simulation, in which a clear downstream transition is observed in the structure of the flow, from the two-dimensional waves upstream to very elongated Λ-shaped vortices Although no transition to small-scale turbulence is observed at this "low" resolution of $300 \times 40 \times 20$ (which, however, implies typical runs of about 20 hours each on the Grenoble Atomic Energy Agency Cray 2), it is possible that these coherent structures may characterize the turbulent boundary layer at Mach 5

These results pose questions about the universality of the vortex structure in turbulent shear flows, submitted or not to the influence of a wall, and to the action of compressibility Let us consider first the incompressible case in a mixing layer, one may also make the distinction between a secondary fundamental mode, yielding the straining of longitudinal hairpin vortices between the primary Kelvin-Helmholtz billows, and a subharmonic mode, corresponding to the *helical-pairing instability* of Pierrehumbert and Widnall (1982), and leading to a *vortex-lattice structure* as demonstrated numerically by Comte and Lesieur (1990) The same calculations show that one of the two spanwise instabilities will develop, according to the relative importance of the two-dimensional and the random three-dimensional forcings. When compressibility is important (convective Mach number of the order of one), the numerical simulations of Sandham and Reynolds exhibit a staggered array of Λ vortices.

Therefore, it is tempting to draw a unified picture of transition to turbulence in any flow submitted to a unidirectional shear: at low Mach number, a quasi two-dimensional forcing will lead to a set of longitudinal hairpin vortices, superposed upon the spanwise billows resulting from the breaking of the primary instability, when such a breaking occurs (as in a mixing layer, but not in the boundary layer) On the other hand, *natural transition* (where no two-dimensional forcing is present) will produce a staggered array of large Λ vortices, tending to be lifted towards the higher velocities, due to self-induction effects. These structures have to undergo some kind of pairing interactions, in order to be consistent with the global self-similarity of the flow. They are likely to survive when small-scale turbulence has developed. At high Mach number, it seems that only the latter flow topology (staggered breaking-up Λ vortices) is selected, whatever the type of forcing. All these conclusions (specially in the compressible case) have to be taken cautiously, and need to be validated by higher resolution calculations and laboratory experiments

Acknowledgments

The authors thank to D. Arnal, M. Morkovin and J Riley for helpful discussions during the course of this study. One of us (X. Normand) is indebted to NASA-Langley and ICASE for being invited to the *Instability and Transition Workshop ICASE/LaRC, June 1989.*

This work was supported by CNES-Avions Marcel Dassault in the frame of the Hermès program (contract n° RDMF 3/86), by DRET (contracts n° 87/808/11 and n° 88/150),

and by CNRS (GDR *Mécanique des Fluides Numérique* and GDR *Hypersonique*). Calculations using a CRAY2 were done on a grant of the *Centre de Calcul Vectoriel pour la Recherche*, and *Centre Grenoblois de Calcul Vectoriel*

References

Bayliss, A , Parikh, P., Maestrello, L , and Turkel, E (1985). *AIAA Paper* 85-1694

Comte, P., Lee, S.S., Cabot, W. and Moin, P. 1990 In Proc. Summer Research Program 1990, Center for Turbulence Research, Stanford, California

Comte, P , and Lesieur, M (1990) Large and small-scale stirring of vorticity and a passive scalar in a 3D temporal mixing layer. *Phys Fluids A*, to appear

Erlebacher, G , and Hussaini, M.Y (1987) *AIAA Paper* 87-1416

Erlebacher, G , and Hussaini, M Y (1990) *Phys Fluids A*, Vol 2, pp. 94-104

Gottlieb, D., and Turkel, E. (1976). *Math. Comp* , Vol 30 (136), pp. 703-723.

Herbert T (1988). *Ann Rev Fluid Mech* , Vol 20, pp. 487-526

Erlebacher, G. and Hussaini, M.Y. (1990). *Phys Fluids* A Vol. 2, pp 94-104.

Klebanoff, P S , Tidstrom, K.D., and Sargent, L M (1962). *J. Fluid Mech.*, Vol. 12, pp. 1-34.

Kleiser, L. and Zang, T.A. (1991). *Ann. Rev. Fluid Mech.*, Vol. 23, pp 495-537

Kline, S.J., Reynolds, W.C., Schraub, F.A., and Runstadler, P.W. (1967). *J. Fluid Mech.*, Vol. 30, pp. 741-773.

Kraichnan, R H. (1976). *J. Atmos. Sci.*, Vol. 33, pp. 1521-1536.

Lesieur, M. (1987). *Turbulence in Fluids.* Martinus Nijhoff Publishers. Revised edition 1990, Kluwer Publishers.

Mack, L M. (1969). Boundary-layer stability theory. Jet Propulsion Lab., Pasadena, Calif., rep. 900-277.

Maestrello, L., Bayliss, A., and Krishnan, R. (1989).*ICASE Report* 89-74.

Masad, J.A., and Nayfeh, A.H. (1990). *Phys Fluids A*, Vol. 2, pp. 1380-1392.

Métais, O., and Lesieur, M. (1990). Spectral large-eddy simulation of isotropic and stably-stratified turbulence *Submitted to the Journal of Fluid Mechanics.*

Nayfeh, A.H., and Harper, R (1989). *Proceedings of the Third IUTAM Symposium on Laminar-Turbulent Transition, Sept. 11-15, Toulouse, France.*, D. Arnal and R. Michel eds, Springer-Verlag.

Normand, X., (1989) *Proceedings of the Instability and Transition Workshop ICASE/LaRC, June 1989.*

Normand, X. (1990) Transition à la turbulence dans les écoulements cisaillés compressibles libres et pariétaux. *Thèse*, Institut National Polytechnique de Grenoble.

Pierrehumbert, R.T., and Widnall, S E. (1982) *J. Fluid Mech.*, Vol 114, pp 59-82. Pierrehumbert and Widnall

Sandham, N.D., and Reynolds, W.C. (1990). Three-dimensional simulations of the compressible mixing layer. *J Fluid Mech.*, to appear

Schlichting, H (1979) *Boundary-layer theory* McGraw-Hill, New-york, seventh edition.

Silveira, A , Grand, D , Metais, O , and Lesieur, M (1990) Large-eddy simulation of the turbulent flow in the downstream region of a backward-facing step. *To appear in Phys Rev letters.*

Smagorinsky, J. (1963) *Monthly Weather Rev* , Vol. 91, pp 99-164.

Spalart, P.R., and Yang, K.-S. (1987) *J Fluid Mech* , Vol 178, pp 345-365.

Strang, G. (1968) *SIAM J Numer Anal.*, Vol 5 (3), pp 506-517

Thumm, A., Wolz, W , and Fasel, H (1989) *Proceedings of the Third IUTAM Symposium on Laminar-Turbulent Transition, Sept. 11-15, Toulouse, France* , D Arnal and R Michel eds, Springer-Verlag.

Zang, T A and Hussaini, M.Y (1987) *Nonlinear Wave Interactions in Fluids*, R W Miksad T R Akylas and T Herbert eds. AMD-87, pp 131-145 New York: ASME

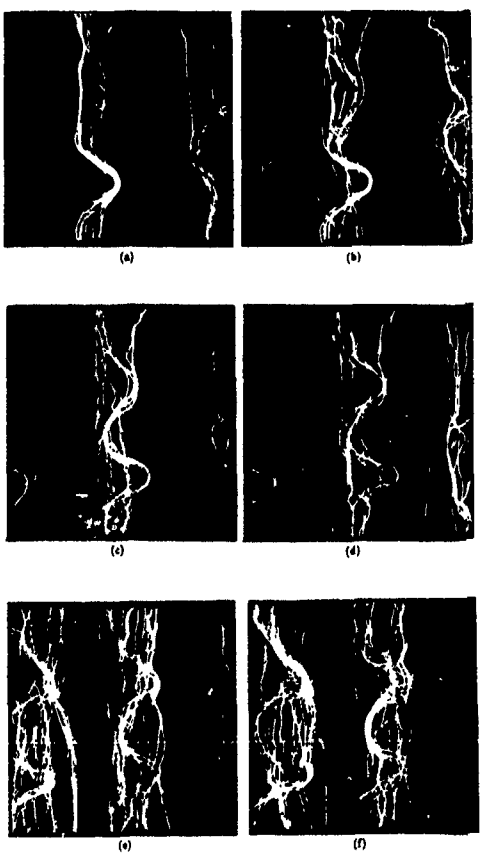

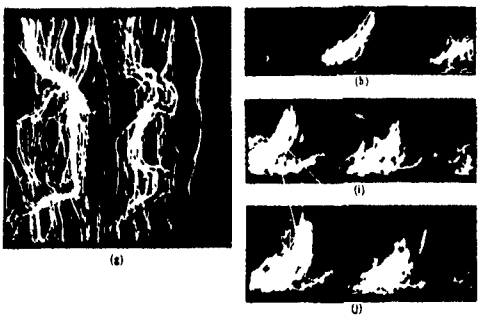

Figure 1 Sets of vortex lines for the simulation at $M = 0.5$ at t=470 (a), 475 (b) and (h), 480 (c), 485 (d), 490 (e) and (i), 495 (f) and (j), 500 (g) δ^*/U_∞. The first ones, (a) to (g), are viewed from the top, and the others, (h) to (i), are viewed from the side.

Figure 2. Streamwise velocity field in the plane $y = 0.5\ \delta^*$ at $t = 300\ \delta^*/U_\infty$ for the temporal simulation at $M = 5$

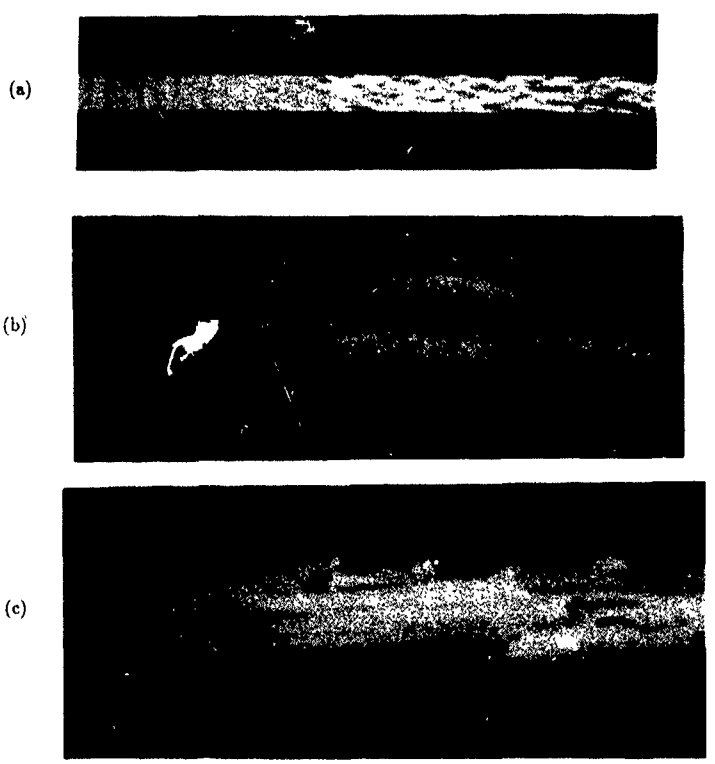

Figure 3. Isosurface $\omega_z = -0.2\ U_\infty/\delta^*$ for the spatial simulation at $M = 5$ [general view (a) and zooms: from the top (b) and perspective (c)].

EIGHTH SYMPOSIUM ON
TURBULENT SHEAR FLOWS
Technical University of Munich
September 9-11, 1991

Breakdown of a circular jet into turbulence

M V Melander*, F Hussain and A Basu
Department of Mechanical Engineering
University of Houston
Houston, Texas

*Department of Mathematics, Southern Methodist University, Dallas, Texas

Abstract

By direct numerical simulation of the Navier-Stokes equations we have studied the near-field organised structures in an incompressible circular jet at a Reynolds number of 1500. In particular, we focus on the breakdown process following the pairing of rolled up vortex rings. The breakdown process seems to involve of strong streamwise hairpin-like vortex loops.

Introduction

The near-field of an axisymmetric jet is rich in the kinds of motions starting with 2D Kelvin-Helmholtz instability, roll-up, pairing, breakdown and perhaps reconnection. This region is also characterised by high level of mixing and aerodynamic noise generation. Unfortunately, our knowledge of this field is extremely limited because of constraints of single-point measurements as well as the intrinsic limitations of flow visualisation Even at Schmidt number equal one, flow visualisation in a 3D flow can be grossly misleading because dynamically significant regions are typically depleted of markers, obscuring them from direct observation. Pending development of 3D flow measurement technology, such as the holographic particle velocimetry (now under development at UH) we used hot-wires (Hussain 1983) In parallel we took advantage of the power of supercomputers which can provide detailed 3D field velocity and vorticity data, although at low Reynolds numbers

In an attempt to complement experimental observations by us and others (e.g. Hussain & Zaman (1980), Crow & Champagne 1971)), as well as to obtain insight into the structure of a circular jet, we have studied by direct numerical simulation a temporally evolving jet as an idealised model. This simulation captures the fundamental mechanisms involved in the transition to turbulence in this geometry, without necessarily accurately giving all the physical measures (such as spread rate). While the periodic geometry admittedly has some undesirable side effects, it also has significant advantages; foremost among these is the easy access to the eigenfunctions of the curl operator. These eigenfunctions are critical for the decomposition of the flow into helically polarized components which are central to the present analysis as they allow us to examine the breakdown of the jet into turbulence in a new fashion. We find that a partial spatial separation of the polarized vorticity components is instrumental in this transition.

Initial Condition

The present results are obtained from a numerical simulation of a temporally evolving circular jet at Re_D=1500. The numerical method used is a spectral (alias-free) algorithm with a fourth order predictor corrector for the time advancement in a $(2\pi)^3$-box of a 64^3-resolution. The diameter of the initial unperturbed jet is D=2.5, the centerline velocity of the jet is W_j=1, and initial momentum thickness is δ_o=0.05. The jet is initially subject to both longitudinal and azimuthal perturbations The longitudinal perturbations are given as variations in the momentum thickness.

$$(1) \qquad \delta(z) = \delta_o \left(1 + a_f \cos(\frac{z}{\lambda_f}+\phi_f) + a_{f/2} \cos(\frac{z}{\lambda_{f/2}}+\phi_{f/2}) + a_{f/4} \cos(\frac{z}{\lambda_{f/4}}+\phi_{f/4})\right),$$

here a_f=0.05, $a_{f/2}$=0.03, $a_{f/4}$=0.01, $\lambda_f=\pi/2$, $\lambda_{f/2}=\pi$, $\lambda_{f/4}=2\pi$, $\phi_f=0$, $\phi_{f/2}=\pi$, $\phi_{f/4}=2\pi$ The azimuthal perturbations are radial displacements of the jet shear layer; these consist of a superposition of 16 waves:

$$(2) \qquad r(\theta)=r_o(1+a\sum \cos(m\theta+\theta_m)),$$

with equal amplitudes a=0.001 and random phases θ_m.

Brief Description of the Evolution

The evolution of the jet over the duration of this simulation naturally divides into three phases. *First*, an axisymmetric phase characterised by roll up of the shear layer into rings and subsequent pairing of the rings *Second*, growth of azimuthal disturbances on the rings and the formation of streamwise structures *Third*, breakdown of the ring structures into smaller structures with significant streamwise vorticity; hence they are apparently helical in nature

During the first phase the shear layer rolls up into four ring vortices at the fundamental perturbation within the computational domain as expected (Fig 1a). The presence of the the initial subharmonic perturbation allows the rings to pair in the periodic geometry (Figs 1b-e). As a result of this pairing event we have only two ring structures within the computational domain These rings have a large core-to-ring-radius ratio which does not permit a second pairing to take place. The jet is thus in "jet column mode". This evolution is almost completely axisymmetric, in that azimuthal disturbances remain small, as illustrated by the vortex lines in Fig 2.

The evolution away from axisymmetry begins by the formation of "ribs" between the ring structures, see Fig 3. The ribs are streamwise structures that form in counter-rotating pairs. Their formation is due to the alignment of vorticity with the principal strain rate direction in between the rings, whereby the streamwise vorticity component is continuously enhanced. Figure 4 illustrates this point by showing a sample of typical vortex lines We notice that the departure from axisymmetry within the rings is small compared to the braid region. Also we observe that the ribs seen in Fig.3 do not consist of vortex lines going from ring to ring, but instead of staggered vortex lines with varying strength, i.e. high amplitude in the rib direction and low amplitude perpendicular to it. At later times the ribs are stronger and the ring structures themselves begin to show significant departures from axisymmetry (Fig.5) This happens as a result of the "Widnall-instability" (Widnall *et al.* 1974). Note that some ribs are stronger than others and that the rings lack symmetry; this is a consequence of the initial azimuthal perturbations (2) which have random phases. A sample of typical vortex lines are shown in Fig 6; from these lines it is evident that the rings are beginning to bend in the streamwise direction, such that the inner loops of the rings are ahead of the outer ones. Moreover, we observe that the waves on the rings are out of phase with the loops in the ribs (Fig 6b). The overall picture at this time is roughly consistent with the sketch of Hussain 1986 (Fig.7).

The ring structures undergo a complete breakdown as they attempt to leapfrog, which they can not do because their cores are too thick (Figs. 8,9). The final result of this breakdown is that the jet region fills up with streamwise loops as shown in Fig 10 We searched this field for ring structures similar to those suggested in Fig 7, but we found none, not even in strongly distorted form.

The evolutions of energy and enstrophy in the computational domain is shown in Figs. 11a,b. Little over half the energy is dissipated by the end of the simulation. The enstrophy

decays rapidly during the first phase of the evolution, this is because the initial momentum thickness is rather small for this Reynolds number and also because the first phase is mainly axisymmetric, lacking any substantial vortex stretching The second phase, however, features a substantial increase in enstrophy, due to the generation of streamwise vorticity, which is subject to vortex stretching. The enstrophy reaches a peak during the breakdown of the ring structures. Subsequently, the enstrophy decays Of particular interest is decomposition of energy and enstrophy into streamwise, radial and azimuthal components, see Figs 11c,d We observe that the azimuthal component of the energy E_θ is negligible until t=20 0 when the rings become unstable Subsequently E_θ grows significantly at the expense of the streamwise energy E_z. The radial component E_r reaches a peak during the pairing event, then decays slightly, but eventually starts to grow at the same rate as E_θ. The corresponding components of the enstrophy Z show the three phases with extraordinary clarity, see Fig 11d During the first phase Z_r and Z_z remain negligible compared to Z_θ, but during the second phase they grow significantly and at the same rate The third phase is characterized by the three components being largely equal, i e. each holding a third of the enstrophy

Spatial Separation of the Polarised Vorticity Components

The jet evolution described above features strong core dynamics in the ring structures as well as in the ribs. We have discovered (Melander & Hussain 1991a,b) that a most revealing way of studying vortex core dynamics is in term of the 'generalised Helmholtz decomposition' (Moses 1971) or the equivalent 'complex helical wave decomposition' (Lesieur 1990)

This decomposition is based on the eigenfunctions of the curl operator. In the periodic as well as in the infinite space the curl operator has only real eigenvalues Moreover, the eigenfunctions can be selected such as to form a complete set of basis functions, which are orthogonal with respect to the inner product,

$$(3) \qquad \langle f, g \rangle \equiv \int f^* \cdot g \, dV,$$

where * means complex conjugation and the integration extends over the periodic box. In Fourier space there are two eigenmodes corresponding to a given wavevector k, one of the eigenmodes has eigenvalue $|k|$ and the other $-|k|$. Vector functions which are linear combinations of eigenfunctions corresponding to positive eigenvalues we call right handed because the trajectories or vector lines locally form right handed helices Similarly we call linear combinations of eigenfunctions corresponding to negative eigenvalues left handed The eigenfunctions corresponding to the eigenvalue zero span the space of potential vector functions An incompressible velocity field can thus be expressed in the form,

$$(4) \qquad u = u_R + u_L + \nabla\phi,$$

where ϕ is a harmonic function (i.e. $\Delta\phi=0$). Note that the periodic geometry allows only one kind of potential vector fields with zero divergence, namely constant vector fields. These three components are unique, rotationally invariant, and constitute the generalised Helmholtz decomposition of Moses (1971). Moreover, in our applications the three components are real because of the conjugate symmetry of u in Fourier space For a solenoidal vector field like a vorticity field ω we have,

$$(5) \qquad \omega = \omega_R + \omega_L,$$

In the following we frequently refer to the left and right handed components of a vector field as its *polarized* components, each of them is by construction solenoidal. We emphasize that the polarized components are Galilean invariant and that the well known frame dependence of the velocity field enters only through the potential component $\nabla\phi$

The significance of the polarised field components is closely related to the concept of helicity (Moffatt 1969, 1985), because the helicity integral H over the periodic domain equals

$$(6) \qquad H = \int \omega \cdot u \, dV = H_R + H_L$$

where

$$(7) \qquad H_R = \int \omega_R \cdot u_R \, dV, \; H_L = \int \omega_L \cdot u_L \, dV$$

Here the H_R is a positive definite and H_L is a negative definite integral. The total helicity H differs from zero when H_R and H_L do not balance exactly Such imbalance typically results from viscous vortex interactions, but can also result from simple viscous decay of partially or fully separated polarized vortical structures (Melander & Hussain 1991c) Spatial separation of ω_R and ω_L is therefore of interest, even when the spatial separation is only partial.

Initially there is pointwise balance between $|\omega_R|$ and $|\omega_L|$ This balance is not significantly disturbed during the first phase where the evolution remains nearly completely axisymmetric However, as the azimuthal disturbances grow during the second phase of the evolution a partial separation of $|\omega_R|$ and $|\omega_L|$ follows both in the ribs and in the ring structures, two examples are shown in Fig. 12. Inside the ring structure the separation is a consequence of core dynamics, similar to that described in Melander & Hussain (1991a,b). In the ribs the separation is of a different nature, as they are generated from the very beginning in partially polarized form, that is, within each pair of ribs one is predominantly right handed and the other is predominantly lefthanded. At the end of the simulation the flow field consists of streamwise hairpin-like loops, where the legs have opposite polarity

At this point we emphasize that this discussion of polarised vortical structures is *not* a repeat of the helicity density ($h=u\cdot\omega$) story (Levich & Tsinober 1983; Pelz *et al* 1986; Shtilman *et al* 1987) There are two reasons for this. *First*, we consider the debate about h and $h_r=u\cdot\omega/(|u||\omega|)$ as being conclusively settled by Rogers & Moin (1987). *Second*, we consider h and h_r to be totally hopeless as pointwise measures for the helical nature of a vortical structure This is not just because of the lack of Galilean invariance of h and h_r, but much more significantly because u is *not a local property of the vorticity field* (i.e. the Biot-Savart integral) Hence if we consider a given vortical structure $\mathcal{S}$ at a given time t_0 then h and h_r depend on the surrounding structures in a totally undesirable fashion. For example, if we consider the exact same vortical structure $\mathcal{S}$ in a different environment then both h and h_r change even though $\mathcal{S}$ is unchanged. [These remarks also apply to a number of other quantities, e g. $|\omega\times u|$, $|\nabla\times(\omega\times u)|$. Note that while the helicity densities h and h_r are quantities that are highly questionable, the helicity integral H, whether over all space or only over a vortical structure bounded by a closed vortex surface, is a well defined quantity with a precise meaning.] Fortunately, the polarised vorticity components do not suffer from these problems, they are in fact true *local* measures of the helical structure of the vorticity field, and they must not be confused with the helicity density h.

In order to diagnose the partial separation of the polarized components during the evolution we have calculated the cross-correlation $\mathcal{R}_\theta$ of $|\omega_R|$ and $|\omega_L|$, i.e

$$(8) \qquad \mathcal{R}_\theta(\Delta r,\Delta\theta,\Delta z) = \langle\, |\omega_R(r,\theta,z)| \; |\omega_R(r+\Delta r,\theta+\Delta\theta,z+\Delta z)| \,\rangle$$

This function is shown in Fig.13 at six times during the evolution. Initially there is a perfect correlation for $(\Delta r,\Delta\theta,\Delta z) = (0,0,0)$. At later times the correlation decreases, but the maximum value of $\mathcal{R}_\theta$ is always obtained for $\Delta r=0$ and $\Delta z=0$ At t=7 the peak correlation is still very high (over 0.995), but there is a noticeable shift in $\Delta\theta$ by approximately 15° This is a sign of the ribs structures starting to form, albeit with very low streamwise vorticity, thus showing that the separation occurs gradually. As the azimuthal perturbations begin to grow in the ring structures the peak in $\mathcal{R}_\theta$ becomes shaper (Figs. 13c,d). When the ring structures break down into streamwise structures the maximum correlation drops further, but also occurs for and increasingly smaller value of $\Delta\theta$, see Figs 13e,f. The reason for the decrease in $\Delta\theta$ is that the organized rib-pairs disappear and get twisted around more independently in the flow

Conclusion

The above analysis of a temporally evolving circular jet suggests that the partial spatial separation of the polarized vorticity components are instrumental in the complete breakdown of the early ring structures and the onset of fully developed turbulence. The turbulent field consists of many vortical structures, roughly like thin hairpins bend in the streamwise direction and with a helical twist to them [note that the ring instability did not produce

secondary ring structures by reconnection as had been conjectured by Hussain 1986, see Fig.7]. The legs in these lobes are not at all symmetric images of each other, but they are, however, characterized by dominance of vorticity of opposite polarity The lack of symmetry between the polarized structures allow them to decay in slightly different ways, thereby producing a volume helicity integral which deviates from zero (Fig. 14). Thus the initial balance between left and right handedness of the jet is broken by the ring breakdown and the onset of turbulence. At the end of the simulation the jet is slightly more lefthanded than right handed We need to explore further the implication of this finding

Acknowledgement This research has been supported by ONR grant N00014-89-J-1361 and DOE grant DE-FG05-88ER13839

References

Crow, S.C & Chempage, F.H. 1971 *J Fluid Mech* 48, 547.
Hussain, F. 1986 *J. Fluid Mech.* 173, 303-356
Hussain,F & Zaman, K.B.M Q 1980 *J. Fluid Mech* 101, 493.
Lesieur, M , 1990 *Turbulence in Fluids*, Kluwer academic publishers.
Melander, M.V & Hussain, F., 1991a Vortex core dynamics, helical waves and organization of fine-scale turbulence. *Phys. Fluids*, (submitted)
Melander, M V & Hussain,F., 1991b Coherent Structure Dynamics. Interaction Between Large and Fine Scales (this volume)
Melander, M.V. & Hussain,F , 1991c Viscous Generation of Helicity, and non-trivial Topology of Vortex Lines in Coherent Structures. *J. Fluid Mech.* (submitted).
Moffatt, H K , 1969 *J Fluid Mech* 35, 117-129
Moffatt, H. K., 1985 *J Fluid Mech* 159, 359-378.
Moses, H E , 1971 *SIAM J Appl Math.*, 21, 114-144.
Rogers, M.M. & Moin, P , 1987 *Phys. Fluids*,30, 2662-2671
Shtilman, L., Levich, E., Orszag, S.A., Pelz, R.B & Tsinober, A., 1985, Phys. Lett 113 A, 32-37.
Tsinober, A & Levich, E , 1983 *Phys. Lett.*, 99 A, 321-324.
Widnall, S.E , Bliss,D.B. & Tsai,C-Y. 1974 *J Fluid Mech* 66, 35-47

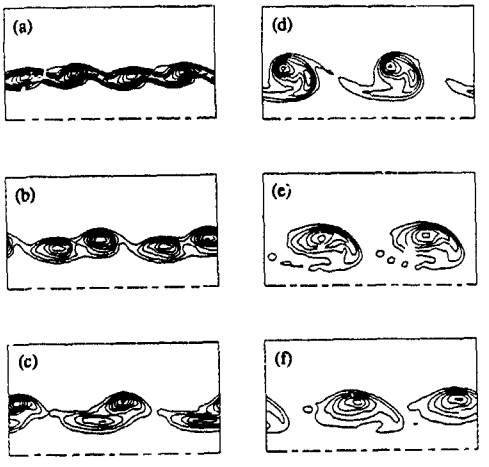

Fig 1 Vorticity contours during roll up and pairing. (a) t=3,(b) t=5, (c) t=7; (d) t=9, (e) t=11, (f) t=13

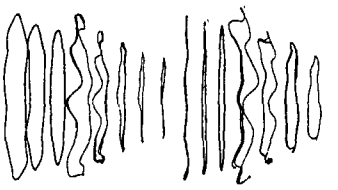

Fig 2 Typical vortex lines at t=9.

Fig 3 A representative surface of $|\omega|$ is shown together with low amplitude ω_3 at t=17, (a) half of the jet viewed from the outside, (b) view from the inside

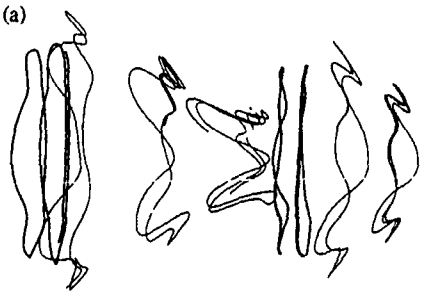

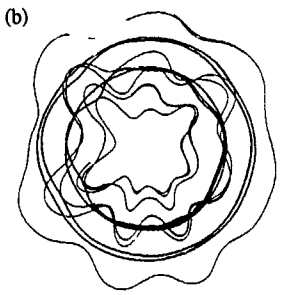

Fig 4 Typical vortex lines at t=17, (a) side view; (b) front view

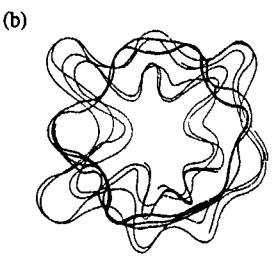

Fig 6 Typical vortex lines at t=23, (a) side view, (b) front view

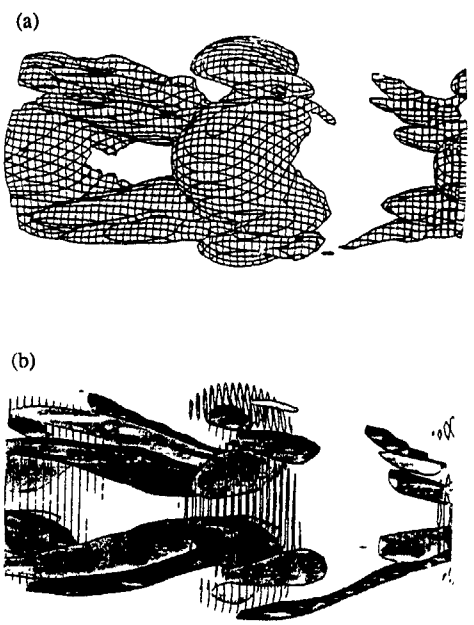

Fig 5 (a) $|\omega|$ in half of the jet at t=23; (b) superimposed plots of $|\omega|$ and ω_z

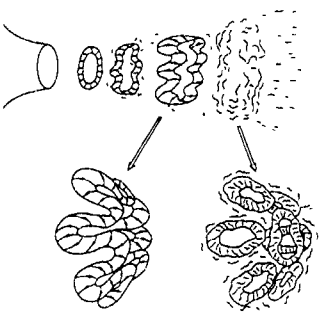

Fig 7 Conjecture about the occurrence of reconnection in a circular jet (Hussain 1986)

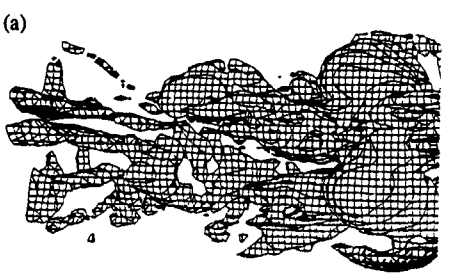

Fig 8 As Fig. 5 but at t=29.

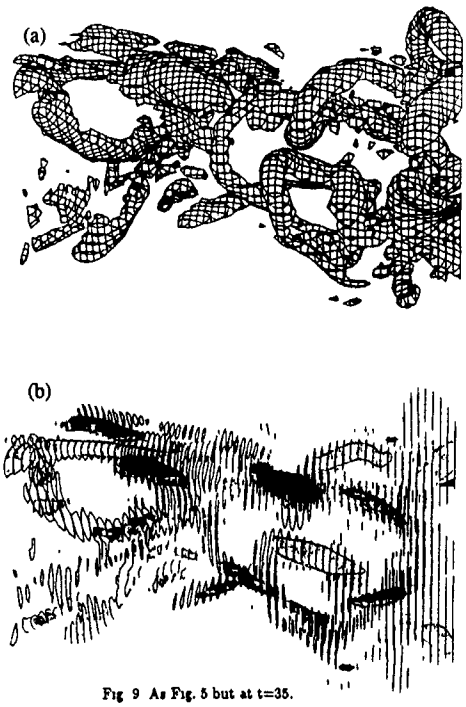

Fig 9 As Fig. 5 but at t=35.

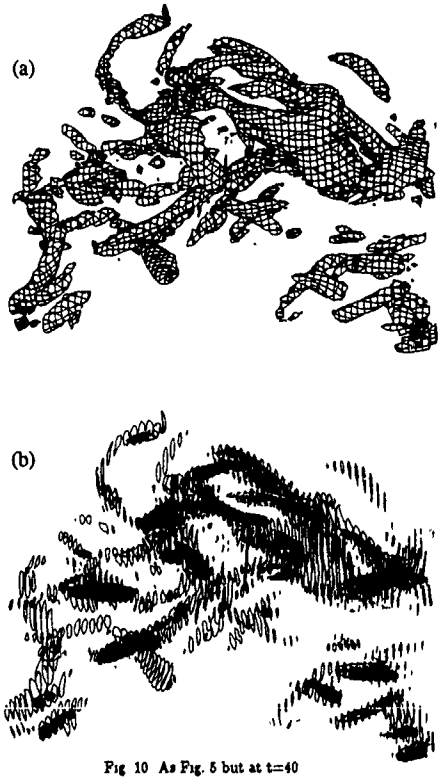

Fig 10 As Fig. 5 but at t=40

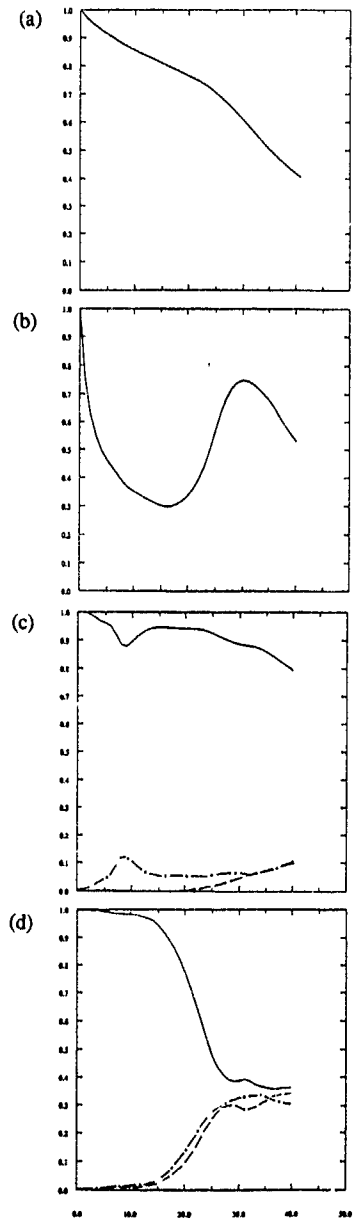

Fig. 11 (a) E/E(0) vs t; (b) Z/Z(0) vs t; (c) E_r/E (···), E_θ/E (- - -), E_z/E (__) vs t, (d) Z_r/Z, Z_θ/Z, Z_z/Z vs t

Fig 13 Cross correlation function $\mathcal{R}_0$, (a) t=0, (b) t=7, (c) t=17; (d) t=23, (e) t=28, (f) t=36

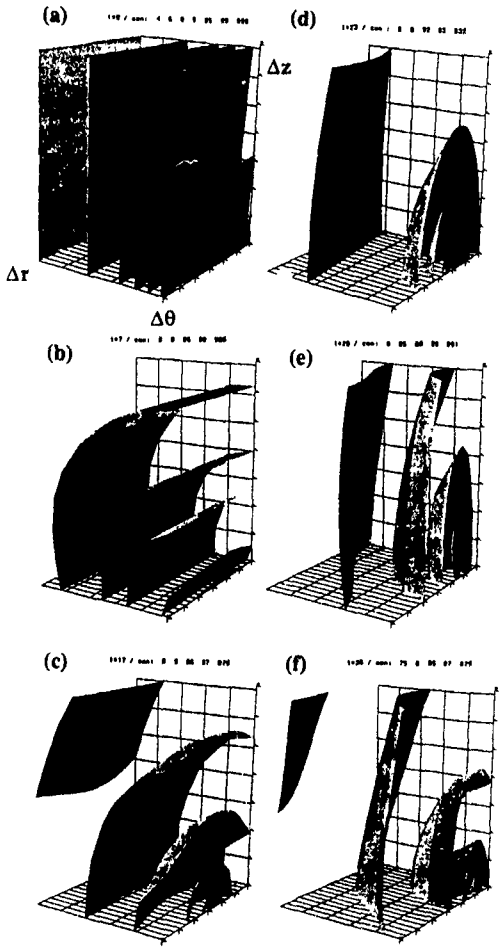

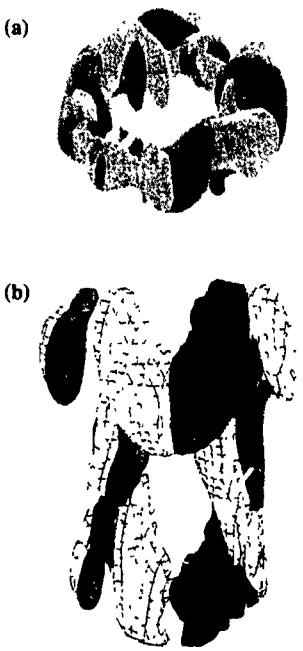

Fig 12 Isovorticity surfaces of ω_R and ω_L at (a) t=17, (b) t=23

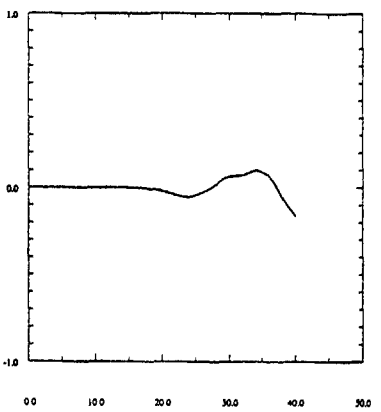

Fig 14 Helicity H versus time

EIGHTH SYMPOSIUM ON
TURBULENT SHEAR FLOWS
Technical University of Munich
September 9-11, 1991

LOCAL TOPOLOGY OF SMALL SCALE MOTIONS IN TURBULENT SHEAR FLOWS

R. Sondergaard†, J. Chen††, J Sona†††, B Cantwell†

† Department of Aeronautics and Astronautics, Stanford University, Stanford, CA, 94305, USA

†† Combustion Research Facility, Sandia National Laboratories, Livermore, CA, 94550, USA

††† Commonwealth Scientific and Industrial Research Organization, Highett, VIC, 3190, Australia

ABSTRACT

An investigation of the local flow geometry of a number of simulated turbulent flows, focusing on the fine scale motions characterized by high dissipation rates and/or high enstrophy, is in progress. The analysis technique consists of constructing the invariants of the velocity gradient tensor (P, Q, and R) and the strain rate tensor (P_s, Q_s, R_s) for every point in the flow. These quantities determine the local linearized flow geometry at each point. Scatter plots of all the points in the flow in P-Q-R and P_s-Q_s-R_s invariant spaces allow study of the distribution of topologies in the flow. Fine scale motions tend to map to regions far from the origin in invariant space. Observed trends suggest that for these motions, the second and third invariants of the rate-of-strain tensor are correlated by $R_s \cong K(-Q_s)^{3/2}$. Preliminary examination of vorticity strain alignments for these scales reveal a preference for the vorticity to align with the intermediate, positive, strain direction.

BACKGROUND

The high wavenumber motions of turbulence are not well understood. The purpose of this project is to study the geometry of these motions using data from recent direct numerical simulations of turbulent flows. Cases studied at the time of the submission of this paper include a time developing compressible plane mixing layer (Chen (1990)), a time developing incompressible plane mixing layer (Rogers and Moser (1990)), a time developing compressible plane wake (Chen (1990)), and preliminary results from a time developing incompressible plane wake (Sona and Sondergaard (1991)). These computations are at Reynolds numbers for which they can be considered to simulate transitional or early turbulent flow. In particular, late stages of the Rogers and Moser mixing layer exhibit tertiary instabilities similar in structure to the so-called "mixing transition" observed in laboratory experiments (Bernal and Roshko, 1986).

Also in progress at this time are studies of simulations of homogeneous turbulence, homogeneous shear flow, and wall-bounded turbulent flow.

APPROACH

Topological methods are useful in the description of fields and are coming increasingly into use as a means to study the large data sets that direct numerical simulations generate. Chong, Perry, and Cantwell (1990) have carried out a classification of the various types of linear three-dimensional flow patterns which can occur in compressible and incompressible flow. This classification method was used by Cantwell, Chen, and Lewis (1989) and Chen, Cantwell, and Mansour (1989) to analyze the topology of the flow structures in direct simulations of a compressible plane wake and experimental measurements of a pulsed low-speed diffusion flame. The method is based on concisely summarizing the flow structure in the space of invariants of the velocity gradient tensor.

The velocity gradient tensor $A_{ij} = \partial u_i/\partial x_j$ is divided into a symmetric and an anti-symmetric part, $A_{ij} = S_{ij} + R_{ij}$, where $S_{ij} = 1/2(\partial u_i/\partial x_j + \partial u_j/\partial x_i)$ is the rate-of-strain tensor and $R_{ij} = 1/2(\partial u_i/\partial x_j - \partial u_j/\partial x_i)$ is the rate-of-rotation tensor. The eigenvalues of A_{ij} satisfy the charactenstic equation

$$\lambda^3 + P\lambda^2 + Q\lambda + R = 0 \qquad (1)$$

where the invariants are given by

$$P = -\text{trace}[A] = -S_{ii} \qquad (2)$$

$$Q = \frac{1}{2}\left[P^2 - \text{trace}[A^2]\right] = \frac{1}{2}\left[P^2 - S_{ij}S_{ji} - R_{ij}R_{ji}\right] \qquad (3)$$

and

$$R = -\det[A] = \frac{1}{3}\left[-P^3 + 3PQ - S_{ij}S_{jk}S_{ki} - 3R_{ij}R_{jk}S_{ki}\right] \qquad (4)$$

The solutions to the characteristic equation at each point determine the local, linearized flow pattern.

Also of interest is the rate-of-strain tensor, whose invariants (P_s, Q_s, and R_s) are generated by setting the components of R_{ij} equal to zero in the above equations.

It can be shown that, in the space of these invariants, the surface which divides characteristic equations that have real solutions from those that have a pair of

complex solutions is given by

$$27R^2 + (4P^3 - 18PQ)R + (4Q^3 - P^2Q^2) = 0 \qquad (5)$$

A detailed discussion of the properties of this surface and a guide to the various possible flow geometries which can occur for all domains in P-Q-R space are given in Chong, Perry, and Cantwell (1990).

Fig 1 shows the flow topologies that can occur for the incompressible (P = 0) case. In this figure, the intersection of the surface dividing real and imaginary eigenvalues with the plane P = 0 is given by

$$R = \pm \frac{2\sqrt{3}}{9}(-Q)^{3/2} \qquad (6)$$

Matrices with invariants below this line have real eigenvalues, while those with invariants above it have one real and two imaginary eigenvalues.

For incompressible flow, the mechanical dissipation of energy due to friction is related to the second invariant of the rate of strain tensor by

$$\phi = 2\nu S_i S_i = -4\nu Q_s \qquad (7)$$

Hence, large negative values of Q_s correspond to large values of the dissipation. Similarly, for incompressible flow,

$$Q = \frac{1}{2}[R_i R_i - S_i S_i] \qquad (8)$$

Therefore large positive values of Q indicate that locally the enstrophy is large and dominates the strain while large negative values of Q indicate the reverse.

RESULTS

Fig. 2 is a scatter plot of Q vs. R for the incompressible mixing layer of Rogers and Moser (1990). The flow shown is at a late stage in the development of the layer and has a Reynolds number based on vorticity thickness of approximately 3000. At this point well developed streamwise vortices (ribs) have formed and the flow has undergone tertiary breakdown. For the velocity gradient tensor, all possible incompressible topologies are observed. However, those points which lie far from the origin tend to have a geometry of either stable focus/stretching or unstable-node/saddle/saddle.

Fig. 3 is the Q_s vs. R_s scatter plot for the same flow. Since the rate-of-strain tensor is symmetric, its eigenvalues are constrained to be real. No other constraints on where the points may lie are known to exist. Despite this, the highly dissipating fine scales tend to lie well into the right half of the accessible space, corresponding to an unstable-node/saddle/saddle flow

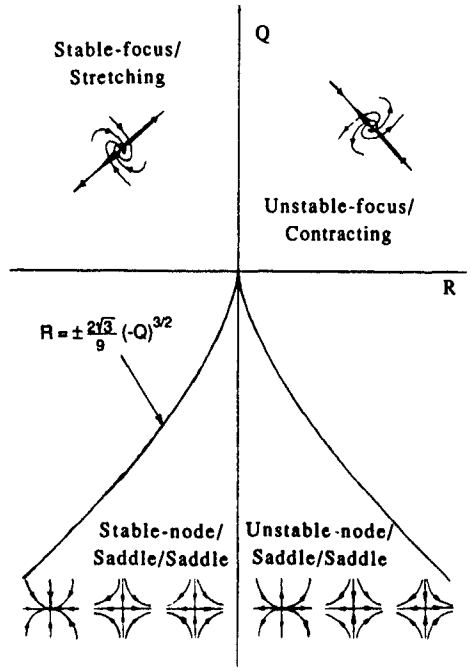

Fig. 1 Q-R invariant space for incompressible flow.

geometry. This is in agreement with the results of a study of homogeneous isotropic and homogeneous sheared turbulence by Ashurst *et. al.* (1987), as well as studies of the development of singularities in the Euler equations by Pumir and Siggia (1990), and the evolution of velocity gradients in homogeneous turbulence by Girimaji and Pope (1990).

Scaling arguments have been put forth by Chen *et. al.* (1990) which indicate that the highly dissipating motions should be expected to lie near a line given by

$$R = K(-Q)^{3/2} \qquad (9)$$

where the coefficient K may be a function of Reynolds number and/or flow type. Further study is required to determine why the unstable-node/saddle/saddle form is so strongly preferred, and to confirm the existence of a functional relationship between the second and third invariant of the rate-of-strain tensor.

Figs. 4 and 6 are plots of Q vs. R and Q_s vs. R_s for the compressible mixing layer. At this time in the simulation, the Reynolds number based on vorticity thickness is approximately 1600. Again the velocity gradient tensor tends to have fine scale motions which lie in the second and fourth quadrants. Similarly, the rate-of-strain tensor has fine scale motions whose geometry is nearly exclusively unstable-node/saddle/saddle. The

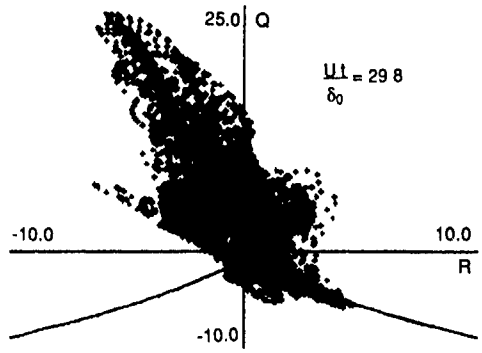

Fig 2 Q vs R for the incompressible mixing layer.

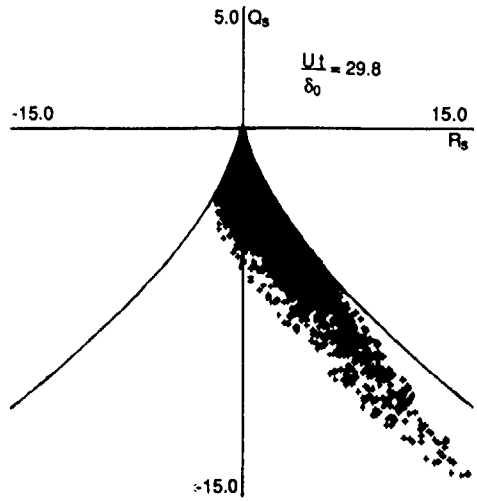

Fig 3 Q_s vs. R_s for the incompressible mixing layer.

scatter in the fine scales are greater than for the incompressible mixing layer. This may be due to the lower Reynolds number of the flow.

Fig. 5 is a plot of Q vs. P for this flow. Note that, for the fine scales, P is small compared to the other invariants. This implies that compressibility has only a weak affect on the local flow geometry of these scales and that the dissipation at these points is very nearly the incompressible dissipation, which is proportional to the second invariant of the rate-of-strain tensor.

Figs 7 and 8 are plots of Q vs. R and Q_s vs. R_s for the incompressible wake This simulation, at a Reynolds number based on the initial half width of 500, is still very early in its development. Despite this, the same trends are present. Although there is more scatter than in the more well developed flows, there is still a tendency for the invariants of the fine scales in the velocity field to lie in the second and fourth quadrants and for the rate-of-strain tensor to have an unstable-node/saddle/saddle

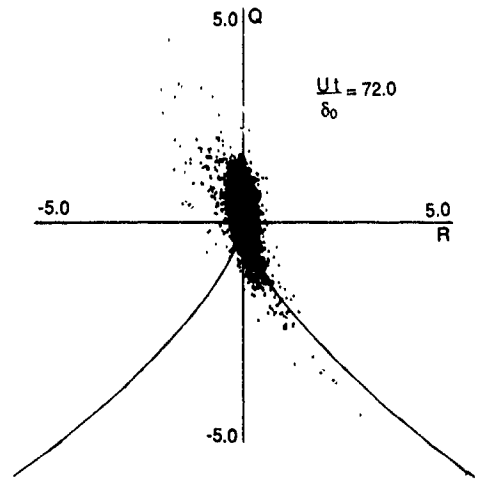

Fig 4 Q vs R for the compressible mixing layer.

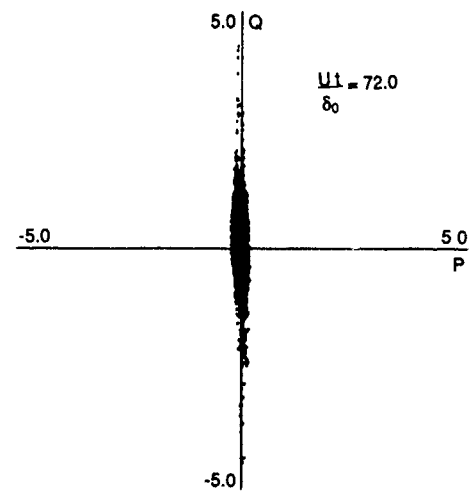

Fig 5 Q vs P for the compressible mixing layer

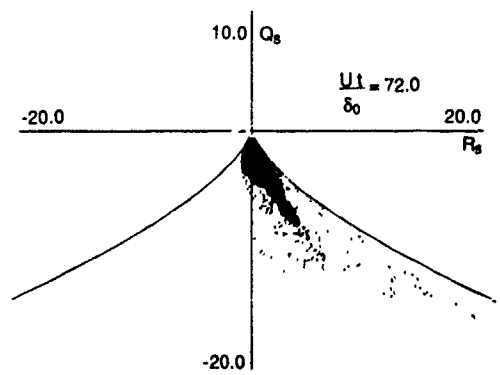

Fig. 6 Q_s vs. R_s for the compressible mixing layer.

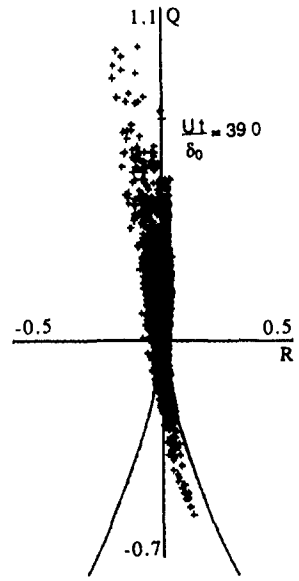

Fig 7 Q vs. R for the incompressible wake

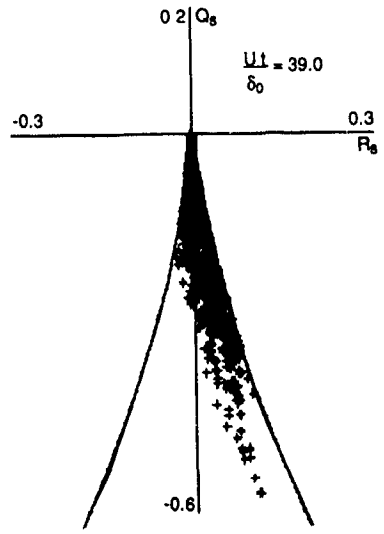

Fig 8 Q_s vs R_s for the incompressible wake

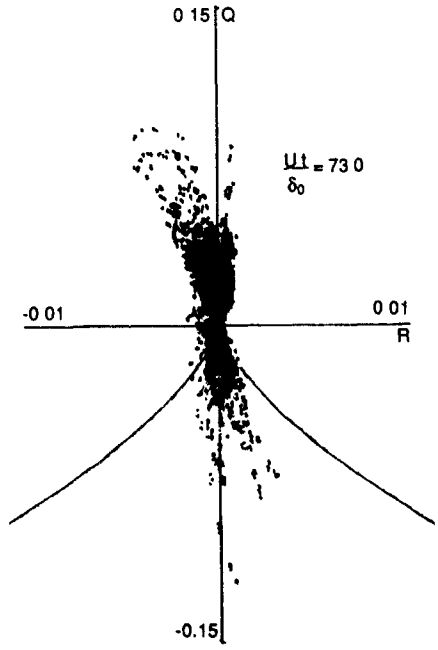

Fig 9 Q vs. R for the compressible wake

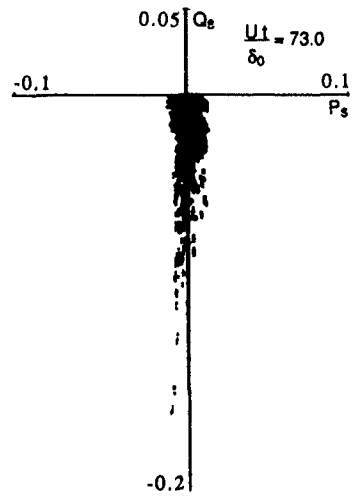

Fig 10 Q_s vs. P_s for the compressible wake.

topolog,

Figs 9 through 11 are plots of Q vs R, Q_s vs. P_s, and Q_s vs. R_s for the compressible wake. Again the same trends in the data occur. Fine scale motions favor the second and fourth quadrants of the Q vs. R plot, P is relatively small, and the rate-of-strain field has unstable-node/saddle/saddle topology. This is the lowest Reynolds number flow presented, with a Reynolds number based on the freestream velocity and the initial half width of 300. This accounts for the sparseness of the fine scale motions and may also account for the wide scatter of these scales in Q_s-R_s space.

To study the relationship between the strain and vorticity, the alignment of the local vorticity vector with the principal strain directions for the fine scale motions in the mixing layers was computed Figs. 12 through 14 are the alignment probability distributions for the incompressible mixing layer for sets of points conditioned on different

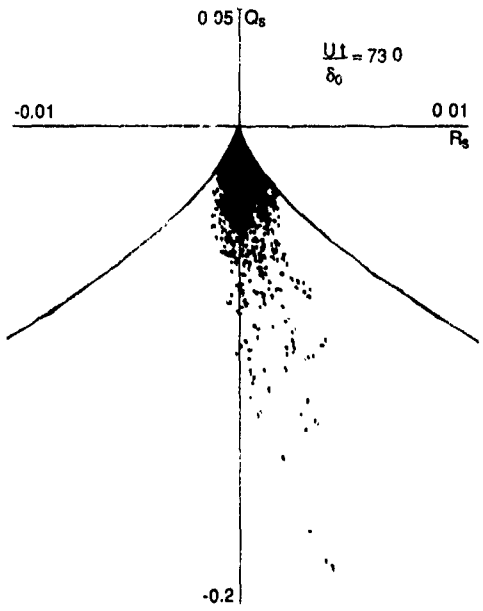

Fig. 11 Q_S vs. R_S for the compressible wake

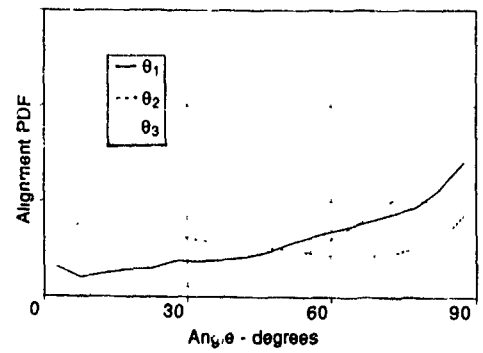

Fig 12 Incompressible mixing layer vorticity alignment with principal strain directions. $|Q_s| \geq 0.09$

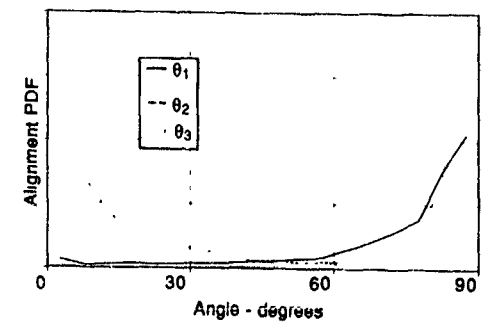

Fig. 13 Incompressible mixing layer vorticity alignment with principal strain directions. $|Q_s| \geq 2.0$.

minimum values of Q_s, hence different levels of dissipation Fig. 12 is the distribution for points which have a $|Q_s|$ greater than 0.09, which is approximately the value which would be produced by the mean shear if the flow were laminar. For this conditioning, there is only a weak preference for the vorticity to align with any given strain direction in the mean Fig. 13 is the same data but with a lower limit cutoff of $|Q_s| = 2.0$, roughly 20 times the value due to mean shear. For this level of dissipation, the vorticity has a distinct tendency to align along the direction of the intermediate (α_2) strain.

Fig 14 is the alignment distribution for only the most dissipating points. Here the vorticity aligns itself very strongly along the intermediate strain direction Note that, since the rate-of-strain topology for these points is unstable-node/saddle/saddle, the intermediate strain is positive Again, this is consistent with the results of Ashurst *et al.* (1987), Girimaji and Pope (1990), and Pumir and Siggia (1990) as well as asymptotic studies of a modified set of Euler equations by Vieliefosse (1984).

Fig. 15 is the alignment distribution for the strongly dissipating points in the compressible mixing layer

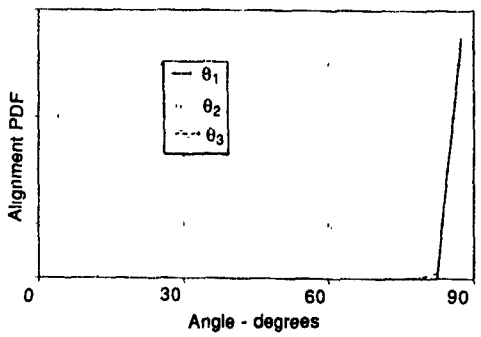

Fig. 14 Incompressible mixing layer vorticity alignment with principal strain directions $|Q_s| \geq 9.1$

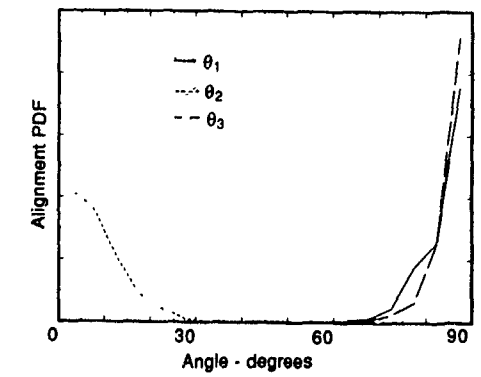

Fig 15 Compressible mixing layer vorticity alignment with principal strain directions. $|Q_s| \geq 2.0$.

Again, the vorticity vector tends to align with the intermediate rate of strain. While this aspect of the wake flows has yet to be studied, it is expected that the same trends will appear

CONCLUSIONS

The fine scale motions of the direct numerical simulations studied appear to be characterized by relatively simple relations between the second and third invariants of the rate-of-strain tensors. The possibility that a triple product (R_S) can be simply related back to a double product (Q_S) is significant in that it could contribute to a closure hypothesis for the contribution of underresolved fine scale motions to momentum and energy transport.

The procedure outlined here needs to be applied to a greater variety of direct numerical simulations, including higher Reynolds number flows, to determine if the trends observed between Q_S and R_S are, indeed, universal.

Work on expanding the study to higher Reynolds number flows, including free and wall-bounded turbulent flows, is in progress. It is expected that these higher Reynolds number flows will reinforce the trends observed thus far

If the trends seen in the completed studies are found to be universal and if, at high Reynolds number, these trends are found to characterize the motions responsible for a significant part of the total dissipation of kinetic energy, this will constitute a significant step towards a better understanding of fine scales in turbulent flow.

ACKNOWLEDGEMENTS

This study is supported by the Center for Turbulence Research, ONR grant N00014-90-J-1976, and the Department of Energy's Office of Basic Energy Sciences, Division of Chemical Sciences.

REFERENCES

CHEN, J 1990 The effect of Mach number on the stability of a plane supersonic wake *Physics of Fluids A* **2(6)**, 984-1004

ROGERS, M. & MOSER, R. 1990 Mixing transition and the cascade to small scales in a plane mixing layer *Proceedings of the IUTAM Symposium on Stirring and Mixing.* UCSD, LaJolla, CA.

SORIA, J & SONDERGAARD, R. 1991 Private Communication

BERNAL, L. & ROSHKO, A. 1986 Streamwise Vortex Structure in Plane Mixing Layers. *J. Fluid Mech.* **179**, 499

CHONG, M , PERRY, A & CANTWELL, B 1990 A general classification of three-dimensional flow fields *Physics of Fluids A* **2(5)**, 765-777

CANTWELL, B., CHEN, J & LEWIS, G 1989 Topology of three-dimensional, variable density flows. *Proceedings of the Tenth Australasian Fluid Mechanics Conference.* Melbourne, Australia.

CHEN, J , CANTWELL, B. & MANSOUR, N. 1989 The topology and vorticity dynamics of a three-dimensional plane compressible wake. *Proceedings of the Tenth Australasian Fluid Mechanics Conference.* Melbourne, Australia.

ASHURST, WM. T , KERSTEIN, A. R., KERR, R. M. & GIBSON, C. H 1987 Alignment of vorticity and scalar gradient with strain rate in simulated Navier-Stokes turbulence *Physics of Fluids* **30(8)**, 2343-2353.

PUMIR, A & SIGGIA, E. 1990 Collapsing solutions to the 3-D Euler equations. *Physics of Fluids A.* **2(2)**, 220-241.

GIRIMAJI, S. S. & POPE, S B 1990 Alignment of vorticity and scalar gradient with strain rate in simulated Navier-Stokes turbulence *Physics of Fluids A.* **2(2)**, 242-256.

CHEN, J , CHONG, M , SORIA, J., SONDERGAARD, R , PERRY, A E., ROGERS, M., MOSER, R., & CANTWELL, B. 1990 A Study of the Topology of Dissipating Motions in Direct Numerical Simulations of Time-Developing Compressible and Incompressible Mixing Layers *Center for Turbulence Research Report CTR-S90.*

VIEILLEFOSSE, P 1984 Internal motion of a small element of fluid in an inviscid flow. Physica 125A, 150-162.

EIGHTH SYMPOSIUM ON
TURBULENT SHEAR FLOWS
Technical University of Munich
September 9-11, 1991

ON THE USE OF THE WEIERSTRASS-MANDELBROT FUNCTION TO DESCRIBE THE FRACTAL COMPONENT OF TURBULENT VELOCITY

J.A.C Humphrey, C A Schuler and B Rubinsky

Department of Mechanical Engineering
University of California at Berkeley
Berkeley, California 94720

ABSTRACT

It is shown that the Weierstrass-Mandelbrot function simulates the irregularity in a turbulent velocity record and yields correct forms for the energy and dissipation spectra. In particular, the universal properties of a corresponding multi-fractal function are demonstrated by showing its ability to reproduce and explain turbulent flow spectra measured near the walls of straight and curved channels and in the obstructed space between a pair of disks corotating in an axisymmetric enclosure. The simulation capabilities of the multi-fractal function strongly suggest that turbulence is fractal in the frequency range of the turbulent energy spectrum where the slope of the logarithm of the spectrum, G, is $-3 < G < -1$. The scale-independent frequency range of the energy spectrum correctly represented by the multi-fractal function includes the isotropic dissipation subrange ($-3 < G < -5/3$), the inertial subrange ($G = -5/3$), and the "inner" portion of the anisotropic large-scale subrange ($-5/3 < G < -1$)

1 INTRODUCTION

The subject of fractal mathematics is important because of the demonstrated ability of fractals to describe and quantify disorderly geometries and chaotic phenomena The fractal properties of fully developed turbulence, a fluid flow phenomenon characterized by disorderly behavior, have recently become the subject of intensive studies. The first to apply fractal mathematics to turbulence was Mandelbrot [1974, 1975, 1976, 1983]. Subsequent researchers include Frisch et al. [1978], Chorin [1981, 1988], Lovejoy [1982], Heutschel and Procaccia [1983a, 1983b], Meneveau and Sreenivasan [1987] and Turcotte [1988]. The research on the fractal properties of turbulent flows has concentrated primarily on characterizing the energy distribution among the various scales of motion, or eddies, and the transfer of this energy from large to small eddies It deals mostly with scaling turbulent energy content as a function of eddy size and representing the scaling process through fractal dimensions. In this regard, we note especially the "curdling" approach of Mandelbrot [1983] to derive a fractal model of turbulence accounting for its intermittent and dissipative nature.

The shape of the time signature for velocity in a statistically steady (stationary) high Reynolds number turbulent flow is a highly irregular line that defies description by analytical functions The fact that previous researchers have found that the eddy structure of turbulent flows can be modeled using fractal concepts suggested to us that the turbulent velocity *itself* might be described by a multi-fractal function In this work we demonstrate that, in addition to producing a time sequence that closely resembles a measured turbulent velocity record, the use of the Weierstrass-Mandelbrot (W-M) fractal function, in the context of a multi-fractal formulation, yields correct forms for the energy and dissipation spectra of turbulence over a frequency range that includes inertial (large and anisotropic) and dissipative (small and isotropic) scales of motion. The simulation capabilities of the multi-fractal formulation are illustrated by showing its ability to reproduce and explain turbulent flow spectra measured near the walls of straight and curved channels and in the obstructed space between a pair of corotating disks in an axisymmetric enclosure

2. FRACTAL REPPESENTATION OF TURBULENT VELOCITY

The fractal properties of the W-M function were recognized by Mandelbrot, and the function is used to describe fractal geometries (Mandelbrot 1983, Peitgen and Saupe 1988, Feder 1988). Mandelbrot [1983] actually suggested using the W-M function to describe the trajectory of a particle in turbulent flow. In this section we argue that the fractal component of turbulent velocity can be represented by a multi-fractal W-M function. In Section 3 we show that this assumption yields correct forms for the energy and dissipation spectra over a wide range of frequencies in both isotropic and anistropic flows and we demonstrate a practical application of our findings to rotating disk flows. Section 4 presents the conclusions of this work.

The basic form of the W-M function employed is:

$$u(t) = A \sum_{n=n_1}^{n_2} \frac{\sin(\omega t)}{\omega^H} \qquad (1)$$

In Eq.(1), t represents time for an analysis performed in frequency space, or the homogeneous direction of the flow for an analysis performed in wavenumber space. Accordingly, the quantity ω represents frequency or wavenumber The variable u(t) represents velocity, A is a constant, H is a constant scaling factor related to the fractal dimension, D, $\omega \equiv b^n$, b is a constant and n is a running integer in the summation The summation limits, n_1 and n_2, are determined by substituting the smallest (ω_1) and largest (ω_2) values of the frequencies (or wavenumbers) to be represented by the fractal function into the definition of ω.

The W-M function has been studied extensively by Singh [1953], Berry and Lewis [1980] and, more recently, by Majumdar [1989]. It has been shown that the function given by Eq. (1) is fractal, i e continuous, non-differentiable and self-affine for $b > 1$ and $0 < H < 1$ The mathematical constraints on H, listed in Table 1, are set by the fact that for $H < 0$ the series does not converge, while for $H > 1$ the series generates an analytical function that is continuous and differentiable: see, for example, Singh [1953], Mandelbrot [1983], or Peitgen and Saupe [1988]. The parameter b determines the density of the spectrum of u(t). To achieve a spectrum that corresponds to a random u(t) profile, b must be chosen in such a way that its powers, which form the frequency spectrum, are not multiples of a basic frequency. Majumdar [1989] has shown that for $b = 1.5$ the simulation of a random profile results.The relation between the scaling factor H, the fractal dimension D and the Euclidean dimension E is given by Peitgen and Saupe [1988]:

$$H = E + 1 - D \qquad (2)$$

where, in the present application, time (or space) has an Euclidean dimension $E = 1$. It should be emphasized that both H and D are representations of fractal dimensions, i.e. scale-independent measures.

Examples of time sequences for the W-M function have been calculated by Berry and Lewis [1980] in a study aimed at characterizing the appearance of the function in terms of its governing parameters, b and D. Figure 1 shows our numerical evaluation of the W-M function corresponding to Eq. (1) in the interval 1.5 - 2.5 seconds for the conditions of the figure.

(Note that while the choice of time interval for representing the function is arbitrary, by avoiding the origin t = 0 we avoid having to deal with a function that contains infinitely many b-periods in the interval of interest.) The irregularity of the calculated profile is not unlike that of a typical turbulent velocity record and raises the question: *Can the W-M fractal function be used to represent the scale-independent turbulent component of velocity?* We note that while other functions might also achieve a similar apparently irregular behavior (for example, Frost [1977] discusses the use of improper Fourier-Stieljes integrals to represent a stationary random process as a sum of sinusoids of all frequencies each having a random amplitude) none of them embodies the simplicity of the present function.

Based on the investigations of the W-M function by Berry and Lewis [1980] and Majumdar [1989], we propose to use a deterministic multi-fractal W-M function to represent the fractal component of turbulent velocity, $u_F(t)$. The form of this function is

$$u_F(t) = \sum_{j=1}^{m} A_j \sum_{n=n_{1j}}^{n_{2j}} \frac{\sin(\omega t)}{\omega^{H_j}} \qquad (3)$$

where, as before, $\omega = b^n$, b is a constant (b > 1), and $b^{n_{2m}}$ is the largest frequency in the series. The A_j and H_j are scale-independent constants, and $0 < H_j < 1$ is a constraint on H_j.

This multi-fractal formulation is a generalization of the observation by Majumdar [1989], that the W-M fractal function can be decomposed into two functions (j = 1 and 2) each of which has the same constant value of b > 1, each of which exists between specified frequencies, given by n_{1j} and n_{2j}, respectively, and each of which has a constant scaling factor H_j (or dimension D_j according to Eq (2)) in its frequency range.The sum of the different dimension functions in Eq. (3) will remain fractal provided that b > 1 and that in each frequency interval the constraint on H_j is obeyed.

In addition to closely resembling a time- (or space-) dependent turbulent velocity record, we now show that the proposed multi-fractal W-M representation of turbulent velocity yields other important turbulent flow properties such as the correct forms for the energy and dissipation spectra for fully developed turbulence. We will also show that through its special characteristics the multi-fractal function encompasses a universal behavior of turbulent flows that is not captured by other analytical formulations of comparable simplicity.

3 THE ENERGY SPECTRUM OF TURBULENT FLOW

Turbulent velocity is an irregularly fluctuating quantity that cannot be exactly represented analytically As a result, turbulent flows are frequently characterized by their energy spectra The energy spectrum in frequency space is obtained according to the well known relation:

$$E(\omega) = \frac{1}{T}\left| \int_0^T u(t) \exp(i\omega t) dt \right|^2 \qquad (4)$$

The discrete energy spectrum, S_j, for the multi-fractal function expressed by Eq (3) follows from that for the W-M function in Berry and Lewis [1980] and is:

$$S_j(\omega) = A_j^2 \sum_{n=n_{1j}}^{n_{2j}} \frac{\delta(\omega - b^n)}{(b^n)^{2H_j}} \quad j = 1 \ldots m, \quad b^{n_{1j}} < \omega < b^{n_{2j}} \qquad (5a)$$

where δ is the Dirac delta function The corresponding continuous energy spectrum is obtained by averaging S_j over a range $\Delta\omega$ including Δn frequencies b^n. The result is:

$$E_j(\omega) = \frac{A_j^2}{2 \ln b} \frac{1}{\omega^{2H_j+1}} \qquad j = 1 \quad m, \quad b^{n_{1j}} < \omega < b^{n_{2j}} \qquad (5b)$$

which is an exact expression in each of the different dimension domains in the limit when $b \to 1$

From Eqs. (2) and (5b) it follows that, in any frequency (or wavenumber) interval, the scaling factor, H_j, and the corresponding fractal dimension, D_j, are related to the slope of the logarithm of the continuous energy spectrum, G_j, through:

$$H_j = -(G_j + 1)/2 \qquad (6)$$

$$D_j = (G_j + 5)/2 \qquad (7)$$

The mathematical constraints on the H_j, listed in Table 1, result in corresponding constraints on the slope, G_j, in the interval of the spectrum that the j'th W-M function represents The constraints imply that the W-M functions composing Eq (3) are fractal, and hence scale-independent and self-affine, only in the range $-3 < G_j < -1$ Therefore, the use of Eq. (3) to represent turbulent velocity implies that the turbulence represented is fractal, and that the representation is valid only in the frequency range of the turbulent energy spectrum for which the slope of the logarithm of the spectrum obeys the constraint.

$$-3 < G_j < -1 \qquad (8)$$

Figure 2 shows numerically computed discrete and continuous spectra for the time record of Figure 1. The slope of the continuous spectrum is very close to G = - 5/3, in agreement with the value for G set by the value for H used to calculate the time record.

We now consider the case of locally isotropic turbulence, to show that Eq. (5b), subject to E_{-1}. (8), includes the equilibrium range of the turbulent spectrum, described below. We also show that Eq (7) predicts a fractal dimension for the inertial subrange of the equilibrium range that is identical to that obtained by other researchers using other methods. Finally, we demonstrate the simulation capabilities of the multi-fractal formulation for some anistropic turbulent flows near walls in straight and curved channels and in the obstructed space between a pair of corotating disks.

3.1 LOCALLY ISOTROPIC TURBULENCE

Turbulent flows are dissipative and, to be maintained, they require a continuous supply of energy to overcome the deformation work performed by the viscous shear stresses Most of the viscous dissipation of turbulent kinetic energy occurs at the smallest (Kolmogorov) scales of motion, while most of the turbulent energy itself is contained in much larger scales of motion, the largest of which interact directly with the mean flow; see Tennekes and Lumley [1972] Calling l and η the length scales characteristic of the energy-containing and dissipative scales of motion respectively, it is readily shown that $l/\eta \approx R_l^{3/4}$, where $R_l = lu/\nu$ is the turbulence Reynolds number based on l and its associated characteristic turbulent velocity, u. The quantity ν is the fluid kinematic viscosity For the high values of R_l typical of turbulent flows, the l and η scales of motion lie several decades apart.

For large values of R_l, the time-averaged dynamics of the microscale turbulent motion become independent of orientation. In this case, the condition of local isotropy prevails; see Kolmogorov in Friedlander and Topper [1961] The range of eddy wavenumbers possessing local isotropy is referred to as the equilibrium range and, in this range, the turbulent energy spectrum is described by the following scaling law, due to Kolmogorov:

$$\frac{E(\kappa)}{\nu^2 \eta} = f(\kappa\eta) \qquad (9)$$

where $E(\kappa)$ is the energy associated with an eddy of size $2\pi/\kappa$ (κ being the eddy wavenumber), $\eta = (\nu^3/\varepsilon)^{1/4}$ is the Kolmogorov microscale, $v = (\nu\varepsilon)^{1/4}$ is the Kolmogorov velocity and ε is the rate of dissipation of turbulent kinetic energy By contrast, the scaling law for the spectrum of the anisotropic large-scale motion is:

$$\frac{E(\kappa)}{u^2 l} = F(\kappa l) \qquad (10)$$

and varies with the flow geometry. Thus, unlike Eq. (9), Eq. (10) is not universal.

Because most of the viscous dissipation occurs about the Kolmogorov scale, the equilibrium range encompasses the dissipation range The spectrum of the dissipation is given by:

$$D(\kappa) = 2\nu \kappa^2 E(\kappa) \qquad (11)$$

Tennekes and Lumley [1972] show that when $\kappa l \to \infty$, $\kappa\eta \to 0$ and $R_l \to \infty$, Eqs (9) and (10) overlap in a viscosity-independent region of the spectrum described by:

$$\frac{E(\kappa)}{v^2\eta} = \alpha(\kappa\eta)^{-5/3} \qquad (12a)$$

or, equivalently,

$$\frac{E(\kappa)}{u^2 l} = \alpha(\kappa l)^{-5/3} \qquad (12b)$$

where $\alpha \approx 1.5$, approximately. Either one of Eqs. (12) describes the scale-independent inertial subrange of the equilibrium spectrum in fully developed turbulent flow. From Eqs. (11) and (12a) it follows that the spectrum of the dissipation in the inertial subrange is:

$$D(\kappa) = 2\alpha\eta\varepsilon\,(\kappa\eta)^{1/3} \qquad (13)$$

Figure 3, from Tennekes and Lumley [1972], shows typical shapes of nondimensional energy and dissipation spectra for $R_l = 2 \times 10^5$, corresponding to $l/\eta \approx 10^4$. The figure also shows the shapes of the spectra near the ends of the inertial subrange where the effects of dissipation (at high wavenumber) and energy production (at low wavenumber) must be considered when evaluating the energy flux across wavenumber space.

Over the wavenumber range in Fig. 3 for which $-3 < G < -1$, the energy spectrum can be correctly represented by that of the proposed multi-fractal function. For example, in the inertial subrange of the equilibrium spectrum we know that $G = -5/3$, which falls within the range of the multi-fractal representation. In addition, substitution of this value of G into Eq. (7) yields $D = 5/3$ as the fractal dimension of turbulent velocity in the inertial subrange. This is the value of D predicted by Chorin [1988] for the support of dissipation by means of a very different analysis involving vortex elements.

The multi-fractal velocity function given by Eq. (3) also represents the dissipation spectrum correctly. This can be shown by substituting Eq. (5b), with ω replaced by κ, into Eq. (11) to obtain that the slope of $\log D(\kappa)$ is $1\text{-}2H_j$ or, equivalently, G_j+2. A value of 1/3 is obtained for the slope of $\log D(\kappa)$ in the inertial subrange of the spectrum, where $G = -5/3$. This result is in agreement with Fig. 2 and Eq. (13).

However, the 1/3 slope for $\log D(\kappa)$ can also be obtained *directly* from du/dt, the time derivative of velocity, without resorting to the arguments leading to Eq. (11). By the definition of the W-M function, its time (or space) derivative will diverge if the series summation is taken over all frequencies (or wavenumbers) to infinity. However, for a finite range of frequencies (or wavenumbers), it can be shown (Mandelbrot, 1983 and Majumdar, 1989) that:

$$\langle \left(\frac{du}{dt}\right)^2 \rangle \sim \omega^2 E(\omega) \qquad (14)$$

where $\langle\ \rangle$ denotes average over time (or space). The spectrum of the dissipation, $D(\kappa)$, is proportional to $\langle (du/dt)^2 \rangle$ and setting $\omega \equiv \kappa$ in Eq. (14) shows the correspondence between Eqs. (11) and (14). Thus, the slope of $\log \langle (du/dt)^2 \rangle$ is also 1/3 in the inertial subrange, which illustrates the consistency embedded in the use of the W-M fractal function when used to describe velocity in fully developed turbulence.

In addition to modeling the inertial subrange correctly, in the high frequency limit corresponding to $G = -3$ the multi-fractal function becomes continuous and differentiable, as is required by a scale of motion ultimately dominated by viscous effects. Thus Eq. (3) yields correct forms for the energy and dissipation spectra of turbulence as a function of increasing frequency (or wavenumber).

3.2 ANISTROPIC FLOWS NEAR SURFACES

The proposed expression for the fractal component of turbulent velocity, Eq. (3), also accounts for the spectral characteristics of more complex anisotropic flows such as those near solid surfaces. For a high Reynolds number flow along a solid surface there is a range of distances y, normal to the surface, where $y\,u_\tau/\nu \gg 1$ and $y/\delta \ll 1$ simultaneously, δ being the thickness of the boundary layer along the surface and u_τ the wall shear velocity. In this region, the structure of the turbulence is scale-independent, since neither η nor l characterize the flow; y itself is the only relevant length scale for nondimensionalizing purposes. This leads to the "inner flow" scaling law discussed by Perry et al [1985], which is the boundary layer analog of Eq. (10) but includes the inertial sublayer (equivalent to the inertial subrange discussed above).

Because the fractal component of turbulence ranges over $-3 < G < -1$ and fractal behavior is scale independent, we expect that within this range of G the shape of the energy spectra should coincide, regardless of the distance from the wall where the spectra are measured. Similarly, because scale invariance is a characteristic only of fractal turbulence, the energy spectra should be observed to diverge outside this range of G.

Typical of the spectra obtained in straight and curved channel flows are the results shown in Fig. 4, taken from Hunt and Joubert [1979]. In the plot, ϕ' is the nondimensional intensity-normalized spectrum function for the streamwise normal stress, u^2. This is plotted against $k' = 2\pi f\, y/U$ where (by the Taylor hypothesis) U is the local mean velocity and f the frequency. Similar results have been measured by Barlow and Johnston [1988] for the boundary layer on a concave surface, and by Bradshaw [1967] and Perry et al [1985] in flat plate boundary layers. From the figure it is evident that the shapes of the spectra coincide in the interval $-3 < G < -1$, and that they can be represented by Eq. (5b) which is based on the proposition embodied in Eq. (3), that the fractal component of turbulence can be simulated by a scale invariant multi-fractal W-M function. Thus, in spite of its simplicity, we find that the multi-fractal function proposed accounts for the coincidence in shape, within the fractal range, of energy spectra measured at various distances from a straight or curved wall, as well as for their divergence where $G > -1$.

3.3 A PRACTICAL APPLICATION

The results presented above suggest that a turbulent velocity record can be decomposed according to:

$$u(t) = u_{SD}(t) + \sum_{j=1}^{m} A_j \sum_{n=n_{1j}}^{n_{2j}} \frac{\sin(\omega t)}{\omega^{H_j}} \qquad (15)$$

where the first term represents the contributions from the nonfractal (scale-dependent or imposed) components of motion and the second term represents the contributions from the fractal (scale-independent) components of motion.

We wish to establish the form of Eq. (15) for the case of high speed flow past an obstruction in the space between a pair of coaxial corotating disks in an axisymmetric enclosure. This flow configuration has been explored by the first two authors in other work using flow visualization and the laser-Doppler velocimetry technique. Measurements of the circumferential component of velocity, with and without the obstruction, have been reported by Usry et al. [1990] and Schuler et al. [1990], respectively. Since the work of Usry et al. [1990], Kawamura et al. [1991] have attached a hot-wire to the downstream side of the obstruction. Figure 5 shows part of a typical time-record of velocity sensed by the hot-wire. The entire record (not shown) consists of 8192 equally-spaced interconnected digitized points measured over a time period of 3.2 seconds in a flow rotating at 60 Hz.

Equation (7) states the relation between the slope, G_j, of the energy spectrum of a fractal curve of dimension D_j generated by a W-M fractal function in the interval $b^{n_{1j}} < \omega < b^{n_{2j}}$. In order to be able to represent the entire experimental velocity record by means of a W-M function, we must first verify that: a) the spectrum of the record presents a power law decay; and, b) *independent* measures of D_j and G_j comply with Eq. (7).

That the experimental velocity record yields a spectrum with a power law decay is shown in Fig. (6). This spectrum is the average of 12 Fourier transforms obtained by dividing the original time record into 12 sequential subrecords of 512 points each and applying a FFT to each subrecord. The peak in the spectrum at $\omega \approx 1130$Hz is believed to be associated with the characteristic (scale dependent) eddy shedding frequency of the obstruction. That at $\omega \approx 10$Hz is known to be due to a circumferentially periodic intensification of axially-aligned component of vorticity known to exist in this flow; see, for example, Usry et al. Two lines, with slopes $G_1 = -1.1$ and $G_2 = -1.76$, respectively, are also indicated in Fig. (6) and they are seen to approximate the spectrum reasonably well over the ranges $30 < \omega \leq 500$ and $500 < \omega \leq 1500$.

For measures of D_1 and D_2 we estimated the Hausdorff dimension of the original time record in each of the above two frequency intervals. This was done by computing the length of the time record on a successively refined grid in the interval $0 < t < T$ with sampling frequencies $N = \frac{2^n}{T}$ $(n = 0, 1, 2, \ldots)$ We know (Mandelbrot [1983]) that the length, L, of the curve and its fractal dimension, D, are related according to

$$L \sim \varepsilon N^{D-1} \qquad (16)$$

from which, in the range $10 < N < 500$, $D_1 = 1.95$ is obtained Similarly, for $N > 500$, a value of $D_2 = 1.62$ is obtained The values for G_1 and G_2 used to draw the straight lines in Fig (6) follow from the substitution of these values of D_j into Eq (7) In positioning the straight lines in Fig (6) we have maintained a correspondence with the frequency ranges for which the values of D_1 and D_2 were determined.

Strictly, we should have measured G_1 and G_2 independently from D_1 and D_2 to show that, within experimental error, the separately determined measures for these quantities comply with Eq. (7). However, this approach introduces a level of uncertainty that is unnecessary to illustrate the point

It should be clear that, subject to unavoidable experimental limitations, higher sampling frequencies would allow a more continuous correspondence in frequency space between pairs of D_j and G_j The choice of only two values of j made here is simply for illustration purposes. The main point is that, for the velocity record under consideration, the second condition set above, that *independent* measures of D_j and G_j comply with Eq (7), has been demonstrated

With just two values of G_j or, equivalently, H_j, known, we now attempt to reproduce the fractal component of the entire experimental velocity record. We first fix the value of $b = 1.005$ This allows us to find the values for n_{1j} and n_{2j} in Eq (3) from the relation $\omega = b^n$ We find $n_{11} = 1050$ and $n_{21} = 1614$ for $j = 1$ over the range $30 < \omega \leq 500$, and $n_{12} = 1615$ and $n_{22} = 1834$ for $j = 2$ over the range $500 < \omega \leq 1500$ (The upper limit of $\omega = 1500$ is arbitrary but was made large enough to include the upper limit in frequency observed in the experimental energy spectrum.)

The choice of $b = 1.005$ is dictated by the desire to obtain a discrete energy spectrum for the W-M function which is as continuous as possible but still relatively easy to calculate numerically From Eq (5a) it is clear that peaks will appear in the discrete energy spectrum, $S_j(\omega)$, at values of $\omega = b^n$, see, for example, Fig. (2) for $b = 1.5$ As $b \to 1^{(+)}$, $S_j(\omega)$ tends to a continuous distribution. However, the range for the summation index, n, also increases with $b \to 1^{(+)}$ and the computational overhead to evaluate the function becomes larger The present choice of $b = 1.005$ represents a compromise between an acceptable continuity in the energy spectrum and a reasonable amount of computational effort.

Values for A_1 and A_2 in Eq (3) were determined as follows The ratio A_2/A_1 was obtained from Eq (5b), subject to the requirement that $E_1(500\text{Hz}) = E_2(500\text{Hz})$ in order to avoid a jump in energy in the average spectrum at the 500 Hz transition point. From this it follows that $A_2/A_1 = \omega^{(G_1 - G_2)/2}$ which, for $\omega = 500\,2\pi$, yields $A_2/A_1 = 14.26$ The value of A_1 was then determined by adjusting the average energy of the artificial signal to match that of the measured time record at $\omega = 100$ Hz which is near the center of the range for $j = 1$. The results obtained were $A_1 = 0.0647$ and $A_2 = 0.923$, respectively

For the present application, the scale-dependent velocity components are given by

$$u_{SD}(t) = A_{SD1}\cos(\omega_{SD1}\,t) + A_{SD2}\cos(\omega_{SD2}) \qquad (17)$$

In this equation, we can immediately set $\omega_{SD1} = 10$ Hz and $\omega_{SD2} = 1130$ Hz from the experimental energy spectrum plotted in Fig (6). The values $A_{SD1} = 0.20$ and $A_{SD2} = 0.05$ were determined in exactly the same way as was done for A_1

The final form of the velocity record *simulated* by Eq. (15) with the above set of values is plotted in Fig (7) The corresponding energy spectrum is shown in Fig. (8). The similarity between these two figures and the corresponding Figs (5) and (6) for the real record is noteworthy It is hard to distinguish between the real and artificial signals merely from an inspection of their respective time records or the associated spectra.

4. CONCLUSIONS

A new multi-fractal function has been proposed for representing the scale-independent component of turbulent velocity The function closely resembles the appearance of a turbulent velocity record and yields correct values for the energy and dissipation spectra over a range of frequencies that includes anisotropic large scale motions at one end, isotropic dissipative scales of motion at the other, and the inertial subrange in between. The function allows the derivation of relatively simple analytical expressions for the representation of both isotropic and anistropic turbulence. In addition to its simulation capabilities, illustrated here for the case of the flow past an obstruction between corotating disks, the properties of the function allow an improved understanding of the physics of turbulence such as, for example, the wall-independent shape of energy spectra in channel flows.

Of potential use for turbulence modeling purposes in the case of high speed turbulent shear flows admitting Taylor's hypothesis (see Hinze [1975]) are the results that the *fractal contributions* to the turbulent kinetic energy,

$$k = 1/2\,\langle u(t)u(t)\rangle = 1/2 \int_0^\infty E(\omega)d\omega \qquad (18)$$

and its (isotropic) rate of dissipation,

$$\varepsilon = \frac{15\,\nu}{U^2}\langle\left(\frac{du}{dt}\right)^2\rangle = \frac{15\,\nu}{U^2}\int_0^\infty \omega^2\,E(\omega)d\omega \qquad (19)$$

can be approximated by

$$k = \frac{1}{2\ln b}\sum_{j=1}^{m}\left[\frac{A_j^2}{4-2D_j}\left[\frac{1}{\omega_{1j}^{4-2D_j}} - \frac{1}{\omega_{2j}^{4-2D_j}}\right]\right] \qquad (20)$$

and

$$\varepsilon = \frac{15\,\nu}{U^2\,2\ln b}\sum_{j=1}^{m}\left[\frac{A_j^2}{2-2D_j}\left[\frac{1}{\omega_{1j}^{2-2D_j}} - \frac{1}{\omega_{2j}^{2-2D_j}}\right]\right] \qquad (21)$$

respectively In these expressions, U is the local mean velocity of the shear flow, and ω_{1j} and ω_{2j} correspond to the piecewise representation of H_j.

We conclude by noting that the multifractal W-M formulation, developed here in frequency space, can also be developed in wavenumber space Likewise, the deterministic nature of the W-M fractal function we employed can be rendered stochastic as explained in Berry and Lewis (1980), by adding a random phase to the argument of the sine term in Eq (3).

ACKNOWLEDGEMENT

This study was supported in part by a grant received by the first author and a postdoctoral appointment received by the second from the IBM Almaden Research Center in San Jose, California We gratefully acknowledge IBM's continued interest and support of our research. The authors appreciate the help provided by Janet Christian in preparing this manuscript.

REFERENCES

Barlow, R.S. and Johnston, J.P. (1988) *J. Fluid Mech.*, **191**, 137-176.

Berry, M V. and Lewis, Z.V. (1980) *Proc R Soc Lond. A*, **370**, 459-484.

Bradshaw, P (1967) *J Fluid Mech*, **30**, 241-258.

Chorin, A.J. (1981) *Comm. Pure Appl. Math*, **34**, 853.

Chorin, A.J. (1988) *Phys. Rev Lett.*, **60**, 1947-1949.

Feder, J. (1988) Fractals, Plenum Press, New York.

Friedlander, S.K. and Topper, L (1961) Turbulence, Classic Papers on Statistical Theory, Interscience Publishers, Inc, New York.

Frisch, U., Sulem, P.L. and Nelkin, J (1978) *J. Fluid Mech.*, **87**, 719-736.

Frost, W. (1977) Spectral Theory of Turbulence, in Handbook of Turbulence, Volume 1, Fundamentals and Applications, Frost, W. and Moulden, T.H. (editors), Plenum Press, New York and London

Heutschel, H G.E and Procaccia, I. (1983a) *Phys Rev A*, **27**, 1266-1269.
Heutschel, H.G E and Procaccia, I (1983b) *Phys Rev A*, **28**, 417-426.
Hinze, J.O. (1975) Turbulence, Second Edition, McGraw-Hill, Inc, New York.
Hunt, I.A and Joubert, P N. (1979) *J Fluid Mech*, **91**, 633-659.
Kawamura, T., Gor, D and Humphrey, J A C. [1991], in preparation
Lovejoy, S (1982) *Science*, **216**, 185-187
Majumdar, A. (1989) Fractal Surfaces and Their Applications to Surface Phenomena, Ph.D. Thesis, University of California at Berkeley
Mandelbrot, B.B. (1974) *J Fluid Mech*, **62**, 331-358.
Mandelbrot, B.B (1975) *Proc Nat Acad Sc*, **72**, 3825-3828.
Mandelbrot, B B (1976) in Turbulence and the Navier-Stokes Equation, Lecture Notes in Mathematics, **565**, 121-145, Temam, R. (ed.), Springer-Verlag, Berlin
Mandelbrot, B.B (1983) The Fractal Geometry of Nature, Freeman, W.H and Co, New York
Meneveau, C and Sreenivasan, K.R (1987) *Phys Rev Lett*, **59**, 1424-1427.
Peitgen, H.-O and Saupe, D (eds) (1988) The Science of Fractal Images, Springer-Verlag, New York
Perry, A E., Lim, K L and Henbest, S.M (1985) A Spectral Analysis of Smooth Flat-Plate Boundary Layers, Proceedings of the Fifth Symposium on Turbulent Shear Flows, Cornell University, Ithaca, August 7-9, 1985.
Schuler, C A., Usry, W, Weber, B, Humphrey, J A.C and Greif, R. (1990) *Phys. Fluids A*,**2**, 1760-1770
Singh, A N (1953) The Theory and Construction of Non-Differentiable Functions, in Squaring the Circle and Other Monographs, Chelsea Publishing Company.
Tennekes, H and Lumley, J L (1972) A First Course in Turbulence, The MIT Press, Cambridge, Massachusetts
Turcotte, D L. (1988) *Ann Rev Fluid Mech.*, **20**, 5-16.
Usry, W.R., Schuler, C.A, Humphrey, J A.C and Greif, R. (1990) Unsteady Flow between Corotating Disks in an Enclosure with an Obstruction, Proceedings of the Fifth International Symposium on Application of Laser Techniques to Fluid Mechanics, Instituto Superior Tecnico, Lisbon, Portugal, July 9-12, 1990

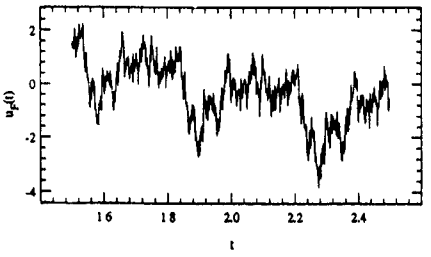

Figure 1 Calculated time sequence of the W-M function using Eq (1) with: A = 1, b = 1.5, H = 1/3 (D = 5/3) In the series n1 = 1 and n2 = 50, respectively.

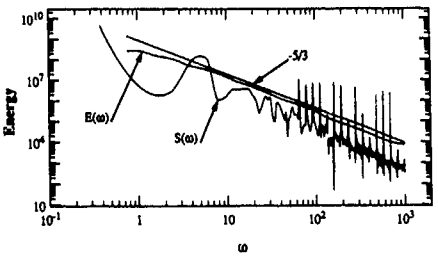

Figure 2 Calculated discontinuous, S(ω), and averaged, E(ω), energy spectra for the time sequence of Fig 1

Table 1. Allowed ranges of the energy spectrum slope, G, that can be represented by the W-M fractal function as a result of the constraints on H or, equivalently D

Character of the W-M Function	Constraint on H (or D)	Corresponding Constraint on G
Diverging	H < 0 (D > 2)	G > -1
Fractal	0 < H < 1 (1 < D < 2)	-3 < G < -1
Differentiable	H > 1 (D < 1)	G < -3

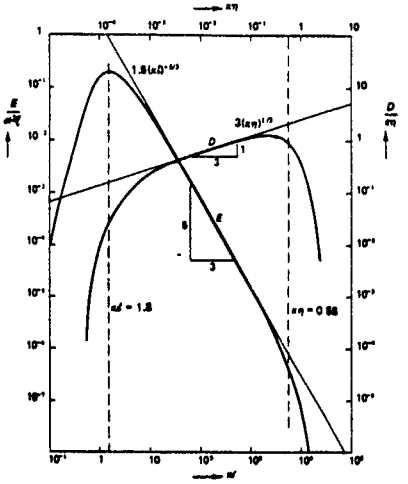

Figure 3. Normalized energy and dissipation spectra for R_λ=2 10^5 according to Tennekes and Lumley [1972]. Dashed lines indicate cutoffs for approximate spectra given analytically by these authors. Reproduced with permission from MIT press.

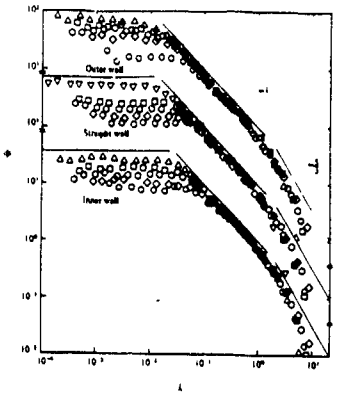

Figure 4. Logarithmic-region spectra in wall coordinates for straight and curved channel flows according to Hunt and Joubert [1979] In the table below $y^* = y\,u_\tau/\nu$ where y is the distance normal to a wall and u_τ is the wall shear velocity; $R_N = D\,U_m/\nu$ is the flow Reynolds number based on the channel width, D, and the maximum velocity, U_m Reproduced with permission from Cambridge University Press

y^*	$R_N \times 10^{-3}$	y^*	$R_N \times 10^{-3}$
80	30	160	60
80	60	160	130
80	130	320	130

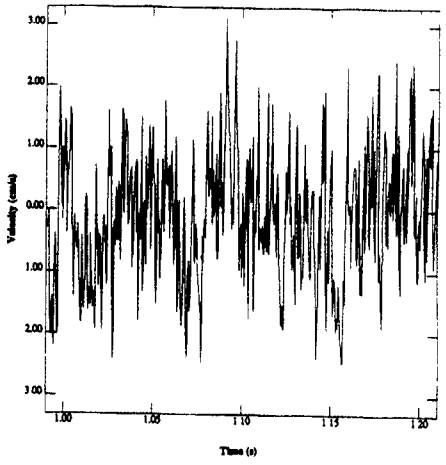

Figure 5 Segment of the velocity time record measured by the hot-wire in the obstructed space between corotating disks

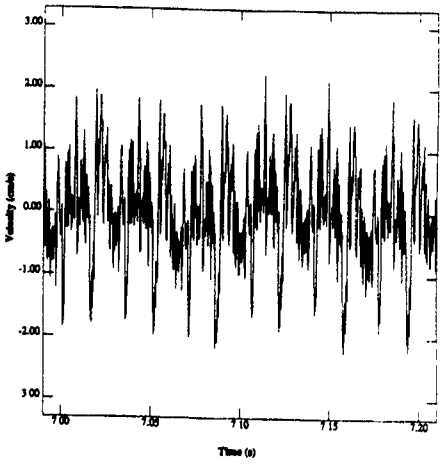

Figure 7 Portion of the velocity time record generated by the multifractal W-M function with its parameters determined as explained in the text

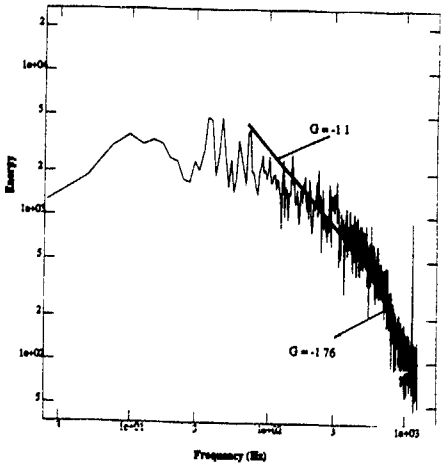

Figure 6. Energy spectrum of the entire velocity time record corresponding to Fig. (5). The peaks at 10 Hz and 1130 Hz correspond to non-turbulent time-dependent phenomena peculiar to this flow and described in the text

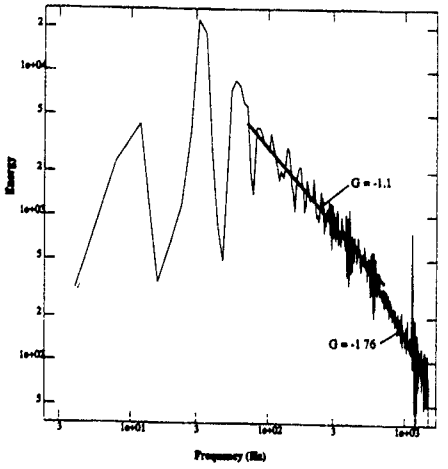

Figure 8 Energy spectrum of the entire velocity time record corresponding to the segment shown in Fig (7).

EIGHTH SYMPOSIUM ON
TURBULENT SHEAR FLOWS
Technical University of Munich
September 9-11, 1991

STUDY OF COUPLED EFFECTS OF PLANE STRAIN AND ROTATION ON HOMOGENEOUS TURBULENCE

O. LEUCHTER and J.P. BENOIT

Office National d'Etudes et de Recherches Aérospatiales (ONERA)
92320 - CHATILLON (France)

ABSTRACT

New configurations of homogeneous turbulence submitted to mean flow gradients are investigated experimentally, ranging from the basic case of plane strain to the domain of rotation dominated elliptical flows. The gradients are produced by combining solid body rotation with plane strain. The state of pure shear is realized for equal rates of rotation and strain. Very satisfactory homogeneity conditions are achieved for all flows. The evolution of the Reynolds stresses and associated length scales are determined by hot wire techniques. The mean flow distortion give rise to a definite decrease of the turbulent energy decay and a pronounced anisotropization of the Reynolds stresses and the associated length scales. The discussion of the results is focussed on the influence of the rotation rate/strain rate ratio.

INTRODUCTION

Various configurations of homogeneous turbulence submitted to uniform mean flow distortions have been investigated in the past. Flows of this type constitute valuable test cases for improving the general physical understanding of the basic mecanisms governing real world turbulence. They further provide useful material for data banks, especially in view of testing turbulence models in physical or spectral space, or for comparing experimental results with those obtained from direct or large eddy simulations.

The particular cases of constant strain, solid body rotation and pure shear have been mostly investigated up to now, see for a general discussion the review paper of GENCE [1]. In the first case, the flow distortion is located in transverse planes and the flow has constant velocity in the direction perpendicular to the distortion plane. This is also the case for pure rotation which has recently been reinvestigated at the ONERA [2]. In the case of homogeneous shear, most of the previous experiments are relative to situations where the shear is created in planes parallel to the mean velocity (as it occurs in most of the shear flows of practical relevance). This implies that the longitudinal velocity component cannot be kept constant in transverse planes. Therefore, the requirements of strictly homogeneous shear flows can only be satisfied partially, and it becomes difficult to avoid the downstream growth of transverse inhomogeneity. A short discussion of the corresponding experiments is given in [3].

Recently, a new method of generating homogeneous turbulent shear flows has been developed at the ONERA, which results from the superposition of solid body rotation with plane strain of the same rates [3],[4]. This provides uniform shear acting in planes perpendicular to the main flow direction, instead in planes parallel to it.

The main features of the action of transverse shear on the turbulence field were found to be a definite decrease of the turbulent energy decay and a pronounced anisotropization of the Reynolds stresses and the associated length scales. Due to the particular mode of shear generation, the flow distortion affects principally the turbulence quantities relative to the distortion plane, whereas those relative to the longitudinal direction are only weakly influenced. The Reynolds stresses and the length scales develop in a quite similar way to that observed i the case of pure strain, except that the principal directions of the Reynolds stress tensor are no longer aligned with those of the strain. The evolution of the shear stress correlation coefficient was found to be in good qualitative agreement with published data for longitudinal shear.

The experimental results relative to the shear case have also been compared with numerical predictions based on two-point closure approach of the EDQNM type developed at the ECL (Lyon), [4]. The numerical results have been found to be in good qualitative agreement with the measurements, including the evolution of the length scales.

In the present work, more general configurations of rotation/strain coupling are examined, based on the same principle of superposition as that used previously for the shear. Beside the limiting case of pure strain (no rotation) and the central case of shear (rotation equal to strain), we consider here two new cases corresponding respectively to the (hyperbolic) domain of dominant strain and to the (elliptic) domain of dominant rotation, with values for the rotation-to-strain ratio $\omega = \Omega/D$ of respectively 0.5 and 2. The case of elliptical flows appears in this context to be particularly attractive, since it corresponds to a periodic gradient tensor (and thus to a periodic distorting duct, see below). The evolution of the turbulence may therefore be expected to exhibit some oscillating behavior. Furthermore, this flow case may be considered in relation with the problem of 3D-instabilities developing in strained vortices, see e.g.[5].

One of the principal objectives of our study consists in comparing the experimental results with those obtained from two-point closure models or from numerical simulations. For this purpose a cooperative work with the ECL is under way aiming at developing spectral models of the EDQNM type able to take into account the distortions studied experimentally. As mentioned above, the case of pure shear has already been examined successfully in this context, [4].

The work presented hereafter is focussed on the description of the experimental methods used for generating the distorting flows and on the discussion of the principal results concerning the evolution of the turbulence during the distortions.

EXPERIMENTAL TECHNIQUES

Principle of flow generation

The flow configurations considered in the present work belong to a family of uniformly distorted mean flows characterized by the deformation matrix:

$$(\lambda_{ij}) = \begin{pmatrix} 0 & 0 & 0 \\ 0 & 0 & D-\Omega \\ 0 & D+\Omega & 0 \end{pmatrix} \qquad (1)$$

with $\lambda_{ij} = \partial U_i / \partial x_j$.

The U_i are the mean velocity components, D is the strain rate and Ω the rotation rate. The flow distortion is located in the x_2,x_3 plane perpendicular to the mean flow, whereas the velocity in the x_1 direction remains constant. This garantees particularly favorable conditions for achieving perfect transverse homogeneity, as required by the theory. In the following we only have to consider the submatrix relative to the distortion plane x_2,x_3. The particular choice of the coordinate system is made here for experimental convenience. The principal axes of the symmetrical part of the strain rate tensor are inclined at $\pm 45^\circ$ with respect to the coordinates, with the stretching in the $+45^\circ$ direction.

The flows defined by eq.(1) include the special cases of solid body rotation (D=0), plane strain (Ω=0) and uniform shear (Ω=D). In this case the shear rate S(=D+Ω) is defined in our coordinate system as $\partial U_3/\partial U_2$. The case of shear separates the regime of rotation dominated "elliptical" flows (Ω>D) from that of strain dominated "hyperbolic" flows (Ω<D). The streamlines, as determined by the stream fonction

$$\psi = -\tfrac{1}{2}\,[(D+\Omega)\,x_2^2 - (D-\Omega)\,x_3^2], \qquad (2)$$

have elliptical shapes in the former case and hyperbolic ones in the latter. For the limiting case of shear they become straight lines parallel to the x_3-axis.

The experimental setup which generates the flows defined by eq.(1) is schematically sketched in Fig.1. Its main components are:

i) a rotating duct of 0.3 m inner diameter containing a fine mesh honeycomb followed by a grid turbulence generator. This part of the facility produces the solid body rotation of rate Ω which can be varied continuously from 0 to 20 π rd/s;

ii) a distorting duct with cross sections of constant area and variable shape ensuring the superposition of plane strain upon the rotation at the required rates.

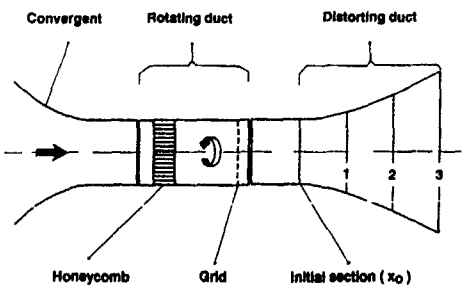

Fig. 1 Schematic view of the experimental setup

For each particular combination of plane strain and rotation, a specific distorting duct is needed. The determination of the corresponding geometry has been described in [4] (see also [6] for more theoretical background). It is based on the requirement that the streamtube originating from the upstream cylindrical pipe must be distorted according to eq.(1). This results in elliptical cross sections of variable aspect ratio and orientation.

The aspect ratio (ratio a/b of the major to minor axes) as well as the inclination angle ψ of the major axis with respect to the x_2 axis are given by:

$$a/b = 1 + G^2/2 + G(1 + G^2/4)^{\frac{1}{2}}$$
$$\psi = 1/2\,[\pi - \tan^{-1}(\sigma/\Omega.\coth \sigma t)]. \qquad (3)$$

with $G = 2D.(\sinh \sigma t)/\sigma$, $\quad \sigma^2 = D^2-\Omega^2$

The time t is taken equal to zero at the initial section of the duct ($x=x_0$). Equation (3) covers all special cases considered above. For elliptical flows (Ω>D), σ becomes imaginary and the hyperbolic functions turn into trigonometric ones.

Then $(\sinh \sigma t)/\sigma = (\sin \sigma' t)/\sigma'$, with $\sigma' = -i\sigma$, and $G = 2D.(\sin \sigma' t)/\sigma'$. In this case the deformation gradient tensor F associated with the deformation rate tensor (eq.1) becomes periodic with a period of $2\pi/\sigma'$ and the distorting duct has a period of $\pi U_1/\sigma'$ corresponding to a half-period of F. In all other cases the aspect ratio is an increasing function of time, and ψ lies in the interval $(\pi/4, \pi/2)$.

The limiting case of pure shear is obtained by letting σ (or σ') go to zero. Then $(\sinh \sigma t)/\sigma$ tends to t and G to St, where S = D + Ω is the shear rate.

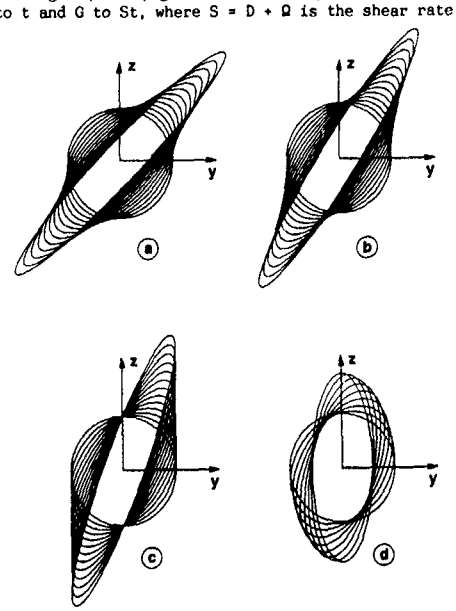

Fig. 2 Evolution of the cross sections of the distorting ducts
a. case 1, $\Omega/D = 0$
b. case 2, $\Omega/D = 0.5$
c. case 3, $\Omega/D = 1$
d. case 4, $\Omega/D = 2$

Figure 2 shows the evolution of the elliptical cross sections for the four cases considered in the present study:

- case 1: pure strain, Ω=0,
- case 2: "hyperbolic" strain-rotation coupling, Ω/D=0.5,
- case 3: pure shear, Ω/D=1,
- case 4: "elliptic" strain-rotation coupling, Ω/D=2.

In the last case, only a half-period of the distorting duct is presented. This portion represents a quarter of the total length of the duct, of L = 1.16 m, which insures an entire period of the flow. For the non-periodic cases, sections 1, 2 and 3 are relative to the three portions of the duct (see figure 1), each of 0.22 m length. The final sections (3) correspond to values of the total strain Dt of 1.04, 1.06 and 1.13 respectively for flow cases 1, 2 and 3. For case 4 the maximum value of Dt is 3.64.

At the nominal conditions of our experiment (axial velocity of 10 m/s), the corresponding values of the strain rate are respectively 15.75, 16.03, 17.05 and 31.4 s^{-1} for flow cases 1 through 4. The (linear) velocity profiles V(z) and W(y) in the distortion plane are given by:

$$V(z) = (D-\Omega)z \qquad W(y) = (D+\Omega)y \qquad (4)$$

according to eq.2.
(Note that hereafter we use rather the notations x,y,z; U,V,W,.... than x_1,x_2,x_3; U_1,U_2,U_3,.... introduced above).

One of the major advantages of the present flow generation method lies in the spatial uniformity of the streamwise velocity, ensuring very satisfactory properties of statistical homogeneity. A further advantage lies in the independence of the initial turbulence field from the mean flow distortion, since the turbulence is created in the rotating duct before strain is applied. The mesh size of the turbulence grid can be varied in order to examine various initial conditions of the turbulence.

The nominal conditions of the experiments reported hereafter are as follows:

- Streamwise velocity: U = 10 m/s
- Mesh size of the grid: M = 15 mm

The correspondin, mesh Reynolds number is of the order of 10^4.

The distorting ducts are connected to the rotating duct via a straight entry section of 0.22 m length. The value for the x/M ratio at the entrance of the duct is

$$x_o/M = 16.67$$

The corresponding turbulence Reynolds number is there approximately 40 (based on the Taylor microscale).

Mean flow and turbulence measurements are performed by hot-wire anemometry using crossed wire probes at four different azimuthal positions for each measuring point. Thus all components of the Reynolds stress tensor can be measured. Digital data acquisition and signal processing is used for the determination of the statistical quantities, evaluated from about 200.000 individual samples of the velocity vector. Frequency spectra of the three fluctuating velocity components are provided by FFT techriques. From these, integral length scales are evaluated via the Taylor hypothesis.

RESULTS AND DISCUSSION

Qualification of the flow

The qualification of the flow field has revealed very satisfactory results with regard to homogeneity. In the central part of the duct, where the flow is free from boundary layer effects, linear evolutions of the mean velocity components (according to eq.4) are achieved, as well as uniform distributions of the turbulence intensity, so that the requirements for the existence of homogeneous turbulence are well satisfied there. Figure 3 shows for the new flow cases 2 and 4 the measured velocity profiles in the distortion plane, in comparison to the theoretical ones (full lines) given by eq.4. (Note that the two figures are plotted here for the same strain rate). The measured gradients can be seen to be perfectly linear; they correspond to the theoretical evolutions, except for V(z) in flow case 4, which exhibits a slightly stronger gradient More detailed measurements for flow case 3 had been performed previously and were reported in ref.[3], mainly for section 2 of the distortion duct which had been completely explored. Outside the boundary layer zone, the Reynolds stresses were found to be uniform within a few percentage points; the axial velocity was found to be constant, the U_2 (or V) component to be zero and the U_3 (or W) component linear in x_2 (or y). The streamlines of the transverse flow were correspondingly straight vertical lines as required by eq.(2).

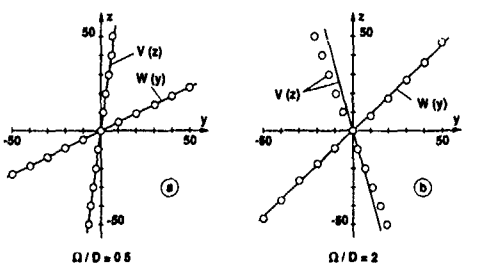

Fig. 3 Mean velocity profiles for case 2 and 4
a. case 2, $\Omega/D = 0.5$
b. case 4, $\Omega/D = 2$

Streamwise evolution of the turbulence

Streamwise evolutions of the normal stresses are shown in Fig. 4 for the four flow cases examined here. All stresses are normalized by their initial value at the beginning of the distortion ($x = x_o = 16.67*M$), and plotted against the normalized longitudinal distance x/M (log-log plot). The reference case without any distortion ($D = \Omega = 0$) is realized by replacing the distortion ducts by a straight cylindrical one.

At first glance, flow cases 1 to 3 show quite similar evolutions: As expected, the distortions act principally on the transverse components v'^2 and w'^2, whereas the u'^2 stress is much less influenced. Whilst in the case of plane strain v'^2 and w'^2 are equally affected, the effect of distortion becomes more pronounced for w'^2 with increasing rotation. Case 4 is seen to exhibit a quite different behavior: The action of distortion (represented mainly by the strain rate D), is here much more pronounced and the onset of the departure from the reference evolution occurs much earlier than in the previous cases. This is obviously due to the higher value of D, but also the periodic nature connected with the elliptic flow regime comes here into play. The evolutions of the individual transverse stresses differ much more from each other than in the previous cases 1 to 3 and the effect on the u'^2 stress is here much more pronounced.

The evolution of the Reynolds stresses as shown in Fig. 4 is more clearly understood when considering the production tensor (P_{ij}) associated with the deformation rate tensor (λ_{ij}) (eq.1). From the definition of the P_{ij}:

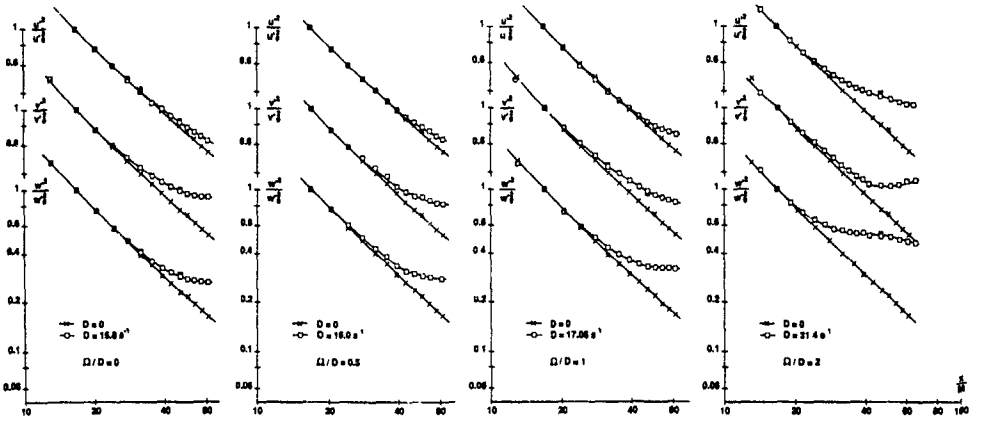

Fig.4 Streamwise evolution of the normal stresses, case 1 to 4

$$P_{ij} = -\overline{u_i u_k}\,\lambda_{jk} - \overline{u_j u_k}\,\lambda_{ik} \qquad (5)$$

and taking into account eq.1, one gets for the non-zero elements of (P_{ij}):

$$\begin{aligned} P_{22} &= -2(D-\Omega)\,\overline{vw} \\ P_{33} &= -2(D+\Omega)\,\overline{vw} \\ P_{23} &= -(D+\Omega)\,v'^2 - (D-\Omega)\,w'^2 \end{aligned} \qquad (6)$$

Thus, for a fixed cross correlation $\overline{vw}$, the difference of the transverse stresses $(w'^2-v'^2)$ is produced only by the rotation and their sum (as well as the whole turbulent energy) only by the strain. This implies that w'^2 becomes greater than v'^2 when Ω increases and that the level of both stresses increases with increasing strain rate (Fig. 4). Furthermore, the production of the negative cross-correlation $-\overline{vw}$ is mainly due to the strain and it is only weakly affected by the rotation which tends to reduce it slightly. These tendencies are also confirmed by the Rapid Distortion Theory (RDT). One notes that there is no production of u'^2 which is only fed by the pressure-strain correlation. The same circumstance occurs for v'^2 in the special case of pure shear (Ω=D).

Figure 5 shows the evolution of the normalized turbulent kinetic energy for all flow cases considered. As expected, there is no obvious effect of rotation; the differences in the evolutions are due to the differences in the strain rate, especially for case 4, which has a strain rate of roughly twice that of the other cases. The independence of the energy from the rotation rate has also been confirmed by RDT calculations.

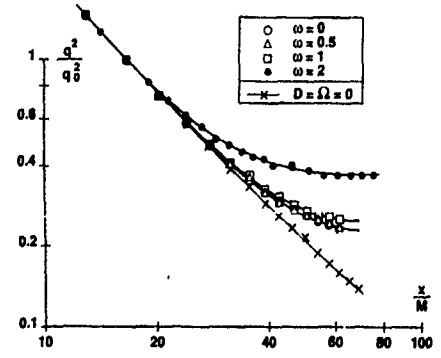

Fig. 5 Evolution of the turbulent energy

The progressive establishment (growing from zero) of the cross correlation $\overline{vw}$ is shown in Fig. 6 in terms of the correlation coefficient $R_{vw}=\overline{vw}/v'w'$, plotted against the total strain Dt. The (thick) solid line represents the evolution of R_{vw} for the case of pure shear (case 3). Considered as a function of the total shear St (twice the strain rate), this evolution had been found to be in good qualitative agreement with data from the literature, see [3]. As expected, there is no major effect of rotation for a fixed strain rate (cases 1 to 3), only a slight decrease with increasing $\omega=\Omega/D$, which is also confirmed by the RDT results. The higher Ω/D ratio of case 4 obviously inhibits the correlation coefficient to reach an asymptotic value of the same level as for the other cases. We have here a typical effect of dominant rotation which is also confirmed by the RDT results.

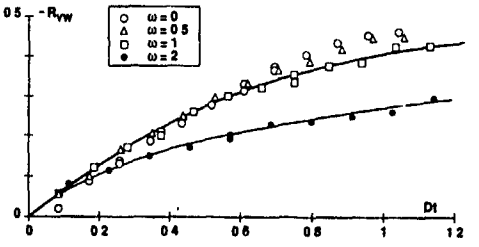

Fig. 6 Evolution of the cross-correlation coefficient

The overall anisotropy of the Reynolds stress tensor is commonly characterized by the second invariant (B_2) of the anisotropy tensor

$$b_{ij} = \overline{u_i u_j}/q^2 - \delta_{ij}/3 \qquad (7)$$

In our experiments, B_2 starts from about 0.015 at the entrance section (reflecting initial anisotropy) and grows continuously for all flow cases. Typical values reached at Dt=1 range from 0.046 for ω=0 down to 0.028 for ω=2, showing a continuous decrease of B_2 for increasing ω. This reflects primarily the diminution of the cross correlation discussed previously, which contributes substantially to the second invariant.

To characterize this, we consider the (2D) second invariant B'_2 relative to the projection of the Reynolds stress tensor on the distortion plane. This quantity starts from 0 at the entrance section and grows continuously during the distortion. As for the 3D invariant, increasing rotation has a rather strong reducing effect on the planar anisotropy. For Dt=1 e.g., B'_2 reaches a value of 0.11 for the pure strain, 0.09 for the shear case, but only 0.05 for the case of dominant rotation.

A more complete insight into the structure of the planar anisotropy is achieved by considering the eigenvalues and the associated principal axes of the Reynolds stress tensor restricted here to the y,z plane. We define a new structural parameter K_σ built with the two eigenvalues σ_1 and σ_2 (where $\sigma_1 > \sigma_2$):

$$K_\sigma = (\sigma_1 - \sigma_2)/(\sigma_1 + \sigma_2) \qquad (9)$$

which is related to B'_2 by the relation $B'_2 = \frac{1}{4} K_\sigma^2$

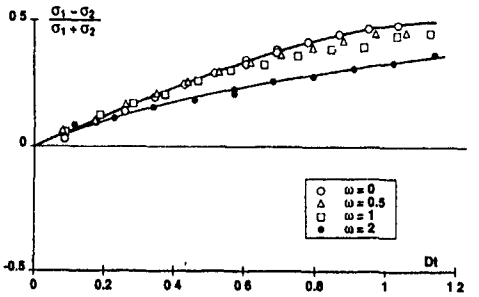

Fig. 7 Evolution of the structural parameter K_σ

Figure 7 shows the evolution of K_σ plotted against Dt, which is also representative for that of the second invariant B'_2. Like in Fig. 6, the isotropizing action of the rotation is clearly evidenced. At Dt=1, the pure strain case reaches a value of K_σ of nearly 0.5 corresponding to a ratio of the two eigenvalues of the order of 3. A substantial reduction is observed for the elliptical flow case, for which the values of K_σ and σ_1/σ_2 reduce to 0.33 and 2 respectively. Figure 7 contains essentially the same information as Fig. 6, since the principal direction corresponding to σ_1 is not very far from that associated with the strain (-45° in our coordinate system). Would the two directions coincide, then $-\overline{vw}$ would be equal to half the difference between the eigenvalues.

Figure 8 shows the evolution of the inclination angle Φ_R associated with σ_1. The (negative) deviation from the reference direction of -45° relative to the case of pure strain increases with increasing rotation. For Dt=1, the deviation is about 18° for ω=2 and much less for the other cases. The homologous plots relative to the production tensor introduced above (eq.5), exhibit very similar evolutions. The values of the deviation for Dt=1 are here 0°, 6°, 12° and 20° for flow cases 1 to 4 respectively. We must emphasize here that the principal axes of the Reynolds stress tensor turn in the opposite sens of the mean flow rotation.

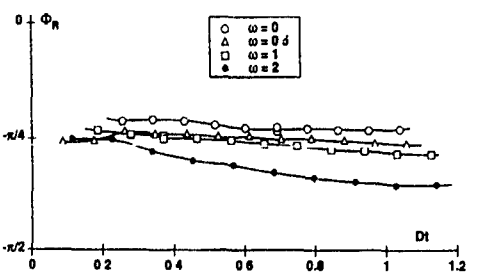

Fig. 8 Angle of the principal axes of the Reynolds stress tensor

Typical variations of the three integral length scales L_u, L_v and L_w as deduced from the frequency spectra are shown in Fig. 9 for the central case of shear. The (broken) reference lines are relative to the basic flow without gradients. The most striking effects of the flow distortion are here the strong reduction of the longitudinal lengthscale and a distinct increment of the lateral scale L_v, whereas L_w is hardly affected. The reduction of L_u, which is observed for all flow cases (included pure strain) is only slightly accentuated when ω increases; this reduction seems therefore to be essentially an effect of strain. In contrast to this, the difference between L_v and L_w, which does not exist for the pure strain (for reasons of symmetry), increases with growing rotation and must be considered as a typical rotation effect. The RDT solution shown at the bottom of the figure clearly displays the same features as the experimental results, unavoidably magnified with respect to the experiment.

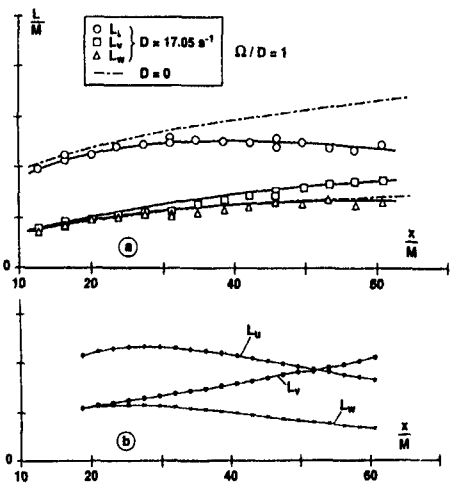

Fig. 9 Evolution of the integral length scales for case 3 (shear)
a. Experiment
b. RDT

The spectral analysis of the turbulence signals also provides the spectral distribution of the cross correlation (P_{vw}), beside that of the normal stresses. The spectral region where P_{vw} is maximum coincides with that where the power spectra P_v and P_w become different from each other, with $P_w > P_v$. This region spans roughly between (streamwise) wavenumbers of 50 and 250 m^{-1}. (The medium wavenumber of 150 m^{-1} corresponds approximately to the longitudinal length scale L_u). Figure 10 shows the evolution of the spectral correlation coefficient $\gamma = P_{vw}/(P_v P_w)^{\frac{1}{2}}$, for the four flow cases 1 to 4. The maximal position corresponds to a value of Dt of the order one. The figure shows that the rotation tends to lower the maximum value of γ, but also that the profiles become somewhat enlarged when the rotation increases. It is interesting to note that the central frequency of the bumps corresponds very closely to the longitudinal length scale L_u.

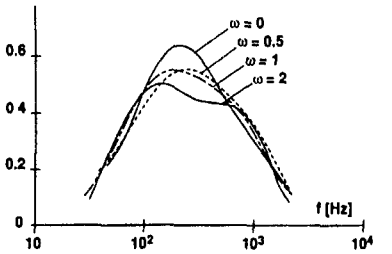

Fig.10 Coherence coefficient of the cross-correlation, case 1 to 4

The last example is related to the specific case of elliptical flows which differs from the other cases for several reasons: The first is that it represents a particular type of flow which exhibits features of periodicity in the turbulence properties, in contrast to the monotonic evolutions of the other flow cases. Furthermore, the amount of distortion is here much larger than in flow cases 1 to 3. The reason for this is that we aimed at achieving at least one period of the flow, within the constraint of limited length of the facility. The ratio of the characteristic "linear" time of the mean flow distortion (1/D) to the "non linear" turn-over time ($\frac{1}{2}q^2/\varepsilon$) is thus significantly lower for the elliptical flow case and the linear effects are here much more pronounced. In addition, the relatively high value of the rotation rate needed for realizing twice the strain rate introduce some additional rotation effects altering the turbulence properties at the entrance before strain is applied. The outstanding character of this flow suggests a more elaborate investigation than could be done in the frame of the present work.

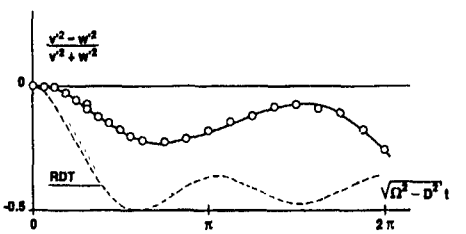

Fig. 11 Evolution of the structural parameter Kvw for case 4

Figure 11 shows for the elliptical flow case the evolution of the structural parameter K_{vw} defined as

$$K_{vw} = (v'^2 - w'^2)/(v'^2 + w'^2) \qquad (10)$$

over the whole period of the flow. The figure clearly indicates the oscillatory character of the evolution. The measurements reveal that this was merely due to an oscillatory variation of the principal direction rather than to that of the eigenvalues. The figure shows also the evolution of K_{vw} as determined from RDT, which can be seen to have more ample variations and a shorter wavelenth than the experiment. These differences may be related to the non-linear damping effects which are not taken into account in the RDT. The experiment revealed oscillatory features also for other turbulence parameters as e.g. for the second invariant of the anisotropy tensor (3D or planar) or for the cross correlation coefficient. More detailed results about this flow case are given in [7].

CONCLUDING REMARKS

The flow configurations studied in the present work constitute useful test cases, especially in view of developing (or improving) turbulence models in physical or spectral space. Among the new configurations involving rotation/strain coupling with non-equal rates, the case of rotation dominated elliptical flows appears as a particularly interesting one, for it provides flow properties that are oscillatory in character. This case needs further detailed investigations, experimentally as well as theoretically. The second new flow case, that of strain dominated hyperbolic flow, presents more "classical" features similar to those observed for plane strain and uniform shear.

The mode of generation of the mean flow gradients by the superposition principle fullfils very satisfactorily the conditions of homogeneity: the mean flow gradients and the turbulence quantities are uniform within an adequate lateral extent, for all flow cases examined. In the hyperbolic flow cases, strain is the principal factor acting on the turbulent field. For a given strain, increasing rotation induces only a slight reduction of the eigenvalues of the Reynolds stresses in the distortion plane, but causes a distinct rotation of the corresponding principal axes in the sens opposite to that of the flow rotation. The elliptical flow case could not be studied here with the same strain rate as for the other cases. The results therefore cumulate the effects of an increased strain and of a higher rotation rate ratio. Further experimental work is needed to clarify this point.

Numerical descriptions using two-point closure techniques developed at the ECL (see e.g.[4]) are in progress for the flow cases examined here; they are aimed at achieving a deeper physical understanding of the experimental findings.

REFERENCES

[1] Gence, J.N., "Homogeneous turbulence", Ann. Rev. Fluid Mech. 1983, pp. 201-222.

[2] Jacquin, L., Leuchter, O., Cambon, C. and Mathieu, J., "Homogeneous turbulence in the presence of rotation", J. Fluid Mech. (1990), vol. 220, pp. 1-52.

[3] Moulin, V., Leuchter, O., and Geffroy, P., "Experimental study of homogeneous turbulence in the presence of transverse shear", 7th Symp. Turb. Shear Flows, Stanford, 1989.

[4] Leuchter, O., Benoit, J.P., Bertoglio, J.P. and Mathieu, J., "Experimental and theoretical investigation of homogeneous turbulent shear flow", 3rd Eur. Turb. Conf., Stockholm, 1990.

[5] Malkus, W.V.R. and Waleffe, F.A., "The transition from order to disorder in elliptical flow: a direct path to shear flow turbulence", 3rd Eur. Turb. Conf., Stockholm, 1990.

[6] Cambon, C., Teissedre, C., Jeandel, D., "Etude d'effets couplés de déformation et de rotation sur une turbulence homogène", J.M.T.A., vol. 4, n° 5, 1985, pp. 629-657.

[7] Leuchter, O. and Benoit, J.P., "Etude de la turbulence homogene soumise à des effets de rotation et de déformation", internal ONERA report, in preparation.

EIGHTH SYMPOSIUM ON
TURBULENT SHEAR FLOWS
Technical University of Munich
September 9-11, 1991

Large and Small-scale Coupling in Homogeneous Turbulence: Analysis of the Navier-Stokes Equation in the Asymptotic Limit

James G. Brasseur & P K. Yeung
Department of Mechanical Engineering, Pennsylvania State University
University Park, PA 16802, U S A

Abstract

The structure of the Navier-Stokes equations in Fourier-spectral space is such that a direct coupling between large and small scales necessarily exists within 'distant' triadic interactions We discuss the consequences of this coupling in light of the Kolmogorov hypotheses of statistical independence between large and small scale turbulent motions and consequent local isotropy at the smallest scales We show that, in the asymptotic limit of large Reynolds numbers, although no *energy exchange* takes place between large and small scales, the *structure* of the small vortical scales is modulated by the structure of the large energy-containing scales Consequently, large-scale anisotropy in the energy-containing scales *induces* anisotropy at the dissipative scales This effect is studied with a direct simulation of forced homogeneous turbulence in which the smallest scales respond directly to spectrally local 'stirring' at the large-scales.

1. Introduction

The large energy-containing scales and the small dissipative scales become increasingly separated as Reynolds number increases Kolmogorov (1941) hypothesized that, in the asymptotic limit of infinite Reynolds numbers, turbulent kinetic energy is transferred from the large energy-containing scales to the small dissipative scales through an inertia-dominated range of intermediate scales with little frictional loss Consequently, $\varepsilon \sim q^3/L$, where $q^2 \sim$ turbulent kinetic energy, L is an integral scale, and ε is turbulent dissipation-rate This conceptual model of an 'energy cascade' assumes no direct energy transfer between the large and small scales but, in principle, does not demand *independence* between the large and small scales. The hypothesis of local isotropy at the smallest scales, however, *does* require independence of large and small scales. In this more restrictive model, the energy-containing and dissipative scales do not interact directly in the asymptotic limit of infinite Reynolds numbers Consequently, the dynamical and structural characteristics of the dissipative scales are governed entirely by spectrally local processes which develop independently of the structure and dynamical processes within the energy-containing scales The point of this necessarily brief paper is to show that, whereas the large and small scales do not directly *exchange* energy, the large and small scales are *not independent* in the asymptotic limit of infinite Reynolds numbers. Consequently, the small scales do not, in principle, attain a locally isotropic state independent of the large scales.

Some clarification of concepts is necessary. In this discussion, the terms 'large scale' and 'small scale' refer to those spectral scales in which energy and dissipation-rate are concentrated, respectively. In homogeneous turbulence, the large energy-containing scales are those residing near the peak in the energy spectrum, k_L, quantified by an integral scale: $k_L \sim 1/L$. Dissipation-rate, strain-rate, and vorticity are most highly concentrated near the peak in the dissipation-rate, or enstrophy spectrum, which resides somewhere between the Taylor microscale, $k_\lambda \sim 1/\lambda$, and the Kolmogorov scale, $k_\eta \sim 1/\eta$ Dimensional reasoning (Tennekes and Lumley, 1975) suggests that, at large Re_λ, $k_\lambda/k_L \sim Re_\lambda$, and $k_\eta/k_L \sim Re_\lambda^{3/2}$ Consequently, the dissipative scales separate infinitely far from the energy-containing scales at asymptotically large Reynolds numbers and the concept of local isotropy applies to the entire dissipative range, from the far intertial range to the smallest scales There is a small amount of experimental evidence to support the approximation that, at large Reynolds numbers, $\varepsilon \sim q^3/L$ (Batchelor 1953, Sreenivasan 1984). By contrast, although considerably more experimental analysis has been directed at the question of local isotropy, the issue remains unresolved and controversial (see the various discussions by Antonia and Brown *et al* 1988, 1987, 1986, Van Atta 1991, and Sreenivasan 1991)

We argue in this paper that the hypothesis of no energy transfer between small and large scales in the asymptotic limit is correct; but the hypothesis of *independence* between large and small scales and local isotropy is not correct Whereas turbulent energy is dissipated primarily in the small scales, at a rate given approximately by $\varepsilon \sim q^3/L$, and whereas a $k^{-5/3}$ spectral form in an inertia-dominated subrange may be anticipated from dimensional arguments, the dynamical processes which govern the dynamical evolution and structure of the small scales are directly affected by the dynamical evolution and structure of the large scales In particular, we argue that an anisotropic energy distribution within the large scales, in principle, leads to an anisotropic structure and energy distribution within the small scales at asymptotically large Reynolds numbers[1].

We should be quick to point out that, whereas *in principle* anisotropy at the large scales induces anisotropy at the small scales, in practice the effect is not necessarily large, other dynamical processes will be briefly mentioned which tend to return the small scales to an isotropic state. On the other hand, the effect is not necessarily small either If the large scales are made strongly anisotropic, by stirring for example, the small scales can be pushed far from an isotropic state over finite time This effect is demonstrated in companion numerical experiments where initially isotropic turbulence is strongly forced locally at the peak in the energy spectrum (Yeung and Brasseur, 1991a) Large levels of anisotropy build up at the smaller scales as a direct consequence of the distant triadic couplings with the large-scale forced modes. More importantly, the effect *stengthens with decreasing scale*, consistent with the asymptotic forms presented in this paper Taken together with the asymptotic analysis, then, we conclude that the large scale couplings which dominate small scale inertial dynamics in the moderate Reynolds number simulations would play the same role had it been possible to simulate very large Reynolds numbers We conclude that the small-scale structure of a high Reynolds number turbulence is coupled to the structure of the large energy containing scales and that this coupling may be exploited to alter small scale structure by manipulating large scale structure

2. The Fourier-spectral Structure of the Navier-Stokes Equation

The underlying concepts may be obtained through a cursory examination of the Fourier-spectral structure of the Navier-Stokes equation in the infinite Reynolds number limit. Expanding the velocity field, $u(x,t)$, into a discrete set of Fourier modes with complex amplitude $u(k,t)$, the Navier-Stokes equations may be written:

[1]Here, 'anisotropic structure' is given in terms of the energy distribution within spherical shells in k-space However, an anisotropic energy distribution within a spectral shell *does* imply anisotropy in physical space structure at those scales

$$\frac{\partial u(k)}{\partial t} \equiv [\dot{u}(k)]_{NL} + [\dot{u}(k)]_{VIS}$$

where $[\dot{u}(k)]_{NL} = -i \sum_{k'} u(k')_{\perp k} [k \cdot u(k-k')]$, (1)

$$[\dot{u}(k)]_{VIS} = -\nu k^2 u(k) \quad ; \quad u_i(k')_{\perp k} \equiv \left[\delta_{ij} - \frac{k_i k_j}{k^2}\right] u_j(k')$$

$u(k')_{\perp k}$ is the vectorial projection of $u(k')$ onto a plane perpendicular to k. Incompressibility requires that $k \cdot u(k) = 0$, and reality of $v(x,t)$ requires that $u(-k) = u^*(k)$. The evolutionary equation for mode energy, $e(k) \equiv u(k) \cdot u^*(k)$ is

$$\frac{\partial e(k)}{\partial t} = u(k) \cdot \dot{u}^*(k) + cc \equiv [\dot{e}(k)]_{NL} + [\dot{e}(k)]_{VIS}$$

$$[\dot{e}(k)]_{NL} = -i \sum_{k'} [u^*(k) \cdot u(k')][k \cdot u(k-k')] + cc \quad ; \quad (2)$$

$$[\dot{e}(k)]_{VIS} = -2\nu k^2 e(k) \ ,$$

where twice the total kinetic energy is $q^2 = \sum e(k)$, 'cc' implies the complex conjugate of the previous term, and ν is the kinematic viscosity.

In the above equations the viscous terms, $[\dot{u}(k)]_{VIS}$ and $[\dot{e}(k)]_{VIS}$, have been separated from the nonlinear terms, $[\dot{u}(k)]_{NL}$ and $[\dot{e}(k)]_{NL}$, because of the separate roles of inertial and viscous effects in spectral evolution. Our interest here is primarily in the role of nonlinear intermodal couplings. Note, however, that viscous dissipation tends to move both the components of the complex amplitude, and the energy in a spectral shell in k-space, towards equipartition. Thus, the linear part provides an isotropizing influence within high wavenumber spectral shells.

The nonlinear interactions among scales are given by the RHS of $[\dot{u}(k)]_{NL}$ or $[\dot{e}(k)]_{NL}$. Central to the discussion is the observation that the nonlinear interactions occur as a *linear sum* of nonlinear terms, each of which describes an interaction among three modes whose wave vectors form a triangle (a triad). This linear-nonlinear combination in the nonlinear structure of the Navier-Stokes equation has important implications which can be best discussed with the help of Fig. 1 where the expansion for $v(x,t)$ is ordered as

$$v(x,t) = \sum_n u(k_n,t)\, e^{i k_n \cdot x} \ , \quad k_1 < k_2 \ . \ . < k_L \ . \ . < k_\lambda \ . \ . < k_\eta \quad (3)$$

The modes are ordered by wave vector magnitude from largest to smallest active scale ($k_n \equiv |k_n|$) and each mode, k_n, evolves through a linear sum of triadic interactions as illustrated in Fig. 1. In the figure, each row describes the evolution of a mode residing within a spectral shell as a sum of triad interactions, where each triad represents those terms on the RHS of either $[\dot{u}(k_n)]_{NL}$ or $[\dot{e}(k_n)]_{NL}$ associated with that triad. Consequently, each triad in the row contains k_n as one leg[2]. The dynamical evolution of a mode is given by the integrated sum of triadic interactions in a row, while the dynamical evolution of the complete spectrum is given by the complete integrated set of triadic interactions.

The linearity in $[\dot{u}(k_n)]_{NL}$ allows the sum of triadic interactions in each row of Fig. 1 to be ordered arbitrarily. We have ordered the triads in each row by first choosing the shortest wave vector, p, of the two wave vectors in the triad other than k_n, and then ordering triads from lowest to highest p magnitude.

[2]For each mode k_n a negative counterpart $-k_n$ must exist (for reality of $v(x,t)$). The complex amplitude of the negative set need not be calculated separately, because it can be obtained directly from the positive set via $[\dot{u}(-k)]_{NL} = [\dot{u}(k)]^*_{NL}$. However, the sum in equations (1) and (2) must include the negative set. Each triad in figure 1 specifies a unique triangle created with combinations $k_n + p_n + q_n = 0$, or $(-k_n) + (-p_n) + (-q_n) = 0$. Consequently, each triadic interaction illustrated in figure 1 represents four terms on the RHS of equations (1) and (2) given by $k' = p_n, -p_n, q_n, -q_n$.

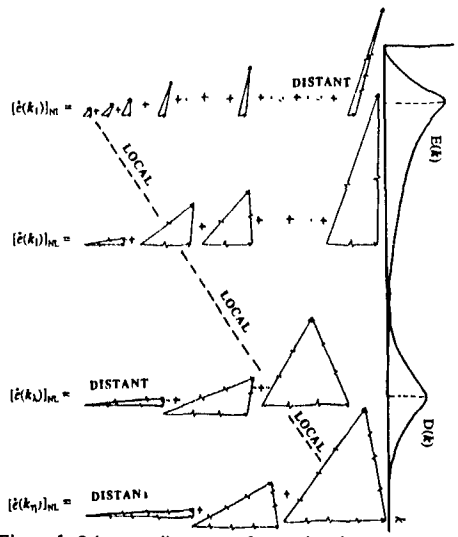

Figure 1. Schematic illustration of spectral evolution in terms of triadic interactions within spectral shells. Fourier modes are ordered by increasing wavenumber, increasing from the lowest wavenumber (k_1) to the highest wavenumber ($\sim k_\eta$), as shown in Eq. (3). Each mode in the spectrum, k_n, evolves due to triadic interactions with every other mode in the spectrum. Each triad which contributes to the evolution of a mode k_n involves k_n and two other modes. The lower wavenumber of the two modes are ordered in each row from the lowest to highest wavenumber. Consequently, in the top row (low k modes), local triadic interactions appear on the left, while distant triadic interactions appear on the right of the row. At the bottom (high k modes), distant triads appear on the left and local on the right. In the inertial range distant triadic interactions with the low/high wavenumber end of the spectrum appear on the left/right, and local triads appear in the middle of a row.

In this way, the triads in the low wavenumber rows are arranged from spectrally 'local' triads to 'distant' triads, whereas triads in the high wavenumber rows are arranged from spectrally 'distant' to spectrally 'local' triads. Note that each unique triad appears three times, in three separate rows for each each mode in the triad.

The distinction between 'local' and 'distant' triads is central to the arguments which follow. Triadic interactions are known to possess global characteristics based solely on triad geometry (Brasseur & Corrsin, 1987). Local triads are those where all three modes within the triad are within a 'narrow' spectral shell — where the three triadic wave vectors about the same length. Distant triads are those which couple modes widely disparate in scale, such as low wavenumber energy-contraining modes with high wavenumber dissipative modes. In these triads one wavenumber is very much smaller than the other two.

3. Triadic Interactions within Spectral Shells

Consider relatively narrow high wavenumber spectral shells between k_λ and k_η. Within a high wavenumber shell consider, with the help of Fig. 1, the following reordering of the triadic interactions in this region:

$$\sum_{\substack{k_n \in \text{ high} \\ \text{waveno. shell}}} \dot{e}(k_n) = \quad (4)$$

$$\sum_{\substack{k_n \in \text{ high} \\ \text{waveno shell}}} \left(\sum_{\substack{\text{local} \\ \text{triads}}} \dot{e}(k_n) + \sum_{\substack{\text{distant triads} \\ \text{with } k_L}} \dot{e}(k_n) + \sum_{\substack{\text{other nonlocal} \\ \text{triads}}} \dot{e}(k_n) \right) .$$

where $\dot{e}(k)$ refers to the nonlinear part, $[\dot{e}(k)]_{NL}$ or $[\dot{u}(k)]_{NL}$. The dynamic evolution within a high wavenumber shell is separated into a linear sum of triadic interactions, where the triads are grouped according to their geometrical characteristics. The procedure we follow is to examine the three groups of triadic interactions on the RHS of Eq. (4) individually for their global characteristics. We draw from the work of Brasseur & Corrsin (1987), who showed that the interactions among three modes within distant triads is fundamentally different from the interactions within local triads.

4. Large and Small-scale Coupling in the Asymptotic Limit

Consider an arbitrary triadic interaction from the middle group in Eq. (4) in comparison with an arbitrary triadic interaction from the first group in Eq. (4). We seek the contribution of a single triad, $k_1+k_2+k_3=0$, to the evolution of the spectrum. That is, we seek the contribution of the *same* triad, $k_1+k_2+k_3=0$, to the evolution of modes k_1, k_2, and k_3, given by the same triangle on the rhs of $[\dot{u}(k_1)]_{NL}$, $[\dot{u}(k_2)]_{NL}$, and $[\dot{u}(k_3)]_{NL}$ in Fig. 1. In particular, we consider the contributions from distant triads, where $k_1 \ll k_2$ or k_3, k_1 is within the energy containing scales, and $k_2 \sim k_3$ lie in a high wavenumber spectral shell between k_λ and k_η; in comparison with the contributions from local triads, where $k_1 \sim k_2 \sim k_3$ and all three modes lie in the high wavenumber spectral shell. The contribution of a single triad to $[\dot{u}(k_1)]_{NL}$, $[\dot{u}(k_2)]_{NL}$, and $[\dot{u}(k_3)]_{NL}$ is, from Eq. (1),

$$[\dot{u}(k_1)]_{NL} = -i\,\{u^*(k_2)_{\perp k_1}[k_1\cdot u^*(k_3)] + u^*(k_3)_{\perp k_1}[k_1\cdot u^*(k_2)]\},$$

$$[\dot{u}(k_2)]_{NL} = -i\,\{u^*(k_1)_{\perp k_2}[k_2\cdot u^*(k_3)] + u^*(k_3)_{\perp k_2}[k_2\cdot u^*(k_1)]\}, \tag{5}$$

$$[\dot{u}(k_3)]_{NL} = -i\,\{u^*(k_1)_{\perp k_3}[k_3\cdot u^*(k_2)] + u^*(k_2)_{\perp k_3}[k_3\cdot u^*(k_1)]\},$$

When $k_1 \ll k_2$, k_3 and $k_1 \sim k_L$, Eqs. (5) describe the basic nonlinear interaction between the large and small scales. We seek the form of this interaction in the limit of infinite Re_λ. It was argued in §1 that, at large Reynolds numbers, $k_\lambda/k_L \sim Re_\lambda$, and $k_\eta/k_L \sim Re_\lambda^{3/2}$. Thus, infinite Re_λ is given by the limit $k_1/k_2 \sim k_1/k_3 \equiv \delta \to 0$. The reduction of Eqs. (5) in the limit of small δ is (Brasseur & Corrsin 1987).

$$[\dot{u}(k_1)]_{NL} = O(\delta),$$

$$[\dot{u}(k_2)]_{NL} = -i\,\{u^*(k_3)[k_2\cdot u^*(k_1)]\} + O(\delta), \tag{6}$$

$$[\dot{u}(k_3)]_{NL} = i\,\{u^*(k_2)[k_2\cdot u^*(k_1)]\} + O(\delta).$$

Similarly, the rate of energy change in each mode is given in the limit $\delta \to 0$ by

$$[\dot{e}(k_1)]_{NL} = O(\delta), \tag{7}$$

$$[\dot{e}(k_2)]_{NI} = -[\dot{e}(k_3)]_{NL} = i\{u(k_2)\cdot u(k_3)[k_2\cdot u(k_1)] + cc\} + O(\delta).$$

The essential elements of the dependence between the large and small scales in the asymptotic limit of infinite Reynolds number are embedded in Eqs. (6) and (7). Several important points can be made. Clearly, the interaction between large and small scales persists in the asymptotic limit of infinite Reynolds number (given by the leading order terms above). Consistent with the Kolmogorov hypotheses, no energy exchange between the large and small scales takes place in the asymptotic limit. However, the rate of evolution of the high wavenumber modes is *directly proportional to the the amplitude of the low wavenumber mode*. Thus, the low wavenumber mode modulates the rate at which the high wavenumber modes evolve.

The last observation is particularly important as it leads to the conclusion that those distant triadic interactions which couple the large energy-containing scales to the small vortical scales dominate over the local triadic interactions entirely among scales of approximately the same size. Applying Eq. (5) to a local triad in the high wavenumber shell, and Eq. (7) to a distant triad coupling the large and small scales, the order of magnitude rates of energy transfer in the high wavenumber associated with distant *vs* local triads may be compared.

$$\frac{[\dot{e}(k_\lambda)]_{distant}}{[\dot{e}(k_\lambda)]_{local}} \sim \sqrt{\frac{e(k_1)}{e(k_\lambda)}} \gg 1 \tag{8}$$

It is clear that, in the asymptotic limit of infinite Reynolds number, local triadic intermodal energy exchange at the small scales is dominated by distant triadic couplings with large energy-containing modes. Indeed, a $k^{-5/3}$ decrease in spherically integrated energy suggests that, on average

$$\frac{[\dot{e}(k_\lambda)]_{distant}}{[\dot{e}(k_\lambda)]_{local}} \sim \left(\frac{k_\lambda}{k_L}\right)^{11/6} \sim Re_\lambda^{11/6} \tag{9}$$

In contrast with classical thinking, it appears that small scale dynamics becomes progressively *more* strongly coupled to large scale characteristics as Reynolds number increases.

The dominance of distant to local triadic interactions has been verified in moderate Reynolds number direct simulations by Domaradzki & Rogallo (1990) and Yeung & Brasseur (1991a). Again, however, we must be quick to point out that, whereas Eq. (8) indicates that, on average, distant triadic interactions dominate local interactions within the dissipative scales, the cumulative dominance of distant triadic interactions to local triadic interactions is not guaranteed. Nevertheless, the cumulative effect of the distant triads must remain finite and the dependence of small scale dynamics on the large scales will persist in the asymptotic limit of infinite Reynolds numbers.

5. The Necessity of Anisotropy at the Small Scales

We have established above that, whereas no energy is directly transferred between the large and small scales, small scale dynamics is coupled to large scale dynamics in the high Reynolds number limit. This interdependence between small and large scales is manifested through the energy exchange among high wavenumber modes, modulated by the energy-containing region of the spectrum. It seems plausible, therefore, to anticipate a structural coupling between the energy-containing scales and the dissipative scales. We present here an argument to show that this is the case, with the consequence that, in principle, anisotropy in the large scales leads to anisotropy in the small scales. Clearly, this conclusion is at variance with the concept of a universal, locally isotropic structure at the small scales.

Consider a fully developed turbulence which is isotropic at all scales except within a narrow spectral shell at low wavenumbers, as schematically illustrated in Fig. 2. Let k_1 be the dominant energy direction on a k-space sphere within the energy-containing scales (k_1 should be interpreted as an average over an ensemble of low wavenumber modes). Now imagine all the *distant* triadic

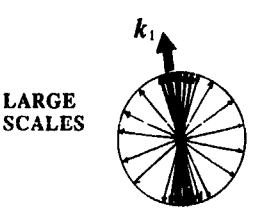

Figure 2. An anisotropic distribution of energy within a spectral shell in the low wavenumber energy-containing modes. The dominant energy direction is k_1.

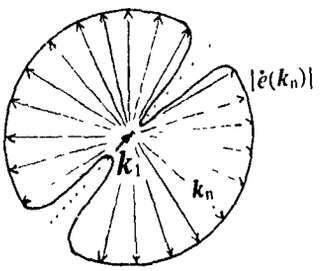

Figure 3. Depletion of energy due to low rates of energy transfer within narrow cones in the directions $\pm k_1$ due to distant triadic interactions with modes in the anisotropic energy-containing scales, shown in Fig 2.

interactions between the dominant energy mode k_1, and all high wavenumber modes k_n in a narrow spectral shell between k_λ and k_η, as illustrated in Fig 3. That is, consider the middle group of triadic interactions in Eq (4). The high wavenumber modes are in an isotropic state, so that energy is distributed uniformly on a sphere of large radius, k_n. We learned from Eqs. (6) and (7) that the rate of energy exchange in every distant triad between k_1 and high wavenumber modes k_2 and k_3 is modulated by the combination $k_n \cdot u(k_1)$, where k_n is either high wavenumber mode. Because the large scales are *anisotropically* distributed with dominant direction k_1, the rate of energy exchange will be reduced in the direction k_1 as compared with other directions on the high-k sphere (N.B , $k_n \cdot u(k_1) = 0$ when k_n and k_1 are colinear). Over time, energy will be depleted in the direction k_1 within the high wavenumber modes[3] and the energy distribution will become nonuniform on high wavenumber shells. Therefore, an isotropic energy distribution at the small scales is moved towards an anisotropic state with a structure related to the anisotropic structure of the large scales In principle, isotropy at the small scales requires isotropy at the large scales and a universal small scale structure independent of large scale structure cannot exist

6. Random Uniform Sweeping of the Small Scales

Random uniform sweeping of small scales is given in the limit $k_1/k_2 \sim k_1/k_3 \equiv \delta \to 0$ by taking k_1 to zero while holding $k_2 \sim k_3$ fixed. Uniform sweeping should have no affect on turbulence evolution. This is easily shown to be the case. In the limit $k_1 \to 0$, $k_3 \equiv -k_2$, $u(k_3) = u^*(k_2)$, $e(k_3) = e(k_2)$, and $\dot{e}(k_2) = \dot{e}(k_3)$ Eq. (7), however, demands that $\dot{e}(k_2) = -\dot{e}(k_3)$ when $\delta = 0$, which can only be the case if $\dot{e}(k_3) = \dot{e}(k_2) \equiv 0$. Thus, modes at $k = 0$ play no role in turbulence evolution

It is instructive to identify the source of this result, which suggests that modes with wavenumbers near zero might, by virtue of their large scale alone, play a weaker role in distant interactions than modes farther from $k = 0$. This, however, is *not* the case $k_1 \equiv 0$ *necessarily* requires $k_2 \equiv -k_3$ and, by the requirement that the velocity field $v(x,t)$ be real, $u(-k_2) = u^*(k_2) \equiv u(k_3)$. Consequently, when $k_1 \equiv 0$, modes k_2 and k_3 are no longer independent—the amplitudes and phases of one mode may be obtained directly from the other mode. However, if $k_1 \neq 0$, *no matter how small*, then modes k_2 and k_3 are independent, $u(k_3) \neq u^*(k_2)$, $e(k_2) \neq e(k_3)$, and $\dot{e}(k_2) \neq \dot{e}(k_3)$ in general. We conclude that the coupling between large and small scales at asymptotically large Reynolds numbers should properly be viewed in the limit $\delta \to 0$ with k_1 finite. In this limit, large and small scales interact directly according to Eqs (6) and (7) regardless of the magnitude of k_1.

[3]Siginificant energy depletion appears to take place within a roughly 20° cone of wave vectors aligned in the direction k_1 (Brasseur & Wei 1991)

7. Response of Small Scales to Large-scale Stirring: a Numerical Experiment

The considerations above indicate that the small scales are directly coupled to the large energy-containing scales through distant triadic interactions which persist to asymptotically large Reynolds numbers, and that, on average, these distant triadic interactions play a dominant role in the inertial dynamics of the small scales Consequently, the large energetic scales impress their structure directly on the small scales, and modification of large scale structure should, in principle, lead to modification of small scale structure[4] Furthermore, the order-of-magnitude estimates in Eq. (9) suggest that a restructuring of the small scales by the energy-containing scales will be felt more strongly with increasing Reynolds number and *will be felt more strongly as the scale decreases* Both of these conclusions are at odds with the notion of a locally isotropic universal spectrum at the small scales.

To test these conclusions, a numerical experiment was performed in which initially isotropic turbulence was forced anisotropically in a narrow shell at the peak of the energy spectrum (Yeung & Brasseur 1991a) Pseudospectral calculations were carried out on a 128^3 grid with periodic boundary conditions. Gaussian initial conditions relax to an asymptotic state of isotropic decay. Forcing was applied continuously to initially isotropic turbulence at $Re_\lambda = 32$. Energy and vorticity were added to the turbulence through the array of 16 two-dimensional counter-rotating vortices shown in Fig. 4 which, in Fourier space, consist of four Fourier modes with wave vectors of length $2\sqrt{2}$ oriented within the x-y plane at ±45° to the x-y axes. $k = 2\sqrt{2}$ lies near the peak in the energy spectrum. Modes up to $k \cong 60$ were well resolved. Consequently, the most distant triads with the forced modes had a high-to-low wavenumber ratio of about 20 ($\delta_{min} \cong 0.05$).

The details of the analysis is given in Yeung & Brasseur (1991a). The primary result is summarized in Fig 5. Here the third principle invariant of the anisotropy of the spherically integrated energy spectrum tensor, $E_{ij}(k)$, is plotted against wavenumber after continuous forcing for two large-scale eddy turnover times. Large levels of anisotropy are built up at $k \cong 3$ due to forcing The structure of the turbulence at these large scales is dominantly two-component in the velocity (x,y) and one-component in the vorticity (z) After an initial time lag of about one eddy turnover time, the small scales respond rapidly to the anisotropic forcing at the large scales and become highly

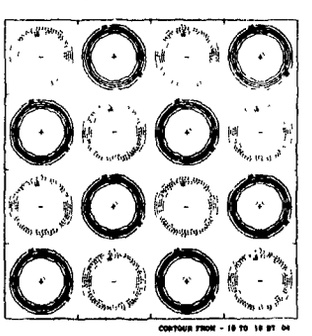

Figure 4. Isocontours of the vorticity distribution of an array of 16 counter-rotating rectilinear vortices which are continuously forced. Forcing is 2D in the velocity (x-y plane) and 1D in the vorticity (z).

[4]One should note that, whereas the influence of the large scales on the small scales in a first order effect, the influence of the small scales on the large is a second order effect which becomes very weak in the high Reynolds number limit.

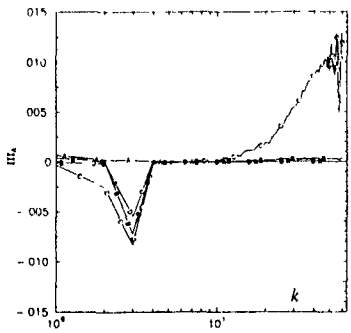

Figure 5. Third principle invariant (III_A) of the spectral anisotropy tensor during continuous anisotropic forcing at the large scales over two eddy turnover times (curves A-C), and relaxation after forcing is removed (curve D). $A_{ij} = E_{ij}(k)/E_{ii}(k) - \delta_{ij}/3$

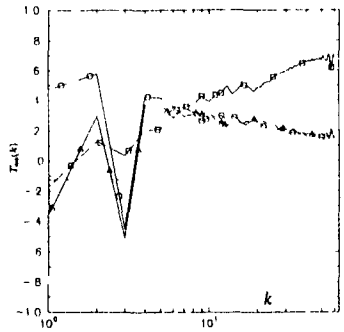

Figure 6 Normalized component energy transfer integrated over spherical shells after forcing continuously for two eddy turnover times. Δ,○,□ represent the α = 1,2,3 diagonal components of $T_{\alpha\alpha}(k)$, respectively (x,y,z directions).

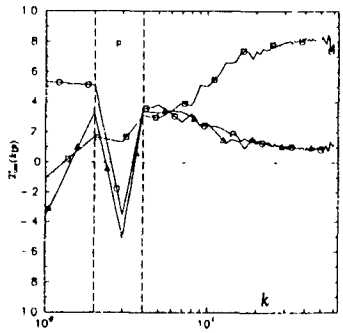

Figure 7 Analogous to Fig 6, however, $T_{\alpha\alpha}(k|p)$ includes only triads with one leg within the shell p where $2 \le p \le 4$. At high wavenumbers, $T_{\alpha\alpha}(k|p)$ is the energy transfer into or out of a high k shell due to nonlocal or distant triadic interactions with low k modes

anisotropic at about two eddy turnover times. However, the anisotropic structure of the small scales is very different from the large scale structure—the dominant energy direction at the small scales is z, and the vorticity strengthens in the x and y directions Significant anisotropy builds up above wavenumbers which are roughly an order of magnitude or higher than the forced modes Particularly significant is the observation that, consistent with Eq (9), the level of anisotropy at the small scales *increases with wavenumber* That is, the smaller the scale, the stronger the effect! It is shown in Yeung & Brasseur (1991a) that this restructuring of the small scales is wholly dominated by the more nonlocal triadic interactions between the high wavenumber and forced modes. In subsequent studies we have shown that in physical space this forced large-small scale interaction is dominated by the convection and stretching of small scale vorticity by the large-scale forced energetic structures, leading to an anisotropic structure at the small scales very different from large scale structure being forced (Yeung & Brasseur, 1991b).

8. Some Comments on Isotropizing Influences at the Small Scales

An important point relative to the study just described is summarized by Figs 6 and 7 In Fig. 6 the diagonal components of the spherically integrated energy transfer spectrum, $T_{\alpha\alpha}(k)$, are plotted against wavenumber after forcing for two eddy turnover times (the $T_{\alpha\alpha}(k)$ are normalized with $|T_{11}(k)|+|T_{22}(k)|+|T_{33}(k)|$, limiting the ratio to values between −1 and +1). Fig. 6 shows that, whereas near the large scale forced modes energy is transferred into the x–y velocity components by the two-dimensional forcing, at the small scales energy is transferred dominantly into the z direction. A similar plot is shown in Fig. 7, however here only those triadic interactions which include one mode in a narrow shell around the forced modes (band p) are included. Consequently, at high k, $T_{\alpha\alpha}(k|p)$ includes only the nonlocal or distant triadic interactions with modes in shell p. Note that Figs. 6 and 7 look similar at high wavenumbers, indicating the dominance of the more nonlocal interactions in the intermodal energy transfer process Note also, however, that when local triadic interactions are excluded at the small scales, the energy transfer process is more anisotropic than when local interactions are included. Thus, the global effect of local triadic interactions in this calculation is to isotropize the small scales.

The global effects of distant and local triadic interactions in the asymptotic limit of large Reynolds numbers have been studied by Brasseur and Wei (1991) through statistical calculations of interconnected 'chains' of local, nonlocal and distant triadic interactions Consistent with the low order, nonstatistical calculations of Brasseur & Corrsin (1987) we have found that local-to-nonlocal triadic interactions at wavenumbers higher than the spectral peak, on average tend to transfer energy from larger to the smaller scales. This forward cascading characteristic appears to be strongest among groups of interlinked triads which are not too close to equilateral ($\delta = 1$), but not highly nonlocal ($\delta \ll 1$). In contrast with interconnected distant triadic interactions which tend to distribute energy only within triads attached to the low wavenumber modes (Brasseur & Corrsin 1987), the local-to-nonlocal triadic interactions tend to transfer energy uniformly through a spectral shell—that is, without preferred direction in k -space. Consequently, as energy is transferred within these local-to-nonlocal triadic interactions, it moves through each successively higher wavenumber shell with an increasingly isotropic distribution

The isotropizing influence of interconnected chains of local-to-nonlocal triadic interactions would suggest that the anisotropizing effects of large scale forcing demonstrated in Fig. 5 (vid. §7) would eventually be reduced when the energy added at the large scales has cascaded to the small scales via local-to nonlocal triadic interactions. Furthermore, this isotropizing effect should be felt within successively higher wavenumber shells at later times. This is found to be the case in the moderate Reynolds number simulations described above, as shown in Fig 8 (from Yeung & Brasseur, 1991b). Here the third principle invariant shown in Fig. 5 is plotted against time within spectral shells of width $\Delta k = 5$ for continuous forcing over 4 eddy turnover times.

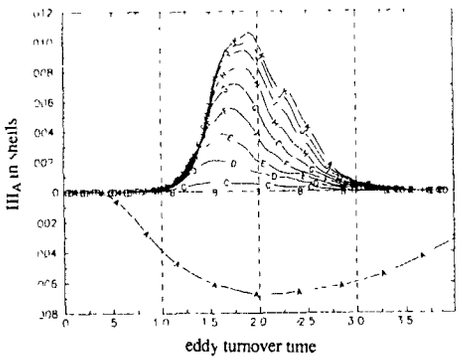

Figure 8. III_A from Fig 5 integrated over spectral shells of width $\Delta\kappa = 5$ is plotted as a function of eddy turnover time. The central wavenumbers for each spectral shell are: (A 3), (B 8), (C 13), (D 18), (E 23), (F 28), (G 33), (H 38), (I 43), (J 48), (K 53)

After reaching peak anisotropy within each spectral shell, the level of anisotropy then decreases Peak anisotropy is reached later at the higher wavenumbers, consistent with the arguments above.

Detailed analysis surrounding Fig 8 is given in Yeung & Brasseur (1991b) It turns out that frictional effects at the small scales begin to dominate small-scale dynamics at roughly two eddy turnover times, providing a strong isotropizing influence at the small scales. The return to an isotropic state at about 3.5 eddy turnover times is due partially to the effects of friction, and partially due to a return towards isotropy at the large scales The final state, however, is very different from the initial state at all scales

9. Summary and Conclusions

We summarize here the primary conclusions from the discussions above All conclusions are applicable in the limit of high Reynolds numbers

Within a spectral shell at the small scales, inertial interscale dynamics is separable approximately into the effects associated with distant triadic interactions with the energy-containing scales, and effects associated with local-to-nonlocal triadic interactions triadic interactions within the shell. The asymptotic form of the Navier-Stokes equation at high Reynolds numbers indicates that individual distant triadic interactions dominate, on average, over local triadic interactions, tending to move the small scales to a structural state directly coupled to the structure of the large scales. An anisotropic structure at the large scales therefore induces an anisotropic structure at the small scales The effect becomes stronger with Reynolds number and is stronger at smaller scales.

The Navier-Stokes equations show that no direct energy transfer takes place between large and small scales in the asymptotic limit Consequently, energy from the large energy-containing scales must reach the small scales through a series of interconnected chains of local-to-nonlocal triadic interactions. As energy is transferred through relatively narrow spectral shells within these more local triadic interactions, it tends to leave the higher k side of the shell more uniformly distributed than as it entered on the lower k side. In this way, as energy moves up the spectrum from the energy-containing to the dissipative scales, it does so in an increasingly isotropic manner.

As a consequence turbulence which has undergone anisotropic restructuring at the large scales will also undergo anisotropic restructuring at the small scale through direct inertial interaction with the large scales After sufficient time for energy from the large scales to reach the small scales, however, a reduction in the level of anisotropy at the small scales may be anticipated. The higher the Reynolds number, the greater range of scales must be traversed for large-scale energy to reach the small scales We argue that, in the asymptotic limit of infinite Reynolds numbers, energy transferred out of the large scales with an anisotropic energy distribution will arrive at the small scales with an isotropic energy distribution, but that it will take infinitely long to get there.

A second isotropizing influence important at the small scales is friction As a linear effect, frictional forces tend to move the energy among Fourier modes, as well as energy among the independent complex amplitude components, towards equipartition within a spectral shell

In summary, two dynamical processes, interconnected chains of local-to-nonlocal triadic interactions triadic interactions and frictional dissipation, are isotropizing influences at the small scales, whereas distant triadic interactions which directly couple small scale structure and large scale structure can move the small scales toward an anisotropic state It is likely that under different conditions one effect may dominate the other for different periods of time However, regardless of the relative importance of isotropizing to anisotropizing influences at the small scales, distant triadic couplings will remain active at infinite Reynolds numbers and the structure of the large scales will always impress itself at some level within the structure of the small scales

Acknowledgements. This work was supported by he U S Air Force Office of Scientific Research and the U R.I. program through AFOSR. Many stimulating discussions were had with K R Sreenivasan, A.J Smits, C-H Wei, J M. McMichael, J L Lumley, J A Domaradzki, R S Rogallo, J R Herring, and some years ago with S Corrsin (who continues to be greatly missed)

References

Antonia, R.A., Shah, D.A. & Browne, L.W B. 1988 *Phys Fluids* **31** 1805

Antonia, R A , Anselmet, F & Chambers, A.J. 1986 *J Fluid Mech* **163**: 365

Batchelor 1952 *The Theory of Homogeneous Turbulence* Cambridge University Press, Fig. 6.1.

Brown, L W.B , Antonia, L W B. & Shah, D A. 1987 *J Fluid Mech* **179**. 307

Brasseur, J.G 1991, manuscript in preparation

Brasseur, J G. & Corrsin, S 1987 in *Advances in Turbulence*, edited by G. Comte-Bellot and J. Mathieu (Springer-Verlag, Heidelberg), pp. 152

Brasseur, J G & Wei, C-H. 1991 , manuscript in preparation (also Wei, C-H., M S. Thesis, in preparation)

Domaradzki, J A & Rogallo, R S. 1990 *Phys. Fluids A* 2. 413

Kolmogorov , A N. 1941 *Dokl Akad Nauk USSR* **30** 299.

Sreenivasen, K R 1991 To appear in the A.N. Kolmogorov commmemerative issue of the *Proc Royal. Soc London A*

Sreenivasan, K.R 1985 *Phys Fluids* **27** 1048

Tennekes, H. & Lumley, J L. 1972 *A First Course in Turbulence*. MIT Press

Van Atta, C. 1991 To appear in the A.N. Kolmogorov commmemerative issue of the *Proc Royal Soc London A.*

Yeung, P.K & Brasseur, J.G 1991a *Phys. Fluids A* 3 884

Yeung, P.K & Brasseur, J.G 1991b To be presented at the European Fluid Dynamics Conference, Cambridge, England, September 14-16, manuscript in preparation

EIGHTH SYMPOSIUM ON
TURBULENT SHEAR FLOWS
Technical University of Munich
September 9-11, 1991

16-5

EVOLUTION OF COHERENT VORTEX STRUCTURES IN SHEARED AND STRATIFIED, HOMOGENEOUSLY TURBULENT FLOWS

Thomas Gerz

DLR, Institut für Physik der Atmosphäre
W-8031 Oberpfaffenhofen, Germany

ABSTRACT

The evolution of coherent vorticity structures is investigated by Direct Numerical Simulation (DNS) with a resolution of 128^3 and 160^3 gridpoints when a homogeneously turbulent flow is forced by vertically oriented mean shear and thermally stable stratification (negative buoyancy). Several types of coherent structures have been detected in flows at different gradient Richardson numbers *Ri*. Besides the well-known, vertically inclined, almost symmetric *horseshoes* or *hairpins* also non-symmetric *hooks* of coherent vorticity dominate the neutrally stratified flow with a constant shear rate. Sometimes several horseshoes are linked together in a *serpentine* form. The structures prevail in the flow as long as *Ri* is subcritical. At supercritical *Ri* the heads of developed horseshoe or hook vortices form into *rings* by self induction whereas the legs are dissolved by viscous forces. The vorticity is then mainly organized in almost horizontal *sheets* and *streaks*. Several video sequences elucidate that evolution of coherent vortices in stratified shear flows.

INTRODUCTION

Within the last decade it became more and more evident from experimental and numerical data that turbulence - despite its rather chaotic and random character in space and time - reveals a remarkable degree of coherence. This is particulary the case in inhomogeneous flows like boundary layer flows, mixing layers, and jets (Head & Bandyopadhyay 1981, Hussain 1986). But - more surprisingly perhaps - coherent structures have also been detected under purely isotropic conditions (Schwarz 1990, She et al. 1990). In inhomogeneous shear flows, as in mixing layers with a curved mean velocity profile, the spanwise (mean) rolls are the preferred vortex modes (see e.g. Hussain 1986). However, it is to be expected that in a homogeneous flow, where perturbations get influenced by the mean properties but not vice versa, different vortex structures will develop. Rogers & Moin (1987) detected horseshoe or hairpin shaped vortex structures in unstratified and sheared homogeneous turbulence. These structures are vertically inclined against the mean flow direction and they transport momentum, heat and other species very efficiently. The findings by Rogers & Moin (1987) and She et al. (1990) clearly demonstrate that coherent structures do form in homogeneous turbulence (as was already suggested by Townsend (1970)) and even in isotropic turbulence. Hence, in those flows coherent structures do not form due to linear instability of time-mean profiles but evolve locally by nonlinear interactions of turbulence itself and grow due to the "one-way" forcing of the mean strain rate.

It is the aim of this contribution to investigate the evolution of coherent vortex structures under statistically *homogeneous* conditions in a highly resolved domain with 128^3 or 160^3 gridpoints using the DNS-method. We consider the development of initially isotropic turbulence under the effects of viscous dissipation, thermally stable stratification (negative buoyancy) and shear, where the external forces consist of uniform vertical gradients of mean velocity dU/dz and mean temperature dT_R/dz. The linear mean profiles guarantee the spatial homogeneity of the turbulence statistics, but still allow different temporal evolutions which depend on three characteristic numbers. The gradient-Richardson number $Ri = \alpha g\, dT_R/dz \,/\, (dU/dz)^2$ (α and g represent volumetric expansion coefficient and gravitational acceleration) measures the relative strength of buoyancy to shear forces; the Reynolds number describes the degree of turbulence activity and the Prandtl number relates kinematic viscosity ν to thermal conductivity γ.

We keep Reynolds and Prandtl numbers fixed but change Ri from run to run, see Table 1

Gerz et al. (1989) and Gerz & Schumann (1991) performed direct numerical simulations of stably stratified, homogeneously turbulent shear flows with a (Taylor length) Reynolds number Re_λ of initially ≈ 26. They analyzed the data statistically and found a separation into subcritically and supercritically stratified flow regimes depending on Ri *Subcritical* regimes are characterized by increasing turbulent kinetic energy in time due to the shear forcing, whereas perturbations are damped out if the flow is *supercritical* At the critical value $Ri_c \approx 0.13$, Gerz & Schumann (1991) observed an almost steady flow state. Since shear dominates in subcritically stratified flows, horseshoe structures are expected to develop as they do in unstratified shear flows However, for the given Reynolds number of $Re_\lambda \approx 26$ in Gerz & Schumann (1991) the resolution with typically 64^3 gridpoints was too low to reveal coherent vortex structures in the computational domain

Holt et al. (1991) introduce a transition Richardson number $Ri_t (> Ri_c)$ at which the ratio of potential energy to kinetic energy is maximum At this Richardson number the flow changes from a shear driven state to a buoyancy driven state and the vertical heat flux approaches zero Hence, depending on the relative importance of buoyancy the coherent structures will evolve differently in flows where $Ri < Ri_c$ than in flows where $Ri > Ri_t$ In a previous study (Gerz 1991) I analyzed structures at $Ri_c \approx 0.13$ and at a much higher Richardson number of 1.32 ($> Ri_t$) Histograms of the inclination angle of the vortices showed maxima at about 30° and well developed horseshoes occured at this angle for the first case whereas inclination angles approached zero and almost horizontally oriented sheets and long and thin streaks of vorticity have been found in the second case. In this study we will see that in the intermediate range of Ri with $Ri_c < Ri < Ri_t$ the shear first stretches vortex filaments and forms horseshoes or hairpins But at a certain vertical extent the structures "feel" the restoring force of buoyancy and then change into Ω shapes and rings. A similar change of structures is observed when a developed unstratified shear flow ($Ri = 0$) suddenly experiences a strong restoring force ($Ri = 0.66$)

METHOD AND PARAMETERS

The three-dimensional Navier-Stokes and temperature equations for perturbation velocities (u, v, w) and temperature T are integrated in a cubic domain with side length L and coordinates (x, y, z) pointing in downstream, spanwise and vertical directions, respectively. The Boussinesq approximation is used Linear gradients of reference temperature $T_R(z)$ and mean velocity $U(z)$ drive the flow Periodic and shear periodic boundaries are applied in the horizontal and vertical directions, respectively. Details see in Gerz et al. (1989)

We consider non-dimensional quantities Scaling parameters are constant density ρ, mean velocity and temperature differences ΔU and ΔT between bottom and top of the domain and box size L The initial temperature perturbations are zero All cases start from the same isotropic velocity fields, except run D which is initiated at shear time $t = 6$ of the fully developed, neutrally stratified shear flow (case A) Initial data are summarized in Table 1

Grid points	M^3					128^3, 160^3
R m s velocity	$v = (\overline{u_i u_i}/3)^{1/2}$					0.020
R m s temperature	$T' = (\overline{TT})^{1/2}$					0
Shear number	$Sh = (dU/dz)(\ell/v)$					3.56
Reynolds numbers	$Re_\lambda = v\lambda/\nu$, $Re_\ell = v\ell/\nu$					26.8, 43.7
Prandtl number	$Pr = \nu / \gamma$					1
Richardson number	$Ri = (\alpha g\, dT_R/dz) / (dU/dz)^2$					
Cases		A	B	C	D	E
$Ri =$		0.	0.13	0.33	0.66	1.32
Integral length	ℓ					0.07428
Taylor micro-length	λ					0.04551
Kolmogorov length	L_K					0.004468

Table 1. Non-dimensional initial data and characteristic parameters For cases A and D $M = 128$, for cases B, C and E $M = 160$. Bars denote ensemble (i.e. 3-d spatial) averages

RESULTS

The evolution of turbulent kinetic energy $E_{kin} = \overline{u_i u_i}/2$ and available potential energy $E_{pot} = Ri\overline{TT}/2$ of all flows is depicted in Fig 1 Turbulence is enhanced by shear and is damped by stratification and viscosity An equilibrium is achieved when E_{kin} is constant in time. This results in a critical Richardson number

$$Ri_{crit} = \frac{\overline{uw}\, dT_R/dz}{\overline{wT}\, dU/dz}\left(1 - \frac{\varepsilon}{P}\right) = Pr_t\left(1 - \frac{\varepsilon}{P}\right) \quad (1)$$

where $P = -\overline{uw}\, dU/dz$ is the production rate, ε the dissipation rate and Pr_t is the turbulent Prandtl number (Rohr et al 1988) As can be seen in Fig 1 and as has been discussed by Gerz & Schumann (1991), the critical Richardson number in our simulations is close to $Ri_{crit} \approx 0.13$. For values of $Ri < (>) Ri_{crit}$ the turbulence is growing

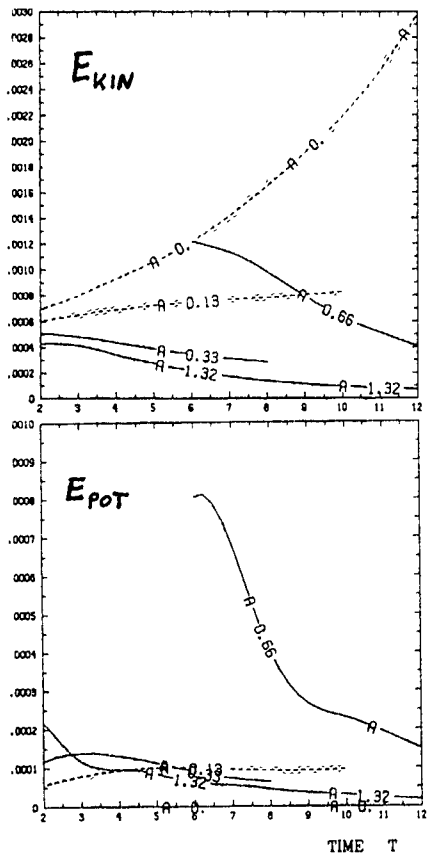

Fig 1 Turbulent kinetic energy and available potential energy for cases A to E versus shear time t

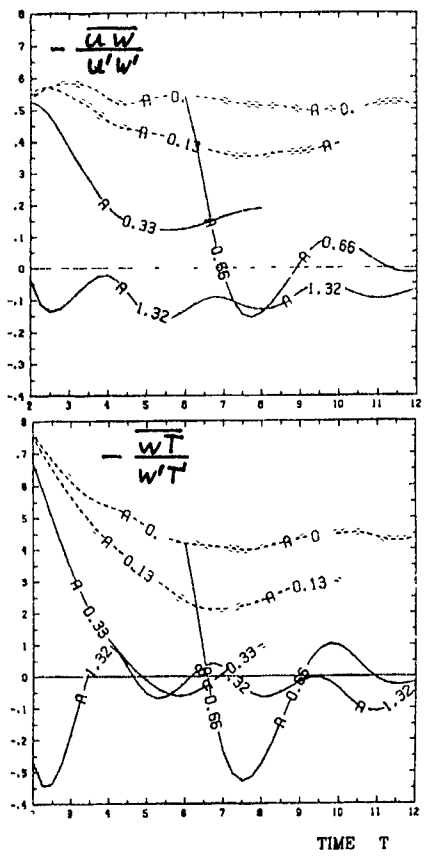

Fig 2. Correlation coefficients of negative fluxes of momentum and heat for cases A to E versus shear time t

(decaying) in time Since in case A the temperature field is passive, large temperature fluctuations do occur but no potential energy is available ($Ri = 0$). But when buoyancy is "switched on" at $t = 6$ in case D, suddenly these temperature perturbations provide a large amount of E_{pot} for the flow Most of E_{pot} is quickly transferred into kinetic energy where it results in a rather smooth decay of E_{kin} untill $t \approx 7.5$ Then the dissipation rate of E_{kin} is increased (not shown) which also increases the decay rate of the kinetic energy at $t \approx 8$.

Fig 2 shows the negative correlation coefficients of the vertical fluxes of momentum and heat, $-\overline{uw}/u'w'$ and $-\overline{wT}/w'T'$ (primes denote rms values), versus time Turbulence very well mixes momentum and heat as long as the Richardson number is not supercritical (dashed lines) For large values of Ri the fluxes quickly approach zero and even become positive (solid lines). Also in case D the correlations drop quickly despite their rather high (but of course unnatural) initial values. The strong decorrelation of horizontal momentum and vertical velocity and of heat and vertical velocity indicates a vertical seperation and decoupling of horizontal layers· The vertical mixing by turbulence is strongly reduced The heat flux becomes zero firstly in case C with $Ri = 0.33$ which indicates that the transient case has a Richardson value of $Ri_t \approx 0.3$ according to Holt et al (1991). However, note that the momentum flux still remains negative due to its direct forcing by shear. This effect explains the strong increase of the turbulent Prandtl number with growing Richardson number (see Eq 1) as observed in various stratified experiments (Komori et al. 1983, Rohr et al. 1988, Gerz et al 1989)

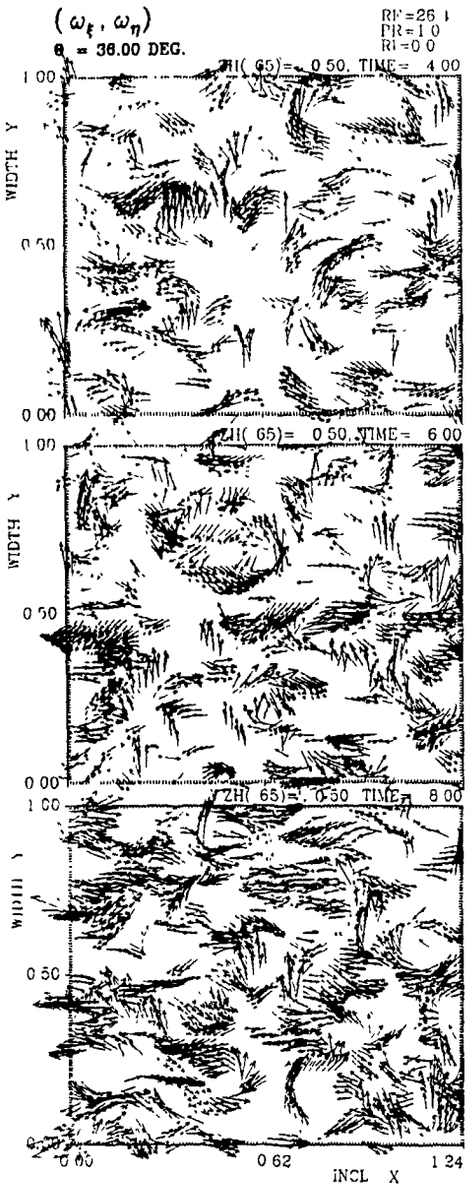

Fig 3 Projection of vorticity vectors on an inclined plane ($\theta = 36°$) for $Ri = 0$ at $t = 4$, 6 and 8 Vectors with magnitude ≥ 2 are displayed

DISCUSSION

After that short review of the statistical behaviour of turbulence in flows with different Richardson numbers we now concentrate on the coherent structure of vorticity in such flows The subsequent figures show vorticity vectors $(\omega_\xi, \omega_\eta)$ projected on a plane $(\xi, \eta = y)$ which is inclined against downstream direction (x) by rotation around the y-axis at an angle θ In most cases the inclination angle is $\theta = 36°$ which is about the angle at which developed coherent vortex structures in shear flows are inclined due to a balance of stretching and rotating of the vorticity filaments by the mean strain rate dU/dz (Rogers & Moin 1987, Gerz 1991)

The development of coherent structures in the projected vorticity field for case A with $Ri = 0$ at times 4, 6 and 8 can be studied in Fig. 3 For reasons of legibility only vorticity vectors are shown which exceed a magnitude of 2. At early times vorticity appears to be organized in tubes and sheets as known from isotropic flows. But when time proceeds more and more *hook*-like structures occur which consist of a "head" with positive lateral vorticity and one "leg" with vorticity oriented in mainly both upstream and downstream tilted directions At $t = 8$ a *horseshoe* vortex can be distinguished in the lower part of the frame It has almost equally developed long legs connected by a strong head which forms like a Ω due to self induction. Vorticity is maximum in the legs Since in homogeneous flows $\varepsilon = \nu \overline{\omega_i \omega_i}$ the legs also suffer from strongest dissipation (Gerz 1991).

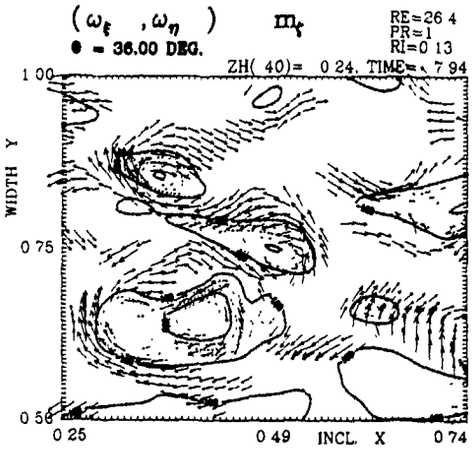

Fig 4 As Fig 3 for $Ri = 0\,13$ at $t = 7\,94$ Focus on a section of the plane. Vectors with magnitude $\geq 1\,5$ are displayed The projected momentum flux m_ξ is shown by contours

If the flow is weakly stratified as in case B with $Ri = 0\,13$ we also observe hairpins as docu-

mented in Fig 4 There we focus on a quarter of the area of the tilted plane in the flow at $t = 7\,94$ Three strong hairpins clearly dominate Note that they are connected with each other sharing legs together and, thus, forming a *serpentine* vortex Between the legs of each structure maximum values of negative momentum flux m_t are observed (as well as heat flux, not shown) which confirmes the important role of these structures for the mixing process

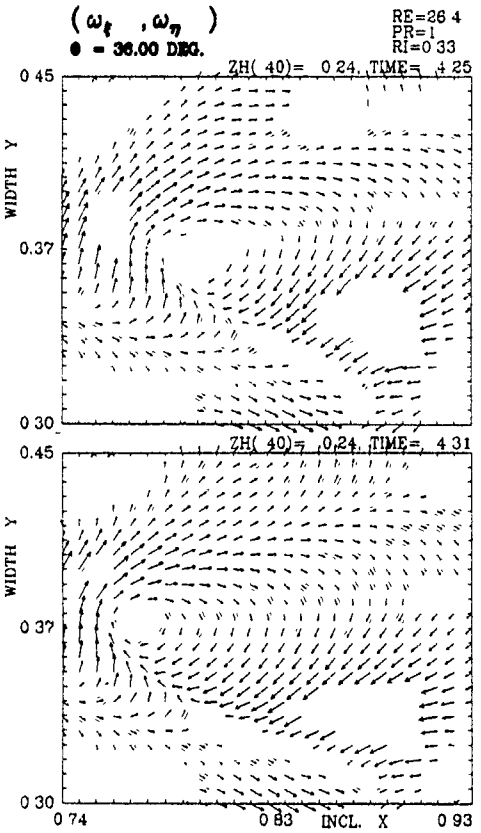

Fig 5 As Fig 3 for $Ri = 0\,33$ at $t = 4\,25$ and $4\,31$ Focus on a section of the plane Vectors with magnitude $\geq 1\,5$ are displayed.

Fig 5 now depicts two vorticity fields at two subsequent times of flow C with $Ri = 0\,33$ A former horseshoe vortex changes into a *ring* vortex With increasing Richardson number the possible vertical extent of an eddy decays since the restoring force increases In other words, the flow develops into horizontal layers which get more and more vertically decoupled (Gerz & Schumann 1991). At $Ri = 0\,33$, which is almost

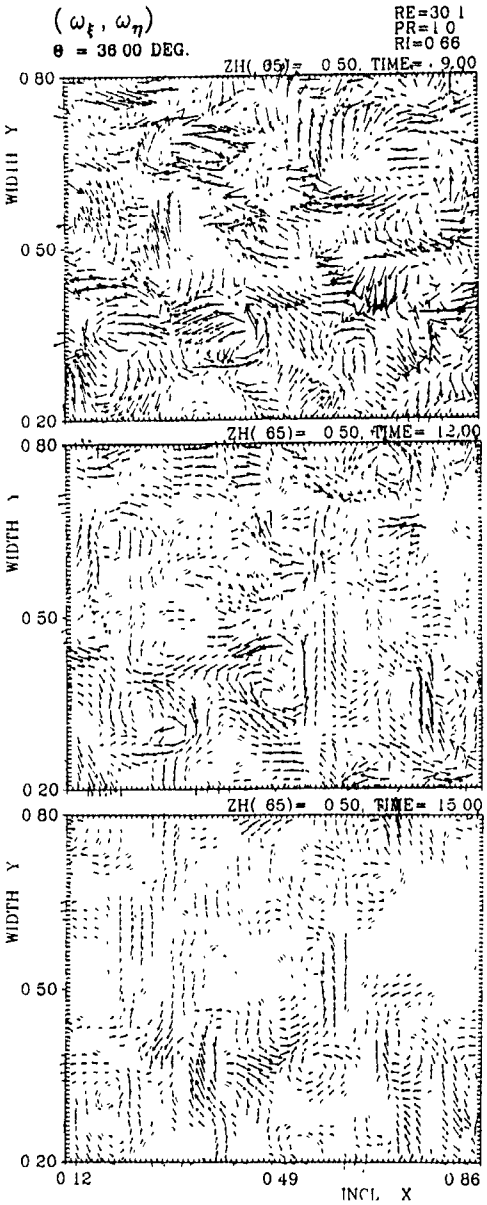

Fig 6 As Fig 3 for $Ri = 0\,66$ at $t = 9$, 12 and 15. Focus on a section of the plane Vectors with magnitude $\geq 0\,5$ are displayed

the transient Richardson number (see Fig 2), the horseshoe structure grows initially by vortex stretching until buoyancy limits a further growth. The legs are then dissolved by viscosity and cannot be rebuild by shear since a further

stretching is prohibited by the restoring force The head of the former horseshoe, however, survives and mutates into a ring due to self-induction forces.

If a fully developed, neutrally stratified flow suddenly experiences strong gravitational forces due to a sudden stable stratification with $Ri = 0.66$ (case D) the horseshoe vortices quickly degenerate to vortex rings which often occur as pairs as can be seen in Fig 6 The vorticity of the same flow has been projected onto a less inclined plane ($\theta = 12°$) in Fig 7 We find sheets of rather weak but equally oriented vorticity similar to the structures found by Gerz (1991) for $Ri = 1.32$ They are typical for vertically almost decoupled shear layers However as Fig 6 reveals, the ring vortices as the remainder of the former horseshoes still exist with a vertical inclination of 36° at this time $t = 15$ due to the self-induction process

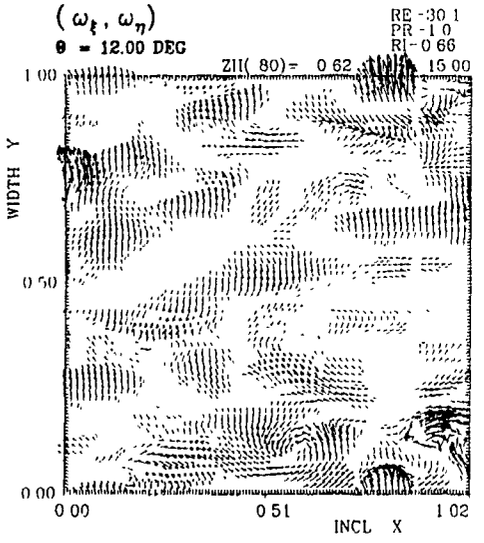

Fig 7 Projection of vorticity vectors on an inclined plane ($\theta = 12°$) for $Ri = 0.66$ at $t = 15$ Vectors with magnitude ≥ 0.5 are displayed

CONCLUSIONS

In stably stratified shear flows with *subcritical* Richardson numbers horseshoe shaped vortex structures evolve as known from homogeneous shear flows without stratification. Buoyancy does not affect the dynamics of the flow considerably. Typically, those structures are not symmetric and often reveal shapes like a hook rather than like a horseshoe The flow at subcritical and critical Richardson numbers is fully turbulent and the observed structures control the dynamics of the flow like heat and momentum transport. In flows with *supercritical* but *subtransient* Richardson numbers, $Ri_c < Ri < Ri_t$, inclined horseshoe vortices form at early stages of the flow evolution When the structures have reached a certain vertical size (which depends on Ri), they get influenced by the restoring force of buoyancy and the curved tips of the horseshoe vortices form into Ω shapes and eventually into rings by self-induction forces A similar evolution of structures is observed when a fully developed, neutrally stratified flow suddenly experiences a strong gravitational force The sheets and streaks of vorticity which are then found in almost horizontal layers are similar to but larger then the structures found in isotropic turbulence with the difference that they only survive horizontally Gerz (1991) argued that these sheets represent vertically decoupled shear layers whereas the streaks can be associated with gravity oscillations

REFERENCES

FRISCH, U & ORSZAG, S. A. 1990 Turbulence: Challenges for theory and experiment Physics Today, January 1990, 25-32

GERZ, T , SCHUMANN, U & ELGHOBASHI, S 1989 Direct numerical simulation of stratified homogeneous turbulent shear flows J Fluid Mech., **200**, 563-594

GERZ, T 1991 Coherent structures in stratified turbulent shear flows deduced from direct simulations In: *Turbulence and Coherent Structures* (O Métais & M. Lesieur, eds), Kluwer Academic Publishers, 449-468.

GERZ, T & SCHUMANN, U. 1991 Direct simulations of homogeneous turbulence and gravity waves in sheared and unsheared stratified flows In. *Turbulent Shear Flow 7*, (W C Reynolds, ed) Springer-Verlag, -...

HEAD, M R & BANDYOPADHYAY, P. 1981 New aspects of turbulent boundary layer structure. J Fluid Mech , **107**, 297-338

HOLT, S E , KOSEFF, J R. & FERZIGER, J H. 1991 The evolution and structure of homogeneous stably stratified sheared turbulence. Subm to J Fluid Mech

HUSSAIN, A K M F 1986 Coherent structures and turbulence J Fluid Mech , **173**, 303-356

KOMORI, S , UEDA, H , OGINO, F & MIZUSHINA, T 1983 Turbulence structure in stably stratified open-channel flow J Fluid Mech , **130**, 13-26

ROGERS, M M & MOIN, P. 1987 The structure of the vorticity field in homogeneous turbulent flows J Fluid Mech , **176**, 33 66

ROHR, J J., ITSWEIRE, E C , HELLAND, K N & VAN ATTA, C W. 1988 Growth and decay of turbulence in a stably stratified shear flow. J Fluid Mech , **195**, 77-111.

SCHWARZ, K W. 1990 Evidence for organized small-scale structure in fully developed turbulence Phys Rev. Letters, **64**, 415-418

SHE, Z -S , JACKSON, E & ORSZAG, S.A 1990 Intermittent vortex structures in homogeneous isotropic turbulence Nature, **344**, 226-228

TOWNSEND, A A 1970 Entrainment and the structure of turbulent flow. J Fluid Mech., **41**, 13-46.

EIGHTH SYMPOSIUM ON
TURBULENT SHEAR FLOWS
Technical University of Munich
September 9-11, 1991

SCRUTINIZING $k-\varepsilon$ EVM AND ASM BY MEANS OF LES AND WIND TUNNEL FOR FLOWFIELD AROUND CUBE

S. Murakami, A. Mochida and Y. Hayashi

Institute of Industrial Science, University of Tokyo,
22 - 1, 7 - Chome, Roppongi, Minato - ku, Tokyo 106, Japan

ABSTRACT

Three - dimensional turbulent flowfield around a cube placed in a surface boundary layer is predicted using Large Eddy Simulation (LES), Algebraic Stress Model (ASM) and the standard $k-\varepsilon$ Eddy Viscosity Model ($k-\varepsilon$ EVM) with similar boundary conditions. The accuracy of these simulations is assessed by comparing the numerical results with those of wind tunnel tests conducted by the authors. The differences between the results given by these three turbulence models are examined precisely by comparing the distributions of velocity vectors, turbulence energy k, turbulence production P_k and normal stress components $<u_i'u_i'>$.

1 INTRODUCTION

In this study, the accuracy of numerical simulations based on LES, ASM and $k-\varepsilon$ EVM is examined for the turbulent flowfield around a surface-mounted cube. Numerical studies of flowfields around bluff bodies placed within channel flows have been carried out by several authors [Durst,F. and Rastogi, A K.(1979),Werner,H. and Wengle,H.(1989),Obi,S.,Peric, M. and Scheurer,G.(1990), etc]. In this study, the cube is placed within a surface boundary layer which has relatively large magnitudes of turbulence intensities in comparison with those of channel flows and this produces some differences between the flowfield treated here and those in previous studies.

The flowfield analyzed here is extremely complex. It consists of stagnation at the windward face, separation at the frontal corner and Karman's vortex street behind the cube. The most distinctive feature of such a flowfield is found in the distributions of each component of the strain - rate tensor $(\partial<u_i>/\partial x_j+\partial<u_j>/\partial x_i)$, which is highly anisotropic and changes significantly depending on the relative position over the cubic body. Therefore, the application of $k-\varepsilon$ EVM, which is based on an isotropic Eddy Viscosity Model, to such an anisotropic flowfield may have serious limitations.

In the first part of this paper, the accuracy and the relative performance of these three turbulence models are assessed by comparison with the experimental data. It is confirmed that the results of LES agree very well with the experimental results. In the latter part, the results of $k-\varepsilon$ EVM and its algebraic extension (ASM) are scrutinized using both the numerical data given by LES and the experimental data from the wind tunnel tests. The shortcomings of these two models are then examined.

2. OUTLINE OF NUMERICAL SIMULATIONS

2.1. Model equations and numerical methods

The standard formulation for $k-\varepsilon$ EVM [Launder, B.E. and Spalding,J.L.(1972,1974)] was adopted. In LES, the Smagorinsky subgrid model [Smagorinsky,J S. (1963),Deardorff,J.W.(1970)] was applied and the value of 0.12 was selected for the Smagorinsky constant C_s. The model equations for ASM are shown in Table 1. The commonly adopted form for ASM was used, following the methods of Rodi,W.(1976), Gibson, M.M. and Launder,B.E.(1978) except for the treatment of the wall reflection term $\Phi_{ij\omega}^{w}$ (cf. APPENDIX 2) [Murakami,S.,Kato,S. and Kondo,Y.(1990)]. The values

NOMENCLATURE

x_i : three components of spatial coordinate (i = 1,2,3 : streamwise, lateral, vertical)
$<f>$: time - averaged value of f
$\bar{f}$: filtered value of f
f' : deviation from $<f>$, $f'=f-<f>$ (In LES, $f'=f-\bar{f}$)
f'' : deviation from $\bar{f}$, $f''=f-\bar{f}$
H_b : height of cube
u_i : three components of velocity vector
u_b : u_1 value at inflow of computational domain at height H_b
p : pressure
ν_t : eddy viscosity
ν_{SGS} : subgrid scale eddy viscosity
k : turbulent kinetic energy, $k=\frac{1}{2}<u_i'u_i'>$
k^* : subgrid component of k, $k^*=\frac{1}{2}\overline{u_i''u_i''}$
P_k : production of k
ε : dissipation rate of k (In LES, $\varepsilon=<\nu_{SGS}\partial\bar{u}_i/\partial x_j(\partial\bar{u}_i/\partial x_j+\partial\bar{u}_j/\partial x_i)>$)
$<u_i'u_j'>$: Reynolds stress
P_{ij} : production of $<u_i'u_j'>$
ε_{ij} : dissipation rate of $<u_i'u_j'>$
C_{ij} : convection term of $<u_i'u_j'>$,
D_{ij} : diffusion term of $<u_i'u_j'>$, $D_{ij}=\frac{\partial}{\partial x_k}(-<u_i'u_j'u_k'>-<p'u_i'>\delta_{jk}-<p'u_j'>\delta_{ik})$
Φ_{ij} : pressure - strain correlation term (consists here of $\Phi_{ij(1)}$, $\Phi_{ij(2)}$ and $\Phi_{ij(1)}^{w}$, cf. APPENDIX 2)
h_i : mesh interval in x_i direction
h : mesh scale, $h=(h_1h_2h_3)^{1/3}$
h_P : mesh interval adjacent to solid wall
$(u_i)_P$: tangential component of velocity vector at the near - wall node
k_P : k value at the near - wall node
ε_P : ε value at the near - wall node
τ_w : wall shear stress
$h_n^{(w)}$: vertical distance from the w - th wall
Re : Reynolds number ($<u_b>H_b/\nu=8.4\times10^4$)

Values are made dimensionless by $<u_b>$, H_b and air density ρ.

of the numerical constants in ASM follow those proposed by Launder,B E ,Reece,G.J and Rodi,W.(1975) and Launder,B E.(1983)

A staggered grid was adopted A second－order upwind scheme (the QUICK scheme) was applied for the convection terms in the cases of k–ε EVM and ASM A second－order centered difference scheme was adopted for the other spatial derivatives The Adams－Bashforth scheme was used for time marching.

2 2 *Mesh arrangements and boundary conditions*

The computational domain covered 15 7 (x_1 direction), 9 7 (x_2 direction) and 5 2 (x_3 direction). This domain was discretized into 50 (x_1) × 49 (x_2) × 28 (x_3) meshes for the cases of k–ε EVM and ASM, and 63 (x_1) × 49 (x_2) × 34 (x_3) meshes for the case of LES The value of h_p was set at 1/24 for all cases.

Boundary conditions are summarized in Table 2 For the inflow boundary of LES, time history of $\overline{u_i}(t)$ in a fully developed channel flow predicted by LES were utilized The profiles of $\langle \overline{u_i}(x_3)\rangle$ and $k(x_3)$ in the boundary layer of the channel given by LES correspond well to those of the experiment (cf.Fig 1). For the boundary conditions at the solid walls, the generalized logarithmic law expressed by eqn.(2 1) [Launder,B.E. and Spalding,J.L.(1974)] was employed in order to estimate the time－averaged wall shear stress $\langle \tau_w \rangle$ for the cases of three models. Furthermore, eqn.(2.4) was used to specify the instantaneous wall shear stress τ_w for the case of LES As shown in Table 2, almost the same boundary conditions were imposed for the calculations of the three models so far as the time averaged flowfields are concerned. Therefore, it can be concluded that the differences observed in the results from these three models are mainly caused by the difference in turbulence modellings.

Table1 Model equations for ASM

$$\frac{\partial \langle u_i\rangle}{\partial t}+\frac{\partial \langle u_i\rangle\langle u_j\rangle}{\partial x_j}=-\frac{\partial p}{\partial x_i}-\frac{\partial \langle u_i'u_j'\rangle}{\partial x_j} \quad (1\,1)$$

$$\frac{\partial \langle u_i\rangle}{\partial x_i}=0 \quad (1.2)$$

$$\frac{\partial k}{\partial t}+\frac{\partial k\langle u_j\rangle}{\partial x_j}=D_k+P_k-\varepsilon \quad (1\,3)$$

$$\frac{\partial \varepsilon}{\partial t}+\frac{\partial \varepsilon\langle u_j\rangle}{\partial x_j}=D_\varepsilon+\frac{\varepsilon}{k}(C_{\varepsilon 1}P_k-C_{\varepsilon 2}\varepsilon) \quad (1.4)$$

$$(P_k-\varepsilon)\frac{\langle u_i'u_j'\rangle}{k}=P_{ij}+\Phi_{ij}-\varepsilon_{ij} \quad (1.5)$$

$$D_k=\frac{\partial}{\partial x_m}(C_k\langle u_m'u_i'\rangle\cdot\frac{k}{\varepsilon}\cdot\frac{\partial k}{\partial x_l}) \quad (1\,6)$$

$$D_\varepsilon=\frac{\partial}{\partial x_m}(C_\varepsilon\langle u_m'u_l'\rangle\cdot\frac{k}{\varepsilon}\cdot\frac{\partial \varepsilon}{\partial x_l}) \quad (1.7)$$

$$P_k=-\langle u_i'u_j'\rangle\frac{\partial \langle u_i\rangle}{\partial x_j} \quad (1.8)$$

$$P_{ij}=-\langle u_i'u_k'\rangle\frac{\partial \langle u_j\rangle}{\partial x_k}-\langle u_j'u_k'\rangle\frac{\partial \langle u_i\rangle}{\partial x_k} \quad (1.9)$$

$$\varepsilon_{ij}=\frac{2}{3}\cdot\delta_{ij}\varepsilon \quad (1\,10)$$

$$\Phi_{ij}=\Phi_{ij(1)}+\Phi_{ij(2)}+\Phi^w_{ij(1)} \text{ (cf APPENDIX 2)} \quad (1\,11)$$

$$\Phi_{ij(1)}=-C_1\frac{\varepsilon}{k}(\langle u_i'u_j'\rangle-\frac{2}{3}\delta_{ij}k) \quad (1\,12)$$

$$\Phi_{ij(2)}=-C_2(P_{ij}-\frac{2}{3}\delta_{ij}P_k) \quad (1.13)$$

$$\Phi^w_{ij(1)}=\sum_{w=1}^{w0}C_1'\frac{\varepsilon}{k}(\langle u_k'u_m'\rangle\cdot n_k^{(w)}\cdot n_m^{(w)}\cdot\delta_{ij}-\frac{3}{2}\langle u_k'u_i'\rangle\cdot n_k^{(w)}\cdot n_j^{(w)}-\frac{3}{2}\langle u_k'u_j'\rangle\cdot n_k^{(w)}\cdot n_i^{(w)})\cdot\frac{k^{3/2}}{C_l\cdot h_k^{(w)}\varepsilon} \quad (1.14)$$

C_μ : 0.09, σ_k : 1.0, σ_ε : 1.3, C_1 : 1.8, C_2 0.6, C_1' . 0.5, C_2' : 0.5, C_k : 0.22, C_ε : 0.16, $C_{\varepsilon 1}$: 1.44, $C_{\varepsilon 2}$: 1 92, C_l : 2.5 (1 15)

Table 2 Boundary conditions

	k–ε EVM, ASM	LES
inflow	$\langle u_1(x_3)\rangle$, $\langle u_1(\tau_w)\rangle \propto x_3^n$ (measured profile in wind tunnel) $\langle u_2(x_3)\rangle = 0$, $\langle u_3(x_3)\rangle = 0$ $k(x_3)$ predicted distribution in plane channel by LES (this distribution corresponds well to that measured in the experiment (Fig 1)) $\nu_t(x_3)=k(x_3)^{1/2}\ell(x_3)$, $\varepsilon(x_3)=C_\mu k(x_3)^{3/2}/\ell(x_3)$ $\ell(x_3)=(C_\mu k(x_3))^{1/2}/(\frac{\partial\langle u_1\rangle}{\partial x_3})$, $(P_k(x_3)=\varepsilon(x_3))$ $\langle u_1'^2(x_3)\rangle \propto \frac{2}{3}k(x_3)$	$\overline{u_1}(t)$, $\overline{u_2}(t)$, $\overline{u_3}(t)$ time history of velocity in boundary layer of plane channel predicted by LES $\begin{pmatrix}\langle\overline{u_1(x_3)}\rangle \propto x_3^n\\ \langle\overline{u_2(x_3)}\rangle=0\\ \langle\overline{u_3(x_3)}\rangle=0\end{pmatrix}$
outflow	$\langle u_1\rangle$, $\langle u_2\rangle$, $\langle u_3\rangle$, k, ε : free slip $(\partial/\partial x_1=0)$	$\overline{u_1}$, $\overline{u_2}$, $\overline{u_3}$, free slip
upper face of computational domain	$\langle u_3\rangle = 0$, $\langle u_1\rangle$,$\langle u_2\rangle$, k, ε , free slip $(\partial/\partial x_3=0)$	$\overline{u_3}=0$, $\overline{u_1}$, $\overline{u_2}$ free slip
side faces of computational domain	$\langle u_2\rangle = 0$, $\langle u_1\rangle$,$\langle u_3\rangle$, k, ε , free slip $(\partial/\partial x_2=0)$	$\overline{u_2}=0$, $\overline{u_1}$, $\overline{u_3}$ free slip
solid wall	The time averaged wall shear stress $\langle\tau_w\rangle$ is given by equation (2 1). The volume averaged value of ε at the near－wall grid used for transport equation of k is expressed by equation (2 2), and defined as $\bar{\varepsilon}$. The value of ε at the near－wall node used for transport equation of ε is defined by equation (2 3). $\frac{\langle(u_l)_P\rangle}{\langle\tau_w\rangle}(C_\mu^{1/4}k_P)^{1/2}=\frac{1}{\kappa}ln(\frac{E\cdot\frac{1}{2}h_P(C_\mu^{1/4}k_P)^{1/2}}{\nu})$ ⋯ (2.1) $\bar{\varepsilon}=\frac{C_\mu^{3/4}\cdot k_P^{3/2}}{\kappa h_P}ln(\frac{Eh_P(C_\mu^{1/4}k_P)^{1/2}}{\nu})$ ⋯ (2 2) $\varepsilon_P=\frac{C_\mu^{3/4}\cdot k_P^{3/2}}{\frac{1}{2}\kappa h_P}$ ⋯ (2 3) κ : free slip $(\kappa=0.4, C_s=0.09, E=9.0)$	$\tau_w=\langle\tau_w\rangle\times\frac{(\overline{u_l})_P}{\langle(\overline{u_l})_P\rangle}$ ⋯ (2.4) $\langle\tau_w\rangle$ is estimated by equation (2.1). $\langle(\overline{u_l})_P\rangle$, k_P are given by using the results of the foregoing time steps

■ experiment

○ k–ε, ASM, LES (predicted distribution in the boundary layer of plane channel by LES)

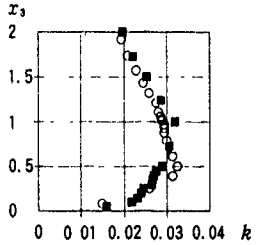

Fig.1 Profiles of $k(x_3)$ at inflow boundary (x_3 : vertical direction)

3 OUTLINE OF WIND TUNNEL TESTS

A cube – shaped model, 200mm in height, was placed in the turbulent boundary layer The Reynolds number based on $\langle u_h \rangle$ and H_h was about 8.4×10^4. The wind velocity was measured by a tandem – type hot wire anemometer which could monitor each component of an instantaneous velocity vector.

4 RESULTS AND DISCUSSION

4.1. Distributions of k and mean velocity vectors

The distributions of k at the central vertical section are illustrated in Fig.2. The result given by LES agrees very well with that of the wind tunnel experiment except for the value in the downstream free shear layer above the recirculation region behind the cube, where the value of k from LES is a little larger than the experiment. Slightly larger values of k in the free shear layer may be attributed to the inadequacy of the value of $C_s = 0.12$ Previous studies reported that the appropriate value of C_s is around 0.14 in such flowfields as free shear layer just behind a backward facing step [Morinishi,Y.and Kobayashi,T. (1990)] On the other hand, the result of k given by k–ε EVM is quite different from the experiments, in particular, the value of k becomes much larger in the area around the frontal corner. The distribution of k given by ASM agrees rather well with that given by the experiment, but its k value is estimated to be a little larger in the area just before the windward face, and too small in the area near the floor behind the cube It should be noted that, in the case of ASM as well as in the case of k–ε EVM, k value near the floor is estimated to be smaller in comparison with the experiment and LES.

Figs.3 and 4 illustrate the distributions of time – averaged velocity fields. The correspondence between LES and the experiment is particularly good. The small reverse flow on the roof and the velocity distribution in the recirculation region behind the cube are reproduced successfully in LES (Figs.3, 4 (2)) In the case of k–ε EVM, there are several significant discrepancies The reverse flow on the roof is not reproduced and the velocity value (reverse flow) is too large in the recirculation region in comparison with the experiment and LES (Figs 3, 4 (2)), although the similar boundary conditions are applied for both LES and k–ε EVM

The overestimation of k near the frontal corner in the case of k–ε EVM gives rise to the large eddy viscosity ν_t, and thereby the large mixing effect produced by this ν_t eliminates the reverse flow on the roof. This discrepancy is caused by overestimation of the turbulence production P_k which is evaluated using Eddy Viscosity Model (EVM) as discussed in the next section and APPENDIX 1

In the case of ASM, the reverse flow on the roof is reproduced But the distribution of velocity value behind the cube is similar to that of k–ε EVM and the correspondence with the experiment is not so good (Fig.4 (2)) This discrepancy is sure to be related to the underestimation of k near the floor behind the cube in both k–ε EVM and ASM as shown in Fig.2 This underestimation of k is mainly caused by the fact that the value of $\tilde{\varepsilon}$ assigned at the solid wall, which is given by eqn.(2.2) in Table 2, is not appropriate for this area. It was pointed out in many previous studies that eqn (2.2) works well as a boundary condition when the local balance of P_k and

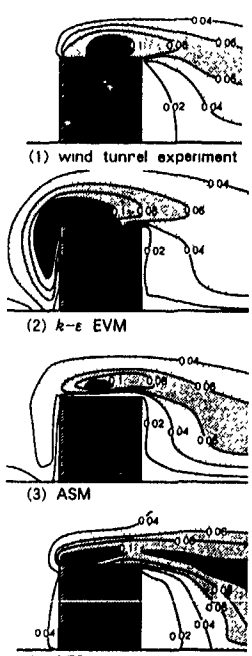

Fig 2 Distributions of k at center section

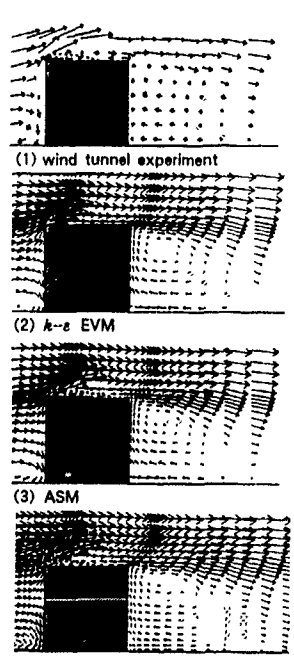

Fig.3 Distributions of velocity vectors

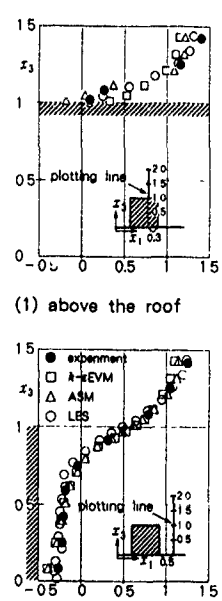

Fig.4 Vertical profiles of $\langle u_i \rangle$ at center section

ε can be assumed Obviously, the recirculation zone is not an area where this assumption applies In this area,the value of $\tilde{\varepsilon}$ is estimated too large and thus the value of k becomes very small as already shown in Fig 2 Consequently the value of ν_t becomes too small and the poor mixing effect caused by this small value of ν_t results in too large velocity value of reverse flow in this area in k-ε EVM and ASM

4 2 Distribution of P_k

The distributions of P_k are illustrated in Fig.5. The result of LES is sure to be reasonable because of the good agreement of its k distribution with the experiment The difference between k-ε EVM and LES is significant The value given by k-ε EVM is much larger in the area around the frontal corner than that of LES It was clarified in our previous studies that this defect of k-ε EVM is mainly caused by overestimation of P_k concerned with the diagonal elements of strain – rate tensor [Murakami,S. and Mochida,A (1988), Murakami,S ,Mochida,A and Hayashi, Y (1990)] (cf APPENDIX 1) This reflects the fundamental shortcoming of k-ε EVM, which is based on the isotropic Eddy Viscosity Model, for the accurate reproduction of flowfields around bluff – shaped bodies

ASM also estimates the larger value of P_k than that of LES in the area just before the windward wall where a negative value of P_k appears in the result of LES. However, the difference between the values from ASM and LES is relatively small in comparison with the large difference observed between the results from k-ε EVM and LES

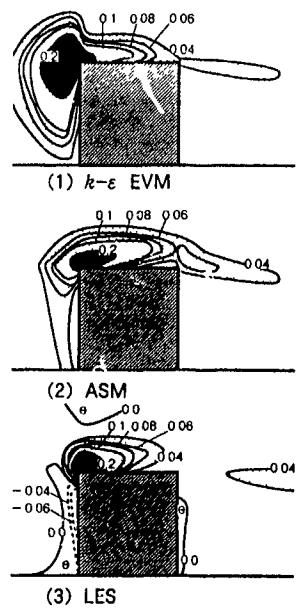

Fig 5 Distributions of P_k ($\in$ denotes the areas where values are negative)

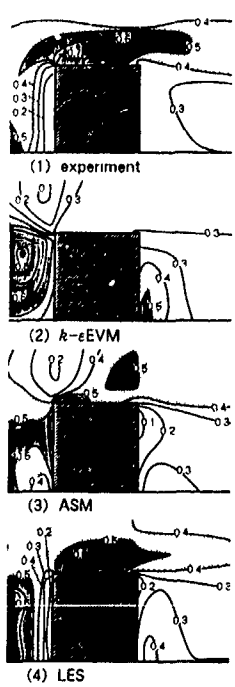

Fig 6 Distributions of $\langle u_1'^2\rangle/2k$

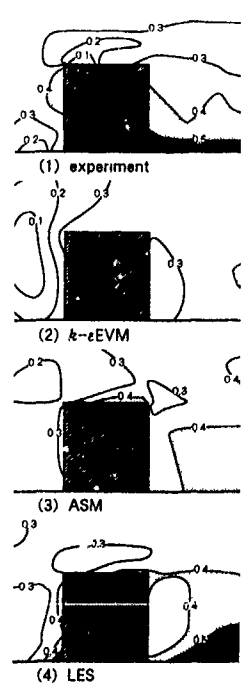

Fig.7 Distributions of $\langle u_2'^2\rangle/2k$

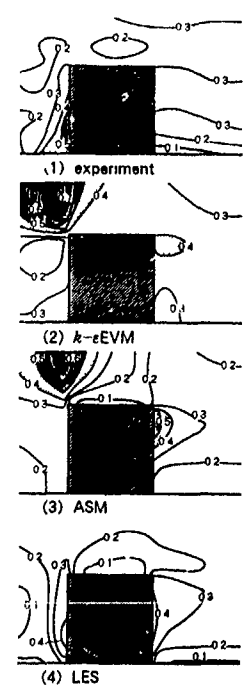

Fig.8 Distributions of $\langle u_3'^2\rangle/2k$

4.3. Distributions of each component of $\langle u_i'^2\rangle/2k$ (with no summation here)

The anisotropic property of each component of normal stress $\langle u_i'^2\rangle$ is examined in Figs 6 – 10, where distributions of $\langle u_i'^2\rangle/2k$ are presented as a measure to judge the anisotropy of turbulence

The results of the wind tunnel experiment illustrate that the value of $\langle u_1'^2\rangle$ dominates in the area on the roof, in the downstream free shear layer (Fig 6) In the recirculation region behind the cube, $\langle u_1'^2\rangle/2k$ has a larger value where Karman's vortex street appears (Fig 7) The value of $\langle u_3'^2\rangle/2k$ is the smallest in general, except for the region in the vicinity of the windward face where $\langle u_3'^2\rangle$ is the largest component (Fig.8)

The anisotropic features given by each component of $\langle u_i'^2\rangle/2k$ in LES correspond very well with those from the experiment (Figs.6 – 8). On the other hand, k–ε EVM cannot reproduce such anisotropic properties at all (Figs 6 – 8) In the case of ASM, the discrepancies observed in the results of k–ε EVM are improved remarkably in the distributions of each component in the recirculation region behind the cube (Figs 6 – 9). In this region, the values given from ASM agree rather well with those of the experiment. However, near the floor ASM underestimates the value of $\langle u_1'^2\rangle/2k$ in comparison with the results of the wind tunnel experiment and LES (Fig.9). It should be mentioned that this inaccuracy of ASM is partly caused by the fact that Φ_{ii2}^* was not involved in this calculation as described in detail in APPENDIX 2

Furthermore, the results of ASM show serious discrepancies in the area above the frontal corner in comparison with both the experiment and LES. In this area, the results of ASM show abnormal maximum and minimum peaks in the distributions of $\langle u_1'^2\rangle/2k$ and $\langle u_3'^2\rangle/2k$ respectively, as is observed identically in the results of k–ε EVM (Figs 6,8,10). These peaks do not appear in the results of the experiment and LES. This serious discrepancy is caused by an inaccuracy in the algebraic approximation $\frac{-\langle u_1'u_3'\rangle}{k}(P_k-\varepsilon)$ for $-(C_0-D_0)$ in the case of ASM. It is well known that this algebraic expression is most effective when the values of $\langle u_i'u_j'\rangle/k$ are almost constant across the flowfield However, Figs.6 – 10 indicate that values of $\langle u_i'u_j'\rangle/k$ are not constant. $\langle u_i'u_j'\rangle$ and k vary in very different manners in the flowfield around the cube, particularly in the area around the frontal corner Thus,the results from ASM are unavoidably inaccurate because of the algebraic approximation for $-(C_0-D_0)$ in this area.

Lastly, the balance of production term P_{33} and convection and diffusion terms $-(C_{33}-D_{33})$ in the transport equation for $\langle u_3'^2\rangle$ is discussed in order to examine the large difference observed in the distributions of $\langle u_3'^2\rangle/2k$ of the results of ASM and LES In this area, the velocity gradient $\partial\langle u_3\rangle/\partial x_3$ has a large negative alue, since a large positive value of $\langle u_3\rangle$ is produced related to the stagnation at the windward wall and decreases in a vertical direction as is illustrated in Fig.3. This large negative value of $\partial\langle u_3\rangle/\partial x_3$ makes the value of P_{33} very large in comparison with those of P_{11} and P_{22} which do not include the terms containing $\partial\langle u_3\rangle/\partial x_3$ Consequently the anisotropic property of turbulence is strongly influenced by the value of P_{33} in this area Fig.11 shows a comparison between the value of P_{33} and two types of $-(C_{33}-D_{33})$. One of $-(C_{33}-D_{33})$ is estimated from the original exact expression and another is given by the algebraic expression introduced in ASM, both using the numerical data given from LES. It is found that $-(C_{33}-D_{33})$ estimated from the original exact

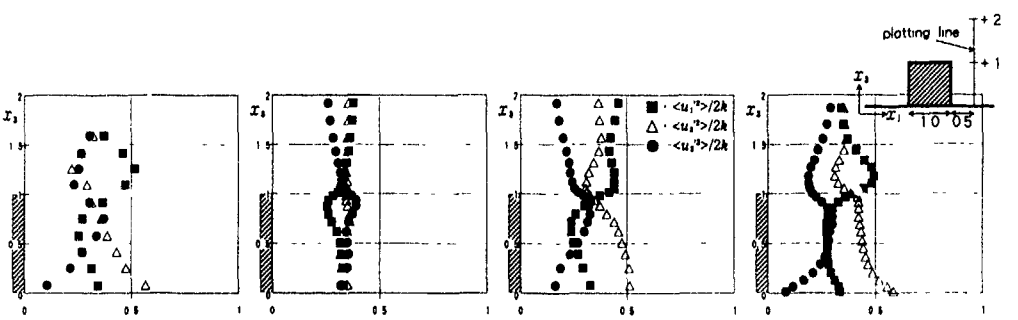

(1) experiment (2) k–ε EVM (3) ASM (4) LES

Fig.9 Vertical profiles of each component of $\langle u_i'u_i'\rangle/2k$ in the recirculation behind the cube (with no summation here)

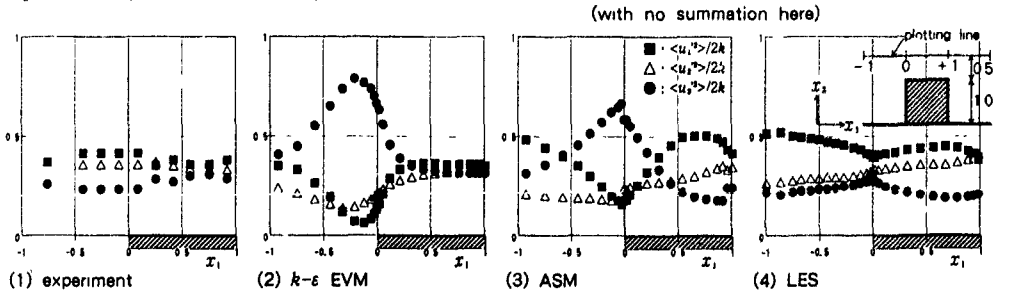

(1) experiment (2) k–ε EVM (3) ASM (4) LES

Fig 10 Longitudinal profiles of $\langle u_i'u_i'\rangle/2k$ above the roof

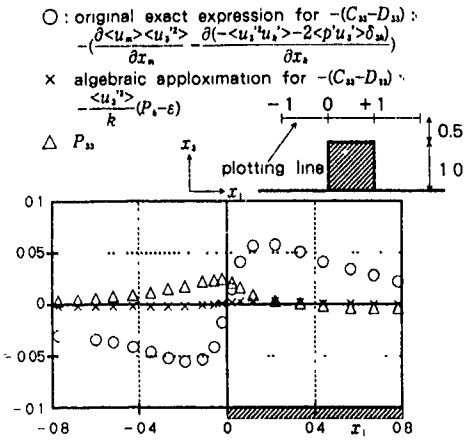

Fig.11 Distributions of $-(C_{33}-D_{33})$ and P_{33} above the roof estimated by using the numerical data given from LES

expression has a large negative value in the area where the distribution of P_{33} indicates a maximum peak, thereby, the increase of $<u_3'^2>$ caused by the positive value of P_{33} is restrained by the effect of $-(C_{33}-D_{33})$. This means that $<u_3'^2>$ increased by P_{33} is convected and diffused to the upper and downstream sides of the flowfield, so that the distribution of $<u_3'^2>/2k$ does not have a sharp peak in the area in front of the windward corner in the cases of the experiment and LES (Figs.8,10 (1),(4)). As is clearly shown in Fig.11, the approximation adopted in ASM cannot reproduce this strong effect of convection and diffusion which should decrease $<u_3'^2>$ in the area in front of the corner. This inaccurate estimation of $-(C_{33}-D_{33})$ causes too large value of $<u_3'^2>$ in the case of ASM. This cannot be improved so long as we remain at a stage where the algebraic expression for $-(C_{ij}-D_{ij})$ is adopted. The results of Differential Stress Model (DSM) will be presented by the same authors in the near future.

5. CONCLUSION

1) The flowfields around a surface-mounted cube as predicted by LES, ASM and k-ε EVM are compared precisely with the experimental data.

2) The results of LES agree very well with the experimental data in terms of the distributions of mean velocity, k and $<u_i'^2>/2k$.

3) The results of k-ε EVM include several serious discrepancies from the experimental data. These shortcomings of k-ε EVM are attributable to the isotropic Eddy Viscosity Model.

4) Significant inaccuracies in the results of k-ε EVM are improved remarkably in ASM. However, there still exist some discrepancies in the results of ASM in the reproduction of the anisotropic properties of turbulence around the frontal corner. This inaccuracy mainly derives from the algebraic expression for $-(C_{ij}-D_{ij})$ employed by ASM. A study of prediction by DSM will be undertaken by the authors.

APPENDIX 1

The value of P_k at the center section is estimated. Considering the symmetrical property and neglecting the small terms, P_k is given as follows:

$$P_k \fallingdotseq -<u_1'^2>\frac{\partial<u_1>}{\partial x_1}-<u_3'^2>\frac{\partial<u_3>}{\partial x_3} \quad (P_{k,n})$$
$$-<u_1'u_3'>\frac{\partial<u_1>}{\partial x_3}-<u_3'u_1'>\frac{\partial<u_3>}{\partial x_1} \quad (P_{k,s}) \qquad \text{(A.1)}$$

where $P_{k,n}$ is the turbulence production by diagonal elements of the strain-rate tensor and $P_{k,s}$ is the one by off-diagonal elements. The expression for $P_{k,n}$ in eqn (A.1) can be rewritten by using the continuity equation as follows:

$$P_{k,n} \fallingdotseq -(<u_1'^2>-<u_3'^2>)\frac{\partial<u_1>}{\partial x_1}. \qquad \text{(A.2)}$$

In the case of k-ε, eqn.(A.2) is transformed into eqn.(A.3) by eddy viscosity modelling.

$$P_{k,n} \fallingdotseq 4\nu_t(\frac{\partial<u_1>}{\partial x_1})^2. \qquad \text{(A.3)}$$

In general, the magnitude of $P_{k,n}$ does not become so large in the cases of LES and ASM, since $P_{k,n}$ is calculated using the exact form of eqn.(A.2) which is expressed as the subtraction of $<u_1'^2>$ and $<u_3'^2>$. On the other hand, the turbulence production due to $<u_1'^2>$ and $<u_3'^2>$ is simply added in the case of k-ε EVM as expressed by eqn (A.3), and hence the value of $P_{k,n}$ becomes very large. This is the fallacy given by EVM. This overestimation of k caused by the diagonal elements of strain-rate tensor is the fundamental shortcoming of eddy viscosity modelling when it is applied to a flowfield involving stagnation where usually large values of $\partial<u_i>/\partial x_i$ exist.

The overestimation of $P_{k,s}$ also occurs in the case of k-ε EVM. The mechanism of overestimation can be shown easily by the same manner as $P_{k,n}$.

APPENDIX 2

$\Phi^w_{ij(2)}$ is not involved in this calculation. This is because the model of $\Phi^w_{ij(2)}$ proposed by Gibson,M.M. and Launder,B.E. (1978) which is most common at present reveals itself to have some shortcomings in the analysis of flowfield with impinging where a main flow $<u_1>$ attacks the windward wall x_2-x_3 perpendicularly. $\Phi^w_{ij(2)}$ may be represented in the following manner.

$$\Phi^w_{11(2)}=2C_2C_2'(P_{11}-2/3P_k)/f_1,\ \Phi^w_{22(2)}=\Phi^w_{33(2)}=-C_2C_2'(P_{11}-2/3P_k)/f_1$$

Here, $f_1=k^{3/2}/(2.5\varepsilon h_1)$.

$\Phi^w_{11(2)}$ is a term which should decrease $<u_1'^2>$ according to its original meaning. Thus, in this case, $(P_{11}-2/3P_k)$ must be negative. However, on the center line of the impinging flow, P_{11} is large. Therefore it does not take a negative value. Hence, in this model, $\Phi^w_{11(2)}$ works to increase $<u_1'^2>$, contrary to its original meaning. As a matter of fact, when $\Phi^w_{ij(2)}$ is involved in the calculation, the normal stress perpendicular to the wall becomes excessively large near the wall and the solution diverged in this study.

REFERENCES

Deardorff,J.W.(1970),J.Fluid Mech.,Vol.41,pp.453 – 480.

Durst,F. and Rastogi,A.K.(1979),1st Symposium on Turbulent Shear Flow,pp.208 – 219.

Gibson,M.M. and Launder,B.E.(1978),J.Fluid Mech.,Vol.86, pp.491 – 511.

Launder,B.E. and Spalding,J.L.(1972),Mathematical Models of Turbulence, Academic Press,New York.

Launder,B.E. and Spalding,J.L.(1974),Computer Methods in Applied Mechanics and Engineering,Vol.3,pp.269 – 289.

Launder,B.E.,Reece,G.J. and Rodi,W.(1975),J.Fluid Mechanics, Vol.68,pp.537 – 566.

Launder,B.E.(1983),University of Manchester, Institute of Science and Technology Report No.TFD/82/4.

Morinishi,Y.and Kobayashi,T.(1990),Engineering Turbulence Modelling and Experiments,Elsevier Science Publishing, pp.279 – 286.

Murakami,S. and Mochida,A.(1988),J.Wind Eng.Ind.Aerodyn., Vol.31,pp.283 – 303.

Murakami,S.,Kato,S. and Kondo,Y.(1990),Engineering Turbulence Modelling and Experiments,Elsevier Science Publishing, pp.205 – 214.

Murakami,S.,Mochida,A. and Hayashi,Y.(1990),J.Wind Eng.Ind Aerodyn.,Vol.35,pp.87 – 100.

Obi,S.,Peric,M.,Scheurer,G.(1990),Engineering Turbulence Modelling and Experiments,Elsevier Science Publishing, pp.185 – 194.

Rodi,W.(1976),ZAMM,Vol.58,T219 – T221.

Smagorinsky,J.S.(1963),Mon.Weather Rev.,Vol.91,pp.99 – 164.

Werner,H. and Wengle,H.(1989),7th Symposium on Turbulent Shear Flow,Vol.1,pp.10.2.1 – 10.2.6.

EIGHTH SYMPOSIUM ON
TURBULENT SHEAR FLOWS
Technical University of Munich
September 9-11, 1991

NUMERICAL SIMULATION OF PERIODICALLY FULLY DEVELOPED TURBULENT FLOW AND HEAT TRANSFER IN A CHANNEL WITH LONGITUDINAL VORTEX GENERATORS

J. X. Zhu, N K. Mitra, M. Fiebig

Institut fur Thermo- und Fluiddynamik
Ruhr-Universität Bochum
W-4630 Bochum 1, Germany

ABSTRACT

A numerical study has been performed to investigate the hydrodynamical and thermal characteristics in the periodically fully developed region of turbulent channel flows with built-in longitudinal vortex generators. The level of turbulent kinetic energy in the flow is considerably elevated by the vortex generators. This contributes to augmentation of flow loss and heat transfer. For a ratio of 10.4 of the channel wall area to the vortex generator area, a mean heat transfer enhancement of 341% accompanied by 32 times of flow loss increase over the flow without vortex generators has been obtained.

INTRODUCTION

Turbulent flows with heat transfer in channels and ducts are of immense technological importance, as they occur frequently in many heating and cooling devices. In order to enhance heat transfer at the channel walls, longitudinal vortices can be introduced in the flows; eg. Edwards et al. (1974), Fiebig et al. (1986). Longitudinal vortices promote mixing of the fluid between the wall and the core regions of the channel, disturb the growth of the boundary layers on the channel walls and thus ensure high rate of heat transfer at the walls. Longitudinal vortices in a channel can be generated either by mounting or by punching out of the channel wall wing type vortex generators such as delta wing, delta winglet pair, rectangular wing or rectangular winglet pair (Fiebig et al. 1991). These are triangular or rectangular pieces which remaining attached at the base to the channel wall project into the flow with an angle of attack. Fiebig et al. (1986) have investigated the heat transfer enhancement and drag increase produced by a single wing or a pair of winglets for laminar flows in a rectangular channel. Effects of a single delta or rectangular wing or a pair of delta or rectangular winglets on the local and global heat transfer enhancement and flow losses in turbulent channel flows have been compared by Fiebig et al. (1991). Results show that when compared to other forms of vortex generators the rectangular winglet pair gives the least increase in flow loss for a nearly equal heat transfer enhancement.

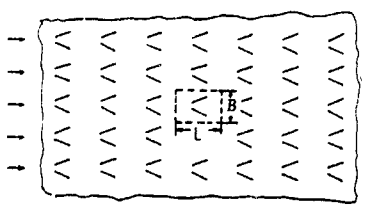

Fig. 1 *Schematic of a parallel wall channel with a series of vortex generators mounted on one channel wall*

The works cited above deal with a single array of vortex generators located in the thermally developing region of the channel where the vortex generators modify thermally developing flows. In practical applications rows of vortex generators have to be used, see Fig. 1. Numerical Simulation of the flow in the complete channel with rows of vortex generators will be tremendous task even for a super computer. However, after a sufficiently large distance from the inlet the flow in the channel with rows of vortex generators will tend to be periodically fully developed in streamwise direction in modules or elements of the channel as shown by the dotted lines in Fig 1.

The purpose of the present work is to predict heat transfer and flow losses in periodically fully developed area of turbulent channel flow with vortex generators (Fig. 1). As vortex generators the rectangular winglet pair is considered.

MATHEMATICAL FORMULATION

The periodical properties of the flow field enables the flow field analysis to be confined to a single isolated module shown in Fig. 2, which can be assumed as an element in periodically fully developed region of the arrangement shown in Fig 1 and serves as computational domain in the present work.

The computational domain consists of a parallel wall channel and a pair of rectangular winglets mounted on the lower wall. Symmetry is assumed at B/2 so that the computation is performed only in the half of the channel width. The geometrical parameters of the computational domain and the

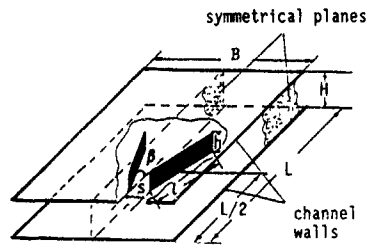

Fig. 2 *Computational domain and geometrical parameters*

vortex generator in Fig. 2 have the following basic values relative to the channel height H:

$$L = 3.75\ H, \quad B = 4\ H, \quad l = 1.2\ H,$$
$$n = 0.6\ H, \quad s = 0.4\ H, \quad \beta = 45^{\circ} \qquad (1)$$

The flow in the channel is described by 3-D Reynolds averaged Navier-Stokes and energy equations for incompressible medium in conjunction with the eddy viscosity concept:

Continuity:

$$\frac{\partial U_i}{\partial x_i} = 0 \qquad (2)$$

Momentum:

$$\rho \frac{DU_i}{Dt} = -\frac{\partial p}{\partial x_j} + \frac{\partial}{\partial x_i}\left[(\mu + \mu_t)\left(\frac{\partial U_i}{\partial x_j} + \frac{\partial U_j}{\partial x_i}\right) - \frac{2}{3}\rho\, k\, \delta_{ij}\right] \qquad (3)$$

Energy:

$$\rho \frac{DT}{Dt} = \frac{\partial}{\partial x_i}\left[(\Gamma + \Gamma_t)\frac{\partial T}{\partial x_i}\right] \qquad (4)$$

Where the turbulent viscosity μ_t and the turbulent dynamic thermal diffusivity Γ_t are given by:

$$\mu_t = c_\mu\, \rho\, k^2/\epsilon\ ; \qquad \Gamma_t = \frac{\mu_t}{Pr_t} \qquad (5)$$

The turbulence kinetic energy k and its dissipation rate ϵ are computed from the standard k-ϵ model of Launder and Spalding (1974):

$$\rho \frac{Dk}{Dt} = \frac{\partial}{\partial x_i}\left(\frac{\mu_t}{\sigma_k}\frac{\partial k}{\partial x_i}\right) + G - \rho\,\epsilon \qquad (6)$$

$$\rho \frac{D\epsilon}{Dt} = \frac{\partial}{\partial x_i}\left(\frac{\mu_t}{\sigma_\epsilon}\frac{\partial \epsilon}{\partial x_i}\right) + c_1 \frac{\epsilon}{k} G - c_2\, \rho \frac{\epsilon^2}{k} \qquad (7)$$

G denotes the production rate of k which is given by:

$$G = \mu_t \left(\frac{\partial U_i}{\partial x_j} + \frac{\partial U_j}{\partial x_i}\right)\frac{\partial U_i}{\partial x_j} \qquad (8)$$

The standard constants are employed:
$c_\mu = 0.09$; $c_1 = 1.44$, $c_2 = 1.92$,
$\sigma_k = 1.0$, $\sigma_\epsilon = 1.3$, $Pr_t = 0.9$

BOUNDARY CONDITIONS

Entrance and Exit

A special method for calculating periodically fully developed flows proposed by Patankar et al. (1977) is applied with some modifications to describe the inlet and outlet boundaries of the computational domain.

$$\varphi(x,y,z) = \varphi(x+L,y,z); \quad \varphi = (U,V,W,P,k,\epsilon,\Theta) \qquad (9)$$

Where P and Θ are a periodical component of the static pressure p and a dimensionless temperature respectively. They are defined as follows:

$$p(x,y,z) = -\beta\, x + P(x,y,z) \qquad (10)$$

$$\beta = \frac{p(x,y,z) - p(x+L,y,z)}{L} \qquad (11)$$

$$\Theta(x,y,z) = \frac{T(x,y,z) - T_w}{\bar{T}_b(x) - T_w} \qquad (12)$$

Symmetry

At the symmetric planes the normal velocity component and the normal derivatives of all other variables are set to zero:

$$W = 0; \quad \frac{\partial \varphi}{\partial z} = 0; \quad \varphi = (U,V,k,\epsilon,T) \qquad (13)$$

Walls

Wall functions given by Launder and Spalding (1974) are employed to prescribe the boundary conditions along the channel walls. The wall functions are applied in terms of diffusive wal fluxes. For the wall-tangential moment these are the wall shear stresses:

$$\tau_w = \frac{\rho U_p c_\mu^{1/4} k_p^{1/2} \kappa}{\ln(Ey^*)} \qquad (14)$$

with the non-dimensional wall distance y^+ defined as:

$$y^+ = \frac{\rho y_p c_\mu^{1/4} k_p^{1/2}}{\mu} \qquad (15)$$

and $\kappa \simeq 0.42$, $E = 9.0$.

The subscript p refers to the grid point adjacent to the wall. The production rate of k and the averaged dissipation rates over the near-wall cell for the k-equation as well as the value of ϵ at the point p are computed respectively from:

$$G_p = \tau_w \frac{U_p}{y_p} \qquad (16)$$

$$\bar{\epsilon} = \frac{1}{y_p}\int_c^{y_p} \epsilon\, dy = \frac{c_\mu^{3/4} k_p^{3/2}}{\kappa\, y_p} \ln(Ey^*) \qquad (17)$$

$$\epsilon_p = \frac{c_\mu^{3/4} k_p^{3/2}}{\kappa\, y_p} \qquad (18)$$

For the temperature boundary condition, the heat flux to the wall is derived from the thermal wall function of Launder and Spalding (1974):

$$q_w = \frac{(T_w - T_p)\,\rho c_p c_\mu^{1/4} k_p^{1/2}}{Pr_t\left[\frac{1}{\kappa}\ln(Ey^*) + P\right]} \qquad (19)$$

where the empirical P function is specified as:

$$P = \frac{\pi/4}{\sin(\pi/4)}\left(\frac{A}{\kappa}\right)^{1/2}\left(\frac{Pr}{Pr_t} - 1\right)\left(\frac{Pr_t}{Pr}\right)^{1/4} \qquad (20)$$

The lower wall is adiabatic and the upper wall has a constant temperature in the present work

NUMERICAL PROCEDURE

A finite difference procedure, based on the SOLA algorithm (Hirt et al., 1975), was modified by the authors' group for the investigation of the velocity and temperature fields in 3-D laminar channel flows with longitudinal vortex generators. In the present work, this procedure has been extended to solve turbulent problems. In order to validate the modified computer program, the code has been used to simulate a well documented 3-D turbulent flow experiment of Pauley and Eaton (1988). The numerical results compare well with experiments (Zhu et al., 1990).

RESULTS AND DISCUSSION

Flows appeared in the configuration of Fig. 2 with a Reynolds number $Re_{Dh} = 3 \cdot 10^5$ and a Prandtl number Pr = 0.7 have been numerically simulated.

The number of grids typically used is 37 x 15 x 20. The computational time on a SUN 4/260 workstation was 38 CPU hours. A grid independence study of the computation has not been performed, but some idea of the grid independence of these results is given by Fiebig et al (1991). A hydrodynamically and thermally fully developed flow with same Reynolds number, same Prandtl number and same thermal boundary conditions in a channel without vortex generator was also computed for the sake of comparison. Henceforth this flow is referred to as the base flow.

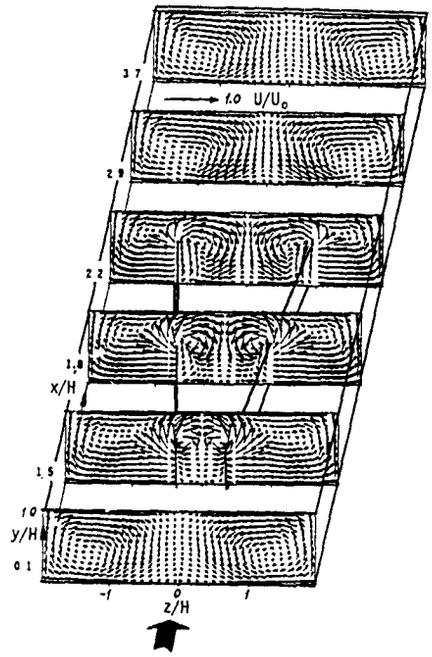

Fig. 3 *Secondary velocity vectors in periodically developed region of a turbulent channel flow with built-in rectangular winglet pair; L = 3.75 H, β = 45°, Re_{Dh} = 3 10^5*

Fig. 3 shows secondary velocity vectors of the flow at some axial cross sections of the channel. The identical secondary velocity distribution at inlet and outlet of the domain illustrates the periodically developed character of the flow. The generation and transport of longitudinal vortices are quite discernible in Fig. 3. In contrast to the thermally developing region, where the vortex generator faces an undisturbed 2-D flow (Fiebig et al., 1991), the vortex generator in periodically fully developed region interact with a three dimensional, longitudinal vortices contained flow. The disturbance of the flow by the vortex generator in this region is much stronger than in the entrance region, the total cross section is filled by the vortices.

Fig. 4 shows the contours of turbulent kinetic energy at the axial cross sections. The influnce of longitudinal vortices on the distribution of turbulent kinetic energy in the flow is obvious. The isolines reveal the vortex structure. In the vortex core the maximal k-value (isoline 10) is 500 times higher as that at the correspondent position in the base flow. The elevation in the turbulent kinetic energy level is much larger tha in the entrance region, where the elevation is about 100 times im comparison with base flow (Fiebig et al., 1991). This means, owing to the repeated interaction of the main flow with the vortex generators in streamwise direction, much more kinetic energy is converted from main flow to turbulence movement in periodically developed region than in entrance region.

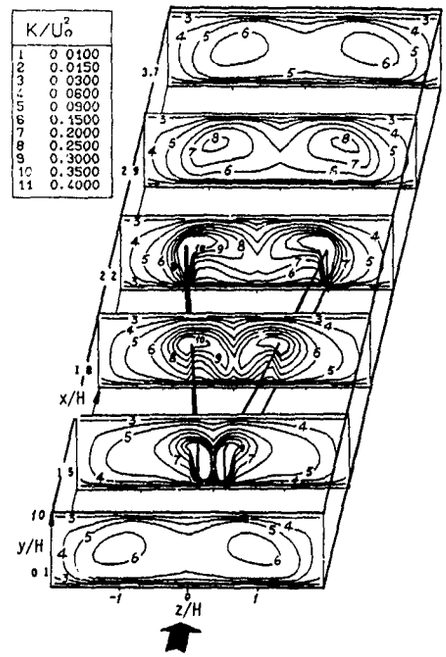

Fig. 4 *Contours of turbulent kinetic energy k/U_0^2 at axial cross sections in periodically developed region of a turbulent channel flow with built-in rectangular winglet pair, L = 3.75 H, β = 45°, Re_{Dh} = 3 10^5*

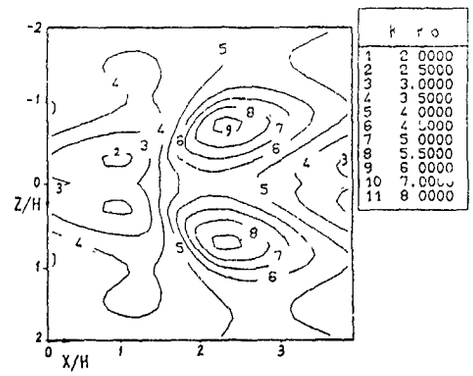

Fig. 5 *Isolines of k/k_0 on a x-z plane near the upper wall ($y^+ \approx 400$), L=3.75 H, β=45°, Re_{Dh}=3 10^5*

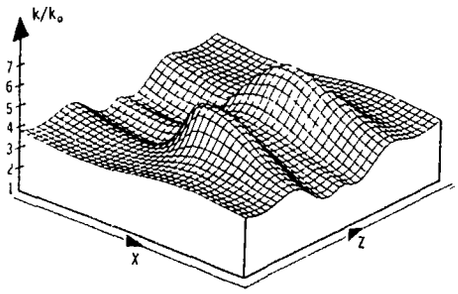

Fig. 6 *k/k_0-distribution on a x-z plane near the upper wall ($y^+ \simeq 400$), L=3.75 H, β=45°, Re_{Dh}=3 10^5*

Fig. 5 shows isolines of k/k_0 on a x-z plane near the upper wall of the channel, which is 0.038 H away from the upper wall and located in full turbulent region of the boundary layer ($y^+ \simeq 400$). Fig. 6 shows the k/k_0-distribution on this plane. Here k_0 is the corresponding turbulent kinetic energy in base flow. One notices that the vortex generator increases k in the near wall area by a factor of 6 over k_0 at maximum. Since large k means large thermal diffusivity, influence on heat transfer due to large k should be prominent. That such is the fact is apparent from the isoline plot of the ratio of the Nusselt numbers on the upper wall Nu/Nu_0 in Fig. 7 The structural similarity of the k/k_0-plots (Fig. 5) and Nu/Nu_0-plots (Fig 7) is remarkable.

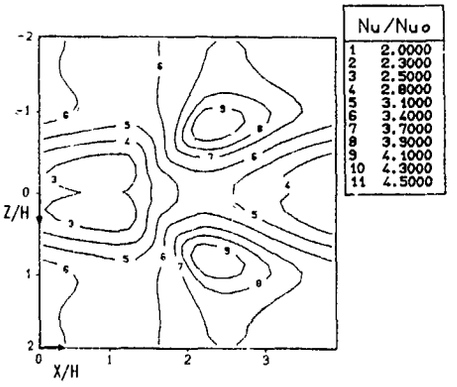

Fig. 7 *Isolines of Nusselt number ratio Nu/Nu_0 on upper wall (T_w= const.); at lower wall q_w= 0, L = 3.75 H, β = 45°, Re_{Dh}= 3 10^5, Pr = 0.7*

Fig. 8 shows Nu/Nu_0-distribution on the upper wall. Here again one notices the structural similarity with Fig. 6 for k/k_0-distribution. Areas of large enhancement in Nu correspond to the areas of large k. In the above plots, Nu_0 stands for the Nusselt number in the channel without vortex generator. The maximum of Nu/Nu_0 takes a value of 4.1 and the minimum a value of 2.5. The mean value of Nu/Nu_0 over the total upper wall area, which is 10.4 times of the face area of the vortex generators, is 3.41.

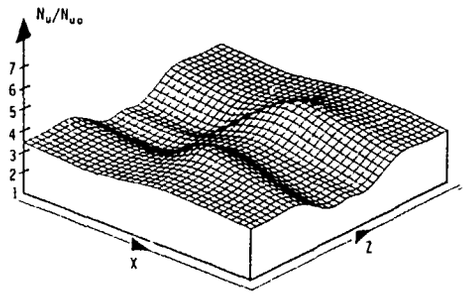

Fig. 8 *Nu/Nu_0-distribution on the upper wall, L = 3.75 H, β = 45°, Re_{Dh} = 3 10^5, Pr = 0.7*

For the estimate of flow losses in the present problem the kinetic energy equation in Gersten (1983) is simplified as follows:

$$\Phi_{12} = \frac{1}{2}(\alpha_1 - \alpha_2)\, U_o^2 + \frac{p_1 - p_2}{\rho} \qquad (21)$$

where

$$\Phi_{12} = \frac{P_D}{M} \qquad (22)$$

is the specific dissipation. The variables α and P_D in Eqs. (21-22) are kinetic energy correction factor and disspation respectively, which are described in detail by Gersten (1983). The dissipation P_D indicates the loss of mechanical energy due to friction and turbulent mixing. For the convenience of analysis, a dimensionless number C_φ, called dissipation number, is derived from Eq. (21) (Fiebig et al., 1991):

$$C_\varphi = \frac{\Phi_{12}}{U_o^2}\frac{H}{\Delta x} = \frac{1}{2}(\alpha_1 - \alpha_2)\frac{H}{\Delta x} + f_{app} \qquad (23)$$

For the present problem the index 1 means inlet, index 2 means outlet of the computational domain and Δx indicates the periodical length L Because of the identical velocity profile at inlet and outlet of the domain ($\alpha_1 = \alpha_2$), it holds in the periodically developed region $C_\varphi = f_{app}$

Based on Eqs.(22-23) the dissipation P_D (a measure for flow loss) can be expressed by:

$$P_D = C_\varphi U_o^2 \frac{L}{H}\rho U_o B H = C_\varphi L B \frac{\rho \nu^3}{D_h^3} Re^3 \qquad (24)$$

For the same medium, Reynolds number and geometrical parameters the flow loss is proportional to the dissipation number C_φ. In present case the increase of flow loss over the base flow $C_\varphi/C_{\varphi o}$ is 32. The computed Nu_o and $C_{\varphi o}$ for the base flow are compared in Tabel 1 with available data from reference.

Tabel 1 *Comparison between numerical and empirical results for Nu_o and $C_{\varphi o}$ in a fully developed turbulent channel flow; Re= 3 10^5, Pr = 0.7, at one wall T_w= const., at the other wall q_w= 0*

	$C_{\varphi o}$ 10^3	Nu_o
empirical	3.71 *	367 **
numerical	3.63	353
deviation	2 %	3.8 %

* - after Eq. (26); ** - after Eq. (27)

Heat transfer in a channel can also be enhanced by just increasing the flow velocity (raising Reynolds number). To judge the goodness of the vortex generator for heat transfer enhancement, the flow loss caused by rise of Reynolds number is estimated according to some empirical relation and used as a criterion in the following. Normally the so called Fanning friction-factor C_f ($= 2\tau_w/\rho U_o^2$) is used to describe the flow losses in fully developed channel flows. It holds in such flows:

$$C_f = f_{app} = C_\varphi \qquad (25)$$

Based on experimental data, a Fanning friction-factor formula:

$$C_f = 0.0868\ Re^{-2\ 75};\ \text{for } 1\ 2\ 10^4 < Re < 1.2\ 10^6 \qquad (26)$$

and a Nusselt number correlation for $0.01 < Pr < 1$ and $10 < Pe < 10^5$ for a parallel-plate channel with uniform temperature at one wall and the other wall insulated:

$$Nu_T = 5.8 + 0.02\ Re^{0\ 8}\ Pr^{0\ 8} \qquad (27)$$

are presented in Bhatti and Shah (1987). With Eq (26) in Eq. (24) a relation between the dissipation P_D and Reynolds number for fully developed channel flow within the range of Reynolds number shown in Eq. (26) can be given by:

$$P_D \sim Re^{2\ 75} \qquad (28)$$

If the heat transfer enhancement of factor 3.41 (in the above case) is achieved by increasing the flow velocity instead of using vortex generators, the Reynolds number should be raised by a factor of 4 55 after Eq. (28). This rise of Reynolds number will result 68 times increase in the flow loss according to Eq. (28), which is much larger than the flow loss caused by the vortex generator ($C_\varphi/C_{\varphi o}$= 32). The flow losses caused by raising Reynolds number accompanied by the same heat transfer enhancement achieved by using vortex generator will be designated in the following with $(P_D/P_{Do})_{crit}$.

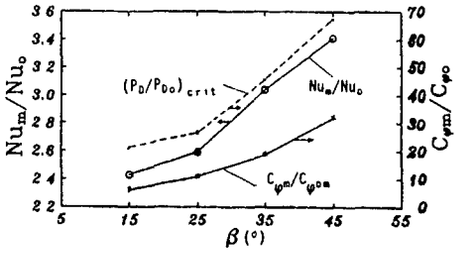

Fig. 9 *Influnce of β on heat transfer enhancement and flow loss increase in periodically developed region, $L = 3.75\ H$, $Re_{Dh} = 3\ 10^5$, $Pr = 0.7$*

In order to investigate the influnce of β and L on heat transfer and flow loss, they are independently varied in this study. Four values of β (= 15°, 25°, 35°, 45°) and three values of L (= 2.5 H, 3.75 H, 5 H) are tested. A smaller L means a denser arrangement of vortex generators at the channel wall. Fig. 9 shows the influnce of β on heat transfer enhancement and flow loss increase. The dotted line indicates those flow losses, which must be put up with, if one tries to obtain the same Nu_m/Nu_o achieved by vortex generator

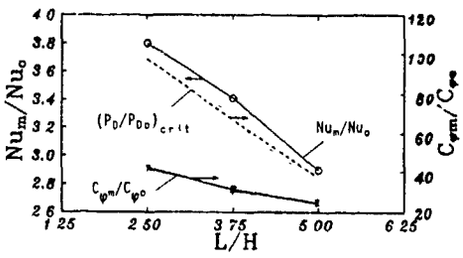

Fig. 10 *Dependence of Nu_m/Nu_o and $C_\varphi/C_{\varphi o}$ on the periodical length L, β = 45°, Re_{Dh}=3 10^5, Pr= 0.7*

through flow acceleration. Although $C_\varphi/C_{\varphi o}$ is rather high at β = 45°, the difference between $C_\varphi/C_{\varphi o}$ and $(P_D/P_{Do})_{crit}$ is also larger than at smaller β. That means, the higher the demand for heat transfer enhancement, the more favourable is the use of vortex generator. The same conclusion can be made from Fig. 10, where the dependence of Nu_m/Nu_o and $C_\varphi/C_{\varphi o}$ on the periodical length L is displayed. Both Nu_m/Nu_o and $C_\varphi/C_{\varphi o}$ increase with the decrease of L. The largest difference between $C_\varphi/C_{\varphi o}$ and $(P_D/P_{Do})_{crit}$ corresponds to the highest heat transfer enhancement.

CONCLUDING REMARKS

Vortex generator in periodically developed region interacts with incoming flows containing longitudinal vortices. In this region, owing to repeated interaction of main flow with vortex generators in streamwise direction, the disturbance of the flow is much stronger, the elevation in turbulent kinetic energy level is much hiher than in thermally developing region. One consequence of these is the large increase of flow loss. To examine the efficiency of vortex generator for heat transfer enhancement with regard to flow loss, another method for heat transfer enhancement, flow acceleration, has been compared with it. For a same heat transfer enhancement in an investigated case (Nu_m/Nu_o= 3.41), the flow loss increase caused by raising Reynolds number is more than double of that caused by the vortex generator. Results show further, the higher the demand for heat transfer enhancement, the more favourable is the use of vortex generator opposed to flow acceleration.

ACKNOWLEDGEMENT

The first author gratefully acknowledge the scholarship provided by the Deutsche Forschungsanstalt fur Luft- und Raumfahrt.

REFERENCES

BHATTI, M.S. & SHAH, R.K., 1987, Turbulent and transition flow convective heat transfer in ducts, Handbook of Single-Phase Convective Heat Transfer, ed. S. akac et al., John Wiley & Sons, New York

EDWARDS, F. J. & ALKER, C. J. R. 1974, The improvement of forced convection surface heat transfer using surface protrusions in the form of (A) cubes and (B) vortex generators, Proc. 5th Intl. Heat Transfer Conf., Tokyo, Vol. 2, 244-248

FIEBIG, M., KALLWEIT, P. & MITRA, N. K., 1986, Wing type vortex generators for heat transfer enhancement. Proc. 8th Intl. Heat Transfer Conf., San Francisco, Hemisphere, Vol 6. 2909-2914.

FIEBIG, M., ZHU, J. X, & MITRA, N. K., 1991, Embedded longitudinal vortex arrays, velocity and temperature fields, loss and heat transfer augmentation, 8th Symposium on Turbulent Shear Flows, Munich

GERSTEN, K., 1983, Fluid Mechanics and Heat Transfer; Introduction and Fundamentals, Heat Exchangers Design Handbook, Hemisphere, Vol. 2, chapter 2.2.1-4

HIRT, C. W., NICHOLS, B. D. & ROMERO, N C., 1975, SOLA - A numerical algorithm for transient fluid flows, Los Alamos Scientfic Laboratory Report LA-5652, Los Alamos, New Mexico

LAUNDER, B. E. & SPALDING, D. B., 1974, The numerical computation of turbulent flows, Computer methods in Applied Mechanics and Engineering, 3, 269-289.

PATANKAR, S. V., LIU, C. H & SPARROW, E. M. 1977, Fully developed flow and heat transfer in ducts having streamwise-periodic variations of cross-sectional area, J. Heat Transfer, Vol. 99, 180-186.

PAULEY, W. R., & EATON, J. K , 1988, Experimental study of the development of longitudinal vortex pairs embedded in a turbulent boundary layer, AIAA J., Vol. 26, No. 7, 816-823

ZHU, J. X., FIEBIG, M., & MITRA, N. K., 1990, Numerical Simulation of a 3-D turbulent flow field with longitudinal vortices, ASME FED-Vol. 103, 131-136.

EIGHTH SYMPOSIUM ON
TURBULENT SHEAR FLOWS
Technical University of Munich
September 9-11, 1991

EMBEDDED LONGITUDINAL VORTEX ARRAYS, VELOCITY AND TEMPERATURE FIELDS, LOSS AND HEAT TRANSFER AUGMENTATION

M. Fiebig, J.X Zhu, N.K. Mitra
Institut für Thermo- und Fluiddynamik
Ruhr-Universitat Bochum
W-4630 Bochum 1, Germany

ABSTRACT

Turbulent Flows in the entrance of a parallel wall channel with mounted longitudinal vortex generator in form of delta wing, rectangular wing, delta winglet pair and rectangular winglet pair are simulated by the numerical solution of the Reynolds averaged Navier-Stokes, energy and standard k-ϵ model equations. Results show that the heat transfer augmentation of 16% to 19% occurs in an area of channel wall which is 30 times larger than the vortex generator area. The ratio of heat transfer enhancement and flow loss increase indicates better performance for the rectangular winglet pair.

INTRODUCTION

In gas-liquid and gas-gas heat exchangers the thermal resistance on the gas side is dominant and extended surfaces in the form of fin plates are frequently used to reduce it, Fig. 1. Compared to the thermal resistance on the liquid side the gas side thermal resistance even with fins is still higher. To reduce it further longitudinal vortex generators can be placed at the fins e.g. Fiebig et al. (1986), and Sanchez et al (1990). The vortex generators, mostly slender wings or winglets at high angle of attack (see Fig. 2), generate strong longitudinal vortices which rotate the flow, substitute fluid from the wall region by fluid of higher momentum from the core (Fig. 3) and thus increase heat transfer and flow losses. Longitudinal vortices have a strong influence on momentum and heat transfer far downstream of their origin even in turbulent flow e.g. Pauly and Eaton (1988). The ordered vortex motion should result in higher heat transfer at lower flow loss increase than a purely higher turbulence level.

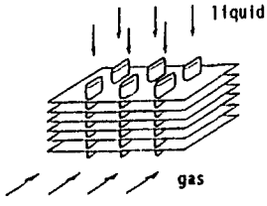

Fig. 1 *Schematic of a compact gas-liquid heat exchanger with extended surfaces (finned tube)*

The purpose of the present work is to investigate numerically effects of different forms of vortex generators such as delta wing, delta winglet pair, rectangular wing and winglet pair (Fig 2) on the heat transfer and flow losses in turbulent channel flows.

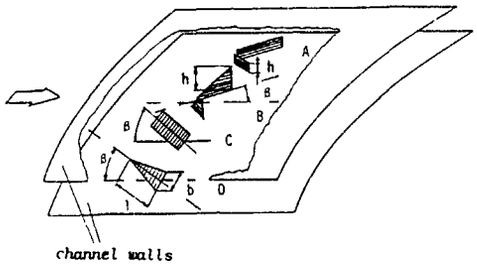

Fig. 2 *Some types of longitudinal vortex generators. A) Rectangular Winglet Pair (RWP), B) Delta Winglet Pair (DWP), C) Rectangular Wing (RW); D) Delta Wing (DW)*

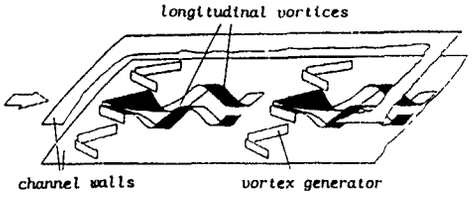

Fig. 3 *Schematic of flow seperation at the edges of the vortex generators and formation of longitudinal vortices in a channel flow*

COMPUTATIONAL DOMAIN

Fig. 4 shows the computational domain consisting of a parallel wall channal and a pair of delta winglets (DWP) which can be replaced by other forms such as rectangular winglet pair (RWP), delta wing (DW) and rectangular wing (RW), see Fig. 2. Table 1 gives the geometrical parameters of the vortex generators with respect to the channel height H. The surface areas of the vortex generators and their angle of attack (β = 25°) are kept equal for all cases.

Tabel 1 *Geometrical parameters of the vortex generators (Figs 2 and 4)*

	DWP	RWP	DW	RW
l	2 H	2 H	2 H	2 H
b			2 H	1 H
h	1 H	0.5 H		
s	0.5 H	0 5 H		

The geometrical parameters of the computational domain (Fig.4) have the following values relative to the channel height H:

$$L = 10\ H, \qquad B = 6\ H, \qquad a = 0.5\ H$$

The flows are assumed to be symmetric about the centre plan (II), so that the computations are performed only in the region between the planes I and II in z-direction.

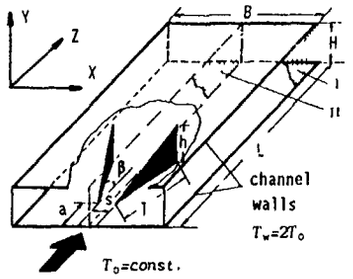

Fig. 4 *Computational domain A parallel wall channel with a delta winglet pair mounted on the channel bottom wall, In a fin-plate heat exchanger the element may be repeated in spanwise and vertical directions*

BASIC EQUATIONS AND NUMERICAL PROCEDURE

The flow in the channel is described by 3-D Reynolds averaged Navier-Stokes and energy equations for incompressible medium in conjunction with the eddy viscosity concept. Details about the governing equations and numerical procedure are given in Zhu et al. (1991).

BOUNDARY CONDITIONS

At the channel entrance the flow has a uniform temperature T_o, the velocity, k and ϵ profiles are obtained from a calculation of 2-D fully developed turbulent channel flow. Symmetry conditions are used on the side planes I and II. At the exit the streamwise gradients of all variables are set to zero.

Wall functions given by Launder and Spalding (1974) are employed to prescribe the boundary conditions along the channel walls. Details have been presented in Zhu et al. (1991). The wall temperature T_w is constant in the present work, $T_w = 2T_o$.

RESULTS AND DISCUSSION

Computations have been performed on a SUN 4/260 workstation. 91 x 15 x 48 grids and 60 CPU hours have been used e.g for the configuration in Fig. 4. A grid-independence study has not been performed in this work, but a grid-independence study for laminar flow computations in a rectangular channel with a tube with a basically same program shows that the average Nusselt number on the channel wall computed with present grids deviates by at most 10% from the grid-independent value, e g Sanchez et al (1990). The Reynolds number Re_H based on the channel height for all calculations is taken to be 50000 and the Prandtl number Pr is 0.7. For the sake of comparison, a hydrodynamically develped thermally developing turbulent channel flow (without vortex generator) is calculated with the same flow and boundary conditions as described above. Henceforth this flow is referred to as the base flow

Fig. 5 shows typical computational results of cross stream velocity vectors at x/H = 1 3, 2 3, 4.3 and 9.3 in the channel with a pair of delta winglets. The generation and transport of the longitudinal vortices, eventual flattening of the vortex cores and their lateral movement towards the side boundaries are evident in this figure.

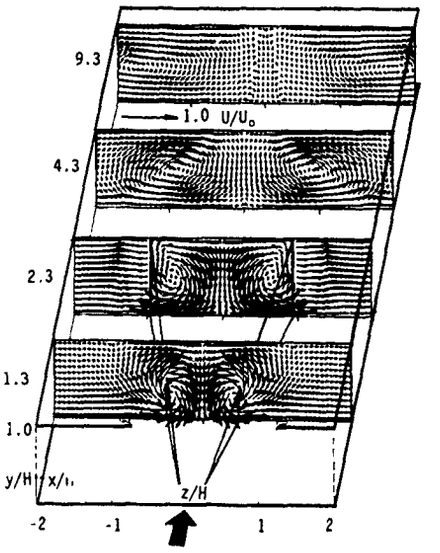

Fig. 5 *Cross sectional velocity vectors at axial locations x/H = 1.3, 2.3, 4.3 and 9.3, showing the formation and development of longitudinal vortices in a channel with a delta winglet pair*

Fig. 6 shows the temperature field for the same case as in Fig. 5. Isotherms in the base flow will be straight lines parallel to the top and bottom walls. In the flow with vortices, however, isotherms with large values appear around the vortex generator due to the high heat transfer there. At x/H = 1.3, the vortex cores are displayed by the variation of the isotherms 2 to 10. The empty white area corresponds to the isotherm 1 ($T/T_o = 1$), i.e. the flow has not yet been heated up. In successive cross sections (x/H = 2.3, 4.3 and 9.3) the mixing of hot and cold fluids due to azimuthal velocities of the vortices become evident and higher isotherms (lines 4 and 5) appear in the middle of the channel The dotted lines (isotherm 2) near the top and bottom walls at sections x/H = 4.3 and 9.3 show the extent of heating

in the base flow. The thermal boundary layer in the channel is strongly disturbed by the longitudinal vortices.

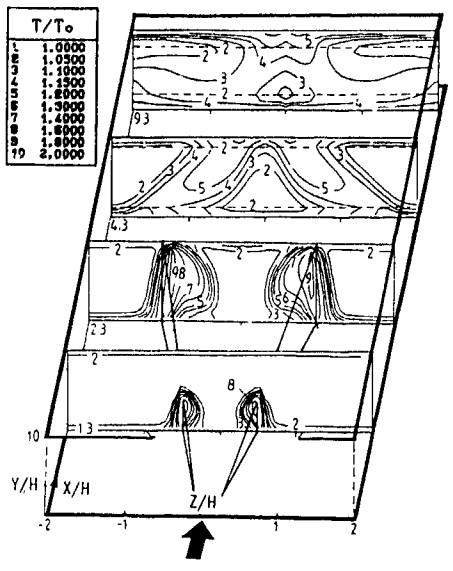

Fig. 6 *Structure of the temperature field in a turbulent channel flow with a pair of delta winglet. Isotherms for a temperature ratio of* $T_W/T_o = 2$ *at cross sections* $x/H = 1.3$, 2.3, 4.3 *and* 9.3, $Re_H = 50000$, $Pr = 0.7$

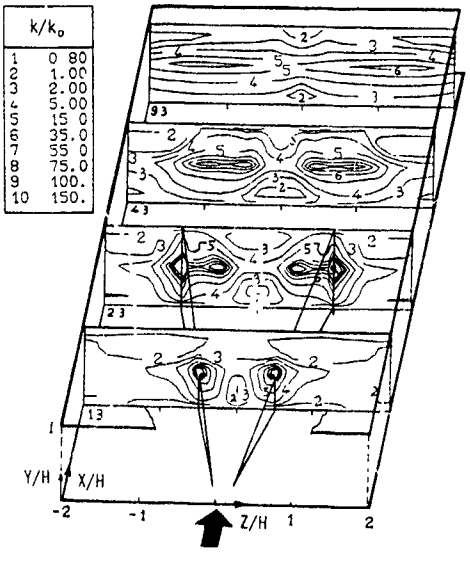

Fig. 7 *Elevation of turbulent kinetic energy in the channel with a built-in delta winglet pair (Fig. 4),* $Re_H = 50000$

Fig. 7 shows the contour of the turbulent kinetic energy ratio k/k_o for the above case, where k_o is the k-value in the base flow. Higher turbulent kinetic energy is produced around the vortex generators by the interaction between the main flow and the vortex generators. In the core region of the vortices at cross section $x/H = 2.3$ the turbulence energy is 100 times of that in base flow (line 9). At $x/H = 9.3$, k diffuses throughout the cross section in such a way that except in the upwash and downwash regions near the top and bottom walls (isoline 2) it is everywhere larger than that in the base flow. Large k signifies large turbulent thermal diffusivity and hence large heat transfer.

The flow and temperature fields with rectangular wing, delta wing and rectangular winglet pair will not be displayed further in the following a comparison of the global characters of the flows with different vortex generators are presented.

Figure 8 compares the average vorticity component $\bar{\omega}_x$ in the channel with **DWP**, **DW**, **RW** and **RWP**. Here $\bar{\omega}_x$ is defined by:

$$\bar{\omega}_x = \frac{1}{A_f/2} \int_0^{A_f/2} |\omega_x| \, dA \Big|_x \quad \text{with} \quad \omega_x = \frac{\partial W}{\partial y} - \frac{\partial V}{\partial z} \quad (1)$$

All configurations show peaks in $\bar{\omega}_x$ distribution slightly before the trailing edge of the wing. The peak values for wings are 40% to 50% larger than for the corresponding winglets. However the decay in $\bar{\omega}_x$ for winglets is much slower than for wings. At the exit ($x/H = 10$), $\bar{\omega}_x$ for **RWP** is 70% larger than for **RW**. Since $\bar{\omega}_x$ can be used as a measure of the circulation, Fig. 8 also shows that the circulation in the channel with winglets has become nearly constant at $x/H = 4$ whereas with wings the circulation has not reached its constant value even at the exit.

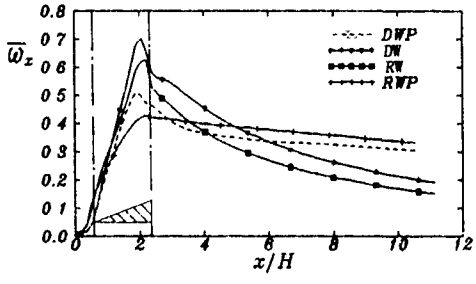

Fig. 8 *Cross sectional averaged vorticity along the streamwise direction for the four vortex generators, showing strength and decay of longitudinal vortices*

Fig. 9 compares the ratios of the spanwise averaged Nusselt numbers with (Nu_x) and without vortices (Nu_{ox}) in the channel for different vortex generator configurations. On the lower wall where the vortex generators are fixed, the Nu_x/Nu_{ox} distributions for the wings show sharp change with peak and minimum near the base of the wing. These are caused by the flow acceleration on the pressure side due to the blockage and the flow separation on the suction side of the wing. Winglets, whose span unlike those of wings are not normal to the main flow, do not generate sharp rise and fall in Nu_x. The Nu_x-enhancement due to

vortices appears downstream of the vortex generators. For delta winglet, the flow does not separate at the suction side and further downstream, the vortices take care of Nu_x-enhancement. Hence is the smooth increase in Nu_x.

On the upper wall the rectangular wings cause the highest enhancement in Nu_x. This is because the vortices generated by the rectangular winglets move closer to the upper wall

The flow losses are evaluated by using the kinetic energy equation in Gersten (1983), which is simplified for the present problem as follows:

$$\Phi_{12} = \frac{1}{2} (\alpha_1 - \alpha_2) U_o^2 + \frac{p_1 - p_2}{\rho} \qquad (2)$$

where

$$\Phi_{12} = \frac{P_D}{M} \qquad (3)$$

is the specific dissipation. The variables α and P_D in Eqs. (2) and (3) are kinetic energy correction factor and disspation respectively, which are described in detail by Gersten (1983). The dissipation P_D indicates the loss of mechanical energy due to friction and turbulent mixing. For the convenience of analysis, a dimensionless number, called dissipation number (Brockmeier, 1987), is derived from Eq. (2):

$$C_\varphi = \frac{\Phi_{12}}{U_o^2} \frac{H}{\Delta x} = \frac{1}{2} (\alpha_1 - \alpha_2) \frac{H}{\Delta x} + f_{app} \qquad (4)$$

with the apparent friction factor f_{app} (Shah and London, 1978)

$$f_{app} = \frac{1}{2} C_p \frac{H}{\Delta x} \qquad (5)$$

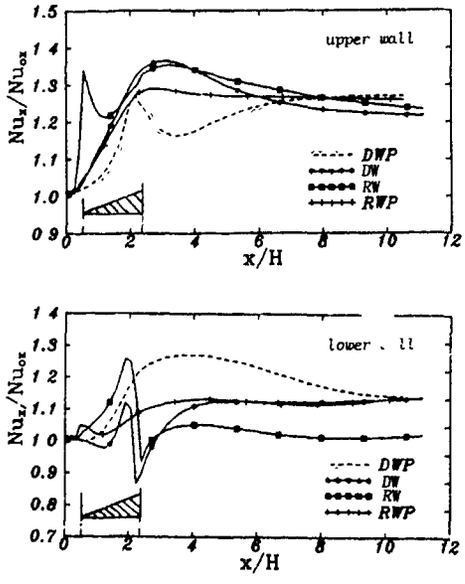

Fig. 9 *Ratios of the spanwise averaged Nusselt numbers on the upper and lower wall for flows with and without vortex generator, comparing the streamwise effects of the four vortex generators on heat transfer, A_L/A_w = 30, β = 25°, Re_H= 50000, Pr = 0.7*

In Eq. (4) the index 1 means inlet, index 2 means an arbitary axial location at the downstream and Δx indicates the distance between the locations 1 and 2

Fig. 10 shows relative increase of the dissipation numbers of the four investigated cases to the base flow $(C_{\varphi x}-C_{\varphi o})/C_{\varphi o}$. $C_{\varphi o}$ is the C_φ-value of the base flow. The peak values of $(C_{\varphi x}-C_{\varphi o})/C_{\varphi o}$ appear at the leading edge for the rectangular wing and rectangular winglet pair whereas for the delta geometries the peaks appear near the trailing edge. From x/H = 8 downwards, the curve for all four vortex generator geometry merge together.

Table 2 compares the global increase of Nusselt numbers and flow losses for the four types of vortex generator relative to the base flow. The ratio of the channel wall to vortex generator areas A_L/A_w is 30 for all cases The subscript m stands for the average value.

Table 2 *Comparison of global effects of the four vortex generators on heat transfer and flow losses in turbulent channel flow, T_w= 2T_o, A_L/A_w = 30, β = 25°, R_H = 50000, Pr = 0.7*

	Nu_m/Nu_{om} upper wall	Nu_m/Nu_{om} lower wall	Nu_m/Nu_{om} average for both walls	$C_{\varphi m}/C_{\varphi o}$
DWP	1.20	1.18	1.19	4.2
RWP	1.14	1.10	1.17	4.0
DW	1.25	1.08	1.165	5.1
RW	1.28	1.04	1.16	4.9

Nu_{om} = 230 , $C_{\varphi om} = 4.6\ 10^{-3}$

The enhancement of Nusselt number averaged over both walls differs by only 2% for different types of vortex generators. The increase in flow losses for the four geometries can differ by more than 20 For a nearly equal heat transfer enhancement the rectangular winglet pair brings the least flow loss increase among the four vortex generators.

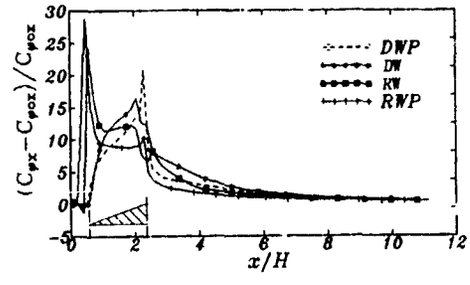

Fig. 10 *Relative increase of the dissipation number C_φ, showing the additional flow losses caused by the vortex generators along streamwise direction, Re_H= 50000*

CONCLUSIONS

Heat transfer augmentation in turbulent flows in a channel with longitudinal vortex generators is caused by the elevation in the turbulent kinetic energy level near the wall and exchange o the fluid between the near wall and core region of the channel.

The mean heat transfer enhancement at an angle of attack of 25° and Re_H = 50000 amounts to 16% to 19% on a channel wall area which is 30 times larger than the face area of the vortex generator, the corresponding increase in flow losses is however 4 to 5 times larger than that in a turbulent channel flow without vortex generator. The ratios of heat transfer enhancement to flow loss increase suggest better performance for the rectangular winglet pair than for other forms of vortex generators.

ACKNOWLEDGEMENT

The scholarship provided by the Deutsche Forschungsanstalt fur Luft- und Raumfahrt for J X. Zhu is greatly appreciated.

REFERENCES

BROCKMEIER, U., 1987, Numerisches Verfahren zur Berechnung Dreidimensionaler Stromungs- und Temperaturfelder in Kanalen mit Langswirbelerzeugern und Untersuchung von Warmeubergang und Strömungsverlust, Dissertation, Ruhr-Universitat Bochum

FIEßIG, M., KALLWEIT, P. & MITRA, N. K., 1986, Wing type vortex generators for heat transfer enhancement, Proc. 8th Intl. Heat Transfer Conf. 6 San Francisco, Hemisphere 2909-2914.

GERSTEN, K., 1983, Fluid Mechanics and Heat Transfer; Introduction and Fundamentals, Heat Exchangers Design Handbook, Hemisphere, Vol. 2, chapter 2.2.1-4

LAUNDER, B. E. & SPALDING, D. B., 1974, The Numerical Computation of Turbulent Flows, Computer Methods in Applied Mechanics and Engineering, Vol. 3, 269-289.

PAULEY, W. R., & EATON, J. K., 1988, Experimental Study of the Development of Longitudinal Vortex pairs Embedded in a Turbulent Boundary Layer, AIAA J., Vol. 26, No. 7, 816-823

SANCHEZ, M., MITRA, N. K., & FIEBIG, M., 1990, Conjugate Heat Transfer in a Three Dimensional Channel with a Built-in Cylinder and Vortex Generators, Proc. 9th Intl. Heat Transfer Conf 4, Jerusalem, Hemisphere, 57-63

SHAH, R.K. & LONDON, A.L., 1978, Laminar Flow in Forced Convection in Ducts, Advances in Heat Transfer, Academic Press New York, San Francisco, London

ZHU, J. X., MITRA, N. K., & FIEBIG, M., 1991, Numerical simulation of periodically fully developed turbulent flow and heat transfer in channel with longitudinal vortex generators, 8th Symposium on Turbulent Shear Flows, Munich

EIGHTH SYMPOSIUM ON
TURBULENT SHEAR FLOWS
Technical University of Munich
September 9-11, 1991

AN EXPERIMENTAL STUDY ON THE SEPARATION OF A TURBULENT BOUNDARY LAYER FROM A SHARP EDGE

Shintaro YAMASHITA*), Ikuo NAKAMURA**),
Takehiro KUSHIDA**) and Hiroya YAMADA***)

*) Dept. Mech Eng., Gifu University, Yanagido, Gifu, Japan
**) Dept Mech. Eng , Nagoya University, Furocho, Chikusaku, Nagoya, Japan
***) Dept. Mech. Eng., Daido Inst. Tech., Daidocho, Minamiku, Nagoya, Japan

ABSTRACT

Results of the measurement of flow properties in the shear layer occurring when a fully developed two-dimensional turbulent boundary layer separates from a sharp edge of a groove are presented, especially focussing on the region near the edge. The effect of the edge on the boundary layer extends slightly upstream of the edge. The mean and fluctuating velocities and Reynolds stress change significantly in the longitudinal direction The turbulent energy production and dissipation are in a state of extreme disequilibrium in the inner mixing layer just behind the edge. The turbulent energy spectrum in the mixing layer has a fold or a peak, suggesting the existence of a coherent structure

NOMENCLATURE

b, h : width and depth of the groove, respectively
k : wave number
$\overline{q}^2/2$: turbulent energy = $(\overline{u}^2 + \overline{v}^2 + \overline{w}^2)/2$
U : mean velocity in the x-direction
U_∞ : main flow velocity out of the boundary layer
U_∞^* : reference main flow velocity at x = −250 mm
u, v, w: fluctuating velocity component in the x-, y- and z-directions, respectively
u', v', w': rms values for u, v and w, respectively
x, y, z: coordinate system (Fig. 1, z: spanwise direction)
δ : boundary layer thickness
Φ_{11}, Φ_{22}: one-dimensional energy spectra of u and v normalized by $\overline{u}^2$ and $\overline{v}^2$, respectively

INTRODUCTION

Although the separation of a turbulent boundary layer is practically important and many investigations have been made on this phenomenon so far, our understanding of the turbulent-flow separation is less developed than our understanding of the laminar separation. The flow separation can be roughly divided into two categories: that which occurs on a smooth surface where the separation line is not predetermined, and that which separates from a sharp edge, i.e., the separation at a fixed line.

The present study deals with the latter case, that is, the separation of a turbulent boundary layer from a sharp edge. The flow field in this study is that which develops when a two-dimensional turbulent boundary-layer flow passes over a groove with large dimensions in comparison with the boundary layer thickness, as shown in Fig. 1. Near the separation point the flow properties change abruptly, and after the edge there develops a new mixing layer called a inner mixing layer. This report mainly concerns itself with this abrupt change and the inner mixing layer, in which there is no significant effect of pressure gradient and streamline curvature. The flow field is the same as for a backward-facing-step flow with no influence due to sudden expansion of the flow passage, except in the reattachment region.

The present flow is, on the whole, a so-called cavity flow with recirculation. It relates to practical engineering problems and there is much research and review (e.g., Chang 1970, Rockwell & Naudascher 1978, Eaton & Johnston 1980), including the pioneering work by Tani et al. (1961) on the flows of a groove or a backward-facing step In these studies, investigations have focussed mainly on the vortical motion within the groove, the release frequency of the vortices, the three dimensionality and instability of the cavity flow, and, for the step flow, the flow properties near the reattachment point and the redevelopment of the flow after the attachment.

The flow phenomena associated with sudden disappearance of the wall-restriction at the sharp edge are also observed at the exit of a nozzle or the trailing edge of a flat plate The reports of

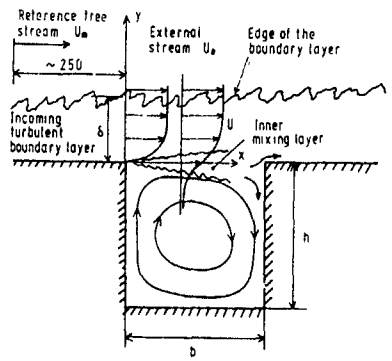

Fig. 1.Flow field

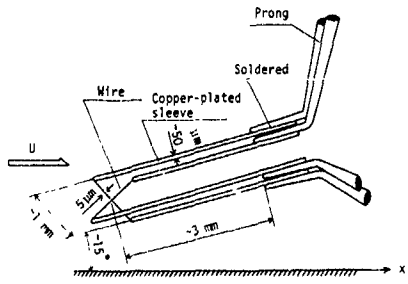

Fig. 2. Miniature X-probe

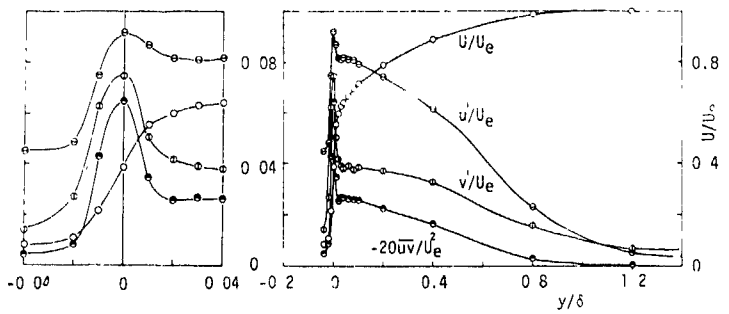

Fig. 3 Distribution of the mean velocity, rms values of the fluctuating velocities and Reynolds stress measured just behind the edge. x = 3 mm

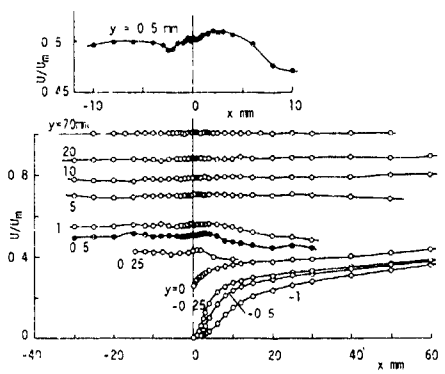

Fig. 4. Variation of the mean velocity in the x-direction

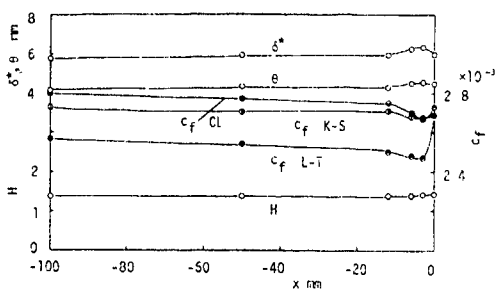

Fig 5 Distribution of the boundary layer parameters in the x-direction upstream of the edge
CL, Method of Clauser chart;
K-S, Method of Karman & Shoenherr,
L-T, Method of Ludwieg & Tillmann

downstream developments of the flows after the edges differ considerably among researchers. Some attribute these differences mainly to the upstream conditions (e.g., Bradshaw 1966, Goldschmidt 1977). However, much attention has been paid so far to the self-preserving region far downstream, and no detailed experiment has been made near the sharp edge.

The present experiment is motivated partly by these circumstances, and deals with the flow geometry shown in Fig. 1, for which it is easy to realize the slight change in upstream conditions. The measurement is carried out for the sudden change and subsequent development in the mean and fluctuating flow properties.

EXPERIMENTAL APPARATUS AND PROCEDURE

The experiment has been made using a wind tunnel with working section of about 500 mm height, 1000 mm width and 3 m length. A trip wire 1 mm in diameter is placed on a flat plate 10 mm downstream from the leading edge. The groove of b = h = 250 mm as shown in Fig. 1 is set about 2.5 m downstream from the leading edge. The origin of the coordinate is at the front edge of the groove. The free stream velocity is kept constant and the Reynolds number $Re = U_e b/\nu$ is 5×10^5.

Mean and fluctuating velocities and Reynolds stress have been measured mainly by means of I- and X-type hot-wire probes, which are specially designed miniature ones to measure in the vicinity of the wall; typical X-type probe is presented in Fig. 2. The boundary layer thickness δ at the edge was about 50 mm with no groove.

RESULTS AND DISCUSSION

The ratio of the width to the depth of the groove b/h is an important parameter governing the structure of the recirculating flow within the groove according to the previous experiments (Maull & East 1963, Kistler & Tan 1967). Depending on this parameter, the recirculating flow varies as two-dimensional flow, three-dimensional cellular structure, and unsteady flow. These structures are reflected on the spanwise distribution of the static-pressure on the groove wall. The square groove (b = h) is considered to realize a two dimensional cavity flow (Maull & East 1963, Kistler & Tan 1967), and in this experiment also the two dimensionality has been confirmed from the measurement of the static pressure on the front-side wall in the groove

Figure 3 shows the dimensionless profiles of the mean velocity, rms values of the fluctuating velocities and Reynolds stress measured at x = 3 mm just behind the edge. The fluctuating velocities and Reynolds stress have peak values at y = 0; in particular v' and $-\overline{uv}$ become relatively larger as shown in the left figure with the enlarged abscissa.

The variation of the mean velocity in the x-direction associated with the edge-separation is presented in Fig. 4. The minimum traversing pitch of probes in the x-direction is 0.25 mm near the edge. The velocity at y = 70 mm, outside of the shear layer, is constant. Hence, in spite of sudden expansion of the flow passage, there is no appreciable effect of the pressure gradient, and a free streamline comes out from the edge. The velocities

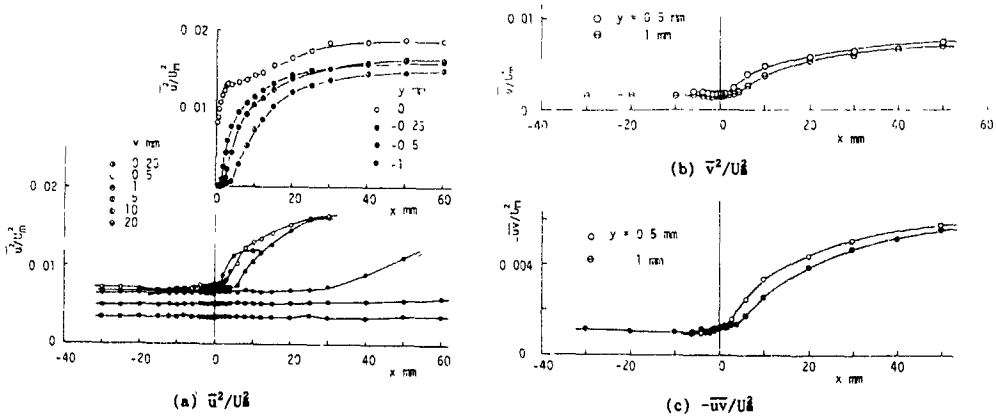

Fig 6 Variation of the fluctuating quantities in the x-direction

are nearly constant along the x-direction down to y = 10 mm, but vary slightly at smaller y. The upper figure is an enlarged profile at y = 0.5 mm, and it can be seen that the profile begins to change somewhat upstream of the edge and the flow is slightly accelerated near the edge. The lower figure reveals that, in the region $y < 0$ in the inner mixing layer, $\partial U/\partial y$ is positive and large just behind the edge. In Fig. 5, the local shear-stress coefficients estimated by three different methods, the displacement and momentum thicknesses, δ^* and θ, and shape factor H in the incoming turbulent boundary layer are presented. These quantities show certain changes just ahead of the edge, and the upstream influence of the edge is evident.

The changes in the turbulent energy $\overline{u}^2$, $\overline{v}^2$ and the Reynolds stress $-\overline{uv}$ are shown in Figs. 6(a)-(c). They are nearly constant in the x-direction on the wall, and those near the wall increase rapidly just behind the edge. The upstream influence of the edge for the turbulence properties seems not so appreciable as for the mean flow. Figure 7 shows the variation of these quantities normalized by each value at x = 0 in the x-direction. The growth rates for $\overline{v}^2$ and $-\overline{uv}$ relative to their values at x = 0 are much larger just behind the edge than $\overline{u}^2$. The change in the turbulent energy production may explain this, but it is more likely the result of the disappearance of the wall restriction. In turbulent shear flow along the wall, $\overline{u}^2$, $\overline{v}^2$, $\overline{w}^2$ and $-\overline{uv}$ vanish as y^2, y^4, y^2 and y^3, respectively, as the wall is approached (e.g., Monin & Yaglom 1965); thus, the decays of $\overline{v}^2$ and $-\overline{uv}$ are faster than $\overline{u}^2$ and $\overline{w}^2$ as the wall is approached. Therefore, when the wall restriction is removed, the growth rates for $\overline{v}^2$ and $-\overline{uv}$ relative to the values in the wall flow should be greater than those for $\overline{u}^2$ and $\overline{w}^2$

From the viewpoint of the response of the turbulent boundary layer to the disturbance, this flow is that in which the state of equilibrium is suddenly disturbed at the edge due to the step change in the boundary condition. This feature is examined using the basic equation for the mean flow and the turbulent energy equation.

The mean flow equation in the x-direction is

$$U\frac{\partial U}{\partial x}+V\frac{\partial U}{\partial y}+\frac{1}{\rho}\frac{dP_e}{dx}+\left(\frac{\partial \overline{u^2}}{\partial x}-\frac{\partial \overline{v^2}}{\partial x}\right)+\frac{\partial \overline{-uv}}{\partial y}-\nu\frac{\partial^2 U}{\partial y^2}=0 \quad \cdots\cdots(1)$$

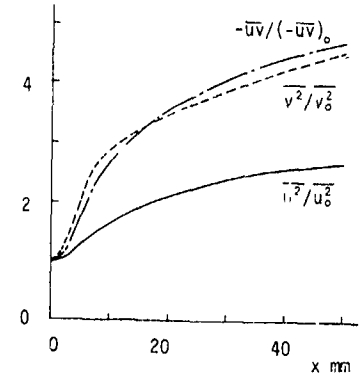

Fig. 7. Variation of the fluctuating quantities normalized by each value at x = 0

Figure 8 shows the variation of the representative terms, $U\partial U/\partial x$, $\partial \overline{u}^2/\partial x$ and $\partial \overline{v}^2/\partial x$, in the above equation near the edge. The change in the mean flow begins slightly upstream of the edge, and is very large near and after the edge On the other hand, the large change in the terms of normal stresses is confined just behind the edge and no effective change upstream of the edge can be seen. Although these terms are relatively smaller than the advection term, they cannot be neglected as in the thin shear layers.

The total turbulent-energy equation, the energy equations for the fluctuating components and the Reynolds stress equation in case of steady two-dimensional flow (e.g , Rotta 1972) are

$$\frac{D}{Dt}\left(\frac{\overline{q^2}}{2}\right)+\overline{uv}\frac{\partial U}{\partial y}+\left\langle \overline{uv}\frac{\partial V}{\partial x}\right\rangle+\left\langle(\overline{u^2}-\overline{v^2})\frac{\partial U}{\partial x}\right\rangle+\varepsilon+D_t=0 \quad \cdots\cdots(2a)$$

$$\frac{D}{Dt}\left(\frac{\overline{u^2}}{2}\right)+\overline{uv}\frac{\partial U}{\partial y}+\left\langle \overline{u^2}\frac{\partial U}{\partial x}\right\rangle-\frac{1}{\rho}\overline{p\frac{\partial u}{\partial x}}+\varepsilon_u+D_{tu}=0 \quad \cdots\cdots(2b)$$

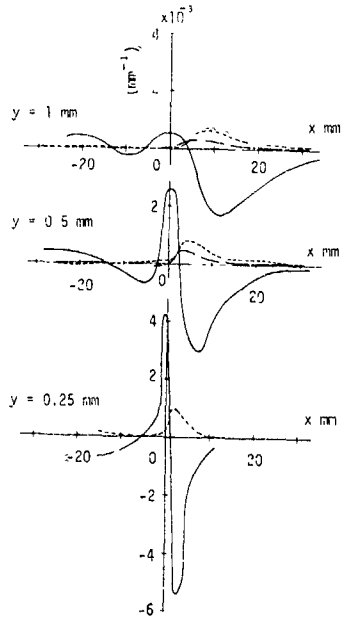

Fig. 8. Change in the representative terms in the mean flow equation
—, $(U/U_e)\partial(U/U_e)/\partial x$;
---, $\partial(\overline{u}^2/U_e^2)/\partial x$;
— · —, $\partial(\overline{v}^2/U_e^2)/\partial x$

$$\frac{D}{Dt}\left(\frac{\overline{v^2}}{2}\right)+\left\langle\overline{uv}\frac{\partial V}{\partial x}\right\rangle-\left\langle\overline{v^2}\frac{\partial U}{\partial x}\right\rangle$$
$$-\frac{1}{\rho}\overline{p\frac{\partial v}{\partial y}}+\varepsilon_v+D_{fv}=0 \quad \cdots\cdots\cdots\cdots \quad (2c)$$
$$\frac{D}{Dt}\left(\frac{\overline{w^2}}{2}\right)-\frac{1}{\rho}\overline{p\frac{\partial w}{\partial z}}+\varepsilon_w+D_{fw}=0 \quad \cdots\cdots \quad (2d)$$
$$\frac{D}{Dt}(-\overline{uv})-\overline{v^2}\frac{\partial U}{\partial y}-\left\langle\overline{u^2}\frac{\partial V}{\partial x}\right\rangle$$
$$+\frac{1}{\rho}\overline{p\left(\frac{\partial u}{\partial y}+\frac{\partial v}{\partial x}\right)}+2\varepsilon_{uv}+2D_{fuv}=0 \quad (2e)$$

respectively, where $D/Dt = U\partial/\partial x + V\partial/\partial y$, and ε, ε_i (i = u, v, w or uv) are the dissipation or destruction terms, and D_f, D_{fi} are the diffusion terms. The terms bracketed by symbols ⟨ ⟩ and « » could be neglected under the usual boundary layer approximation, and the latter is one order smaller than the former.

The variation of two terms in the turbulent energy equation for u-fluctuation [Eq. (2b)' is presented in Fig. 9, one of the advection term $(1/2)U\partial\overline{u}^2/\partial x$ and minus the turbulent energy production $\overline{u}^2\partial U/\partial x$ which can be usually neglected under the thin shear layer approximation. In the figure the usual production of turbulent energy is also given for reference, which is estimated from the wall shear stress and the logarithmic velocity distribution since the Reynolds stress cannot be measured in the vicinity of the wall. As shown in this figure, the production $\overline{u}^2\partial U/\partial x$ cannot be ignored near the edge. Then another production $\overline{v}^2\partial U/\partial x$ will not be small either. These production terms will be important in the turbulence field associated with the edge-separation. In particular,

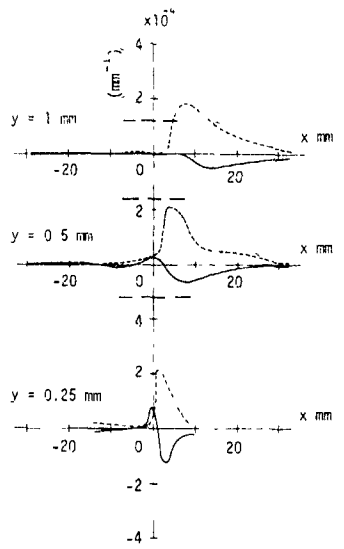

Fig. 9 Change in the representative terms in the turbulent energy equation in the x-direction.
---, $(U/U_e)\partial(\overline{u}^2/2U_e^2)/\partial x$;
—, $(\overline{u}^2/U_e^2)\partial(U/U_e)/\partial x$;
— · —, $[(-\overline{uv}/U_e^2)\{\partial(U/U_e)/\partial y\}]_{x=0}$

at the initial stage of the development of the inner mixing layer. $\overline{v}^2\partial U/\partial x$ makes a positive contribution to v-energy, while $-\overline{u}^2\partial U/\partial x$ makes a negative contribution to u-energy as seen from Eq. (2b, c), since $\partial U/\partial x$ is positive for $y \lesssim 0$ behind the edge (see Fig. 4).

Figure 10 shows the profiles of the main production $-\overline{uv}\partial U/\partial y$ and dissipation ε, the most essential terms in the turbulent energy budget [Eq. (2a)], at the x-station just behind the edge (x = 3 mm). The dissipation is estimated by using $k^{-5/3}$-spectrum for turbulent energy after Bradshaw (1967). Figure 10(a) is for $y > 0$ where the flow is boundary-layer like since the inner mixing layer is very thin and confined near $y = 0$ at this section. The profile of the production coincides very much with that in a flat-plate boundary-layer of Klebanoff (1954), and the dissipation estimated from the u- or v-spectrum also seems reasonable compared with Klebanoff's profile. Figure 10(b) shows the profiles of the production and dissipation around y = 0 with the abscissa contracted and the ordinate enlarged. The profiles for the flat-plate boundary-layer are given for comparison by chain lines. There is a thin inner-mixing layer around y = 0, and in this layer the production takes a maximum value which is considerably greater than the flat-plate value. The dissipation near $y = 0$ is smaller than in the turbulent boundary layer and its absolute value takes a maximum at $y/\delta = -0.01$ (y = -0.5 mm). It can be seen that the production and dissipation are far from a state of equilibrium at the initial section of the inner mixing layer. Hence, the turbulent energy produced is not dissipated here and must be transported downstream.

The normalized energy spectra of u and v, Φ_{11} and Φ_{22}, respectively, just behind the edge are presented in Fig. 11. The outer layer at this station (x = 3 mm) is a boundary-layer flow in effect, and the spectra in the outer layer are those of the boundary layer. However, the spectra in the inner mixing layer (y = 1, 0.5, 0, -1 mm) show a large

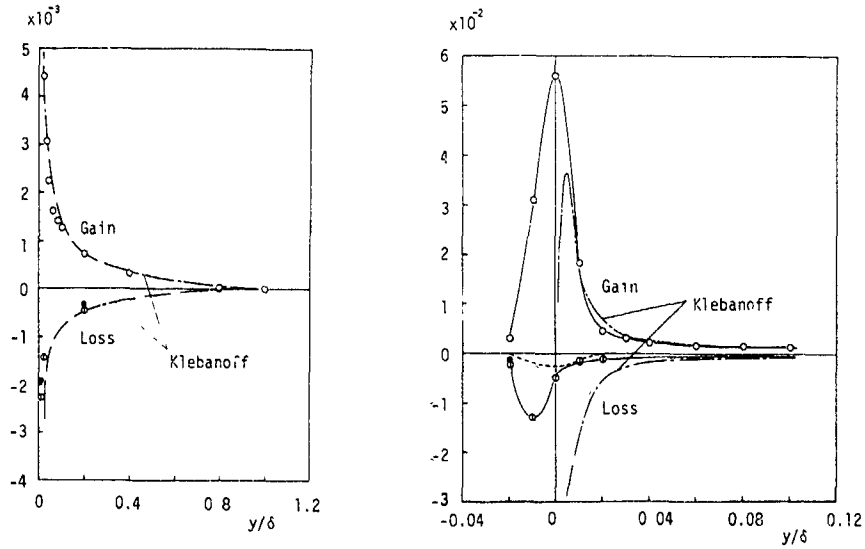

(a) Region of boundary-layer like of y > 0

(b) Inner mixing layer

Fig. 10. Production and dissipation of the turbulent energy: x = 3 mm.
o, Production,
●, Dissipation estimated from u-spectrum;
●, Dissipation estimated from v-spectrum

variation; the contribution to the turbulent energy from the high-wavenumber component increases as y decreases.

The changes in the energy spectra when the flow near the wall undergoing change from the wall-flow to the boundary-free flow over the edge are shown in Fig. 12. In Fig. 12(a) the u-spectra in the wall-flow region ($x \leq 0$) and at $x = 1$ mm are similar and contain ranges where $\Phi_{11} \propto k^{-1}$ is followed. The spectrum at x = 50 mm, the most downstream station in this experiment, is bent at $k \cong 120\ m^{-1}$. The profiles of v-spectra shown in Fig. 12(b) also do not change appreciably down to x = 1 mm as in the u-spectra, but have pronounced peaks at more downstream stations corresponding to the bend of the u-spectra. Eaton & Johnston (1980) have found the same spectral peak in the shear layer of the backward-facing step flow in which the incoming boundary layer is laminar and the momentum-thickness Reynolds number is 240, unlike the present flow in which the boundary layer is turbulent and the momentum-thickness Reynolds number is about 9000 The existence of this spectral peak or bend in this experiment illustrates that there

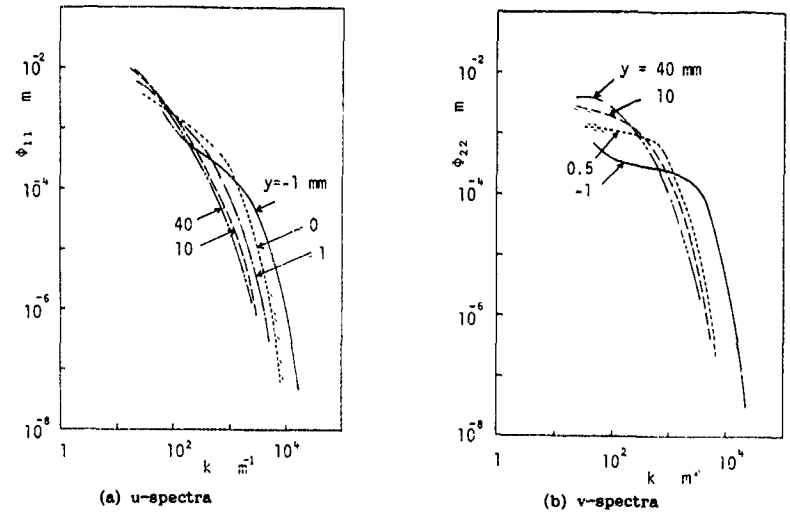

(a) u-spectra

(b) v-spectra

Fig. 11. Normalized turbulent energy spectra: x = 3 mm

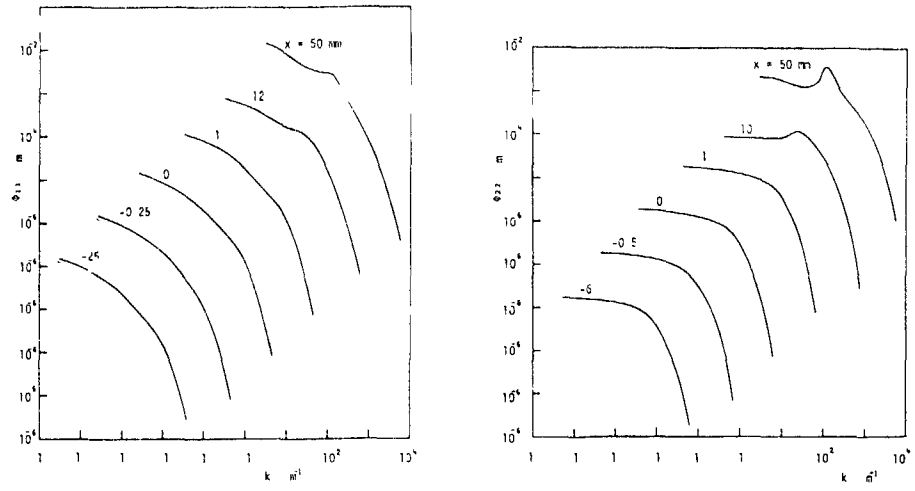

(a) u-spectra: y = 0.25 mm

(b) v-spectra: y = 0.5 mm

Fig. 12. Variation of the energy spectra in the x-direction

exists a coherent structure in an early stage of the development of the inner mixing layer even when the incoming flow is a turbulent boundary layer of a high Reynolds number.

CONCLUDING REMARKS

The present study on the abrupt change in the flow properties associated with the edge-separation of a turbulent boundary layer leads to the following conclusions.

The effect of a sharp edge on the turbulent boundary layer extends slightly upstream of the edge. This effect especially is manifest in the mean velocity, wall shear-stress and integral thicknesses.

The mean and fluctuating velocities and Reynolds stress change markedly in the x-direction near the edge. The change in the fluctuating velocities is specially important in the basic equation for the mean flow, and the terms such as $\partial\overline{u^2}/\partial x$ and $\partial\overline{v^2}/\partial x$, usually neglected in thin shear layers, cannot be ignored.

The fluctuating velocities and Reynolds stress increase suddenly at the initial stage of the development of the inner mixing layer; the removal of the turbulence-suppression effect by the wall and the additional production term $\overline{v^2}\partial U/\partial x$ contribute to these increases. In this region the main production and dissipation are remarkably unbalanced.

In the inner mixing layer just behind the edge, the contribution to the turbulent energy from the high-wavenumber component increases relatively. The turbulent energy spectrum in the inner mixing layer has a peak, and it is conjectured that there exists a coherent structure in an early stage of the development of this layer

REFERENCES

Bradshaw, P. 1966 *J. Fluid Mech.* 26, 225.

Bradshaw, P. 1967 *A.R.C. R. & M.* 3603.

Chang, P.K. 1970 *Separation of Flow*, Pergamon Press.

Eaton, J.k. & Johnston, J.P. 1980 *Thermo. Div., Dept. Mech. Eng., Stanford Univ.* Rep. MD-39.

Goldschmidt, V.W. 1977 *Structure and Mechanics of Turbulence* II, ed. Fiedler, H. *Lecture Notes in Physics* 76, 1.

Kistler, A.L. & Tan, F.C 1967 *Phys. Fluids* Suppl., 165.

Klebanoff, P.S. 1954 *NACA TR* 1247, 1135

Maull, D.J. & East, L.F. 1963 *J. Fluid Mech.* 16, 620.

Monin, A.S. & Yaglom, A.M. 1965, tr. 1971 *Statistical Fluid Mechanics*, 270, The MIT Press.

Rockwell, D. & Naudascher, E. 1978 *Trans. ASME J Fluids Eng.* 100, 152.

Rotta, J.C. 1972 *Turbulente Stromungen*, 132, B.G. Teubner.

Tani, I. et al. 1961 *Aero. Res. Inst., Univ. Tokyo* Rep. 364, 119.

EIGHTH SYMPOSIUM ON
TURBULENT SHEAR FLOWS
Technical University of Munich
September 9-11, 1991

MEASUREMENTS AND MODELLING OF THE TURBULENT NEAR WAKE FLOW OF A DISK WITH A CENTRAL JET

by

D.F.G. Durão, G. Knittel, J.C.F. Pereira and J.M.P. Rocha

Instituto Superior Técnico
Technical University of Lisbon
Mechanical Engineering Department
Av Rovisco Pais
1096 Lisboa Codex
Portugal

ABSTRACT

LDV measurements of the velocity and turbulence characteristics and their comparison with numerical solutions are reported for the near wake recirculating flow around a disk with a central jet. Both the two-equation k-ε eddy-viscosity model and the second-moment Reynolds stress transport closure (RSM) were used to close the mean-field equations. The 13-point Quadratic Weighted Upstream scheme was used for convection discretization and employed in all transport equations. It was found that the present flow configuration requires a very high computational resolution for numerical accuracy. Like other disk flow predictions, significant differences were noticed between the two levels of turbulence closure. The RSM provides a significantly better description of mean field compared with k-ε eddy viscosity model. None of the models is able to predict accurately the turbulence field.

INTRODUCTION

The velocity characteristics of the flow in the near wake of a disk play an important role in many engineering applications Measurements of the flow in the disk near wake were reported previously e.g. Carmody (1969), Durão and Whitelaw (1974), Durão and Firmino (1983), Taylor and Whitelaw (1984) and Heitor and Whitelaw (1987). The few numerical simulations of isothermal disk flows reported have shown that the numerical accuracy of flow computation is crucial in order to provide a meaningful assessement of turbulence models, see McGuirk *et al* (1985a). Concerning turbulence modelling, McGuirk *et al* (1985b) have applied two versions of a second-moment closures to the prediction of the confined disk flow with comparison with k-ε eddy viscosity model results. A noticeable feature is that second-moment closure did not show notorious superiority over k-ε model.

The present study is concerned with the flow configuration of the unconfined recirculating flow behind a disk with a central jet similarly to the bluff-body stabilized flame investigated by Scheffer *et al.* (1987). The selected momentum ratio between the annular flow around the disk and central jet originates a complex recirculating flow structure. The objective of this study is to obtain measurements of mean and fluctuating velocity characteristics and to investigate the performance of a second-moment turbulence closure, in this separated flow.

EXPERIMENTAL INVESTIGATION

Experiments were conducted in the recirculation region behind a disk with a central orifice. Air was discharged at a velocity of 30 m/s at the nozzle surrounding the disk and also through the central disk jet. Air was supplied independently to the inner pipe and discharged through the disk central orifice. The Reynolds numbers of the two incoming streams were respectively $Re_a = 1.2 \times 10^5$ and $Re_j = 10^4$ based on disk diameter and disk orifice diameter respectively.

Velocity measurements were obtained with one-component dual beam LDV in forward scattering mode. The optical system consisted of an 0.8 Argon-Ion laser using the green line and OEI transmitting optics The signal was processed by a counter (TSI 1980B) interfaced with a computer which provided the velocity moments. The air in both streams was seeded with nominal 1μm diameter TiO_2 particles. Mean axial and radial variances were calculated from 10 to 50 thousand samples. The maximum uncertainties in the mean and variances velocity at 95% confidence interval were 2% and 4% respectively. Detailed tests were carried out regarding flow axisymmetry, influence of seeding conditions, etc. and excellent long-term repeatability of the measurements was obtained. Details concerning the LDV system and data averaging procedure may be found in Durão *et al* (1990).

MATHEMATICAL MODEL

The continuity and momentum equations for a steady, two-dimensional, incompressible fluid flow at high Reynolds number are

$$\frac{\partial U_j}{\partial x_j} = 0 \,, \tag{1}$$

$$\frac{\partial U_j U_i}{\partial x_j} = -\frac{1}{\rho}\frac{\partial P}{\partial x_i} - \frac{\partial \langle u_i u_j \rangle}{\partial x_j} \,. \tag{2}$$

Upper and lower cases relate to mean and turbulence quantities, respectively; <> denotes temporal average of the variable; P represents pressure variable. To close the above equations either a second-moment model and the standard k-ε eddy viscosity (EVM) model were considered. The transport equations for the components of Reynolds stress tensor can be written as

$$\frac{\partial U_k \langle u_i u_j \rangle}{\partial x_k} = \mathcal{D}_{ij} + \mathcal{P}_{ij} + \Phi_{ij} - \varepsilon_{ij} \,, \tag{3}$$

where the terms in RHS of Eq. (3) represent diffusion, production, pressure redistribution and dissipation rate of $\langle u_i u_j \rangle$ Apart from $\mathcal{P}_{ij}$ terms all the remaining ones in RHS need to be modelled.

Diffusion term is represented by a generalised gradient diffusion model Daly and Harlow (1970):

$$\mathcal{D}_{ij} = \frac{\partial}{\partial x_k}\left[C_s \frac{k}{\varepsilon} \langle u_k u_l \rangle \frac{\partial \langle u_i u_j \rangle}{\partial x_l}\right] \,. \tag{4}$$

Pressure-redistribution term by Rotta (1951) and Naot *et al.* (1970) "slow" and "rapid" models·

$$\Phi_{ij} = \Phi_{ij,1} + \Phi_{ij,2} \tag{5}$$

$$\Phi_{ij,1} = -C_1 \frac{\varepsilon}{k}\left[\langle u_i u_j \rangle - \frac{\delta_{ij}}{3} \langle u_k u_k \rangle\right] \,, \tag{6}$$

$$\Phi_{ij2} = -C_2\left[P_{ij} - \frac{\delta_{ij}}{3}P_{kk}\right] \quad (7)$$

where the production term is given by

$$P_{ij} = -\langle u_i u_k\rangle \frac{\partial U_j}{\partial x_k} - \langle u_j u_k\rangle \frac{\partial U_i}{\partial x_k} . \quad (8)$$

For the basic model, the dissipation rate of $\langle u_i u_j\rangle$ is represented by an isotropic tensor as $\varepsilon_{ij} = 2/3\,\varepsilon\delta_{ij}$ The scalar dissipation rate is computed from solving a transport equation in the form

$$\frac{\partial U_j \varepsilon}{\partial x_j} = \frac{\partial}{\partial x_j}\left(C_\varepsilon \frac{k}{\varepsilon}\langle u_i u_k\rangle \frac{\partial \varepsilon}{\partial x_k}\right) + C_{\varepsilon 1}\frac{\varepsilon}{k}P_k - C_{\varepsilon 2}\frac{\varepsilon^2}{k} \quad (9)$$

where $P_k = P_{kk}/2$

The value of model constants are taken as previous studies and presented in Table 1.

Table 1 — Model Constants Used.

C_1	C_2	C_s	C_ε	$C_{\varepsilon 1}$	$C_{\varepsilon 2}$
1.8	0.6	0.24	0.15	1.44	1.92

Together with the above model the standard form of the k-ε eddy-viscosity model was considered (Launder and Spalding, 1974).

NUMERICAL MODEL

A finite-volume method using a staggered variable arrangement is used for solving the equations system. The pressure and mean velocity fields are coupled with SIMPLE algorithm (Patankar and Spalding, 1972). The 13-point quadratic upstream weighted scheme (QUDS: Leonard, 1979) was used for convection discretization in all transport equations At each control volume face the dependent variable ϕ was interpolated by the quadratic surface yielding e.g. for $\phi_{i-1/2,j} > 0$ the following expression when $U_{i-1/2,j} > 0$, $V_{i-1/2,j} > 0$,

$$\phi_{i-1/2,j} = a_o + a_1\frac{\Delta x_i}{2} + a_2\frac{\Delta x_i^2}{4} - a_4\frac{1}{3}\frac{\left(C_y^3+1\right)}{\left(C_y+1\right)^3}\left(\frac{\Delta y_i + \Delta y_{i+1}}{2}\right)^2 \quad (10)$$

where $C_y = \Delta y_j/\Delta y_{j-1}$ takes into account the grid non-uniformity and a_i denotes coefficients that contain the dependent variable ϕ in the surrounding grid nodes, (see for more details Durão and Pereira, 1989). The strongly implicit method, (Stone, 1968; Azevedo *et al*, 1988) was used to solve the system of algebraic equations including only 5 diagonals in the coefficients matrix. The other coefficients were appropriately incorporated in the source term.

The stabilizing practices suggested by Huang and Leschziner (1985) were used in the numerical solution of the second moment closure. The under-relaxation form of the $\langle u_i u_j\rangle$ finite-difference equations was used in the splitting procedure of $\langle u_i u_j\rangle$ in apparent diffusion and source terms included in the momentum equations. The use of under-relaxation form prevents large variations of the value of the variables to occur during the iterative olution procedure.

The solution domain was extended in order to cover 2.7 disk diameters in the axial direction and 1.4 diameters in the radial direction. This computational domain was shown to be adequate to compute the recirculating flow region up to 1.2 diameters.

Boundary conditions for U, V and the stresses along the jet-exit plane were taken from experimental values. The inlet unknown turbulence-energy dissipation ε was prescribed according to $\varepsilon = k^{3/2}/0.3$ D. Along the entrainment boundary, the pressure was prescribed and the radial momentum equation solved with the assumption of zero axial velocity in this boundary and arbitrary very small values were assigned to all turbulent quantities. At the exit plane the grid was refined and a zero second derivative was used for the axial velocity component. Special care was taken to evaluate the radial velocity at the entrainment boundary outside the domain to ensure mass conservation at the exit plane.

Calculations with EVM and RSM closures were made with non-uniform meshes consisting of 30 x 23, 60 x 46 and 100 x 94 control volumes; the last grid is shown in Fig. 1. Solution

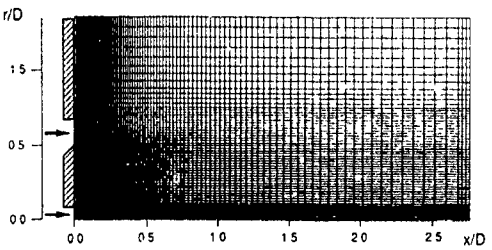

Figure 1. Computational Grid, 100 x 66 nodes.

convergence problems were encountered for both eddy viscosity and second moment closure computations due to high negative coefficients in the finite difference equations and also rapidly varying gradients of dependent variables. Three approaches have been investigated to overcome this problem:

i) A mixed quadratic upstream (QUDS) and first order upwind scheme which shifts from QUDS to first order upwind on the basis of local cell Peclet number, similar to that used by McGuirk *et al* 1985b;

ii) A blending flux correction of the form.

$$\left[A\right]^{n+1}\left[\phi\right]^{n+1} = \left[S\right]^n + \beta\left(\left[A\right]^n\left[\phi\right]^n - \left[A\right]^n\left[\phi\right]^n\right), \quad (11)$$

where L and H denote lower and higher order convection discretization schemes and n the iteration counter. If $\beta = 1$ the converged solution corresponds to the higher order scheme,

iii) A mixed procedure, with option i) adopted for momentum equations and option ii) for the other transport equations.

Option i) was applied with the shift from QUDS to first order Upwind at Peclet greater than 10^3. For eddy-viscosity calculations, more than 80% of the computational domain was calculated with QUDS. In this region, the negative coefficients were appropriately incorporated in the source term. For RSM calculations, the shift Peclet number had to be reduced in turbulence variables equations. To avoid this reduction, option ii) was tried and surprisingly, it was possible to obtain converged solutions either with central differences, quadratic upstream or high-order upwind depending on the correct choice of β. However, for $\beta > 0.5$ solution wiggles were found in almost all quantities and mainly in steep gradients regions. The best compromise was provided by option iii). For turbulence variables equations, β was assigned to 0.5 and option i) was used in momentum equations with the limit Peclet number Pe = 500. This procedure was required as first order Upwind results obtained with 60 x 48 and 100 x 94 control volumes were far from to be grid independent.

As our attention was focussed only in the separated flow region no solution grid independence was found even with the finer grid. Deviations up to 10% in the location of the first stagnation point were encountered for RSM calculations using the two finer grids. However, it was concluded that the grid comprising 100 x 66 control volumes was sufficiently fine to permit the response of turbulence-model variations to be interpreted on the assumption that the solutions were not biased by numerical errors.

RESULTS

Fig 2 shows the flow visualization results. The measured mean flow velocities are presented in Fig 3 in the form of vector plots and streamlines. The figures show that the annular air jet converges towards the centreline downstream of the disk and forms a wake region which extends approximately 1 23 diameters. A toroidal recirculating flow region is formed within the wake region by the interaction of the outer annular air with the central jet flow The central jet stagnates and is turned upstream and outward by the opposing reverse flow of the annular air. The stagnation point location is dictated by both high shear stresses generated along central jet boundary and by the adverse pressure gradient

Figure 2. Flow Visualization.

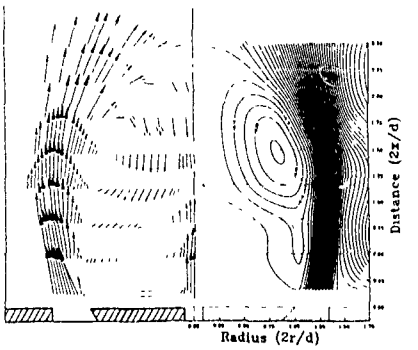

Figure 3 Measured Velocity Patterns (U + V) and Evaluated Stream Functions.

Fig. 4a) and b) presents computed streamlines for RSM and EVM, respectively. Broadly, the main features of the flow are captured in the computations. The two-stagnation points located along the centreline are also reproduced in the predictions, but their locus vary depending on the turbulence model used, specially the first stagnation point.

The centreline U-velocity evolution is presented in Fig 5 for EVM and RSM models. The size and minimum flow velocity within recirculation zones is correctly predicted by RSM, while EVM underpredicts the location of the first stagnation point by almost 50%. The centreline velocity decay is also rather differently predicted by the two models.

Fig. 6 shows radial profiles of U-velocity. Notably, RSM predictions follow quite well the experimental data across all axial stations. Only small discrepancies are observed, mainly within the outer region bounding the annular flow, where experimental values are larger than the predicted ones. This is probably due to flow intermittency in this zone, a feature previously identified by Scheffer *et al* (1987) and that none of the present turbulence models include. As a consequence of erroneous prediction of the first stagnation point, large discrepancies with the measurements are displayed in radial profiles obtained with EVM.

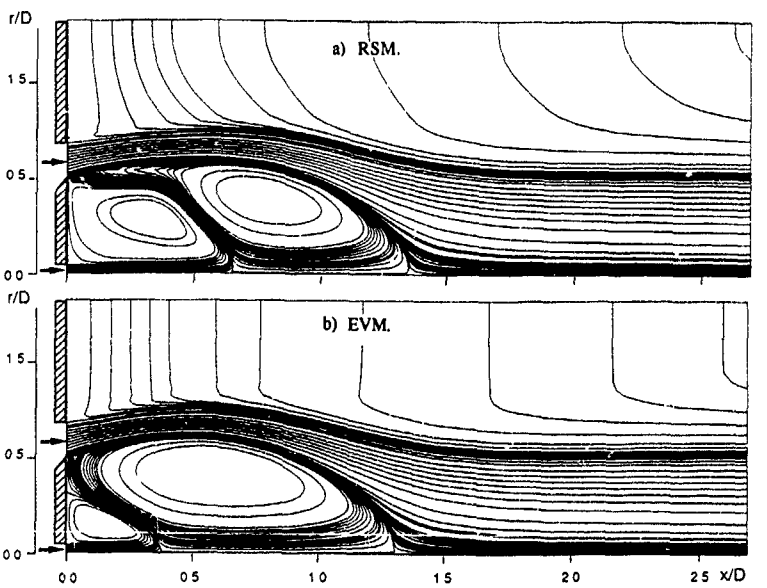

Figure 4. Computed Streamlines.

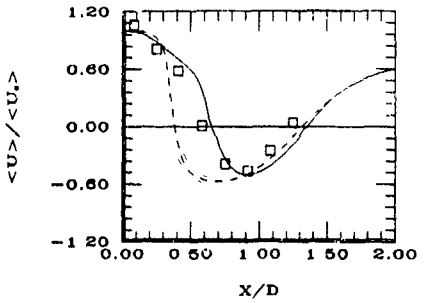

Figure 5. Centreline Velocity Development. Predictions. ——— RSM; - - - - , EVM; Measurements: Symbols, Durão *et al.* (1990)

The radial profiles of V-velocity component are shown in Fig 7 RSM predicted profiles are close to measurements, denoting that the flow entrainment rate is correctly predicted. EVM predictions are in severe error in the zone upstream of the first stagnation point inside the central vortex. In this zone, the transition of an inward flow (negative V-velocities) to a outward flow (positive V-velocities) observed near the first stagnation is correctly captured by RSM, while EVM is in error both in magnitude and in sign of the V-velocity.

Figs. 8, 9 and 10 show the radial development of Reynolds stress tensor components $\langle u^2 \rangle$, $\langle v^2 \rangle$ and $\langle uv \rangle$ near the stagnation points, respectively. A striking feature, already observed in the computations of McGuirk *et al.* (1985b), is the strong underprediction of stresses levels in the core region of the flow, and specially at centreline.

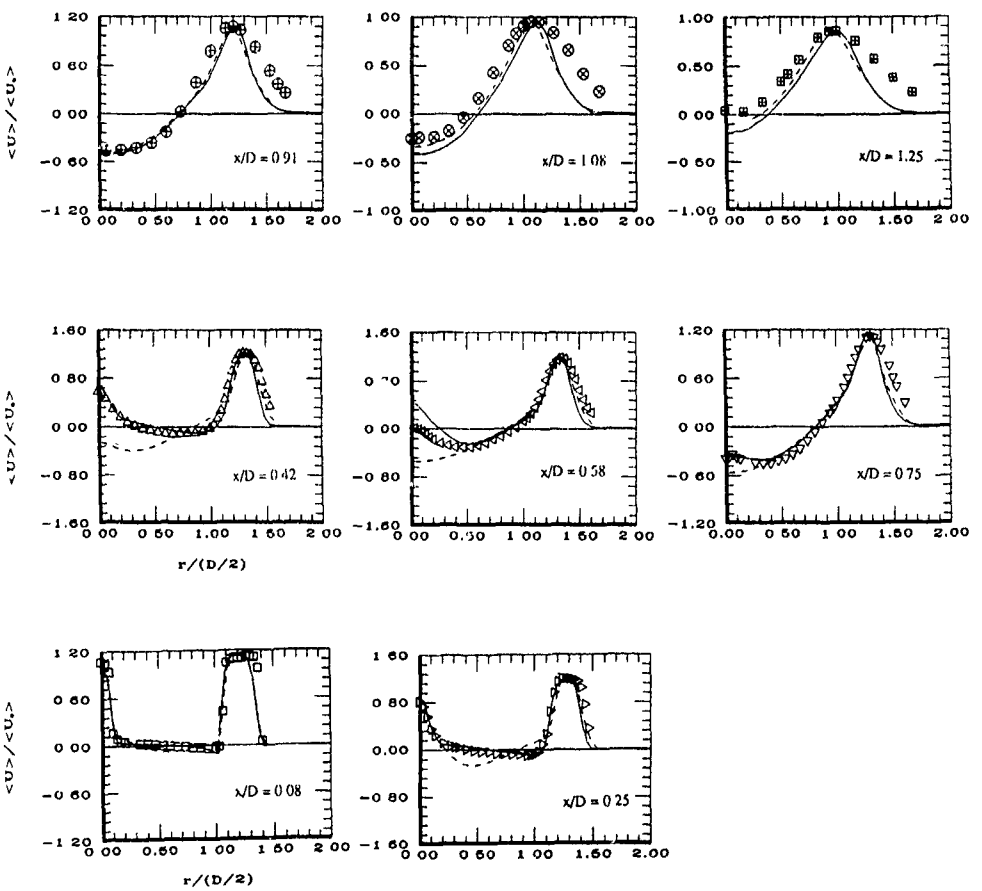

Figure 6. U-velocity Radial Development. Predictions: ——— RSM; - - - - , EVM; Measurements. Symbols, Durão *et al* (1990).

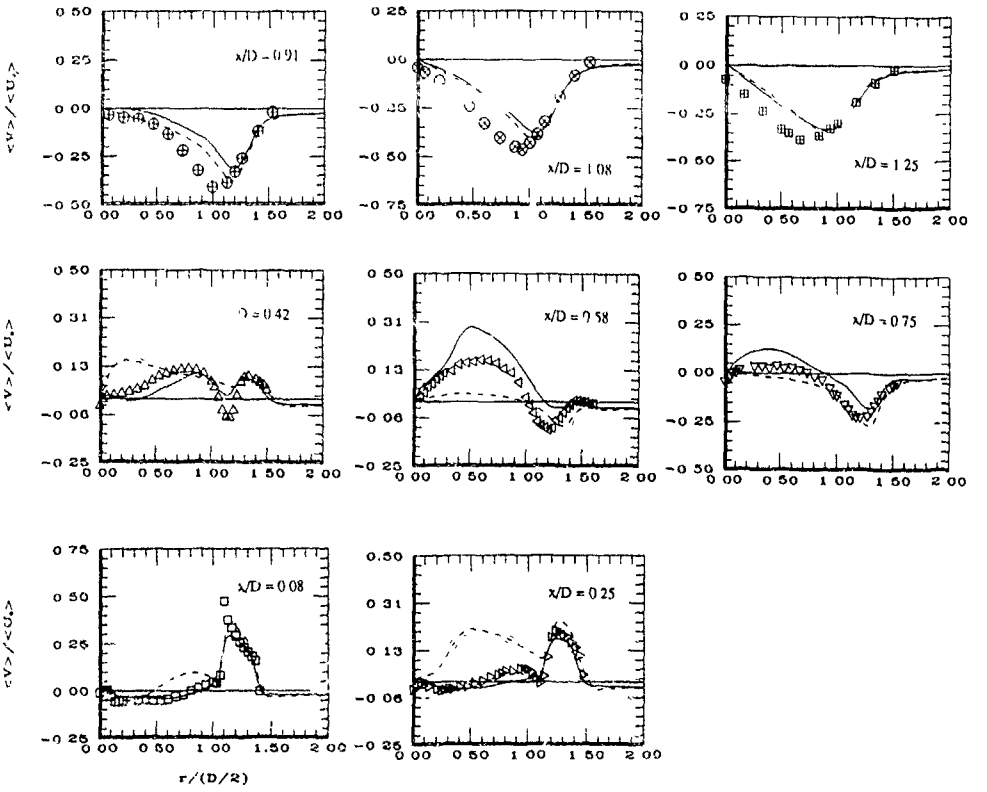

Figure 7. V-velocity Radial Development Predictions. ——— RSM; - - - - , EVM, Measurements Symbols, Durão *et al* (1990).

This major defect of both RSM and EVM can not be attributable to an erroneous computation of mean-field, which if true, would yield biasing effects in Reynolds stresses production rates via mean-strain. However, this is not the case as RSM predictions of mean-flow field are quite close to measurements. It was speculated by McGuirk *et al.* (1985b) that the problem could arise from a deficient representation of pressure-strain process by the present model in the prediction of Reynolds stress anisotropy near stagnation points. Although this argument can be valid concerning the modelling of the intercomponent energy transfer, it is believed that is not enough to justify the systematic

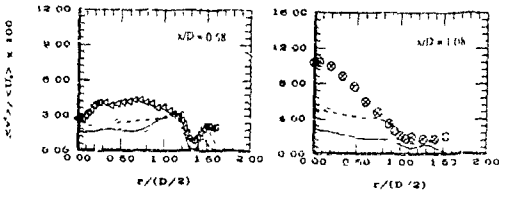

Figure 9. Normal Radial Reynolds Stress, Radial Development. Predictions: ——— RSM, - - - - , EVM; Measurements Symbols, Durão *et al.* (1990).

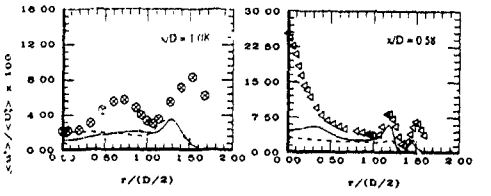

Figure 8. Normal Axial Reynolds Stress, Radial Development. Predictions: ——— RSM; - - - - , EVM; Measurements: Symbols, Durão *et al.* (1990).

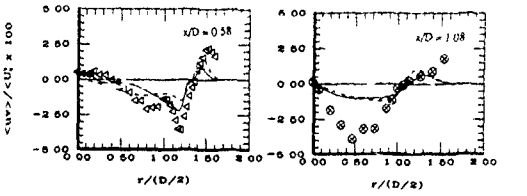

Figure 10. Reynolds Shear Stress, Radial Development. Predictions: ——— RSM; - - - - , EVM; Measurements: Symbols, Durão *et al* (1990).

underprediction of values of turbulence energy components observed, as pressure strain process mainly represents an energy redistribution mechanism. Previous studies (Weinstock and Burk, 1985, Sreenivasan, 1985, Daly and Harlow, 1970) have attempted to explore a functional dependence of pressure-strain model coefficients C_1 and C_2 on mean strain after some initial trials, this route was not pursued no further in the present study as, one believes, the major weakness stem from ε-equation. Moreover, EVM predictions show also the same discrepancies.

However, due to the complexity of the flow and variety of effects present, it is not an easy task to identify which mechanisms are not represented by ε-equation in its standard form and in which flow zones their influence is dominant, and consequently to devise any reasonably correction term. Two agencies are likely to be responsible: The first is the strong pressure gradient, which drives the central jet flow and establishes the first stagnation point together with shear stresses generated in the border of the jet; the second is the curved shear layer developing within the annular flow which is responsible for the formation of the second stagnation point. This shear layer dictates the levels of turbulence energy across the annular flow and by transport is of influence on the values of k at second stagnation region. However, and this point must be emphasized, experimental measurements of probably density distribution functions show clearly a bimodality in U-velocity components at the first stagnation point and in V-velocity component near the second stagnation point. No bimodality was identified within the annular flow bordering shear layer. This may indicate that high levels of normal stresses found near stagnation regions are due also to the contribution to turbulence energy budjet from oscillating behaviour of the flow. This speculation may be supported by the comparison of present measurements with those reported previously by Sheffer *et al* (1987).

Recently Hallbäck *et al* (1990) have proposed an algebraic model for dissipation rate of Reynolds stress tensor, ε_{ij}, aiming to include small scale anisotropy in modelling $\langle u_i u_j \rangle$-equation The model has the form

$$\varepsilon_{ij} = \left(e_{ij} - \frac{2}{3}\delta_{ij}\right)\varepsilon \qquad (12)$$

where

$$e_{ij} = \left[1 - \alpha\left(\frac{1}{2}II - \frac{2}{3}\right)\right] b_{ij} - \alpha\left(b_{ik}b_{kj} - \frac{1}{3}II\,\delta_{ij}\right) \qquad (13)$$

where $b_{ij} = \langle u_i u_j \rangle / k - 2/3\,\delta_{ij}$ is the Reynolds stress anisotropy tensor and II is the second invariant of b_{ij}. This algebraic model basically relaxes the isotropic assumption for ε_{ij}, allowing that non-normal components ($\langle uv \rangle$ in the present case) to have a dissipating process other than pressure-strain. This relation was incorporated in the RSM closure and predictions of the flow were obtained for several values of α, the only model constant. These computations have not shown an improvement in the maximum values of energy components, since the same model for ε-equation was used with the above mentioned supposed drawbacks. However, as a noticeable effect, the locus of maximum normal stress component at centreline was found to change if the model is employed. Moreover, this locus was found to be dependent of the value of α. More stringing tests are required before to conclude about of the validity and general applicability of this model.

CONCLUSIONS

In the present study a numerical and experimental study of an unconfined wake recirculating flow behind a disk with a central jet A second-moment closure as well as k-ε eddy-viscosity model were incorporated in an appropriate numerical solver and predictions of mean and turbulence characteristics of the flow were compared against experiments. It was shown that, although the flow being basically pressure-driven, RSM mean field predictions are substantially in close agreement with experiments compared to EVM ones. Another finding of the present study and consistently with previous ones, RSM or EVM are unable to capture the rising of turbulence energy levels near the stagnation regions. This inability can arise from different agencies, the more likely the ε-equation. Future modelling research is needed in improving ε-equation. The successful incorporation of more sophisticated effects as anisotropic dissipation as was done in the present study is depending on the adequate simulation of turbulence energy dissipation rate

ACKNOWLEDGEMENTS

The authors wish to acknowledge the financial support of CEC contract No. PL890926 under the JOULE Programme

REFERENCES

AZEVEDO, J.L.T., DURST F. & PEREIRA J.C.F. 1988. Comparison of strongly implicit procedures for the solution of the fluid flow equations in finite-difference form. *App Math. Modelling*, Vol. 12, pp 51-62

DALY, B.J & HARLOW, F.H., 1970. *Physics Fluids*, Vol. 13, No. 11, pp. 2634-2649.

DURÃO, D.F.G. & FIRMINO, F.C. 1983 Velocity field around a disk. 4th Symposium on Turbulent Shear Flows.

DURÃO, D.F.G. & PEREIRA, J.C.F., 1989. A numerical-experimental study of confined unsteady laminar flow around a square obstacle Fifth International Conferenceon Numerical methods and Turbulen Flow, Montreal Canada, pp. 261-272.

DURÃO, D.F.G. & WHITELAW, J H. 1978. Velocity Characteristics of the flow in the near wake of a disk. *J. Fluid Mech* , Vol. 85, pp. 369-385.

HALLBÄCK, M., GROTH, J. & JOHANSSON, A.V 1991 An algebraic model for non-isotropic turbulent dissipation rate in Reynolds stress closures *Physics Fluids*, A2 (10), pp 1859-1866.

HEITOR, M.V , TAYLOR, A.M K.P & WHITELAW J H. 1987. The interaction of turbule ice and pressure gradients in a baffle-stabilised premixed flame. *J. Fluid Mech* , 181, pp. 387-413.

HUANG, P G. & LESCHZINER, 1985. Stabilization of recirculating flow computations performed with second-moment closures and third-order discretization. Proc. 5th Symp. Turbulent Shear Flows, Cornell University, 20.7-20.12.

LAUNDER, B.E. & SPALDING D.B 1974 The numerical computation of turbulent flows. *Comp. Meth. Appl Mech Eng* , Vol. 3, pp. 269-289.

LEONARD, B.P. 1979. A stable and accurate convective modelling procedure based on quadratic upstream interpolation. *Comp Meths. Appl. Mech Engng* , Vol. 19, pp. 59-98.

MCGUIRK, J.J., PAPADIMITRIOU, C. & TAYLOR, A.M.K.P 1985b. Reynolds stress model calculation of two-dimensional plane and axisymmetric recirculating flows. 5th Symposium Turbulent Shear Flows.

MCGUIRK, J.J., TAYLOR, A.M.K.P. & WHITELAW, J.H. 1985a. The assessment of numerical diffusion in upwind difference calculations of turbulent recirculating flows. Turbulent Shear Flows - 3, Springer Verlag, pp. 206-224.

NAOT, D. A. SHAVIT & WOLFSHTEIN M. 1970. Interactions between components of the turbulent velocity correlations tensor. *Israel Journal of Technology*, Vol. 88, pp. 259.

PATANKAR, S.V. & SPALDING D.B 1972. A calculation procedure for heat, mass and momentum transfer in three-dimensional parabolic flows. Int J. Heat Mass Trans , Vol 15, pp. 1787-1806

ROTTA, J.C. 1951. Statistische theorie nichthomogener turbulenz. *Zeitschr fur Physik*, Vol. 129, pp. 547-572.

SCHEFER, R.W., NAMAZIAN, N. & KELLY, J. 1987. Velocity measurements in a turbulent nonpremixed bluff-body stabilised flame. *Combustion and Science and Technology*, 56, pp. 101-138.

SREENIVASAN, K.R., 1985. *J. Fluid Mech.*, Vol. 154, pp 187-213.

STONE, H.L 1968. Iterative solution of implicit approximations of multi-dimensional partial differential equations. SIAM J. Numer. Anal. Vol. 5, No. 3, pp. 530-558

TAYLOR, A.M.K P. & WHITELAW, J. 1984. Velocity characteristics in the turbulent near wakes of confined axisymmetric bluff bodies. *J. Fluid Mech.*, 139, pp. 391-416.

WEINSTOCK, J. & BURK, S., 1985. *J Fluid Mech* , Vol 154, pp. 429-443.

EIGHTH SYMPOSIUM ON
TURBULENT SHEAR FLOWS
Technical University of Munich
September 9-11, 1991

A MODEL EQUATION FOR TRANSITION AND TURBULENCE IN PLANE CHANNEL FLOW

N D Sandham

DLR, Institute for Theoretical Fluid Mechanics
Gottingen, Germany

ABSTRACT

A predictive model for the mean velocity profile in wall-bounded turbulent flow is developed. The model is conceptually based on the dynamical processes known to occur in near-wall turbulence. Ejections, sweeps and outer-layer motions are modelled directly as momentum transfer processes. These combine with viscous and pressure gradient effects to keep the mean velocity profile in a state of balance. A quantitative model is developed for the case of plane channel flow and is shown to correctly give an inner law, a logarithmic region, and a wake region. Predictions of skin friction, channel centreline velocity and shape factor agree well with experiments over a wide range of Reynolds numbers, including the transitional and low-Reynolds-number régimes. The procedure adopted represents a new and fundamentally non-local approach to turbulence prediction.

1. INTRODUCTION

The turbulent flow near a wall has been the subject of intense research over a large number of years. Significant progress has been made, resulting from studies using many different approaches. Although a complete understanding has not yet been achieved, there is substantial agreement on the main features of the flow. As a background to the current paper, a brief review of our current understanding will be presented.

Central to the current view of the turbulent boundary layer are the flow visualisations from Kline et al. (1967) which showed elongated streaks in the region very close to the wall, indicating a degree of organisation within the flow that was previously unsuspected. Streaks containing lower momentum fluid ('low-speed streaks') were observed to rise slowly, and break up in a high-activity process termed 'bursting'. Work since then has focussed on using increasingly sophisticated methods to try to understand this process. Motions have been identified based on the quadrant of $u'v'$ in which they occur (in the usual notation u' and v' are the velocity fluctuations relative to the mean in the streamwise and wall-normal directions respectively). For example if u' is negative and v' is positive the event falls in quadrant 2, and is termed an ejection. It is interpreted as the movement of low momentum fluid away from the wall. An event with u' positive and v' negative falls in quadrant 4 and is termed a sweep. It represents the motion of high momentum fluid towards the wall. Ejections and sweeps are common in the buffer region between the linear sublayer and the logarithmic region of the mean velocity profile.

Another approach has been to construct conceptual models of turbulent flow based on the vortical structures in the flow. A recent review has been given by Robinson (1991). In the near-wall region a popular vortical structure has been the hairpin vortex. In the region between the legs of the hairpin fluid is moved away from the wall, which could correspond to an ejection process. As well as these near-wall vortices, there are also large-scale motions in the outer portion of the boundary layer. An example of the kind of motion proposed for this part of the flow can be found in Brown and Thomas (1977). The relation between the vortices in the inner and outer regions is relatively poorly understood.

The most recent input to studies of the turbulent boundary layer has come from direct numerical simulations of the Navier-Stokes equations for flows in simple geometries. The resulting databases provide a wealth of information, including quantities that cannot be measured in experiments. Statistics from a computation of turbulent channel flow have been presented by Kim, Moin and Moser (1987). One important result from the simulations has been the observation that near-wall vortical motions do not contain the symmetries that had been previously supposed. Instead of hairpin vortices, Robinson (1991) found asymmetric structures, with single quasi-streamwise vortices common in the buffer region. It is increasingly apparent (Kline, 1990) that there are many mechanisms at work and the processes and vortical structures may be non-unique.

What has been largely absent from all the studies, of both the inner and outer regions, has been the application of the new facts and concepts to generating new *prediction* schemes for turbulent flows. The intention of this paper is to present one possible approach to this problem. One of the simplest turbulent flows, incompressible two-dimensional channel flow, is considered. In section 2 the procedure is introduced, and a quantitative model developed. Section 3 presents a comparison with experimental data. Further discussion is then made in section 4. Standard notation is employed throughout. The mean velocity profile is $u(y)$, where y is the distance from the lower wall. Wall-coordinates are $y^+ = yu_\tau/\nu$ and $u^+ = u/u_\tau$, where $u_\tau^2 = \nu(du/dy)_w$, ν is the kinematic viscosity and the subscript w refers to the wall.

2. MODEL

2.1 CONCEPTS

Turbulent flow in a channel can be considered as a state held in balance by the competing actions of eddies and viscosity. The eddying motions bring high-momentum fluid towards the wall, while viscosity tries to damp these motions, especially near the wall. The limiting cases resulting from these effects are sketched on figure 1. If the viscous effects

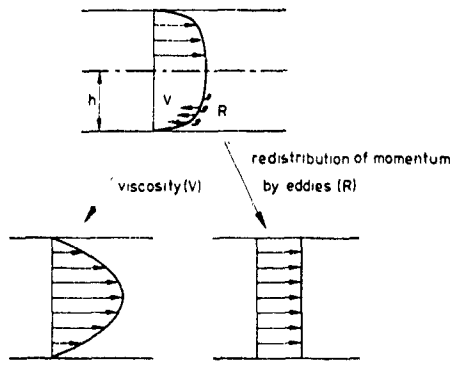

Figure 1 Schematic of the mean turbulent flow in a channel, showing the balance between eddy motions and viscosity. Viscosity tries to return the mean flow to the parabolic laminar profile, while the eddying motions try to redistribute momentum uniformly across the channel.

act alone we would return to laminar flow with a parabolic velocity profile. If the eddying motions are allowed to act alone, unchecked by viscosity or walls, we would have a perfect redistribution of momentum, leaving a uniform velocity profile. The latter state can never practically be obtained, since there is always viscosity present, but it is conceptually useful. The state of turbulence can therefore be considered at a simple level as a balance between the two effects.

This conceptual picture suggests the approach of predicting the mean velocity profile in a turbulent flow by modelling individually the momentum redistributions caused by certain classes of eddy motions. The three types of eddying motions which will be considered are ejections, sweeps and outer-layer motions. The model terms, describing the momentum redistribution caused by each of these motions, were developed by a trial and error method

2.2 FORMULATION

The balance between momentum redistribution and viscosity can be expressed in the following form

$$0 = T(E + S + O) + \nu\frac{d^2u}{dy^2} - \frac{1}{\rho}\frac{dp}{dx}, \tag{1}$$

where the last term is the streamwise pressure gradient Incompressible flow with constant density ρ is assumed The terms are here formulated as 'velocity' redistributions rather than 'momentum' redistributions. However, the latter terminology is retained since it is more meaningful physically. For variable density flows one would have to include the density in the terms representing the eddying motions These motions are referred to as E (ejections), S (sweeps) and O (outer-layer motions) and are modelled as follows.

Ejections (E).

$$E = -c_1(u - u_e)^2\frac{2h}{y(2h-y)}, \tag{2}$$

where u_e is the velocity at the edge of the linear region of the viscous sublayer, y is the wall-normal coordinate and h is the channel half width. The last factor is simply $1/y$, but applied for both walls in the channel. This term reduces the momentum at any point in the channel, and models the ejection process It is strongest in the buffer region, and small further away from the wall due to the $1/y$ effect The significance of u_e will be discussed later

Sweeps (S):

$$S = c_2(u_s - u)\left(\frac{du}{dy}\right)_w, \tag{3}$$

where the subscript w denotes the wall The action of this term is to move high momentum fluid towards the wall If u_s were equal to the mean velocity in the channel (averaged over y) then this term would act to force the channel towards a uniform flow, as in figure 1 In the current implementation the actual value of u_s has little effect, and is chosen so that global mass is conserved during the redistribution of momentum process.

The two terms above give a reasonable model for near-wall turbulence The mean velocity profile is realistic up to $y^+ = 100$, but results in too strong a wake in the outer portion of the channel. To get the correct behaviour in this region an additional term is required.

Outer-layer motions (O):

$$O = \frac{c_3(du/dy)_w^2}{2h/[y(2h-y)] - c_4/h + c_5O^*}, \tag{4a}$$

with

$$O^* = \frac{\nu}{u\overline{u}^2}\left(\frac{du}{dy}\right)_w^2, \tag{4b}$$

where $\overline{u}$ is the mean velocity in the channel (averaged over y) Near the wall the first term in the denominator of equation (4a) is dominant and the whole term then acts like $y(du/dy)_w^2$ and combines with E and S to generate the logarithmic law The remaining terms in the denominator are the most ad hoc part of the model. They serve to give the correct Reynolds number trend of the wake size

Transitional effects are handled in a simple manner, by reducing the size of the momentum redistribution term in accordance with the size of the ratio y_e/h, where y_e is the value of y at the edge of the linear region of the sublayer. Hence:

$$T = 1 - c_t\frac{y_e}{h}, \tag{5}$$

where c_t is a (single) transition constant. This term reduces the momentum redistribution as if it were cramped at the lower Reynolds numbers, where y_e becomes significant compared to the channel half-width. When T drops to zero laminar flow becomes the solution to (1).

2.3 NUMERICS

To focus attention on the model equation the numerical method for solution has been kept as simple as possible. The solution is obtained by two nested iteration processes. For the inner iteration equation (1) is reformulated into two steps:

$$\begin{aligned} u^{(1)} &= u^n + \Delta t\left\{T(E + S + O) + \nu\frac{\delta^2u}{\delta y^2}\right\} \\ u^{n+1} &= u^{(1)} - \Delta t\frac{1}{\rho}\frac{dp}{dx}, \end{aligned} \tag{6}$$

where Δt is the time step and δ^2 represents a second-order central difference The pressure gradient is assumed to be independent of y, with the magnitude determined as a correction to the first step, to ensure that a constant channel throughflow is maintained Equation (6) is iterated until a steady state is obtained.

The outer iteration consists of adjusting y_e until the solution to (6) gives a prescribed value of u_e^+, the velocity of the edge of the sublayer in wall coordinates The velocity profile for $y < y_e$ is assumed to be linear, so $u^+ = y^+$ up to y_e This procedure ensures that the point y_e is at the same position in wall coordinates for all cases This fixes the behaviour in wall-coordinates and is essential in producing an inner law (u^+ a function of y^+ alone). The secant method was used for the iterations.

The basic solution can be made on a uniformly spaced mesh, with the first inner point at y_e. However a little more flexibility and speed is obtained if a stretched mesh is used Results will be presented for a grid with the first mesh point at the wall, the second at y_e, the third at $2y_e$ and with succeeding points following

$$y_{j+1} = y_j + \alpha[y_j - y_{j-1}] \tag{7}$$

In the computations $\alpha \approx 1\,1$ was used, adjusted slightly so that the last point fell at the channel centreline The results are not sensitive to α, which can be made as large as 1 4 with only a one percent error in skin friction Tests showed that a complete resolution of the buffer region required adjustments to the constants. This did not lead to different results, but did lead to very small time steps An implicit treatment of the viscous term would probably cure this problem For the current explicit scheme a CFL number can be defined as

$$CFL = \frac{\nu \Delta t}{(\Delta y)^2_{min}}. \tag{8}$$

The scheme was found by trial to be stable for $CFL < 0\,38$

As a start point for the iterations the laminar solution was used. Symmetry was exploited so that only one channel half needed to be computed The number of points required for $\alpha = 1\,1$ varied from 7 at $Re = 1700$ to about 60 at $Re = 10^8$. The whole iteration process required less than 5 seconds on a 386 personal computer, even at the highest Reynolds numbers considered.

2 4 CONSTANTS

Dimensionless constants used in the model are. $u_e^+ = 9.0$, $c_1 = 0.074$, $c_2 = 0.0051$, $c_3 = 4.3 \times 10^{-6}$, $c_4 = 2\,0$, $c_5 = 2.6$ and $c_t = 5.4$. It is possible that c_4 doesn't need to be counted as a constant - it makes the combination of the first two terms in the denominator of (4a) equal to zero at the channel centreline. The constants u_e^+, c_1, c_2 and c_3 were determined so that (a) a logarithic region was obtained, and (b) the constants for this region matched the law of the wall constants. An explicit rule connecting the constants from the current model with the law of the wall constants has not so far been obtained. The remaining constants were determined in order to give a reasonble behaviour in the outer region of the channel and in the transition region

3. RESULTS

Throughout this section the Reynolds number is defined as:

$$Re = \frac{2h\overline{u}}{\nu}, \tag{9}$$

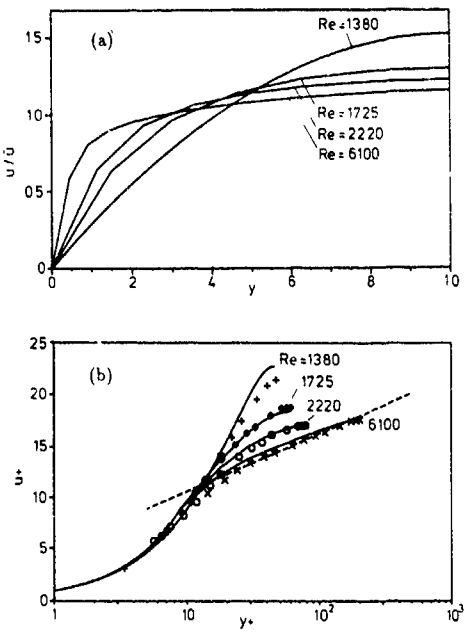

Figure 2. Model results in the low-Reynolds-number régime (a) in physical coordinates, (b) in wall units, compared with experimental data from Patel and Head (1969) The solid line is from the model at Reynolds numbers 1380 (laminar flow), 1725, 2220 and 6100. The symbols are the experimental data. The dashed line is the logarithmic law (10)

where h is the channel half-width, $\overline{u}$ is the average velocity and ν is the kinematic viscosity For comparison purposes the standard logarithmic law is used

$$u^+ = \frac{1}{\kappa} \ln y^+ + b, \tag{10}$$

with $\kappa = 0\,41$ and $b = 5.0$.

3.1 TRANSITIONAL FLOW

Solutions to equation (6) exist for Reynolds numbers greater than 1700. Below this the flow is considered to be laminar. The low Reynolds number region was investigated experimentally by Patel and Head (1969), who found that the trend from a laminar profile to a turbulent profile (approximately satisfying equation (10)) took place in the Reynolds number range 1380 to 6100 The change in the mean velocity profile from the model over this range is shown on figure 2(a) in physical coordinates for Reynolds numbers 1380 (laminar), 1725, 2220 and 6100. The same profiles are shown in wall units on figure 2(b) and compared with the results from Patel and Head. Agreement with the experimental results is good, both for the trends in the mean flow towards the logarithmic law, and in the shapes of the profiles. Skin friction and channel centreline velocities also agree well with the experimental values.

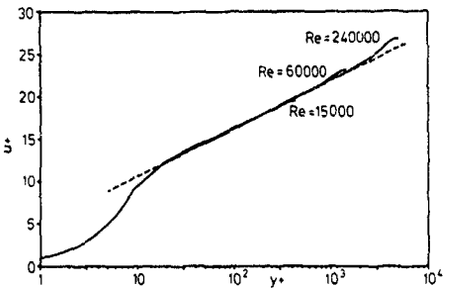

Figure 3 Evolution of the mean velocity profile in wall coordinates, showing the development of a logarithmic region and a small wake

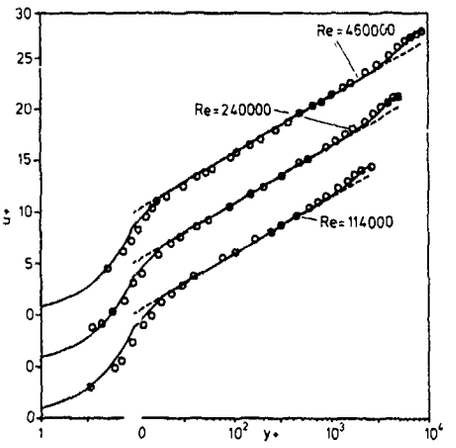

Figure 4 Comparison of the model velocity profile (solid line) with data from Comte-Bellot (1965) (symbols) The experimental value of u_τ was adjusted so that the data matched the logarithmic law (10)

3.2 EFFECT OF REYNOLDS NUMBER

As the Reynolds number is increased further one expects the logarithmic law to be more closely approched, to extend to higher values of y^+, and for a 'wake' region to form in the outer part of the channel. Figure 3 shows these effects for Reynolds numbers 15000, 60000 and 240000. The size of the wake at the highest Reynolds number is about one u_τ unit Figure 4 shows a comparison of velocity profiles with the data from Comte-Bellot (1965) for Reynolds numbers of 114000, 240000 and 460000, which represent the highest channel flow Reynolds number data available In order to compare the profiles, the values of u_τ from the experiment have been adjusted so that the same logarithmic law (10) is satisfied in each case. The value of u_τ was multiplied by 1.09, 1.03 and 1.085 for the three Reynolds numbers respectively. Agreement between the model and the data is very good, across the whole of the channel. The size of the wake in turbulent channel flow is known to be significantly smaller than that of a boundary layer. A trend towards slightly increasing wake size as the Reynolds number increases is obtained.

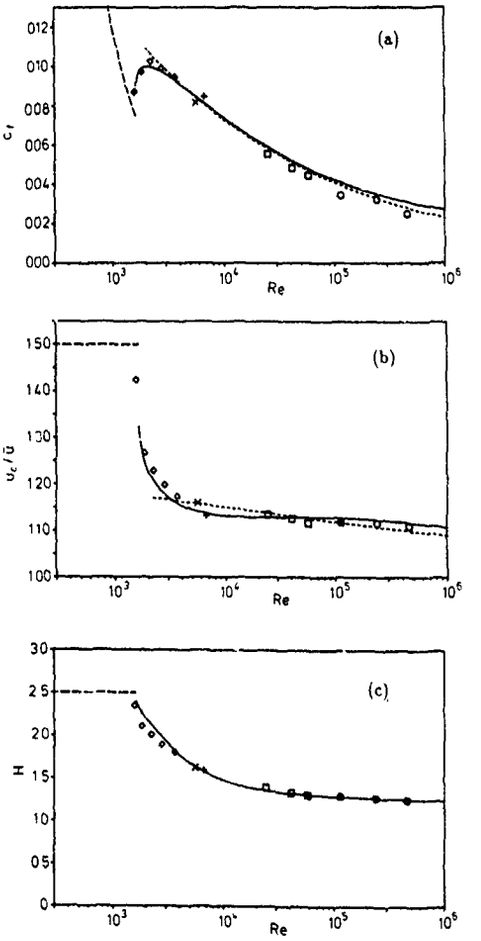

Figure 5 Variation with Reynolds number of (a) skin friction $c_f = 2\nu/\overline{u}^2(du/dy)_w$, (b) centerline velocity $u_c/\overline{u}$ and (c) shape factor $H = \delta_1/\delta_2$, where δ_1 is the displacement thickness and δ_2 is the momentum thickness. ——, model; - - - -, Dean correlations ($c_f = 0.073Re^{-1/4}$, $u_c/\overline{u} = 1.28Re^{-0.0116}$), — — —, laminar flow, ◇, Patel and Head (1969), □, Hussain and Reynolds (1975); ○, Comte-Bellot (1965); ×, Kim, Moin and Moser (1987); +, Gilbert (1988)

A large quantity of experimental data was collated by Dean (1978), who produced empirical laws for the variation of skin friction and centreline velocity with Reynolds number. On figure 5 the model predictions and Dean's correlations are compared with experimental data from Patel and Head (1969), Hussain and Reynolds (1975) and Comte-Bellot (1965), as well as direct numerical simulation results from Kim, Moin and Moser (1987) and Gilbert (1988). Figure 5(a) shows the skin friction $c_f = 2\nu/\overline{u}^2(du/dy)_w$, figure 5(b) the channel centreline velocity $u_c/\overline{u}$ and figure 5(c) the shape factor H. The shape factors for the experimental data were

computed from the original velocity profiles using trapezoid integration The model quantitatively predicts all the quantities correctly Especially notable is the ability of the model to give the correct behaviour of skin friction at low Reynolds numbers.

3 3 MODEL TERMS

It is of interest to examine the behaviour of the individual terms in the model The variations with y of the ejection term (E), the sweep term (S), the outer-layer term (O), the viscous term (V) and the pressure gradient term (P) at Reynolds number 114000 are shown on figure 6(a) in the near-wall region and on figure 6(b) across half the channel width At this Reynolds number the premultiplying transition factor T is equal to 0.996, and can be ignored The ejection term is strongest in the buffer region $20 < y^+ < 40$ as expected. In fact the shape of this term is similar to the conditionally sampled streamwise velocity during a burst (see figure 6 in Blackwelder and Kaplan, 1976) In the model this term reduces to zero at $y^+ = u_c^+ = 9.0$. At y_c there is basically a balance between the sweep term S and the effect of viscosity V The viscous term uses the physical viscosity ν, and should not be confused with a 'turbulent' viscosity. In the logarithmic region the viscous term has much less influence, and the important terms are the ejections, sweeps and outer-layer motions. In the central part of the channel the ejection term, the sweep term (here producing a decrease in momentum) and the outer-layer term all play a role The pressure gradient acts uniformly across the channel, but is of negligible importance compared with the other terms.

4 DISCUSSION

The idea for the current model came during a study of the late stages of transition to turbulence (Sandham and Kleiser, 1991) High wall shear was observed to develop, caused by vortices in the flow. The question was then posed why does the shear at the wall not increase indefinitely? The obvious answer of viscosity led directly to the picture sketched on figure 1, with the idea of a balance between the effects of eddies and viscosity in the near wall region Further development of this picture was pursued in the hope that by considering the direct effects of certain eddy motions in the near-wall region some of the basic physics would be modelled, and the final model would be of more general applicability than the usual empirical approaches via the Reynolds-averaged equations Whether this new approach can be turned into an engineering tool remains to be seen, but the experience from channel flow is encouraging.

Several informal rules were followed during this work. One was to keep all constants independent of Reynolds number, and another was to avoid the use of any functions (logarithms, exponentials etc.) in the model terms. Thus the logarithmic region of the velocity profile develops naturally rather than being imposed This leads to the hope that turbulent flows in which there is no logarithmic region (for example 'relaxing' flows) may also be correctly treated. In this respect the low Reynolds number effects in the channel flow can be cited – the model, in agreement with the experiments, does not give a logarithmic region

The current model has several features which are incorrect, or which it would be preferable to avoid One problem is that a velocity-defect law is not quite obtained. Figure 7 shows the velocity defect $(u_c - u)/u_\tau$ at $y = h/2$ from the model plotted against Reynolds number and compared with

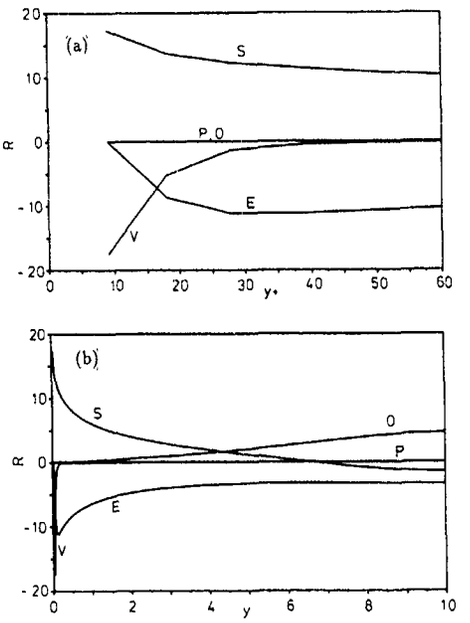

Figure 6 Terms in the model equation (a) in near-wall region, (b) over one channel-half. E = ejection term, S = sweep term, O = outer-layer term, V = viscous term and P = pressure gradient term

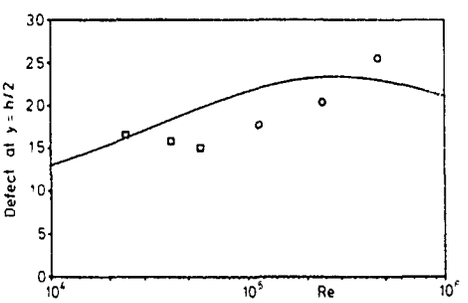

Figure 7. Variation of the velocity defect $(u_c - u)/u_\tau$ at $y = h/2$ with Reynolds number, showing how a defect law is not quite obtained at the higher Reynolds numbers

data from Hussain and Reynolds (1975) and Comte-Bellot (1965). It can be seen that the defect is not independent of Reynolds number, suggesting that the treatment of the outer-layer is not quite correct. The deviations are generally too small to show up against the experimental velocity profiles (figure 4) and it should be noted that the experiments themselves do not convincingly display a constant velocity defect. However, conceptually one would like the model to give a defect law in the limit of infinite Reynolds number. Also, the very near-wall region could perhaps be improved. The

current formulation applies only down to y_e, below which the profile is assumed to be linear The y_e point is fundamental to the success of the model, but it does lead to a discontinuity in the derivative of the velocity profile A continuous formulation would be preferable in the near-wall region, would avoid the numerical problem of where to put the first few points and would possibly simplify analytical treatment of the model system

As a general classification the current model could perhaps be described as non-local, although this term has been used elsewhere in different contexts The idea of non-local transport of mass appears in the meteorology literature, termed transilient turbulence by Stull (see for example Ebert et al , 1989). However, the applications have been to model the vertical motion of matter in the atmosphere, rather than the redistribution of momentum near a wall Perhaps a step in this direction was taken by Rüdiger (1982), who proposed to model the Reynolds stress with a linear integral equation (the current model leads to a nonlinear integral equation for the Reynolds stress). However, to the best of the author's knowledge nothing like the current model has appeared in the literature

The change from laminar to turbulent flow is an interesting part of the model When the Reynolds number is too low there is no solution to the model system and the flow is assumed to be laminar What the model is really saying is whether turbulent flow can be sustained. Thus the transition processes are really those of 'bypass' transition (where large initial disturbances lead directly to breakdown, bypassing primary and secondary instabilities) or of relaminarisation. Thus a simplified form of the model may perhaps be useful, not for predicting transition, but for prediction of locations in a flow where wall-bounded turbulence would self-sustain

5. CONCLUSIONS

A simple model equation has been developed, which contains as its solution many of the observed features of the mean velocity profile in transitional and turbulent channel flow. Solutions to the model equation exist above a certain Reynolds number. As the Reynolds number is increased the mean profile develops a logarithmic region, and at higher Reynolds numb a small wake forms Good quantitative agreement with experiments is obtained for the mean velocity profile, together with the associated measures of skin friction, centreline velocity and shape factor.

Individual terms in the model equation can be considered as modelling directly the transfer of momentum in a channel due to certain types of eddy motions. One term models ejections and transfers low momentum fluid away from the wall Another models sweeps and carries high momentum fluid towards the wall. A third term is interpreted as modelling motions in the outer region Each transfer of momentum is a non-local process, depending on conditions near the wall

ACKNOWLEDGEMENT

I would like to thank L. Kleiser for constructive comments on a draft version of this paper.

REFERENCES

Blackwelder, R. F. and Kaplan, R E. 1976 On the wall structure of the turbulent boundary layer. *J. Fluid Mech* **76**, 89-112.

Brown, G L. and Thomas, A. S. W. 1977 Large structure in a turbulent boundary layer *Phys Fluids* **20**, S243-S252

Comte-Bellot, G 1965 Écoulement turbulent entre deux parois parallèles *Publications Scientifiques et Techniques du Ministère de l'Air*, No. 419

Dean, R B 1978 Reynolds number dependence of skin friction and other bulk flow variables in two-dimensional rectangular duct flow *J Fluids Eng* **100**. 215-223.

Ebert, E E , Schumann, U and Stull, R B. 1989 Nonlocal turbulent mixing in the convective boundary layer evaluated from large-eddy simulation. *J. Atm. Sci* **46**, 2178-2207.

Gilbert, N. 1988 Numerische Simulation der Transition von der laminaren in die turbulente Kanalstromung *DFVLR* FB 88-55

Hussain, A. K M. F and Reynolds, W C 1975 Measurements in fully developed turbulent channel flow *J Fluids Eng.* **97**, 568-580

Kim., J , Moin, P and Moser, R 1987 Turbulence statistics in fully developed channel flow at low Reynolds number. *J Fluid Mech.* **177**, 133-166.

Kline, S. J., Reynolds, W. C., Schraub, F A. and Runstadler, P. W 1967 The structure of turbulent boundary layers. *J Fluid Mech.* **30**, 741-773

Kline, S J. 1990 Comment in Whither Turbulence? Turbulence at the Crossroads J. L. Lumley, ed , *Lecture Notes in Physics*, Springer-Verlag, 383-388

Patel, V C and Head, M. R 1969 Some observations on skin friction and velocity profiles in fully developed pipe and channel flows. *J Fluid Mech* **38**, 181-201.

Robinson, S K. 1991 Coherent motions in the turbulent boundary layer *Ann Rev Fluid Mech* **23**, 601-639

Rüdiger, G. 1982 A heuristic approach to a non-local theory of turbulent channel flow. *ZAMM* **62**, 95-101.

Sandham, N. D. and Kleiser, L 1991 Vortex formation in the late stages of transition to turbulence. *Roya. Society of Aeronautics, Conference on Boundary Layer Transition and Control*, April 8-11, Cambridge, UK

EIGHTH SYMPOSIUM ON
TURBULENT SHEAR FLOWS
Technical University of Munich
September 9-11, 1991

TRANSITION TO TURBULENCE IN CURVED CHANNEL FLOW

O John E. Matsson*), Alessandro Bottaro**) and P Henrik Alfredsson*)

*)Department of Gasdynamics, Royal Institute of Technology
S-100 44 Stockholm, Sweden

**)DME-IMHEF, Swiss Federal Institute of Technology
CH-1015 Lausanne, Switzerland

ABSTRACT

Experiments and numerical simulations have been carried out for the developing flow in a curved channel. This flow is susceptible to a centrifugal instability, which results in the formation of streamwise oriented vortices Linear stability theory is able to accurately predict the critical Reynolds number, i e. the Reynolds number for which the primary instability starts to develop. If the Reynolds number is increased above the critical a number of supercritical bifurcations occurs before a developed turbulent state is reached The focus here is on the initial stages of transition to turbulence of the flow from its original laminar state. Our measurements and simulations show that even at Reynolds numbers six times the critical one the longitudinal vortex structure persists.

INTRODUCTION

The flow in curved passages is important in several practical applications, as for instance most types of turbo-machinery, flow along guide vanes, in heat exchangers and past airfoils. In many of these applications the Reynolds number is fairly low and the stability of the laminar flow and the laminar-to-turbulent transition phase may be of great importance to determine the efficiency or performance of the application in question. The understanding of the transition phase is less developed in these cases where body forces (of centrifugal and/or Coriolis type, the latter in the case of system rotation) play an important role (see for instance Alfredsson & Persson, 1989 and Matsson & Alfredsson, 1990) Furthermore no practical engineering methods, of e.g. the e^n-type, have been developed for these cases. The instability in a flow field subject to body forces usually takes the form of streamwise oriented roll cells or vortices which dramatically alter the basic laminar velocity field These roll cells seem to persist even in the turbulent state and they have a profound influence on, for instance, the skin friction and possibly also on heat transfer

In this study experimental and computational techniques are used to investigate the route to transition of the flow in a curved channel (Fig 1) which can serve as a canonical case for flows with streamline curvature. The basic laminar flow is unidirectional and has a near-parabolic profile with the maximum slightly shifted towards the inner (convex) wall. The object of this work is the understanding of the transition sequence past the curved channel Poiseuille type flow, once centrifugal forces reach a "critical" magnitude. The flow undergoes a sequence of supercritical bifurcations before a fully developed turbulent state is reached The control parameter is the so called Dean number defined as

$$De=Re\sqrt{\gamma},$$

where γ is the channel width over radius of curvature ratio $\gamma=2d/(r_o+r_i)$, r_i is the inner and r_o the outer radius of the channel, and Re is defined through the bulk velocity, U_b, and the channel height, $d=r_o - r_i$). From linear stability analysis one finds that the critical Dean number (De_c), i.e the Dean number above which streamwise vortices may grow, is 36 (assuming $\gamma \ll 1$). The wave number (β) that corresponds to the critical Dean number is 3.95 (Drazin & Reid, 1981). At higher Dean numbers ($De/De_c \geq 1.3$) an analysis by Guo & Finlay (1991) indicates that the streamwise vortex structure is unstable to spanwise perturbations (denoted by them as a generalized Eckhaus instability, see also Eckhaus, 1965 and Stuart & DiPrima, 1978), which would give rise to merging

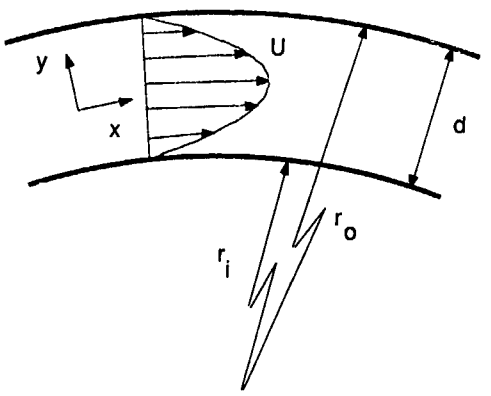

Fig. 1. Definitions of geometry for curved channel flow

and splitting of the streamwise vortices Bottaro, Matsson & Alfredsson (1991) performed numerical simulations of a spatially developing flow with a large spanwise box to allow for natural spanwise wave number selection and compared this with experimental measurements at De=2 4 De_{cr} The overall agreement was good both qualitatively and quantitatively. Furthermore merging and splitting of vortex pairs was observed in both the experiment and the simulation In experiments at higher De ($De/De_c > 3$) a secondary instability in the form of oblique travelling waves with a streamwise wavelength of the same order as the spanwise wavelength of the primary instability has been detected both from flow visualization and hot-wire experiments (Kelleher, Flentie & McKee, 1980, Ligrani & Niver, 1988 and Matsson & Alfredsson, 1990, 1991) and in numerical simulations (Finlay, Keller & Ferziger, 1988) In this paper we present results at higher De which give information of the transition stages before developed turbulence is obtained. The report is both a study of the flow field itself and a comparison between a full numerical simulation with inflow-outflow boundary conditions and a physical experiment.

EXPERIMENTAL ARRANGEMENT

The experiments were carried out in an air channel made of Plexiglass designed for hot-wire measurements of curved channel flow The radius of curvature of the channel at the centreline was 400 mm and the channel width was 10 5 mm, giving an inner to outer radius ratio of 0.974. The spanwise aspect ratio was 29 to 1 thereby avoiding end wall effects in the major part of the channel A radial fan blew air into the inlet chamber where the flow was distributed by a perforated pipe and two wire screens A two-dimensional contraction with an area ratio of 14 further reduced the mean flow variations. The channel consisted of a straight part followed by a curved section of 270 degrees. The straight inlet section was 40 channel heights long and the curved section corresponded to a length of 180 channel heights

The traversing system was a three degree of freedom system, for which the motion normal to the walls and in the spanwise direction was computer controlled The upper end wall had a tight slit of rubber which allowed streamwise positioning of the hot-wire support This was made manually. The hot-wire probe was mounted on a vertical rod of 4 mm diameter spanning the channel along the centerline. This rod was connected to a stepper motor which traversed the hot-wire in the vertical direction The rod was guided by a 4 mm hole at the bottom wall (holes were located at different streamwise positions) and at the top of the channel by a brass tube that fitted tightly between the channel walls The rod could also be rotated by another stepper motor to allow for radial traversing In this way the hot-wire sensor could be traversed in contact with the outer concave channel wall and as close as 0 3 mm from the inner wall. In the spanwise direction measurements were made across the full channel section and at a distance of 3 mm from the bottom and top walls. Measurements were usually taken across a full y-z-plane consisting of 20*300 measurements points which were sufficient to allow detailed plotting of contour lines of the streamwise velocity

The measurements of the streamwise velocity was obtained with a hot-wire probe, where the sensor had a diameter of 2 5 μm and a length of 0 5 mm connected to a CTA hot-wire anemometer (DISA 55M01) The hot-wire was calibrated against the parabolic Poiseuille profile ($1-y^2$) at the end of the straight part of the channel (which was assumed to be fully developed) and the calibration so obtained was directly in U/U_{CL}, where U_{CL} is the centerline velocity The flow velocities encountered were low (typically between 0 5-4 m/s) Data sampling and stepper motor movements were controlled by a Macintosh II. The fan was running at maximum speed and the flow rate could be regulated by a mechanical throttle and determined from the pressure drop over an orifice-plate flow meter located between the fan and the inlet section

NUMERICAL PROCEDURE

The numerical simulation considers the spatially developing flow with inflow-outflow boundaries. The spanwise direction is chosen periodic with a width of 9 channel heights This is large enough to contain several vortex pairs The streamwise length corresponds to 100° or 67 channel heights No-slip Dirichlet conditions for the velocity were applied at the solid boundaries The inlet condition was the slightly modified parabola, corresponding to the fully developed subcritical one-dimensional curved channel flow (Matsson & Alfredsson, 1990) A steady periodic inlet perturbation was adopted (superimposed on the shifted parabola) to drive the vortex development The steady inlet perturbation is indispensable to avoid a continuous forcing of the flow at the inlet of the channel (Buell & Huerre, 1988). At the outflow convective boundary conditions such as the ones described by Lowery and Reynolds (1986) and Bottaro (1990) were judged to be acceptable These conditions are suited for time-dependent problems and have been shown to produce negligible upstream reflection of outgoing waves in a Poiseuille/Benard travelling wave problem (Bottaro, 1990) In non-dimensional units they read

$$\frac{\partial u}{\partial t} + U\frac{\partial u}{\partial x} = 0, \quad \frac{\partial v}{\partial t} + U\frac{\partial v}{\partial x} = 0, \quad \frac{\partial w}{\partial t} + U\frac{\partial w}{\partial x} = 0$$

where the u, v and w are the disturbance velocities in the streamwise, normal and spanwise directions, respectively. Once the outlet velocity components are computed by the use of the above expressions, the streamwise velocity u at the exit cells is adjusted to satisfy global mass balance The correction factor is a multiplying constant which is always contained within 1±0.001. Deviations from unity should be ascribed to the fact that the divergence of the velocity is not exactly equal to zero during the iteration procedure; as such global mass conservation is not exactly satisfied.

The computational grid was 130*24*160 in the x,y,z-directions. The streamwise resolution was felt to be adequate to resolve the large streamwise scales of the flow but may be only marginally adequate to resolve the secondary instabilities of the flow. A fine resolution was employed in the cross-section and the grid was composed of 160 spanwise points and 24 normal points, the latter smoothly stretched to resolve boundary layers near the walls. The mesh was fully staggered. Its adequateness was assessed on the basis of comparisons with experimental measurements as well as one dimensional spanwise spectra. The good comparison with linear stability theory for spatial growth (which is reported in Fig. 4) is particularly reassuring with respect to the streamwise numerical resolution. The spatial discretization, in the finite volume approximation, adopted a second order central difference scheme to treat total (convective and diffusive) fluxes. Solutions were obtained by fully implicit time-marching, with up to 5 internal iterations performed at each time step to ensure that the maximum pressure and velocity residuals decrease to acceptable levels (10^{-4} was the level required for streamwise velocity and pressure, while normally the other two velocity components were reduced to $0.5\ 10^{-5}$). The time step was chosen to be about one tenth the Courant condition. The pressure coupling is treated with the SIMPLER pressure correction technique described by Patankar (1980). The computational domain was scanned with radial and azimuthal zebra sweeps which do not eliminate the (inevitable) recursion, but allow vectorization of all inner loops. Three sweeps were performed for pressure and pressure correction equations and one each for the three velocity components. The resulting tridiagonal systems of linear equations are solved by the use of the Thomas algorithm.

RESULTS

The results presented here are for a De of 235 which is more than six times the critical De. At this Dean number the flow was not steady, however the vortex pattern was quite consistent and some individual vortex pairs could be followed in the streamwise direction. Depending on the downstream position the hot-wire signal was typically averaged over a period of 5 seconds. In Fig. 2 the velocity field at five different downstream positions is plotted (at x/d= 22, 52, 82, 112 and 142). Shown are lines of constant streamwise disturbance velocity, i.e. the measured streamwise velocity from which the undisturbed parabolic profile has been subtracted. The contour lines are spaced 0.10 U_{CL} apart and negative values are shown as dotted lines while the zero contour as well as positive lines are full-drawn. The measurements span the entire width of the channel and the effects of the top and bottom walls are strongly localized. At x/d=22 the vortex pairs have given rise to "mushroom" shaped regions of low velocity fluid which are typical for boundary layer flows along concave surfaces (see e.g. Swearingen & Blackwelder, 1987). We call this the inflow regions. In channel flow at lower De than the present, the inflow region does not exhibit such a clear mushroom-shape (see Bottaro et al., 1991).

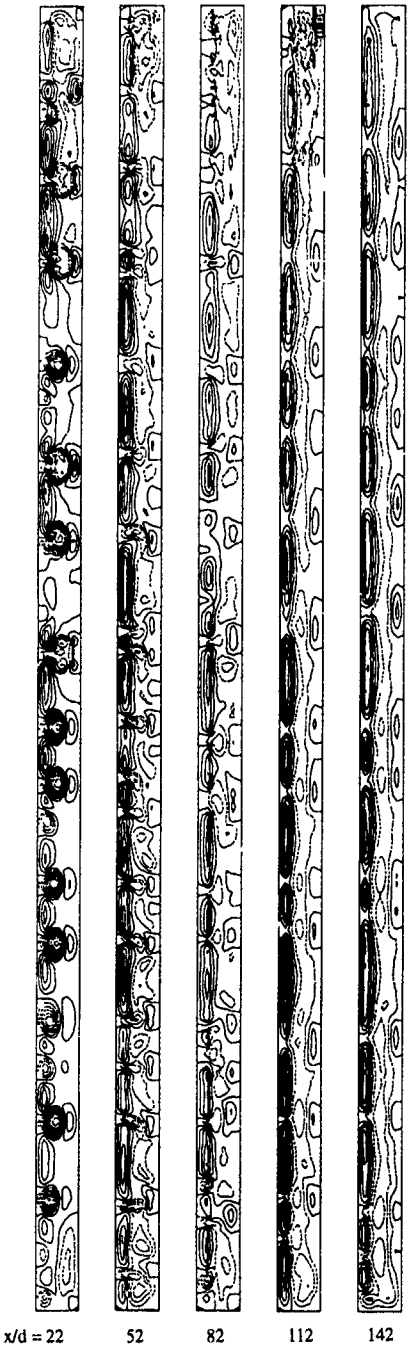

Fig. 2. Contours of the streamwise perturbation velocity for De=235 in the y-z plane at five different x/d. The outer and inner channel walls are to the left and right, respectively. Contour lines are separated by 0.10 U_{CL}.

The mushrooms consist of fluid with low streamwise velocity which is moved from the concave wall towards the convex side between a pair of counter rotating vortices The magnitude of the disturbance velocity reaches values as high as 50 % of U_{CL} The effect of this motion is also seen close to the convex side as a high speed region which originates from fluid in the centre of the channel. At this streamwise position the strength of the vortices is fairly equal and in the central part of the channel the average spanwise wave-number of the vortices is 3.6. Further downstream the mushroom shape pattern of the low-speed regions disappears and the flow is instead dominated by a periodic pattern of elongated regions of positive disturbance velocity at the concave wall The regions of negative disturbance velocity are not as clearly visible as at smaller x/d This may be due to the fact that the flow is unsteady and that the vortices move irregularly in the z-direction thereby "erasing" the narrow low-speed regions when taking a long-time average. The downstream development of the vortex pairs leads to merging of neighbouring pairs and the average spanwise wave number decrease with downstream distance (at x/d=142 β is 3.0)

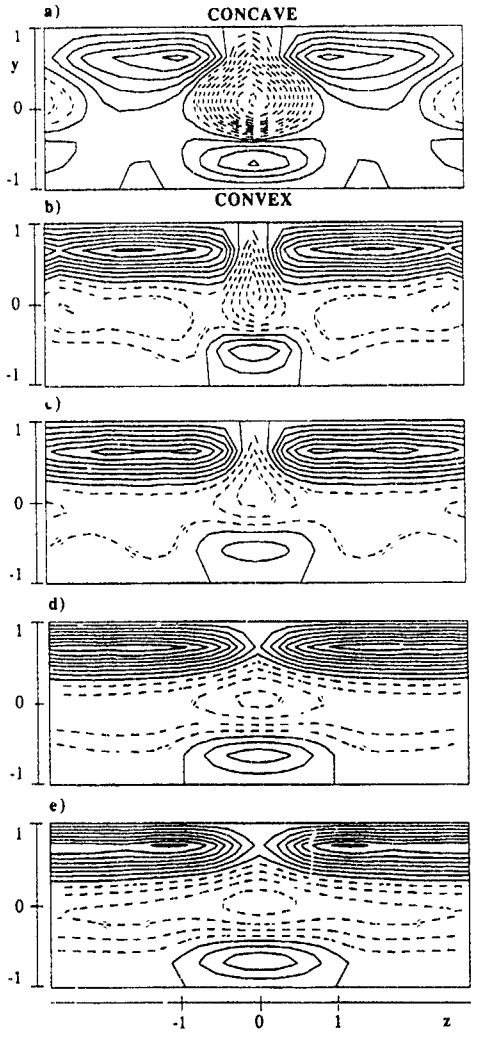

Fig. 3. Ensemble averages of the streamwise perturbation velocity for De=235 at five different x/d Contour lines are separated by 0.05 U_{CL}.

a) x/d=22 b) x/d=52 c) x/d=82 d) x/d=112 e) x/d=142

In order to get a clearer picture of the average development of the flow field, ensemble averages of the vortex pairs were constructed This was done by first identifying the centre of each vortex pair, i.e. the regions of maximum negative disturbance velocity in the flow field and using this as a reference point for the ensemble averages. About thirteen vortex pairs were identified at each streamwise position and were used in the ensemble average (which also was made symmetrical) shown in Fig 3. Although slightly smeared compared to the individual vortices the development is clearly seen, at first the mushroom shape, which decreases in size further downstream whereas the positive disturbance regions become more elongated. Noticeable is also how the vortex pair give rise to a positive disturbance region on the convex wall, which is consistent with the idea that the vortex pair moves high speed fluid from the centre of the channel towards the convex wall.

The development of the vortex structure is illustrated in Fig 4 where a measure of the streamwise disturbance velocity is shown The measure is defined as

$$e = \sqrt{\frac{1}{A}\int_A (u')^2 \, dA} \quad ,$$

The initial development in the numerical simulation is close to the exponential growth as predicted by linear theory up to quite high disturbance amplitudes. Further downstream the disturbance amplitude reached a maximum before it decreased and reached its

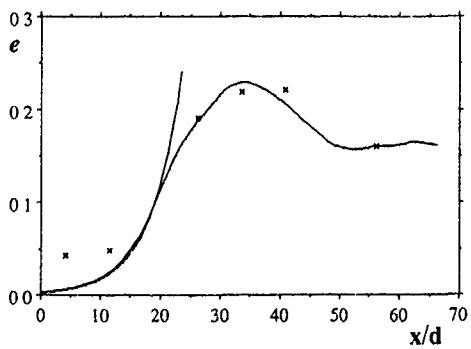

Fig. 4. Amplitude of the average disturbance velocity at different x/d for De=235. For comparison the linear spatial growth rate is also plotted ——: simulation, x: experiments

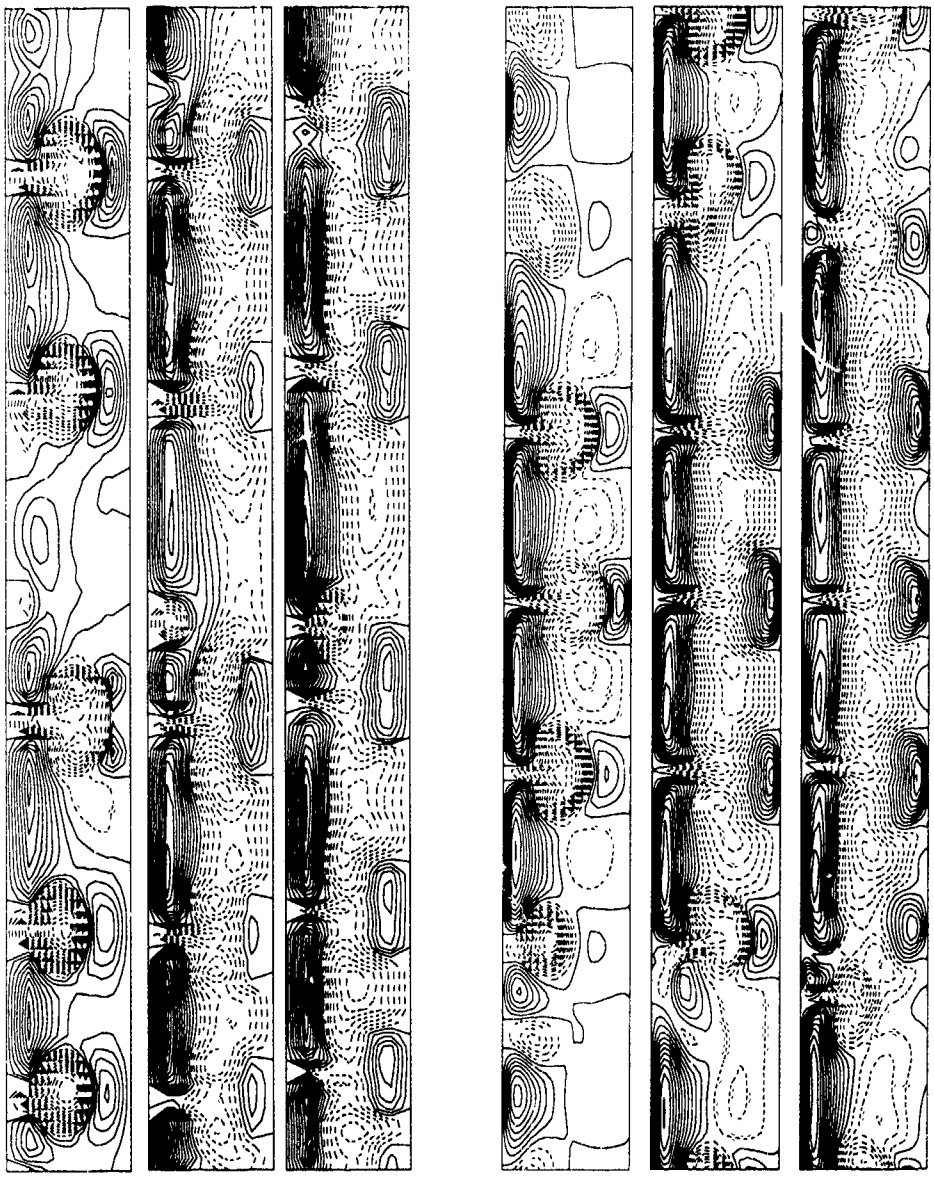

Fig 5 Comparison of measured and computed streamwise disturbance velocity field in the y-z plane at three different streamwise positions for De=235 Contour lines are separated by 0 05 U_{CL}

asymptotic level The experimental data, after being shifted by x/d=5 to match the "virtual" origin of the experiment and the simulation, agree nicely with the simulation Note that in the simulation the flow is stationary up to x/d=40, and that above x/d=50 a distinct wobbling of the vortices in space and time is noticeable

Fig. 5 is a comparison between the experimental and numerical results at three different downstream positions. The experimental data are taken from the middle of the channel in order to minimize influence of the side walls. The downstream spacing is the same in the figure for the experiment and the simulation, however the virtual origins for the two cases are different and are shifted according to the results in Fig 4. There is a close correspondence between the experiments and the simulation both of the qualitative development of the vortex structure as well as quantitative measures of the streamwise disturbance velocity

CONCLUSIONS

A combined experimental and numerical study of the route towards turbulence in curved channel flow has been made. The experimental data show a remarkably regular spanwise pattern, reflecting the development of a dominating pattern of streamwise vortices The numerical simulation seems to be able to predict the general features of the flow development accurately The details of these processes and its development into turbulent curved channel flow will be further investigated by us in the future. It is interesting to compare the present numerical approach with that of other simulations. Bland & Finlay (1991) simulated the transition in a box with periodic streamwise and spanwise boundary conditions. The spanwise size of the box was chosen to fit only one vortex pair. This of course restrict the possibility of interaction between neighbouring vortices which in both our experiment and simulation seems to be an important ingredient in the flow development. Also the use of periodic streamwise boundary conditions may be questionable since the spatial development is not accurately modelled. We believe that such a simulation can only be of limited value in order to understand the later stages of transition in this and similar flows The study of Yang & Kim (1991), which is a study of rotating plane channel flow, on the other hand uses a wide box in order to let the flow itself develop its spanwise structure. The development there is close to the experiments by Alfredsson & Persson (1989) (both merging and splitting are observed for instance), however their use of streamwise periodic boundary conditions also restricts the validity of that approach if one wants to get adequate information on the physical processes leading to transition in general and to use them as input to transition models in particular

The experiments were carried out with support from STU, the Swedish National Board for Technical Development, whereas Cray-2 time was provided by the Swiss Federal Institute of Technology, Lausanne The authors want to thank Professor Inge Ryhming for supporting and encouraging this cooperative effort.

REFERENCES

ALFREDSSON, P H & PERSSON, H. 1989 Instabilities in channel flow with system rotation *J Fluid Mech* **202**, 543

BLAND, S B. & FINLAY, W H 1991 Transition toward turbulence in a curved channel *Phys Fluids. A* **3**, 106

BOTTARO, A. 1990 Note on open boundary conditions for elliptic flows *Num Heat Transfer* B **18**, 243.

BOTTARO, A , MATSSON, O.J.E. & ALFREDSSON, P.H. 1991 Numerical and experimental results for developing curved channel flow. Accepted for publication in *Phys Fluids* A.

BUELL, J C & HUERRE, P. 1988 Inflow/outflow boundary conditions and global dynamics of spatial mixing layers Stanford University/ NASA Ames Report CTR-S88, 19

DRAZIN, P G. & REID, W.H. 1981 *Hydrodynamic Stability* Cambridge University Press

ECKHAUS, W 1965 *Studies in Nonlinear Stability Theory* Springer

FINLAY, W H , KELLER, J.B. & FERZIGER, J H. 1988 Instability and transition in curved channel flow *J Fluid Mech* **194**, 417.

GUO, Y & FINLAY, W H 1991 Splitting, merging and wavelength selection of vortices in curved and/or rotating channel flow due to Eckhaus instability. Accepted for publication in *J. Fluid Mech*

KELLEHER, M D., FLENTIE, D L. & MCKEE, R. 1980 An experimental study of the secondary flow in a curved rectangular channel *ASME J Fluids Eng.* **102**, 92

LIGRANI, P M. & NIVER, R.D 1988 Flow visualization of Dean vortices in a curved channel with 40 to 1 aspect ratio *Phys Fluids.* **31**, 3605.

LOWERY, P.S , & REYNOLDS, W C. 1986 Numerical simulation of a spatially-developing, forced, plane mixing layer Stanford University Rep. TF-26.

MATSSON, O J E. & ALFREDSSON, P H 1990 Curvature and rotation induced instabilities in channel flow *J. Fluid Mech* **210**, 537.

MATSSON, O J E. & ALFREDSSON, P.H. 1991 Experiments on instabilities in curved channel flow. Submitted to *Phys. Fluids* A

PATANKAR, S.V. 1980 *Numerical Heat Transfer and Fluid Flow* McGraw-Hill.

SWEARINGEN, J. D & BLACKWELDER, R. F., The growth and breakdown of streamwise vortices in the presence of a wall *J Fluid Mech.* **182**, 255 (1987)

STUART, J T & DIPRIMA, R C 1978 The Eckhaus and Benjamin-Feir resonance mechanisms *Proc R Soc Lond* A**362**, 27.

YANG, K.S. & KIM J 1991 Numerical investigation of instability and transition in rotating plane Poiseuille flow *Phys Fluids* A **3**, 633

EIGHTH SYMPOSIUM ON
TURBULENT SHEAR FLOWS
Technical University of Munich
September 9-11, 1991

Evolution of Coherent Structures During Transition in a Flat-Plate Boundary Layer

D. Rempfer
Institut für Aerodynamik und Gasdynamik, University of Stuttgart
Stuttgart, Germany

H. Fasel
Department of Aerospace and Mechanical Engineering, University of Arizona
Tucson, Arizona, USA

Abstract

A theoretical investigation is described that attempts to gain additional insight into the later stages of the transition process and initial turbulence in the flat-plate boundary layer. For this purpose the coherent structures of the flow were calculated from the data of a numerical simulation by Rist et al. [10] and the spatio-temporal behaviour of these structures was investigated. The coherent structures were determined using the Proper Orthogonal Decomposition technique (POD) leading to an expansion of the flow field variables into Karhunen-Loève (KL) eigenfunctions. This decomposition was performed in planes normal to the flow direction and in three dimensions. In the two-dimensional case, in addition to the eigenfunctions for the velocity vector the eigenmodes of nonlinear functionals like turbulent production and viscous dissipation were calculated. The three-dimensional KL eigenfunctions are demonstrated to represent the structures seen in experiments.

1 Introduction

The last decades of turbulence research have seen growing interest in the study of coherent structures of turbulent flows. One of the reasons for this interest is the expectation that investigating the dynamical behaviour of the characteristic structures of a turbulent flow might increase our understanding of such flows. It has already been demonstrated [1,8] that certain prominent features of turbulent flow can be represented as the action of coherent structures, and it is hoped that—at least for some flows—the turbulent flow as a whole can be explained in terms of its coherent structures.

Furthermore, three-dimensional coherent structures of a flow can be used as a system of 'natural' eigenmodes along which the Navier-Stokes equations may be projected yielding a system of ordinary differential equations for the dynamical behaviour of these structures [1,12]. If most of the energy of the turbulent flow can be captured by only few of these modes, such a system of ODE's forms a low-dimensional model of the turbulent flow that can be analysed using the well developed tools of dynamical systems theory.

As a first step towards such a low-dimensional model we therefore calculated the coherent structures of the canonical flow over a flat plate. For these calculations, data from the numerical simulation of transition in a flat-plate boundary layer by Rist [9] and Rist et al. [10] were used. In their work, Rist et al. performed a direct Navier-Stokes simulation of the spatial development of an incompressible flow as observed in the experiments on 'controlled' transition by Kachanov et al. [2]. Like Rist in [9], where the details of this simulation can be found, we use the symbols x, y and z for the streamwise, normal and spanwise coordinate, respectively; the corresponding velocity components for the fluctuating flow we are only dealing with in this paper are u, v and w.

From the data generated by the above simulation we only used the values of the velocity vector within a certain three-dimensional window of the computational domain. The region investigated corresponds to a rectangular box 8.85 mm high and 24.5 mm wide in the spanwise direction. In the streamwise direction the box extends from $x = 300$ mm to $x = 500$ mm, with x being the distance from the flat-plate leading edge. With the free-stream velocity of 9.09 m/s the Reynolds-number based on momentum thickness can be calculated as $\mathrm{Re}_{\delta_2} = 283$ at the inflow and $\mathrm{Re}_{\delta_2} = 575$ at the outflow boundary of our domain. Thus the region considered here comprises the stages of the transition process from the beginning three-dimensional, nonlinear development of Tollmien-Schlichting waves up to just beyond the spike stages.

From the data given above it can be inferred that the flow we are considering here certainly does not show fully developed turbulence although certain features of it—like mean-flow profiles—begin to approach the turbulent ones near the end of our domain. On the other hand, as will be shown below, certain processes that we found show striking similarities to events like bursting that are generally

agreed to be of importance in the case of fully developed turbulent boundary layers.

In the next section of this paper, we briefly describe the proper orthogonal decomposition (POD) method we used for the calculation of coherent structures of our flow. We then present a discussion of the structures of the flow within planes perpendicular to the streamwise direction. In section 4 we finally give some of our latest results concerning three-dimensional structures of the flat-plate boundary layer

2 The Proper Orthogonal Decomposition

In connection with the problem of identification of characteristic eddies in a random turbulent flow, Lumley [7] proposed a method for determining coherent structures which is now widely known as Proper Orthogonal Decomposition (POD). We will outline this method briefly in the following.

Before proceeding, a few remarks concerning our prerequisites and the validity of the derivations below are in order. We will confine ourselves to finite regions in space, so that all functions appearing in the formulas below can be viewed as being of finite support and hence, on physical grounds, being square-integrable. Thus, all the integrals used below are well defined in the ordinary Riemannian sense, the integration domain D being a finite region in space. Furthermore, as the simulation that produced our data assumed symmetry of the flow field with respect to the x-y-plane, the fields we are investigating are not homogeneous in the spanwise direction so that the continuous translation group does not apply. Rather the flow field shows distinct qualitative variations with the spanwise coordinate that can be summarised under the term 'peak-valley splitting' [3]. Because of this situation, the POD will yield well-defined structures for the spanwise direction as well and not just sinusoids as in the case of homogeneous directions [12].

In our evaluation of averages we make use of the ergodic hypothesis by substituting time averages for the ensemble averages denoted by $\langle\cdot\rangle$. Finally, the spatial variable $\boldsymbol{x}$ can stand for a one-, two- or three-dimensional vector of any combination of the x-, y-, and z-coordinates. The scalar product $(\cdot,\cdot)$ in the Hilbert-space of square-integrable functions is then defined by

$$(a,b) = \int_D a(\boldsymbol{x}) \cdot b(\boldsymbol{x})\, d\boldsymbol{x}. \tag{1}$$

Suppose now we are given a set of realisations (an ensemble) of some flow field variable $\boldsymbol{u}$ as a function of a coordinate $\boldsymbol{x}$ at different times t_i, $\boldsymbol{u}^i(\boldsymbol{x}) = \boldsymbol{u}(\boldsymbol{x}, t_i)$. What we are looking for is a function $\boldsymbol{\phi}(\boldsymbol{x})$ that is, in some average sense, as similar as possible to the realisations $\boldsymbol{u}^i$. Mathematically this can be expressed as

$$\frac{\langle (\boldsymbol{u}^i, \boldsymbol{\phi})^2 \rangle}{\|\boldsymbol{\phi}\|^2} \stackrel{!}{=} \text{Max.}, \tag{2}$$

where the symbol $\|\cdot\|$ is used for the norm

$$\|\boldsymbol{\phi}\|^2 = (\boldsymbol{\phi}, \boldsymbol{\phi}) \tag{3}$$

in function space. In other words, we are looking for a function $\boldsymbol{\phi}$ whose projection on the flow realisations $\boldsymbol{u}^i$ is maximum in quadratic mean. Using the calculus of variations we can reduce the above problem to the Fredholm integral equation of the second kind

$$\int_D \boldsymbol{R}(\boldsymbol{x}, \boldsymbol{x}') \cdot \boldsymbol{\phi}(\boldsymbol{x}')\, d\boldsymbol{x}' = \lambda \boldsymbol{\phi}(\boldsymbol{x}) \tag{4}$$

representing an eigenvalue problem for the structure $\boldsymbol{\phi}$ (see [7] for details of the derivation). The kernel $\boldsymbol{R}$ of this equation is the autocorrelation function defined by

$$\boldsymbol{R}(\boldsymbol{x}, \boldsymbol{x}') = \langle \boldsymbol{u}(\boldsymbol{x}) \boldsymbol{u}(\boldsymbol{x}') \rangle, \tag{5}$$

where the term inside the brackets denotes a dyadic product. This kernel is symmetric and nonnegative-definite so that from Hilbert-Schmidt theory it follows that Eq. (4) has a denumerable infinite set of solutions $\boldsymbol{\phi}_j$ and corresponding eigenvalues λ_j. Methods for the solution of (4) are described in [7] and in [12] and shall not be dealt with here. The eigenfunctions of (4) are known as 'Karhunen-Loève eigenfunctions' from probability theory [6]. Some of the most important properties of these solutions shall be repeated here.

The different eigenfunctions are orthogonal and can be normalised so that

$$(\boldsymbol{\phi}_j, \boldsymbol{\phi}_k) = \delta_{jk}, \tag{6}$$

where δ_{jk} is the Kronecker-symbol. The flow fields $\boldsymbol{u}^i$ can be expanded in the eigenfunctions via

$$\boldsymbol{u}^i(\boldsymbol{x}, t_i) = \sum_{j=1}^{\infty} \zeta_j(t_i) \boldsymbol{\phi}_j(\boldsymbol{x}), \tag{7}$$

where

$$\zeta_j(t_i) = (\boldsymbol{u}^i, \boldsymbol{\phi}_j). \tag{8}$$

The coefficients in the expansion (7) have the property

$$\langle \zeta_j \zeta_k \rangle = \lambda_j \delta_{jk}, \tag{9}$$

which means that they are uncorrelated with each other and that the eigenvalues of (4) represent the mean square values of the coefficients in equation (7). Thus the eigenvalues of Eq. (4) are nonnegative and are a measure for the importance of

the corresponding structure to the flow. In the following we will make use of this property by defining

$$\Lambda_j = \frac{\lambda_j}{\sum_{k=1}^{\infty} \lambda_k} \tag{10}$$

as the 'activity' of the corresponding coherent structure ϕ_j. Like the eigenvalues, these activities show an exponential decay with their 'quantum number' j.

The most significant property of the decomposition (7) can be seen immediately by comparing (7) and (2). There it becomes clear that the eigenfunctions were chosen such that the convergence of a representation of the flow field is optimally fast in the mean-square. This means that of all possible systems of modes the one described by (4) needs the smallest number of terms to represent the flow field to a given accuracy. Thus, if one is aiming at a low-dimensional description of a turbulent flow via a system of ordinary differential equations, once one has decided that time should be the independent variable of this system of ODE's—which although not being mandatory seems to be a natural choice—the POD delivers an optimum system of eigenfunctions for such a description. Furthermore, apart from an application of its eigenfunctions in models for turbulent flows, the modes of the POD allow to describe the spatial structure of a flow in an optimally compact form.

3 Two-Dimensional Structures

In this section, structures in planes normal to the flow direction shall be discussed. The set of two-dimensional eigenfunctions representing these structures forms a complete decomposition of the flow fields that occur within such planes and thus provides a description of the spatial structure of the flow depending on the streamwise coordinate. In section 2 it has been shown that the POD furnishes a minimum system of eigenmodes in the sense that there is no other set of eigenmodes possible that could capture the structure of the flow using fewer modes than the POD. Therefore, the number of KL eigenfunctions needed for the approximation of the flow fields to a given accuracy can be used as an 'intrinsic' dimension that measures the spatial complexity of these flow fields [13]. As the precise value of this dimension d_{KL} depends on the accuracy prescribed, we will use as an informal definition of d_{KL} the number n of eigenfunctions needed, so that

$$\Lambda_{n+1} \leq 1.0 \cdot 10^{-6}, \tag{11}$$

which means that we require the root mean square error of the KL expansion Eq. (7) to be of the order of 0.1%. We now calculated this 'Karhunen-Loève dimension' for decompositions of the field of the velocity vector u, for the field of the instantaneous turbulent production

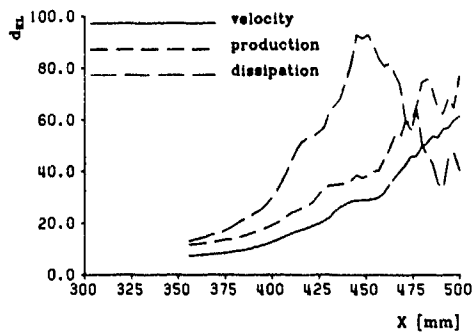

Figure 1: Karhunen-Loève dimension d_{KL} for fields of velocity, turbulent production and viscous dissipation

$$P = -u_i u_j S_{ij}, \tag{12}$$

where S_{ij} is the mean rate of strain,

$$S_{ij} = 1/2 \left(\frac{\partial \langle u_i \rangle}{\partial x_j} + \frac{\partial \langle u_j \rangle}{\partial x_i} \right) \tag{13}$$

and for the field of viscous dissipation

$$E = 2\nu s_{ij} s_{ij}, \tag{14}$$

with s_{ij} denoting the fluctuating rate of strain, defined by

$$s_{ij} = 1/2 \left(\frac{\partial u_i}{\partial x_j} + \frac{\partial u_j}{\partial x_i} \right), \tag{15}$$

where we have made use of the summation convention in the equations above. The results of the calculation of d_{KL} for these fields are shown in Fig. 1. First of all, it can be seen that the spatial complexity of the velocity field rises during the transition process, and the gradient of this increase is almost constant during the last 20% of the domain. The curve for the dimension of the turbulent production field is qualitatively similar to the one of the velocity field with a shift towards somewhat higher values. As turbulent production basically is a product of velocities, a higher complexity of this field was to be expected. In contrast, the behaviour of the decomposition of the field of viscous dissipation does not meet such expectations. After an initial steep increase, the complexity of the dissipation field decreases just behind an x-position corresponding to the beginning of the spike stages [2] and at the end of our domain even seems to be lower than that of the velocity field. And in fact, if the most energetic eigenfunction of dissipation at a location near the maximum of d_{KL} is compared to the one at the end of our domain (Fig. 2) it is found that the latter is significantly less complex in shape. We can

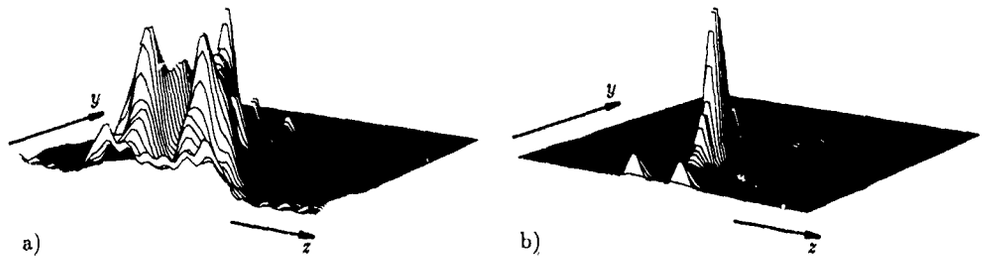

Figure 2: First eigenfunction of viscous dissipation at a) 442 mm b) 500 mm distance from the leading edge.

therefore conclude that just after the spike stages a process of organisation of viscous dissipation sets in This phenomenon seems to be connected to the well-known intermittent character of viscous dissipation [5], as Fig. 3 indicates, where the behaviour in time of the coefficients $\zeta_1(t)$ in Eq. (7) for an expansion of the dissipation field are shown. The

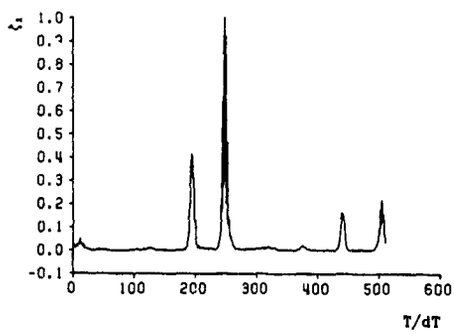

Figure 3. Expansion coefficients $\zeta_1(t)$ for viscous dissipation at $x = 500$ mm.

flow at this position seems to be in a state where highly dissipative structures are embedded in an almost inviscid flow, a situation described by the term 'internal intermittency' [5]. It has been conjectured [5] that such a situation arises due to the action of vortex stretching that created thin filaments of high vorticity and corresponding dissipation. In contrast, the dissipative structure we found is highly localised in the y-z-plane and—judging from the extremely narrow spike in Fig. 3—also in the x-direction, forming something like a 'dissipative blob' rather than a filament. Furthermore, we did not find structures with a behaviour similar to the ones of the dissipation field neither in the velocity nor in the vorticity field. This indicates that the attributes of the dissipative structures we found are due to an interaction of two or more of the structures of the velocity field rather than being a signal of the passage of a single coherent structure possessing special dissipative properties.

The observations above also confirm the prominent role of the spike stages of transition to turbulence. We will therefore discuss the structure of the flow field as captured by the eigenfunctions of the POD in some more detail at a streamwise location of $x = 442$ mm which is at the so-called 'two-spike stage'. Fig. 4 shows the behaviour in time of the

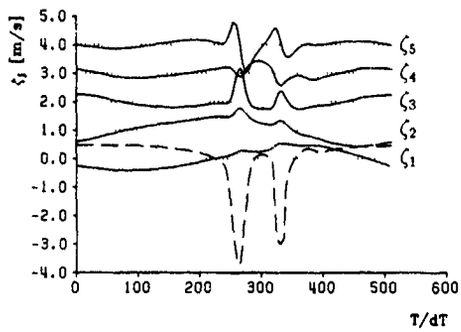

Figure 4: Expansion coefficients $\zeta_j(t)$ and signal of u (dashed line)at $y = 3.11$ mm in the peak plane. Curves of the ζ_j have been shifted in the ordinate as indicated by the dotted lines and were multiplied by the maximum velocity in the y-z-plane of the corresponding eigenfunction.

first five coefficients $\zeta_j(t)$ of the expansion (7) of the velocity field together with the signal of u. Three of these coefficients show a particularly noticeable behaviour simultaneously with the occurence of the spikes. This indicates that the characteristic processes of the spike stage are captured by these three structures which we therefore want to lock at more closely. Since the instantaneous flow field induced by a given eigenfunction ϕ_j is given by $\zeta_j(t)\phi_j(x)$, one can get a precise idea of the events that are responsible for the spikes by combining the information on the coefficients ζ_3, ζ_4 and ζ_5 with the velocity vectors in the y-z-plane as plotted in Fig. 5. The process starts with a movement of fluid towards the peak plane of the boundary layer (5th eigenfunction) that is immediately followed by an intense updraught of fluid away from the wall (3rd eigenfunction). After this motion has settled, a somewhat weaker motion of fluid back towards the wall

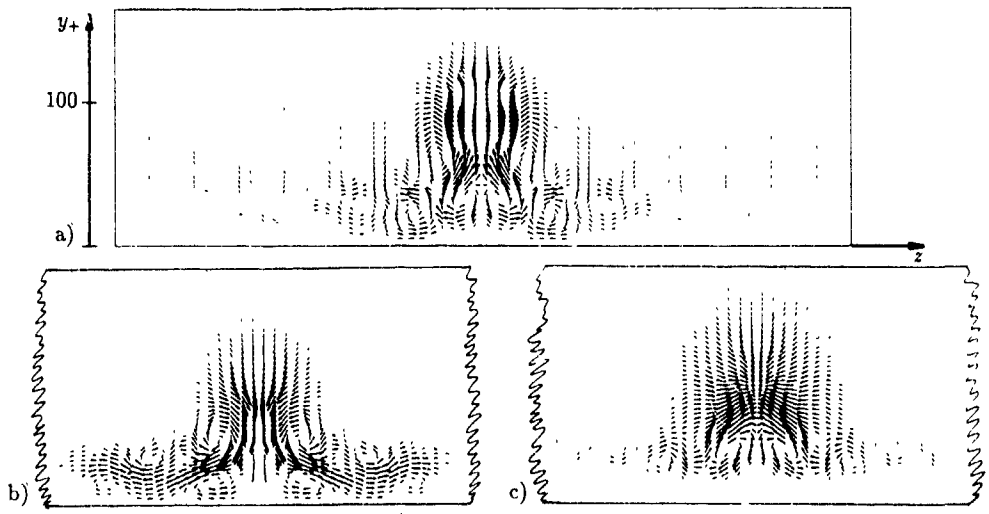

Figure 5: Velocity vectors in y-z-plane for a) 3rd b) 4th c) 5th eigenfunction of velocity field at $x = 442\,\mathrm{mm}$

(4th eigenfunction) follows. This cycle is repeated during the second spike in an only slightly modified fashion.

It has to be noted that the processes described above are taking place within a flow field that is already disturbed by the flows that are represented by the eigenfunctions 1 and 2. Thus it would have been difficult to get a clear picture of what happens during a spike by just looking at the instantaneous fields of the complete flow.

Finally we would like to draw attention to the striking similarity of the events during a spike as described above to the characterisations of the 'bursting-event' that can be found in the literature [4,11]. The fluid motions that are being described by the third eigenfunction correspond to the descriptions given of the 'ejection-phase' of the bursting event, and the ones described by the fourth eigenfunction are very similar to what is reported on the 'sweep-phase' of the bursting phenomenon.

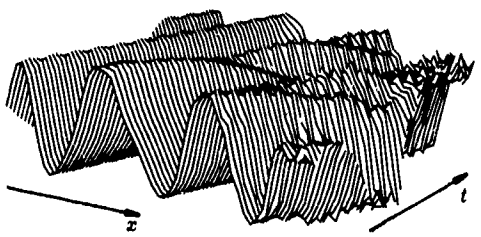

Figure 6: Coefficient $\zeta_1(t)$ of velocity decomposition at different streamwise locations

$\lambda_1 = 4.1 \cdot 10^{-7}$	$\lambda_3 = 4.5 \cdot 10^{-8}$	$\lambda_5 = 8.2 \cdot 10^{-9}$
$\lambda_2 = 3.9 \cdot 10^{-7}$	$\lambda_4 = 4.4 \cdot 10^{-8}$	$\lambda_6 = 8.0 \cdot 10^{-9}$

Table 1: Eigenvalues of three-dimensional POD

4 Three-Dimensional Structures

In Fig. 6 we show a plot of the time behaviour of the coefficient $\zeta_1(t)$ of an expansion of the 2D velocity flow fields within planes normal to the flow at different streamwise locations. Although the two-dimensional structures have been calculated independently at the different positions there is obviously a coherence of the behaviour of the 2D-structures in the streamwise direction as well. The ζ_1-coefficient appears to be a simple wave travelling in the streamwise direction. This observation suggests that the structures found within the cross-stream planes are due to the passage of three-dimensional coherent structures. To find these structures, we solved Eq. (4) for the three-dimensional velocity field within different regions of the domain covered by our data. In the following we will show some results for a region starting at $x = 369\,\mathrm{mm}$, being 69 mm long, 8.1 mm high and 24.5 mm wide. In Table 1 the first six of the eigenvalues of (4) are given. What is noticeable about these eigenvalues is that they occur in pairs of almost equal value. Looking at the eigenfunctions of such a pair one finds that these are approximately two realisations of the same structure that are phase shifted in the x-direction. Also, the coefficients $\zeta(t)$ of an expansion of the flow field into such pairs of functions are analogously phase

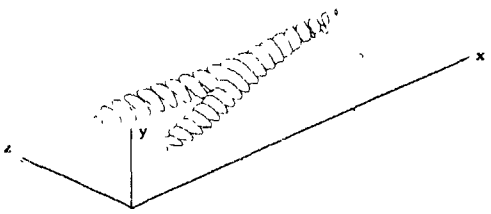

Figure 7: First 3D coherent structure between $x=369$ mm and $x=438$ mm. Shown is a contour surface of the u-velocity component.

shifted in time. This behaviour is a consequence of the convective character of the spatially developing boundary layer. If coherent structures exist in such a flow, these are transported downstream, additionally being deformed as they move From the pairs of eigenfunctions the POD yields, the actual coherent structure can be reconstructed at any instant by multiplying the eigenfunctions of a pair by their corresponding coefficient ζ and adding them. Thus such a pair of eigenfunctions does not only contain complete information about the shape of the coherent structure but also shows the evolution such a structure undergoes while moving downstream. An example of such a coherent structure as calculated by the POD is shown in Fig. 7. This structure clearly shows the shape of the well-known lambda-vortex demonstrating that the POD indeed can yield the coherent structures that have been identified in the experiment.

5 Conclusions

In this paper we have shown that the POD can be employed as a useful tool to organise the information present in complex flow fields. From the eigenvalues of this decomposition the evolution of complexity in a transitional flow can be deduced and the eigenfunctions show the spatial structures present in the flow. Phenomena like internal intermittency and 'bursting'-like processes are captured in an intuitively satisfying way by a representation of the flow field using Karhunen-Loève eigenfunctions. Our investigations show a similarity between transitional structures and those found in fully developed turbulent flows. The detailed analogies between the two suggest corresponding similarities in the underlying mechanisms. The three-dimensional structures calculated by the POD are similar to experimentally observed ones, like the 'lambda-vortex'. These structures are represented by the POD as a pair of eigenfunctions that shows the structure of the corresponding 'characteristic eddy' as well as its spatial evolution.

It can be easily shown [12] that the three-dimensional structures of the POD constitute a complete set of orthogonal eigenfunctions each of which satisfies all of the boundary conditions of the problem. In the case of incompressible flow, each of the eigenfunctions represents a solenoidal vector field satisfying the continuity equation As a next step, we have therefore started to construct a low-dimensional model of our flow via Galerkin-projection of the Navier-Stokes equations. This way we hope to be able to find out to what extent the ideas of deterministic chaos are relevant to the flow phenomena at the onset of turbulence in the flat-plate boundary layer.

Acknowledgements

This research was supported by a grant of Studienstiftung des deutschen Volkes, Germany and by the Office of Naval Research, USA.

References

[1] AUBRY, N.; HOLMES, P.; LUMLEY, J. L.; STONE, E. 1988 The Dynamics of Coherent Structures in the Wall Region of a Turbulent Boundary Layer. *J. Fluid Mech.*, **192**, 115–173.

[2] KACHANOV, Y. S.; KOZLOV, V. V.; LEVCHENKO, V. Y.; RAMAZANOV, M. P. 1985 On Nature of K-Breakdown of a Laminar Boundary-Layer. New Experimental Data. In *Laminar-Turbulent Transition*. (ed. V. V. Kozlov), 61–73. Springer.

[3] KLEBANOFF, P. S.; TIDSTROMM, K. D.; SARGENT, L. M. 1962 The Three-Dimensional Nature of Boundary-Layer Instability. *J. Fluid Mech.*, **12**, 1–34.

[4] KIM, H. T.; KLINE, S. J.; REYNOLDS, W. C. 1971 The Production of Turbulence Near a Smooth Wall in a Turbulent Boundary Layer. *J. Fluid Mech.*, **50**, part 1, 133–160.

[5] LESIEUR, M. 1990 *Turbulence in Fluids* Kluwer Academic Publishers.

[6] LOÈVE, M. 1955 *Probability Theory*. Van Nostrand.

[7] LUMLEY, J. L. 1970 *Stochastic Tools in Turbulence*. Academic Press.

[8] MOIN, P.; MOSER, R. D. 1989 Characteristic-Eddy Decomposition of Turbulence in a Channel. *J. Fluid Mech.*, **200**, 471–509.

[9] RIST, U. 1990 Numerische Untersuchungen der räumlichen, dreidimensionalen Strömungsentwicklung beim Grenzschichtumschlag. Dissertation, University of Stuttgart.

[10] RIST, U.; KLOKER, M.; FASEL, H. 1991 Numerical Simulation of Transition in a Flat Plate Boundary Layer. (submitted for publication in JFM).

[11] ROBINSON, S. K. 1991 Coherent Motions in the Turbulent Boundary Layer. *Ann. Rev. Fluid Mech.*, **23**, 601–639.

[12] SIROVICH, L. 1987 Turbulence and the Dynamics of Coherent Structures. *Quart. Appl. Math.*, **45**, 561–590.

[13] SIROVICH, L. 1989 Chaotic Dynamics of Coherent Structures. *Physica D*, **37**, 126–145.

EIGHTH SYMPOSIUM ON
TURBULENT SHEAR FLOWS
Technical University of Munich
September 9-11, 1991

INFLUENCE OF SUCTION THROUGH A SLOT ON A TURBULENT BOUNDARY LAYER

G. PAILHAS* - J. COUSTEIX* - F. ANSELMET** - L. FULACHIER**

* ONERA/CERT - Aerothermodynamics Department
2 avenue E. Belin - 31055 TOULOUSE Cedex (FRANCE)

** Institut de Mécanique Statistique de la Turbulence
Unité Mixte 380033 - Univ D'AIX-MARSEILLE II CNRS
12 avenue du Général Leclerc - 13003 MARSEILLE (FRANCE)

ABSTRACT

The goal of the study is to analyze the effects of slot suction on a turbulent boundary layer and the relaxation of the flow downstream of the slots

The present study is also devoted to the understanding of the bursting phenomenon occurring in a boundary layer the turbulence of which is manipulated by localised suction

Two experiments are presented One of them, in a water tunnel, is concerned with visualisations and measurements of mainly mean velocity with laser Doppler anemometry The other one is carried out in a wind tunnel, by means of hot wire anemometry, with one or several slots, in order to mostly determine the influence of suction on velocity fluctuations and their correlation A spectral analysis has also been made.

In order to educe the general effect of suction on the coherent structures, a conditional analysis has been performed.

I INTRODUCTION

The effectiveness of various devices for turbulence control in wall flows has motivated many studies over the last years (Bushnell and McGinley, (1989)), in particular for applications in aeronautics, with the view of reducing the drag of the aircraft

If the Reynolds number is large, so that the boundary layer is turbulent, we have to interfere on the structure of the turbulence

Among the various devices used in this way riblets or lebus are mainly attractive because of their ability in reducing drag when the flow is turbulent

The intrusion of such devices in the boundary layer contributes to the modification of the structure of the turbulence in the inner or outer part of it. So, the natural interaction between these two regions is modified and consequently the exchange and production phenomena of turbulent energy are affected

A local suction applied on a turbulent boundary layer, not with the view of resorbing it, but of modifying its structure, deserves to be analyzed.

Moreover, suction seems mostly active for delaying transition (laminar flow control) or for attempting at avoiding the development of parasitic vortices.

In the case of a swept wing, for instance, the boundary layer which develops on the fuselage contaminates the wing leading edge : turbulent spots are created and their spreading along the swept wing is such that the boundary layer on it is turbulent from the leading edge ; it seems that sucking the fuselage wall flow through a slot may be a way to reduce this shortcoming.

The effects of a localised suction on a boundary layer developing on a flat plate are investigated in the present experimental study.

The effects of suction have been studied on the mean and turbulent velocity fields, on the turbulent kinetic energy production and on the spectral distribution of energy

Finally, a conditional analysis is performed with the view of educing the general effect of suction on the coherent structures in the inner region of the boundary layer

II PRELIMINARY STUDY

A preliminary study has been carried out in the IMST water tunnel ($20 \times 20 \times 120\ cm^3$), in order to perform visualisations and measurements of mainly the longitudinal mean velocity, with laser-Doppler anemometry. A metallic plate made of specially treated stainless steel has been installed in one of the vertical walls of the tunnel, within which a 1.5 mm wide slot, spanning 120 mm and inclined at 45° relative to the mean flow direction, has been cut

Visualisations showed that when the slot is orientated in the same way as the flow, the boundary layer is disturbed even with no suction (scheme (a)) ; so, the slot has been positioned so that the suction occurs in the opposite direction of the flow (scheme (b))

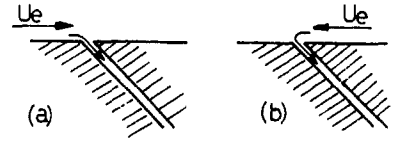

At the station where the slot is located, the fully developed turbulent boundary layer (tripped by three-dimensional roughness elements) is such that its thickness δ is about 4 cm when the freestream velocity U_e is $15.5\ cms^{-1}$; the Reynolds number R_θ , based on the momentum thickness, is about 600 The most commonly used suction rate $A = -V_p/U_e$ (defined as the ratio of suction velocity to the freestream velocity) is 0.23.

The influence of suction on mean longitudinal velocity profiles has been investigated in the water tunnel with LDA. This allows us to perform measurements in the wall vicinity ($y^+ = yu^*/\nu \sim 2$, for $A = 0$, u^* being the friction velocity) without any wall correction. The skin friction values are inferred from the slopes of velocity profiles at the wall. Figure 1 gives an example of distributions obtained with and without suction at the distance $X = 10$ mm (0.4δ) from the slot With no suction, the standard law of the wall is obtained It must be noticed that the wake region is practically non-existent and the logarithmic law is limited to a narrow range of y^+ since the Reynolds number is small.

With suction, an effect similar to that obtained over a porous wall is observed in the region corresponding to the logarithmic law of the velocity profile with no suction. But this effect is of course not similar to that obtained with the suction rate A, estimated from the actual suction velocity V_p through the slot, but with a fictive suction rate $\tilde{A}$ much lower than A We have calculated this suction rate $\tilde{A} = -\tilde{V}_p/U_e$ -where $\tilde{V}_p$ is the equivalent suction velocity that would be applied

through a porous wall- fitting a pseudo-velocity law in the wall region (Verollet et al (1977))

$$\frac{2}{\tilde{A}^+}\left[1 - \left(1 - \tilde{A}^+U^+\right)^{1/2}\right] = U_0^+ = 5.75 \log y^+ + 5.24$$

$\tilde{A}^+ = -\tilde{V}_p/u^*$ is the equivalent suction rate relative to the wall friction velocity ; $U^+ = U/u^*$ is the mean velocity relative to u^* with suction and $U_0^+ = U/u_0^*$ without suction From fig 1, one gets the equivalent suction rate $\tilde{A}^+ = 0.058$, which is much lower than that actually applied through the slot $A^+ = 3.2$. As far as the viscous sublayer is concerned, it seems the law $U^+ = y^+$ is still valid, but with a friction velocity ($u^* = 1.09\ ms^{-1}$) larger than the one ($u_0^* = 0.86\ ms^{-1}$) corresponding to the case without suction.

A similar study has been performed further downstream of the slot ($X = 75$ mm $\approx 2.7\delta$) An effect on the mean velocity profile is still noticeable and quite important over the boundary layer ; however, close to the wall, there is almost no modification due to suction

The aim of this preliminary study was particularly to assess the effect of the width and orientation of the slot, with and without suction, on the flow.

The influence of suction on mean and turbulent velocities fields has been mostly investigated in a CERT wind tunnel

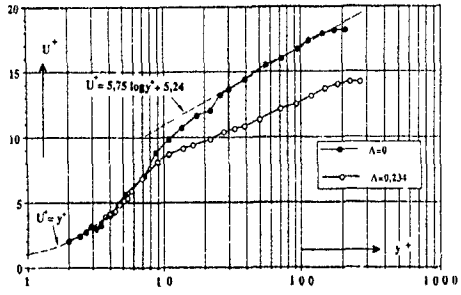

Fig. 1 - Influence of suction on the mean velocity in the water channel (X=0,4 δ ; 1 slot)

III EXPERIMENTAL SET-UP AND MEASURING TECHNIQUES

The most detailed study which includes the use of several slots, has been performed in a EIFFEL-type wind tunnel ($30 \times 40 \times 120\ cm^3$) ; the experimental set-up is given figure 2. On the test section floor, a 1 mm wide slot, spanning 200 mm and inclined at 45° relative to the mean flow direction, (as required from the preliminary study) has been located. The experimental device allows that 2 or 3 slots are added upstream of the previous one in such a way that the distance between the last slot and a fixed measurement station remains constant whatever the number of slots. The suction rate is precisely adjusted with the help of a sonic flow-meter

Measurements are mainly carried out with one single slot, but also with three or four slots ; the streamwise spacing between two consecutive slots is 11.5 mm ($\approx 0.58\delta$). The boundary layer which develops on the test section floor is fully turbulent in the area where slots are located ; $U_e = 20 ms^{-1}$, $\delta \approx 2$ cm, $R_\theta \approx 3\,500$.

The boundary layer has been probed at various X-stations downstream of the slots using hot-wire constant temperature anemometry.

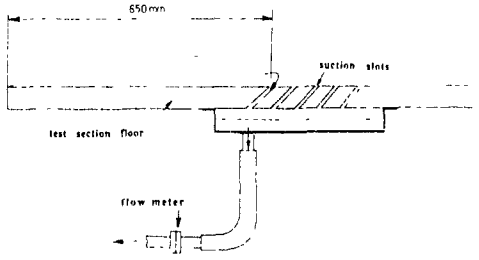

Fig 2 - Experimental set-up

IV EXPERIMENTAL RESULTS

IV 1 Selection of the suction mode

Figure 3 shows, at the distance $X = 10$ mm (0.5δ) downstream of the slot, the evolution of u'^+ (u'^+ being the ratio of the standard deviation $\sqrt{\overline{u'^2}}$ of streamwise velocity fluctuation u' to the friction velocity u_0^* without suction ; $u'^+ = \sqrt{\overline{u'^2}}/u_0^*$) in the vicinity of the wall for various suction rates.

One can notice (at the measurement station near the slot) that a quasi asymptotic state is reached quite quickly, in spite of an increasing suction rate.

Beyond a suction rate $A = 0.7$, the wall suction does not play an important role on the turbulence any longer

At the farthest measurement station ($X = 5\delta$), the u'^+ profiles superimpose each other for distances y^+ to the wall below 100

So, in the present experiment, the suction rate which was chosen is 0.70, corresponding to a suction velocity through the slot of $14\ ms^{-1}$ and a freestream velocity of $20\ ms^{-1}$.

Close to the wall -at $y^+ = 15$-, where the maximum of turbulence production is roughly located, it is shown (figure 4) that with respect to the station upstream of the slot ($X = -0.25\delta$) corresponding to the no suction case, u'^+ is decreasing with X in the close vicinity of the slot (up to values of $X = 0.5\delta$) and then increasing to values larger than that obtained without suction.

This evolution of the longitudinal turbulent fluctuation velocity considered close to the wall, at a constant value of y^+ ($y^+ = 15$, for example) and relating to various X measurements in the vicinity of the slot, reflects the fact that, in this area, the shear stress is very important, due to the suction effect, and the phenomenon of turbulent energy production is probably modified, being constantly renewed

Due to the turbulence relaxation effect which seems to occur at a distance $\delta/2$ downstream of the slot, the experimental device has been modified ; several slots have been located on the test section wall, the spacing of which being adjustable.

In configuration with several slots, the suction rate $A = 0.7$ is applied to each slot so that the quantity of flow sucked up through 3 slots for example, is three times greater than the one corresponding to one slot.

Then, experiments have been performed for various configurations obtained in varying the number of slots and their spacing ; the influence of these two parameters on the turbulence especially has been widely investigated.

Owing to the behaviour of u'^+, in the vicinity of the slot ($X < 0.75\delta$) depicted on figure 4, the slots have been, at first, fitted on the wall with a spacing of order $\delta/2$. However, this configuration is not the one providing the most significant results.

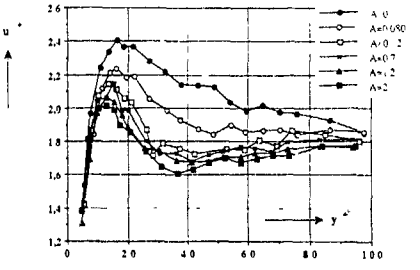

Fig. 3 - Influence of suction on turbulence (x=.5δ ; 1 slot)

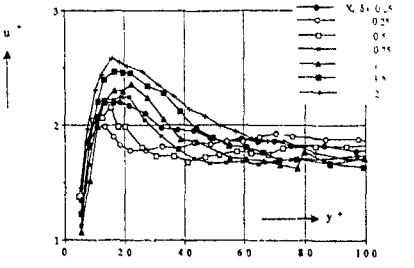

Fig. 4 - Longitudinal evolution of near wall turbulence (A=.7 ; 1 slot)

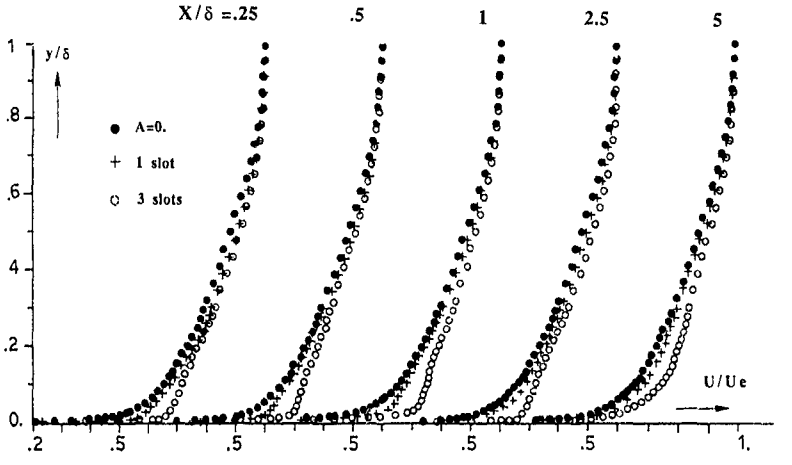

Fig. 5 - Longitudinal mean velocity profiles

In fact, suction effects are more sensitive when the experimental device is fitted with 3 slots, the distance between each one being about 1 7δ.

We present in this paper a comparison of results inferred from experimental configurations with suction, by means of 1 or 3 slots, and those from the reference configuration (that is to say without suction)

IV 2 Influence of suction on the longitudinal mean velocity

Figure 5 shows the evolution of the longitudinal component of the mean velocity when 1 or 3 slots are respectively working and when no suction is applied.

It can be noted that suction increases notably the mean velocity in the inner region of the boundary layer

The velocity profile relating to 3 slots is more affected by suction than the other one where suction is active through one slot only

Moreover, the spreading of the disturbed area in the boundary layer is noticed when the distance downstream of the slot (or of the last slot) increases

At the last measurement station (X = 5δ), the suction effect (when the experimental set-up is fitted with 3 slots) is still very pronounced

IV 3 Effect of suction on $\overline{u'v'}$

The suction effect on $\overline{u'v'}$ is very strong in the inner wall region ; the quantity $\overline{u'v'}/U_e^2$, the value of which attains about $1\,8\,10^{-3}$ when there is no suction ($3\,10^{-3}$ corresponding approximately to the skin friction coefficient deduced from the logarithmic law of the velocity profile), decreases dramatically and has a local minimum below $5\,10^{-3}$, at the first measurement station when suction is applied

At the downstream measurement stations, in the inner wall region $\overline{u'v'}$ recovers quickly its level without suction Then, there is a spreading of the area where $\overline{u'v'}$ is disturbed by suction ($0.05 < y/\delta < 0\,3$ for $X = 1\delta$ - Fig 6) and then disturbances reach all the boundary layer thickness. As a matter of fact, the disturbance on the $\overline{u'v'}$ profile first appears in the inner wall region and propagates in the whole inner region of the boundary layer ; after that, the propagation attains the outer part of the boundary layer.

In a general way, it appears that the evolution of $\overline{u'v'}$ with suction is similar to longitudinal or transverse fluctuation velocity one However the behaviour of the correlation coefficient (with suction) given in figure 7 shows that the decrease of $\overline{u'v'}$ near the wall is certainly closely linked to a strong decorrelation between u' and v' fluctuations. This means that the structure of turbulence is affected.

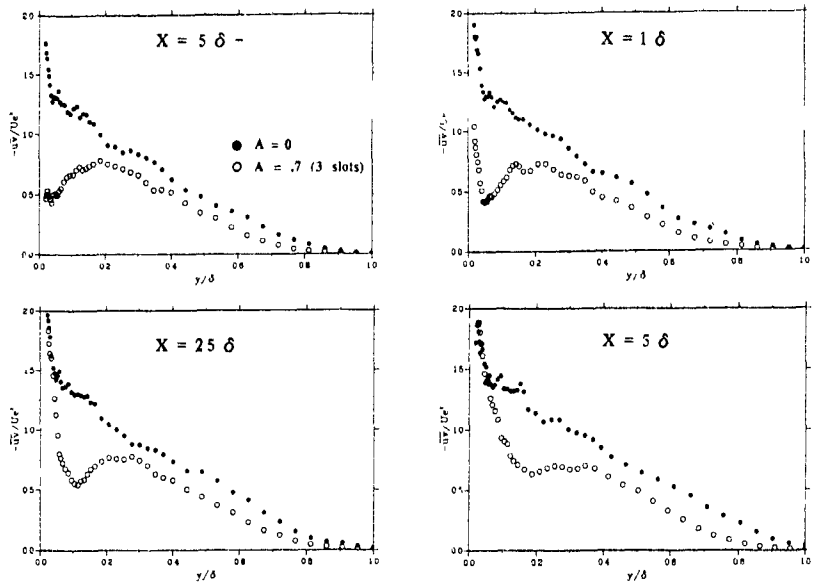

Fig. 6 - Effect of suction on $\bar{u'v'}$

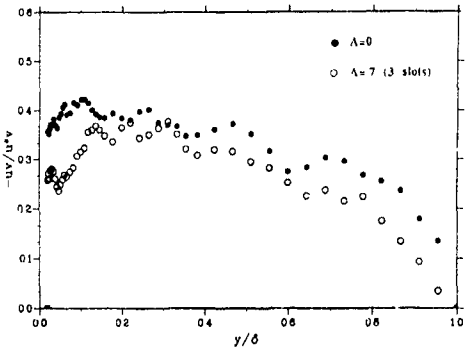

Fig. 7 - Correlation coefficient (X=1δ)

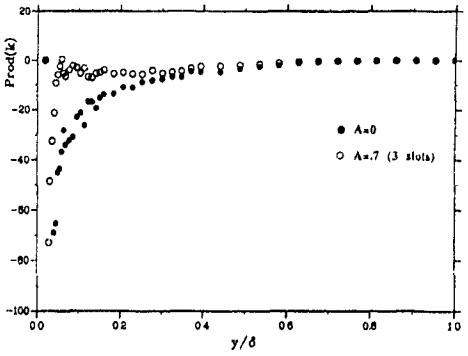

Fig. 8 - Turbulent kinetic energy production (X=1δ)

IV 4 u'v' and k production

Figure 8 gives the turbulent kinetic production at the measurement station located one boundary layer thickness behind the last slot.

In the inner part of the boundary layer, the production of turbulent kinetic energy is strongly reduced (being approximately zero above $y/\delta = 0.1$) with suction. In the inner wall region ($y/\delta < 0.05$), the production of k does not seem to be disturbed by suction. This is not an unexpected result, reminding u'v' and mean velocity behaviours (previously depicted) with suction.

The r m s value $\sqrt{\overline{v'^2}}$ of the transverse fluctuation velocity associated to the mean derivative $\frac{\partial U}{\partial y}$ is the main term in the expression of $\overline{u'v'}$ production.

The evolution of $\overline{u'v'}$ production ($P_{u'v'} = \overline{u'^2}\frac{\partial V}{\partial x} + \overline{v'^2}\frac{\partial U}{\partial y}$) across the boundary layer is similar to the k production one.

It can be mentioned that, even with suction, the production of k and the production of u'v' behave in the same way and have the same order of magnitude.

IV 5 Spectral analysis

A spectr l analysis, at one measurement station, has been made in order to establish the frequency distribution of the two fluctuation velocities u' and v' submitted to the suction effect. figure 9 gives the normalized spectra of u' and v' (in a fF(f) representation) at the measurement station located one boundary layer thickness downstream of the last slot.

On the u' as well as on the v fluctuation, suction seems to have virtually no effect on their frequency distribution in spite of an important variation of $\sqrt{\overline{u'^2}}/U_e$ and $\sqrt{\overline{v'^2}}/U_e$ when suction is applied

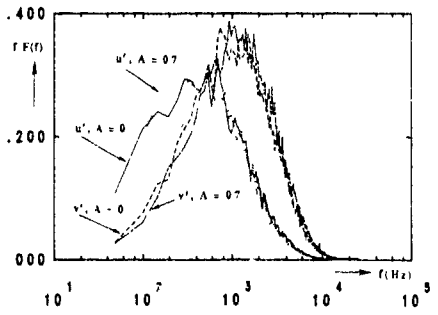

Fig 9 - Streamwise and transverse fluctuations spectra (X=1δ ; y=.05δ)

This result is fundamentally different from that obtained with a porous wall where spectra are clearly shifted towards low frequencies (Ref 6)

The co-spectra fE(f) of the quantity $\overline{u'v'}$ ($\int fE(f)\,df = R_{uv}$) are given on figure 10

These co-spectra confirm the strong reduction of the correlation coefficient (as previously mentioned) when the boundary layer is disturbed by suction

From spectral density information, it could be deduced the coherence function related to u' and v' fluctuations (figure 11)

The loss of coherence at the lower frequencies (when suction is working), probably reflects the fact that bigger structures in the boundary layer are essentially affected by suction ; so, the strong decorrelation between the two fluctuating components of the velocity is clearly pointed out.

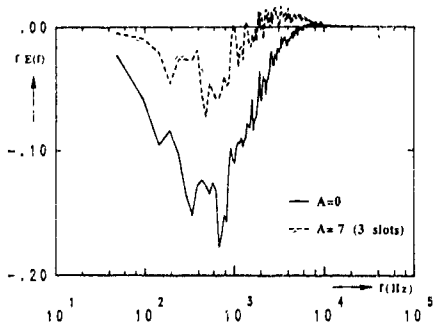

Fig. 10 - $\overline{u'v'}$ co-spectra (X=1δ ; y=.05δ)

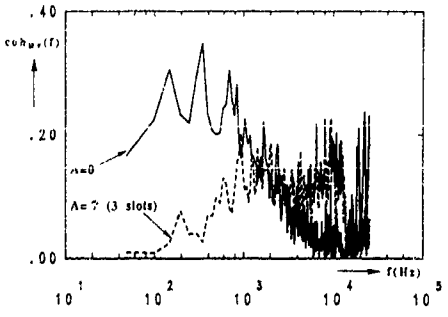

Fig. 11 - Coherence function

IV 6 Conditional analysis

In order to educe the general effect of suction on the coherent structures of the boundary layer, the quadrant method as advocated by Boggard and Tiedermann (Ref 3), Alfredson and Johanson (Ref 1), has been applied to analyse the u' and v' fluctuations

It can be briefly reminded the mechanism occurring in a boundary layer and giving rise to the turbulence phenomenon According to the scheme given by Kline et al (Ref. 8), thin strips of flow develop in the inner region of the boundary layer ($y^+ < 40$) ; strips, the velocity of which is lower, rise towards the outer part of the boundary layer ; then, it can be observed a strong oscillation leading to the breakdown of the structure ; correlatively high velocity flow from the outer part of the boundary layer moves towards the wall and "sweeps" it

The occurrence on the boundary layer successively composed of rising , ejection and breakdown is called "bursting" ; this phenomenon schematically depicted is the main responsible of turbulence production in the boundary layer

The aim of the quadrant method is to assign to various quadrants the instantaneous u' and v' fluctuations velocity according to their sign.

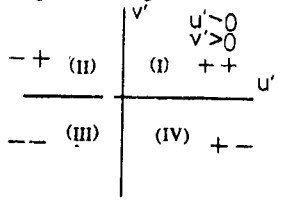

Boggard and Tiedermann showed that quadrant technique was the most effective detector of ejections occurring in the second-quadrant u'v' where u' is negative and v' positive

We present, in this paper, results relating to only one measurement station ($X = 1\delta$, $y/\delta = 0.05$), this conditional investigation being in progress.

The following data table gives an example of the measured values of the correlation u'v' normalized with the total r.m.s. values $\sqrt{\overline{u'^2}}$ and $\sqrt{\overline{v'^2}}$ affected to the corresponding quadrant ; the percentage in time of u'v' contribution in each quadrant is also given with and without suction

	X = 1δ				Y = 0.05δ			
A	$\frac{\overline{u'^+v'^+}}{\sqrt{\overline{u^2}}\sqrt{\overline{v^2}}}$	T++	$\frac{\overline{u^-v^+}}{\sqrt{\overline{u'^2}}\sqrt{\overline{v'^2}}}$	T -+	$\frac{\overline{u^-v^-}}{\sqrt{\overline{u^2}}\sqrt{\overline{v^2}}}$	T	$\frac{\overline{u^+v'}}{\sqrt{\overline{u^2}}\sqrt{\overline{v^2}}}$	T+
0	0.07	19	0.31	31	0.07	18	-0.22	32
0.7	0.14	25	0.22	25	0.14	25	0.14	25

For example, $\overline{u'^+v'^+}$ represents the correlation of the velocity fluctuations relating to quadrant (I), T^{++} represents the percentage in time of $u'^+v'^+$ contribution to the quadrant (I), i.e the ratio of the occurrence time of $u'^+v'^+$ to the total time.

It can be noted that the contributions to the correlation coefficient R_{uv} are significantly modified by suction ; the decrease of $|R_{uv}|$ is due to both a reduction of contribution from quadrants (II) and (IV) and an increase of those from quadrants (I) and (III) ; the least affected quadrant is quadrant (II)

corresponding to ejection ; a similar trend is observed for the distribution of occupation time Without suction, contributions from quadrant (II) and (IV) corresponding to ejection and sweep motion respectively, are practically equal and significantly larger than those from quadrants (I) and (III) ; this is underlining the organisation of the flow On the other hand, with suction, the occupation times relative to the four quadrants are equal, suggesting that organized motions are strongly affected, resulting in the attenuation of their contribution to the flow dynamics

The iso-probability curves with suction are symmetric with regards to α ($\alpha = u'/\sqrt{\overline{u'^2}}$) and β ($\beta = v'/\sqrt{\overline{v'^2}}$) confirming the equi-distribution of occupation time in all quadrants

The correlation coefficient can be expressed from the joint probability density function $P(\alpha, \beta)$ associated with the pair of random variables α and β

$$R_{uv} = \iint_{-\infty}^{+\infty} \alpha\beta\, P(\alpha, \beta)\, d\alpha d\beta$$

Figure 12 shows the iso-contours of $\alpha\beta\ P(\alpha, \beta)$ revealing the contribution to the correlation coefficient from each of the four quadrants ; it clearly shows the decrease of the covariance term R_{uv} that results mainly from the attenuation of quadrants (II) and (IV) and the enhancement of the quadrants (I) and (III)

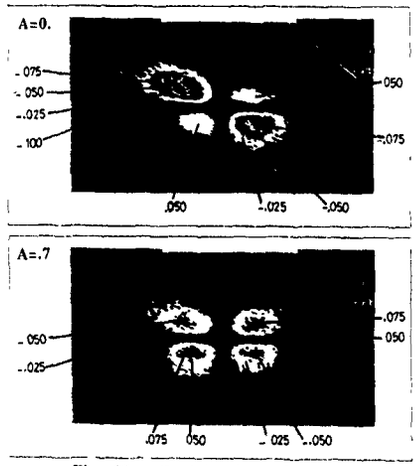

Fig. 12 - Contribution of the correlation coefficient in the four quadrants

CONCLUSION

The experimental study which has been undertaken is devoted to the control of the turbulence, in a turbulent boundary layer, by means of localised wall suction Measurements have been performed on the test section floor fitted with one or three slots

It could be noticed the increase of the mean velocities in the vicinity of the wall when suction is applied

With slot suction, the standard deviations of longitudinal and transverse velocity fluctuations are mainly modified in a region close to the wall ; however suction effects very close to the wall are not as important as those relative to a porous wall where suction is continuously applied.

The longitudinal component of the shear stress $\overline{u'v'}$ is strongly affected by suction in the inner wall region ; there is a spreading of the disturbed area when X increases in such a way that disturbances reach all the boundary layer thickness

In fact, disturbances generated by suction, on the Reynolds stress tensor components, first appear in the inner wall region of the boundary layer ; quickly, the whole inner region is concerned by suction effects ; after that, the propagation attains the outer part of the boundary layer

However, in the inner wall region, the Reynolds stress tensor components u'^2, v'^2 and $u'v'$ affected by suction (in the vicinity of the suction area) recover quite rapidly, one half boundary layer thickness downstream the slot, their level without suction

A spectral analysis has revealed that the frequency distribution of u' and v' fluctuations did not seem to be disturbed by suction as it occurred in the case of a porous wall The co-spectrum of $u'v'$ has confirmed the strong reduction of the correlation coefficient whereas coherence investigation pointed out the strong decorrelation between the two fluctuating components of the velocity and the main effect of suction on the bigger structures inside the boundary layer

A conditional analysis by means of a quadrant method has been undertaken From the first results, (this analysis being in progress), it could be observed that the occurrence time of $u'v'$ in each quadrant is strongly disordered by suction in the inner wall region

This conditional analysis will probably allow us to better understand the suction effect on the boundary layer structure close and far from the section area In particular, conditional information will allow us to analyse effect of suction on the bursting phenomenon.

Finally a space time correlation analysis of the u' and v' fluctuation at various y-locations in the boundary layer would allow us to clearly define if the outer part of the boundary layer is submitted to suction effects in the same way as the inner one ; propagation of disturbances from the latter region to the former one would then be detected and analysed

REFERENCES

[1] ALFREDSON P H., JOHANSSON A.Y , On the detection of turbulence-generating events, 1984, J F.M 139, 325-345

[2] ANTONIA R A., FULACHIER L , KRISHNAMOORTHY L.V , BENABID T., ANSELMET F , Influence of wall suction on the organized motion in a turbulent boundary layer, 1988,J.F.M 190, 217-240

[3] BOGGARD D G., TIEDERMAN W G., Characteristics of ejections in turbulent channel flow, 1987,J F.M. 179

[4] BUSHNELL D.M , McGINLEY C.B., Turbulence control in wall flows, 1989, Ann Rev Fluid Mech., 21, 1-20

[5] FAVRE A , DUMAS R , VEROLLET E , COANTIC M., Couche limite turbulente sur paroi poreuse avec aspiration, 1966, J de Mécanique 5, 1, 3-28

[6] FULACHIER L., Contribution à l'étude des analogies des champs dynamique et thermique dans une couche limite turbulente - Effet de l'aspiration, 1972, Thèse

[7] FULACHIER L , VEROLLET E , DEKEYSER I , 1977, Résultats expérimentaux concernant une couche limite turbulente avec aspiration et chauffage à la paroi, 1977, Int. J. Heat and Mass Transfer 20, 7, 731-739

[8] KLINE S.J., REYNOLDS W C , SCHRAUB F.A., RUNSTADLER P W , The structure of turbulent boundary layer, 1967, J F M 30

[9] VEROLLET E , FULACHIER L , DEKEYSER I., 1977, Int J Heat and Mass Transfer. 20, 2, 107-112

EIGHTH SYMPOSIUM ON
TURBULENT SHEAR FLOWS
Technical University of Munich
September 9-11, 1991

EXPERIMENTAL AND NUMERICAL INVESTIGATION OF A TURBULENT BOUNDARY LAYER OVER RIBLETS.

M. BENHALILOU, F. ANSELMET, J. LIANDRAT, L. FULACHIER

Institut de Mécanique Statistique de la Turbulence
Unité Mixte N° 380033 Université d' Aix-Marseille II / C.N.R.S.
12, Avenue du Général Leclerc, 13003 Marseille, France.

ABSTRACT

The effect of triangular riblets on a turbulent boundary layer is investigated both experimentally and numerically. Measurements are performed in a water tunnel with laser-Doppler velocimetry extending within the grooves: mean values and Reynolds stresses relative to the longitudinal and spanwise velocity components are presented. Numerical predictions, assuming that the mean spanwise velocity is zero, are developed with a mixing length model.

INTRODUCTION

It has now been widely demonstrated that turbulent skin friction drag can be reduced, by about 6-8 % under a variety of flow conditions, with a modified wall geometry in the form of continuous uniform U- or V-profile longitudinal surface grooves or riblets.

Extensive experimental studies (Bushnell (1985), Coustols (1989), Squire and Savill (1987), Walsh and Lindemann (1984)) have been concerned with drag estimates from global measurements in order to determine the most effective riblet geometry and dimensions under various flow conditions. Triangular grooves with $h^+ \approx 15$ and $h^+ < s^+ < 3h^+$ (where h denotes the rib height, s the spacing between two adjacent grooves, and $h^+ = hu^*/\nu$, with u^* the friction velocity and ν the kinematic viscosity) are effective for both low-speed and transsonic flows. From more detailed measurements, Choi (1989) has shown that the restriction of spanwise movement of the longitudinal vortices is a prime mechanism for the turbulent drag reduction. Nevertheless, the influence of riblets on the bursting process seems quite weak and results from various authors relative to the variation of the burst frequency are conflicting. Thus, the physical mechanism responsible for the turbulent flow stabilisation is still quite unclear and not sufficient for providing strong enough guidelines for the development of accurate modelisations. Recent studies by Djenidi et al. (1989) and Liandrat et al. (1990) have shown from a combined experimental and numerical investigation of a laminar boundary layer over riblets that viscous effects are very important in drag reduction. In particular, the velocity field reorganisation within a rib is such that the balance between the increase of wall velocity gradients in the crest vicinity and their strong reduction within the groove with respect to the gradient over a flat plate is compensating the very large wetted area enhancement (more than 100 % for V-grooves with $s \approx h$) : a weak drag reduction of about 2 % can even be obtained.

Spatially resolved velocity measurements in the close vicinity of a ribbed wall are quite difficult owing to the tiny size of riblets suitable for wind-tunnel investigations so that very few data are available. Hooshmand et al. (1983) have found that the mean streamwise velocity over the crest plane varies periodically in the spanwise direction with the wavelength of the riblets, and that this periodicity almost completely disappears at $y^+ \approx 13$ (y is the normal to the wall distance relative to the crest plane). Nevertheless, when the overall mean velocity profile is plotted logarithmically, several authors have found an upward shift suggesting an increase of viscous sublayer thickness similar to drag-reducing polymers. This result is clearly evidenced by the visualisations of Clark (1990). It is also similar to the shift of the velocity profile origin towards a location that lies somewhat below the tips of the ridges indicated by the calculations of Bechert and Bartenwerfer (1989) and named "protrusion height".

As far as we know, the only quantitative measurements within a large triangular groove are those by Vukoslavcevic et al. (1987). They measured the mean U and fluctuating u streamwise velocity field with the hot wire anemometry technique : the local wall shear stress varies greatly in the spanwise direction and u' ($= \sqrt{\overline{u^2}}$) is nearly zero below the midpoint of the groove. But, in particular, no information is given about the spanwise mean W and fluctuating w velocities, which are both of prime importance. The former one - W - to know whether the assumption $W \approx 0$ - which was shown to be valid for the laminar case (Djenidi, 1989) - can be made in numerical predictions, and the latter one - w - to determine to what extent the flow is stabilized by longitudinal grooves.

The present paper is concerned with experimental results relative to U, u', W, w' as well as the correlation $\overline{uw}$ extending within the riblets obtained by laser-Doppler anemometry. Modelisations based on the concept of a mixing length, assuming that the spanwise mean velocity is equal to zero, are also performed.

EXPERIMENTAL CONDITIONS

Experiments are carried out in the IMST water tunnel (20 x 20 x 120 cm³). On one of the side walls of the vertical working section three dimensional roughness elements have been placed in order to trip the boundary layer (Antonia et al., 1988). With the centreline mean velocity U_e about 9 cm/s, a fully

developed turbulent boundary layer is obtained at the downstream distance X = 430mm from the trip where is located the riblet wall (190 x 280 mm^2) At this station, the friction velocity u^* is about 0 5 cm/s, the boundary layer thickness δ is 32 mm and the momentum thickness Reynolds number R is about 300 Very good agreement with the classic Van Driest law is observed in the boundary layer inner region and especially in the region very close to the wall. Nevertheless, the law of the wall is only extending over a quite narrow zone owing to the low value of the Reynolds number. In the external zone, the wake law is almost nonexisting since turbulence is tripped with large roughnesses In addition, in the viscous sublayer, the distribution of u'/u^* is the same as that usually obtained in larger Reynolds number flows (see Antonia et al., 1988). However, further away from the wall, turbulence intensities u'/U_e and w'/U_e are larger than those of natural boundary layers and their peaks are located at a greater distance from the wall : this is probably related to a quite large outer turbulence level and to the use of quite big roughnesses

Large triangular grooves ($s = 2h = 7$ mm, $h^+ \approx 15$) are considered in order to perform velocity measurements extending within the riblets These riblets are machined in a stainless steel plate and polished. Crests are flush with the upstream and downstream smooth plates. All measurements relative to the riblet wall are performed at the station X = 700 mm = 20δ just before the ribbed plate trailing edge.

Velocity components in the streamwise and spanwise directions are inferred from data obtained with a one component LDA system (He - Ne, 15 mW) fitted with a Bragg cell and a Burst Spectrum Analyser. The backscatter technique is used and the measuring volume is 0.12 x 1.3 x 0.12 mm^3. At each position, measurements are performed for three beam inclinations in order to determine U, W, u', w' and $\overline{uw}$.

NUMERICAL PROCEDURE

The numerical simulations over riblets are performed using the Reynolds averaged equations. The flow is assumed incompressible and statistically steady. As a first step, calculations presented herein are carried out with the assumption that the spanwise mean velocity W is equal to zero. In the laminar regime we have shown both experimentally and numerically (Djenidi et al., 1987) that W is actually equal to zero even within the grooves which is in good agreement with Khan's calculations (1986). However, the latter numerical study has also pointed out that, when the flow is turbulent, W differs from zero : this result seems consistent with data (not presented herein) obtained in our experimental study despite the difficulty of such measurements. Classical boundary layer approximations are applied, and the pressure gradient term is considered as a prescribed quantity ($dP/dx = 0$ herein) Thus, the governing equations are given, in their conservative form, by

$$\partial(UU)/\partial x + \partial(UV)/\partial y = -1/\rho\, dP/dx + \partial(\nu\partial U/\partial y - \overline{uv})/\partial y + \partial(\nu\partial U/\partial z - \overline{uw})/\partial z \quad (1)$$

$$W = 0 \quad (2)$$

$$\partial U/\partial x + \partial V/\partial y = 0 \quad (3)$$

where ρ is density.
The boundary conditions are :

$U=V=0$ at the wall,
$U=U_e$ at the upper boundary of the calculation domain,
$\partial U/\partial z = \partial V/\partial z = 0$ at the lateral boundaries

Only one groove is considered in these numerical predictions and it is thus assumed that the adjacent ribs do not influence the flow over this groove this hypothesis is obviously valid inside the riblet and in the outer part of the boundary layer, but it is doubtful in the vicinity of the crest plane This objection is all the more justified since the length scale λ characteristic of the spanwise organization of the near wall coherent structures -which are playing an important role in the dynamics of the motion in this region- is several times larger than the rib spacing ($s^+ \approx 30$, $\lambda^+ \approx 100$) and since it seems that the influence of riblets on these structures might be significant (Choi, 1989).

The parabolic feature of equation (1) is amenable to a forward marching procedure such as that presented by Cousteix et al. (1985). The computation is then carried on step by step in the x direction. At each x station, this equation is solved -using the known upstream values to estimate the advection terms- and V is then deduced from the continuity equation (3) Finally, a finite volume discretization of equation (1) provides a system of equations that is solved using the Modified Strongly Implicit algorithm developed by Schneider and Zedan (1981). The computational domain is presented on figure 1. The grid is divided in two sets : the first one, covering the groove, is such that the meshes are regularly spaced along the y and z directions ; in the second set, above the rib, the mesh repartition along z is the same as the previous one whereas that along y is following a geometrical progression. As it has been shown in the previous study relative to the laminar regime (Llandrat et al , 1990), the evaluation of the crest velocity gradient is very crucial and a systematic study of the grid refinement is necessary to ensure calculation convergence : the first step over the crest plane has been chosen less than 10^{-3} wall units The number of grid points is 81 x 29 (relative to y and z respectively)

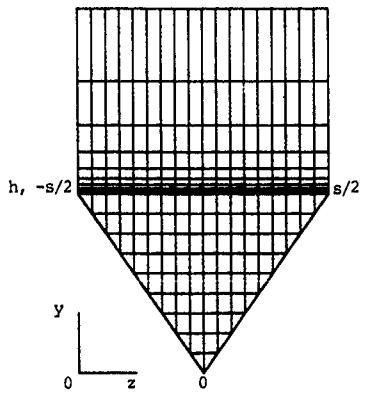

Fig.1. Computation mesh grid

The calculation is initialized with the experimental velocity profile ($U/U_e = f(y/\delta)$) obtained just upstream the riblet plate. It is run over a smooth wall until the longitudinal evolution of skin friction coefficient Cf satisfies the usual law ($Cf = 0.06\ Re^{-0.2}$, with Re the Reynolds number based on streamwise distance x). When this condition is verified, the corresponding velocity profile is considered as the reference profile used to initialize computations on the riblet. In fact, when the experimental Reynolds number R = 300 is used, the computed velocity profiles do not retain turbulent features and it has been decided to work with R=1000 the resulting reference profile somewhat differs from the experimental one.

Turbulence closure models have been derived using Boussinesq hypothesis to estimate $\overline{UV}$ and $\overline{UW}$ in equation (1). The eddy viscosity is computed from a mixing length model propounded by Cebeci and Smith (see Cousteix, 1988). In the inner region ($y/\delta \leq 0.15$), ν_t is given by $\nu_t = \chi^2 d^2 (1-e^{-d/A})^2 \partial U/\partial n$ where χ (=.41) is the Karmann constant, d a local length to be defined later, $A = 26\ \nu\ (\tau_w/\rho)^{-.5}$ (with τ_w wall friction stress) and $\partial U/\partial n$ is the velocity gradient normal to the wall. In the outer region, ν_t is calculated from $\nu_{te} = 0.0168\ U_e \delta_1\ (1+5.5(d/\delta)^6)^{-1}$ where δ_1 is the displacement thickness. The connection between these two regions is obtained, for $y/\delta > 0.15$, by $\nu_t = \nu_{te}(1-e^{-\nu_{ti}/\nu_{te}})$. On the flat plate, d = y is the distance from the wall. Over the V groove, two models have been used to estimate d. The first one is deduced from Buleev (1963) who studied the flow in a square pipe. The computational domain is divided in two parts D_1 and D_2. In D_1, d is defined by $1/d = .5\ (1/d_1+1/d_2)$, whereas in D_2, d is the distance PH, where H belongs to the fictive wall built from the borderline AO'B using the previous relationship. In the

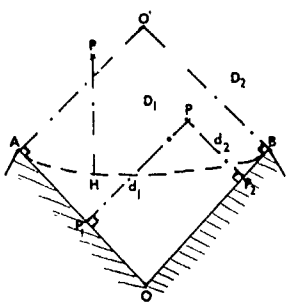

second model, d is obtained from the conformal mapping relating the flat plate to the triangular groove (Bechert and Bartenwerfer, 1989) presented on figure 2 . transversal lines correspond to iso-d-lines. Thus, d is estimated from the grid presented on figure 2b and equation (1) is solved using the grid shown on figure 1

RESULTS AND DISCUSSION

Mean longitudinal velocity profiles obtained at various spanwise positions z/s (X = 700 mm = 20δ), within and over a groove, are shown on figure 3. The y_1 distance is the separation along the direction normal to the crest plane between the considered point and the wall. Generally speaking, it is found that, with respect to the smooth wall, the velocity gradient over the crest

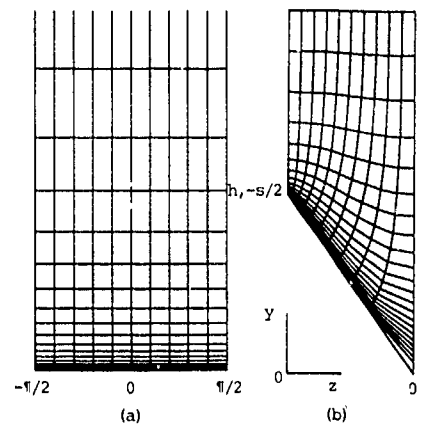

Fig.2. Grids used for determining the distance to the wall d involved in the mixing length model
(a) Initial cartesian grid
(b) Curvilinear grid deduced from conformal mapping

is enhanced by about 100 % whereas, over most of the rib, gradients are weakened ; this is especially apparent over the trough where friction is almost zero This is similar to what had been previously observed for both the laminar regime (Djenidi et al., 1989) and the turbulent one (Vukoslavcevic et al., 1987). The spanwise position at which the velocity profile is the same as that over the flat plate is z/s about 0.1 This is in very good agreement with the conformal mapping analysis showing the distance d, involved in the eddy viscosity, is the same as that over the smooth plate for z/s = 0.1. Concerning numerical predictions, it appears that the two models give almost identical profiles, so that only results computed with the first model will be presented later on. But, though experimental and numerical velocity profiles are very similar over the crest, they differ noticeably within the groove These discrepancies might result from the use of the mixing length model -but this kind of model is usually efficient in describing wall flows-, or from the Reynolds number which retains significantly different values for experiments and calculations- but this would probably induce more differencies over the crest than over the trough unlike what is actually observed. It seems more reasonable to think that the assumption W = 0 is the main cause, especially since this is not verified experimentally : there would exist two counter-rotating vortices, one of them sitting on each side of the trough. Even very low W values -with respect to U- may result in significant contributions from the $W\partial U/\partial z$ term which could not be neglected anymore in equation (1)

Indeed, figure 4 shows that spanwise U variations are significant in the region close to the crest plane, and that $|\partial U/\partial z|$ is about one third of $\partial U/\partial y$ at the place where it is greatest (z/s = 0.2 and 0.8) : thus, there may exist positions where $W\partial U/\partial z$ could even be larger than $V\partial U/\partial y$. Moreover, these velocity distributions are in very good agreement with Hooshmand et al.'s (1983) experiments pointing out the rapid dumping of spanwise U variations when moving away from the crest plane. The magnitudes of variations deduced

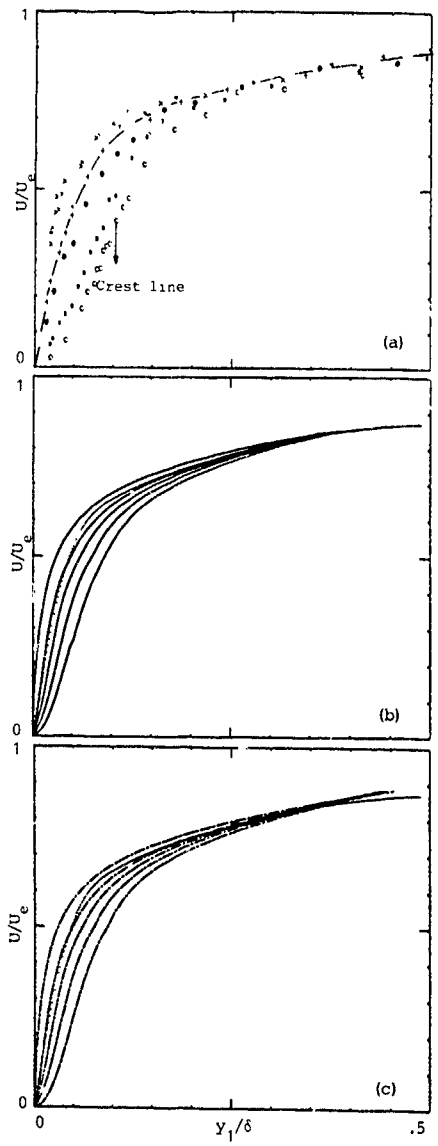

Fig.3. Longitudinal mean velocity profiles over and within riblets.
a) Experiments : X/δ = 20, U_e =9 cm/s, s=2h=7mm ; •:z/s=0 (peak), +:z/s=0.14, ● : z/s=0 25, ■ : z/s = 0.36, o. z/s =0.50 (trough), x:z/s=1 (peak), – –:smooth plate.
(b) Computations with the first model (same z/s as (a)).
(c) Computations with the second model (same z/s as (a)) ; ..... : smooth plate (for computations).

from experiments and from computations are quite similar, though the distribution obtained experimentally at the position closer to the crest plane does not exhibit the quite flat plateau extending over about one third of the groove which is present in the three other profiles. In addition, the ∂U/∂z evolutions resulting from these distributions are completely consistent with the $\overline{uw}$ profiles presented on figure 5 (at 0.05 δ from the crest plane) and the Boussinesq hypothesis, $\overline{uw} = -\nu_t\, \partial U/\partial z$, despite the difficulty of $\overline{uw}$ measurements close to a wall with a one component laser-Doppler velocimeter : this result clearly supports the validity of the mixing length model used in our computations. It is worth mentioning that the lines drawn on figures 4 and 5 are not best fits of experimental points but they rather represent average curves insuring the coherence between these results and the Boussinesq hypothesis. In addition, on figure 4, for the distance y = 0.05 δ, the relative positions of experimental and numerical curves for various z/s locations are not consistent with velocity profiles reported on figures 3a and 3b : since, at this distance y, the velocity gradients along the direction normal to the crest plane are very strong, a small error on the experimental estimation of y could both explain why velocities are not equal on the crests and why the experimental velocity is not smaller than the numerical one over the trough.

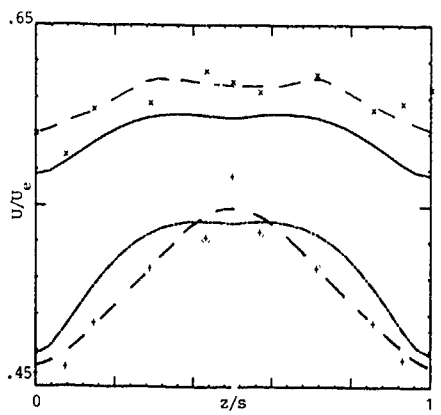

Fig.4. Spanwise distributions of longitudinal mean velocity over riblets.
-x- : y = 1.75 mm = 0.05δ ; -+- : y = 1.50 mm = 0.04δ ; —, –.– : computations.

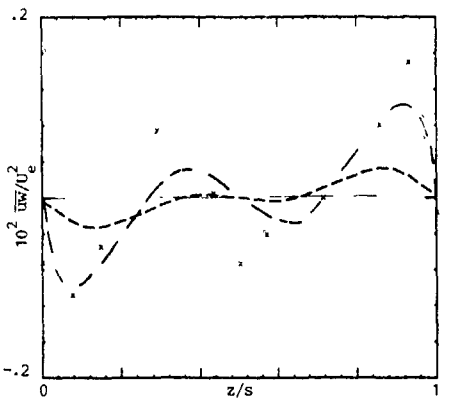

Fig.5 Spanwise distribution of Reynolds shear stress $\overline{uw}$ over riblets
y = 1.75 mm = 0.05δ , —x— experiments ,
-- computations

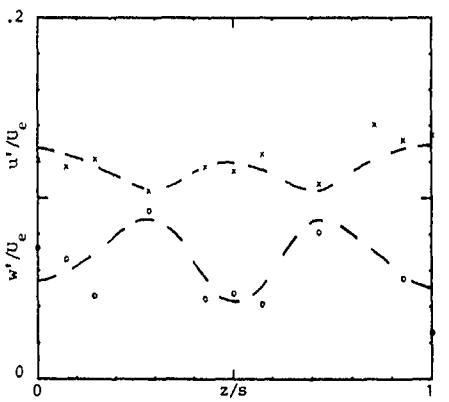

Fig.6. Spanwise distribution of standard deviations over riblets
y = 1.75 mm = 0.05δ ; x : u', o : w'

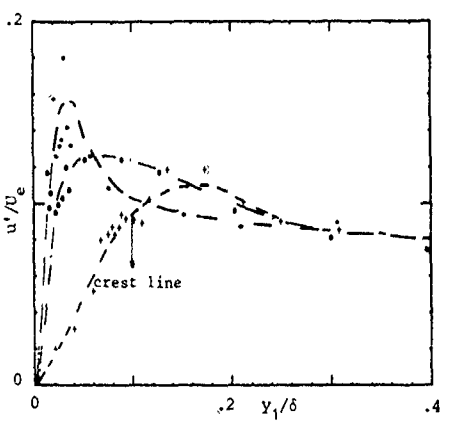

Fig.7. Standard deviation of longitudinal velocity fluctuations over and within riblets.
*, peak, + trough, ● : smooth plate.

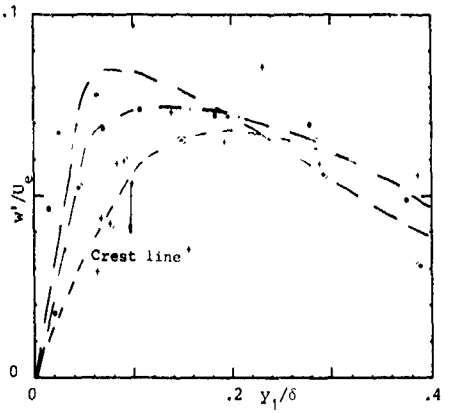

Fig.8. Standard deviation of spanwise velocity fluctuations over and within riblets.
*, peak, + trough, ● : smooth plate.

The spanwise variations of velocity standard deviations u'/U_e and w'/U_e obtained experimentally at the same distance from the crest plane are shown on figure 6 : there seems to be a minimum for u'/U_e and a maximum for w'/U_e at the same spanwise position z/s = 0.3 (and 0.7 as well), where is located the crossover of $\overline{uw}$. It is interesting to notice that these locations are also those where $|\overline{uw}|$ is greatest (not presented herein) : this is the place where the counter-rotating vortices have the most important contribution to the spanwise velocity characteristics. It is also worth mentioning that the numerical $\overline{uw}$ distribution (figure 5) exhibits the same behaviour as the experimental one -but with a significantly lower level- though these computations are based on the assumption W = 0, so that it is reasonable to think that these vortices are enhancing the correlation $|\overline{uw}|$. The corresponding correlation coefficient obtained experimentally (not presented herein) presents exactly the same feature as that of the correlation $\overline{uw}$, and its maximum value is about 0.2.

Figures 7 and 8 give longitudinal and spanwise standard deviations, u'/U_e and w'/U_e respectively, as a function of the actual distance to the wall y_1/δ, measured straight over the peak and straight over the trough extending within the groove. These profiles are compared with that determined over the smooth wall just downstream the riblet wall (X = 730 mm = 21 δ) which is practically identical with the upstream one (X = 420 mm = 13 δ). One observes quite large turbulence reduction in the trough vicinity and significant increase close to the peak. Nevertheless, one could imagine that, since mean velocities U are very small within the grooves, turbulence intensities u'/U and w'/U are strong close to the wall, in the trough vicinity. But it appears (not presented here) that the u'/U and w'/U profiles determined over the peak and over the trough are almost the same as the smooth wall one. This result supports the concept of flow stabilisation by riblets and strengthens the argument relative to the relevance of viscous effects in the mechanism of turbulent drag reduction by riblets.

CONCLUSION

In spite of the large wetted area increase there may exist a turbulent drag reduction resulting from the new velocity distribution within riblets since it appears that, over most of a groove, friction is much lower than on the smooth wall. A similar effect has been obtained in laminar flow but detailed mechanism concerning the mean velocity field is somewhat different since, in the turbulent regime, on one hand, over the crests the relative friction enhacement is smaller and, on the other hand, over the trough the friction reduction is also weaker : this seems to be related to turbulent mixing tending to smooth velocity gradients. In addition, the existence of two counter-rotating vortices relative to each groove-which are not present in the laminar regime- is also an important feature to be studied more thoroughly to explain the observed stabilisation of the turbulent flow. Moreover it is necessary to take into account in numerical computations the existence of these vortices which are inducing non zero mean spanwise velocity. It is also crucial to investigate experimentally v' and the shear stress $\overline{uv}$ in order to better understand the influence of riblets on the structure of turbulence and to improve modelling

ACKNOWLEDGEMENTS

This work is supported under a "Service Technique des Programmes Aéronautiques" grant. We are grateful to M. Astier for his technical assistance. Thanks are also due to Drs J. Cousteix and E. Coustols (ONERA-CERT).

REFERENCES

ANTONIA, R.A., FULACHIER, L., KRISHNAMOORTHY, L.V., BENABID, T. & ANSELMET, F. 1988 Influence of wall suction on the organized motion in a turbulent boundary layer J. Fluid Mech. 190, 217-240

BECHERT, D.W & BARTENWERFER, M. 1989 The viscous flow on surfaces with longitudinal ribs J. Fluid Mech. 206, 105-129.

BULEEV, N.I. 1963 Theoretical model of the mechanism of turbulent exchange in fluid flows, AERE trans. 957, Harwell, 1-39.

BUSHNELL, D.M. 1985 Turbulent drag reduction for external flows. AGARD Rep. 723, 5,1-5.26.

CHOI, K.S. 1989 Near-wall structure of a turbulent boundary layer with riblets. J. Fluid Mech 208, 417-458.

CLARK, D.G. 1990 Boundary layer flow visualization patterns on a riblet surface. In Turb. Control by Pass. Means, ed Coustols, E., Kluwer Acad. Press, 79-96.

COUSTEIX, J. 1988 Aérodynamique en fluide visqueux, cours E.N.S.A.E. Toulouse

COUSTEIX, J., de SAINT-VICTOR, X. & HOUDEVILLE, R. 1985 X - marching methods to solve the Navier Stokes equations in two and three - dimensional flows in proc. 3rd Symp. on Num. Phys. Aspects of Aerod. Flows, Long Beach, California.

COUSTOLS, E. 1989 Behaviour of internal manipulators-riblets models in subsonic and transonic flows AIAA Paper n° 89-0963, 1-14

DJENIDI, L. 1989 Contribution à l'étude de couches limites sur parois rainurées Ph. D. Thesis, I.M.S.T., Univ. d'Aix-Marseille II.

DJENIDI, L., ANSELMET, F. & FULACHIER, L. 1987 Influence of a riblet wall on boundary layers in proc. Turb. Drag Red. by Pass. Means Conf., Royal Aeron. Society, London, 310-329

DJENIDI, L., LIANDRAT, J., ANSELMET, F. & FULACHIER, L. 1989 Viscous effects in drag reduction over riblets in Drag Red. in Fluid Flows, eds. Sellin, R.H.J. & Moses, R.T., Ellis Horwood Publ., 35-41.

HOOSHMAND, D., YOUNGS, R., WALLACE, J.M. & BALINT, J.L. 1983 An experimental study of changes in the structure of a turbulent boundary layer due to surface geometry changes. AIAA Paper n° 83-0230, 1-10

KHAN, M.M.S. 1986 A numerical investigation of the drag reduction by riblets surface. AIAA Paper n° 86-1127, 1-11.

LIANDRAT, J., COUSTOLS, E., DJENIDI, L., ANSELMET, F., de SAINT-VICTOR, X., FIOC, F. & FULACHIER, L. 1990 Effect of riblets on either fully developed boundary layers or internal flows in laminar regime in Turb. Control by Pass. Means, ed. Coustols, E., Kluwer Acad. Press., 141-157.

SCHNEIDER, G.E. & ZEDAN, M. 1981 A modified strongly implicit procedure for the numerical solution of field problems. Num. Heat Transfer 4, 1-19.

SQUIRE, L.C. & SAVILL, A.M. 1987 Some experiences of riblets at transonic speeds in proc. Turb. Drag Red. by Pass. Means Conf., Royal Aeron. Society, London, 392-407.

VUKOSLAVCEVIC, P., WALLACE, J.M. & BALINT, J.L. 1987 On the mechanism of viscous drag reduction using streamwise aligned riblets : a review with some new results in proc. Turb. Drag Red. by Pass. Means Conf., Royal Aeron. Society, London, 290-309.

WALSH, M.J. & LINDEMANN, A.M. 1984 Optimization and application of riblets for turbulent drag reduction AIAA Paper n° 84-0347, 1-10.